Digitized by the Internet Archive
in 2024

https://archive.org/details/physica-scripta_1955_9

QC
1
S923

634

ARKIV FÖR FYSIK

UTGIVET AV

K. SVENSKA VETENSKAPSAKADEMIEN

Band 9

Med 36 avhandlingar

STOCKHOLM
ALMQVIST & WIKSELLS BOKTRYCKERI AB

LONDON
H. K. LEWIS & CO., LTD
136, GOWER STREET

1955

PARIS
LIBRAIRIE C. KLINCKSIECK
11 RUE DE LILLE

NIONDE BANDETS INNEHÅLL

Sid.

1. Hertz, C. H., Der Einfluss isolierender Schichten auf den Koronastrom und die Durchschlagspannung von Funkenstrecken . . . . 1—28
2. Hertz, C. H., Die Einwirkung von Lackschichten auf die Wechselstromkorona an Spitzen und Drähten . . . . 29—37
3. Ahnlund, K., Proton groups from deuteron bombardment of Ne^{20} by magnetic analysis. Part II . . . . 39—40
4. Mladjenović, M., and Slätis, H., Auger transitions in Bi^{212} (ThC) . . . 41—47
5. Ekspong, G., On multiple scattering measurements in nuclear research emulsions . . . . 49—75
6. Siksna, R., Two different breakdowns between a positive electrode with small curvature and a plane . . . . 77—82
7. Siksna, R., Some peculiarities of the current-potential characteristics of positive corona discharge . . . . 83—91
8. Fröman, P. O., Concerning the statistical calculation of cohesive energies of ionic crystals . . . . 93—99
9. Brogren, G., Bromine-quenched and iodine-quenched Geiger-Müller counters . . . . 101—105
10. Thulin, S., Studies in nuclear spectroscopy with electromagnetically separated gaseous isotopes. I . . . . 107—136
11. Thulin, S., Studies in nuclea rspectroscopy with electromagnetically separated gaseous isotopes. II . . . . 137—196
12. Ingelstam, E., Measurements of optical path gradients by means of birefringence interferences. Part I. General and approximately linear gradients. Part II. Liquid gradients, in particular determination of diffussion constants . . . . 197—226
13. Huldt, L., und Lagerqvist, A., Termschemata von CaO, SrO und und BaO 227—228
14. Grabe, B., A theoretical study of the coloured alkali oxides . . . . . . 229—243
15. Hultberg, S., An investigation of the longitudinal angular distribution of photoelectrons at gamma ray energies of 0.41, 0.66 and 1.33 Mev . . . 245—280
16. Eriksson, T, and Swiatecki, W. J., Polarization of neutrons in high energy scattering . . . . 281—285
17. Brogren, G. On line width determinations with bent crystal spectrometers 287—292
18. Larsson, K.-E., The use of the ^{3}T (d, n) ^{4}He reaction for a comparison of some methods for the absolute measurements of a fast neutron flux. The yield of a Ra-α-Be source . . . . 293—333
    Erratum . . . . 603—604
19. Sato, M., The weakening effect on paraffin and waxes with its application for determining their surface tensions in solid state . . . . 335—339
20. Erlandsson, G., Microwave spectrum of cyclopentene oxide . . . . . . 341—343
21. Kleman, B., and Liljeqvist, B., On the band spectrum of CrH . . . . 345—347
22. Brogren, G. and Nordling, C., The anomalous X-ray transmission through a crystal on both sides of the K absorption edge of an element in the crystal . . . . 349—351

Sid.

23. Ekspong, G., A note on mean life-time determinations on small samples of radioactive nuclei . . . . 353—355
24. Flodmark, S., A quantum theoretical study of the covalent boron-boron bonds in crystals of some metal borides . . . . 357—376
25. Kleman, B. and Liljeqvist, B., Emission spectra in the near infra-red . 377—383
26. Kleman B. and Lindqvist, S., The band spectrum of the Ag_2 molecule . 385—390
27. Anzelius, A., Two flow problems in a viscous fluid . . . . 391—398
28. Erlandsson, G., A microwave spectrometer and its applications to some organic molecules . . . . 399—434
29. Lundqvist, S. O., On the limiting vibrational frequencies of a cubic ionic lattice . . . . 435—455
30. Bockasten, K., A study of C III by means of a sliding vacuum spark . . 457—481
31. Risberg, P., The spectrum of singly-ionized magnesium, Mg II . . . . 483—494
32. Beckman, O., Relative intensities of the X-ray K lines of heavier elements 495—529
33. Ekspong, A. G., Energy loss of fast electrons. An investigation into the absolute total cross-section for Bremsstrahlung in nuclear research emulsions . . . . 531—554
34. Siksna, R., Photographs of the light phenomena of positive corona . . . 555—560
35. Johansson, S. A. E., The RaC-RaC′ decay . . . . 561—569
36. Pauli, R. T., Low energy levels in N^{16} . . . . 571—601
Erratum 602

ARKIV FÖR FYSIK Band 9 nr 1

Mitgeteilt am 2. Juni 1954 durch MANNE SIEGBAHN und BENGT EDLÉN

Der Einfluss isolierender Schichten auf den Koronastrom und die Durchschlagspannung von Funkenstrecken

von C. H. HERTZ

Mit 21 Abbildungen im Text

I. Einleitung

Wird an eine leitende Spitze, z.B. eine Nadel, eine genügend hohe Spannung gelegt, so erhält man in Luft bei Atmosphärendruck an der Spitze eine sogenannte Korona oder Spitzenentladung. Diese Gasentladungsform ist von verschiedenster Seite untersucht worden [1, 2]. Von LOEB und Mitarbeitern wurde speziell das Verhalten der Koronaentladung für den Fall, wo die Spitze einer ebenen Metallplatte gegenüber steht, unter den verschiedensten Verhältnissen studiert, wobei Gasart und Gasdruck, Polarität der Spitze, Spitzenform usw. variiert wurden. Einen Übersichtsartikel über diese Arbeiten hat LOEB [3] gegeben.

In der hier vorliegenden Arbeit werden zunächst die Resultate beschrieben, die man erhält, wenn man in der Spitzen-Plattenanordnung die Metallplatte mit gewissen dünnen isolierenden Schichten, z.B. einer Schellackschicht, überzieht. Eine kurze Zusammenfassung preliminärer Ergebnisse für diesen Fall ist bereits gegeben worden [4]. Die mit einer Lackschicht erhaltenen Strom-Spannungskennlinien weichen bei positiver und bei negativer Spitze von den mit metallischer Plattenelektrode erhaltenen stark ab, und ausserdem tritt der Funkendurchschlag zwischen Spitze und lackierter Platte in vielen Fällen bei wesentlich geringeren Spannungen ein.

Im folgenden soll zunächst an Hand eines typischen Falles die Einwirkung einer Lackschicht als solche beschrieben und die Erklärung der gefundenen Erscheinung gegeben werden.

II. Einfluss eines Lacküberzuges auf der Plattenelektrode auf die Strom-Spannungskennlinie der Koronaentladung

Über einer grossen ebenen Metallplatte, die über ein Amperemeter mit dem geerdeten positiven Pol einer Spannungsquelle verbunden ist, befinde sich im Abstand von 7,5 cm eine leitende Spitze. Die Spitze, welche mit dem negativen Pol der Spannungsquelle in Verbindung steht, bestehe aus einem 0,3 mm dicken Platindraht. Die Anordnung befindet sich in Luft von Atmosphärendruck und 30 % relativer Feuchtigkeit. Erhöht man nun kontinuierlich die Spannung an der Spitze, so kann oberhalb einer Spitzenspannung von ca. 10 kV eine kleine Gasentladung (Korona) an der Spitze beobachtet werden, wobei gleichzeitig ein Strom durch das Amperemeter

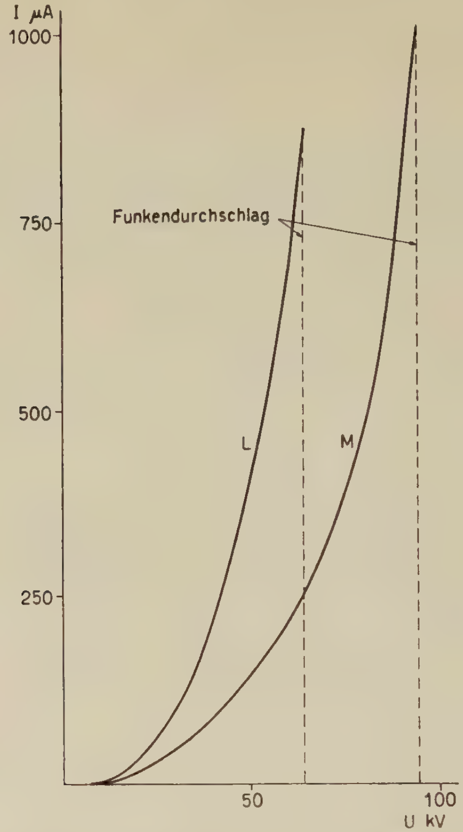

Abb. 1. Strom-Spannungskennlinie einer Spitzenkorona gegen eine Plattenelektrode. Kurve *M* ohne Lackschicht auf der Plattenelektrode, Kurve *L* mit Lackschicht auf der Plattenelektrode. Spitzenabstand 7,5 cm.

angezeigt wird. Die bekannte Abhängigkeit des Stromes von der Spannung zeigt die Kurve *M* in Abb. 1. Bei einer Spannung von 94 kV tritt schliesslich der Funkendurchschlag ein.

Ist nun die metallische Plattenanode mit einer dünnen Schellackschicht bedeckt, so erhält man eine Strom-Spannungskennlinie wie sie die Kurve *L* der Abb. 1 zeigt. Man sieht deutlich, dass der Koronastrom im letzteren Falle bei gleicher Spannung wesentlich grösser ist, wenn die Plattenelektrode mit einer Schellackschicht bedeckt ist. Weiterhin tritt der Funkenüberschlag bei einer wesentlich geringeren Spannung ein.

Diese etwas unerwartete Einwirkung einer isolierenden Lackschicht auf den Koronastrom ist ziemlich unabhängig vom Abstande Spitze – Plattenelektrode und tritt ebenfalls, wenn auch nicht ganz so ausgeprägt, bei positiver Spitze auf. Ähnliche Einwirkungen isolierender Materialien in der Nähe von Hochspannungsgasentladungen sind schon von anderer Seite beobachtet worden [5, 6, 7, 8], jedoch fehlte bisher eine Erklärung des starken Ansteigens des Koronastromes in diesen Fällen. Im

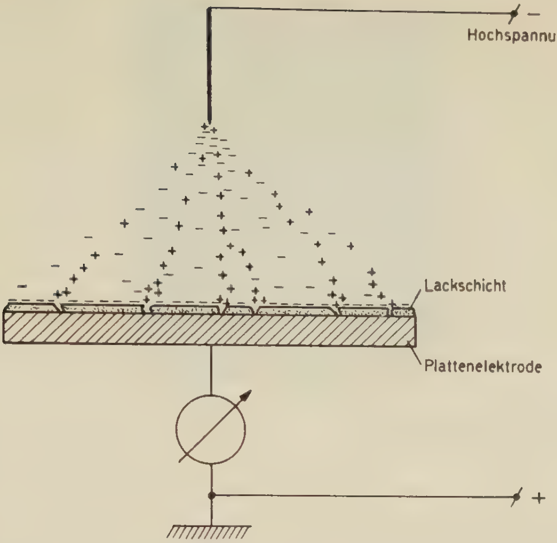

Abb. 2. Zur Deutung des Lackschichteffektes. In den Poren der Lackschicht L entstehen wegen der hohen Aufladung der Lackschichtoberfläche neue Ionisationsbereiche.

Folgenden soll nun erst die Erklärung dieser Erscheinung gegeben und danach die Versuchsresultate, die zu dieser Erklärung geführt haben, geschildert werden.

1. Erklärung des Lackschichteffektes

Legt man in der oben beschriebenen Anordnung die negative Spannung plötzlich an die Spitze, so wird die isolierende Schicht über der Plattenelektrode durch die von der Spitze kommenden negativen Ionen oder Elektronen in kurzer Zeit negativ aufgeladen. Diese Ladung kann auf Grund der isolierenden Eigenschaften der Schicht nicht von deren Oberfläche verschwinden und man sollte deshalb ein sofortiges Erlöschen der Koronaentladung an der Spitze erwarten. Dies tritt auch bei der Verwendung idealer isolierender Schichten ein.

Nimmt man nun aber an, dass die verwendete Schellackschicht feine Löcher oder Poren besitzt (vgl. Abb. 2), welche die Lackschicht in beliebiger Weise zur Metallplatte hin durchlaufen [9, 10], so werden in diesen Poren auf Grund der hohen Aufladung der dünnen Lackschicht grosse Feldstärken entstehen. Negative Ionen oder Elektronen, die von der Spitze kommend in diese feinen Poren eintreten, werden hier so kräftig beschleunigt, dass sie das Gas in den Poren ionisieren können. Die hierbei entstehenden positiven Ionen treten aus den Poren aus und wandern auf die Spitze zu. Diese zusätzlichen Ionisationsbereiche erhöhen erklärlicherweise den Koronastrom, da nun nicht nur negative Ionen von der Spitze zur Plattenelektrode, sondern auch positive Ionen in umgekehrter Richtung laufen. Da sich auf diese Weise der auf der Spitze einfallende Ionenstrom um die aus den Ionisationsbereichen in den Poren der Lackschicht kommenden Ionen erhöht, steigt auch die Anzahl der durch Ionenstoss aus der Spitze befreiten Elektronen, was ebenfalls zur Erhöhung des Koronastromes beiträgt. Schliesslich vermindern die von der Plattenelektrode

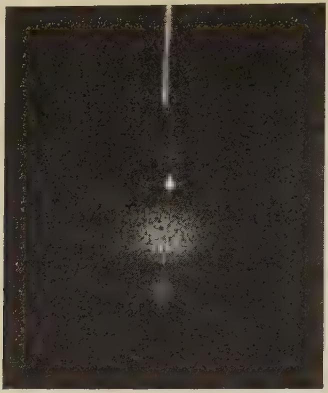

Abb. 3. Spitzenkorona über Lackschicht, schräg von oben gesehen. Spitzenabstand 5 mm, Spitzenspannung — 5000 V, Strom 200 μA.

kommenden positiven Ionen die negative Raumladung vor der Spitze, was zu einer nicht unwesentlichen Erhöhung des Spitzenfeldes führen kann.

Ist die Spannung der Spitze positiv, so tritt ein ähnlicher Vorgang ein. Der Effekt ist in diesem Falle jedoch nicht so ausgeprägt, da Elektronenbefreiung durch Ionenstoss an der Spitze nicht stattfinden kann. Es wird jedoch weiter unten gezeigt, dass dann ein ähnlicher Prozess in den Poren der Lackschicht an der Plattenelektrode auftritt. Praktisch können jedoch alle die im Folgenden beschriebenen Versuche zur Bestätigung der hier vorgeschlagenen Erklärung des Lackschichteffektes mit positiver sowie mit negativer Spitze durchgeführt werden.

Es sollte vielleicht an dieser Stelle darauf hingewiesen werden, dass es sich hierbei um einen anderen Effekt als den von PAETOW [11] beschriebenen handelt, da der Paetoweffekt auf Feldemission von Elektronen zurückgeführt wird. Diese Erklärung kann eventuell für den Fall einer positiven Spitze teilweise herangezogen werden, für den Fall der negativen Spitze ist sie nicht anwendbar, da ja hier positive Ionen aus den Poren der Schicht austreten.

2. Experimentelle Bestätigung der Theorie

Im Folgenden sollen einige der Experimente beschrieben werden, die zu der oben gegebenen Erklärung der Einwirkung einer Lackschicht auf den Koronastrom geführt haben. Soweit nicht ausdrücklich anders angegeben, sind alle Versuche in Luft von Atmosphärendruck, Zimmertemperatur und 30–50 % relativer Feuchtigkeit ausgeführt worden.

Die Abb. 3 zeigt schräg von oben das Aussehen der mit einer Lackschicht bestrichenen Plattenelektrode. Die negative Spitze ist direkt darüber sichtbar. Neben der deutlich leuchtenden Koronaentladung an der Spitze sieht man im Dunkeln eine grosse Menge leuchtender Punkte auf der Lackschicht, welche bei Verwendung einer unlackierten Plattenelektrode nicht auftreten. Jeder dieser leuchtenden Punkte wird nun als die Mündung einer Pore in der Lackschicht gedeutet, da, falls in diesen Poren Ionisation des Gases stattfindet, auch Anregung der Gasatome durch Elektronenstoss vorkommen muss. Deshalb muss die Mündung jeder Pore durch das hierbei erzeugte Licht sichtbar werden.

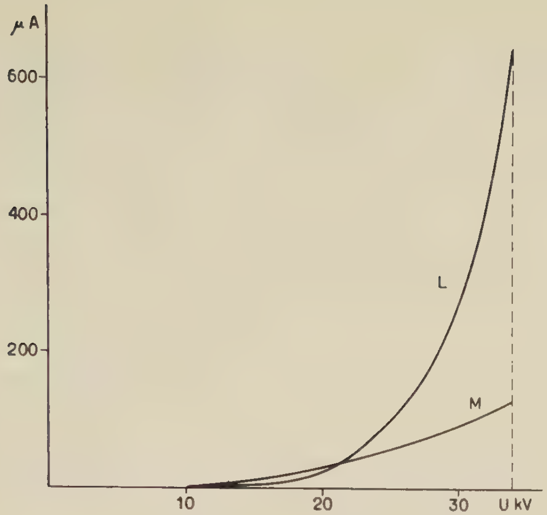

Abb. 4. Zur Untersuchung des Lackschichteffektes (vgl. Text).

Diese Deutung lässt sich auf folgende Weise leicht bestätigen. Legt man ein genügend dickes Papier oder gewisse Plastfolien (z. B. Pliofilm oder Alkathen) auf die unlackierte Plattenelektrode, so erlischt die Koronaentladung ganz und der Koronastrom geht auf Null zurück. Dies ist zu erwarten, da sich die Oberfläche des Papieres so lange auflädt, bis die Feldstärke an der Spitze nicht mehr zur Aufrechterhaltung einer Koronaentladung ausreicht. Die starke Aufladung der Papieroberfläche bewirkt fernerhin, dass das Papier an die Plattenelektrode angepresst wird.

Sind nun in das Papier vorher einige feine Löcher mit einer Nähnadel gestochen worden, so fliesst wieder ein kräftiger Koronastrom. Gleichzeitig beobachtet man in jedem Loch deutlich eine leuchtende Gasentladung (Abb. 8), deren Aussehen ganz den in den Poren der Lackschicht gefundenen Gasentladungen entspricht. Auch in diesem Falle bemerkt man eine Anpressung des Papieres auf der Plattenelektrode, welches wieder von den auf der Papieroberfläche angesammelten Ladungen herrührt.

Das Auftreten dieser Gasentladungen in den Poren der Lackschicht oder den Löchern des Papieres ist unabhängig von der Polarität der Spitze und dem Spitzenabstande; bei grösserem Spitzenabstand benötigt man natürlich eine höhere Spannung an der Spitze, gleichzeitig sind jedoch auf einem grösserem Gebiet der Lackschicht die leuchtenden Poren zu sehen.

Der Nachweis, dass von der Lackschicht wirklich positive Ionen zur negativen Spitze hinwandern, lässt sich leicht durch seitliches Anblasen der Anordnung erbringen. Stellt man hinter der Koronaspitze in den Weg des Luftstromes eine mit der negativen Spitze über ein Messinstrument verbundene Kollektorelektrode auf, so fliesst ein positiver Strom von der Kollektorelektrode zur Spitze. Dieser rührt von den positiven Ionen her, die auf dem Wege von der lackierten Plattenelektrode zur Spitze zum Kollektor hin weggeblasen wurden. Leider lässt sich auf diese Weise nicht messen, ein wie grosser Anteil des Gesamtspitzenstromes von den von der lackierten Plattenelektrode kommenden positiven Ionen getragen wird, da man durch den Luftstrom gleichzeitig die Spitzenentladung stört.

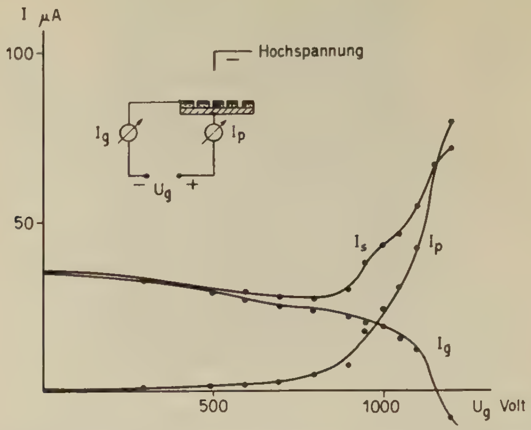

Abb. 5. Künstliche „Lackschicht" mit veränderlichem Oberflächenpotential. I_g = Strom zur Oberfläche und I_p = Strom durch die Poren als Funktion der Oberflächenspannung U_g.

Indirekt kann man die Einwirkung der den negativen Ionen entgegenlaufenden positiven Ionen auch durch die Verminderung des elektrischen Windes an der negativen Spitze messen. Bringt man in der Nähe der Spitze einen glühenden Platindraht an, so wird dieser durch den elektrischen Wind abgekühlt, was teils am Heizstrome durch den Draht und teils an seiner Farbe erkennbar ist. Wird nun die der Spitze gegenüber liegende Plattenelektrode lackiert, so kann mit Hilfe des Platindrahtes eine starke Verminderung des elektrischen Windes nachgewiesen werden.

Um zu zeigen, dass der Koronastrom wirklich vorzugsweise zu den lackierten Teilen der Plattenelektrode hinfliesst, wurde folgender Versuch angestellt. 27 Metallstreifen, jeder 2 mm breit und 70 mm lang, wurden parallel nebeneinander gelegt. Jeder Metallstreifen war von seinem Nachbar etwa 0,3 mm entfernt und isoliert. Nun wurde jeder zweite Metallstreifen mit Schellack überstrichen und danach alle lackierten Streifen miteinander leitend verbunden. Ebenso wurden auch alle unlackierten Streifen miteinander leitend verbunden. Auf diese Weise wurde eine Ebene in der Grösse 70 × 60 mm erhalten, die aus wechselweise lackierten und unlackierten Metallstreifen bestand. 3 cm über dieser Anordnung wurde nun eine Koranaspitze in Luft angebracht und die Spannung an dieser langsam erhöht. Die Abb. 4 zeigt den Koronastrom zu den unlackierten Streifen (Kurve *M*) und zu den lackierten Streifen (Kurve *L*) als Funktion der Spitzenspannung. Unterhalb von ca. 21 kV fliesst der Koronastrom vorzugsweise zu den unlackierten Streifen. Dies beruht auf der negativen Aufladung der Lackschicht der lackierten Streifen, die ihrerseits jedoch noch nicht genügend stark ist, um zur Ionisation der Luft in den Poren zu führen. Steigt die Spitzenspannung über 21 kV, so fliesst der grössere Teil des Koronastromes wie erwartet zu den lackierten Streifen hin. Es entstehen also in diesem Falle eine Art von bevorzugten Wegen zwischen der Spitze und den Poren der Lackschicht, in denen positive und negative Ionen gegeneinander wandern.

Um schliesslich eine Auffassung über die Aufladung der Lackschicht zu erhalten, wurde folgender Versuch angestellt. Eine 0,12 mm dicke Glimmerplatte wurde einseitig mit einer leitenden Graphitschicht belegt. Danach wurden auf einer Fläche von ca. 1 cm² 25 feine Löcher mit einer Nadel gestochen und die Glimmerplatte mit der Graphitschicht nach oben auf die Plattenelektrode unter die 6 mm entfernte Spitze gelegt. Bei einer Spannung von ungefär 5700 V an der Spitze konnten trotz der Graphitschicht die üblichen Glimmerscheinungen in den Löchern leicht beobachtet werden. Die Graphitschicht muss sich also auf ein gewisses negatives Potential aufgeladen haben. Verbindet man nun die Graphitschicht über eine variable Spannungsquelle mit der Plattenelektrode, so kann man das Potential der Graphitschicht und somit die Feldstärke in den Löchern der Glimmerplatte beliebig einstellen. Die Abb. 5 gibt die Schaltung und das Ergebnis des Versuches. Die negative Spitzenspannung war dabei konstant 5700 V, geändert wurde nur die Spannung der Graphitschicht von 0 bis -1200 V. Die Abb. 5 zeigt die Abhängigkeit des Spitzenstromes I_s, des Stromes zur Graphitschicht I_g und des durch die Löcher der Glimmerplatte hindurch zur Plattenelektrode fliessenden Stromes I_p von der Spannung der Graphitschicht U_g. Mit steigender Spannung U_g sinkt zunächst der Spitzenstrom I_s auf Grund der hierdurch bewirkten Verkleinerung des Feldes an der Spitze. Der Strom I_p zur Plattenelektrode ist sehr gering, da die Fläche der Löcher im Vergleich mit der mit Graphit belegten Oberfläche der Glimmerplatte sehr klein ist. Übersteigt U_g etwa 600 V, so setzt jedoch die Ionisierung des Gases in den Löchern der Glimmerplatte ein, was sich durch ein Ansteigen des Stromes I_p zur Plattenelektrode bemerkbar macht. Bei noch höherem U_g wird dieser Effekt so kräftig, dass der Gesamtstrom wieder steigt, um bei $U_g = 1150$ V fast das Doppelte des Wertes bei $U_g = 0$ V zu erreichen. Bei dieser Spannung ($U_g = 1150$ V) ist der Strom I_g zur Graphitschicht gleich null, d.h. die auf die Graphitschicht treffenden negativen und positiven Ionenströme heben sich gegeneinander genau auf. Die hier gemessene Spannung U_g entspricht also ungefähr derjenigen, die sich auf einer gewöhnlichen Lackschichtoberfläche automatisch einstellt. Auch in diesem Falle sind wieder die Glimmentladungen in den Löchern zu sehen. Man erhält also als eine ungefähre Abschätzung der Spannung der Lackschichtoberfläche unter der Koronaspitze ca. 1000 V, der Wert hängt aber sicher sehr von der Dicke und Leitfähigkeit der verwendeten Schicht ab. Steigert man U_g weiterhin, so wird der zur Graphitschicht fliessende Strom positiv, was darauf hinweist, dass nun die Anzahl der auf die Graphitschicht auffallenden positiven Ionen grösser ist als die der von der Spitze kommenden negativen Ionen oder Elektronen. Eine Steigerung von U_g über 1200 V hinaus war wegen der in den Löchern auftretenden Funkenüberschläge zwischen der Graphitschicht und der Plattenelektrode nicht möglich.

Auf Grund der hier beschriebenen Versuche scheint es dem Verfasser erwiesen, dass es sich bei der beobachteten Erscheinung wirklich um den in der vorausgeschickten Erklärung angegebenen Mechanismus handelt. Auch die im Folgenden beschriebenen Messungen unterstützen nur diese Annahme.

3. Herabsetzung der Durchschlagspannung durch Lackschichten

Eine weitere typische Eigenschaft der hier behandelten Erscheinung ist die Herabsetzung der Durchschlagspannung durch den Lacküberzug der Plattenelektrode. Diese lässt sich ebenfalls leicht durch die Annahme einer Bildung von Ionen oder Elektronen in den Poren der Lackschicht verstehen. Diese neutralisieren auf ihrem Wege zur Spitze nämlich einen Teil der Raumladungen der von der Spitze kommenden Ionen entgegengesetzter Polarität und erhöhen so das Feld vor der Spitze. Weiterhin bilden sich bereits vor dem Überschlag zwischen Spitze und den

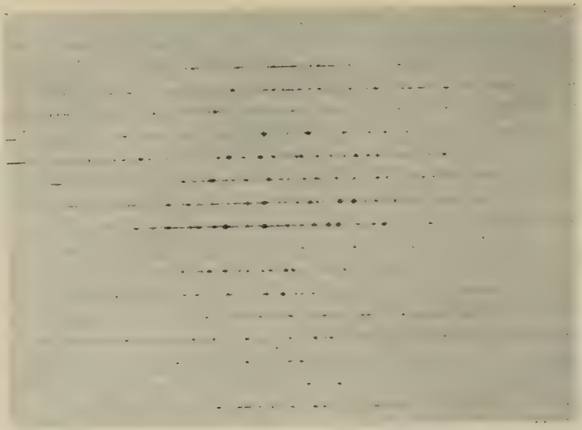

Abb. 6. Durchschlagstellen eines Funkens durch geritztes Papier (vgl. Text).

Poren der Lackschicht bevorzugte Ionenwege aus, in denen positive und negative Ionen in entgegengesezter Richtung laufen. Dies wurde schon oben durch den Versuch mit der abwechselnd aus lackierten und unlackierten Streifen zusammengesetzten Plattenelektrode gezeigt. Wird die Spitzenspannung weiterhin gesteigert, so werden diese Ionenwege einen Funkendurchschlag erleichtern.

Dass der Funke beim Durchschlag sich wirklich zu den Poren der Lackschicht sucht, kann direkt visuell beobachtet werden, da in jeder getroffenen Pore im Augenblick des Funkendurchschlages ein intensives punktförmiges Leuchten auftritt. Noch besser kann dies jedoch auf folgende Weise gezeigt werden. Bedeckt man die Plattenelektrode mit einem genügend dicken Papier, in welchem mit einem scharfen Messer einige feine Schnitte gemacht worden sind, so hat dieses Papier die gleiche Wirkung auf den Koronastrom wie eine Lackschicht, da die Schnitte im Papier wie Löcher wirken. Es wird also auch hierdurch die Durchschlagspannung stark gesenkt. Beim Durchschlag auf das Papier hinterlässt der Funke überall dort, wo er durch das Papier hindurchschlägt, ein kleines Loch. Auf diese Weise können die Durchschlagpunkte des Funkens leicht festgestellt werden. Die Abb. 6 gibt das Aussehen eines solchen Papieres nach einigen Funkendurchschlägen wieder (Spitzenabstand 10 cm, Durchschlagspannung ca. 100 kV). Die durch den Durchschlag entstandenen Löcher liegen alle genau in den Ritzen im Papier. Dies bestätigt die Annahme, dass der Funke sich bevorzugt die Ionenwege entlang in die Poren der Lackschicht sucht. Wie weiter unten gezeigt wird, wurde jedoch ebenfalls festgestellt, dass der Funke einen wesentlich kürzeren Weg zu einer nicht lackierten Stelle der Plattenelektrode einem längeren entlang eines solchen Ionenweges vorzieht.

4. Anwendung der Erscheinung zur Prüfung von Lackschichten und isolierenden Folien

Da, wie oben gezeigt wurde, die Poren in isolierenden Schichten mit Hilfe einer Koronaentladung leicht erkennbar werden, wurde hierzu eine geeignete Anordnung gebaut und einige Lackschichten und isolierende Folien untersucht. Das Auffinden dieser Poren bereitete technisch bisher grosse Schwierigkeiten. Ein Mikroskop kann zum Beispiel deshalb nicht angewendet werden, weil der Lack meistens nicht auf

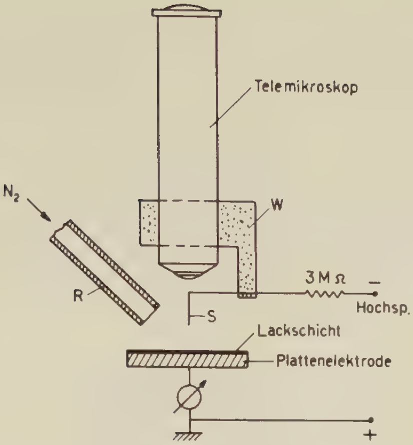

Abb. 7. Anordnung zur Untersuchung von Lackschichten.

einer durchsichtigen Unterlage aufgebracht ist und die Poren unter Aufsichtsbeleuchtung nicht erkennbar sind. Bringt man, um dies zu umgehen, einen schwarzen Lack z. B. auf einer Glasplatte an und betrachtet ihn unter dem Mikroskop, so findet man erstaunlich wenige Poren. Dies ist darauf zurückzuführen, dass die Poren im allgemeinen nicht senkrecht durch die Lackschicht hindurchgehen, sondern sich auf schrägen oder sogar spiralförmigen Wegen von der Oberfläche zur Unterlage suchen. Da das Vorhandensein solcher Poren die Güte einer Lackschicht wesentlich verschlechtert, sind bisher verschiedene Methoden zur Prüfung von Lack- und Farbschichten zur Anwendung gekommen [9, 12, 13]. Gemeinsam für alle diese Methoden ist, dass sie sehr zeitraubend sind — ein Versuch nimmt oft mehrere Monate in Anspruch — und dass die Resultate auch dann oft noch nicht ganz einwandfrei sind. Es liegt daher nahe zu untersuchen, ob die Koronaentladung ein besseres Hilfsmittel für solche Prüfungen sein könnte.

Als erstes wurde untersucht, ob die Koronaentladung die Poren in der Lackschicht nicht erst künstlich erzeugt. Dass dies nicht der Fall ist zeigt man leicht, indem man eine Koronaentladung längere Zeit über einer Lackschicht aufrechterhält und die Zahl der Poren in der Lackschicht beobachtet. Diese ist während einer Beobachtungszeit von etwa 10 Minuten vom Einschalten der Spitzenspannung an praktisch vollkommen konstant, die ganz selten auftretenden neuen Poren lassen sich auf schwache Stellen in der Lackschicht oder auch darauf zurückführen, dass für die Gasentladung in einer Pore erst geeignete Bedingungen vorliegen müssen, bevor sie zünden kann. Dies kann z. B. der Fall sein, wenn zwei Poren sehr nahe beieinander liegen und ihr Feld gegenseitig beinflussen. Erst nach längerer Zeit kann man beobachten, dass die Gasentladungen in den Poren die Lackschicht angreifen und die Poren langsam vergrössern. Der Verlauf dieses Prozesses ist natürlich von dem verwendeten Isolationsmaterial oder Lackschicht abhängig.

Um die zu untersuchenden isolierenden Schichten unter der Spitzenentladung besser beobachten zu können, wurde folgende Anordnung verwendet (vgl. Abb. 7). Mit Hilfe eines isolierenden Winkelarmes *W* wurde die Spitze *S* (0,3 mm Platindraht, am Ende zu einer Spitze angefeilt) etwa 5 mm über der Gegenstandsebene eines Telemikroskopes mit 25facher Vergrösserung in der Mitte unter dessen Objektiv angebracht. Die Spitze wurde über einen Schutzwiderstand von 3 MΩ mit dem negativen Pol einer Spannungsquelle verbunden, die bis zu 6 kV und 1 mA abgeben konnte. Der Schutzwiderstand verhindert ernstere Folgen, falls man bei der Untersuchung unwillkürlich die Spitze berühren sollte. Stellt man das Mikroskop nun scharf auf die zu untersuchende Fläche ein, so befindet sich die Spitze automatisch im richtigen Abstand von dieser Fläche; die an ihrem Ende befindliche Koronaentladung erscheint jedoch selbst nicht störend im Gesichtsfeld, da sie sich nicht in der Gegenstandsebene des Mikroskopes befindet. Wird nun die Spannung zwischen die Spitze und die metallischen Unterlage der Lackschicht gelegt, so können alle Poren in der Lackschicht an den in ihnen auftretenden Glimmerscheinungen mit dem Mikroskop sofort entdeckt werden.

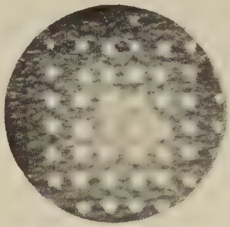

Abb. 8. Glimmentladungen in künstlichen Löchern in Millimeterpapier. Abstand zwischen den Löchern 1 mm, Durchmesser der Löcher ca. 0,1 mm (5000 V, 150 μA).

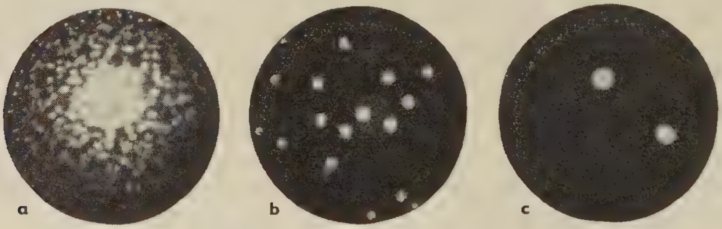

Abb. 9. a.) Poren in einer einfachen Schellackschicht. b.) Poren in einer dreifachen Schellackschicht. c.) Poren in einer sechsfachen Schellackschicht. — Gleiche Vergrösserung wie Abb. 8.

Die Abbildungen 8 und 9 zeigen Aufnahmen, die durch Einführen eines Filmes in die Bildebene des Objektives des Mikroskopes gewonnen wurden. Abb. 8 zeigt ein Blatt Millimeterpapier, in welchem die Ecken jedes Millimeterquadrates mit einer feinen Nadel durchstochen waren, und welches danach auf die unlackierte Plattenelektrode gelegt wurde. Man sieht deutlich die Glimmerscheinungen in jedem Loch. Um auch die Oberfläche des Millimeterpapieres sichtbar zu machen, wurde sie während der Aufnahme gleichzeitig von oben beleuchtet. Da die Abb. 9 a–c mit der gleichen Vergrösserung aufgenommen sind, kann die Abb. 8 gleichzeitig als Massstab für diese Abb. dienen. Schon hier sei darauf hingewiesen, dass der Durchmesser der Glimmerscheinungen in den Löchern auf der Photographie in keiner Weise dem wahren Durchmesser der Löcher entspricht, dieser war in Wirklichkeit bei Abb. 8 etwa 0,1 mm.

Die Abb. 9 a, 9 b und 9 c zeigen die Poren in Schellackschichten, die auf einer ebenen Kupferplatte mit dem Pinsel aufgetragen wurden. Die Abb. 9 a zeigt die Kupferplatte nach einer Streichung mit Schellack (Schichtdicke ca. $2–3 \cdot 10^{-3}$ mm).

Die Abb. 9 b wurde nach 3maliger Streichung mit Schellack erhalten, zwischen jedem Anstrich wurde die Schicht 24 Stunden lang bei 80° C getrocknet. Abb. 9 c zeigt schliesslich die Schellackschicht nachdem 6 separate Anstriche aufeinander angebracht waren. In allen Aufnahmen der Abb. 9 wurde die Lackschicht im Dunkeln photographiert, so dass nur die Glimmerscheinungen in den Poren zu erkennen sind.

Wie erwartet verringert sich die Anzahl der Poren mit jedem neu hinzukommenden Anstrich. Dagegen wäre es falsch anzunehmen, dass die zurückbleibenden Poren ihren Durchmesser mit zunehmender Anzahl der Anstriche vergrössern, wie man dies vielleicht den Aufnahmen nach anzunehmen geneigt ist. Der Grund für den wesentlich grösseren Durchmesser der Glimmerscheinungsbilder bei 6 Schellackanstrichen ist auf die wesentlich grössere Stromdichte in den Poren zurückzuführen (vgl. auch Abb. 13 c), da nun der gesamte Strom durch die wenigen noch vorhandenen Poren hindurchfliesst. Dies ist an dem wesentlich intensiveren Leuchten der Poren erkennbar. Da das Licht der Glimmerscheinungen zu einem sehr grossen Teil aus ultraviolettem Licht besteht, ist die Vergrösserung des Bildes der Glimmerscheinungen in den Poren wohl teilweise auf deren Verstärkung und teilweise auf die chromatische Abberration des Mikroskopobjektives zurückzuführen. Beobachtet man die Glimmerscheinungen visuell durch das Mikroskop, so erscheinen sie bei weitem nicht so gross wie auf der Photographie, wenn auch ihre Helligkeit bei fallender Anzahl der Poren stark wächst. Es kann also schon hier vermutet werden, dass der Strom der Spitzenentladung keineswegs proportional zur Anzahl der Poren in der Lackschicht ist (vgl. Abb. 13 c).

Um schliesslich auch sehr dünne isolierende Schichten, ($d < 1-2\,\mu$), untersuchen zu können, ist es notwendig, zu vermeiden, dass die von der Spitze kommenden Elektronen auf ihrem Wege zur Plattenelektrode mit den Sauerstoffmolekülen der Luft negative Ionen bilden, da diese in den Poren wesentlich schlechter ionisieren [19]. Dies kann vermieden werden, wenn man die Koronaentladung in einer Stickstoffatmosphäre laufen lässt, oder, was in diesem Falle einfacher und ausreichend ist, durch ein Rohr *R* (vgl. Abb. 7) von schräg oben einen schwachen Stickstoffstrom in den Entladungsraum hineinbläst. Die Reinheit des technischen Stickstoffes, den man in Bomben erhalten kann, reicht hierfür vollkommen aus. Mit diesem Kunstgriff kann man auch in sehr dünnen Lackschichten und sogar in dünnen Aluminiumoxydschichten (Eloxalschichten [14] und chemisch oxydiertem Aluminium) leicht Poren nachweisen. Dieser Kunstgriff sollte immer angewandt werden, wenn die normale Koronaprüfung in Luft keine klaren Resultate ergibt.

5. Untersuchungen an verschiedenen isolierenden Schichten

Im Folgenden sollen einige Beispiele von isolierenden Schichten gegeben werden, bei denen der Effekt gefunden bzw. nicht gefunden wurde.

Leicht zu finden sind Poren in folgenden Materialien: fast alle Lacke und Farbanstriche, Kollodium, dicke Eloxalschichten, die durch einstündiges Elektrolysieren von Al in 6 % Oxalsäure bei einer Stromdichte von 10 mA/cm^2 Wechselstrom entstanden sind [14], dünne Piceinschichten (ca. 0,05 mm dick), dünne Paraffinschichten (ca. 0,05 mm dick), dünnes Papier, besonders Zigarettenpapier und Seidenpapier, und dicke Oxydschichten, z.B. MgO und CuO.

Da die Korona gegen CuO für das Koronaverhalten von Kupferhochspannungsfreileitungen von Interesse ist, ist die zeitliche Änderung des Koronastromes von einer negativen Spitze gegen eine 4 mm entfernte Kupferplatte bei konstanter Spitzen-

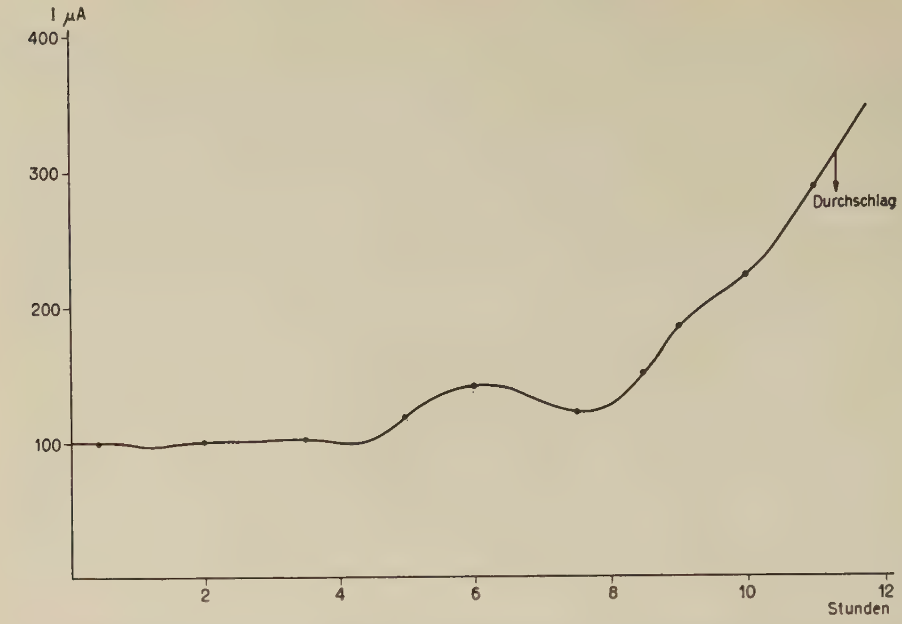

Abb. 10. Spitzenkoronastrom gegen eine Kupferplatte. Der Strom steigt auf Grund der Oxydierung der Platte. Spitzenspannung — 4900 V; Spitzenabstand 4 mm.

spannung gemessen worden (Abb. 10). Die Luftfeuchtigkeit während des Versuches war 30 %. Die Koronaentladung bewirkt eine langsame Oxydation des Kupferbleches in der Nähe der Spitze, welche ihrerseits mit der Zeit eine Erhöhung des Koronastromes mitführt. Der Grund hierfür ist im Aufkommen von isolierenden Oxydschichten zu suchen, was durch das Auftreten der charakteristischen Glimmerscheinungen auf den oxydierten Teilen der Kupferelektrode bewiesen wird. In diesem Falle musste der Versuch nach 12 Stunden abgebrochen werden, da Durchschläge zwischen Spitze und Plattenelektrode eintraten. Der von KÜHN [15] gefundene Effekt, dass alte Hochspannungsfreileitungen für Gleichspannung aus Kupfer wesentlich grössere Koronaverluste zeigen als neue oder solche aus Aluminium, dürfte wohl auf die gleiche Ursache zurückzuführen sein.

Streicht man eine nicht zu dicke Fettschicht auf die Plattenelektrode der in Abb. 7 gezeigten Anordnung, so kann man auch hier kräftige, meist punktförmige Glimmerscheinungen auf der Fettschicht beobachten. Das Auftreten dieser Glimmerscheinungen hängt nicht von der Oberflächenbeschaffenheit der Fettschicht ab: ganz glatte Fettschichten unterscheiden sich nur unwesentlich von rauhen. Ist die Fettschicht genügend dick, so findet man keine Poren mehr, jedoch treten Glimmerscheinungen am Rande der Fettschicht, also an der Grenze Metall – isolierende Schicht, auf. Je grösser die Viskosität des Fettes ist, umso weniger ausgeprägt erscheint der Effekt. Die Tatsache, dass der Lackschichteffekt ebenfalls bei Fettschichten auftritt, dürfte eine Erklärung für die an Hochspannungsfreileitungen gefundenen Alterungserscheinungen bieten.

Allgemein kann der hier beschriebene Effekt an jeder Grenze zwischen Metall und

Isolator gefunden werden, da Oberflächenladungen auf dem Isolator zu Feldverzerrungen an der Grenze Metall – Isolator Anlass geben, die die Ionisation des Gases an diesen Stellen erleichtern.

In den folgenden Materialien konnten Poren durch Glimmerscheinungen nachgewiesen werden, wenn in den Raum der Koronaentladung Stickstoff geblasen wird: den meisten Papiersorten, dünne Eloxalschichten und chemisch oxydiertes Aluminium, sehr dünne Lackschichten und Cellophan.

Schliesslich sollen noch einige Beispiele für Materialien gegeben werden, in denen mit Hilfe der Koronamethode keine Poren nachgewiesen werden konnten: Pliofilm (0,05 mm), Alkathen (0,05 mm), Teflon (0,15 mm), Glimmer (0,1 mm), Paraffin (0,3 mm), dünnes Glas und Emailschichten auf Metallunterlage.

III. Einfluss einer Schellackschicht auf Koronaentladungen und Funkendurchschlag unter verschiedenen Versuchsbedingungen

Um ein besseres Verständnis des Einflusses der Lackschicht auf den Koronastrom in dem speziellen Falle Spitze-Plattenelektrode zu erhalten, wurden verschiedene Parameter wie Spitzenpolarität, Spitzenabstand, Lackschichtsdicke, Luftfeuchtigkeit, Luftdruck usw. variiert und die dabei auftretenden Erscheinungen untersucht. Im Folgenden sollen die Ergebnisse dieser Messungen samt dazugehörige eventuelle Erklärungen dargestellt werden.

1. Versuchsanordnung

Für Spitzenabstände von 1–10 cm und Atmosphärendruck wurde ein zylindrisches Gefäss G benutzt (siehe Abb. 11), welches auf der Innenseite mit dünnem Aluminiumblech ausgekleidet war. Der luftdicht schliessende Deckel D war aus Plexiglas gefertigt und mit zwei Durchführungen versehen, durch welche das Gefäss durchlüftet werden konnte. Weiterhin ragte durch die Mitte des Deckels D noch die in ihrer Längsrichtung verschiebbare Spitze S senkrecht in das Gefäss hinein. Sie bestand aus einem gut abgerundeten Messingzylinder, in welchem ein 6 mm langer Pt-Draht von 0,3 mm Durchmesser als Spitze eingelötet war. Das untere Ende des Platindrahtes war zu einer Kugel mit dem Durchmesser 0,5 mm geformt, welche also die eigentliche Spitze bildete. Unter der Spitze befand sich die runde Plattenelektrode P aus 2 mm Messingblech, die um die Achse AB drehbar gelagert war. Die eine Seite dieser Plattenelektrode war mit der zu untersuchenden Schellackschicht bestrichen, die andere Seite hingegen von jeglichem Lack oder Schmutz befreit. Auf diese Weise konnte durch Drehen der Achse AB von aussen der Spitze die lackierte oder die unlackierte Seite der Plattenelektrode je nach Wunsch zugekehrt werden, ohne dass die anderen Bedingungen im Gefässe geändert wurden. Der Abstand zur Spitze änderte sich dabei weniger als 0,5 mm. Soweit nicht ausdrücklich anders erwähnt, kam bei den Versuchen eine Schellackschicht von 2–3 μ Dicke zur Verwendung, die durch Aufstreichen einer gereinigten Schellack-Alkohollösung (300 g Schellack auf 1 Liter Alkohol) mit einem feinen Pinsel erhalten wurde. Die Lackschicht wurde direkt nach dem Streichen bei 80° C 24 Stunden lang getrocknet. Es wurde festgestellt, dass trotz häufigen Funkenüberschlägen auf die Schicht die Messwerte innerhalb eines zu erwartenden Fehlers von ca. 3 % reproduzibel waren, so dass die Schicht nur selten erneuert wurde. Auch nach einer solchen Erneuerung konnten die alten

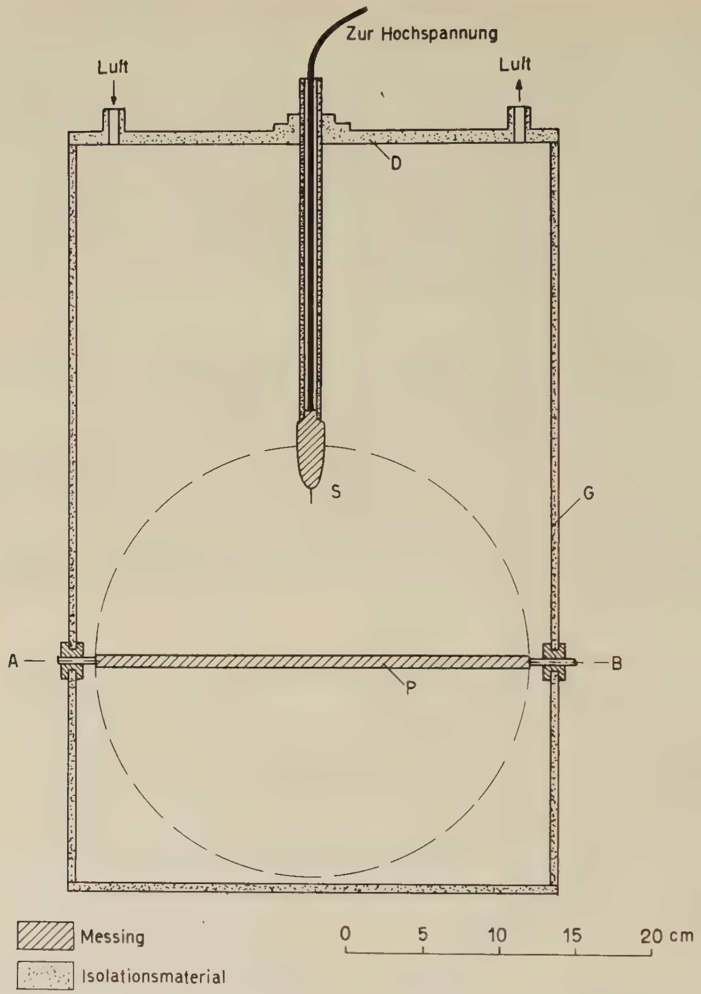

Abb. 11. Versuchsgefäss zur Untersuchung des Lackschichteffektes bei hohen Spannungen.

Messwerte zufriedenstellend reproduziert werden. Der Gasdruck bei den in diesem Gefässe angestellten Messungen war immer gleich dem Luftdruck und die Temperatur gleich der Zimmertemperatur (ca. 21° C), es wurde also bei den Versuchen weder auf eine genaue Einhaltung eines konstanten Luftdruckes von 760 mm Hg noch auf grosse Konstanz der Temperatur geachtet. Diese Massnahmen wurden deshalb nicht ergriffen, da die zu untersuchende Erscheinung von den normal vorkommenden Schwankungen dieser Grössen (755 ± 10 mm Hg, 21 ± 2° C) nicht sehr wesentlich beeinflusst wird. Ausserdem spielen andere schwer kontrollierbare Grössen in den Versuchen eine Rolle (z. B. Spitzenform etc.), die die Ergebnisse in ähnlichen Grenzen beeinflussen. Trotzdem waren jedoch alle Durchführungen in das Gefäss soweit ab-

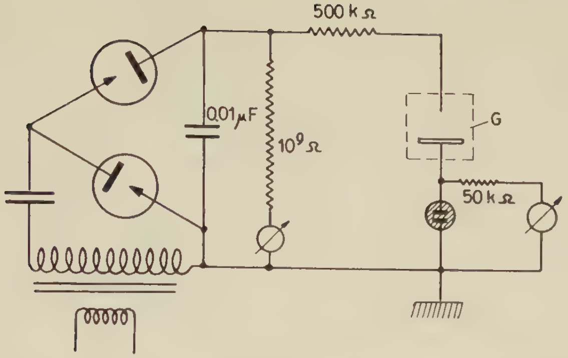

Abb. 12. Versuchsanordnung zur Untersuchung des Lackschichteffektes bei hohen Spannungen.

gedichtet, dass ein wesentliches Hinein- oder Hinausdiffundieren von Gas oder Feuchtigkeit aus dem Gefäss während der Messungen unmöglich war.

Die Versuche in dem hier beschriebenen Gefässe wurden also bei ungefähr konstantem Luftdruck und Temperatur ausgeführt. Die Luftfeuchtigkeit wurde dagegen geändert, wobei die relativen Luftfeuchtigkeiten von 0 %, 30 % und 50 % zur Anwendung kamen. Diese wurden auf folgende Weise erhalten: Um eine Luftfeuchtigkeit von so nahe wie möglich 0 % zu erreichen, wurde auf dem Boden des Gefässes Silicagel ausgebreitet und das Gefäss danach luftdicht verschlossen. Mit Hilfe eines Haarhygrometers konnte das Fallen der relativen Feuchtigkeit im Gefässe laufend beobachtet werden. Nach etwa 24 Stunden änderte sich das Haarhygrometer nicht mehr. Da das Silicagel seine blaue Farbe nicht geändert hatte, muss die relative Feuchtigkeit sehr nahe 0 % gewesen sein. Nach weiteren 24 Stunden wurde daher mit den Versuchen begonnen. Ein Nachteil dieser Methode ist der, dass während des Versuches kein Luftstrom durch das Gefäss geblasen wird. Es konnte jedoch bei Versuchen mit 30 % und 50 % relativer Feuchtigkeit festgestellt werden, dass die Abwesenheit des Luftstromes des verhältnismässig grossen Gefässes wegen die Ergebnisse nur unbedeutend verändert.

Die Feuchtigkeiten von 30 % und 50 % wurden direkt durch Durchblasen des Gefässes mit Luft entsprechender Feuchtigkeiten erhalten. Die Luftgeschwindigkeit betrug dabei ca. 5–10 l/sec. Die Luftfeuchtigkeit wurde laufend mit einem Haarhygrometer kontrolliert, welches in regelmässigen Abständen mit einem Taupunkthygrometer verglichen wurde.

Zur Untersuchung des Effektes bei kleineren Spitzenabständen als 1 cm wurde die in der Abb. 7 wiedergegebene Anordnung benutzt. In diesem Falle bestand die Spitze aus einem 0,3 mm Pt-Draht, der am Ende zu einer 90°-Spitze angefeilt war.

Als Spannungsquelle für Spannungen von mehr als 6 kV wurde ein Kaskadengenerator verwendet, welcher bei einer maximalen Spannung von 200 kV einen Strom von 10 mA hergeben konnte (vgl. Abb. 12). Die Welligkeit der Gleichspannung an der Spitze war bei den hier vorliegenden Versuchen immer besser als 3 %.

Die Messung der Spannung wurde mit Hilfe eines Hochohmwiderstandes durchgeführt, der aus 20 Stück 50 MΩ S.S. White Dental Co Widerständen bestand. Die Abhängigkeit des Stromes durch diesen Widerstand von der Spannung wurde sorgfältig bis zu hohen Spannungen mit Hilfe von elektrostatischen Voltmetern kalibriert, was wegen der Spannungsabhängigkeit der S.S. White Dental Widerstände notwendig war. Die Genauigkeit der Spannungsmessung ist besser als 3 %, was für die vorliegenden Messungen als ausreichend betrachtet wurde.

Um den Strom beim Funkendurchschlag zu begrenzen war ein Schutzwiderstand von 500 kΩ zwischen dem negativen Pol des Kaskadengenerators und der Koronaanordnung eingeschaltet. Es wurde experimentell festgestellt, dass dieser keinen merkbaren Einfluss auf die bei den Messungen bestimmte Durchschlagspannung hatte. Um schliesslich das empfindliche Amperemeter zur Messung der Koronaströme vor Überlastung beim Funkendurchschlag zu schützen, wurde parallel dazu eine Glimmstrecke angebracht, die über einen Widerstand von 50 kΩ mit dem Messinstrument verbunden war. Auf diese Weise wurde erreicht, dass beim Funkendurchschlag der grösste Teil des Stromes über die parallelgeschaltete Glimmstrecke floss.

Die Messreihen wurden durch eine langsame Steigerung der Spitzenspannung bis zum Durchschlag erhalten, wobei bei geeigneten Spannungen Messungen des Koronastromes vorgenommen wurden. Die auf diese Weise erhaltenen Resultate waren innerhalb von 3 % reproduzibel.

2. Versuchsergebnisse mit negativer Spitze

Als erstes wurde die Abhängigkeit der Koronakennlinie und der Durchschlagspannung vom Spitzenabstand untersucht. Die Abb. 13 gibt die Resultate der Messungen für Spitzenabstände ≥ 2 cm wieder. Die Kurven L zeigen die Abhängigkeit des Koronastromes von der Spitzenspannung bei einer mit Lack bedeckten Plattenelektrode, die Kurven M denselben ohne Lackschicht auf der Plattenelektrode. Die senkrecht gestrichelten Linien am Ende jeder Kurve geben die Spannung an, bei welcher der Funkendurchschlag eintrat. Diese Spannung wurde jedesmal wiederholt gemessen, um einen Mittelwert festzustellen; die auf Grund von statistischen Schwankungen [16] gefundenen Abweichungen von diesem Mittelwert waren jedoch selten grösser als 1–2 %. Die bei den Versuchen verwendete relative Luftfeuchtigkeit war 29 %. An sich hätten die Dimensionen des Gefässes (Abb. 11) auch Messungen mit grösseren Spitzenabständen als 10 cm zugelassen, es zeigte sich jedoch, dass dann auf Grund der elektrostatischen Einwirkung der Gefässwände die in diesen Versuchen angestrebte Spitzen-Plattengeometrie zu stark gestört wurde.

Die Messergebnisse zeigen zwei auffallende Eigenschaften der Spitzenentladung gegenüber einer lackierten Plattenelektrode. Erstens ist das Verhältnis der Durchschlagspannung ohne und mit Lackschicht unabhängig vom Abstand immer ungefähr $1{,}63 \pm 0{,}03$. Dieses Verhältnis ist jedoch abhängig u.a. von der Geometrie, wie die Resultate mit der Kugel-Plattengeometrie zeigen (Abb. 18).

Wesentlich auffallender ist jedoch die Unabhängigkeit des Spitzenstromes kurz vor dem Durchschlag vom Spitzenabstande im Falle der lackierten Plattenelektrode (Kurven L). Wie die Abb. 13 zeigt, ist dieses nicht der Fall bei Verwendung einer unlackierten Plattenelektrode. Dies scheint darauf hinzuweisen, dass beim Funkendurchschlag zwischen Spitze und lackierter Plattenelektrode nur die Verhältnisse an der Spitze und nicht der Spitzenabstand ausschlaggebend ist. Es ist deshalb vermutlich anzunehmen, dass in diesem Falle der Funkenkanal von der negativen Spitze zur Plattenelektrode vorstösst, wie dies von der positiven Spitze her bekannt ist [17]. Im letzteren Falle ist der Spitzenstrom vor dem Funkenüberschlag mit und ohne Lackschicht nämlich ebenfalls praktisch unabhängig vom Spitzenabstand, was entsprechende Messreihen mit positiver Spitze gezeigt haben.

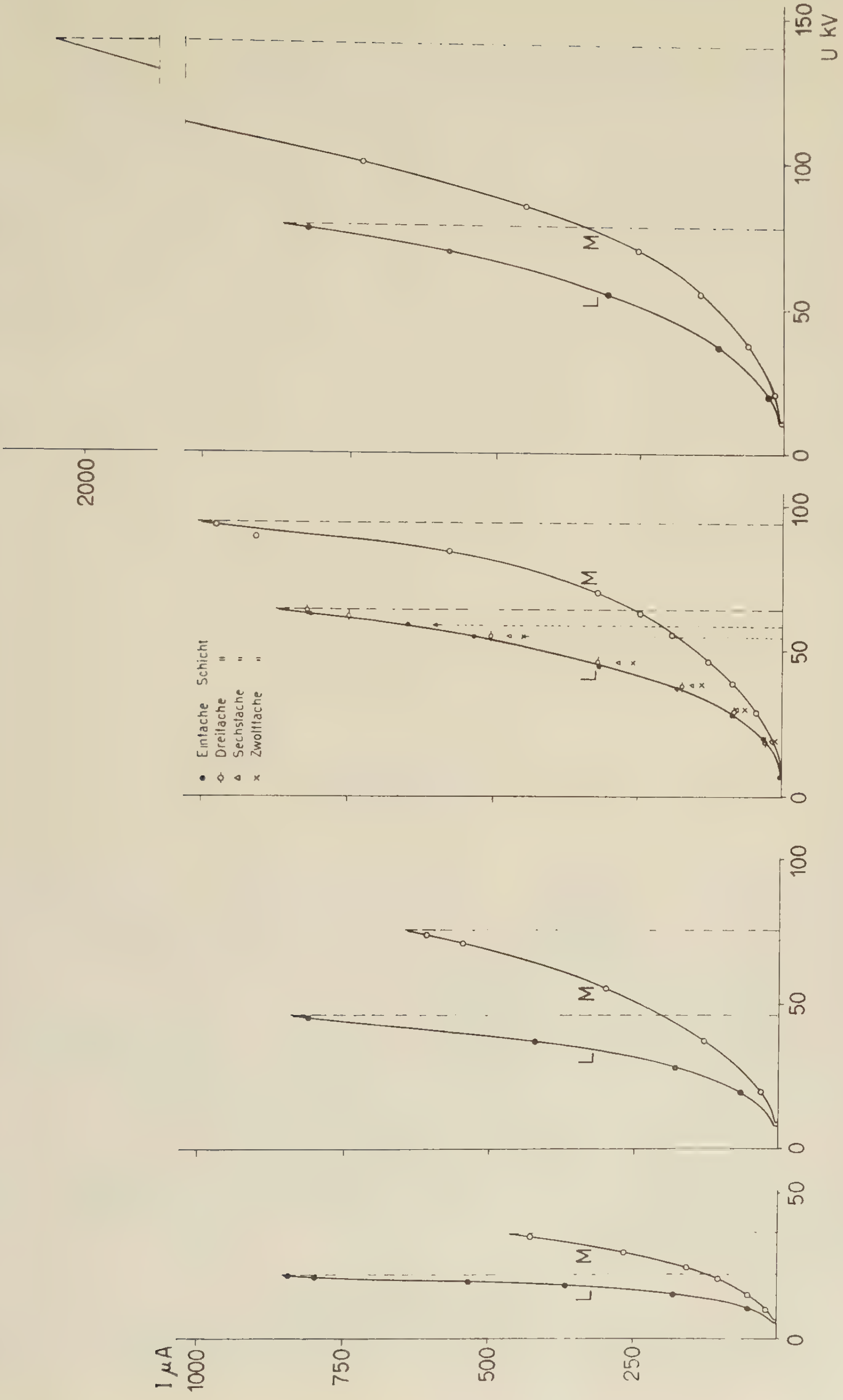

Abb. 13. Strom-Spannungskennlinien bei verschiedenen Spitzenabständen. Relative Luftfeuchtigkeit 29 %. Spitze negativ. Spitzenabstände von links nach rechts: 2 cm, 5 cm, 7,5 cm und 10 cm.

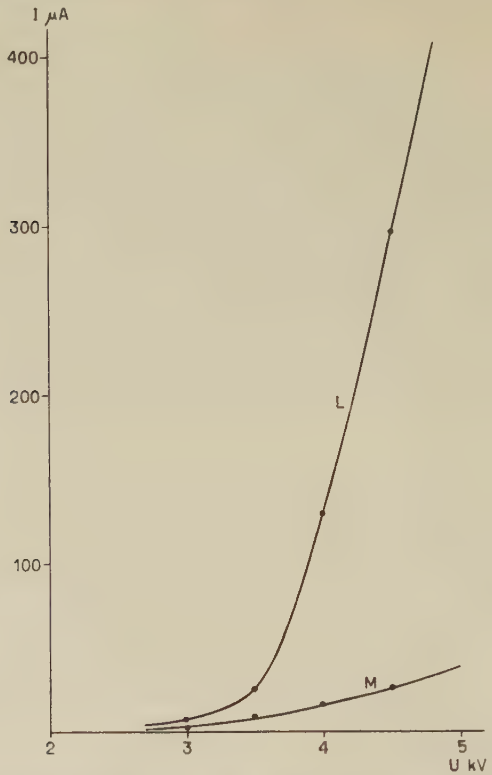

Abb. 14. Strom-Spannungskennlinie für 5 mm Spitzenabstand. Spitze negativ. Relative Luftfeuchtigkeit 20 %.

Die Annahme, dass der den Funkendurchschlag einleitende Prozess von der negativen Spitze ausgeht, wird weiterhin durch folgenden Versuch bekräftigt. Legt man zwei rechteckige Plattenelektroden, von denen die eine lackiert ist, nahe isoliert nebeneinander und stellt die negative Spitze darüber so ein, dass der Strom zur lackierten Elektrode doppelt so gross wie der zur unlackierten Elektrode ist, so befindet sich die Projektion der Spitze bei 7 cm Spitzenabstand ca. 2 cm von der Grenzlinie zwischen den beiden Plattenelektroden entfernt über der unlackierten Elektrode. Steigert man nun die Spitzenspannung bis zum Funkenüberschlag, so schlägt der Funken den geometrisch kürzesten Abstand entlang zur unlackierten Elektrode durch. Falls der Funkenkanal [18] von der lackierten Elektrode gegen die Spitze vorwachsen würde, sollte man wegen des sehr geringen Unterschiedes des Spitzenabstandes von der lackierten und der unlackierten Plattenelektrode einen Durchschlag zur lackierten Elektrode erwarten. Ein klares Verständnis des Mechanismus lässt sich jedoch wohl erst mit der von ALLIBONE & MEEK (17) angewandten Technik erhalten.

3. Einwirkung negativer Ionen

Arbeitet man bei negativer Spitze mit wesentlich geringeren Spitzenabständen, so tritt der Einfluss der Lackschicht noch deutlicher hervor. Die Abb. 14 gibt die

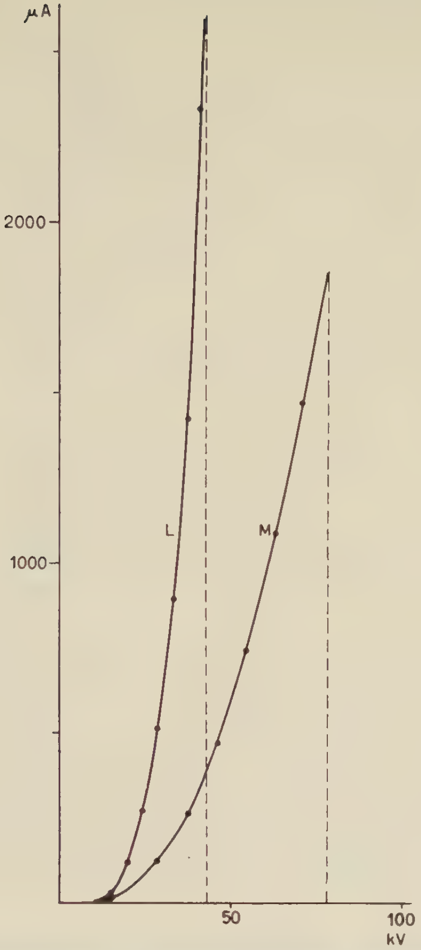

Abb. 15. Strom-Spannungskennlinie in technisch reinem Stickstoff. Spitzenabstand 7,5 cm. Spitze negativ.

Spannungsabhängigkeit des Koronastromes gegen eine Plattenelektrode mit und ohne Schellackschicht (Kurve *L* und *M*) bei einem Spitzenabstand von 5 mm wieder. Der Versuch wurde offen im Laboratorium bei einer Temperatur von 24° C und einer relativen Luftfeuchtigkeit von 20 % durchgeführt. Eine Ansicht der Anordnung schräg von oben wurde bereits in der Abb. 3 gezeigt.

Die ungewöhnlich grosse Verstärkung des Spitzenstromes durch die Schellackschicht bei Spitzenabständen von weniger als 1 cm kann leicht durch die von Franck [19] untersuchte Bildung von negativen Sauerstoffionen in der Umgebung einer Koronaentladung erklärt werden. Franck fand, dass unter gewissen Annahmen alle Elektronen, die von einem negativ geladenen Sprühdraht (Durchmesser 0,05 mm) zu einer konzentrischen Zylinderanode wanderten, nach 5–6 mm in Luft bei Atmosphärendruck negative Ionen gebildet hatten. Diese werden in unserem Falle mit grosser Wahrscheinlichkeit, bevor sie in den Poren der Lackschicht ionisieren können,

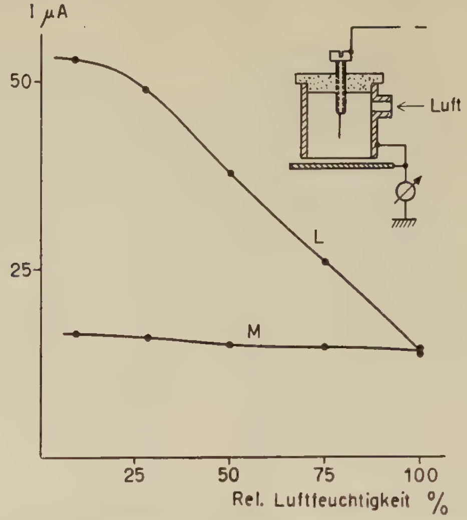

Abb. 16. Abhängigkeit des Koronastromes von der relativen Luftfeuchtigkeit, Kurve *M*: unlackierte Plattenelektrode, Kurve *L*: lackierte Plattenelektrode. Spitzenabstand 5 mm. Spitze negativ.

erst wieder in Elektron und neutrales Atom bzw. Molekül aufgespalten. Falls diese Aufspaltung nicht eintritt, so ist ihre Ionisierungswahrscheinlichkeit auf Grund ihrer kleinen freien Weglänge wesentlich geringer als die der freien Elektronen [21]. Bei kleinen Spitzenabständen in der Grössenordnung von wenigen Millimetern erreichen noch viele freie Elektronen die lackierte Plattenelektrode und ionisieren also leichter in den Poren der Lackschicht. Dies erklärt die sehr hohe Verstärkung des Spitzenstromes durch die Lackschicht. Bei Spitzenabständen von mehr als 2 cm treffen dagegen praktisch ausschliesslich negative Ionen auf die Plattenelektrode auf, wo sie wegen ihres geringeren Ionisierungsvermögens den hier untersuchten Effekt nicht so stark hervortreten lassen.

Ein anderer Beweis für diese Vorstellung gibt die Untersuchung der Erscheinung bei grossen Abständen in genügend reinem Stickstoff, wo keine Bildung von negativen Ionen möglich ist [22]. Der Stickstoff wurde zu diesem Zwecke solange durch das Versuchsgefäss (Abb. 14) geleitet, bis alle Luft daraus verdrängt war. Die Spannungsabhängigkeit des Koronastromes bei 7,5 cm Spitzenabstand in technisch reinem Stickstoff (weniger als 0,3 % Verunreinigung, meist wohl O_2) bei Atmosphärendruck zeigt Abb. 15. Auch hier tritt trotz des grossen Spitzenabstandes der Lackschichteffekt wesentlich kräftiger hervor als in Luft bei gleichem Abstand (vgl. Abb. 1). Dies muss ebenfalls darauf zurückgeführt werden, dass die meisten negativen Ladungsträger als freie Elektronen und nicht als negative Ionen die Lackschicht erreichen. Es soll jedoch darauf hingewiesen werden, dass die Messungen sehr schlecht reproduzibel waren, da unter der Einwirkung der Gasentladung während der Messung Gasreste aus den Elektroden usw. frei wurden, welche den Stickstoff weiterhin verunreinigten. Hierdurch erhöhte sich die Wahrscheinlichkeit für die Bildung negativer Ionen beträchtlich, was ein starkes Absinken des Koronastromes zur Folge hatte. In absolut reinem Stickstoff dürfte der Lackschichteffekt also noch deutlicher hervortreten.

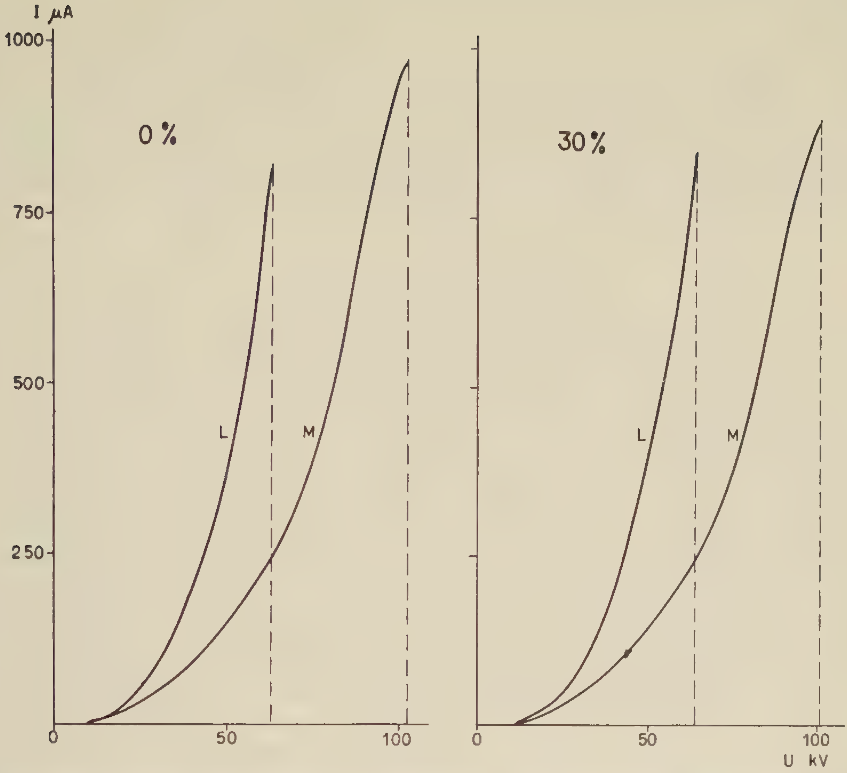

Abb. 17. Strom-Spannungskennlinie bei verschiedener Luftfeuchtigkeit. Spitzenabstand 7,5 cm. Spitze negativ.

4. Einwirkung der Luftfeuchtigkeit

Bei Spitzenabständen von weniger als 10 mm war der Koronastrom bei lackierter Plattenelektrode stark von der Luftfeuchtigkeit abhängig. Dies ist ohne Lackschicht nicht der Fall. Umgibt man die von der Lackschicht ca. 5 mm entfernte Koronaspitze mit einem kleinen Gehäuse und lässt dieses von Luft durchspülen, so kann die Abhängigkeit des Koronastromes von der Luftfeuchtigkeit leicht beobachtet werden. Abb. 16 zeigt diese Abhängigkeit für eine normale Zaponlackschicht (Kurve L) und eine unlackierte Plattenelektrode (Kurve M), bei konstanter Spitzenspannung. Die Form der Kurve L kann dabei recht verschieden bei verschiedenen Lackschichten ausfallen. Das gleiche Verhalten zeigen auch alle anderen Schichten, bei denen die hier untersuchte Erscheinung beobachtet wird, z.B. Papier mit feinen Löchern. Es kann weiterhin beobachtet werden, dass das Leuchten in den Poren der Lackschicht bei erhöhter Luftfeuchtigkeit stark abnimmt. Dagegen ist der Spitzenstrom bei unlackierter Plattenelektrode fast vollkommen unabhängig von der Luftfeuchtigkeit, was die Kurve M zeigt.

Bei grösserem Spitzenabstande ist der Einfluss der Luftfeuchtigkeit wesentlich weniger ausgeprägt. Die Abb. 17 zeigt die Spannungsabhängigkeit des Spitzenstromes bei 7,5 cm Spitzenabstand für zwei verschiedene Luftfeuchtigkeiten. Macht man den

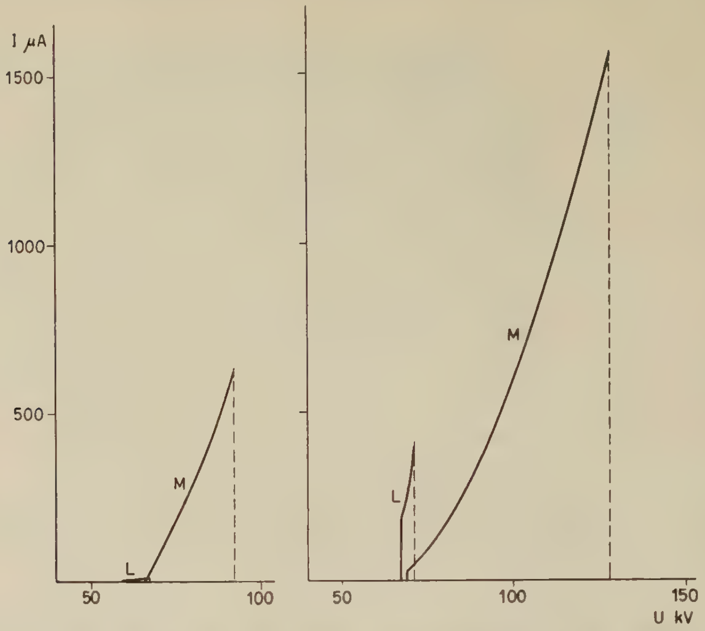

Abb. 18. Strom-Spannungskennlinie bei Kugel-Plattengeometrie. Kugel negativ, Kugelradius 19 mm. Abstand Kugelmitte–Plattenelektrode 9,4 und 11,9 cm. Rel. Luftfeuchtigkeit 29 %.

gleichen Versuch bei 50 % relativer Luftfeuchtigkeit, so fällt der Spitzenstrom gegen eine lackierte Metallelektrode langsam während der Messung ab, bis er die Charakteristik des Spitzenstromes bei unlackierter Plattenelektrode angenommen hat. Dies ist wohl durch den Niederschlag einer Wasserhaut auf der Lackschicht zu erklären, die die Oberflächenleitfähigkeit der Lackschicht steigert. Dass dieselbe Erscheinung nicht bei kleinen Spitzenabständen auftritt, liegt an der wesentlich höheren Stromdichte durch die Lackschicht in dem letzteren Falle. Diese lässt einen solchen Niederschlag im allgemeinen nicht zu, mit gewissen Schichten kann jedoch auch dieser Effekt manchmal gefunden werden.

Für die starke Feuchtigkeitsempfindlichkeit des Lackschichtseffektes bei kleinen Abständen muss vermutlich die Bildung von negativen Ionen bei Anwesenheit von Wasserdampf verantwortlich gemacht werden [20]. Dass es sich hierbei nicht nur um eine Veränderung der Leitfähigkeit der Lackschichtoberfläche handelt, geht daraus hervor, dass die Änderung des Koronastromes der Änderung der Luftfeuchtigkeit praktisch trägheitslos folgt, was gegen das Niederschlagen oder Verdunsten von Feuchtigkeit auf der Oberfläche spricht. Dies kann auch rein visuell beobachtet werden, da in den Teilen der Lackschicht, die von einem feuchten Luftstrom getroffen werden, der z. B. aus einer seitlich angebrachten Düse austritt, sofort die Glimmerscheinungen in den Poren erlöschen. Weiterhin kann gezeigt werden, dass auch Dämpfe von CCl_4, HCl, $CH_2{:}CH\,Cl$, und HNO_3 trotz sehr geringer Konzentration eine starke Verminderung des Koronastromes bewirken, wogegen dieser nicht für kleine Konzentrationen der Dämpfe von Aceton, Äther oder Alkohol empfindlich ist. Bei den erstgenannten Dämpfen ist die Bildung von negativen Ionen zu erwarten, bei den letzteren nicht. In beiden Fällen dürfte sich aber die Oberflächenleitfähigkeit der Lackschicht nicht ändern.

Es liegt nahe zu versuchen, die Feuchtigkeitsabhängigkeit des Koronastromes gegen eine Lackschicht bei kleinen Abständen als trägheitsloses Hygrometer zu verwenden. Versuche in dieser Richtung ergaben keine guten Resultate, da die Lackschicht von der elektrischen Entladung angegriffen und langsam verändert wird. Deshalb ändert sich die Kalibrierung eines solchen Hygrometers mit der Zeit, schon nach etwa 10 Minuten sind im allgemeinen Abweichungen zu erwarten.

5. Änderung der Elektrodenform

Um festzustellen, ob die Einwirkung einer Lackschicht auf den Koronastrom und die Durchschlagspannung auch bei anderer Form der Elektroden vorhanden ist, wurde die Spitze im Versuchsgefässe (Abb. 11) durch eine blankpolierte und gut gesäuberte Messingkugel mit einem Durchmesser von 38 mm ersetzt. Bei Elektrodenabständen von weniger als 7,5 cm trat bei dieser Anordnung direkt ein Durchschlag ein, ohne dass ein Koronastrom vorher nachgewiesen werden konnte. In diesen Fällen war die Durchschlagspannung unabhängig davon, ob die Plattenelektrode von einer Lackschicht bedeckt war oder nicht. Wie die Abb. 18 jedoch zeigt, traten grosse Unterschiede in der Durchschlagspannung mit und ohne Lackschicht auf der Plattenelektrode ein, sobald ein Koronastrom vor dem Durchschlage nachgewiesen werden konnte. Dieses Verhalten ist der Erklärung der Einwirkung der Lackschicht auf den Funkenüberschlag nach zu erwarten, da sich die den Funkenüberschlag begünstigenden Ionen in den Poren der Lackschicht erst bilden können, wenn wirklich ein Koronastrom fliesst, der die Oberfläche der Lackschicht aufladen kann.

6. Dicke der Lackschicht

Weiterhin wurde untersucht, ob die Eigenschaften der Lackschicht, in diesem Falle hauptsächlich die Anzahl der Poren pro cm², die Grösse des Koronastromes und der Durchschlagspannung beeinflussen. Es wurden deshalb Versuche mit einem Schellacküberzug von 1, 3, 6 und 12 Schellackschichten übereinander angestellt, die bereits in Abb. 13 (Spitzenabstand 7,5 cm) wiedergegeben sind. Wie die Abb. 9 zeigt, verkleinert sich die Anzahl der Poren pro cm² wesentlich mit steigender Zahl der übereinander liegenden Schellackschichten. Trotzdem ändert sich der Spitzenstrom bei gleicher Spannung nur unwesentlich. Da die Zahl der Poren mit steigender Lackschichtanzahl stark fällt, muss die Stromdichte in den Poren steigen, was durch stärkeres Leuchten der Glimmerscheinungen in den Poren auch wirklich sichtbar wird. Macht man ähnliche Messungen bei kleinen Spitzenabständen, z.B. 5 mm, so sinkt der Koronastrom wegen der allzu geringen Anzahl der Poren stark ab. Dies wird auch bei grossen Spitzenabständen beobachtet, wenn wirklich nur 5–10 Poren vorhanden sind.

Je kleiner die Anzahl der Poren ist, desto unsicherer wird die Bestimmung der Durchschlagspannung, die bei mehrfachen Lackanstrichen oft geringer ist als bei einem einfachen. So wurde bei 12 Schellackschichten aufeinander oft schon ein Durchschlag bei 55 kV erhalten, während dieser bei nur einer Schellackschicht erst bei 64 kV eintrat. Ein solches Verhalten ist zu erwarten, da bei wenigen Poren der Koronastrom längs wenigen Ionenwegen zwischen diesen und der Spitze verläuft und so günstigere Voraussetzungen für den Aufbau eines richtigen Funkenkanales [18]

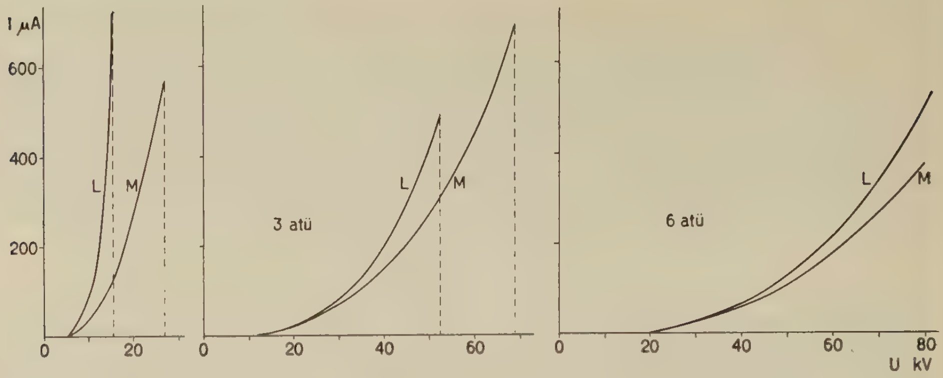

Abb. 19. Strom-Spannungskennlinie bei verschiedenem Luftdruck.

schafft. Ausserdem tritt dann nicht selten auf Grund der hohen Aufladung der Lackschichtoberfläche ein Flächengleitfunke längs derselben auf, der seinerseits in den meisten Fällen einen Funkendurchschlag zur Spitze initiiert [23]. Dies tritt besonders dann ein, wenn die isolierende Schicht sehr wenige oder keine Poren hat. Falls keine Poren vorhanden sind, so tritt immer zuerst ein solcher Flächengleitfunke ein, welcher Löcher in die isolierende Schicht schlägt.

7. Einwirkung höherer Gasdrucke

Schliesslich wurde noch die Einwirkung der Lackschicht auf den Koronastrom bei verschiedenen Drucken gemessen. Diese Untersuchungen wurden hauptsächlich im Hinblick auf die Anwendung von hohen Gasdrucken zur Isolation von Bandgeneratoren und anderen Hochspannungsgeräten durchgeführt. Der hierbei verwendete Spitzenabstand konnte wegen dem zur Verfügung stehenden Druckgefässe nicht grösser als 16 mm gemacht werden, ohne dass eine Beeinflussung der Spitzen-Plattengeometrie durch die Wände stattgefunden hätte. Die Spitze hatte sonst die gleiche Form wie die bei den oben beschriebenen Versuchen mit grossen Spitzenabstand verwendeten Spitzen. Als Gas wurde trockene Luft (Trocknung durch Silicagel) von verschiedenen Drucken verwendet. Die Abbildung 19 zeigt die Ergebnisse: bei höherem Luftdruck tritt der Lackschichteffekt mehr und mehr zurück. Auch der relative Unterschied in der Durchschlagspannung mit und ohne Lackschicht wird geringer. Dies erklärt sich leicht durch die verminderte mittlere freie Weglänge von Elektronen und Ionen im Gas bei höheren Drucken. Im Falle von 6 atü konnte kein Durchschlag über die Koronastrecke erzielt werden, da Überschläge ausserhalb des Druckgefässes den Messungen bei höherer Spannung eine Grenze setzten.

8. Versuchsergebnisse mit positiver Spitze

Wie schon oben erwähnt, wird ein der negativen Spitze ganz ähnlicher Effekt einer Lackschicht auf der Plattenelektrode auch mit positiver Spitze beobachtet. Auch hier ist der Spitzenstrom zwischen Spitze und lackierter Plattenelektrode grösser als ohne Lackierung der Elektrode, und die Poren in der Lackschicht sind ebenfalls durch die Glimmerscheinungen in ihnen zu erkennen. Die Lackschicht

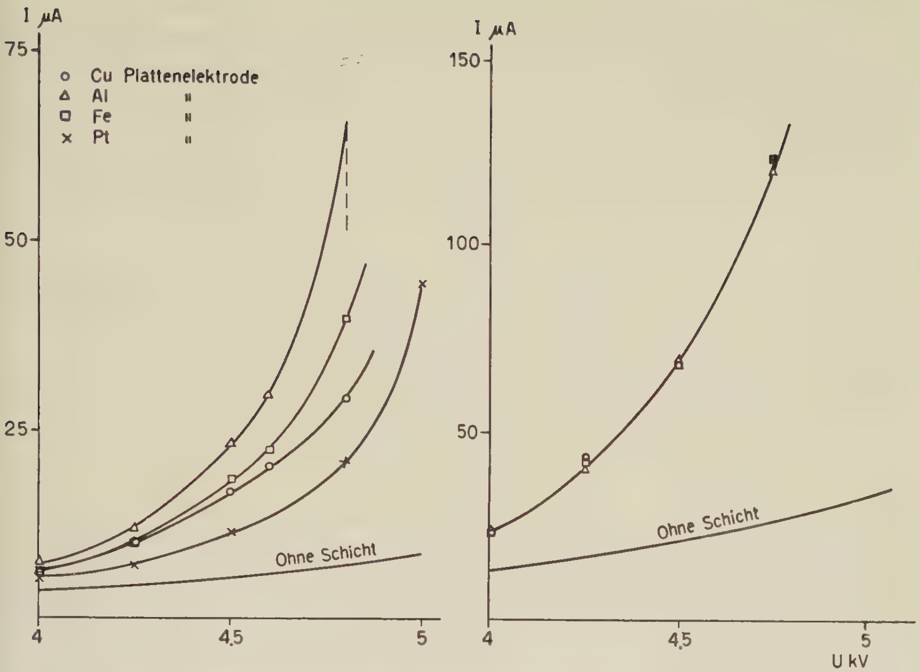

Abb. 20. Strom-Spannungskennlinien bei verschiedenem Material der Plattenelektrode. a.) positive Spitze b.) negative Spitze. Spitzenabstand 5 mm.

kann wieder durch eine isolierende Folie mit feinen Löchern ersetzt werden. Der Lackschichteffekt tritt aber nicht ganz so deutlich hervor wie im Falle der negativen Spitze.

Der diese Erscheinung hervorrufende Mechanismus bei positiver Spitze kann verschiedener Ursache sein. In diesem Falle wandern positive Ionen von der Spitze zur lackierten Plattenelektrode und laden die Lackschicht auf bzw. treten in die Poren derselben ein. Offenbar sind hier dann zunächst zwei Möglichkeiten gegeben: a) die positiven Ionen ionisieren im hohen Felde im Inneren der Poren und erzeugen dadurch Elektronen, die wegen ihrer grösseren Ionisierungswahrscheinlichkeit die Ionendichte in den Poren weiterhin stark erhöhen, bis sie die Poren auf ihrem Wege zur Spitze verlassen; b) die Ionen werden durch das hohe Feld in den Poren beschleunigt und befreien durch Ionenstoss Elektronen aus dem Metall der Plattenelektrode, sobald sie auf diese am unteren Ende einer Pore auftreffen. Diese Elektronen wandern ihrerseits in entgegengesetzter Richtung durch die Pore hindurch und ionisieren Gasmoleküle auf diesem Wege. Schliesslich ist hier noch eine dritte Möglichkeit c) denkbar, mit welcher die u.a. von PAETOW [11] bei Glimmentladungen zwischen mit isolierenden Schichten bedeckten Elektroden gefundenen Erscheinungen gedeutet wurden. PAETOW nimmt eine hohe, meist durch Photonen hervorgerufene positive Aufladung der isolierenden Partikel auf der Kathode an, wodurch Elektronen durch Feldemission aus der Kathode befreit werden.

Die Wahrscheinlichkeit, dass der unter a) angedeutete Mechanismus die wichtigste Rolle spielt, ist wegen der geringen Ionisierungswahrscheinlichkeit von positiven

Ionen nicht allzu gross [21]. Dass dagegen der unter b) vorgeschlagene Mechanismus eine Rolle spielt, konnte auf folgende Weise gezeigt werden. In eine isolierende Folie (Alkathen) wurden etwa 25 feine Löcher gestochen. Danach wurde die durchlöcherte Folie auf Plattenelektroden aus verschiedenen Metallen gelegt. Auf diese Weise wurde erreicht, dass in jedem Falle genau die gleiche isolierende Schicht zur Verwendung kam. Die anderen Versuchsbedingungen wie Spitzenabstand, Spitzenspannung, Luftfeuchtigkeit usw. wurden sehr genau konstant gehalten und der Spitzenstrom bei positiver Spitze für jede Plattenelektrode in Abhängigkeit von der Spannung gemessen.

Die Abb. 20 a zeigt das Resultat der Messungen, bei denen der Spitzenabstand 5 mm und die relative Feuchtigkeit 24 % betrug. Es zeigt sich, dass die Stromspannungskennlinie für verschiedene Elektrodenmaterialien bei gleicher isolierenden Schicht stark voneinander abweichen. Um festzustellen, ob dieses wirklich auf die verschiedenen Elektrodenmaterialien und nicht auf andere Faktoren zurückzuführen ist, wurde die gleiche Messung mit negativer Spitze ausgeführt, wobei innerhalb kleiner Messfehler keinerlei Unterschiede festgestellt werden konnten (Abb. 20 b). Dies ist auch nicht anders zu erwarten, wenn der unter b) genannte Prozess der Elektronenbefreiung durch Ionenstoss auf die Metalloberfläche wirklich in den Poren stattfindet.

Die Tatsache, dass der Spitzenstrom für verschiedene Elektrodenmetalle so grosse Unterschiede zeigt, lässt vermuten, dass die Elektronenbefreiung durch Ionenstoss auf die Metalloberfläche am Ende der Lackschichtporen eine wesentliche Rolle für die Aufrechterhaltung des Prozesses bei positiver Spitze spielt. Die für die verschiedenen Elektrodenmetalle erhaltenen Messwerte liegen auch einigermassen in der richtigen Reihenfolge, die nach den wenn auch recht ungenügend bekannten γ-Werten für langsame Ionen [24] und den Elektronenaustrittsarbeiten der verwendeten Metalle zu erwarten ist. Dass diesen Kurven nach γ für Fe höher als für Cu gefunden wird, was im Widerspruch mit den bei KNOLL angegebenen γ-Werten steht, mag auf ungenügende Reinheit des bei den hier beschriebenen Versuchen verwendeten Eisens zurückzuführen sein. Da es sich hier nur um qualitative Versuche handelte, wurde hierauf sowie auf die Einwirkung eventueller leichter Oberflächenverunreinigungen auf den Metallen keinen besonderen Wert gelegt [25].

Die Abhängigkeit des Koronastromes bei positiver Spitze und lackierter Plattenelektrode vom Elektrodenmaterial ist jedoch auch unter Annahme der Möglichkeit c) zu erwarten. Da es nicht unwahrscheinlich ist, dass die an der Metalloberfläche auftretenden Felder genügend gross sind, um Feldemission zu verursachen (vgl. Abb. 5), kann diese Möglichkeit also nicht ausgeschlossen werden. Welcher der beiden Prozesse b und c den wirksameren Anteil liefert, konnte bisher nicht entschieden werden. In beiden Fällen durchlaufen die Elektronen die Poren von der Metalloberfläche zur positiven Spitze und ionisieren die Gasmoleküle im hohen Felde der Poren.

Auch mit positiver Spitze wurden die selben Versuchsreihen durchgeführt wie mit negativer Spitze. Die Versuchsergebnisse sind qualitativ denen mit negativer Spitze erhaltenen recht ähnlich, waren jedoch wesentlich schlechter zu reproduzieren. Es sollen deshalb hier nur in aller Kürze die wichtigsten Ergebnisse wiedergegeben werden.

Auch für die positive Spitze gilt, dass bei Spitzenabständen von weniger als 1 cm der stromverstärkende Effekt der Lackschicht wesentlich stärker hervortritt als bei grossen Abständen und ebenfalls eine starke Abhängigkeit von der Luftfeuchtigkeit gefunden wird. Die Erklärung dürfte hier die gleiche wie die für die negative Spitze

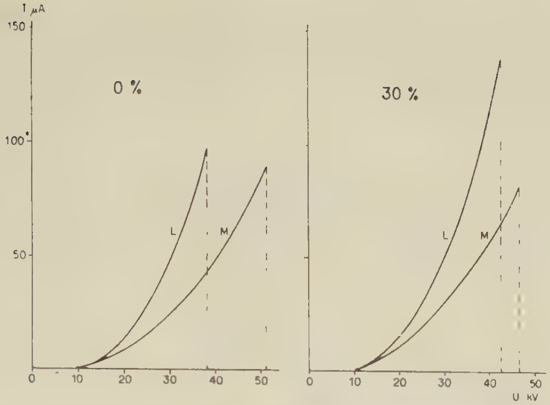

bb. 21. Strom-Spannungskennlinie bei verschiedener Luftfeuchtigkeit. Spitzenabstand 7,5 cm. Spitze positiv.

egebene sein. Auffallend ist, dass bei grossen Spitzenabständen und 30 % relative uftfeuchtigkeit der Unterschied der Durchschlagspannungen mit und ohne Lackhicht gering war und ausserdem die Durchschlagspannung mit Lackschicht starke chwankungen aufwies. Im Gegensatz zur negativen Spitze schien hier die relative uftfeuchtigkeit eine starke Rolle für die Bestimmung der Durchschlagspannung zu pielen. Die Abb. 21 zeigt die Spannungsabhängigkeit des Koronastromes bei erschiedenen Luftfeuchtigkeiten und einem Spitzenabstande von 7,5 cm. Zu einer laren Entscheidung, ob der Effekt der Lackschicht auf die Durchschlagspannung uch dann noch verhanden ist, wenn die positive Spitze durch eine Kugel von 38 mm urchmesser ersetzt wurde, konnte nicht gekommen werden, da bei den zur Verigung stehenden Abständen nie ein Koronastrom vor Eintritt des Durchschlages eobachtet werden konnte. Ein Einfluss der Lackschicht auf die Durchschlagspannung ar somit nicht zu erwarten und wurde auch nicht gefunden. Die Untersuchungen Überdrucken bis zu 6 atü Luft bei 16 mm Spitzenabstand und 0 % relative Feuchgkeit ergaben ähnlich wie bei der negativen Spitze ein langsames Verschwinden des ackschichtseffektes bei höheren Drucken.

ZUSAMMENFASSUNG

An einer Spitze, die einer Plattenelektrode gegenüber steht, wird durch Anlegen iner hohen Spannung in Luft von Atmosphärendruck eine Koronaentladung erzeugt. s wurde gefunden, dass der Koronastrom sehr viel grösser wird, wenn die Plattenlektrode mit einer Schellackschicht überzogen ist, was ebenfalls die Funkendurchhlagspannung von der Spitze zur Platte stark senkt. Es wird gezeigt, dass der rund für dieses unerwartete Verhalten feine Poren in der Lackschicht sind, in enen wegen der hohen Aufladung der Lackschichtoberfläche die Luft ionisiert wird. urch diese zusätzlichen Ionisationsbereiche wächst der Koronastrom und beeinflusst benfalls die Durchschlagspannung. Der Einfluss der Lackschicht auf Koronastrom nd Durchschlagspannung findet sich bei negativer und positiver Spitze. Der gleiche ffekt kann auch mit anderen isolierenden Schichten gefunden werden. Es wird ezeigt, dass der Lackschichteffekt zum Nachweis von Poren in Lackschichten und

isolierenden Folien benutzt werden kann. Weiterhin wird der Einfluss einer Lackschicht auf den Koronastrom und die Durchschlagspannung unter verschiedenen Versuchsbedingungen untersucht und auf die Auswirkungen des Effektes in der Hochspannungstechnik hingewiesen.

Für seine Unterstützung und sein stetes inspirierendes Interesse an dieser Arbeit möchte ich Herrn Professor S. von Friesen meinen warmen Dank aussprechen.

Physikalisches Institut der Universität Lund, im Mai 1954.

LITERATUR

1. A. Bouwers, Elektrische Höchstspannungen (1939).
2. R. Gänger, Der elektrische Durchschlag von Gasen (1953).
3. L. B. Loeb, J. Appl. Phys. *19*, 882 (1948).
4. C. H. Hertz, Arkiv för Fysik *7*, 399 (1953).
5. E. Warburg, Ann. d. Ph. (4) *2*, 301 (1900).
6. F. W. Peek, Dielectric Phenomena in High Voltage Engineering, S. 54 u. 116 (1929).
7. W. N. English, Phys. Rev. *74*, 170 (1948).
8. W. E. Slepian and Berkey, W. E., J. Appl. Phys. *11*, 765 (1940).
9. Hansen, ASEA's tidning *36*, 2 (1944).
10. R. C. Bacon, J. J. Smith, and F. M. Rugg, Ind. & Eng. Chem. *40*, 161 (1948).
11. H. Paetow, ZS f. Phys. *111*, 770 (1939).
12. W. W. Kittelberger, Ind. & Eng. Chem. *44*, 326 (1952).
13. H. Grinsfelder, Ind. & Eng. Chem. *44*, 563 (1952).
14. W. Birett, Siemens ZS *16*, 1 (1936).
15. E. Kühn, ETZ *56*, 609 (1935).
16. L. B. Loeb, Rev. Mod. Phys. *20*, 151 (1948).
17. T. E. Allibone and Meek, J. M., Proc. Roy. Soc. A *169*, 246 (1938).
18. H. Raether, Erg. d. exakten Naturwiss. *22*, 73 (1949).
19. J. Franck, Ann. d. Phys. *21*, 972 (1905).
20. H. Schüler, L. Reinebeck, und Michel, A., ZS d. Naturf. *9 a*, 279 (1954).
21. Engel-Steenbeck, Elektrische Gasentladungen, *Bd. 1*, S. 168 (1932).
22. G. L. Weissler, Phys. Rev. *63*, 96 (1943).
23. W. Weizel und Meyer, C., ZS f. Phys. *136*, 263 (1953).
24. M. Knoll, Gasentladungstabellen, S. 79 (1935).
25. Llewellyn Jones, F., and Morgan, C. G., Proc. Roy. Soc. A *218*, 88 (1953).

Tryckt den 30 december 1954

Uppsala 1954. Almqvist & Wiksells Boktryckeri AB

ARKIV FÖR FYSIK Band 9 nr 2

Mitgeteilt am 22. September 1954 durch MANNE SIEGBAHN und BENGT EDLÉN

Die Einwirkung von Lackschichten auf die Wechselstromkorona an Spitzen und Drähten

Von C. H. HERTZ

Mit 3 Abbildungen im Text

Zusammenfassung

In der vorliegenden Arbeit wird die Einwirkung von Lackschichten auf Wechselstromkoronaentladungen untersucht. Als erstes wird die Spitzenkorona über einer mit Lack überzogenen Metallplatte betrachtet, wobei ähnliche Erscheinungen wie bei der Gleichstromkorona gefunden werden. Danach wird die Wechselstromkorona am freien Drahte untersucht, die für Hochspannungsfreileitungen von besonderem Interesse ist. Es wird gezeigt, dass das Aussehen der Wechselstromkorona am sauberen Drahte sich stark von dem an einem lacküberzogenen Drahte unterscheidet und dass im letzteren Falle die Koronaeinsatzspannung tiefer und die Koronaverluste höher liegen. Die Versuchsergebnisse können auch hier wieder durch die isolierenden Eigenschaften der Lackschicht erklärt werden. Der Zusammenhang zwischen der hier untersuchten Erscheinung und den an technischen Hochspannungsfreileitungen gemachten Erfahrungen wird diskutiert (Alterungserscheinungen, Koronaverluste bei Eisbildung).

1. Einleitung

In einer früheren Arbeit [1] wurde gezeigt, dass der Strom einer Spitzenkorona sich wesentlich erhöht, wenn die gegenüberliegende Elektrode mit gewissen Lackschichten, z.B. Schellack, bedeckt ist. Es konnte nachgewiesen werden, dass der Grund für diesen unerwarteten Effekt die Aufladung der Lackschichtoberfläche durch von der Spitze kommende Ionen ist, welche zu hohen Feldern in den Poren der Lackschicht Anlass gibt. In diesen Poren entstehen hierdurch neue Ionisationsbereiche, was u.a. an den in den Poren auftretenden Glimmerscheinungen zu erkennen ist. Da der Einfluss der Lackschicht auf den Koronastrom bei positiver und negativer Polarität der Spitze gefunden wurde, lag es nahe, ähnliche Untersuchungen auch mit Wechselspannungen (50 Hz) zu machen.

2. Spitzen-Plattengeometrie

Als erstes wurde auch hier die Spitzen-Plattenanordnung untersucht, wobei wiederum das in [1] Abb. 11 angewandte Gefäss zur Verwendung kam. Die im Folgenden beschriebenen Versuche wurden in Luft von Atmosphärendruck, 21° C und 28 %

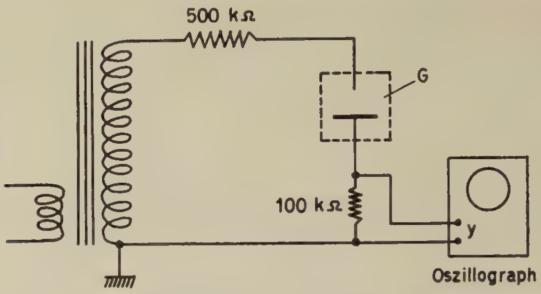

Abb. 1. Versuchsanordnung zur Aufnahme von Stromoszillogrammen der Spitzenkorona über einer Plattenelektrode.

relativer Feuchtigkeit ausgeführt. Die verwendete Schaltung zeigt Abb. 1. Das Stromoszillogramm wurde ähnlich wie bei Cobine [2] mit dem Kathodenstrahloszillographen beobachtet. Eine direkte Messung des Koronastromes für sich ist in diesem Falle schwieriger, da neben dem eigentlichen Koronastrom auch auf Grund der Kapazität Spitze–Plattenelektrode eine kapazitive Stromkomponente auftritt. Es wurden jedoch auch solche Messungen durchgeführt, die aber nur die mit dem Oszillographen erhaltenen Ergebnisse bestätigten.

Abb. 2*a–c* zeigen die mit den Oszillographen erhaltenen Stromkurven des Gesamtstromes (= Koronastrom und kapazitiver Strom) für einen Spitzenabstand von 2 cm (Abb. 2*a*, 16 kV_{eff}), 5 cm (Abb. 2*b*, 27 kV_{eff}) und 10 cm (Abb. 2*c*, 44,5 kV_{eff}). Das linke Bild wurde jeweils ohne, das rechte mit einer Lackschicht auf der Plattenelektrode erhalten. Die Spannung wurde wie bei [2] gleichzeitig mitgeschrieben, so dass die Phasenverschiebung des Stromes erkennbar ist. In allen drei Fällen wurde eine Spitzenspannung gewählt, die wenig unter der Durchschlagspannung lag, um einen möglichst grossen Koronastrom zu erhalten.

Abb. 2*a* zeigt deutlich, dass die Koronastromkomponente bei einer lackierten Plattenelektrode (rechtes Bild) wesentlich grösser als die mit unlackierter Plattenelektrode erhaltene (linkes Bild) ist. Im ersteren Falle sind die Koronaverluste dieser Anordnung also wesentlich grösser. Die Oszillogramme zeigen, dass wie erwartet der positive und negative Koronastrom durch die Lackierung der Plattenelektrode vergrössert wird. Dies setzt jedoch voraus [1], dass die Oberfläche der Lackschicht in jeder Halbperiode des Wechselstromes umgeladen wird und die Polarität der Spitze annimmt. Dies muss durch die ersten Ionen, die in jeder Halbperiode von der Spitze kommen, geschehen. Die nachfolgenden Ionen erzeugen dann in den Poren der Lackschicht in der in [1] beschriebenen Weise neue Ionisationsgebiete und tragen so zu einer Vergrösserung des Ionenstromes bei. Auch hier können wieder die Glimmerscheinungen in den Poren visuell beobachtet werden. Man sieht weiterhin (Abb. 2), dass der Lackschichteffekt im Falle einer negativen Spitzenpolarität wesentlich stärker hervortritt als bei positiver Spitze, worauf schon früher [1] hingewiesen wurde.

Vergrössert man den Spitzenabstand auf 5 cm (Abb. 2*b*), so wird der Unterschied zwischen den beiden Oszillogrammen jedoch wesentlich geringer, und bei 10 cm Spitzenabstand (Abb. 2*c*) ist kein Unterschied im Koronastrom mit und ohne Lackschicht mehr zu finden. Die direkten Messungen des Koronastromes ergaben das gleiche Resultat.

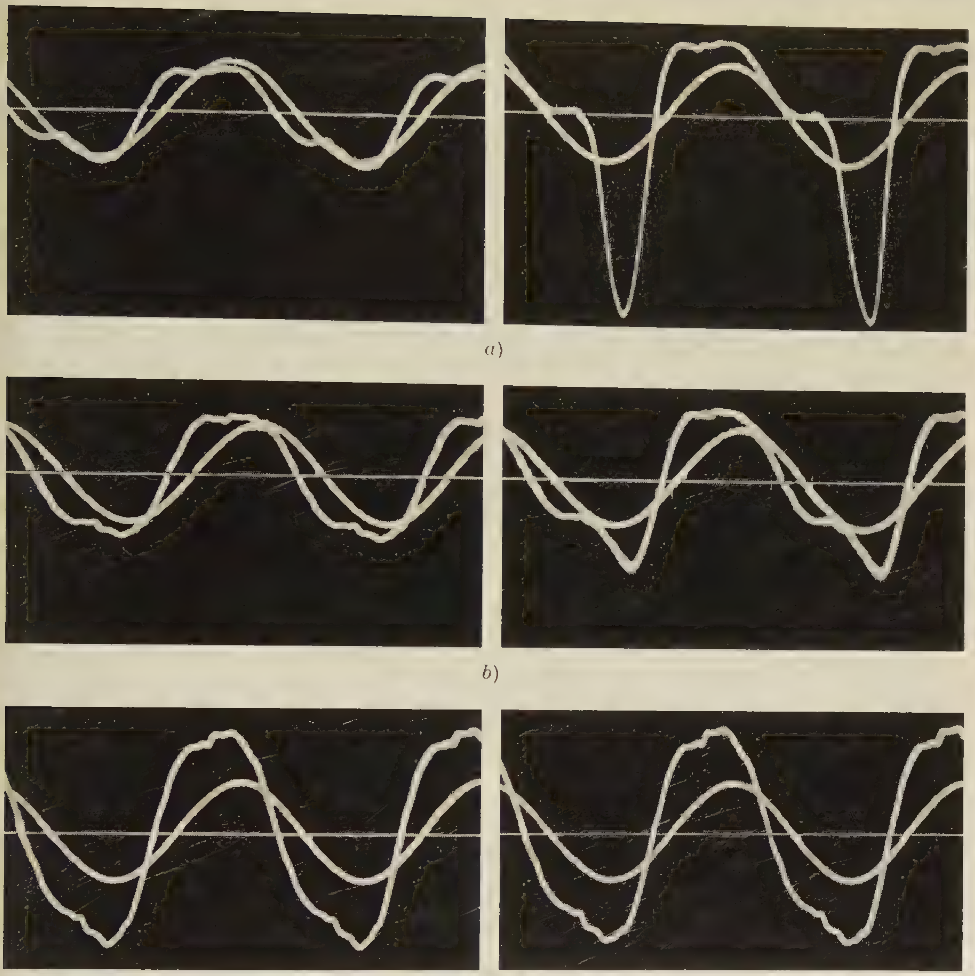

a)

b)

c)

Abb. 2. Oszillogramme des Wechselstromes zwischen Spitze und Plattenelektrode bei verschiedenem Spitzenabstand. — *a*) Spitzenabstand 2 cm, Spitzenspannung 16 kV$_{\text{eff}}$. *b*) Spitzenabstand 5 cm, Spitzenspannung 27 kV$_{\text{eff}}$. *c*) Spitzenabstand 10 cm, Spitzenspannung 44,5 kV$_{\text{eff}}$. — *Linke Bilder:* unlackierte Plattenelektrode. *Rechte Bilder:* lackierte Plattenelektrode.

Zur Veranschaulichung der Strom- und Phasenverhältnisse ist die Spannungskurve der an der Spitze liegenden Wechselspannung mitgeschrieben. Sie entspricht einem Wechselstrom $I_{\max} = 100\ \mu$A durch den Messwiderstand 100 kΩ (Vgl. Abb. 1).

Die Ursache hierfür ist durch die Annahme der oben beschriebenen notwendigen Umladung der Lackschichtoberfläche in jeder Halbperiode durch von der Spitze kommende Ionen zu verstehen. Bei Spitzenabständen von 10 cm und mehr gelangen die Ionen wegen ihrer geringen Wanderungsgeschwindigkeit während einer Halbperiode nicht mehr zur Plattenelektrode. Deshalb kann die Lackschicht nicht während einer Halbperiode entsprechend der Spitzenpolarität aufgeladen werden, weshalb die hohen Feldstärken in den Poren nicht auftreten, die zur Ionisation des Gases in denselben notwendig sind. Der hier gefundene Abstand von ca. 10 cm für die Reichweite der vor der Spitze hin- und herpendelnden Ionenwolken beider Polarität stimmt gut mit dem für Wechselspannungskorona an freien Leiterseilen gefundenen [2, 3] überein.

Die Funkendurchschlagspannung zwischen Spitze und Platte war jedoch unabhängig von der Anwesenheit einer Lackschicht. Dies ist nach den mit Gleichspannung gemachten Erfahrungen zunächst nicht zu erwarten. Da der Durchschlag aber bei positiver Polarität der Spitze bei tieferen Spannungen eintritt als bei negativer, so ist zu erwarten, dass der Funkendurchschlag bei der mit Wechselspannung von 50 Hz betriebenen Spitze während der positiven Halbwelle eintritt. Tatsächlich stimmen auch die mit positiver Gleichspannung gemessenen Durchschlagspannungen innerhalb eines Fehlers von 4 % mit den maximalen Wechselspannungswerten an der Spitze beim Durchschlag überein. Bei der Untersuchung der Durchschlagspannung mit positiver Spitze bei verschiedener Luftfeuchtigkeit [1] wurde jedoch bei 30 % rel. Luftfeuchtigkeit sehr wenig Unterschied mit und ohne Lackschicht gefunden. Da die hier beschriebenen Untersuchungen bei einer rel. Luftfeuchtigkeit von 28 % durchgeführt wurden, ist ein solcher Unterschied also nicht zu erwarten.

3. Freihängende Drähte

Eine technisch wesentlich wichtigere Form der Wechselstromkorona ist die Korona an Hochspannungsfreileitungen, die zu sehr beträchtlichen Verlusten führen kann und deshalb bei Spannungen über 100 kV den Seilradius der Leitungen bestimmt. Da in den letzten Jahren eine Tendenz vorhanden ist, für Hochspannungsfernleitungen Spannungen von ungefär 400 kV zu verwenden, sind viele Versuche über die Koronaverluste an verschiedenen Seiltypen und unter variierenden Witterungsbedingungen gemacht worden. Eine Zusammenfassung dieser Arbeiten hat in letzter Zeit Gänger [3] gegeben. Die Versuchsergebnisse zeigen, dass die die Verluste hervorrufenden Faktoren noch recht wenig bekannt sind und ein theoretisches Verständnis der Resultate oft schwer möglich ist. Es liegt deshalb nahe zu untersuchen, ob eine isolierende Schicht auf einem freihängenden Leitungsseile auch die Wechselstromkoronaverluste beeinflusst. Dass dies für Gleichspannungen der Fall ist, geht aus den Messungen von Kühn [4] hervor. Kühn fand, dass das Kupferoxyd an gealterten Kupferfreileitungen die Verluste stark heraufsetzte, was durch die bei [1] gefundene und erklärte Einwirkung von Kupferoxyd auf den Koronastrom zu verstehen ist.

Der Mechanismus der Wechselstromkorona an freihängenden Drähten ist von verschiedener Seite beschrieben [5] und von Holm [6] berechnet worden. Bei diesen Überlegungen wird eine ideal glatte und leitende Drahtoberfläche vorausgesetzt, so dass sich der Draht oberhalb der Koronaeinsatzspannung mit einer leuchtenden Koronahaut gleichmässig überzieht, die aus mit Wechselspannungsfrequenz hin- und herpendelnden elektrischen Ladungsträgern entgegengesetzter Polarität besteht [2, 5]. Da bei Hochspannungsfreileitungen eine solche Koronahaut erst bei Spannungen auftritt, die wesentlich über der Einsatzspannung von einzelnen büschelförmigen Koronaentladungen an der Leitung liegt [3, 7, 8, 9], muss nach anderen Ursachen für das Auftreten der beobachteten punktförmigen Büschelentladungen gesucht werden. Als eine dieser Ursachen werden Kratzer und Unebenheiten am Seile angegeben [3, 7, 9], die durch Angriff von Werkzeugen usw. entstanden sind. Weiterhin wird in vielen Arbeiten die Rauhigkeit der Leiteroberfläche hierfür verantwortlich gemacht. Durch Abtragen dieser Rauhigkeit und Unebenheiten bei längerem Betriebe der Freileitungen wird der allgemein beobachtete Effekt erklärt, dass sich die Koronaverluste einer Freileitung nach einer Betriebszeit von ½–1 Jahr oft erheblich vermindern [3, 10]. Weitere Ursachen, die zu starken Verlusten an Freileitungen führen, sind Wassertropfen, die sich bei Regen and den Seilen bilden [7, 11], Fettschichten [10, 11], sowie Rauhreif [11] und Eisüberzüge der Seile [12, 13].

Da das Aussehen der in der Praxis an Hochspannungsfreileitungen gefundenen Koronaentladungen sich von den theoretisch erwarteten und auch an idealen Drähten beobachteten stark unterscheidet, wurde versucht, ob ausser Unebenheiten und Kratzern auf dem Leiter eventuell auch die Anwesenheit einer glatten Lackschicht das Koronaverhalten derselben ändert. Zu diesem Zwecke wurde ein Aluminiumrohr von 8 mm Durchmesser und 1,8 m Länge auf der Drehbank mit feinem Schmirgelpapier von allen isolierenden Schmutzteilchen befreit und danach poliert, so dass eine reine glatte Oberfläche entstand. Danach wurde die eine Hälfte des Rohres mit einer dünnen sauberen Zaponlackschicht überzogen, die keinerlei Spitzen oder Unebenheiten aufwies. Die Dicke der Lackschicht betrug ca. 5 μ. Das Rohr wurde mit der Hochspannungselektrode eines Röntgentransformators verbunden und wagerecht in einem Zimmer aufgehängt. Der Abstand zu den Wänden des Zimmers war überall grösser als 1 m.

Abb. 3 zeigt das Aussehen des Rohres bei verschiedenen Spannungen im Dunkeln. In allen Aufnahmen verläuft das Rohr etwa in der Mitte des Bildes horizontal von einer Bildseite zur anderen, wobei die rechte Hälfte mit Zaponlack überzogen war (der Pfeil in Abb. 3*a* zeigt die Grenze der Zaponlackschicht an). Die relative Luftfeuchtigkeit betrug 20 %, die Temperatur 22° C.

Der Unterschied im Aussehen der Korona in den beiden Fällen ist deutlich zu erkennen: an dem lackierten Teile des Rohres treten Koronabüschel auf [7, 8], während der saubere Teil sich mit der theoretisch erwarteten Koronahaut überzieht (Abb. 3*d*). Weiterhin wird beobachtet, dass bei einer Spannung von 75,5 $\mathrm{kV_{eff}}$ keine Korona mehr an dem unlackierten Teil des Rohres auftritt, während man die Spannung bis unter 68–70 $\mathrm{kV_{eff}}$ senken muss, bis die letzten Büschelentladungen an dem lackierten Teile verschwinden. Um die Büschelentladungen nach dem Erlöschen wieder zur Zündung zu bringen, muss man die Spannung bis auf 72–75 $\mathrm{kV_{eff}}$ erhöhen. Die sichtbare Einsatzspannung der Büschelentladungen auf der Lackschicht unterscheidet sich also stark von ihrer Löschspannung, sie liegt jedoch fast immer unter der Einsatzspannung der Koronahaut auf dem sauberen Teile des Rohres. Die sichtbare Einsatz- und Löschspannung für die „normale" Korona auf dem sauberen Teile des Rohres unterschieden sich dagegen nur um höchstens 1 kV und waren wesentlich besser definiert als die des lackierten Rohrteiles. Befand sich eine Koronaentladung in der Nähe des Rohres, z. B. an der Aufhängung desselben, so setzte diese die Einsatzspannung (sehr wesentlich) und ebenfalls die Löschspannung der Büschelentladungen am lackierten Rohre herunter.

Weiterhin wurde ein gewisser Einfluss der Luftfeuchtigkeit gefunden. Bei höherer Luftfeuchtigkeit verringert sich der Unterschied zwischen Einsatz- und Löschspannung des lackierten Rohrteiles und betrug bei einer relativen Feuchtigkeit von 70 % nur noch 0,5 kV. Dagegen schien die Senkung der Koronaeinsatzspannung durch die Lackschicht unabhängig von der Luftfeuchtigkeit immer etwa 2–3 kV zu betragen.

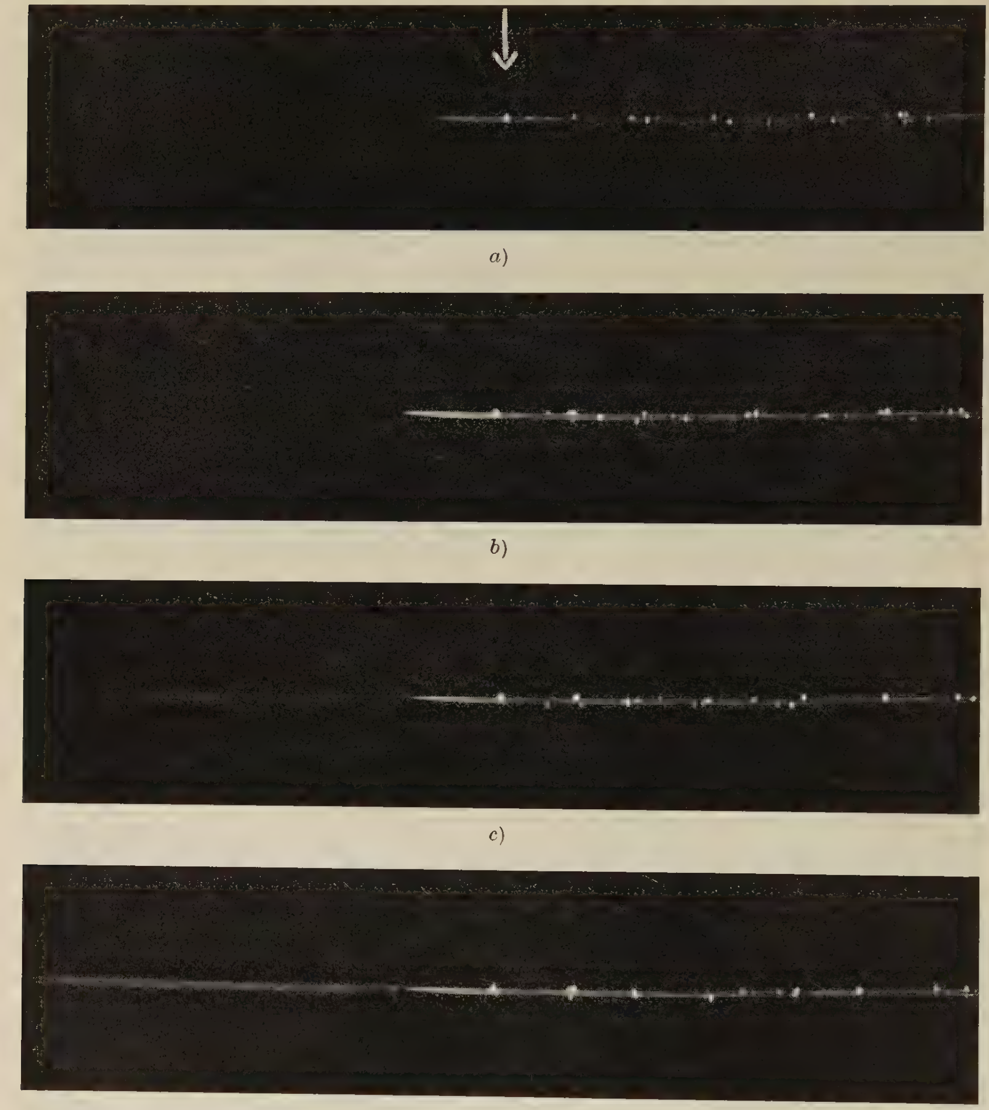

a)

b)

c)

d)

Abb. 3. Wechselstromkorona an einem Aluminiumrohr (Durchmesser 8 mm) bei verschiedenen Spannungen. Die rechte Hälfte des Rohres ist mit einer dünnen Zaponlackschicht überzogen. — *a)* 70,5 kV_{eff}, *b)* 75,5 kV_{eff}, *c)* 76 kV_{eff}, *d)* 77,5 kV_{eff}.

Sobald Büschelentladungen auftreten, überzieht sich das Rohr in der unmittelbaren Umgebung derselben auch mit einer Koronahaut. Dies geschieht anscheinend unabhängig davon, ob das Rohr an dieser Stelle lackiert ist oder nicht, was man auf den Abb. 3 erkennen kann. Die erste Büschelentladung von links gesehen sitzt nämlich genau an der Stelle, wo die Lackschicht anfängt, d.h. in der Mitte des Rohres (Pfeil in Abb. 3*a*). Links von dieser Büschelentladung beobachtet man eine von ihr unterhaltene Koronahaut auch auf dem unlackierten Teil des Rohres (Abb. 3*b* und 3*c*). Diese Koronahaut ist vermutlich auf die Herabsetzung der Durchbruchfeldstärke der Luft durch Photoionisation in der Nähe einer Büschelkorona zurückzuführen.

Auch die geringere Einsatz- und Löschspannung der Weckselstromkorona am lackierten Drahte ist wieder unter Annahme der Poren in der Lackschicht zu verstehen. Die radial zum Rohre hin- und herpendelnden Ionenwolken entgegengesetzter Polarität laden im Takte der Wechselspannung wechselweise die Lackschicht auf. Diese Aufladung gibt in den Poren der Lackschicht zu einer höheren Feldstärke Anlass als die Feldstärke, die sich ohne Lackschicht an der Rohroberfläche ausbildet, da sich die in den Poren durch die Aufladung der Lackschicht entstandene Feldstärke zu der Feldstärke am unlackierten Rohre addiert. Dies führt zu einer wesentlich tieferen Löschspannung der Wechselstromkorona am lackierten Drahte. Auch die Koronaeinsatzspannung ist etwas erniedrigt, da sich immer einige Ionen in der Luft befinden, die eine Aufladung der Lackschicht im Takte der Wechselspannung bewirken.

Nach dieser Erklärung sollte jedoch ebenfalls eine gleichmässige Koronahaut über der Lackschicht erwartet werden, da sich in dieser nach früheren Messungen [1] etwa 500 Poren/cm^2 befinden. Das Auftreten der Koronabüschel ist aber wohl auf eine gegenseitige Beeinflussung derselben zurückzuführen, wie sie schon von anderer Seite bei Regentropfen an Hochspannungsfreileitungen beobachtet worden ist [3]. Die Bildung von Stellen besonders hoher Ionisation (Büschelentladungen) auf der Lackoberfläche ist etwa durch folgende Überlegung zu verstehen. An einer Stelle, wo durch statistischen Zufall die Koronaentladung etwas stärker ist, wird auch die Lackschicht stärker aufgeladen, wodurch die Voraussetzungen für eine Koronaentladung an diesem Punkt begünstigt werden. Dies bewirkt eine weitere Verstärkung der durch den statistischen Zufall geschaffene Ungleichmässigkeit der Ionendichte über der Rohroberfläche, was schliesslich zu einer Entstehung einer Büschelentladung an dieser Stelle führt. Dies gilt auch für die Wechselstromkorona, obwohl hier die Polarität der Oberflächenladung auf der Lackschicht dauernd mit der Wechselspannungsfrequenz wechselt, da die Ionenkonzentration in der Nähe der Büschelentladungen immer am grössten und daher die nötige statistische Ungleichmässigkeit beim Einsetzen der folgenden Spannungswelle vorhanden ist. Schaltet man die Wechselspannung zwischen zwei Versuchen vollkommen ab, so findet man, dass die meisten Büschelentladungen sich beim erneuten Einschalten an anderen Stellen auf der glatten Lackschicht ansetzen. Dieses spricht gegen die Annahme von Unregelmässigkeiten oder Rauhigkeiten der Lackschicht, die ein bevorzugtes Ansetzen der Büschelentladungen an bestimmten Stellen bewirken würden.

Überzieht man den sauberen Teil des Rohres mit einer Fettschicht, so treten auch hier Büschelentladungen auf. Diese liegen oft dichter nebeneinander als die bei der Lackschicht beobachteten, und ändern öfters ihren Ansatzpunkt am Rohre. Die Koronaeinsatz- und Löschspannung zeigen noch ausgeprägter die mit der Lackschicht gefundene Tendenz, jedoch änderten sie ihre Werte stark mit der Dicke und der Qualität der verwendeten Fettschicht. Es wurden hierbei Werte gefunden, die bis zu 20 % unterhalb des Wertes der Einsatzspannung am unlackierten Rohre lagen. Diese hier beschriebene Ähnlichkeit zwischen Lackschicht und Fettschicht ist nach den in [1] gefundenen Resultaten zu erwarten.

Eine Voraussetzung zur Vermeidung von Büschelentladungen am unlackierten Teil des Rohres ist, dass das Rohr gut gereinigt ist und keine grösseren Staubpartikel oder isolierenden Teilchen an dem Rohre haften. Flache Paraffin- oder Fettflecke von nur 1–3 mm Durchmesser geben Anlass zu Büschelentladungen, deren Einsatz- und Löschspannung ebenfalls unter der Einsatzspannung der Koronahaut beim reinen Rohre liegt. Die Messergebnisse variierten sehr je nach Art und Dicke der Schichten, die Erniedrigung der Einsatzspannung konnte aber bis zu 20 % der normalen Einsatzspannung betragen.

Die Erklärung für dieses Verhalten ist die gleiche wie die oben für die Lackschicht gegebene. Auf den isolierenden Paraffin- oder Fettschichten können sich ebenfalls Ladungen ansammeln, die zu einer Feldverzerrung an der Grenze Isolator–Metall und somit zu einer Erhöhung der Feldstärke an der Rohroberfläche führen. Dass dies wirklich der Fall ist, kann mit der bei [1] angegebenen Anordnung zur Prüfung von Lackschichten nachgewiesen werden. Als weiterer Beweis hierfür kann angeführt werden, dass die einzige Stelle, an der bei den in Abb. 3 gezeigten Versuchen immer eine Büschelentladung auftrat, der Anfang der Lackschicht in der Mitte des Rohres war. Die anderen Büschelentladungen wechselten fast immer Platz, wenn die Wechselspannung kurzzeitig abgeschaltet wurde. Die Grenze Isolator–Metall kann also sowohl bei Gleich- wie bei Wechselspannung wie eine Spitze wirken und günstige Verhältnisse für das Auftreten von Koronaentladungen schaffen. Die Ursache für die an Hochspannungsfreileitungen beobachteten Büschelentladungen können also entweder Spitzen und Kratzer oder isolierende Schichten oder Partikel auf der Leiteroberfläche sein.

Diese Feststellung lässt verschiedene an Hochspannungsfreileitungen gemachte Erfahrungen verstehen. Es ist von verschiedener Seite beobachtet worden [10, 13], dass Fett an den Leitungsseilen die Koronaverluste erhöht, welches nach dem Obigen hauptsächlich auf die Isolationseigenschaften der Fettschicht zurückgeführt werden muss [1]. Ein Verdampfen der Fettschicht an den Stellen der Büschelentladungen kann die Ausbildung von Korona weiterhin begünstigen, was erklären würde, weshalb die Erniedrigung der Koronaeinsatzspannung bei Fettschichten grösser als bei Lackschichten gefunden wurde. Durch gründliches Entfetten der Leitung [10, 11] verringern sich die Verluste stark, was nach der hier angeführten Erklärung erwartet werden muss. Der gleiche Rückgang der Verluste wird nach etwa einjähriger Alterung der Seile am Maste beobachtet. Dies kann auf langsames Abtragen und Verkohlen der isolierenden Fettschichten zurückgeführt werden [7], wodurch diese ihre guten Isolationseigenschaften verlieren. Die starke Erhöhung der Verluste durch Eisschichten [12, 13] müssen vermutlich ebenfalls auf die Isolationseigenschaften des Eisüberzuges auf dem Seile zurückgeführt werden, da Eis auch einen relativ grossen spezifischen Widerstand hat [14]. Schliesslich dürfte das von Strigel [9] gefundene Resultat, dass oxydierte Kupferseile bei hohen Koronaverlusten grössere Verluste zeigen als reine Seile, auch auf der hier behandelten Erscheinung beruhen.

Um die Vergrösserung der Koronaverluste am lackierten Draht auch elektrisch nachzuweisen, wurde wieder die in Abb. 1 gezeigte Anordnung benutzt, anstelle der Spitze wurde hier aber ein 15 m langer Kupferdraht mit einem Durchmesser von 4 mm an die Hochspannungselektrode des Transformators angeschlossen. Der Draht war in einem Gange wagerecht ausgespannt, der Abstand zu den Wänden betrug überall mindestens 80 cm. Die relative Luftfeuchtigkeit während des Versuches war 22 %. Wie bei den in Abb. 2 gemachten Messungen wurde die Summe des kapazitiven

Stromes und Koronastromes mit dem Oszillographen bei verschiedenen Spannungen bestimmt. Auch hier wurde gefunden, dass die Koronaverluste des sauberen Drahtes geringer als die des lackierten Drahtes waren.

Herrn Professor S. VON FRIESEN sei an dieser Stelle für sein stetes Interesse an dieser Arbeit gedankt.

Physikalisches Institut der Universität Lund, im September 1954.

LITERATUR

1. HERTZ, C. H., Arkiv för Fysik *9*, 1 (1954).
2. COBINE, J. D., Gaseous Conductors (1941).
3. GÄNGER, B., Elektrischer Durchschlag von Gasen (1953).
4. KÜHN, E., ETZ *56*, 609 (1935).
5. ENGEL, A. v. und STEENBECK, M., Elektrische Gasentladungen, Bd. 2 (1934).
6. HOLM, R., Wiss. Veröff. Siemens-Werke *4*, 14 (1925).
7. CAHEN, F. und PÉLISSIER, R., Bull. S.F.E. *6*, VIII, 111 (1948).
8. LÄPPLE, H., ETZ *65*, 25 (1944).
9. STRIGEL, R., Wiss. Veröff. Siemens-Werke *13*, 27 (1934).
10. CAROLL, J. S. and COZZENS, B., A.I.E.E. *52*, 178 (1933).
11. BELDI, F., CIGRE *408* (1948).
12. AILLERT, P. und CAHEN, F., CIGRE *410* (1948).
13. PEEK, F. W., Dielectric Phenomena in High Voltage Engineering (1929).
14. JOHNSTONE, J. H. L., The electrical resistance and temperature coefficient of ice. Proc. Trans. Nova Scotian Inst. Science *13*, 126 (1912).

Tryckt den 30 december 1954

Uppsala 1954. Almqvist & Wiksells Boktryckeri AB

ARKIV FÖR FYSIK Band 9 nr 3

Communicated 22 September 1954 by MANNE SIEGBAHN

Proton groups from deuteron bombardment of Ne^{20} by magnetic analysis

Part II

By KATARINA AHNLUND

With 1 figure in the text

Introduction

An earlier report [ref. 1] described a magnetic analysis, performed at the Nobel Institute, of two proton groups of long range from the reaction $Ne^{20}(d,p)Ne^{21}$ obtained with thin separated Ne^{20}-targets. They correspond to transitions to the ground state and first excited state in the nucleus Ne^{21} and had previously been analysed magnetically by VAN PATTER *et al.* [2, 3]. The work has been extended to a search for the next two proton groups—earlier most accurately studied with range methods by ZUCKER and WATSON [4] and MIDDLETON and TAI [5]. In Table 2 the results of the present work are summarized together with corresponding data from refs. 2–5.

Procedure and results

The experimental procedure is described in refs. 1 and 6. The energy of the deuterons from the Cockcroft-Walton accelerator was 855 keV and the observation angles of the nuclear spectrometer relative to the incident deuteron beam were $\theta = 134.7^\circ$ and 91.0°. The solid angle of the spectrometer was 0.43×10^{-2} steradians and detection in nuclear emulsions was used.

The group Q_3 gave about 1,000 proton tracks in the plates at $\theta = 134.7^\circ$ by 2400 μC deuteron bombardment on the target. The group Q_2 did not appear at any of the two observation angles in the energy region supervised (see Table 1). Its intensity at our experimental conditions must be less than 4% of the intensity of Q_0 as determined by subsequent runs at one target spot. The approximate relative intensities at $\theta = 134.7^\circ$ are given in Table 1.

The reaction energy Q_3 was measured by comparison with protons of known energy from $O^{16}(d,p)O^{17}$ $Q_0 = 1.917 \pm 0.004$ MeV. See Fig. 1. The distance between

Table 1. Relative intensities of proton groups.

Group	Q_0	Q_1	Q_2	Q_3
Intensity	1	1	<0.04	2

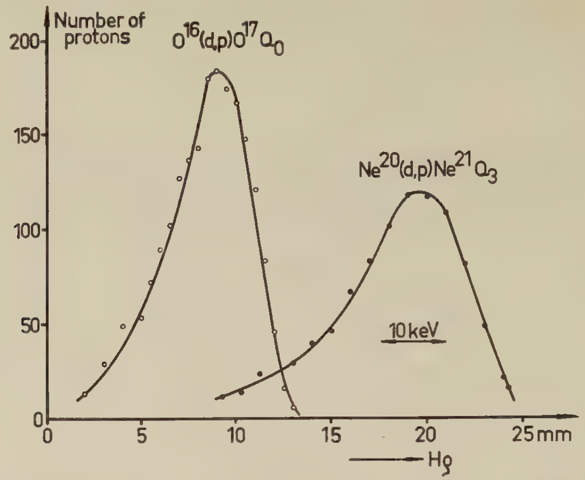

Fig. 1. Spectra of protons from $O^{16}(d,p)O^{17}$ at $\theta = 134.7°$ and from $Ne^{20}(d,p)Ne^{21}$ at $\theta = 91.0°$. Deuteron energy 853 keV. Deuteron bombardment 320 μC on the O^{16}-target and 2400 μC on the Ne^{20}-target. The number of tracks/0.8 mm plate is given in the figure. An oxidized O^{16}-target on Cu and a separated Ne^{20}-target on Ag were used.

the peaks was determined from the high energy edges using the minimum angle and external layer corrections. We get for $Ne^{20}(d,p)Ne^{21}$ the reaction energy $Q_3 = 1.738 \pm 0.008$ MeV.

Table 2. Recent experimental Q-values of $Ne^{20}(d,p)Ne^{21}$ in MeV.

	ZUCKER-WATSON 50 [ref. 4]	MIDDLETON-TAI 51 [ref. 5]	v. PATTER *et al.* 51 [refs. 2, 3]	Present work
Q_0	4.50 ± 0.09	4.54 ± 0.04	4.529 ± 0.007	4.526 ± 0.009 [ref. 1]
Q_1	4.19 ± 0.07	4.21 ± 0.03	4.177 ± 0.010	4.177 ± 0.009 [ref. 1]
Q_2	2.73 ± 0.06	2.86 ± 0.04		(No group 2.62–2.96 MeV)
Q_3	1.68 ± 0.07	1.75 ± 0.02		1.738 ± 0.008

ACKNOWLEDGEMENT

Tekn. lic. S. THULIN kindly prepared the separated Ne^{20}-targets in the electromagnetic isotope separator of the Nobel Institute.

REFERENCES

1. AHNLUND, K., Ark. f. Fys. *7*, nr 14, 155 (1953).
2. VAN PATTER, D. M., SPERDUTO, A., ENDT, P. M., BUECHNER, W. W., and ENGE H. A., Phys. Rev. *85*, 142 (1952).
3. SPERDUTO, A., BUECHNER, W. W., and VAN PATTER, D. M., M.I.T. Progress Report (May 1951).
4. ZUCKER, A., and WATSON, W. W., Phys. Rev. *78*, 14 (1950).
5. MIDDLETON, R., and TAI, C. T., Proc. Phys. Soc. *64*A, 801 (1951).
6. MILEIKOWSKY, C., Ark. f. Fys. *7*, nr 8, 89 (1953).

Tryckt den 30 december 1954

Uppsala 1954. Almqvist & Wiksells Boktryckeri AB

ARKIV FÖR FYSIK Band 9 nr 4

Communicated 8 September 1954 by MANNE SIEGBAHN and ERIK HULTHÉN

Auger transitions in Bi^{212} (ThC)

By MILORAD MLADJENOVIĆ[1] and HILDING SLÄTIS

With 2 figures in the text

Introduction

The energy of a KLL Auger electron $E_{KL_pL_q}$ may be represented by the relation

$$E_{KL_pL_q} = E_K^Z - E_{L_p}^Z - E_{L_q}^{Z+\Delta Z}$$

where E_K^Z and $E_{L_p}^Z$ are the binding energies of the K and L_p electrons respectively, while $E_{L_q}^{Z+\Delta Z}$ is the binding energy of an L_q electron in an atom already once ionized [1]. If the Auger transition is taking place in an atom with the charge number Z, then one can expect for $E_{L_q}^{Z+\Delta Z}$ a value between $E_{L_q}^Z$ and $E_{L_q}^{Z+1}$, that is

$$E_{L_q}^Z < E_{L_q}^{Z+\Delta Z} \leq E_{L_q}^{Z+1}$$

The increase in binding energy is due to the reduction of screening caused by the absence of an L_p electron. Quantitatively, the reduction of screening may be described by an effective incremental charge ΔZ, defined by [1]

$$\Delta Z = \frac{E_{L_q}^{Z+\Delta Z} - E_{L_q}^Z}{E_{L_q}^{Z+1} - E_{L_q}^Z} \tag{1}$$

BERGSTRÖM and HILL have recently measured the KLL Auger electrons from mercury and found that ΔZ is equal to 0.55 for L_{I} and L_{II} electrons while for L_{III} elctrons it is equal to 0.76. Earlier measurements of ROBINSON and CASSIE [2] give $\Delta Z = 0.75$ for L_{I} electrons of copper.

In order to obtain the value of ΔZ with an accuracy of ± 10 % it is necessary in the case of heavy elements to have the $B\varrho$ values of Auger electrons measured with an accuracy of 5 parts in 10,000. The active deposits of radon and thoron represent convenient sources for accurate energy measurements. Since the earlier measurements of the Auger spectra of Bi^{212} (ThC) and Bi^{214} (RaC) made by ELLIS [3], and of Bi^{214} (RaC) made by MLADJENOVIĆ and SLÄTIS [4], were made with an accuracy of 1 ‰, we have undertaken a remeasurement of the Auger spectrum of Bi^{212} in order to obtain the values of ΔZ for KLL Auger electrons accurate within ± 10 %.

---

[1] On leave from the Institute for Nuclear Sciences "Boris Kidrič", Beograd.

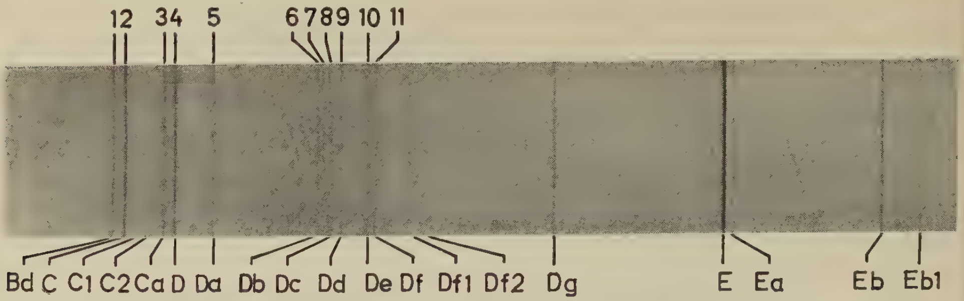

Fig. 1. Auger lines in the beta spectrum of ThB + C + C″ recorded photographically in a permanent magnet beta ray spectrometer.

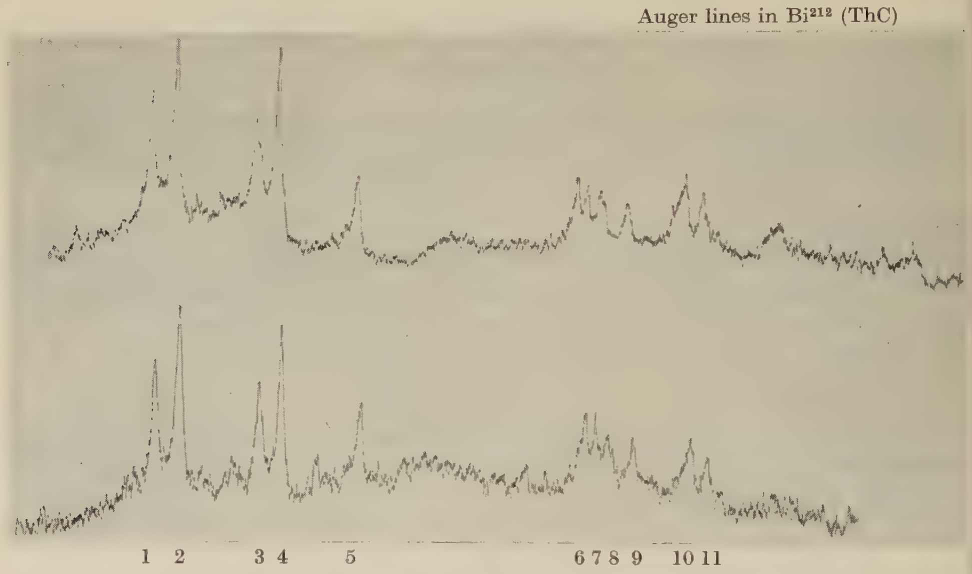

Fig. 2. Microphotometer record of the Auger lines shown in Fig. 1.

Measurements

The measurements were made with the permanent magnet beta ray spectrometer described by SLÄTIS [5]. Figs. 1 and 2 show a reproduction of the Auger lines obtained and a microphotometer record of the spectrum, respectively. Line No. 10 very probably consists of two unresolved lines. A number of low intensity peaks may be present on the microphotometer record. They are not included into the analysis.

The energies of the lines were determined by the method described by SLÄTIS [5] and by MLADJENOVIĆ and SLÄTIS [4]. As energy standards we have taken the recent measurements of the *A*, *B*, and *F* lines of ThC made by K. SIEGBAHN with his ironfree double focusing spectrometer. (Private communication. In course of publication.)

By taking the *F* line as a standard and calculating the $B\varrho$ values of the *A* and *B*

Table 1. The momenta of the A, B, and F lines of ThB measured by K. SIEGBAHN and the authors, obtained by taking SIEGBAHN's value for the F line as a standard.

Line	SIEGBAHN	MLADJENOVIĆ and SLÄTIS
A	534.20	534.03
B	652.38	652.40
F	1388.44	1388.44

lines we find that the values agree with the values found by SIEGBAHN within three parts in 10,000. A comparison of SIEGBAHN's and our values for the A, B, and F lines is shown in Table 1.

The estimated error of the energies of the KLL lines is about 0.03 % while the KLM lines, which are weaker and more difficult to measure, have an error of about 0.05 %. It should be pointed out that all the Auger lines are situated between the B and F lines.

The intensities were measured according to the method described by SLÄTIS [6] and used for RaB + C measurements by MLADJENOVIĆ and SLÄTIS [4]. The blackening of lines was within the linear region, and caused no important error in the intensity measurements. The largest uncertainty in the intensity determinations comes from the fact that several lines, especially KLM lines are not completely resolved. For these lines the error in the intensity measurements may be of the order of 20 %, while the error in the intensity of resolved lines should be about 10 %.

The energies and intensities of the Auger lines of Bi^{212} are given in Table 2.

Table 2. Energies and relative intensities of Auger lines of Bi^{212}.

No.	Transition	$B\varrho$	Energy KeV	Rel. intensity
1	KL_1L_1	830.77	57.466	1
2	KL_1L_2	836.17	58.186	1.8
3	KL_1L_3	853.00	60.417	1.1
4	KL_2L_3	858.01	61.090	1.6
5	KL_3L_3	875.04	63.404	0.8
6	KL_1M_1	922.35	70.020	0.4
7	KL_1M_2	924.95	70.391	0.5
8	KL_2M_1	927.54	70.761	0.8
9	KL_2M_3	933.04	71.553	0.7
10	KL_3M_2	925.13	73.301	0.7
11	KL_3M_3	949.07	73.873	1.0

In the above table we have written, as is usually done, only one transition formula for each line, but it should be noted that the transitions KL_pL_q and KL_qL_p have the same initial and final states, and cannot be distinguished.

Values of ΔZ

In order to compare the experimentally determined energies of Auger electrons $E_{KL_pL_q}$ with the calculated values of $E_K^Z - E_{L_p}^Z - E_{L_q}^Z$ and $E_K - E_{L_p}^Z - E_{L_q}^{Z+1}$ it is necessary to have precise values of the electron binding energies in the K and L shells. The energies of the emission lines can be used for the values of $E_K^Z - E_{L_p}^Z$ because they are known with a higher accuracy than the binding energies. We give in Table 3 the values of some emission lines by CAUCHOIS and HULUBEI [7] which we have used for the calculation of Auger electron energies in bismuth. For comparison we also give the values obtained using HILL, CHURCH and MIHELICH [8] values of binding energies. The energy of the K–L_1 transition was obtained by subtracting the values for two emission lines which involve K, L_1 and a third level. The mean was taken from four different values.

Table 3. The energy of some emission lines in keV.

Transition	CAUCHOIS, HULUBEI	HILL, CHURCH, MIHELICH
K–L_1	$(K-M_{II})-(L_I-M_{II})=86.832-12.691=74.141$	
	$(K-M_{III})-(L_I-M_{III})=87.340-13.209=74.131$	
	$(K-N_{II})-(L_I-N_{II})=89.725-15.581=74.144$	
	$(K-N_{III})-(L_I-N_{III})=89.955-15.708=74.148$	
	Mean 74.141	74.135
K–L_2	74.815	74.812
K–L_3	77.108	77.104

In Table 4 we give the values of the effective L subshell binding energies obtained by taking the mean of all the transitions involving the given subshell electron. We also compare our values of ΔZ with the values obtained by BERGSTRÖM and HILL [1].

Table 4. The values of the effective L subshell binding energies for doubly ionised bismuth

Transition	Energy keV	Mean energy	$E_{L_p}^{83}$	$E_{L_p}^{84}$	ΔZ	
					MLADJENOVIĆ and SLÄTIS	BERGSTRÖM and HILL
$E_{L_I}^{83+\Delta Z}=E_K^{83}-E_{L_I}^{83}-E_{KL_IL_I}$	16.675	16.665	16.384	16.93	0.51	0.54
$E_{L_I}^{83+\Delta Z}=E_K^{83}-E_{L_{II}}^{83}-E_{KL_IL_{II}}$	16.629					
$E_{L_I}^{83+\Delta Z}=E_K^{83}-E_{L_{III}}^{82}-E_{KL_IL_{III}}$	16.691					
$E_{L_{II}}^{83+\Delta Z}=E_K^{83}-E_{L_I}^{83}=E_{KL_IL_{II}}$	15.955	15.986	15.718	16.23	0.52	0.55
$E_{L_{II}}^{83+\Delta Z}=E_K^{83}-E_{L_{III}}^{83}-E_{KL_{II}L_{III}}$	16.018					
$E_{L_{III}}^{83+\Delta Z}=E_K^{83}-E_{L_I}^{83}-E_{KL_IL_{III}}$	13.724	13.718	13.426	13.81	0.76	0.76
$E_{L_{III}}^{83+\Delta Z}=E_K^{83}-E_{L_{II}}^{83}-E_{KL_{II}L_{III}}$	13.725					
$E_{L_{III}}^{83+\Delta Z}=E_K^{83}-E_{L_{III}}^{83}-E_{KL_{III}L_{III}}$	13.704					

Table 5. Values of ΔZ for M subshells in bismuth.

Subshell	Transition	Transition energy, keV	ΔZ	mean ΔZ
M_{I}	$KL_{\mathrm{I}}M_{\mathrm{I}}$	70.020	0.81	0.59
	$KL_{\mathrm{II}}M_{\mathrm{I}}$	70.761	0.36	
M_{II}	$KL_{\mathrm{I}}M_{\mathrm{II}}$	70.391	0.38	0.58
	$KL_{\mathrm{III}}M_{\mathrm{II}}$	73.301	0.77	
M_{III}	$KL_{\mathrm{II}}M_{\mathrm{III}}$	71.553	0.75	0.61
	$KL_{\mathrm{III}}M_{\mathrm{III}}$	73.873	0.51	

Mean for M shell ~ 0.60.

The close agreement between our ΔZ values and those obtained by Bergström and Hill is remarkable. It should be pointed out that the two energy measurements were independent of each other.

The values of ΔZ for the KLM transitions are less accurate because these lines are more difficult to measure. In addition the difference $E_M^{Z+1} - E_M^Z$ is about four times smaller than $E_L^{Z+1} - E_L^Z$ so that the relative error is increased. We give these ΔZ values in Table 5.

Intensities of the Auger lines

It may be of interest to compare our intensity values with other heavy element values as well as with the non-relativistic calculations by Burhop [9] and the relativistic calculations by Massey and Burhop [10]. The comparison is given in Table 6.

Table 6. Experimental and theoretical relative intensities of Auger lines.

Author	Mihelich	Bergström and Hill	Ellis	Mladjenović and Slätis	Experimental mean	Johnson and Foster, exp.	Burhop Theor non-rel.	Massey and Burhop Theor.rel.
Transition	79	80	83	83	~ 80	47	47	79
$KL_{\mathrm{I}}L_{\mathrm{I}}$	1	1	1	1	1	1	1	1
$KL_{\mathrm{I}}L_{\mathrm{II}}$	1.7	1.2	1.8	1.8	1.6	1.3	1.13	5.5
$KL_{\mathrm{I}}L_{\mathrm{III}}$	1.2	0.7	1.3	1.1	1.1	1.3	2.26	5.3
$KL_{\mathrm{II}}L_{\mathrm{II}}$	0.3	0.2	0.2	< 0.2	0.2	0.5	0.38	
$KL_{\mathrm{II}}L_{\mathrm{III}}$	1.4	1.4	2.3	1.6	1.7	3.2	4.03	
$KL_{\mathrm{III}}L_{\mathrm{III}}$	0.8	0.6	1.3	0.8	0.9	1.8	2.30	

Table 6 shows that the experimentally measured relative intensities of the KLL Auger lines for the elements 79–83 are not in agreement with the theoretical predictions. The values by Burhop are calculated for $Z = 47$, but should be almost independent on Z in the non-relativistic theory. The experimental values by Johnson and Foster [12] for $Z = 47$ are, however, in somewhat better agreement with these non-relativistic values.

Table 7. Experimental and relative intensities of some groups of lines.

Group	MLADJENOVIĆ and SLÄTIS	JOHNSON and FOSTER	PINCHERLE	BURHOP
KLL	1	1	1	1
$KL_{\mathrm{I}}M_{\mathrm{I,II,III}}$	0.14	0.18	0.10	0.16
$KL_{\mathrm{II,III}}M$	0.5	0.45	0.49	0.30

Our intensity values can also be compared with the theoretical calculations of PINCHERLE [11]. In Table 7 we give the values of the relative intensities of some groups of lines compared with the calculations of PINCHERLE, and with the corresponding theoretical values obtained from BURHOP's calculations.

Our experimental results and also those of JOHNSON and FOSTER [12] seem to indicate that PINCHERLE's value for $KL_{\mathrm{I}}M_{\mathrm{I,II,III}}$ is too low.

Fluorescence yield

The Auger yield A_K for the K shell is defined as the ratio of the number of K-vacancies resulting in K Auger electrons to the number of primary vacancies in the K-shell. Hence A_K is the ratio between the intensities of the K Auger lines to the sum of the intensities of the K lines. For ThB the F line gives rise to most of the K vacancies or 92% according to the intensities by ELLIS. We found the intensity ratio 2.3 for the KLL and KLM Auger lines to the E line and $E{:}F = 0.019$, hence $A_K = 2.3 \cdot 0.019 : 0.92 = 0.043$. This gives for the fluorescence yield $f_K = 1 - A_K$ the value 0.96. Table 8 gives a comparison of this value with theoretical values and other experimental values for bismuth as derived by KINSEY [13] from ELLIS' and FLAMMERSFELD's results. The experimental values for $Z = 78$ and 84 are also included.

Table 8. Experimental and theoretical values of fluorescence yield.

Author	STEFFEN *et al.* [14]	KINSEY (ELLIS)	KINSEY (FLAMMERSFELD)	MLADJENOVIĆ and SLÄTIS	GERMAIN [15]	Theoretical	
						non-rel.	rel.
Element	78	83	83	83	84		
Fl. yield	0.94	0.93	0.97	0.96	0.894	0.97	0.94

Thus our fluorescence yield value is in good agreement with that calculated by KINSEY from FLAMMERSFELD's measurements and with the theoretical nonrelativistic value.

Summary

1. The energies and intensities of the Auger electrons in the beta spectrum of ThB + C + C″ have been studied by means of a semicircular permanent magnet beta-ray spectrometer with photographic recording.

2. The effective incremental charge ΔZ was calculated for different L-subshells. The values obtained were in excellent agreement with the ΔZ values for double ionized mercury measured by BERGSTRÖM and HILL.

3. The intensities of the Auger lines were compared with measurements of other authors as well as with theoretical calculations by MASSEY and BURHOP.

4. The fluorescence yield for the K-shell was found to be 0.96.

Nobel Institute of Physics, Stockholm 50, Sweden.

REFERENCES

1. BERGSTRÖM, I. and HILL, R. D., Arkiv f. Fysik *8*, nr 2 (1954).
2. ROBINSON, H. R. and CASSIE, A. M., Proc. Roy. Soc. *A 113*, 282 (1926).
3. ELLIS, C. D., Proc. Roy. Soc. *A 138*, 318 (1932); *A 143*, 350 (1934).
4. MLADJENOVIĆ, M. and SLÄTIS, H., Arkiv för Fysik *8*, No. 5 (1954).
5. SLÄTIS, H., Arkiv f. Fysik *6*, No. 41 (1953).
6. SLÄTIS, H., Arkiv f. Fysik *8*, No. 43 (1954).
7. CAUCHOIS, Y. and HULUBEI, C. R., Longeurs d'onde des emission X et des discontinuités d'absorption X. Paris, Hermann, 1947.
8. HILL, R. D., CHURCH, E. L., and MIHELICH, J. W., Rev. Sci. Inst. *23*, 523 (1952).
9. BURHOP, E. H. S., The Auger Effect and Other Radiationless Transitions. Camb. Univ. Press, London 1952, and private communication.
10. MASSEY, H. W. S. and BURHOP, E. H. S., Proc. Roy. Soc., *A 153*, 661 (1936).
11. PRINCHERLE, L., Nuovo Cimento *12*, 81 (1935).
12. JOHNSON, F. A. and FOSTER, J. S., Can. J. of Phys. *31*, 469 (1953).
13. KINSEY, B. B., Can. J. Res. *A 26*, 404, 421 (1948).
14. STEFFEN, R. M., HUBER, O., and HUMBEL, F., Helv. Phys. Acta *22*, 167 (1949).
15. GERMAIN, L. S., Phys. Rev. *80*, 937 (1950).

Tryckt den 31 december 1954

Uppsala 1954. Almqvist & Wiksells Boktryckeri AB

ARKIV FÖR FYSIK Band 9 nr 5

Communicated 26 May 1954 by AXEL E. LINDH and I. WALLER

On multiple scattering measurements in nuclear research emulsions

By A. GÖSTA EKSPONG

With 13 figures in the text

Introduction

Measurements of the multiple Coulomb scattering on tracks of particles passing through nuclear research emulsions yield the quantity pv, where p is the momentum of the particle and v its velocity. From this quantity the energy of the particle may be evaluated when its rest mass is known. For a particle which ends in the emulsion a measurement of its range combined with the scattering measurements gives values of the mass and the energy. For a particle which does not end in the emulsion a combined measurement of its ionization and scattering gives the desired result, provided the energy is below a certain limit, depending on the particle and the precision of the measurements.

The accuracy in energy determinations based on scattering measurements is limited by statistical fluctuations, due to the limited number of independent determinations of scattering angles along the path of the particle. The measurements are however disturbed by various sources of errors, which produce angular deflections superimposed as noise on the scattering signal. An increase of the accuracy of the measurements often results in a slower speed in the determinations. This effect may be counteracted by automatizing the registrations and computations.

This paper contains a description of the performance of scattering measurements, discusses various sources of errors, the elimination of some systematic errors and describes a semi-automatic method to raise the speed of scattering determinations.

Theory

When a charged particle traverses matter, it interacts with the surrounding atoms through its electromagnetic field. One result of these collisions is a loss of energy of the particle. The study of this phenomenon yields the range-energy relation. The energy taken up by the surrounding atoms results partly in an ionization, the measurement of which is of great importance in many applications. Part of the energy is lost as radiation (Čerenkov-radiation) under certain conditions and as Brehmsstrahlung.

Another result of the collisions is the deviation of the path of the particle from a straight line. This effect is the basis of the scattering measurements.

The theoretical relations between the deflections in the path of particle and the properties of the particle and the scattering medium is treated by several authors [1, 2, 3, 4].

The problem may be said to be twofold; firstly to calculate the differential cross section of single scattering, and, secondly, to derive the statistical distribution of deflections due to many successive single scatterings in a finite path length of the scatterer.

Of importance to the following applications is the result that the deflections, α_r, are nearly normally distributed in the case of small deviations. In that of larger deviations the normal distribution is superimposed by a single-scattering tail. Further, the mean angle of deflection to the projection of the track in a plane is given by

$$\alpha_t = \frac{K z t^{\frac{1}{2}}}{p v} = \alpha_{100} \cdot t^{\frac{1}{2}}, \tag{1}$$

α_{100} here called the scattering parameter.

In this formula those factors are separated which depend on the particle, viz. its charge z in units of the electron charge, its momentum p, and velocity v, and those which chiefly depend on the scattering medium, viz. the scattering factor K and the cell length t.

The scattering factor, which is explicitly given by the theory, is but slightly dependent on the particle velocity and the cell length used in the measurements.

A comparison of the theories of WILLIAMS and MOLIÈRE shows that that of MOLIÈRE deals with the single-scattering cross section in a more stringent quantum-mechanical way by using the partial wave method. Thus it is shown that the scattering factor $K = f(\Omega_b)$, where Ω_b corresponds to the average number of collisions made by the particle on a path t of the scattering medium. For a given velocity, Ω_b is simply proportional to the cell length t. Its dependence on the velocity is given graphically in the paper by GOTTSTEIN *et al.* [5]. For very fast particles ($\beta^2 \simeq 1$) the relation is $\Omega_b = 310\ t$, when t is measured in units of 100 μ.

Investigations into the scattering factor

Several papers have appeared which deal with the experimental verification of the value of the scattering factor. The method used consists of measuring the absolute mean deflection, $\bar{a}$, for particles of known energy, and to calculate the K-factor from equation (1). The particles used in most of these experiments have been electrons, pi-mesons and protons.

In investigations with not too large a number of independent cells the absolute mean deviation, $\bar{a}$, is subject to rather great fluctuations on account of the appearance of a few very large deflections due to single scattering. If these are eliminated, the statistical accuracy of the mean will be better. The mean itself will be smaller, which is taken into account by replacing K by K_0, the value of the scattering factor being calculated with a cut-off procedure. Usually, values of $a_r > 4 \times |\bar{a}_c|$ are eliminated, where $|\bar{a}_c|$ is the absolute mean deviation calculated with "cut-off".

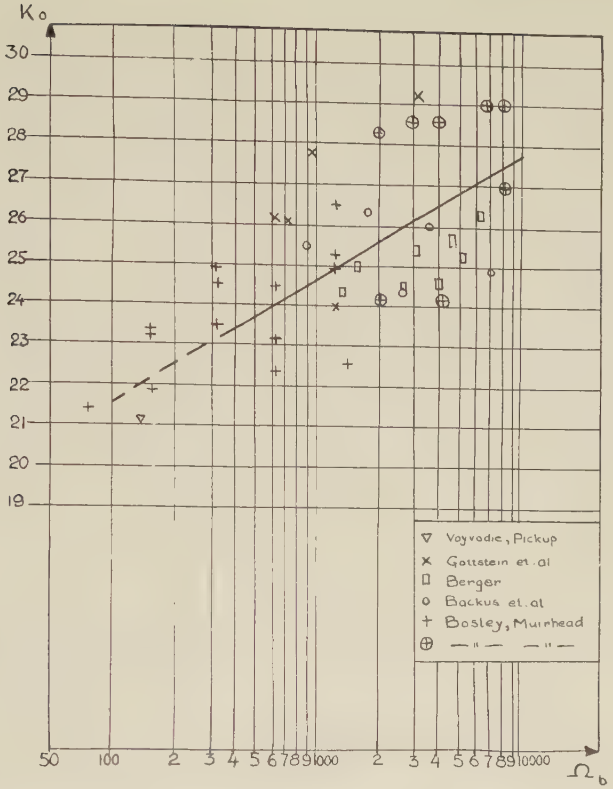

Fig. 1. Experimental results in determinations of the scattering factor, K_0, with cut-off. The line drawn represents the values obtained from theory. Ω_b corresponds to the average number of collisions in the cell. References are: Voyvodic, Pickup (electrons, positrons) Phys. Rev. *85,* 91. Gottstein *et al.* (positrons, protons, mesons) Phil. Mag. *42,* 708. Berger (protons) Phys. Rev. *88,* 59. Backus *et al.* (mesons) Phys. Rev. *88,* 1431. Bosley, Muirhead (electrons) Phil. Mag. *43,* 63. Bosley, Muirhead (protons) Ibidem *43,* 63.

Fig. 1 shows the results obtained by various observers. In order to draw a comparison with the theory of Molière, K_0 is plotted as a function of Ω_b. The line drawn in the figure represents the value of K_0 (with the cut-off) obtained from the theory [5]. In most cases of the listed number of 40 determinations of K_0 the experimentally obtained value agrees with the value deduced from the theory within three times the probable error. In two cases the experiments give higher values. Fig. 2 shows mean values of experimentally determined results. It is seen that the theory represents the data quite well. Therefore, in determining energy by the scattering method the quantity pv is calculated from equation (1) with the proper value of the scattering factor taken from Fig. 2. The systematic error in pv introduced by the uncertainty in K_0 is probably less than 4%.

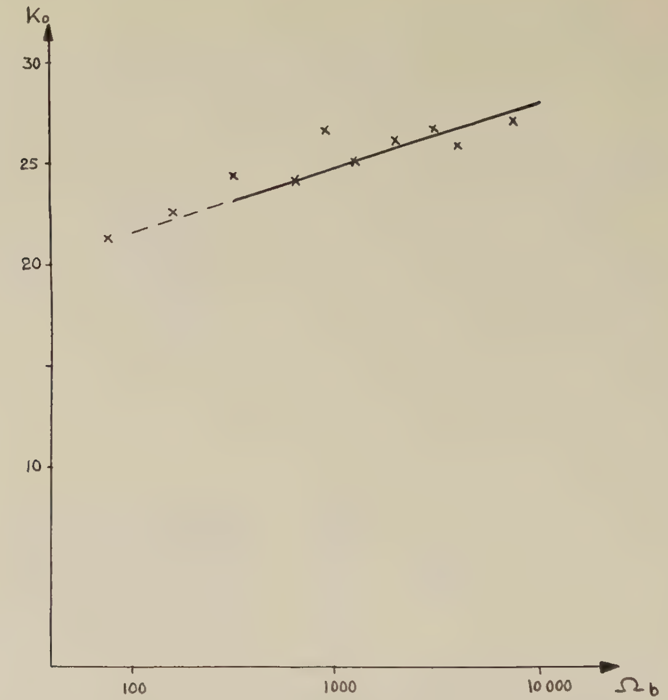

Fig. 2. Mean experimental values of the scattering factor, K_0, compared with the theory (line). The agreement is 4 % in general.

Experimental method for determining the scattering parameter

There are four different methods described to determine α_t. One, which is most in accordance with the theory, is based on a determination of the angle between "best lines" fitted to the track of the particle. Tangents cannot be drawn, because the path is not well enough defined by the grains in the emulsion. This method needs a correction, which accounts for the fact that the lines fitted to the track deviate somewhat from the tangents of the path. The method is discussed in great detail by various investigators [6, 7].

A method that has been used for low-energy electrons is based on the determination of the center of the gravity of a number of grains [8]. For low-energy electrons a special method has been worked out by H. ÖVERÅS [9].

The coordinate method of FOWLER [10] is a widely used and very convenient and rapid one. The microscope stage defines an x-y-plane, with the x-axis along the main movement. The optical axis of the microscope points along the z-axis. In applying this method the track is aligned approximately parallel to the x-axis of the microscope stage. The intersections of the track with the y-axis is read in the ocular in a series of points along the x-axis. In a modification used [11] the z-coordinate is read instead of the y-coordinate, i.e. studying the scattering in a plane at right angles to that used in the first method. This procedure, however, requires very accurate dip measurements.

Here the original method is used—as the best for our purposes—where the y-readings are taken at equally spaced intervals along the x-axis, the distance between the reading points being the cell length t. It is assumed that the energy is practically constant over the portion of the track measured.

By this method a series of y-coordinates is obtained: $Y_1, Y_2, \ldots Y_r, Y_{r+1}, Y_{r+2} \ldots$

From these observations the first difference $\Delta Y_r = Y_{r+1} - Y_r$ gives a measure of the slope of the track. The second difference $\Delta^2 Y_r = Y_{r+2} - 2 Y_{r+1} + Y_r$ is a measure of the scattering.

The observed Y-coordinate is composed of two parts, viz. one the genuine scattering, y_r, and the other, e_r, the result of various sources of error. If all sorts of systematic errors are eliminated (see below), e is a random error, which is distributed approximately normally with zero mean and standard deviation α_n. By measuring the noise-level, this assumption is justified and α_n is obtained.

An angle between chords is defined by $a_r = \frac{Y_{r+2} - 2 Y_{r+1} + Y_r}{t}$. Thus

$$a_r = \frac{\Delta^2 y_r}{t} + \frac{\Delta^2 e_r}{t}. \tag{2}$$

It follows that the angles a_r are not independent, successive values (a_r, a_{r+1} and a_{r+2}) being somewhat correlated.

According to a treatment due to MOYAL [12] the y-coordinate may be given by

$$y_r = \int_0^{x_r} (x_r - x)\, d\phi(x),$$

where ϕ is the angle between the path of the particle and the x-axis.

If the further assumption is made that the contribution of the error—conveniently called the noise—in one cell is independent of that in another (which is certainly true as to reading noise and grain noise and not far from correct as to stage noise), one obtains expressions for the expectation values of the first and second moments and the product-moments (the symbol E means "expectation value of"):

First moment (the mean):

$$E\left(\frac{1}{n} \sum a_r\right) = 0 \tag{3}$$

Second moment (m_2):

$$E\left(\frac{1}{n} \sum a_r^2\right) = \alpha_t^2 + \alpha_n^2 \tag{4}$$

Product-moment (m_{11}):

$$E\left(\frac{1}{n-1} \sum a_r a_{r+1}\right) = \frac{1}{4} \alpha_t^2 - \frac{2}{3} \alpha_n^2 \tag{5}$$

Product-moment (m_{101}):

$$E\left(\frac{1}{n-2}\sum a_r\,a_{r+2}\right)=\frac{1}{6}\alpha_n^2 \tag{6}$$

Product-moments $(|j-k|\geq 3)$:

$$E\left(\sum a_j\,a_k\right)=0 \tag{7}$$

Here α_t is the signal-angle, related to the scattering parameter by (1), and α_n the noise-parameter.

The signal-angle $\alpha_t=\alpha_{100}\cdot t^{\frac{1}{2}}$ increases with the size of the cell, where $\alpha_{100}=\dfrac{K\cdot z}{p\,v}$ is dependent on the energy of the particle, see eq. (1).

The noise-parameter $\alpha_n=\alpha_0\cdot t^{\ p}$ decreases with the cell-size. The exponent p of a real microscope is somewhat less than one ($p=1$ in the case of an ideal microscope).

From equations (4), (5) and (6) several estimators may be constructed giving the signal-angle in terms of the quantities a_r observed.

It is one of the objects of this paper to study the relative merits of a simple estimator obtained from (4), *viz.*

$$\alpha_t^2=m_2-\alpha_n^2,$$

i.e. (8)

$$\alpha_t^2=\frac{1}{n}\sum a_r^2-\alpha_n^2.$$

The sampling variance of this estimator and its comparison with others is treated in a later section.

Closely related to this estimator is another utilizing absolute mean values:

$$\alpha_t^2=\left(\frac{1}{n}\sum|a_r|\right)^2-\alpha_n^2. \tag{9}$$

A semi-automatical scattering recorder

In most applications of the coordinate method the Y-coordinates of the track are read on an eyepiece graticule. From these readings the first and second differences are calculated. At last the mean absolute deviation (with cut-off) is calculated. For long tracks and when many significant figures are involved these computations are relatively lengthy.

In order to facilitate the recordings and computations, a device may be constructed which takes over most of the routine work. The observer may then concentrate on the settings in the microscope.

In this laboratory the microscopes (of Cooke, Troughton & Simms type M 40000) are equipped with eyepiece filar micrometers consisting of a carefully made slide, the movement of which is controlled by a good micrometer screw, 0.5 mm per turn. The slide carries a glass plate with two horizontal lines engraved, i.e. the lines are adjusted parallel to the x-axis of the stage. The distance between the lines has been made equal to the image of one grain in the highest

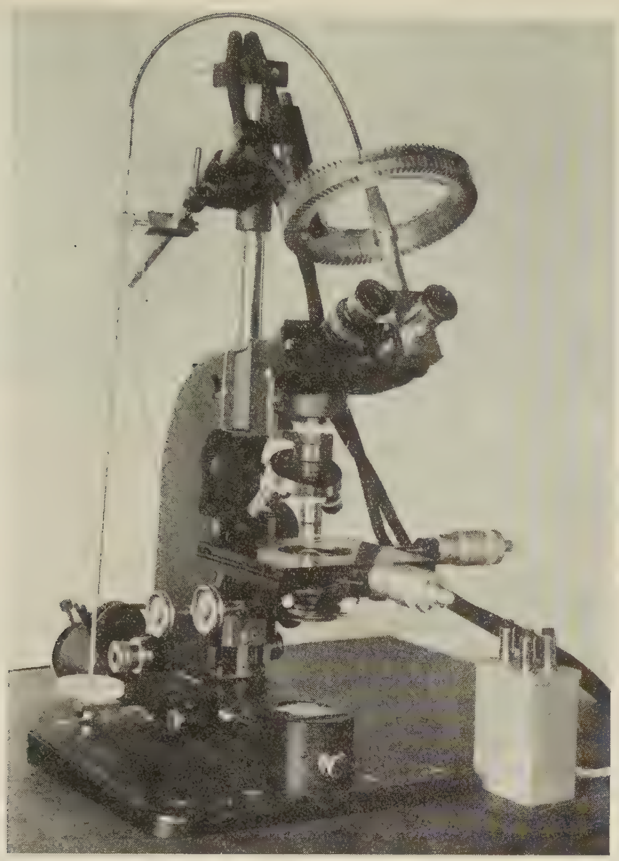

Fig. 3. *The microscope with the transmitter of the scattering-recorder.* The right eyepiece is equipped with a filar micrometer, to which is coupled the sliding-contact of the transmitter. From the operating head at the bottom left the rotations are transmitted by means of a flexible wire to the micrometer.

magnification. The track is thus seen to fit in between the lines after a proper adjustment. Vertically there are two lines engraved whose distance corresponds to 10 μ in the object plane. These two lines define the reading-interval for the smoothing of grain noise. The position of the slide along the y-axis is readable with a precision corresponding to about 0.01 μ in the object plane at the highest magnification. By experiment it is found that the position of a grain is at best reproducible within 0.02 μ.

The first difference, ΔY_r, corresponds to a certain angular movement of the micrometer screw. Instead of reading the screw divisions, the angle may be automatically recorded. This can be done either continuously or in steps. The latter method is adopted here. One revolution of the ocular micrometer screw is divided into 100 equal steps, each step corresponding to about 0.045 μ. This value was considered to match the various mean errors, these being 0.02 μ, 0.05 μ, 0.03–0.08 μ of the reading error, the grain position error and that of the stage

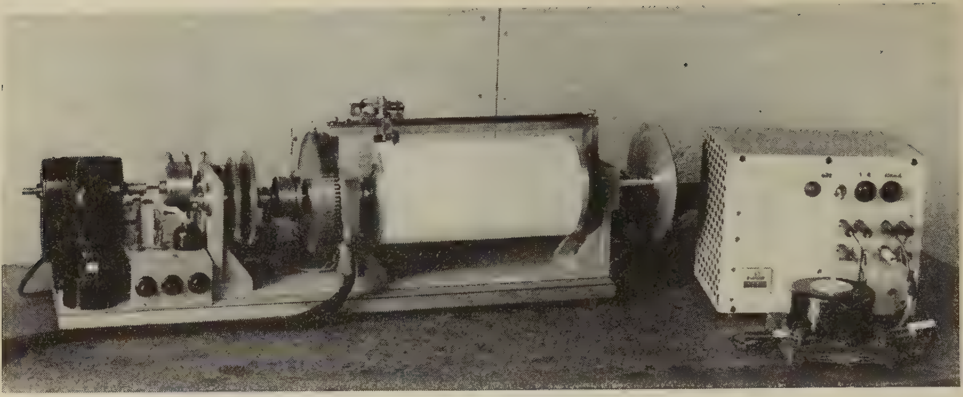

Fig. 4. *The scattering-recorder.* From the left is seen the reversing-motor, the coupling-magnet on its axis, and a speed-changer, below which is seen the drum-stop magnet. Between the gears and the receiver are placed the zero-position contact and the searching contact. In the mid-region are the recording drum and its ink-pen. Behind the drum are the four control-relays. To the right are the optical impulse-generator and the register.

movement respectively, the total mean error thus being found in region 0.065–0.10 μ. The angle of revolution may be recorded in several possible ways. One thing that must be remembered when doing this, is that the ΔY-difference has to be recorded with its sign.

In order to avoid a rigid coupling between the recorder and the ocular micrometer, and further to allow the observer to search back and forth for the best position when making a coincidence between track and micrometer lines, the following system is used.

The micrometer screw is rigidly coupled to a sliding contact made of silver threads, which runs across the 100 contacts situated on the periphery of an isolated ring. The arrangement, called the transmitter, is seen in Fig. 3. In the same figure the very convenient position of the driving mechanism may be seen, placed in such a way that the observer may, without moving his left hand, either control the fine focusing screw or the ocular micrometer. The contact ring and sliding contact are duplicated in the recording machine, here called the receiver. Each contact of the transmitter is electrically connected with its corresponding contact of the receiver. The sliding contact of the receiver is called the searching contact.

After the position of the ocular micrometer screw has been chosen, the observer starts a motor which drives the searching contact along the periphery of the receiver until it arrives at the corresponding position, and there it is locked by an electromagnet. The angle of revolution of the searching contact is proportional to the ΔY-difference. The sign is taken into account by the motor running backwards or forwards. The motor also drives a recording drum on the same axis as that of the receiver. After the searching contact has been locked, the recording drum is returned to its zero position by the motor, and there the drum is locked and the motor stopped. A stationary pen has then drawn an ink-line, which measured from the zero position is proportional to the first difference in Y. The pen is moved by an electromagnet 1 mm to the side between each recording. The recording drum is 25 cm long, thus having a capacity of 250 registrations. Changing recording paper on the drum takes less time than a minute. The construction may be seen in Fig. 4.

The observer has to start the motor in the desired direction; then the control of the other operations described above is carried out by electromagnetic relays. Four relays are used in this construction, as is seen in Fig. 5. One of the first two relays, labelled F and B, is energized by the observer pressing either the F or B manual switch to start the motor. The third relay, S, is energized when the searching contact comes to the corresponding contact of the receiver. Via the contacts driven by the S relay, the motor is then made to revolve in the opposite direction, and the searching contact is locked in its new position by an electromagnet. The fourth relay, labelled Z, is disenergized during the starting, thereby closing a magnet which couples the motor to the the axis of the drum, and providing necessary contacts for the F and B relays. The Z relay is reenergized when the drum arrives at its zero position again, thus disconnecting the motor-current and via some contacts of the F and B relays closing a magnet which locks the drum in its zero position. This locking magnet is used to stabilize the zero position of the drum, and by a proper adjustment of the contact that closes when the drum is near its zero position, a satisfactory reproducibility of the zero position is obtained.

As is seen in Fig. 5, the F and B relays are self-energized, provided the Z relay is opened. So is the S relay via a contact driven by the Z relay. By this arrangement the observer is free to move the ocular micrometer screw into a new position as soon as the searching contact has been locked in its end position, i.e. while the drum is returning to its zero position.

The case of $\Delta Y > 100$ *units.* In this case the micrometer screw is turned more than one revolution. The drum, however, is made to record only the excess value and a special sign is made on the recording paper to mark that 100 units should be added to the value recorded. For this purpose the observer makes use of the third manual switch, R, which is kept closed until the S relay operates as described above. The recording pen will thereby jump 1 mm aside at the very moment the drum has arrived at its turning point. The pen track being a rectangle then shows that $100 < \Delta Y < 200$. Two consecutive connections made by the R-press-button is used to mark that the recorded value exceeds 200 units and so on. However, in most cases, these rules are not necessary to apply, because 100 units cover most values met with in practice.

In the special case of $Y = 0$ the S relay is already energized at the start. By a special coupling (Fig. 5) the Z relay is self-energized in such a manner as to make it impossible to start the motor. The only thing that happens, when the observer makes use of one of the press-buttons F or B, is a pen-movement. The machine thus records $\Delta Y = 0$ correctly.

Evaluation of the sum ($\sum |\Delta^2 Y|$). Up to this point no computations or readings have been called for by the observer. In order to fulfill this program, a minimum of computations should be aimed at in order to get the mean absolute deviation out of the values recorded. On remembering that the second difference is simply obtained by measuring the distance from one peak to the next on the scattering diagram, this is done semiautomatically by fixing, to the drum axis, a disc with 100 contacts, which gives impulses to an electro-mechanical register. The contacts are placed along the periphery of the disc and equally

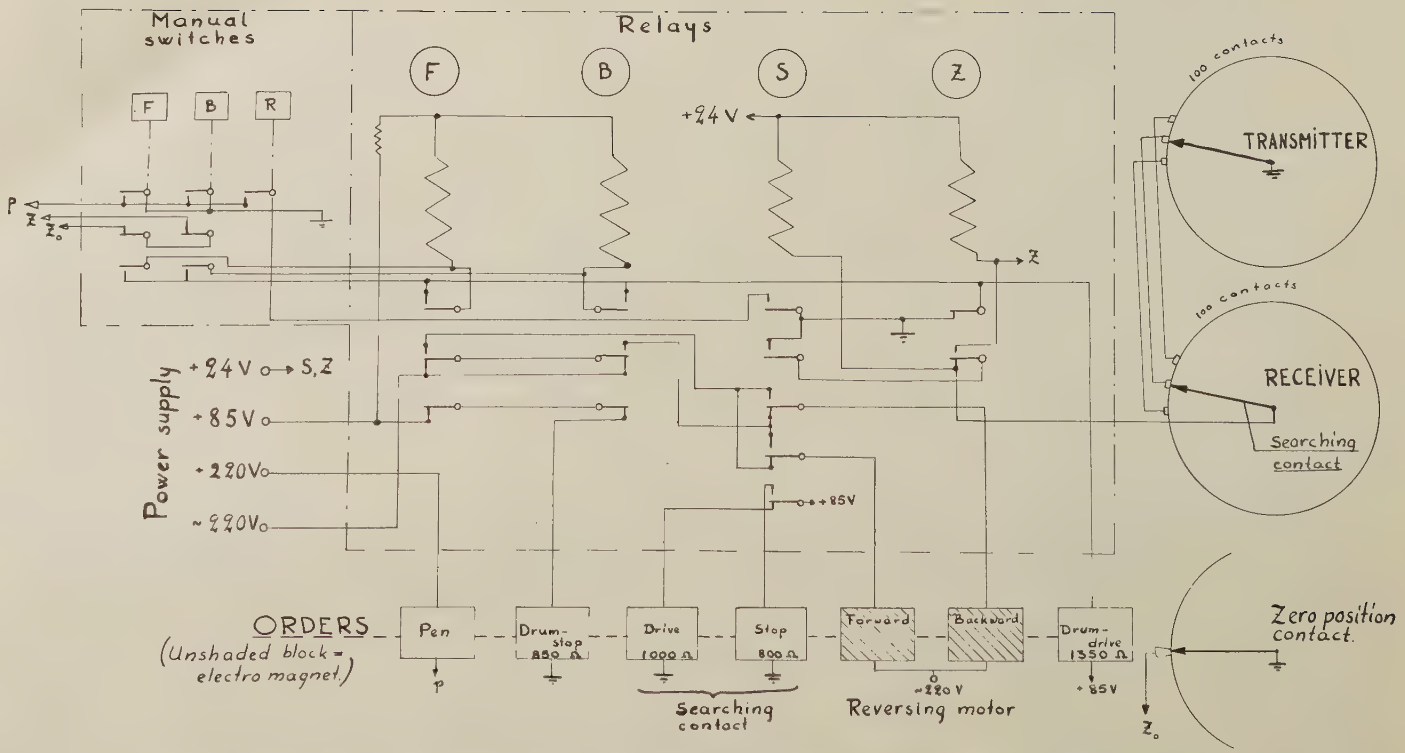

Fig. 5. *The scattering-recorder.* The four control relays are labelled, *F* (forward), *B* (backward), *S* (stop) and *Z* (zero position). Via their contacts, power is transmitted to the five electromagnets and the motor.

spaced. It has been found that the register operates more safely and at a higher speed when there are "optical contacts". By this is meant that the impulses are generated in a photocell, this in turn being illuminated by a beam of light passing through one of the 100 holes in the disc. The drum is forced by hand to move from peak to peak on the scattering diagram. During this operation the register adds up the various absolute values, and in the end contains the sum $\sum|\Delta^2 Y|$. By inspecting the scattering diagram and measuring large terms in the sum, corrections for single scatterings are easily made. At last the mean absolute deviation is computed.

Advantage of using the recorder. Besides the time gained by using the recorder, a few further points deserve mentioning. No large mistakes in reading are possible—either the recorder operates properly or not at all. Further there is no mental stress during operation. The observer is in fact not reading a scale; he only makes coincidences between the lines of the micrometer and the track, and operates one of the press-buttons. By experience it is found that the possible error of making a wrong contact is not to be feared. In an investigation of the gain of time a very long track was selected for determining energy, and measured both without and with the use of the scattering recorder. The time gained in the latter case was found to be about 45 %.

The recorder just described operates in two separate steps in order to obtain the final result, viz. the absolute mean deviation. It is obviously also possible to construct a recorder which performs both the necessary steps automatically. Such a recorder has to be a little more complicated in construction, but should be very convenient in practice. One solution is to build the recorder on the same principles as before, but with two axes, the ΔY-axis (memory) and the $\Delta^2 Y$-axis. After a recorded value (a first difference $+a_r$) has been fed both into the ΔY- and the $\Delta^2 Y$-axis, the latter is returned to its zero position, generating impulses for the register. Not until then is the ΔY-axis returned to its zero position, coupled so that it feeds $-a_r$ into the second axis. No impulses for the register are generated during this phase of the operation. The next first difference (a_{r+1}) fed in, sets the second axis in a position corresponding to the second difference $(a_{r+1}-a_r)$. The absolute value of this quantity is transferred to the register when the described operations start again. By use of a stamping register, or a recording drum, the individual values could be registered, which is of importance for single scattering corrections and in such cases as where the scattering in a larger cell is to be studied. The main advantage of such a recorder is that the result, the mean deviation, may be obtained immediately after the measurements in the microscope are concluded. The speed of the apparatus may be made to match or surpass that of the observer. Thus the apparatus must not prolong the time for measurements. Magslips, coupled as a synchronous link, are intended for being used as the transmitter and the receiver.

A discussion of errors, accuracy, and best conditions of measurement

The measurements in the microscope are usually performed under such conditions as to yield first differences in Y in the approximate range of 0 10 μ, second differences in that of 0-3 μ, with mean values of about 0.4 μ. By comparing these figures with the wavelength of the light used, about 0.5 μ, or, more precisely, with the resolution of the objective, which calculated from the numerical aperture is 0.2 μ, and further the diameter of a developed grain being about 0.6 μ, it is clear that a discussion of errors involved in the measurements is important.

In order to cover the field of errors, the subject is in the following discussion divided into two main groups dealing with 1) systematic errors, and 2) random errors. In both groups a subdivision is made, classifying the errors according to the sources. As such we look upon (*a*) the photographic plate, (*b*) the microscope, (*c*) the observer, and (*d*) the sampling. This division makes sense if the errors are, as a rule, regarded in individual second differences or their corresponding chord-angles. The case of sampling errors deals, on the other hand, with some measure of dispersion of the chord-angles.

1 a. *Systematic errors arising in the photographic plate. Distortion.*

Very careful handling of the plates during processing and good properties of the emulsion are needed so as not to change the shape of the emulsion. A wet emulsion is several times (≈ 4) thicker than a fresh one; and the thickness of a processed emulsion is about 43 % of the nominal value. The precautions that may be taken in order to prevent a distortion of the tracks are described elsewhere [13]. If an emulsion shows some slight regular distortion, it may still be used in scattering work, since the distortion may be eliminated. In the case of uniform distortion, the change of equations (3)–(7) is that (3) then reads $E\left(\frac{1}{n}a_r\right) = D \cdot t$, the other formulae being formally unchanged if $a_r' = a_r - D \cdot t$ is substituted for a_r. Here $D = R^{-1}$, where R is the radius of curvature of the distortion. A closer study of the distortion may be made by utilizing the concept of the distortion vector as introduced by COSYNS and VANDERHAEGHE [14, 15]. It is noted that the distortion of a given track is a function of the angle of its dip; tracks nearly parallel to the surface on the emulsion reveal very little or no distortion. The presence of distortion is detected either by inspecting very steep tracks in the same region of the plate as that of the track under investigation (the distortion-vector method), or by testing whether the mean value of the second differences differ significantly from zero (statistical method), or by studying how the mean scattering angle observed, varies with the cell-size. The elimination of distortion may be performed in several ways, three being listed here:

Each value of the second differences is corrected for distortion by eq. $a_r' = a_r - D \cdot t$, where $D \cdot t$ is found either from a knowledge of the distortion vector and the position of the track relative to this vector, or from the mean value of the second differences, which means that in this case a statistic

$$\bar{a}_r = \frac{\frac{1}{n}\sum \left| \Delta^2 Y - \frac{1}{n}\sum \Delta^2 Y \right|}{t}$$

is used and inserted in eq. (9) in order to compute the scattering parameter. Thirdly, the distortion is eliminated by taking third differences, $\Delta a_r' = \Delta a_r$. In the Gaussian approximation the expectation value of third differences is related

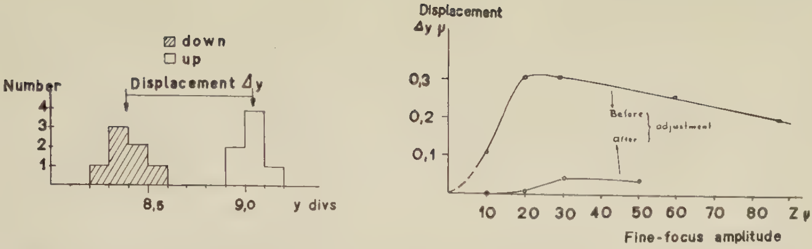

Fig. 6. Effect on the Y-coordinate by hysteresis in the fine focusing movement. The histogram shows the effect to be well outside the reading errors (an eyepiece graticule used). The curves show the displacement before and after the adjustment.

to that of second differences in a simple way. In most work at this institute, when a distortion correction has been necessary, one of the first two methods has been used. The relative merits of their accuracy in the final result do not seem to have been investigated.

1b. *Systematic errors caused by the microscope*

The instrument used for studying the small quantities involved in multiple scattering must have good mechanical and optical properties. An instrument especially designed for such measurements is studied in this section. It is a Cooke, Throughton & Simms microscope M 40171. It is presumed that the main methods of investigation may have a wider interest.

Temperature-effect. When the microscope is heated, e.g. by absorption of radiation, either from the sun or from lamps nearby, it is found that the Y-coordinate of one and the same grain is not reproducible. The heat from the microscope lamp is also of influence, although it is cut down considerably by the lamp being detached from the main body of the microscope. However, it is advisable to have a heat-absorption filter or a reflection filter (as is used here) in the light beam. The effect of taking these precautions may be demonstrated by an example showing the speed of the systematic trend in the Y-coordinate:

Microscope heat unshielded: 0.12 μ/min. for a period of about 10 min.
,, ,, shielded: 0.00 ,, ,, ,, ,, ,, ,, 10 ,,

It is recalled that the reproducibility of one grain is about 0.02 μ.

The effect of hysteresis in the fine focusing movement. It was found that the Y-coordinate reading of one and the same grain was dependent on the history of the fine focusing adjustment. As is shown in Fig. 6, the effect is well outside the limits of reading errors. The displacement in the Y-coordinate was further shown to depend on the amplitude of the fine focusing movement by focusing on the grain by alternatively going down or up. The displacement saturates, more or less, at a z-amplitude of about 25 μ, as is shown in Fig. 6. This fact may be used to eliminate the detrimental effect of hysteresis. If one strictly performs the measurements by utilizing a constant z-amplitude in the region of saturation, no appreciable error remains in the second difference. However, by a careful adjustment of the slide controlling the fine focusing

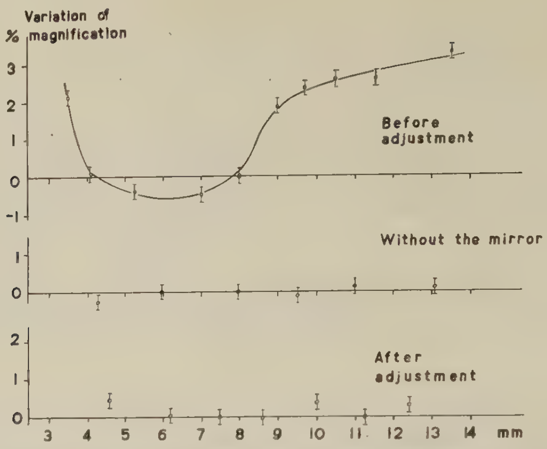

Fig. 7. Variation of the apparent size of an object as a function of its position in the field of view; *a*, before any adjustment made; *b*, by-passing mirror and prism-system; *c*, after adjustment of the mirror. The errors shown are maximum errors in the sense that the probability of the value lying inside the interval is about 95 %.

movement, the effect may be diminished. A good result was obtained here by removing one of the two springs pressing the bar, which transmits the movement of the fine focusing head to the objective changer.

Errors caused by an imperfect optical system. In an attempt to calibrate the ocular micrometer carefully it was found that the magnification varied across the field of view by as much as 3.5 %. The method of investigating this effect consists in selecting a convenient object (in the highest magnification two well-defined grains at the same depth in a nuclear emulsion having a distance of about 10 μ are suitable), and in measuring the variation of the apparent size by the ocular micrometer. The result is plotted as a function of the midpoint of the object in the field of view. Typical results in an actual experiment is shown in Fig. 7 a. In order to trace the cause of this variation a series of measurements was undertaken. By using the method described above, but without the binocular attachment, thus by passing the mirror and the prism-system, a test is obtained of the quality of the lenses. The effect disappeared (Fig. 7 b). Various tests of this kind showed that the mirror was the weak point. However, by adjusting the screws holding the mirror, its shape could be changed, and made to approach that of a plane. At last a satisfactory result was obtained, Fig. 7 c. A test made about one year later revealed no measurable change.

Calibration. The scale divisions of the ocular micrometer screw are calibrated carefully against a ruled grating. The spacing of the grating rules has been determined in a spectrometer with the results $d = 4.5161$ μ and $d = 4.5162$ μ as determined from measurements with the yellow sodium light doublet. The value $d = 4.516$ μ is considered good up to about 0.01 %. With this grating, the scale of a Zeiss objective micrometer was checked in a magnification of the microscope of $\times 45 \times 10$. For a calibration of the highest magnification the Zeiss scale was used, as it is difficult to see the lines of a ruled grating under these conditions.

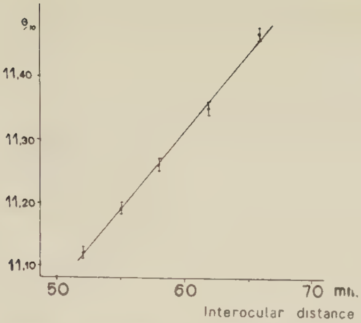

Fig. 8. The magnification G as a function of the interocular distance. One scale division $= 10/G\,\mu$ (95 %-level errors).

The calibration was performed for each of the objectives of the microscope. The most important calibration is that of the highest magnification, because practically all scattering measurements are performed with this objective.

Besides the objectives, the tube length is of some influence on magnification. Thus, in accurate work the interocular distance of the binocular attachment has to be specified, and its influence on magnification taken into account. The relationship between magnification G and the interocular distance x, is linear, and may be put in the form $\frac{\Delta G}{G_0} = \frac{\Delta x}{2\,L_0}$, where L_0 is the tube length corresponding to G_0. This relation is verified experimentally, Fig. 8. Various observers use different interocular distances. Values of $\Delta x \lesssim 10$ mm being common, systematic errors of the order of 2 % may be made in case this variation is neglected.

The design of the Cooke microscopes is such as to separate the suspension of the revolving objective changer from that of the binocular attachment. Fine focusing movements are transmitted to the objective changer alone, thereby changing the effective tube length. This construction is in some respects an advantage, especially as it makes the position of the image of an object rather insensitive to mechanical disturbances emanating from the binocular eyepiece attachment. An undesired effect of the construction, however, is that the magnification becomes, to some degree, dependent on the fine focusing setting. In the type of microscopes discussed here the fine focusing, or z-movement, can cause the tube length to vary 3 mm, which corresponds to a maximum variation of the magnification of 1.25 %.

To sum up the above discussion, the magnification, G, of this type of microscope may be written

$$G = G_0\,(1 + a\,(x - x_0) + b\,z) \tag{10}$$

where $a = 1/2\,L$, and $b = 1/L$ with L = the effective tube length. The range of x is approximately given by $52 \leq x < 70$ mm, that of z by $-1.5 \leq z \leq 1.5$ mm. One scale division of the ocular micrometer screw is given by

$$1\ \text{div.} = \frac{10.00}{G}\ \mu. \tag{11}$$

As for the particular microscope discussed here (M 40171) this relation is calculated and experimentally verified to be $G = 111.9 + 0.24\,(x - 58) + 0.47 \cdot z$ for the × 80 apochromatic objective.

The calculation of scattering angles depends also on the value of the cell-size as measured by the micrometer screw controlling the x-movement of the stage. The divisions of the screw were checked by counting the number of lines of the ruled grating in a certain interval. The screw divisions were found to agree with their nominal values within the reading errors. In the long run—in an interval of 5.400 μ—the agreement was found to be good up to 0.024 % (this being again of the order of magnitude of reading errors).

The curvature of the microscope stage. All but the last of the preceding microscope errors have been investigated with the stage stationary. When the stage, the movement of which is controlled by ball-bearings, is moved, it is important that the motion should be rectilinear. In this context we are interested not in the random departure from a straight line, but in the case of a curvature of the stage. In order to test this, one needs an object which is a very good approximation to a straight line. Most investigators have used tracks of particles of extremely high energy, a procedure that is possible, provided distortion is absent and the cell-sizes not too large. It occurred to the author that artificially made lines should be possible to obtain with sufficient precision. However, lines engraved on glass plates by a good lathe are still rather bad for these purposes. The objects used in this investigation are a series of lines engraved on a glass plate by an accurate grating machine.[1]

The lines are of a width of about 1 μ and a length of about 4 cm. Older grating lines were tested and found to have a relatively strong curvature; in one case the radius of curvature being 5.5 m.

In order to make the lines visible a phase-contrast equipment was used for these measurements. The line selected was lined up approximately parallel to the x-axis of the stage. All the readings were taken on one side of the 1 μ thick line, the constant thickness of the line first being checked.

So as to obtain a good conception of the situation and to guide the interpretation the following considerations are made:

Were the movement of the stage ideal, the first difference of the readings on a straight line would follow the relation $\frac{\Delta Y}{\Delta x} = \text{constant}$. In the case of a real stage, one may apply a stage-function $y = f(x) = a_1 + a_2 x + \frac{a_3 x^2}{2} \ldots$, where without loss of generality we may put $a_1 = a_2 = 0$. We limit ourselves to studying the effect of the second approximation, thus $y = a_3 \frac{x^2}{2}$. The radius of curvature is given by $R = \frac{1}{a_3}$. The test line is represented by a similar function $y = b_1 + b_2 x + b_3 \frac{x^2}{2}$. The readings in the microscope are taken at intervals $= \Delta x$. Their first differences follow a relation

---

[1] The author wishes to express his gratitude to Professor M. SIEGBAHN and Mr. L. LUNDIN for supplying the high-quality grating-lines.

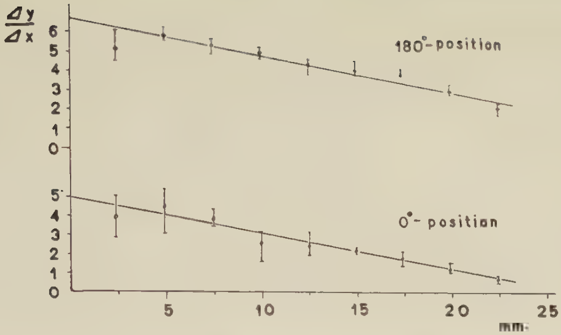

Fig. 9. *The stage curvature.* The ordinates are given in scale divs. per 5 mm, the abscissas in mm. Every point is the mean of six readings; the total spread of the points are shown by arrows. The radius of curvature is calculated to be 62 meters.

$$\frac{\Delta y}{\Delta x} = b_2 + (b_3 - a_3)\,x, \tag{12}$$

representing a straight line with the slope $k_1 = b_3 - a_3$. The measurements are repeated with the test plate turned 180°. In the new position the corresponding relation to (12) is

$$\frac{\Delta y}{\Delta x} = b_2' - (b_3 + a_3)\cdot x,$$

representing another straight line with the slope $k_2 = -(b_3 + a_3)$. From the experimental estimation of the slopes one obtains $a_3 = -\frac{1}{2}(k_1 + k_2)$ for the curvature of the stage, and $b_3 = \frac{1}{2}(k_1 - k_2)$ for the curvature of the test line.

The experimental results of M 40171 are given in Fig. 9, yielding $a_3 = 1.6 \cdot 10^{-4}\,\mu/(100\,\mu)^2$. The corresponding radius of curvature is 62 ± 10 meters. The curvature of the test line is too small to be measurable with this method; the value actually obtained is $b_3 = 2.10^{-10}\ \mu^{-1}$, indicating the radius of curvature of the test line to be $\gtrsim 5000$ meters. For practical purposes the test line may be regarded as a straight one. The systematic error in the second differences introduced by stage curvature is: $1.6\ 10^{-4}\ t^2\ \mu$ for a cell-size t (in units of $100\ \mu$).

In Table 1 there is a computation of typical cases, and it should be regarded as approximately giving the magnitude of the errors involved. The systematic error contribution is considered negligible if the error in Y is below $0.02\ \mu$ or below $0.06\ \mu$ in $\Delta^2 Y$, this error level being obtained by a comparison with the reading errors, or more exactly the reproducibility. The latter is about $0.02\ \mu$ in Y, corresponding to an error of $0.06\ \mu$ in $\Delta^2 Y$ on the average. For a well adjusted microscope this is seen to be the case. The hysteresis effect requires some attention. As long as the track goes steadily downwards or upwards there is no measurable influence. It occurs to some extent when the focusing is made alternatively up and down. Further it is seen that the errors caused by fine focusing movement and stage curvature need not in general be taken into account. Usually the cell-sizes are less than $1000\ \mu$. For cells larger than about $2000\ \mu$ a correction for stage curvature should be made, i.e. for particles with $p v \geq 6000$ MeV.

Table 1. Summary of the "1 b" systematic errors, i.e. those caused by imperfections of the microscope.

	Remaining error with microscope adjusted and after proper corrections		Error before adjustment and corrections	
	In Y	In $\Delta^2 Y$	In Y	In $\Delta^2 Y$
Temperature error	$\lesssim 0.01\ \mu$		$\sim 0.1\ \mu$	
Hysteresis in z	$\lesssim 0.05\ \mu$	$\lesssim 0.10\ \mu$	$\sim 0.3\ \mu$	
Optical error	$\lesssim 0.01\ \mu$		$\sim 0.1\ \mu$	
Calibration		None		—
Interocular distance		None		$0.01\ \mu$
Fine focusing setting		None		$0.006\ \mu$
Curvature of stage:				
cell-size $\leq 500\ \mu$		None		$0.004\ \mu$
,, $\leq 1000\ \mu$		None		$0.016\ \mu$
,, $\leq 2000\ \mu$		$\sim 0.01\ \mu$		$0.064\ \mu$
,, $\leq 5000\ \mu$		$\sim 0.06\ \mu$		$0.40\ \mu$

1 c. *Personal error*

When an eyepiece graticule is used for the Y-readings, the observer's ability to judge decimals of a scale-division may, as is well known, introduce a systematic error. This effect has been investigated here by taking 404 decimal readings at random and testing their distribution. It was found that the decimals in the mid-region (around 0.5) were underrepresented. The mean error introduced was calculated as amounting to $0.04\ \mu$. In the case described, one scale division was divided into ten subunits. Another case with only five subunits gave a much better distribution with no single decimal significantly underrepresented. The material (300 readings) gave a mean error of $0.03\ \mu$.

With the eyepiece micrometer these errors are highly reduced and need not be considered.

1 d. *Sampling errors*

One type of systematic errors caused by the sample drawn has to be considered in each experiment and it is mentioned here only for the sake of completeness. It has been pointed out by several investigators in this field that special care in interpreting the results should be exercised when long tracks in thin emulsions are being selected for measurements, the difficulty being that the tracks selected may be deficient in large signals.

The interval grouping of the measurements when evaluated by the scattering recorder causes the computed standard deviation or mean absolute deviation to be somewhat too large. By an application of Sheppard's corrections this effect may be diminished. However, as shown by a calculation, the correction is of very little significance in general. If h is the interval ($h = 0.045\ \mu$ for the M 40171 microscope) one obtains, in practice, a standard deviation of $6h$ to $15h$, say nh. The corrected standard deviation is $\sqrt{(nh)^2 - \frac{h^2}{12}} \approx nh\left(1 - \frac{1}{24n^2}\right)$. The correction is thus generally less than 0.1 %. It is regarded unnecessary to apply this correction in view of other errors being of even greater influence.

2. *Random errors*

Even if all systematic errors are eliminated or kept at an insignificantly low level, there are additional errors of a random character which build up the noise level.

2a. *Grain noise*

The developed grains belonging to a track are distributed at random around the path of the particle. The position of the path is not defined better than to a certain amount, due to the linear dimensions of the silver-bromide crystals — to some extent also owing to the size of the developed grains. If the mean position of a few neighbouring grains is taken, the Y-coordinate of the path is somewhat better defined.

By starting from simplified assumptions as to the formation of spherical grains, a detailed calculation has been made. Thereby it is possible to obtain a distribution of the distance from the center of a grain to the path. From this distribution one can derive that of the second difference in the case of a perfectly straight path. The mean absolute deviation has been calculated to amount to $1.02\,r$, where $2\,r$ is the diameter of a grain ($0.27\,\mu$) [16, 17]. The mean grain noise in the second differences is thus $0.14\,\mu$. An experimental investigation did agree with this value within 8 %. When the micrometer screw is applied, it is convenient to set the reading at the mean position of several close grains (n grains). In this case the grain noise in the chord-angle is $\alpha_g = \frac{0\overset{\circ}{.}079}{\sqrt{n \cdot t}}$. For minimum tracks $n = 4$ is usually chosen. The corresponding grain-noise function $\alpha_g = \frac{0\overset{\circ}{.}039}{t}$, where t is the cell-size in units of $100\,\mu$, is plotted in the noise-line diagram, Fig. 10.

2b. *Stage noise*

The movement of the stage is somewhat irregular, thereby causing random deviations in the Y-coordinate readings. The error thus introduced in the chord-angle is called stage noise. In order to measure its magnitude and dependence on cell-size—in the absence of grain noise and true scattering—measurements have been performed on the straight test line used in the determination of stage curvature. The magnitude of the stage noise is crucial in judging the applicability of a microscope for scattering measurements with the coordinate method. The distribution of stage noise seemed from histograms to be somewhat more peaked than a normal distribution. The goodness of fit to a normal law with zero mean and the same variance as that of the experimental frequency curve has been tested with the χ^2-test; the results showed agreement on the 20 % level. The measured mean absolute deviations turned out to increase with cell-size, an effect found by other observers [7, 5]. The resultant angular stage noise is displayed in Fig. 10, after correcting reading errors (see below), and the stage curvature contribution in the case of $1000\,\mu$ and $2000\,\mu$ cells.

2c. *Reading noise*

The observer has to judge the best position of the eyepiece micrometer. The precision of reproducing the position of one grain is about $0.02\,\mu$. The second difference will on the average be in error of $\sqrt{6} \cdot 0.02\,\mu$. The actual figure measured

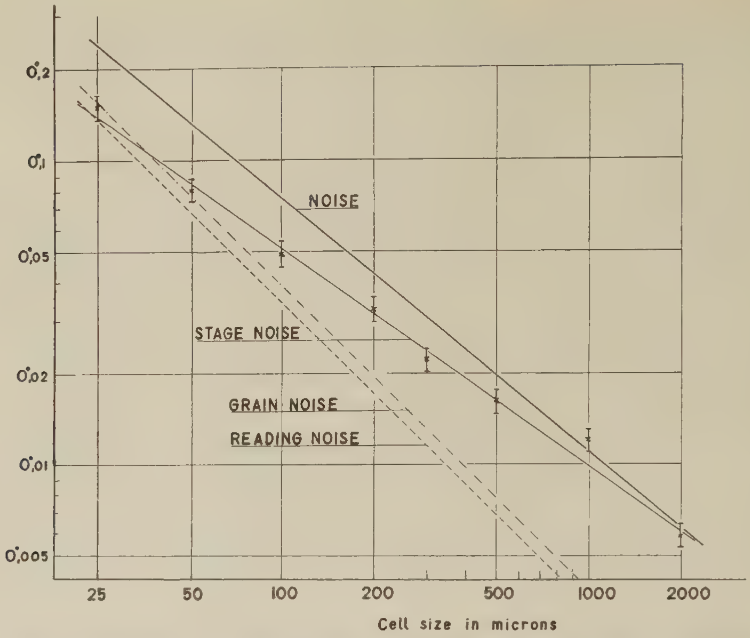

Fig. 10. *Noise-line diagram.* The total noise is calculated from its three components, viz. read ing noise, grain noise, and stage noise. Errors are standard errors.

amounted to 0.056 μ. The reading noise is thus $\alpha_r = \frac{0^{\circ}.032}{t}$. This function is als plotted in the noise-line diagram, Fig. 10.

It is evident that the scattering recorder may introduce small deviations fro the actual settings recorded. In three test runs the error in the mean deviatio calculated by the recorder was + 0.28 %, + 0.24 %, and − 0.69 % respectivel as compared with the value obtained by a direct reading of the micrometer screw The accuracy of the recorder is thus better than 1 %.

Summary of random errors. The three sources of random errors mentioned d cover all the errors that contribute to the noise. Their values are summarize below and plotted in the noise-line diagram of Fig. 10.

2 a. Grain noise (for 4 grains) $\alpha_g = \frac{0^{\circ}.039}{t}$

2 b. Stage noise ($25 \leq 100\,t \leq 2000\ \mu$) $\alpha_s \simeq 0^{\circ}.053\, t^{-0.72}$

2 c. Reading noise $\alpha_r = \frac{0^{\circ}.032}{t}$

The total noise level: $\alpha_n = (\alpha_g^2 + \alpha_s^2 + \alpha_r^2)^{\frac{1}{2}}$ has been plotted in Fig. 10. It i seen that this is very nearly a straight line in the log-log-diagram of Fig. 1 The corresponding function is (if $50 \leq 100\,t \leq 500\ \mu$)

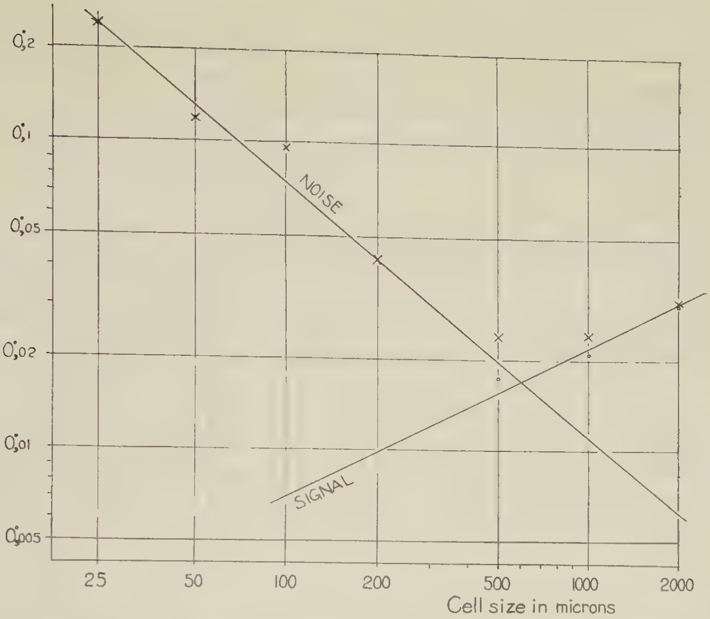

Fig. 11. Verification of noise level by measurements on a fast electron track. The noise line plotted is that of Fig. 10. The crosses are obtained by actual measurements on the track. The signal line is obtained from the measurements by subtracting noise, actual values being represented by points.

$$\alpha_n = 0^\circ073\, t^{-0.84}.$$

As an independent check of the noise, long tracks of high energy electrons have been selected and measured several times with different cell-sizes. A typical result is plotted in Fig. 11 together with the noise line. It is found that the measurements follow the noise line within the errors for small cells. When larger cells are used (in the case discussed as to cells $\geq 500\,\mu$) the true scattering signal comes in and raises the measurements above the noise level. Another check of the noise has been made by another observer, who after some training practically attained the same noise line. Repeated checks were made to control the noise level. As long as the microscope is kept clean, the moving parts oiled, and the systematic errors insignificantly low (temperature effect must be checked), it is found that the noise level is constant. This situation implies that it is worth while to consider the possibility of using the expression (9), $\alpha_t^2 = \left(\frac{1}{n}\sum |a_r|\right)^2 - \alpha_n^2$, for estimating the true scattering signal.

Accuracy of the noise-level. In utilizing (9) it is essential to know the noise level, α_n, with some accuracy. In the evaluation of the stage noise, the error of the result depends on the number of readings taken, in the present case being 40 to 60 readings for each cell. The value for each single cell is further supported from those of the neighbouring cells. In short one may say that the relative standard error in the stage-noise determination is less than about 12 %. For cells less than 500 μ, about 10 %. Reading noise is regarded to be equally accurate, 12 %, and grain noise about 8 %. As the various contributions to the total noise play relatively different roles, one calculates the relative standard error in noise to be $(12\,t^{-0.64}+28\,t^{0.48})^{\frac{1}{2}}\,10^{-2}$. In the region of the greatest interest, viz. cell-sizes ranging from 50 μ to 500 μ, the error quoted is 6 % to 8 %.

2 d. *Statistical error*

If measurements are repeated on the same grains of a track given, the resultant signal angles will be different due to variations of the noise level. If the signal-to-noise ratio, λ, is kept high the various scattering results may lie within relatively narrow limits. In some test experiments this effect was demonstrated by first measuring with $\lambda=1.5$, when the relative standard error amounted to 9 %, then measuring with $\lambda=9$, when a relative standard error of 1.3 % was obtained. In each case the material consisted of about 20 repeated series of 25 scattering angles.

The reproducibility discussed above does not imply the same degree of accuracy in estimating the scattering parameter (α_{100}) or the product momentum × velocity ($p\cdot v$). One has to regard the scattering angles on the track selected for measurement as a sample of n drawn from a universe emanating from monoergic particles of the same kind. The standard error of any statistic used to estimate the scattering parameter will mainly depend on $n^{-\frac{1}{2}}$. The main error of the final result comes in fact from the limited number of independent readings. Starting from (8), $\alpha_t^2=m_2-\alpha_n^2$, one obtains from the sampling variance of m_2 the following expression for the standard error, σ, in α_{100}:

$$\frac{\sigma}{\alpha_{100}}=\frac{\sqrt{\operatorname{var} m_2}}{2\,\alpha_t^2}. \tag{13}$$

To this error has to be added the systematic one arising from the uncertainty of α_n:

$$\pm\frac{\alpha_n\,\delta\,\alpha_n}{\alpha_t^2}. \tag{14}$$

The sample moments are denoted by m_2, m_{11}, and m_{101}, their expectation values by μ_2, μ_{11}, and μ_{101}. The moments are defined by equations (4), (5) and (6).

It is the object of the present calculation to evaluate the expressions (13) and (14) in terms of the number of scattering angles, n, and the signal-to-noise ratio, λ, thus defined by $\lambda=\frac{\alpha_t}{\alpha_n}$. It is pointed out that λ is a function of the cell-size.

The sampling variance of m_2 is calculated from

$$\operatorname{var} m_2=E\,(m_2-\mu_2)^2=\frac{1}{n^2}E\,(\sum a_r^2)^2-\mu_2^2. \tag{15}$$

The calculation is somewhat complicated by the fact that the a_r are correlated to a certain extent, as shown in the relations (5) to (7).

$$E\left(\sum a_r^2\right)^2 = \sum_{r=1}^{n} E\left(a_r^4\right) + 2\sum_{r=1}^{n-1} E\left(a_r^2 \cdot a_{r+1}^2\right) + 2\sum_{r=1}^{n-2} E\left(a_r^2 \cdot a_{r+2}^2\right) + \sum_{j,k} E\left(a_j^2 \cdot a_k^2\right).$$

The last summation extends over all such j and k as where a_j and a_k are uncorrelated, i.e. in the case of $|j-k| \geq 3$, according to (7). From the fact that the a_r are approximately normally distributed, being a sum of variables having nearly a normal distribution, it follows that

$$E\left(\sum a_r^2\right)^2 = n \cdot 3\mu_2^2 + (n-1) \cdot 2\left(\mu_2^2 + 2\mu_{11}^2\right) + (n-2) \cdot 2\left(\mu_2^2 + 2\mu_{101}^2\right) + (n-2)(n-3)\mu_2^2.$$

The sampling variance of m_2 is then, from (15),

$$\operatorname{var}(m_2) = \frac{1}{n}\left[2\mu_2^2 + 4\left(\mu_{11}^2 + \mu_{101}^2\right) - \frac{4\left(\mu_{11}^2 + 2\mu_{101}^2\right)}{n}\right]. \tag{16}$$

The last term in var (m_2) is an end-effect, emanating from the beginning and end of the track. The magnitude of this term is generally a fraction of 1 % of the other terms and is left out. Introducing the expectation values from (4) to (6) in (16), expression (13) reads

$$\frac{\sigma}{\alpha_{100}} = \frac{1}{\sqrt{n}}\left[\frac{9}{16} + \frac{2}{3}\lambda^{-2} + \frac{35}{36}\lambda^{-4}\right]^{\frac{1}{2}} \tag{17}$$

Optimum conditions. With a given track length, L, the standard error given by expression (17) will vary with the cell-size, because both n and λ depend on t in the following way:

$$n = \frac{L}{t} - 1 \simeq \frac{L}{t},$$

$$\lambda = \frac{\alpha_t}{\alpha_n} = \frac{\alpha_{100}}{\alpha_0} \cdot t^{\frac{2p+1}{2}}.$$

After the elimination of t, one obtains

$$n = L\left(\frac{\alpha_{100}}{\alpha_0}\right)^{\frac{2}{1+2p}} \cdot \lambda^{-\frac{2}{1+2p}}. \tag{18}$$

The introduction of (18) into (17) allows an investigation of the minimum standard error (Fig. 12). The solution shows that the optimum condition, when defined by the value assigned to λ, is independent of all track properties and most microscope properties; λ depends only on p, the noise exponent. With very good approximation the solution may be written

$$\lambda^2 = 1.56 + 2.80\,p, \quad \text{if } 0.5 \leq p \leq 1.0. \tag{19}$$

For each microscope given and when p is a constant, the optimum condition is defined by the constant value of the signal-to-noise ratio, as given by (19). The value of λ is inserted into (17) to give the error at the optimum condition. The influence of p is very slight, as may be seen from Table 2.

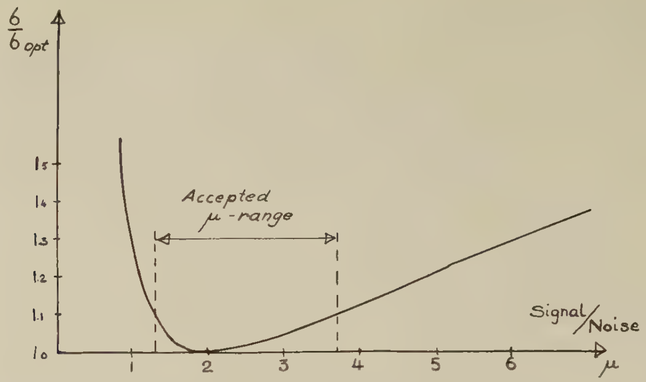

Fig. 12. The standard deviation, σ, in units of its value at the optimum condition as a function of the signal/noise ratio.

Table 2. The optimum condition as a function of p, and the relative standard error.

p	1.0	0.84	0.75	0.50
$\lambda_{\text{opt.}}$	2.09	1.98	1.91	1.72
Standard error at optimum	$\frac{0.88}{\sqrt{n}}$	$\frac{0.89}{\sqrt{n}}$	$\frac{0.90}{\sqrt{n}}$	$\frac{0.95}{\sqrt{n}}$
Instrument	Ideal	M 40171	—	—

The optimum condition is given by a signal-to-noise ratio $= 2.0$ for the microscope discussed here, and it is approximately the same for all noise-exponents met with in practice. The relative standard error of α_{100} may according to (17), be written as $\frac{A}{\sqrt{n}}$. The value of A at the optimum condition is 0.89. In the vicinity of the optimum value its magnitude is given by (17). A 10 % increase of the relative error is according to this theory made if the signal-to-noise ratio is 1.3 or 3.7. As is seen in Fig. 12 the theoretical error is more sensitive to a change in the λ-value on the side below $\lambda = 2$ than above. As one does not know the signal accurately enough in practice it is safer to keep the signal-to-noise ratio within the interval $1.6 \lesssim \lambda \lesssim 3.0$ to get no more than a 10 % increase of the error as compared to that at the optimum condition. To this error comes the uncertainty in α_n as given in (14), $0.07\,\lambda^{-2}$. At the optimum condition this is about 2 %. In view of this error the minimum of the total error is shifted towards higher values of λ; values of λ between 2 and 3 being common. Thus it is best to keep the signal-to-noise ratio in the region $2 \lesssim \lambda \lesssim 4$, in which case the systematic error is 1–2 %.

Simplification of calculations. Instead of computing the root-mean-square deviation in (8), one usually computes the absolute mean deviation of eq. (9). The

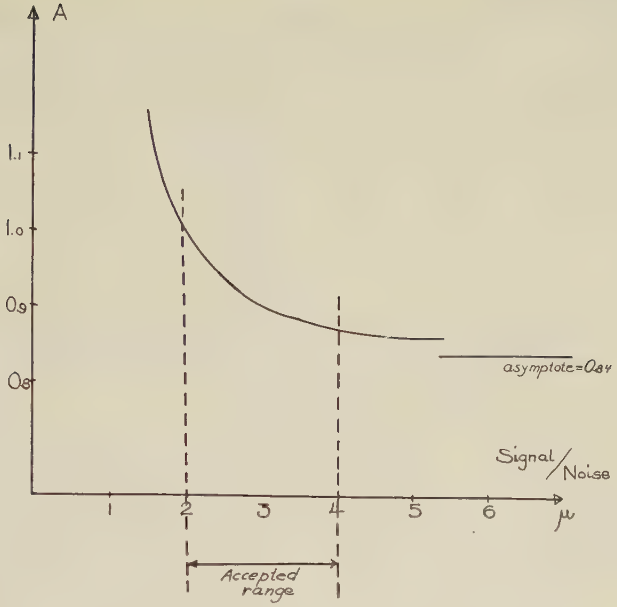

Fig. 13. The relative standard error is written $\frac{A}{\sqrt{n}}$, where the value of A is given in the figure. In view of the influence of the systematic error arising from incomplete knowledge of the noise parameter, the accepted range is shifted to $2 \lesssim \frac{\text{sign.}}{\text{noise}} \lesssim 4$.

effect on the magnitude of the error is expected to increase the error by a factor $\sqrt{\pi - 2} = 1.07$ [18]. The cut-off procedure raises the error by a factor 1.05 [6]. The sampling error of estimator (9) is thus expected to be given by (17) multiplied by 1.12. The function thus obtained is drawn graphically in Fig. 13, from which the appropriate error may be obtained.

The problem of noise-elimination. In several papers a use of (9) has been made, but with the signal-to-noise ratio $\lambda > 4$, in which case the noise has been completely neglected. In this paper the use of (9) has been re-examined and the estimated error deduced.

Other methods of noise-elimination have been proposed. From two or more relations of type (4) with different cell-sizes the scattering parameter may be computed, e.g. the t-$2t$-method [19], and further the noise may be eliminated from the measurements in one and the same cell using equations (4) and (5), i.e. the method of product-moments [20].

A comparison of sampling errors shows that the methods mentioned are all substantially equally accurate. Table 3 contains the estimated standard error of the three methods. n/n_1 is the number of readings normalized to that of the first method. Thus in about 40–50 % of the labour (including readings and computations) approximately the same sampling error is achieved by the method of this paper as compared with the other two methods. The difference lies obviously in

Table 3.

Method of noise elimination	Signal/noise at optimum	n/n_1	Relative standard error	Ref.
Preknowledge of noise	2.1	1.0	$\frac{0.88}{\sqrt{n_1}}$	this paper
Product-moments . .	0.91	1.75	$\frac{1.13}{\sqrt{n_2}}=\frac{0.86}{\sqrt{n_1}}$	20
t-$2t$-method	0.63	2.24	$\frac{1.25}{\sqrt{n_3}}=\frac{0.84}{\sqrt{n_1}}$	21

the circumstance that the other methods must be so performed as to determine the noise also.

However, the 1–2 % error arising from the uncertainty of the noise-parameter is not present in the other methods. On the other hand these methods suffer from another systematic error due to the variation of the noise level with cell-size [21].

In work with $n \lesssim 50$ and when individual tracks are not of paramount interest it is considered justified to use the rapid method of this paper, provided the noise level is accurately known and further kept constant from time to time. In order to attain this state the precautions discussed in earlier sections should be taken so as to suppress disturbing systematic errors. In routine work one usually starts by measuring the signal-angle in a cell larger than the optimum cell. By comparing the following measurements with this first value, a check is made on the constancy of the noise level.

The range of validity of the formula of the relative standard error. The formula is derived by assuming a normal distribution, a large sample and by using the second moment instead of the absolute mean deviation. From some experiments made by O'CEALLAIGH and O. ROCHAT [22] on samples of 7 ($n=7$), it seems that the formula can be applied with confidence even in the case of so small a value as $n=7$. The approximate normal distribution (with cut-off) is actually remarkably good. W. T. SCOTT [23] has calculated the standard error in a similar case numerically. The calculation is based on the theoretical distribution law. His results are not immediately comparable with the formula (17). But, if noise is negligible ($\lambda^{-2}\rightarrow 0$), and a factor 1.05 is multiplied into SCOTT's formula to account for the effect of the correlation between successive chord-angles, the two are comparable. For $200 < \Omega_b < 1000$, SCOTT arrived at a relative standard error of about $\frac{0.84}{\sqrt{n}}$ with regard to the absolute mean deviation with cut-off. The same result is obtained by eq. (17) multiplied by the factor 1.12.

ACKNOWLEDGEMENTS

I should like to express my gratitude to Professor AXEL E. LINDH for his unfailing encouragement, and his kind help in facilitating this work. It is through the financial support of *Atomkommittén* that much of the research has been made possible.

Institute of Physics, University of Uppsala, Sweden, May 1954.

REFERENCES

1. WILLIAMS, E. J., Proc. Roy. Soc. A, *169*, 531, 1939, and Phys. Rev. *58*, 292, 1940.
2. GOUDSMIT, S. A. and J. L. SAUNDERSON, Phys. Rev. *57*, 24, 1940.
3. MOLIÈRE, G., Z. Naturforsch. *2a*, 133, 1948, Ibid. *3a*, 78, 1948.
4. SNYDER, H. S. and W. T. SCOTT, Phys. Rev. *76*, 220, 1949.
5. GOTTSTEIN, K., M. G. K. MENON, J. H. MULVEY, C. O'CEALLAIGH, and O. ROCHAT, Phil. Mag. *42*, 708, 1951.
6. GOLDSCHMIDT-CLERMONT, Y., Nuovo Cim. *7*, 331, 1950.
7. LEVI SETTI, R., Nuovo Cim. *8*, 96, 1951.
8. HISDAL, E., Phil. Mag. *43*, 790, 1952.
9. ÖVERÅS, H., Phil. Mag. *45*, 158, 1954.
10. FOWLER, P. H., Phil. Mag. *41*, 169, 1950.
11. MABBOUX, C., C. R. Acad. Sci., Paris, *232*, 1091, 1951.
12. MOYAL, J. E., Phil. Mag. *41*, 1058, 1950.
13. BONETTI, A., C. C. DILWORTH, and G. P. S. OCCHIALINI, Bull. Cent. Phys. Nucléaire Bruxelles, N° 13 b, 1951.
14. COSYNS, M. and G. VANDERHAEGHE, Bull. Cent. Phys. Nucléaire Bruxelles, N° 15, 1950.
15. CAULTON, M., Rev. Sci. Instrum. *24*, 569, 1953.
16. DODD, E. C. and G. WALLER, Fundamental Mechanisms of Photographic Sensitivity. Butterworths Scientific Publ., London 1951, p. 266.
17. PICKUP, E., Canad. J. Phys. *31*, 898, 1953.
18. KENDALL, M. G., The Advanced Theory of Statistics, Vol. 1. Ch. Griffin & Co. Lim., London 1948, p. 375.
19. See e. g. MENON, M. G. K, C. O'CEALLAIGH, and O. ROCHAT, Phil. Mag. *42*, 932, 1951.
20. D'ESPAGNAT, B., J. Phys. Radium, *13*, 74, 1952.
21. D'ESPAGNAT, B., C. MABBOUX, A. ORKIN-LECOURTOIS, and J. TREMBLEY, Congrès International, Bagnères-de-Bigorre, 1953.
22. O'CEALLAIGH, C., and O. ROCHAT, Phil. Mag. *42*, 1050, 1951.
23. SCOTT, W. T., Phys. Rev. *85*, 245, 1952.

Tryckt den 31 december 1954

Uppsala 1954. Almqvist & Wiksells Boktryckeri AB

ARKIV FÖR FYSIK Band 9 nr 6

Communicated 12 May 1954 by Axel E. Lindh and Harald Norinder

Two different breakdowns between a positive electrode with small curvature and a plane

By Reinhards Siksna

With 8 figures in the text

1. Introduction

During the investigation of positive corona around various electrodes an arrangement was used where corona was formed around a wire loop with various radii of curvature. All the different stages of positive corona were obtained by using narrow bent loops without a breakdown in the gap—loop to plane. When the loop radius of the same diameter wire was greater, the corona phenomena appeared only partly, but a breakdown in form of a spark occurred at a comparatively low potential (Fig. 1). In order to clarify the phenomenon, the following experiments were performed.

2. Experimental arrangement

In the middle of a brass rod A fixed between two plexiglas plates B in a stage, wire loops L of various shapes were installed (Fig. 2). The geometric dimensions of the loops used are characterized by the wire diameter $2r$ and the radius of the curvature of the loop, $R = 2r$, 2.5 mm, 15 mm and ∞. The discharge gap was built between the loop and a 60 mm diameter, 10 mm thick metallic plate P, having rounded edges and adjustable by a micrometric screw S for the desired spacing. It was also possible to install a straight wire opposite the plate P. Aluminium and brass plates were used. No influence by the material of the plates was observed. The material of the wires did not influence the phenomena observed either. The high tension required was supplied by a high tension rectifier HTR with a condenser at the output. A Starke–Schröder high tension voltmeter kV was connected in parallel to the gap. The same simple arrangement was used for determination of the corona current. For this purpose all the system (condenser of the rectifier, being 0.42 μF, + the high tension voltmeter + the corona gap) was charged up to a definite high potential, after that the rectifier was switched off and the dropping of the potential with time was measured. By differentiating the potential-time curve and by multiplying the derivative by the capacity of the system, the corona current-time curve was determined. From the two curves the current-potential characteristics were obtained.

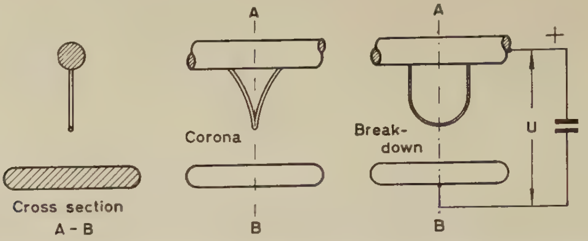

Fig. 1. By using a narrow wire loop corona were built, but when the curvature of the loop was greater a breakdown was observed at the same distance from a negative plate.

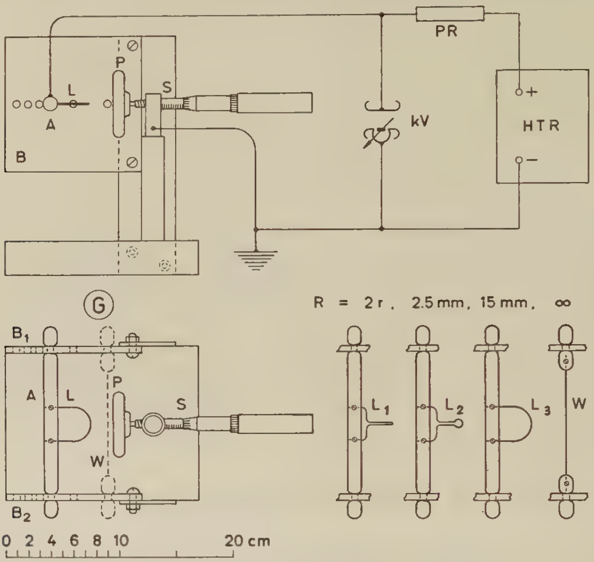

Fig. 2. Experimental arrangement. Gap (G), B_1 and B_2 plexiglas plates, A brass rod, L_1, L_2, L_3 wire loops, W straight wire, P a metallic plate with rounded edges, S micrometer screw; high tension rectifier (HTR), PR protection resistance, kV Starke-Schröder high tension voltmeter.

3. Results

The feature of the obtained potential characteristics in dependence on the spacing δ is shown in Figs. 3, 4, 5. By increasing the potential, a spark or a complete breakdown was observed at a definite potential for a definite shape of the loop and for a definite spacing. However, frequently this first breakdown could be passed over with a more rapid increasing of the potential and thereafter a potential c. twice as high had to be reached for obtaining a breakdown. Therefore we shall call the breakdown at the lower potential the *first breakdown* and that at the higher potential the *second breakdown*. Indeed it was not possible to establish both the breakdowns in all the cases. The first breakdown was not established at a smaller spacing for the straight wire (Fig. 3), likewise some of the first breakdowns did not occur in case of the thinner wire (Fig. 5). In this last case perhaps it was not possible to approach the potential required sufficiently slowly.

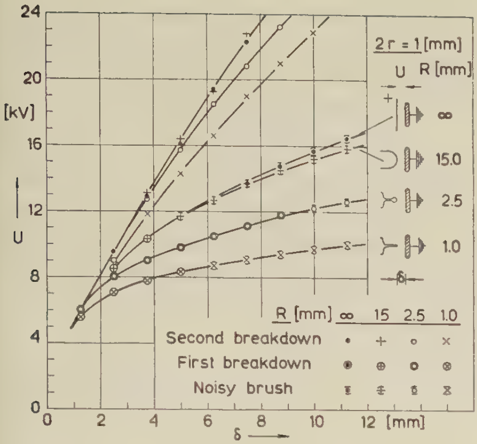

Fig. 3.

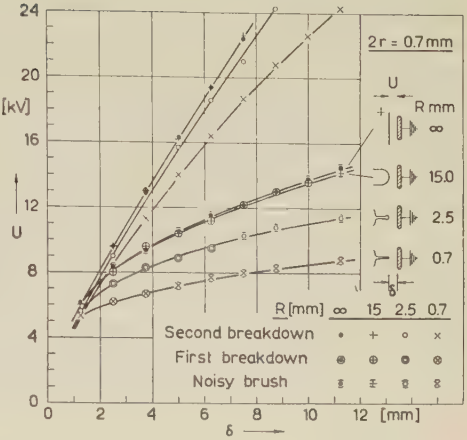

Fig. 4.

Fig. 3. Positive breakdown potential U as a function of the spacing δ between 1 mm wire loops of various forms and a plane.

Fig. 4. Positive breakdown potential U as a function of the spacing δ between 0.7 mm wire loops of various forms and a plane.

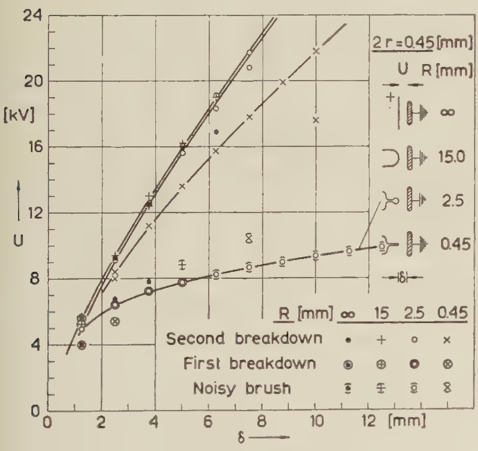

Fig. 5.

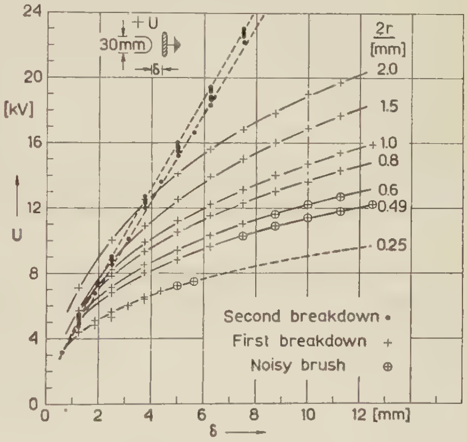

Fig. 6.

Fig. 5. Positive breakdown potential U as a function of the spacing δ between 0.45 mm wire loops of various forms and a plane.

Fig. 6. Positive breakdown potential U as a function of the spacing δ between 30 mm loops of various diameter wires and a plane.

For greater spacing the first breakdown was no longer a complete breakdown, but at the potential at which the first breakdown could be expected, a more or less intense noise was heard and a light phenomenon was observed. This form of the discharge could be identified with what FITZSIMMONS [1] calls "noisy brush". All the three mentioned names: first breakdown, noisy brush and second breakdown, are used in the presented figures. As may be seen, the points for the first breakdown and the noisy brush lie on the same curves and therefore the first breakdown and the noisy brush must be regarded as stages of different intensity of the same phenomenon. By other experiments we have shown that the stage of noisy brush also can be indicated by other means when it is so weak that it may not be heard or seen. These means are (1) the current-potential characteristics, and (2) a cathode ray oscillograph connected to the discharge gap. Especially the last mentioned method was very sensitive and we have used it in some cases in this work. A description in detail of the use of an oscillograph for detection of noisy brush will appear in another publication. Thus, possibilities were indicated by which the first breakdown may be investigated from different aspects.

Returning to the curves it may be seen that no difference is indicated for the second breakdown in the case of the straight wire and that of 30 mm loop. Moreover if the curvature of the loop was smaller, the potentials of the second breakdown were also smaller. For the first breakdown a difference is also indicated for the straight wire and the 30 mm loop, in the last case the first breakdown is lower, for loops with smaller curvatures still lower. The tendency of the dependence on the wire diameter is similar, for wires with smaller diameter the potentials are lower. This fact is shown in Fig. 6 for series of curves for 30 mm loops of wires with various diameters. The points of the first breakdown lie on very smooth curves which form a family. The points of the second breakdown are not so definitely dependent on the wire diameter and lie in a comparatively tight band of another feature. The dependence of the first breakdown on the wire diameter is shown in Fig. 7 for different spacing δ.

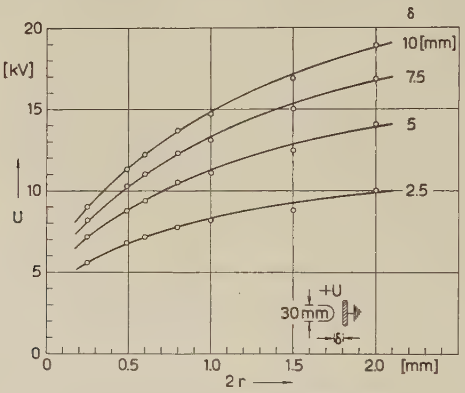

Fig. 7. Positive breakdown potential U as a function of the wire diameter in case of 30 mm wire loops for various spacing δ.

By experiments with noisy brush from other aspects, the importance of the space charge in the gap was indicated. Some correlations could be expected between the space charge and the current through the discharge gap before the breakdown or during the corona stage. The current-potential characteristics are shown therefore in Fig. 8 for the 0.7 mm diameter wire. These characteristics were obtained with the above-mentioned method by measuring the dropping of the potential of the system with time. As may be seen, at smaller spacing already at low potentials the current

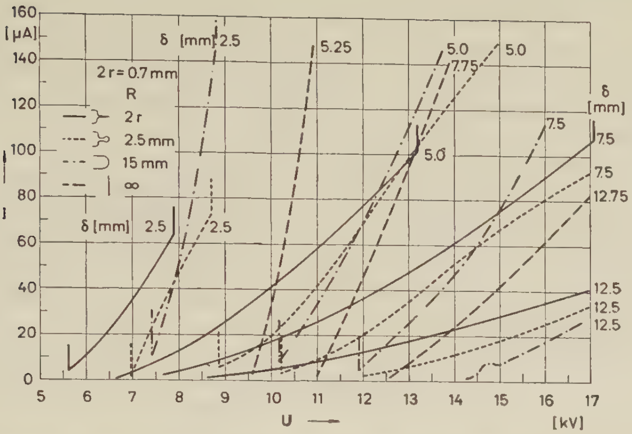

Fig. 8. Current-potential characteristics for various gaps δ between wire loops of various forms and a plane.

was great for smaller curvature of the loops, thus favouring perhaps the appearance of the second breakdown.

The existence of two breakdowns has also been shown by other authors. Uhlmann [6] had observed two breakdowns in a cylindric arrangement. The conditions for appearance of the phenomenon were described as follows: Whether the event appeared in the way mentioned, or whether the potential could be increased to the higher values with dropping out of the lower values, or whether at last the higher value was not reached (the lower breakdowns did not cease in this case), was evidently fortuitous. Reliable conditions for appearance of one or the other case could not be inferred. The higher values could be obtained in general, but not certainly, when the device was connected as quickly as possible to a potential lying between the both mentioned. Then the potential could be slowly increased up to the higher values.

It seems to us, that with our arrangement the conditions for obtaining both the potentials were more reliable. At first, by using the wire loops it was possible to vary the curvature of the electrodes in a simple manner without the difficulties which occur when it is necessary to round the end of a rod with smaller diameter. By using a loop towards an adjustable plate one more advantage is obtained. If the first breakdown was reached and could not be passed over by rashly increasing the potential, as was frequently observed at low spacing, the following procedure was used. The spacing was greater at the outset than that to be examined, then the potential was raised in the region of steady corona and afterwards the desired spacing was adjusted. Although the potential now was higher than that at which the first breakdown had been observed by increasing potential, only corona discharge appeared. But, when the potential now decreased because of the corona discharge, the first breakdown followed at a lower potential. This event is obviously shown by the current-potential curves in Fig. 8. Here the curious effect is shown that at higher potentials only the intense corona discharge was observed, indicated by a comparatively high corona current. However, if this current and the potential decreased, the conditions were finally such that a breakdown in form of a spark followed at a potential corresponding to that at which the first breakdown had been observed by increasing the pontential. Likewise, two positive breakdowns have been established by GÄNGER [2] for a 5 mm sphere to a plane when the spacing was above 10 mm. If now the gap was irradiated by ultraviolet light, the first breakdown dropped out as a surprise for GÄNGER [2].

It seems that the phenomenon of the two positive breakdowns is caused by the positive space charge formed in the gap as indicated first by MARX [3], [4]. The space charge diminishes the field near the anode, increasing it in the rest space. It could be of importance, therefore, to measure the field in the gap during the described different stages of the development of the discharge. If the importance of the space charge was as mentioned here, it might be understandable that by irradiating the gap with ultraviolet light the first breakdown dropped out, as indicated by GÄNGER. In the air irradiated by ultraviolet light large ions are formed [5], negative ions in excess, and perhaps also electrons. By these negative charges the positive space charge may be diminished or even removed.

Acknowledgements

The author is grateful to the Director of the Institute of High Tension Research of the University of Uppsala, Professor H. NORINDER, for providing him with facilities to carry out this work and for his interest in its progress. The Swedish Natural Science Research Council deserves to receive thanks for placing means at the disposal of the Institute to perform this investigation. The author gratefully acknowledges the assistance of Mr. A. METNIEKS.

Institutet för högspänningsforskning vid Uppsala Universitet, March 1954.

REFERENCES

[1] FITZSIMMONS, K. E., Threshold field studies of various positive corona phenomena. *Phys. Rev.*, *61*, 175–182, 1942.

[2] GÄNGER, B., Die elektrische Festigkeit verdichteter Gase. *Arch. f. Elektrotechn.*, *34*, 633–652, 1940.

[3] MARX, E., Der Durchschlag der Luft im unhomogenen elektrischen Felde bei verschiedenen Spannungsarten. *ETZ*, *51*, 1161, 1930.

[4] MARX, E., Der Durchschlag von Luft im unhomogenen Felde. *Arch. f. Elektrotechn.*, *24*, 61–70, 1930.

[5] NORINDER, H. and SIKSNA, R., Ions produced in the air at atmospheric pressure by ultraviolet light from a quartz-mercury arc. *Ark. fysik*, *5*, Nr 23, 471–491, 1952.

[6] UHLMANN, E., Der elektrische Durchschlag von Luft zwischen konzentrischen Zylindern. Dissertation: 1929, T. H. Braunschweig.

Tryckt den 30 december 1954

Uppsala 1954. Almqvist & Wiksells Boktryckeri AB

ARKIV FÖR FYSIK Band 9 nr 7

Communicated 12 May 1954 by Axel E. Lindh and Harald Norinder

Some peculiarities of the current-potential characteristics of positive corona discharge

By Reinhards Siksna

With 6 figures in the text

1. Introduction

During measurements of ions formed by corona, a stage of development of positive corona discharge in a cylindric device was encountered which could be identified with a phenomenon called "noisy brush" by Fitzsimmons [1]. This name seemed to us to be reasonable because a noise and intense light phenomena were observed during this stage of the corona. Because of the intensive discharge observed in the noisy brush, a greater current might also be expected through the corona gap and, therefore, an attempt was made to measure it. Already Fitzsimmons [1] using confocal paraboloid electrodes in air at atmospheric pressure, had shown a very great rise of rather unsteady current as the potential increased. The current soon reached a peak value and then dropped less rapidly toward a minimum with further increase of potential. Recently, phenomena which could also be identified with the noisy brush stage of corona had been described by Wagner [2], but the specific current-potential characteristics were not mentioned, evidently because the current was too small.

2. Experimental arrangement

2.1. *Corona gap.* The corona gap used was the same as for series of experiments with corona (Fig. 1). It was constructed of a piece of c. 35 mm long, and 0.5 mm diameter kanthal wire placed axially in a 30 mm diameter aluminium cylinder. The wire was connected with the positive terminal of a high tension source, the cylinder and the negative terminal of the high tension source were grounded.

2.2. *High tension source.* The source of high tension was a rectifier by which a condenser C_R was charged. At the beginning C_R was $0.22\ \mu$F, later on it was $0.42\ \mu$F. As the proper high tension source, the charged condenser could be considered in the following measurements because in accordance with the method used, the current through the gap was determined by the lapse of the potential of the condenser. At the beginning, it was charged by the rectifier and during the measurements disconnected from it. In this way it was attempted to avoid the necessity of a stabilised high tension source.

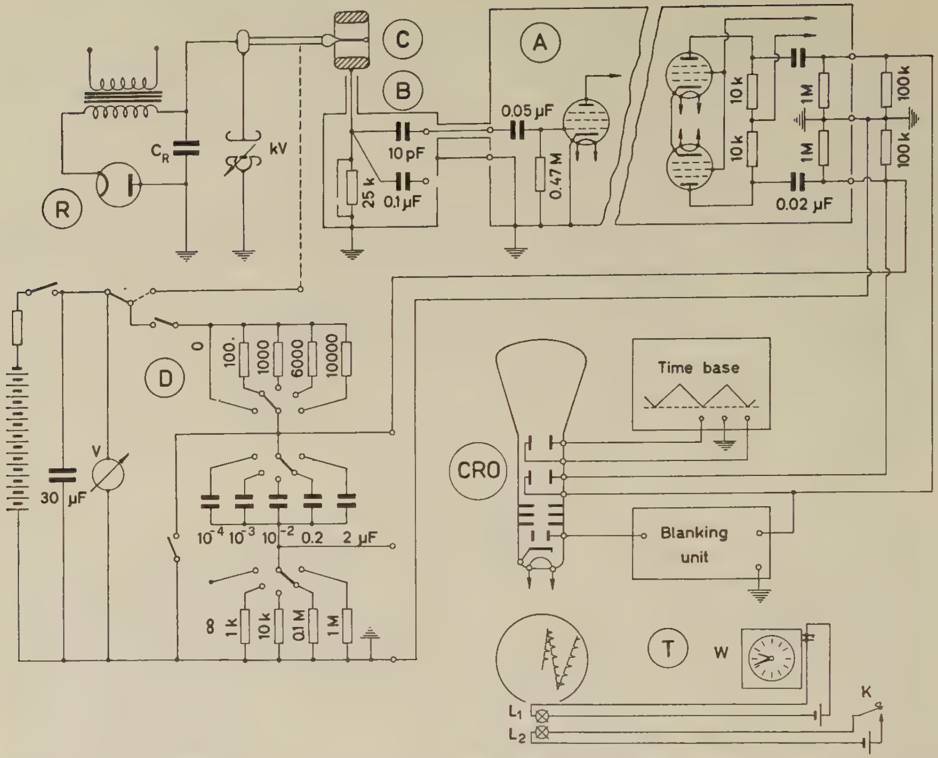

Fig. 1. Schematic diagram of the experimental arrangement. (R) high tension rectifier, $C_R = 0.22$ µF and 0.42 µF, kV Starke-Schröder high tension voltmeter; (C) cylindrical corona gap; (B) coupling box; (A) amplifier; (CRO) cathode ray oscillograph with time base and blanking unit; (D) device for additional deflection; (T) arrangement for time recording, W clockwork, K key, L_1, L_2 incadescent lamps.

2.3. *The method used for determination of corona current.* The following method was used for determination of the current through the gap. The condenser was charged up to c. 14 kV. Thereafter the rectifier was disconnected from the condenser. It was observed that the lapse of the potential of the condenser connected only with the Starke-Schröder high tension voltmeter was very small (from 14 to 13 kV for 5–6 minutes) but when the corona gap was switched on too, dropping of the potential from 14 to 13 kV followed for c. 5 seconds with $C_R = 0.22$ µF and for c. 10 seconds with $C_R = 0.42$ µF. Thus it was possible to determine the dropping of the potential without the corona gap and correct the lapse when it was switched on. In this way a simple method for determination of the corona current was given. For this purpose the lapse of the potential U was determined and the potential-time curves $U = U(t)$ were plotted (Figs. 3, 4, 5). As shown in the figures, a characteristic shape may be seen in the region of potentials at which the noisy brush, indicated oscillographically as will be shown later, occurred. By differentiating $U = U(t)$ curves and by multiplying the derivative with the capacity of the system, the corona current may be obtained

$$I = C_R \, dU/dt.$$

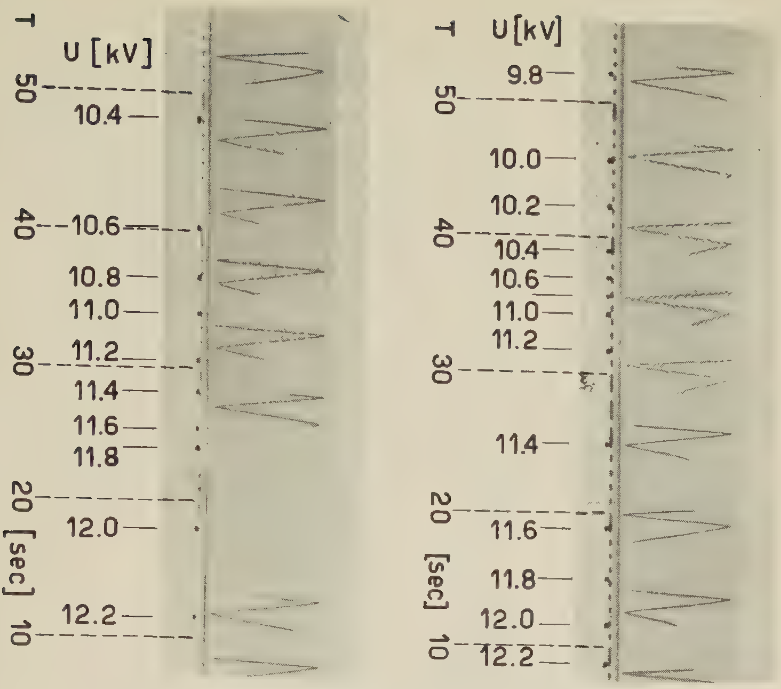

Fig. 2. Examples of films with recorded pulses and time marks.

2.4. *Indication of the noisy brush region.* From our earlier experiments it was known that the region of noisy brush was very sensitively indicated by an oscillograph connected with the corona device. Fitzsimmons [1] and Wagner [2] have also indicated oscillographically intense pulses in the noisy brush region. Arrangement of the apparatuses used by us is shown in Fig. 1. The outer cylinder of the corona gap was grounded through a 20–50 kΩ resistor. The ungrounded end of the resistor was connected by means of a small coupling condenser with a wide band amplifier to a cathode ray oscillograph. Intense pulses were observed on the oscillograph in case of noisy brush. It was, however, not possible to measure the magnitude of the pulses with the device used because of difficulties due to the coupling elements. The frequency of the pulses was measurable. For this purpose an additional sweep was switched on to the impulse plates of the oscillograph. The obtained oscillograms are shown in Fig. 2. When the period of the time base sweep is known the frequency of the pulses may be determined from these oscillograms.

2.5. *Recording of the time.* The dropping of the potential was a comparatively fast event in the case of noisy brush and for recording of the lapse of the potential the photographic recording film of the oscillograph was therefore used. The film was evenly driven and at definite times the additional sweep was switched on to the oscillograph for obtaining the oscillograms shown in Fig. 2. On one side of the oscillograph screen two incadescent lamps were placed, one of which L_1 was switched on every second by a clockwork. The second one L_2 was switched on by means of a hand key K when the high tension voltmeter showed a definite voltage. Marks of seconds and time for the chosen potentials were obtained in this way on the film as shown in Fig. 2.

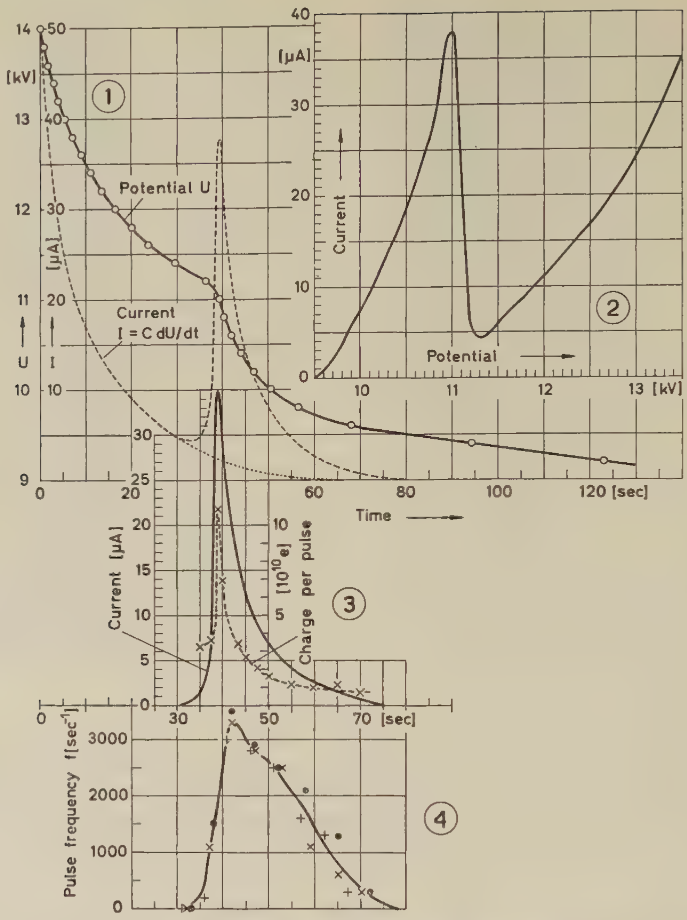

Fig. 3. (1) Dropping of potential U with time; current $I = C\,dU/dt$, $C = 0.22$ μF; (2) current-potential characteristic; (3) current due to noisy brush; number of elementary charges $[10^{10} e]$ per pulse; (4) pulse frequency f during noisy brush.

3. Results

The results of measurements are shown in Figs. 3, 4 and 5.

3.1. *Dropping of the potential.* A characteristic shape of the curves of dropping of potential with time $U = U(t)$ is shown in the figures (1). The potential dropped comparatively fast at the beginning, thereafter slower, but during the noisy brush region again quickly. The presence of the noisy brush is indicated on the lower parts of the figures where the frequency of the pulses is shown (4). The rapid decrease of the potential was observed during this phenomenon.

3.2. *Current and current-potential characteristics.* From the dropping of the potential with time, the corona current I was determined. When the potential decreased in the region of noisy brush the current I increased very much, and after reaching a maximum decreased again. The current-potential characteristics computed from the

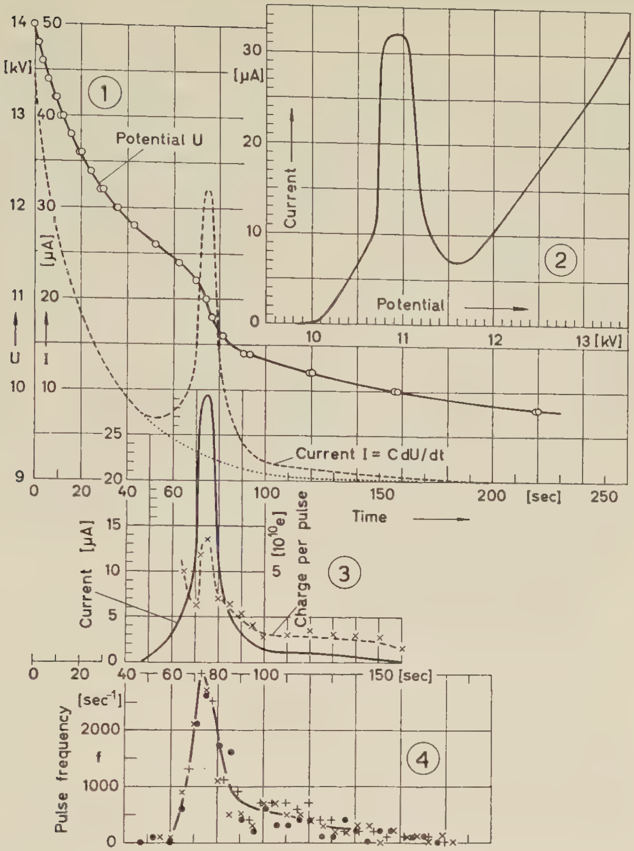

Fig. 4. (1) Dropping of potential U with time; current $I = C\,dU/dt$, $C = 0.42$ μF; (2) current-potential characteristic; (3) current due to noisy brush; number of elementary charges $[10^{10}e]$ per pulse; (4) pulse frequency f during noisy brush.

measured potential and the computed current are shown in Figs. 3, 4, 5 (2). With increasing potential the current rose also at the beginning, reached a maximum, afterwards decreased reaching a comparatively low minimum and increased again. Although it was not possible to increase the potential by the method used and to measure the current (the potential decreased during the observation period), experiments with the observed phenomenon during rising potential showed that its characteristic properties were the same in both cases. Thus the characteristics obtained with decreasing potential could be considered as valid also in the case of increasing potential. The shapes of the potential and of the current curves were not identical in all cases, but in general the phenomenon was the same. The variations may have been caused by the variation of the conditions in the gap. The curves shown in the figures were obtained at $t = 20$–$27°$ C and at the relative humidity of c. 60 % or above that. The dropping of the potential with time was determined several times in each case. Mostly the points coincided almost completely, and in cases when they did not coincide (Fig. 4) the shape of the curve was not changed.

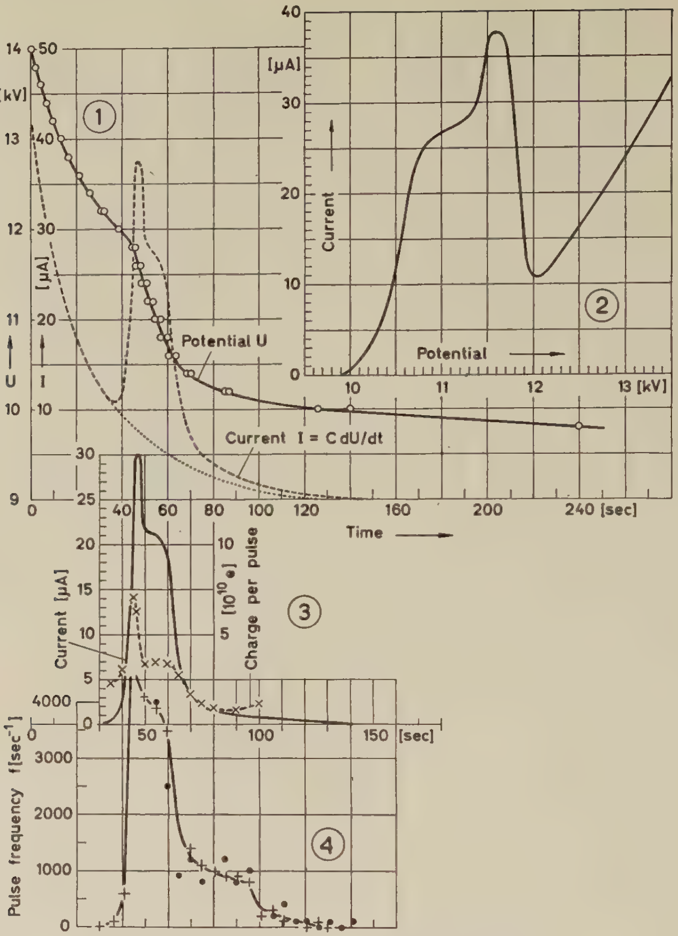

Fig. 5. (1) Dropping of potential U with time; current $I = C\,dU/dt$, $C = 0.42$ μF; (2) current-potential characteristic; (3) current due to noisy brush; number of elementary charges [$10^{10}e$] per pulse; (4) pulse frequency f during noisy brush.

3.3. *Characterization of the noisy brush.* The frequency of the pulses varied perhaps more, but again in each case the points of series of measurements coincided very well, as shown by the points for several series of measurements in the lower parts of the figures (4). The maximal frequency of the pulses was 3000–4000 sec^{-1}. The data by which the noisy brush could be characterized are given in Table 1. The charge per pulse (in 10^{10} elementary charges e) was determined by dividing the current with the frequency. Some variations of the characteristic data may be seen, but the conditions for appearance of the noisy brush are comparatively definite as shown by all the presented material. The causes of the variation of the ranges were preliminarily not clarified, but it seems that the atmosphere where the discharge happened was decisive for that.

3.4. *Noisy brush from the end of a razor blade.* With the used cylindrical arrange-

Table 1. Characteristic data of observed noisy brush.

Start	Maximal frequency of pulses		End	Maximal current		Maximal charge per pulse	
at [kV]	at [kV]	f [sec^{-1}]	at [kV]	at [kV]	[μA]	[10^{10} e]	
11.2	10.6	3300	9.6	11.0	35	11	Fig. 3
11.6	11	3000	9.9	10.9	30	6.8	Fig. 4
12.1	11.8	>4000	10.0	11.6	30	~ 7	Fig. 5

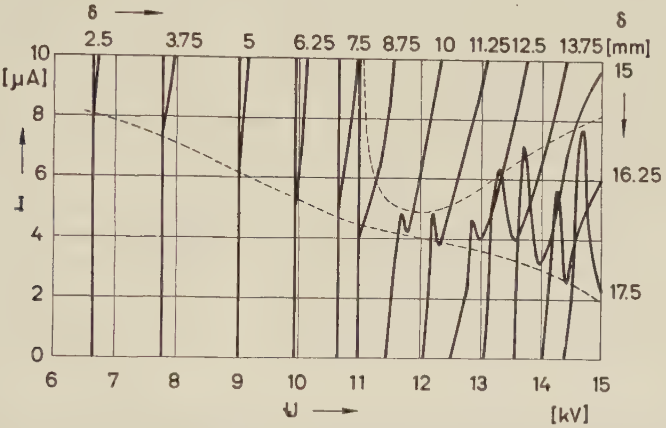

Fig. 6. Current-potential characteristics for various separation δ of the electrodes in case of positively charged end of a razor blade to a grounded negative plate.

ment of the corona gap, it was not possible to change in a simple manner the separation of the electrodes in order to see the variation of the effect at different spacing. Therefore, an attempt was made to use a sharp point towards a plate. The effect was indicated oscillographically, but the current was too small to be determined by the used method. The sharp point was therefore replaced with the end of a razor blade. The corona current was, in this case, sufficient to be determined by the dropping of the potential. The obtained current-potential characteristics are shown in Fig. 6 for different spacing δ of the electrodes. It may be seen that at greater δ (above 10 mm) the characteristics are similar to those observed for the used cylindrical arrangement. With increasing of δ, the peak of the current was more marked, its height increased and the minimal current decreased. For spacings $\delta < 10$ mm another phenomenon appeared. At a potential at which noisy brush could be expected, a spark was observed. The potential at which this spark was observed we call the *first breakdown* potential because at δ only a little below 10 mm, it was possible to pass over this first breakdown and to reach the steady corona region after which a *second breakdown* followed at a much higher potential. At lower δ it was not possible to pass over the first breakdown potential with its rash increasing. In these cases therefore, the following procedure was used. The spacing was taken at first greater than that under examination, the potential was raised in the region of steady corona and after that the desirable spacing δ was adjusted. Now when the potential decreased because of the steady corona discharge, the first breakdown was reached. With increasing potential the second breakdown was reached.

3.5. *Some factors determining the appearance of noisy brush.* FITZSIMMONS [1] has said that he had observed noisy brush only when the relative humidity was above 60 %. Such humidity conditions are usually present in the atmospheric air and the appearance of noisy brush could therefore be expected in the normal atmospheric air if only the humidity conditions were decisive for the phenomenon. But FITZSIMMONS [1] had also observed noisy brush in dry air when the gap was poorly ventilated, and had explained this by the formation of nitric oxides which are produced in the gap in considerable quantities. We can also accept the last mentioned statement. We have not used dry air, because our first intention was to investigate the phenomenon at such conditions which are normally present in the air, with relative humidity above 60 % consequently. But our cylindrical gap was arranged so that it was possible to blow a comparatively strong air-stream along the corona wire. It was possible to diminish the intensity of the noisy brush or even to remove it by using a steady air-stream. On the other hand, if the corona gap was not used for a time, the noisy brush did not appear. However if some air was blown into the gap from the mouth, the noisy brush appeared and the conditions for it were present henceforth although the air was sucked from the gap. The light phenomena around the positive corona electrode during the noisy brush were of the kind which might be explained if the origin of the brush at the electrode was concentrated at definite points or smaller areas at the surface of the positive electrode. Thus it might be concluded that the properties of the surface of the positive corona electrode could also be of importance for the development of noisy brush. It seemed also that by blowing moistened air, the properties of these active surfaces were influenced so that the conditions for appearance of noisy brush were created. From the considered facts it might be concluded that two factors could be mentioned which can favour the appearance of noisy brush: (1) the "atmosphere" in the gap (definite humidity conditions and chemical products formed during discharge), and (2) some still unknown properties of the surface of the positive corona electrode. Investigation of these factors could be a problem in itself.

It was not of importance to compute the electrical field on and around the corona electrode because such a computation could only be geometrical. It is evident that the field around the corona electrode is also determined by the corona discharge in the gap and the properties of the discharge are shown by the current, pulses and also the light phenomena. Therefore a problem of importance could be to measure the field distribution in the corona gap. It seems that the solution of this problem may be facilitated by consideration of the relations between the partial individual processes indicated by various means during corona discharge.

Acknowledgements

The author is grateful to the Director of the Institute of High Tension Research of the University of Uppsala, Professor H. Norinder, for providing him with facilities to carry out this work and for his interest in its progress. The Swedish Natural Science Research Council deserves to receive thanks for placing means at the disposal of the Institute to perform this investigation. The author gratefully acknowledges the assistance of Mr. A. Metnieks.

Institutet för högspänningsforskning vid Uppsala Universitet, March 1954.

REFERENCES

[1] Fitzsimmons, K. E., Threshold field studies of various positive corona phenomena. *Phys. Rev., 61,* 175–182, 1942.
[2] Wagner, L., Korona-Entladungen an der Spitze-Platte-Funkenstrecke. *Arch. f. Elektrotechn. 40,* 331–342, 1952.

Tryckt den 30 december 1954

Uppsala 1954. Almqvist & Wiksells Boktryckeri AB

ARKIV FÖR FYSIK Band 9 nr 8

Communicated 2 June 1954 by IVAR WALLER

Concerning the statistical calculation of cohesive energies of ionic crystals

By PER OLOF FRÖMAN

Although the connection between the one-electron approximation and the statistical approximation[1] is well known, the discusson in this paper gives some new points of view which may be of a certain interest.

In the one-electron approximation the most satisfactory wave function of an ionic crystal (with ions having complete electron shells) is the Slater determinant of the Hartree-Fock functions $\Phi_\mu(\boldsymbol{x})$ $(\mu = 1, 2, \ldots, N)$ of the whole crystal. (The symbol $\boldsymbol{x}$ denotes both the space coordinate $\boldsymbol{r}$ and the spin coordinate ζ of an electron. N is the total number of electrons in the crystal.) The electron density $n(\boldsymbol{r})$ is defined by

$$n(\boldsymbol{r}) = \sum_{\zeta} \sum_{\mu=1}^{N} \int \ldots \int |\Psi(\boldsymbol{x}_1; \ldots; \boldsymbol{x}_{\mu-1}; \boldsymbol{x}; \boldsymbol{x}_{\mu+1}; \ldots; \boldsymbol{x}_N)|^2 \, d\boldsymbol{x}_1 \ldots d\boldsymbol{x}_{\mu-1} \, d\boldsymbol{x}_{\mu+1} \ldots d\boldsymbol{x}_N, \quad (1)$$

where Ψ denotes the normalized Slater determinant of the functions $\Phi_\mu(\boldsymbol{x})$, and $\int d\boldsymbol{x}_\nu$ denotes both an integration over $\boldsymbol{r}_\nu$ and a summation over the two possible values of ζ_ν. From (1) and the ortho-normality properties of the functions $\Phi_\mu(\boldsymbol{x})$ one easily finds that

$$n(\boldsymbol{r}) = \sum_{\zeta} \sum_{\mu=1}^{N} |\Phi_\mu(\boldsymbol{x})|^2. \quad (2)$$

Let E denote the expectation value of the energy of the ionic crystal, calculated with the Slater determinant of the functions $\Phi_\mu(\boldsymbol{x})$ as wave function. Because of the ortho-normality properties of the functions $\Phi_\mu(\boldsymbol{x})$ one obtains the following simple and well-known formula

$$\begin{aligned} E = {} & \tfrac{1}{2} e^2 \sum_{g} \sum_{g^1}{}^{(g)} \frac{z_g z_{g^1}}{|\boldsymbol{r}_g - \boldsymbol{r}_{g^1}|} + \sum_{\mu} \int \Phi_\mu^*(\boldsymbol{x}) \left\{ -\frac{\hbar^2}{2m} \Delta - e^2 \sum_{g} \frac{z_g}{|\boldsymbol{r} - \boldsymbol{r}_g|} \right\} \Phi_\mu(\boldsymbol{x}) \, d\boldsymbol{x} + \\ & + \sum_{\mu} \sum_{\nu} \int \int \Phi_\mu^*(\boldsymbol{x}_1) \Phi_\nu^*(\boldsymbol{x}_2) \frac{e^2}{2|\boldsymbol{r}_1 - \boldsymbol{r}_2|} \Phi_\mu(\boldsymbol{x}_1) \Phi_\nu(\boldsymbol{x}_2) \, d\boldsymbol{x}_1 \, d\boldsymbol{x}_2 - \qquad (3) \\ & - \sum_{\mu} \sum_{\nu} \int \int \Phi_\mu^*(\boldsymbol{x}_1) \Phi_\nu^*(\boldsymbol{x}_2) \frac{e^2}{2|\boldsymbol{r}_1 - \boldsymbol{r}_2|} \Phi_\nu(\boldsymbol{x}_1) \Phi_\mu(\boldsymbol{x}_2) \, d\boldsymbol{x}_1 \, d\boldsymbol{x}_2, \end{aligned}$$

---

[1] P. GOMBÁS, Die statistische Theorie des Atoms (Springer-Verlag, Wien 1949), p. 125.

in which the notations are rather self-explanatory. In terms of the density matrix $(\boldsymbol{x}_1|\varrho|\boldsymbol{x}_2)$ which we define by

$$(\boldsymbol{x}_1|\varrho|\boldsymbol{x}_2)=\sum_{\mu=1}^{N}\Phi_\mu^*(\boldsymbol{x}_1)\,\Phi_\mu(\boldsymbol{x}_2) \tag{4}$$

and the symbol $(\boldsymbol{x}|\Delta|\boldsymbol{x})$ which we define by

$$(\boldsymbol{x}|\Delta|\boldsymbol{x})=\sum_{\mu=1}^{N}\Phi_\mu^*(\boldsymbol{x})\,\Delta\,\Phi_\mu(\boldsymbol{x}) \tag{5}$$

(Δ being the Laplacian operator), the formula (3) can be written

$$\begin{aligned}E=\tfrac{1}{2}e^2\sum_g\sum_{g^1}{}^{(g)}\frac{z_g z_{g^1}}{|\boldsymbol{r}_g-\boldsymbol{r}_{g^1}|}-\frac{\hbar^2}{2m}\int(\boldsymbol{x}|\Delta|\boldsymbol{x})\,d\boldsymbol{x}-\\ -e^2\sum_g z_g\int\frac{(\boldsymbol{x}|\varrho|\boldsymbol{x})}{|\boldsymbol{r}-\boldsymbol{r}_g|}\,d\boldsymbol{x}+\\ +\tfrac{1}{2}e^2\int\int\frac{(\boldsymbol{x}_1|\varrho|\boldsymbol{x}_1)\,(\boldsymbol{x}_2|\varrho|\boldsymbol{x}_2)}{|\boldsymbol{r}_1-\boldsymbol{r}_2|}\,d\boldsymbol{x}_1\,d\boldsymbol{x}_2-\\ -\tfrac{1}{4}e^2\int\int\frac{|(\boldsymbol{x}_1|\varrho|\boldsymbol{x}_2)|^2}{|\boldsymbol{r}_1-\boldsymbol{r}_2|}\,d\boldsymbol{x}_1\,d\boldsymbol{x}_2.\end{aligned} \tag{3'}$$

The usual statistical approximation for E can be obtained from (3′) by approximating locally all functions $\Phi_\mu(\boldsymbol{x})$ by plane waves, i.e., by introducing in (3′) the statistical approximations

$$\begin{aligned}(\boldsymbol{x}|\varrho|\boldsymbol{x}^1)_{\text{statistical}}&=\delta_{\zeta,\zeta^1}\cdot\frac{1}{h^3}\int e^{-\frac{2\pi i}{h}\boldsymbol{p}\cdot\boldsymbol{r}}\,e^{\frac{2\pi i}{h}\boldsymbol{p}\cdot\boldsymbol{r}^1}\,d\boldsymbol{p}\\ &=\delta_{\zeta,\zeta^1}\cdot\tfrac{1}{2}n(\boldsymbol{r})\frac{3(\sin\alpha-\alpha\cos\alpha)}{\alpha^3},\ \left(\text{where }\alpha=\sqrt[3]{3\pi^2 n(\boldsymbol{r})}\,|\boldsymbol{r}^1-\boldsymbol{r}|\right)\end{aligned} \tag{6}$$

and

$$(\boldsymbol{x}|\Delta|\boldsymbol{x})_{\text{statistical}}=\delta_{\zeta,\zeta}\cdot\frac{1}{h^3}\int e^{-\frac{2\pi i}{h}\boldsymbol{p}\cdot\boldsymbol{r}}\,\Delta\,e^{\frac{2\pi i}{h}\boldsymbol{p}\cdot\boldsymbol{r}}\,d\boldsymbol{p}=-\,\delta_{\zeta,\zeta}\cdot\tfrac{3}{10}(3\pi^2)^{\frac{2}{3}}\{n(\boldsymbol{r})\}^{\frac{5}{3}}. \tag{6'}$$

The integrations over p in (6) and (6′) are extended over the region in $\boldsymbol{p}$-space which is defined by

$$\frac{2}{h^3}\cdot\frac{4\pi}{3}p^3\leq n(\boldsymbol{r}).$$

When (6) and (6′) are substituted into (3′), one gets the well-known formula[1]

---

[1] See P. GOMBÁS, Die statistische Theorie des Atoms.

$$E_{\text{statistical}} = \tfrac{1}{2} e^2 \sum_g \sum_{g'}{}^{(g)} \frac{z_g z_{g'}}{|\boldsymbol{r}_g - \boldsymbol{r}_{g'}|} - e^2 \sum_g \int \frac{z_g}{|\boldsymbol{r} - \boldsymbol{r}_g|} n(\boldsymbol{r})\, d\boldsymbol{r} + \tag{7}$$

$$+ \tfrac{1}{2} e^2 \int\int \frac{n(\boldsymbol{r}_1)\, n(\boldsymbol{r}_2)}{|\boldsymbol{r}_1 - \boldsymbol{r}_2|} d\boldsymbol{r}_1\, d\boldsymbol{r}_2 +$$

$$+ \varkappa_k \int \{n(\boldsymbol{r})\}^{\frac{5}{3}} d\boldsymbol{r} - \varkappa_a \int \{n(\boldsymbol{r})\}^{\frac{4}{3}} d\boldsymbol{r},$$

where

$$\varkappa_k = \tfrac{3}{10} (3\pi^2)^{\frac{2}{3}} e^2 a_0 = 2.871\, e^2 a_0$$

and

$$\varkappa_a = \tfrac{3}{4} \left(\frac{3}{\pi}\right)^{\frac{1}{3}} e^2 = 0.7386\, e^2,$$

a_0 denoting the Bohr radius, i.e.,

$$a_0 = \frac{\hbar^2}{m e^2}.$$

For the electron density $n(\boldsymbol{r})$ in (7) one should use the expression (2). Strictly speaking $n(\boldsymbol{r})$ is not exactly equal to the sum of the electron densities $n_g(\boldsymbol{r})$ of the free ions, but it seems natural to assume that the approximations inherent in the statistical treatment are rougher than the approximation to replace $n(\boldsymbol{r})$ by

$$\sum_g n_g(\boldsymbol{r}).$$

If this is done, and if the energies of the free ions are also calculated according to the statistical approximation[1], one obtains from (7) the following approximate expression for the cohesive energy E_{coh} of the ionic crystal[2]:

$$(E_{\text{coh}})_{\text{statistical}} = \tfrac{1}{2} e^2 \sum_g \sum_{g'}{}^{(g)} \frac{z_g z_{g'}}{|\boldsymbol{r}_g - \boldsymbol{r}_{g'}|} - e^2 \sum_g \sum_{g'}{}^{(g)} \int \frac{z_g}{|\boldsymbol{r} - \boldsymbol{r}_g|} n_{g'}(\boldsymbol{r})\, d\boldsymbol{r} +$$

$$+ \tfrac{1}{2} e^2 \sum_g \sum_{g'}{}^{(g)} \int\int \frac{n_g(\boldsymbol{r}_1)\, n_{g'}(\boldsymbol{r}_2)}{|\boldsymbol{r}_1 - \boldsymbol{r}_2|} d\boldsymbol{r}_1\, d\boldsymbol{r}_2 + \tag{8}$$

$$+ \varkappa_k \int \{[\sum_g n_g(\boldsymbol{r})]^{\frac{5}{3}} - \sum_g [n_g(\boldsymbol{r})]^{\frac{5}{3}}\}\, d\boldsymbol{r} -$$

$$- \varkappa_a \int \{[\sum_g n_g(\boldsymbol{r})]^{\frac{4}{3}} - \sum_g [n_g(\boldsymbol{r})]^{\frac{4}{3}}\}\, d\boldsymbol{r}.$$

---

[1] This really corresponds to the approximation that the Hartree-Fock functions for each ion g are approximated by plane waves. Therefore in the derivation of (8) the total energy of the crystal is calculated by approximating the Hartree-Fock functions for the whole crystal by plane waves, while the energy of the free ions is calculated by approximating the Hartree-Fock functions for each ion by plane waves.

[2] H. Jensen, Zs. f. Phys. *101*, 164 (1936).

The cohesive energy is defined as the difference between two large terms (the total energy of the crystal and the total energy of the free ions), each of which is much larger than the cohesive energy itself. Even if the energy of the free ions is calculated so accurately that one uses the numerically tabulated Hartree-Fock one-electron wave functions for the free ions, the error in this calculation cannot be neglected compared with the quantum mechanical part of the cohesive energy (i.e., the cohesive energy with the Madelung part disregarded).[1] As the statistical approximation is, of course, much rougher than the approximation to use the numerically tabulated Hartree-Fock functions, the usefulness[2] of the statistical expression (8) must be due to the fact that the error in the statistical expression for the energy of the crystal and the error in the statistical expression for the energy of the free ions cancel to a large extent when the difference between these two expressions is calculated.

In applications one often uses the Slater determinant of the normalized Hartree-Fock functions $\psi_\mu(\boldsymbol{x})$ $(\mu = 1, 2, \ldots, N)$ for the free ions instead of the more satisfactory Slater determinant of the Hartree-Fock functions $\Phi_\mu(\boldsymbol{x})$ for the whole crystal. For the functions $\psi_\mu(\boldsymbol{x})$ the deformations of the ions in the crystal are obviously not taken into account. Two functions $\psi_\mu(\boldsymbol{x})$ and $\psi_\nu(\boldsymbol{x})$ $(\mu \neq \nu)$ are orthogonal if they belong to the same ion in the crystal. In general they are, however, not completely orthogonal if they belong to different ions in the crystal. By forming linear combinations of all the functions $\psi_\mu(\boldsymbol{x})$ one can obtain a set of ortho-normalized one-electron wave functions[3] $\varphi_\mu(\boldsymbol{x})$ $(\mu = 1, 2, \ldots, N)$.

It is easily verified that the normalized Slater determinant of the functions $\psi_\mu(\boldsymbol{x})$ is identical with the normalized Slater determinant of the functions $\varphi_\mu(\boldsymbol{x})$ (except for an arbitrary phase factor of unit modulus).[4] From the physical point of view these two Slater determinants are therefore completely equivalent. Mathematically it is, however, in certain respects much easier to handle the Slater determinant of the functions $\varphi_\mu(\boldsymbol{x})$ than the other one. The previous treatment can be modified by using the functions $\varphi_\mu(\boldsymbol{x})$ instead of the functions $\Phi_\mu(\boldsymbol{x})$. This is achieved by replacing everywhere the $\Phi_\mu(\boldsymbol{x})$ by the $\varphi_\mu(\boldsymbol{x})$. It is, however, more satisfactory to use the functions $\Phi_\mu(\boldsymbol{x})$ than to use the functions $\varphi_\mu(\boldsymbol{x})$.

We have previously mentioned that the electron density (defined by means of the functions $\Phi_\mu(\boldsymbol{x})$) is not exactly equal to the sum of the electron densities of the free ions. This statement is also true if we had defined the electron density by means of the Slater determinant of the $\psi_\mu(\boldsymbol{x})$ (or $\varphi_\mu(\boldsymbol{x})$) instead of by means of the Slater determinant of the functions $\Phi_\mu(\boldsymbol{x})$. In fact,

$$\sum_{\zeta} \sum_{\mu=1}^{N} |\Phi_\mu(\boldsymbol{x})|^2 \neq \sum_{\zeta} \sum_{\mu=1}^{N} |\psi_\mu(\boldsymbol{x})|^2$$

---

[1] S. O. LUNDQVIST, and P. O. FRÖMAN, Arkiv för Fysik, Band *2*, nr 40 (1950).

[2] The formula (8) has been successfully used for the calculation of cohesive energies, lattice constants and compressibilities of ionic crystals. See P. GOMBÁS, Die statistische Theorie des Atoms.

[3] This ortho-normalization was first carried out by R. LANDSHOFF, Zs. f. Phys. *102*, 201 (1936). Later P. O. LÖWDIN has done it very elegantly by matrix algebra, Thesis, Uppsala 1948.

[4] P. GOMBÁS, Theorie und Lösungsmethoden des Mehrteilchenproblems der Wellenmechanik (Verlag Birkhäuser, Basel 1950), p. 81.

and

$$\sum_{\zeta}\sum_{\mu=1}^{N}|\varphi_\mu(\boldsymbol{x})|^2 \mp \sum_{\zeta}\sum_{\mu=1}^{N}|\psi_\mu(\boldsymbol{x})|^2.$$

In the Heitler-London treatment of ionic crystals, which is based on the use of the Slater determinant of the functions $\psi_\mu(\boldsymbol{x})$ (or $\varphi_\mu(\boldsymbol{x})$) as wave function, one can derive an expression for the cohesive energy[1] by using (3) (with the $\Phi_\mu(\boldsymbol{x})$ replaced by the $\varphi_\mu(\boldsymbol{x})$) and (9) (to be given later) and by using the fact that the functions $\psi_\mu(\boldsymbol{x})$ shall satisfy the Hartree-Fock equations for the free ions. In the final expression which one then obtains the terms are of comparable order of magnitude and the cohesive energy no longer appears as the difference between two larger terms which nearly cancel each other. If the functions $\psi_\mu(\boldsymbol{x})$ in this expression for the cohesive energy are approximated by plane waves within each ion g, one would get a new statistical method for the calculation of cohesive energies of ionic crystals. This idea is due to Professor I. WALLER (unpublished). Along these lines the present author performed some preliminary calculations on RbJ in 1949 (unpublished). The result was not good, but the reason for this may be due to the fact that some very rough approximations were introduced in the calculations.

It seems natural that those wave functions, which are locally replaced by plane waves in the statistical approximation, should form an ortho-normalized set, because these plane waves are themselves supposed to be ortho-normalized. Therefore one has three obvious possibilities: either to approximate all functions $\Phi_\mu(\boldsymbol{x})$ by plane waves, or to approximate all functions $\varphi_\mu(\boldsymbol{x})$ by plane waves, or to approximate for each ion those functions $\psi_\mu(\boldsymbol{x})$ that belong to that ion by plane waves. The former two possibilities both lead to the expression (7) for the energy E, the only difference between these two cases being that $n(\boldsymbol{r})$ is defined as

$$\sum_{\zeta}\sum_{\mu}|\Phi_\mu(\boldsymbol{x})|^2$$

in the first case but as

$$\sum_{\zeta}\sum_{\mu}|\varphi_\mu(\boldsymbol{x})|^2$$

in the second case. The third possibility leads to the previously mentioned treatment suggested by WALLER.

If one tries to draw conclusions concerning finer details of the properties of matter by means of statistical methods one must, of course, by very careful and critical. This is easily seen from the following remarks on the Cauchy relations. As was first pointed out by LÖWDIN[2] and later supplemented by LUNDQVIST,[3] the Heitler-London approximation leads to the conclusion that the Cauchy relations are in general not valid for ionic crystals. An application of the statistical formula (8) would, however, lead to the conclusion that the Cauchy relations are in general valid. This is easily seen as follows. In the statistical theory the ions have finite radii, and in most crystals the regions where three or more ions overlap are so small that their contributions to the integrals in (8) can be entirely neglected. In this approximation the right-hand side of (8) is in reality a sum of two-center integrals in which each integral depends only on the distance between the ions, whence it immediately follows that the Cauchy relations are valid in the statistical treatment which is based on the formula (8). In the previously mentioned statistical treatment of ionic crystals which was suggested by WALLER, it is, however, very probable that the Cauchy relations would not be valid in general. For the question of the validity of the Cauchy relations in statistical treatments it is of importance which one of the function systems $\Phi_\mu(\boldsymbol{x})$ or $\varphi_\mu(\boldsymbol{x})$ or $\psi_\mu(\boldsymbol{x})$ one approximates by plane waves. The functions $\psi_\mu(\boldsymbol{x})$ are, so to speak, rigidly connected with the ions in the lattice and do therefore not change by a deformation of the lattice in other respects than being bodily displaced. The functions $\varphi_\mu(\boldsymbol{x})$ and $\Phi_\mu(\boldsymbol{x})$ on the other hand are intrinsically changed in a complicated way by lattice deformations. These remarks on the Cauchy relations in statistical treatments of ionic crystals are not meant as an attempt to decide whether there are theoretical reasons to believe that the Cauchy relations should be valid or not, but rather as an example of a case where the statistical methods are too rough to give a significant result.

---

[1] This expression for the cohesive energy, as well as references to earlier papers which contain similar expressions, can be found on p. 15 in LÖWDIN's thesis (l.c.).

[2] P. O. LÖWDIN, l.c.

[3] S. O. LUNDQVIST, Arkiv för Fysik, Band *6*, Nr 3 (1952).

Although the use of the Slater determinant of the functions $\psi_\mu(\boldsymbol{x})$ (or $\varphi_\mu(\boldsymbol{x})$) as wave function of the crystal need not necessarily be a very good approximation, we shall apply LÖWDIN's ortho-normalization formulae to derive a formula for

$$\sum_\zeta \sum_\mu |\varphi_\mu(\boldsymbol{x})|^2 - \sum_g n_g(\boldsymbol{r}).$$

According to LÖWDIN[1]

$$\varphi_\mu(\boldsymbol{x}) = \sum_\nu \{(1+S)^{-\frac{1}{2}}\}_{\nu\mu}\, \psi_\nu(\boldsymbol{x}), \tag{9}$$

where the elements of the matrix S are defined by

$$S_{\mu\nu} = \int \psi_\mu^*(\boldsymbol{x})\, \psi_\nu(\boldsymbol{x})\, d\boldsymbol{x} - \delta_{\mu\nu}. \tag{10}$$

From (9) we get

$$\sum_\zeta \sum_{\mu=1}^{N} |\varphi_\mu(\boldsymbol{x})|^2 - \sum_g n_g(\boldsymbol{r}) = -\sum_\zeta \sum_{\mu=1}^{N} \sum_{\nu=1}^{N} \left(\frac{S}{1+S}\right)_{\mu\nu} \psi_\nu^*(\boldsymbol{x})\, \psi_\mu(\boldsymbol{x}) \tag{11}$$

by using the facts that

$$\sum_g n_g(\boldsymbol{r}) = \sum_\zeta \sum_\mu |\psi_\mu(\boldsymbol{x})|^2$$

---

[1] The most general ortho-normalization is obtained by multiplying $(1+S)^{-\frac{1}{2}}$ in (9) by an arbitrary unitary matrix. See LÖWDIN's thesis, Eq. (2.3), p. 14.

and $S^{\dagger}=S$. If the overlap integrals $S_{\mu\nu}$ are sufficiently small, we have[1]

$$\frac{S}{1+S}=S-S^2+S^3-+\cdots.$$

By approximating every matrix element of $\frac{S}{1+S}$ by the corresponding first non-vanishing matrix element in the series $S-S^2+S^3-+\cdots$ and by substituting the expression (10) for the matrix elements of S, one can write the right-hand side of (11) in terms of the density matrices $(\boldsymbol{x}'|\varrho_g|\boldsymbol{x}'')$ which we define by

$$(\boldsymbol{x}'|\varrho_g|\boldsymbol{x}'')=\sum_{\mu}^{g}\psi_{\mu}^{*}(\boldsymbol{x}')\,\psi_{\mu}(\boldsymbol{x}''),$$

$\sum_{\mu}^{g}$ denoting a summation over those μ for which μ belongs to the ion g.

As far as the author knows, very few direct numerical comparisons have been carried out between integrals calculated by using the tabulated Hartree-Fock functions and the same integrals calculated by using the statistical approximation. It would, however, surely be of value if such purely numerical comparisons were done, because one could then get reliable quantitative estimates of the accuracy of the statistical approximation.

Finally I wish to thank Professor I. WALLER for suggesting to me a problem which directed my interest to the questions which are treated in this paper, and also for the many valuable discussions which I have had with him at various times. I am also much indebted to Drs. S. O. LUNDQVIST and P. O. LÖWDIN for their valuable suggestions and criticism concerning my manuscript.

---

[1] A mathematical condition for the validity of this expansion can be found in COURANT-HILBERT, Math. Physik I, p. 16.

Tryckt den 31 december 1954

Uppsala 1954. Almqvist & Wiksells Boktryckeri AB

ARKIV FÖR FYSIK Band 9 nr 9

Communicated 22 September 1954 by Axel E. Lindh and Harald Norinder

Bromine-quenched and iodine-quenched Geiger-Müller counters

By Gösta Brogren

With 1 figure in the text

In a discharge in a Geiger-Müller counter filled with a rare gas and a quenching agent (commonly a suitable organic vapour) a positive space charge is formed around the centre wire. It has the form of a positive ion cylinder, which moves outwards towards the cathode under the influence of the electric field between the anode and the cathode. During the path every ion undergoes many collisions with neutral atoms and vapour molecules (approximately 10^5). Since the ionization potential of the vapour molecule must be less than that of the rare gas, electron transfer occurs between gas ions and vapour molecules so that only vapour ions reach the cathode. At the same time all metastable rare gas molecules formed during the discharge must be de-excited by collisions with vapour molecules. The released energy is either transferred to the molecule or gives rise to a photon. If the energy of the photon is so great that a photo-electron can be released from the cathode the radiation must be absorbed by the quenching vapour.

When the vapour ions are within about 10^{-7} cm from the cathode they are neutralized and get an excitation energy of $I - \Phi$, where I is the ionization energy of the vapour molecule and Φ is the work function of the cathode. If $I > 2\,\Phi$, the excitation energy is so great that a secondary electron can be released from the cathode, for instance by radioactive de-excitation followed by a released photoelectron. For the commonly used polyatomic organic vapours the life of the excited molecule is about 10^{-13} sec. in the case of predissociation, but about 10^{-8} in the case of radioactive de-excitation. Hence, only about one excited molecule of 10^9 can give rise to a secondary electron. The molecule undergoes predissociation and the discharge is self-quenched [1].

The following conditions are necessary for the counter to be self-quenching:

1. the ionization potential of the vapour molecules must be less than that of the rare gas molecules;
2. the vapour must have a continuous absorption for all radiation with a higher photon energy than the work function of the cathode surface and it must undergo predissociation. This also means that the excess energy radiated by an excited neutral gas atom after inelastic collision between a gas ion and a vapour molecule is absorbed if the difference between the ionization potentials of the gas and the vapour is greater than the work function of the cathode.

Table 1. The ionization potential and the energy of the metastable states of rare gases and vapours, used in G.-M. counters.

		Ionization potential in volts	The energy of the metastable states in volts	
Helium	He	24.5		
Neon	Ne	21.7	16.58	16.78
Argon	A	15.77	11.57	11.77
Krypton	Kr	14.01	9.99	10.60
Xenon	Xe	12.14	8.39	9.53
Ethyl alcohol	C_2H_5OH	11.3		
Ethyl ether	$(C_2H_5)_2O$	9.72		
Methylal	$CH_2(OCH_3)_2$	11.0		
Hydrogen	H_2	15.37		
Chlorine	Cl_2	13.2		
Bromine	Br_2	12.8		
Iodine	J_2	9.7		

On account of the dissociation a large number of vapour molecules are decomposed in every discharge so that the lifetime of the counter is finite. The decomposition products, which are partly polymerized, contaminate the electrodes and this rather than the removal of the vapour is the reason for the ageing of the counter. The contamination can easily be studied with a microscope. In order to refit a counter that has broken down, the wire and the cathode must be cleaned before refilling.

Some of these disadvantages can be eliminated if chlorine, bromine or iodine vapour is used as a quenching agent [2]. Chlorine and bromine have continuous absorption for wavelengths below about 2500 Ångströms. The absorption is followed by predissociation. Iodine has no continuous absorption in this region but its ionization potential is only 9.7 volts. The work function Φ is 5 volts or more for nearly all cathode surfaces, so that the energy $I - \Phi$ released when the iodine ion is neutralized is less than the work function. Hence no secondary electron can be released from the cathode.

Chlorine and bromine-quenched Geiger-Müller counters filled with argon and neon have been used with good results [3]. These counters were intended for use in nuclear physics research. When Geiger counters are to be used as X-ray detectors it is desirable to utilize counters containing krypton or xenon, which gives much higher sensitivity to hard X-radiation. We have here investigated the possibility of using these rare gases in halogen-quenched counters. As appears from Table 1 the ionization potential of xenon is 12.14 volts. Among the halogens only iodine has a lower ionization potential. As this element has not been used as quenching agent previously, we have investigated the possibility of using it together with the other rare gases.

Different cathode materials were used in the counters, but only chromium-iron and some types of stainless steel were resistant against chemical attacks from iodine and bromine. These materials were not attacked by the vapours themselves, but stainless steel was slowly affected on account of the discharges. During these, positive halogen ions are formed, which are dissociated to atomic halogen during neutralization. This again reacts so that halogen molecules are reformed, which is the reason why counters of this type have a nearly infinite life and why they are not destroyed y too high voltages. However, the atomic halogen is much more reactive than the nolecular one, and this probably explains the slow attack on stainless steel.

Bromine was purifed by destillation in vacuum. Before the counter was filled, the valls were saturated with halogen, after which pumping was carried out. Bromine apour with a pressure of 10 mm was mixed with krypton in a glass container until he total pressure was 100 mm (all pressure in mm of Hg). This mixture and pure rypton were inserted into the counter so that the intended mixture was obtained. ll investigations were carried out at a total pressure of 100 mm. The partial pressure f bromine varied between 0.03 mm and 20 mm.

When the bromine pressure was low (less than 0.1 mm), oscillations were observed n the counters before the beginning of the plateau, a phenomenon which agreed with arlier observations [3].

As the partial pressure of bromine became greater, the number of negative bromine ons formed in the discharge increased and more multiple pulses were formed. At the ame time the efficiency of the counter diminished somewhat. The dead time also ncreased with the partial pressure of bromine. The best results were obtained at a romine pressure of about 0.2 mm of Hg. Such counters were compared with normal rypton-alcohol counters (krypton 90 mm of Hg, and ethyl alcohol 10 mm of Hg). The bromine counters had a threshold voltage that was 10–20 per cent less. They ad good plateaux with a slope of about 0.04 %/volt. Simultaneous investigations vith an oscilloscope showed that multiple pulses appeared when the working voltage vas more than 50 volts above the threshold voltage. The reason for this is probably hat the number of metastable krypton atoms excited in the discharge increases with he overvoltage. At last so many are formed that some reach the cathode before they re de-excited. A secondary electron can now be released and a new discharge takes lace. As the ionization potential of bromine vapour (Br_2) is higher than the energy f the metastable state, the de-excitation probability when collision takes place with bromine molecule is much less than in a neon-bromine counter, where the metastable state can be de-excited by an inelastic collision. Also, in such counters the ercentage of multiple discharges is increased for a relatively slight overvoltage. For his reason the working voltage of a halogen-quenched counter should not exceed he threshold voltage with more than some ten volts.

The properties of iodine vapour as a quenching agent were investigated in Geiger-Müller counters filled with neon, argon, krypton or xenon. The ionization potential f iodine is less than that of the rare gases, but it is also less than the energies of the netastable states of neon, argon and krypton. (See Table 1.) When a collision takes lace between an iodine molecule and an excited metastable atom of one of these lements, the latter is as a rule de-excited. The released energy ionises the iodine nolecule so that a positive ion and an electron are liberated. In this way the electron valanche increases more rapidly, which in its turn causes the potential difference etween the anode and the cathode necessary for a discharge to be much reduced. he threshold voltage of krypton counters with a total pressure of 100 mm of Hg vas 1350 volts with an admixture of 10 mm Hg of methylal ($CH_2[OCH_3]_2$), 1140 volts vith 0.2 mm of bromine and 640 volts with 0.2 mm of iodine. The corresponding rgon-iodine counter had a threshold voltage of 550 volts, and the neon-iodine ounter 390 volts. In a xenon counter with 100 mm total pressure and 0.2 mm iodine dmixture the threshold voltage was 1150 volts, which is only 200 volts lower han the value obtained in a counter with 90 mm xenon and 10 mm ethyl ether.

In all iodine-quenched counters multiple pulses appeared when the working voltage

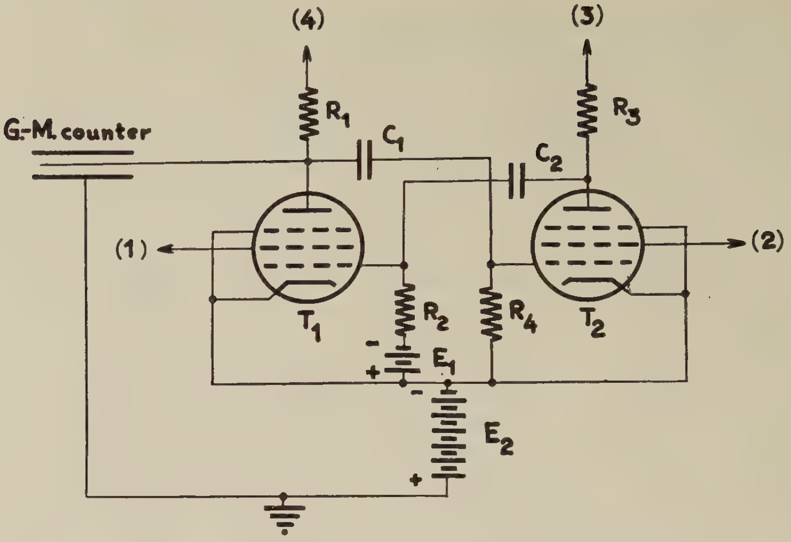

Fig. 1. The quenching circuit.

R_1	50–100 kohm	E_1	6–10 volts
R_2	100 kohm	E_2	100–150 volts
R_3	50 kohm	(1)	100 volts above methode potential
R_4	100 kohm	(2)	60 ,, ,, ,, ,,
C_1	12 μμF	(3)	100 ,, ,, ,, ,,
C_2	25 μμF	(4)	Working voltage of the counter.

exceeded the threshold by about 40 volts. Iodine-quenched krypton and xenon counters as well as bromine-quenched krypton counters were tested with high over voltages. Overvoltages that caused direct discharges between anode wire and cathode cylinder did not destroy the counters, contrary to what happens to ordinary counters quenched with some organic vapour; these are destroyed immediately if overvoltage is applied. The above counters were also tested by continuous counting for long periods. Counting of $5 \cdot 10^9$ pulses influenced the counters very slightly. In counters where the wire and the cathode cylinder were made of stainless steel the plateaux were displaced towards higher voltages. Such a counter kept on counting until he plateau was too small for reliable counting. Refilling did not restore the original properties. Observations in a microscope showed that the wire was attacked during the discharge so that metal iodine was formed on it. When the wire was exchanged for a new one, refilling gave a good counter. Counters with tungsten wire and a chromium-iron cathode were more resistant against chemical attack.

The counters were also used together with a potential reversing flip-flop circuit, shown in Fig. 1. Tube T_1 is normally non-conducting. A negative pulse from the Geiger-Müller counter of about 0.2 volts is sufficiently amplifed in T_2 to cause the grid in tube T_1 to come above cut-off; a new negative pulse is added to the grid of the second tube and the action proceeds until the second grid is below cut-off. The time during which the first tube is conducting is determined by the time constant C_1R_4. As the grid of T_2 recovers, the plate current of T_2 starts and a negative pulse on the grid of tube T_1 abruptly brings this below cut-off. The time required for the entire cycle of the circuit operation is 25–30 μsec.

When the first tube is conducting, the anode wire of the counter is brought below the earth potential. The electron avalanche takes place very near the wire. As the mobility of the positive ions is small and as the time between the initial ionization and the potential reversing action is less than one μsec., the positive ions will be drawn back to the wire and be neutralized there. In this way the dead time of the counter is reduced to about 30 μsec. However, as the time between the initial ionization and the potential drop of the counter wire is short, the discharge is interrupted before it has spread along the whole wire, which must be partly due to the improvement in the dead time.

When the halogen-quenched counters were tested with this circuit, chlorine and bromine quenched counters as well as counters quenched with organic vapours functioned very well. Iodine-quenched argon and krypton counters also worked together with the circuit, but multiple pulses appeared about 30 volts above the threshold voltage. Iodine-quenched xenon counters did not work, as they gave almost exclusively multiple pulses. The ionization potential of iodine is higher than the energy of the metastable state of xenon but lower than that of the other rare gases. Hence a metastable xenon atom cannot be de-excited by an inelastic collision with an iodine molecule. De-excitation can only take place by radioactive emission or by collision with the walls of the counter. The life-time of the metastable state is so long that a great number metastable xenon atoms still exist after the quenching of the electric discharge. The ultraviolet radiation emitted in the de-excitation has an energy of 8.4–9.5 volts (see Table 1). In the ultraviolet wavelength range the iodine molecule is characterized by absorption bands. The absorption is often followed by fluorescent radiation and the iodine molecule does not undergo predissociation as do the bromine and the chlorine molecules. The probability that protoelectrons will be released from the cathode cylinder and give rise to a new discharge when the metastable xenon atoms are de-excited is so great that this will generally happen. Hence xenon-iodine counters can only be used in connection with a quenching circuit with a dead time long enough to make the probability of obtaining multiple pulses small. Bromine is to be preferred as quenching gas in connection with the other rare gases, as it gives fewer multiple pulses than the iodine-quenched counters. This seems to be due to the fact that the iodine molecule does not predissociate when absorbing ultraviolet radiation. In all halogen-quenched counters the working voltage should be kept rather near the threshold of the plateau so that the risk of multiple pulses is kept as low as possible.

REFERENCES

1. Korff, S. A., Electron and Nuclear Counters, New York 1946.
2. Present, R. D., Phys. Rev. *72*, 243 (1947).
3. Liebson, S. H. and Friedman, H., Rev. Sci. Instr. *19*, 303 (1948).

Tryckt den 9 december 1954

Uppsala 1954. Almqvist & Wiksells Boktryckeri AB

ARKIV FÖR FYSIK Band 9 nr 10

Communicated 27 October 1954 by MANNE SIEGBAHN and ERIK HULTHÉN

Studies in nuclear spectroscopy with electromagnetically separated gaseous isotopes. I

Isotope separator and sample preparation

By SIGVARD THULIN

With 16 figures in the text

Contents

Page
Acknowledgements 108
Introduction: Electromagnetic mass separators and their application to nuclear physics 108
  1. Short review and classification of existing separators 108
  2. "Production capacity" of a separator. Isotope quantities required 110
Chapter I. The isotope separator at the Nobel Institute of Physics 111
  1. General 111
  2. Improvement of the resolving power by operation as a symmetrical sector field instrument 113
  3. Improved stabilization of the mass spectrum 116
Chapter II. Isotope collection and properties of targets prepared in the isotope separator 118
  1. Introduction 118
  2. Collection of gaseous stable isotopes for nuclear reaction studies 119
  3. Temperature stability of gas targets 121
  4. Collection of radioactive isotopes 123
    a. General 123
    b. Preparation of sources for β- and γ-spectrometer measurements 124
Chapter III. An experimental study of saturation effects occurring in the collection of rare gas isotopes 126
  1. Introduction 126
  2. Saturation studies by means of tracer technique 126
  3. Saturation studies using stable isotopes 128
  4. Results 129
Chapter IV. Concluding remarks 133
Summary 135
References 135

Acknowledgements

The present investigation has been carried out at the Nobel Institute of Physics, Stockholm. I am very much indebted to the head of the Institute, Professor MANNE SIEGBAHN, for placing all the facilities of the Institute at my disposal, and for his continuous encouragement throughout the course of these investigations.

Many of the measurements reported here are of a nature which requires the uninterrupted operation of several machines: the cyclotron, the isotope separator and the β- and γ-spectrometers. It is impossible to perform such measurements without the assistance of several people. It is a great pleasure for the author to express his sincere thanks to all the members of the Institute who have contributed, in various respects, to the completion of the present investigations.

I am greatly indebted to Professor K. SIEGBAHN, who in 1949 suggested an investigation of the Kr^{88} decay. In fact this initiated the present work an rare gas isotopes.

In particular, I am most grateful to Dr. I. BERGSTRÖM for valuable suggestions and discussions and for his stimulating assistance during the whole of this work, a great deal of which is based on mutual experience gained during operations with the separator. It should also be pointed out that the improvements to the separator, described in the present paper, were effected as the result of common efforts.

The skilled assistance in the separator work given by Mr. E. WÅHLIN and, more recently, Fil. kand. T. ALVÄGER must be acknowledged here.

Most of the β-spectroscopy was performed using the intermediate image β-spectrometer, designed by Professor H. SLÄTIS and Professor K. SIEGBAHN. The author is indebted to them for discussions on problems arising from these measurements.

Many of the disintegration studies have been performed using scintillation spectrometers designed by Civ. ing. B. ÅSTRÖM. I wish to express my most sincere thanks to him for enlightening discussions and for indispensable help in maintaining various pieces of electronic equipment.

Special mention should be made of the considerable assistance given by Dr. H. ATTERLING, Dr. K. G. MALMFORS and also their cyclotron personnel, for providing the irradiations.

Finally, I must thank the Cockcroft-Walton accelerator group, Dr. D. MILEIKOWSKY, Dr. R. PAULI and Tekn. lic. K. AHNLUND, for cooperation and discussions in the study of gas collection phenomena.

Stockholm, October 1954. *Sigvard Thulin*

Introduction

Electromagnetic mass separators and their application to nuclear physics

1. *Short review and classification of existing separators*

As is well known, the method of electromagnetic isotope separation originated with the experiments of J. J. THOMSON 1910 [T1], A. J. DEMPSTER 1918 [D1], and F. W. ASTON 1919 (A11] on positive ray analysis in electric and magnetic fields. The application of the method was soon developed along two quite different branches; mass spectrography (photographic ion detection) and mass spectrometry (electrometric ion detection). The mass spectrographs were designed for measurements of isotopic masses and mass differences with the highest precision. The mass spectrometers were constructed for accurate measurements of relative isotopic abundances. The electromagnetic separation method, as applied in these two types of apparatus, has made important contributions to our fundamental konwledge of nuclear physics. For example, measurements of isotopic masses supported the hypothesis that all nuclei are built up of particles of the same mass as that of the proton; the packing fraction curve gives information about nuclear stability; the fine structure of this curve and the isotopic abundance statistics give support to nuclear shell theory.

It was recognized at an early stage that the electromagnetic separation method offered the possibility of preparing isotopically pure samples for nuclear investigations. Considerable attention was devoted to this problem in the nineteen thirties, when particle accelerators became available for the study of nuclear reactions. However, the ion currents obtainable in mass spectrometers at that time were of the order of 10^{-10} A, which is far too small for the collection in a reasonable period of the quantities required. New instruments were therefore developed [O1, S1, W1, Y1], some of which were able to produce milligram quantitites of certain light isotopes. The high ion beams were obtained by using new types of ion sources, and increasing the transmission of the spectrometers at the expense of resolving power. This can be done by enlargement of the beam defining slits and the introduction of ion optical systems. Isotopic samples produced in these instruments were used for the study of some nuclear reactions and for mass assignments of the natural radioactive isotopes of K and Rb.

During the war, tremendous efforts were made in the development of electromagnetic isotope separators (calutrons) for the production of kilogram quantities of U^{235}. The constructional details of these machines are still partly classified. Since the end of the war, calutrons have been used for the enrichment of large quantities (up to several grams) of stable isotopes of most elements [K2]. Such isotopic samples are now available commercially.

As will be seen below, however, many important types of nuclear investigation do not require even milligram quantitites of isotopes. This explains why several smaller isotope separators have been built in the last ten years. These machines are able to separate milligram quantities, but some of them normally work with microgram quantities. In 1944, J. Koch and B. Bendt-Nielsen reported the completion of a 90° separator [K4], which since then has been used for various types of nuclear investigations. In 1949 a description of the separator at the Nobel Institute was published [B2]. It is of a similar construction to that of Koch *et al.* At present (1954) two smaller separators of the same general design are in operation in this country [A10, L2]. These four separators normally operate with ion currents of the order of tenths to hundreds of microampere, although milliampere currents may be realized.

In 1952, R. Bernas described a separator of the 60° type, which has produced several milligrams of enriched isotopes [B15]. Recently, C. J. Zilverschoon [Z1] described in detail a 180° separator, built by Kistemaker and Zilverschoon [K3] in Amsterdam. This machine has also produced milligram quantities of isotopes.

It seems convenient to classify the electromagnetic mass separators into the following four grous, although, of course, several boundary cases occur.

1. *Mass spectrographs* are characterized by extremely high resolution (up to 50,000 [E1]) and extremely low ion currents. These instruments are used for precision measurements of atomic masses.

2. *Mass spectrometers* have lower resolving power (up to some hundreds [B1]) and low ion currents. They are used for isotopic abundance measurements. Modified mass spectrometers have been used for mass assignment of isotopes formed in nuclear reactions [L1, I1]. Other applications in nuclear physics are reviewed in ref. [I1].

3. *Low intensity isotope separators* are able to produce milligram quantities of isotopic sample. Proper fields of application are the preparation of (*a*) targets for nuclear reaction studies, (*b*) pure samples of active isotopes for the study of their decay properties, and (*c*) samples for hyperfine structure measurements [cf. K6].

4. *High intensity isotope separators* are designed to produce gram quantities of isotopes. Isotopic samples from the calutrons have been used for many investigations in nuclear physics, as well as in classical physics, biology and medicine [K1, A8].

2. *"Production capacity" of a separator. Isotope quantities required*

Generally, the use of separated isotopes in nuclear physics presumes that the quantities required can be produced in a reasonable time. It may therefore be justified to discuss briefly the "production capacity" of an electromagnetic separator and the isotope amounts needed for various types of nuclear investigation.

The quantity m of an isotope, separated in a time interval of t hours, is computed from Faraday's law:

$$m = 0.0373\ I \cdot t \cdot A$$

where I is the ion current and A is the mass number. The collection of one milligram-atom thus corresponds to 27 milliamp-hours, assuming 100% collection efficiency.

The most powerful ion sources, those of the calutrons, are able to produce ion currents of the order of 100 mA. This means that in favourable cases gram quantities of separated isotopes may be produced in a day. In fact, such amounts are available from the calutron plants at Oak Ridge and Harwell. The use of large ion currents, however, entails difficulties in the resolution of the mass lines; the isotope samples produced are therefore usually not pure, the degree of enrichment varying within wide limits [K2].

In the low intensity separators milliampere ion currents are obtainable, although those used are normally much smaller. The production rate of these machines is therefore often less than a milligram per day.

Fortunately, the quantities of separated isotopes required for many important nuclear investigations, are very small. In some cases, indeed, the sample thickness is required to be extremely small (cf. p. 120). As a rough guide we quote in Table 1 orders of magnitude for the isotope quantities used in measurements of various types. The figures for the first three items are based mainly on our experience with the separator at the Nobel Institute. In the last four cases the figures are based on published data. For the mass assignments and nuclear spectrometer measurements, we have given the total amounts of material (active and inactive) separated in actual cases, since this quantity is the only one of importance for our discussion.

Apparently the low intensity separators are well suited for the first types of measurement, while calutron capacity is needed in the other cases. Of course, this is a very rough classification. It is evident, however, that the different separators complement each other very well.

Table 1. Orders of magnitude of isotope quantities used in various types of investigation.

Type of work	Quantity, mg
Mass assignment of isotopes*	10^{-4}– 10^{-1}
Nuclear spectrometer measurements*	10^{-3}– 1
Nuclear reaction studies	10^{-4}– 10^{-1}
Hyperfine structure measurements	10^{-1}–100
Nuclear reaction cross section measurements	100
Nuclear magnetic moment measurements	100
Super conductivity measurements	100

* The figures give the total amounts of material (active and inactive) separated for use in some actual investigations.

Chapter I. The isotope separator at the Nobel Institute of Physics

1. General

A short description of the separator was published in 1949 [B2], soon after it was put into operation. The changes made since then have been mainly of a technical nature, except for the recent fundamental improvements discussed in Sections 2 and 3.

The main features of the apparatus are as follows. In the ion source, a gas discharge is maintained through the vapour of the substance to be separated. The ions formed are extracted through a 2.5 mm diameter aperture by the first cylindrical electrode of an electrostatic lens system. This consists of four electrodes of diameter 150 mm. The divergent beam from the source was focussed by this lens system so that it was parallel at the entrance of the magnetic field. After 90° of deflection the ions were collected at the edge of the magnet. Following the modifications described in Section 2, the beam is now still slightly divergent on entering the magnetic field, and the collector is now at a distance of 1.6 m from the edge of the magnet.

The acceleration voltage is 40–60 kV and the mean deflection radius 160 cm. The pole gap distance is 10 cm. The main vacuum system is maintained at a pressure of about 5×10^{-6} mm by means of a NRL diffusion pump (HD 16) of capacity 1400 l/sec at 10^{-4} mm. This pump is backed by a Kinney rotary pump. The importance of a good vacuum is evident from our experience that the mass lines are markedly broadened when the pressure increases above $\sim 1 \times 10^{-5}$ mm.

The adjustment to best focus of the mass lines is performed by means of a fluorescent screen at the target position (cf. Fig. 7). The mass lines appearing on this screen are visually inspected and their shape is adjusted by means of the variable voltage of the first and third electrodes of the electrostatic lens system. The second and fourth electrodes are earthed.

In many cases it is desirable to change the vertical position of the mass spectrum at the target. For this purpose a pair of horizontal deflection plates has been mounted at the entrance end of the deflection chamber. The electrical field between these plates is adjusted from the control table at the target end.

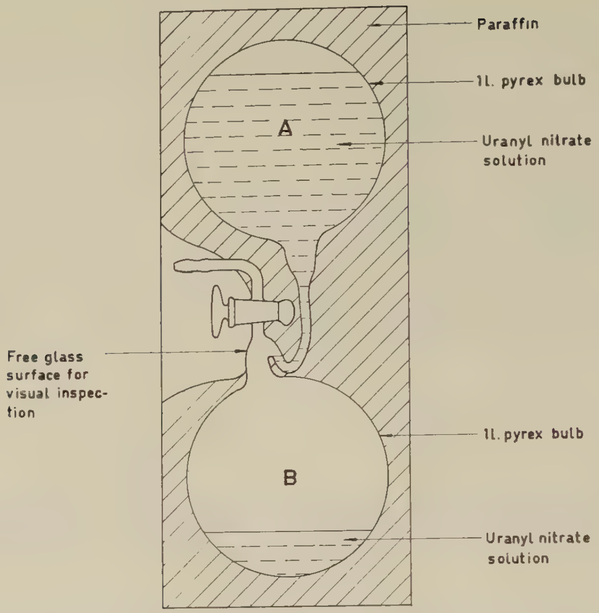

Fig. 1. Arrangement for extraction of fission gases from uranyl nitrate solution.

The ion source is, in principle, the same as described in ref. [B2]. It was designed for the separation of substances which can be introduced in gaseous form. Isotopes of O (from H_2O), N, rare gases, halogens, Ti (from $TiCl_4$), As (from AsH_3) and Hg have been separated in this way. However, solid charge materials (e.g. Li, Mg, Se, HfF_4, and ZrF_4) have also been used. In such cases a small lava boat, containing the substance, was placed in such a position that the heat radiated from the filament produced an appropriate evaporation rate. In a separation of Mo, chlorine was passed over the molybdenum charge in the ion source. A volatile chloride is then formed, which is ionized in the gas phase.

As most of our disintegration studies concern fission gas isotopes (cf. Part II), a technique of preparing fission gas samples for isotope separation has been developed. This is described in ref. [T6]. Since then, however, an essential improvement of the gas sampling apparatus has been introduced. Fig. 1 shows the new arrangement. Two spherical pyrex bulbs, each of volume one litre, and a vacuum tap are assembled in an all-glass unit, imbedded in a cylindrical block of paraffin. Since paraffin, if left unsupported, tends to creep, a reinforcing tube was embedded in the paraffin block to prevent damage to the glass tubes. The glass bulbs contain about 1.3 l of saturated uranyl nitrate solution. Before irradiation with neutrons in the cyclotron, the apparatus is evacuated, and a small amount of carrier gas is introduced. After irradiation, the fission gases are extracted in the following manner. The paraffin piece is placed horizontally, with half of the solution in each container, and shaken for about ten minutes. The solution is then transferred to bulb *A* by lowering it. When *A* is filled, the apparatus is turned upside down, and the solution is allowed to flow into *B*, as shown in the figure. The bend of the glass tube joining *A* and *B* prevents the gas from bubbling back into A. In this way all the fission gas is collected in the small volume below the stop-cock, from which it is transferred to the gas storage chamber of the ion source.

2. Improvement of the resolving power by operation as a symmetrical sector field instrument

When the isotope separator was put into operation in 1948, it was designed for ion beam focus at the exit boundary of the magnetic field. With this arrangement the machine was used for the preparation of sources for β-spectrometer investigations and for preparation of targets for nuclear reaction studies in various accelerators (cf. Table 2). Most of the nuclei studied were in the mass region below 135. The resolution of the separator was in most cases adequate. However, it sometimes is the case that the isotope A_1 of interest is of much lower intensity than a neighbouring isotope A_2. Then a "tail" from A_2 may cause a serious contamination of A_1 even though it is of low intensity compared to the peak height of A_2. Moreover, considerable attention has recently been given to the study of nuclei in the heavy mass region, where the resolution with this arrangement was not always sufficient.

In order to make the separator more generally useful, it was considered desirable to increase the resolving power. This can be done by increasing the mass dispersion $(\Delta r)_M$ and minimizing the line width B. A simple and well-known way of increasing the mass dispersion is to arrange matters so that the point at which the beam is focused is located at a distance l from the exit boundary of the magnet. The focusing properties of magnetic sector fields have been extensively studied in mass spectroscopy (cf. [E1] and [B1] and the references therein). As the present separator differs in some essential details from the mass spectroscopes, it may be worth while to discuss its resolving power as a function of l.

The mass dispersion $(\Delta r)_M$ for a 90° magnetic sector field, with normal entrance and exit of the beam, is (cf. e.g. [E1])

$$(\Delta r)_M = \frac{r}{2}\frac{\Delta M}{M}\left(1+\frac{l}{r}\right) \tag{1}$$

where l is the image distance from the exit boundary of the magnet. If the resolving power P is defined as the mass number for which

$$\underset{\Delta M=1}{(\Delta r)_M} = B_l \tag{2}$$

where B_l is the half width of the mass lines, we obtain from (1) and (2)

$$P = \frac{r}{2\,B_l}\left(1+\frac{l}{r}\right). \tag{3}$$

Thus the resolving power increases with increasing l, if B_l increases more slowly than $\left(1+\frac{l}{r}\right)$. The l-dependence of the line width B_l is therefore of importance. For comparison with preliminary experimental results it will be briefly discussed below.

The line width B_l may be considered as the sum of a number of components b_i, arising from different effects. These are:

b_1, due to aberration of the magnetic sector field
b_2, ,, ,, energy spread ε of the ions, which originates mainly in the ion source
b_3, ,, ,, magnet current fluctuations ΔI
b_4, ,, ,, acceleration voltage fluctuations ΔV
b_5, ,, ,, angular spread resulting from initial velocity components normal to the accelerating field
b_6, ,, ,, spherical aberration of the electrostatic lens system
b_7, ,, ,, space charge broadening
b_8, ,, ,, scattering by residual gas atoms.

The l-dependence of the first four components is (cf. e.g. [E1])

$$b_1 = \frac{d^2}{8r}\left[1+\left(\frac{l}{r}\right)^3\right] \tag{4}$$

where d is the ion beam diameter at the entrance of the magnetic field,

$$b_2 = \frac{r}{2}\frac{\varepsilon}{V}\left(1+\frac{l}{r}\right) \tag{5}$$

$$b_3 = r\frac{\Delta I}{I}\left(1+\frac{l}{r}\right) \tag{6}$$

$$b_4 = \frac{r}{2}\frac{\Delta V}{V}\left(1+\frac{l}{r}\right). \tag{7}$$

b_5 is approximately independent of l, since ion trajectories diverging from a point at the entrance of the magnet field become parallel at the exit. b_6 may *decrease* by increasing l, for the following reason. When the image position is moved outwards from the magnet edge, the virtual object moves from infinity towards the magnet. As the geometrical arrangement of ion source and lens system remains unchanged, this means that the focal length of the electrostatic lens is increased. The increase of this focal length on the other hand results in a decrease of the spherical aberration.

The space charge repulsion (we are in this discussion dealing with ion currents of the order of 10 μA) acts mainly as a negative lens, and is maybe partly compensated by decreasing the focal length of the electrostatic lens system.

The line broadening due to gas scattering, b_8, has been discussed by ZILVERSCHOON [Z1], who found it to be negligible in the case of the Amsterdam separator. Since our working pressure is considerably less than that used by ZILVERSCHOON in his calculation, we assume b_8 to be negligible in our case.

With reasonable assumptions for the values of d (20 mm), ε (5 eV), $\frac{\Delta I}{I}$ ($\leq 0.05\,\%$) and $\frac{\Delta V}{V}$ ($\leq 0.05\,\%$) we obtain: $b_1 = 0.06$ mm, $b_2 = 0.08$ mm, $b_3 \leq 1.6$ mm and $b_4 \leq 0.8$ mm.

If we choose $l = r$, the mass dispersion $(\Delta r)_M$ is increased by a factor 2, compared with the case when $l = 0$. The line width components b_1, b_2, b_3 and b_4 also increase by a factor 2, b_5 is unchanged and b_6 probably decreases. b_8 is neglected for reasons

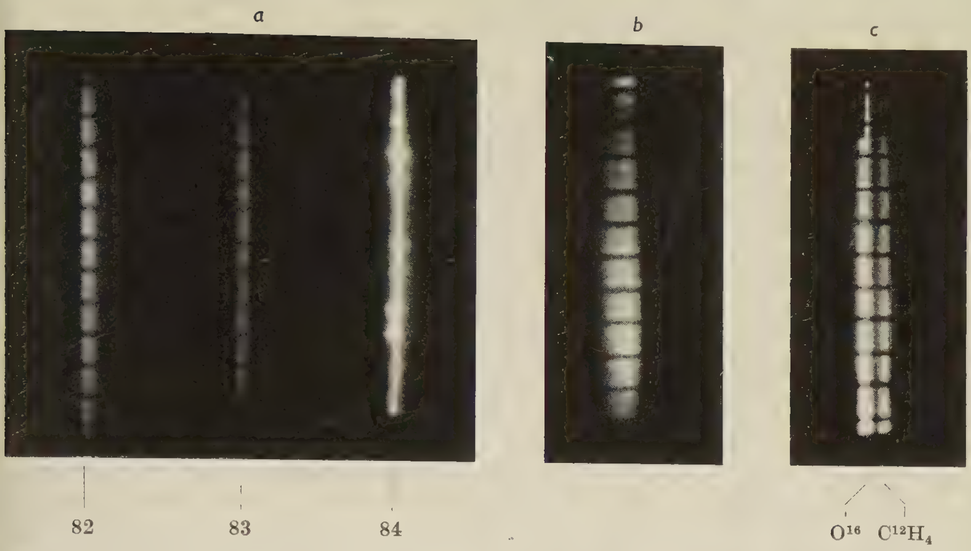

Fig. 2. Photographs of mass lines displayed on a fluorescent screen, placed at a distance of 1.6 m from the magnet edge. *a*: Krypton lines, stabilized with the new arrangement described in section 3. *b*: O_{16}-CH_4 doublet with the previous stabilization. *c*: O_{16}–CH_4 doublet with the new stabilizer. The shadow of the slit strips is seen in the upper part of the CH_4 line (cf. text).

given above. The change of b_7 is uncertain but it possibly decreases because of the increased divergence of the entrance beam. An increase of the resolving power, corresponding to the increase in mass dispersion, will therefore be achieved, if:

(*a*) the decrease in the term b_6 is appreciable (or at any rate, is larger than any possible increase of b_7);

(*b*) the stabilization of magnet current or acceleration voltage is improved, thereby decreasing b_3 or b_4.

In the next section a device for stabilization of the mass spectrum is described, which seems to reduce the terms b_3 and b_4 below the magnitude of other terms.

In order to decide if the condition (*a*) above is fulfilled, some measurements have been performed with the focus at the distance $l = r$. Fig. 2a shows a photograph (full scale) of krypton lines displayed on a flourescent screen, placed at the distance r from the magnet edge. The line widths, as observed on the fluorescent screen, seem to be narrower than those obtained with the focus at $l = 0$. (In the visual inspection, intermittent instabilities in I and V are eliminated.) This strongly indicates that the spherical aberration term b_6 really decreases considerably when l increases.

Activity measurements showed half widths of 2.8 and 3.0 mm respectively for Kr^{85} and Xe^{135} mass lines focussed at $l = r$. The Xe^{135} activity measurement is shown in Fig. 5.[1] These half widths correspond to a resolving power of 520 and 570 respectively. With $l = 0$ a half width of 3.7 mm has been measured for Kr^{88} (resolving power 220).

---

[1] In these separations the new stabilizer, described in Section 3, was in operation.

3. Improved stabilization of the mass spectrum

The magnet current and the acceleration voltage of the separator are each stabilized to better than 1 in 10^3. A change of 0.05 % in the magnet current produces a mass line displacement of 0.8 mm at the edge of the magnet. In the new arrangement with focus 160 cm from the magnet edge, all instabilities cause displacements twice as large as those at the magnet edge (cf. p. 114). The stabilization therefore had to be considerably increased if the higher resolution obtained should not be nullified by the instability of the mass lines.

A solution of this problem was accomplished by introducing a modified "slit stabilization", as shown schematically in Fig. 3. A reference mass line F is focused between two narrow metal strips A and B, which are individually insulated and mounted 1 mm apart. The strips are connected to a differential amplifier. When the mass line F is centered relative to the slit, the two strips receive equal ion currents. If the mass spectrum tends to move, the strips receive current increments of opposite sign, which are amplified and applied in the appropriate manner to the plates C and D. The resulting field across CD deflects the ion beam so that the reference line is kept in the centered position. In this way both the magnet current and acceleration voltage instabilities are counteracted. Due to the negative feed back, the amplifier unit need not itself be well stabilized.

The mechanical arrangement of the stabilizer slit is shown schematically in Fig. 4. The two slit halves *3* are mounted 1 mm apart on a perspex plate. This is fixed to the end of a shaft *5* through a vacuum-tight seal, permitting the slit to be displaced perpendicular to the mass spectrum *2* under operating conditions. It is therefore easy to bring the reference mass line to any desired position within the useful target region. The slit can also be rotated by the shaft, so that only the upper part of the reference line affects the amplifier (cf. Fig. 2c).

The new stabilizer has so far been checked only with a trial set-up, but the results are promising. Fig. 2b and c show two photographs of the O^{16}–CH_4 mass doublet, displayed on a fluorescent screen 1.6 m from the magnet edge. Fig. 2b was taken with the old arrangement, that is, separately stabilized magnet current and accelera-

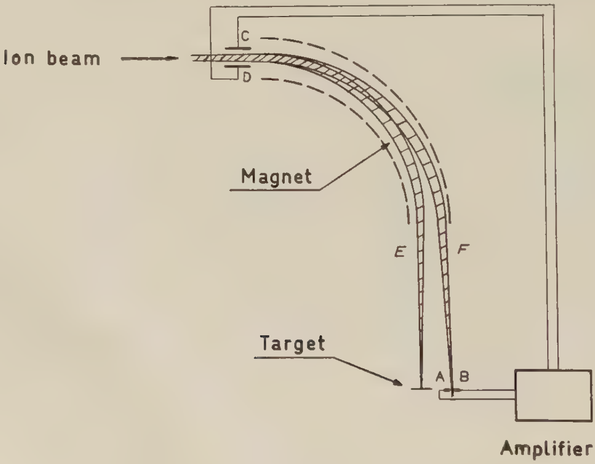

Fig. 3. Illustration of the stabilizer principle.

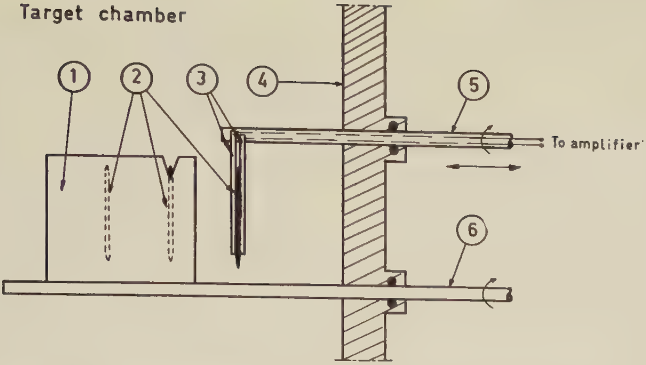

Fig. 4. Stabilizer slit and target arrangement. 1, target plate; 2, mass lines; 3, slit strips; 4, wall of target chamber; 5, shaft for adjustment of slit position; 6, water-cooled support for target plate.

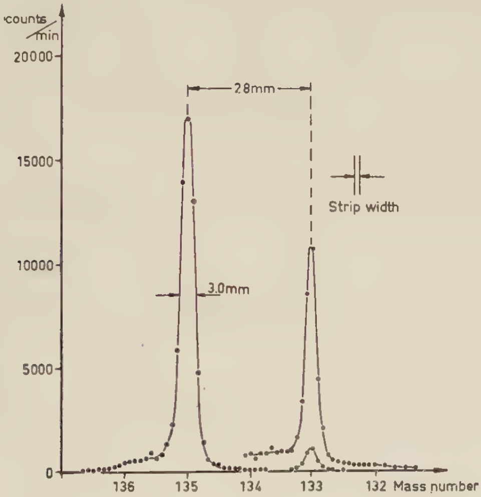

Fig. 5. Activity spectrum of xenon isotopes collected at a distance of 1.6 m. from the magnet edge. The target foil was cut into 1 mm strips, the activity of which was recorded with a G.M.-counter.

tion voltage. Fig. 2 c was taken with the slit stabilizer. The components of the doublet are now clearly resolved, indicating a resolving power better than 500. Fig. 5 shows an activity spectrum, measured after a separation of fission gas, containing mainly Xe^{135}. Although the stabilizer was not working under optimum conditions, the result is satisfactory. The resolving power, deduced from the half width and the mass dispersion, is about 520.

Chapter II. Isotope collection and properties of targets prepared in the isotope separator

1. Introduction

The collection of the separated isotopes is an essential part of the separation process. The problems involved in a particular case depend on the ion beam intensity and the purpose of the separation. For comparison with collection problems later discussed we will briefly mention some difficulties met with in the collection of large isotope quantities. In this case, the comparatively high electrical power (of the order of hundred watts), dissipated in the target material, necessitates efficient cooling. The ions often cause sputtering, that is, the isotopic material already deposited may be knocked off by the impinging ions, together with some target material. For example, BERNAS [B15] reports a case, in which 7.5 mg of separated Zn^{64} became contaminated by 1.1 mg of molybdenum sputtered from the target plate (cf. below). In order to minimize losses due to reflection and sputtering, a target arrangement as shown in Fig. 6 has been used [cf. Z1]. The surface AB is bombarded by the ion beam, and most of the reflected or sputtered material is deposited on the surface CD. For the operation of this technique it is necessary that the deposited material should have a very low vapour pressure, as is normally the case with metals. In other cases, the isotopes to be collected are trapped in the target material by some chemical reaction. For example, oxygen and sulfur were collected on copper shavings. and mercury has been collected in silver.

After the electromagnetic separation the collected isotopes are chemically separated from the target material. This work often demands a refined chemical technique. As a final result of the high intensity separation, the isotopic samples are usually supplied as a chemical compund, which is not often directly useful for nuclear investigations. On the other hand, the technique described in Sections 2 and 3 gives isotopic samples having the properties required for the measurements to be made with them.

The present separator has been frequently used to prepare samples of stable isotopes for nuclear reaction studies in various accelerators (cf. Table 2). More than 50 separations of this kind have been made, and about 120 targets have been delivered. With a few exceptions, the stable isotope production has so far been concerned with isotopes of oxygen, nitrogen and neon. The amounts collected are normally of the order of

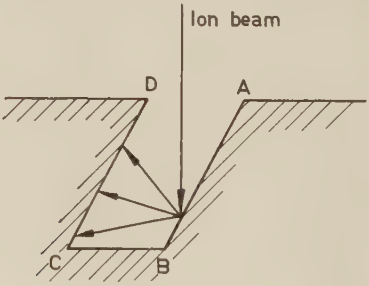

Fig. 6. Collection principle used in high intensity separators.

micrograms. The method of preparing gaseous targets by ion bombardment of metal surfaces is discussed in detail in Section 2.

Although many stable isotope samples have been prepared, the main part of the separator work has been devoted to the preparation of active isotopes for nuclear spectrometer investigations. In particular, rare gas isotopes have been studied (cf. Table 2). The technique developed for active isotope collection is discussed in Section 3.

2. Collection of stable gaseous isotopes for nuclear reaction studies

When ions of a gaseous element strike a metal surface and have sufficient kinetic energy, they penetrate into the surface layer. Due to the extremely low diffusion rate, the gas atoms are trapped in the metal lattice. This phenomenon has been experimentally demonstrated by J. Koch [B 17] who prepared silver targets containing neon isotopes in this way (cf. [L3]). These targets were shown to withstand moderate temperatures ($\leq 200°$ C) in high vacuum for one hour. At 350° C the gas content of the silver plates disappeared within 20 minutes. From nuclear reaction yields of targets bombarded with different amounts of neon ions, it was concluded that saturation of the metal lattice occurs at a neon density of about 2 μg per cm², corresponding to a relative neon concentration in the surface layer of at least 10 %.

The penetration depth of heavy ions may be roughly calculated according to the theory of Bohr [B 16]. For certain cases specified below, the range R (in cm) may be written according to eq. 5.4.2. of ref. [B 16]

$$R\,(\mathrm{cm}) \sim \frac{1}{2\pi N a_0^2}\,\frac{1}{Z_1^{2/3}+Z_2}\,\frac{m_1}{\mu}\left(\frac{v_1}{v_0}\right)^2 \tag{8}$$

where m_1 = mass of impinging ion

v_1 = velocity of impinging ion
v_0 = electron velocity in the hydrogen atom
a_0 = radius of the hydrogen atom
μ = electronic mass
Z_1 and Z_2 = atomic numbers of impinging and target atoms respectively
N = number of target atoms per cm³.

For our purpose it is convenient to rewrite this expression in the form

$$R\,(\mu\mathrm{g/cm^2}) \sim 0.7\,\frac{A_1 E_1}{Z_1^{2/3}+Z_2} \tag{9}$$

where A_1 is the mass number of the impinging ion and E_1 the ion energy in kev. This expresion is valid [B 16], if

(a) $A_1 \gg A_2$, where A_2 is the mass number of the target atoms
(b) $v_1 < v_0$ and
(c) $0.027\; Z_1 Z_2 \sqrt{Z_1^{2/3}+Z_2^{2/3}}\left(\frac{A_1}{A_2}+1\right)\frac{1}{E_1} \gtrsim 1.$

Condition (b) may be written as

$$\frac{A_1}{E_1} > 0.04,$$

which holds in all practical cases ($E_1 \leq 60$, $A_1 \geq 20$). Condition (*c*) is also fulfilled in the examples below.

Assuming eq. (9) to be applicable, we obtain for example, $R \sim 75$ μg/cm² for 50 kev Xe ions impinging on beryllium, and $R \sim 20$ μg/cm² for 50 kev Kr ions on aluminium. For 45 kev Xe ions on carbon, R would be ~ 50 μg/cm². An experimental study of a similar case, described in Section 4 b, appeared to give ~ 6 μg/cm².

The theoretical penetration depth gives a rough upper limit to the gas quantity which can be collected in this way, assuming a reasonable maximum value (say 0.1) for the ratio of gas atoms to metal atoms. The saturation amounts may be of the order of 0.1 microgram-atoms per cm² of the metal surface. The small thickness of such gas targets makes them very useful, e.g. for precision measurements of reaction energies, since energy straggling of bombarding and emitted particles is small (cf. also Section 4 b).

In this collection process there is considerable freedom in the choice of collector material. In the present separations, targets of Be, Al, Cu, Fe, Ag, and Au have been used, depending on the purpose of the subsequent investigation.

The actual collection technique used is simple; Fig. 7 a shows schematically the target arrangement. The circular target plate *1* is screwed to the copper support *2*, which is fixed to a watercooled shaft *3*. This can be rotated from outside the vacuum system (cf. Fig. 4), so that the target is shielded from the ion beam when adjusting the line shape, which is visually inspected on the fluorescent screen *4*.

In most cases of stable gas collection, thick target plates (2 mm) have been used. In some nuclear reaction studies, however, the distribution of bombarding particles, scattered from a thick target, masks the particle groups to be studied in the nuclear reaction. By choosing a thin target backing one can eliminate, partly at least, the scattered particles in favour of the emitted particles. Several thin targets have been prepared, using the following types of foil: aluminium, 150 μg/cm² (commercial), aluminium, ~ 100 μg/cm² (evaporated), silver, ~ 100 μg/cm² (evaporated), and gold, ~ 300 μg/cm² (evaporated). The aluminium foils have been exposed to ion currents (~ 40 kev) of ~ 1 μA for up to 30 min. without being destroyed. Corresponding values for the silver and gold foils are respectively ~ 0.5 μA, (2 h) and ~ 0.2 μA (4 h). The foils were fixed between two copper frames, which were screwed to a watercooled copper support. The free area of the foils was usually about 5 × 7 mm.

Immediately before the separation, the target plates were machined with a sharp and clean tool, in order to ensure that the collecting surface was clean. Traces of surface contaminations may seriously affect the measurements, because of the sensitivity of the detection methods. As is well known, surface layers are often deposited during particle bombardment of metal surfaces. These layers are probably building up by the adsorption and subsequent decomposition of organic molecules from the diffusion pump oil. The same phenomenon also occurs in the isotope separator. In the following, we will call these external layers "carbon layers" or "carbon deposits" although the true composition is not known.

In earlier separations, carbon layers corresponding to a stopping power of 1–10 kev (for 1 Mev protons), were usually deposited on the targets during the separation. Later, a liquid air trap was installed near the target. Although no systematic comparison has been made, it appeared that targets prepared with this arrangement were covered with carbon layers of only ~ 0.5 kev thickness.

Because of the small area (a few mm²) of the particle beam used in the precision measurements in the accelerator, only a very small part of the target area was

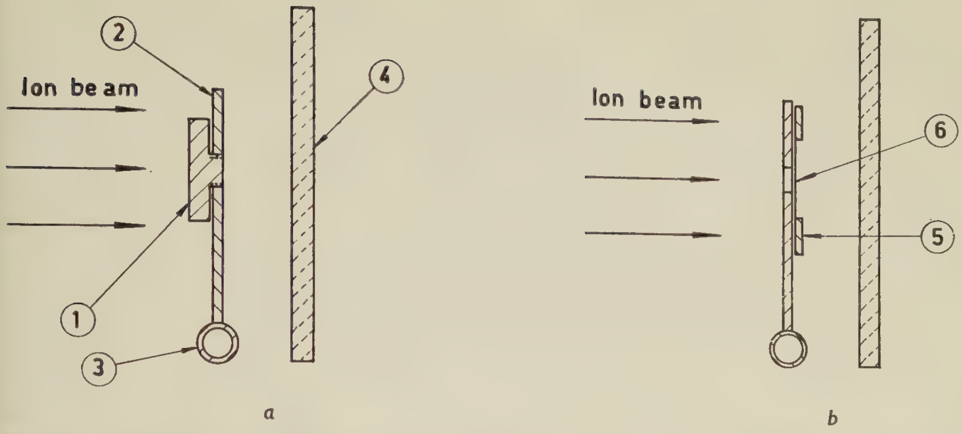

Fig. 7. Collector arrangements: *a* for the preparation of stable gas targets for nuclear reaction studies; *b* for preparation of β-spectrometer samples. 1, target plate; 2, copper support; 3, water-cooled shaft; 4 fluorescent screen; 5, ring-shaped support for the thin collector foil 6.

utilized. The gas concentration had therefore to be as high as possible. The saturation effect discussed above places a limit on this concentration. The isotope amounts collected were, however, sufficient for nuclear reaction studies (cf. Table 2). The cross-sectional area of the ion beam at the target of the isotope separator has been of the order of 50 mm². Therefore a target can be used in several measurements by bombarding a new part of the target each time.

The limited temperature stability of gaseous targets (cf. Section 3) necessitates a limitation of the bombarding particle intensity to a value for which the surface temperature of the target can be kept below 200°C. In quantitative measurements, corrections may be necessary for gas losses during particle bombardment. For example, the loss of nitrogen from a target was found to be about 2 % per hour, when the bombarding proton current was 1 μA [M4].

3. Temperature stability of gas targets

The usefulnes of separated gaseous targets depends on their stability against increases in temperature, resulting from the energy dissipated by bombarding particles. The temperature stability is, however, also of interest for other reasons. A systematic study of the thermal properties may give information about the diffusion of rare gases through solid substances.

Some measurements of the temperature stability of gaseous targets will be reported below. In the measurements described in Section 2 of Chapter III, various metal foils (thickness 13 mg/cm²) were saturated with stable krypton or xenon, containing suitable fractions of tracer isotopes. Some of these targets were used for the present temperature measurements. As discussed in Chapter III it is not yet clear whether or not the gases were, in these cases, distributed only in the metal lattice. Therefore no detailed discussion of the diffusion phenomena has been attempted. The results obtained so far are merely to be regarded as providing some guidance in the manipulation of such targets.

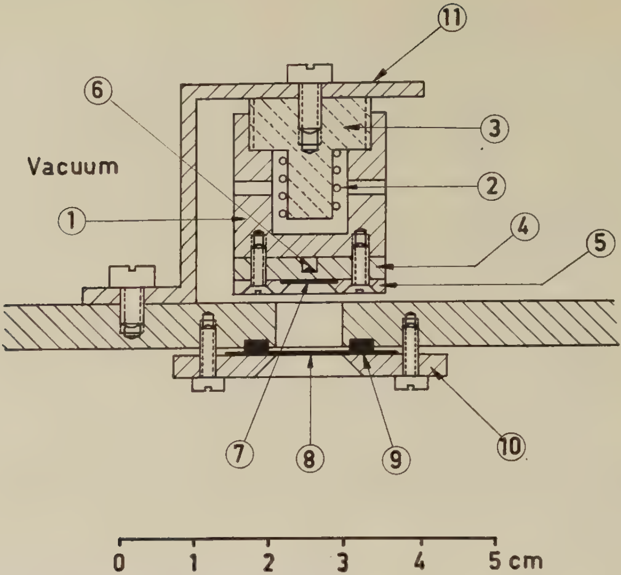

Fig. 8. Device for measurements of temperature stability of gaseous targets. The target foil 7, containing the active gas, is fixed to the copper block 1 by two copper discs 4 and 5. The block is heated by the filament 2, and the temperature is measured by a thermocouple at 6. The target activity is followed by a G.M.-counter outside the thin aluminium foil 8. 9, rubber gasket.

The present method makes use of the tracer technique for the purpose of studying the disappearance of the gas trapped in a metal surface. The surface is heated in high vacuum ($\sim 5 \times 10^{-6}$ mm Hg), and the activity is measured as a function of time. The experimental arrangment is shown in Fig. 8. A cylindrical copper block *1* is heated by a tungsten wire *2*. This is supported by a lava cylinder *3*, screwed to *1*. At the other end of the copper cylinder are screwed very tightly two copper plates *4* and *5*. Between them lies the target foil *7* to be investigated. The surface of the foil containing the gas is freely exposed to the vacuum. β-particles emitted from this surface pass through the foil *8* and are recorded with a GM-counter outside the vacuum system. The temperature is measured by means of a thermocouple (copper-constantan), having one joint soldered at the position *6* in the center of the copper plate *4*. The thermo-couple joint and the target foil were separated by 1 mm of copper.

Fig. 9 shows the temperature and the foil activity as a function of time for an aluminium target saturated with xenon. For comparison, a corresponding measurement of a xenon-gold target is indicated by a broken line. The experimental accuracy of the two curves are comparable. The points of the Au-curve were omitted for clarity.

We observe that in both cases part of the gas disappears comparatively rapidly when the target is heated to 200°C. With the temperature maintained at this value the activity curves soon become parallel to the time-axis. When the temperature is raised to 250°C, the activity curves fall again. This behaviour may be explained by the assumption that the gas atoms first disappearing are distributed in an external carbon layer with a higher diffusion constant than that of the target metal.

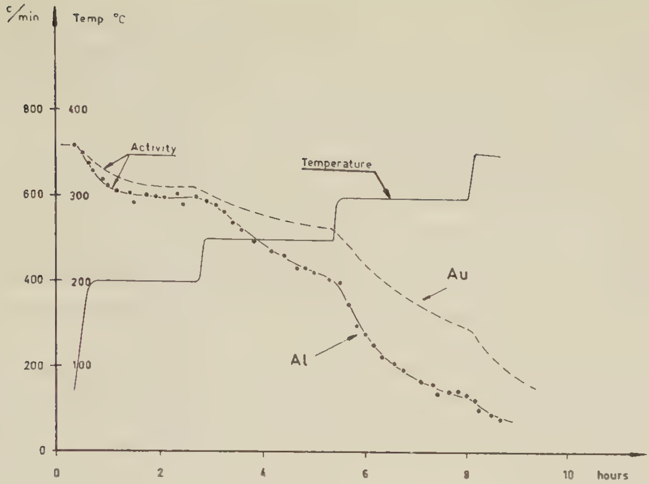

Fig. 9. Temperature stability curves for xenon in aluminium and gold. (Counting intervals 4 min).

The temperature sensitivity of the diffusion process is clearly demonstrated by the marked change of the diffusion rate, when the temperature is increased by 50° C.

The different slopes of the two activity curves indicate that the rate of diffusion in the two targets is different. This would give additional support to the assumption above, that only a small part of the gas is distributed in a carbon layer. However, the reproducibility of the present method has not yet been checked sufficiently well for definite conclusions of this kind to be drawn.

A similar study of the thermal stability of krypton in aluminium showed that the diffusion becomes serious at 300° C. In 2 hours ~ 40 % of the activity disappeared. The temperature was then raised to 350° C. After 2 more hours only ~ 20 % of the total activity was left.

We can conclude that gaseous targets of this kind should be prevented from reaching temperatures above 200° C. These results are in accordance with the experience of J. Koch on the stability of neon-silver targets (cf. p. 119).

4. Collection of radioactive isotopes

a. *General*

In principle, radioactive and stable isotopes are collected in the same way. However, there are some significant differences in the target technique. The ion beams of the radioactive isotopes (10^{-3}–10^{-9} μA) are several orders of magnitude smaller than the stable ion currents. Therefore saturation effects are normally absent. Exceptions may occur when the active isotope is an isomer of a stable isotope (cf. the preparation of β-sources of Xe^{129m} [B 11, T6]). The extremely low intensities of the active isotopes require the introduction of carrier gas in order to assure normal operation of the ion source and to display a visible mass spectrum on the fluorescent screen. Owing to the low ion currents, extremely thin foils may be used as collectors (cf. p. 126).

b. *Preparation of sources for β- and γ-spectrometer measurements*

There are several requirements for a good β-spectrometer source:

1. The sample should be uniform and have a thickness small enough to give negligible backscattering and energy straggling.
2. The area of the sample should be well defined and small enough to permit good energy resolution in the β-spectrometer.
3. If covering material is necessary, it should be thin enough to give negligible energy straggling.
4. Thin backings are necessary to minimize backscattering effects.
5. The source should be free from contaminations from other activities.

The preparation of good samples is, in fact, one of the most important problems in experimental β-spectroscopy, and considerable effort has gone into the development of various techniques such as careful chemical separation, evaporation, and electroplating. However, these special methods are not always applicable, and a compromize is often necessary in the choice of source properties.

The electromagnetic isotope separation technique, on the other hand, is in principle generally applicable, and allows the preparation of "ideal" β-samples. Fig. 7 b shows a target arrangement often used in the present work. A ring-shaped aluminium plate *5*, covered with a thin foil *6* is placed behind an aperture in a target plate. By means of the visible mass lines of the carrier isotopes, the position of the spectrum is adjusted so that ions of the required mass strike the aperture. In order to avoid contamination during this adjustment, the collector may be turned downwards by means of the shaft *3* (cf. Fig. 7 a), or the ion beams may be deflected vertically by means of the deflection plates at the entrance to the magnet (p. 111). One or more small triangular notches in the edge of the collector plate (cf. Fig. 4) facilitate a continuous check of the position of the mass spectrum. Behind these notches the upper parts of stable mass lines are visible on the fluorescent screen.

The collected activities are uniformly deposited. From the discussion in Section 2 it follows that the deposited samples, even of rare gas isotopes, are fixed in the collector foil without the use of any additional covering material. The activities collected on aluminium backings will be distributed within a layer whose thickness is of the order of ten micrograms per cm^2 according to theoretical estimates (p. 120). Such samples may therefore not be suited for β-measurements at very low energies. However, the penetration depth can be reduced by decreasing the ion energy (cf. also below).

Normally, the source is carrier-free, the exceptions being due to (*a*) contamination from stable isotopes of neighbouring mass number in the case of incomplete mass resolution; (*b*) collection of active isotopes, which are isomers of stable isotopes.

By means of the aperture in front of the foil, the shape and size of the sample area can be varied as desired. Generally, a circular aperture of diameter 5 mm has been used for measurements in magnetic lens spectrometers. For the double focusing β-spectrometer appropriate sample dimensions are approximately 2×20 mm. In this case therefore, most of the activity is used.

In most cases, commercial aluminium foils of thickness 0.15 mg/cm^2 have been used as backings. They were supported by aluminium rings with an inner diameter of 12 mm. For β-measurements in the very low energy region, much thinner backing foils are required. It is of interest to know if the present preparation method is

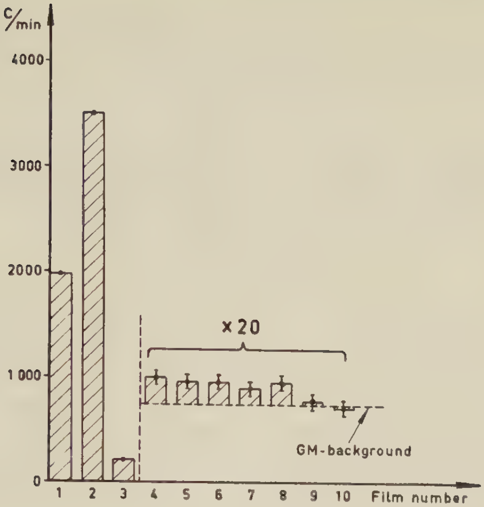

Fig. 10. Stopping of 45 kev Xe ions in formvar foils, each of thickness 2 μg/cm².

applicable in such cases. We have therefore tried to collect active gas isotopes in thin formvar films. It was found possible, for example, to prepare a 9.4 y Kr^{85} sample, deposited in a film of thickness 40 μg/cm², which was strong enough for β-spectrometer measurements. However, the collection efficiency was an order of magnitude less than for the aluminium foils. This is probably due to heating of the formvar films.

An attempt has also been made to collect 9 h Xe^{135} in extremely thin formvar films (2 μg/cm²). These were prepared from a solution of formvar in chloroform in the conventional manner. The thickness of the target films was determined by weighing identically prepared films of dimensions 7 × 8 cm on a microbalance. From several weighings, a value (2.0 ± 0.5) μg/cm² was obtained. As the thickness of these films was much less than the penetration depth estimated from the expression (1), ten films were stacked together. They were supported by 0.5 mm thick metal rings with diameters 19 and 8 mm. The stack was fixed behind an aperture of diameter 3 mm in a water-cooled copper target.

The active Xe^{135} was prepared from neutron irradiated uranium (p. 112). Carrier gas was added sparingly in order to reduce possible contamination by stable isotopes at mass 135. This is important since the thin films are easily destroyed. The target was exposed to a Xe^{135} ion beam of energy 45 kev for 15 minutes; the total ion current to the copper support was 0.01 μA. From this value we estimate the total electric power dissipated in the formvar foils to be much less than 5 μwatt.

After the separation, the stack of films was dismantled and their activities measured with a GM-counter. Fig. 10 shows the activity of each film, numbered in the order they were penetrated by the ions. The total activity deposited in the films was estimated to be less than 0.1 % of the activity collected in an equal area of an aluminium foil around the target aperture. This may indicate that serious heating occurred during the collection.

We notice that practically all the Xe^{135} activity was deposited in the first three layers, corresponding to a total thickness of 6 μg/cm^2. This is much less than the penetration depth ~ 40 μg/cm^2, estimated from Eq. (1). Autoradiograms of these three films showed black spots of approximately the same size.

Chapter III. An experimental study of saturation effects occurring in the collection of rare gas isotopes

1. Introduction

As discussed in Chapter II, gaseous targets which are very suitable for nuclear reaction studies may be prepared by bombarding metal surfaces with ions of the gas in question. When preparing such targets, it is of interest to know what amounts of gas can be collected, how deeply the gas atoms are distributed in the metal lattice, and the optimum collection conditions. It is evident that a metal lattice, when bombarded with ions of a gas, cannot retain more than a certain amount. For rare gases, where chemical effects are presumably absent, this amount will depend on the penetration depth of the impinging ions, the lattice structure, and the rate of diffusion of the gas through the metal. A study of saturation phenomena for inert gases may therefore provide a method of studying the properties of metal lattices. As will be shown below, it is in principle possible to determine the penetration depth of the gas as well as the total amount of gas distributed within the corresponding volume of the surface structure.

The purpose of the present investigation was to study the conditions under which saturation occurs when inert gases are collected in metal surfaces. Two different methods have been used. In the first, the increase in the amount of gas collected in a foil is followed continuously during the collection by means of a tracer isotope. In the other case, metal plates are exposed, under various conditions, to ion beams of a stable gas isotope. The gas content of the metal plates is then analyzed from measurements of the scattering of high energy protons or deuterons. A series of measurements by this method has been started. Unfortunately, some difficulties have been encountered in the operation of the Cockcroft-Walton accelerator, and therefore, the data so far obtained by this method are very incomplete. However, it seems worth while to mention the method here, since a combination of the two lines of approach seems to be a useful way of studying the problem. The results of the present saturation measurements are collected in Section 4.

2. Saturation studies by means of tracer technique

In principle, the isotope separator is not usually a suitable instrument for studying the behaviour of stable isotopes by the tracer method, since it normally separates the tracer isotope from the stable isotope which is of interest. However, this is not so in the case of isomeric states of stable isotopes. For example, the stable nucleus Xe^{131} has a 12.3 day isomer, which is suitable for the present purpose. Therefore, the collection of Xe can be studied with a mixture of Xe^{131} and Xe^{131m}, using the radiation intensity from the latter as an indicator of the total xenon quantity collected. If the specific activity of the Xe^{131} gas introduced into the ion source is known, it is possible to evaluate quantitatively the amount of Xe^{131} collected.

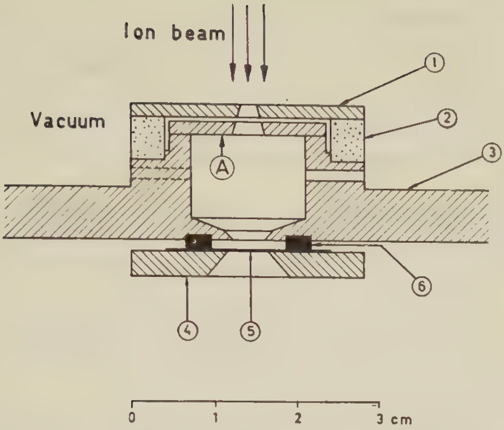

Fig. 11. Target arrangement used in saturation measurements. 1 and 3 are brass pieces, forming part of a Faraday cage; 2, perspex ring; 6, rubber gasket. The increase of activity in the target foil 5 was followed with a G.M.-counter close to the brass plate 4.

In the case of krypton, there is no corresponding isomer with suitable decay characteristics. For saturation measurements with krypton we therefore used another method, described in detail below.

Saturation measurements with xenon.—The collector arrangement used in the xenon tracer measurements is shown schematically in Fig. 11. It is composed of three electrically insulated metal parts, *1*, *3*, and *4*, constituting a cylindrical Faraday cage. Part *3* was held at a negative potential (-100 V), part *1* was earthed, and part *4* was earthed via a galvanometer. The circular aperture (diameter 2.5 mm) in plate *1* is much smaller than the dimensions ($\sim 20 \times 5$ mm) of the Xe mass lines which were somewhat defocused. This was necessary in order that the variations of ion density across the exposed target area should be negligible. The target consisted of an aluminium foil *5*, (thickness 13 mg/cm^2) covered with an evaporated layer of the target metal. The evaporation technique was used in order to ensure reproducible properties of the target surfaces.

In order to reduce the deposition of carbon, a large liquid air trap was installed a few centimeters from the arrangement of Fig. 11. As there is a rubber gasket between plates *3* and *4*, the possibility of formation of carbon deposits is, however, not excluded.

12 d Xe^{131m} decays by the emission of a highly converted (internal conversion coefficient $=30$) γ-ray of energy 163 kev. This fact makes it suitable for our purpose, since the counting background from the comparatively large amount of Xe^{131m}, collected on plate *1*, becomes very small. On the other hand, the target foil absorbed less than 25 % of the β-particles to be counted.

The active xenon used in these measurements was obtained from the decay of 8 d I^{131}. An I^{131} solution of 10–20 mC activity was introduced into a 30 ml glass bulb, provided with a high vacuum tap. The liquid was frozen and the bulb evacuated. The iodine was left to decay for some days, after which a suitable amount of stable xenon was introduced. After shaking, the xenon gas mixture was transferred to a gas store, and the solution in the glass bulb was left to decay for another few days, when a new Xe^{131m} extraction was carried out.

The saturation measurements were performed with the collector at the magnet edge. The slightly defocused mass lines were held in the correct position by means of the slit stabilizer, using the Xe^{136} mass line as a reference (p. 116). The mass line corresponding to $Xe^{131} + Xe^{131m}$ was centered at the small aperture of plate *1*. The increase of the activity of the target foil was followed by an end-window GM-counter outside the vacuum system, close to the target foil. The ion current was kept constant during the measurement.

The results of the measurements are discussed in Section 4.

Saturation measurements with krypton.—As already mentioned, the technique described above cannot be applied in the case of krypton, since there is no suitable isomer of a stable krypton isotope. On the other hand, 9.4 y Kr^{85}, which is commercially available in large quantities, has suitable decay characteristics. It decays mainly by 672 kev β-particles; less than 1 % of the decaying nuclei emits a γ-ray. The GM-background is therefore negligible in this case also. In order to make the tracer technique applicable the following procedure was used. A mixture of Kr^{85} and stable krypton was introduced into the ion source, and the krypton spectrum was focused at the magnet edge. By applying a (variable) alternating voltage (50 c/s) across the deflection plates *CD* of Fig. 3, the whole mass spectrum was swept to and fro across the circular aperture of plate *1* in Fig. 11. As the stabilizer could not be used in this case, we had to switch off the sweep frequently, and check the position of a reference line. The target activity was measured as a function of time, the ion current being constant. Some results are discussed in Section 4.

3. Saturation studies using stable isotopes

The method of observing the elastic scattering of protons or deuterons has been frequently used for the analysis of target composition in connection with nuclear reaction studies. It is briefly discussed, for example in ref. [M2]. The target is bombarded with deuterons (or protons) of known energy and intensity. The energy distribution of the elastically scattered deuterons is analysed by a heavy particle spectrometer, using photographic detection [M1]. Suppose that the target is a metal plate with a gas deposited in the surface layers, and with a thin layer of carbon (or organic molecules) covering the surface. The energy distribution of the scattered particles is then of the form shown in Fig. 12. The continuum *a* is due to deuterons scattered in the thick metal plate. The peak *b* corresponds to scattering by the gas atoms in the metal (The atomic number of the gas is assumed to be higher than that of the metal). The broken curve *c* is the distribution obtained for deuterons scattered by a clean metal plate, i.e. without energy absorption in an external carbon layer. The energy difference E_2–E_1 between the scattering edges gives a measure of the carbon lyer thickness. The difference E_4–E_3 gives information about the depth of the gas distribution in the metal. From the area under *b*, the total amount of gas within the exposed region may be estimated.

It is evident that this method would, in principle, be suited to a study of saturation effects occurring when gases are collected in metal lattices, since it gives essentially the information required. However, the technique involved is comparatively elaborate, and the appropriate values of collection parameters for each of a series of targets must be predetermined by trial. Therefore the results of the tracer method were used in planning measurements by the scattering method.

The gas collection in the isotope separator was carried out in the same way as

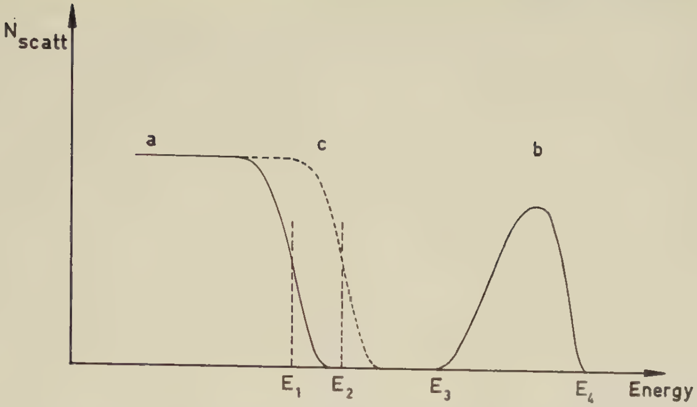

Fig. 12. Energy distribution of light particles scattered from a metal plate with a heavier element (gas) distributed in the surface layer.

in the tracer measurements with krypton. An additional requirement is that the area exposed in the separator should be considerably larger than the cross section of the deuteron beam. The exposed area was, in our set up, circular, with a diameter of 6 mm. Thick aluminium plates were used as targets. Some preliminary results are mentioned below.

4. Results

Fig. 13 shows a typical result of collection measurements, performed by bombarding a gold surface with a xenon current of 1.6 $\mu A/cm^2$. The target activity is plotted as a function of the electrical charge carried to the target by the ion beam. At *b* of Fig. 13 the flow of active xenon gas to the ion source was switched off, and ordinary inactive xenon was introduced. In this way it was possible to study the exchange of active xenon, already collected, with impinging stable xenon. It is evident that the experimental points of Fig. 13 follow an exponential curve. The curve *aa* of Fig. 13 represents the function

$$y = C_1 (1 - e^{-C_2 t}) \tag{10}$$

with $C_1 = 12{,}500$ and $C_2 = 0.0018$, obtained by a trial and error fit to the experimental points. For several collection curves, functions of the type (10) could be fitted. This phenomenon may be interpreted as follows. Suppose that the total number of positions, which can be occupied by a gas atom, is n_0. At the time t, n places are filled. If the rate of filling, $\frac{dn}{dt}$, is proportional to the number of empty places, we obtain

$$\frac{dn}{dt} = k(n_0 - n) \tag{11}$$

where k is a constant. Eq. (11) gives

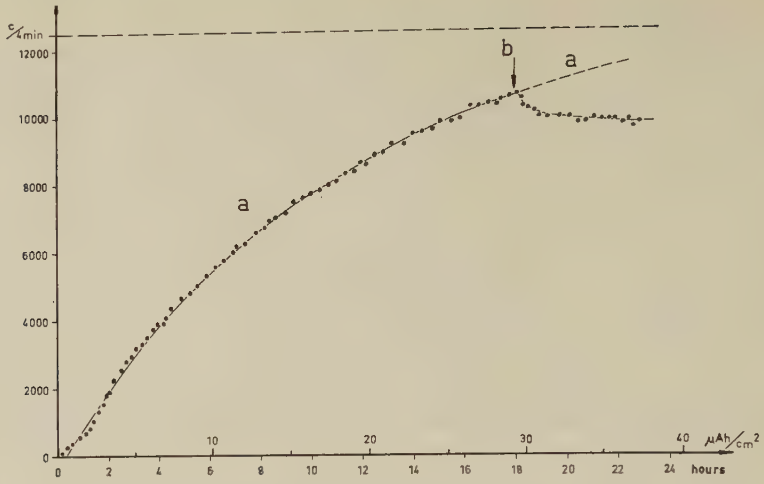

Fig. 13. "Saturation curve", obtained by recording the activity of a gold foil as a function of time, while bombarding it with a mixture of Xe^{131} and 12 d Xe^{131m}. At b, the active gas fed to the ion source was replaced by inactive xenon. Ion current 1.6 μA/cm².

$$n = n_0(1 - e^{-kt}) \tag{12}$$

which is identical with Eq. (10), if $C_1 = n_0$ and $C_2 = k$.

A knowledge of the specific activity of the charging gas, introduced into the ion source, and the value of C_1 would give the total number of xenon atoms collected in the metal lattice. (The specific activity was unknown in these measurements.)

The curve *c* of Fig. 13 is quite interesting. Apparently, only about 10 % of the collected Xe atoms was removed by further ion bombardment. This leads to the conclusion that destruction of the metal lattice by sputtering was negligible.

Fig. 14 shows a collection curve, obtained on bombarding an aluminium surface with a xenon ion density of 3.7 μA/cm². At *b*, the active gas fed to the ion source was replaced by inactive xenon. The difference between this curve and that of Fig. 13 is evident. Saturation occurred after a comparatively small amount of gas had reached the target. Moreover, more than 70 % of the gas content was displaced by further bombardment.

It should be noticed that the ion current density was much higher in this latter case. A comparison with other similar curves supported the assumption that the significant variable determining the behaviour of the process was the ion current. This was clearly demonstrated by a later measurement, the result of which is shown in Fig. 15. In this case xenon was collected in aluminium. Part *ab* of the curve corresponds to an ion current density of 4.1 μA/cm² while *bc* corresponds to 1.8 μA/cm². From this curve, we conclude that by decreasing the ion current density, it is possible to increase the saturation amount of gas considerably. In the present case, the saturation amount probably increased by a factor of 10–20. This fact is, of course, important for the production of gaseous targets.

The existence of two different types of saturation curve is supported by several measurements. The exponential function (10) could be fitted satisfactorily only to

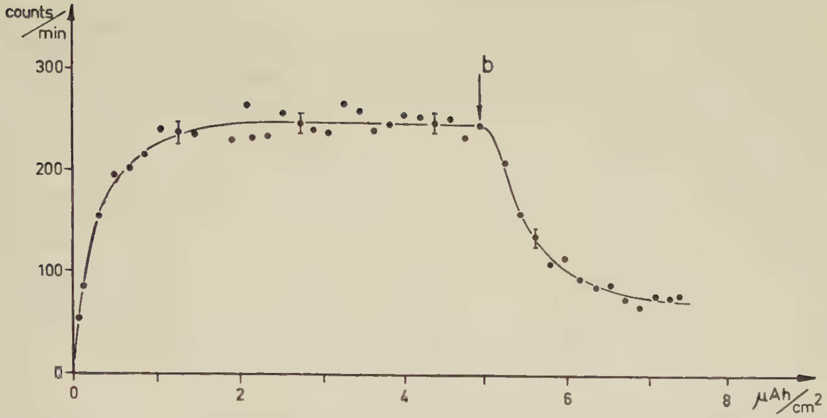

Fig. 14. "Saturation curve" of xenon in aluminium, obtained analogously to Fig. 13. Ion current 3.7 $\mu A/cm^2$.

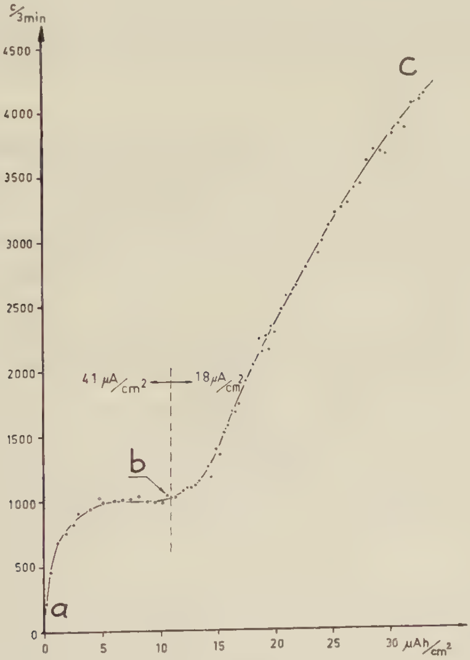

Fig. 15. "Saturation curve" of xenon in aluminium (cf. Fig. 14 and 13). At b, the ion current was decreased from 4.1 $\mu A/cm^2$ to 1.8 $\mu A/cm^2$.

those curves, obtained with low ion currents. This phenomenon may be tentatively explained in either of two different ways, both of them assuming that the surface temperature of the target governs the mode of behaviour. When the ion current increases, a greater amount of power is dissipated in the few atomic layers corresponding to the penetration depth of the ions. The surface temperature may therefore rise considerably. This could lead to one or both of the following consequences.

1. The diffusion rate increases so that the diffusion out of the metal competes with collection. The high temperature sensitivity of the diffusion process (cf. Fig. 9) supports this assumption.

2. A lower surface temperature, corresponding to a low ion current, may permit organic molecules, which may be present in the residual gas, to adhere to the target. They are then partly decomposed by ion impact. This external layer is continuously building up during the separation, and most of the gas is collected in this layer. When the layer grows thicker, the surface temperature increases since the thermal conductivity of the organic layer is less than that of the metal. Finally, the temperature becomes high enough to make diffusion important (and new organic molecules do not adhere to the surface; the layer ceases to grow).

On the other hand, when using a high ion current, the metal surface may be kept at so high a temperature that the molecules in question do not adhere to the surface. The saturation curve would then represent only collection in the metal lattice.

As was discussed on p. 122, temperature stability measurements on targets prepared during the saturation measurements, indicated that only a small part of the activity was deposited in an external layer. These targets were those prepared using a low ion current. Therefore this result would favour the alternative 1 above. More definite conclusions on the existence of carbon layers may be possible from scattering measurements on the targets.

During the bombardment, backscattering of ions by target atoms occurs. Any activity deposited on the surface *A* of the Faraday cage (Fig. 11) should be due to this effect. The two discs with central apertures (Fig. 11) could be removed; after a saturation measurement the activity of the surface *A* was measured in a standard GM-arrangement. It was found to be less than 0.1 % of the activity of the target, measured in the same geometry.

Some results, obtained by the scattering method, may be mentioned here. A series of targets have been exposed in the separator with various ion currents and collection times. Only parts of the scattering distributions, corresponding to the peak *b* of Fig. 12, have so far been recorded.

1. Xenon was collected in three aluminium targets with about the same ion density (4.2 $\mu A/cm^2$) as in the measurement of Fig. 14. Exposure times of 10 min, 30 min and 1 h were used. Figs. 16 a and b show the scattering distribution due to Xe for the first and third targets. It is evident, that saturation is already reached after an exposure of 0.7 $\mu Ah/cm^2$, in agreement with the value 0.6 $\mu Ah/cm^2$ obtained in a corresponding measurement with the tracer method (Fig. 14).

2. Xenon was collected in three aluminium targets with an ion density of 1.8 $\mu A/cm^2$. The exposure times were 1 h, 3 h, and 10 h respectively. The intensity of scattered deuterons was considerably higher in the third target than in the second one. This is in accordance with the corresponding results shown in Fig. 15. Fig. 16 c shows the scattering peak from the xenon in the first target of this series. A comparison with Figs 16 c and b shows that a larger amount is collected in case c, in accordance with the effect shown in Fig. 15. Moreover the xenon gas in the case of Fig. 16 c is distributed within a deeper layer of the target than in the other two cases. This may be due to the presence of carbon deposits as discussed above. However, it might also be explained as the result of a "forced diffusion" into the metal. The impinging gas ions would then give up part of their kinetic energy to xenon

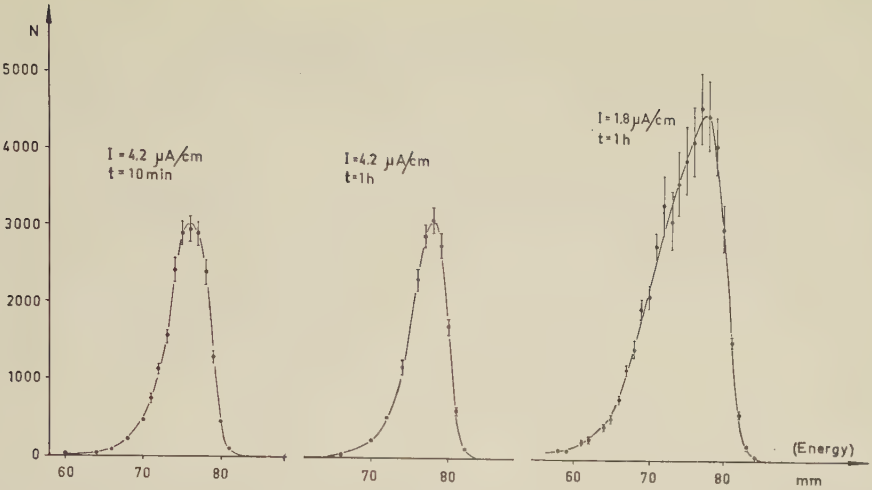

Fig. 16. Energy distribution of protons, scattered from xenon atoms in aluminium targets prepared in different ways. The targets were exposed to the proton beam under identical conditions. N is the number of proton tracks in the photographic detection plate, obtained per unit momentum interval.

atoms already trapped in the lattice, so that these atoms move deeper into the metal. This hypothesis would also explain why the slowly saturated targets loose only a small part of their gas content under further bombardment. On the other hand, the increased stopping power of the saturated lattice, due to the presence of heavier atoms, may also contribute to this effect.

Chapter IV. Concluding remarks

The usefulness of low intensity isotope separators in conjunction with various types of nuclear investigation may be illustrated by the compilation in Table 2 of various isotopes prepared in the present separator, which have been used in published investigations. References to the corresponding publications are given in the third column. Column 2 indicates the type of investigation performed with the isotopic sample.

The preparation of gaseous targets of stable isotopes, discussed in Chapter II, has made possible a systematic study of nuclear reactions in oxygen, nitrogen and neon isotopes. Precision determinations of Q values for such reactions have contributed to the establishment of a mass scale for the light nuclei, based entirely on nuclear reaction data.

The technique of preparing β- and γ-spectrometer samples, described in Chapter II, has been used in the study of several disintegration schemes. Especially, a systematic study of the decay characteristics of krypton and xenon isotopes has been performed (cf. Table 2). Some recent investigations of this type are described in the following paper.

The performance of correct mass assignments, though in principle trivial, is of critical importance for comparison of nuclear properties with predictions based on

Table 2. Isotopes prepared in the present isotope separator, which have been used in published investigations.

n = nuclear reaction studies, s = nuclear spectrometer measurements, m = mass assignment, earlier uncertain.

Element	Mass number	Type of work	Reference
N	15	n	(M 4)
O	17	n	(A 4) (A 5)
	18	n	(A 3) (M 2) (M 4) (M 5) (P 1)
Ne	20	n	(V1) (A 1) (A 6)
	21	n	(M 3)
	22	n	(A 2)
Mg	24	n	(G 1) (A 9)
	25	n	(A 9)
	26	n	(A 9)
Ti	51	m	(F 1)
As	71	s	(A 12) (T 7)
	73	m, s	(J 1)
Se	81	m, s	(B 4)
Kr	76	s	(T 10)
	77	m, s	(T 10)
	79	m, s	(B 10) (B 13) (T 8) (T 10)
	83 m	s	(B 5) (B 12) (B 13)
	85 m	s	(B 6) (B 13) (B 14) (T 10)
	85	s	(B 13) (T 10)
	87	s	(T 4) (T 10)
	88	s	(T 5) (T 10)
Mo	93 m	m, s	(A 7)
Xe	125	m, s	(B 9) (B 13)
	127	s	(B 11) (B 13)
	129 m	m, s	(B 11) (B 13) (B 14) (T 3) (T 6)
	131 m	s	(B 8) (B 13) (B 14)
	133 m	m, s	(B 7) (B 13) (B 14)
	133	s	(B 13) (B 14)
	135	s	(B 10) (B 13) (T 9) (T 10)
	137	m, s	(T 2)
	138	s	(T 2) (T 10)
Hf	175	m, s	(H 1)
	181	m, s	(H 1)
Hg	199 m	m	(B 3)
	203	m, s	(B 2)

nuclear shell theory, because the proton and neutron numbers are fundamental parameters, determining the nuclear properties. An interesting example is Mo^{93m} [A7]: its interpretation as due to "core isomerism" [G2] presumes an unambiguous mass assignment.

Practically all of the separations were performed using a target arrangement with ion beam focus at the magnet edge. The improved resolving power, discussed in Chapter I, in combination with an ion source for solid substances, will make the instrument more generally useful.

Summary

The isotope separator of the Institute is briefly discussed. Recent improvements have increased the resolving power which is now about 550 with ion currents of several μA.

The collection of stable gas isotopes is discussed, mainly with reference to experience gained with the present separator. A study of saturation phenomena occurring when rare gas isotopes are collected in metal surfaces has been undertaken. Preliminary measurements show that the maximum amount of gas which can be collected in this way is very sensitive to the beam intensity at the collector. Sputtering of target material and backscattering of energetic ions from the target were found to be negligible under the experimental conditions given.

The preparation of active isotopic samples for nuclear spectrometer measurements is discussed. Usually, aluminium foils of thickness 0.15 mg/cm² have been used as collectors. It is shown that active rare gas isotopes can be collected in formvar films of thickness 2 μg/cm², but the collection efficiency was, in this case, very small.

The temperature stability of gaseous targets prepared by ion bombardment of metal surfaces has been studied. Rare gas targets were found to be stable below 200° C. Measurements of this kind may give information about the diffusion of gases in metals.

The frequent use of the present instrument in conjunction with nuclear measurements is illustrated by Table 2 (p. 134).

Nobel Institute of Physics, Stockholm 50.

REFERENCES

A1 K. Ahnlund, Ark. f. fysik *7*, 155 (1953).
A2 K. Ahnlund, Ark. f. fysik *7*, 459 (1954).
A3 K. Ahnlund and C. Mileikowsky, Ark. f. fysik *8*, 161 (1954).
A4 K. Ahnlund, S. Thulin and Rolf Pauli, Ark. f. fysik (1954).
A5 K. Ahnlund, Phys. Rev. (1954).
A6 K. Ahnlund, Ark. f. fysik (1954).
A7 D. E. Alburger and S. Thulin, Phys. Rev. *89*, 1146 (1953).
A8 W. D. Allen, Nature, *168*, 451 (1951).
A9 J. Ambrosen, Nature *169*, 408 (1952).
A10 G. Andersson, The Gustaf Werner Institute for Nuclear Chemistry, Uppsala, unpublished.
A11 F. W. Aston, Phil. Mag. 38, 709 (1919).
A12 H. Atterling and S. Thulin, Nature *171*, 927 (1953).
B1 G. P. Barnard, Modern Mass Spectroscopy, London 1953.
B2 I. Bergström, S. Thulin, N. Svartholm and K. Siegbahn, Ark. f. fysik *1*, 281 (1949).
B3 I. Bergström and S. Thulin, Phys. Rev. *76*, 313 (1949).
B4 I. Bergström and S. Thulin, Phys. Rev. *76*, 1718 (1949).
B5 I. Bergström, S. Thulin and G. Andersson, Phys. Rev. *77*, 851 (1950).
B6 I. Bergström and S. Thulin, Phys. Rev. *79*, 537 (1950).
B7 I. Bergström and S. Thulin, Phys. Rev. *79*, 538 (1950).
B8 I. Bergström, Phys. Rev. *80*, 114 (1950).
B9 I. Bergström, Phys. Rev. *82*, 111 (1951).
B10 I. Bergström, Phys. Rev. *82*, 112 (1951).
B11 I. Bergström, Nature *167*, 634 (1951).
B12 I. Bergström, Phys. Rev. *81*, 638 (1951).
B13 I. Bergström, Ark. f. fysik *5*, 191 (1952).
B14 I. Bergström, S. Thulin, A. H. Wapstra and B. Åström, Ark. f. fysik *7*, 255 (1953).

B 15 R. Bernas, Journ. de Phys. et le Rad. *14*, 34 (1953).
B 16 N. Bohr, Det Kgl. Danske Vidensk. Selsk. Mat. Fys. Medd. *18:8*, 1 (1948).
B 17 K. J. Broström, T. Huus and J. Koch, Nature *160* 498 (1947).
D 1 A. J. Dempster, Phys. Rev. *11*, 316 (1918).
E 1 H. Evald and H. Hintenberger, Methoden und Anwendungen der Massenspektroskopie. Weinheim 1953.
F 1 W. Forsling and A. Ghosh, Ark. f. fysik *4*, 331 (1952).
G 1 T. Grotdal, O. M. Lönsjö, R. Tangen and I. Bergström, Phys. Rev. *77*, 296 (1950).
G 2 M. Goldhaber, Phys. Rev. *89*, 1146 (1953).
H 1 A. Hedgran and S. Thulin, Phys. Rev. *81*, 1072 (1951).
I 1 M. G. Inghram, N. B. S. Circular n:r *522*, 151 (1953).
J 1 S. Johansson, Ark. f. fysik *4*, 273 (1952).
K 1 C. P. Keim, Annual Review of Nuclear Science, Vol. *1*, Stanford, Calif., 1952.
K 2 C. P. Keim, J. Appl. Phys. *24*, 1255 (1953).
K 3 J. Kistemaker and G. J. Zilverschoon, N.B.S. Circular no. *522*, 179 (1953).
K 4 J. Koch and B. Bendt-Nielsen, Det Kgl. Danske Vidensk. Selsk. Mat. Fys. Medd. *21*, No. 8 (1944).
K 6 J. Koch, N.B.S. Circular no. *522*, 165 (1953).
L 1 L. G. Lewis and R. J. Hayden, Rev. Sci. Instr. *19*, 599, 915 (1949).
L 2 A. Lundén and O. Almén, Chalmers Institute of Technology, Gothenburg, unpublished.
L 3 A. E. Lindh and Å. Nilsson, Ark. f. Matem. Astr. o. Fys. *31 A*, N:o 7 (1944).
M 1 C. Mileikowsky, Ark. f. fysik *7*, 33 (1953).
M 2 C. Mileikowsky, Ark. f. fysik *7*, 98 (1953)
M 3 C. Mileikowsky and W. Whaling, Phys. Rev. *88*, 1254 (1952).
M 4 C. Mileikowsky and R. Pauli, Ark. f. fysik *4*, 299 (1952).
M 5 C. Mileikowsky and K. Ahnlund, Phys. Rev. (1954).
O 1 M. L. E. Oliphant, E. S. Shire and B. M. Crowther, Proc. Roy. Soc. London, *146*, 922 (1934).
P 1 R. Pauli, Ark. f. fysik (1954).
S 1 W. R. Smythe, L. H. Rumbaugh and S. S. West, Phys. Rev. *45*, 724 (1934).
T 1 J. J. Thomson, Phil. Mag. *20*, 752 (1910), *21*, 255 (1911).
T 2 S. Thulin, I. Bergström and A. Hedgran, Phys. Rev. *76*, 871 (1949).
T 3 S. Thulin and I. Bergström, Phys. Rev *85*, 1055 (1952).
T 4 S. Thulin, Phys. Rev. *87*, 684 (1952).
T 5 S. Thulin, Ark. f. fysik *4*, 363 (1952).
T 6 S. Thulin, Ark. f. fysik *7*, 269 (1953).
T 7 S. Thulin, J. Moreau and H. Atterling, Ark. f. fysik *8*, 219 (1954).
T 8 S. Thulin, J. Moreau, and H. Atterling, Ark. f. fysik *8*, 229 (1954).
T 9 S. Thulin, Phys. Rev. *94*, 734 (1954).
T 10 S. Thulin, Ark. f. fysik *9*, 137 (1955).
V 1 D. M. Van Patter, A. Sperduto, P. M. Endt, W. W. Buechner and H. A. Enge, Phys. Rev. *85*, 142 (1952).
W 1 W. Walcher, Zeitschr. für Phys. *108*, 376 (1938).
Y 1 E. L. Yates, Proc. Roy. Soc. London, *168*, 148 (1938).
Z 1 C. J. Zilverschoon, thesis, University of Amsterdam (1954).

Tryckt den 8 december 1954

Uppsala 1954. Almqvist & Wiksells Boktryckeri AB

ARKIV FÖR FYSIK Band 9 nr 11

Communicated 27 October 1954 by MANNE SIEGBAHN and G. BORELIUS

Studies in nuclear spectroscopy with electromagnetically separated gaseous isotopes II

Disintegration of some krypton and xenon isotopes

By SIGVARD THULIN

With 42 figures in the text

Contents

Page

Introduction 138

Chapter I. Apparatus and technique 139

- 1. Isotope separator and sample preparation (See preceding paper) 139
- 2. Nuclear spectrometer equipment 139
  - a. Beta-spectrometers 139
  - b. Scintillation spectrometer 139
  - c. Coincidence equipment and technique 140

Chapter II. Some remarks on the interpretation of the empirical data 142

- 1. Interpretation of pulse-height distributions 142
- 2. Estimation of relative intensities 143
- 3. Analysis of disintegration data 145

Chapter III. Measurements and interpretation of decay data 146

- 1. 9.7 h Kr^{76} and 17.2 h Br^{76} 146
- 2. 73 min Kr^{77} 149
- 3. 34.5 h Kr^{79} 157
- 4. 4.4 h Kr^{85m} and 9.4 y Kr^{85} 161
- 5. 78 min Kr^{87} 164
- 6. 2.77 h Kr^{88} and 18 min Rb^{88} 170
- 7. 9.2 h Xe^{135} 180
- 8. 17 min Xe^{138} and 32 min Cs^{138} 183

Chapter IV. Concluding remarks 186

- 1. General 186
- 2. Interpretation of some decay schemes in terms of the modified single particle model 188
  - a. Kr^{85} and Xe^{135} 188
  - b. Kr^{87} 189
  - c. Kr^{77} and Kr^{79} 191
  - d. Kr^{88}, Rb^{88} and Xe^{138} 192

Summary 192
References 194

Introduction

The isotope separator at the Nobel Institute of Physics [B1] has been used for the preparation of (*a*) targets of stable isotopes for precision determination of Q values, and (*b*) pure radioactive samples for disintegration measurements. Radioactive isotopes of Ti, As, Br, Kr, Rb, Mo, I, Xe, Cs, Hf, Hg, and Pb have been studied in this way. These applications of the isotope separator are discussed in the preceding paper.

Most decay scheme investigations have been concerned with the isotopes of krypton and xenon. The disintegration data earlier reported for these nuclei were very incomplete, certainly due to the difficulties in preparing proper β-sources with conventional techniques. On the other hand, it was found that the isotope separator technique could successfully be applied for the preparation of pure, mass-determined, carrierfree sources of rare gases, deposited in very thin backing foils without disturbing covering material. Furthermore, the disintegration schemes of the krypton and xenon isotopes are of special interest, since we are here dealing with two sets of nuclei with members on both sides of a single closed nucleon shell. A comparison of the decay properties of these nuclei with predictions of nuclear shell models might therefore be fruitful.

Except for those isotopes of half-lives shorter than 15 minutes and longer than 9.4 years, all krypton nuclei in the mass region 79–88 and all xenon nuclei in the region 125–138 have been studied. In several cases decay schemes were suggested. In other cases, however, the available equipment was not sufficient for a detailed analysis of the disintegration schemes. At present, a higher neutron flux is available for the production of fission gas isotopes and the nuclear spectrometer equipment has been considerably improved. It has therefore now been possible to clear up several uncertainties in earlier measurements and to collect new experimental data. Thus our knowledge on the decay of these isotopes has been considerably increased.

The present investigation concerns a further study of the fission gas isotopes Kr^{85m}, Kr^{87}, Kr^{88}, Xe^{135} and Xe^{138} and the two daugther isotopes Rb^{88} and Cs^{138}. The 9.4 y Kr^{85} has also been measured, using a strong source prepared from a commercial Harwell sample. Some additional decay data of Kr^{79} are reported. The radiations from 1.1 h Kr^{77} have also been studied by means of nuclear spectrometers. Finally, preliminary scintillation measurements are reported for the genetic pair $Kr^{76} \rightarrow Br^{76}$.

In order to avoid unnecessary repetitions in the following, the nuclear spectrometer equipment is discussed in the first section. Then the investigations are presented in order of increasing mass number of the isotopes. Some general conclusions are presented in the last section.

Chapter I. Apparatus and technique

1. Isotope separator and sample preparation

This topic is treated in detail in the preceding paper.

2. Nuclear spectrometer equipment

a) Beta-spectrometers

The intermediate image spectrometer, designed by H. SLÄTIS and K. SIEGBAHN [S2], has been extensively used. The main advantage of this instrument is the high transmission, up to 8 % [S2], which makes possible the measurement of weak β-samples sometimes prepared in the electromagnetic isotope separator. With β-sources of diameter 5–10 mm, a resolution of 3.5–5 % is obtained. The spectrometer has been provided with a continuously variable central slit (H. SLÄTIS, 1952). The radial width of this slit can be changed from zero to about 11 mm by means of a shaft through a vacuum seal. With a sample of diameter 4 mm and a 3.5 mm central slit, a resolution of 2.2 % was obtained. However, the transmission was then considerably less.

The GM-counters used in the spectrometer had a window diameter of 8–12 mm. Formvar windows of thickness corresponding to a "cut off" of 5–7 kev have been frequently used. (The "cut off" is here defined by a straight line extrapolation of a continuous β-distribution to the energy axis.) In the study of low energy electron lines formvar windows with a "cut off" at about 2 kev have been used. They were supported by brass grids of ~ 50 % transmission.

The main disadvantage of the intermediate image spectrometer in its present performance is the inability to focus β-particles of energies higher than ~ 1.8 Mev with high transmission. This fact has seriously influenced some of the present measurements, especially those on Kr^{87} and Kr^{88}. For the measurement of high energy β-continua, e.g. those of Kr^{87} and Kr^{88}, we have earlier used a *short lens spectrometer* [S1]. With special arrangements, this instrument was able to focus the 5.3 Mev β-particles of Rb^{88}. The transmission of this instrument was about 1 %.

The double focusing β-spectrometer, of mean radius 50 cm [H2], has been used in some cases because of the high resolution obtained. Comparatively strong β-sources are needed. In principle, however, this type of instrument is well suited for measurements on β-samples prepared in the isotope separator. The dimensions of the correct β-source shape are very similar to those of the focused mass lines. Therefore most of the activity collected is utilized. For the lens spectrometer samples only a central circular part of the deposited activity can be used. An example illustrating the usefulness of this instrument is the case of Kr^{79} [T4], having fifteen converted γ-rays. Most of the γ-energies were accurately determined in the double focusing instrument with a resolution of 0.25 %. For several γ-rays $K/(L+M)$ ratios have also been determined in this β-spectrometer, when the other instruments could not resolve the K and $(L+M)$ conversion lines.

b. Scintillation spectrometer

The scintillation spectrometer units used were designed by B. ÅSTRÖM [Å1]. They are single channel instruments with variable channel width. Earlier, EMI 5311 photomultipliers were used together with small NaI(Tl) crystals as detectors. Recently, a rapid development of the scintillation technique has taken place. The introduction of large NaI(Tl) crystals (up to 1.5″ thickness and 1.5″ diameter) and the use of Dumont 6292 photomultipliers have considerably improved the resolution of the scintillation spectrometers. With the equipment used in the present work a half width of 8 % is normally obtained for the 661 kev line of Cs^{137}. The improved scintillation spectrometer equipment has made possible the collection of much new nuclear data, reported in the following sections (cf. Table 7).

Most of the γ-spectra measured in the present work cover the energy region up to 3 Mev. In order to utilize the accuracy of the scintillation spectrometer, the measurements have been performed in two or more steps, each of them covering a proper region of the γ-spectrum, and overlapping the next region sufficiently for normalization purpose.

The *energy calibration* of the pulse height scale was performed by means of known γ-rays emitted from a set of standard samples (e.g. Mn^{54}, Co^{57}, Zn^{65}, Y^{88}, Cs^{137}, Bi^{207}). These calibration standards covered the energy region up to 2.76 Mev. For higher energies linear extrapolation of the energy scale was used. In most cases calibration points were taken both before and after the γ-measurements in order to check the constancy of the instrument. The γ-spectra were normally recorded twice. Most energy values reported in this paper are therefore mean values of two or more measurements.

c. Coincidence equipment and technique

β- and γ-spectrometer measurements alone are normally not sufficient to establish the disintegration scheme of an isotope. Coincidence measurements of various types are needed to determine the correlations between different β- and γ-transitions. In the present work we have used coincidence equipment which could be assembled to include either two energy-selective γ-channels or one β- and one γ-channel.

γ-γ coincidences.

Two single channel scintillation spectrometers of the type described above [Å 1] were connected with a coincidence circuit of resolving time $\sim 3 \times 10^{-7}$ sec. [Å 2]. $1'' \times 1''$ cylindrical NaI(Tl) crystals and Dumont 6292 photomultipliers were used as detectors. These units were mounted with the common symmetry axis horizontal and the sample was placed between the crystals.

The interpretation of the results from γ-γ coincidence measurements is often rendered difficult by the complexity of the pulse-height distributions. Generally, this technique is useful only for the most favourable γ-transitions. Some ambiguities may be eliminated by the following measuring procedure. In one measurement channel A is fixed at the photo peak of energy E_1 and channel B is moved in steps across the energy region of interest, for example a photo peak of energy E_2. In the next measurement channel A is fixed above or below the photo peak and channel B is moved across the same energy region as before. The difference between the two coincidence distributions then gives information as to whether the two photopeaks E_1 and E_2 are in coincidence or not. In some cases, the simultaneous absence of coincidences between two photopeaks and presence of coincidences between one of them and a third one may be conclusive. Although γ-γ coincidence results are not always unique, they may be of importance when compared with data obtained in β- and γ-measurements, and in β-γ and e-γ coincidence measurements.

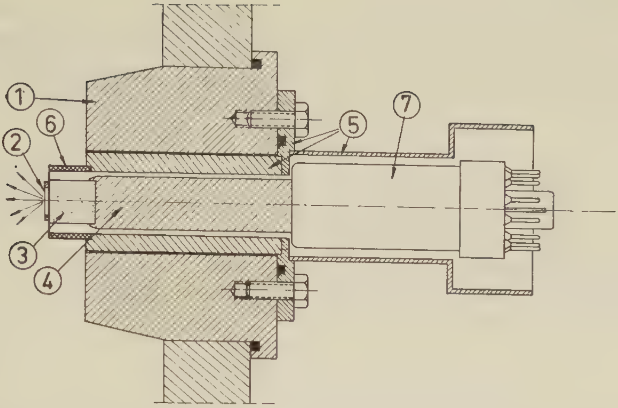

Fig. 1. Schematic drawing of crystal arrangement in the coincidence equipment. 1. Spectrometer pole piece. 2. β-source. 3. NaI crystal. 4. Light guide. 5. Iron shields. 6. Brass hood. 7. Photomultiplier.

β-γ coincidences.

A useful coincidence technique is that of mounting a scintillation counter behind the β-sample in a high transmission β-spectrometer. An arrangement of this kind was assembled at this institute by J. Moreau, using existing electronic components [M6]. It was used in investigations on Sb^{125} [M6], Kr^{79} [T4] and As^{71} [T7]. However, the transmission of the γ-spectrometer channel was low because of a simplified mounting of the scintillation counter [M6]. This equipment was therefore not suited for coincidence measurements with weak samples or on low intensity branches in stronger samples. As such types of measurements were required in the present investigations, the crystal arrangement has been redesigned. A larger NaI crystal was placed much closer to the β-source than in the earlier arrangement. This became possible by the introduction of a light guide (Fig. 1). The total crystal efficiency thereby increased by a factor 10 or more. As this equipment has been frequently used in the present work, it will be briefly described here.

The crystal arrangement is schematically shown in Fig. 1. The NaI(Tl) crystal, of diameter 25 mm and height 25 mm, is placed 3 mm behind the β-source in the intermediate image β-spectrometer [S2]. The chamber containing the crystal is at atmospheric pressure. The wall thickness between this chamber and the vacuum system is ~ 0.3 mm at the position between sample and crystal. The crystal is fixed to a perspex light guide of length 12 cm. This is optically coupled to the glass envelope of a Dumont 6292 multiplier. The pulses from the photomultiplier were analysed in the conventional manner. The energy resolution of this arrangement was 12 % at 660 kev. The β-pulses from the GM-counter of the β-spectrometer and the γ-pulses from the scintillation spectrometer were fed to the same coincidence circuit as was alternatively used in the γ-γ coincidence measurements [Å2].

This coincidence arrangement is useful in recording β-γ, e-γ and C-γ coincidences. Here e denotes conversion electrons, and C denotes K-capture events, detected by means of the corresponding Auger electrons.

Chapter II. Some remarks on the interpretation of the empirical data

1. Interpretation of pulse-height distributions

The interpretation of pulse-height distributions, recorded with a NaI scintillation spectrometer, necessitates a consideration of the various phenomena occurring when γ-quanta interact with matter. The experimental pulse distribution due to a γ-ray of energy E_γ may consist of the following components:

a. The *photopeak*, at energy E_γ, corresponding to the complete absorption of the γ-energy by photoabsorption in the iodine of the phosphor or by various multiple processes.

b. The *Compton distribution*, due to a partial absorption of the quantum by single or multiple Compton scattering processes. The high energy edge of the Compton distribution corresponds to the energy

$$E_c = \frac{E_\gamma}{1 + \dfrac{0.256}{E_\gamma}} \quad \text{(energies in Mev).} \tag{1}$$

3. Especially for low energy γ-rays, the photopeak is accompanied by a noticeable *escape peak* at the energy

$$E_{esc} = E_\gamma - 0.028 \quad \text{(Mev).} \tag{2}$$

This peak is due to the fact that low energy γ-quanta are absorbed in the part of the crystal closest to the source. The iodine X-ray quanta accompanying the photoprocess then have a certain chance of escaping from the crystal. This effect has been studied theoretically and experimentally [see, e.g., M7] for NaI crystals similar to those used in the present work. The escape peak to photopeak intensity ratio is shown to be very small (of the order of one per cent) for $E_\gamma > 150$ kev (cf. also page 174).

d. The *backscatter distribution*, arising from Compton quanta from the surroundings of the phosphor. Quanta scattered through about 180 degrees (mainly from the photocathode and crystal support) may give rise to a peak at energy

$$E_b = \frac{1}{3.91 + \dfrac{1}{E_\gamma}} \quad \text{(energies in Mev.)} \tag{3}$$

This expression gives the energy limit 0.256 Mev for back-scattered quanta.

e. For high energy γ-rays *pair peaks* may occur at energies $(E_\gamma - 1.02)$ and $(E_\gamma - 0.511)$ Mev. The former one is due to pair formation by the γ-quantum and escape from the phosphor of both 0.511 Mev quanta formed in the subsequent annihilation of the positron. In the latter case only one of the annihilation quanta escapes the phosphor. The intensity of such peaks becomes important at energies above ~ 2 Mev in our case. The energy determination of such γ-rays is sometimes facilitated by the presence of pair peaks (cf. page 175).

f. When recording radiations from very strong sources, one has also to consider the possible existence of *coincidence peaks*. These represent accidental or real coincidences between quanta from intense γ-transitions. The intensity of coincidence peaks drops quadratically with the total counting rate in the crystal (cf. Fig. 35).

g. Sometimes the γ-distributions of β^--emitters may contain a weak peak at energy 0.511 Mev. This is due to annihilation of positrons created in the surrounding material by high energy γ-quanta from the β^--emitter.

2. Estimation of relative intensities

a. Pulse-height distributions. The relative intensity γ_1/γ_2 of two γ-rays may be estimated from the corresponding pulse-height distribution by the expression

$$\frac{\gamma_1}{\gamma_2}=\frac{A_1}{A_2}\,\frac{\varepsilon_2}{\varepsilon_1} \tag{4}$$

where A is the photopeak area and ε is the "*relative photopeak efficiency*", i.e. the probability that a γ-quantum entering the crystal produces a pulse contributing to its photopeak. Relative intensity estimates therefore presume a knowledge of the efficiency curve for the crystal arrangement used. Such a curve was obtained by comparing the photopeak areas of γ-γ cascades and γ-X-ray cascades with known relative intensities (cf. [Å3]). In such cases γ_1/γ_2 is konwn, and a measurement of A_1/A_2 gives $\varepsilon_1/\varepsilon_2$. The establishment of an efficiency scale from these values follows from the assumption that the efficiency for recording radiations below 100 kev is approximately 100 %. The values determined in this way were plotted on a double logarithmic diagram of ε versus energy. The experimental curve extended to 1.85 Mev (Y^{88}). The crystal efficiency for higher energies was obtained by linear extrapolation of the efficiency curve.

Several of the intensity estimates given in the following are probably not accurate to more than 50 %, partly because of uncertainties in the efficiency calibration, and partly because of difficulties in defining the area of a photopeak in complex pulse height distributions (see, e.g., Figs. 20 and 28). However, in many cases rough intensity estimates are of importance in deciding between decay scheme alternatives with different γ-sequences. Moreover, a knowledge of approximate intensity relations may sometimes be of value in checking spin- and parity assignments of the corresponding levels.

b. β-γ coincidence distributions. By determining the "absolute photopeak efficiency" (defined below) of the γ-detector, it is possible to get quantitative intensity information from the coincidence measurements. It is for example possible to estimate the relative intensity of a β-decay branch β_1, followed by a certain γ-transition γ_1. This method is briefly discussed below.

The *absolute photopeak effeciency* is here defined as

$$\boldsymbol{e}=\Omega\,\varepsilon \tag{5}$$

where Ω is the effective solid angle subtended by the crystal at the β-source, and ε is the *relative photopeak efficiency* for the γ-ray in question (cf. above). Assume now that the value of $\boldsymbol{e}$ for a γ-ray γ_1 is known. The β_1–γ_1 coincidence distribution $N_{\beta_1\gamma_1}$ and the total β-distribution N_β of the β-particles are recorded. The total β-decay intensity I_β is proportional to the area A_β of the β-distribution:

$$I_\beta = C_1 A_\beta = C_2 \int N_\beta T \, dB\varrho \tag{6}$$

where C_1 and C_2 are constants, and T is the β-spectrometer transmission. Correspondingly, the intensity I_{β_1} of the β-component β_1 is

$$I_{\beta_1} = C_1 A_{\beta_1} = C_2 \int N_{\beta_1} T \, dB\varrho \tag{7}$$

where N_{β_1} is the momentum distribution of β_1. In a case when we do not directly measure N_{β_1}, but rather the coincidence distribution,

$$N_{\beta_1\gamma_1} = \frac{N_{\beta_1} e}{1+\alpha} \tag{8}$$

where α is the internal conversion coefficient of γ_1, we obtain from (7) and (8)

$$I_{\beta_1} = C_2 \frac{1+\alpha}{e} \int N_{\beta_1\gamma_1} T \, dB\varrho. \tag{9}$$

This gives

$$I_{\beta_1} = C_1 \frac{1+\alpha}{e} A_{\beta_1\gamma_1} \tag{10}$$

where $A_{\beta_1\gamma_1}$ is the area of the coincidence distribution. The intensity ratio I_{β_1}/I_β then is

$$\frac{I_{\beta_1}}{I_\beta} = \frac{A_{\beta_1\gamma_1}(1+\alpha)}{e A_\beta}. \tag{11}$$

In the present measurements α is much smaller than 1 and has been neglected, since the correction would be small compared with other errors. Intensity estimates by this method were found to be in accordance with branching values obtained from other methods (see, e.g., p. 158 and 181).

The total crystal efficiency e was determined for the 565 kev γ-ray in Bi^{207}. The γ_{565} photoline was integrated by the γ-channel and the conversion electrons of the 1.1 Mev γ-ray of Bi^{207} were recorded in the β-channel. Each of these conversion electrons was assumed to be followed by 0.9 γ_{565}-quanta (the internal conversion coefficient of γ_{565} is ~ 0.1). From the ratio of the coincidence rate and the GM-counting rate we compute $e_{565} = 0.025$. The relative efficiency curve discussed on page 143 is then used to obtain the corresponding total efficiency e for other γ-energies, since according to eq. (5)

$$e_x = \frac{e_{565} \cdot \varepsilon_x}{\varepsilon_{565}}, \tag{12}$$

if the solid angle Ω is assumed to be approximately independent of energy. In many cases the γ-channel cannot properly be set to integrate the whole photoline. Corrections are then applied for the part of the photoline not recorded in the γ-channel.

It is to be understood that the method outlined above has not been worked out with any degree of precision in the present work. However, the rough intensity estimates obtained appear to be of value, especially in computing log *ft* values. The classification of β-transitions by means of their log *ft* value is not very sensitive to the error in the estimated β-intensity.

3. *Analysis of disintegration data*

The main purpose of our measurements has been to explore the disintegration schemes of various isotopes and, if possible, to use the experimental data for spin and parity assignments of the excited levels. A brief review of the method used in analysing the empirical data is given below.

From β-spectrometer measurements the following data may be obtained:

a. The β-continuum gives the energies and relative intensities of the various β-transitions. From these data log *ft* values are computed for the β-transitions.
b. The electron line spectrum gives the energies and relative intensities of conversion electrons. From the conversion line energies the corresponding γ-ray energies are computed.
c. In some cases conversion coefficients can be deduced from a comparison of conversion electron intensity and β-decay intensity.
d. The intensity ratio of K and L conversion electrons may be compared with theoretical or semi-empirical K/L values, to give the multipole order of the corresponding γ-ray.
e. For positron emitters the Auger line intensity may be used to compute the ratio of K-capture and positron emission.

From γ-spectrometer measurements we obtain the energies and intensities of γ-transitions.

The coincidence measurements give information about cascade relations and branching ratios.

Generally, the first step of the analysis was performed by combining β- and γ-spectrometer data to give a probable, often fragmentary decay scheme. This was then checked by coincidence measurements. The results obtained sometimes suggested a remeasurement of part of the β- or γ-spectrum. Finally we arrived at a probable disintegration scheme, consistent with regard to energies and estimated intensities. Spin- and parity assignments were then attempted, starting with the known spin of one of the ground states involved in the decay. From the log *ft* values of the β-transitions various spin and parity alternatives of the corresponding levels were obtained. It is to be noticed that this method of spin assignment is sometimes uncertain because of the existence of anomalous log *ft* values (cf. p. 188). The next step in the spin assignment is to compare the various spin alternatives with predictions of the shell model, when this is assumed to be applicable. Several spin alternatives may thus be excluded. If there are still several alternatives left, some of them may be excluded by comparing the empirical relative γ-intensities with theoretical predictions. In cases where the internal conversion coefficient or the K/L ratio of a γ-ray is determined, the spin change of this transition is often determined by comparison with theoretical calculations. In the present work such cases are rare because of the high γ-ray energies and the complexity of the decay schemes.

Chapter III. Measurements and interpretation of decay data

Section 1. 9.7 h Kr^{76} and 17.2 h Br^{76}

Introduction

Recently, A. A. Caretto and E. O. Wiig [C1] reported a new neutron deficient isotope of Kr, produced by the spallation of yttrium. They assigned a 9.7 ± 0.5 h activity to Kr^{76} by showing its genetic relationship to 17.2 h Br^{76}. Caretto and Wiig stated that Kr^{76} decays predominantly by emission of positrons of energy ≤ 0.6 Mev.

The decay of 17.2 h Br^{76} has been studied by S. C. Fultz and M. L. Pool (F2), who produced this isotope by α-bombardment of enriched selenium. The activity was measured in a 180° spectrometer. Source and backing had a density of ~ 10 mg cm^{-2} and the thickness of the GM counter window was 2.5 mg cm^{-2}. Five positron groups of energies 3.57, 1.7, 1.1, 0.8 and 0.6 Mev were reported. The conversion electrons of eight γ-rays of energies 0.25, 0.33, 0.37, 0.42, 0.68, 0.75, 0.96 and 1.2 Mev were also assigned to Br^{76}. Some of these energies were evaluated by "a statistical method" because of the weak samples used. Coincidence measurements indicated that the high energy positron transition leaves the Se^{76} nucleus in the ground state.

In the following we will discuss some preliminary measurements performed on Kr^{76} and its daughter Br^{76}.

Sample preparation. Mass assignment

In the Kr^{77} measurements later reported (p. 149) the first two Kr samples were obtained by bombarding KBr with protons of energy ≤ 50 Mev. No investigation of Kr^{76} was undertaken in these cases. The activity plot of Fig. 5 (p. 149) showed no certain indication of an activity at mass number 76. The corresponding mass separation was performed with the ion beam focus at the magnet edge (cf. preceding paper), and the mass resolution was not very good.

It was tempting, however, to see if Kr^{76} could be produced in measurable quantities by a $(p, 4n)$ reaction on Br^{79}. In the last KBr irradiation, the maximum proton energy was therefore increased to 60 Mev. The mass separation of the Kr activities was performed with ion beam focus at 1.6 m from the magnet edge. Fig. 2 shows the activity plot of the collector foil (2.5 mg cm^{-2}). This was cut into strips, two mm broad, the activities of which were measured with a GM counter. (Only a minor part of the intensity of the mass lines was used for this measurement. The main part was kept for scintillation spectrometer studies.) Fig. 3 shows the decay of the activity at mass number 76 (curve *a*). For each decay point the GM counting rate was normalized by means of a standard sample. The straight line *b* defines a half life of 17.5 h, in accordance with the half life 17.2 h, reported for Br^{76} [F2]. The difference between line *b* and the experimental points is represented by the circles to which curve *c* is fitted. This line apparently bends somewhat towards the time axis. The straight line *d* gives a half life of 10.5 h. However, this curve should be remeasured before definite conclusions can be made. In the measurements of Caretto and Wiig [C1], the line corresponding to *c* of Fig. 3 showed a single period of 9.7 h.

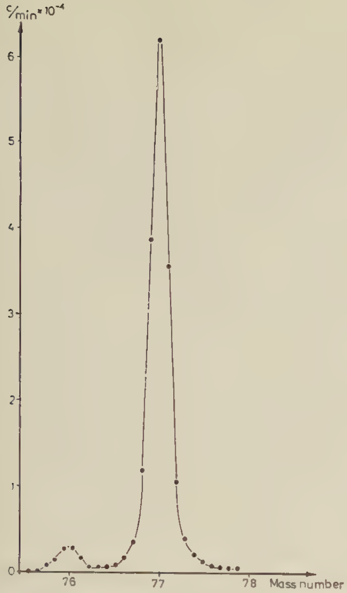

Fig. 2. Activity spectrum of electromagnetically separated Kr isotopes formed in Br (p, xn) reactions. Proton energy ≤ 60 Mev. The activity of 2 mm broad collector strips is plotted as a function of mass number.

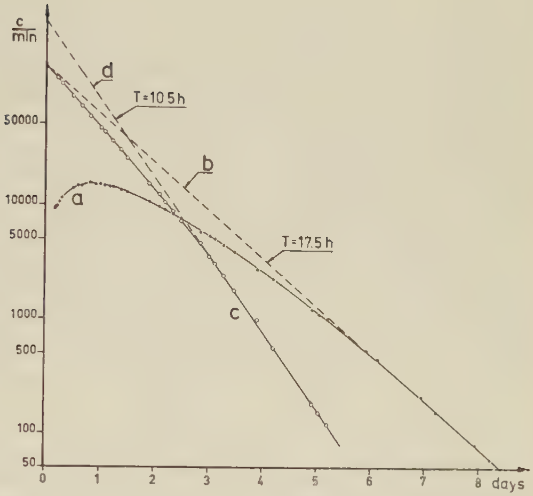

Fig. 3. Decay of electromagnetically separated Kr^{76} + Br^{76}.—*a*, Experimental curve; *b*, extrapolated decay curve of Br^{76}; *c*, difference between *b* and *a*; *d*, straight line defining the final slope of *c*.

Scintillation spectrum

As our main interest was in the decay of 73 min Kr^{77}, we investigated it first, and did not begin the scintillation spectrometer measurements of Kr^{76} + Br^{76} until ~ 12 h after the mass separation. The Kr^{76} activity was then considerably mixed up with Br^{76}. The γ-spectrum appears to be very complex, as seen from Fig. 4 a and b. The inset of Fig. 4 b shows a separate analysis of the double line at 0.55 Mev. This analysis was performed by normalizing the annihilation peak of Na^{22} to the low energy slope of the 0.55 Mev doublet. The γ-spectrum of Fig. 4 shows the presence of peaks at energies 0.028, 0.093, 0.13, 0.20, 0.267, 0.316, 0.40, 0.511 (annihilation peak), 0.560, 0.660, 0.85, ~ 1.2, and 1.86 Mev. The peak at 0.13 Mev may be due to backscattered quanta from 0.267 and 0.316 Mev γ-transitions (cf. p. 142). The existence of "peaks" at 0.20 and 0.85 Mev is not certain. The other peaks of Fig. 4 are probably genuine photopeaks. The "peak" at ~ 1.2 Mev is probably double.

By remeasuring the low energy region of the γ-spectrum (Fig. 4 a) after 9, 15, and 32 hours, the peaks of energies < 0.5 Mev were found to decay with a period of about 12 h. The relative decay of the doublets at 0.3 and 0.5 Mev was studied separately. In the beginning, the 0.3 Mev doublet was roughly twice as strong as the 0.5 Mev doublet. After three days the 0.3 Mev doublet had disappeared, whereas the decay of the complex 0.55 Mev line could be followed for another two days. It turned out that the 0.511, 0.560, and 0.660 Mev peaks decayed with an apparent half life of about 19 h. The decay of the 1.86 Mev peak apparently proceeded with a half life of about 30 h.

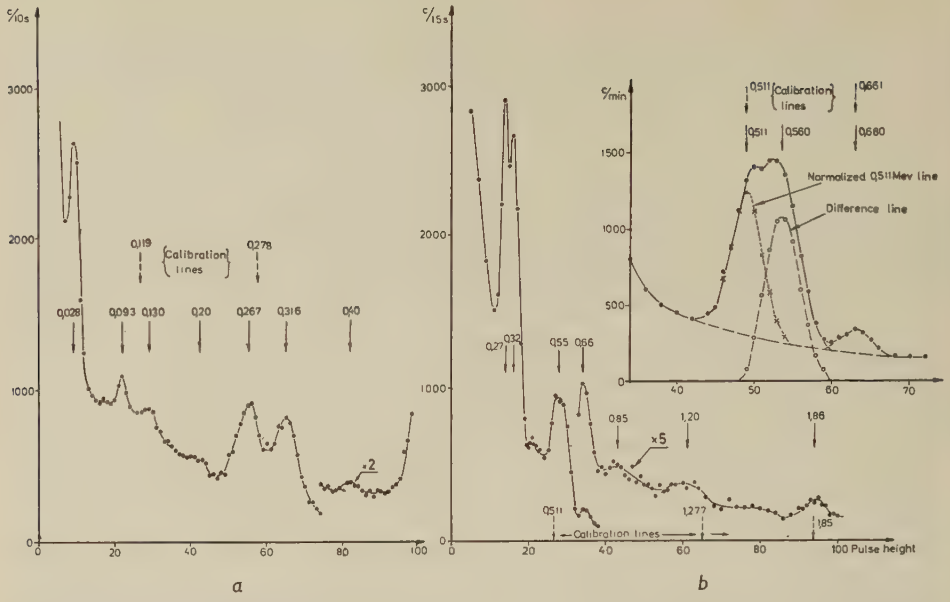

Fig. 4. Pulse height distributions of $Kr^{76} + Br^{76}$, recorded in the NaI scintillation spectrometer. —*a*, Low energy region; *b*, high energy region. (Energies in Mev.)

By measurements on comparable strips of the collector foil at mass 77 and 76.5, it was shown that the contamination of mass 77 by Br^{77} was negligible in the γ-source of $Kr^{76} + Br^{76}$.

Discussion

As was pointed out before, the present measurements are of a preliminary character and therefore incomplete. It will certainly be possible to prepare sources of Kr^{76}, sufficiently strong for a more extensive investigation of the decay of Kr^{76} and Br^{76}.

The 0.560 Mev peak and part of the "peak" at about 1.2 Mev may be due to the 0.557 and 1.22 Mev γ-transitions reported in the decay of As^{76} (H3). They would then occur in the Br^{76} decay. This conclusion is supported by the half life found for the 0.5 Mev doublet. Some of the γ-rays found in the present measurement may be identified with γ-rays reported by FULTZ and POOL [F2].

The decay periods of the isotopes of mass 76 should be accurately checked. If our measurements are correct, the nuclei of mass 76 would decay with three different half lives. This would indicate the existence of an isomeric state in either of the nuclei Kr^{76}, Br^{76} or Se^{76}.

Our measurements show that the 0.560 Mev peak and the annihilation peak decay with the same period. This would mean that the contribution from Kr^{76} to the 0.511 Mev peak was relatively small at the time when the measurement started. Kr^{76} would then decay mainly by K-capture and low energy positrons. This conclusion is partly in accordance with the results of CARETTO and WIIG [C1].

Section 2. 73 min Kr^{77}

Introduction

The experimental data on Kr^{79} have shown that the decay of this isotope is much more complicated than predicted by the extreme on particle model (p. 161). It is therefore of interest to know if Kr^{77} behaves in a similar manner.

The decay of 1.1 h Kr^{77} had so far only been investigated by means of absorption measurements [cf. H 3]. It is reported by WOODWARD *et al.* [W 1] to decay partly by K-capture (70 %) and partly by positron emission to 57 h Br^{77}. The maximum energy of the positrons was determined to be 1.7 Mev by absorption measurements. γ-radiation also occurs. In the Tables of HOLLANDER *et al.* [H 3] Kr^{77} is classified as a B isotope, that is the mass number is not regarded as unambiguously established.

In the present investigation, 1.1 h Kr^{77} has been produced by a $(p, 3n)$ reaction on Br^{79}. β- and γ-spectrometer samples were prepared by means of the electromagnetic isotope separator. Several β- and γ-transitions were found and some coincidence measurements were performed. A tentative level scheme (Fig. 13) is proposed, which includes the main decay branches of Kr^{77}.

Sample preparation. Mass assignment

In earlier work Kr^{77} has been prepared by means of α-bombardment of selenium. Using enriched Se^{74} and assuming an (α, n) reaction WOODWARD *et al.* [W 1] assigned the 1.1 h Kr activity to Kr^{77}. Another way of preparing this isotope would be a $(p, 3n)$ reaction on Br^{79}. In fact, we obtained strong Kr^{77}-samples by bombarding KBr-powder with protons of maximum energy 50 Mev in the Uppsala synchrocyclotron[1]. The powder was packed in a small tube, made of a thin aluminium foil (~ 10 mg cm^{-2}). In addition to Kr^{77}, 34 h Kr^{79} was formed by the Br^{81} $(p, 3n)$ reaction.

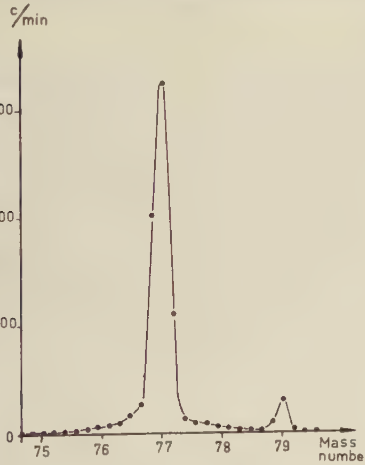

Fig. 5. Activity spectrum of electromagnetically separated Kr isotopes formed in Br (p, xn) reactions. Proton energy ≤ 50 Mev. The activity of 1 mm broad collector strips is plotted as a function of mass number.

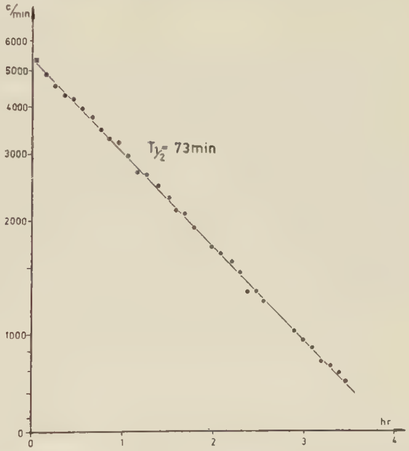

Fig. 6. Decay curve of electromagnetically separated Kr^{77}.

---

[1] The author is very much indebted to the cyclotron group at Uppsala for these irradiations.

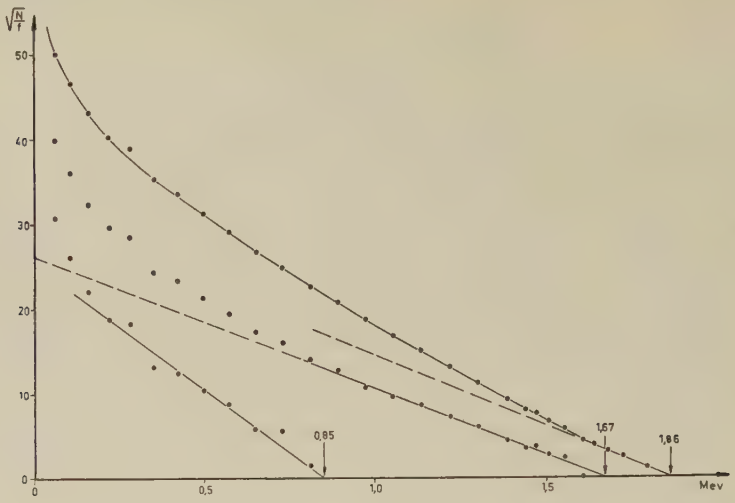

Fig. 7. Fermi plot of the positron distribution of Kr^{77}.

The krypton gas formed in the nuclear reactions was extracted from the irradiated KBr-powder and separated electromagnetically in the same way as described in ref. [T4]. In this way the mass number of Kr^{77} was also uniquely established. Fig. 5 shows the activity of a target foil as a function of mass number. The activity peak at mass 77 is much more intense than that corresponding to Kr^{79}. This is to be expected from the short irradiation time used (~ 1 h). The half life of Kr^{77} was found to be 73 min. The decay curve is shown in Fig. 6.

Positron spectrum

The positron spectrum of Kr^{77} was measured in the intermediate image β-spectrometer [S2], using a source of diameter 5 mm, deposited on an aluminum foil of thickness 0.15 mg cm^{-2}. The resolution was 3 %. Fig. 7 displays the Fermi plot [N 1] of the positron distribution. It is evident that the positron spectrum is complex. The analysis of the plot is performed on the assumption that the last five points define a straight line representing a high energy component. Thus we find three β-components of energies 1.86, 1.67 and 0.85 Mev. The relative intensities of these components would be 61, 32 and 7 % and the corresponding log *ft* values [M3] 5.4, 5.4 and 4.8 respectively. These values classify all β-transitions as belonging to the allowed group, occurring with $\Delta I = 0,1$ and no parity change [M4].

Electron line spectrum

Using a helical baffle to eliminate the positrons, the conversion electron spectrum was measured in the intermediate image β-spectrometer. In addition to the Auger lines nine conversion electron lines were recorded, as shown in Figs. 8 and 9. Part of the spectrum (Fig. 8 b and c) was measured with a central slit of 4 mm radial width, giving a resolution of 3.5 %. The three low intensity lines of Fig. 9 were recorded with a 7 mm slit, resolution 4.5 %. The interpretation of the electron lines follows from Figs. 8 and 9 and from Table 1. The line at 22.6 kev cannot be a *K*-line of a 36.1 kev γ-ray, since we failed to find a corresponding L-line. The counting rate measured at the position calculated for an L_{36} line was less than 1/80 of the counting rate at 22.6 kev. We therefore conclude that the 22.6 kev line is the L-line of a 24.2 kev γ-ray. The corresponding K-line (energy 10.7 kev) could not be resolved from the KLL Auger line (energy 10.2 kev) (cf. Fig. 8 a). The existence of a K_{24} line, superposed on the KLL Auger line, is however evident from the anomalous intensity ratio $KLL/KLM = 4.2$ obtained for the main Auger line components KLL and KLM of Kr^{77}. In Kr^{79} the corresponding ratio is found to be 3.3. The interpretation of the line group at energies 94–149 kev seems to be justified from the internal consistency of the γ-energies computed from the line pairs denoted K_{108}, L_{108}, and $(K_{149}+L_{131})$, L_{149} (see Table 1). The $(K_{149}+L_{131})$ line is broader than the others, indicating that it is really double. The γ-energy 148.4 kev, obtained from this line, is 1.6 kev lower than that deduced from the L_{149} line. This may partly be due to the influence of the L_{131} electrons (129.5 kev) on the position of the $(K_{149}+L_{131})$ peak (cf. also the discussion below).

The decay of the lines L_{24}, K_{108}, L_{108}, K_{131} and $K_{149}+L_{131}$ was checked by repeated measurements at 1 h intervals. All these lines decayed with the period found for Kr^{77}. The very weak lines K_{245}, K_{281} and K_{313} were found to have disappeared after 7 hours. Thus none of them could be due to the 57 h daughter nucleus Br^{77}.

Intensity comparisons

The relative line intensities, given in Table 1, were estimated from the areas of the corresponding lines, setting the K_{108} intensity equal to 100. Correction was applied for differences in β-spectrometer transmission, due to different width of the central slit of the spectrometer in the different measurements. From the estimated intensities we obtain the $K/(L+M)$ ratios

$$\frac{K_{108}}{(L+M)_{108}} = 3.6 \pm 0.4$$

and

$$\frac{K_{149}}{(L+M)_{149}} \leq 6.$$

The latter value is somewhat high, because it is not corrected for the L_{131} line superposed on the K_{149} line. A rough analysis of the double line is however possible, making use of the fact that the position and the half width of the L_{131} peak are known. The line components obtained from such an analysis, are shown in Fig. 8 c. Of course, the L_{131} intensity cannot be accurately determined in this way. We obtain, however, an upper intensity limit of 14 for this line ($K_{108} = 100$). Using the relative L_{131} intensity 5.4, obtained in the analysis of Fig. 8 c, we compute

$$\frac{K_{131}}{(L+M)_{131}} = 8.2 \pm 4.$$

Furthermore

$$\frac{K_{149}}{(L+M)_{149}} = 4{,}9 \pm 1,$$

from the K_{149} line intensity derived in the same analysis. (It should be noticed that these results are supported by an earlier measurement of the conversion lines, but the statistical errors were then larger.)

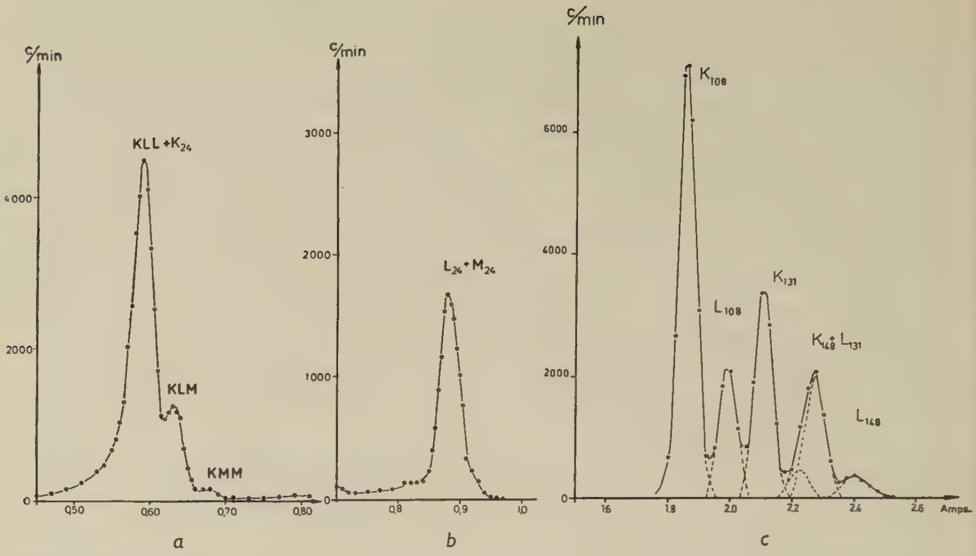

Fig. 8. Auger lines (a) and conversion electrons (b and c) of Kr^{77}, measured in the intermediate image β-spectrometer. The Auger line intensity given in a corresponds to a sample 2.7 times weaker than was used in measuring the lines of b and c. Subscripts give γ-ray energies in kev. Correction: the subscripts 148 should be 149.

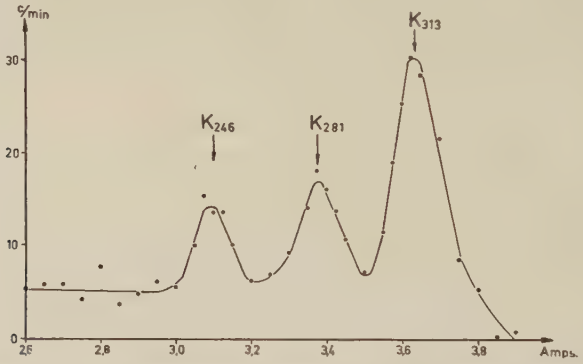

Fig. 9. "High energy" region of conversion spectrum of Kr^{77}, recorded in intermediate image β-spectrometer. Subscripts give γ-energies in kev.

The Auger line intensities given in Table 1 are corrected for absorption in the GM counter window, which was shown to have a "cut off" (cf. p. 139) of 4.8 kev. Assuming that the absorption curves of LANE and ZAFFARANO [L1] are applicable in our case, we obtain approximate absorption correction factors 1.2 and 1.1 for the KLL and KLM Auger electrons respectively. The error in these corrections is probably less than 25 %, and the error in the ratio between them is much smaller.

Assuming that the intensity ratio $KLL/KLM = 3.3$ as measured for the Auger electrons of Kr^{79} (p. 151) also holds for Kr^{77}, we estimate the relative K_{24} line intensity ($K_{108} = 100$) to be 36. This would give

Table 1. Electron line data of Kr^{77}.

Line	Interpretation	Electron energy kev	γ-ray energy kev	Final γ-ray energy kev	Relative line intensity
1	$KLL+K_{24}$	10.2			171
2	KLM	11.6			41
3	KMM	13.4			3
4	L_{24}	22.6	24.2	24.2 ± 0.5	25
5	K_{108}	94.0	107.5	107.6 ± 0.8	100
6	L_{108}	106.4	108.0		28
7	K_{131}	117.6	131.1	131.1 ± 1	45
8	$K_{149}+L_{131}$	134.9	148.4		30
9	L_{149}	148.4	150.0		5.5
10	K_{246}	232.2	245.7	246 ± 3	~ 0.2
11	K_{281}	267.8	281.3	281 ± 3	~ 0.2
12	K_{313}	299.9	313.4	313 ± 3	~ 0.4
1a*	KLL				135
1b*	K_{24}				~ 36
8a*	K_{149}	135.8	149.3	149.3 ± 1	26
8b*	L_{131}				~ 5

* These data were obtained from line analysis discussed in text.

$$\frac{K_{24}}{(L+M)_{24}} = 1.3 \pm 1.$$

The branching ratio C/β^+ between K-capture and positron emission may be computed by the expression

$$\frac{C}{\beta^+} = \frac{1}{A_{\beta^+}} \left(\frac{\Sigma A_A}{1-\omega_K} - \Sigma A_K \right)$$

where A_{β^+} = area of the positron spectrum
ΣA_A = total area of the K-Auger lines
ΣA_K = total area of the K-conversion lines
ω_K = the K-fluorescence yield.

For Kr, we put ω_K equal to 0.57 (B6). The area A_{β^+} was found to be 1000 ($K_{108}=100$), and the Auger line area, corrected for the K_{24} intensity, 180. We obtain

$$\frac{C}{\beta^+} = 0.21 \pm 0.1.$$

This value is not in accordance with the ratio $C/\beta^+ \approx 2.3$ given by WOODWARD *et al.* [W1]. We notice that also for Kr^{79} these authors report a much higher C/β^+ ratio ($C/\beta^+ = 49$, ref. [W1]) than has been obtained in recent β-measurements ($C/\beta^+ = 9.3$, ref. [T4]). The theoretical C/β^+ ratios, obtained from the curves of FEENBERG and TRIGG (F1) are 0.20, 0.28 and 2.7 for the 1.86, 1.67 and 0.85 Mev components respectively. From these figures we compute a total C/β^+ ratio of 0.30, in accordance with our experimental value.

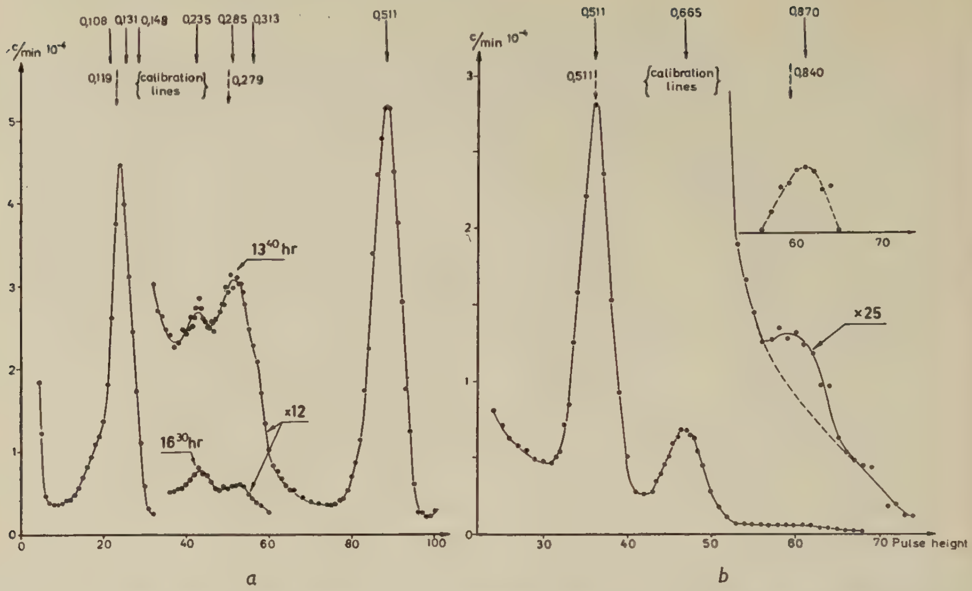

Fig. 10. Pulse-height distributions of Kr^{77}, recorded with the NaI scintillation spectrometer. —*a*, low energy region; *b*, high energy region. (Energies in Mev.)

Scintillation spectrum

The low and high energy regions of the scintillation spectrum of a Kr^{77} sample are shown in Figs. 10 a and b. The strong line at about 125 kev is probably complex, consisting of photopeaks of the three γ-rays of energies 108, 131 and 149 kev recorded in our β-measurements. The components of the weak line group around 250 kev were shown to decay with different half lives. In Fig. 10 a are shown two records taken with a time interval of about 3 h. The peak at 285 kev decays with the Kr^{77} period. It corresponds to the 281 kev γ-ray found in the β-measurements. The 235 kev line is long lived and is probably identical with the 237 kev γ-ray of the 57 h daughter nucleus Br^{77} [H3]. In Fig. 10 a is also shown the expected position of the photopeak of the 313 kev γ-ray found in the β-measurements.

The upper region of the γ-spectrum (Fig. 10 b) shows the presence of two photopeaks at 665 and 870 kev, in addition to the annihilation peak at 511 kev. Both of them decayed with a half life of about 1 h. We therefore conclude that there are also two γ-rays of energy 665 ± 6 and 870 ± 15 kev in the decay of Kr^{77}.

After one day the γ-spectrum of the Kr^{77} sample was recorded once again. We then found several weak γ-rays of energies corresponding to those reported for 57 h Br^{77}.

Coincidence measurements

The coincidence equipment has been discussed on p. 140.

γ-γ coincidences.

Fig. 11 a shows the coincidence distribution, obtained when γ-quanta of ~ 140 kev energy were recorded in one channel and γ-quanta of various energies around 665 kev were accepted in the other. Fig. 11 b shows the corresponding coincidence distribu-

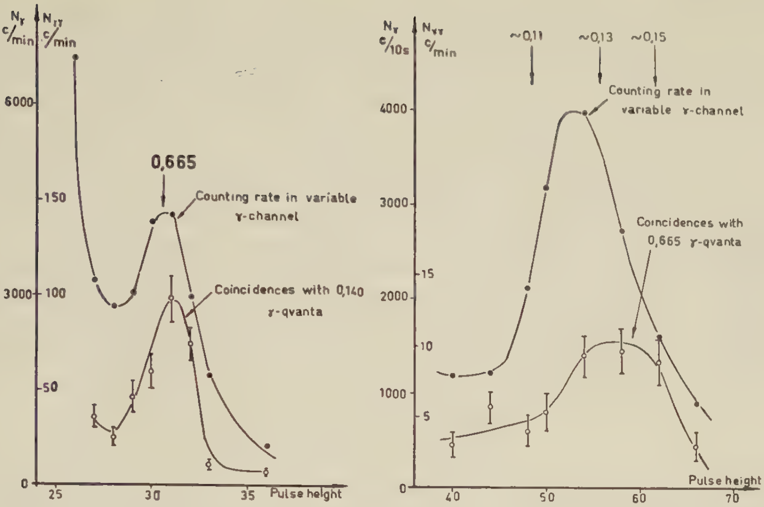

a *b*

Fig. 11. *a*, $\gamma_{0.140}$–γ coincidences; *b*, $\gamma_{0.665}$–γ coincidences in Kr^{77}. (Energies in Mev.)

tion when one channel was fixed at 665 kev and the other recorded γ-quanta of various energies around 130 kev. A comparison with the counting rate in the latter channel shows that the 665 kev γ-ray is probably emitted in cascade with γ-rays of energy 125–150 kev, but not with γ-rays of energy 100–125 kev. (The peak of the γ-line group lies at 123 kev, according to the γ-measurement of Fig. 10.)

e-γ coincidences.

The γ-channel was set to record pulses corresponding to energies >0.62 Mev, and the β-spectrometer was adjusted to focus successively the conversion electrons of the 108, 131 and 149 kev γ-rays. The coincidence intensity measured at the various conversion electron peaks is shown in Fig. 12. Apparently the 665 kev γ-ray is emitted in cascade with both of the 131 and 149 kev γ-rays, but not with the 108 kev γ-ray. This result is in agreement with our γ-γ coincidence measurements.

Discussion

According to our measurements, Kr^{77} decays by means of K-capture and positron emission to Br^{77} with a branching ratio $C/\beta^+ = 0.21 \pm 0.1$. The half life is 73 min. Three allowed positron transitions of energies 1.86, 1.67 and 0.85 Mev were found, as well as nine γ-rays of energies 24.2, 107.6, 131.1, 149.3, 246, 281, 313, 665 and 870 kev. The 665 kev γ-ray is probably in coincidence with the 131 and 149 kev γ-rays, but not with the 107 kev γ-ray.

Although these data are not sufficient to interpret all details of the Kr^{77} decay, they may indicate the structure of the main decay branches. Fig. 13 shows a tentative decay scheme which fits the energy data and partly also the coincidence data. The broken vertical lines are drawn only to indicate the existence of the corresponding γ-transition in the Kr^{77} decay. The positions of the β-transitions are also tentative. It should be noticed that β-transitions to the two lowest levels may also exist. In

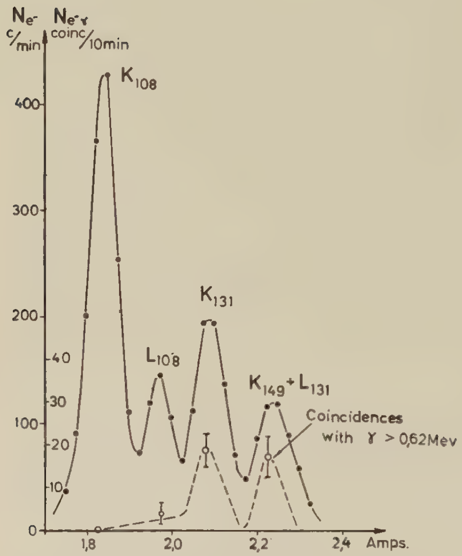

Fig. 12. Coincidences of conversion electrons of Kr^{77} and γ-pulses corresponding to energies >0.62 Mev.

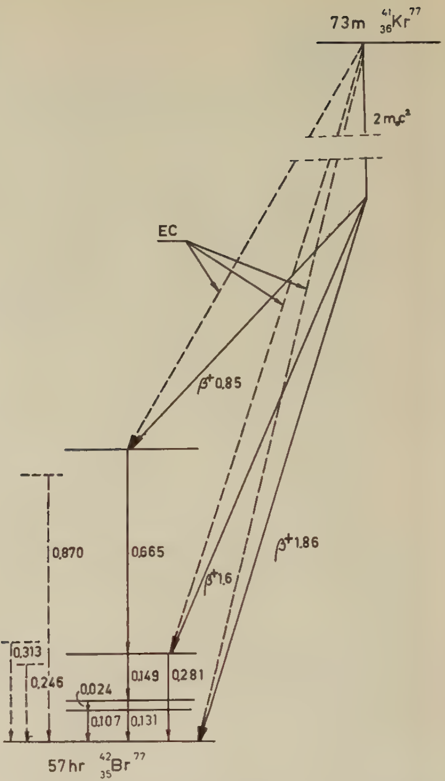

Fig. 13. Tentative scheme of the main decay branches of Kr^{77} discussed in text. (Energies in Mev.)

our Fermi analysis it was impossible to resolve such components. The theoretical C/β^+ ratio discussed on page 153 would not be influenced by such a change. The positions of the 24 and 108 kev γ-rays are only suggested from energy consideration; their order is arbitrary. In order to explain the absence of coincidences between the 665 and 108 kev γ-rays in the decay scheme of Fig. 13, we may assume that the latter one is of so high multipole order that its half life is longer than the resolving time 2.5×10^{-7} sec of the coincidence circuit. This conclusion may be compatible with other experimental data: A comparison of the experimental $K/(L+M)$ ratio with the semi-empirical K/L curves of GOLDHABER and SUNYAR [G2, S9] classifies the 108 kev γ-transition as being of $M4$ or $E2$ type. The $M4$ alternative is excluded because the corresponding half-life [G2] would be much longer than the half-life of Kr^{77}. The theoretical half-life of an 108 kev $E2$ transition would be $\sim 8 \times 10^{-7}$ sec. [B5]. Considering the uncertainty in the theoretical estimate, this result can account for the apparent absence of coincidences between the 108 and 665 kev γ-rays. We also notice the possibility that the 108 kev level may also be fed from β-transitions. Only a fraction of the 108 kev γ-transitions would then occur in cascade with another γ-transition.

The $K/(L+M)$ ratio of the 24.2 kev γ-ray (p. 153) indicates an E2, E1 or M3 transition (G2, S9), which correspond to theoretical half lifes (B5) of the order of 10^{-3}, 10^{-9} or 10^{8} sec respectively. The M3 alternative is excluded since the experimental half life is less than 4×10^3 sec. If the transition is of E2 type, it cannot occur from the 0.281 Mev level, for intensity reasons; the order of the 24.2 and 108 kev transitions given in Fig. 13 should then be reversed.

The $K/(L+M)$ ratio of the 149 kev γ-ray suggest and $E2$ radiation [G2, S9]. The theoretical half-life of the 149 kev γ-transition would then be $\sim 2 \times 10^{-7}$ sec. Our coincidence results are not in contraction with such a value.

Even if the level scheme of Fig. 13 is not right in all details, it is evident that there are probably more than five excited levels in Br^{77}. The Kr^{77} decay is therefore in some respects similar to that of Kr^{79} (Fig. 16). We notice that the total decay energy of Kr^{79} is 1.62 Mev and that of $Kr^{77} \geq 2.89$ Mev. This explains the difference in the branching ratio C/β^+, which is 9.3 for Kr^{79} and only 0.2 for Kr^{77}.

Section 3. 34 h Kr^{79}

Introduction

In an earlier investigation by S. THULIN *et al.* [T4], the decay of Kr^{79} was shown to be very complex, including at least fifteen γ-transitions. Two decay scheme alternatives were suggested, mainly based on accurate energy determinations of the γ-transitions. Some details were supported by coincidence measurements.

Since then, additional coincidence data have been collected by means of the improved coincidence arrangement discussed on p. 141. (In this case an EMI 5311 photomultiplier was used, giving an energy resolution of 16 % at 661 kev with the light quide arrangement.) As the new coincidence data give preference to one of the two suggested decay schemes (*a* of ref. [T4]), we will discuss the measurements in some detail here. Further evidence for this decay scheme has also been obtained from Coulomb excitation experiments, which are also mentioned below.

Coincidence measurements

β-γ coincidences.

Fig. 14 shows a Fermi plot [N1] of the coincidence distribution obtained between positrons of various energies and γ-quanta of energy > 80 kev. The upper energy

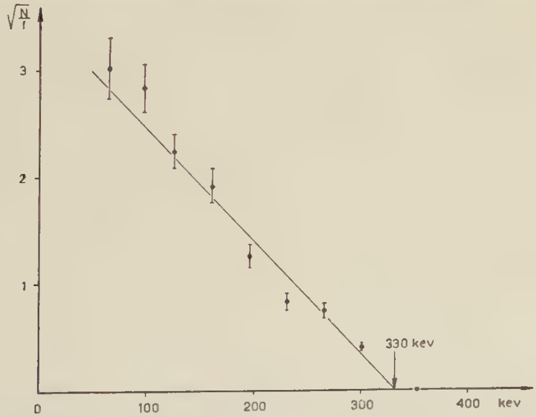

Fig. 14. Fermi plot of coincidence distribution between positrons of Kr^{79} and γ-quanta of energy > 80 kev.

limit is 330 kev, in accordance with the value 325 ± 20 kev, obtained in our β-measurements [T4]. From a comparison of the area of the coincidence distribution and the corresponding area of the total β^+-distribution (p. 143) we estimate the relative intensity of the 330 kev β^+-component to be about 9 % of the total β^+-decay. This value agrees with the intensity value 7 %, obtained for the 325 kev β^+-component in β-measurements.

e-γ coincidences.

$K_{606}-\gamma$ and $K_{84}-\gamma$. As was pointed out in ref. [T4] it is difficult to perform conclusive coincidence measurements on Kr^{79} because of the complex nature of the decay. However, some information has been obtained. Two measurements concern the 606.4 and 84.0 kev γ-rays respectively. Table 2 gives the coincidence rate $N_{e\gamma}$ obtained when recording simultaneous emission of the corresponding conversion electrons and γ-quanta of energy > 40 kev. N_{acc} is the computed contribution of accidental coincidences. $(N_{e\gamma})_{\text{calc}}$ is the coincidence rate to be expected if the conversion electrons were emitted in cascade with a γ-ray. Our results indicate that the 84.0 kev γ-ray is emitted in cascade with one or more γ-rays, whereas the 606.3 kev γ-ray seems not to be associated with any other γ-transition.

Table 2. Results of e-γ coincidence measurements on Kr^{79}.

Electron line	$N_{e\gamma}$ coinc/min	N_{acc} coinc/min	$(N_{e\gamma})_{\text{calc}}$ coinc/min
K_{606}	0.13 ± 0.1	0.07	≥ 1.5
K_{84}	1.5 ± 0.4	0.05	≥ 1.3

$K_{44}-\gamma$, $K_{136}-\gamma$ and $K_{261}-\gamma$. The cascade relations between K-conversion electrons of either of the 44.5, 136.1 and 261.3 kev γ-rays on the one hand and γ-rays of various energies on the other were also studied. The β-spectrometer selected the conversion

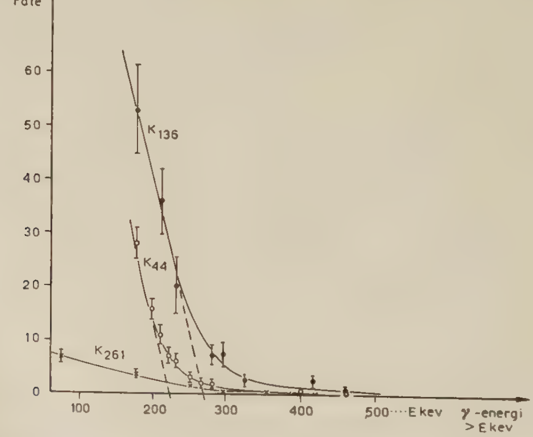

Fig. 15. Coincidence distributions of K_{44}, K_{136} and K_{261} electrons of Kr^{79} on the one hand and γ-quanta of energy $> E$ on the other hand. Subscripts give γ-ray energies in kev.

electrons and the γ-detector recorded γ-quanta above an energy E. The coincidence rate was measured as a function of E. The results are collected in Fig. 15. The coincidence rates have been normalized to the same electron intensity. A straight line through the steep part of the K_{136} curve cuts the energy axis at about 270 kev. The corresponding value for the K_{44} curve is $\sim$220 kev, and for the K_{261} curve $\sim$300 kev. The smooth bending of the curves is probably due to the low resolution of the γ-channel.

We note that the coincidence rate per recorded conversion electron is very small for the K_{261} line compared with that of the K_{44} line, which in turn is less than that of the K_{136} line.

Discussion

In Table 3 are compared the coincidence results presented above and the γ-cascade relations expected from the two decay schemes *a* and *b* of ref. [T4]. It is evident that the decay scheme *b* is improbable. On the other hand, the measurements give additional support to the level scheme *a*. As pointed out in ref. [T4], there are two possible positions of the 345.5 kev γ-ray in the level scheme. Both of them may still be valid, but the K_{261} coincidence curve may indicate that a 345.5 kev γ-transition really feeds the 261.3 kev level. Fig. 16 shows the scheme *a* of ref. [T4] with a minor change. The 345.5 kev transition is here placed according to the conclusion above, and the alternative position is shown with a broken line.

Table 3. Comparison of coincidence results for Kr^{79} with the γ-cascade relations expected from the two decay schemes a and b of ref. (T4).

Conversion electrons	In cascade with γ-rays of energy* (kev)		
	Scheme *a*	Scheme *b*	Experimental result
K_{44}	84, 136, 209, 217	84, 217, 261	$\leq$220
K_{136}	45, 209, 217, 261	45, 209, 217	$\leq$270
K_{261}	84, 136, 209, (346)	45, 84, (346)	$\lesssim$300

* The energy values are rounded off.

The relative coincidence rates of the K_{44} line on the one hand and the K_{136} and K_{261} lines on the other are in accordance with the decay scheme of Fig. 16 since the 261.3 kev level is mainly fed by positron and K-capture transitions.

The existence of the 606.3 kev level in Br^{79} is supported by the coincidence measurements of Table 2. The position of the 84.0 kev γ-transition is still somewhat arbitrary. According to the coincidence measurements, it may go to any of the excited levels in Br^{79}, but not to the ground state.

As was mentioned in the introduction, Coulomb excitation studies of Br^{79} have given further evidence for part of the decay scheme of Fig. 16. N. P. HEYDENBURG and G. M. TEMMER [H4] obtained only three γ-rays of energies 44, 213 and 266 kev when bombarding Br with α-particles. These three γ-rays are therefore probably associated with the lowest excited levels in Br^{79}.

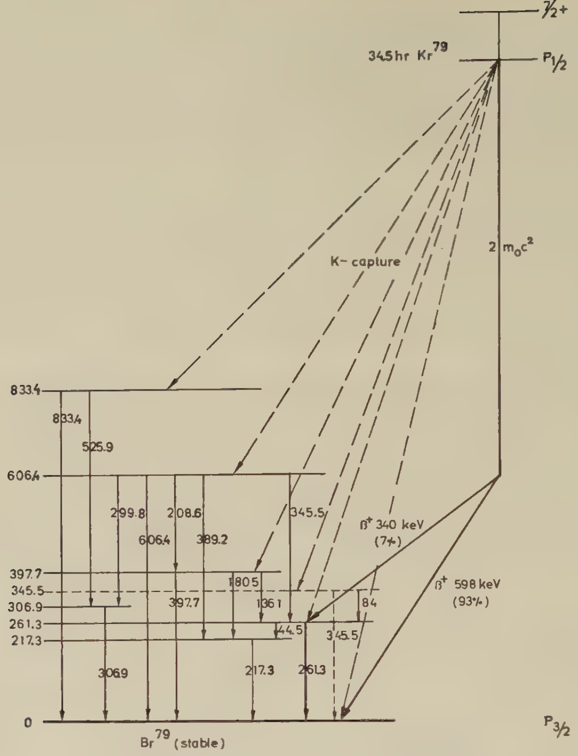

Fig. 16. Decay scheme of Kr^{79} discussed in text. (Energies in kev.)

Spin- and parity assignments

The experimental data are still insufficient for unique spin assignments of the various levels in Br^{79}. However, the 261.3 kev level may be assigned by means of the β-data and Coulomb excitation results. The ground states of Br^{79} and Kr^{79} are most probably $p_{3/2}$ and $p_{1/2}$ respectively [T4]. The 330 kev β-transition to the 261.3 kev level is shown to be of allowed type, occuring with $\Delta I = 0{,}1$ and no parity change [T4]. This level might then be $p_{1/2}$ or $p_{3/2}$, in terms of the shell model. In the Coulomb excitation experiments the 261 kev transition is relatively intense, and it is therefore interpreted as probably being of $M1 + E2$ type [T6]. The 261 kev level could then be 1/2–, 3/2–, or 5/2–. No decision can therefore at present be made between the two alternatives $p_{1/2}$ and $p_{3/2}$, obtained from β-data.

Recently G. Scharff-Goldhaber and M. McKeown [S6] reported an isomeric transition of energy 210 ± 10 kev and half-life 5.0 ± 0.2 sec in Br^{79}. Apparently none of the γ-transitions in the decay scheme of Fig. 16 can be identified with this isomeric transition. The only two γ-transitions of Fig. 16, falling within the energy limits of the reported isomer, would be $\gamma_{208.6}$ and $\gamma_{217.3}$. The former one cannot be delayed, since several competing γ-rays occur. The latter γ-ray has a relatively high $K/L + M$ ratio. Furthermore, it is apparently excited primarily in the Coulomb excitation experiments [H4]. This fact excludes the possibility that this transition might be isomeric. Finally, our coincidence measurements indicate coincidences between the 24 and 217 kev rays. The one particle level corresponding to the reported isomeric transition would probably be $g_{9/2}$. It would not be excited in measurable intensity by a β-transition from the ground state of Kr^{79}. As we do not observe the isomeric γ-ray in the Kr^{79} decay, we may conclude that the excited levels of Fig. 16 probably have relatively low spin values. This also follows from the fact that all levels seem to be easily deexcited by transitions to the $p_{3/2}$ ground state in competition with other γ-transitions.

It is evident that the level scheme of Br^{79} cannot be explained by the extreme one particle model. This is briefly discussed on p. 191.

Section 4. 4.3 h Kr^{85} and 9.4 y Kr^{85}

Introduction

The neutron number of Kr^{85} differs by one unit from the magic number 50. According to nuclear shell theory the nuclear core of such isotopes has approximately spherical symmetry. The conditions for application of the one particle shell model is therefore considered most favourable in the neighbourhood of magic numbers. For this reason, there is considerable interest in completing the experimental data on Kr^{85}, in order to make a comparison with the predictions of the one particle shell model still more reliable.

The decays of Kr^{85} and Kr^{85m} have earlier been investigated at this institute [B2, B4]. It was shown that 4.3 h Kr^{85m} decays in two ways: partly by emission of 305.0 ± 0.2 kev γ-quanta to the ground state of Kr^{85} and partly by 830 ± 10 kev γ-particles to an excited level of 149.5 ± 0.1 kev energy in Rb^{85}. The 9.4 y ground state of Kr^{85} decays by γ-emission partly to the ground state of Rb^{85} [Z1, B4] and partly to an excited level of 540 kev energy [Z1]. The level scheme (cf. Fig. 19) first seemed to be well established, and most experimental data fitted the predictions of the one particle shell model [M1, H1] quite well. However, there appeared to be some inconsistencies both in the intepretation and in the experimental data. The present investigation was performed in order to study the following problems, discussed in detail in paragraphs a, b, and c of this section.

a. The β-energy values reported by different authors for 9.4 y Kr^{85} were inconsistent.

b. The 540 and 513 kev γ-transitions reported in the decay of Kr^{85} and Sr^{85} respectively were assumed to be identical. However, the identity had not been experimentally established.

c. The $K/(L+M)$ ratio reported for the 305 kev $M4$ transition in Kr^{85} seemed to be high compared with experimental data for other similar cases.

a. β-decay energies of Kr^{85} and Kr^{85m}

The decay schemes of Kr^{85} and Kr^{85m} (cf. Fig. 19) offer a means of checking the internal consistency of β-energies determined from the β-decay of Kr^{85} and Kr^{85m} respectively. The total energy released when Kr^{85} decays to the ground state of Rb^{85} may be computed from two different branches, each consisting of one β- and one γ-transition. The γ-energies are accurately determined (cf. above). However, the β-energy values reported are inconsistent. The maximum β-energy of Kr^{85} was reported by BERGSTRÖM [B4] to be 666 kev, and by ZELDES *et al.* [Z1] to be 695 ± 5 kev. As BERGSTRÖM's value was obtained with a very weak Kr^{85} source, his error limits were expected to be larger than those given by ZELDES *et al.* However, using the energy value of ZELDES *et al.*, the total decay energy would differ by 21 kev in the two branches, as compared with a total error sum of 15 kev. In order to decide if this discrepancy was significant, the β-continua of Kr^{85} and Kr^{85m} have been carefully remeasured.

Kr^{85m} was produced in uranium fission by neutron bombardment in the 225 cm cyclotron [A1] and Kr^{85} was obtained from fission gas commercially produced at Harwell. Both β-sources were prepared in the isotope separator, using thin aluminium foils (0.15 mg cm^{-2}) as collectors. In both cases the source diameter was 5 mm. The strong Kr^{85} source (cf. below) was obtained in a separation time of about one hour.

The β-measurements were performed in the intermediate image β-spectrometer [S2]. The counting rate at the maximum of the β-continuum was ~ 2500 c/min for Kr^{85} and ~ 1000 c/min for Kr^{85m}. The spectrometer was calibrated by means of the F-line of ThB. In the case of Kr^{85m} the K-conversion line of the 305.0 kev γ-ray was also used for calibration.

The Fermi plot [N1] of the Kr^{85m} β-spectrum showed an upper energy limit of 824 ± 8 kev. This value is in accordance with the earlier values 830 ± 10 kev [B4] and 817 kev [B2].

The conventional Fermi plot [N1] of the β-distribution of Kr^{85} showed a forbidden shape, as earlier reported [Z1, B4]. Correction with the factor $G = (W_0 - W)^2 + W^2 - 1$ yields a straight line with a small deviation below 200 kev. This line cuts the energy axis at 672 ± 7 kev. This value is in accordance with the value 666 kev reported by BERGSTRÖM [B4].

The new values for the β-energies and the earlier determined γ-ray energies give a good internal consistency for the energy cycle of Fig. 19. The energy difference is only 4.5 kev, as compared with a total error sum of 15 kev. We therefore conclude that the maximum β-energy value of Kr^{85}, published by ZELDES *et al.* [Z1], is too high.

b. Scintillation spectrum of 9.4 y Kr^{85}

The 9.4 y Kr^{85} is reported to decay in two ways; either by emission of 672 kev β-particles (cf. above) to the ground state of Rb^{85}, or by β-particles of ~ 150 kev energy to an excited level of energy 540 ± 20 kev in Rb^{85} [Z1]. The 150 kev β-branch has a relative intensity of only 0.65 % [Z1]. On the other hand a 513 kev level in Rb^{85} has been found from the decay of 65 *d* Sr^{85} [H3]. This level is isomeric with a half life of 0.9×10^{-6} sec [S4], in accordance with the $g_{9/2}$ level assignment of the one particle shell model (cf. Fig. 19).

The two γ-transitions of energies 540 and 513 kev in the decay of Kr^{85} and Sr^{85} respectively have been tentatively assumed to be identical by SUNYAR *et al.* [S4]. As a consequence of this assumption, the low intensity β-transition of Kr^{85} would occur between two $g_{9/2}$ levels (cf. Fig. 19). The extremely high log *ft* value for this apparently allowed transition has been explained by SUNYAR *et al.* [S4], in terms of the one particle shell model, as due to the occurrence of mixed nucleon configurations (cf. Chapter IV, and ref. [D1]).

The apparent importance of the assumed identity of the two γ-transitions suggested a remeasurement of the γ-ray energy of 9.4 y Kr^{85}. The pulse height distribution is shown in Fig. 17. The scintillation spectrometer was calibrated immediately before and after recording the Kr^{85} photoline (calibration lines: annihilation radiation of

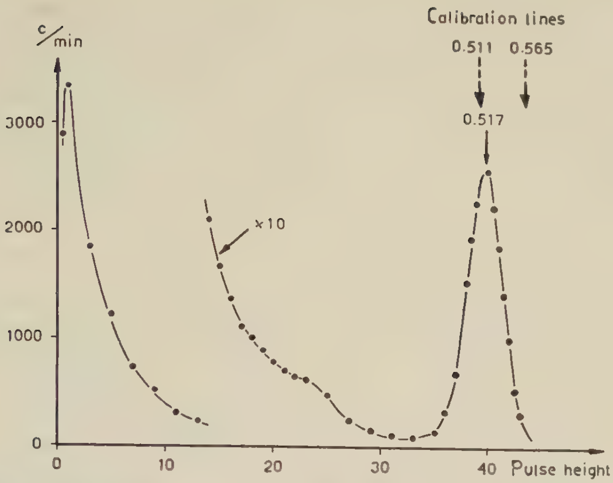

g. 17. Pulse height distribution of 9.4 y Kr^{85}, recorded with the NaI scintillation spectrometer. (Energies in Mev.)

a^{22} and the 565 kev γ-ray of Bi^{207}). The γ-energy appeared to be 517 ± 5 kev. iis is in accordance with the values 513 and 514 kev reported for the isomeric vel in Rb^{85} [H3]. We therefore conclude that the two γ-transitions most probably e identical. As a consequence the low intensity β-branch would have an upper ergy limit of 159 kev. The relative intensity of this branch (0.65 %) was calculated om coincidence measurements by ZELDES *et al.* [Z1]. In their paper, no corrections e reported for the delay of the cascade. Therefore the calculated intensity (0.65 %) the 159 kev branch may be too low.

c. $K/(L+M)$ ratio of the 305.0 kev γ-ray in Kr^{85m}

The 305.0 kev γ-transition in Kr^{85m} has been shown to be of $M4$ type by measure-ents of the K-conversion coefficient [B7]. The $K/(L+M)$ ratio was reported by ERGSTRÖM [B4] to be 7 ± 1. This value seems to be high compared with exprementa data for other $M4$ transitions, as presented by GRAVES *et al.* [G4]. The $K/(L+M)$ io of the 305 kev γ-ray has therefore been remeasured, using the double focusing pectrometer [H2]. The $K/(L+M)$ ratio appears to be 6.2 ± 0.6. In Fig. 18 this ult is plotted together with the values of GRAVES *et al.* [G4] for some other $M4$ nsitions. Even the new value for Kr^{85m} lies above the line drawn through the ier points. The deviation may not be considered significant, especially since it been shown that $K/(L+M)$ ratios for isotopes of low Z-values commonly lie her than those of higher Z-values, for the same Z^2/E value (see, e.g., [S9]). Kr^{85m} resents the lowest Z-value of Fig. 18.

Discussion

The experimental data presented here eliminates the energy discrepancy in the ay data of Kr^{85m} and Kr^{85}. The $K/(L+M)$ ratio of the 305 kev γ-transition of ^{5m} seems to be consistent with $K/(L+M)$ data for $M4$ transitions. The good

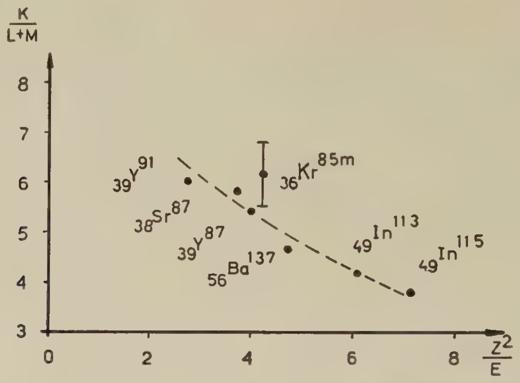

Fig. 18. $K/(L+M)$ ratio of the 305 kev γ-ray in Kr^{85m}, plotted together with $K/(L+M)$ ratios of some $M4$ radiations, reported by GRAVES *et al.* [G4].

agreement with predictions of the one particle shell model, earlier found for the main decay branches [B4, G6], still holds. The weak 159 kev β-transition (0.7 %) in Kr^{85} most probably goes to the 513 kev isomeric level in Rb^{85}, known from the Sr^{85} decay. This level is also in agreement with the shell model (cf. also discussion on p. 188).

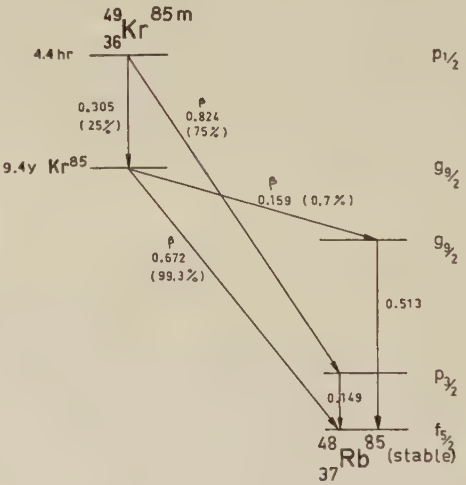

Fig. 19. Decay schemes of Kr^{85m} and Kr^{85}. (Energies in Mev.)

Section 5. 78 min Kr^{87}

Introduction

The decay of Kr^{87} has earlier been studied by the author [T2]. The β-spectrum was found to be complex with two components of energies 1.27 and 3.63 Mev and intensities 25 and 75 % respectively. Due to the low resolution of the scintillation spectrometer used, most details of the γ-spectrum were lost in the measurement of ref. [T2]. However, a strong γ-ray of 0.405 Mev energy was found, and a small peak at 0.89 Mev was interpreted as the pair line of an 1.89 Mev γ-ray, the photoline of which could not be resolved from the Compton distribution. The continuous end of the spectrum was interpreted as due to a γ-ray of about 2.4 Mev energy. In the present investigation the γ-spectrum of Kr^{87} has been reinvestigated, using the improved detector arrangement mentioned on page 140. Four γ-rays of energies 0.403, 0.847, 2.05 and 2.57 Mev were now found. β-γ and γ-γ coincidence measurements were also performed. A probable decay scheme is suggested (Fig. 25).

Scintillation spectrum

Figs. 20 a and b show respectively the low and high energy regions of the γ-spectrum of Kr^{87}. They are interpreted as follows. The peaks at energies 0.403 ± 0.004, 0.847 ± 0.009, and 2.57 ± 0.004 Mev are genuine photopeaks. The peak at 1.20 Mev may be due to coincident recording of 0.403 and 0.847 Mev quanta, which are very intense. The peak at 1.55 Mev is certainly the pair line of the 2.57 Mev γ-ray, since there is no Compton distribution corresponding to a γ-ray of 1.55 Mev energy. The peak at 2.05 Mev seems to be broader than the other lines. It may therefore be complex, consisting partly of a photopeak of energy 2.05 ± 0.05 Mev and partly of a pair peak of energy 2.57–0.511 Mev. The peaks at 1.75 and 2.3 Mev finally, coincide approximately with the Compton peaks of 2.05 and 2.57 Mev γ-transitions.

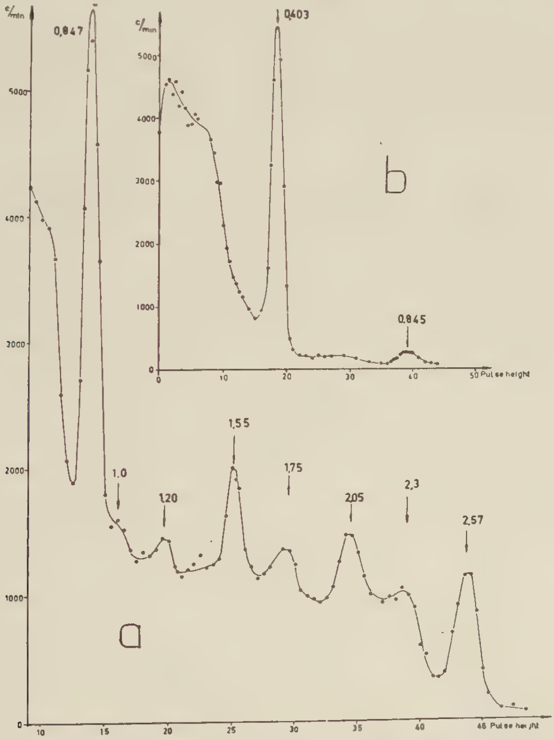

Fig. 20. Pulse-height distributions of Kr^{87}, recorded with the NaI scintillation spectrometer. —*a*, High energy region; *b*, low energy region. (Energies in Mev.)

However, we note that the 1.75 Mev peak seems to be more pronounced than ordinary Compton peaks. The existence of a 1.75 Mev γ-transition in the decay of Kr^{87} may therefore not be excluded.

The intensity ratio of the 0.403, 0.847, 2.05 and 2.57 Mev γ-rays were estimated (cf. p. 143) to be $100:19:\leq 6:42$. At least half of the 2.05 Mev peak area was assumed to be due to the annihilation peak discussed earlier (cf. [B9]).[1]

β-spectrum

Earlier β-measurements on Kr^{87} [T2] showed the presence of two β-components of energies 3.63 and 1.27 Mev energy. However, present β-γ coincidence measurements (cf. below), give some evidence for the existence of a β-component of about 3.3 Mev in the decay of Kr^{87}. Moreover, the coincidence data and energy considerations (cf. Fig. 25) strongly indicate that the maximum β-energy is 3.8 Mev. An inspection of the Fermi plot of our earlier β-measurement (cf. Fig. 1, ref. [T2]) shows that the last points at the high energy end of the Fermi plot might be used to define a straight line, cutting the energy axis at 3.8 Mev. As a result of such an analysis, we obtain a second β-component of low intensity and about 3.3 Mev energy and a third component of about 1.25 Mev energy. Although such a Fermi analysis is not a priori justified from the experimental data, it shows that our β-measurements are not in contradiction with the coincidence results reported below.

Coincidence measurements

From energy considerations, the decay scheme of Fig. 25 appeared to be the most probable one. As will be seen below, it is also supported by β-γ and γ-γ coincidence measurements. The coincidence arrangements are described in chapter I c.

β-γ coincidences.

β–$\gamma_{2.57}$. In the γ-channel pulses of amplitude corresponding to energies higher than 2.4 Mev were accepted. Coincidences were recorded for various β-spectrometer

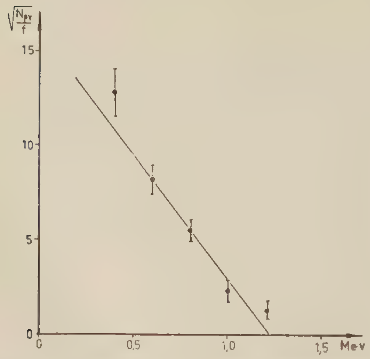

Fig. 21. Fermi plot of β-γ coincidence distribution of the 2.57 Mev γ-ray in Kr^{87}.

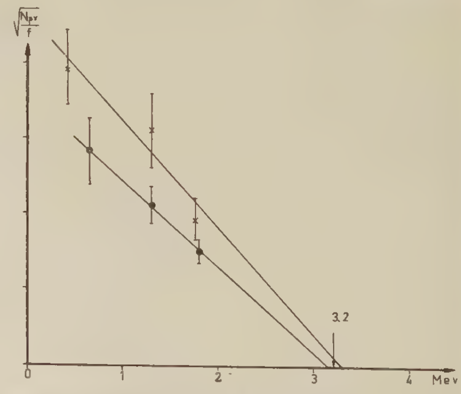

Fig. 22. Fermi plots of β-γ coincidence distributions of the 0.847 Mev γ-ray in Kr^{87}.

---

[1] *Note added in proof:* A recent measurement of the 2.75 Mev γ-ray of Na^{24} with the same Na I crystal has shown that this assumption is reasonable: the intensity ratio of the pair peak $E_\gamma - 0.511$ and the photopeak was 0.3 for $E_\gamma = 2.75$ Mev, whereas the ratio of the 2.05 and 2.57 Mev peaks of Kr^{87} was 0.5.

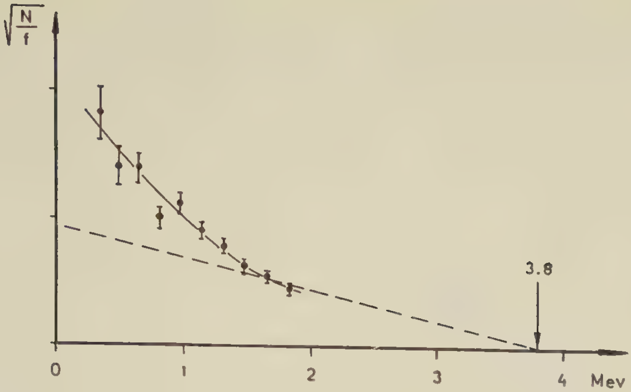

Fig. 23. Fermi plot of β-γ coincidence distribution of the 0.403 Mev γ-ray in Kr^{87}.

settings. A Fermi plot of the coincidence distribution is shown in Fig. 21. We conclude that the 2.57 Mev γ-ray is emitted in cascade with a β-transition af 1.2 ± 0.1 Mev energy.

β–$\gamma_{0.847}$. In the same way, coincidences were recorded between γ-pulses corresponding to energies >0.78 Mev and β-particles. Unfortunately, the scintillation spectrometer was not stable during the whole measurement. We therefore had to check the counting rate before and after each coincidence point, and discard all measurements where this counting rate had changed significantly. Two different series of points were obtained, each consisting of three useful points. Fig. 22 shows the Fermi plots of these coincidence distributions. A check of β-γ coincidences with γ-energies >0.95 Mev showed no significant coincidence effect at β-energy 1.8 Mev. Although the measurements were performed under unfavourable conditions, it may still be concluded from Fig. 22 that 0.847 Mev γ-quanta are emitted in cascade with a β-transition of ~ 3.2 Mev energy. The relative intensity of this β-transition would be less than 10 %, as estimated from the coincidence rate at 1.8 Mev (p. 143).

β–$\gamma_{0.403}$. The 0.403 Mev peak in the γ-spectrum of Kr^{87} is by far the strongest one. The β-γ coincidence distribution of this γ-ray is therefore of special interest. Unfortunately, the β-spectrometer used [S2] cannot focus β-particles of energies higher than 1.8 Mev with high transmission. The Fermi plot of the coincidence distribution (Fig. 23) therefore ends at 1.8 Mev, and the extrapolation to the energy axis is very uncertain. However, it is evident from Fig. 23, that the 0.403 Mev γ-ray is emitted in cascade with β-particles of energy higher than 2 Mev. From the coincidence rate at 1.8 Mev we estimate the fraction of 1.8 Mev β-particles that is in coincidence with 0.403 Mev γ-quanta to be 50–100 %. According to the discussion above, Kr^{87} decays by emission of β-particles of energies 1.3, 3,3 and 3.8 Mev and intensities 25 %, <10 % and ≥ 65 % respectively. We therefore interpret the coincidence results of Fig. 23 as indicating that the 0.403 Mev γ-ray is emitted in cascade with 3.8 Mev β-particles. This interpretation is roughly illustrated by the broken line of Fig. 23, which cuts the energy axis at 3.8 Mev. A further analysis of the Fermi plot gives a second β-component of energy about 1.4 Mev. This leads to the conclusion that 0.403 Mev γ-quanta are also emitted in cascade with the 1.3 Mev β-component.

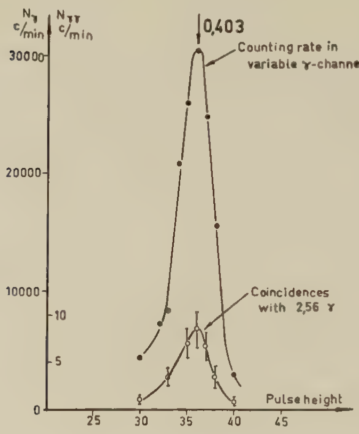

Fig. 24. Coincidences between 0.403 Mev and 2.57 Mev γ-rays in Kr^{87}. (Energies in Mev.)

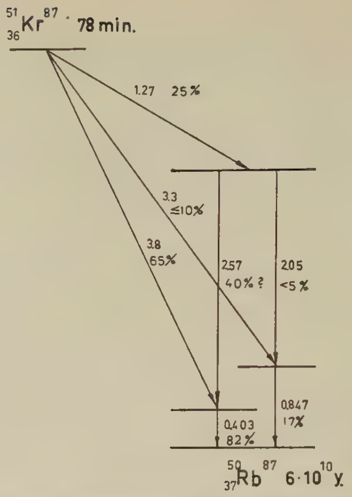
$^{51}_{36}Kr^{87}$ · 78 min.
1.27 25%
3.3 ≤10%
3.8 65%
2.57 40% ?
2.05 <5%
0.847 17%
0.403 82%
$^{50}_{37}Rb^{87}$ $6 \cdot 10^{10}$ y.

Fig. 25. Decay scheme of Kr^{87} discussed in text. (Energies in Mev.)

γ-γ coincidences.

In one γ-channel, pulses of amplitudes corresponding to energies higher than 2.4 Mev were accepted. In the other γ-channel pulses of various amplitudes were recorded. Coincidences were found between the 2.57 and the 0.403 Mev γ-rays, as shown in Fig. 24. No coincidences were found between the 0.403 and 0.847 Mev γ-rays.

Discussion

Our experimental data are consistent with the decay scheme of Fig. 25. The cascade branch $\gamma_{2.05}$–$\gamma_{0.847}$ Mev is not directly proved by coincidence measurements, but the existence of the 0.847 Mev level is suggested from β-γ coincidence measurements. In Fig. 25 are given relative intensities of the β-transitions deduced from β-measurements [T2] and β-γ coincidence data (cf. above). The γ-branching intensities are given in per cent of the total decay and are computed from the relative intensity estimates with the assumption that the sum of the $\gamma_{0.847}$ and $\gamma_{0.403}$ intensities is 100 %. The two sets of intensity values agree within the error limits in the individual estimates, although the intensity of the 2.57 Mev γ-branch (Fig. 25) is high.

As there are no conversion data on the γ-rays of Kr^{87}, we have to start out from the log *ft* values for the β-transitions in assigning the levels of Kr^{87} and Rb^{87}. The large number of spin and parity alternatives thus obtained is considerably reduced after comparison with shell model predictions. The estimated relative γ-intensities may then be used to check the level assignments.

The ground state of $^{50}Rb^{87}$ has a measured spin 3/2 [H3], in accordance with the level prediction $p_{3/2}$ of the shell model. The ground state of $^{51}_{36}Kr^{87}$ would be $d_{5/2}$ or $g_{7/2}$. From the apparent nonexistence of a 4.2 Mev β-transition between the ground states of Kr^{87} and Rb^{87} we conclude that the ground state of Kr^{87} is $g_{7/2}$ rather than $d_{5/2}$. A 4.2 Mev β-transition would then occur with a spin difference of 2 and parity change and have low intensity (cf. discussion on page 189).

Our conclusion that the ground state of Kr^{87} (51 neutrons) is $g_{7/2}$ is in accordance with the analogous cases of Sb^{125} and Sb^{123}, which have an odd proton number of 51. These nuclei also have the ground state spin 7/2 [H3].

Table 4. Spin- and parity assignments of the levels in Rb^{87}, as obtained from β-data of Kr^{87}.

β-transition Mev	Final level Mev	Log ft	Change of		Possible spins and parities	
			spin	parity	from log ft value	from shell model
4.2	0	> 8.2	(2)	(yes)	(3/2, measured)	$p_{3/2}$
3.6	0.403	7.3	0, 1	yes	$9/2-$, $7/2-$, $5/2-$	$f_{5/2}$
3.3	0.847	8.1*	2	yes	$11/2-$, $3/2-$	$p_{3/2}$**
1.25	3.0	5.8	0, 1	no	$9/2+$, $7/2+$, $5/2+$,	$g_{9/2}$, $g_{7/2}$, $d_{5/2}$
			0, 1	yes	$9/2-$, $7/2-$, $5/2-$,	$f_{5/2}$

* $\log (W_0^2 - 1)\, ft = 9{,}8$.

** see discussion on p. 189.

In order to facilitate the discussion of spin and parity assignments to the energy levels in Rb^{87}, we have collected our data in Table 4. In column 6 are given possible spin- and parity assignments of the energy levels displayed in column 2. Thess assignments follow from a comparison of log ft values of the various β-transitions with the β-decay statistics of M. G. MAYER *et al.* [M4]. The classification of the β-transitions is shown in columns 4 and 5. It should be noticed that $\log (W_0^2 - 1)\, ft$ [S3] for the 3.3 Mev β-transition appears to be 9.8. This fact strongly supports a classification of this β-branch as belonging to the group of first forbidden transitions, occurring with $\Delta I = 2$ and parity change [M4]. The Fermi plot of the 3.6 Mev β-transition has an allowed shape [T2]. This β-branch can therefore not be classified as occurring with $\Delta I = 2$, yes.

We are now able to eliminate most of the spin alternatives in column 6 by a comparison with the one particle shell model [M1, H1], which is assumed to be valid in the extended form later discussed. According to the one particle model, the following energy levels are available in this nucleon region (37 protons): $p_{1/2}$, $p_{3/2}$, $f_{5/2}$ and $g_{9/2}$. At very high excitation energies a $d_{5/2}$ or $g_{7/2}$ level in the (51–82) shell might also be imaginable. Assuming that some of these spin terms are to be identified with the experimental levels in Rb^{87}, the numerous spin alternatives in column 6, Table 4, are reduced to those shown in column 7. The ground state and the first excited state would then be identified as $p_{3/2}$ and $f_{5/2}$. The $p_{3/2}$ assignment of the second excited level is discussed on p. 189. The assignment of the third level is uncertain. There remain the possibilities $f_{5/2}$, $g_{9/2}$, $g_{7/2}$ and $d_{5/2}$. Of these, the $f_{5/2}$ alternative seems to be least probable, since it follows from the classification of the 1.25 Mev β-transition as first forbidden. In the statistics of MAYER *et al.* [M4] the mean values of the log ft values for allowed and first forbidden transitions are 5.2 and 6.8 respectively. The classification of the 1.25 Mev β-branch ($\log ft = 5.8$) as belonging to the allowed group therefore seems to be preferred.

An observation of importance for the discussion on p. 189 should be noted. The assumption that the ground to ground state β-transition occurs with $\Delta I = 2$, yes, implies that $\log (W_0^2 - 1) ft$ should be about 10 [S3]. The relative intensity of the 4.2 Mev β-branch, computed from this condition, would be 20–30 %. We would certainly have been able to detect such a β-component in the β-spectrum of Kr^{87}. This anomaly is discussed on p. 189.

The assignments of the 2.97 Mev level may now be checked by comparing the

Table 5.

Assignment of 2,97 Mev level	Theoretical ratio		
	2.1	2.57	2.97
$d_{5/2}$	0.5	1	1.3
$f_{5/2}$	0.5	1	1.3
$g_{7/2}$	$1.6 \cdot 10^6$	1	10^7
$g_{9/2}$	$2 \cdot 10^{-3}$	1	0.02
Experimental values	< 0.2	1	< 0.05

estimated relative γ-intensities with theoretical estimates from WEISSKOPF's formulas [B5], which are derived for one particle transitions. In Table 5 are given the theoretical relative γ-transition probabilities $\gamma_{2.1} : \gamma_{2.57} : \gamma_{2.97}$ computed from WEISSKOPF's formulas for various spin assignments of the 2.97 Mev level in Rb^{87}. The experimental γ-intensity ratios seem to favour the $g_{9/2}$ assignment rather than $d_{5/2}$ and $f_{5/2}$. The $g_{7/2}$ alternative seems to be excluded.

It is evident that the extreme one particle model is not successful in explaining the excited levels of Rb^{87}. However, the excitation mechanism may be explained by assuming the existence of mixed nucleon configurations [S4, D1]. This is discussed in detail on p. 189.

Section 6. 2.77 h Kr^{88} and 18 min Rb^{88}

Introduction

The β-spectrum of the genetic pair $Kr^{88} \rightarrow Rb^{88} \rightarrow Sr^{88}$ has been previously studied by the author [T3]. At that time the available equipment was not sufficient to settle the details of the decay scheme of Kr^{88}. The measurements are complicated by the simultaneous presence of the 18 min daughter activity Rb^{88}. As the main result, Kr^{88} was shown to decay by emission of two β-particle groups of energies 2.8 and 0.52 Mev and possibly also one of energy ~ 0.9 Mev. The relative intensities of these groups were estimated as 20, 68, and 12 % respectively Moreover, conversion electrons of a γ-ray of energy 28 kev were recorded. In a separate investigation of Rb^{88} [T3], the β-spectrum of this isotope was shown to consist of at least three β-components of energies 5.30, 3.6 and 3.5 Mev and intensities 78, 13, and 9 % respectively. A fourth β-component of ~ 0.7 Mev energy and low intensity (~ 7 %) also appeared from the analysis of the Fermi plot, but its existence was regarded as uncertain.

In the present work, the decay of Kr^{88} and Rb^{88} has been investigated by means of the improved scintillation spectrometer and coincidence equipment discussed in chapter 1. The γ-spectrum of Kr^{88} was obtained in the same way as the β-spectrum [T3], i.e. as the difference between the γ-spectrum of $Kr^{88} + Rb^{88}$ and that of a pure Rb^{88} sample. In the decay of Kr^{88} seven new γ-transitions of energies 0.166, 0.191, 0.36, 0.84, 1.55, 2.2 and 2.4 Mev were found. This data together with intensity estimates and earlier β-data formed the basis for suggesting a decay scheme, which has then been partly checked by coincidence measurements.

In the decay of Rb^{88} two new γ-rays of energies 2.18 and 4.2 Mev were found. They seem to fit the earlier established decay scheme of Rb^{88} [B3, T3], if one assumes the presence of an additional excited level of 4.1 Mev energy in Sr^{88}.

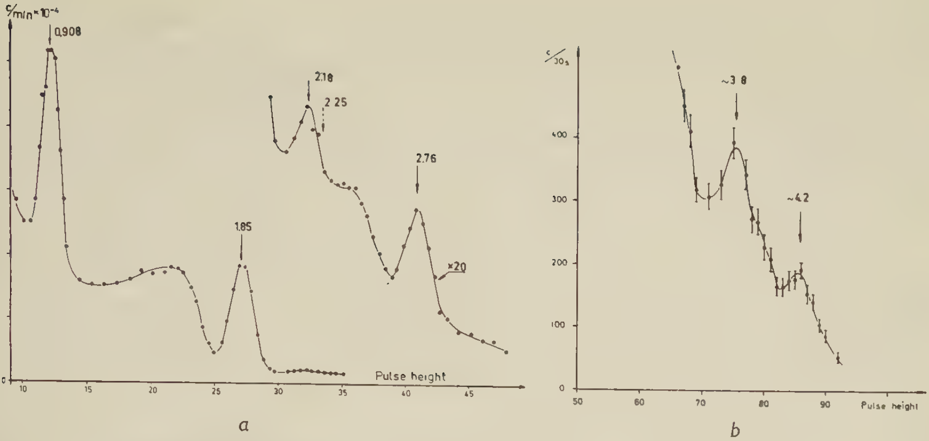

Fig. 26. Pulse-height distributions of Rb^{88}, recorded with the NaI scintillation spectrometer. —*a*, 0.8–3 Mev region; *b*, 3–4.5 Mev region. (Energies in Mev.)

18 m Rb^{88}

Scintillation spectrum

The samples of Rb^{88} were prepared by means of electrostatic precipitation from fission gas as described in our previous paper on Kr^{88} and Rb^{88} [T3].

The pulse height distribution of Rb^{88}, recorded with a NaI scintillation spectrometer (p. 139) is shown in Fig. 26 a and b. In addition to the photopeaks of γ-rays of energy 0.908, 1.853 and 2.76 Mev, earlier reported by other investigators [H3], we find three more peaks at $2.18 + 0.03$, 3.8 ± 0.1 and 4.2 ± 0.1 Mev energy, which were reproduced in three measurements. The 3.8 Mev peak is probably a coincidence peak due to the strong 1.85 Mev γ-transition, since its relative intensity did not seem to be proportional to the source strength. The other two peaks are interpreted as photopeaks due to 2.18 and 4.2 Mev γ-rays. There was also an indication of a pair line at 3.2 Mev. The peak at 2.18 Mev cannot be a pair peak of energy 2.76–0.511 Mev. The expected position of such a peak is shown by an arrow at 2.25 Mev in Fig. 26 a. It is apparently of relatively low intensity, which supports the assumption that the 2.76 Mev peak is partly due to coincident recording of 1.85 and 0.908 Mev quanta (cf. below).

The relative intensities of the γ-rays of energies 0.908, 1.85, 2.18, 2.76, and 4.2 Mev were estimated from the corresponding peak areas (cf. p. 143) to be 60:100:4:10:0.2. The value of the relative intensity $\gamma_{2.76}/\gamma_{0.908}$ is 15 times larger than that reported by G. R. GAMERTSFELDER [G1] in the decay of 104 *d* Y^{88}. His value is estimated from the relative neutron yield in four (γ, n) processes. The 2.76 Mev γ-intensity given above is probably overestimated, since part of the corresponding photopeak may be due to coincident recording of 1.85 and 0.91 Mev quanta.

A comparison of the line intensities in the scintillation spectra of Y^{88} and Rb^{88} may be used to estimate the branching ratio $\beta_{3.5}/\beta_{2.5}$ between the 3.5 and 2.5 Mev β-components in the decay of Rb^{88}. In the Y^{88} decay, practically all ($\sim 99\%$) of the nuclei decay by K-capture to the 2.76 Mev excited level in Sr^{88} [H3]. This level is then mainly de-excited by the 0.908 and 1.853 Mev γ-cascade. These two γ-transitions therefore are of approximately equal intensity in the Y^{88} sample. In the Rb^{88} decay, however, the 2.76 Mev level of Sr^{88} is excited by a 2.5 Mev β-transition, and the 1.85 Mev level is excited either by 0.908 Mev γ-transitions from the 2.76 Mev level or by 3.5 Mev β-particles [T3]. The ratio of the areas of the 0.908 and 1.85 Mev photolines in the γ-spectrum of Y^{88} was found to be 3.1 as compared with the corresponding value 2.0 in the Rb^{88} spectrum. From these figures we calculate a branching ratio $\beta_{3.5}/\beta_{2.5} = 0.5 \pm 0.2$. This value is to be compared with the ratio 1.4 obtained in our β-measurements [T3] and the ratio 1.3 computed from the data of BUNKER *et al.* [B3]. The error in the two latter values may be of the order of 50 %, since an overestimate of the 3.5 Mev β-intensity may involve an underestimate of the 2.5 Mev β-intensity. If the $\beta_{3.5}/\beta_{2.5}$ discrepancy were real, it would mean that the K-capture branch from Y^{88} to the 1.85 Mev level in Sr^{88} is not negligible, as has been assumed (cf. [H3]). This problem may be solved by a more precise measurement of the relative γ-ray intensities in the decay of Y^{88} and Rb^{88}.

Discussion

A decay scheme of Rb^{88}, comprising the 0.908, 1.853 and 2.76 Mev γ-transitions has earlier been established [T3, B3]. Due to the short half life of Rb^{88} and the low intensities of the new γ-transitions no coincidence measurements could be performed in order to determine the relation of these transitions to the known levels in Sr^{88}. It is plausible, however, to assume the existence of an excited level of 4.1 Mev energy in Sr^{88}. (In fact, the 4.2 Mev γ-peak was discovered in a separate investigation, performed in order to check this assumption.) The resulting decay scheme of Rb^{88} is shown in Fig. 27. The relative γ-intensities have been transformed to per cent of the total decay, assuming the intensity relation

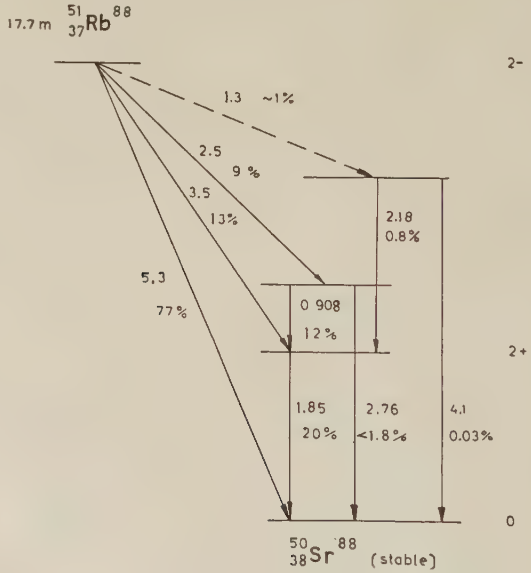

Fig. 27. Decay scheme of Rb^{88} discussed in text. (Energies in Mev.)

$$\gamma_{1.85}+\gamma_{2.76}+\gamma_{4.1}=24\,\%$$

to be valid. The 4.1 Mev level would be excited by a β-transition of energy 1.4 Mev and intensity about 1 %.

According to the decay scheme of Fig. 27 the γ-rays of energies 2.18 and 4.1 Mev would not occur in the Y^{88} decay, since the total decay energy of this nucleus is only 3.7 Mev [H3].

Spin- and parity assignments

On the basis of β-measurements, BUNKER *et al.* [B3] assigned both the 1.85 and 2.76 Mev levels of Sr^{88} to be $2+$. However, this assignment is not in accordance with experimental data reported by PEACOCK and JONES [P1] and by METZGER and AMACHER [M5]. From measurements of the internal conversion coefficient of the 0.908 Mev γ-ray in Y^{88}, these authors conclude that the 0.908 Mev γ-transition is of $E1$ type. This would mean that the 1.85 and 2.76 Mev levels are not of equal parity. The assignment $2+$ for both of these levels is also inconsistent with the β-decay data of Y^{88}, as will be discussed later.

As shown below, it seems, however, possible to obtain consistent assignments of the 1.85 and 2.76 Mev levels of Sr^{88}. The ground state of this isotope is $0+$, since it is even-even (cf. also [H3]). The first excited state is most probably $2+$, according to the rule that the first excited state of even-even nuclei is $2+$. Only two exceptions from this rule are known so far [P3].

Using the relative β-intensities given in Fig. 27, we compute the log ft values 6.5, 6.9, 7.3 and 7.4 for the 1.3, 2.5, 3.5 and 5.3 Mev β-components respectively. As the Fermi plot of the 5.3 Mev β-component has forbidden shape [B3, T3], this transition occurs with $\Delta I=2$, yes. As the ground state of $^{50}_{38}Sr^{88}$ has spin 0 and even parity, the ground state of $^{51}_{37}Rb^{88}$ would be $2-$ [cf. B3]. The log ft values of the 1.3, 2.5 and 3.5 Mev β-components are all consistent with a classification as first forbidden with $\Delta I=0$, yes or as l-forbidden with $\Delta I=1$, No and $\Delta l=2$ (M4). The spin and parity alternatives of each of the levels in Sr^{88} might thus be $1\pm$, $2+$, $3\pm$.

The results of PEACOCK and JONES [P1] and METZGER and AMACHER [M5] strongly indicate that the 0.908 Mev γ-transition proceeds with $\Delta I=0$, 1 and parity change. This would mean that only the $1-$ or $3-$ alternative can be valid for the 2.76 Mev level.

Furthermore, the β-data on Y^{88}, reported by PEACOCK and JONES [P1], eliminates the $1-$ alternative for the following reasons. The non-existence of a β-transition from the ground state of Y^{88} to the ground state of Sr^{88} implies a high spin of the former state. From the relative intensity of the β-transition to the 1.85 Mev level we compute a log ft value of 9.6. Log $(W_0^2-1)ft$ appears to be 10.0, indicating that this transition occurs with $\Delta I=2$, yes [S3]. If the 1.85 Mev level is $2+$, the ground state of Y^{88} would be $4-$, as suggested from the shell model (cf. [B3]). The log ft value for the β-transition to the 2.76 Mev level is 6.8, classifying this level as first forbidden, occurring with $\Delta I=0$, yes or l-forbidden with $\Delta I=1$, no, $\Delta l=2$ [M4]. This gives the alternatives $4+$, $3-$ and $5-$ for the 2.76 Mev level. A comparison with the results above leaves the $3-$ assignment as the only one which fits all the data discussed above.

Recent angular correlation data on the $\gamma_{9.08}$–$\gamma_{1.85}$-cascade in the Y^{88} decay are also in accordance with the assignments $2+$ and $3-$ of the first and second excited levels of Sr^{88}. R. STEFFEN [S7] and J. VARMA *et al.* [V1] independently reported directional correlation functions indicating a mixture of $E1$ and $M2$ radiations for the 0.908 Mev γ-transition. The $M2$ to $E1$ intensity ratio vould be 10^{-4} [S7]. Steffen also stated that the experimental intensity ratio of the 0.908 Mev $M2$ transition and the $E3$ cross over transition of energy 2.76 Mev seems to be in good agreement with the intensity ratio computed from Weisskopf's formula.

From the discussion above we conclude that the assignments $0+$, $2+$ and $3-$ for the ground state and the first two excited states of Sr^{88} seem to be in accordance with all existing experimental data from the decay of Rb^{88} and Y^{88}.

As mentioned earlier, the log *ft* value of the 1.3 Mev β-transition suggests the alternative assignments $1\pm$, $2+$, or $3\pm$ for the 4.9 Mev level in Sr^{88}. The experimental intensity ratio $\gamma_{2.18}/\gamma_{4.1} \geq 30$ gives preference to a $2+$ assignment of the 4.1 Mev.

2.77 h Kr^{88}

Scintillation spectrum

The $Kr^{88} + Rb^{88}$ samples were prepared in the isotope separator as described in ref. [T3].

Figs. 28 a and b show the low and high energy regions of the γ-spectrum of an electromagnetically separated Kr^{88} sample containing Rb^{88} in equilibrium. The main γ-line of 0.194 Mev energy has a "satellite" line at 0.166 Mev. This might be the escape peak of the 194 kev γ-ray. To examine this possibility, we measured the 0.150 Mev γ-ray in Kr^{87}, using the same geometry as in the Kr^{88} measurement. No escape peak was detected (cf. also p. 142). We therefore conclude that the peak at 166 kev really corresponds to a γ-ray. From the half width of the line at about 0.90 Mev we conclude that it is double, containing both the 0.908 Mev line of Rb^{88} and another line due to Kr^{88}. The inset of Fig. 28 a shows an analysis of this line, using the 0.908 Mev line of Rb^{88} as a "window" curve. The energy of the Kr^{88} line

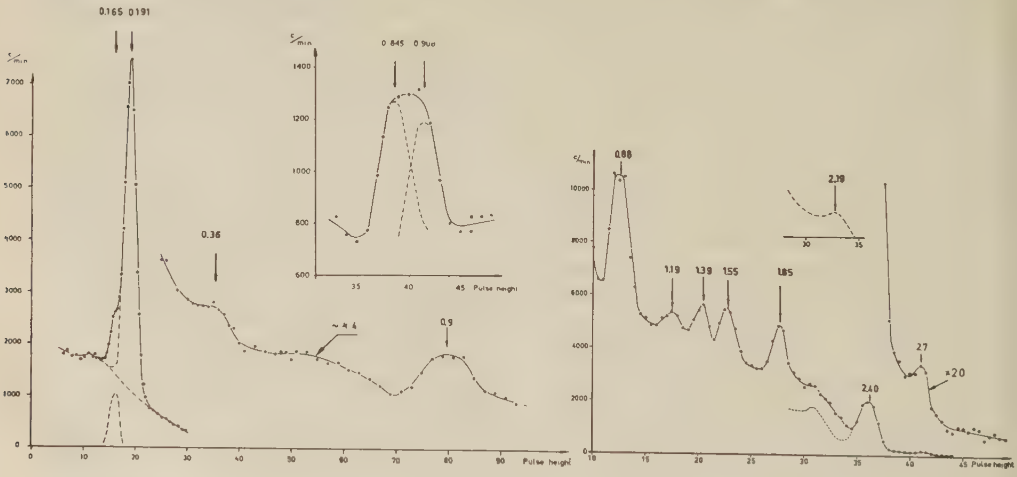

a *b*

Fig. 28. Pulse-height distributions of $Kr^{88} + Rb^{88}$, recorded with the NaI scintillation spectrometer.—*a*, Low energy region; *b*, high energy region (Energies in Mev). The inset of *b* shows the difference between the corresponding region of the γ-distribution and the dotted curve, obtained by normalization of the high energy region of fig. 20 *a* (cf. text).

appears to be 0.845 Mev. (The same value was obtained in the analysis of another Kr^{88} spectrum.)

The peaks at 1.55 and 2.40 Mev are interpreted as the photolines of two γ-rays of the corresponding energies. The lines at 1.85 and 2.76 Mev are due to the known γ-rays in Rb^{88} (cf. p. 171). The peak at 1.39 Mev is most probably the pair line of the 2.40 Mev γ-ray. The peak at 1.19 Mev might be a photopeak. However, there are very strong indications that it is the pair line of a 2.2 Mev γ-ray. An inspection of the Compton distribution of the 2.57 Mev γ-ray in Kr^{87}, Fig. 20 a, shows that its height is somewhat smaller than the height of the corresponding photoline. This means that the height of the Compton distribution of the 2.40 Mev γ-ray in Kr^{88} definitely should be lower than the photopeak of the same γ-ray. It is then clear from Fig. 28 b that the high energy part of the 2.40 Mev Compton distribution has superimposed on it another distribution. A rough analysis (cf. Fig. 28 b), performed by means of the high energy part of the pulse-height distribution of the 2.57 Mev γ-ray, indicates the presence of a photoline of about 2.2 Mev energy. This interpretation is confirmed in γ-γ coincidence measurements (cf. below). It should be noticed that in this case the occurrence of the pair line made possible a satisfactory energy determination of the 2.2 Mev γ-ray.

According to our interpretation of the γ-spectrum, Kr^{88} decays with the emission of γ-rays of energies 0.166, 0.191[1], 0.36, 0.845, 1.55, 2.19, and 2.40 Mev. In addition, the existence of a 0.028 Mev γ-ray has earlier been reported from β-spectrometer measurements [T3]. The relative γ-ray intensities were estimated from the photopeak areas to be $20:100:14:65:40:\leq 50:100$.

β-spectrometer measurements

A rough calculation indicated that the conversion electrons of the strong 0.194 Mev line might be of measurable intensity. A reinvestigation of the corresponding part of the Kr^{88} β-spectrum proved the existence of such conversion electrons. Fig. 29

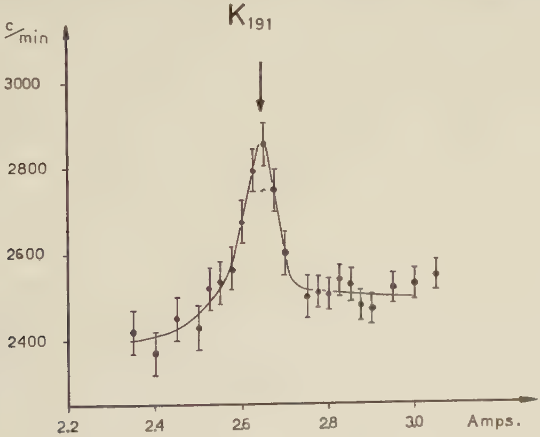

Fig. 29: Conversion electrons of 0.191 Mev γ-ray in Kr^{88}, recorded in the intermediate image β-spectrometer.

---

[1] The energy value 0.191 Mev obtained in conversion electron measurements (cf. below) is considered more accurate than the value 0.194, obtained in scintillation spectrometer measurements.

shows the unresolved $(K+L)$-lines, measured in the intermediate image β-spectrometer [S2]. The γ-ray energy appeared to be 191 ± 2 kev. The intensity of the K_{191}-line is only $\sim 5\,\%$ of the K_{28} intensity. The ratio $K/(L+M)=8$ for the 28 kev γ-ray, reported in ref. [T3], is therefore not affected by the discovery of the K_{191} line, since the number of Auger electrons, due to K-vacancies produced by 0.191 Mev γ-transitions, is negligible.

Coincidence measurements

The coincidence equipment is described on p. 140.

β-γ coincidences.

β–$\gamma_{0.191}$. The γ-channel was fixed at the 0.191 Mev photopeak and coincidences were recorded for various β-spectrometer settings. The Fermi plot [N1] of the coincidence distribution of 0.191 Mev γ-quanta and β-particles is shown in Fig. 30.

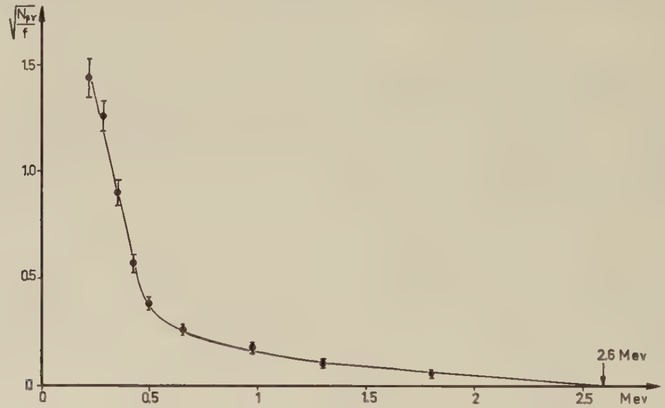

Fig. 30. Fermi plot of β-γ coincidence distribution of the 0.191 Mev γ-ray in Kr^{88}.

Evidently, this γ-transition occurs in cascade with two β-particle groups of energies ~ 0.5 Mev and ~ 2.5 Mev. Due to the few points defining the high energy component, the energy of this is uncertain. It might be identical with the value 2.8 Mev obtained in β-spectrometer measurements (T3).

γ-γ coincidences.

As a consequence of the complexity of the $Kr^{88}+Rb^{88}$ γ-spectrum, it is difficult to get unique results from γ-γ coincidence measurements. Most photoline peaks are superimposed on Compton distributions of more energetic γ-rays. Compton-Compton and Compton-photo-coincidences will therefore obscure the results. For this reason, we have only investigated the coincidence relations between the very strong 0.191 Mev photoline and the high energy region of the γ-spectrum.

$\gamma_{0.191}$–$\gamma_{2.2}$. In one channel the photopeak of the 0.191 Mev γ-ray was recorded, and in the other channel γ-quanta of energy >2.3 Mev. No coincidences above the accidentals were found. However, there was a comparatively large coincidence effect between the 0.191 Mev γ and γ-quanta >2.0 Mev. Part of the coincidence

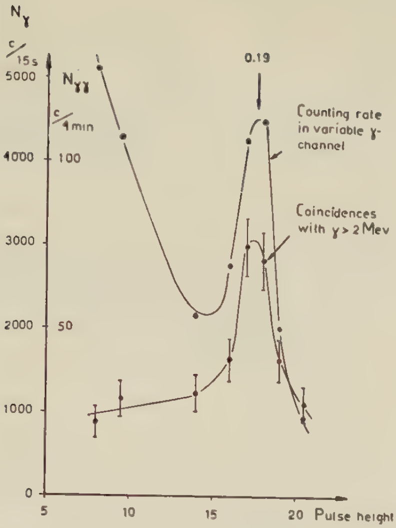

Fig. 31. Coincidences between 0.191 Mev γ-transitions and γ-quanta of energy > 2.0 Mev.

distribution $\gamma_{0.191}-\gamma$ was then recorded with the first channel still fixed at 0.191 Mev, and moving the other channel in steps from 2.4 Mev to ~ 1.5 Mev. The coincidence distribution ended at ~ 2.3 Mev. In the next run, the second channel was fixed to accept pulses corresponding to γ-quanta of energy > 2.0 Mev while the first channel was moved across the 0.191 Mev photoline. The coincidence distribution is shown in Fig. 31. These measurements show that the 0.191 Mev γ-transition occurs in cascade with the 2.2 Mev γ-transition but not with the 2.4 Mev transition.

$\gamma_{0.191}-\gamma_{0.845}$. One γ-channel was fixed at the 0.191 Mev photopeak. The other channel was moved across the 0. 845 Mev photopeak. There were no coincidences above the background of Compton-Compton and 0.191 Mev photoline-Compton coincidences. We therefore conclude that the 0.191 Mev γ-ray is probably not emitted in cascade with the 0.845 Mev γ-ray.

e-γ coincidences.

The conversion electrons of the 0.028 Mev γ-ray were focussed into the GM-counter of the intermediate image β-spectrometer. Coincidences were recorded between these electrons and γ-quanta of various energies. Such measurements in the high energy region of the γ-spectrum showed a coincidence effect, which dropped down at somewhat lower energy than the maximum energy of the γ-distribution. This result is interpreted as indicating that the 0.028 Mev γ-ray is probably in coincidence with the 2.19 Mev γ-ray but not with the 2.40 Mev γ-ray.

The coincidence distribution between the $K_{0.028}$ conversion line and γ-quanta in the low energy region is shown in Fig. 32. It is evident from this measurement that the 0.028 Mev γ-transition occurs in cascade with the 0.165 Mev γ-transition but not with the 0.191 Mev γ-transition.

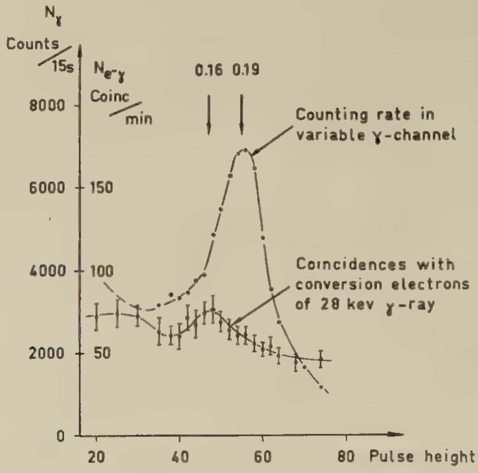

Fig. 32. Coincidence distribution of K_{28}-conversion electrons of Kr^{88} and γ-quanta in the energy region ~0.190 Mev.

Discussion

Considering all the experimental data on the decay of Kr^{88} we arrive at the decay scheme of Fig. 33. The intensities of the various γ-branches in Fig. 33 are given in per cent of the total β-decay. The 0.350 Mev γ-ray is here assumed to be emitted in cascade with a γ-ray of 1.85 Mev energy. The existence of this cascade is not proved. It would in fact be hard to distinguish this postulated 1.85 Mev γ-ray from the 1.85 Mev γ-ray in the decay of the daughter nucleus Rb^{88}, which would be of much higher intensity. The assumed γ-cascade, which is indicated by broken lines in Fig. 33, would also support the presence of a 0.9 Mev β-component, indicated in the earlier measurements [T3]. This γ-cascade branch should, however, be considered tentative.

The $\gamma_{1.55}$–$\gamma_{0.845}$ - cascade is mainly suggested from energy considerations. It is also supported by the absence of $\gamma_{0.191}$–$\gamma_{0.845}$ coincidences. The order of the γ-transitions is somewhat arbitrary, although the intensity estimates favour the order given in Fig. 33. It is to be noticed, that the energy difference between the third and fourth levels of Fig. 33 is 1.2 Mev. The 1.2 Mev line in the γ-spectrum of Kr^{88} might then possibly be due to a 1.2 Mev γ-ray. The intensity of such a γ-transition would be appreciably lower than 4 % of the total β-decay.

The order of the 0.028 and 0.165 Mev γ-transitions is arbitrarily given in Fig. 33. It is discussed below.

When trying to make spin- and parity assignments of the levels in Rb^{88} we have to start from the ground state spins and the log *ft* values of the β-transitions. As a check of the result we may then use the relative γ-intensities. The ground state of the even-even nucleus Kr^{88} should have spin zero and even parity. From the Rb^{88} β-decay the ground state of this nucleus has been shown to be 2 − (cf. p. 173). The log *ft* values of the 2.8, 0.9 and 0.52 Mev β-transitions are 7.7, 5.9, and 4.8 respectively. The last value indicates an allowed transition, occurring with $\Delta I = 1$, no [M4]. The 2.40 Mev level in Rb^{88} would then be uniquely characterized as a 1 + level.

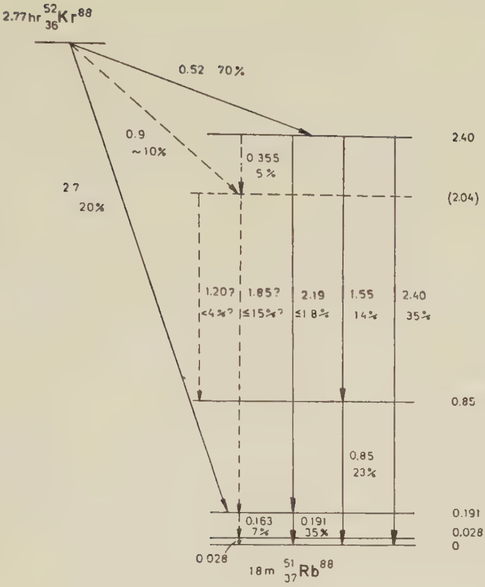

Fig. 33. Decay scheme of Kr^{88} discussed in text. (Energies in Mev.)

The log ft value of the 0.9 Mev β-transition would classify it as occurring either with $\Delta I = 1$, no, or $\Delta I = 0$, yes. The 2.04 Mev level could then be $1+$ or $0-$.

As the possible β-transition to the 0.85 Mev level is certainly of lower intensity than 10 %, it would neither occur with $\Delta I = 1$, no, nor with $\Delta I = 0$, yes. The assignments $1+$ or $0-$ for this level may therefore be excluded. The same argument holds if the order of the 1.55 and 0.85 Mev γ-rays were reversed.

As already shown in ref. [T3], the 2.7 Mev β-transition probably belongs to the first forbidden group with $\Delta I = 2$, yes. This transition was therefore assumed to occur between the ground states of Kr^{88} and Rb^{88}. However, our coincidence measurements indicate that the 0.191 Mev γ-ray is emitted in cascade with high energy β-particles. β-transitions to the ground state and first excited state of Rb^{88} may therefore belong to the same class ($\Delta I = 2$, yes). It seems therefore justifiable to assume that the high energy region of the β-distribution of Kr^{88} [T3] is complex, containing one 2.7 and one 2.9 Mev component, both with log $ft > 7.7$. Both of them would then occur with $\Delta I = 2$, yes. The 0.191 Mev level would then have spin 2 and odd parity.

The order of the 0.028 and 0.166 kev levels in Rb^{88} cannot be established at present. We have somewhat arbitrarily placed the former one lowest in Fig. 33. The 0.028 Mev γ-ray has a $K/(L+M)$ ratio of 8 [T3], which classifies this transition as being of $M1$ type [S9, G2]. If both the ground state and the 0.191 Mev level are $2-$, the 0.028 (or 0.163) Mev level would be $2-$, $1-$, or $3-$. The $1-$ alternative is excluded from the log ft value > 7.7, computed for a possible β-transition to this level.

As a result of our analysis, the ground state of Rb^{88} would be $2-$, the 0.028 (or 0.163) Mev level $2-$ or $3-$, the 0.191 Mev level $2-$, the 0.85 Mev level uncertain, but probably not $1+$ or $0-$, the 2.04 Mev level(?) $1+$ or $0-$ and the 2.40 Mev level $1+$.

Section 7. 9.2 h Xe^{135}

The decay scheme of Xe^{135} is expected to be in good agreement with the predictions of the one particle shell model [M1, H1]. This is because the nucleon configurations are near closed shells, where the conditions for pure one particle excitations are satisfactorily fulfilled. It was therefore considered of interest to complete the experimental data on this isotope.

The decay of Xe^{135} has earlier been studied at this laboratory. In 1949 a preliminary measurement of the β-spectrum was made with an electromagnetically separated sample, obtained from uranium fission [T1]. Later the results of a more detailed investigation were reported [B4]. A list of references to earlier work on Xe^{135} is given in ref. [B4]. It was shown that Xe^{135} decays by means of a 0.910 Mev β-transition to an excited level of 0.250 Mev energy in Cs^{135}. A very weak γ-ray of energy 0.610 Mev was also reported but a complete decay scheme could not be established at that time. In the investigation to be reported here, a low intensity decay branch of Xe^{135} has been established by means of coincidence technique. The resulting decay scheme of Fig. 36 seems to be well established. A preliminary report of the main results of this investigation has been published elsewhere [T5].

Coincidence measurements

A problem of interest was to determine the position of the weak 0.604 Mev γ-transition (cf. p. 181) in the level scheme of Cs^{135}. For this purpose β-γ coincidences were recorded in the intermediate image β-spectrometer with the arrangement described on page 141. γ-quanta of energy higher than 0.550 Mev were accepted in the γ-channel, and β-particles of various energies were focussed into the GM-counter of the β-spectrometer. The coincidence distribution showed that there are no coincidences between K- conversion electrons of the 0.250 Mev γ-ray and γ-quanta of energy higher than 0.550 Mev. However, the high energy γ-ray is in coincidence with part of the β-continuum. A Fermi plot (N1) of the coincidence distribution is shown in Fig. 34. The maximum energy of the continuum is found to be 0.550 Mev.

The coincidence measurements thus prove that a small fraction of the Xe^{135} nuclei decay by 0.550 Mev β-particles to an excited level of energy 0.604 Mev in Cs^{135}.

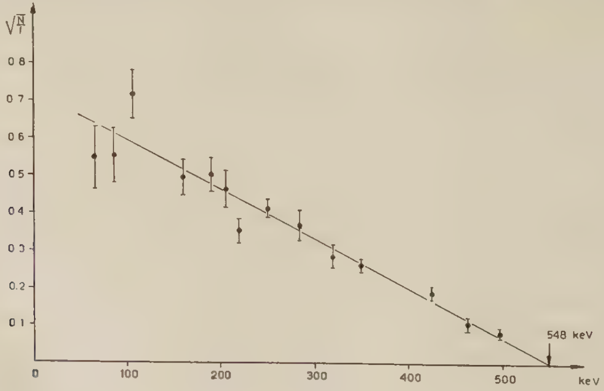

Fig. 34. Fermi plot of the β-γ coincidence distribution of the 0.604 Mev γ-ray in Xe^{135}.

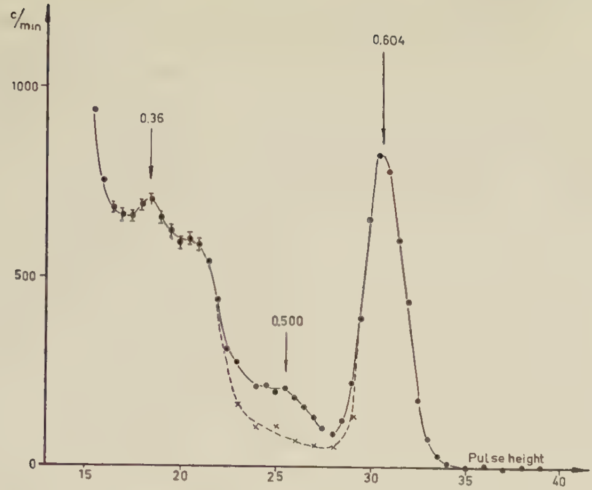

Fig. 35. High energy region of Xe^{135} scintillation spectrum. The "peak" at 0.500 Mev was shown to be due to coincident recording of 0.250 Mev γ-quanta. The broken line shows the normalized pulse distribution obtained with a weaker sample. The 0.250 Mev γ-line, rising to the left, is ~200 times stronger than the 0.604 Mev line. (Energies in Mev.)

Scintillation spectrum

The experimental data presented above indicate the presence of two excited levels of energy 0.250 and 0.604 Mev in Cs^{135}. The theoretical interpretation would be facilitated if the relative intensity of the possible γ-transition between these levels could be estimated. Therefore the scintillation spectrum of Xe^{135} was carefully remeasured, using a strong source and a crystal arrangement of high resolution. Fig. 35 shows the result. The small bump at 0.36 Mev was reproduced in three different measurements. It is interpreted as the photoline of a 0.36 Mev γ-ray.

The high energy γ-line of Xe^{135} was also remeasured. The γ-spectrometer was calibrated before and after the γ-measurement using γ-rays of 511 and 840 kev as reference lines. We obtained the energy value 604 ± 6 kev.

The relative γ-intensities were estimated from the areas of the corresponding photopeaks (cf. p. 143). They were found to be 100, 3, and 0.09 for the 0.250, 0.604, and 0.36 Mev γ-rays respectively.

Discussion

The empirical data on the decay of Xe^{135} are consistent with the decay scheme of Fig. 36. Both branches are established by means of coincidence measurements. The internal energy consistency lies within the errors in the individual measurements.

The branching ratio $\beta_{0.550} : \beta_{0.910}$ may be estimated in two ways. From the relative photopeak intensities we obtain $\beta_{0.550} : \beta_{0.910} \sim 0.03$, neglecting the internal conversion. (The K-conversion coefficient is 0.058 for the 0.250 Mev γ-ray [B4] and probably less for the other two γ-transitions.) Another estimate of $\beta_{0.550} : \beta_{0.910}$ is obtained from the β-$\gamma_{0.604}$ coincidence measurement. By comparing the normalized areas under the β-continuum and the β-γ coincidence distribution (p. 143), we arrive at

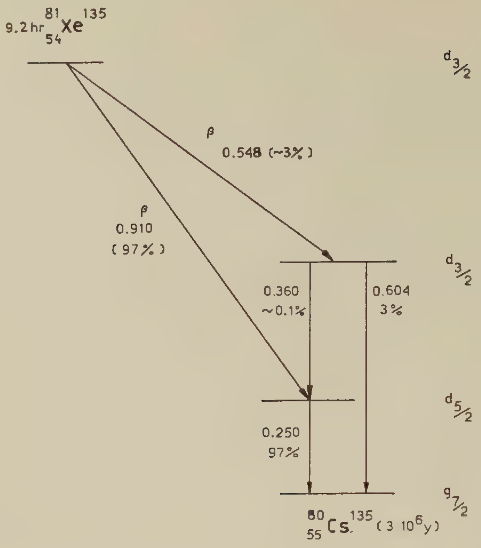

Fig. 36. Decay scheme of Xe^{135} discussed in text. (Energies in Mev.)

a branching ratio of 0.025. We thus conclude that the branching ratio $\beta_{0.550} : \beta_{0.910}$ is about 0.03. The log *ft* values then appear to be 6.6 and 5.8 for the 0.550- and 0.910-Mev β-components respectively [M3]. According to the systematics of M. G. Mayer *et al.* [M4] the 0.910-Mev transition would then be classified as allowed, with $\Delta I = 0{,}1$ and no parity change. The 0.550 Mev β-transition would be of first forbidden type, occurring with $\Delta I = 0{,}1$ and parity change.

The empirically established decay scheme of Xe^{135} is consistent with the level predictions of the one particle shell model [M1, H1] for an odd nucleon number of 55 ($^{80}_{55}$Cs^{135}). The ground state of Cs^{135} is known to have the spin 7/2 [H3], in accordance with the level prediction $g_{7/2}$ of the one particle model. From earlier data, the ground state of Xe^{135} is interpreted as a $d_{3/2}$ level, and the 0.250 Mev level in Cs^{135} as a $d_{3/2}$ level [cf. B4, G6]. According to the shell model, two more excited levels are possible, namely $s_{1/2}$ and $d_{3/2}$. The former alternative can hardly be identified with the 0.604-Mev level, since then the γ-transition to the ground state would be of the $M3$ type. The half life of the 0.604-Mev level would then be $\sim 10^{-2}$ sec, according to the semiempirical formula of Goldhaber and Sunyar [G2]. This would be in contradiction to our coincidence data. The $d_{3/2}$ alternative, however, fits the experimental data. The 0.604-and 0.360-Mev γ-transitions would then be of $E2$ and $M1$ type respectively. The ratio of the theoretical half lives for $M1$ and $E2$ transitions [B5] gives a branching ratio $\gamma_{0.360} : \gamma_{0.604}$ of about 0.05, in accordance with our empirical value 0.03.

According to the level assignments of Fig. 36, the 0.910-Mev β-transition should occur with no parity change and $\Delta I = 1$, in accordance with the experimental log *ft* value. The apparent nonexistence of an 1.16 Mev β-transition can be accounted for by the high spin difference ($\Delta I = 2$, no) between the two ground states. The 0.550-Mev β-transition, however, seems to violate the ordinary selection rules. This is discussed in detail on page 188.

Section 8. 17 min Xe^{138} and 32 min Cs^{138}

The decay data on Xe^{138} are fragmentary (cf. [H3]). It is shown by G. N. Glasoe and J. Steigman [G3] to be a β-emitter with a half life of 17 min. A rough β-measurement by S. Thulin *et al.* [T1] indicated a maximum β-energy of $\sim$2.7 Mev. A study of the decay of this isotope is highly complicated by the fact that the daughter nucleus Cs^{138} is radioactive with a half life of 32 min. The problems involved are similar to those met with in the study of the genetic pair $Kr^{88} + Rb^{88}$ (cf. T3). However, a study of the $Xe^{138} + Cs^{138}$ pair is much more difficult, partly because of the shorter half lives involved, and partly because the daughter nucleus in this case has the longer half life. In the Xe-Cs case therefore no equilibrium is reached, and the application of proper decay corrections is in most cases very difficult.

The radiations from Cs^{138} have been investigated by Langer *et al.* [L2], who reported a maximum β-energy of 3.4 Mev and three γ-transitions of energies 0.463, 0.98 and 1.44 Mev. β-γ and γ-γ coincidence measurements indicated that the 0.463 and 0.98 Mev γ-rays are emitted in cascade with the 1.44-Mev. The high energy β-transition was shown to leave the Ba^{138} nucleus in an excited state of 1.44 Mev energy.

The measurements to be reported here concern only the γ-spectrum of the isotope mixture $Xe^{138} + Cs^{138}$. A number of new γ-transitions were found, but the information obtained is not sufficient to suggest unambignous decay schemes.

Scintillation spectrum of $Xe^{138} + Cs^{138}$

The sources were prepared as described in Part I. The scintillation spectrometer arrangement is described on p. 139. Fig. 37 a and b show the low and high energy regions of a pulse height distribution of γ-rays from $Xe^{138} + Cs^{138}$. By repeated measurements it was shown that the 1.78 and 2.01 Mev peaks decayed with a shorter half life than that of Cs^{138}. The energies and assignments of the various γ-transitions

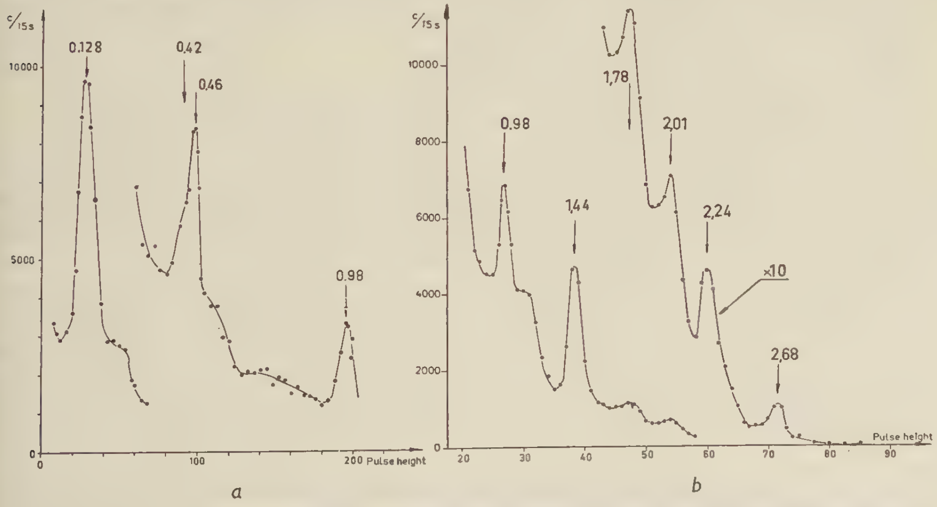

Fig. 37. Pulse-height distributions of $Xe^{138} + Cs^{138}$ recorded with the NaI scintillation spectrometer.—*a*, Low energy region; *b*, high energy region. (Energies in Mev.)

Table 6. Assignment of γ-rays in the γ-spectrum of $Xe^{138} + Cs^{138}$.

Nr	γ-ray energy Mev	Assigned to	Estimated relative intensity
1	0.128 ± 0.006	Cs^{138}	20
2	0.460 ± 0.005	Cs^{138}	20
3	0.550 ± 0.01	Cs^{138}	3
4	0.980 ± 0.02	Cs^{138}	25
5	1.44 ± 0.02	Cs^{138}	100
6	2.24 ± 0.03	Cs^{138}	20
7	2.68 ± 0.03	Cs^{138}	10
8	0.42 ± 0.02	Xe^{138}	100*
9	0.51 ± 0.02	Xe^{138}	20*
10	1.78 ± 0.03	Xe^{138}	
11	2.01 ± 0.03	Xe^{138}	

* This intensity scale is not the same as for Cs^{138}.

are presented in Table 6. An analysis of the line group around 0.460 Mev was performed in a separate measurement. The line group was remeasured seven times at about 15 min intervals with emphasis on reproducibility in the measuring procedure. The seventh distribution obtained was assumed to represent the Cs^{138} components of the line group, after a small correction for a residual Xe^{138} component. This curve was used in analysing the earlier six curves. Two of the cases are shown in Fig. 38 a and b. The Cs^{138} distribution was normalized at the top of the 0.55-Mev peak. The Xe^{138} difference distribution indicates the presence of two γ-lines at 0.42 and 0.51

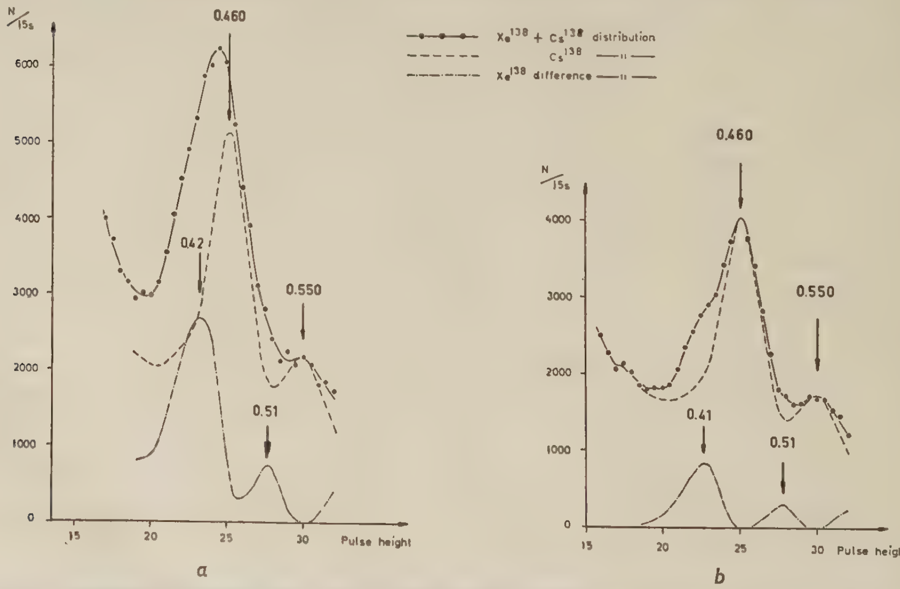

Fig. 38. Analysis of complex line group in the $Xe^{138} + Cs^{138}$ γ-spectrum.—*a*, First run; *b*, third run. The pure Cs^{138} distribution was obtained from the seventh run. (Energies in Mev.)

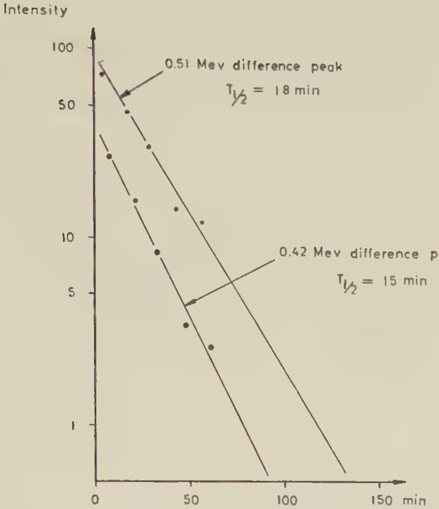

Fig. 39. Decay curves of 0.42 and 0.51 Mev lines of Xe^{138}.

Mev. The latter might be due to annihilation quanta produced by pair formation in the surroundings (p. 143). However, this interpretation seems unlikely, since the Cs^{138} distribution would then also contain a 0.511 Mev peak. Moreover, other similar γ-spectra recorded in the same arrangement, showed no indications of a 0.511 peak. The peak heights of these two lines are plotted logarithmically as a function of time in Fig. 39. The half life of the two peaks was found to be 15 and 18 min respectively, in accordance with the half life 17 min reported for Xe^{138} [H3].

The relative γ-intensities given in Table 6 were roughly estimated from the areas under the corresponding photopeaks.

Discussion

Xe^{138}. According to our measurements, four γ-transitions of energies 0.42, 0.51, 1.78 and 2.01 Mev are associated with the decay of Xe^{138}. It is not excluded that there are still more γ-rays, since we have not covered the whole energy region by measurements taken in a short time after the Xe^{138} source preparations. The present information on Xe^{138} is not sufficient for any discussion of the decay scheme, although it can be said that it is probably rather complex and that the total β-decay energy of this isotope is higher than 2 Mev.

Cs^{133}. The γ-rays 2, 4 and 5 of Table 6 are certainly identical with the γ-rays of energy 0.463, 0.98 and 1.44 Mev, reported by LANGER *et al.* [L2]. Our measurements indicate the presence of four more γ-transitions in the decay of Cs^{138}. It is tempting to see how these γ-rays may be arranged to fit the results obtained by LANGER *et al.*

The daughter nucleus of Cs^{138}, ${}^{82}_{56}Ba^{138}$, is even-even with a closed neutron shell. There is strong empirical evidence that the first excited state of such nuclei is of high energy [S5, S8]. It seems therefore justified to assume that the 1.44-Mev level really is the lowest one, as indicated by the coincidence measurements of LANGER *et al.* [L2]. Fig. 40 shows some possible interpretations of our results, based on this

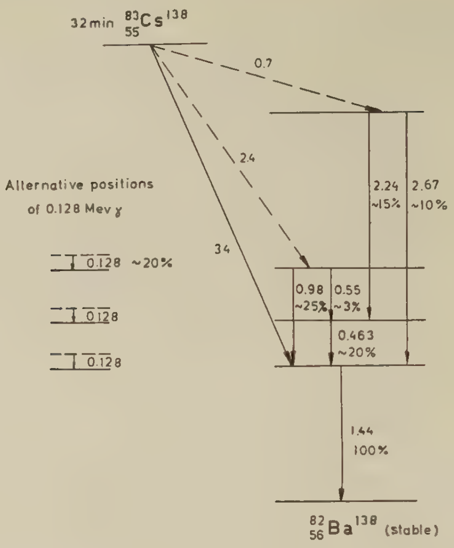

Fig. 40. Possible decay scheme of Cs^{138} discussed in text. (Energies in Mev.)

assumption. The internal energy consistency lies within the error limits. The estimated γ-intensities also seem to be consistent with the γ-sequences of Fig. 40. The position of the 0.128-Mev γ-transition cannot be determined yet; but intensity considerations make a 0.128-Mev transition to the second excited level improbable.

The tentative decay scheme of Fig. 40 necessitates that Cs^{138} decays with at least four β-transitions. It should also be noticed that only one γ-transition goes to the ground state. For the highest level, a cross over transition to the ground state would be of 4.1 Mev energy. A search for such a γ-transition in a strong Cs^{138} sample would be of interest (cf. Rb^{88}, Fig. 27).

Chapter IV. Concluding remarks[1]

1. *General*

In the preceding chapter an account was given of some disintegration measurements and their interpretation by current methods. Decay schemes were discussed for most isotopes investigated. Some of them are not unambiguously established and may therefore not be suitable for detailed comparisons with nuclear shell theory. However, some general observations are discussed in the present chapter, and some decay shemes are treated in more detail. As a background to the following discussion we will first briefly mention some features of current nuclear shell theory, which are of special interest in the present case. For a systematic review of the shell model the reader is referred to existing review articles, e.g. refs. [G5, F3, P3], where also further references are found.

Although based on assumptions which are theoretically unexplained, the single particle shell model [M1, H1] has been very successful in its experimental applications. We may here mention the simple interpretation of spin and parities of ground states and excited levels, the successful predictions regarding nuclear isomerism, and the smooth variation of level schemes of isotope sequences differing by a nucleon pair. Since its publication in 1949, this model has been frequently used by experimental physicists as a guide in planning new measurements and in interpreting experimental results. In this way a vast amount of new experimental data was obtained, which supported the validity of this rough model. However, in the same time an increasing amount of nuclear data appeared, which could not be explained with the extreme one particle model. It was also to be expected that the rough approximations of the one particle model might only be valid for nuclei in the neighbourhood of closed shells. This situation may be illustrated by the set of decay shemes reported in the present paper; the cases of Kr^{85m}, Kr^{85} and Xe^{135} (near closed shells) are for the most part in accordance with the single particle model, whereas the decay of Kr^{77} and Kr^{79} cannot be interpreted in this simple manner.

---

[1] *Note added in proof.* My sincere thanks are due to Professor M. H. L. Pryce for reading this chapter and offering his comments.

The difficulties mentioned above seem to be partly overcome by recent modifications of the one particle model, which take into account the excitation of more than one particle. In the extreme one particle model excited levels of an odd A nucleus were assumed to be due to the excitation of the odd nucleon into higher shells, whereas the "core" of paired nucleons remains unaffected. According to current ideas, excited levels may also occur by the excitation of a nucleon pair to a higher shell. Furthermore, a nucleon pair in an unfilled shell may be broken up, and the two nucleons may appear in different orientations in the same shell, or in different shells.

In several cases the energy corresponding to the excitation of a nucleon pair would be comparatively high, if no interaction energy were assumed between nucleons in a pair. However, the difference in pairing energy [M2] of a nucleon pair in the higher and lower levels may cause a considerable decrease of the total excitation energy.

Of special interest for our discussion is the possible existence of mixed nucleon configurations, treated by different authors [S8, D1, D2]. In particular, the theory of A. de Shalit and M. Goldhaber [D1] seems to be directly applicable in some of the present cases. These authors assume an interaction between an odd nucleon and a nucleon pair of the other kind, when this pair is situated in a shell of similar angular momentum as the odd nucleon. In some cases the corresponding interaction energy cancels the excitation energy required to lift the nucleon pair from its "normal" position to the shell where it interacts with the odd nucleon. The effect of the interaction may be expressed as a "stabilization" of the nucleon pair by the odd nucleon [D1]. In this way an experimentally obtained nuclear level might correspond to two or more nucleon configurations. de Shalit and Goldhaber showed that several experimental anomalies in the decay of nuclei near closed shells could be successfully explained as due to the presence of such mixed nucleon configurations. One example which they discussed is Kr^{85}, which has also been studied experimentally in the present work (p. 161). As will be shown below, the decay of Xe^{135} probably constitutes an analogous case (p. 188). Furthermore, the decay of Kr^{87} may be interpreted in a similar manner (p. 189).

Another approach to the interpretation of nuclear phenomena has been made by A. Bohr and B. Mottelson [B8], who consider nuclear properties due to collective particle motion in the nucleus. This model works successfully in the regions of large nuclear deformations (large quadrupole moments), i.e. nuclei far from closed nucleon shells. The decay schemes discussed in detail below concern isotopes near closed shells; consequently, we have not tried to apply the collective particle model in interpreting the results.

2. *Interpretation of some decay schemes in terms of the modified single particle model*

a. Kr^{85m}, Kr^{85} and Xe^{135}

It has earlier been pointed out that the decay schemes of these isotopes are consistent with predictions of the one particle model. An exception is, however, the extremely high log *ft* value 9.0 of the 0.159 Mev β-transition in Kr^{85}. According to the shell model interpretation this transition would occur between the $g_{9/2}$ ground state of Kr^{85} and the $g_{9/2}$ level of 0.513 Mev energy in Rb^{85} (Fig. 19), and therefore be of the allowed type (log *ft* (4.5–5.5)). A. W. SUNYAR *et al.* [S4, cf. also D1] suggested the following explanation of this discrepancy (cf. above). The significant part of the proton configuration of the 0.513 Mev level of Rb^{85} would normally be $(g_{9/2})^1$, and the neutron configuration $(p_{1/2})^2$ $(g_{9/2})^8$. The $g_{9/2}$ proton is, however, assumed to interact with $g_{9/2}$ neutron pairs, so that the neutron configuration $(p_{1/2})^0$ $(g_{9/2})^{10}$ is energetically favoured. If the population of the latter configuration is very high, a β-transition from the ground state of Kr^{85} (neutron configuration $(p_{1/2})^2$ $(g_{9/2})^9$) is correspondingly delayed. That is to say, a β-transition, ending in the neutron configuration $(p_{1/2})^0$ $(g_{9/2})^{10}$, is very unlikely, since it involves a three particle transition ($g_{9/2}$ proton $\rightarrow$ $g_{9/2}$ neutron and neutron pair $(g_{9/2})^2 \rightarrow (p_{1/2})^2$).

According to our measurements, Xe^{135} would constitute an analogous case to Kr^{85}. As pointed out on p. 182, the log *ft* value 6.6 of the 0.548 Mev β-transition in Xe^{135}

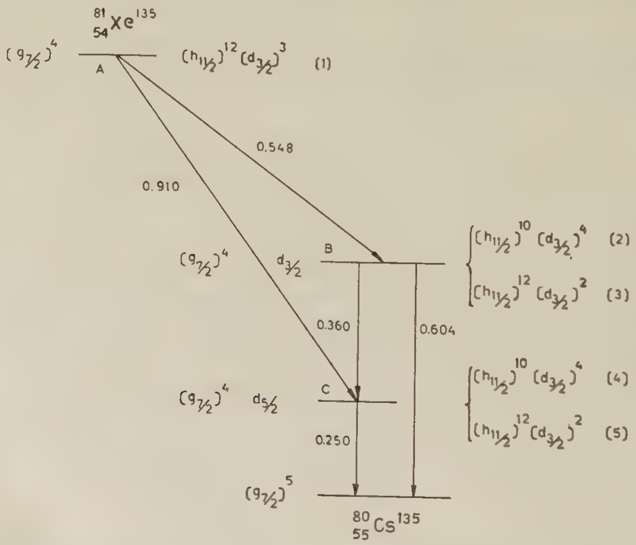
${}^{81}_{54}Xe^{135}$
$(g_{7/2})^4$
A
$(h_{11/2})^{12}(d_{3/2})^3$ (1)
0.548
0.910
$(g_{7/2})^4$
$d_{3/2}$
B
$(h_{11/2})^{10}(d_{3/2})^4$ (2)
$(h_{11/2})^{12}(d_{3/2})^2$ (3)
0.360
0.604
$(h_{11/2})^{10}(d_{3/2})^4$ (4)
$(g_{7/2})^4$
$d_{5/2}$
C
$(h_{11/2})^{12}(d_{3/2})^2$ (5)
0.250
$(g_{7/2})^5$
${}^{80}_{55}Cs^{135}$

Fig. 41. Mixed neutron configurations in Cs^{135}, explaining the anomalous log *ft* value for the β-transition $A \rightarrow B$. Significant parts of the proton configurations are shown to the left and of of the neutron configurations to the right of the levels.

(Fig. 36) seems to be in disagreement with the level assignments $d_{3/2}$ of both the initial and final state. These assignments classify the β-transition as being of the allowed type. However, the log ft values of allowed β-transitions lie in the region around 5.0, between the limits 4.5 and 6.0. The discrepancy may be explained by assuming the presence of mixed nucleon configurations. In Fig. 41 are shown significant parts of the proton configurations to the left of the levels and neutron configurations to the right. The $d_{3/2}$ proton of level B is now assumed to interact with $d_{3/2}$ neutron pairs so that the neutron configuration (2) of Fig. 41 occurs together with the normal configuration (3). A β-transition A → B, ending in configuration (2), is very unlikely, since it involves a three particle transition. Therefore the total probability (and the log ft value) for the transition $A \to B$ depends on the population p_3 of the neutron configuration (3). Assuming a log ft value of 4.5–5.5 for a normal allowed transition would lead to $p_3 = 0.7 - 8\,\%$ from the experimental log ft value 6.6.

Similarly, the rather high log ft value 5.9 for the transition $A \to C$ may be explained. In this case the $d_{5/2}$ proton of the level C might stabilize the $d_{3/2}$ neutron pairs, so that the neutron configuration (4) of level C competes with (5). If this effect occurs, it would apparently be smaller than in the case of level B, that is, the relative population p_5 of configuration (5) would be higher than p_3.

b. Kr^{87}

The decay of Kr^{87} is of special interest, because the resulting nucleus, Rb^{87}, has the magic neutron number 50. The level scheme of this isotope might therefore be expected to be in accordance with the single particle model. However, it seems clear that the experimental data cannot be fitted to the level predictions $p_{1/2}$, $(f_{5/2})$ and $g_{9/2}$ of this model. Assuming that our decay scheme of Kr^{87} (Fig. 25) is essentially correct, we will try to find a reasonable interpretation of the excited levels in Rb^{87} and the excitation mechanism leading to these levels. The following anomalies are then to be explained:

1. The high excitation energies, especially of the third level.
2. The occurrence of an excited $^3/_2-$ level besides the $p_{3/2}$ ground state.
3. The apparent absence of a β-transition to the $p_{3/2}$ ground state, compared with the normal intensity of the corresponding β-transition to the excited $^3/_2-$ state.

We will now try to analyze the situation when the 51st neutron in Kr^{87} transforms to the 37th proton in Rb^{87}, using the experimental data as a guide in choosing between various alternatives. The significant part of the neutron configuration of ${}^{51}_{36}Kr^{87}$ is $(g_{9/2})^{10}$ $(g_{7/2})^1$, giving the ground state $g_{7/2}$, as deduced from β-data. As the ground state of ${}^{50}_{37}Rb^{87}$ is 3/2, its proton configuration would probably be $(f_{5/2})^6$ $(p_{3/2})^3$. The most likely proton configuration of Kr^{87} would then be $(f_{5/2})^6$ $(p_{3/2})^2$. Finally, the closed shell structure of the 50 neutrons in Rb^{87} is $(g_{9/2})^{10}$.

The discussion of the nucleon transition may be facilitated by means of the configuration shemes of Fig. 42. (a) and (b) representing the nucleon configurations of the ground states of Kr^{87} and Rb^{87} respectively.

If we assume that the β-transitions are due to one particle transitions, it is evident from Fig. 42 (a) and (b) that an $f_{5/2}$ state in Rb^{87} cannot be excited, if the proton configuration (a) really represents the ground state of Kr^{87}. *We are therefore forced*

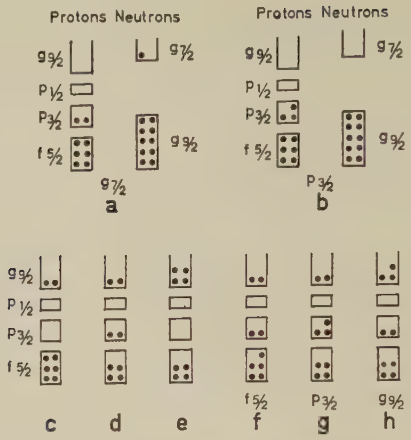

Fig. 42. Nucleon configurations in the Kr^{87} decay discussed in text.—*a*, Ground state of Kr^{87}; *b*, ground state of Rb^{87}; *c*, *d*, and *e*, proton configuration alternatives arising from the stabilization effect of the $g_{7/2}$ neutron on proton pairs in the $g_{9/2}$ shell; *f*, *g*, and *h*, tentative proton configurations of excited levels in Rb^{87}.

to assume a proton configuration of the ground state of Kr^{87} *with two protons lacking in the* $f_{5/2}$ *shell.* It would then be interesting to see, if the theory of DE SHALIT and GOLDHABER [D1, cf. p. 187] might be applied in this case. The odd $g_{7/2}$ neutron in Kr^{87} would then be expected to "stabilize" one or more proton pairs in the $g_{9/2}$ shell. Any of the proton configurations (*c*), (*d*) and (*e*) could then occur in the ground state of Kr^{87}. Without analyzing in detail here the other possibilities, we state that —assuming the configuration (*d*) to be predominant—it seems possible to explain the experimental data fairly well, whereas the other two alternatives do not fit all the data. (It seems indeed plausible that a "stabilization" of a proton pair from $f_{5/2}$ to $g_{9/2}$ is most likely, since it involves the smallest spin change.)

The particularly low intensity of the 4.2 Mev ground to ground state β-transition is now simply explained by the assumption that the population of the proton configuration (*a*) in the ground state of Kr^{87} is very low.

The configurations of three excited states $f_{5/2}$, $p_{3/2}$ and $g_{9/2}$ are shown in Fig. 42 (*f*), (*g*) and (*h*). They may be excited by a transformation of the $g_{7/2}$ neutron into a proton occupying either of the corresponding empty positions of configuration (*d*). We tentatively identify these configurations with the corresponding experimental energy levels in Rb^{87}. The γ-transitions $g_{9/2} \rightarrow p_{3/2}$ and $g_{9/2} \rightarrow f_{5/2}$ take place as single particle transitions. It might be argued that the $p_{3/2}$ configuration (*g*) does not correspond to the lowest $p_{3/2}$ state, since a proton-pair transition $p_{3/2} \rightarrow f_{5/2}$ (see Fig. 42, *g*) would give a $p_{3/2}$ state of lower energy. However, this level should be of lower energy than the $f_{5/2}$ level (cf. Fig. 42, *f* and *g*). We therefore conclude that the 0.847 Mev level rather corresponds to the configuration (*g*). In the same way one would also expect $g_{9/2}$ levels of lower energy, e.g. those corresponding to the proton configurations $(f_{5/2})^6$ $(g_{9/2})^3$ and $(f_{5/2})^6$ $(p_{3/2})^2$ $(g_{9/2})^1$. The energy of the latter would be ~ 2 Mev, since it differs from the 2.97 Mev level by the excitation energy $f_{5/2}$–$g_{9/2}$ of a proton pair (cf. below). The existence of such a level would perhaps not be inconsistent with the experimental data; it would mean that the 2.05 Mev and 0.847 Mev photolines in the Kr^{87} γ-spectrum were double. If this is true, the experimental intensity ratio between the 2.05 Mev γ-transition to the 0.847 Mev level and the 2.57 Mev γ-transition to the 0.403 Mev level would be still lower than given in Table 5, that is the experimental value $\gamma_{2.1}/\gamma_{2.57}$ would lie closer to the theoretical estimate for the $g_{9/2}$ alternative of Table 5. Moreover, a transition between the hypothetical 2.05 Mev level and the 0.847 Mev level would correspond to the γ-energy 1.20 Mev. As is seen from Fig. 20, there is really a peak at energy 1.20 Mev in the γ-spectrum of Kr^{87} (cf. also discussion on p. 165). The $g_{9/2}$ level corresponding to the configuration $(f_{5/2})^6\ (g_{9/2})^3$ would have an energy between 2 and 3 Mev. None of these two $g_{9/2}$ levels would be excited in significant intensity by a β-transition, because of the low population earlier assumed for the proton configurations (*a*) and (*c*) (Fig. 42) in the Kr^{87} ground state.

The normal intensity of the 3.3 Mev β-transition to the 0.847 Mev $p_{3/2}$ level implies that the population of the proton configuration (*d*) (Fig. 42) in the ground state of Kr^{87} is high, as was stated at the beginning of this discussion. The high excitation energies of the levels in Rb^{87} are an expected consequence of the excitation mechanism proposed here, since all of the levels are due to the excitation of both an odd particle and a proton pair or only a proton pair. A more detailed interpretation might give some information on the excitation energies of nucleon pairs. For example, the energy 0.847 kev of the $p_{3/2}$ level would correspond to the excitation energy of a proton pair in the transition $f_{5/2} \rightarrow g_{9/2}$.

According to the one particle model, a $p_{1/2}$ level would also occur in Rb^{87}. We have not found any evidence for the existence of such a level. This is in accordance with our interpretation above, since a β-transition from the $g_{7/2}$ ground state of Kr^{87} to a $p_{1/2}$ level in Rb^{87} would be highly forbidden. Moreover, γ-rays resulting from plausible transitions of any of the configurations (*f*), (*g*) and (*h*) of Fig. 42 to a configuration with an odd nucleon in a $p_{1/2}$ state would involve a comparatively high spin change. Such γ-transitions would therefore be of low intensity.

It is understood that the considerations above are very tentative, and therefore all excitation possibilities have not been discussed here. However, it seemed worth while to present this simple model here because of its apparent ability to explain the experimental level scheme of Rb^{87}, which does not seem to be in accordance with the extreme one particle shell model.

c. Kr^{77} and Kr^{79}

As was stated on pages 157 and 161, the decay schemes of Kr^{77} (Fig. 13) and Kr^{79} (Fig. 16) are more complex then can be accounted for by the extreme one particle model. Br^{79}, for example, has seven excited levels, while only three single particle excitations are predicted. The information about spin and parities of the experimentally determined levels in Br^{79} is very incomplete, but most of them probably have low spin values (p. 161). Although no detailed interpretation is possible at present, it might be plausible to assume the excited levels of Kr^{79} to be due to the excitation of nucleon pairs. If this interpretation is correct, the excitation of such levels might be explained analogously to the case of Kr^{87}. The proton configuration of the ground state of Kr^{79} would be $(f_{5/2})^6\ (p_{3/2})^2$ and the neutron configuration $(g_{9/2})^4\ (p_{1/2})$, according to the extreme one particle model. The $p_{1/2}$ neutron may now be assumed to interact with $p_{1/2}$ or $p_{3/2}$ proton pairs, so that the proton configurations $(f_{5/2})^6\ (p_{3/2})^0\ (p_{1/2})^2$, $(f_{5/2})^4\ (p_{3/2})^4$ and $(f_{5/2})^4\ (p_{3/2})^2\ (p_{1/2})^2$ are also present in the ground state of Kr^{79}. From these initial configurations, it is possible to derive six proton configurations (with one additional proton), corresponding to excited levels in Br^{79}. Of these levels, two would be $p_{1/2}$, two $p_{3/2}$ and two $f_{5/2}$.

The apparent similarity of the level schemes of Br^{77} and Br^{79} indicates that the same excitation mechanism may be working in both cases.

d. Kr^{88}, Rb^{88} and Cs^{138}

The interpretation of level schemes of even A nuclei is often highly complicated by the large number of coupling possibilities for the nucleons. This is especially the case for odd-odd nuclei with several excitation possibilities for the odd nucleons. Rb^{88} constitutes such an example, having 37 protons and 51 neutrons. The ground state may have the proton configuration $(f_{5/2})^6$ $(p_{3/2})^3$ and the neutron configuration $(g_{9/2})^{10}$ $(g_{7/2})$ (cf. Rb^{87}, p. 189). The odd proton may be excited in either of the empty $p_{1/2}$ or $g_{9/2}$ levels. Furthermore, an $f_{5/2}$ pair may be broken up and one of the protons paired to the odd $p_{3/2}$ proton, giving the excited proton configuration $(f_{5/2})^5$ $(p_{3/2})^4$. The odd neutron might be excited in any of the levels $g_{7/2}$, $d_{5/2}$, $d_{3/2}$, $s_{1/2}$, and $h_{11/2}$. It is evident that there are several resulting excited states. We notice that the only odd nucleon combination giving an 1+ state (the 2.40 Mev level of Rb^{88}, Fig. 33), is a $g_{9/2}$ proton together with a $g_{7/2}$ neutron. The nucleon configurations of this level might therefore be $(f_{5/2})^6$ $(p_{3/2})^2$ $(g_{9/2})$ (protons) and $(g_{9/2})^{10}$ $(g_{7/2})$ (neutrons).

In the case of Sr^{88}, we are dealing with an even-even nucleus with a closed neutron shell (50 neutrons, 38 protons). The excited states are therefore probably due entirely to proton excitations. The proton configuration of the ground state might be $(f_{5/2})^6$ $(p_{3/2})^4$. The first excited level is 2+ and the second one 3− (p. 173). We notice that the only possibility of obtaining an excited level of odd parity would be a combination of a $g_{9/2}$ term with a p or f term. Assuming that the intrinsic spins of the two odd particles are antiparallel, a 3− state would result only from the proton configuration $(p_{3/2})^3$ $(g_{9/2})$.

The decay scheme of Cs^{138} (Fig. 40) is only tentative and is therefore not discussed here. However, we note that the level scheme of Ba^{138} (82 neutrons, 56 protons) seems to be more complex than that of the other closed-shell nucleus Sr^{88}. Also in the case of Ba^{138}, the excited levels are probably due to proton excitations. The higher complexity of this scheme is to be expected, because there are more excitation possibilities for the protons of Ba^{138} than for the protons of Sr^{88}.

According to level statistics of even-even nuclei the energies of the first excited levels show pronounced maxima for closed shell nuclei [S 5, S8]. The excitation energies of the first levels of Sr^{88} (50 neutrons) and Ba^{138} (82 neutrons) are therefore expected to be high. Earlier decay data on these isotopes were considered to confirm this rule. (The first levels of Sr^{88} and Ba^{138} were reported to be 1.85 and 1.44 Mev respectively.) As shown in the present work, these data were incomplete. However, the new γ-transitions reported give no evidence for the existence of levels of lower energy than 1.85 and 1.44 Mev respectively.

Summary

The present investigation deals with the decay of 9.7 h Kr^{76}, 17.2 h Br^{76}, 73 min Kr^{77}, 34.5 h Kr^{79}, 4.4 h Kr^{85m}, 9.4 y Kr^{85}, 78 min Kr^{78}, 2.8 h Kr^{88}, 18 min Rb^{88}, 9.2 h Xe^{135}, 17 min Xe^{138}, and 32 min Cs^{138}. The disintegration of these isotopes has

Table 7. Summary of nuclear data reported in the present investigation and in the related works of refs. [T3] and [T4].

Data printed in italics have been reported before, but are in several cases measured with higher accuracy in the present work. In the second column are given mass numbers identified by electromagnetic isotope separation. All energy values are expressed in Mev. Bracketed figures after a γ-energy value give the experimental $K/(L+M)$ ratio of the γ-transition. The last column refers to the Figure of the present paper, showing the corresponding decay scheme discussed in text. The results of coincidence measurements are not included in the Table, but the presence of such results is indicated by the abbreviation coinc. in the sixth column.

Isotope	Mass number	Type of decay	Half life	β-particles	Gamma-radiations	Method of production	Decay scheme Fig.
Kr+ +Br	76	*EC*, β^+	*~11 h* *17.5 h* ~30h?		0.028, 0.093, 0.267, 0.316, 0.40, 0.560, 0.660, ~1.2 1.86	Br (p, 4n)	
Kr	77	*EC*, β^+ C/β^+ = 0.21 ± ± 0.1	*73 m*	1.86 61 % 1.67 32 % 0.85 7 %	0.0242, (~1.3), 0.1076, (3.6), 0,131, (~8), 0.149, (5), 0.246, 0.281, 0.313, 0.665, 0.870 Coinc.	Br (p, 3n)	13
Kr	*79*	*EC*, β^+ C/β^+ = 9.3 ± 2	*34.5 h*	*0,598* 93 % 0.33 7 %	*0.0445*, (7.2), 0.0840, (5?), 0.1361, (8.6), 0.1805, 0.2086, (6.9), 0.2173, (10.6), *0.2613*, (8.0), 0.2998, (10.8), 0.3069, (9.4), 0.3455, 0.3892, 0.3977, (10), 0.5259, 0.6064, (7.8), 0.8334 Coinc.	Br (d, 2n)	16
Kr	*85m*	β^-	*4.3 h*	*0.824 ± 0.008*	*0.1495, (6.2 ± 0.6)*	*fission U*	19
Kr	*85*	β^-	*9.4 y*	*0.149 0.7 %* *0.672 ± 0.007 99.3 %*	*0.517 ± 0.005*	*fission U*	19
Kr	*87*	β^-	*78 m*	3.8 65 % 3.3 ≤ 10 % 1.25 25 %	0.403, 0.847, 2.05, 2.57, $\gamma_1/\gamma_2/\gamma_3/\gamma_4 \sim 100/19/\leq 6/42$ Coinc.	*fission U*	25
Kr	*88*	β^-	*2.77 h*	2.7 20 % 0.9? ≤ 10 % *0.52* 70 %	0.028, (8), 0.166, 0191, 0.355, 0.845, 1.55, 2.2, 2.40 $\gamma_2/\gamma_3/\gamma_4/\gamma_5/\gamma_6/\gamma_7/\gamma_8 \sim \sim 20/100/14/65/40/\leq \leq 50/100$ Coinc.	*fission U*	33
Rb^{88}		β^-	*17.8 m*	*5.3* 77 % *3.5* 13 % 2.5 9 % 1.3* ~1 %*	*0.908*, *1.85*, 2.18, *2.76*, 4.2 $\gamma_1/\gamma_2/\gamma_3/\gamma_4/\gamma_5 \sim 60/100/4/\leq 10/0.2$	*decay* Kr^{88}	27

* Deduced from tentative decay scheme.

Table 8 (cont.)

Isotope	Mass number	Type of decay	Half life	β-particles	Gamma-radiations	Method of production	Decay scheme Fig.
Xe	*135*	β^-	*9.2 h*	*0.910* 97 % 0.548 ~ 3 %	*0.250*, 0.360, *0.604*, $\gamma_1/\gamma_2/\gamma_3 \sim 100/3/0.1$ Coinc.	*fission U*	36
Xe	*138*	β^-	*17 m*		0.42, 0.51, 1.78, 2.01 $\gamma_1/\gamma_2 \sim 10/2$	*fission U*	
Cs^{138}		β^-	*32 m*	*3.4* ~ 50 %* 2.4* ~ 25 %* 0.7* ~ 25 %*	0.128, *0.460*, 0.548, *0.980*, *1.44*, 2.24, 2.68, $\gamma_1/\gamma_2/\gamma_3/\gamma_4/\gamma_5/\gamma_6/\gamma_7 \sim$ 20/20/3/25/100/20/10	*decay* Xe^{138}	40

* Deduced from tentative decay scheme.

been studied by means of beta- and scintillation spectrometers, as well as γ-γ and β-γ coincidence spectrometers. The nuclear spectrometer equipment and the experimental techniques are briefly discussed in Chapter 1.

Most of the isotopes were produced by uranium fission. Others were successfully prepared by nuclear reactions not reported before. Thus Kr^{76} was produced by Br^{79} $(p, 4n)$, Kr^{77} by Br^{79} $(p, 3n)$, and Kr^{79} by Br^{79} $(d, 2n)$ reactions. β- and γ-samples were prepared by means of electromagnetic isotope separation. A discussion of the sample preparation technique appears in the preceding paper.

The new experimental data reported in this paper are collected in Table 7. Decay schemes of all isotopes, except Kr^{76}, Br^{76} and Xe^{138}, are discussed on the basis of available experimental data. (References are given in the last column of Table 7 to the figures showing decay schemes discussed.)

Those decay schemes which were considered sufficiently established have been compared with level predictions of nuclear shell theory. The extreme one particle model seems not to account completely for any of the decay schemes presented. However, by applying recent extensions of the one particle model, it seems possible to account qualitatively for most level schemes.

Nobel Institute of Physics, Stockholm 50, Sweden.

REFERENCES

A1. H. Atterling and G. Lindström, Nature *169*, 432 (1952).

B1. I. Bergström, S. Thulin, N. Svartholm, and K. Siegbahn, Arkiv f. fysik *1*, 281, (1949).

B2. I. Bergström and S. Thulin, Phys. Rev. *79*, 537 (1950).

B3. M. E. Bunker, L. M. Langer, and R. J. D. Moffat, Phys. Rev. *81*, 30 (1951).

B4. I. Bergström, Arkiv f. fysik *5*, 191 (1952).

B5. J. M. Blatt and V. F. Weisskopf, Theoretical Nuclear Physics. New York 1952.

B6. E. H. S. Burhop, The Auger Effect. Cambridge University Press, p. 48 (1952).

B7. I. Bergström, S. Thulin, B. Åström, A. H. Wapstra, and K. Nybö, Arkiv f. fysik *7*, 255 (1953).

B8. A. Bohr and B. R. Mottelson, Kgl. Danske Videnskab. Selskabs Mat.-fys. Meddel. *27*, No. 16 (1953).

B9. C. I. Borkowski and R. L. Clark, Rev. Sci. Instr. *24*, 1046 (1953).
C1. A. A. Caretto, Jr., and E. O. Wiig, Phys. Rev. *93*, 175 (1954).
D1. A. de Shalit and M. Goldhaber, Phys. Rev. *92*, 1211 (1953).
D2. A. de Shalit, O. Huber, and H. Schneider, Helv. Phys. Acta, *25*, 298 (1952).
F1. E. Feenberg and G. Trigg, Rev. Mod. Phys. *22*, 399 (1950).
F2. S. C. Fultz and M. L. Pool, Phys. Rev. *86*, 347 (1952).
F3. B. H. Flowers, The Nuclear Shell Model: O. R. Frisch, Progress in Nuclear Physics 2, London 1952.
G1. G. R. Gamertsfelder, Phys. Rev. *66*, 288 (1944).
G2. M. Goldhaber and A. W. Sunyar, Phys. Rev. *83*, 906 (1951).
G3. G. N. Glasoe and J. Steigman, Phys. Rev. *58*, 1 (1940).
G4. G. A. Graves, L. M. Langer, and R. D. Moffat, Phys. Rev. *88*, 344 (1952).
G5. O. Haxel, J. H. D. Jensen, and H. E. Suess, Ergebnisse der exakt. Naturwiss. *26*, 244 (1952).
G6. M. Goldhaber and R. D. Hill, Rev. Mod Phys. *24*, 179 (1952).
H1. O. Haxel, J. H. D. Jensen, and H. E. Suess, Phys. Rev. *75*, 1766 (1949).
H2. A. Hedgran, K. Siegbahn, and N. Svartholm, Proc. Phys. Soc. *63*, 960 (1950).
A. Hedgran, Arkiv f. fysik *5*, 1 (1952).
H3. J. M. Hollander, I. Perlman, and G. T. Seaborg, Rev. Mod. Phys. *25*, 469 (1953).
H4. N. P. Heydenburg and G. M. Temmer, Phys. Rev. *93*, 906 (1954).
L1. R. O. Lane and D. J. Zaffarano, Phys. Rev. *94*, 960 (1954).
L2. L. M. Langer, R. B. Duffield, and C. W. Stanley, Phys. Rev. *89*, 907 (1953).
M1. M. G. Mayer, Phys. Rev. *75*, 1969 (1949).
M2. M. G. Mayer, Phys. Rev. *78*, 22 (1950).
M3. S. A. Moszkowski, Phys. Rev. *82*, 35 (1951).
M4. M. G. Mayer, S. A. Mozkowski, and L. W. Nordheim, Rev. Mod. Phys. *23*, 315 (1951).
M5. F. R. Metzger and A. C. Amacher, Phys. Rev. *88*, 147 (1952).
M6. J. Moreau, Arkiv f. fysik *7*, 391 (1953).
M7. F. K. McGowan, Phys. Rev. *93*, 163 (1954).
N1. Nat. Bur. Stand.; Tables for the Analysis of Beta Spectra, AMS. 13, 1952.
N2. L. W. Nordheim, Phys. Rev. *78*, 294 (1950).
P1. W. C. Peacock and J. W. Jones, AECD-1812 (March 1948).
P2. M. H. L. Pryce, Proc. Phys. Soc. *A 65*, 773, 962 (1952).
P3. M. H. L. Pryce, Nuclear Shell Structure: A. C. Stickland, Reports on Progress in Physics XVII, London 1954.
R1. M. E. Rose, G. H. Goertzel, B. J. Spinrad, J. Harr, and P. Strong, Phys. Rev. *83*, 79 (1951).
S1. K. Siegbahn, Arkiv f. fysik *30 A*, No. 20 (1944).
S2. H. Slätis, and K. Siegbahn, Phys. Rev. *75*, 1955 (1949).
H. Slätis and K. Siegbahn, Arkiv f. fysik *1*, 339 (1949).
S3. F. B. Shull and E. Feenberg, Phys. Rev. *75*, 1768 (1949).
S4. A. W. Sunyar, J. W. Mihelich, G. Sharff-Goldhaber, M. Goldhaber, N. S. Wall, and M. Deutsch, Phys. Rev. *86*, 1023 (1952).
S5. G. Scharff-Goldhaber, Phys. Rev. *90*, 587 (1953).
S6. G. Scharff-Goldhaber and M. Mckeown, Phys. Rev. *95*, 613 (1954).
S7. R. Steffen, Phys. Rev. *91*, 443 (1953).
S8. P. Stähelin and P. Preiswerk, Il Nuovo Cimento *10*, 1219 (1953).
S9. J. B. Swan and R. D. Hill, Australian Journal of Physics, 6 *4*, 371 (1953).
T1. S. Thulin, I. Bergström and A. Hedgran, Phys. Rev. *76*, 871 (1949).
T2. S. Thulin, Phys. Rev. *87*, 684 (1952).
T3. S. Thulin, Arkiv f. fysik *4*, 363 (1952).
T4. S. Thulin, J. Moreau and H. Atterling, Arkiv f. fysik *8*, 229 (1954).
T5. S. Thulin, Phys. Rev. *94*, 734 (1954).
T6. G. M. Temmer, Carnegie Institution, Washington, private communication.
V1. J. Varma, B. L. Saraf, and W. B. Todd, Jr,. Phys. Rev. *91*, 484 (1953).
W1. L. L. Woodward, D. A. McCown, and M. L. Pool, Phys. Rev. *74*, 761 (1948).
Z1. H. Zeldes, B. H. Ketelle, and A. R. Brosi, Phys. Rev. *79*, 901 (1950).
Å1. B. Åström, Arkiv f. fysik *7*, 241 (1953).
Å2. B. Åström, unpublished.
Å3. B. Åström, A. H. Wapstra, S. Thulin, and I. Bergström, Arkiv f. fysik, *7*, 247 (1953).

Tryckt den 8 december 1954

Uppsala 1954. Almqvist & Wiksells Boktryckeri AB

ARKIV FÖR FYSIK Band 9 nr 12

Communicated 2 June 1954 by MANNE SIEGBAHN and ERIK HULTHÉN

Measurements of optical path gradients by means of birefringence interferences

By ERIK INGELSTAM

With 15 figures in the text

Part I. General and approximately linear gradients

1. Introduction, and methods of birefringence interferences

In order to measure optical path or phase gradients, several interferometric methods are possible. As a parallel to the phase contrast method especially worked out, with variation in one dimension only, in order to measure small gradients fairly accurately, the writer has tried to find a more direct method.

A phase gradient, which is equivalent to a wave front of vibrations of constant amplitude being inclined with respect to its straight direction perpendicular to the rays, is here assumed to vary only in one dimension, called x. The phase, called φ, or the corresponding path z, which is

$$z = -\frac{\lambda}{2\pi}\varphi = -\varphi/k \tag{1}$$

thus forms the gradient function considered here, $\partial z/\partial x$.

Referring to Figs. 1 a and b, this gradient may have its origin in a wedge-shaped transparent medium through which the monochromatic light has passed, or from reflection at planes which are not parallel. While the phase contrast method works thanks to the fact that we have large portions of the field of view outside the gradient, the present method can be applied also when the field contains only the details forming the gradient. Thus, as indicated in Fig. 1 c, a single break in the wave front can be examined, with reference to one side of the neighbouring field which is nominated as the phase-constant x axis.

For the two origins of a gradient, cases a and b, the path values are obviously:

$$\frac{\partial z}{\partial x} = z'(x) = (n-1)\frac{\partial h}{\partial x} \tag{2 a}$$

$$\frac{\partial z}{\partial x} = z'(x) = \operatorname{tg} 2v. \tag{2 b}$$

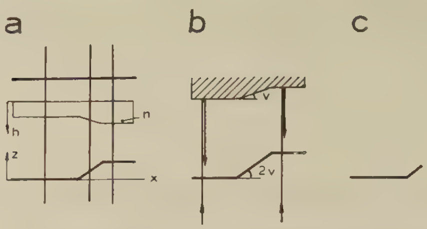

Fig. 1. Wave fronts containing gradients.

Often, as is assumed in the figure, the gradient is constant, and thus the phase is a linear function of x. In case b, this means that angles between reflecting plane parts of the specimen are considered. These are, of course, only special cases, as the gradients may have, and often have in practice, any shape as a function of x.

In 1868, JAMIN [1] drew attention to the possibility of utilizing the birefringence of calcite in such a way that the two rays emerging from a crystal are used as the two coherent rays of an interferometer, and thus a transparent specimen inserted in one of them changes the optical path. In order to bring the two rays together, a second equivalent calcite plate is used with such an orientation that the ordinary and extraordinary rays are interchanged. This is important, as no path difference must be introduced by the calcite plates themselves. The auxiliary components were nicols and a $\lambda/2$ plate, and, as may easily be shown, fringes of equal thickness result, or if a strictly plane parallel specimen is inserted, we have an intensity corresponding to its thickness. In spite of some technical difficulties in making the calcites, which with modern technique are easier to overcome, this interferometric technique is sometimes used, as recently by SCHOPPER [2].

LEBEDEFF [3], in 1930, made the important modification of using the birefringence interferences in microscopy, not letting the two rays be separated so far sideways as to let only one of them pass through the specimen, but by using relatively thin crystals (calcite or quartz) only displacing them a small amount and letting both of them go through the transparent specimen to be examined. JAMIN had already mentioned this possibility, and similar interferometers have been suggested. It is this method that we want to apply for the gradients of interest here, but with several modifications. This method, ideally, gives the gradient itself.[1]

In recent years, several constructors of interference microscopes, especially F. H. SMITH (Baker, London), have adopted more or less related constructions using birefringent plates or lenses as wave-splitting optical elements. The most direct continuation of LEBEDEFF's work, however, is that of FRANÇON [4, 5]. He has dimensioned the crystal plates so that, for microscopy, he obtains sensitive effects for objects having sizes near the resolving limit of the microscope, which makes it possible to incorporate the whole interferometric device in or at the eyepiece of the microscope. Further, he has combined the optical components, and in particular worked with white light and utilized the "sensitive colour" for obtaining good visual contrast.

---

[1] *Note added in proof:* My attention has been drawn to an earlier work of G. VALLET (Mém. serv. chim. de l'État *33*, 247, 1947), which, using calcites as a phase-differentiating device for measuring diffusion constants as done here in Part II, is based on much the same ideas. They mainly differ in the following respects, that V. uses differences of several wavelengths in optical path (here: below one), that V. measures on fringe positions in a Babinet compensator (here: photometric measurements on a rotatable ring) and that the arrangement of V. works with a fixed distance b (here: variable by change of magnification G, of use as treated in Sections 2 and 12).

It should be added that this technique is very closely related to that used in examining birefringence phenomena themselves, with very many applications.

2. Differentiating procedure

As starting point for our considerations, we examine gradients of all the types shown in Fig. 1 with very wide variations in $\partial z/\partial x$. In the case of Fig. 1 a, it may be the question of fixed plates as indicated there, but more likely of a liquid field with gradients on account of diffusion or the like, or an aerodynamic field, where gradients, more or less steep and often linear, occur at supersonic and subsonic velocities. The cases of Fig. 1 b are present also in practical cases, and in the testing of mirrors etc., but we had special interest in measuring angles in metallographic specimens of small extension, in the microscopic region. Common to all these aims is the need to obtain the interferometric accuracy necessary, with simple accessories.

We assume at first that the entrance slit of the collimator giving the initial plane wave fronts of Fig. 1 is of negligible width. This means that the wave fronts are strictly parallel.

In Fig. 2, the wave front having passed the specimen is seen to fall on the differentiating crystal double plate. This is the principle of the Savart polariscope, which has been treated extensively in theory by F. E. WRIGHT [6], the ordinary use of this unit being to detect or analyze polarization by viewing fringes of equal inclination. Here, this operation is of use when adjusting to phase-uniformity, but in this case this is not the main purpose of the unit. The double plate is traversed by strictly parallel light, and the doubling of the wave front in the x direction, which we will call b and which, on account of the equal thickness of the single plates and of the adjustment perpendicular to the wave front, does not introduce any phase shift between the two wave fronts, is determined by

$$b = \sqrt{2} \cdot e \cdot \frac{n_e^2 - n_0^2}{n_e^2 + n_0^2}, \tag{3}$$

where e is the thickness of each part of the double plate [4, 6].

The two wave fronts transmitted through the crystal double-plate, being polarized perpendicularly to one another, together form elliptically polarized light. It can be analysed by any of the classical methods, and our experiments result in a very simple device.

Irrespective of the analysing device, the information about the phase gradient function is due to the fact that the differentiating double plate can combine light from two adjacent parts of the gradient. At a coordinate x one of the rays has the path $z(x)$ and the second $z(x+b)$. The light vectors have (see Fig. 2) the values A_1 and A_2, which are independent of the phase shift angles but depend on orientations of polarizers and double plate, so far undetermined,

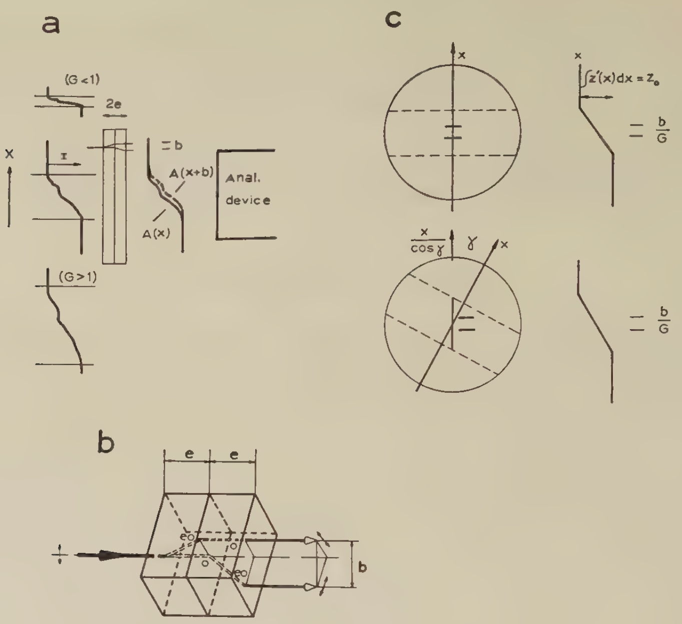

Fig. 2. *a*. Principle of differentiating plate. *b*. Detail showing the rays within the differentiating device: extraordinary-ordinary and ordinary-extraordinary rays. The arrows at the rays indicate polarization directions. *c*. Differentiating difference (see the text) in relation to the extent of the gradient strip, also including turning through an azimuth angle γ.

$$A\,(x) = A_1\,e^{ikz\,(x)}; \quad A\,(x+b) = A_2\,e^{ikz\,(x+b)}, \tag{4}$$

and the difference in phase is, expanded in series,

$$k\,z\,(x) - k\,z\,(x+b) = \varphi\,(x+b) - \varphi\,(x) = b \cdot \varphi'\,(x) + \frac{b^2}{2!}\,\varphi''\,(x) + \frac{b^3}{3!}\,\varphi'''\,(x) + \cdots \tag{5 a}$$

or, interrupting with the first term as residual,

$$= b\,\varphi'\,(x + r\,b) \qquad [0 < r < 1] \tag{5 b}$$

If b is small, the gradient value multiplied by b enters directly as a phase-turning angle in forming elliptically polarized light, and is thus capable of direct measurement.

So far, our treatment is only formally different from that of earlier writers. Contrary to them, we are in the following interested in keeping b low, as we want a measuring device for the gradients themselves. There are two important ways of varying the phase function given by the object so that a good measurement can be made even when retaining this condition of a small differential displacement b.

Three wave fronts before the differentiating plate are indicated in Fig. 2 a, differing as regards magnification (G) of the phase object. Instead of letting the direct wave front through the differentiator, a geometrical image of it can be used, magnified ($G > 1$) or reduced ($G < 1$). This possibility of variation was implicitely advised by FRANÇON [5] for gain of microscopic phase sensitivity. The undisturbed wave front through the crystal double plate should be plane, and it will be shown later, in Fig. 6, how this may be done in practice. The phase function, $z(x)$, is retained as always in imagery, but the gradient value is to be divided by G. The phase angle of (5 a), accordingly, is more generally written $[b/G] \cdot \varphi'(x)$.

A second efficient possibility of suiting accurate measurement applicable on linear gradients is used here, namely to vary the azimuth angle γ of the gradient with respect to the differentiating-analysing optical system. This can be done by rotating either the sample or the system mentioned, whichever is the more convenient technically. This last variation means that the two wave fronts to interfere pass the differentiating system obliquely, and that thus $\cos \gamma$ of the gradient value is subject to displacement.

Realizing this, it is possibly more instructive to consider how both these procedures affect the object itself, as they are directly observable and measurable in the image given by any of the experimental arrangements. From Fig. 2 c, which ought to be self-explanatory, it is seen that b/G is the apparent magnitude of the birefringence effect, and that in the second case this is still valid in the $x/\cos \gamma$ scale, but that the apparent magnitude in the x scale has the value $[b \cos \gamma/G]$.

We could generalize b in (5 a) and (5 b) introducing the generalized differentiating difference b_g as $b_g = b \cos \gamma/G$ when the variations of G and/or γ are of importance in the applications.

3. A $\lambda/2$ ring analyser as direct phase meter

As is well known, a great variety of devices are available for analysing fields containing elliptically polarized light and measuring phase differences causing the ellipticity [7]. Extensive and modern reviews have recently been given by JERRARD [8]. We have had access to a Soleil-Babinet compensator, which is useful for checking the much simpler components used in constructing the present apparatus.

In describing the procedures step by step, we anticipate a set-up that will be shown later in Fig. 6. The question here is to analyse what comes from the

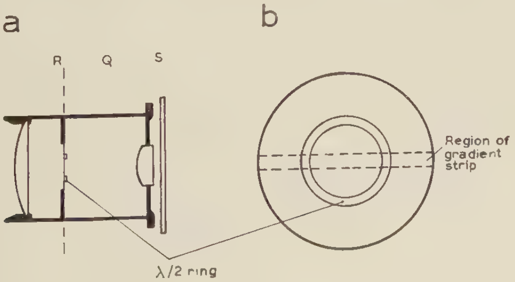

Fig. 3. *a*. Eyepiece Q with analysing $\lambda/2$ ring inserted in the plane R, and Polaroid screen S in fixed position. *b*. Field of view; the eyepiece is turned so that the intensity of the ring should equal that of the gradient region (except for the crossing areas).

double plate, Fig. 2, and L, Fig. 6. The object plane and the planes conjugate to it are marked by dotted lines in Fig. 6. The analysing device finally used consists mainly of a turnable $\lambda/2$ ring inserted in a conjugate plane, here the focal plane of the eye lens of the eyepiece, and a Polaroid sheet S, as shown in Fig. 3 a. The field of view is shown in Fig. 3 b. The Polaroid sheet S is always kept crossed with respect to the polarizer (K in Fig. 6), which is situated anywhere in front of the differentiating plate. This plate itself is always adjusted so that its vibration directions are in 45° with the polarizer, which means that the two rays, the ordinary-extraordinary and the extraordinary-ordinary, have equal intensity, which is to be preferred in order to have maximum constructive or destructive interference.

a. Intensity variation of gradient strip with $\varphi'(x)$. If we normalize the first amplitude of light vibration, before the differentiating plate, to $A\sqrt{2}$, we have for the final amplitudes A_1 and A_2, being their components outside the gradient

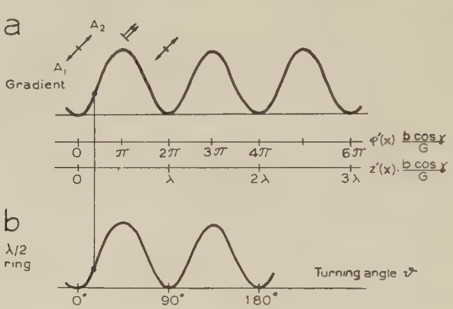

Fig. 4. Evaluation principle using the $\lambda/2$ ring. Two intensities of "flat fields" are set equal (vertical line).

$A_1 = -A_2 = A$, and the field for $\varphi'(x)$ is dark on account of destructive interference. Within the gradient we have a light amount, which, as emerging from the two parts of the image dealt with in (4), is found to be

$$I = 2\,A^2 \sin^2 \frac{b\cdot\varphi'(x)}{2}\,. \tag{6}$$

This function is of course an ordinary interference variation, but it could be of some value to give it also in the evident form of Fig. 4 a. The interfering vector positions are outlined, and scales given in $\varphi'(x)$ and $z'(x)$ for convenience. The differentiating device has transformed a phase gradient to an intensity value. On taking out only the first of the terms of (5 a), we have neglected higher derivatives, and for a constant value of the gradient, giving constant intensity over the strip, not considered border effects.

b. Evaluation intensity. The most direct way of measuring an unknown set of values of any kind, ξ, from an experimentally accessible function $\eta = \eta(\xi)$, is of course to reproduce the *same* function with a known set of values (evaluation values), say ζ, thus realizing the function $\eta = \eta(c \cdot \zeta)$, and to adjust ζ for equal η. In such a case, the unknown set of values are given directly by the evaluation values: $\xi = c \cdot \zeta$, the proper scale factor c being known from the way the functions were constructed.

This is a convenient method when polarized light is present, as intensity functions ($I = \eta$) are of the same sinusoidal shape. If a $\lambda/2$ plate is superimposed on the background of the field, before the light enters the second polarizer, we introduce such an intensity function. Every time the axis of the $\lambda/2$ ring coincides with either the first or the second polarizer here (K and S), its area is dark, and if ϑ denotes the angle of rotation counted from it, the intensity function is

$$I = 2A^2 \sin^2 2\vartheta. \tag{7}$$

Fig. 4 b shows the congruent evaluation curve and how a reading of angle ϑ directly gives the phase. We have, combining (6) and (7) and taking the generalized differentiating factor,

$$\varphi'(x) \cdot \frac{b \cos \gamma}{G} = 4\vartheta \tag{8 a}$$

which shows that 4ϑ directly is the transferred phase value, or, expressing it in degrees, denoted ϑ°, and taking the dimensionless slope value

$$z'(x) \cdot \frac{b \cos \gamma}{G} = \frac{\vartheta^\circ}{90} \cdot \lambda. \tag{8 b}$$

4. Dependence on *b* of the phase function obtained

As shown in (5), we produce by this method a first-difference ratio of the phase function, namely $[\varphi(x+b) - \varphi(x)]/b_g$, and we aim at the first-derivative $\varphi'(x)$. This differentiating method thus is approximate in so far as it neglects the higher derivatives.

For the exactly straight gradients, such as of the shape shown in Fig. 1, we have disturbances only where the first derivative has discontinuities (compare Eq. 5 b). As should be obvious from Fig. 5, the resulting phase function has rising and falling regions bordering to the "corners". If the gradient has a more general shape, depicted in the second column, the real curves can be traced graphically for a certain assumed value of b_g. As is also directly obvious, the largest deviations in shape are obtained near the maxima or minima of the gradient, where $\varphi''(x)$ goes through zero points. The corresponding maxima or minima are flattened out, and discontinuities, (which, of course, are never really present for physical reasons), appear as slopes. For the important case of a distribution of phases according to a Gaussian function, as in a diffusion field, the question will be treated in detail in Part II.

It is important also to consider the real intensity distribution across the field in the measurement chosen here, as shown in the last line of Fig. 5. The bordering slopes are greatly reduced near the zero axis on account of the $\sin^2$ function for the intensity. The disturbances at variations in the non-linear

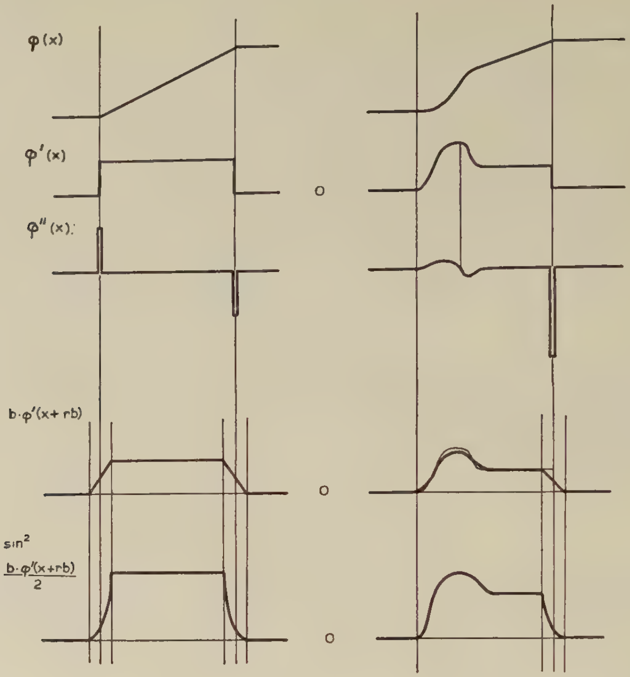

Fig. 5. Influence of finite width of b, or b_g in general. The narrow line of fourth figure second column represents the ideal curve (that of $\varphi'(x)$), the main line the real curve, as in all other cases.

gradient to be examined (second column, compare also fourth figure) have on the other hand an importance which is fairly proportional to $\varphi'(x)$ when, as convenient, one prefers to measure the intensity at the approximately linear parts of the sinusoidal intensity function, Fig. 4 a.

In summary, the method is the more true the smaller b/G is compared to the extent of the gradient curve or gradient details to be examined, and this ratio and especially $\cos\gamma$ should be chosen accordingly. If a detail of a gradient to be measured is linear and has the width w, we are quite safe that the phase in the centre will be true if

$$b_g = \frac{b\cos\gamma}{G} < w. \tag{9}$$

This demand is of course much too severe if it deals with finding out the detailed shape of an approximately straight phase curve, and when more than half a wavelength is inherent in the total phase decrement of the gradient, it is possible to go by means of successive approximations in changing γ, or have estimates of the upper limits of the error.

5. Additional experimental influences

a. Influence of finite entrance slit width. The slit, still assumed to be illuminated with monochromatic light, should have a finite width, compromising between intensity and detoriating influence on the exact phase conditions. An increase of slit width means oblique rays through the birefringent plates, and the exact treatment of these problems in crystal plates of the type used here is tedious. If the slit width is equal to b, (the scale magnification imaging the slit D by means of H (Fig. 6) taken to unity), the rays from either edge of the entrance slit make the same angle as the rays of the extraordinary wave with the ordinary wave, which means that the influences are of the same order.

This may, abstaining from a complicated integration, hold as a rule: the slit width must not exceed b, and this is in fact a severe limitation in some cases, as those of Section 7, or, rather, a limit of accessible light intensity. Variation of the slit width experimentally has definitively confirmed this fact.

b. Non-ideal polarizers. When aiming at great accuracy in applying (7), the deviations of the Polaroid sheets from the ordinary simple assumptions must of course be taken into account, by making a calibration.

c. Imperfections of the $\lambda/2$ ring. An inconvenience of plates with thicknesses fixed in respect to a wavelength, as a $\lambda/2$ plate, is that they apply only to that special wavelength. The results must accordingly be corrected when they are used for other wavelengths, if they can be used at all. In this application, an erroneous phase shift means that the amplitude variation seen in Fig. 4 b is smaller than for the ideal case, and thus the maxima and minima are changed. This should also be paid attention to in checking the apparatus. Here, a cellulose acetate sheet was used for the ring, which was fairly accurate for 5461 A light. The minima however (which could be positioned very accurately) were not quite 90° apart (see Table 2 later), which should be due to a disorientation of the optic axis within the streched sheet. The readings were always taken on both slopes bordering a minimum, and in the average no influence at all enters from this imperfection.

6. Monochromatic and "sensitive colour" interferences

In order to increase visual contrast, and also with the aim of measuring phases by means of colour matching, FRANÇON has, mainly for microscopy, worked with white light and, using a technique familiar from other branches of interferometry, attenuated the yellow colour at 5600 A by a $\lambda/2$ plate inserted behind the double crystal plate so that destructive interference is obtained for this wavelength. The phase-even field stands out in the sensitive redviolet colour, and phase differences appear as differences in hue.

Parallel to the measurements with monochromatic light, we have also used this method. This was easily done by arranging a tungsten lamp so that its light was projected onto the entrance slit instead of the light from the mercury lamp and monochromator. The only further change is that a mica $\lambda/2$ plate for 5600 A is inserted after the differentiating plate. The results of this comparison will be given below.

On changing between the two types of interferences, and also for making adjustments before each experiment, it is necessary that the double crystal plate be tiltable with precision about an axis which is parallel to the entrance slit: in this way any desired change of phase between the two interfering bundles can be introduced. This is the procedure for adjusting to the sensitive colour. If the $\lambda/2$ plate is not removed on changing from coloured interferences to those of monochromatic type, we obtain nearly the case of destructive interference on account of the small difference between 5600 and 5461 A.

7. Some technical details of an arrangement for macroscopic gradients

Fig. 6 gives the essentials of the set-up and need not to be described in detail, except for the parts requiring careful dimensioning and adjustment. Entrance slit *D* is the transparent part of a glass plate aluminized by evaporation except for the part masked by a tungsten wire: it was ordinarily 45 microns wide. *K* and *S* are Polaroid screens of the modern type which are very dense in the crossed position; the more transparent types give background light equivalent to stray light. The parts *K* and *L* are joined in a unit with a micrometer adjustment for the angle of tilt and separate rotations read by indices on a common scale. Parts *J–S* are seen in the photograph Fig. 7.

As differentiating crystal plates *L*, the following are available for various measuring regions of gradients:

Material	Half-thickness e (mm)	Birefringence displacement b (microns)
1. Calcite	5.0	790
2. Calcite	2.0	305
3. Quartz	10.0	82.8
4. Quartz	3.20	26.5
5. Quartz	2.0	16.0
6. Quartz	1.0	8.0

The first two were prepared by Bernh. Halle Nachfolger, those of quartz by Steeg & Reuter, all of excellent quality. Quartz is of course to be preferred on account of its durability if the larger thickness is not an inconvenience when choosing the other dimension.

The magnification of the microscope with the analysing eyepiece should be chosen so that the extension of the gradients fits the ring (Fig. 3 b) which serves as reference. As is obvious from the figure, all adjustments are simple, and if the method is used for routine work the following parts may be made rapidly interchangeable if placed in a revolving device: *J*, *L* (interdependent, only one of them needing to be changed in general), *M*, and the eyepiece of the microscope.

As strict parallelity is necessary in the wave fronts traversing the crystal plate, the entrance slit (or the lens system *H*) is adjusted in position by means of a telescope set to infinity mounted in place of the microscope.

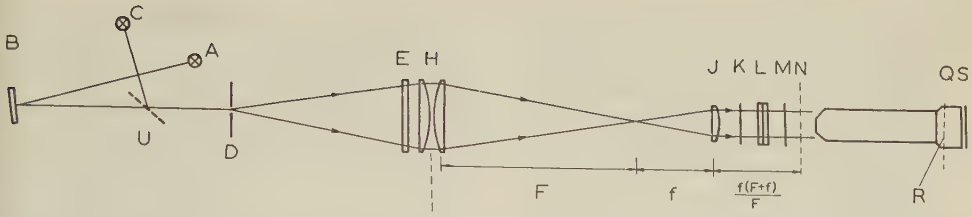

Fig. 6. Schematic outline of macroscopic set-up. *A*, mercury lamp; *B*, grating providing the monochromator dispersion; *C*, tungsten band lamp followed by mirror *U*; *D*, entrance slit (lenses before *D* not shown); *E*, specimen under test (may as well, or in some applications better, be symmetrically placed within lens system *H*); *H*, lens system; *J*, collimating lens; $(K+L)$ differentiating unit; *K*, Polaroid sheet; *L*, crystal double plate; *M*, $\lambda/2$ plate which may alternatively be inserted; *N*, plane conjugate to *E* or *H*; *Q*, analysing eyepiece containing *R*, $\lambda/2$ ring (see Fig. 3 a); *S*, Polaroid sheet in fixed position. All reading scales omitted.

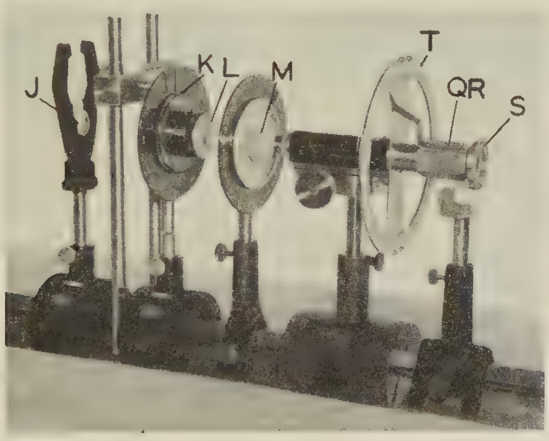

Fig. 7. Last part of the set-up outlined in Fig. 6. Same notation; *T*, reading scale of the $\lambda/2$ eyepiece.

8. Measurements of approximately straight gradients

In order to make an extensive test of the possibilities of the method, two different fixed-gradient specimens denoted *A* and *E* were used, inserted at *E*, Fig. 6. As it was advisable to change the azimuth angle γ, the specimens were mounted in a turning device made from a ball-bearing. The specimens were the same as those used for examination with phase contrast, as reported elsewhere [20], and consisted of glass plates of which one half was coated with magnesium fluoride. The total path difference between the two halves were: for gradient *A* 222 mμ and for gradient *E* 57 mμ, as measured by multiple-beam interferences on afterwards silvered parts. By means of this mapping with interferences (which is suitable in this case, but not in others, where this method is of the greatest importance, see Part II), detailed knowledge of the gradients at the borders between the two halves was obtained. The mapping of the whole gradient $z(x)$ is represented in the curves Fig. 8 and 9.

Table 1. Results of the measurements on gradients *A* and *E*. The values in brackets should not be approved, as b_g is near to its limit value, Eq. (9). Magnification 0.120 ± 0.000.

Sequence	Object	Data	γ	ϑ	$\frac{\vartheta}{\cos\gamma}$	$z'(x)$	$z'(x)$ measured from multiple-beam interferograms
1	*A*	Hg 5461, $e = 10.0$, without $\lambda/2$ plate	0°	(36°)	(36°)		*A:* For measurements of the slopes, see Fig. 8, especially the construction lines with different inclination. Average slope 1.85×10^{-4} Maximum slope, in centre 2.50×10^{-4} Flat part at one of the flanks 1.27×10^{-4}
			15°	30.0°	31.2°	2.74×10^{-4}	
			30°	28.0°	31.4°	2.76×10^{-4}	
			45°	18.0°	25.5°	2.24×10^{-4}	
			60°	9°	18°		
2	*A*	Hg 5461, $e = 10.0$, with $\lambda/2$ plate for 5600	0°	(33°)			
			15°	28.0°	29.0°	2.55×10^{-4}	
			30°	24.0°	27.9°	2.45×10^{-4}	
			45°	19.0°	27.0°	2.37×10^{-4}	
			60°	(too near stray light level)			
3	*A*	Hg 5461, $e = 3.2$, with $\lambda/2$ plate for 5600	0°	10.5°	10.5°	2.08×10^{-4}	
				11.2°	11.2°	2.21×10^{-4}	
			180°	12.4°	12.4°	2.45×10^{-4}	
				9.8°	9.8°	1.94×10^{-4}	
4	*A*	White, 3.2, $\lambda/2$ plate, sensitive colour	0° (brownish red)	10.7°	10.7°	2.12×10^{-4}	
			180° (azur blue)	10.7°	10.7°	2.12×10^{-4}	
5	*E*	Hg 5461 $e = 3.2$	0°	4°	4°	0.79×10^{-4}	*E:* Average slope, see Fig. 9 0.52×10^{-4} Maximum slope 0.70×10^{-4}
6	*E*	White $e = 3.2$	0°	5.7°	5.7°	1.12×10^{-4}	
			180°	6.2°	6.2°	1.23×10^{-4}	

The magnification *G* used for these measurements was fixed at the value given in Table 1. We aimed at examining the accuracy of the method, and *G* and *e* were thus chosen accordingly. The quartz crystal plates of $e = 10.0$ and 3.2 were both used. The important condition for b_g was further tested by inserting a second differentiating crystal plate of negligible *e* compared to the main one between *Q* and *S* Fig. 6, thereby producing fringes of equal gradient values [5], which were photographed. They give, although in this case with very low accuracy, the curves No. 4 of Fig. 5 directly. Fairly flat tops resulted in all these cases.

The maximum gradient value is obtained for $\gamma = 0°$ (or $= 180°$, the appearance of the fields being the same for monochromatic light in this case, but for white light the colour of the gradient changes to the opposite side of the sensitive colour), and for the two gradients we are on the rise of the first order interference curve, thus between 0° and 45° of ϑ of Fig. 4. The double plate is

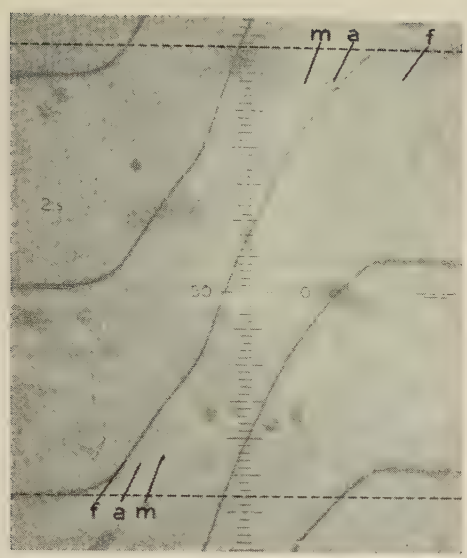

Fig. 8.

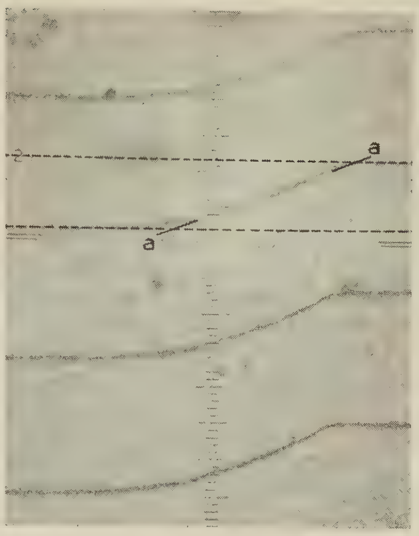

Fig. 9.

Fig. 8. Multiple-beam interferograms of specimen A; see the text, a = end of straight lines approximating average slope, m = maximum slope, f = slope of a flat portion. x scale (along the dotted lines) is 1 mm = 25 scale divisions of height scale. Fig. 9. Corresponding interferogram of specimen E.

adjusted through tilting, and, it wanted, we check that the first order of interference in the crystal plate is present by looking (behind L of Fig. 7) at the Savart fringes in white light, seeing the slit at the same time (it should fall near zeroth order fringe). In this way, the background value, $I = 0$, for $\varphi'(x) = 0$, or, the sensitive colour, for white light, is obtained for all parts except for the gradient. The measurements are made by turning the eyepiece, as already indicated. The same procedure is repeated for other values of γ, the requirements at b_g being better fulfilled.

a. Monochromatic light 5461 A. The settings of the ring are astonishingly reproducible. In general, all eight settings of a turn were used, although two are sufficient. The minimum points may be set with an average deviation of less than 1° in ϑ, and the measuring points generally to within 2°.

Table 1 shows all the values obtained in the various measurements. From Eq. (6) and (7) we realize that the best measurements are made at about 22.5°. However, the low values for the plates $e = 3.2$ mm, especially at E, were of interest as the measured gradient is very low and we have a comparison of the two methods of monochromatic and sensitive-colour measurements in this region.

A deviation of $\pm 2°$ in ϑ makes, regarding (8 b), for the differentiated path function, $\pm 0.04\,\lambda$, and an absolute uncertainty in $z'(x)$, of $\pm 0.18 \cdot 10^{-4}$. The possible greater deviations between individual values of $z'(x)$ in Table 1 on the same object for white light should indicate either that bordering effects have disturbed the visual judgement, or, that the gradient has been as far from being linear that the intensity is not uniform enough within the measuring accuracy. The former reason should hold for sequence 1, where b_g is about 20 %, falling with γ, which is confirmed by the tendency of the values. The later reason is the main cause of the variation: it belongs to the object, the slope of which varies in most of its region with about three times the limits of accuracy of measurement just given according to the multiple-interference mappings. The agreement is, as seen in the last two columns of the table, satisfactory.

These deviations being random, it is of greater interest to judge if greater systematical errors of the type indicated in Section 5 b and c are present. A systematic photographic-photometric test run was thus made in order to find out how the maxima ($\vartheta = 45°$) and minima ($\vartheta = 0°, 90°$) and some intermediate values of the intensity transmitted through the rotated ring onto a phase-even field agree with the theoretical values. The result was: (a) that for crossed Polaroids as used here the intensities were those predetermined (measured in respect to the background) within a limit not giving rise to inaccuracies above 1° in ϑ, but (b) that when the background is light, the presence of stray light may falsify the results. For the measurements reported here under Parts I and II, this means no correction. If for any other more qualified purpose stray light ought to be reduced, many parts of the differentiating and analysing devices can be cemented together to avoid reflexions, and polarizing equipment improved.

Table 2. Example of readings, in degrees, for the values given in Table 1, first sequence, object A, $\gamma = 30°$.

h	*a*	*b*	*c*	*d*	*e*	*f*	*g*
31	88	120	170	197	265	299	346
31	102	123	170	194	262	301	345
27	98	124	167	201	264	295	350
28	99	123	168	201	263	299	349
30	85	122	169	205	265	303	355
29	94	122	169	200	264	299	349

Minima 57.0 145.0 237.0 324.0
(readings not
given here) (0) (88.0) (180.0) (267.0)

$8\vartheta = (a+c+e+g) - (b+d+f+h)$; $\vartheta = 28.0°$

b. White light. It was of great interest to examine the possibilities of making parallel measurements with sequences 1 and 2 of the table, as for these large phases colours are very far from the sensitive region, namely yellow at one side and bluish-pale green at the other side of phases (for γ in the first or second quadrant). When matching equal hues, it also showed that this is more uncertain the more the phase-indicating colours differ from the violet-purple sensitive region. This has two reasons, one systematical and one of more instrumental type. The systematical reason is the well-known fact that the eye's ability to judge equal hues is much inferior in these colour regions [9]. The cond is that slightly different dispersion of birefringence in mica and in the llulose acetate sheet enters, being shown as a trend to asymmetry of the z' lues, because the hues of the field of the ring and that of the gradient cannot brought to coincide. This suggests choosing exactly the same material for th $\lambda/2$ details, most conveniently those now available as plastic sheets with eatly variable dispersion properties [10].

The closer, however, we approach $\vartheta = 0$, the better the circumstances, which is nfirmed by a comparison of sequences 3 and 4. At sequences 5 and 6, the uch better reproducibility of the coloured field of 6 is prominent, but a systemical deviation due to stray light (less colour saturation) is detectable. In this gion of low ϑ values we could claim the same accuracy for the coloured interrences (sequence 6), namely $\pm 0.04\,\lambda$ in our set-up as stated for the monoromatic interference method applicable at all the approximately straight regions the successive interference variations according to Fig. 4 a.

c. Comparison. On making this comparison between monochromatic birefrinnce interferences and coloured interferences, with reference to their suitability r measuring phases, it is clear that monochromatic interferences are especially nvenient for precise measurements (as always in interferometry using intensities) nere the slopes of curves such as those in Fig. 4 a are great, which is the ct on the major part of the periodical function (except for the maxima and e minima). The lower precision obtained in the maxima or minima when ing monochromatic light is complemented by the coloured interferences, utiing a special physiological property of the eye, which is of course a very fferent phenomenon. As already stated, the good information obtainable by eans of this fortunate circumstance is only restricted to a very limited scale hue, corresponding to about $\lambda/10$ of a path difference at either side. We ve found the accuracy of measurement by coloured interferences in this reon to be about $\lambda/25$; FRANÇON has estimated from the literature that $\lambda/1000$ uld be detected using the best field shapes of "flat" colour. These statements e not contradictory, as the accuracy obtainable is dependent on the shape d size of the objects and also colour saturation.

9. Angles in metallographic specimens

An interesting method is to combine the variation of azimuth γ indicated re with the use of the method at very high magnification. This should make possible to measure directly the angles between flat portions of a specimen, ese angles extending to the order of several degrees, which is quite another ler of magnitude, $z'(x) \sim 0.1$, than those previously examined.

In practice, following closely the ideas of FRANÇON [4], this is done by inporating the whole device in the eyepiece. We had at our disposal a Vickers ojection Microscope, and a differentiating eyepiece is constructed as shown Fig. 10, the details of which may be understood by the legend of the figure, ntaining the same notation as before. Here also a $\lambda/2$ ring was present, and same procedure as before could be used for equalizing intensities.

The angle in the specimen, v, Eq. (2 b), could however be directly read by ans of varying γ, so that the gradients show maximum or minimum of insity. In the combination of (2 b) and (8 b) with $\vartheta^\circ = k \cdot 45$ we thus have a relation between γ and v only, so that $\operatorname{tg} 2v$ is equal to an apparatus constant times a whole number of $1/\cos\gamma$. To achieve this, the metallic specimen is placed directly on the rotating stage of the microscope which is provided with a good azimuth scale, adjusted in relation to the differentiating unit, and turned round till the eye judges the image of the gradient to be maximally light or dark. As test objects, we have so far used very narrow (between 1 and 10 microns wide) grooves in a flat-polished surface of stainless steel, these grooves being pressed or cut by a diamond.

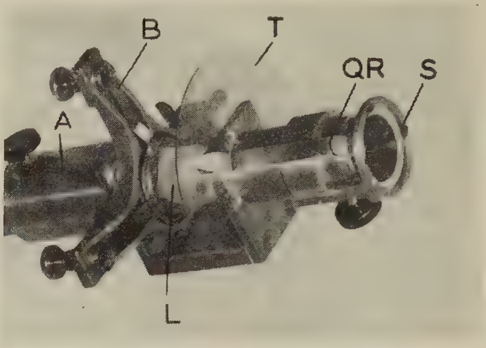

Fig. 10. Auxiliary parts forming a special differentiating eyepiece for the Vickers Microscope: *A*, ring to be fixed in a position which fits the optic axis directions of *L*. Collimating lens is situated inside *A* and adjusted with parts *Q R S* removed. Polarizing sheet is also inside *A* fixed in respect to *A*. *L*, differentiating plate; *B*, tilting device for the adjustment of *L*; *Q*, *R*, eyepiece with turnable $\lambda/2$ ring (not used when only azimuths are varied); *T*, scale of the $\lambda/2$ ring; *S*, Polaroid sheet.

Although the principle is simple, we must be aware of the complications which may arise for large angles of metallic reflexion, and in approaching the interesting region near the resolving power. The parts of a traced groove and still more those of a natural metallographic specimen may consist of differently reflecting and polarizing materials, and accordingly the surface should be coated e.g. with silver in order to secure an amplitude-uniform gradient. The domain of angles v is limited upwards by the need of large apertures of the microscope objective, which have aberrations influencing the interfering wavefronts, and for still larger angles by metallic polarization effects.

The settings on a maximum or a minimum are easily performed and reproducible. Accuracies of about 1° in angle for angles v of the order of 10° can be reached with certainty, but more experience must be gained with the instrument before the ultimate accuracy can be stated. As is well known, these measurements of angles between planes of only a few microns extent are also a difficult problem with Fizeau interferometry, using fringes of multiple reflection, or twobeam interferences. The present method has transformed the measurements to "flat field" interferometry, which simplifies the problem.

Summary of Part I

The factors entering into practical measurements of one-dimensional path gradients by means of birefringence interferences (using calcite or quartz) are examined. The arrangement used is in effect a phase-differentiating device, and special attention is paid to the influence of the amount of displacement of the two interfering beams due to the presence of higher derivatives in the phase gradient. This factor can be favourably modified mainly by variation of the azimuth angle of the specimen under test in relation to the analysing optical device. A special direct phase meter using a rotatable $\lambda/2$ ring has been constructed. The procedures are applied for (a) gradients in transparent specimens, and (b) angles between metallographical surfaces, which in this case can be obtained directly from a single azimuth measurement.

References, see end of Part II.

Part II. Liquid gradients, in particular determination of diffusion constants

10. Detailed treatment of application to a gradient following Fick's diffusion law

It is of special interest to examine in more detail the application of this differentiating interference method to gradients following the Gaussian error curve which is the natural shape given by the differential equation for diffusion. This application is suited to the method as it gives directly with considerable accuracy the derivative of the concentration function, which is often required.

The limitation in accuracy from the theoretical point of view lies in the fact treated in Section 4, namely, that the method gives, not directly the first derivative, but the first difference, and this includes some higher derivatives. If the function to be studied is mathematically known, these higher derivatives can of course be calculated and thus their influence can be corrected for if suitable dimensions are chosen.

We write the well-known Fick's diffusion law, also known in mathematics as the differential equation of Laplace, in the one-dimensional form, c being the concentration and D the diffusion constant:

$$\frac{\partial c}{\partial t} = D \frac{\partial^2 c}{\partial x^2} \cdot \tag{11}$$

Assuming the refractive index to be proportional to the concentration, $n = r \cdot c$, which is always valid within the accuracy required here, and thus the equation will be expressed in terms of the index n instead of c. As, further, the optical path z of a ray within a plane parallel cell of thickness a, for a monochromatic ray of air wavelength λ, is the same function of x as of c and n:

$$z(x) = n_\lambda (x) \cdot a, \tag{12}$$

the diffusion law can, if desired, also be expressed in terms of path differences:

$$\frac{\partial z}{\partial t} = D \frac{\partial^2 z}{\partial x^2} \cdot \tag{13}$$

The validity of (13), or (11), assumes that D be independent of the concentration, which in special cases should be very carefully considered, as this is a physical-chemical question. If this is not the case, the right member of (11) is modified, as $D = D(c)$ and an additional term $\frac{dD}{dc}\left(\frac{\partial c}{\partial x}\right)^2$ enters. For the solution of the unmodified (11), the boundary conditions further are such that the concentration function is assumed to take its asymptotical values at both sides of the gradient irrespective of surfaces and other neighbouring gradients; yet, slight deviations from the exact fulfilment of these conditions have only a negligible influence on the solution in the centre of the function. If $x = 0$ is taken at the centre of the gradient, the solution is

$$z(x) = \frac{z_0}{2}\left(1 + \frac{1}{\sqrt{\pi D t}}\int_0^x e^{-\frac{\xi^2}{4Dt}}\,d\xi\right), \tag{14}$$

and the derivative of the gradient is

$$\frac{dz(x)}{dx} = \frac{z_0}{2}\cdot\frac{1}{\sqrt{\pi D t}}\cdot e^{-\left(\frac{x}{\sqrt{4Dt}}\right)^2}. \tag{15}$$

It is convenient, in order to use the same notation of light vibration phases as in Section 4, to multiply both sides of equations (12)–(15) by $-k = -2\pi/\lambda$, so that φ may replace z, as in Equation (5).

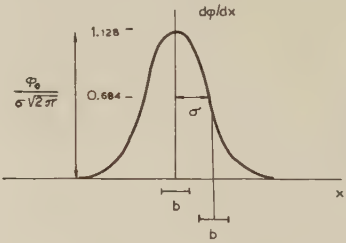

Fig. 11. Gaussian curve as obtained from a diffusion boundary. The two b regions are for the two procedures: at the top and at the slope, compare Sections 11 and 12.

When examining the correction to the registration or measurement of the derivative as found by our method, it is useful to denote a specific characteristic x value of the function (15) by a symbol directly comparable with the b value of the birefringence: let us take the inflexion point of the Gaussian error curve and denote it by σ:

$$\sigma = \sqrt{2Dt}. \tag{16}$$

As shown in Fig. 11, the height of the curve is also determined by this quantity, and the total decrement of phase, and the equation takes the formally simpler shape

$$\varphi'(x) = \varphi_0\frac{1}{\sigma\sqrt{2\pi}}\cdot e^{-\frac{x^2}{2\sigma^2}}. \tag{17}$$

The phase angle φ_0 is here equivalent to z_0 in Eq. (14) or to the corresponding concentration c_0, the total phase increment (or decrement) of the gradient, as was assumed in obtaining (14).

The differentiating crystal double plate gives, instead of the derivative (17), the differences as defined in equation (5), which is, assuming for convenience $x=-b/2$ and $x=+b/2$ for the two interfering rays:

$$\varphi(x+b/2)-\varphi(x-b/2), \tag{18}$$

where

$$\varphi(x)=\varphi_0\cdot\frac{1}{\sigma\sqrt{2\pi}}\int_0^x e^{-\frac{\xi^2}{2\sigma^2}}d\xi.$$

The difference in (18) may be developed in series, in terms of b, giving the result

$$\varphi(x+b/2)-\varphi(x-b/2)=2\frac{b}{1!\cdot 2}\varphi'(x)+2\frac{b^3}{3!\cdot 2^3}\varphi'''(x)+2\frac{b^5}{5!\cdot 2^5}\varphi^{\mathrm{V}}(x)+\cdots \tag{19}$$

or, taking out the wanted gradient, and multiplying it by a correction factor

$$\begin{aligned}\varphi(x+b/2)-\varphi(x-b/2)&\\ &=b\cdot\varphi'(x)\left[1+\frac{b^2}{6}\cdot\frac{\varphi'''(x)}{2^2\cdot\varphi'(x)}+\frac{b^4}{120}\cdot\frac{\varphi^{\mathrm{V}}(x)}{2^4\cdot\varphi'(x)}+\cdots\right]\\ &=\frac{b\,\varphi_0}{\sigma\sqrt{2\pi}}\cdot e^{-\frac{x^2}{2\sigma^2}}\left[1+\frac{b^2}{6}\cdot\frac{\varphi'''(x)}{2^2\varphi'(x)}+\frac{b^4}{120}\cdot\frac{\varphi^{\mathrm{V}}(x)}{2^4\varphi'(x)}+\right.\\ &\qquad\left.+\cdots\frac{b^{2\nu}}{(2\nu+1)!}\,\frac{\varphi^{2\nu+1}(x\pm r\,b/2)}{2^{2\nu}\varphi'(x\pm r\,b/2)}\right].\end{aligned} \tag{20}$$

The successive derivatives of the error integral are tabulated in the tables of JAHNKE-EMDE, which also contain the expressions used in their computation.

When b is smaller than or of the same order of magnitude as σ, the corrections at different parts of the curve are not great. In the following, two measuring (recording) devices will be dealt with, one of them using the maximum, equivalent to the methods used in Part I, the second measuring at the slopes on both sides, thus in the neighbourhood of the inflexion points, see Fig. 11. It may be mentioned that the half width value of the curve (the width of the curve at half the peak value) is $2\cdot 1.18\,\sigma$, thus 18 % more than the width at the inflexion points.

In order to give direct observational material for this correction some values are given in Table 3. These apply to the maximum and to the point of half value, and directly give the correction values which should be added to a determined value of $\varphi'(x)$ in these cases. The maximum, where the corrections are of course positive, is somewhat flattened out as composed of two gradient curves. We see that for $b=\sigma$, the correction is $+4.0$ %, for $b=2\,\sigma$, $+14.2$ % and for the very large value of $b=3\,\sigma$ it is about $+25$ %.

Table 3. Terms of the parenthesis of Eq. (20) following the first term which is unity. The values of columns 4 and 7 with opposite signs are the corrections to a measured phase value in either of the two procedures: at the top (column 4) or at the slope of the Gaussian curve at the half width value (column 7).

$b/2\sigma$ (width of birefringence effect relative to distance between inflexion points of G. curve)	Values in % for $x=0$			Values in % for $x=1.18\sigma$		
	second term	third term	sum	second term	third term	sum
(1)	(2)	(3)	(4)	(5)	(6)	(7)
0	0	0	0	0	0	0
0.212			<1			
0.283	− 1.33	+ 0.01	− 1.32	+ 0.37	− 0.02	+ 0.35
0.354	− 2.08	0.03	− 2.05	0.58	− 0.04	+ 0.54
0.424	− 3.00	0.07	− 2.93	0.84	− 0.08	+ 0.76
0.495	− 4.08	0.13	− 3.95	0.14	− 0.15	+ 0.99
0.566	− 5.33	0.22	− 5.11	1.49	− 0.26	+ 1.23
0.636	− 6.75	0.36	− 6.39	1.89	− 0.42	+ 1.47
0.707	− 8.33	0.55	− 7.78	2.33	− 0.63	+ 1.70
0.849	− 12.00	1.14	− 10.9	3.36	− 1.31	+ 2.05
0.990	− 16.33	2.11	− 14.2	4.57	− 2.43	+ 2.14
1.061	− 18.75	2.78	− 16.0	5.25	− 3.21	+ 2.04
1.202	− 24.08	4.59	− 19.5	6.74	− 5.30	+ 1.4
1.414	− 33.3	8.8	− 25	9.33	− 10.13	− 0.8
1.768	− 52.1	+ 21.5		14.6	− 24.8	
2.122	− 75	+ 44		21	− 31	

For the points on the sides of the curve, columns (5)–(7) of Table 3, φ''' is practically zero, and the corrections are much smaller till b will be as large as to comprise also other parts of the curve shown in Fig. 11. Here, corrections are practically negligible up to $b = 3\sigma$. The accuracy of the calculations of the corrections is sufficient up to the values marked by a horisontal line. For higher values, more terms may be included, but it seems that if corrections are to be applied with certainty, their absolute value must not exceed 20 %, as is the case here.

This is for b values of the same order as the extension of the gradient, or preferably less. When b is very large, another case occurs which is of less interest for the present discussion. For intermediate values of b the identification and evaluation of the interferometric field is complicated by the fact that the derivatives change sign: as higher derivatives must be taken into account, the correction function passes through an increasing number of zeros. For this reason this case should be avoided unless it is required for the examination of some special gradient field.

11. Measurements at the maxima of diffusion gradients in very dilute solutions

Series of observations and measurements on liquid gradients were performed with only slight modifications of the set-up described and used for the fixed gradients. The modification consists in changing the unit containing the gradient plate E and lenses H of Fig. 6 for a cell holding the two liquids whose boundary is to be studied.

Fig. 12 shows the cell used: it consists of a plano-parallel space, round in shape and formed as a hole in a plastic (Bonoplex) plate fitted with the necessary connections, and onto both sides of which are pressed two plano-convex lenses selected and polished very carefully to meet the requirement of phase-uniformity in the wave fronts passing through them. The circumstance that the cell had no special arrangements for securing a sharp boundary from the beginning of mixing mainly determined the concentration chosen and the time used for the observations, as will be dealt with in the discussion of the method given below.

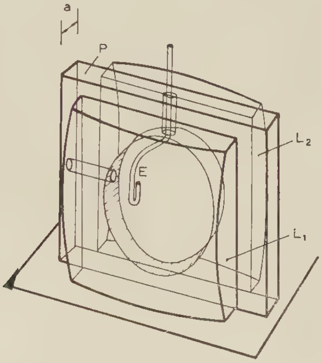

Fig. 12. Cell for studying liquid boundaries. Lenses L_1 and L_2 are pressed against the plastic plate P, the thickness a of which determines the geometrical path through the liquids. (Clamps etc. not shown, and curvature of the lenses exaggerated.) A liquid can be stratified on another by feeding it slowly into the cell through the capillary ending at E.

The differentiating and analysing unit were as before (with the addition that provision was made for inserting a camera at the place where the sharp image of the interference field falls, at N, Fig. 6). On viewing the field in white light, a very bright display of colours is seen, which gives considerable information about the detailed phase changes occurring when the two liquids mix. The optical path difference between the two interfering rays need not be greater than of the order of one wavelength in order to get the whole spectrum of saturated colours.

As an example of an actual measurement, under conditions chosen so that the correction is quite negligible, we arbitrarily chose to study dilute solutions of amino-acetic acid (glycine) in water, this being a solution having medium refractivity and diffusion constants [11]. We do not need to take more than the order of or a fraction of one wavelength for the increment, which determines the concentration. As the difference between the refractive index of water and of a solution of 1 gram glycine in 100 cm³ of water (in the following called a 1 % solution) gives a retardation of 33.5 (air) wavelengths for $t = 10.0$ mm, we have taken 0.01 %, giving 0.335 wavelengths, and have especially worked with 0.025 %, corresponding to an optical path difference of 0.837 wavelengths.

Table 4. Visual interferometric determination of diffusion constant for glycine aqueous solution/water. Conc. 0.025 g in 100 cm³. Differentiating plate and optical constants: $e = 10.0$ mm, $b = 82.8$ microns, $G = 0.0663$, $\gamma = 0$. First half of table: Run 3.5. 54. Temp. 24°–25°. Second half: Run 6.5. 54. Temp. 24°–24°.

Time t (min.)	$\lambda/2$ ring reading (degrees)	$\sqrt{t}$	$\vartheta\sqrt{t}$	$\|\Delta\|$
30	22.8	5.48	125	11
37	19.5	6.09	119	5
45	16.3	6.70	109	5
48	15.7	6.92	109	5
60	15.6	7.73	120	6
78	10.7	8.82	93	21
108	11.4	10.4	119	5
142	10.5	11.9	125	11
178	9.3	13.4	125	11
335	5.3	18.3	97	17
			114	
(12)[1]	(36)	(3.47)	(121)	
37	17.5	6.08	106	2
45	15.0	6.70	100	8
53	12.2	7.42	94	14
69	12.0	8.30	100	8
102	10.6	10.1	107	1
116	11.1	10.8	120	12
172	9.3	13.1	122	14
178	8.8	13.3	117	9
210	7.5	14.5	109	1
219	7.2	14.8	107	1
			108	

[1] These first measurements were made on another boundary situated sideways to the main boundary: the point is not taken into account in the average, for although the result agrees fairly well, it has lower accuracy.

Everything is reckoned in terms of the 5461 A line used both in the present investigation and in that quoted before [11].

We used ammonia-free Aminoacetic acid, Eastman Organic Chemical Nr. 445, and dissolved it in the same distilled water as was used for forming the boundary. The magnification was lower in this case than for the specimens of Part I due to different focal distances of the main lenses now 1700 mm, instead of 1000 mm. The choice of plate thickness e was made so that there was no influence on the correction due to b_g. We accordingly worked with plates for which $e = 10.0$ mm. All data are given in Table 4.

In these experiments, as previously, we could change between white light and mercury light, but measurements were always made with the latter. Especially for the first stages when the gradient is formed out, it is however very convenient to have the coloured field, as it is then easy to make sure that phases outside are the same to within say 0.05 of a period; any asymmetry in a gradient reveals itself. By turning the mirror U, Fig. 6, out of the path the monochromatic field from the spectral line is restored. It was shown that a fairly good gradient could be obtained in the following way. The solution, 0.0250 %, was brought to fill the whole cell, phase-uniformity was adjusted by means of tilting the differentiating plate, and half of the contents was let out. Pure solvent, at the same temperature, was allowed to collect on top of the solution by inserting it through a capillary with a speed chosen by trial to avoid inconvenient turbulences. As the procedure is kept under accurate control, as mentioned, even this very crude method of forming a gradient succeeds. Measurements were begun after about half an hour, when all detectable irregular motions of the field had disappeared. This delay also means that the gradient maximum value for this concentration had passed the maximum at $\lambda/2$ (Fig. 4), which for obvious reasons is not so accurate to measure upon, and further that the settling of the zero time (taken to be the very beginning of the mixing) is not critical.

The readings, all made on the maximum gradient value (peak of intensity curve), were taken most frequently when the boundary was new, and were stopped when this value had fallen to about 0.05 wavelengths. At this stage the photometric accuracy is lower, and also imperfections in the lenses are of the same magnitude, which makes readings less reliable.

The evaluation of a diffusion constant D, when measurements of the intensity of the peak of the Gaussian error curve are made, is done as follows.

Referring to Eq. (15), our measurements will give us

$$\frac{dz(x)}{dx}_{x=0} = \frac{z_0}{2} \cdot \frac{1}{\sqrt{\pi D t}}, \tag{21}$$

since the method gives directly

$$\frac{b}{G} \cdot \frac{dz(x)}{dx} = \frac{\vartheta^\circ}{90} \cdot \lambda, \tag{22}$$

bearing in mind that a rotation of $\vartheta = 90^\circ$ gives an intensity variation equivalent to one wavelength of interference. We thus obtain the following expression for D:

$$D = \frac{45^\circ}{\pi} \left(\frac{b}{G}\right)^2 \left(\frac{z_0}{\lambda}\right)^2 \cdot \frac{1}{\vartheta^{\circ 2} \cdot t} \cdot \tag{23}$$

By inserting the values for this case, from Table 4, with $\vartheta^\circ \sqrt{t} = 111$ degrees $\cdot$ $\cdot\,\text{min}^{\frac{1}{2}}$, and $z_0/\lambda = 0.837$, we obtain the value

$$D = 9.6 \cdot 10^{-6}\ \text{cm}^2/\text{s}.$$

The main methodical uncertainty in this value lies in the photometric determination of intensity. To this must also of course be added the possibility that other influences than diffusion, such as small turbulences etc., may increase the values of D obtained. The reliability may be judged by the scatter in the settings of ϑ: as may be seen from Table 4, the averages of deviations from the mean value of $\vartheta \sqrt{t}$ are seen to be 10 and 7 units in the two runs, and the standard deviations of the mean values calculated in the usual way are 3.7 and 2.9 units respectively. Taking half of the first-mentioned value, about 4.5 units, as the ± maximum error, we obtain a relative error in D of ± 8 per cent. It should be stressed that this error can definitely be decreased if an improved device for equalizing the two light intensities is used, as discussed in the last section.

With this error, it is to some extent a matter of chance that the value found agrees so well with the values of D extrapolated to zero concentration found by measurements at much higher concentrations of the same chemical, such as those performed with the LAMM scale method and the GOUY interferometer, both sets of values given in the investigation already quoted. When going to another decade of small concentration in measurements of this kind, it seems to the writer preferable to use the logarithmic scale of concentration: in Fig. 13 such a diagram is plotted, with the point measured here included. The temperatures are also different, and the extensive measurements of the authors cited and this preliminary work should not be directly compared. However, these determinations suffer from greater uncertainty the smaller is the concentration, and in spite of the coincidences of the points in the diagram shown the lowest points are in fact uncertain to the order of a few per cent due to the measuring methods, though performed with great care. We shall later return to the question of the ultimate accuracy obtainable.

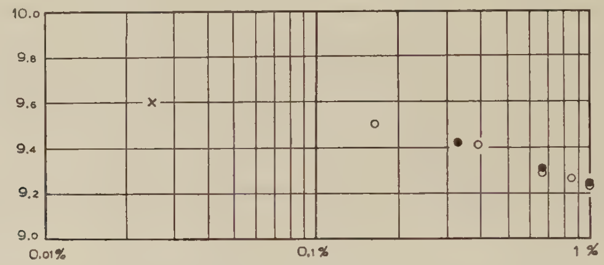

Fig. 13. Determinations of diffusion constant for aminoacetic acid; values in 10^6 cm²/s, concentrations see the text. Filled circles, POLSON, 20°C [11]; empty circles, reference [11], 20°C; cross, this investigation, 24°C.

12. Outline of a modification to the method using photographic registration

With the method discussed above the measurements are made at the top of Gaussian distribution curve, and the known value of z_0 is used.

It is also of some interest to examine a registering procedure of the type now often used in interferometry at very many wavelengths, where the interferometer fringes themselves are traced. This of course works very well with photoelectric devices, but when simplicity is desired some other methods are more attractive.

During a run the gradient changes as is indicated in Fig. 14, the curve retaining its Gaussian form but gradually flattening out and spreading, while keeping the same area. This process could be photographed directly from time to time,

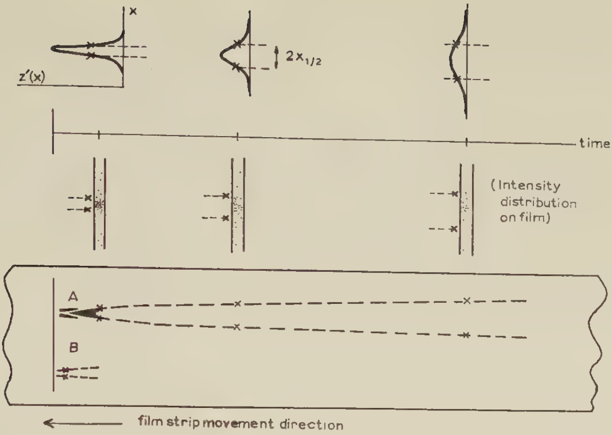
x
z'(x)
2x1/2
time
(Intensity distribution on film)
A
B
film strip movement direction

Fig. 14. Principle of photographic recording and measurement at the slope of the gradient curve.

as was also done here in the last of the runs, and the image of the boundary photometered, in order to determine a characteristic fall-off x value, for example the half-width value, which is $x_{\frac{1}{2}} = 1.18\ \sigma$. It is obvious that these values for different t, evaluated considering the intensity function given in (6) and Fig. 4, give the diffusion constant D directly, this being a purely kinematic quantity given in (length)^2/time.

A continous registration on a single photographic film strip may be obtained by placing a slit in the field of view, extended in the x direction, and moving the photographic film slowly in the direction indicated at the bottom of the figure. This movement should preferably be linear with time, in order to maintain a constant "time of exposure". The width of the slit is dimensioned so that the $x_{\frac{1}{2}}$ of the diffusion process does not appreciably change during the time it takes for the film strip to move a path equal to this width, this requirement being of course most critical at the beginning of the run. In our set-up, one minute was sufficient exposure time, and compared to the times of Table 4 the width of the equivalent slit is appropriate.

The interesting period at the very beginning of the run, in which the diffusion boundary is very sharp (indicated at A of Fig. 14) deserves special attention: partly because the corrections dealt with in Section 13 may be required, and partly because if there is more than half a wavelength of optical path increment in the difference between the two liquids, not a single maximum but minima or maxima are present (compare the dotted curves of Fig. 15, and the following text). If it is desired to make measurements at very small t values, these circumstances may be varied by setting the apparatus to another constant b/G, which can be done without changing any other adjustment. In this way, several recorded blackened bands with different constants can be traced on the same strip. In the figure, the band B indicated at the bottom of the figure represents such a record, where the interferometric sensitivity has been decreased by taking a smaller b value, G being unchanged, in order to maintain $b z'(x)/G$ below $\lambda/2$ which is more convenient. This means only a change of differentiating scale.

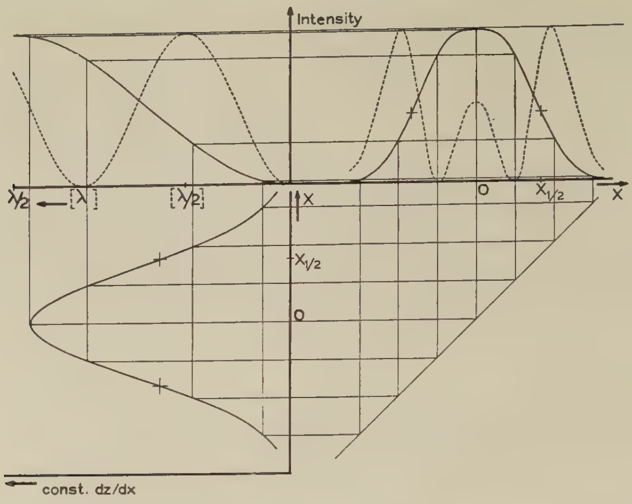

Fig. 15. Transform from differentiated phase curve to intensity curve for using the method in photometrical measurement at the slope of the curve. x coordinate is in the same scale on the two curves, as is seen from the 45° construction line. Full curves:

$$b\,z'(x)/G = b\,z_0/2\,G\sqrt{\pi D t} < \lambda/2;$$

the measurements reported here began at about half of this value, see Tables 4 and 5. Dotted curves: the ratio mentioned about 1.25 λ, which can be the case in the beginning of a run as indicated at A, Fig. 14.

We have also made measurements by means of this method using the photographs taken during the second run given in Table 4 for the visual measurements on the top of the intensity curves. On commenting their evaluation, a more detailed explanation of the function which transforms the phase curve to the intensity curve could be of some value. In Fig. 15, the phase derivative curve, or refractive index gradient curve, which has the Gaussian shape, is measured by means of the interferometric function shown at the top left-hand corner of the figure for two different b values, as is explained in the legend of the figure. If only the total phase increment z_0/λ is of the order of unity, we can always make this choice of b and still retain a low or negligible correction by means of Table 3. For measuring technique reasons it is in this case most favourable to take b as small as to realize the case of the full curve. This case is automatically obtained when z_0/λ is less than 0.5 for any value of b.

During the diffusion process the top of the Gaussian curve decreases proportionally with the square root of time. Our method consists primarily in measuring the half width $x_{\frac{1}{2}}$ of the Gaussian curve at the intensity curve, and Fig. 15 shows how the points on the latter curve are found. The height on which the $x_{\frac{1}{2}}$ or $2\,x_{\frac{1}{2}}$ values should be measured is of course 0.5 when the peak extends to $\lambda/2$ at the transform curve, and somewhat less for lower peak values. In our case, we had about 0.27.

Our values obtained in this way are found in Table 5. The random variations in this case are not astonishing, mainly due to the gradient itself, but

Table 5. Determination of diffusion constant for glycine solution from half width values of the Gaussian curve using photographic intensity registration. This run is the same as the second half of Table 4, where the data are given, *a* and *b* are two parts of the photograph.

Time t, min.	$2x_{\frac{1}{2}}$, cm	$(2x_{\frac{1}{2}})^2$, cm	$16\,t\,\ln 2$, s	D, cm²/s
41.5	*a* 0.579	3.35×10^{-1}	2.73×10^4	12.1×10^{-6}
	b 0.586	3.43	2.73	12.4
50.5	*a* 0.660	4.36	3.36	13.0
	b 0.601	3.61	3.36	10.7
105	*a* 0.755	5.70	6.99	8.5
	b 0.630	4.00	6.99	5.7
				10×10^{-6}

yet the values of D, from (15) found to be $D=(x_{\frac{1}{2}})^2/4\,t\ln 2$, are consistent with the other measurements. Also in these (Table 4), the values at the corresponding times give higher value than the average.

A modified method which avoids this precalculation of a height is to incorporate in the image plane small reference "spots" of birefringent material oriented at determined angles in respect to the polarizing devices, e.g. of $\lambda/2$ material. In this way a photographic run as outlined in Fig. 14 contains strips which serve as reference intensities for the different parts of the recorded intensity curve, giving them directly as phase values.

13. Relative merits of the present method and earlier refraction and interferometric methods

In both modifications of this method, that in which the peak is measured and that of determining the half-width value, the accuracy is dependent on an intensity measurement. The conservative limits of error in the provisional measurements reported in Sect. 11 are based on a visual judgement of different fields in a microscope not especially adapted for precision measurements: they correspond to a relative intensity error of $\pm 7\,\%$. As shown elsewhere [12] in discussing a set-up having very similar characteristics as regards intensity, colour and fields of view, $\pm 2\,\%$ can be reached without special precautions. In this modification only some stops and prisms in the present eyepiece are needed. If a photographic-photometrical or simple photoelectrical device is used, the same intensity accuracy requires only routine procedures. Doubling this relative error for the diffusion constant value, because of the formula in which it enters, this means that the method determines D to within 4 %. In order to compare the present procedure with other interferometric methods, this limit of error should be recalculated into wavelengths: when measuring in the region used here it corresponds to $0.015\,\lambda$.

These errors, which are also valid for the positioning of an interference fringe, may seem astonishingly small in this connection, but in fact they are not. It should be of didactical value to remember that depth information of the order of thousandths of a wavelength, or even one or two decades less, is easily obtained even in routine instruments when dealing with phases transformed to *intensities*. For example, in a polarimeter, the setting of the angle to one minute of arc means an accuracy in optical path (transformed by means of the circularly polarized light) of 0.0001 λ, and many analysers come up to this [8].

There are, however, reasons why the theoretically unlimited accuracy when measuring path differences by methods utilizing interferometric techniques is seldom achieved in practice. The more wavelengths are incorporated in the two light paths, the more disturbances of a more or less trivial kind occur. This is especially so when the two paths travel far away from one another, pass through different optical surfaces etc., which is very often the case in conventional interferometers. The present method, where the two rays to interfere are only separated, by means of the birefringence of a very prefect and smoothly polished crystal such as quartz, by a very small amount, namely the limited number of wavelengths sideways necessary to perform the differentiating procedure, is very nearly ideal for obtaining the information wanted.

It does not, however, give more than the derivative of the concentration function, not the function itself, which should sometimes be of interest as well. If only the constant value of z_0 is to be measured, the double slit method is attractive. The most direct connection to this method however is to use birefringence interferometry as suggested JAMIN, and such as it is used in most cases. This method applies especially well if there is only one gradient present in the field and it is not too extensive, and consists in using a birefringence device with a b_g sufficiently large as to superimpose the gradient on a phase-even field. In this case the $z(x)$ function is obtained by the same means as $z'(x)$ here. Several other methods are accessible for scannings of the $z(x)$ function, and skilled combinations of methods which give $z(x)$ at the same time as $z'(x)$ are very often used by workers in this field [13]. This would be necessary if a detailed study is to be made when D is not independent of the concentration for the conditions to be examined. This assumption is also made for example in evaluating results from a Gouy interferometer [11].

The differentiating interferometric principle can be regarded as a very simple and effective method of studying extremely dilute solutions, as it avoids working with, and the technical difficulties in arranging, the long boundaries necessary for obtaining sufficiently many wavelengths in optical path difference along the optical axis, with their attendant lack of precision. With a cell like the present one of 10 mm thickness, this means a convenient concentration region ($\lambda/2$ in path difference) of, for example,

for KCl in water	0.01 %	(D about $17 \cdot 10^{-6}$ cm^2/s)
for glycine	0.015 %	(D about $10 \cdot 10^{-6}$ cm^2/s)
for albumine etc.	0.005 %	(D about or less than $1 \cdot 10^{-6}$ cm^2/s).

The present accuracy of the determination of D (per cent) is still retained. It seems that there is a definite interest in examining these low-concentration regions, as in them several physical and chemical effects come into play. As is well known, this is the case for electrolytes, where the D values are often greatly changed at small concentration differences in a boundary [14], and it would be of still more interest to develop simple and accurate methods for the high-molecular organic substances.

Regarding the interest in the physical-chemical questions in this field, it seems attractive to improve the accuracy by modifying the present very simple technique. For comparison, the accuracy in determinations by SVENSSON [15 a] using the Rayleigh interferometer and those very precise ones by means of the Gouy interferometer performed by GOSTING et al. [15 b] is a few tenths of a per cent, yet at concentrations 20 to 100 times as large as here.

The ultimate accuracy limit for low concentrations is set by the presence of stray light or lack of phase equality over the whole field of view. It seems convenient to replace the Polaroid screens by crystal polarizers: a perfect Nicol prism should be placed in a part of the system where the field angle is not too large, and a Glan-Thomson prism in the eyepiece. Further, dispersion-free retarding plates ($\lambda/2$) would help by making monochromatization less critical [10].

The speed of a determination is of some interest, especially for liquids with high values of D. This is often a question of starting with a very sharp boundary and beginning the measurements quickly. In this respect, the methods of forming a sharp boundary by "flowing" the two liquids onto one another, or by withdrawing liquid from the boundary, as elaborated [16, see also 11, 15 b] are important, but before this interferometric principle has been applied to these types of cells nothing definite can be stated about its quantitative merits in this respect. As already indicated, the b value of the differentiating unit should be chosen lower the sharper is the boundary, and different plates could be interchanged during a measurement, if required. The time scale used here (Table 4) seems to be quite suitable for medium D values.

Returning, finally, to the question of the accuracy of the different methods used in analysing gradients in liquids, it is interesting that ANTWEILER [17] has pointed out the relative merit of "coloured" interferences, using white light, for giving greater sensitivity than the methods he cites. He discusses in some detail the reasons why the geometrical-optical method such as the Lamm scale method has about the same limiting accuracy as interferometric methods with very many wavelengths, and points out that generally the least decrement of path difference perceptible with certainty is about 1 λ. The use of the Jamin method, technically well applied by LABHART, STAUB [18], and later also, in collaboration, by LOTMAR [19] improves the conditions so that the limit becomes 0.6 λ. This is at the many wavelengths and far from the acheivable accuracy on account of the reasons mentioned. The addition of observation with colours, according to ANTWEILER, is reported to give 0.02 λ as this limit. This should not be impossible as sensitivity, and it corresponds to what was said in the first part of this paper on the fact that the sensitivity of colour matching by the eye, if physiologically favourable, is the same as an ordinary interferometric accuracy, or even, a decade better.

The relative merits of the phase contrast method for measurements similar to those reported here will be discussed in a subsequent paper [20].

Summary of Part II

As it is especially interesting, the case of a distribution of phases according to a Gaussian "error integral", the gradient following the "error curve", is investigated in detail, the corrections necessary in some cases being computed. Liquid gradients were produced experimentally, and it is proved that diffusion constants can be measured with an accuracy of a few per cent with very simple means. Improvements in the photometric procedure give the higher accuracies that may be required. The main merit of the method is that the concentrations of solution may be so low as to correspond to an optical path increment over the solvent of less than one wavelength, i.e. in general concentration of the order of 0.01 % for a cell of 10 mm thickness.

The experiments and measurements were performed in collaboration with Mr. LARS JOHANSSON of this laboratory, who has also made the valuable suggestion that the phase reference field be shaped as a ring instead of as strips, as previously done. The metallic specimens were skilfully prepared by Mr. S. AMBERG, First Assistant, and Mr. JOHANSSON. These investigators were interested in applying the method to the measurement of angles in metallographic specimens.

The writer greatly appreciates the kindness of Dr. HARRY SVENSSON in reading the manuscript, making suggestions for improvements and giving valuable information about the current state of related methods for examining liquids.

This work was made possible thanks to support given to our laboratory in recent years by the State Council of Technical Research and the Swedish Natural Science Research Council.

Optics and Physics Laboratory, Royal Institute of Technology, Stockholm 70.

REFERENCES

1. M. J. JAMIN, Comptes rendus (Paris) *67*, 814 (1868).
2. H. SCHOPPER, ZS. f. Physik *135*, 516 (1953).
3. A.-A. LEBEDEFF, Revue d'Optique *9*, 385 (1930).
4. M. FRANÇON, Revue d'Optique *31*, 65; 170 (1952).
5. M. FRANÇON, Revue d'Optique *32*, 349 (1953).
6. F. E. WRIGHT, J. O. S. A. *24*, 206 (1934).
7. G. BRUHAT, Traité de Polarimétrie. Ed. de la Revue d'Optique. Paris 1930.
8. H. G. JERRARD, J. O. S. A. *38*, 35 (1948); *44*, 289 (1954).
9. Text-books in physiological Optics, e.g. The Science of Color, Thos. Y. Crowell Co, New York 1953. Measurements mainly by D. L. MACADAM, J. O. S. A. 32, 247 (1942).
10. C. D. WEST and A. S. MAKAS, J. O. S. A. *39*, 793 (1949).
11. C. A. COULSON, J. T. COX, A. G. OGSTON, and J. S. L. PHILPOT, Proc. Roy. Soc. A *192*, 382 (1948).
12. E. INGELSTAM and L. JOHANSSON, Appl. Sci. Res. B *4*, 100 (1954).
13. Elucidating surveys are given by H. SVENSSON, e.g. in Transactions of Instruments and Measurements Conference, Stockholm 1952.
14. Data are given in LANDOLT-BÖRNSTEIN's tables up to their time of issue. Optical measurements were efficient, e.g. those by ZUBER *et al.*, ZS. f. Physik *79*, 280; 291; 306 (1932), E. MÜNTER, Ann. der Physik [5] *11*, 558 (1931), and G. FRANKE, Ann. der Physik [5] *14*, 675 (1932), which however do not come up to the precision of later techniques.
15. a) H. SVENSSON, Acta Chem. Scand. *5*, 72 (1951); b) L. J. GOSTING and M. S. MORRIS, Journ. Amer. Chem. Soc. *71*, 1998 (1949).
16. H. SVENSSON, Arkiv Kemi Min. Geol., A *22*, Nr 10 (1946); D. S. KAHN and A. POLSON, J. Phys. Coll. Chem. *51*, 816 (1947).
17. H. J. ANTWEILER, Mikrochemie *34*, 561 (1951).
18. H. LABHART and H. STAUB, Helv. Chim. Acta *30*, 1954 (1947).
19. H. LABHART, W. LOTMAR, and P. SCHMID, Helv. Chim. Acta *34*, 154 (1951); W. LOTMAR, Rev. Sci. Instr. *22*, 886 (1951).
20. E. INGELSTAM (to appear).

Tryckt den 26 januari 1955

Uppsala 1955. Almqvist & Wiksells Boktryckeri AB

ARKIV FÖR FYSIK Band 9 nr 13

Mitgeteilt am 10. November 1954 durch ERIK HULTHÉN

Termschemata von CaO, SrO und BaO

Von LENNART HULDT und ALBIN LAGERQVIST

Kürzlich haben wir eine Methode veröffentlicht[1], durch welche die Höhen angeregter Elektronenterme approximativ bestimmt werden können. Wir untersuchten mittels einer Azetylen-Luftflamme die Oxyde der Erdalkalien Ca, Sr und Ba und machten auf Grund der Messergebnisse einen Vorschlag für die Termschemata dieser Moleküle. Nach diesem Vorschlag konnte keines der bekannten Bandensysteme von CaO und SrO mit dem Grundzustand kombinieren. Um dieses überraschende Resultat nochmals zu prüfen, haben wir jetzt die Untersuchung unter veränderten Bedingungen, die eine Erweiterung des Temperaturgebietes enthalten, wiederholt.

Die von uns entwickelte Methode besteht in Messungen der Bandenintensitäten der betreffenden Moleküle bei verschiedenen Temperaturen. Aus der Änderung der Intensität mit der Temperatur kann die Anregungsenergie der Bande, unter Voraussetzung thermischen Gleichgewichtes, berechnet werden. Wir konnten durch Änderung des Mischungsverhältnisses der Flammengase die Temperatur der Azetylen-Luftflamme zwischen etwa 2100 und 2400° K variieren. Mit einer Knallgasflamme (Beckmanntypus) haben wir jetzt Temperaturen von 2300 bis etwa 2750° K erreicht. Die übrige Apparatur war die gleiche wie bei unseren früheren Untersuchungen, nur wurde die Bandlampe durch eine Wolframspirallampe ausgetauscht.

Die Messungen wurden wie früher[1] ausgeführt. Die Auswertung ist hier jedoch nicht einfach nach den Gleichungen (5) und (6)[1] vorzunehmen, weil diese Flamme, im Gegensatz zu der Azetylen-Luftflamme, ihre Form stark mit dem Mengenverhältnis der Flammengase ändert. Zur Prüfung der Methode eignet sich das grüne Bandensystem von BaO, dessen unterer Zustand nach Untersuchungen verschiedener Art[1, 2, 3, 4] mit dem Grundterm identisch ist. Die Messpunkte im $\log I_{\mathrm{BaO}}/\log I_{\mathrm{Na}}$-Diagramm geben auch hier eine Gerade, jedoch ist die nach der obengenannten Gleichung (5) berechnete Anregungsenergie E_{BaO} viel zu hoch. Die Ursache ist offenbar die auffällige Zunahme des Flammendiameters mit wachsender Temperatur. Da nun die Anregungsenergie E_{BaO} als bekannt anzusehen ist, kann der Unterschied zwischen der tatsächlichen Neigung der Gerade und der nach Gl. (5) erwarteten zur Berechnung der Abhängigkeit des Flammendiameters d von der Temperatur dienen. Setzen wir für diese Abhängigkeit an:

$$d = \text{Konst.} \times e^{-A/kT}, \tag{1}$$

---

[1] A. LAGERQVIST und L. HULDT, Arkiv f. Fys. *8*, 427, 1954.

[2] L. HULDT und A. LAGERQVIST, Ark. f. Fys. *2*, 333, 1950.

[3] A. LAGERQVIST, E. LIND und R. F. BARROW, Proc. Roy. Soc. A *63*, 1132, 1950.

[4] A. LAGERQVIST und L. HULDT, ZS. f. Naturforsch. *9 a*, Heft 12, 1954.

so wird die Intensität einer Bande

$$I = \text{Konst.} \times e^{-(E+A)/kT}. \tag{2}$$

Unsere frühere Gl. (5)[1] wird jetzt

$$\log I = \frac{E+A}{E_{\text{Na}}} \log I_{\text{Na}} + \text{Konst.} \tag{3}$$

Die für alle untersuchten Banden gefundene Linearität zwischen log I und log I_{Na} berechtigt den Ansatz (1). Aus den Messungen des BaO-Systems ergibt sich $A = 20000$ K.

Die Methode bedingt unbedeutende Dissoziation der Oxyde. Aus der Temperatur, der Zusammensetzung der Flamme und den bekannten Dissoziationsenergien[4] wird der Dissoziationsgrad für CaO und SrO auf höchstens 0,1 berechnet. Die Dissoziation von BaO ist im ganzen Temperaturgebiet sehr gering. Wegen der logarithmischen Beziehung ist somit die Dissoziation stets zu vernachlässigen.

Die Ergebnisse sind in der nachstehenden Tabelle zusammen mit den früher erhaltenen[1] gegeben. Die Übereinstimmung ist als befriedigend anzusehen.

Molekül	Wellenzahl K	E in K Azetylen-Luftflamme	E in K Knallgas-Flamme
CaO	11 500	27 000	27 000
	16 000	32 000	38 000
	18 000	36 000	40 000
SrO	10 900	24 000	25 000
	15 000	27 000	28 000
	16 500	28 000	29 000

Stockholm, Physikalisches Institut der Universität, November 1954.

Tryckt den 26 januari 1955

Uppsala 1955. Almqvist & Wiksells Boktryckeri AB

ARKIV FÖR FYSIK Band 9 nr 14

Communicated 2 June 1954 by ERIK HULTHÉN and OSKAR KLEIN

A theoretical study of the coloured alkali oxides

By BARBRO GRABE

With 5 figures in the text

Contents

Summary 229
1. Introduction 229
2. Crystal structure 230
3. Methods 232
  i. Valence bond method 232
  ii. Molecular orbital method 234
4. Calculation of the orbital energy and the molecular orbital 235
  i. Choice of atomic orbitals for oxygen 236
  ii. Choice of an atomic orbital for rubidium 236
  iii. The potential function of oxygen 237
  iv. The potential function of rubidium 238
  v. Determination of the orbital energy and the coefficients in the molecular orbital 239
5. Results 240
6. Discussion 240
Appendix 242
References 243

Summary[1]

The sesquioxides of $Rb_4(O_2)_3$ and $Cs_4(O_2)_3$ are coloured. Most probably, the colour depends on the structure of the crystal lattice. To explain the dark colour we have described the electron distribution of $Rb_4(O_2)_3$ in terms of semi-localized orbitals. We have considered an Rb atom and the three nearest O atoms. We have assumed that the valence electron of Rb can be assigned to a molecular orbital of this group. The parameters of the orbital are determined by minimizing the energy of the electron. Two electronic states are obtained, having an energy difference between them which corresponds to a wavelength in the visible part of the spectrum. Thus a transition between these states can explain the colour of the crystal. A valence bond method is also discussed.

1. Introduction

There are three oxides common to all the alkali metals: Me_2O, Me_2O_2 and MeO_2. All these oxides are almost colourless. Furthermore, the sesquioxides $Me_4(O_2)_3$ have been prepared from at least two metals: rubidium, Rb, and

---

[1] A preliminary report has been published in J. Chem. Phys. *22* (1954) 1259.

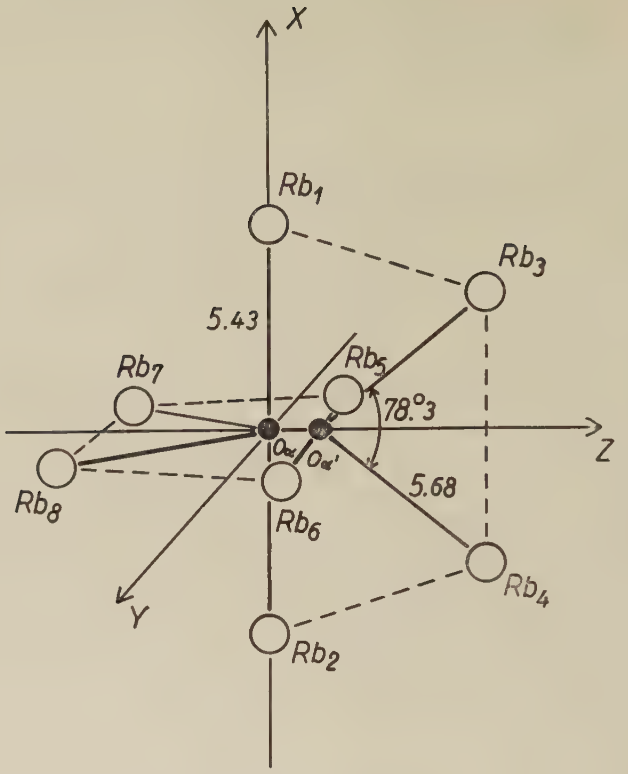

Fig. 1. An O_2 pair, O_α–$O_{\alpha'}$, and its nearest Rb neighbours. O_α–$O_{\alpha'}$, Rb_1, Rb_2, Rb_3 and Rb_4 are in the plane of the paper. Rb_5, Rb_6, Rb_7 and Rb_8 are in a plane through the symmetry axis of O_α–$O_{\alpha'}$, perpendicular to the plane of the paper.

caesium, Cs. Attempts to prepare the corresponding potassium compound do not seem to have been successful hitherto. The sesquioxides are characterized by a dark colour. This feature can hardly be attributed to any of the separate ions. Most probably the colour depends on the special configuration of the ions in the lattice of the crystallized sesquioxides. In the present paper an attempt is made to describe the electron distribution in terms of wave functions, and the two lowest energy levels of the valence electron have been computed. It is suggested that the dark colour of the compound is due to a transition between these two levels, the energy difference of the levels corresponding to a radiation frequency in the region of visible light. The computations have been carried out using the parameters of the $Rb_4(O_2)_3$ crystal, but analogous results could obviously be obtained in the case of $Cs_4(O_2)_3$.

2. Crystal structure

Helms and Klemm [1], who have prepared the various alkali oxides, have determined their crystal structures. The structure of $Rb_4(O_2)_3$ can approximately be described as follows. The O atoms are placed in pairs, the distance

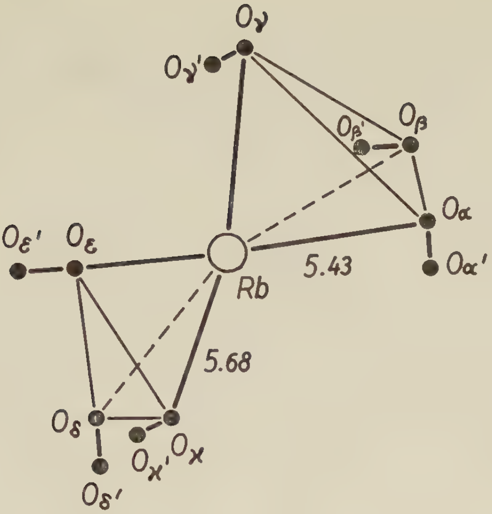

Fig. 2. An Rb atom and the six nearest O_2 pairs.

between the two O atoms of a pair being 1.3 A = 2.4 a.u. The symmetry axis of each O_2 pair is directed in one of three orthogonal directions.

Let us now consider the nearest Rb neighbours of a pair of oxygen atoms, e.g. the pair O_α–$O_{\alpha'}$, of Fig. 1. In a plane through the symmetry axis of the pair (in the present case the plane of the paper) there are two Rb atoms, Rb_1 and Rb_2, at a distance of 5.43 a.u. from O_α on a line through O_α perpendicular to the symmetry axis. Furthermore, there are two Rb atoms, Rb_3 and Rb_4, at a distance of 5.68 a.u. from the other O atom, $O_{\alpha'}$, symmetrically placed in relation to the O_α–$O_{\alpha'}$ axis. The angle $Rb_3O_{\alpha'}Rb_4$ is 78°.3. In another plane through the symmetry axis, orthogonal to the first plane, there are also four Rb atoms placed in a similar way, but here two of them are at a distance of 5.43 a.u. from $O_{\alpha'}$ and two at a distance of 5.68 a.u. from O_α.

Consider now the nearest oxygen neighbours of an Rb atom. There are three O_2 pairs (Fig. 2. O_α–$O_{\alpha'}$, O_β–$O_{\beta'}$ and O_γ–$O_{\gamma'}$), so situated that one of the atoms in each pair is at a distance of 5.43 a.u., and the other at a distance of 5.97 a.u. from the Rb atom. In the following we shall refer to these atoms as "a group of one Rb atom and three O_2 pairs". Any two of the vectors $\overrightarrow{RbO_\alpha}$, $\overrightarrow{RbO_\beta}$ and $\overrightarrow{RbO_\gamma}$ form an angle of 80°.1 with each other. The symmetry axis of an O_2 pair is orthogonal to its own vector from Rb, e.g. $\overrightarrow{O_\alpha\text{–}O_{\alpha'}}$ is orthogonal to $\overrightarrow{RbO_\alpha}$, and almost parallel to one of the other vectors (angle 10°) in such a way that all the three symmetry axes are orthogonal. Each O_2 molecule is a member of four such groups around different Rb atoms (Figs. 1 and 3). There are three additional O_2 pairs (Fig. 2. O_δ–$O_{\delta'}$, O_ε–$O_{\varepsilon'}$ and $O_\varkappa$–$O_{\varkappa'}$) rather near the Rb atom, the nearest atom in each pair being at a distance of 5.68 a.u. and the other at a distance of 7.75 a.u. The vectors $\overrightarrow{RbO_\delta}$, $\overrightarrow{RbO_\varepsilon}$ and $\overrightarrow{RbO_\varkappa}$ form angles of 76°.2 with each other. The symmetry axes are orthogonal, and the angle between, e.g. $\overrightarrow{O_\delta\text{–}O_{\delta'}}$ and $\overrightarrow{RbO_\delta}$, is 39°.2 (Fig. 1). Between the vectors

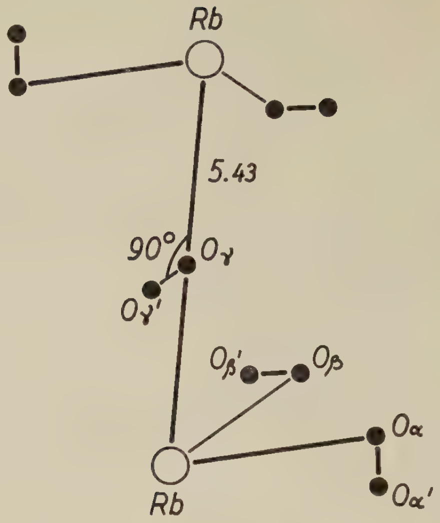

Fig. 3. The same group of Rb and O_α–$O_{\alpha'}$, O_β–$O_{\beta'}$ and O_γ–$O_{\gamma'}$ as in Fig. 2. Here it is seen how O_γ is also part of another group of the same kind. In the same manner $O_{\gamma'}$ takes part in two similar groups, compare Fig. 1.

$\overrightarrow{RbO_\alpha}$, $\overrightarrow{RbO_\beta}$ ... $\overrightarrow{RbO_\varkappa}$ there are fifteen angles in all. Their magnitudes are given in Table 1.

Table 1.

Number of angles	3	3	3	3	3
Magnitude of angle	80°.1	76°.2	88°.3	124°.6	150°.2

3. Methods

Here we will discuss two possible approaches to the problem, the one following the valence bond method and the other following the molecular orbital method. In crystals electrons which are strictly localized to one atom, molecule or ion can be described by atomic or molecular wave functions, but when this condition is not fulfilled they may be described by Bloch functions. As a first approximation, however, it seems to us that it would also be reasonable to represent the valence electrons by functions composed of atomic orbitals of a group of atoms, e.g. one or several Rb atoms together with one or more O atoms. These orbitals are chosen in different manners in the two methods.

i. Valence bond method

The difference between the energy of an electron in a $5s$, $5p$ or $4d$ orbital of Rb is so small, that spd hybridization is likely to occur. (The difference between $5s$ and $5p$ is 0.057 a.u. and between $5s$ and $4d$ is 0.088 a.u. [2].)

R. HULTGREN [3] has studied the orbitals in *spd* hybridization. For a trigonal prism he has found a distribution in which the directions of greatest bond strength form the angles with each other given in Table 2.

Table 2.

Number of angles	9	6
Angles between bonds	81°47′	135°35′

For an $Rb_4(O_2)_3$ crystal the mean value of the first nine angles given in Table 1 is 81°.5 and of the six last 137°.4. These mean values are in good agreement with the angles of Table 2. When we, following PAULING [4], apply the valence bond method to our problem we choose the trigonal prism *spd* hybrid orbitals of Rb and some suitable orbitals of the oxygen atoms.

The electron configuration of an oxygen molecule is commonly written

$$(\sigma_g\,1\,s)^2\,(\sigma_u\,1\,s)^2\,(\sigma_g\,2\,s)^2\,(\sigma_u\,2\,s)^2\,(\sigma_g\,2\,p)^2\,(\pi_u\,2\,p)^4\,(\pi_g\,2\,p)^2. \tag{1}$$

MECKLER [5] has found that the wave function for the ground state is mostly composed of the wave function symbolized by (1), with only a very small contribution from other wave functions. However, when the distance between the two O atoms increases, he finds that the wave function symbolized by

$$(\sigma_g\,1\,s)^2\,(\sigma_u\,1\,s)^2\,(\sigma_g\,2\,s)^2\,(\sigma_u\,2\,s)^2\,(\sigma_g\,2\,p)\,(\pi_u\,2\,p)^3\,(\pi_g\,2\,p)^3\,(\sigma_u\,2\,p) \tag{2}$$

begins to be of more importance. Although MECKLER has not used hydrogenlike atomic orbitals, but Gaussian functions, his results indicate that the importance of the orbital $(\sigma_u\,2\,p)$ should be investigated and that the energy of $(\sigma_u\,2\,p)$ is not very much higher than that of the other $2\,p$ orbitals, when the distance between the atoms is large. For this reason it is probably acceptable, under the conditions existing in the crystal, to use the following configuration of the oxygen molecule, which we have assumed,

$$(\sigma\,1\,s)^2\,(\sigma_u\,1\,s)^2\,(\sigma_g\,2\,s)^2\,(\sigma_u\,2\,s)^2\,(\sigma_g\,2\,p)^2\,(\sigma_u\,2\,p)^2\,(2\,p_y\,(\alpha))^2\,(2\,p_x\,(\alpha'))^2, \tag{3}$$

where $2\,p_y\,(\alpha)$ and $2\,p_x\,(\alpha')$ are atomic orbitals of O_α and $O_{\alpha'}$. (For the direction of the coordinate axes, see Fig. 1.) The orbitals $2\,p_x\,(\alpha)$ and $2\,p_y\,(\alpha')$ are not occupied by electrons from the neutral O_2. We assume that the electrons in the $(\sigma_g\,2\,p)$ and $(\sigma_u\,2\,p)$ orbitals are somewhat delocalized, so that $(\sigma_g\,2\,p)$ and $(\sigma_u\,2\,p)$ should be replaced by ψ_A and ψ_B, where

$$\psi_A = a_1\,(\varphi_{\mathrm{Rb}_7} + \varphi_{\mathrm{Rb}_8}) + a_2\,(\sigma_g\,2\,p) + a_1\,(\varphi_{\mathrm{Rb}_3} + \varphi_{\mathrm{Rb}_4}) \tag{4}$$

and

$$\psi_B = b_1\,(\varphi_{\mathrm{Rb}_7} + \varphi_{\mathrm{Rb}_8}) + b_2\,(\sigma_u\,2\,p) - b_1\,(\varphi_{\mathrm{Rb}_3} + \varphi_{\mathrm{Rb}_4}). \tag{5}$$

In (4) and (5) the φ_{Rb} are the above-mentioned *spd* hybrid orbitals of the Rb atoms; the indices indicate which Rb atom the orbital is referred to, using the notation in Fig. 1. The coefficients a_1 and b_1 measure the degree of delocalization.

The inner electrons of the Rb atom including the $4s$ and $4p$ electrons are regarded as localized at the Rb atom. For the valence electron of e.g. Rb_1 in Fig. 1 we assume the wave function

$$\psi_c = c_1 \varphi_{Rb_1} + c_2 (2p_x(\alpha)), \tag{6}$$

where the φ_{Rb} is again an spd hybrid orbital. Our suggestion is that this one-electron bond resonates between the three nearest O atoms in the group around the Rb. (O_α, O_β and O_γ, Figs. 2 and 3.) (See PAULING [4].)

All the six hybrid orbitals of an Rb atom are in this manner at least partly occupied by electrons: one electron resonates between three bonds which are described by wave functions of the type (6) and three electron pairs are described by wave functions of the types (4) and (5). In this description all the $2s$ and $2p$ orbitals of the oxygen atoms are fully or partly occupied.

The coefficients in (4), (5) and (6) should be determined by minimizing the expression for the energy. Very likely a_1 and b_1 in (4) and (5) are small, because the distance between the paired O atoms is close to the ordinary distance for an oxygen molecule. Nevertheless, the delocalization of the oxygen orbitals should stabilize the structure which has been found for the crystal.

ii. Molecular orbital method

In the application of this method we assume that with the exception of the valence electron of Rb, all electrons are localized to the Rb atoms or to the O_2 molecules. We want to assign the Rb valence electron to a suitable molecular orbital of the group of one Rb atom and three O_2 pairs (cf. p. 231 and Figs. 2 and 3.) The $5s$ orbital of the Rb atom has its largest density at a distance from about 3.5 a.u. to about 7.5 a.u., that is, where the three nearest O atoms of the group are situated. It is therefore reasonable to assume that the molecular orbital ψ is composed of the $5s$ orbital of the Rb atom and atomic orbitals of the three nearest O atoms, O_α, O_β and O_γ:

$$\psi = a\,\varphi_{Rb} + b\,(\varphi_\alpha + \varphi_\beta + \varphi_\gamma). \tag{7}$$

Here, φ_α is a $2p_x$ orbital referring to the electron configuration (3) which we have assumed for the oxygen molecule. The x-axis is directed as in Fig. 1 if Rb in (7) is Rb_1. φ_β and φ_γ are the corresponding orbitals for the other two oxygen atoms. φ_α also enters in the analogous orbital for the valence electron of Rb_2. This molecular orbital is composed of a $5s$ orbital of Rb_2, φ_α and two other oxygen orbitals (Figs. 1 and 3). The spin is, however, antiparallel to that of (7). Similarly the $2p_y$ orbitals of $O_{\alpha'}$ enter in molecular orbitals around Rb_5 and Rb_6. The coefficients a and b of (7) can be determined by minimizing the expression:

$$E = \frac{\int \psi^* H \psi\, d\tau}{\int \psi^* \psi\, d\tau}, \tag{8}$$

where H is the hamiltonian of the valence electron.

Both the valence bond method and the molecular orbital method can only be approximate, although they are very tedious. The application of the valence bond method includes the difficulty of choosing good wave functions for the $4d$ orbitals of the Rb atom. Moreover, it is very laborious to compute all the expressions (4), (5) and (6). Although it would be of interest to make a comparison between the two methods, this has been too tedious for our limited resources, and we have chosen to make the thorough calculations only for the molecular orbital method. The methods differ in two respects: (i) the bonds between an Rb atom and the three O atoms at a distance of 5.68 a.u. have been allowed for in the valence bond method, cf. (4) and (5), but neglected in the molecular orbital method; (ii) the bonds between the Rb atom and the three nearest O atoms have been described in the first method by a one-electron bond resonating between the three atoms and in the second method by one molecular orbital.

4. Calculation of the orbital energy and the molecular orbital

As the wave function (7) is composed of atomic orbitals we must first construct approximate expressions of these orbitals: a $5s$ orbital of Rb, φ_{Rb}, and $2p$ orbitals of O, φ_α, φ_β and φ_γ. Using these we shall determine the coefficients a and b of (7) by minimizing (8). The hamiltonian H in (8) is

$$H = T + V_{\mathrm{Rb}} + V_\alpha + V_{\alpha'} + V_\beta + V_{\beta'} + V_\gamma + V_{\gamma'} + V_{\mathrm{add}}, \tag{9}$$

where V_{Rb} is the potential from Rb^+, $V_\alpha + V_{\alpha'}$ is the potential from one of the O_2 pairs nearest to Rb^+, and $V_\beta + V_{\beta'}$ and $V_\gamma + V_{\gamma'}$ are analogous expressions for the two other oxygen molecules. V_{add} is the potential from all additional rubidium and oxygen ions in the lattice. To get a suitable expression of the interaction it has been necessary to introduce some approximations. For this purpose the interaction with the other electrons has been replaced by a simple potential. Thus, V_{Rb} and e.g. $V_\alpha + V_{\alpha'}$ have been put equal to the potential from an Rb^+ ion and an $O_2^{-0.5}$ ion respectively (cf. the following paragraph). For the determination of $O_2^{-0.5}$ it is necessary to have expressions for the orbitals of the inner electrons. In Sections i and ii of the following we determine all the wave functions which are needed. In Sections iii and iv we calculate the potentials of (9), and finally in Section v we minimize (8).

The reason for our choice of the approximate potential field from an O_2 pair of the group will be apparent from the following discussion. In addition to the electrons in the neutral O_α–$O_{\alpha'}$ molecule (cf. (3)), we have assigned one of the valence electrons of the three nearest Rb atoms to a $2p_x\,(\alpha)$ orbital and the other two to $2p_y\,(\alpha')$ orbitals, see p. 234. Each of these three electrons is assigned to an orbital analogous to (7). Thus every electron is shared between O_α–$O_{\alpha'}$, one Rb atom and two other O_2 pairs. Anticipating our result, we note that an extremum of (8) can be obtained by two different orbitals (7). In one of them the ratio $a:b$ is $\ll 1$, in the other it is $\gg 1$. It is probable that the electron jumps between the two corresponding states. We therefore assume that the electron is equally shared between the Rb atom on the one hand and the three O_2 pairs on the other. Thus on an average it is one-sixth of the time at O_α–$O_{\alpha'}$. Three such electrons give O_α–$O_{\alpha'}$ the charge -0.5, more exactly $O_\alpha^{-\frac{1}{6}}$ and $O_{\alpha'}^{-\frac{1}{3}}$. Consequently the last term in (9), V_{add}, is composed of the potentials from ions of $Rb^{+0.5}$ and $O_2^{-\frac{2}{3}}$. (The charge on $O_2 = -4 \cdot \frac{1}{6}$.)

i. Choice of atomic orbitals for oxygen

For the oxygen we have used the analytical form of the atomic orbitals suggested by DUNCANSON and COULSON [6]:

$$\psi_{1s} = \sqrt{\frac{\mu_1^3}{\pi}}\, e^{-\mu_1 r} = R_{1s}(r)\, S_{00}(\vartheta, \varphi) \qquad \text{(2 electrons)} \tag{10}$$

$$\mu_1 = 7.68$$

$$\psi_{2s} = \sqrt{\frac{\mu_2^5}{3N\pi}} \left(r\, e^{-\mu_2 r} - \frac{3A}{\mu_2}\, e^{-\mu_2 b r} \right) = R_{2s}(r)\, S_{00}(\vartheta, \varphi) \qquad \text{(2 electrons)} \tag{11}$$

$$\mu_2 b = 7.06$$

$$\psi_{2p} = 2 \sqrt{\frac{\mu_3^5}{3}}\, r\, e^{-\mu_3 r}\, S_{1m}(\vartheta, \varphi) = R_{2p}(r)\, S_{1m}(\vartheta, \varphi) \qquad \text{(4 electrons).} \tag{12}$$

A and N of (11) are constants determined by orthonormalization conditions. $S_{lm}(\vartheta, \varphi)$ are normalized spherical harmonics. The parameters μ_2 and μ_3 have been determined in the following way. HARTREE *et al.* [7] have published tables of the electron density of O^- as a function of the distance from the nucleus. These values were determined by self-consistent field computations. We have determined the parameters in the above-mentioned analytical functions (11) and (12) so that the maximum density becomes equal to that given by HARTREE *et al.* The values obtained are $\mu_2 = 2.29$ and $\mu_3 = 1.58$. The density curves obtained from (11) and (12) agree quite well with HARTREE's corresponding curves, but the curve obtained from (12) is displaced somewhat towards larger r values, so that the r value for maximum density is about 0.4 a.u. larger than that of HARTREE. The use of HARTREE's curves for O^- is not quite correct. Under the conditions which we have assumed, the negative charge of an oxygen atom is 0.25–1.25. The values of μ_2 and μ_3 obtained from the curves for neutral O of HARTREE *et al.* [7] are 2.36 and 1.88. Thus our choice of μ values can only be slightly incorrect, provided the μ values of molecular and atomic orbitals are almost equal.

The atomic orbital φ_α of (7) is one of the orbitals (12): $\varphi_\alpha = R_{2p}(r)\, S_{10}(\vartheta, \varphi)$, where ϑ is measured from the x-axis of Fig. 1.

ii. Choice of an atomic orbital for rubidium

For the valence orbital of Rb, φ_{Rb}, we have put

$$\varphi_{\mathrm{Rb}} = A\, r^4\, e^{-\nu r}\, S_{00}(\vartheta, \varphi).$$

The parameter ν should preferably be determined analogously to μ_2 and μ_3 of (11) and (12). Unfortunately, no values of $\psi_{5s}(\mathrm{Rb})$ have been published, as far as we are aware. We have therefore determined ν by an extrapolation from GIBBONS and BARTLETT's tables [8] for $\psi_{4s}(\mathrm{K})$ in the following way: The potentials of K^+ and Rb^+ are obtained from HARTREE's tables [9] and [10]. From a comparison of the potential curves it was found that the curves have the same shape, but that the curve of Rb^+ is displaced towards larger distances r from the nucleus compared to that of K^+. The difference in distance is about 0.1–0.2 a.u., when $r = 1$–2.5 a.u., and decreases for larger r-values. We have thus assumed that the density of $\psi_{5s}(\mathrm{Rb})$ has the same maximum value, $D_{\max}$, as that of $\psi_{4s}(\mathrm{K})$, but that the former maximum corresponds to an r value, $r_{\max}$, 0.15 a.u. larger than that of K. In this way we have determined A from the value of $D_{\max}$, and ν from the assumed value of $r_{\max}$. The function obtained is not exactly normalized to unity as the maxima nearest the nucleus are neglected, $\int \varphi_{\mathrm{Rb}}^* \varphi_{\mathrm{Rb}}\, d\tau = 0.85$. We have preferred to use a function that coincides with GIBBONS and BARTLETT's curve in the interval that is of most importance for our problem. The coincidence is fairly good for r values between 4 and 7 a.u., that is, where the O_2 pairs are placed. HARTREE and HARTREE [11] have also published tables of the electron density of $\psi_{4s}(\mathrm{K})$. Their curve is shifted towards somewhat smaller r values than that of GIBBONS and BARTLETT. The difference is not likely to have any significant influence on our calculations.

The wave function obtained is

$$\varphi_{\mathrm{Rb}} = 0.018557\, r^4 e^{-0.97 r}. \tag{13}$$

iii. Estimation of the potential function of oxygen

$V(\mathrm{O}_2^{-0.5})$, the potential from $\mathrm{O}_2^{-0.5}$, e.g. $V_\alpha + V_{\alpha'}$, has been calculated as the potential from two oxygen atoms, each carrying the charge -0.25:

$$V(\mathrm{O}_2^{-0.5}) = 2\, V(\mathrm{O}^{-0.25}), \tag{14}$$

where

$$V(\mathrm{O}^{-0.25}) = \frac{1}{r}\int_0^r [2\,|R_{1s}(r_1)|^2 + 2\,|R_{2s}(r_1)|^2 + 4.25\,|R_{2p}(r_1)|^2]\, r_1^2\, dr_1 +$$

$$+ \int_r^\infty \frac{1}{r_1}[2\,|R_{1s}(r_1)|^2 + 2\,|R_{2s}(r_1)|^2 + 4.25\,|R_{2p}(r_1)|^2]\, r_1^2\, dr_1. \tag{15}$$

The angular dependence has been neglected in (15). To simplify (15) we have plotted $V(\mathrm{O}^{-0.25})$ against r, and constructed an expression which gives almost the same plot as (15) except for small r values. We have made two different approximations

$$V = -14\, \mu_3^2\, r\, e^{-2\mu_3 r} + \frac{0.25}{r} \tag{16}$$

and

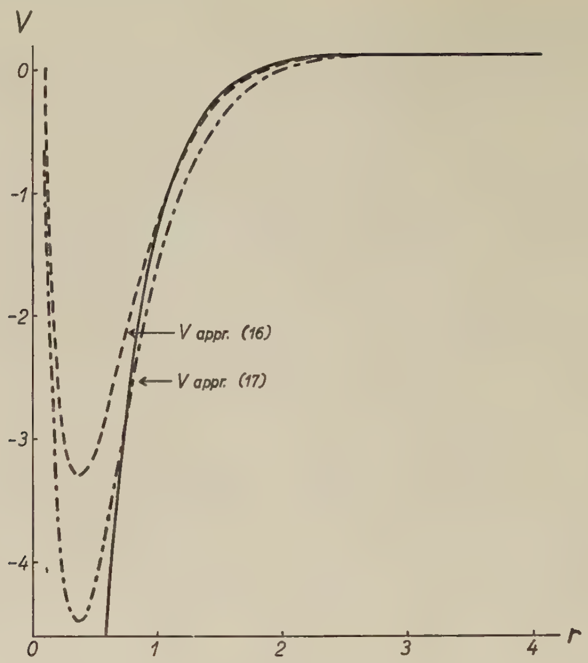

Fig. 4.

———— $V(O^{-0.25})$ according to (15).

— — — V according to (16).

—·—·— V according to (17).

$$V = -18\,\mu_3^2\, r\, e^{-2\mu_3 r} + \frac{0.25}{r}. \tag{17}$$

All the following calculations have been carried out using both (16) and (17). Fig. 4 shows that for r larger than 1 a.u. the plot of (16) coincides well with that of (15), but that the plot of (17) is somewhat too low. For smaller r values the plots of both (16) and (17) lie above that of (15), but (17) agrees satisfactorily with (15) for r values between 1 a.u. and 0.5 a.u. As the calculation of $V(O^{-0.25})$ is itself an approximation, especially for small r values, we have not found it justifiable to look for a still better approximation of (15).

For each $O^{-\frac{1}{3}}$ in V_{add} we have determined the potential by means of (15), but making allowance for the difference in charge. The last term in the approximations (16) and (17) in this case becomes $+\frac{1}{3r}$.

iv. The potential function of rubidium

Hartree [10] gives a table of $Z_p = r\,V(\mathrm{Rb}^+, r)$ where $V(\mathrm{Rb}^+, r)$ is the potential at a distance r from the Rb^+ ion. From this table we have calculated $V(\mathrm{Rb}^+, r)$ (which is V_{Rb} in (9)). The potential is plotted against r in Fig. 5.

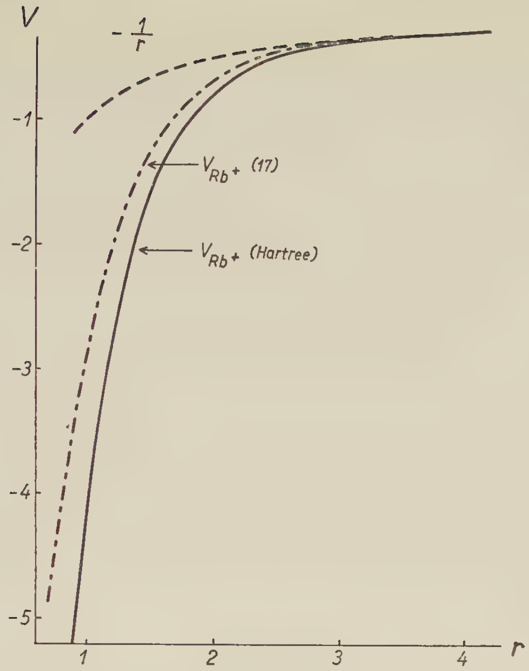

Fig. 5.

——— $V(\mathrm{Rb}^+)$ according to HARTREE [10].

— — — $V = -\frac{1}{r}$.

—·—·— $V = -\frac{1}{r} - 18\,\mu_3^2\,r\,e^{-2\mu_3 r}$. (See Discussion.)

In the following calculations V_{Rb} has been approximated as $-\frac{1}{r}$. The approximated value differs from that of HARTREE by 0.024 a.u. for $r = 3.0$ a.u., and still less for larger r values. For smaller r values the atomic orbitals of (7) have comparatively small values, φ_{Rb} being the dominant term. As we have used the experimental value of the ionization energy of Rb for the integral $\int \varphi_{\mathrm{Rb}}^* (T + V_{\mathrm{Rb}})\, \varphi_{\mathrm{Rb}}\, d\tau$, the approximation of V_{Rb} is quite satisfactory.

For the potential from each $\mathrm{Rb}^{-0.5}$ in V_{add} we have used the approximation $-\frac{0.5}{r}$, in agreement with V_{Rb} above. This approximation will be discussed below.

v. Determination of the orbital energy and the coefficients *a* and *b* in the molecular orbital

We have determined the coefficients a and b of (7) by minimizing the orbital energy (8). We have used a semi-empirical method for finding better values for the orbital energy. Thus we have replaced $\int \varphi_{\mathrm{Rb}}^* (T + V_{\mathrm{Rb}})\, \varphi_{\mathrm{Rb}}\, d\tau = E_{\mathrm{Rb}}$ by the ionization energy of Rb [2], -0.1535 a.u., and $\int \varphi_\alpha^* (T + V_{\mathrm{Rb}}) \varphi_{\mathrm{Rb}} \, d\tau$ by $E_{\mathrm{Rb}} \cdot \int \varphi_\alpha^* \varphi_{\mathrm{Rb}} \, d\tau$. It is true that the vertical ionization potential E_{Rb} is not identical with the experimental value. In the present case the difference is, however, probably very small. We also need a value for the ionization energy E_{O} of $\mathrm{O}^{-1.25}$ for the integral $\int \varphi_\alpha^* (T + V_\alpha) \varphi_\alpha \, d\tau$. We have obtained the value $E_{\mathrm{O}} = -0.004$ a.u. by extrapolation from the ε values of HARTREE *et al.* [7] for O and O^-.

The values found for all the integrals are found in the Appendix. The three-centre integrals e.g. $\int \varphi_\alpha^* f(\varrho) \varphi_{\mathrm{Rb}} \, d\tau$ have been approximated as

$$\int \varphi_\alpha^* f(\varrho) \varphi_{\mathrm{Rb}} \, d\tau = \tfrac{1}{2} \int \varphi_\alpha^* \varphi_{\mathrm{Rb}} \, d\tau \left[\int \varphi_\alpha^* f(\varrho) \varphi_\alpha \, d\tau + \int \varphi_{\mathrm{Rb}}^* f(\varrho) \varphi_{\mathrm{Rb}} \, d\tau \right], \tag{18}$$

where ϱ is the distance from the third centre.

The integral $E_{\mathrm{add}} = \int \psi^* V_{\mathrm{add}} \psi \, d\tau$ can be calculated taking into account all the N surrounding groups $\mathrm{Rb}_4(\mathrm{O}_2)_3$ lying within a sphere of radius R. We have calculated E_{add} for 6 values of $R \leq 1$ crystal unit $= 17.6$ a.u., corresponding to $N \leq 16$. It is found that the value of E_{add} is independent of R when $R > 16$ a.u., and the potential from complete $\mathrm{Rb}_4(\mathrm{O}_2)_3$ groups at larger distances can therefore be neglected.

5. Results

The computed values of the coefficients a and b of (7), and the corresponding energy values, are given in Table 3. The calculation gives two orthogonal molecular orbitals, and the difference of energy between these orbitals is given in the last column of Table 3. The lower orbital is composed of the three oxygen atomic orbitals with a small contribution from φ_{Rb}, and the higher orbital is almost a pure Rb orbital, only slightly disturbed by the presence of the surrounding oxygen atoms. The energy difference corresponds approximately to light in the visible spectrum, and it can be assumed that the transition of the electron between these two states is the cause of the dark colour of the crystal.

Table 3.

Approximate potential used	$\frac{a}{b}$	E	Energy difference
. (16)	0.3 -5.7	-0.30 a.u. -0.23 a.u.	0.07 a.u. = 6 500 A
(17)	0.6 -4.1	-0.31 a.u. -0.25 a.u.	0.06 a.u. = 7 500 A

6. Discussion

In the preceding chapters we have discussed two different theoretical descriptions of the electron distribution of the dark-coloured crystals of the alkali sesquioxides. On the basis of one of the descriptions we have carried out a calculation of the frequency of the absorbed radiation. According to this treatment the absorption should be within the range of visible light, which is in agreement with the experimental evidence. This calculation is, however, subject to several uncertainties, some of which will be discussed below. We have estimated that the influence of the uncertainties on the final result is a few per cent, at most about 15 per cent, and thus none of the points mentioned below is likely to invalidate the main result of the present study, although the actual figure for the absorption wavelength is perhaps somewhat in error.

The various approximations made in the calculation were made in order to keep the computations from becoming too laborious. Thus we have used simple atomic orbitals of the type $A r^n e^{-ar}$ without any modification of the parameters a to allow for surrounding nuclei. Moreover, we have neglected the correlation energy and the exchange part of the electron potential. In the following we will first discuss the influence of the simplified wave functions and then the neglected parts of the potentials.

We have tried to bring the wave functions into agreement with HARTREE's wave functions in the interval where the electron density has its largest value. As far as the φ_{Rb} (13) is concerned, this is the interval where the nearest oxygen atoms are situated. As a matter of fact, the integrals $\int \varphi^* V_{\mathrm{add}} \varphi \, d\tau$, where φ can have the indices Rb, α, β, γ, contribute considerably to the energy, and the wave function at larger distances from the nucleus is therefore also of importance. It is, however, the difference between φ_{Rb} and φ_α which enters into the expression for the absorption frequency. This difference is probably of the correct magnitude even with the approximations made.

$V_\alpha + V_{\alpha'}$ is calculated as the potential from two $\mathrm{O}^{-0.25}$ instead of the potential from $\mathrm{O}^{-\frac{1}{6}}$ and $\mathrm{O}^{-\frac{1}{3}}$. This would give an error of about 0.01 a.u. Moreover, we have neglected the angular dependence and the influence of the σ bond of the oxygen on the electron distribution.

The uncertainty of the potential functions close to the nuclei seems to be the most significant approximation, because φ_{Rb} has large values at the sites of the nuclei of the nine nearest O atoms, and moderate values at the nuclei of at least three O atoms and five Rb atoms. Since we have neglected the correlation energy and the exchange part of the electron potential, the potential (15) of oxygen as well as the potential $V(\mathrm{Rb}^+)$ from HARTREE's curves are surely too low in the region close to the nuclei. This is especially so for the Rb^+ ion, where so many electrons are collected. HJALMARS [12] has determined the repulsion from the $1s$, $2s$ and $2p$ electrons in oxygen by numerical integration of HARTREE's curves. To get the same repulsion by our method we must use an approximation between (16) and (17). This gives a support for the assumption that (16) and (17) are reasonable approximations. When we tried to estimate the error in the energy difference, we used the first term in (17) as a correction also of the potential of rubidium.

It is difficult to estimate the error in the results caused by all these approximations. Some of them cause an increase and other a decrease of the energy difference between the two lowest states. Our opinion is that the resulting energy difference is perhaps somewhat too large. The absorption wave length should therefore be a little too short.

ACKNOWLEDGEMENT

I would like to express my sincerest thanks to Professor O. KLEIN for his kind interest, and for many stimulating discussions. I am also much indebted to Docent I. HJALMARS, who has suggested the present investigation, and I would like to express my gratitude for her stimulating guidance and for her encouragement and unfailing interest.

Institute of Theoretical Physics, University of Stockholm, June 1954.

Appendix

All the integrals are one-electron, two-centre integrals. R is the distance between the two centres in atomic units. For φ_{Rb} we use the notation Rb and for φ_α the notation p_x or p_z. The line through the two centres is chosen as z-axes. The two centres are A and B.

Coulomb Integrals

$$\int a^* f(r_B)\, a\, d\tau = C(f(r); a, a)$$

R	$C\left(\frac{1}{r}; p_z, p_z\right)$	$C\left(\frac{1}{r}; p_x, p_x\right)$	$C\left(\frac{1}{r}; \mathrm{Rb}, \mathrm{Rb}\right)$
2.42	0.4727	0.3719	
5.40			0.1414
5.43	0.1917		
5.70	0.1818	0.1721	0.1371
6.00			0.1328
7.00	0.1464	0.1411	
8.00			0.1055
8.80	0.1154	0.1128	
10.0	0.1012	0.0994	0.0852
11.0	0.0918	0.0905	0.0775
11.5			0.0742
12.0	0.0840	0.0830	0.0711
12.5			0.0682
13.0	0.0775		0.0656
13.5			0.0632
14.0	0.0719		0.0609
14.5			0.0588
15.0	0.0670		0.0569
15.5			0.0550
16.0	0.0628		0.0533
16.5			0.0517
17.0	0.0591		0.0502
17.5			0.0487
18.0	0.0558		0.0474

R	$C(re^{-2\cdot 1.58\,r}; p_z, p_z)$	$C(re^{-2\cdot 1.58\,r}; p_x, p_x)$	$C(re^{-2\cdot 1.58\,r}; \mathrm{Rb}, \mathrm{Rb})$
2.42	0.00773	0.001511	
5.70			0.000343
7.20	0.0000003		
7.84			0.000081

Exchange integrals

$$\int a^* f(r_k)\, b\, d\tau = E(f(r_k); a, b) \qquad (k = A \text{ or } B)$$

R	$E\left(\frac{1}{r_A}; p_z, \text{Rb}\right)$	$E\left(\frac{1}{r_B}; p_z, \text{Rb}\right)$	$E(r_A e^{-2\cdot 1.58 r_A}; p_z, \text{Rb})$
5.43	0.0290	0.0225	
5.70	0.0317	0.0220	0.000426

Overlap integrals

R	$\int \varphi_\alpha^* \varphi_{\text{Rb}}\, d\tau = (p_z, \text{Rb})$	R	$\int \varphi_\alpha^* \varphi_\beta\, d\tau$
5.43	0.0656	6.99	0.0102

REFERENCES

1. A. Helms and W. Klemm, Z. anorg. und allgem. Chem. *242* (1939) 201.
2. Atomic Energy Levels, Circular of the National Bureau of Standards *467*, Vol. II (1952).
3. R. Hultgren, Phys. Rev. *40* (1932) 891.
4. L. Pauling, The Nature of the Chemical Bond, 2nd ed. Ithaca (1948) p. 106, 259.
5. A. Meckler, J. Chem. Phys. *21* (1953) 1750.
6. W. E. Duncanson and C. A. Coulson, Proc. Roy. Soc. Edinb. A *62* (1943) 37.
7. D. R. Hartree, W. Hartree and B. Swirles, Phil. Trans. Roy. Soc. London A *238* (1938) 229.
8. J. J. Gibbons Jr. and J. H. Bartlett Jr., Phys. Rev. *47* (1935) 693.
9. D. R. Hartree, Proc. Roy. Soc. A *143* (1934) 506.
10. D. R. Hartree, Proc. Roy. Soc. A *151* (1935) 96.
11. D. R. Hartree and W. Hartree, Proc. Camb. Phil. Soc. *34* (1938) 550.
12. I. Hjalmars, unpublished calculations.

Tryckt den 27 januari 1955

Uppsala 1955. Almqvist & Wiksells Boktryckeri AB

ARKIV FÖR FYSIK Band 9 nr 15

Communicated 27 October 1954 by Manne Siegbahn and G. Borelius

An investigation of the longitudinal angular distribution of photoelectrons at gamma ray energies of 0.41, 0.66 and 1.33 Mev

By Sölve Hultberg

With 20 figures in the text

Introduction

Ever since directional effects in the distribution of photoelectrons around the direction of incidence of X-rays impinging on thin metal foils was observed in the early years of this century, several attempts have been made in order to work out a satisfactory theory for the photoelectric emission, and many experiments have been performed to check the theoretical formulas. Before 1947 the Wilson cloud chamber method was used almost exclusively [1] and thereafter magnetic spectrometers have been utilized in a few cases [2, 3]. In spite of the many reported investigations, most of which were carried out before 1931 in the X-ray region, no really reliable quantitative determinations of the longitudinal distribution of photoelectrons have ever been made, because (a) the statistics in the Wilson method are very poor (some 300–500 tracks are usually measured), and (b) the magnetic spectrometer measurements [2, 3], where the statistics are good, are incomplete and reported only as by-products of larger investigation schemes and are not analyzed; they are merely included to demonstrate the effect.

Thus the Wilson chamber experiments remain as the only investigations trying to determine the true longitudinal intensity distribution of photoelectrons at specified energies, but they suffer seriously from the drawback mentioned above.

These considerations led to the conclusion that a closer examination of the magnetic spectrometer method could be worth while, because a large double-focusing spectrometer ($\varrho = 50$ cm) was available, which would allow the use of strong gamma sources and thus would permit good statistics. The present paper is concerned with the details of an investigation of the angular distribution of photoelectrons at three gamma-ray energies: 0.41 Mev, 1.33 Mev (the preliminary results of which were reported in the form of a letter in *Phys. Rev.* [4]) and 0.66 Mev.

The two experiments first mentioned have been carefully reanalyzed, and the figures given in the present paper are to be regarded as final. The drawing and the value of $\vartheta_{\max}$ for $\beta = 0.96$ given in reference [4] have been slightly corrected.

The present paper is divided in three parts:

A. A short survey of the development and present status of the theory for the longitudinal photoelectric intensity distribution from gamma-radiation of different energies.

B. Details of four experiments performed at the gamma energies 411 kev ($\beta = 0.79$), 662 kev ($\beta = 0.88$), and 1330 kev ($\beta = 0.96$).

C. A compilation of the formulas and tables needed for the computation of multiple scattering from the theory of MOLIÈRE [5].

Section C is included in order to show how readily the scattering of electrons in thin metal foils can be computed from the Molière theory without having to penetrate the whole mathematical formalism of the original articles by Molière or the subsequent treatment of the same theory by BETHE [6]. From this section the multiple scattering of electrons can be easily computed without much labour in the case of spatial distribution, which is obtained in the form of an analytical function of Gaussian character.

In the text the following notations will be used:

(a) Sections are referred to by capitals followed by Roman numbers: A, B II, C etc., with or without parentheses.

(b) Equations and formulas are indicated by section capitals followed by Arabic numbers: (A 10), (B 2), and so on.

(c) Numbers in brackets without capitals always mean references; these are listed after the text.

A. The development of the theory for the ejection of photoelectrons from the atomic *K*-shells

In the photoelectric process the incident gamma quantum disappears completely and its energy E is converted into ionization energy of, say, the K-shell and kinetic energy E_{kin} of the electron, where

$$E = E_{\text{kin}} + E_K . \tag{A 1}$$

According to HEITLER [7] one can roughly estimate the photoelectric absorption in the K-shell at high energies as 80 % of the total photoelectric absorption. All formulas presented in the following discussion refer to the atomic K-shells.

The direction of emission of the photoelectron is usually defined in the way shown in Fig. 1. Here a linearly polarized light wave is considered with the propagation direction along the z-axis of the rectangular coordinate system with the electric vector oscillating along the x-axis. The direction of emission is defined by the longitudinal angle ϑ and the azimuthal angle φ, as shown in the figure. The dependence on ϑ defines the longitudinal intensity distribution[1] and the dependence on φ gives the azimuthal intensity distribution of the photoelectrons.

---

[1] This distribution in ϑ will be referred to as "the angular distribution", since we shall not be concerned with the azimuthal distribution.

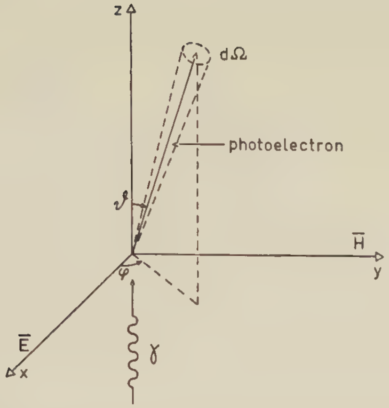

Fig. 1. Definition of the emission direction of a photoelectron. The z-axis is taken as propagation direction of the gamma quantum.

Denote a small solid angle around the emission in the direction ϑ by $d\Omega$ and let $J(\vartheta)$ describe the angular distribution for unpolarized radiation, i.e. the photoelectric emission rate into $d\Omega$ is $J(\vartheta)\cdot d\Omega$. Choosing $d\Omega = 2\pi\cdot\sin\vartheta\cdot d\vartheta$ we have for the change of total rate N

$$dN = 2\pi\cdot\sin\vartheta\cdot J(\vartheta)\cdot d\vartheta = n(\vartheta)\cdot d\vartheta. \tag{A 2}$$

Integrating over all ϑ we obtain

$$N = \int_0^\pi n(\vartheta)\cdot d\vartheta. \tag{A 3}$$

The asymmetry A is defined from [ref. 1]

$$A = \frac{\int_0^{\frac{\pi}{2}} n(\vartheta)\cdot d\vartheta}{\int_{\frac{\pi}{2}}^{\pi} n(\vartheta)\cdot d\vartheta} \tag{A 4}$$

and the bipartition angle ϑ_b can be calculated from [ref. 1]

$$\int_0^{\vartheta_b} n(\vartheta)\cdot d\vartheta = \int_{\vartheta_b}^{\pi} n(\vartheta)\cdot d\vartheta. \tag{A 5}$$

Thus ϑ_b is the semi-vertical angle of a cone which divides the total number of photoelectrons in two equal parts. An approximate calculation gives for ϑ_b [1]

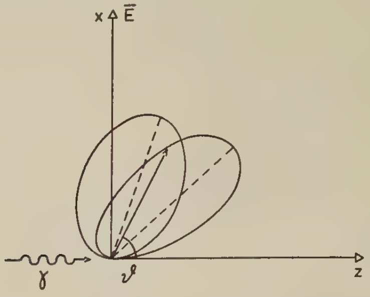

Fig. 2. Polar diagram showing the intensity distribution of the photoelectrons at two different gamma ray energies. $\vartheta_{\max}$ is a characteristic function of $\beta = v/c$.

$$\cos\vartheta_b \sim \frac{\beta}{1+k} \qquad \begin{cases} \beta = \dfrac{v}{c} \\ k = \dfrac{h\nu}{2\,m_0\,c^2} \end{cases} \tag{A 6}$$

The directional dependence of the intensity is usually illustrated by polar diagrams such as the one in Fig. 2.

For unpolarized radiation there is rotational symmetry around the z-axis. $\vartheta_{\max}$ is the angle that the direction of maximum intensity makes with the z-axis. This angle decreases as the energy of the radiation increases and a knowledge of $\vartheta_{\max}$ at different electron energies obviously may be of interest. The main object of the investigation reported here is the determination of $\vartheta_{\max}$ at large β's, where accurate values of $\vartheta_{\max}$ are completely lacking. The results are then compared with theoretical predictions.

On the basis of radiation pressure on the ejected photoelectron WENTZEL [8] in 1926 deduced an expression for J which was asymmetric in ϑ

$$J \sim \sin^2\vartheta\cdot(1 + 2\,\beta\cdot\cos\vartheta)\,\cos^2\varphi. \tag{A 7}$$

The factor $(1 + 2\,\beta\cdot\cos\vartheta)$ gives $J_{\max}$ for $\vartheta < \pi/2$. The experiments showed, however, that the calculated asymmetry in ϑ from (A 7) is far too small; that is, classical mechanics cannot explain the observed longitudinal asymmetry quantitatively.

In 1930 SOMMERFELD and SCHUR [9] calculated the following expression starting from the Schrödinger equation

$$J \sim \sin^2\vartheta\cdot(1 + 4\,\beta\cdot\cos\vartheta)\cdot\cos^2\varphi. \tag{A 8}$$

This relationship holds for small β's and has been verified experimentally in the X-ray region with Wilson cloud chambers.

Then J. FISCHER [10] gave the following formula, also founded on the Schrödinger equation

$$J \sim \frac{\sin^2\vartheta}{(1-\beta\cdot\cos\vartheta+k)^4}\cdot\cos^2\varphi\,; \quad k = \frac{h\nu}{2\,m_0\,c^2}, \tag{A 9}$$

to which (A 8) is an approximation if k is neglected.

Finally F. SAUTER [11, 12] published two papers in 1931, and on the basis of the relativistic electron theory by Dirac he obtains the following extended formula for the dependence of J on ϑ and φ:

$$J(\vartheta,\varphi)\sim\tfrac{1}{4}\cdot\frac{(1-\sqrt{1-\beta^2})^2}{(1-\beta^2)^{3/2}}\cdot\frac{\sin^2\vartheta}{(1-\beta\cdot\cos\vartheta)^3}-$$

$$-\tfrac{1}{2}\cdot\frac{1-\sqrt{1-\beta^2}}{1-\beta^2}\cdot\frac{\sin^2\vartheta}{(1-\beta\cdot\cos\vartheta)^3}\cdot\cos^2\varphi+\frac{\sin^2\vartheta}{(1-\beta\cdot\cos\vartheta)^4}\cdot\cos^2\varphi. \qquad \text{(A 10)}$$

For relativistic β ($\beta>0.5$) this relation is, however, subject to the limiting conditions of the Born approximation ($\beta\sim 1$ and $Z\ll 137$). In practice β often lies in the range 0.5–1 and, because the photoelectric cross section increases as Z^5, heavy radiators are generally used, hence the second condition $Z\ll 137$ is almost never fulfilled. These facts mean that Eq. (A 10) has to be used with discretion and that it should be checked experimentally in order to see how far it is true. The first two terms on the right-hand side of Eq. (A 10) can be considered as relativistic corrections to the third one, which is similar to Eq. (A 9).

Multiplying by the surface element $dS=\sin\vartheta\cdot d\vartheta\cdot d\varphi$ ($r=1$) and integrating over all polarization directions φ of the gamma radiation Eq. (A 10) becomes

$$J(\vartheta)\cdot 2\pi\cdot\sin\vartheta\cdot d\vartheta\sim a\cdot\frac{\sin^3\vartheta}{(1-\beta\cdot\cos\vartheta)^3}\cdot d\vartheta\cdot\int_0^{2\pi}d\varphi-$$

$$-b\cdot\frac{\sin^3\vartheta}{(1-\beta\cdot\cos\vartheta)^3}\cdot d\vartheta\cdot\int_0^{2\pi}\cos^2\varphi\cdot d\varphi+\frac{\sin^3\vartheta}{(1-\beta\cdot\cos\vartheta)^4}\cdot d\vartheta\cdot\int_0^{2\pi}\cos^2\varphi\cdot d\varphi. \qquad \text{(A 11)}$$

Thus

$$J(\vartheta)\sim\left(a-\frac{b}{2}\right)\cdot\frac{\sin^2\vartheta}{(1-\beta\cdot\cos\vartheta)^3}+\tfrac{1}{2}\cdot\frac{\sin^2\vartheta}{(1-\beta\cdot\cos\vartheta)^4} \qquad \text{(A 12)}$$

where for convenience

$$a=\tfrac{1}{4}\cdot\frac{(1-\sqrt{1-\beta^2})^2}{(1-\beta^2)^{3/2}};\qquad b=\tfrac{1}{2}\cdot\frac{1-\sqrt{1-\beta^2}}{1-\beta^2} \qquad \text{(A 13)}$$

$$a=b^2\cdot\sqrt{1-\beta^2}. \qquad \text{(A 14)}$$

Thus the angular distribution $J(\vartheta)$ for non polarized radiation can be written

$$J(\vartheta)\sim(2a-b)\cdot J_{\mathrm{r}}+J_{\mathrm{n}}$$

$$J_{\mathrm{r}}=\frac{\sin^2\vartheta}{(1-\beta\cdot\cos\vartheta)^3};\quad J_{\mathrm{n}}=\frac{\sin^2\vartheta}{(1-\beta\cdot\cos\vartheta)^4};\quad \begin{cases}\mathrm{r}=\text{relativistic}\\ \mathrm{n}=\text{non relativistic}\end{cases} \qquad \text{(A 15)}$$

We now want to know how the position of the intensity maximum varies with energy. Differentiating Eq. (A 15) with respect to ϑ and putting $dJ/d\vartheta=0$

we get an equation which on solving for ϑ gives $\vartheta_{\max}$ as a function of β. We thus obtain

$$\frac{dJ}{d\vartheta}=(2a-\mathrm{b})\cdot\frac{dJ_{\mathrm{r}}}{d\vartheta}+\frac{dJ_{\mathrm{n}}}{d\vartheta}=0 \tag{A 16}$$

and by means of Eq. (A 15)

$$(2a-b)(1-\beta\cos\vartheta)(\beta\cos^2\vartheta+2\cos\vartheta-3\beta)+2(\beta\cos^2\vartheta+\cos\vartheta-2\beta)=0. \tag{A 17}$$

From Eq. (A 17) we can find $\vartheta_{\max}(\beta)$ for J_{r} and J_{n} separately:

$$\beta\cos^2\vartheta+2\cos\vartheta-3\beta=0 \quad \text{gives} \quad \cos\vartheta=-\frac{1}{\beta}+\sqrt{\frac{1}{\beta^2}+3}, \tag{A 18}$$

$$\beta\cos^2\vartheta+\cos\vartheta-2\beta=0 \quad \text{gives} \quad \cos\vartheta=-\frac{1}{2\beta}+\sqrt{\frac{1}{4\beta^2}+2}. \tag{A 19}$$

Eqs. (A 18, 19) give a fairly good idea of $\vartheta_{\max}$ as they do not differ by much, and on account of their simplicity they have formerly been used exclusively to obtain practical estimates of $\vartheta_{\max}$ by interpolation. Eq. (A 17) is discussed in greater detail in section B V.

Finally, it may be mentioned that the formula of FISCHER and SAUTER (A 9) is considered as rather well established for small β's as it agrees very well with most Wilson chamber experiments. In these cases the comparison between theory and experiments was, however, not based on a determination of the angle of maximum emission $\vartheta_{\max}$, as will be done in the present paper. In the earlier investigations the bipartition angles were the quantities most frequently determined from the obtained distributions. They were then compared with the theoretical values from Eqs. (A 5) and (A 6). This is quite natural because it is very difficult to determine $\vartheta_{\max}$ from the distribution curves of the Wilson chamber experiments [1], which very well may give reliable estimates of the total spatial distribution $n(\vartheta)$ (A 2) but cannot be expected to deliver correct values of the intensity per unit solid angle $J(\vartheta)$, for statistical and practical reasons. In the spectrometer method, on the other hand, $J(\vartheta)$ is the measured quantity (constant slit opening for all angles) and therefore it is suitable to try to get accurate values of $\vartheta_{\max}$ and compare with Eq. (A 17). The reader is referred to the article by EGGLESTON & MARTIN [1] for a general survey of the results of the earlier Wilson chamber experiments.

Thus no precise experimental values of $\vartheta_{\max}$ exist at any energy and, accordingly, the aim of the present paper is to supply this lack of information for large β's.

B. The angular distributions at $\beta=0.79$, 0.88 and 0.96

For the reasons outlined in the Introduction three experiments were performed in 1953 and 1954 at gamma energies of 0.41 Mev from Au^{198}, 0.66 Mev from Cs^{137} and 1.33 Mev from Co^{60}. Apart from the intrinsic interest, an experimental knowledge of the variation of $\vartheta_{\max}$ with β for high energies might prove useful for some applica-

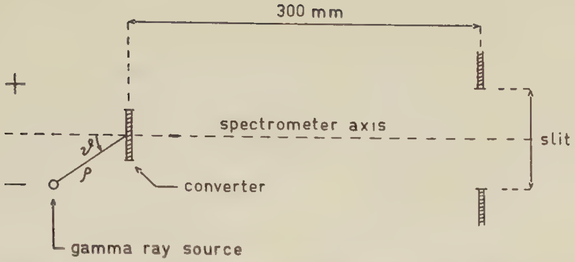

Fig. 3. Schematic view of the spectrometer arrangement. + and − refer to different directions of ϑ with respect to the spectrometer axis ($\vartheta = 0$).

tions in β-spectrometric investigations of gamma radiation.[1] This applies, of course, to the use of thin converter foils so that the electrons have not completely lost their original directions of emission by scattering in the foil.

I. The case of $\beta = 0.79$

Experimental.—The experimental setup is shown schematically in Fig. 3.

The circular converter (diameter 11 mm) was placed at the usual source position in the double focusing spectrometer of mean radius 50 cm, and the active gold was fixed to an arm which could be moved horizontally around the vertical axis through the converter centre. The size of the mounting for the converter and source holder was chosen so as to minimize the necessary material near the converter but was at the same time limited by the volume of the vacuum lock device. The construction can be understood from Fig. 4.

As the gamma source was rather strong (~ 400 mC) a coincidence GM-counter was used and with a considerable amount of lead shielding between source and counter, this arrangement reduced the background to a satisfactory level (~ 20 counts/min).

In the choice of converter (cf. discussion in Section B II) the multiple scattering

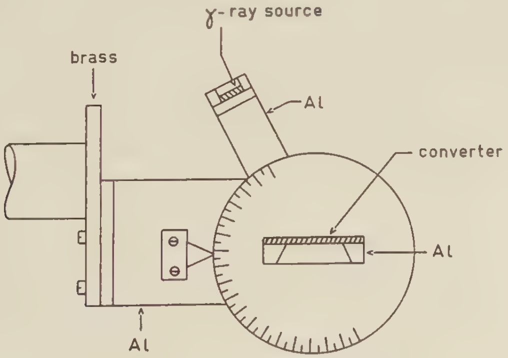

Fig. 4. Experimental setup for the Au-198 experiment (schematic).

---

[1] An attempt in this direction was made by K. SIEGBAHN and H. SLÄTIS, Arkiv f. Mat., Astr. o. Fysik 32 A, No. 9 (1945).

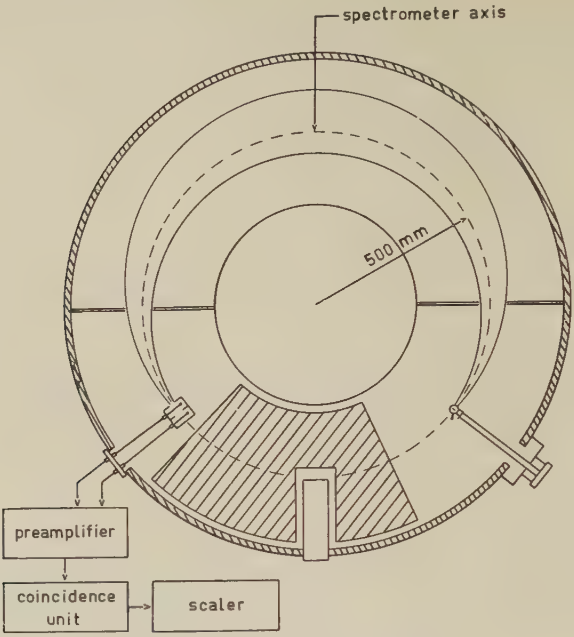

Fig. 5. Arrangement in the double focusing spectrometer.

of the photoelectrons in the material must be considered, and a rough calculation from a nomogram [13], which is founded on an approximate theory by W. BOTHE [14], gives a thickness of about 1 mg/cm², if a probable deviation of 10° of the photoelectrons is allowed. A gold foil of 0.8 mg/cm² gave an intensity which was too low, so another foil of 1.68 mg/cm² was used. The probable deviation in this converter, however, turned out to be far lower than that calculated from the nomogram.

The gamma radiation source consisted of neutron-irradiated gold, which had the shape of a disc (diameter 5 mm, thickness 1 mm) encased in aluminium in order to cut off all decay electrons from Au^{198}.

Measurements.—The investigation was carried out by measuring the K conversion line of the 411 kev gamma ray for different ϑ's over a range of 150°. By taking the backgrounds, Compton electrons and other secondaries could then be subtracted. The recorded photo-lines are shown in Fig. 6 after correcting for decay (half life 2.7 days).

The following data about these recordings should be mentioned:

1) The spectrometer iron was demagnetized before the runs but did not have to be demagnetized between each measurement of a photo-line because of the extremely small variation of the magnetic field over a line.

2) The current was always varied in only one direction over a line.

3) The photo-lines were measured by 1 min. counts and the backgrounds by 2 min. counts. After some preliminary tests the line series shown in Fig. 6 was run. A few lines were then repeated.

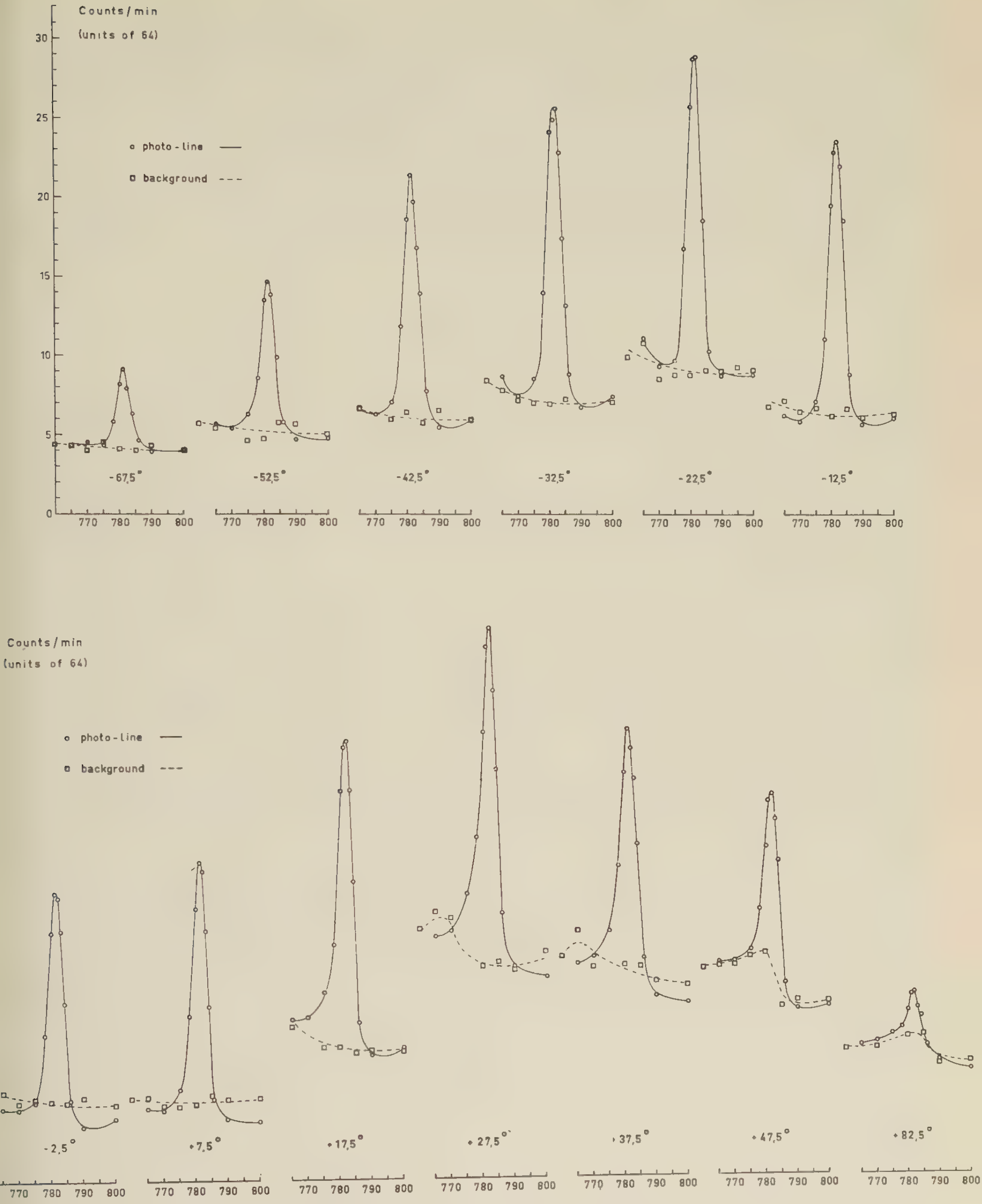

Fig. 6. Photo-lines from the 411 kev gamma ray of Au-198 shown for different angles ϑ. 1.68 mg/cm^2 gold converter. $\beta = 0.795$.

4) The backgrounds of the lines were measured immediately before and after the peaks, and in the diagram the mean value of the two background runs is plotted. Photo-lines and backgrounds were measured under identical experimental conditions; only the converter was taken away in the latter case.

5) ϱ, the source-to-converter distance, was 33 mm (Fig. 3).

6) The plateau of the GM-counter was frequently checked during the measurements; its behaviour was found to be resonably constant.

Discussion of results.—The fraction dJ of photoelectrons emitted into a solid angle $d\Omega$ around a certain direction can be written

$$\frac{dJ}{d\Omega} = N \cdot \varrho_a \cdot x \frac{d\sigma}{d\Omega}, \tag{B 1}$$

which results from the definition of the cross section. N is the number of incident photons, ϱ_a is the number of atoms/cm^3, x is the thickness of the converter and $\frac{d\sigma}{d\Omega}$ is the differential cross section per unit solid angle, which is a function of photon energy, the nature of the absorber and the angle between the direction of the incident photon and the outgoing electron. Eq. (B 1) regards the direction of the photons as fixed and considers various positions of $d\Omega$, whereas, for natural reasons, we study the intensity of photoelectrons scattered into a $d\Omega$ around the spectrometer axis as a fixed direction, and, accordingly, vary the position of the gamma source (cf. Fig. 3). This means that the quantity $N \cdot \varrho_a \cdot x$, which is proportional to the absorption of the quanta in the converter material, has to be independent of the position of the source. This is in fact so, because N is determined by the solid angle, that the converter subtends at the source, and is consequently proportional to $\cos \vartheta$ while x, being the traversed path inside the converter, has to be multiplied by $1/\cos \vartheta$, ϑ thus exactly cancelling from the product. Consequently $N \cdot \varrho_a \cdot x$ is a constant for a given converter.

The photo-line peak heights, which represent the electron intensity per unit solid angle, are therefore proportional to the differential cross sections for the corresponding ϑ and thus, by plotting the peak heights versus ϑ, we can obtain the intensity distribution $J(\vartheta)$, which is represented by the full line curve in Fig. 7.

The curve was drawn through the experimental points, and then the centre line corresponding to the direction of the spectrometer axis ($\vartheta = 0$) was drawn to give the best fit for symmetry over the whole curve. In this way the positions of the symmetrical intensity distribution maxima relative to $\vartheta = 0$ could be determined already from the experimental curve. Before any conclusive figures are given, one has, however, to consider the possible influences on the result from (a) geometry and (b) scattering of the electrons in the converter material as discussed below.

The uncertainties in the drawing of the distribution curve of Fig. 7 arise from the setting of the angle ϑ and the determination of the peak heights from Fig. 6. The question of basing the distribution curve on peak heights or on the areas of the photo-lines is discussed in section B IV. The graduation of the circular disc in intervals of 5° was very accurately done in a machine and, as interpolated settings between the marks were never used, a certain ϑ could easily be reproduced to 0.1°, which in turn means that the errors resulting from inaccurate angle settings are quite negligible.

The errors in the estimates of the peak heights from the photo-lines of Fig. 6 arise in about equal parts from the uncertainties in the determinations of maxima and

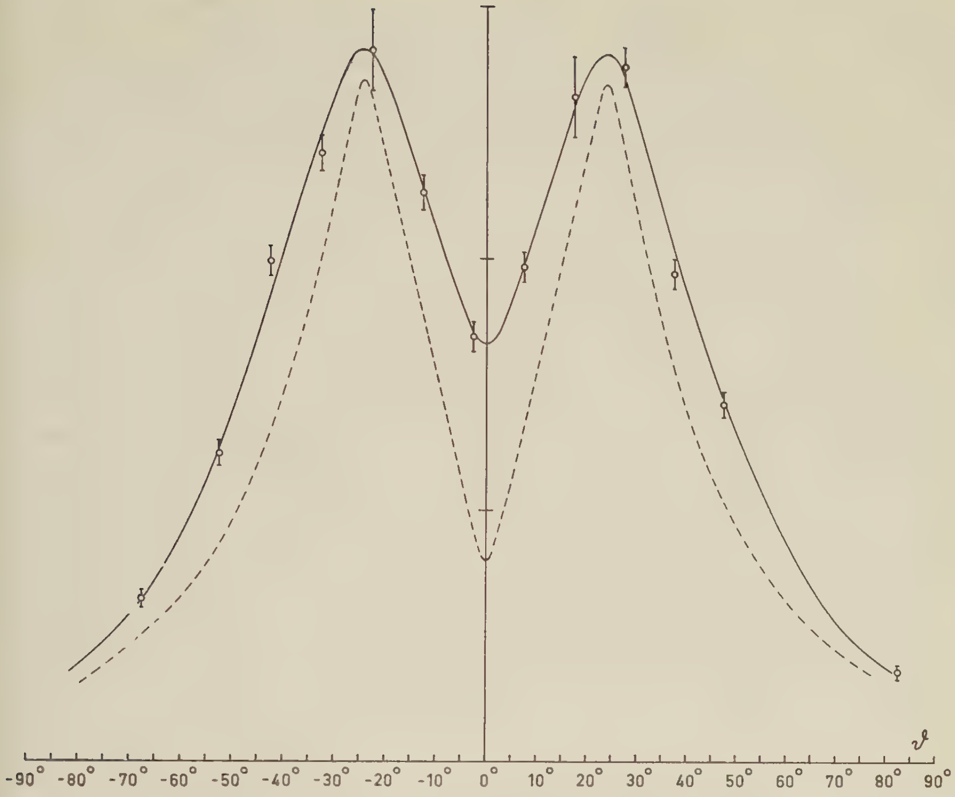

Fig. 7. The experimental (full line) and true (dotted line) photoelectric intensity distributions for $\beta = 0.795$. Units of 500 counts/min. are indicated on the ordinate axis.

backgrounds. The maxima mainly suffer from a greater statistical error, while the background level in this case is subject to an effect somewhat similar to the variation of the peak heights with ϑ. The effect is more pronounced for "positive" ϑ's and probably has to do with (a) the geometry of the arrangement shown in Fig. 4 (a small photo-effect in the brass part of the support may be quite possible), and (b) the fact that secondary electrons liberated from the brass of the vacuum chamber walls and passing through the first slit are more easily recorded by the counter when originating in the outer wall. This means that the intensity of these secondaries can be expected to be larger for angles ϑ denoted positive (Fig. 3) because of the flat cylindrical shape of the radiation source (Fig. 4). These considerations, however, do not seriously affect the result of the experiment because the photoelectric intensity for a certain ϑ is determined as the difference between two measured quantities and thus the photo-line peak heights generally could be accurately determined.

The backgrounds were measured twice, immediately before and after the recording of the lines, and in Fig. 6 the mean values are shown.

The determination of $\vartheta_{\max}$, with which we are mainly concerned here, is not much affected by the above fluctuations, because (a) the errors are small compared with the peak heights, and (b) $\vartheta_{\max}$ is determined by the whole curve, not by a single point. The highest points of Fig. 7 being somewhat more critical than the rest, two of them were remeasured and in Fig. 7 the mean values are plotted. For these two points the maximum deviations from the mean values are given while in the other cases the statistical errors are indicated. The former are somewhat larger which means that the latter may be a little too small; however, the points lie on a well-defined curve of the expected shape, and we feel justified in considering $\vartheta_{\max}$ rather well determined.

The full line curve of Fig. 7 shows the *experimental* intensity distribution obtained for the special conditions of this investigation. In order to get something that is independent of the chosen parameters (source-converter distance; converter size, material and thickness; magnitude of slit openings), that is, something representing the *true* distribution, one has, as mentioned above, to try to correct for the effects distorting the true distribution into the experimental one.

Let us, for this reason, first consider the geometry shown schematically in Fig. 3 neglecting the multiple scattering in the converter for the moment. For infinitely small widths of source, converter and slit aperture (only the first slit is of importance here) the instrumental response or "window curve" would be represented by an infinitely narrow rectangle for every ϑ, which means that, for a certain setting of ϑ, there will be no influence on the counting rate from adjacent ϑ's. The finite geometrical widths, which are necessary in practical work, have, however, the effect of distorting the ideal window curve into a distribution, which is approximately a Gaussian, and can be characterized by its full width at half maximum. The maximum ordinate is arbitrarily chosen $=1$ for convenience, and by inspecting the points where the window curve intercepts the abscissa axis ($=$ axis of ϑ), one obtains an angular interval $=2\,\Delta\vartheta$, the midpoint of which (at ordinate $=1$) represents the value ϑ_0 of ϑ just set for recording. Thus every ϑ for which $|\vartheta_0-\vartheta|\leq\Delta\vartheta$ contributes to the counting rate at ϑ_0 in a proportion given by the corresponding ordinate on the window curve, which means that the experimental value of the intensity at ϑ_0 will generally differ from the true intensity because of this influence from nearby ϑ's.

By replacing source, converter and slit opening by a number of infinitely narrow apertures, the window curve for this experiment could be constructed geometrically, compare Fig. 12 b. It had a width of 18° at half maximum.

The window curve could be constructed two-dimensionally because of the circular symmetry of source, converter and slit, which means that the size of $\Delta\vartheta$ is quite correct even for three dimensions. The construction shows that the size of the gamma source is of little importance between limits, which are not too critical. The size of the converter, on the other hand, is mainly responsible for the width of the window curve and should therefore be minimized. A practical limit is, of course, set by the necessary intensity.

The question of multiple scattering is discussed in some detail in Section C, to which the reader is generally referred.

An inspection of Fig. 20 gives for the parameters of this experiment a point outside the region where Molière's theory is strictly valid. A computation of the multiple scattering from Eq. (C 1) for half the converter thickness[1] gives 6° as an estimate of the probable scattering angle, which probably is about right even if Molière's theory is not strictly applicable to this case.

---

[1] $\frac{\sigma}{2}$ is a mean value of the thickness σ, inside which the photoelectrons are generated uniformly.

The distortion of the true intensity distribution due to multiple scattering is then superimposed on the straggling from the geometrical arrangement, and the result is a broadened window curve with a full width at half maximum of 21.6°. This resultant curve is the one which will be referred to as the *straggling curve.*

Knowing the shapes of the experimental intensity distribution and of the straggling curve it is now possible to obtain the true distribution by using the well-known folding procedure [15] represented by the integral

$$F(x) = \int_{-\infty}^{+\infty} f(\xi) \cdot g(x-\xi) \cdot d\xi. \tag{B 2}$$

Here $f(\xi)$ stands for the true distribution, $g(x-\xi)$ for the straggling curve, and $F(x)$ for the expected experimental distribution.

The simplest way to use Eq. (B 2) is to assume a certain shape for $f(\xi)$, compute $F_c(x)$ from (B 2) and finally compare $F_c(x)$ with the measured distribution $F_m(x)$. If, after division by a constant, $F_c(x)$ is a good fit to $F_m(x)$ inside experimental errors, the assumption was good; if not, the shape of $f(\xi)$ has to be changed. This method is one of trial and error but usually a few trials are sufficient.

Through calculations of this type we obtained as the true photoelectric intensity distribution the dotted curve in Fig. 7. The calculations were carried on until $F_c(x)$ everywhere agreed with $F_m(x)$ inside the experimental errors. From the dotted curve one can conclude that the preferred directions of the photoelectrons are separated by $48° \pm 1°$. Thus we have found $\vartheta_{\max} = 24° \pm 0.5°$ for $\beta = 0.795$.

II. The case of $\beta = 0.96$

Experimental.—For the following investigation, which was performed using the Co^{60} 1.33-Mev gamma-ray (half-life ~ 5 years), a new mechanical arrangement was devised in order to improve the experimental conditions and facilitate the adjustment of the apparatus. The main reasons were briefly these:

(a) The strength of the Co^{60} source was 500 mC. Because of the much stronger penetrating power compared with the former case health hazards required a minimum of exposure to the radiation, which in turn meant that, while remaining inside the spectrometer, the source had to be operated from the outside.

(b) The equipment of Fig. 4 did not so easily permit a variation of the distance between source and converter. This is of importance for choosing best experimental conditions.

(c) It was desirable to measure the corresponding background directly after the run of a line; because of the short half-life and the less convenient arrangement this could not be done for $\beta = 0.79$.

These requirements led to the design and construction of a mechanism that was permanently placed inside the spectrometer, which meant that the heavy upper pole piece of the spectrometer had to be lifted each time the gamma source had to be put in or taken out. The converter was now fixed to the end of the sample holder rod, thus permitting an easy shift of converters. As the position of the source could be

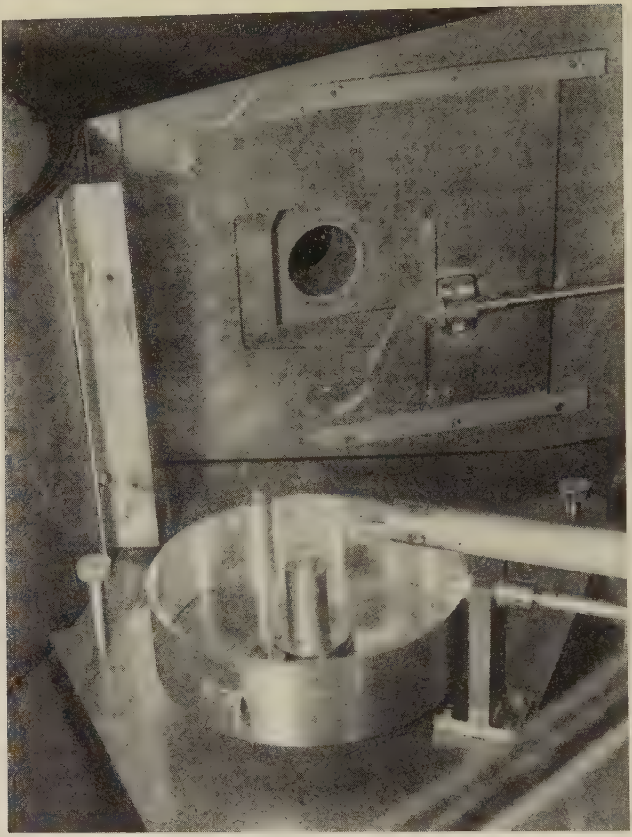

Fig. 8. The experimental arrangement inside the spectrometer, used with the Co-60 and Cs-137 radiation sources. Lead bricks behind the first slit reduced the backgrounds considerably. Part of the central lead brick with a circular opening (diameter 50 mm) can be seen.

operated from the outside, this device fulfilled the requirements stated above. The arrangements are shown in Fig. 8.

With this setup the precision of angle setting became very high.

Lead bricks had to be put up outside the spectrometer also so that the continuous radiation intensity at the operator's place could be reduced to a few mR/hour.

The gamma radiating source consisted of 0.46 g Co^{60} from Harwell enclosed in a cylindrical 4 × 4 mm aluminium capsule (strength 525 mC at delivery).

The choice of converter depends mainly upon the required intensity and on the amount of multiple scattering which can be tolerated. The first point requires a high Z because the photoelectric cross section for the K-shell varies as Z^5 while the second means that the thickness of the converter must not be too great. In fact, a very rough calculation from the nomogram [13], mentioned in B I, gave a maximum thickness of ~ 7 mg/cm^2 if an average deflection of about 10° from the original direction of emission was allowed. Three lead foils of 14, 8.25 and 6.98 mg/cm^2, respectively, were made and fixed onto Al backings. The converters of 14 and 8.25 mg/cm^2

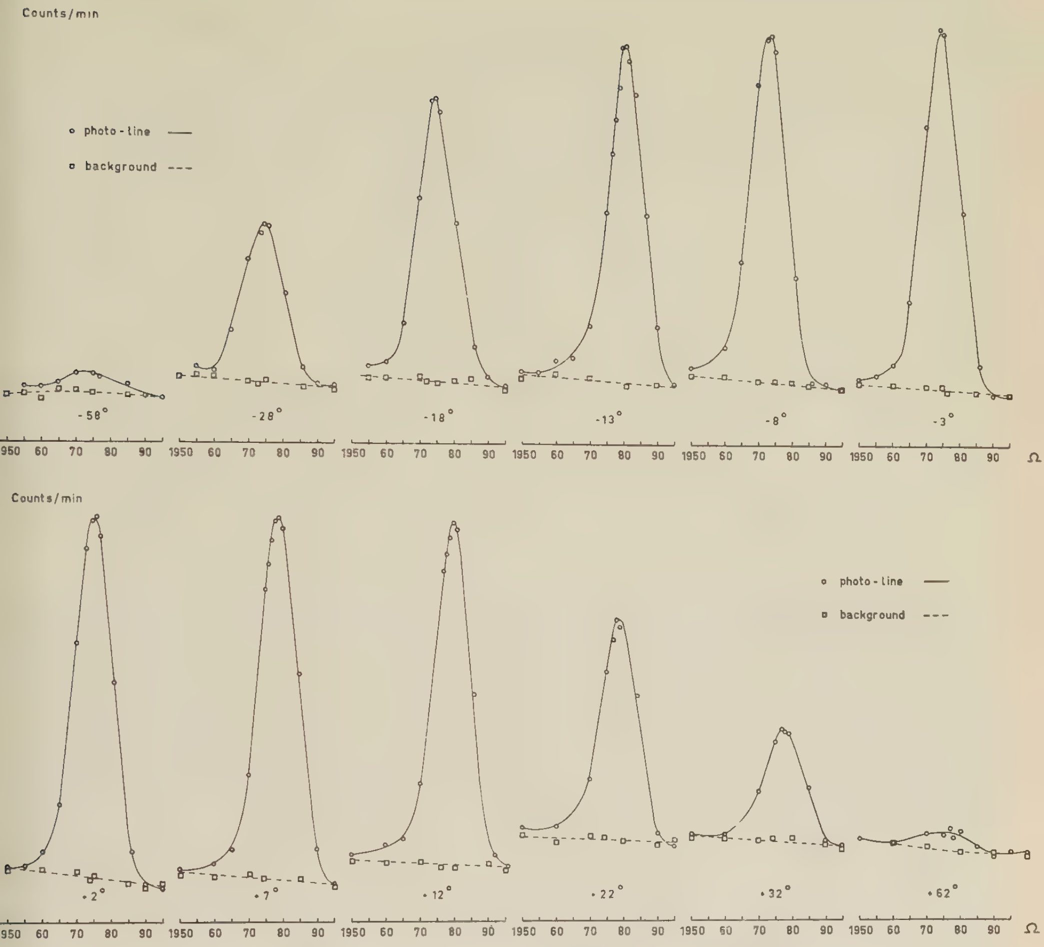

Fig. 9. Photo-lines from the 1.33 Mev gamma ray of Co-60 shown for different angles ϑ. 6.98 mg/cm² lead converter. $\beta = 0.957$.

were used for preliminary measurements and with the third one the final runs were performed. Three different source-to-converter distances were possible: $\varrho = 30$, 45, and 60 mm.

Measurements.—The general principles of spectrometer and GM-counter operation were the same as in the preceding section. For every setting of ϑ the photo-line was recorded and then the converter was taken out and replaced by an exact copy of the converter holder, with the converter missing. It was observed in the first runs that (a) the low energy tails of the lines were generally much more intense than the high energy tails, and (b) the backgrounds often did not coincide with the photo-line tails but were generally higher. Because a sloping background necessitates a more careful determination than a horizontal one, it was desirable to improve the ratio between peak heights and backgrounds by trying to reduce the latter considerably.

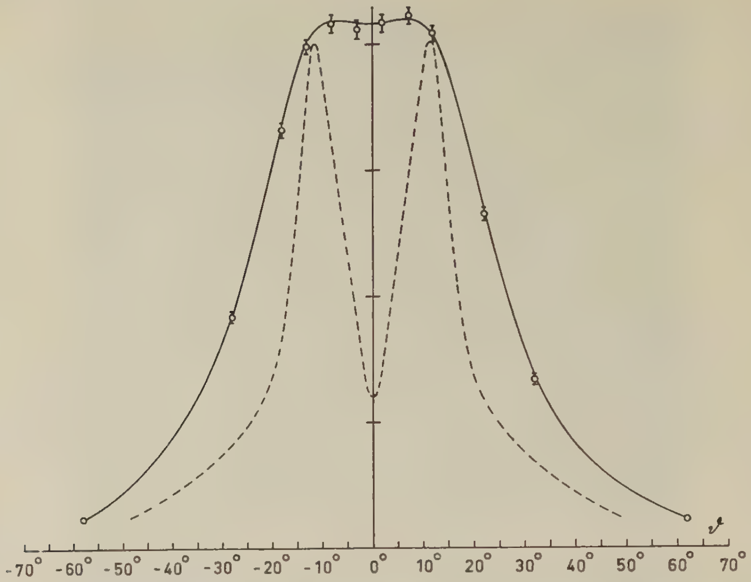

Fig. 10. The experimental (full line) and true (dotted line) photoelectric intensity distributions for $\beta = 0.957$. Units of 500 counts/min. are indicated on the ordinate axis.

This could in fact be done because it was likely that the intense low energy tails of the photo-lines mainly consisted of secondary electrons from the first slit and the brass walls of the spectrometer behind this slit. Thus, by putting some lead bricks (all shielded by thick aluminium) behind the first slit, most of the radiation was absorbed, and the background curves became straight and almost horizontal. The difficulty mentioned under (b) indicated that the converter acted as an absorber for secondary electrons produced around the gamma source and by substituting for the converter an Al foil of the same mass during the background runs, the agreement between line tails and background ends was considerably improved and became almost perfect. Two values of the source-converter distance were tried: $\varrho = 45$ mm and 60 mm. The angular resolution being about the same in both cases, the former distance was chosen because of better intensity.

The final runs were made with the thinnest lead foil (6.98 mg/cm^2) and the photo-lines obtained are shown in Fig. 9. The same coincidence GM-counter as before was used and the background without magnetic field was about 60 counts/min.

The peaks and backgrounds were measured by 2 min. counts. For every setting of ϑ the background was measured directly before or after the corresponding peak, and, with the precautions described above, a rather good series of lines was obtained. It is to be noticed that the background level is practically constant over the whole range of ϑ. Because the 1.33 Mev line is the most energetic transition of Co–60 the number of secondary electrons from the surrounding material, which are energetic enough to be focussed in the spectrometer, is very small, and the background level can be expected to be low.

Discussion of results.—In Fig. 10 the peak heights are plotted versus ϑ, showing the experimental intensity distribution for $\beta = 0.96$

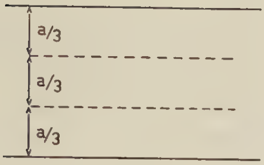

Fig. 11.

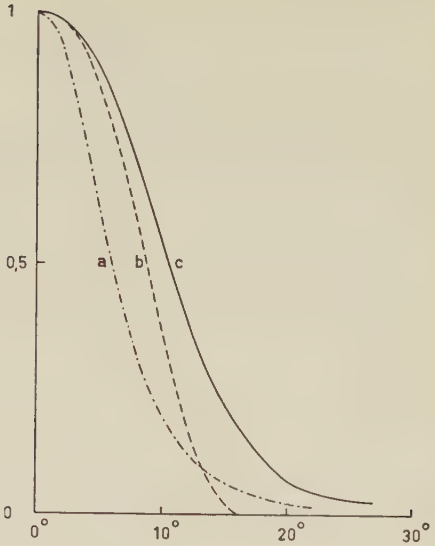

Fig. 12.

Fig. 11. Division of the converter material in partial thicknesses to compute multiple scattering.

Fig. 12. Curves showing factors influencing the angular resolution of the experiment at 1.33 Mev.—*a*, contribution from multiple scattering in the converter material; *b*, contribution from the geometry of the setup; *c*, total effect of *a* and *b* (straggling curve).

Most of the photo-lines were remeasured and a very good agreement was obtained. In Fig. 10 the plotted points represent mean values between the runs, and in all cases the maximum deviation between the mean value and successive runs of the same photo-line peak is less than the statistical error. For every point in Fig. 10 the statistical deviation is indicated.

From the full curve in Fig. 10 it is not, as before, possible to find $\vartheta_{\max}$ because the distance between the maxima is so small that they mask each other, producing a flattened top with a slight indication of a minimum. The distribution for the 8.25 mg/cm² converter had an exactly similar shape, while the 14 mg/cm² converter did not show any appreciable flattening, because of the greater scattering of the photoelectrons in the thicker converter material.

The analysis was similar to that carried out in the former case. The window curve was constructed geometrically and turned out to have a full width at half maximum of 17° (Fig. 12 b). This case was found to be more satisfactory for the application of Molière's theory, as the actual parameters (3.5 mg/cm²,[1] 1240 kev) gave a point in Fig. 20 inside the permitted region for lead. Because the photoelectrons are generated everywhere in the converter material one should, theoretically, apply the theory to a thickness dx at a distance x in the converter and then sum up by integrating over the whole thickness a. In practice, the integral is replaced by a sum of a small number of scattering functions, mainly because Molière's theory itself puts a lower limit to the chosen value of the partial thickness Δx ($n \cdot \Delta x = a$, $n =$ number of partial functions).

---

[1] See footnote, p. 256.

The converter thickness a was divided into three equal partial layers $\Delta x = a/3$ by two borderlines, each of which gives one partial scattering function. This can be made clear in the following way, which perhaps is somewhat rough but may serve to clarify the point (cf. Fig. 11).

Suppose n photoelectrons are generated in the converter at a certain arbitrary moment. Because they are produced uniformly in the material they have, on the average, to traverse half the converter thickness or $a/2$, which gives a total path length of $n \cdot a/2$ in the foil. According to Fig. 11 the converter is divided into three equally thick layers and half the photoelectrons are imagined to be produced at each of the two borderlines between the layers. This is consistent with the statistical idea of the process (average path length $= a/2$) because in Fig. 11 the total path length is $\frac{n}{2} \cdot \frac{a}{3} + \frac{n}{2} \cdot \frac{2\,a}{3} = \frac{n}{2} \cdot a$, exactly as before.

In order to get an idea of the scattering of the photoelectrons in the 7 mg/cm^2 converter Molière's function (C 1) was computed for the thicknesses $a/3$ and $2 \cdot a/3$. Because these curves apply to equal numbers of electrons they can be added to give the total scattering function for the converter (Fig. 12 a). This function had a full width of 12° at half maximum and gave, together with the window curve above, a straggling curve with a full width at half maximum of $\sqrt{17^2 + 12^2} \sim 21°$. It is shown in Fig. 12 c.

In precisely the same way as for $\beta = 0.79$ the function representing the true distribution was found from the experimental distribution in Fig. 10 (full line) and the straggling curve just computed, by applying the folding procedure. The result is shown in Fig. 10 (dotted line), from which we obtained $\vartheta_{\max} = 11.5° \pm 0.5°$.

III. The case of $\beta = 0.88$

In order to be able to test SAUTER's theory more completely in the relativistic region (somewhat arbitrarily defined by putting $\beta_{\text{rel}} > 0.5$) where, at least for heavy elements, Born's approximation is not valid, a knowledge of $\vartheta_{\max}$ somewhere between the two cases just described would be of great interest. We have investigated case B I and case B II which approximately fit the unrelativistic (A 18) and the relativistic (A 19) terms respectively, so that a measurement of a suitably chosen intermediate $\vartheta_{\max}$ would permit a determination of the "transition" between the regions of strict validity of (A 18) and (A 19). This having been accomplished, the dependence of the angular distribution on the energy of the incident gamma quanta (disregarding the slight differences in binding energies of various converters) may be considered as rather well determined.

Because caesium 137 has a prominent gamma ray of 662 kev and because very strong sources are now available, this isotope was chosen for the final investigation. For this gamma ray we should obtain a very satisfactory interpolation midway between the preceding cases, since the photoelectrons produced in heavy converters (Pb, U) will have $\beta \sim 0.88$.

Experimental.—The setup described in Section B II was used. The radiation source consisted of a 300 mC Cs-137 sample, containing about 30 mC Cs-134, and was obtained from Harwell. The source had cylindrical shape (diameter 2 mm, height 2 mm) and was enclosed in an aluminium capsule. The whole arrangement was exactly similar to that of the preceding section shown in Fig. 8.

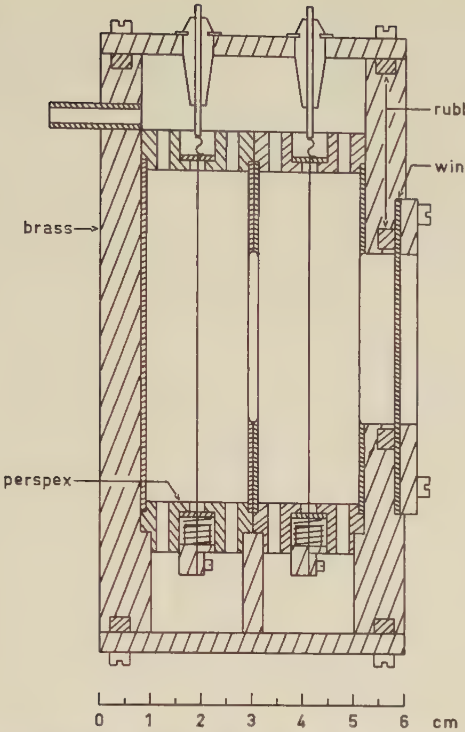

Fig. 13. A double GM-counter for gas-filling (schematic). The cathodes (made from brass tubing) together with wire holding arrangements fit very smoothly in the common brass housing and can easily be pushed out. The wires are stretched by springs (indicated in the lower part of the drawing).

In this experiment two converters were used: the lead foil of 7 mg/cm^2 from B II and a uranium foil of 4.25 mg/cm^2. The latter was made by painting uranyl nitrate solution in ethyl alcohol on a 0.1 mm aluminium foil, followed by evaporation and heating to about 450°C. The layer mainly consisted of uranium oxide UO_3, and its homogeneity was found to be satisfactory.[1]

Measurements.—After some preliminary tests and general adjustments the following runs were made

(a) 6.98 mg/cm^2 Pb converter. $\varrho = 45$ mm. Slit opening 50 mm diameter. (Fig. 3)

(b) 4.25 mg/cm^2 U converter. $\varrho = 45$ mm. Slit opening 50 mm diameter.

The purpose of the preliminary adjustments was to get the best operating conditions possible, which in turn meant the requirement of a good peak to background ratio of the photo-lines, reduction of the slopes of the backgrounds and, for the sake of comparison, a counting rate not too different from those of B I and B II.

Photo-line peaks and backgrounds were measured by 2-min. counts, and many lines were remeasured in order to test the stability and reproducibility of the spectro-

---

[1] My thanks are due to Dr. W. Forsling for the preparation of the uranium converter.

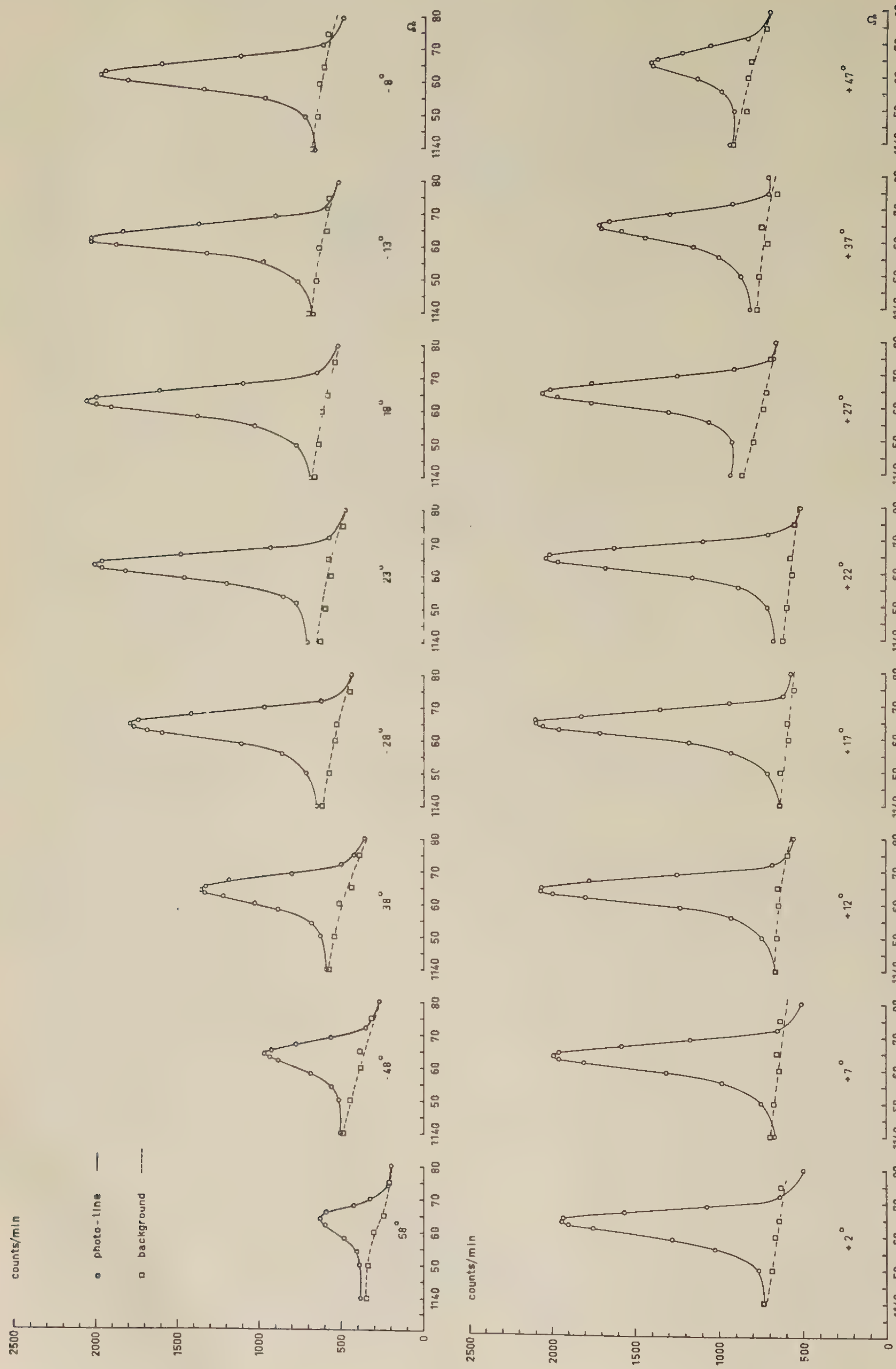

Fig. 14. Photo-lines from the 662 kev gamma ray of Cs-137 shown for different angles ϑ. 6.98 mg/cm² lead converter. $\beta = 0.882$.

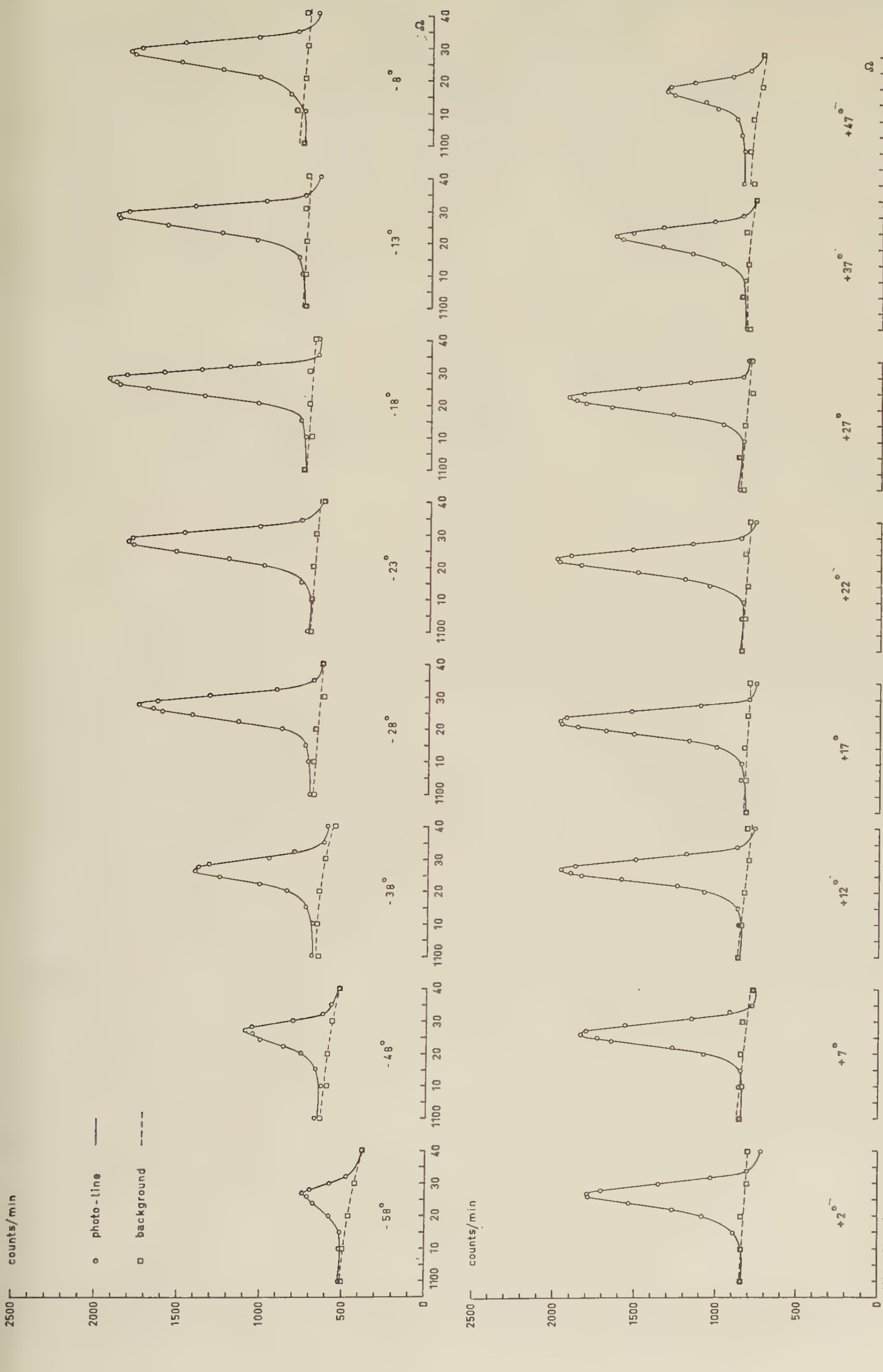

Fig. 15. Photo-lines from the 662 kev gamma ray of Cs-137 shown for different angles ϑ. 4.25 mg/cm^2 uranium converter. $\beta = 0.876$.

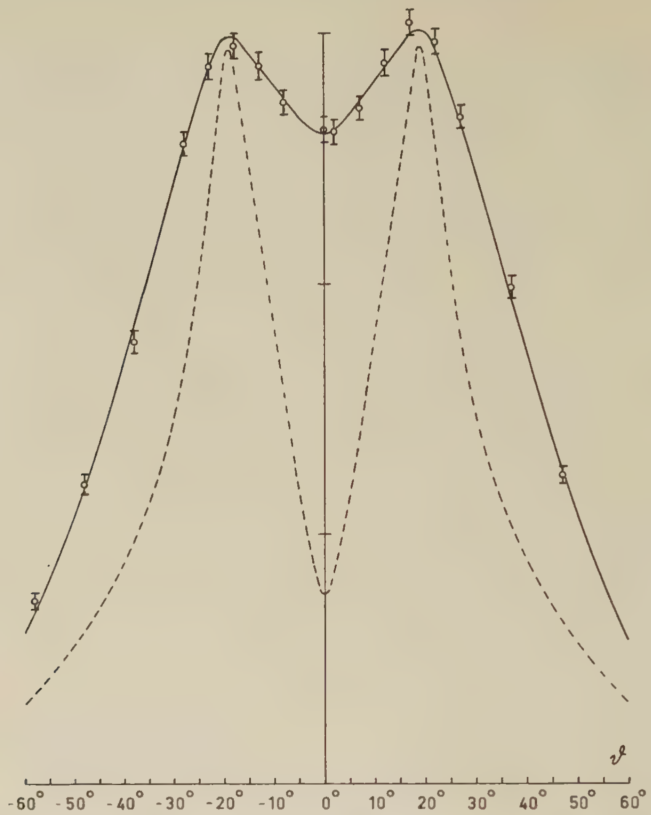

Fig. 16. The experimental (full line) and true (dotted line) photoelectric intensity distributions for $\beta = 0.882$. Units of 500 counts/min. are indicated on the ordinate axis.

meter operation, especially that of the GM-counter. During this experiment a new coincidence counter was used, and because it has performed reliably for about six months without any difficulties, it is shown schematically in Fig. 13.

The counter has been used with a mixture of 12 mm propane gas and 36 mm argon and the window consisted of a thin rubber hydrochloride foil ~ 300 $\mu g/cm^2$. Extremely thin formvar layers can also be used with a supporting metal grid. To be independent of each other the counting volumes had to be optically shielded from one another by means of an extremely thin aluminium foil (150 $\mu g/cm^2$). Rubber gaskets are used exclusively for sealing the counter.

Operating this counter in coincidence, a background as low as ~ 10 counts/min. was obtained when no magnetic field was applied. This was, of course, primarily due to the effective lead shielding between source and counter. The coincidence arrangement then reduced the counting rate 4–5 times.

Careful tests showed a perfect reproducibility of the photo-lines and it was not found necessary to measure the backgrounds immediately after or before the corresponding lines. Thus the photo peaks for different ϑ's were measured first and then the converter plus Al backing were replaced by a similar Al backing plus an Al foil

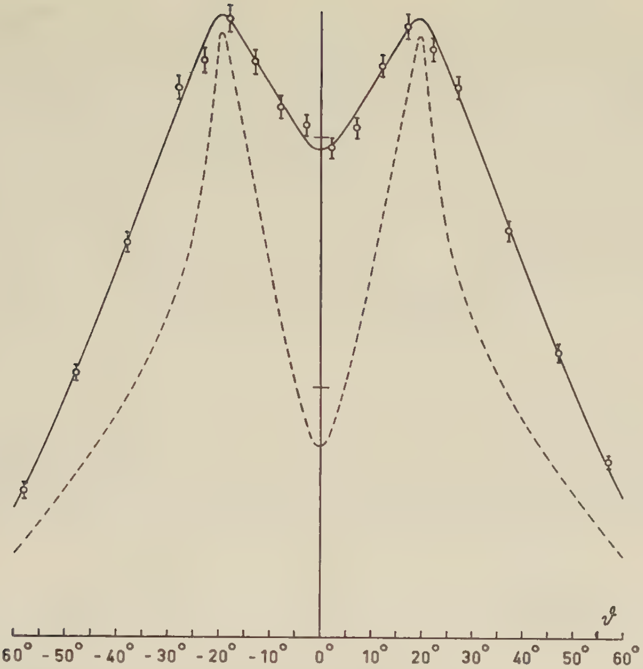

Fig. 17. The experimental (full line) and true (dotted line) photoelectric intensity distributions for $\beta = 0.876$. Units of 500 counts/min. are indicated on the ordinate axis.

of the same mass, and all backgrounds were measured. In this way the operation was greatly facilitated and a complete series (comprising about 20 lines and as many backgrounds) could be taken in about 15 hours' continuous operation. The spectrometer was operated as described in B I.

With the 7 mg/cm^2 lead converter the series shown in Fig. 14 was obtained. The photo-lines are plotted versus ϑ, as usual.

The low energy tails are somewhat broadened because the lead foil is a little too thick for this energy; the calculated probable scattering angle was 11.4° as mentioned below. The foil is, however, sufficiently thin to permit an accurate determination of $\vartheta_{\max}$ as can be seen from Fig. 16. On the other hand, the gold foil from B I could not be used here as the intensity obtained turned out to be far too low to allow a satisfactory comparison.

In Fig. 15 the photo-lines obtained from the 4.25 mg/cm^2 uranium converter are given versus ϑ. These lines do not show any appreciable broadening on the low energy sides and thus the foil thickness is suitably chosen. In fact, the probable multiple scattering amounts to 8.1°.

As well as the main runs just described, a preliminary run with the lead converter, at somewhat different slit settings, and an additional series with the uranium converter, using a smaller source-converter distance (30 mm), were performed.

Discussion of results.—Figs. 16 and 17 show the photo-line peak heights from Figs. 14 and 15, respectively, plotted against ϑ (full lines).

Some of the photo-lines were remeasured as mentioned before and in these cases mean values of the peak heights are shown in Figs. 16 and 17, where the larger one of the experimental and statistical deviations is indicated for each point.

As in B I it is here possible to get an idea of $\vartheta_{\max}$ directly from the experimentally determined photoelectric distributions in Figs. 16 and 17 (full lines). In order to get accurate values of $\vartheta_{\max}$ the experimental distributions were analyzed precisely as in B I and B II. The geometry being exactly similar to that in B II the window curve of this section could be used directly. For the computation of the multiple scattering, each foil was divided into three equal thicknesses and the partial scattering functions were calculated as in B II. The total probable multiple scattering was thus found from the Molière theory to be 11.4° for the lead foil and 8.1° for the uranium converter. Together with the window curve the total straggling was obtained as two Gaussians with full widths at half maximum of 28.6° for lead and 23.4° for uranium.

The centre lines in Figs. 16 and 17 are drawn to give best fit for symmetry over the whole full line curves.

Through use of the folding procedure (B I) the true photoelectric intensity distributions were obtained as the dotted curves in Figs. 16 and 17. The procedure was carried on until $F_c(x)$ lay inside the indicated errors of $F_m(x)$ (same notations as in B I). From the dotted curves $\vartheta_{\max}$ was finally determined to

$19.0° \pm 0.5°$ for $\beta = 0.882$ (Pb converter)
$19.5° \pm 0.5°$ for $\beta = 0.876$ (U converter)

The errors indicated are the estimated uncertainties in the folding procedure; they are certainly not greater because the experimental distributions are rather well determined and the dotted curves are unique.

The additional runs mentioned above agreed perfectly within the indicated errors with the main series, but were not completely analyzed.

IV. The dependence of the photo-line width upon the angle ϑ

As pointed out in the following Section C the deflection of a particle from its original direction of propagation by multiple scattering is brought about by a random number of small angle deflections. It is then generally assumed that the energy loss of the scattered particles is negligible, though Molière's theory permits correction for this simplification. Now, the low energy sides of the measured photo-lines are practically always less steep than the high energy side. This is connected with scattering because the assumption of negligible energy loss becomes poorer when the deviation of a particle increases. In the present investigations, as outlined in the section on $\beta = 0.79$, the angular resolution is not infinitely high. This means that the area of a certain recorded photo-line gives not only a measure of the intensity actually belonging to the direction set for recording, but is also (apart from the geometrical distortion, which is the same for all settings) made up of a number of scattered electrons originally belonging to neighbouring angles inside a region, which is given to a good approximation by the calculated straggling curves (cf. Fig. 12). This effect gives rise to a broadening of the photo-lines on the low energy side, and, considering the intensity variation of the dotted curves (Figs. 7, 10, 16, 17), it is evident that this broadening varies with ϑ. Furthermore, it is to be expected that the line broadening will have a minimum at $\vartheta = \vartheta_{\max}$, because then the broadening depends on angles representing lower intensities, compared with that of $\vartheta_{\max}$.

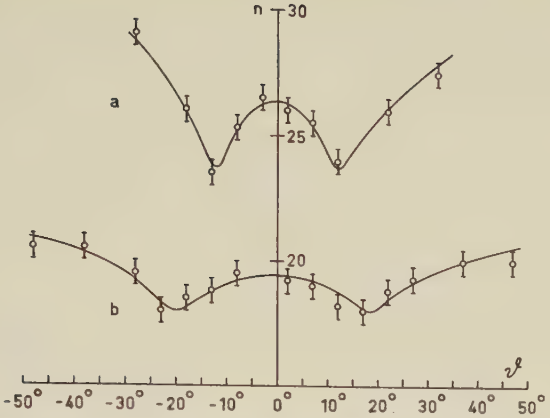

Fig. 18. Curves showing the variation of the photo-line half widths with ϑ. This is due to multiple scattering in the converter material. Ordinate n is proportional to $\Delta H\varrho$.
a, Lead converter 6.98 mg/cm² at 1.33 Mev. Full width at half maximum of a photo-line is $\Delta H\varrho/H\varrho = n \times 0{,}0253\,\%$. *b*, Lead converter 6.98 mg/cm² at 662 kev. Full width at half maximum of a photo-line is $\Delta H\varrho/H\varrho = n \times 0{,}0429\,\%$.

These considerations constitute the reasons for basing the intensity distributions (full line curves in Figs. 7, 10, 16, 17) on the peak heights (which are not subjected to the described effects) rather than on the photo-line areas.

In consequence of these arguments the widths at half maximum of all recorded photo-lines were inspected and plotted versus ϑ.

Fig. 18 shows the results for the 7 mg/cm² lead converter at $\beta = 0.96$ (B II) and $\beta = 0.88$ (B III). The angular distances between the symmetrically distributed minima were determined to be $24° \pm 2°$ and $38° \pm 2°$, respectively, showing a very good agreement with $\vartheta_{\max}$ obtained from the experimental intensity distributions by the folding procedure. The widths of the photo-lines are, as expected, sensitive to ϑ and their variation with ϑ directly gives good values of $\vartheta_{\max}$ and provides tests on the values obtained before.

The errors indicated in Fig. 18 are the estimated uncertainties in the determinations of the half widths from the diagrams.

Thus assuming that the magnitude of the variation of the half widths phenomenologically depends on large angle multiple scattering of the photoelectrons, it is to be expected that this phenomenon, which is effectively observed in the two cases of Fig. 18, will be quite negligible for very thin converters. That this is really so was in fact confirmed by the photo-lines from the 1.7 mg/cm² gold radiator (probable scattering about 6°) in B I and from the 4.25 mg/cm² uranium converter (probable scattering 8°) in B III, which show half widths that are nearly constant within the estimated errors over the whole ranges of observed ϑ's. Consequently, in these cases the converters were properly chosen.

The described observations mean that at large β's, where $\vartheta_{\max}$ becomes small, one has to be careful about the choice of converter material in order to get a good angular resolution (which may be characterized by the sharpness of the minimum of the experimental intensity distribution).

The 4.25 mg/cm² uranium radiator would probably have given a better resolution at 1.3 Mev but was unfortunately not available at the time.

V. General conclusions

Equation (A 17) is rewritten

$$\frac{dJ(\vartheta)}{d\vartheta}=J'(\vartheta)\sim(2a-b)(1-\beta\cos\vartheta)(\beta^2\cos^2\vartheta+2\cos\vartheta-3\beta)+ \\ +2\cdot(\beta\cdot\cos^2\vartheta+\cos\vartheta-2\beta)=0. \qquad \text{(B 3)}$$

Rearranging the terms one gets

$$J'(\vartheta)\sim\beta^2\cdot(2a-b)\cdot x^3-[2\beta-\beta\cdot(2a-b)]\cdot x^2-[2+(2+3\beta^2)(2a-b)]\cdot x+ \\ +3\beta\cdot(2a-b)+4\beta=0, \qquad \text{(B 4)}$$

where $x=\cos\vartheta$. This equation was solved for some values of $\beta\geqq 0.6$ and the result is shown as the full line in Fig. 19.

The experimentally obtained values of $\vartheta_{\max}$ are indicated with the estimated uncertainties and a function of the character of Eq. (B 4) is drawn to satisfy the experimental points inside the errors.

The general agreement with Sauter's theory is seen to be reasonable. There is, however, a marked deviation of the theory from the experiments in the strictly relativistic region, which is consistently outside the experimental errors. In view of the dependence of Sauter's theory on Born's approximation in the relativistic region, the agreement is to be considered as rather satisfactory, the maximum deviation being about 10% for $\beta=0.88$.

For $\sqrt{1-\beta^2}=\frac{1}{2}$, i.e. $\beta=0.866$, the first term of equation (B 3) drops out because then $2\cdot a-b\equiv 0$ and $\vartheta_{\max}$ is obtained from the purely unrelativistic equation $J'_n(\vartheta)=0$ (A 19). Because the factor $(2\cdot a-b)$ is negative for $\beta<0.866$ and positive for $\beta>0.866$ the functions $J'(\vartheta)=0$ and $J'_n(\vartheta)=0$ actually intersect at $\beta=0.866$. It is surprising that this happens for such a large value of β and quite naturally the discrepancy between theory and experiment reaches a maximum around this value of β. One possible way of correcting the function (B 3) empirically would then be to replace the factor $(2a-b)$ by $(n\cdot a-b)$, where $n>2$, thus shifting the point of intersection towards smaller β's. Some numerical calculations led to the result that $n\sim 11$ modifies (B 4) in such a way that the function

$$\frac{dJ_{\exp}(\vartheta)}{d\vartheta}=J'_{\exp}(\vartheta)\sim\beta^2\cdot(11a-b)\cdot x^3-[2\beta-\beta(11a-b)]\cdot x^2- \\ -[2+(2+3\beta^2)\cdot(11a-b)]\cdot x+3\beta\cdot(11a-b)+4\beta=0 \qquad \text{(B 5)}$$

satisfies the experimental values of $\vartheta_{\max}$ within 1%, which is inside the experimental errors. The function intersects $J'_n(\vartheta)$ at $\beta=0.533$, which seems more reasonable than before, but it has not been investigated beyond the range covered by these experiments. Because $|11\cdot a-b|$ decreases with β, Eq. (B 5) probably does not deviate much from (B 4) for small β's. The whole distributions according to (A 12) and its modification for $n=11$ have been computed and are, of course, quite similar except

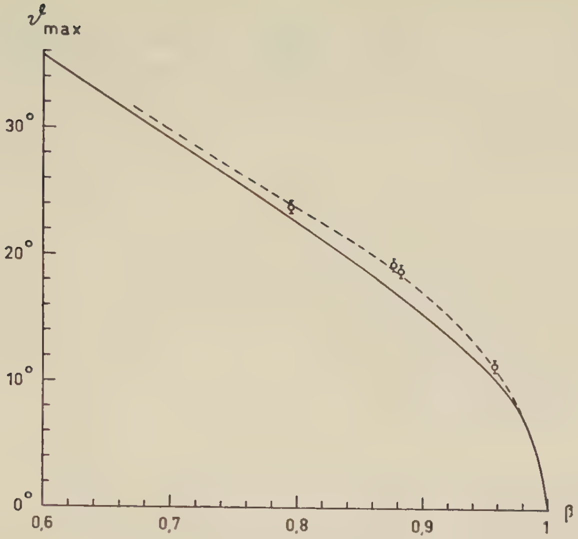

Fig. 19. Comparison between Sauter's theory (full line) and the experimental values of ϑ_{max}. The dotted curve represents a slightly modified form of Sauter's formula.

that $J_{exp}(\vartheta)$ [the integral of (B 5)] gives a better value of ϑ_{max} but represents a somewhat broader distribution curve. A comparison with the dotted curves of Figs. 7, 10, 16, 17 shows that these give distributions that are narrower than the theoretical ones. The main discrepancy lies in the fact that all experiments give finite photoelectric intensities for $\vartheta = 0$, whereas theory requires that $J(0) = 0$. This means that, except for the position of ϑ_{max}, it is difficult to compare theory and experiment as long as the former depends on the Born approximation, which is not strictly valid under the conditions of the described experiments.

Finally, it may be pointed out that the distribution curves of the Wilson chamber experiments in all cases are drawn so that $J(0) = 0$ [1]. This is, however, not so much at variance with the present experiments as may seem at first sight because (a) the Wilson experiments have been made for $\beta < 0.6$ where (A 9) is valid, and (b) the magnitude of the "zero" intensity does not vanish *exactly* but depends to some extent on the positions of the angular intervals (usually about 20°) when the tracks are counted. These facts, together with the poor statistics of the cloud chamber experiments, mean that the question of zero intensity must be left open for discussion and further investigation, both theoretical and experimental.

C. A compilation of the formulas needed for the computation of the multiple scattering spatial distribution according to the theory of Molière

I. List of symbols used

χ, θ = deflection angle of electron from direction of incidence $\chi, \theta = 0$

χ_0 = angular constant $= \dfrac{\lambda}{2\pi a} = \dfrac{1}{a k_0}$

χ_α = Molière's "screening" angle

χ_c = Molière's "characteristic" angular constant

Q = differential scattering cross section

α = parameter (see text)

Ω_b, Ω = letters representing number of collisions

B = parameter (see text)

N = number of atoms/cm^3 of the scatterer

Z = atomic number of scatterer

A = atomic weight of scatterer

σ = density of scattering material (g/cm^2)

l = length of electron path in scatterer

λ = de Broglie wave length of electron

$v = \beta c$ = speed of electron

p = momentum of electron $= \dfrac{h}{2\pi} \cdot k_0 = \dfrac{h}{\lambda}$

m_0 = rest mass of electron

e = electrostatic charge of electron (esu)

N_0 = Avogadro's number

a = Thomas-Fermi radius $= Z \times 0.466 \times 10^{-8}$ cm

$\ln \gamma$ = Euler's constant $= 0.577 \cdots$

II. Theoretical introduction (short survey of the general ideas)

Scattering of charged particles plays an important role in many physical experiments, especially when the scattering events take place in thin foils, so that the original directions of the particles are not completely lost. Depending on the number of collisions encountered by a particle on traversing a foil it is common practice to differentiate between various scattering regions. The region of multiple scattering, which is of interest here, is said to predominate when the deviation of the electron from the original direction is caused by a great number of small-angle deflections. These come about when the electron is moving in the resulting electrostatic field from nuclei + atomic electrons, which means that the screening of the nuclear charges by the atomic electrons plays an important role. On the other hand, if the incident electron passes through the electron cloud of an atom and gets very near to the nucleus, it will be deflected through a large angle. In this case the shielding effect of the atomic electrons can be neglected if the electron energy is a few hundred kev or more [16] and we have the Rutherford single scattering. Thus, if the foil thickness at a given electron energy is chosen so that multiple scattering is not too severe, the observed *large* deviations are mainly due to Rutherford scattering. Therefore, on account of the statistical nature of the small-angle scattering, a theory

Table 1.

W. Bothe	Z. Physik *4*, 161 and 300 (1921)	
	Z. Physik *5*, 63 (1921)	
E. J. Williams	Proc. Roy. Soc. *169*, 531 (1939)	
	Phys. Rev. *58*, 292 (1940)	
S. Goudsmit & J. L. Saunderson	Phys. Rev. *57*, 24 (1940)	
	Phys. Rev. *58*, 36 (1940)	
G. Molière	Z. Naturforsch. *2 a*, 133 (1947):	M I
	Z. Naturforsch. *3 a*, 78 (1948):	M II
H. S. Snyder & W. T. Scott	Phys. Rev. *76*, 220 (1949)	
H. W. Lewis	Phys. Rev. *78*, 526 (1950)	
W. T. Scott	Phys. Rev. *85*, 245 (1952)	
F. Sauter & H. Wanke	Z. Naturforsch. *7 a*, 33 (1952)	
G. Molière & F. Sauter	Z. Naturforsch. *7 a*, 280 (1952)	
H. Bethe	Phys. Rev. *89*, 1256 (1953):	B

of the multiple scattering distribution would be expected to be composed of a Gaussian with a tail describing the gradual transition to single scattering.

A very good general survey of electron scattering in solids is given by H. S. W. Massey in *Advances in Electronics*, vol. IV, p. 2–68. For the sake of completeness Table 1 above contains references to the theories of multiple scattering of charged particles advanced up to date.

For the influence from the screening of the nucleus by the atomic electrons on the distribution of the scattered electrons the parameter

$$\alpha = \frac{2\pi Z e^2}{h\beta c} = \frac{Z}{137\beta}$$

is of great importance. Only for a pure Coulomb field Rutherford's law (cf. below) holds exactly for all values of α; every distorted field form introduces a dependence on this parameter.

In his first paper (M I) Molière treats single scattering and works out an analytical expression for the differential scattering cross section per unit solid angle $Q(\chi)$ in terms of the Rutherford cross section $Q_R(\chi)$, where χ denotes the scattering angle, valid for any central field $V(r)$. Introducing the Thomas-Fermi field distribution Molière then obtains an integral, which on evaluation gives the following asymptotic expression

$$q(\chi) = \frac{Q(\chi)}{Q_R(\chi)} \sim 1 - \frac{8.85}{\left(\frac{\chi}{\chi_0}\right)^2} \cdot \left[1 + \alpha^2 \cdot 2.303 \cdot {}^{10}\log\left(\frac{\chi^4}{\chi_0^4} \cdot \frac{0.00072}{\alpha^4 + \frac{1}{3}\alpha^2 + 0.13}\right)\right]$$

valid for large χ and any α in contrast with the Born approximation solution, which requires $\alpha \ll 1$. The formula is good for $q(\chi) > 0.9$, and for $q(\chi) < 0.9$ Molière gives interpolation formulas of the type

$$\chi_q = \chi_0 \cdot \sqrt{A_q + B_q \alpha^2}$$

where χ_q is the scattering angle for a fixed value of $q(\chi)$ and A_q, B_q are tabulated in M I for a number of values of $q(\chi)$. The connexion between $q(\chi)$ and χ for any α so obtained is exact for the limiting cases $\alpha \to 0$ and $\alpha \to \infty$ and is, according to Molière good to about 10% for the calculated angles χ for intermediate values of α. The theory holds for $\chi \leq 90°$, any α and for kinetic energies of the incident electrons $E_{\text{kin}} \gtrsim Z^{4/3} \cdot 100$ ev. Further the theory is valid for any kind of particles, but here only electrons are of interest.

It must be noted that this treatment neglects the effect of spin, and for the upper part of this angular range and for high energies the latter effect is much greater than that of screening, at least in the case of electrons [17]. However, the multiple scattering theory is concerned with very small angles of single scattering, and here the single scattering cross section is given quite accurately by Molière's theory [18].

For the development of the theory of multiple scattering (M II), where all χ are small ($\cos\chi \sim 1$, $\sin\chi \sim \chi$), it is sufficient to describe the influence on $Q(\chi)$ from the screening by one constant χ_α, the "screening" angle. According to Molière it is convenient to write

$$q(\chi) = \frac{Q(\chi)}{Q_R(\chi)} = \frac{\chi^4}{(\chi^2 + \chi_\alpha^2)^2}$$

where χ_α is given by an expression of the form (similar to that of χ_q)

$$\chi_\alpha = \chi_0 \cdot \sqrt{1.13 + 3.76\,\alpha^2}$$

The probability $W(\chi) \cdot \sin\chi \cdot d\chi$ that an electron is scattered into the solid angle between χ and $\chi + d\chi$ (assuming cylindrical symmetry) can be written in terms of $Q(\chi)$ calculated above

$$W(\chi) \cdot \sin\chi \cdot d\chi \sim W(\chi)\,\chi\,d\chi = N\,l \cdot Q(\chi) \cdot 2\pi\chi\,d\chi.$$

The Rutherford scattering cross section can be written

$$Q_R(\chi) = \left(\frac{2\alpha}{k_0}\right)^2 \cdot \frac{1}{\left(2\sin\frac{\chi}{2}\right)^4} = \left(\frac{2\alpha}{k_0}\right)^2 \cdot \frac{1}{\chi^4} \cdot \left(1 + \frac{\chi^2}{6} + \cdots\right).$$

For small χ it is sufficient to write $Q_R(\chi) = \dfrac{4\alpha^2}{k_0^2 \cdot \chi^4}$ and thus

$$Q(\chi) = q(\chi) \cdot Q_R(\chi) \sim q(\chi) \cdot \frac{4\alpha^2}{k_0^2 \cdot \chi^4}.$$

We now get

$$W(\chi)\,\chi\,d\chi \sim N\,l \cdot 2\pi\,q(\chi) \cdot \frac{4\alpha^2}{k_0^2} \cdot \frac{1}{\chi^4} = 2\chi_c^2 \cdot \frac{q(\chi)}{\chi^4}$$

with

$$\chi_c = \frac{2\alpha}{k_0} \cdot \sqrt{\pi N l}$$

which Molière calls the "characteristic angular constant".

Molière then defines a number Ω_b, which characterizes the number of collisions encountered by an electron on traversing the foil

$$\Omega_b = \frac{\gamma^2}{e} \cdot e^b \qquad \left(\frac{\gamma^2}{e} = 1.167\right)$$

where $\ln \gamma = 0.577 \cdots =$ Euler's constant and $\ln e = 1$. The meaning of b is immaterial for the present purpose. From the definition of b (cf. M II) and the expression for $q(\chi)$ it can easily be shown that

$$\Omega_b = \frac{\chi_c^2}{\chi_\alpha^2}.$$

Following a method already used by WENTZEL, Molière calculates the contributions to the total angular distribution from the particles scattered 0, 1, 2, 3, ..., n, ... times. The total distribution then results as the sum over these contributions. Using Fourier transformations and Hankel functions Molière finally obtains a series expression for the angular distribution of the multiply scattered particles

$$F(\vartheta) = \vartheta \cdot d\vartheta \cdot \left[2e^{-\vartheta^2} + \frac{1}{B} \cdot f_1(\vartheta) + \frac{1}{B^2} \cdot f_2(\vartheta) + \cdots\right] = \vartheta \cdot d\vartheta \cdot f(\vartheta) \qquad \text{(C 1)}$$

where $\chi_c \cdot \sqrt{B}$ is introduced as a convenient angular unit according to

$$\vartheta = \frac{\theta}{\chi_c \cdot \sqrt{B}}.$$

Further Molière has put $b = B - \ln B$ and thus it follows that

$$\Omega_b = \frac{\gamma^2}{e} \cdot e^b = \frac{\gamma^2}{e} \cdot \frac{e^B}{B} = \frac{\gamma^2}{e} \cdot \Omega$$

where $\Omega = e^b$ is a convenient measure of the number of collisions.

Fig. 1 in M II shows the bracketed functions in (C 1) plotted versus ϑ.

Molière has obtained analytical expressions for the functions $f_1(\vartheta)$ and $f_2(\vartheta)$, which become dominant for large angles ($\vartheta > 2$) and they consequently represent the gradual transition to the large angle Rutherford scattering. For very large angles $f_1(\vartheta)$ becomes predominant and actually takes the value $2 \cdot \vartheta^{-4}$, the single scattering law. According to BETHE 1953 (Table 1) the series (C 1) converges even faster at large ϑ's than at moderate ones, which means that $2 \cdot e^{-\vartheta^2} + \frac{1}{B} f_1(\vartheta)$ will be a good approximation of (C 1) at any angle. If B is of order 10 and an accuracy of $\sim 1\%$ is wanted the function $f_2(\vartheta)$ must be included.

Because of the statistical nature of multiple scattering the average number of collisions for the particles in traversing the scatterer must be $\gg 1$. In fact, Molière puts $\Omega_b \sim 20$ as a practical lower limit for the applicability of the theory. The value of B usually lies between 5 and 20. Another limit for (C 1) is set by the condition that $\theta < 20°$. A very useful diagram giving the regions of validity of (C 1) for three elements is shown in Fig. 20.

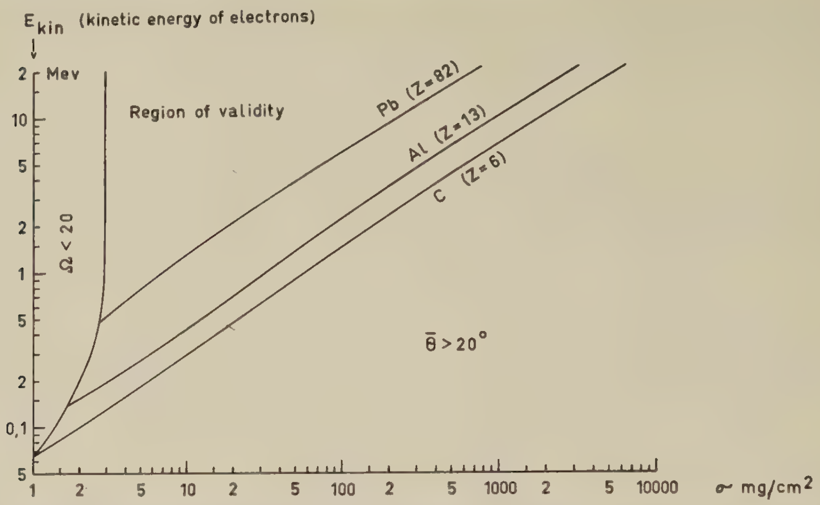

Fig. 20. Diagram showing approximately the regions of validity of Molière's theory for three different materials. From W. HEISENBERG, *Kosmische Strahlung*, p. 486, Springer Verlag 1953.

III. Numerical evaluation of the distribution function

To evaluate Molière's distribution function

$$\vartheta\, d\vartheta \cdot f(\vartheta) = \vartheta\, d\vartheta \cdot \left[f_0(\vartheta) + \frac{1}{B} f_1(\vartheta) + \frac{1}{B^2} f_2(\vartheta) + \cdots \right] \qquad \text{(C 1)}$$

numerically in actual applications it is practical to proceed in the following way.

1) *Calculate speed parameter* β.

2) *Calculate parameter* α.

$$\alpha = \frac{Z}{\beta} \cdot \frac{2\pi e^2}{h c} = \frac{Z}{137\beta}.$$

3) *Calculate parameter* χ_c.

$$\chi_c^2 = \frac{4\alpha^2}{k_0^2} \cdot \pi N l = \frac{4\alpha^2}{k_0^2} \cdot \pi N_0 \cdot \frac{\sigma}{A} \qquad (\sigma = \text{g/cm}^2).$$

Insert

$$k_0 = \frac{2\pi}{\lambda} = \frac{p}{h} \cdot 2\pi; \qquad p = \frac{m_0 \cdot v}{\sqrt{1-\beta^2}} = \frac{m_0 \cdot \beta \cdot c}{\sqrt{1-\beta^2}}.$$

Then

$$\chi_c^2 = \frac{4 e^4 \cdot \pi \cdot N_0}{c^4 \cdot m_0^2} \cdot \frac{Z(Z+1) \cdot (1-\beta^2)}{\beta^4 \cdot A} \cdot \sigma$$

or

$$\chi_c^2 = 0.6009 \cdot \frac{Z(Z+1) \cdot (1-\beta^2)}{\beta^4 \cdot A} \cdot \sigma.$$

Following BETHE (paper B), Molière's factor Z^2 has here been replaced by $Z \cdot (Z+1)$ to take into account the scattering by the atomic electrons, as first suggested by KULCHITSKY & LATYSHEV.

4) *Calculate "number of collisions"* Ω.

$$\Omega = e^b = \Omega_b \cdot \frac{e}{\gamma^2} = \frac{\chi_c^2}{\chi_\alpha^2} \cdot \frac{e}{\gamma^2}.$$

Insert

$$\chi_c^2 = \frac{4\,\alpha^2}{k_0^2} \cdot \pi\, N_0 \cdot \frac{\sigma}{A}$$

$$\chi_\alpha^2 = \chi_0^2 \cdot (1.13 + 3.76\,\alpha^2) = \frac{1}{a^2\, k_0^2} \cdot 1.13 \cdot (1 + 3.33\,\alpha^2).$$

It follows that $\left(\text{since } \frac{\gamma^2}{e} = 1.167\right)$

$$\Omega = \frac{1}{1.167} \cdot \frac{\chi_c^2}{\chi_\alpha^2} = \frac{4 \cdot Z(Z+1) \cdot 4\pi^2 \cdot e^4}{h^2 c^2} \cdot \pi\, N_0 \cdot \frac{\sigma}{A} \cdot \frac{Z^{-2/3} \cdot (0.466)^2 \cdot 10^{-16}}{1.13 \cdot (1 + 3.33\,\alpha^2)}$$

or

$$\Omega = 6680 \cdot \frac{(Z+1) \cdot \sqrt[3]{Z}}{\beta^2 A \cdot (1 + 3.33\,\alpha^2)} \cdot \sigma.$$

Table 2. $^{10}\log \Omega$ against B.

$^{10}\log \Omega$	B
1	3.58
1.5	5.08
2	6.47
2.5	7.81
3	9.12
3.5	10.40
4	11.67
4.5	12.92
5	14.16
5.5	15.40
6	16.63
6.5	17.85
7	19.07
7.5	20.28
8	21.49
8.5	22.69
9	23.90

Table 3. Values of $f_0(\vartheta)$, $f_1(\vartheta)$ and $f_2(\vartheta)$ for some ϑ's as calculated by BETHE 1953.

ϑ	$f_0(\vartheta)$	$f_1(\vartheta)$	$f_2(\vartheta)$
0	2	0.8456	2.4929
0.2	1.9216	0.7038	2.0694
0.4	1.7214	0.3437	1.0488
0.6	1.4094	−0.0777	−0.0044
0.8	1.0546	−0.3981	−0.6068
1	0.7338	−0.5285	−0.6359
1.2	0.4738	−0.4770	−0.3086
1.4	0.2817	−0.3183	0.0525
1.6	0.1546	−0.1396	0.2423
1.8	0.0783	−0.0006	0.2386
2	0.0366	+0.0782	0.1316
2.2	0.01581	0.1054	0.0196
2.4	0.00630	0.1008	−0.0467
2.6	0.00232	0.08262	−0.0649
2.8	0.00079	0.06247	−0.0546
3	0.000250	0.04550	−0.03568
3.2	7.3×10^{-5}	0.03288	−0.01923
3.4	1.9×10^{-5}	0.02402	−0.00847
3.6	4.7×10^{-6}	0.01791	−0.00264
3.8	1.1×10^{-6}	0.01366	0.00005
	$1000 \times f_0$	$1000 \times f_1$	$1000 \times f_2$
4	2.3×10^{-4}	10.638	1.0741
4.5	3×10^{-6}	6.140	1.2294
5	2×10^{-8}	3.831	0.8326
5.5	2×10^{-10}	2.527	0.5368
6	5×10^{-13}	1.739	0.3495
7	1×10^{-18}	0.9080	0.1584
8	3×10^{-25}	0.5211	0.0783
9	1×10^{-32}	0.3208	0.0417
10	1×10^{-40}	0.2084	0.0237

5) *Calculate parameter B.*

$$b = B - \ln B$$

$$\Omega = e^{b} = e^{B}/B.$$

B can be obtained by linear interpolation from Table 2.

6) *Calculate scattering angle θ.*

$\theta = \vartheta \cdot \chi_c \cdot \sqrt{B}$ degrees.

7) *Calculate distribution function from Eq. (C 1).*

Table 3 gives $f_0 = 2 \cdot e^{-\vartheta^2}$, $f_1(\vartheta)$ and $f_2(\vartheta)$ for some values of ϑ.

Remarks

1) The distribution function $f(\vartheta)$ is normalized in the following way:

$$\int_0^\infty f(\vartheta)\cdot\vartheta\cdot d\vartheta=1$$

$$\int_0^\infty f_1(\vartheta)\cdot\vartheta\cdot d\vartheta=\int_0^\infty f_2(\vartheta)\cdot\vartheta\cdot d\vartheta=0.$$

2) As a rough estimate of the useful region of the theory Molière puts

(a) $\Omega_b>20$. At $\Omega_b=20$ collisions the accuracy still is $\sim 1\,\%$.

(b) $\theta<20^\circ$. Cf. Fig. 20.

3) As pointed out by BETHE 1953, the factor in the expression for Ω

$$(Z+1)\cdot Z^{1/3}/[A\cdot(1+3.33\,\alpha^2)]$$

is nearly constant; it never deviates much from 1. Its values for $v=c$ and different Z's are given in table I of BETHE's paper B. Thus the effective "number of collisions" Ω per g/cm² is nearly independent of Z at $v=c$.

Summary

The longitudinal angular intensity distributions of K-shell photoelectrons from different radiators at the gamma ray energies 0.41 Mev (Au-198), 0.66 Mev (Cs-137) and 1.33 Mev (Co-60) have been studied. The distribution functions $J(\vartheta)$ are referred to $\vartheta=0$ as direction of incidence of the quanta. ϑ is the longitudinal angle in a polar coordinate system ϑ, φ, r.

The recorded photo-lines are shown and the angular distributions are obtained by plotting the photo-line peak heights versus ϑ. In order to get the true distributions the experimental curves are corrected for geometrical distortion and multiple scattering in the converter (MOLIÈRE's theory is used).

From the true distributions the preferred directions of emission $\vartheta_{\max}$ of the photoelectrons were accurately determined. Results:

Gamma source	Radiator	Thickness mg/cm²	β	$\vartheta_{\max}$
Au-198	Au	1.68	0.795	24° ±0.5°
Cs-137	U	4.25	0.876	19.5° ±0.5°
Cs-137	Pb	6.98	0.882	19° ±0.5°
Co-60	Pb	6.98	0.957	11.5° ±0.5°

The half widths of the photo-lines are shown to depend on ϑ. Thus, optimal resolution is found to occur for the direction of maximum emission $\vartheta_{\max}$. The effect seems to be closely connected with multiple scattering and can be considerably reduced by using very thin converters.

The results are compared with SAUTER's theory, which is found to be essentially in agreement with the results of the experiment. A consistent deviation is, however, found; the theoretical value of $\vartheta_{\max}$ is about 10 % too small at $\beta = 0.88$. A slightly corrected form of SAUTER's distribution is attempted, which satisfies the experimental values of $\vartheta_{\max}$ within 1 %.

A schematical drawing of a double GM-counter of reliable operation is included. Rubber gaskets are exclusively used for the sealing and the counter can be used with any kind of window.

A scheme for an easy computation of multiple scattering from MOLIÈRE's theory is included together with useful numerical tables and a diagram showing the region of applicability of the theory for a few values of Z.

ACKNOWLEDGEMENTS

The present investigation has been carried out at the Nobel Institute of Physics, Stockholm. I am greatly indebted to the Head of the Institute, Professor MANNE SIEGBAHN, for his never-failing interest and for providing me with all the necessary facilities. My deep gratitude is also due to Professors ERIK HULTHÉN and HILDING SLÄTIS for their kind interest in my work.

I wish to take the opportunity to express my sincere thanks to Dr. ARNE HEDGRAN, who suggested the investigation and with whom I have had several valuable discussions. Further I am most grateful to Dr. STIG BRIMBERG for helpful advice concerning Sections A and C.

I want to thank Dr. JOHN A. MCDONELL for several profitable discussions; Springer Verlag, Göttingen, has kindly permitted the reproduction of a diagram from W. HEISENBERG: *Kosmische Strahlung*, p. 486 (1953), shown in Fig. 20 of this paper.

Nobel Institute of Physics, Stockholm 50.

REFERENCES

1. F. F. H. EGGLESTON & L. H. MARTIN, Proc. Roy. Soc. *A 162*, 95 (1937).
2. G. D. LATYSHEV, Rev. Mod. Phys. *19*, 132 (1947).
3. A. HEDGRAN, Arkiv för Fysik *5*, 13 (1952).
4. A. HEDGRAN & S. HULTBERG, Phys. Rev. *94*, 498 (1954).
5. G. MOLIÈRE, Z. Naturforschung *3 a*, 78 (1948).
6. H. BETHE, Phys. Rev. *89*, 1256 (1953).
7. W. HEITLER, The Quantum Theory of Radiation, p. 127 (Oxford 1944).
8. G. WENTZEL, Z. Phys. *40*, 574 (1926).
9. A. SOMMERFELD & G. SCHUR, Ann. Phys. *4*, 409 (1930).
10. J. FISCHER, Ann. Phys. *8*, 821 (1931).
11. F. SAUTER, Ann. Phys. *9*, 217 (1931).
12. F. SAUTER, Ann. Phys. *11*, 454 (1931).
13. M. WALTER, O. HUBER & W. ZÜNTI, Helv. Phys. Acta *23*, 715 (1950).
14. W. BOTHE, Handbuch der Physik XXII:II, p. 1 (1933).
15. P. WHITE & G. MILLINGTON, Proc. Roy. Soc. *A 120*, 701 (1928).
16. C. B. O. MOHR & L. J. TASSIE, Proc. Phys. Soc. *A 67*, 711 (1954).
17. N. S. MOTT & H. S. W. MASSEY, The Theory of Atomic Collisions, p. 57 ff. (2nd ed.).
18. C. B. O. MOHR & L. J. TASSIE, Austr. J. Phys. *7*, 217 (1954).

Tryckt den 27 januari 1955

Uppsala 1955. Almqvist & Wiksells Boktryckeri AB

ARKIV FÖR FYSIK Band 9 nr 16

Communicated 2 June 1954 by IVAR WALLER

Polarization of neutrons in high energy scattering

By T. ERIKSSON and W. J. SWIATECKI

With 4 figures in the text

In connection with the recent experiments on the polarization of nucleons in high energy nuclear reactions[1] we have made some calculations with the object of learning about the type of polarization effects to be expected in the elastic scattering of neutrons by a heavy nucleus, assuming the polarization to be due to a spin-orbit coupling of a magnitude suggested by the shell model[2]. The nucleus was represented by a spherical, complex, square-well potential with spin-orbit coupling, of the type

$$\begin{aligned} V &= -B - iD - C\,(\boldsymbol{l}\cdot\boldsymbol{s}) \qquad &&\text{for } r<R \\ V &= 0 &&\text{for } r>R \end{aligned}$$

where B, D, C are constants.[3]

The present note concerns a calculation in which the parameters were chosen to correspond to the scattering of 150 Mev neutrons by a copper nucleus. The values $R = 5.8\times10^{-13}$ cm, $B = 15$ Mev, $D =$ about 8 Mev (corresponding to an inverse mean free path of neutrons in nuclear matter $K = 0.15\times10^{13}$ cm^{-1}) were taken from TAYLOR (1953).[4] The constant C was taken as 0.5 Mev or 1 Mev. (The sign is such that states with $\boldsymbol{l}$ and $\boldsymbol{s}$ parallel lie lower.) The phase shift analysis was carried out according to the WKB method, valid for $kR \gg 1$, where $k =$ wave number of the incident neutrons. In our case $kR = 15.6$. The presence of the $\boldsymbol{l}\cdot\boldsymbol{s}$ term in the potential gives rise to two phase shifts for each value of $\boldsymbol{l}$, corresponding to the two possible orientations of the spin. Using the WKB approximation the formulae for these phases are simple generalizations of the expressions for the phase shifts obtained using the so-called optical model[5], to which they reduce when $C = 0$.

---

[1] See for instance C. L. OXLEY *et al.*, Phys. Rev. *93*, 806 (1954).

[2] This question has been considered recently by several authors. See, for instance, E. FERMI, Nuovo Cimento *11*, 407 (1954). The present investigation was suggested by Drs A. BOHR and B. R. MOTTELSON in Copenhagen.

[3] The treatment of the problem is essentially the same as that given by A. SJÖLANDER and S. KÖHLER in Arkiv för Fysik *8*, 521 (1955).

[4] T. B. TAYLOR, Phys. Rev. *92*, 831 (1953). These values reproduce the experimental total cross sections.

[5] S. FERNBACH *et al.*, Phys. Rev. *75*, 1352 (1949)

Ta

Polarization in per cent as a function of scattering angle. C is the coupl

	Scattering angle		0°	3°	6°
Polarization in per cent	$C = 0.5$ Mev	$K = 0$	0	-3.2	-6.8
		$K = 0.15 \times 10^{13}$ cm^{-1}	0	0.8	1.7
	$C = 1$ Mev	$K = 0$	0	-5.8	-12.1
		$K = 0.15 \times 10^{13}$ cm^{-1}	0	1.9	4.0

If the incident beam is unpolarized, then after scattering there is a polarization perpendicular to the plane of scattering. We give our results in terms of the polarization P (expressed as a percentage) defined as the average of the expectation value of the spin operator σ in the scattered beam.[1] Table 1 gives P as a function of scattering angle. The results are also plotted in Figs. 1 and 2. Figures 3 and 4 give the differential cross sections averaged over final spin directions.

The results suggest that, on this model at least, the polarization is a rather

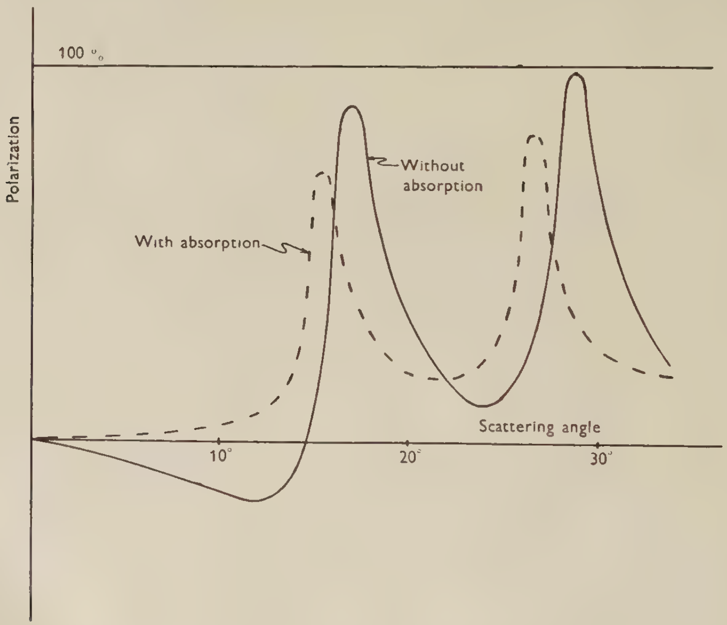

Fig. 1. The polarization as a function of scattering angle, with a spin-orbit coupling strength corresponding to $C = 0.5$ Mev with and without absorption ($K = 0.15 \times 10^{13}$ cm^{-1} and $K = 0$).

---

[1] Compare L. Wolfenstein, Phys. Rev. 75, 1664 (1949). Positive P means polarization in the direction of a right-handed screw specifying the rotation of the beam in the scattering.

stant and K the inverse mean free path of neutrons in nuclear matter.

9°	12°	15°	18°	21°	24°	27°	30°	33°
11.2	−15.9	8.5	71.4	24.8	9.9	36.1	68.0	26.2
3.1	6.9	62.0	29.4	17.2	21.4	80.4	25.9	18.5
19.0	−24.5	3.5	99.3	51.3	24.6	44.8	88.2	50.1
6.7	12.8	65.3	51.2	34,5	41.5	84.5	41.6	35.6

sensitive function of the scattering angle. It appears that around certain angles (which are related to the positions of the diffraction minima in the differential scattering cross section) the polarization may reach large values. Recently we had the opportunity of comparing these results with the similar calculations of G. A. Snow *et al.*[1] and the above qualitative features appear to be confirmed. Certain differences are, however, apparent, presumably due to the different choice of parameters in the two cases, especially the different strengths and radial dependences of the spin-orbit coupling term in the potential. (Snow *et al.* consider also higher energies and a smaller nucleus, but the ratio of wavelength to nuclear radius, which determines the angular scale of the diffraction patterns,

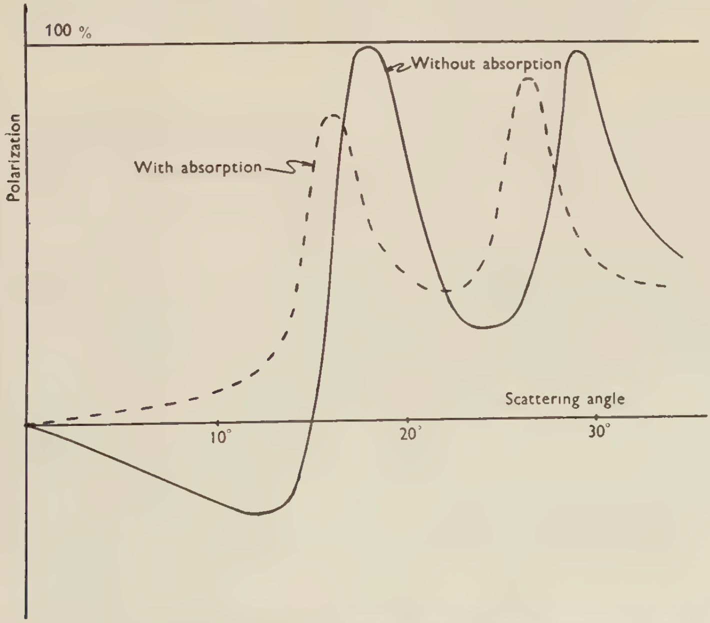

Fig. 2. The polarization as a function of scattering angle, with a spin-orbit coupling strength corresponding to $C=1$ Mev with and without absorption ($K=0.15\times10^{13}$ cm^{-1} and $K=0$).

---

[1] G. A. Snow, R. M. Sternheimer, and C. N. Yang, Phys. Rev., *94*, 1073 (1954).

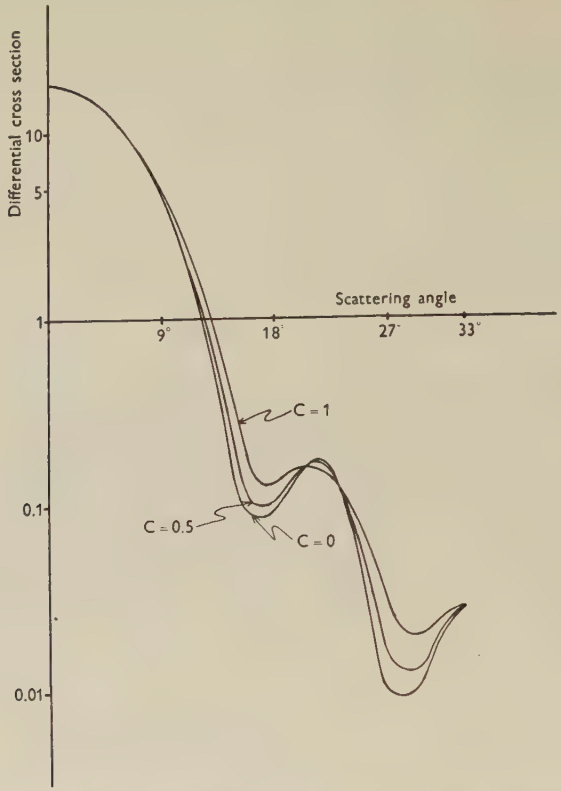

Fig. 3. The differential cross section in barns, for the different coupling strengths corresponding to $C = 0$; 0.5; and 1 Mev, in the case of no absorption ($K = 0$).

happens to be only some 15 % greater than in our case. Their absorption, $K = 0.17 \times 10^{13}$ cm^{-1},[1] is also close to our $K = 0.15 \times 10^{13}$ cm^{-1}.)

The different cases treated so far are too few to justify detailed conclusions about the dependence of the polarization on the various parameters entering the calculation, but the following features are perhaps significant. At small angles our results suggest small polarization, negative without and positive with absorption, and increasing in magnitude with increasing strength of coupling. With increasing angle there is a rather sudden increase of P in the region of the first peak. Snow *et al.*, on the other hand, find rather large (positive) values of P, even for small angles, and for the larger coupling strengths this region merges with the first peak. For smaller coupling strengths the small angle polarization decreases and the peak stands out more clearly, as in our case.

Another feature is the depth of the dip in P between the first and second maximum, which, according to Snow *et al.*, is large and negative for strong couplings but becomes less negative with decreasing coupling. In our case P remains positive in the region of the dip.

---

[1] The imaginary part of the potential is stated by Snow *et al.* to be +25.6 Mev. We find that their K leads to about (minus) half this value.

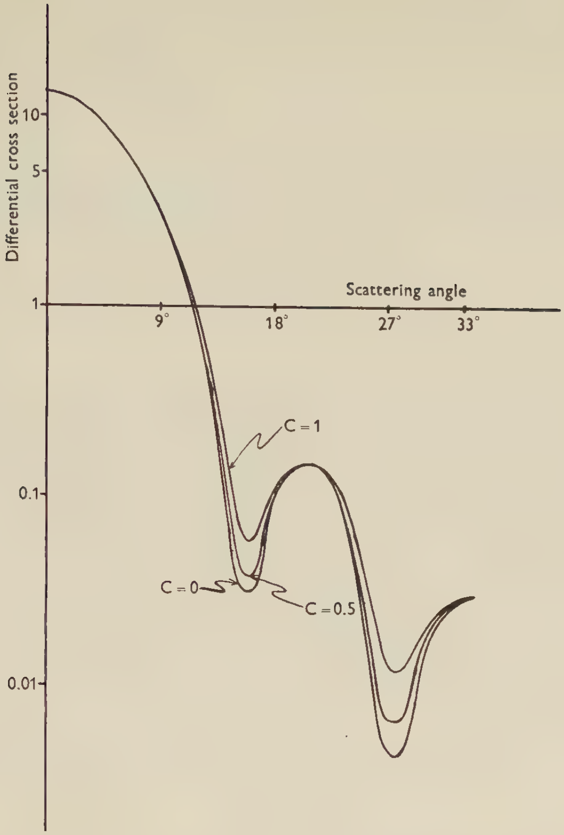

Fig. 4. The differential cross section in barns, for the different coupling strengths corresponding to $C=0$; 0.5; and 1 Mev, in the case of absorption ($K=0.15\times 10^{13}$ cm^{-1}).

In general the curves of SNOW *et al.* become more like ours with decreasing coupling strength. Owing to the different radial dependence of the coupling term in the different sets of calculations a unique comparison of the coupling strengths cannot be made, and differences characteristic of the different types of coupling are in any case to be expected. If, as a rough measure of the strength of coupling, we take the average over the nucleus of the term in front of $(\boldsymbol{l}\cdot\boldsymbol{s})$, then for the 3 cases considered by SNOW *et al.* ($\varepsilon_1=4.0$; 7.5; 15.0 Mev) we find 1.8; 3.5; 6.9 Mev respectively (for both the $\delta\ (r-R)$ and $(r/R)^2$ types of radial dependence). The corresponding figures in our case are 0.5 and 1.0 Mev. This is consistent with the above-mentioned greater similarity of our results with the weaker coupling cases of SNOW *et al.* The same is true of the comparison of the differential cross sections plotted in Figs. 3 and 4 with the corresponding curves given by SNOW *et al.*

We should like to thank Professor I. WALLER for his interest in the problem, Fil. lic. A. SJÖLANDER for an illuminating discussion, and Fil. mag. S. KÖHLER for assistance with the numerical work.

Tryckt den 27 januari 1955

Uppsala 1955. Almqvist & Wiksells Boktryckeri AB

ARKIV FÖR FYSIK Band 9 nr 17

Communicated 22 September 1954 by Axel E. Lindh and Harald Norinder

On line width determinations with bent crystal spectrometers

By Gösta Brogren

With 2 figures in the text

The resolving power of a bent crystal X-ray spectrometer is as a rule investigated by registering the contour curve of a well-known X-ray emission line. The line width obtained is then compared with the hitherto accepted standard value, viz. that obtained with a two-crystal spectrometer using the first order reflection from the cleavage face of calcite. Very often the bent crystal spectrometers have produced line widths less than the commonly accepted calcite values. This is remarkable, since the crystal bending introduces effects that must give rise to an increase in the line width. This fact is partly explained by recent observations from two-crystal spectrometer investigations. Before discussing the matter further, we must consider the properties of the focusing spectrometers, especially the broadening due to the bending of the crystal.

According to Johann [1], the widening b along the Rowland circle in a spectrometer where the radius of curvature of the bent crystal is R, is

$$b = \frac{\sigma^2 \cot \vartheta}{8R}, \tag{1}$$

σ being the opening of the crystal holder along the Rowland circle and ϑ the Bragg angle for the wavelength under consideration. When the broadening is calculated in X.U., we get

$$b_\lambda = \frac{\lambda \cot^2 \vartheta}{8} \frac{\sigma^2}{R^2}. \tag{2}$$

(In the Cauchois spectrometer cot ϑ must be replaced by tan ϑ.) If the crystal is first ground to radius R and then bent to radius $R/2$, the Johann broadening disappears [2].

The theory of X-ray diffraction in crystals shows that, for a given wavelength, reflection will take place only within a very small angular region around the Bragg angle, the width of which may be roughly estimated as twice the full width of the diffraction pattern at half maximum intensity. In consequence, it is necessary to investigate whether reflection takes place over the whole geometric opening of the crystal. Fig. 1 is a diagram of the Johann spectrograph. A is a point focal spot on the Rowland circle. B_1BB_2 is the bent crystal. The ray AB strikes the crystal at the Bragg angle ϑ, and the ray AB_1 at angle ϑ_1. Using the symbols in the figure, and applying the sine rule to the triangle ABB_1, we have

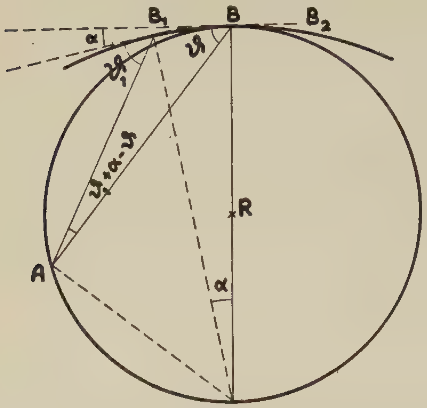

Fig. 1.

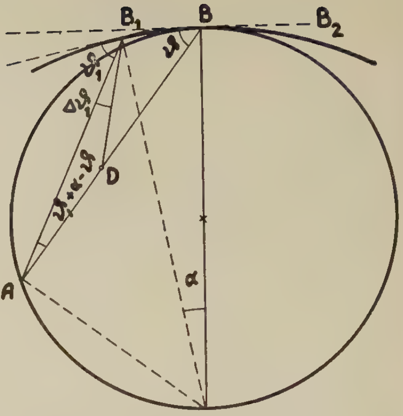

Fig. 2.

$$\frac{BB_1}{\sin(\vartheta_1+\alpha-\vartheta)}=\frac{AB}{\sin(\vartheta_1+\alpha/2)} \tag{3}$$

But $BB_1=R\sin\alpha=2R\sin\frac{\alpha}{2}$ (α is very small)

$AB=R\sin\vartheta$.

Introduce $\vartheta_1-\vartheta=\Delta$.

Substitution and expansion (α and Δ both very small) give us

$$\Delta=\frac{\alpha^2}{2}\cot\vartheta. \tag{4}$$

The maximum value of α is $\sigma/2R$. If $\sigma/R=0.01$, the maximum value of Δ is 4.5″ at 30°, 3.1″ at 40°, 2.2″ at 50°, and 1.5″ at 60°.

However, the focal spot is usually nearer the crystal. If it is displaced from A to D along the line AB between the crystal and the Rowland circle (see Fig. 2), there will be another increment $\Delta\vartheta_1$ in the glancing angle for the ray DB_1, so that it becomes $\vartheta_1+\Delta\vartheta_1$. $\Delta\vartheta_1$ will be positive between B and B_1; negative between B and B_2, so that $|\vartheta_1+\Delta\vartheta_1-\vartheta|$ will increase along the whole crystal.

The sine rule applied to triangles BB_1D and B_1DA gives

$$\frac{BD}{\sin(\vartheta_1+\Delta\vartheta_1+\alpha/2)}=\frac{B_1D}{\sin(\vartheta-\alpha/2)}, \tag{5}$$

$$\frac{AD}{\sin\Delta\vartheta_1}=\frac{B_1D}{\sin(\vartheta_1+\alpha-\vartheta)}. \tag{6}$$

Substituting

$$AB=R\sin\vartheta$$

$$BD=k\cdot AB=kR\sin\vartheta$$

we get

$$\sin \Delta \vartheta_1 = \frac{1-k}{k} \cdot \frac{\sin(\vartheta_1 + \alpha - \vartheta) \cdot \sin(\vartheta_1 + \Delta \vartheta_1 + \alpha/2)}{\sin(\vartheta - \alpha/2)}. \tag{7}$$

But $\Delta\vartheta_1$ must also be very small because reflection can only take place in a very narrow angular region around the Bragg angle; so that when $k \neq 1$

$$\Delta \vartheta_1 \approx \alpha \frac{1-k}{k}. \tag{8}$$

Therefore,

$$\vartheta_1 + \Delta \vartheta_1 - \vartheta = \Delta \vartheta_1 + \Delta = \alpha \left(\frac{1-k}{k} + \frac{\alpha}{2 \tan \vartheta} \right), \tag{9}$$

$$\text{but } \frac{1-k}{k} \gg \frac{\alpha}{2 \tan \vartheta}, \text{ so that}$$

$$\vartheta_1 + \Delta \vartheta_1 - \vartheta \approx \frac{1-k}{k} \cdot \alpha. \tag{10}$$

If $\vartheta_1 + \Delta \vartheta_1 - \vartheta$ is put equal to the width w of the diffraction pattern, we get

$$\alpha = w \frac{k}{1-k}. \tag{11}$$

The angular width γ of the beam that will be reflected is then

$$\gamma = 2(\alpha + \Delta \vartheta_1) = \frac{2\alpha}{k}. \tag{12}$$

Hence

$$\gamma = \frac{2w}{1-k}. \tag{13}$$

In practice it is impossible to obtain a point focus. If the focal spot is not too large, however, the radiation from every point of it will be reflected as above.

It will be seen that often only a part of the crystal opening is utilized when the focal spot is small. It may be remarked that if the properties of the focal spot remain unchanged, the intensity produced by the spectrometer is proportional to angle γ but inversely proportional to the optical distance from the focal spot to the "image" point on the Rowland circle, so that

$$I = c I_0 \frac{\gamma}{1+k} \approx c I_0 \frac{2w}{1-k^2} \tag{14}$$

when the whole focal spot is utilized. The intensity increases when the spot is displaced from the crystal towards the Rowland circle. A strict derivation shows this to be correct also near the Rowland circle.

In a focusing spectrometer of the Cauchois type eq. (10–13) are valid if the sign of k is changed from $-$ to $+$. k is there the ratio between the distance from the focal spot to the crystal and the radius of curvature. The opening angle γ is very small [$\gamma = 2w/(1+k)$]. If the whole crystal opening is to be utilized there, the linear extension a of the focal spot must be

$$a = \sigma(1 + k). \tag{15}$$

Normally, however, the focal spot is much smaller, so that only part of the crystal is utilized when a certain wavelength is reflected. When the wavelength changes, the reflecting part also changes. For this reason it is necessary to examine the bent crystal with a large focal spot, so that the whole opening is utilized.

After this discussion of the reflecting properties of focusing spectrometers we return to the line width measurements and confine ourselves to the cases where calcite and quartz crystals are used. Both these crystals have a nearly perfect structure. When a quartz crystal is bent in a holder, the bending is purely elastic. We have investigated a plane parallel crystal plate in a two-crystal spectrometer before and after bending, and found no change in the reflecting properties. The bent quartz crystal may therefore still be considered a perfect crystal.

In the bent crystal spectrometer three broadening factors have to be taken into account, besides the widening inherent in the diffraction pattern. They are the broadening due to the crystal aperture, discussed above, the broadening due to the slit that must be used in front of the registering instrument, and the broadening due to elastic deformations of the crystal and deviations from the exact cylindrical form. (The broadening effect of the heights of the focal spot and the counter slit is so slight that it can be neglected.) If the slit width is w_s, the uncorrected line width w_1 and the width, corrected for the slit w_1', measurements with varying w_s were found to satisfy the relation

$$w_1' = \sqrt{w_1^2 + w_s^2}. \tag{16}$$

The maximum value of w_s used in these measurements was about $w_1'/2$. In normal line width determinations w_s is as a rule of the order of $w_1'/10$, which makes its broadening effect negligible.

The effect of the bending is more difficult to estimate. In an ideally bent perfect crystal the interatomic distances are not the same as in the undisturbed crystal. This must influence the diffraction in about the same way as would be the case if the perfect structure had become a little more mosaic. The width of the diffraction pattern must increase. This behaviour is shown experimentally in γ-ray investigations with bent quartz crystals [3–4].

WATSON, WEST, LIND and DUMOND investigated the properties of their 2-meter focusing curved crystal gamma-ray spectrometer by means of the $K\alpha$ lines of tungsten. In order to obtain information about the quartz crystal used, they cut two optically flat 1-mm thick plates of quartz with the reflection $(13\bar{4}0)$ planes perpendicular to the surfaces of the plates. These were cut from the same crystal specimen as the lamina used in the 2-meter curved crystal spectrometer and in all respects identical with the lamina. The reflections were studied with the beams transmitted through the plates. The rocking curve had the full width $2.8'' = 0.016$ X.U. for W$K\alpha_1$. The full width of the line in position $(1 + 1)$ was $28.8'' = 0.164$ X.U. With the curved crystal spectrometer they got the width 0.22 X.U. of W$K\alpha_1$. The crystal was ground before bending so as to eliminate the Johann broadening.

The diffraction pattern of an unstressed crystal cut for symmetric Laue reflection (with the reflecting planes perpendicular to the surfaces of the crystal plate) is given by

$$I = \frac{I_0 e^{-\frac{\mu d}{\gamma}}}{2(1 + y^2)} \cosh \frac{2 \varkappa A}{\sqrt{1 + y^2}} \tag{17}$$

where y is the angular coordinate. $(\varkappa A)$ is a factor that depends on the wavelength, the crystal thickness, the structure factor of the crystal, the polarization, and the anomalous contributions to the atomic scattering factors from the K electrons. For the crystal plates used in transmission spectrometers the value is less than 0.3 and decreases rapidly with decreasing wavelength. After expanding (17) into series, we get

$$I = \frac{I_{\max}}{1+y^2}\left(1 + 2\,\frac{(\varkappa A)}{1+y^2}\right) \tag{18}$$

as higher order terms of $(\varkappa A)$ are so small that they can be neglected. The diffraction pattern of the transmission crystal given by (18) thus has the same or nearly the same shape as the symmetric line and the rocking curve of the double crystal spectrometer. (When both crystals in the double crystal spectrometer are adjusted for symmetric Laue reflection, the diffraction pattern of positions $(n, +n)$ and $(n, -n)$ are identical.) Hence, it ought to be possible to use the same way of correcting the obtained line width for the influence from the diffraction pattern as in double crystal spectrometer measurements. However, the above measurements of the width of W$K\alpha_1$ show that this is not the case. The main reasons seem to be the broadening caused by the elastic deformation during the bending and the fact that larger crystal areas are irradiated in the curved crystal spectrometer, so that slight deficiencies may occur there. It is of course also possible that small deviations from the exact cylindrical form appear. The elastic deformations give rise to another difference between the plane unstressed crystal and the curved one. The integrated reflection power has in the first case a wavelength dependence in agreement with the dynamical theory for perfect crystals but in the latter case the bent crystals follow the predictions for mosaic crystals. This behaviour is not yet theoretically explained. If the influence of bending is to be investigated, this can be done by carrying out comparative recordings of line contour curves by means of double crystal spectrometers and curved crystal spectrometers, using the same crystal lattices.

The properties of the Johann spectrometer are generally examined by registering the contour curve of a well-known emission line, usually a $K\alpha_1$ line. Commonly higher order reflections are used. A high order corresponds to another atomic plane than that involved in the first order reflection. It has a smaller spacing and a higher resolution, so that no direct comparison can be made. Only very few profile curves have been registered in the first order. OHLIN [5] recorded the $K\alpha_1$ lines of Ca, Ti and Va in a curved crystal spectrometer, using the first order reflections from the cleavage plane of calcite (plane 211). The registrations were carried out with Geiger-Müller counters. The line widths obtained from his profile curves are about 0.3–0.5 X.U. larger than those obtained by PARRATT [6] with a double crystal spectrometer using the same reflections. The double crystal spectrometer has a higher resolving power than a single crystal spectrometer. BEARDEN and ROGOSA [7] recorded the width of the copper $K\alpha_1$ line with a plane single crystal spectrometer and a Geiger counter with a very narrow slit. The best result was obtained with a perfect calcite crystal, which was one of a pair that gave theoretical widths of the rocking curves in the double crystal spectrometer. The narrowest line width obtained with the single crystal spectrometer was at 0.64 X.U. and with the double crystal spectrometer 0.58 X.U. The above differences between OHLIN's and PARRATT's values are much larger than what was obtained by BEARDEN with the Cu$K\alpha_1$ line. The additional broadening arises from the effects of bending, which may be rather great here, as calcite has relatively poor elastic properties. This is confirmed by HAGLUND [8], who registered the Cu$K\alpha_1$ photographically and found the width 0.63 X.U. in the second order with the same bent calcite crystal as was used by OHLIN. The corresponding double crystal spectrometer value is 0.45 X.U. (recorded by the author).

The quartz crystal has been used extensively in Johann spectrometers but very few registrations have been carried out with instruments that record the intensity directly. This crystal has excellent elastic properties and is easily bent to the desired radius in cylindrical holders. Using plane (0003) bent to radius 991 mm we obtained the width 0.79 X.U. for the Co$K\alpha_1$ line (the calcite double spectrometer value is 0.69 X.U. and the value obtained with quartz 0003 in the double spectrometer, 0.59 X.U.). With the same plane bent to radius 750 mm the width of the Cr$K\alpha_1$ and $K\alpha_1$ were 1.00 and 1.10 X.U. respectively. The calcite values are 1.08 and 1.30 X.U. respectively. The $(20\bar{2}2)$ plane bent to radius 991 mm gave for Fe $K\alpha_1$ and $K\alpha_2$ the widths 0.87 X.U. and 0.89 X.U. The calcite values are 1.00 and 1.06 X.U. respectively. We have recorded the $K\alpha_1$ line in the double crystal spectrometer using quartz plane $(11\bar{2}0)$ which has not as high a resolving power as $(20\bar{2}2)$ and got the value 0.82 X.U.

The opening of the crystal holders was 3×12 mm. The total spot was so large that the whole opening was utilized. The registrations were made at different time and no comparative investigation has been carried out as yet. The present results show that some broadening effects owing to the bending appear, but it is not possible to explain how they are caused. To a great extent they may be results of inexact curvature. When "higher order" reflections are utilized their influence is diminshed and narrower lines are obtained. Line widths narrower than the uncorrected calcite double crystal spectrometer values are also often reported in literature. It seems at present impossible to construct a formula that gives the relation between the natural line width and the width obtained with a curved crystal spectrometer. Further information can be obtained by comparative recordings with double crystal and bent crystal spectrometers, using the same crystal gratings in both. Such an investigation is planned, and it is to be extended also to longer wavelengths by means of a vacuum double crystal spectrometer now under construction.

The Physical Institute, University of Uppsala, Uppsala, Sweden. April 1954.

REFERENCES

1. JOHANN, H. H., Zs. f. Phys. *69*, 185 (1931).
2. JOHANSSON, T., Zs. f. Phys. *82*, 507 (1933).
3. WATSON, B. B., WEST, W. J., LIND, D. A., and DUMOND, J. W. M., Phys. Rev. *75*, 505 (1948).
4. LIND, D. A., BROWN, J. R., and DUMOND, J. W. M., Phys. Rev. *76*, 1838 (1949).
5. OHLIN, P., Dissertation, Uppsala Universitets Årsskrift 1940.
6. PARRATT, L. G., Phys. Rev. *44*, 695 (1933).
7. BEARDEN, J. A. and ROGOSA, G. L., Phys. Rev. *75*, 1304 (1949).
8. HAGLUND, PH., Arkiv för Mat., Astr. o. Fys., Bd. *28A*, No. 8, 1941.

Tryckt den 27 januari 1955

Uppsala 1955. Almqvist & Wiksells Boktryckeri AB

ARKIV FÖR FYSIK Band 9 nr 18

Communicated 24 November 1954 by LISE MEITNER and ERIK HULTHÉN

The use of the ^{3}T (d, n) ^{4}He reaction for a comparison of some methods for the absolute measurement of a fast neutron flux

The yield of a Ra-α-Be source

By KARL-ERIK LARSSON

With 17 figures in the text

Introduction

Ever since the discovery of the neutron, one of the most frequently used methods for the measurement of a fast neutron flux has been the recoil particle method. The advantage of this method is that it can be successfully used for neutron energies from a few hundred keV up to the several hundred MeV permitted by modern accelerators. If reasonably good precision is wanted in the absolute determination of the flux, the recoil particle method may be used only for monoenergetic neutron spectra. In the general case with a complicated neutron spectrum, it is preferable to use some form of the slowing down technique, which involves the slowing down of the fast neutrons to thermal energies and the subsequent absolute measurement of the thermal neutron density. For the measurement of thermal neutron densities a great number of methods has been developed, some of them to very good accuracy. Two factors, however, limit the usefulness of this slowing down technique, i.e. the long slowing down length required for neutrons of high primary energy, and the probability of absorption of fast neutrons in the moderator by the (n, α) and (n, p) reactions, which generally become important above certain threshold energies. Furthermore the slowing down methods only give the total number of neutrons emitted by the source. These methods, however, are useful up to a primary neutron energy of 15 MeV. In addition to these two classical types of absolute flux measurements, there exist some special methods useful for certain nuclear reactions or for certain neutron energies, such as the associated particle method, the use of fission detectors and the threshold detectors. The associated particle method is especially well suited to the accurate measurement of neutron fluxes from some reactions such as $^3\mathrm{T}(d, n)^4\mathrm{He}$, $^3\mathrm{T}(p, n)^3\mathrm{He}$, $^2\mathrm{D}(d, n)^3\mathrm{He}$ and $^2\mathrm{D}(\gamma, n)^1\mathrm{H}$. This method is based on the counting of the charged recoil nuclei created simultaneously with the neutron. If this counting of charged particles is combined with a measurement of the angular distribution of either of the two types of particles, it is possible to obtain an accurate estimate of the neutron flux.

The purpose of the following investigation is to compare directly some different methods with regard to accuracy and also with regard to the mutual agreement between the different estimates of the fluxes obtained. As a typical example of direct flux measurement the recoil particle method has been chosen. As this method requires a monoenergetic neutron flux in order to give accurate results, the $^3T(d,n)^4He$ reaction was used as a neutron source, the advantage of this reaction being its high Q value—17.58 MeV—giving to the α-particle an energy of 3 MeV. This means that the α-particles are easily counted, and thus the associated particle method may be directly compared with the recoil particle method. Moreover, it is possible to surround the target with a suitable moderator and use the slowing down technique for a third absolute measurement of the flux.

CHAPTER I

Comparison between the recoil particle method and the associated particle method

1. Theory for the methods

There are a great number of recoil particle methods, each with their special advantages [1, 2]. These may be generally divided into counting methods including the counting of each recoil nucleus, and integrating methods measuring the total ionization caused by the recoil particles. Since the $^3T(d,n)^4He$ reaction is not accompanied by disturbing energetic γ-radiation, an integrating method using the homogeneous ionization chamber as detector was chosen. This type of chamber was introduced by Bragg [3] and was perfected later by the investigations of Gray and others [4, 5]. It was used for the first time for the measurement of neutron fluxes by Bretscher [6]. Its operation depends on the principle that in a medium of a given composition exposed to a homogeneous flux of primary radiation, the flux of secondary radiation is also homogeneous and independent of the density of the medium. In practice, the chamber may be made with walls of polythene, $(CH_2)_n$, and filled with ethylene, C_2H_4. The chamber walls and the gas thus have the same atomic composition, and the wall thickness should equal the range of the most energetic recoil nuclei, i.e. the recoil protons. The energy absorption in the active volume of the chamber is measured by the current caused by the ionization of the recoil nuclei. This current is given by the expression

$$i = \phi \cdot \frac{ev}{W} (N_H \sigma_H \bar{E}_H + N_C \sigma_C \bar{E}_C), \tag{1}$$

where ϕ = neutron flux (n/cm^2/sec)
e = the electronic charge
v = the sensitive volume of the chamber
W = the amount of energy in electron volts required to form an ion pair in ethylene or polythene
N_H, N_C = the number of nuclei per cm^3 of hydrogen + carbon respectively.
σ_H, σ_C = the scattering cross sections of hydrogen and carbon.
$\bar{E}_H$, $\bar{E}_C$ = the mean energy of the recoil nuclei of hydrogen and carbon respectively.

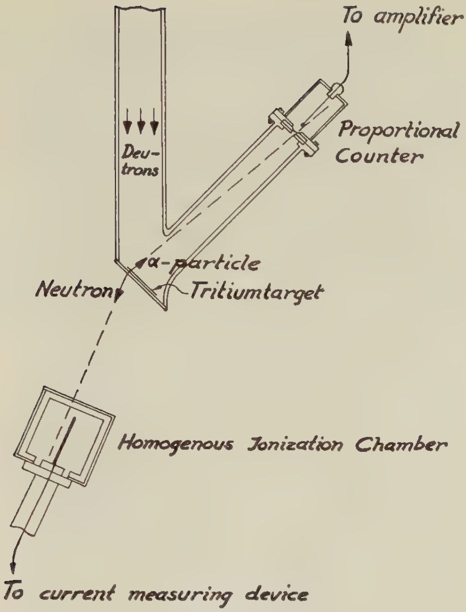

Fig. 1. Principle of the associated particle method and the comparison with the recoil particle method.

The neutron flux is thus directly proportional to the measured current. At higher neutron energies the measurement is complicated by certain inelastic processes occurring in the collision between the neutron and the carbon nucleus. At an energy of 14 MeV these processes are, however, of minor importance. This will be shown later.

In order to measure the flux from the $^3\mathrm{T}(d, n)^4\mathrm{He}$ reaction the associated particle method is also used. In principle this is accomplished by bombarding the tritium target with deuterons, thereby causing α-particles to leave the target in all directions. A constant fraction of these α-particles is counted by placing a proportional counter at a fixed distance from the target (see Fig. 1). This proportional counter thus counts all α-particles falling within a given solid angle ω. The intensity of α-particles measured at the angle θ in the laboratory system is given by

$$I_\alpha(\theta_\alpha)=\frac{N_\alpha}{t\cdot\omega}\ \alpha\text{-particles/unit solid angle/sec}, \tag{2}$$

where N_α is the number of α-particles counted in the time t sec, θ_α is the angle, which α-particles falling within the collimator form with the incoming deuteron beam. On the other hand the corresponding quantity measured by the homogeneous ionization chamber is

$$I_n(\theta_n)=\phi r^2\ n/\text{unit solid angle/sec}, \tag{3}$$

where θ_n is the mean angle between the directions of the deuteron beam and the neutron flux falling within the solid angle subtended by the chamber as seen from the target, and r is the distance from the target to the effective centre of the chamber. The ratio between the fluxes given by the two methods and measured in the laboratory system is thus

$$\left(\frac{I_n(\theta_n)}{I_\alpha(\theta_\alpha)}\right)_{\text{exp}} = \frac{W \cdot \omega \cdot r^2}{ev\,(N_{\text{H}}\sigma_{\text{H}}\bar{E}_{\text{H}} + N_{\text{C}}\,\sigma_{\text{C}}\,\bar{E}_{\text{C}})} \cdot \frac{q}{N_\alpha}, \tag{4}$$

where $q = i \cdot t$, i.e. the charge collected on to the collecting electrode of the chamber in time t. This ratio, however, is preferably transformed to the c.m. system, which implies the transformation of the solid angles. The observed intensities I satisfy the following relations [7], which follow from the laws of conservation of energy and momentum

$$I_{\text{lab}} = \frac{\sin^2 \phi}{\sin^2 \theta \, \cos(\phi - \theta)} I_{\text{cm}}, \tag{5}$$

where ϕ = the angle between the incoming deuteron and the outgoing particle in the c.m. system.
θ = the angle between the incoming deuteron and the outgoing particle in the lab. system.
I_{lab} = the observed intensity at the angle θ per unit solid angle in the lab. system.
I_{cm} = the corresponding intensity at the angle ϕ per unit solid angle in the c.m. system.

The calculated ratio between the intensity of neutrons measured at the angle θ_n and α-particles measured at θ_α is thus

$$\left(\frac{I_n(\theta_n)}{I_\alpha(\theta_\alpha)}\right)_{\text{theor.}} = \frac{\sin^2 \phi_n}{\sin^2 \phi_\alpha} \cdot \frac{\sin^2 \theta_\alpha}{\sin^2 \theta_n} \cdot \frac{\cos(\phi_\alpha - \theta_\alpha)}{\cos(\phi_n - \theta_n)}, \tag{6}$$

where the subscripts n and α refer to neutron angles and the corresponding angles for the α-particles, respectively. If the angular distribution of the particles is spherically symmetrical in the c.m. system the factors I_{cm} cancel.

As the calculation of the angles ϕ_n and ϕ_α implies the use of the laws of conservation of energy and momentum, the expression (6) becomes a complicated function of the effective deuteron energy. Finally, transformed to the c.m. system, the ratio between the neutron fluxes measured by the two methods is

$$\left(\frac{I_n}{I_\alpha}\right)_{\text{cm}} = \frac{\left(\frac{I_n}{I_\alpha}\right)_{\text{exp}}}{\left(\frac{I_n}{I_\alpha}\right)_{\text{theor.}}} \tag{7}$$

2. Apparatus. Investigation of the chamber and proportional counter

a) The accelerating system

The most prominent characteristic of the $^3\text{T}(d,n)^4\text{He}$ reaction is its high cross section [8]—between 2.5 and 5 barns—at deuteron energies of 100–200 keV. This makes this reaction an extremely intense source of monoenergetic neutrons, if deuterons

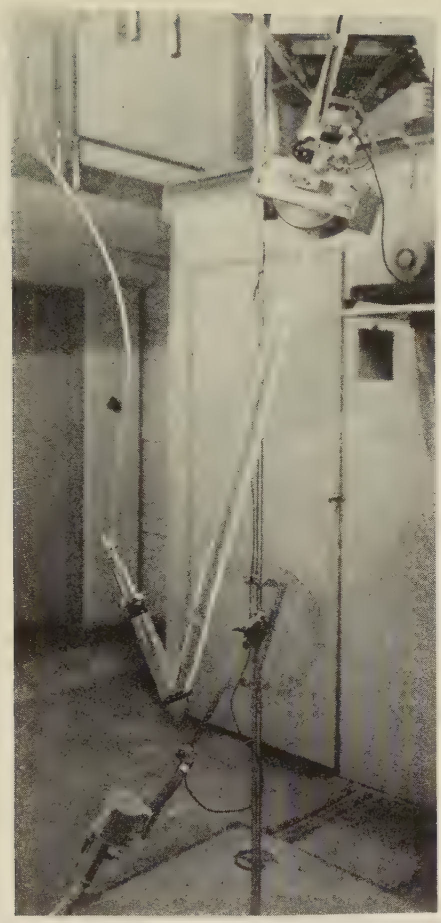

Fig. 2. Target arrangement with magnets, proportional counter and homogeneous ionization chamber.

of these energies are used. In the experiments described below a 200 kV accelerator [9], described in detail earlier, was consequently used. The ion source, which was of high frequency type, delivered a total maximum current of 500 μA. As it is essential in these experiments to know the deuteron energies accurately, the beam was analyzed in a magnet giving a 14° deviation, and only the D^+ component of the beam was used for the bombardment of the target. The high voltage, which was varied between 100 and 200 kV, was measured by measuring the current through a 500 MΩ wire wound precision resistance cooled by oil. A circular zirconium evaporation of a diameter of 25 mm on a Mo backing, in which was absorbed about 10 mC of tritium, was used as a target, the target thickness being 200 μg/cm^2. As zirconium-tritium targets of this type are rather sensitive to an excessive concentration of the ion beam on one point, a second smaller magnet was placed below the larger analyzer magnet in order to oscillate the beam over the target surface. This was accomplished by feeding the magnet with 50 cycle A.C., which was amplitude-modulated with a saw tooth voltage having a 5-second period. In this way the whole surface area was uniformly irradiated, which, moreover, is important for the determination of the effective centre of the target. Some investigators [10] have found that targets of this type deteriorate quickly if coated with an organic film, suggesting that heating to 70–90° may be necessary. For that reason a small heating unit was at first placed under the target, but the experiment showed that no heating was necessary, hence it was removed later. No cold trap between the pumping system and the target tube was used. At the end of the experiment after a total irradiation of 15 mAh the target still gave a neutron intensity 30 % of the primary intensity. The magnitude of the currents to the target was varied between 1 and 8 μA. Because of the risk of backscattering of neutrons from the magnet system and the lower parts of the acceleration tube a target tube of 100 cm of length was used. The distance between the target and the floor also was 100 cm. The target assembly with target tube made of pyrex glass, magnets, α-counter and homogeneous ionization chamber will be shown in Fig. 2. The angle between the incoming deuteron beam and the target plate is 45°, and at right angles to this, thus forming an angle of 135° to the incoming deuteron beam, a side tube of 17 cm of length protrudes, at the end of which an end window proportional counter for the counting of α-particles is situated (see also Fig. 1).

b) The proportional counter

In all experiments involving an absolute measurement of radiation the construction and performance of the detector is of decisive importance. As the detector, which in this experiment should give an absolute measure of the α-particle flux within a small solid angle from the target, must necessarily be exposed to the rather strong neutron irradiation, it was of importance to choose a detector counting a neutron flux with low efficiency. The most suitable detector fulfilling the requirements of counting the α-particles with 100 % efficiency and at the same time showing a low efficiency in counting neutrons is the proportional counter, if the appropriate filling is used.

In order to ensure that the α-particles are counted with 100 % efficiency, two different proportional counters were constructed, one with an end window and the other with a side window. The construction of the end window counter is shown in Fig. 3. The counter with side window has the same geometrical dimensions, the only difference being the location of the window. The counters were filled with a number of different gases and gas mixtures such as argon, argon + CO_2, argon + methane, argon + methylal in different ratios, and the same gases were tested simultaneously in both counters. To perform these investigations a very fine beam of well collimated α-particles from a Po source was used. Approximately the same intensities were used as could be expected in the subsequent measurement of the neutron flux. Since the energy of the Po α-particles is ~ 5.5 MeV, and the α-particles from the $^3T(d,n)^4He$ reaction have an energy of only ~ 3 MeV, the Po α-particles were allowed to traverse 2 cm of air before they reached the mica window of the proportional counter, which had a thickness of ~ 1.4 mg/cm². A typical result of these investigations are the bias curves shown in Fig. 4. The end window counter with the α-particle beam going parallel to the collecting wire shows a good plateau, whereas the counter with side window and the α-particles going at right angle to the wire shows a strongly sloping bias curve. Both counters, however, show the same counting

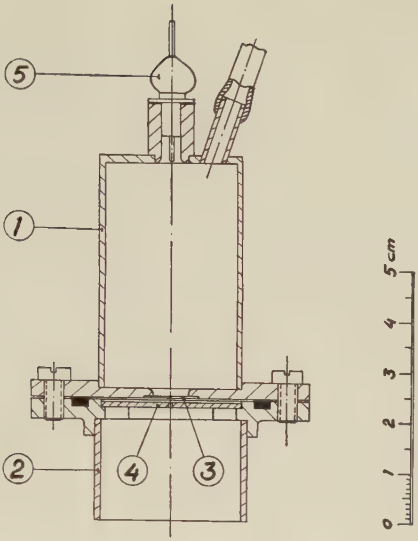

Fig. 3. Construction of the proportional counter. 1. Brass housing. 2. Kovar ring connection to the glass tube. 3. Mica window. 4. Collimator with small circular hole. 5. Kovar seal for the collecting wire, which was of diameter 0.12 mm.

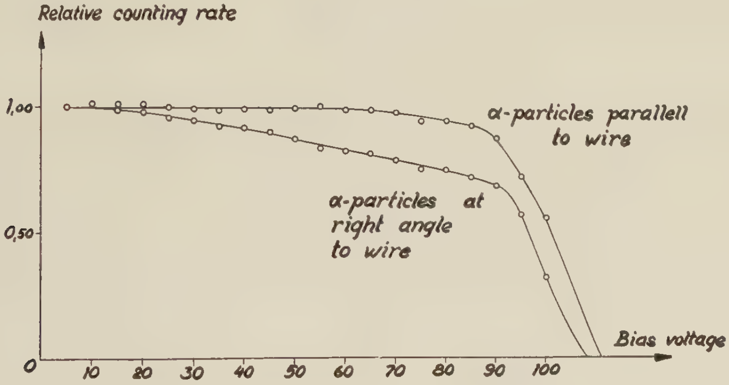

Fig. 4. Bias curves of the two proportional counters.

rate at low bias energies. Similar results were obtained for all the gases tested. In order to investigate whether or not electron capture in oxygen residues or other electro-negative gases was the reason for this difference in characteristics, the clipping times of the amplifiers were changed from 1.5 μs to 5 ms, resulting in ion collection. Independent of this and of the collecting voltage used, the same result was obtained. In the case where the particle beam enters the counter at right angle to the wire, columnar recombination may occur (see WILKINSON [11], p. 53). The greatest probability of such a recombination exists, of course, when the α-particle produces an ionization along a path parallel to the collecting field in the counter. If this were

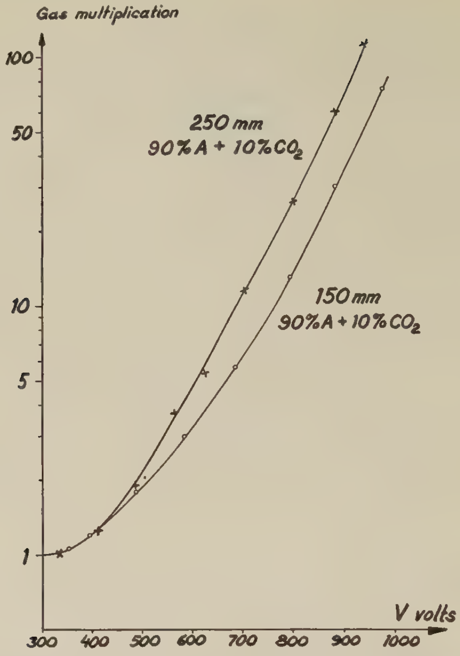

Fig. 5. Gas multiplication as a function of voltage applied to the collecting wires of the two proportional counters. Upper curve refers to the end window counter and lower curve to the side window counter.

the only reason for the spread in pulse size, the gas amplification of the two counters should vary in the same manner with the applied voltage. By studying the pulse size as a function of the collecting voltage with the aid of a Tektronix-514 D oscilloscope the gas amplification curves shown in Fig. 5 were received. The same gas mixture was used in both counters, but in spite of the fact that the counter with a side window was filled to a lower pressure than the end window counter, its gas amplification increased more slowly. A possible explanation to this might be that on account of the dense ionization of α-particles, a very great number of electrons are likely to be liberated within a very small distance from the wire when the particles arrive at right angles to the wire, causing the electrons which first arrive at the wire and produce multiplication to form a cloud of ions, which then lowers the potential near the wire to such a degree, that the following electrons are not multiplied. This would result in a systematic decrease of multiplication with increasing voltage, compared with the multiplication for the much lower ionization density resulting when the particles arrive parallel to the wire. This should be a possible explanation of the sloping bias curve, as even good collimation allows the incoming α-particles to make different angles with the wire, and consequently the same number of primary electrons give a strongly varying number of secondary particles. This investigation also showed, as will be seen in Fig. 4, that the counting of the α-particles is very probably 100 % efficient as the bias curves of the two counters coincide at the low amplitude end. For the final counting of the α-particles from the $^3T(d,n)^4He$

reaction the end window counter was chosen, filled to a pressure of 250 mm by a mixture containing 95 % argon and 5 % CO_2. Before using the counter for the main investigation a long term test of its stability was carried out, bias curves being taken daily for one month. Within the statistical limits of errors of ± 0.5 % the counting rate was constant and the pulse amplitude showed only minor variations.

c) The homogeneous ionization chamber and the method of the current measurement

The homogeneous ionization chamber has previously been used for the measurement of neutron fluxes [6, 12] and the construction employed here is similar to that developed by Bretscher and French [6]. The details of the construction are given in Fig. 6. Two cardinal points must be observed in constructing the chamber. In the first place the wall thickness must equal the range of the most energetic recoil particles as exactly as possible. Every increase in thickness exceeding this limit means a distortion of the measured primary neutron radiation. As the maximum energy of the proton recoils in this experiment should be slightly more than 15 MeV, the walls of the chamber were coated with a polythene film of a thickness of 250 mg/cm², in reasonable agreement with the range of 15 MeV protons in paraffin,

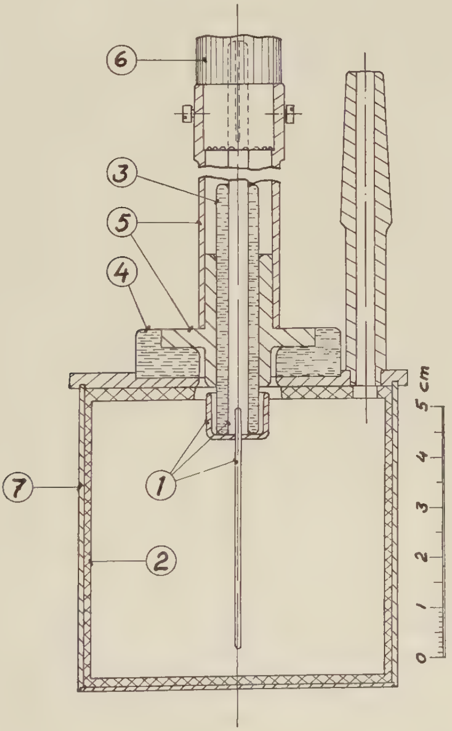

Fig. 6. Construction of the homogeneous ionization chamber. 1. Collecting electrode. 2. Polythene coating of chamber walls. 3. Quartz insulator. 4. Polyesterol insulator. 5. Guard ring. 6. Standard plug for connection with cable. 7. Brass housing.

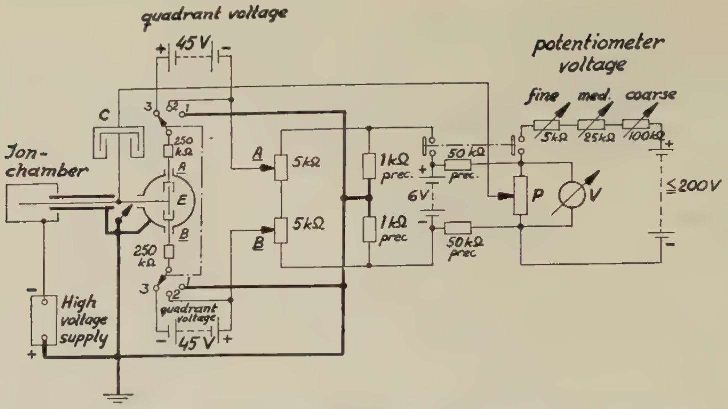

Fig. 7. Principle of the method of measuring the small currents. *E*, Lindemann electrometer; *C*, condenser; *P*, potentiometer to keep the condenser uncharged.

which is 226 mg/cm² [13]. In order to make the inner walls of the chamber conducting, a very thin gold film was evaporated inside the polythene container. In the second place the insulation of the collecting electrode of the chamber must be very good. As the neutron flux which should be measured was of the order of 10^4/sec, the corresponding ionization currents were expected to fall between 5×10^{-13} and 10^{-11} Amp. The greatest care was necessary in choosing insulators. To begin with polysterol was used as insulator next to the collecting electrode but it was found that its resistance changed during irradiation [14]. Then clear quartz glass was tested and found to be satisfactory as it gave an insulation resistance greater than $10^{15}\,\Omega$. Concerning the measurements of these resistances more will be mentioned later.

For the measurements of currents of 10^{-12} Amp. many methods are possible. The method elected should be specially suitable to the measurement of small quantities of electricity (cf. eq. 4). The classical electrometer method for the measurement of small currents is distinguished by its simplicity and its dependence of very few components, the principle being that the current collected in the ion chamber is allowed to charge a system consisting of one plate of a condensor and the sensitive system of a detecting instrument. If the second plate of the condensor is varied in potential from V_1 to V_2 in time t sec so that the condensor remains uncharged, the detecting instrument apparently shows no deviation, and the quantity of electricity collected in the ion chamber in time t is

$$q = \int_0^t i\,dt = C \cdot (V_1 - V_2), \tag{8}$$

The only things needed for the measurement of the current are thus a knowledge of the capacity, C, of the condensor and the change in potential of the second plate of the condensor in t sec.

The details of the circuit are shown in Fig. 7. The collecting electrode of the ion chamber is connected to one plate of the condensor and the needle of the Lindemann electrometer [15], which is used as a null-detector. All wires and the earthing device are made of silver. When the earthing device is disconnected the electrometer

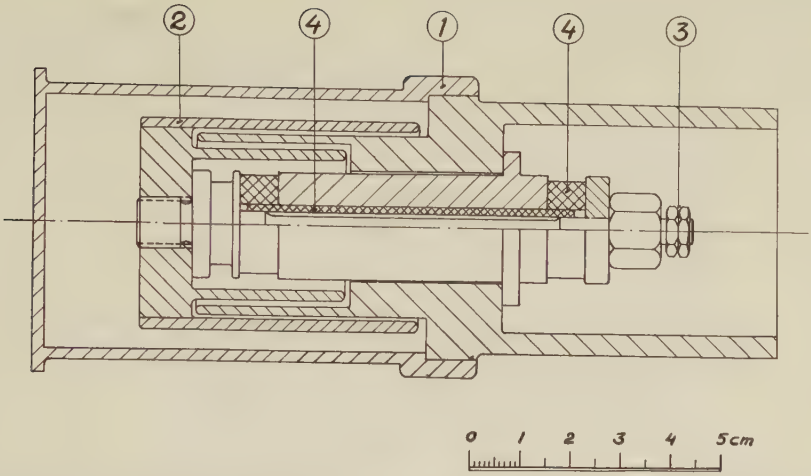

Fig. 8. Construction of the condenser. 1. Brass housing. 2. Cylindrical electrode with high insulation. 3. Connection to the collecting system of the homogeneous ionization chamber and to the electrometer. 4. Clear quartz insulator.

needle begins to move; this movement is compensated by applying a voltage to the other plate of the condensor at appropriate speed. This is effected by moving the sliding contact over the wire wound precision potentiometer P. The voltage applied to the potentiometer is measured by a Cambridge precision instrument. The sensitivity of the Lindemann electrometer was varied according to the currents to be measured. The electrometer needle was observed in a microscope with ocular scale divided into 100 units and it was possible to vary the sensitivity up to 4 mV/scale division before the electrometer became unstable. At this sensitivity it is possible to achieve a stability about a given scale division of ± 0.5 scale divisions, which corresponds to an exceedingly small error in the calculated value of the current or quantity of electricity.

Of special importance for the accuracy of the measurements are the properties of the condensor. The condensor finally used was a quartz-insulated air condensor, the construction of which is given in Fig. 8. Insulators other than clear quartz were tested, especially polyesterol and other plastic materials. Many of these show very pronounced surface charging, which might easily completely mask the weak currents to be measured. Of the same importance is the insulation of the cable between the chamber and the condensor. No commercial cables were found to fulfill the requirements, i.e. to give an insulation resistance higher than $5 \times 10^{14}\,\Omega$ and to be free from surface charge effects. A special cable consisting of a thin aluminum tube with a central silver wire insulated at a few points by clear quartz gave the required result. The insulation resistance of the whole system (chamber-cable-electrometer-condensor) varied somewhat during measurements about the value $10^{15}\,\Omega$. This was measured in such a manner that the system was charged up to about 0.5 V, whereupon the leakage was studied by the aid of the electrometer, and when the capacitance of the system was known, the resistance was calculated from the measured time constant.

The first investigation of the homogeneous ionization chamber concerned its

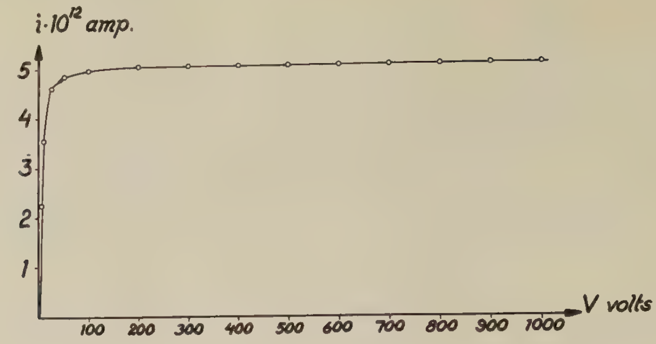

Fig. 9. Saturation curve of the homogenous ionization chamber.

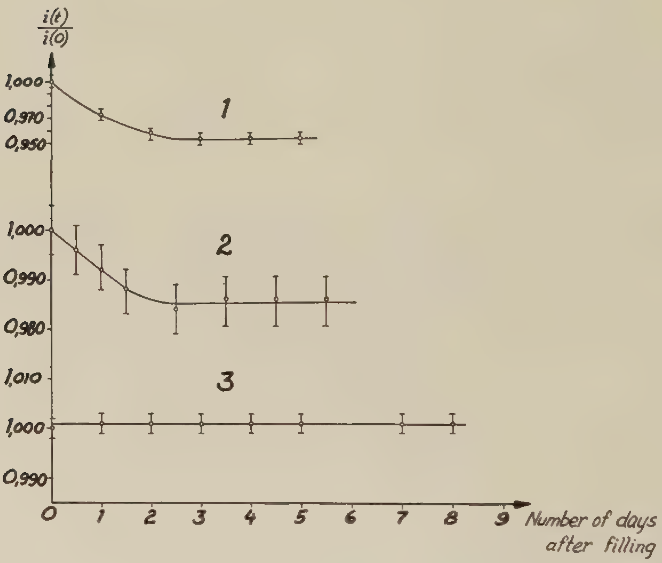

Fig. 10. Test of constancy of ion current.

saturation curve. As will be seen from Fig. 9 which gives an example of a saturation curve after a filling of C_2H_4 to a pressure of 735 mm Hg, saturation is quickly reached, whereupon the current is constant over several hundred volts. In the following experiments a voltage of 600 V was applied to the chamber. In making these investigations a small Ra-α-Be source was employed as a neutron source.

Another essential question is that of the constancy of current with time. After the first filling it was found that the current decreased by about 5 % during the first two days. Measurement of the pressure showed that this was due to the pressure of C_2H_4 in the chamber having decreased. Constancy was reached after a few days. After a new evacuation it was refilled to the same pressure as at the first filling and now it was found that constancy was reached more quickly and with a pressure decrease of 1.5 %. A third filling to a pressure corresponding to the constant value of the second filling now resulted in a constant current value (see Fig. 10). This decrease

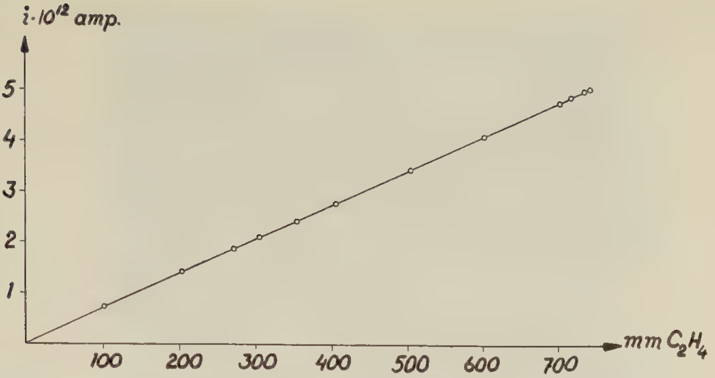

Fig. 11. Variation of ionization current as a function of the gas pressure in the chamber.

of ionization current might depend on gas absorption of the polythene walls. It is also possible that some unpolymerised material was left in the polythene from the production process, and that part of the gas was used up in new polymerisation. After the third filling, however, constancy was reached. The ionization current proved to be strictly proportional to the gas pressure as it should be if the condition of homogenity of walls and gas is fulfilled (see Fig. 11). As the various points were taken at intervals of several days, this curve indicates a high degree of reproducibility in the apparatus—an important feature for this work.

3. Measurements with the complete apparatus

a) A study of background effects

The complete target arrangement as it was used in the measurements of the angular distribution of neutrons from the $^3\mathrm{T}(d,n)^4\mathrm{He}$ reaction is shown in Fig. 12. There are many background effects which must be studied before the starting of the main measurements. Such effects may arise both in the proportional counter and the ionization chamber. Concerning the proportional counter the situation is as follows:

Since the total number of neutrons leaving the target at reasonable target currents is of the order of 5×10^7/sec, the proportional counter will be irradiated by a flux of about 10^5 n/sec. As the neutrons have an energy of 14 MeV they produce a number of nuclear reactions in the atoms of the chamber walls and the atoms of the filling gas, such as $^{16}\mathrm{O}(n,\alpha)\mathrm{C}^{13}$, $^{12}\mathrm{C}(n,n')3\mathrm{He}^4$ etc., and also undergo elastic collisions with the nuclei of the filling gas. These processes give a background of spurious pulses. The situation is complicated by the fact that a collimator with a small hole must be mounted in front of the window of the counter in order to reduce the counting rate of the α-particles (Fig. 3). This collimator has a circular aperture of a diameter of 1.36 mm, while the neutrons irradiate the whole area of the counter which is circular with a diameter of 30 mm. In order to study the background of particles other than α-particles, a bias curve was first taken of all the particles counted by the proportional counter, the homogeneous ionization chamber being used as monitor. An absorber of a thickness of 4 mg/cm² was then placed in front of the collimator so that all α-particles were absorbed, and a new bias curve was taken. The result of this experi-

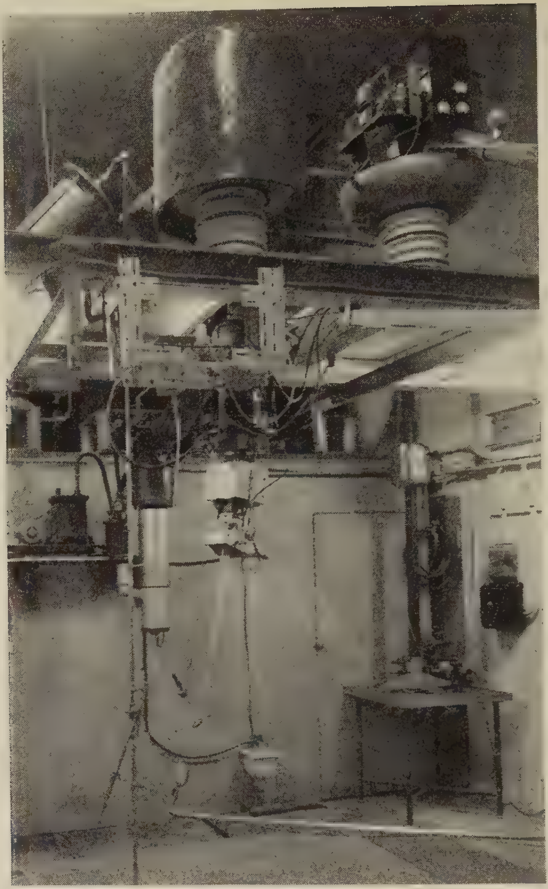

Fig. 12. The accelerator and the counter arrangement for the measurement of the angular distributions of neutrons from the ^{3}T$(d, n)^4$He reaction.

ment is given in Fig. 13. Curve I shows the integrated pulse spectrum of all the particles, curve II the spectrum of background particles, and curve III the difference between I and II, which gives the pulse spectrum of the α-particles from the ^{3}T$(d, n)^4$He reaction. In the subsequent measurements the discriminator was fixed at 25 V, which means a constant correction to the measured value of N_α (cf. eq. 2 and 4). This correction was repeatedly measured during the subsequent measurements and was found to be constant for all the accelerating voltages between 100 and 200 kV used. Still another source of error might arise in the counting of α-particles, namely the backscattering of α-particles from the target. In order to study this, a Po α source of 1 mC was placed above the target in the target tube, so as to give information about the suspected backscattering. With different positions of this source with respect to the target no pulses whatever could be detected by the α-counter, the conclusion being that no backscattering of α-particles from the target occurs.

Concerning the homogeneous ionization chamber there are mainly two sources of background effects to be expected, namely neutrons emitted from D(d, n) reactions

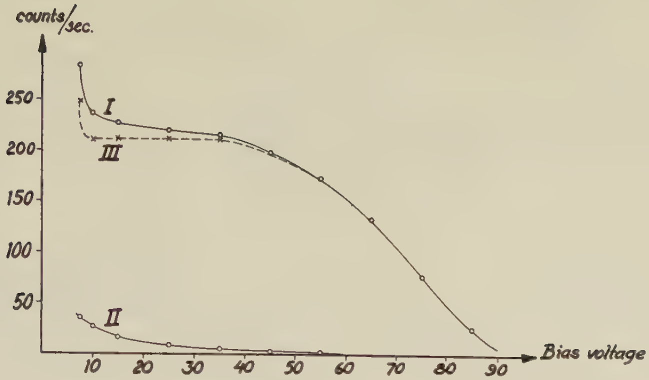

Fig. 13. Bias curves of the proportional counter. Curve I: α-particles + neutron background. Curve II: Neutron background only. Curve III: α-particle spectrum only.

occurring in the collimating system of the analyzing magnet, and γ-radiation from the upper parts of the acceleration tube. By first irradiating the blank Cu target and measuring the ionization current, then mounting the tritium-zirconium target in position, and making a new irradiation under otherwise identical conditions, a measure of the background effects was obtained. This amounted to 2–3 % of the total ionization current. The same result was obtained if, instead of dismounting the T-Zr target and irradiating the Cu target, the magnet current in the analyzing magnet was reversed. In this case no irradiation of the target was effected but the first collimator, which the ion beam had to pass, remained irradiated. This result is reasonable as the currents hitting this collimator are of the order of 200–300 μA while those hitting the target are only ~ 3 μA. It was also observed that these background currents, caused by neutrons from $D(d, n)$ reactions taking place in the collimating system of the analyzing magnet, reached a constant value after an irradiation of 20–30 min. Becuase of this, no measurements were started until the whole system had been irradiated for half an hour. After that the background current was measured between every measurement of the total current, so that a reliable correction varying between 1 and 3 % could be applied to the various values found (cf. eq. 4). That the background effects could be kept as low as 2–3 % was due to the favourable circumstance that the cross section of the $T(d, n)$ reaction is about 100 times bigger than the corresponding cross section of the $D(d, n)$ reaction at the acceleration energies concerned, and that the distance between the source of background neutrons and the homogeneous ionization chamber was never less than 100 cm, while the distance between chamber and target was never more than 20 cm.

The question of backscattering of 14 MeV neutrons from the surroundings is of the utmost importance for the subsequent measurements. The distance between the target and the floor, which was the shortest distance to scattering material, was 100 cm. Upwards and sideways all distances to the walls were greater than 150 cm. To investigate the extent of this reflection of neutrons the following experiment was performed. The ionization current of the chamber is inversely proportional to the square of the distance between the target and the effective centre of the chamber. If noticeable backscattering of the neutrons should occur, deviations from this law must arise. Measurements were therefore made of the ionization current as a function

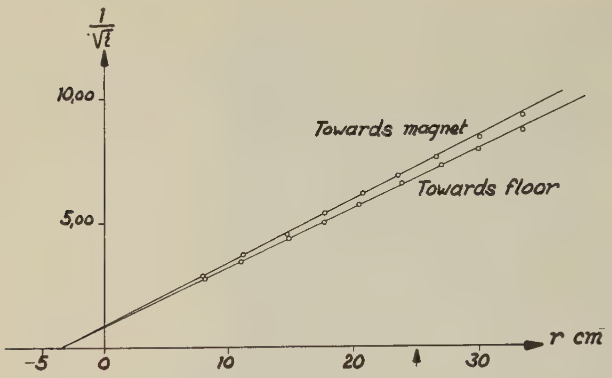

Fig. 14. Determination of the effective centre of the chamber and demonstration that the background of scattered neutrons is small.

of the distance from target in different directions. The result of two such measurements upwards and downwards is shown in Fig. 14, where $\frac{1}{\sqrt{i}}$ is given as a function of the distance r. As will be seen no deviations from the anticipated dependence were found. The intercept of both the lines with the r-axis gives the location of the effective centre of the chamber, which very nearly coincides with its geometrical centre [6]. This quantity was later determined several times, as it is of great importance to know the effective distance between the target centre and the chamber centre accurately (cf. eq. 3). This test, however, does not demonstrate with certainty that the backscattering is negligible; it only indicates that this backscattering must be small.*

b) The angular distribution of neutrons from the ^{3}T (d, n) ^{4}He reaction

As will be seen in Fig. 12 the chamber was mounted on an arm which could rotate round the target. The angles between the incoming deuteron beam and the direction of observation of neutrons could be directly read on the protractor. The distance between the chamber and the target could be arbitrarily changed along this arm. The molybdenum backing on to which the zirkonium evaporation was made, was fixed to a copper plate having a thickness of 1.5 mm in the first series of experiments. Later on it was replaced by a thinner copper plate of thickness 0.4 mm. The angular distribution of the neutrons was determined at several acceleration energies. The result of these distribution measurements on a relative scale, with points at 15° intervals measured at an acceleration energy of 175 kV, is given in Fig. 15. As will be seen the angular distribution found agrees well with the assumption of spherical symmetry in the c.m. system. (For the calculation of the theoretical distribution curve the effective deuteron energy must be known. This involves the use of results to be described in the next chapter.) The irregularities in this distribution in the angular interval 60° to 105° are due to the fact that the neutrons from the thin target must pass through the copper plate, which causes scattering and absorption. These

---

* As a rough calculation shows, the ratio of scattered to direct radiation at the chamber is of the order of $\frac{r^2}{R^2}$, where r = distance between target and chamber and R = radius of the room in which the experiment is performed, this room being supposed to be spherical of radius ≥ 150 cm with the target at its centre. As $r \approx 20$ cm, the ratio becomes ≤ 2 %, which must be considered as an upper limit.

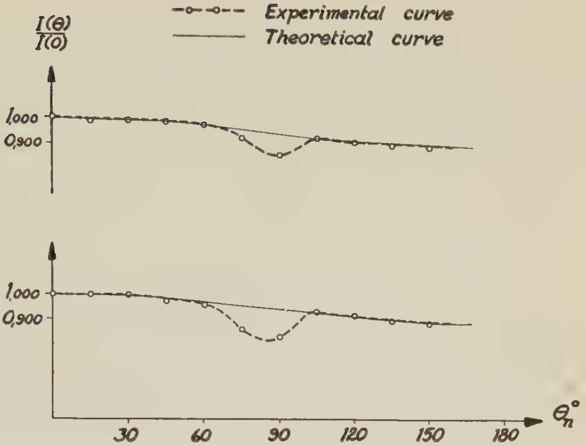

Fig. 15. Angular distribution of neutrons from the $^3T(d, n)^4He$ reaction showing the disturbing effect of the target plate. Lower curve obtained with a 1.5 mm target plate. Upper curve obtained with a 0.4 mm target plate.

effects are especially pronounced in the neighbourhood of 90°, where the neutrons had to pass through the copper plate longitudinally, corresponding to a copper absorber of 15 mm. The thick target plate was replaced by a thin one, and the perturbation decreased correspondingly. The elimination of this absorption is, in the author's opinion, impossible and it must be considered to be particularly serious in experiments utilizing the neutron beam in the 90° direction, when the flux is simultaneously determined by α-particle counting. An error in the determination of the flux of the order of 10 % might then easily arise. Likewise wrong interpretations of the measured angular distribution might easily be made if the detector used subtends a large solid angle at target. In this measurement the chamber diameter was 6 cm, and the chamber was rotated at a distance of 20 cm from the target. If the values between 60° and 105° are left out of consideration, there is good agreement between this result and the results of other workers [16, 17], who have found isotropy in the c.m. system.

c) Determination of the absolute ratio $\left(\frac{I_n}{I_\alpha}\right)_{\text{c.m.}}$

In order to determine the absolute ratio between the fluxes measured by the two methods, a knowledge of a great number of geometrical quantities and atomic constants is needed, according to eq. 4. Moreover a knowledge of the effective energy, $\bar{E}_D$, at which the deuterons react with the tritium nuclei in the target is necessary. The latter must be known in order to calculate the angles ϕ_n and ϕ_α determining $\left(\frac{I_n}{I_\alpha}\right)_{\text{theor.}}$ according to eq. (6).

Determination of the absolute ratio $\left(\frac{I_n}{I_\alpha}\right)_{\text{exp.}}$ from the experimentally determined ionization currents and counting rates follows from equation 4, which may be written:

$$\left(\frac{I_n}{I_\alpha}\right)_{\text{exp.}} = \frac{W\,\omega}{2\,e\,v\cdot N_{C_2H_4}}\cdot\frac{1}{(2\,\sigma_H\bar{E}_H+\sigma_C\bar{E}_C)}\cdot\frac{q\,r^2}{N_\alpha}, \tag{4'}$$

where $N_{C_2H_4}$ is the number of ethylene molecules per cm³ in the chamber. The expression above is purposely divided into three factors, the first of which is considered to be a constant of the apparatus, the second a function of the neutron energy, which in turn is dependent on the effective deuteron energy and the angle of observation θ_n, and the third includes the variables determined in the investigation.

Concerning the quantities determining the constant of the apparatus, there does not exist any direct measurement of the energy W eV, required to create an ion pair in ethylene for protons or ^{12}C nuclei at the energies involved here. There are, however, older [18, 6] as well as some newer determinations of W in ethylene made with Po and Pu α-particles [19, 20, 21]. The mean value of these results, if some older results [18] are excluded, is 28.0 eV/ion pair. According to BETHE [22] and GREY [4], one can expect to find a constant or slowly varying value of W at low particle energies. That W has a constant value for α-particles, in argon at least up to 9 MeV, has been shown in experiments by JESSE *et al.* [23]. In the latter work, however, it is shown that W for air decreases with increasing energy. Theoretical indications as well as certain experiments give the result that W is constant or slowly varying with energy, and as no reliable experiments give evidence to the contrary, the value of 28.0 eV/ion pair is accepted for the proton energies between 0–15 MeV. The same result is considered to be valid for the ^{12}C recoils, the maximum energy of which is about 4 MeV. In the work of JESSE *et al.* cited above, an example of ionization by heavy particles is to be found. There the recoil nucleus ^7Li gives the same mean energy per ion pair as a Po α-particle.

The solid angle was calculated from the known geometry. The distance between the target surface and the collimator was found to be 170.2 mm. The circular collimator had a diameter of 1.36 mm and the effective target surface a diameter of 25 mm. The calculation of the solid angle is given in Appendix I.

The value of $N_{C_2H_4}$, the number of molecules per cm³ of ethylene in the chamber, follows from the fact that the chamber was filled to a pressure of 735 mm Hg at a temperature of 20°C. The volume v of the chamber was 111.1 cm³, which was determined by filling the chamber with water and weighing.

The denominator of the second factor of eq. (4′) contains four variables, σ_H, σ_C $\bar{E}_H$ and $\bar{E}_C$, all of which depend upon the neutron energy. Accurate measurements of the total cross sections for 14 MeV neutrons have been made. COON *et al.* [24] have found $\sigma_H = 0.686 \pm 0.007$ barn at 14.12 MeV, POSS *et al.* [25], $\sigma_H = 0.689 \pm \pm 0.005$ barn at 14.08 MeV. Concerning σ_C many measurements have been made around 14 MeV. POSS *et al.* have found $\sigma_C = 1.279 \pm 0.004$ and the mean value of some older measurements is $\sigma_C = 1.27$ barn. On the basis of this accurate data and older measurements performed by SLEATOR [26] combined with newer ones made at Los Alamos [27], the extrapolation of σ_H and σ_C towards lower and higher energies was made. A series of values of reasonable reliability in the energy region 13–15 MeV was thus obtained. The values of the cross sections used in the calculations are given in Table 1.

For the calculation of the mean energies of the two types of recoil nuclei, ^1H and ^{12}C, a knowledge of the angular distribution of these particles in the c.m. system is required. Concerning the n-p scattering there are several results indicating spherical symmetry in the c.m. system. Thus BARSCHALL and TASCHEK [28] have found spherical symmetry within 6 % for 14 MeV neutrons. ALLRED *et al.* [29] have found the same result within 4–5 %. For the scattering of neutrons by ^{12}C nuclei fewer results exist.

The results of COON and DAVIS [30], who have studied the elastic scattering of 14 MeV neutrons by ^{12}C in the angular interval 6°–50° indicate a strong forward maximum in the scattering. By an estimation of the cross sections they found that only

Table 1.

Neutron energy E_nMeV	$\sigma_H(E_n)$ barn	$\sigma_C(E_n)$ barn
13.0	0.732	1.315
13.5	0.710	1.295
14.0	0.688	1.279
14.5	0.660	1.262
15.0	0.641	1.255

20 % of the elastic scattering occurs through angles larger than 50°. BALDINGER *et al.* [31] have made measurements at neutron energies of 3–4 MeV which indicate a strong anisotropy. The same is shown by experiments made by REMUND and RICAMO [32] with 3.7 MeV neutrons. There does not exist, however, any data on which an accurate calculation may be based for 14 MeV neutrons, hence the author has assumed spherical symmetry in the c.m. system for the elastic scattering of neutrons by ^{12}C nuclei. Besides the elastic scattering processes there are also some inelastic ones. However, it will later be shown with the aid of experimental data, that the final result is almost independent of these deviations of the scattering from spherical symmetry. It might seem that all these facts should give a great uncertainty to the measurement of neutron fluxes with the homogeneous ionization chamber. The influence of the uncertainty in the mean energy of the ^{12}C recoils is, however, relatively small, as only $^1/_4$ of the ion current is caused by ^{12}C recoils and $^3/_4$ of the ionization by proton recoils. This follows from the cross sections and the masses of the recoil nuclei. In calculating the factors $\bar{E}_H$ and $\bar{E}_C$ relativistic effects must be taken into consideration as a result of the high neutron energy. The calculation of $\bar{E}_H$ and $\bar{E}_C$ is given in Appendix II. Fig. 16 gives the factor $2\sigma_H \bar{E}_H + \sigma_C \bar{E}_C$ as a function of the neutron energy. It is necessary to calculate the appropriate neutron energy before $\left(\frac{I_n}{I_\alpha}\right)_{\text{exp.}}$ can be calculated from the measurements of the angular distribution. The neutron energy in turn is dependent on the mean energy at which the deuterons react with the tritium nuclei in the zirconium target. According to the manufacturer, Atomic Energy Research Establishment, Harwell, England, the thickness of the target evaporation is 200 μg/cm^2. The energy loss of protons of energies between 50 and 600 keV for copper (atomic number 29) and silver (atomic number 47) has been studied by WARSHAW [33]. For deuterons within the present energy interval, 100–200 keV, these loss esare almost constant and ~ 225 MeV per g/cm^2 for copper and ~ 140 MeV per g/cm^2 for silver. For zirconium with atomic number 40, which is the slowing down medium in the target, a constant energy loss of ~ 180 MeV per g/cm^2 is assumed. As a simple calculation shows, the energy loss of the deuterons calculated from this assumption is 36 keV. The average energy at which the deuterons react with the target nuclei then follows from

$$\bar{E}_D = \frac{\int_{E-36}^{E} \sigma_{T,D}(E)\, E\, dE}{\int_{E-36}^{E} \sigma_{T,D}(E)\, dE}, \tag{9}$$

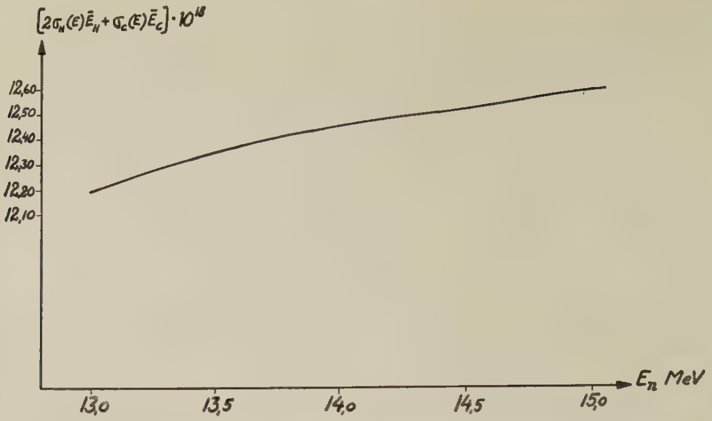

Fig. 16. Calculated energy dependence of the ionization chamber within the energy limits appearing in the experiment.

where $\sigma_{T,D}$ = the reaction cross section for the T-D reaction, and E = the acceleration energy in kV.

A calculation of $\bar{E}_D$ has been made with values for $\sigma_{T,D}$ taken from measurements of CONNER *et al.* [8]. For $E = 175$ kV, which was the acceleration energy used during the measurement of the angular distribution, $\bar{E}_D = 156$ keV. The neutron energies are then uniquely determined by the angle of observation, θ_n, and $\bar{E}_D$.

With the two first factors in eq. (4′) determined, it is now possible to calculate the absolute ratio $\left(\frac{I_n}{I_\alpha}\right)_{\text{exp.}}$ from the experimentally determined values of q, N_α and r for every angle θ_n chosen. To transform this ratio to the c.m. system a division by the ratio $\left(\frac{I_n}{I_\alpha}\right)_{\text{theor.}}$ should be made, the latter ratio being dependent on the angles ϕ_n and ϕ_α in the c.m. system. ϕ_n and ϕ_α are functions of $\bar{E}_D$ and θ_n, $\bar{E}_D$ being taken as 156 keV. Excluding the angles between 60–105° the results obtained from the measurements of the angular distribution described above are given in Table 2.

As will be seen in columns 5 and 6 of this table the ratio $\left(\frac{I_n}{I_\alpha}\right)_{\text{c.m.}}$ is very close to 1.03. The theoretical value, assuming the angular distribution to be spherically symmetrical in the c.m. system and the methods of measurement free from errors, is exactly 1, i.e. experimentally there exists a disagreement of 3 % between the absolute flux measurements. A further conclusion from these measurements is that the angular distribution of the neutrons (compare the discussion of sources of error below) is spherically symmetrical to within ± 2 % at a deuteron energy of 175 keV.

In order to get another series of values of the ratio $\left(\frac{I_n}{I_\alpha}\right)_{\text{c.m.}}$ and, if possible, to estimate the importance of the assumption of a target thickness of 200 μg/cm², a new comparative measurement was made in such a manner that the angle θ_n and the distance r were kept constant and only the acceleration energy E was varied. As it is conceivable that the distribution of tritium in the thin target film is changed by the long irradiation, a position was chosen for the homogeneous ionization chamber,

Table 2.

Neutron angle θ_n	$\left(\frac{I_n}{I_\alpha}\right)_{\text{theor.}}$	$\left(\frac{I_n}{I_\alpha}\right)_{\text{exp.}}$		$\left(\frac{I_n}{I_\alpha}\right)_{\text{c.m.}}$	
		1.5 mm target plate	0.4 mm target plate	1.5 mm target plate	0.4 mm target plate
0°	1.268	1.322	1.296	1.042	1.022
15°	1.267	1.319	1.281	1.041	1.011
30°	1.258	1.306	1.297	1.038	1.031
45°	1.247	1.283	1.287	1.029	1.032
60°	1.232	1.262	1.271	1.024	1.032
105°	1.177	1.227	1.203	1.042	1.022
120°	1.160	1.207	1.180	1.041	1.017
135°	1.145	1.174	1.168	1.025	1.020
150°	1.135	1.162	1.156	1.024	1.019
			Mean values	1.034	1.023

such that its end surface was parallel to the target surface, i.e. $\theta_n = 45°$ (see Figs. 2 and 12). At every other angle such a change in the distribution of tritium must give larger systematic errors in the r value, r being the distance between the effective target centre and the chamber centre. With this distance well defined in the manner described, q and N_α with their corrections for backgrounds were measured at acceleration voltages between 100 and 200 kV. With the new values found, the ratios $\left(\frac{I_n}{I_\alpha}\right)_{\text{c.m.}}$ were calculated for three different assumed values of the target thickness. Firstly the target was assumed to be thin, i.e. $\bar{E}_{\text{D}} = E$ according to earlier notations. Secondly the given value of 200 μg/cm^2 was used for the target thickness and finally the target was assumed to be thick. The calculations of the mean energies $\bar{E}_{\text{D}}$ according to the last two assumptions were made as described earlier. The results of this determination of $\left(\frac{I_n}{I_\alpha}\right)_{\text{c.m.}}$ for the three cases are given in Table 3. As will be seen, the two assumptions of a thin and a semi-thin target gives for $\left(\frac{I_n}{I_\alpha}\right)_{\text{c.m.}}$ values, which, within experimental limits of error, are constant. On the other hand those values, calculated under the assumption of a thick target, show a systematic increase which indicates that the transformation of the experimental values to the c.m. system had been made with an incorrect estimate of the mean energy of the deuterons in the target. The true target thickness may also be estimated from other data previously obtained, namely the yield. The yield of this target was about 5×10^7 n/sec at a target current of 2 μA and at 200 kV. According to the results of other investigators the yield of a thick tritium-zirconium target is of the order 10^8 n/microcoulomb at 200 kV, while the yield of a thin target is considerably lower. The value found here for the yield favours the assumption of a semi-thin target. The value of 200 μg/cm^2 is therefore accepted as the most probable. The error in the transformation factor $\left(\frac{I_n}{I_\alpha}\right)_{\text{theor.}}$ caused by the uncertainty in the target thickness

Table 3.

Acc. energy E kV	Thin target				200 μg/cm²				Thick target			
	$\bar{E}_D$ keV	$\left(\frac{I_n}{I_\alpha}\right)_{\text{theor.}}$	$\left(\frac{I_n}{I_\alpha}\right)_{\text{exp.}}$	$\left(\frac{I_n}{I_\alpha}\right)_{\text{c.m.}}$	$\bar{E}_D$ keV	$\left(\frac{I_n}{I_\alpha}\right)_{\text{theor.}}$	$\left(\frac{I_n}{I_\alpha}\right)_{\text{exp.}}$	$\left(\frac{I_n}{I_\alpha}\right)_{\text{c.m.}}$	$\bar{E}_D$ keV	$\left(\frac{I_n}{I_\alpha}\right)_{\text{theor.}}$	$\left(\frac{I_n}{I_\alpha}\right)_{\text{exp.}}$	$\left(\frac{I_n}{I_\alpha}\right)$
100	100	1.191	1.219	1.024	85	1.175	1.219	1.037	79	1.168	1.220	1.04
112.5	112.5	1.205	1.230	1.021	98	1.190	1.231	1.034	88	1.179	1.231	1.04
125	125	1.217	1.244	1.022	107	1.200	1.244	1.038	97	1.187	1.245	1.04
137.5	137.5	1.230	1.265	1.029	119	1.211	1.266	1.045	101	1.193	1.267	1.06
150	150	1.241	1.268	1.021	131	1.223	1.269	1.038	106	1.198	1.271	1.05
162.5	162.5	1.253	1.292	1.031	143	1.234	1.293	1.048	113	1.205	1.294	1.07
175	175	1.264	1.301	1.029	156	1.247	1.302	1.044	118	1.210	1.304	1.07
187.5	187.5	1.276	1.298	1.017	169	1.259	1.299	1.032	123	1.216	1.301	1.07
200	200	1.286	1.305	1.015	181	1.269	1.305	1.028	127	1.219	1.308	1.07
		Mean value		1.023		Mean value		1.038				

will not be great, as will be shown later. As may be seen in Table 3 the mean value of the different comparative measurements falls in the neighbourhood of 1.04, agreeing with earlier results within experimental limits of error. The scatter in the values is probably mainly due to varying background effects.

4. Experimental accuracy and final results

The uncertainty in the determination of $\left(\frac{I_n}{I_\alpha}\right)_{\text{c.m.}}$ depends upon a great number of factors. Factors not studied in this experiment are the values of the cross sections σ_H and σ_C and the value of the energy $W_{C_2H_4}$ required to form an ion pair in ethylene. Factors directly determined in this experiment are the value of the capacity C of the condensor, the voltage V applied to the potentiometer, the effective distance r between target and chamber, the sensitive volume of the chamber, the pressure and temperature of the filling gas C_2H_4 in the chamber, the counting rate N_α of α-particles with its corrections, the effective diameter R of the collimator in front of the α-counter, and the distance z between the target and the collimator. In the region between these two groups there is the semi-empirical determination of the mean energies $\bar{E}_H$ and $\bar{E}_C$ of the recoil nuclei. Finally an uncertainty in the calculated transformation factor $\left(\frac{I_n}{I_\alpha}\right)_{\text{theor.}}$ arises as a result of the uncertainty in the effective deuteron energy.

The total cross sections σ_H and σ_C seem to be known to an accuracy of $\pm 1\,\%$ at a neutron energy of 14 MeV according to the investigations of COON *et al.* and POSS *et al.* cited above. For other neutron energies between 13 and 15 MeV it seems that σ_H is determined rather more accurately than σ_C. With the values at 14 MeV as a guide, supported by other measurements, the error in σ_H is assumed to be limited to $\pm 2\,\%$ and the error in σ_C to $\pm 3\,\%$.

For α-particle energies of about 5 MeV $W_{C_2H_4}$ seems to be accurately determined by the investigations of JESSE *et al.* who have found the value 28.0 eV per ion pair, BORTNER and HURST, who found 28.0, and DAINTY, who found 28.2 eV/ion pair. The older work of BRETSCHER gave 27.8 eV/ion pair. At the high proton energies in question here, it is possible that the mean value of $W_{C_2H_4}$ should be somewhat lower, as W might be expected to decrease with increasing energy. In the work by BETHE cited above, the value of W for Po α-particles is compared with W for protons of an energy of 340 MeV. The result of this comparison is that W varies very slowly with energy for the gases investigated. On the other hand the energies of the ^{12}C recoils correspond to such low velocities, that an increase of W above the measured value 28 eV/ion pair should be theoretically expected. The results of JESSE *et al.* do not throw very much light on the problem as the only conclusion that might be drawn from their measurements is that W_{argon} is independent of the energy of the α-particles up to 9 MeV but that W_{air} seems to vary with energy. Considering that a value lower than 28.0 eV per ion pair should be theoretically expected for the proton recoils and a value bigger than 28.0 eV ion pair would be conceivable for the ^{12}C recoils, the net effect would be a tendency to eliminate the energy dependence. For that reason, and considering the good agreement between the results cited above, the value 28.0 eV/ion pair (± 2 %) is adopted for $W_{C_2H_4}$.

Of the quantities determined in this experiment the capacity C of the condensor was measured by a comparison with a standard condensor in a bridge circuit, the result being 98 ± 1 pF.[1] The voltage V across the potentiometer was measured to an accuracy of ± 0.2 %. The instrument used for this measurement was calibrated against Weston Standard cells. The effective distance r between the centres of the target and the chamber was determined by measuring and calculating with the method of least squares the position of the centre of the chamber as discussed on p. 308 above. The possible error in r is estimated to be 0.3 % (e.g. 180.0 ± 0.5 mm). The volume v of the chamber was determined by filling with water and weighing. A very small uncertainty exists concerning the difference between the geometrical volume and the effective sensitive volume depending on the construction; the value of 111.1 ± 0.2 cm^3 is found for v. Concerning the pressure and temperature of the filling gas, the uncertainty is of the order of ± 0.1 %. The determination of the solid angle within which the α-particles were counted, depends upon three quantities of which the distance z between the target and the circular collimator was 170.1 ± 0.1 mm; the diameter of the target, which only enters in a small correction term (see Appendix I), was 25 mm; and the diameter $2\,R$ of the circular collimator, which was measured under a microscope having an ocular micrometer, was 1.36 ± 0.01 mm. Generally the measuring times during the experiment were of the order of 2–3 minutes, which gave a statistical accuracy in N_α of about 0.7 %. The correction for background effects, which varied somewhat with the acceleration energy, increases the uncertainty in N_α by about 0.5 %, the total uncertainty in N_α being ± 1.2 %.

The uncertainty in the mean energies $\bar{E}_H$ and $\bar{E}_C$ of the two types of recoil nuclei is dependent upon some different phenomena. A source of uncertainty for both of them is the lack of knowledge of the neutron energy E_n. By the laws of conservation of energy and momentum this is connected with the effective deuteron energy and the Q value of the reaction, the resulting uncertainty ΔE_n being proportional to the uncertainties $\Delta \bar{E}_D$ in $\bar{E}_D$ and ΔQ in the Q value. If $|\Delta \bar{E}_D|$ is assumed to be 10 keV, which corresponds to an uncertainty of 30 % in the calculation of the energy losses in the target and $|\Delta Q| = 20$ keV, the latter resulting from the given mass values

---

[1] These measurements were made by *Statens Provningsanstalt.*

[34], the mean value $|\Delta E_n|$ becomes ≤ 50 keV, which corresponds to an uncertainty of $< 0.5\%$ in E_n and consequently in $\bar{E}_{\text{H}}$ and $\bar{E}_{\text{C}}$. The current in the ionization chamber might be imagined to be composed of two parts: current caused by proton recoils determined by $\bar{E}_{\text{H}}$ and σ_{H}, and current caused by carbon recoils determined by $\bar{E}_{\text{C}}$ and σ_{C}. The calculation of these two parts of the current is simple if only elastic scattering occurs, and if the angular distribution of the scattered particles in the c.m. system is known. Concerning the proton recoils, these conditions are fulfilled, as discussed earlier. For the recoils of ^{12}C the situation is different. Lack of data prevents a reliable calculation of $\bar{E}_{\text{C}}$, but the following example might serve as some guide. The total cross section of ^{12}C at 14 MeV is 1.279 barn. According to measurements of GRAVES and ROSEN [35] with 14 MeV neutrons the mean cross section for all inelastic scattering from 12 down to 0.5 MeV is 0.52 barn, the mean energy of all inelastic scattered neutrons being about 7 MeV. An important reaction in ^{12}C contributing to a changed value of the ion current is $^{12}\text{C}(n,n')3\text{He}^4$, the cross section of which is ~ 0.16 barn at 14 MeV, the mean energies of the three α-particles together being about 5.5 MeV according to measurements of GREEN and GIBSON [36]. The cross section of all other inelastic collisions—$^{12}\text{C}(n,n')3\text{He}^4$ excluded—is consequently 0.36 barn. By the laws of momentum and energy this gives an energy of ~ 0.6 MeV for the ^{12}C recoils, as the mean energy of the scattered neutrons was 7 MeV. If now $\sigma_{\text{C}}\bar{E}_{\text{C}}$ is assumed to be composed of three parts caused by elastic scattering, the reaction $^{12}\text{C}(n,n')3\text{He}^4$ and remaining inelastic scattering, the result is that $\sum_i \sigma_{i\text{C}}\bar{E}_{i\text{C}}$ takes approximately the value 2.65×10^{-18}. If, on the other hand, the elastic scattering is assumed to be the only process occurring, and if the angular distribution is assumed to be isotropic in the c.m. system, $\sigma_{\text{C}}\bar{E}_{\text{C}}$ takes the value 2.61×10^{-18}, the difference being 1.5%. Furthermore, since only $\sim 1/4$ of the ion current is caused by ionisation from ^{12}C recoild, the relative weight of the uncertainty decreases to about 0.5%. However, in order to take these uncertainties and the uncertainty in the assumption of elastic scattering into consideration, the uncertainty in $\bar{E}_{\text{C}}$ is assumed to increase to $\pm 10\%$, and the uncertainty in $\bar{E}_{\text{H}}$ remains, as discussed earlier, $\pm 0.5\%$. The uncertainty in $\bar{E}_{\text{C}}$ might also include the possible error in the current measurement that might arise due to the chamber wall being too thick compared to the range of the most energetic ^{12}C recoils, according to the principle of the homogeneous ionization chamber. This condition is, however, impossible to fulfill, as the range of the proton recoils must determine the wall thickness.

For the transformation of $\left(\frac{I_n}{I_\alpha}\right)_{\text{exp.}}$ to the c.m. system the theoretical ratio $\left(\frac{I_n}{I_n}\right)_{\text{theor.}}$ must be calculated. This ratio is a function of the Q value of the reaction and of the mean energy $\bar{E}_{\text{D}}$ of the deuterons in the target. A straightforward calculation of the uncertainty in $\left(\frac{I_n}{I_\alpha}\right)_{\text{theor.}}$ gives a relative error of approximately $\pm 0.6\,|\Delta\bar{E}_{\text{D}}|$, where $\bar{E}_{\text{D}}$ is expressed in MeV. As $|\Delta\bar{E}_{\text{D}}|$ is assumed to be 0.010 MeV, the result is that the uncertainty in $\left(\frac{I_n}{I_\alpha}\right)_{\text{theor.}}$ is $\pm 0.6\%$.

All of the above sources of error and their respective contributions to the uncertainty in $\left(\frac{I_n}{I_\alpha}\right)_{\text{c.m.}}$ are set out in Table 4.

Table 4.

Source of error		Relative contribution Δ_i to the error in $\left(\frac{I_n}{I_\alpha}\right)_{\text{c.m.}}$ %
Capacity of condensor	(C)	1.0
Potentiometer voltage	(V)	0.2
Distance between target and chamber	(r)	0.6
Sensitive volume of the chamber	(v)	0.2
Gas pressure	(p)	0.1
Gas temperature	(T)	0.1
Distance between target and collimator	(z)	0.1
Diameter of collimator	$(2R)$	1.5
Corrected counting rate	(N_α)	1.2
Mean energy of proton recoils	$(\bar{E}_{\mathrm{H}})$	0.4
Mean energy of C^{12} recoils	$(\bar{E}_{\mathrm{C}})$	2.1
Total cross section	(σ_{H})	1.6
” ” ”	(σ_{C})	0.6
Energy to create an ion pair in $\mathrm{C_2H_4}$	(W)	2.0
Transformation factor $\left(\frac{I_n}{I_\alpha}\right)_{\text{theor.}}$		0.6

If the final uncertainty is calculated from $\sqrt{\sum \Delta_i^2}$, the resulting relative mean error is 4.1 %. The mean value of the ratio $\left(\frac{I_n}{I_\alpha}\right)_{\text{c.m.}}$ between the fluxes measured by the two methods determined from the three series of measurements described above is thus

$$\frac{\text{Neutron flux determined by homogeneous ionization chamber}}{\text{Neutron flux determined by counting of associated particles}} = 1.03 \pm 0.04.$$

An examination of the distribution of the sources of error in the two methods of flux measurement indicates that the associated particle method allows an absolute flux determination to a precision of about 2 %. The use of this method is also preferable whenever possible, for the result is independent of any natural constants. In the application of counting associated particles described here, a knowledge of the differential cross section of the reaction is necessary if the flux is to be measured within intervals of solid angle other than that corresponding to the α-counter. The method with the homogeneous ionization chamber or the recoil particle method cannot, in general, give an accuracy comparable to that possible with an associated particle method, as the result is dependent on a great number of variables such as cross sections, background effects which are difficult to measure, the energy to create an ion pair, etc. The measurements made by ALLEN *et al.* [12], who compared four different recoil particle methods, give a good example. The maximum deviation between the different methods was found to be 6 %, which is indicative of the difficulties that the direct absolute measurement of fast neutron fluxes presents, even when monoenergetic neutrons are used and there is no γ-ray background.

CHAPTER II

The use of ^{3}T (d,n) ^{4}He reaction for the determination of the yield of a Ra-α-Be source

1. Principle of the method

As was mentioned in the Introduction, another absolute measurement of the flux from the T (d,n) reaction may easily be made if the target is surrounded by a suitable moderator, and the thermal neutron density integrated. This means an absolute measurement of the flux by some of the existing slowing down techniques [37]. At the same time as this measurement is made, a flux determination may also be carried out by the associated particle method described above, making possible a comparison between flux measurements at thermal neutron energies and at 14 MeV. All methods including the integration of the thermal flux with radioactive detectors such as foils, $MnSO_4$ bath etc., suffer from the weakness that corrections for the time variations in the neutron flux from the target must be applied. Integration with some type of counter is to be preferred as this makes possible a direct comparison between counting rates. Since, however, the neutron source—T (d,n) reaction—is anisotropic in the lab. system, the measurements ought to be made with long counters, so that the integration is automatically made in one direction in the moderator. The flux being cylindrically symmetrical around the incoming deuteron beam, it will be sufficient to integrate the density in the radial direction, if the counters automatically integrate in the axial direction. As great difficulties are met with in the construction of very long thin neutron detectors intended to count with a 100 % efficiency nuclear reactions of some kind, e.g. the $B^{10}(n,\alpha)Li^7$ reaction, some counters are more easily calibrated using α-particle counting. With these calibrated counters, the flux from the neutron source, e.g. a Ra-α-Be source, is integrated, the yield of the source being determined in advance by some slowing down technique. By comparing the integrated neutron density from the T (d,n) reaction with that from the Ra-Be source, an independent value of the yield of this source is thus obtained by counting associated particles. This value is finally compared with other direct determinations of the yield of the Ra-Be source, the result of such an experiment being twofold: (1) A new value of the yield of the Ra-Be source is obtained; (2) A comparison between the associated particle method and the slowing down method for measuring neutron fluxes is made.

In practice, the measurements are made in such a manner that the neutrons leaving the target are slowed down in a large hydrogeneous medium, the thermal neutrons then being counted in long BF_3 counters placed at different distances from the target. The associated particles are simultaneously counted in the proportional counter described in Chapter I. As the angular distribution of fast neutrons from the T (d,n) reaction is isotropic in the c.m. system, the total number of neutrons, Q_n, leaving this source is

$$Q_n = 4\pi (I_{\text{c.m.}})_n = 4\pi (I_{\text{c.m.}})_\alpha = 4\pi I(\theta_\alpha)_{\text{lab.}} \frac{\sin^2\theta_\alpha \cos(\phi_\alpha - \theta_\alpha)}{\sin^2\phi_\alpha}\, n/\text{sec} \qquad (10)$$

where $(I_{\mathrm{c.m.}})_n$, $(I_{\mathrm{c.m.}})_\alpha$ and $I(\theta_\alpha)_{\mathrm{lab.}}$ are the intensities of neutrons and α-particles per unit solid angle in the c.m. and lab. systems, the angles θ_α and ϕ_α being defined in the previous chapter. Since

$$I(\theta_\alpha)_{\mathrm{lab.}} = \frac{n_\alpha}{\omega_\alpha}, \tag{11}$$

where n_α is the intensity of α-particles counted within the solid angle ω_α, the intensity of the neutrons leaving this source is

$$Q_n = 4\pi \frac{n_\alpha}{\omega_\alpha} \frac{\sin^2\theta_\alpha \cos(\phi_\alpha - \theta_\alpha)}{\sin^2\phi_\alpha} \quad n/\mathrm{sec.} \tag{12}$$

If $n(r)$ is the number of boron disintegrations in the BF_3 counter per counted α-particle at a distance r from the target, it follows that

$$\frac{4\pi}{\omega_\alpha} \frac{\sin^2\theta_\alpha \cos(\phi_\alpha - \theta_\alpha)}{\sin^2\phi_\alpha} = \mathrm{const.} \int_0^\infty n(r)\, r\, dr \quad n/\alpha\text{-particle}, \tag{13}$$

where the integration is performed from the target centre up to a distance from the target where the neutron density is negligible. The integration in the direction at right angles to the r direction is automatically made by the long counter. If the tritium target is now replaced by the Ra-Be source and the neutron density thus created is integrated with the same counter the yield will be

$$Q_{\mathrm{RaBe}} = \mathrm{const.} \int_0^\infty n_1(r)\, r\, dr \quad n/\mathrm{sec.}, \tag{14}$$

or if the value of the constant following from eq. (13) is used, one obtains

$$Q_{\mathrm{RaBe}} = \frac{4\pi}{\omega_\alpha} \frac{\sin^2\theta_\alpha \cos(\phi_\alpha - \theta_\alpha)}{\sin^2\phi_\alpha} \frac{S_{\mathrm{RaBe}}}{S_{\mathrm{T},d}} \quad n/\mathrm{sec}, \tag{15}$$

where S_{RaBe} and $S_{\mathrm{T},d}$ are the values of the density integrals for the Ra-Be source and the $\mathrm{T}(d,n)$ source respectively. This method for the determination of the yield of a Ra-Be source is thus independent of any natural constant such as absorption cross sections etc. The only thing that must be known is the relative angular distribution of α-particles from the $\mathrm{T}(d,n)$ reaction, which has previously been shown to be spherically symmetrical in the c.m. system.

2. Experimental equipment

For the experimental determination of the yield of a Ra-Be source with the associated particle method, the same acceleration system, target system and proportional counter described in the previous chapter were used. Because of the high primary neutron energy it is necessary to choose a hydrogeneous type of moderator round the target. The slowing down length of 14 MeV neutrons in water is of the order of magnitude 18 cm [38]. As this length, in connection with the diffusion length, determines the geometrical dimensions of the moderator, a hydrogeneous medium must be chosen, if the leakage of thermal neutrons across the boundary is to be kept small, e.g. $\leq \frac{1}{1000}$ of the total number of neutrons leaving the target. The diffusion length of thermal neutrons in water is 2.85 cm, while the migration length of 14 MeV neutrons in water is of the order of 18–19 cm. An aluminum tank of diameter and height 2 m was placed under the acceleration tube, so that the target was at the centre of the tank. This meant that the shortest distance from the target to the walls of the tank was 1 m, i.e. 5–6 migration lengths for water, giving a completely negligible leakage. In order to measure the distribution of thermal neutrons in the moderator, two BF_3 proportional counters were used. These were made of brass tubes with a length of 2 m and a diameter of 15 mm and filled with BF_3 to a pressure of about 500 mm. Provided that the sensitivity of these long counters is constant along their total length, they integrate the neutron density correctly. This was investigated by moving a paraffin block containing a Ra-Be neutron source along the total length of the counters, the result being that no variations in counting rate could be found within the statistical limits of error which were $\pm 0.5\,\%$. The BF_3 counters were supported by two thin metal strips, one in the bottom of the tank and one at the upper edge. The BF_3 counters could be moved on each side of the target in such a way that the distance between the target and the counter was changed in steps of 2 cm. As the upper surface of the moderator reached a level only 20 cm from the collimating system of the analyzing magnet, the influence of stray neutrons from $D(d,n)$ targets in these surroundings became disturbing. In order to decrease the effect of these stray neutrons, the collimating system and the upper parts of the analyzing magnet were surrounded by Cd covered paraffin. In spite of this, every value of the counting rate must be corrected for the background of scattered thermal neutrons. The same principle was applied to the integration of neutron density with the BF_3 counters as in the measurements of the angular distributions with the homogeneous ionization chamber described in the previous chapter: Firstly the total number of pulses caused by neutrons from the $T(d,n)$ and $D(d,n)$ sources were counted during a given interval of time, secondly the magnet current was reversed and only pulses from $D(d,n)$ sources were counted. The background determined in this way varied with the distance between target and counter, its maximum value being about 10 % of the total counting rate for the largest distances used, i.e. at about 60 cm from the target. As the proportional counter in this case was immersed in the moderator, the background in this counter could be expected to be changed somewhat in comparison with its value when used in free air. Repeated determinations of these backgrounds, measured with and without absorber in front of the circular collimator, gave a correction of 4.1 % at the same discriminator level as was used earlier. As might be expected this is slightly higher than the value obtained with the counter in free air.

In order to integrate the neutron density from a Ra-Be source, the source was fixed in a thin aluminum holder in contact with the target and supported by wires from the bottom and top of the tank. Since the target system could be expected to absorb neutrons and the absorption might be different for the two widely differing neutron spectra represented by the $T(d,n)$ source and the Ra-Be source, this absorption was studied by placing the Ra-Be source first in contact with the target and then halfway between the target and the bottom of the tank. In the latter case the absorption of the target system was negligible as the distance between the source and the target was about 50 cm. The Ra-Be source used during this investigation was a 250 mg source previously calibrated by several different methods.

3. Measurements

a) Water as moderator

In the first experiment to determine the yield of the Ra-Be source, water was used as moderator. With a water depth of 195 cm in the tank, the distribution of thermal neutrons from the T(d, n) reaction was measured at an acceleration energy of 125 keV for the deuterons. The BF_3 counters and α-counters were started synchronously and the intensities so chosen, that a statistical accuracy better than 0.5 % was reached relatively quickly. A typical result of the measurement is given in Fig. 17, where the neutron distributions from the T(d, n) reaction and from the Ra-Be source are given. Because of the construction of the target and for intensity reasons the integration could not be performed at points closer to the target than 4 cm or at distances from the target greater than ~ 60 cm. This means that an extrapolation of the distribution curves must be made both in the region near the target or the source and in the region very far from the source, as the ratio between the areas under these curves determines the yield of the Ra-Be source according to eq. (15). In Table 5 these areas are given for three cases studied, namely for the T(d, n) source and for the Ra-Be source placed at the target and halfway between the target and the bottom of the tank. The extrapolations of the curves have been made as described in a previous article [37]. As will be seen in this table and in Table 6, the absorption of thermal neutrons in the target system is small, ~ 1 %. This might seem peculiar as the target tube was made of 2 mm pyrex glass, which strongly absorbs thermal neutrons, but the explanation is that practically the same amount of absorbing material in the form of water was displaced by the target tube as was contained in its walls. This means that no correction for the absorption of neutrons by the target tube will be applied in this and following calculations of the measured neutron yields, the value of S_{RaBe}

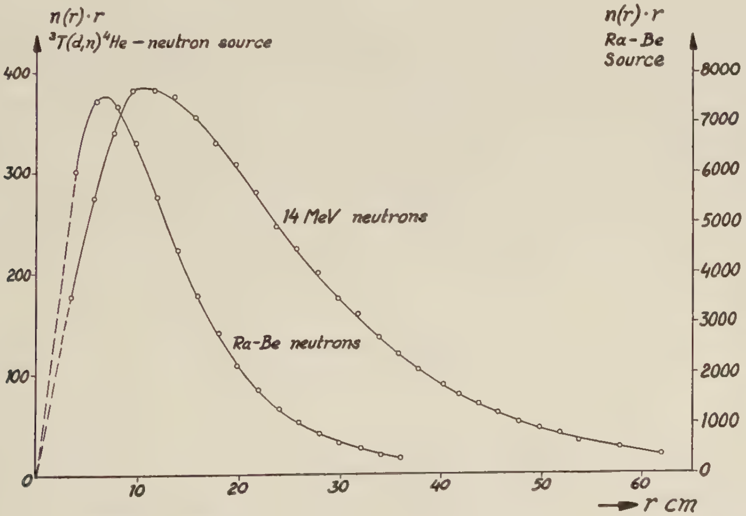

Fig. 17. Neutron density distributions from the Ra-Be source and T(d, n) source measured with long BF_3 counters in water.

					Areas S under ne
Neutron source	BF_3 counter (number)	Region (calculated)	Area	% of total area	Region (measu
^{3}T (d,n) ^{4}He	1 2	$0 \le r \le 3.62$ $0 \le r \le 4.18$	320 940	3.0 4.0	$3.62 \le r \le 61.$ $4.18 \le r \le 62.$
250 mC Ra-Be (in contact with target)	1 2	$0 \le r \le 3.87$ $0 \le r \le 3.88$	11670 25220	10.3 10.2	$3.87 \le r \le 36.$ $3.88 \le r \le 36.$
250 mC Ra-Be (40 cm from target)	1 2	$0 \le r \le 3.77$ $0 \le r \le 3.84$	11790 26820	10.4 10.6	$3.77 \le r \le 42.$ $3.84 \le r \le 41.$

corresponding to the source in contact with target being used without corrections. Justification for this lies in the small differences between the values in column 3 of Table 6 and the fact that only ratios between areas are of interest. The calculation of the final absolute value of the yield of the source from eq. (15) requires a knowledge of the effective neutron energy $\bar{E}_D$, as the transformation factor $\dfrac{\sin^2\theta_\alpha \cos(\phi_\alpha - \theta_\alpha)}{\sin^2\phi_\alpha}$ is dependent on the angle ϕ_α in the c.m. system. $\bar{E}_D$ at the acceleration energy of 125 kV was calculated as previously described in Chapter I, giving $\bar{E}_D = 107$ keV. With these assumptions and with the values found for the ratio of the areas S_{RaBe} and $S_{T,\,d}$, the values of the source strength given in the last column of Table 6 were obtained. These values are corrected for the self-absorption of the source. This correction was found by both measurement and calculation from the composition of the source to be $+1\,\%$. If these values of the yield are compared with values determined by other methods, which give a mean value of $Q_{RaBe} = 2.64 \times 10^6\ n/\mathrm{sec}$ (see the following discussion of the results), one finds a discrepancy of more than 20 %. The main reason for this deviation must be the widely differing spectra presented by the two neutron sources: the $T(d,n)$ source with a primary neutron energy of ~ 14 MeV, and the Ra-Be source with a broad energy spectrum ranging from 0–13 MeV with a mean energy of ~ 5 MeV. With water as moderator, it might be assumed that the absorption of fast neutrons in oxygen causes a neutron loss during the slowing down phase, which is considerable at such a high primary energy as 14 MeV, but of less importance for the spectrum of the Ra-Be neutrons. At least three reactions in oxygen might give considerable contributions to this absorption, namely

$$
\begin{aligned}
O^{16} + n^1 &\rightarrow He^4 + C^{13} - 2.2\ \mathrm{MeV}\\
O^{16} + n^1 &\rightarrow H^1 \ + N^{16} - 9.9\ \mathrm{MeV}\\
O^{16} + n^1 &\rightarrow H^2 \ + N^{15} - 9.9\ \mathrm{MeV}
\end{aligned}
$$

According to measurements by LILLIE [39] the cross sections of these reactions at 14 MeV are 0.310, 0.035 and 0.015 barn respectively, or a total of 0.36 barn. Other measurements made at Los Alamos have resulted in still higher cross sections for the (n,p) reaction at the energy in question. As the total cross sections of hydrogen and oxygen at 14 MeV are 0.687 and 1.60 barn respectively, the loss at only the first

bution curves					
rea	% of total area	Region (calculated)	Area	% of total area	Total area S
10120 21890	95.0 94.0	$61.90 \le r \le \infty$ $62.63 \le r \le \infty$	220 470	2.0 2.0	10660 23300
99570 14700	87.4 87.4	$36.00 \le r \le \infty$ $36.09 \le r \le \infty$	2620 5820	2.3 2.4	113900 245700
00700 23300	88.4 88.3	$42.10 \le r \le \infty$ $41.96 \le r \le \infty$	1300 2900	1.2 1.1	113800 253000

collision becomes as large as 12 %. The total energy dependence of these cross sections is, however, unknown as far as the author knows, hence no complete calculations of the absorption are possible. A direct measurement of this absorption effect in oxygen for Ra-Be neutrons in water has been made by TAVERNIER and TROYER [40]. These investigators found a loss of 2.5 % caused by fast neutron absorption in oxygen. The only possibility of determining this absorption loss experimentally is to substitute the oxygen of the moderator by an element not absorbing neutrons. One possible solution is to use paraffin oil as a moderator instead of water, which in principle means an exchange of the oxygen with carbon. Even the carbon reacts with these highly energetic neutrons, but this reaction, the reaction $^{12}\mathrm{C}(n,n')3\,^{4}\mathrm{He}$, does not result in a neutron loss.

b) Paraffin oil as moderator

In order to study the absorption effects of fast neutrons in oxygen, a medical oil, Mayoline 248 L, was chosen as moderator. This oil is distinguished by a great resistance to oxidation. With 6000 litres of this oil instead of water, the experiments described in a) above were repeated. Special attention was paid to the determination of background effects i.e. the stray neutrons from $\mathrm{D}(d,n)$ reactions and the background of recoil particles in the proportional counter. Measurements were never started until the background had reached a constant value, i.e. when deuterium targets

Table 6.

Ratio between areas				Yield of 250 mg source $Q \times 10^{-6}$ n/sec
Position of 250 mg Ra-Be source	Counter No.	$\dfrac{S_{\text{Ra-Be}}}{S_{\mathrm{T},\,d}}$	Mean value	
In contact with target	1 2	10.68 10.55	10.62	3.13
40 cm from target	1 2	10.68 10.86	10.77	3.17

				Areas S under ne	
Neutron source	Maximum deuteron energy (KeV)	BF_3 count (Number)	Region (calculated) (cm from target)	Area	% of t are
$^3T\ (d, n)\ ^4He$	125	1 2	$0 \leq r \leq 3.66$ $0 \leq r \leq 4.25$	400 1160	3.4 4.5
$^3T\ (d, n)\ ^4He$	175	1 2	$0 \leq r \leq 3.66$ $0 \leq r \leq 4.25$	400 1210	3.4 4.6
250 mC Ra-Be in contact with target		1 2	$0 \leq r \leq 3.66$ $0 \leq r \leq 4.25$	10800 30700	10.4 13.2

had been built up and reached equilibrium in the collimator system. To investigate if some systematic sources of error might be hidden in the background effects, the integration of the neutron flux from the $T(d, n)$ reaction was carried out at two different acceleration voltages, 125 kV and 175 kV. The yield of the $T(d, n)$ reaction decreases somewhat from 125–175 kV, while the yield of the $D(d, n)$ reaction increases. Hence an incomplete correction for $D(d, n)$ sources would be expected to increase the value of the density integral $S_{T,d}$, which means that the experimentally found yield Q of the Ra-Be neutron source should be smaller at 175 kV than at 125 kV acceleration voltage. The results of the experiments in oil are collected in Table 7, where the different parts of the areas S under the distribution curves $n(r) \cdot r = f(r)$ are given. The extrapolated parts of the curves are calculated as in the experiments in water described above. Table 8 gives the final values of the ratios of the total areas given by the counters at both acceleration voltages.

At the acceleration voltage of 125 kV the mean energy $\bar{E}_D$ of 107 keV is adopted, and at 175 keV, $\bar{E}_D = 156$ keV as previously discussed. The agreement between this value and the values obtained by other methods is now very good, which proves that the absorption effect in oxygen at a primary neutron energy of 14 MeV amounts to 25 %. As the hydrogen content of the oil is not exactly known, it is impossible to calculate the corresponding absorption for the neutrons of the Ra-α-Be source from

Table 8.

Ratio between areas				Yield of 250 mg source $Q \times 10^{-6}\ n/\text{sec}$
Maximum deuteron energy (keV)	Counter No.	$\frac{S_{\text{Ra-Be}}}{S_{T,d}}$	Mean value	
125	1 2	8.93 8.92	8.93	2.63
175	1 2	8.72 8.79	8.76	2.66
			Mean value	2.65

ibution curves

gion (measured) n from target)	Area	% of total area	Region (calculated) (cm from target)	Area	% of total area	Total area
$.66 \leq r \leq 59.98$ $.25 \leq r \leq 60.73$	10960 24190	94.0 93.0	$59.98 \leq r \leq \infty$ $60.73 \leq r \leq \infty$	300 630	2.6 2.5	11660 26000
$.66 \leq r \leq 59.98$ $.25 \leq r \leq 60.73$	11240 24550	94.1 93.0	$59.98 \leq r \leq \infty$ $60.73 \leq r \leq \infty$	300 640	2.5 2.4	11940 26400
$.66 \leq r \leq 39.85$ $.25 \leq r \times 28.59$	92200 191100	88.6 82.4	$39.85 \leq r \leq \infty$ $28.59 \leq r \leq \infty$	1080 10100	1.0 4.4	104100 232000

the measured distributions. The result with the 14 MeV neutrons, however, gives strong support to the result of TAVERNIER and TROYER, mentioned above, that the absorption of fast neutrons in water for the Ra-Be source is 2.5 %, which seems reasonable as such a source emits neutrons of energies of up to 13 MeV. The results of the measurements at the two acceleration voltages show that the correction for the background neutrons has, in all probability, been correctly made, as the value of the yield Q at 175 kV is somewhat higher than that found at 125 kV.

4. Sources of error and final result

The associated particle method for determining the yield of an arbitrary neutron source is distinguished by its simplicity and independence of natural constants. Of the quantities determining Q, only the transformation factor for the solid angle is dependent on other nuclear data. The uncertainty in this factor is, as previously discussed, dependent on the degree of accuracy to which the effective deuteron energy $\bar{E}_D$, at which the deuterons react with the tritium nuclei, is known. A calculation of the error in this factor gives the result that this uncertainty is $\leq 0.8\,|\Delta \bar{E}_D|$. As $|\Delta \bar{E}_D|$ is assumed to be 0.010 MeV, the uncertainty in the factor $\frac{\sin^2 \theta_\alpha \cos(\phi_\alpha - \theta_\alpha)}{\sin^2 \phi_\alpha}$ becomes ± 0.8 %. The uncertainty in the determination of the solid angle is 1.4 % as the diameter of the circular collimator is measured to an accuracy of 0.7 %. In the determination of the area S_{RaBe} the greatest uncertainty arises in the extrapolation of the distribution curve $n(r)$ to $r = 0$. The error in the determination of the experimentally measured part of this area is very small, as the calculation is based on a large number of experimental points, and each point is determined with a statistical accuracy better than 0.5 %. Since only about 15 % of the total area is covered by the extrapolated parts of the distribution curve and the error in this extrapolation should not exceed 5 %, an uncertainty of 1 % is estimated for the whole area S_{RaBe}. Concerning the area $S_{\mathrm{T},d}$ the uncertainty arising in the extrapolation is smaller, as only 5 % of the surface is covered by those parts, due to the much more slowly decreasing neutron density. In this case the main sources of uncertainty arise from the background effects of stray neutrons and recoil nuclei in the α-counter. The first of these corrections is very small, of the order of 0.5 % for small r values, increases monotonically and reaches a magnitude of 3 % for $r < 40$ cm. For $r > 40$ cm it increases more rapidly, reaching a value of 10 % for the greatest r values used. As the weight of this correction decreases for the greater distances from the target, the uncertainty caused by the stray neutrons remains small. The second correction, which was found to be 7.5 % in several experiments, has an uncertainty not greater than 0.2–0.3 %. The total uncertainty in $S_{T,d}$ is, for this reason, assumed to be no greater than for S_{RaBe}, i.e. 1 %. These sources of error combined give a relative mean error of ± 2 %, hence the final result is that the neutron yield of the 250 mC source, determined by the associated particle method, is

$$Q = (2.65 \pm 0.06) \cdot 10^6 \ n/\text{sec}.$$

CHAPTER III

A comparison between methods of measurement and the standardization problem

The measurements described in Chapter II, in conjunction with the work of TAVERNIER and TROYER (loc. cit.), clearly show that the absorption of fast neutrons in oxygen, when water is used as moderator, must be taken into account. The effect of this conclusion is that the values of the yield of the 250 mg Ra-Be source obtained in the earlier work using slowing down methods [37] must be corrected for this absorption effect. On the basis of the accurate work of TAVERNIER and TROYER the values of the yield are increased by a factor 1.025. Since the above measurements of the yield by the gold foil method were made, newer and probably more reliable values of the absorption cross sections of gold and hydrogen have been published. According to measurements made at Brookhaven [41] $\sigma_{Au} = 98.7 \pm 0.6$ barn, and a new value found at Harwell [42] is $\sigma_{Au} = 98.4 \pm 0.9$ barn. As these measurements include better corrections for scattering and other minor effects, a value of 98.6 barn (± 1 %) is accepted for σ_{Au}. Concerning σ_H, the tendency of newer measurements has been to give higher values than those obtained from earlier measurements. Besides the value of 0.329 ± 0.004 barn found by HAMMERMESH, RINGO and WEXLER [43], the values 0.332 ± 0.007 barn according to HARRIS *et al.* [44] and 0.333 ± 0.003 barn by VON DARDEL and SJÖSTRAND [45] have been published. As the first two of these measurements depend on a comparison with the boron cross section, and the last one is independent of such a comparison, the greatest importance is attached to this third measurement. If the value 0.333 ± 0.003 barn is accepted for σ_H and the correction factor given above for the absorption of fast neutrons is applied, the results of the measurements in the work cited above are changed to the values given in the first two lines of Table 9. This table also gives the results of the measurements described in Chapters I and II, showing that there is very satisfactory agreement between the results obtained with the different methods. Only the indirect measurement of the yield obtained by the measurement of the fast flux from the T(d,n) reaction deviates perceptibly from the mean value of the yield determined by the remaining methods. This deviation might depend upon an erroneous choice of constants as well as on the background effects which were very difficult to control in this measurement. In the calculation of these values the Po growth in the Ra-Be source has not been taken into consideration, the maximum change of the yield caused by this growth

Table 9.

Yield of 250 mg Ra-Be source		Ratio between yields measured by the different methods. The value of 2.65 of the ass. part. method is put=1	Dependence of absolute value on cross sections	Date of measurement
Method used for absolute determination	Yield $\times 10^{-6}$ corrected for fast neutron absorption			
Space integration of neutron density in H_3BO_3 solution with small BF_3-chambers. Absolute counting of boron disintegrations	2.63 ± 0.12	0.992	No (Slight dependence in the correction term)	January 1952
Space integration of neutron density in pure water with gold foils. Counting of absolute activity. $\sigma_H = 0.333$ barn $\sigma_{Au} = 98.6$ barns	2.64 ± 0.08	0.996	Yes	March 1953
Comparison with the yield of the $^3T\ (d, n)\ ^4He$ reaction. Absolute counting of the associated α-particles from this reaction	2.65 ± 0.06	1.00	No	October 1954
Comparison with the yield from the $^3T\ (d, n)\ ^4He$ reaction. Absolute measurement of the fast neutron flux from this reaction by means of a homogeneous ionization chamber	2.73 ± 0.12	1.03	Yes	October 1954
Subcritical pile method for comparison with a Harwell standard source. Absolute counting of ^{24}Na disintegration	2.64 ± 0.13	0.996	No	July 1952

being about 1 % from the date of the first measurement to the last one. By using the associated particle method for the determination of the yield of the Ra-Be source calibrated earlier, as well as for the comparison with a recoil particle method, a link has been established between the methods for measurement of thermal fluxes and those for the measurement of fast fluxes. The associated particle method is superior to many other methods as the results obtained by it are independent of other natural constants especially cross sections. If reactions between nuclei such as $T(d, n)$, $T(p, n)$ and $D(d, n)$ reactions are used for comparison of neutron fluxes, the tritium reactions are superior on account of the high yield, which decreases the effect of backgrounds. This fact is considered to justify taking the value of the neutron yield, Q, obtained by the associated particle method as the standard and compare the remaining ones with this value as has been done in column 3 of Table 9. If this is accepted the following conclusions may be drawn:

1. Of the remaining methods for the absolute measurement of total neutron yields of point sources such as natural sources (Ra-Be) and of accelerators allowing extraction of the beam, the slowing down technique is the most reliable one. If, in the future, great accuracy can be reached in the determination of cross sections, the slowing down methods should give results accurate to within 1–2 %. The present limit of accuracy is about 3 %.

2. The absolute measurement of fast neutron fluxes with "direct" methods such as the recoil particle method cannot give results of an accuracy better than 4–5 % at present, due to the difficulties in eliminating spurious effects of different kinds. Moreover such measurements are complicated by the energy sensitivity of the detectors, which implies that the neutron spectra should be known.

3. When comparing neutron sources of widely different spectra using any type of slowing down technique, the choice of the moderator is of paramount importance. In particular, water is unsuitable as moderator if either source has an energy spectrum with neutron energies ≥ 3 MeV, as the (n, α) reaction in oxygen might then cause noticeable absorption. This fact also complicates the accurate comparison between photo-neutron sources and e.g. Ra-Be sources, which is of importance for the comparison between so-called standard photo-neutron sources and laboratory substandards.

4. The good agreement between the results of these measurements and the measurement made at Harwell implies that the results of the Stockholm measurements agree within ± 5 % with the measurements made in other laboratories, particularly those from Argonne, Los Alamos, Union Minière, Brussels, and CEA, Paris. This is evident from the series of comparative measurements described by TAVERNIER and TROYER.

5. The results of the measurements show that the yield of the Ra-Be source is constant, at least within 1 %. During the experiments the source has been sharply tapped several times without any measurable change in the yield.

The last conclusion concerning the Ra-Be neutron source is of importance in discussing the standardization of the neutron standards of different laboratories. The neutron standard must, above all, be reproducible and constant. The photo-neutron source proposed by VON HALBAN [46] utilizing the nuclear photo disintegration of deuterium is probably quite reproducible, and it is possible to measure its yield accurately by using the associated particle method in counting the protons from the reaction $D(\gamma, n)^1H$. Its disadvantage is, however, the difficulty of comparing the photo source and another laboratory substandard, e.g. a Ra-α-Be source, a difficulty which is of the same nature as the difficulty of comparing the neutron flux from the $T(d, n)$ reaction with the flux of a Ra-α-Be source. As has been shown in these investigations, this problem may be solved by using a suitable moderator. Generally speaking the most reliable standard neutron sources are those making use of the associated particle method. All the reactions $D(\gamma, n)^1H$, $D(d, n)^3He$, $T(p, n)^3He$ and and $T(d, n)^4He$ are well suited to accurate absolute determination of the flux. Other methods utilizing the particles associated with neutron production are conceivable, e.g. when neutron production leads to a radioactive product nucleus. The activity of the target is then a measure of the neutron flux.

By a further refinement of these methods it may be possible to produce neutron standards having an accuracy of 1 %.

ACKNOWLEDGEMENTS

It is a pleasure for me to express my sincere gratitude to the Director of the Physical Department of AB Atomenergi, Dr. SIGVARD EKLUND, for his interest in my work and for his strong support in many ways, supplying me with all facilities.

In the experimental work I have enjoyed the highly skilful technical assistance of Ing. ERIK ÅSTRÖM and Ing. MAURITZ HÖIJERTZ, to whom I am much indebted.

Finally, I am indebted to AB Svenska Esso for supplying me with the large quantity of high quality paraffin oil.

AB Atomenergi, Department of Physics. Stockholm.

APPENDIX I

Calculation of the solid angle

Pariticles are assumed to leave the surface Σ (target) isotropically and the problem is to calculate the percentage of particles passing the surface Σ_1 (collimator) at a distance z from Σ. The total number of particles passing the surface element $d\sigma_1$ of Σ_1 is

$$\phi(r_1, z) = N \oint_{\Sigma} d\sigma\, d\omega, \tag{1}$$

where N is the number of particles leaving Σ per cm^2 per sec, and $d\omega$ is the solid angle subtended by $d\sigma_1$ as seen from $d\sigma$. The integration is performed over the total surface Σ. $d\omega$ is determined by

$$d\omega = \frac{d\sigma_1 \cos\theta}{4\pi\varrho^2}, \tag{2}$$

where ϱ is the distance between the surface elements $d\sigma$ and $d\sigma_1$, and θ is the angle between the line connecting $d\sigma$ and $d\sigma_1$ and the perpendicular to the surfaces Σ and Σ_1. Substituting for $d\omega$ in eq. (1), remembering that $\cos\theta = \frac{z}{\varrho}$, gives

$$\phi(r_1, z) = N \oint_{\Sigma} \frac{z\, d\sigma\, d\sigma_1}{4\pi\varrho^3}, \tag{3}$$

the total flux of particles passing $\sum_1$ is then

$$n = \frac{N}{4\pi} \oint_{\Sigma_1} \oint_{\Sigma} \frac{z\, d\sigma\, d\sigma_1}{\varrho^3}. \tag{4}$$

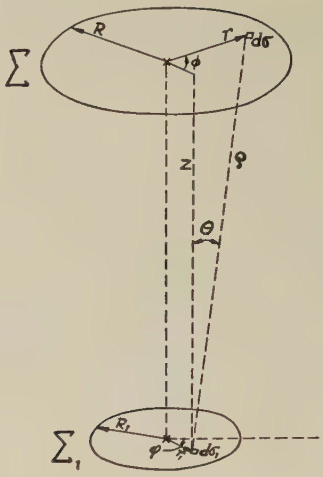

If polar coordinates are used, remembering that $\varrho = (r^2 - 2 r r_1 \cos\phi + r_1^2 + z^2)^{1/2}$, the integral becomes

$$n = \frac{N}{4\pi} \int_0^{R_1} r_1\,d r_1 \int_0^{2\pi} d\varphi \int_0^{R} r\,d r \int_0^{\pi} \frac{z\,d\phi}{(r^2 - 2 r r_1 \cos\phi + r_1^2 + z^2)^{3/2}}. \tag{5}$$

R and R_1 are the radii of the circular surfaces Σ and Σ_1 respectively. As R and R_1 are $\ll z$, a series expansion of the integrand is made, the result being a series of elementary integrals. The result of this calculation is that

$$n = N \frac{\pi R^2}{4} \left(\frac{R_1}{z}\right) \left\{ 1 - \frac{3}{4}\left(\frac{R}{z}\right)^2 - \frac{3}{4}\left(\frac{R_1}{z}\right)^2 + \text{higher terms} \right\}. \tag{6}$$

Considering that $N\pi R^2$ is the total number of particles, $n_{\text{tot.}}$, leaving $\sum$ per second and neglecting $\left(\frac{R_1}{z}\right)^2$ the result is

$$n = n_{\text{tot}} \frac{1}{4} \left(\frac{R_1}{z}\right)^2 \left\{ 1 - \frac{3}{4}\left(\frac{R}{z}\right)^2 \right\}. \tag{7}$$

The solid angle ω is the fraction $\frac{n}{n_{\text{tot}}}$ of 4π, i.e.

$$\omega = \pi \left(\frac{R_1}{z}\right)^2 \left\{ 1 - \frac{3}{4}\left(\frac{R}{z}\right)^2 \right\}. \tag{8}$$

With $R_1 = 0.68$ mm, $R = 12.5$ mm and $z = 170.2$ mm the result is

$$\omega = 4.99 \times 10^{-5} \text{ steradian.}$$

APPENDIX II

Calculation of the mean energies $\bar{E}_{\mathrm{H}}$ and $\bar{E}_{\mathrm{C}}$ of the recoil unclei

As a result of the high primary neutron energy it is necessary to take the relativistic corrections into account in the calculation of the mean energies of the recoiling nuclei ^{1}H and ^{12}C. Considering only elastic collisions, the kinetic energy, T, of a recoil nucleus as measured in the laboratory system is as follows (see SEGRÉ: Experimental Nuclear Physics, Vol. II, p. 3–9, Wiley & Sons, Inc. 1953):

$$T = m_r c^2 (\gamma'^2 - 1)(1 - \cos\theta), \tag{1}$$

where m_r = the mass of the recoil nucleus
c = the velocity of light

$$\gamma' = \frac{\gamma + \frac{m_r}{m_n}}{\left(1 + 2\frac{m_r}{m_n}\gamma + \left(\frac{m_r}{m_n}\right)^2\right)^{1/2}}$$

$$\gamma = (1-\beta^2)^{-1/2}$$

$$\beta = \frac{v}{c}$$

v = the velocity of the neutron before collision
m_n = the mass of the neutron
θ = the angle of scattering of the neutron in the c.m. system.

If the scattering is assumed to be isotropic in the c.m. system the mean energy $\bar{T}$ is calculated from

$$\bar{T} = m_r c^2 (\gamma'^2 - 1)\int_0^\pi (1-\cos\theta)\frac{\sin\theta\, d\theta}{2}, \tag{2}$$

i.e.

$$\bar{T} = m_r c^2 (\gamma'^2 - 1). \tag{3}$$

Series expansion finally gives

$$\bar{T} = \frac{2 m_r m_n}{(m_r + m_n)^2} E_n \left\{1 + \frac{m_n^2 + m_r^2 + m_r m_n}{(m_r + m_n)^2}\beta^2\right\} \tag{4}$$

where $E_n = \frac{m_n v^2}{2}$ = the energy of the neutron before collision, measured in the laboratory system. By substituting the values of the masses of the neutron, the proton and the ^{12}C nucleus respectively in eq. (4), the mean energies $\bar{E}_{\mathrm{H}}$ and $\bar{E}_{\mathrm{C}}$ become

$$\bar{E}_{\mathrm{H}} = \frac{E_n}{2}(1 + 0.75\beta^2), \tag{5}$$

$$\bar{E}_{\mathrm{C}} = 0.142\, E_n (1 + 0.93\beta^2). \tag{6}$$

Using these relation, $\bar{E}_H$ and $\bar{E}_C$ have been calculated for a series of values of E_n between 13 and 15 MeV, which are the energy limits occurring in the experiments. These values are given in the table below.

Neutron energy MeV (E_n)	β^2	Mean energies of recoil nucleus in MeV	
		$\bar{E}_H$	$\bar{E}_C$
13.00	0.028	6.64	1.90
13.50	0.029	6.90	1.97
14.00	0.030	7.16	2.04
14.50	0.031	7.42	2.12
15.00	0.032	7.68	2.19

REFERENCES

1. H. H. Barschall, L. Rosen, R. F. Taschek, and J. H. Williams, Rev. Mod. Phys. *24,* 1 (1952).
2. A. Wattenberg, Annual Review of Nuclear Science *3,* 119 (1953).
3. W. H. Bragg, Studies in Radioactivity, Chapter IX. Macmillan and Company, London, 1912.
4. L. H. Gray, Proc. Cambridge Phil. Soc. *40,* 72 (1943).
5. U. Fano, Radiation Research, *1,* 237 (1954).
6. E. Bretscher and A. P. French, Brit. Decl. Doc. 386 (1944).
7. A. O. Hanson, R. F. Taschek, and J. H. Williams, Rev. Mod. Phys. *21,* 635 (1949).
8. J. P. Conner, T. W. Bonner, and J. R. Smith, Phys. Rev. *88,* 468 (1952).
9. N. G. Sjöstrand, Appl. Sci. Res., Vol. *B 2,* 227 (1951).
10. E. R. Graves, A. A. Rodrigues, M. Goldblatt, and D. I. Meyer, Rev. Sci. Instr. *20,* 579 (1949).
11. D. H. Wilkinsson, Ionization Chambers and Counters. Cambridge University Press, 1950.
12. K. W. Allen, D. L. Livesey, and D. H. Wilkinson, Proc. Cambridge Phil. Soc. *46,* 339 (1950).
13. J. O. Hirschfelder and J. L. Magee, Phys. Rev. *73,* 207 (1948).
14. J. H. Coleman and D. Bohm, Journ. Appl. Phys. *24,* 497 (1953).
15. F. A. & A. F. Lindemann, and T. C. Keeley, Phil. Mag. *47,* 577 (1924).
16. E. Bretscher and A. P. French, Phys. Rev. *75,* 1154 (1949).
17. D. L. Allan and M. J. Poole, Proc. Roy. Soc. *A 204,* 500 (1950–51).
18. K. Schmieder, Ann. Physik *35,* 445 (1939).
19. T. E. Bortner and G. S. Hurst, Phys. Rev. *90,* 160 (1953).
20. W. P. Jesse and J. Sadauskis, Phys. Rev. *90,* 1120 (1953).
21. J. Dainty, National Research Council of Canada, Atomic Energy Project Report CRM-482, 1950 (unpublished).
22. H. A. Bethe and J. Ashkin, Experimental Nuclear Physics, Vol. I, p. 166–252. Wiley & Sons, Inc. N.Y., 1953.
23. W. P. Jesse, H. Forstat, and J. Sadauskis, Phys. Rev. *77,* 782 (1950).
24. J. H. Coon, E. R. Graves, and H. H. Barschall, Phys. Rev. *88,* 562 (1952).
25. H. L. Poss, E. O. Salant, and L. C. L. Yuan, Phys. Rev. *85,* 703 (1952).
26. W. Sleator, Phys. Rev. *72,* 207 (1947).
27. Neutron Cross Sections, AECU-2040; Supplements 1 and 2, Nov. 20, 1952, June 15, 1953. Office of Technical Services, Department of Commerce.
28. H. H. Barshall and R. F. Taschek, Phys. Rev. *75,* 1819 (1949).
29. J. C. Allred, A. H. Armstrong, and L. Rosen, Phys. Rev. *91,* 90 (1953).
30. J. H. Coon and R. W. Davies, Phys. Rev. *94,* 785 (1954).
31. E. Baldinger, P. Huber, R. Ricamo, and W. Zünti, Helv. Phys. Acta *23,* 503 (1950).
32. A. E. Remund and R. Ricamo, Helv. Phys. Acta *25,* 447 (1952).
33. S. D. Warshaw, Phys. Rev. *76,* 1759 (1949).

34. C. W. Li, W. Whaling, W. A. Fowler, and C. C. Lauritsen, Phys. Rev. *83*, 512 (1951).
K. Ogata and H. Matsuda, Phys. Rev. *89*, 27 (1953).
35. E. R. Graves and L. Rosen, Phys. Rev. *89*, 343 (1953).
36. L. L. Green and W. M. Gibson, Proc. Phys. Soc. *62 A*, 296 (1949).
37. K. E. Larsson, Arkiv f. Fysik, *7*, 323 (1954).
38. R. E. Marshak, Rev. Mod. Phys. *19*, 185 (1947).
39. A. B. Lillie, Phys. Rev. *87*, 716 (1952).
40. A. de Troyer and G. C. Tavernier, Bull. de la Classe des Sciences *XL*, 150 (1954).
41. R. S. Carter, H. Palevsky, V. W. Myers, and D. J. Hughes, Phys. Rev. *92*, 716 (1953).
42. Private communications at a Harwell Conference, 1954.
43. B. Hamermesh, G. R. Ringo, and S. Wexler, Phys. Rev. *90*, 603 (1953).
44. S. P. Harris, C. O. Meuhlhause, D. Rose, H. P. Schroeder, G. E. Thomas, and S. Wexler, Phys. Rev. *91*, 125 (1953).
45. G. von Dardel and N. G. Sjöstrand, Phys. Rev. *96*, 1245 (1954).
46. See ref. 2 and private communications at a Harwell Conference 1954.

Tryckt den 18 februari 1955

Uppsala 1955. Almqvist & Wiksells Boktryckeri AB

ARKIV FÖR FYSIK Band 9 nr 19

Communicated 13 October 1954 by Carl Benedicks

The weakening effect on paraffin and waxes with its application for determining their surface tensions in solid state

By Mizuho Sato

With 5 figures in the text

The change in the bending tensile strength of paraffin, beeswax and Japan wax due to wetting by several liquids is studied experimentally. The bending tensile strength of these materials is lowered by wetting, showing a regularity between the change in the strength and the surface tension of the wetting liquid.

Applying this weakening effect for determining their surface tensions in solid state, it is found that the surface tensions of paraffin, beeswax and Japan wax are 46.1, 45.1 dyn/cm (at $8 \sim 10^\circ$C) and 59.6 dyn/cm (at 14°C) respectively.

Some twenty-five years ago, Benedicks and Sederholm[1] carried out experiments on the change in the breaking strength of solids due to wetting, which seems to be the first scientific work concerning the so-called wetting effect. Since then, this effect has experimentally been studied by Benedicks and his co-workers[2] on several materials, concluding that the breaking strength of solids should be affected by the surrounding medium. No doubt, this effect plays an important role in the strength of materials which is always measured in the presence of some kind of surrounding medium. It has been studied by eminent scientists[2, 3] in Europe and America on glass and similar brittle solids. For paraffin and waxes, experimental difficulties have been overcome by the author and the results are briefly reported below.

In order to measure the change in bending tensile strength, a special apparatus has been devised by making some modifications of the ordinary Brinell hardness tester. The ball was replaced by a knife edge whose vertical displacement is read on a sensitive dial gauge indicating the amount of bending of a specimen. In this

---

[1] In his personal communication to the author, Prof. Benedicks wrote that the first experiment was made by himself and Sederholm, in 1931, to explain the cause of accidents such as the bolt burst at a Swedish water power station, the result of which was communicated to the Swedish Metallographer's Society (Nr. 32) May 22 (1944). Splitting of the mineral mica, which occurs more easily in the presence of water, was known as early as 1892 to be a remarkable phenomenon.

[2] C. Benedicks and G. Ruben: Jernk. Ann. *129* (1945), 37; C. Benedicks and R. Härdén: Ark. Fys. *3* Nr. 22 (1951), 407; C. Benedicks: Comptes rendus *232* (1951), 2435; *233* (1951), 409, 482; Intern. Symp. React. Solids, Gothenburg (1952), 477.

[3] T. C. Baker and F. W. Preston: J. Appl. Phys. *17* (1946), 170, 179. J. L. Glathart and F. W. Preston: J. Appl. Phys. *17* (1946), 170, 179. J. L. Glathart and F. W. Preston: J. Appl. Phys. *17* (1946), 189.

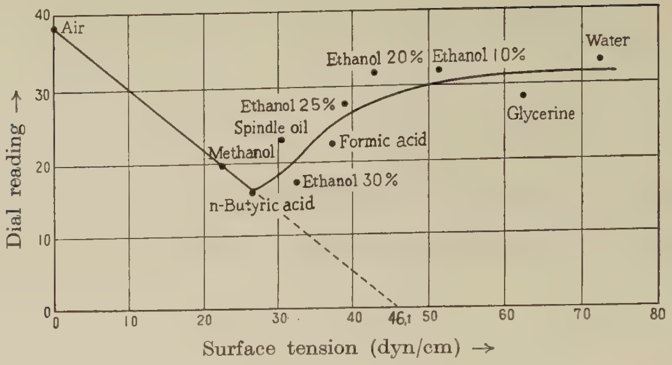

Fig. 1.

way, the amount of maximum bending without crack in dry state is compared with that in wet state. It is obvious that the maximum bending is large when the bending tensile strength is large. Therefore, the former is taken as the measure for the latter.

To prepare specimens, a block of paraffin or wax is melted and cast in a parallel plate mould consisting of two glass plates. When it is solidified, the mould is dipped for a moment into a vessel containing hot water and the glass plates are removed. One thus obtains a plate of paraffin or wax of uniform thickness. From this plate, a large number of rectangular bars are cut as specimens. The dimensions of the paraffin, beeswax and Japan wax specimens were $3.0 \times 7.5 \times 33$ mm, $1.5 \times 7.5 \times 33$ mm, and $3.1 \times 7.5 \times 33$ mm respectively; the span used was 26 mm. These specimens were annealed in a thermostat at 30°C for 5 h to remove internal stresses, and then kept in a desiccator containing $CaCl_2$.

To illustrate the experimental procedure, paraffin is taken. The melting point was determined to be ca. 46°C. At least, 6 ~ 10 specimens in both dry and wet states were tried. The duration of loading was 5 ~ 8 sec. The surface tension of the wetting liquids was determined at a room temperature by an ordinary capillary tube method. Data obtained at 8 ~ 10°C are plotted in Fig. 1.

As seen in the figure, the relation between the dial reading and the surface tension is first represented by a descending straight line and then by an ascending curve, the slope of which successively decreases toward an horizontal line. The straight line means that paraffin in the presence of methanol or *n*-butyric acid becomes more brittle than in dry state; the wetting effect due to *n*-butyric acid is more pronounced than that due to methanol, the former being ca. –49.3 per cent, while the latter is ca. –60 per cent of the dry value. The wetting effect due to spindle oil, 30 per cent ethanol, formic acid etc. is smaller than that due to *n*-butyric acid. From the surface tension of 42.8 dyn/cm (of 20 per cent ethanol onwards), the bending tensile strength becomes almost constant (the wetting effect being *c.* –18 per cent).

Besides the liquids plotted in Fig. 1, mercury was also tried, giving apparently a decrease of ca. –19 per cent.

In Figs. 2 and 3, two similar curves obtained with beeswax and Japan wax are given, the melting points being 59 ~ 61°C and 52 ~ 53°C respectively. In both cases, the weakening effect follows a sequence similar to that seen in Fig. 1.

The influence of thickness and width of the specimen was studied in paraffin using three specimens of (1) 1.25 mm, (2) 3.0 mm and (3) 4.0 mm in thickness but of the

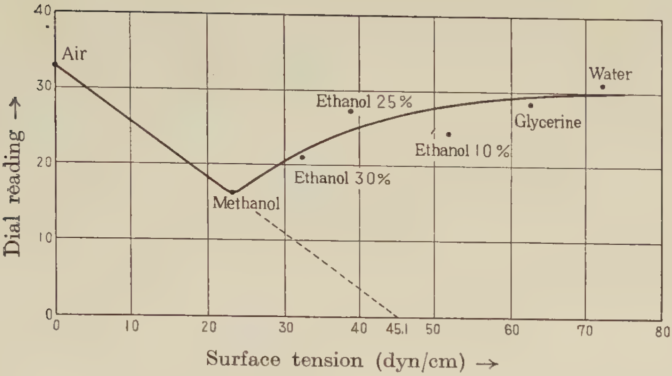

Fig. 2. Weakening effect on beeswax.

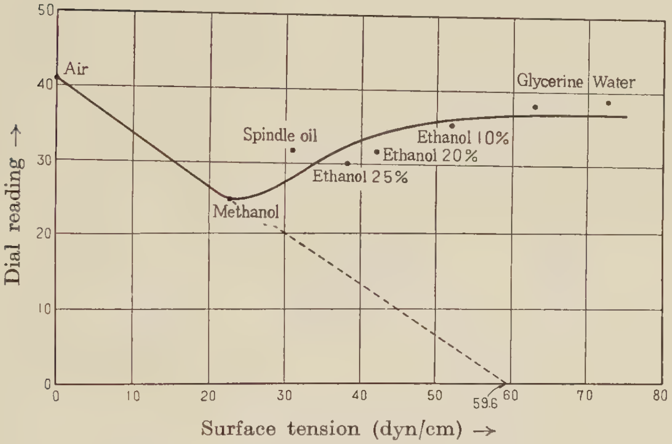

Fig. 3. Weakening effect on Japan wax.

same width of 7.5 mm, and another three of (4) 5.5 mm, (5) 6.5 mm and (6) 7.5 mm in width but of the same thickness of 3.0 mm (the specimen (6) is, of course, the same as the specimen (2)). The weakening effects observed by the wetting of methanol at 8 ~ 10°C are shown in Figs. 4 and 5 in which the line numbers refer to the specimen numbers given above. As seen from these figures, the wetting effect does not depend either on thickness or on width since the lines converge to a certain point in each case, which fact shows that the surrounding medium affects the strength by a ratio, as remarked by BAKER and PRESTON[1], forming a simple rule as to the change of breaking strength of glass due to wetting. This means that in determining the wetting effect, specimens need not have quite the same dimensions. But the duration of loading should be equal for any pair of tests in dry and wet states as it affects the breaking strength considerably.

As for the origin of the weakening effect, BENEDICKS[2] has proposed a theory of lines of force. According to him, some lines of force emanating from atoms on the

---

[1] See footnote 3 on p. 335.
[2] See footnote 2 on p. 335.

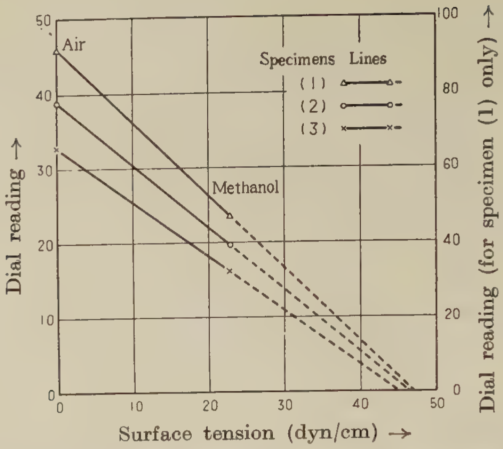

Fig. 4. Weakening effect on paraffin plates of different thicknesses due to methanol.

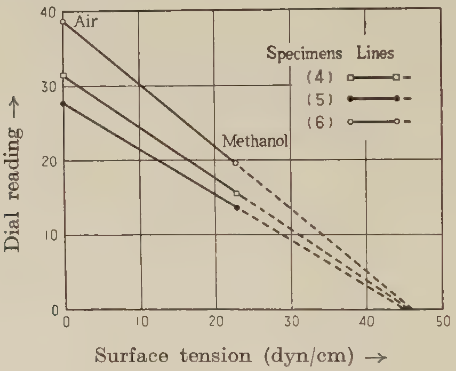

Fig. 5. Weakening effect on paraffin plates of different widths due to methanol.

solid surface are bound by atoms of the wetting liquid so that the mutual attraction between the atoms along the solid surface will decrease if the solid is wetted by the liquid. It is noteworthy that the surplus of lines of force emerged from the surface atoms goes towards the liquid side. If a solid were wetted by a liquid whose surface tension is equal to that of the solid, then the bending tensile strength of this solid would actually vanish, as already remarked by BENEDICKS.

On this basis, the surface tension of the solid can be determined to be the abscissa of the point of intersection of the first (straight) line with the axis of surface tension in the Figs. 1–3, where a dotted line represents a linear extrapolation of the straight line. Thus, we have found the surface tensions of paraffin, beeswax and Japan wax to be 46.1, 45.1 dyn/cm (at 8 ~ 10°C) and 59.6 dyn/cm (at 14°C) respectively.

The surface tensions of paraffin and beeswax have been determined by ANTONOFF[1] to be 41 and 46 dyn/cm respectively at room temperature. Thereby a certain assumption was made regarding the rising or falling of a liquid in a tube of the solid. Anyhow it seems interesting that ANTONOFF's figures agree fairly well with those found here.

---

[1] G. N. ANTONOFF: Phil. Mag., Jan.–June (1926), 1258.

For Japan wax no comparison can be made as no other determination is known to exist in literature.

The author wishes to express his hearty thanks to Professor Dr. C. BENEDICKS of Stockholm for his valuable suggestion, and also to Messrs. T. KAJIMA and S. FUJITA for their experimental assistance.

Scientific Research Institute Ltd., Tokyo, October 1954.

Tryckt den 18 februari 1955

Uppsala 1955. Almqvist & Wiksells Boktryckeri AB

ARKIV FÖR FYSIK Band 9 nr 20

Communicated 14 April 1954 by ERIK HULTHÉN

Microwave spectrum of cyclopentene oxide

By GUNNAR ERLANDSSON

In a previous paper (1) an analysis has been reported of the microwave spectrum of cyclopentanone. In connection with that investigation it was considered interesting to investigate also the isomeric molecule cyclopentene oxide[1] (1.2 epoxy-cyclopentane). This molecule is supposed to have the structure formula

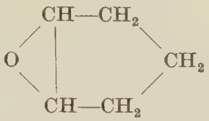

From considerations of bond angles it is clear that the oxygen atom must be out of the approximate plane of the carbon ring. This molecule has therefore, contrary to the cyclopentanone molecule, two active components of electric dipole moment. The microwave spectrum is therefore rather complicated showing some 30–40 absorption peaks of appreciable magnitude in each interval of 1 kMc/sec in the K-band region.

By recording the spectrum several times with different DC and square wave voltages applied to the Stark-effect electrode it was possible to identify five lines as belonging to the transition $J=2–3$. It was found that these lines must be the transitions associated with the a-component of the dipole moment. Preliminary values of the rotational constants were then evaluated and from these it was possible to identify a number of Q-branch lines having $J=10$, 11 and 12. The constants $\varkappa$ and $\frac{1}{2}(A-C)$ were adjusted to give a best fit for these lines. A final value was then calculated for $\frac{1}{2}(A+C)$ to fit the lines $J=2–3$. The results are:

$$\varkappa=0.0502;\quad \tfrac{1}{2}(A-C)=1.2300\ \text{kMc/s};\quad \tfrac{1}{2}(A+C)=4.4786\ \text{kMc/s}$$

$$\text{giving:}\quad A=5.7086,\quad B=4.5404,\quad C=3.2486\ \text{kMc/s}$$

$$\text{and:}\quad I_A=88.536,\quad I_B=111.316,\quad I_C=155.580\ \text{AÅ}^2.$$

Calculated and observed frequency values are found in Tables 1 and 2. Frequency measurements are accurate to ±5 Mc/s. Frequency calculations have been carried out by means of the continued fraction method (2). The relative intensities of the identified lines show that the a- and c-components of electric dipole moment are of the same order of magnitude.

---

[1] A sample of this substance was obtained as a gift from Dr. STIG ANDERSSON, Department of Chemistry, University of Lund.

Table 1. Type *a*-transitions.

Transition	ν_{calc}	ν_{obs}
$2_{0.2} - 3_{0.3}$	21450	21446
$2_{1.2} - 3_{1.3}$	21095	21094
$2_{1.1} - 3_{1.2}$	24746	24751
$2_{2.1} - 3_{2.2}$	23367	23365
$2_{2.0} - 3_{2.1}$	25284	25286
$10_{3.7} - 10_{5.6}$	22135	22140
$11_{4.8} - 11_{4.7}$	24470	24470
$11_{3.8} - 11_{5.7}$	25301	25304
$11_{4.7} - 11_{6.6}$	22773	22775
$12_{5.8} - 12_{5.7}$	22569	22568
$12_{4.8} - 12_{6.7}$	25128	25133
$12_{5.7} - 12_{7.6}$	24963	24968

Table 2. Type *c*-transitions.

Transition	ν_{calc}	ν_{obs}
$10_{7.3} - 10_{8.3}$	23721	23717
$10_{7.4} - 10_{8.2}$	24221	24221
$11_{6.6} - 11_{7.4}$	23025	23028
$11_{7.4} - 11_{8.4}$	22070	22070
$11_{7.5} - 11_{8.3}$	23902	23900
$12_{8.4} - 12_{7.6}$	24264	24262

Stark-effect observations on the Q-branch lines show that lines having one $\Delta K = 0$ have their components on the low frequency side, whereas lines having one $\Delta K = 2$ have their components on the high frequency side. This seems to be consistent with the expressions for the Stark-effect splitting (3) and with the structure of the energy level diagram which shows neighbouring pairs of levels. The Stark-effect increases the splitting of these pairs causing a decrease in frequency for the transition from the upper component in the low energy pair to the lower component in the high energy pair and vice versa.

The values obtained for the moments of inertia have been used in an attempt to get some information about the molecular structure. For this purpose the following simplifying assumptions have been made

(*a*) The carbon ring forms a plane regular pentagon.

(*b*) The C–H bonds lie in radial planes normal to the carbon plane and make 55° angles with this plane, the C–H distance being 1.08 Å. The two single H-atoms are on the same side of the carbon plane.

(*c*) The oxygen atom is situated somewhere in the symmetry plane of the C–H skeleton.

Under these assumptions the C–C distance may be calculated from $I_A + I_C - I_B$ independently of the oxygen bonds. The result is $d_{CC} = 1.516$ Å. The position of the O-atom may then be calculated from I_A and I_C. This gives a bond distance $d_{CO} = 1.47$ Å and an angle between the carbon ring and the COC-triangle of 98.1°.

The value obtained for d_{CC} depends upon the assumption of a regular pentagonal carbon ring and upon the assumed positions of the hydrogen atoms. A comparison with ethylene oxide (4) which has $d_{CC} = 1.472$ Å indicates that the carbon ring is in fact not regular but has a shorter distance between the 1–2 carbon atoms. Also the 1 and 2 C–H bonds probably make larger angles than 55° with the carbon plane.

If the same method of calculation as above is applied to the cyclopentanone molecule, one obtains $d_{CC} = 1.507$. This value depends like the previous one upon the assumed positions of the hydrogen atoms. A larger value is obtained if these are assumed to lie nearer the symmetry plane normal to the carbon ring.

The value of d_{CO} obtained above is rather high compared to the value 1.436 Å btained for ethylene oxide (4). It is, however, a sensitive function of the sum $\sum m_i z_i^2$ calculated for the other atoms with a z-axis normal to the carbon plane. This sum depends upon the planarity of the carbon ring and the positions of he hydrogen atoms. It was shown for cyclopentanone that the non-planarity of he carbon ring gives a considerable contribution to $\sum m_i z_i^2$. If this sum is given he same value for cyplopentene oxide as found experimentally for cyclopentanone, one obtains $d_{\mathrm{CO}} = 1.39$ Å, which is certainly too small. It seems probable herefore that the carbon ring is more nearly plane in cyclopentene oxide than n cyclopentanone.

I wish to express my thanks to Dr. STIG SUNNER in Lund for suggesting this investigation and for helpful advice, and to Dr. STIG ANDERSSON in Lund for the sample of cyclopentene oxide.

Department of Physics, University of Stockholm March 1954.

REFERENCES

1. G. ERLANDSSON, Microwave spectrum of cyclopentanone. J. Chem. Phys. *22*, 563 (1954).
2. G. W. KING, R. M. HAINER and P. C. CROSS, J. Chem. Phys. *11*, 27 (1943).
3. S. GOLDEN and E. B. WILSON Jr., J. Chem. Phys. *16*, 669 (1948).
4. G. L. CUNNINGHAM Jr., A. W. BOYD, R. J. MYERS, W. D. GWINN and W. I. LE VAN, J. Chem. Phys. *19*, 676 (1951).

Tryckt den 1 mars 1955

Uppsala 1955. Almqvist & Wiksells Boktryckeri AB

ARKIV FÖR FYSIK Band 9 nr 21

Communicated 24 November 1954 by Erik Hulthén

On the band spectrum of CrH

By Bengt Kleman and Bengt Liljeqvist

With 2 figures in the text

An infra-red band system ascribed to the CrH molecule appears in the spectrum from a King's furnace. The bands of the system are degraded to the red, and the 0–0 band has its head at λ 8611 Å. Vibrational data for the band system are given in this paper.

The earlier known single band of CrH at λ 3675 Å also appears under the same experimental conditions, as well as another band with its strongest head at λ 3290 Å. The two ultra-violet bands represent different electronic transitions.

Introduction

During the recording of the emission spectrum from a King's furnace with a PbS cell as detector a red-degraded band with its head at 0.86 μ was found [1]. The furnace was loaded with chromium and run in an atmosphere of hydrogen. The appearance of the band and the experimental conditions led us to attribute the band to the CrH molecule.

The infra-red system was subsequently photographed in a glass-spectrograph in order to carry out a vibrational analysis. Gaydon and Pearse [2], using a high-tension arc as light-source, have observed a single band at λ 3675 Å, which they ascribe to CrH. We found it of interest to photograph the ultra-violet part of the spectrum to see if this band also appears with a King's furnace as light-source.

The infra-red band system

The red and infra-red parts of the spectrum from a King's furnace have been photographed in a Zeiss three-prism spectrograph. The dispersion of the spectrograph varies from about 35 Å/mm at λ 6900 Å to about 110 Å/mm at λ 10000 Å. For the infra-red range ammonia hypersensitized Kodak IQ(2) and IZ plates were used. The hydrogen pressure in the furnace was kept somewhat lower than one atmosphere and the temperature at 2000–2200°C. With exposure times of 3 to 5 minutes a system of bands degraded to the red covering the region from λ 6900 Å to λ 10000 Å was found. With argon as filling gas only the strong head at 0.86 μ could be detected on the plates, but it was appreciably weaker than with hydrogen. This is the normal behaviour of those hydride bands which appear strongly in the furnace with hydrogen as filler, that the strongest ones still appear in an atmosphere of another gas than hydrogen.

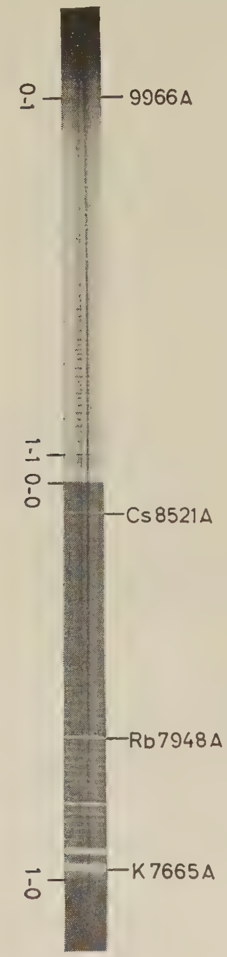

Fig. 1. The infra-red band system of CrH.

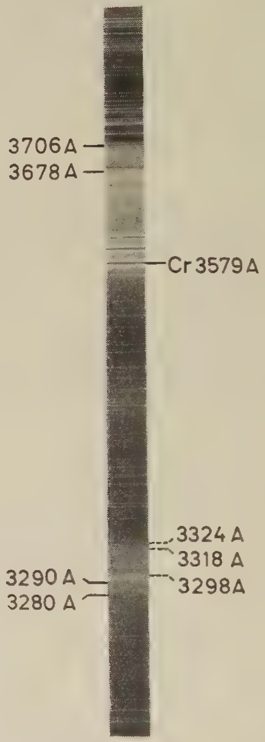

Fig. 2. The ultra-violet band systems of CrH.

The infra-red band system is shown in Fig. 1. The following heads have been measured.

$v'v''$	λ (Å)	σ (K)	Int.
2.0	6892	14505	1
1.0	7642	13082	4
0.0	8611	11610	10
1.1	8696	11497	3
0.1	9966	10031	3

The position of the heads is described by the following equation

$$\sigma_{v',v''} = 11610 + 1497\ v' - 25\ v'^2 - 1582\ v''.$$

The ΔG values obtained are of the expected size for CrH. If we assume that the observed lower state is the ground-state we may compare $\Delta G''_{\frac{1}{2}}$ with the corresponding value for MnH, which is 1491 K.

As far as can be seen from the low dispersion plates, the bands are single-headed and have a simple appearance. For CrH we expect low-lying electronic terms of high multiplicities, and it is not out of the question that the observed system represents a $^6\Sigma - ^6\Sigma$ transition.

The ultra-violet systems

In the spectrum of a high-tension arc between chromium electrodes in a flame of hydrogen GAYDON and PEARSE [2] found a single band of complicated nature which they ascribed to CrH. The band was degraded to the violet and had its strongest head at λ 3675 Å.

The spectrum from a King's furnace has now been photographed in a Hilger medium quartz spectrograph on Ilford Zenith plates. With an exposure time of a couple of seconds the 3675 Å band appeared, as well as another somewhat weaker band degraded to the red and with its strongest head at λ 3290 Å. The distance between the two bands indicates that they do not belong to the same electronic transition. The 3290 Å band is shorter than the other one and has, moreover, sharp limits to the red. It may be that this band is pre-dissociated and that the red limits represent cut-offs. There is, however, also the possibility that the branches on both sides of the origin have heads. We have measured the following heads:

3675 Å band			*3290 Å band*		
	λ (Å)	Int.		λ (Å)	Int.
Degr. to the violet	3706	5	Degr. to the red . . .	3280	2
Degr. to the violet	3678	10	Degr. to the red . . .	3290	5
Limits of the band: between the head at λ 3706 Å and the chromium line at 3579 Å			Degr. to the violet . .	3298	4 (cut-off?)
			Degr. to the violet . .	3318	3 ,,
			Degr. to the violet . .	3324	1 ,,
			Limits of the band: between the heads at λ 3280 Å and λ 3324 Å		

Physics Department, University of Stockholm, November 1954.

REFERENCES

1. KLEMAN, B., and LILJEQVIST, B., Arkiv för Fysik *9*, 377 (1954).
2. GAYDON, A. G., and PEARSE, R. W. B., Nature, *140*, 110 (1937).

Tryckt den 1 mars 1955

Uppsala 1955. Almqvist & Wiksells Boktryckeri AB

ARKIV FÖR FYSIK Band 9 nr 22

Communicated 12 January 1955 by AXEL E. LINDH and HARALD NORINDER

The anomalous X-ray transmission through a crystal on both sides of the K absorption edge of an element in the crystal

By GÖSTA BROGREN and CARL NORDLING

With 2 figures in the text

In an earlier investigation [1] of the anomalous X-ray transmission through calcite a theoretical derivation of the intensity of the transmitted beam was carried out. It was found that the anomalous transmission is caused by the anomalous contributions to the atomic scattering factors which can be calculated from HÖNL's equations [2–3]. The intensities of the transmitted as well as of the Laue reflected radiation are functions of a product ($\varkappa A$), where $\varkappa$ is the ratio between the imaginary and the real parts of the crystal structure factor and A a factor that depends on the wavelength. The anomalous contributions to the atomic scattering factor are greatest around the critical K absorption wavelength. The imaginary part has its maximum on the short wave side of the K edge but is nil on the long wave side of it. This gives us an experimental possibility of checking the theoretical predictions qualitatively by investigating the anomalous X-ray transmission through a crystal where the wavelength of the K absorption edge of one of the elements that build up the crystal is much shorter than those of the other elements. The factor $\varkappa$ will reach its maximum value on the short wave side of this edge but it will be very small on the long wave side of it. If an investigation is carried out with two wavelengths, λ_1 and λ_2, one on each side of the edge, the factor A will be kept nearly constant if the difference $\lambda_2 - \lambda_1$ is slight. The changes in the shapes of the transmission curves must then be due to the variation in the factor $\varkappa$. When $\varkappa$ is small, a pure extinction effect should be obtained, i.e. the sum of the intensities of the transmitted beam and the beam reflected through the crystal should be constant when the crystal is cut for symmetric Laue reflection.

The theory is valid only for perfect crystals. This has also been verified by investigations of the transmission through calcite and quartz crystals in a wavelength range on the short wave side of the K absorption edges rather far from the shortest edge. In an ideal mosaic crystal there appears only a pure extinction effect. The real crystals are built up as intermediate forms between the perfect crystal type and the ideal mosaic one. Single perfect crystal specimens have been found only among calcite and quartz crystals.

When the real crystal is an intermediate form between the two above types, the anomalous transmission pattern must be smoothed out more or less. In some cases, for instance the topaz crystal, the form of the pattern is clearly distinguishable, though the structural details are broadened and the peaks depressed (G. BROGREN *et al.* To be published). In other crystals like mica and rock salt, the mosaic structure

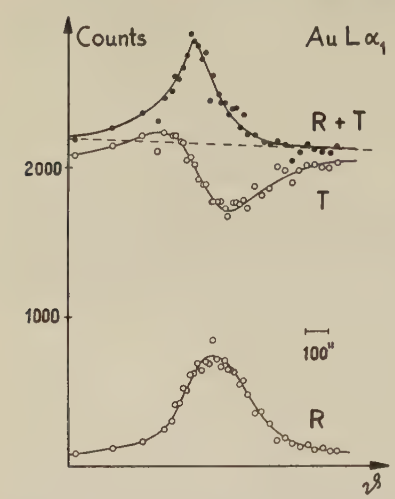

Fig. 1. Recordings with Au $L\alpha_1$ radiation.

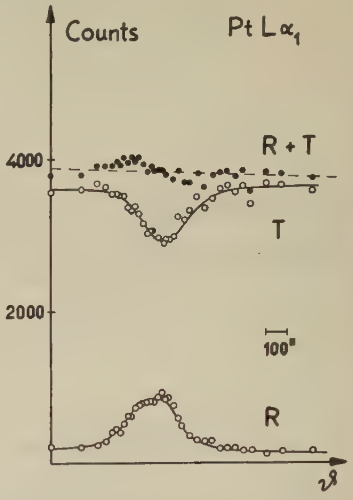

Fig. 2. Recordings with Pt $L\alpha_1$ radiation.

R is the intensity of the Laue reflected beam. T is the intensity of the transmitted beam. The background counts are not withdrawn. The normal sum of R and T is indicated by a dotted line. This is leaning due to the fact that the path through the crystal increases with increasing glancing angle.

is so pronounced that only a pure extinction effect appears. The experimental conditions for obtaining the anomalous transmission are greatly improved if the investigation can be carried out in the region around a critical K absorption edge where the effect has its extreme values. It ought to be possible to check the theory qualitatively even for a rather mosaic crystal if the sum of the intensities of the transmitted and the Laue reflected intensities is investigated on each side of the edge.

The double-crystal spectrometer available for the investigation was constructed for work in air. Wavelengths over 2000 X.U. could not be used. By courtesy of the head of the Mineralogical Department of the Royal Swedish Museum of Natural Sciences (Riksmuseet), Professor F. Wickman, we were able to make an investigation with zinc blende crystals. This crystal belongs to space group T_d^2 and is rather easily cleavable along the (110) plane. The unit cell contains four molecules ZnS. The coordinates of the atoms are:

Zn atoms: $000,\ 0\tfrac{1}{2}\tfrac{1}{2},\ \tfrac{1}{2}0\tfrac{1}{2},\ \tfrac{1}{2}\tfrac{1}{2}0;$
S atoms: $\tfrac{1}{4}\tfrac{1}{4}\tfrac{1}{4},\ \tfrac{1}{4}\tfrac{3}{4}\tfrac{3}{4},\ \tfrac{3}{4}\tfrac{1}{4}\tfrac{3}{4},\ \tfrac{3}{4}\tfrac{3}{4}\tfrac{1}{4}.$

The investigation was carried out with Au $L\alpha_1$ radiation (wavelength 1274 X.U.) and Pt $L\alpha_1$ radiation (wavelength 1310 X.U.), using the (220) reflections. The wavelength of the critical K absorption edge is for zinc 1280.5 X.U. and for sulphur 5008 X.U. If the crystal structure factor and $\varkappa$ are calculated in the usual manner we obtain for Au $L\alpha_1$ $\varkappa = 0.14$ and for Pt $L\alpha_1$ $\varkappa = 0.014$. According to the theory we should get a pronounced extinction effect for the latter radiation but anomalous transmission in the first case. (The calculations are made for the thickness 0.1 mm.)

The investigation was carried out with the monochromator crystal adjusted for Bragg reflection and the analyser crystal for symmetric Laue reflection. The zinc blende crystal, obtained from Picos de Europa in Spain, had a honey-yellow colour due to iron impurities. The monochromator crystal was obtained by cleavage. A pair of split faces were adjusted in Bragg-Bragg position and the rocking curve registered. The great breadth, 90 seconds of arc, indicated that the crystal was very mosaic. The width was independent of the irradiated area when this varied between 0.2 and 3.0 mm^2.

As transmission crystal we first used a crystal lamina, 0.2 mm thick, which was split off from a larger crystal. This thickness was too great, so that nearly all radiation was absorbed. A larger crystal was ground to a thickness of 0.1 mm, its unground surface being a cleavage face. It was fixed into the crystal holder and adjusted until the front face (i.e. the cleavage face) and the cleavage direction perpendicular to it were parallel to the rotation axis of the holder. (It should be mentioned that the qualities of the ground surface could not be improved by subsequent etching.)

The intensities of the transmitted and the Laue reflected beams were registered simultaneously with two Geiger-Müller counters. The latter were carefully compared so that their relative sensitivity was well known. Fig. 1 gives the results obtained with Au $L\alpha_1$ radiation and Fig. 2 those with Pt $L\alpha_1$. The reflection curves are much broader than those obtained with two split faces in Bragg-Bragg position. The mosaic structure of the transmission crystal broadens the curves much more. Partly this may be due to defects introduced by grinding. Between the two registrations there are some differences. In the registrations with Au $L\alpha_1$, the wavelength of which is shorter than that of the zinc K absorption edge, there is a slight maximum in the transmission curve, followed by a pronounced minimum. The maximum in the reflection curve does not fall on the same glancing angle as this minimum but is displaced towards a smaller glancing angle. When the values of the reflected and the transmitted intensities are added together, we obtain a curve with a distinct maximum. Pt $L\alpha_1$ has a wavelength that falls above the K edge of zinc. The transmission curve has no maximum and its minimum occurs at the same glancing angle as the maximum in the reflection curve. The sum intensity curve is a straight line. These results show that in accordance with the predictions of the theory there is no anomalous transmission on the long wave side of the K edge of zinc.

Since the crystal has a very pronounced mosaic structure, no quantitative comparison with the theory can be made. Our intention is to carry out a similar investigation of the anomalous transmission in calcite on both sides of the K absorption edge of calcium. This crystal is nearly perfect so that both qualitative and quantiative comparisons with the theory can be made. A vacuum double crystal spectrometer intended for this purpose is under construction.

We want to express our gratitude to Professor F. WICKMAN for the loan of the zinc blende crystals.

Physics Department, University of Uppsala, Sweden, November 1954.

REFERENCES

1. G. BROGREN, and Ö. ADELL, Ark. f. Fys. *8*, 97 (1954).
2. H. HÖNL, Zs. f. Phys. *84*, 1 (1933).
3. —— Ann. der Phys. *18*, 625 (1933).

Tryckt den 1 mars 1955

Uppsala 1955. Almqvist & Wiksells Boktryckeri AB

ARKIV FÖR FYSIK Band 9 nr 23

Communicated 24 November 1954 by Ivar Waller

A note on mean life-time determinations on small samples of radioactive nuclei

By G. Ekspong

Introduction

The widely used method for determining half-lives of radioactive substances by following the decay curve $\frac{\Delta N}{\Delta t}=\left(\frac{dN}{dt}\right)_0 e^{-kt}$ is not applicable to extreme cases, as when the number of radioactive atoms is very small, or when the half-life is very long.

It is possible by statistical methods to derive formulae that are quite general, and therefore applicable to all cases. Treatments of this kind may be found in the papers by Peierls [1], Bartlett [2, 3], Hole [4, 5], Ruark and Devol [6], and Schiff [7]. This note is intended to draw attention to a useful relation first given by Peierls, and to derive the same relation in an elementary way.

Discussion on the experimental method

It seems obvious that the maximum amount of information about the half-life, or alternatively the mean life-time, is obtained by designing the experiment so as to give the life-time of each individual particle recorded. The conventional method of determining the number of counts in successive finite time-intervals will yield less information. When the experiment deals with a very limited number of disintegrations it may be important to obtain as much information as possible. The experiment starts at the time $t=0$ with an unknown number, N_0, of active atoms. The experimental information consists of individual life-times, $t_1, t_2, \ldots t_m$. During the total time of observation T the total number of counts is m. In references [1, 2, 3, 4, 5, 8] a formula is derived from which the best value of k may be obtained:

$$\frac{1}{kT}-\frac{1}{e^{kT}-1}=\frac{\frac{1}{m}\Sigma t_i}{T}, \tag{1}$$

where k is the decay-constant to be determined. Formula (1) is derived as a maximum-likelihood estimator in the case when background counts may be neglected. It may be changed into another form, by introducing $T_0=\frac{1}{m}\Sigma t_i$, where T_0 is the observed or apparent mean life-time, and $\frac{1}{k}=\tau$, where τ is the best estimated value of the mean life-time:

$$\tau=T_0+\frac{T}{e^{\frac{T}{\tau}}-1}. \qquad (2)$$

Formula (2) shows that, in the first approximation, $\tau=T_0$, the experimentally obtained mean life-time, provided the measurements have been taken on a time $T\gg\tau$. The solution of (2) may be obtained by successive approximations. The correction term is due to the finite observation time, T. It should be emphasized that (2) does not include the unknown N_0.

An elementary deduction of formula (2)

The rigorous treatments given for instance by BARTLETT [2, 3], HOLE [4, 5], and RANKIN [8] may obscure the very elementary character of relation (2).

It occurred to the author that as Eq. (2) contains the mean observed life-time, it should be possible to derive the relation direct from the formula describing the mean decay $N=N_0 e^{-kt}$, thus disregarding fluctuations. When the finite observation time is T, one gets the mean observed life-time

$$T_0=\frac{\int_0^T t\,|dN|}{\int_0^T |dN|}=\frac{\int_0^T te^{-kt}\,dt}{\int_0^T e^{-kt}\,dt}.$$

By evaluating the expression, the relation $T_0=\frac{1}{k}-\frac{T}{e^{kT}-1}$ is obtained, which has the same form as Eq. (2). If the integration is extended to $T\to\infty$ the well-known relation $\tau=\frac{1}{k}$ is obtained. The above deduction, however, does not reveal the fact that Eq. (1) is a sufficient estimator for k. A similar, but not quite as direct a deduction is given by FRETTER *et al.*, in a paper on Neutral V-particles [8].

Accuracy

The above simplified deduction of relation (2) does not state anything about the accuracy. One has to go back to the rigorous treatment in order to get an estimation of the error; e.g., formula (8) in HOLE's paper [5] gives the standard deviation in the case of a large number of counts, or one can consult Table I of PEIERL's paper, or Table I of BARTLETT's paper [3]. As to a small number of counts (e.g. $m\lesssim 10$–25) no simple expression for the error exists. In the following a comparison of two methods is made. It is supposed that the number of counts, m, is sufficiently great to allow the use of asymptotic formulae for the errors.

The two methods are: 1, all individual life-times are measured and k solved y Eq. (1); 2, the number of counts (X_i) are taken during successive timentervals of length l, and k solved by Eq. (11) of Hole's paper [5].

In both cases the error will depend particularly on the total number of counts, . Background is neglected in this treatment. One may write the relative tandard error of the mean life-time as $\frac{A}{\sqrt{m}}$. By comparing the values of A iven by the two methods their relative merits may be judged.

To be specific, one example is worked out; it is assumed that the mean lifeime is $\tau = 33.3$ min. and the total observation time $T = 100$ min. The relative tandard errors may be found in the Table.

	Method 1 (m individual life-times)	Method 2 (intervals $=l$ min.)	
		$l=5.0$ min.	$l=8.35$ min.
Rel. standard error	$\frac{1.409}{\sqrt{m}}$	$\frac{1.411}{\sqrt{m}}$	$\frac{1.414}{\sqrt{m}}$

It is to be seen that for large m the gain arrived at by using Method 1 is egligible. As for small m, the situation is complicated, and no comparison has een made. Bartlett (1953), dealing with the estimation of the mean lifeimes of unstable cosmic ray particles, gives a fairly simple method to derive confidence interval for τ. However, one advantage of Eq. (2) in the case of small number of counts is the simplicity of the equation and the fact that Eq. (2) offers all the information about τ that the observations can give, irespective of the number of counts. The background counts are disturbing in ll methods of estimation. In case the background correction is small, it is uggested to eliminate at random a number of counts corresponding to the executed background.

A comparison with the accuracy obtained by graphical methods is not posible since it is difficult to estimate the error in that case.

Institute of Physics, University of Uppsala, Sweden, October 1954.

REFERENCES

1. Peierls, R., Proc. Roy. Soc. A, *149*, 467 (1935).
2. Bartlett, M. S., Proc. Roy. Soc. A, *154*, 124 (1936).
3. ——, Phil. Mag. *44*, 249 (1953).
4. Hole, N., Arkiv f. Mat. Astr. o. Fysik Bd *34 B*, No. 12 (1947).
5. ——, Arkiv f. Fysik *Bd 3*, No. 25 (1952).
6. Ruark, A., and Devol, L., Phys. Rev. *49*, 355 (1936).
7. Schiff, L. I., Phys. Rev. *50*, 88 (1936).
8. Fretter, W. B., May, M. M. and Nakada, M. P., Phys. Rev. *89*, 168 (1953), (including remarks on results given by B. Rankin).

Tryckt den 1 mars 1955

Uppsala 1955. Almqvist & Wiksells Boktryckeri AB

ARKIV FÖR FYSIK Band 9 nr 24

Communicated 13 October 1954 by Oskar Klein and Erik Hulthén

A quantum theoretical study of the covalent boron-boron bonds in crystals of some metal borides

By Stig Flodmark

With 9 figures in the text

Contents

Page

Summary 357

1. Introduction 358

2. Methods of calculation 360

3. The method of maximum probability of orbital composition 361

4. The charge distribution 364

5. Charge density in the case of configurational interaction 365

6. The method of maximum charge density 367

7. Variation of the effective charge 371

8. Discussion of the results 372

Appendix I: The correspondence between the Zimmerman & van Rysselberghe determinantal wave function and Pauling's directed orbitals of tetrahedral carbon 374

Appendix II: Calculation of the D_{kl} functions 375

References 376

Summary[1]

The electronic distribution around the boron atoms in metal borides with stable space lattices has been theoretically determined and interpreted as covalent bonds in the directions of adjacent boron atoms. Two methods have been used. In the first method the wave function is assumed to have an extreme value, when the valence electrons of a given boron atom are located in the bond directions. Hydrogen-like atomic orbitals (AO's) have been used. There is reason to believe that the metal atoms are ionized, with the result that every boron atom has between three and four valence electrons instead of three as usual. As it is impossible in this case to compose an antisymmetric wave function for the electrons of one atom, the electron density has also been determined by the condition of maximum values in the bond directions. Both methods gave the result that the excited $3d$ orbitals play an important role in describing the bonds, as they make it possible to arrange the electrons according to the

---

[1] A preliminary report has been published in J. Chem. Phys. 22 (1954) 1950.

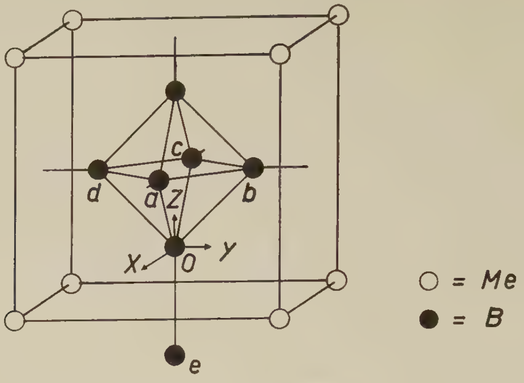

Fig. 1. Part of the MeB_6 crystal. The five B atoms equidistant from the one denoted by O are numbered *a b c d e*.

crystallic symmetry. However, the approximations made probably give an overestimation of this effect. By using the method of maximum density the excited orbitals were found to dominate almost completely. In spite of this, variation of the effective charge parameter of the *d* orbitals gave interesting results.

1. Introduction

Experimental investigations of the borides of some transition elements have been made by KIESSLING [1]. He studied the electron density by means of X-rays. The types of borides investigated experimentally are as follows, mainly in order of increasing percentage of boron:

1. Metal lattices that without being deformed can "alloy" unlimited quantities of boron.
2. Crystals of Me_2B type. The metal atoms (Me) occupy stable layers of tetrahedra with the boron atoms (B) loosely filling up the interstices.
3. Crystals of MeB type. Me forms different types of trigonal prism lattices and B forms simple zig-zag chains in the channels of the Me lattice. The proportion between B and Me varies slightly.
4. Crystals of Me_3B_4 type. B forms hexagonal double chains with the atomic radius a little shorter in the directions of bonds connecting two simple chains (double bonds).
5. Crystals of MeB_2 and Me_2B_5 types. B forms two-dimensional hexagonal nets with metal lattices in sheets between them.
6. Crystals of MeB_6 type and UB_{12}. B forms simple stable three-dimensional frameworks with Me at the interstices.

It is interesting to note the increasing stability of the B lattices with an increasing percentage of B in these crystals. Especially in the last types, where the metal atoms are situated at too great distances to be engaged in strong chemical bonds of covalent type, it is very remarkable that B forms such simple and stable frameworks. This is especially noteworthy, because the crystal structure of pure B is so complicated that it has not even been possible to determine it experimentally. In the borides with chains and nets there are planar types of bond formations, which can be described by sp hybridizations as has been done earlier for similar structures. The present author has therefore only been interested in the borides of MeB_6 type, the structure of which is seen in Fig. 1.

The Me atoms form a cubic lattice, each cube with six B atoms inside it, forming regular octahedra. Every B atom has five other adjacent B atoms at equal distances. The coordination number of Me is 24. According to [1], the shortest B–B distances of MeB_6 are almost independent of the participating metals, as is seen in Table 1.

Table 1. Distances between adjacent atoms in MeB_6, cf. Kiessling [1], Table 9.

Me	Normal radius r_{Me}[1] (Å)	Shortest distance					
		B–B (Å)	$\frac{\text{B–B}}{2 r_B}$	Me–B (Å)	$\frac{\text{Me–B}}{r_B + r_{Me}}$	Me–Me (Å)	$\frac{\text{Me–Me}}{2 r_{Me}}$
(B)	(0.87)						
Ba	2.22	1.78	1.02	3.16	1.02	4.29	0.97
Sr	2.15	1.74	1.00	3.09	1.03	4.20	0.98
Ca	1.97	1.72	0.99	3.06	1.08	4.15	1.05
Yb	1.93	1.71	0.98	3.05	1.09	4.14	1.07
La	1.87	1.72	0.99	3.06	1.12	4.15	1.11
Ce	1.82	1.71	0.98	3.05	1.13	4.14	1.14
Nd	1.82	1.71	0.98	3.04	1.13	4.13	1.14
Pr	1.82	1.71	0.98	3.04	1.13	4.13	1.13
Gd	1.80	1.71	0.98	3.04	1.14	4.13	1.15
Th	1.80	1.72	0.99	3.07	1.15	4.16	1.16
Y	1.80	1.69	0.97	3.01	1.13	4.08	1.14
Er	1.75	1.70	0.98	3.03	1.16	4.11	1.18

[1] Values given by Pauling [2] for twelvefold coordination of Me.

When the values of the ratios in Table 1 are less than 1, it is reasonable to assume that there are strong covalent bonds. Thus the B–B bonds are strong in all cases reported in the table. It therefore seems natural to make an investigation of covalent B–B bonds in the crystal. An attempt to explain the stability of MeB_6 has been made in the present work by assuming Me to have lost (part of) its valence electrons in accordance with Pauling's theory [3].

A theoretical investigation of the electronic structure of MeB_6, carried out by Longuet-Higgins and de V. Roberts [4], was published after the completion of the present work. By assuming that the valence electrons occupy the B_6 octahedra, these authors used the molecular orbital (MO) method, which gave the result that there were twenty bonding orbitals for every B_6 octahedron, the others being anti-bonding. This would give a closed-shell description of the eighteen valence electrons of B combined with two ionized electrons of Me. The results were also confirmed by a treatment by means of Bloch functions. Thus, these authors have found that the stability of the borides depends on ionization of the Me atoms, which is also a result of the present investigation.

In the present investigation two different methods have been used (see Sections 3 and 6). In spite of the many obvious approximations interesting results have been obtained which might provide material for new views in addition to the results of [4]. In [4] special attention has been devoted to obtaining the energy levels, whereas the present methods yield the electronic distribution. The orbitals in the present investigation have been chosen in agreement with the symmetry of the crystal, which necessitates the presence of d orbitals neglected in [4]. The present work thus presents some new points of view on the problem and may therefore be found suitable for publication.

2. Methods of calculation

The correct wave function describing the electronic distribution in a molecular structure can only be found by solving the complete SCHRÖDINGER equation with the kinetic and potential energy operators arising from the whole system of electrons and nuclei. It is in most cases a practical impossibility to obtain the accurate solution of this problem, and many approximations must be made. The present investigation only considers the SCHRÖDINGER wave equation of the three valence electrons relative to a B atom. The solution is formed as an antisymmetric sum of products of atomic orbitals (AO's) of the $2s$, $2p$ and $3d$ types. A rough estimation of the electrostatic interaction between binding electrons of different atoms and between an electron and a neighbouring nucleus shows that this interaction is of the same order of magnitude as the electrostatic energy of a free B atom. This means that the electrons of the B atoms in the crystal are decoupled and, thus, it is not sensible to talk about atomic states of the B atoms in the crystal.

To find suitable hybrid atomic orbitals (HAO's), which are linear combinations of simple AO's, it would be satisfactory if it were possible to use the variation principle. However, there are several difficulties. As a matter of fact, the potential energy arising from adjacent atoms is not known. In these circumstances it is necessary to rely on less satisfactory approximate methods. In the present paper certain forms of valence bond (VB) methods have been used. It is reasonable to assume that the energy of the whole system will be less, the larger the bond energy of the molecular structure is. A minimum of the total energy then corresponds to a maximum of the bond energy, and the variation principle corresponds to the *condition of maximum bond strength*. Many approximate methods exist built on this basis, the one most often applied being the *condition of maximum overlapping*, originally formulated by PAULING [5] and subsequently revised by MACCOLL [6].

It is interesting to note that it is not necessary to form PAULING's directed HAO's [5] in order to obtain the corresponding approximate wave function of the system. The same result can be reached by considering the complete antisymmetric wave function of AO's of a single atom, the condition being that the wave function shall have an extreme value, when the electrons are located in the bond directions. This was found independently by ARTMANN [7] and by ZIMMERMAN and VAN RYSSELBERGHE [8]. The principle may be referred to as the equivalent *condition of maximum probability of orbital composition*, since the squared wave function reaches an extremum at the same time as the wave function itself (cf. (3) in the next section). LINNETT and POË [9] used the notation of electronic *configuration of maximum probability* for the corresponding wave function. According to this method, tetrahedral carbon, for example, can be described with a determinant of the SLATER type, formed by four simple AO's s, p_x, p_y and p_z of the L shell. The corresponding determinant, formed by PAULING's non-orthogonal sp HAO's, which are concentrated in the tetrahedral directions, is directly proportional to the determinant of [8] (see App. I). The method has the advantage that the radial parts need not be neglected, which is the case with PAULING's directed orbitals. By assuming the electrons to be distributed on the surface of a sphere, the radial functions can be taken outside the determinant. In the present treatment this method has been adopted by way of a preliminary trial (see the next section). However, the presence of an sd HAO in the determinantal wave function here necessitates some additional approximation of the radial function. Some of the inadequacies of this method have recently been pointed out by TA-YOU WU [10].

Another alternative condition, known as the *condition of maximum penetration*, is suggested by FISCHER [11]. Here the bond-forming power of a valence electron is supposed to depend mainly on the potential field of the nuclei suitably screened by the other electrons.

A new approximate treatment of the VB theory has been introduced by McWEENY [12]. This treatment is based on grounds similar to the above-mentioned principle. Attention is drawn here to the importance of the charge distribution in the formation of covalent bonds. This affords satisfactory support for the second principle used in the present paper, named the *condition of maximum charge density.* However, the results of this method can only be qualitative, since the valence electrons of one single atom alone are considered.

3. The method of maximum probability of orbital composition

In this section, the wave function is determined by the condition that the probability of finding the valence electrons in the five directions of neighbouring B atoms should be as great as possible. These directions, which we denote by $a\ b\ c\ d\ e$ (cf. Fig. 1), can be described by spherical angles as follows:

$$\begin{aligned} &\vartheta_a=\vartheta_b=\vartheta_c=\vartheta_d=\pi/4, \quad \vartheta_e=\pi, \\ &\varphi_a=0, \quad \varphi_b=\pi/2, \quad \varphi_c=\pi, \quad \varphi_d=3\pi/2. \end{aligned} \tag{1}$$

The ground state of the B atom, which has five electrons, is $(1s)^2(2s)^2(2p)$. We now construct an approximate three-electron wave function, Ψ, of the three valence electrons as an antisymmetric product of real one-electron HAO's, χ_1, χ_2 and χ_3:

$$\Psi(123)=\frac{1}{\sqrt{3!}}\,\mathrm{Det}\,\chi_i(k), \qquad (i, k=1, 2, 3). \tag{2}$$

The orbital numbers i and the electron numbers k here correspond to row and column numbers respectively of the determinantal elements, and k stands for the space vector of the kth electron in the ordinary space. According to DIRAC [13], the probability density of finding the electrons at three given points, 1, 2 and 3, is:

$$P(123)=\frac{1}{3!}\,\mathrm{Det}\sum_k \chi_k(i)\,\chi_k(j), \qquad (i, j=1, 2, 3). \tag{3}$$

It will readily be seen that this is merely the square of the wave function (2). (3) will then reach maximum values at the same time as (2) attains extreme values. We now assume that the maximum bond strength is equivalent to the maximum probability of finding the electrons in three of the five bond directions. This corresponds to the methods [7] and [8]. Let us write the HAO's as linear combinations of simple AO's:

$$\chi_k=\sum_i C_{ik}\,\Phi_i.$$

The Φ_i's are chosen from the hydrogen-like AO's

$$\begin{aligned}&\Phi_1=(2s)=s, \quad \Phi_2=(2p_x)=p_x, \quad \Phi_3=(2p_y)=p_y,\\ &\Phi_4=(2p_z)=p_z, \quad \Phi_5=(3d_{z^2})=d_{z^2}, \quad \Phi_6=(3d_{x^2-y^2})=d_{x^2-y^2}.\end{aligned} \tag{4}$$

(4) are those orbitals of the lowest energy outside the K shell, which have the symmetrical properties required by the experimentally determined atomic arrangement. In the following, we write them without the principle quantum number. An eligible set of orthonormalized HAO's is as follows:

$$\chi_1=p_z, \quad \chi_2=d_{x^2-y^2}, \quad \chi_3=\frac{1}{\sqrt{1+C^2}}\,(s+C\,d_{z^2}),$$

where C is a suitably chosen parameter. χ_3 is the only hybridized orbital, and we introduce some approximation of its radial part. Following PAULING and HULTGREN [14], we write the radial parts equal for the s and d_{z^2} functions, although the approximation is still less exact here, because s and d have different principal quantum numbers:

$$d_{z^2}=\frac{\sqrt{5}}{2}\,(3\cos^2\vartheta-1)\,s.$$

The angular part of d_{z^2} thus is normalized to 4π. If, in accordance with [7] and [8], we now neglect the radial correlation and assume the electrons to be located on a spherical surface, we can take the radial part as a factor outside the three-electron wave function. This is, of course, a rough approximation in our case. In spherical coordinates of the three electrons, and with $r_1=r_2=r_3=r$, we obtain:

$$\Psi=f(r)\,\mathrm{Det}\left\{\begin{matrix}\cos\vartheta_k\\ \sin^2\vartheta_k\cos 2\varphi_k\\ 1+C\dfrac{\sqrt{5}}{2}\,(3\cos^2\vartheta_k-1)\end{matrix}\right\}, \qquad (k=1, 2, 3), \tag{5}$$

where k indicates a column of the determinant. With the value of

$$C=(5+3\sqrt{2})/\sqrt{5}=4.13,$$

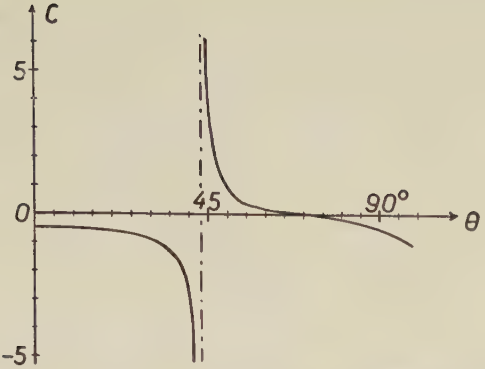

Fig. 2. The coefficient C of d_{z^2} in χ_3, found by the method of maximum probability of orbital composition, and given as a function of the crystallic angle θ.

the angular part of (5) has (equal) maxima, when the electrons occupy the following combinations of directions:

$$abe,\quad bce,\quad cde,\quad dae.$$

For the other combinations of three of the five bond directions

$$ace,\quad bde,\quad abc,\quad bcd,\quad cda,\quad dab,$$

Ψ equals zero. This can be interpreted in the way that one electron manages the b and d bonds, another the a and c bonds and the third the e bond. Thus two electrons can never occupy either the a and c directions or the b and d directions simultaneously. We can write (5) in a form in which the directional properties of the three orthogonal bonding orbitals are seen more clearly (cf. App. I):

$$\Psi=\frac{1}{\sqrt{3!}}\,\mathrm{Det}\begin{vmatrix} \frac{1}{2\sqrt{1+C^2}}\left(s+C\,d_{z^2}+\sqrt{1+C^2}\,p_z-\sqrt{2\,(1+C^2)}\,d_{x^2-y^2}\right)\\ \frac{1}{2\sqrt{1+C^2}}\left(s+C\,d_{z^2}+\sqrt{1+C^2}\,p_z+\sqrt{2\,(1+C^2)}\,d_{x^2-y^2}\right)\\ \frac{1}{\sqrt{2\,(1+C^2)}}\left(s+C\,d_{z^2}-\sqrt{1+C^2}\,p_z\right) \end{vmatrix}.$$

The high value of $C=4.13$ causes almost two of the three valence electrons to assume excited d states. If, however, we abandon the condition that the four "upper" bond directions shall form the angle $\vartheta=45^\circ$ with the z direction, and simply use the notation θ for the common angle, we obtain the following connection between C and θ corresponding to maximum probability of orbitals in the directions thus distorted:

$$C=\frac{3\cos\theta-1}{\sqrt{5}\,(1+3\cos\theta-6\cos^2\theta)}.$$

The diagram $C(\theta)$ is seen in Fig. 2.

If we wish to make all the bonding orbitals equivalent in the sense that they shall have equal bond strengths[1], we find the values of $C=0.04$ and $\theta=69^\circ$. On account of repulsion between the "upper" orbitals, the θ value may really be expected to be somewhat greater than 45° (but less than 60°), the bonds being assumed to be curved. From Fig. 2 we see that the extension of θ to 50° gives $C \approx 1$, which yields 50 % d orbitals. The corresponding orbitals are:

$$\chi_{b,\,d}=0.35\,s+0.35\,d_{z^2}+0.50\,p_z-0.71\,d_{x^2-y^2},$$

$$\chi_{a,\,c}=0.35\,s+0.35\,d_{z^2}+0.50\,p_z+0.71\,d_{x^2-y^2},$$

$$\chi_e=0.50\,s+0.50\,d_{z^2}-0.71\,p_z,$$

with the bond strengths[1] $B(\chi)$:

$$B(\chi_{b,\,d})=B(\chi_{a,\,c})=0.35+0.14+0.55+0.81=1.85,$$

$$B(\chi_e)=0.50+1.12+1.23=2.85.$$

It seems to be natural that the e bond should be stronger than the other four equivalent bonds.

4. The charge distribution

In order to compare the result of the last section with that which has been found by using the method of maximizing the charge density (see Section 6), we compute the charge density corresponding to our wave function. This is:

$$\varrho=3\iint \Psi^*\,\Psi\,d\tau_2\,d\tau_3, \tag{6}$$

where τ_k is the vector space of the kth electron. For a wave function formed by a single determinant, as in the preceding section, this is identical with the diagonal element

$$\varrho=\sum_k \chi_k^2 \tag{7}$$

of DIRAC's charge density matrix [13]. Using the wave function of Section 3 for $\theta=45^\circ$, we obtain the following charge distribution of the valence electrons of one B atom:

$$\varrho=p_z^2+(d_{x^2-y^2})^2+0.0045\,s^2+0.95\,(d_{z^2})^2+0.41\,s\,d_{z^2}.$$

This function is unchanged by reflection in the xy plane and is at a maximum in the z direction ($\vartheta=0$), and a minimum in the xy plane ($\vartheta=\pi/2$), for arbitrary values of the spherical coordinates, r and φ. Other maxima occur, when $\varphi=0,\ \pi/2,\ \pi,\ 3\pi/2$, independently of r and ϑ. The radial distance of the sur-

---

[1] The bond strengths are calculated according to PAULING's definition [5], which gives a rough estimation of the bonding energy.

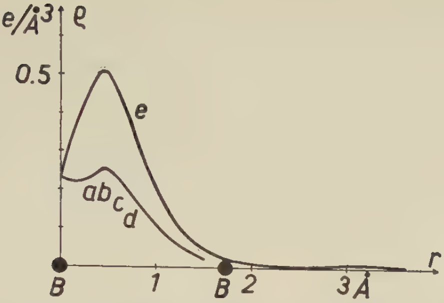

Fig. 3. The charge density of the valence electrons, ϱ, found by maximizing Ψ, and given as a function of the atomic distance r in the five bond directions.

face of maximum density only depends to a small extent on the direction. The diagrams of Fig. 3 give $\varrho(r)$ in the five directions (1).

It will be seen that the p_z electron contributes largely to the maximum charge density between the B nuclei. The other valence electrons have their maxima at distances, much greater than the shortest B–B distance. It is therefore very probable that the remote d orbitals are in reality bent, being distorted by even more distant B atoms. LÖWDIN [15], for example, has pointed out the great importance of taking more distant atoms into account. In our case, the d orbitals would more probably belong to the whole B_6 octahedron in form of MO's (cf. LONGUET-HIGGINS [4]). The large amount of d electrons might explain the electric conductivity of MeB_6.

Thus far, we have not considered the role of Me. Next, we shall assume the crystal to be ionized (see Section 7) and make an investigation as to how this alters the electronic distribution near a B atom. Here too, we shall only take into account the nearest B neighbours which are assumed to give the bond directions of a single atom. However, the number of electrons per atom is no longer an integer, and we are not able to write an antisymmetric wave function of the electrons of one atom only. We shall therefore rest content with the rough method of studying the charge density of the electrons of one single atom. As a preparatory step, in the next section we start by expressing the connection between a three-electron wave function, composed of the AO's (4), as a linear combination of the possible SLATER determinants (configurational interaction) and the corresponding charge density.

5. Charge density in the case of configurational interaction

Now, we write the wave function

$$\Psi = \sum_k c_k D_k, \tag{8}$$

where c_k are constants and D_k $(k = 1, 2 \ldots, 20)$ are the possible SLATER determinants, composed of the six AO's (4). The D functions are numbered according to the following table:

D	Φ
1	123
2	124
3	125
4	126
5	134
6	135
7	136
8	145
9	146
10	156
11	234
12	235
13	236
14	245
15	246
16	256
17	345
18	346
19	356
20	456

This implies, for example, that

$$D_{20} = \frac{1}{\sqrt{3!}} \begin{vmatrix} \Phi_4(1) & \Phi_4(2) & \Phi_4(3) \\ \Phi_5(1) & \Phi_5(2) & \Phi_5(3) \\ \Phi_6(1) & \Phi_6(2) & \Phi_6(3) \end{vmatrix}.$$

Using (8), the charge density (6) will be

$$\varrho = 3 \int\int \sum_{ik} c_i^* c_k D_i D_k \, d\tau_2 \, d\tau_3 = \sum_{ik} c_i^* c_k \cdot 3 D_{ik}, \tag{9}$$

where we have introduced the notation

$$D_{ik} = \int\int D_i D_k \, d\tau_2 \, d\tau_3.$$

With the short notation $(p_i q_k)$ for the product of the pth AO of D_i and the qth AO of D_k, we obtain the following symbolic formula (see App. II):

$$3 D_{ik} = \frac{d}{d\tau} \operatorname{Det} \int (p_i q_k) \, d\tau,$$

which is to be understood as follows:

$$3 D_{ik} = \begin{vmatrix} (11) & (12) & (13) \\ \int(21) & \int(22) & \int(23) \\ \int(31) & \int(32) & \int(33) \end{vmatrix} + \begin{vmatrix} \int(11) & \int(12) & \int(13) \\ (21) & (22) & (23) \\ \int(31) & \int(32) & \int(33) \end{vmatrix} + \begin{vmatrix} \int(11) & \int(12) & \int(13) \\ \int(21) & \int(22) & \int(23) \\ (31) & (32) & (33) \end{vmatrix}. \tag{10}$$

Here we have omitted the indices i and k and the volume elements of integrations. By means of this formula, we can easily compute the D_{ik}'s. We note that most of the integrals cancel on account of the orthogonality of the Φ functions. By evaluating (9), we find that the charge density forms a homogeneous quadratic polynomial of the Φ_k's:

$$\varrho = \sum_{i \leq j = 1}^{6} C_{ij} \Phi_i \Phi_j. \tag{11}$$

There are 21 quadratic equations, which combine the C_{ij}'s with the 20 c_k's:

$$C_{ij} = C_{ij}(c_k), \qquad (i, j = 1, 2 \ldots, 6). \tag{12}$$

The total number of electrons, $\int \varrho \, d\tau = 3$, gives the condition

$$\sum_{k=1}^{6} C_{kk} = 3, \tag{13}$$

which corresponds to $\sum_{k=1}^{20} c_k^* c_k = 1$.

6. The method of maximum charge density

We shall now investigate the possibility of finding a charge density function of type (11) with maxima at equal distances from the origin and in the directions (1). According to McWeeny [12], the charge density plays an important part in the formation of covalent bonds, provided, however, that the whole system of electrons is taken into account. Thus, the method presented here is very rough, and the results should not be taken too literally. As a matter of fact, we see that the method used in Section 3 does not produce any density peaks in the bond directions. Similarly, for tetrahedral carbon (see App. I), the charge density of a single atom is spherically symmetrical.

For our purpose, we now write the AO's (4) in full as follows:

$$s = \frac{1}{2\sqrt{\pi}} R_s, \qquad p_x = \frac{1}{\sqrt{\pi}} R_p \Theta_{11} \cos \varphi,$$

$$p_y = \frac{1}{\sqrt{\pi}} R_p \Theta_{11} \sin \varphi, \qquad p_z = \frac{1}{\sqrt{2\pi}} R_p \Theta_{10},$$

$$d_{x^2-y^2} = \frac{1}{\sqrt{\pi}} R_d \Theta_{22} \cos 2\varphi, \quad d_{z^2} = \frac{1}{\sqrt{2\pi}} R_d \Theta_{20},$$

where the Θ_{nl} functions in ordinary notations are:

$$\Theta_{10} = \frac{\sqrt{6}}{2} \cos \vartheta, \qquad \Theta_{11} = \frac{\sqrt{3}}{2} \sin \vartheta,$$

$$\Theta_{20} = \frac{\sqrt{10}}{4} (3 \cos^2 \vartheta - 1), \quad \Theta_{22} = \frac{\sqrt{15}}{4} \sin^2 \vartheta.$$

The radial functions, R_{nl}, are:

$$R_s = R_{20} = \frac{1}{2\sqrt{2}} \left(\frac{Z_s}{a_0} \right)^{3/2} \cdot \left(2 - \frac{Z_s}{a_0} r \right) e^{-\frac{Z_s r}{2 a_0}},$$

$$R_p = R_{21} = \frac{1}{2\sqrt{6}} \left(\frac{Z_p}{a_0} \right)^{5/2} \cdot r \, e^{-\frac{Z_p r}{2 a_0}},$$

$$R_d = R_{32} = \frac{4}{81\sqrt{30}} \left(\frac{Z_d}{a_0} \right)^{7/2} \cdot r^2 \, e^{-\frac{Z_d r}{3 a_0}}.$$

Here a_0 is the radius of the hydrogen atom in the ground state, and the Z's are effective charges of the different orbitals, $Z_s = 2.68$, $Z_p = 2.41$ [16], and $Z_d = 1.0$ [17]. These values correspond to three valence electrons. To take ionization of Me into account, the value of Z_d will be decreased later on, because of the increased screening of the B nuclei.

In the expression of the charge density, we can immediately omit terms which do not have suitable symmetrical properties. Thus, we can write our charge density as follows:

$$\varrho = C_1 s^2 + C_2 (p_x^2 + p_y^2) + C_3 p_z^2 + C_4 s p_z + C_5 (d_{x^2-y^2})^2 + C_6 s d_{z^2} + C_7 p_z d_{z^2} + C_8 (d_{z^2})^2.$$

This function belongs to the same symmetry group, C_{4v}, as the atomic system. We denote the points of maximum values (cf. (1)) as follows:

$$\text{I}: \begin{cases} r = r^I, \\ \text{directions } abcd; \end{cases} \qquad \text{II}: \begin{cases} r = r^I, \\ \text{direction } e. \end{cases} \tag{14}$$

For, according to [1], the B–B distances are equal in all the bond directions. Furthermore, we assume the other points of extreme values to be given by

$$\text{III}: \begin{cases} r = r^{III}, \\ \vartheta = \pi/4, \\ \varphi = \pi/4,\ 3\pi/4, \\ \quad 5\pi/4,\ 7\pi/4; \end{cases} \qquad \text{IV}: \begin{cases} r = r^{III}, \\ \vartheta = \pi/2, \\ \varphi = \pi/4,\ 3\pi/4, \\ \quad 5\pi/4,\ 7\pi/4; \end{cases} \qquad \text{V}: \begin{cases} r = r^{III}, \\ \vartheta = 0. \end{cases} \tag{15}$$

Assuming these space points of extreme values, we get the following conditions, which are obtained by cancelling those partial derivatives in the points (14) and (15), which do not vanish identically:

$$\varrho_r'^{I} = \varrho_\vartheta'^{I} = \varrho_r'^{II} = \varrho_r'^{III} = \varrho_\vartheta'^{III} = \varrho_r'^{IV} = \varrho_\vartheta'^{IV} = \varrho_r'^{V} = 0.$$

Together with the normalization condition (13), we obtain nine equations, which can be written as follows:

$$C_1 + 2C_2 + C_3 + C_5 + C_8 = 3, \quad \sum_{k=1}^{8} a_{ik} C_k F_{ik}(r^I, r^{III}) = 0, \qquad (i = 1, 2 \ldots, 8), \tag{16}$$

where a_{ik} are numerical factors and $F_{ik}(r^I, r^{III})$ are products of the values of R_{nl} and their derivatives at the points of extreme values. The unknowns are r^I, r^{III} and the eight coefficients C_k, that is, there is one more unknown than the number of conditional equations. This is compensated by the system of equations (12), where we have one more equation than the number of unknowns. Hence, we note that if we also wish to determine the coefficients c_k of the determinants in the wave function, we have 20 + 10 unknowns and 21 + 9 equations, which, theoretically, might provide a possible solution. For convenience, however, only numerical solutions of (16) for different values of C_8 will be given. With $C_8 = 0$, the solution yields:

$$r^I = 0.855 \text{ Å}, \qquad r^{III} = 0.468 \text{ Å};$$

$$\begin{aligned} \varrho = {} & 0.00787\, s^2 + 0.00198\,(p_x^2 + p_y^2) + \\ & + 0.00360\, p_z^2 + 0.00464\, s\, p_z + \\ & + 2.985\,(d_{x^2-y^2})^2 - 0.321\, s\, d_{z^2} - 0.139\, p_z\, d_{z^2}. \end{aligned} \tag{17}$$

We find the values of the second derivatives of ϱ at the points of extreme values I, II and III in Table 2.

Table 2. Second derivatives of ϱ at the points of extreme values.

Point of extreme value	ϱ''_{rr}	$\varrho''_{r\vartheta}$	$\varrho''_{r\varphi}$	$\varrho''_{\vartheta\vartheta}$	$\varrho''_{\vartheta\varphi}$	$\varrho''_{\varphi\varphi}$
I.	−0.0028	0.0010	0	−0.0005	0	−0.0022
II.	−0.0260	0	0	−0.0151	0	0
III.	0.0266	0.0011	0	−0.0014	0	0.0003

The variation of ϱ at the points I,

$$\delta \varrho^I = \tfrac{1}{2}\left(\varrho''^I_{rr}\, \delta r^2 + \varrho''^I_{\vartheta\vartheta}\, \delta\vartheta^2 + 2\varrho''^I_{r\vartheta}\, \delta r\, \delta\vartheta + \varrho''^I_{\varphi\varphi}\, \delta\varphi^2\right),$$

is always negative, which really corresponds to genuine maxima. The extreme values of ϱ at the points (14) and (15) are:

$$\begin{array}{ll} \varrho^I = 0.00154 & (\text{max. point}), \\ \varrho^{II} = 0.00644 & (\;\;,,\qquad ,,\;), \\ \varrho^{III} = 0.00119 & (\text{saddle } ,,\;), \\ \varrho^{IV} = 0.00096 & (\text{min.}\quad ,,\;), \\ \varrho^{V} = 0.00104 & (\;\;,,\qquad ,,\;). \end{array}$$

The values of ϱ are measured in electrons per Å^3. We can demonstrate symbolically the charge density (17) of the three valence electrons in the surroundings of a B atom, as in Fig. 4. However, we see from Fig. 5, which

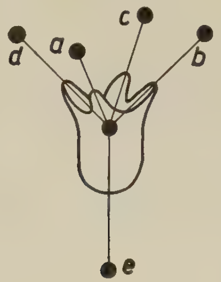

Fig. 4.

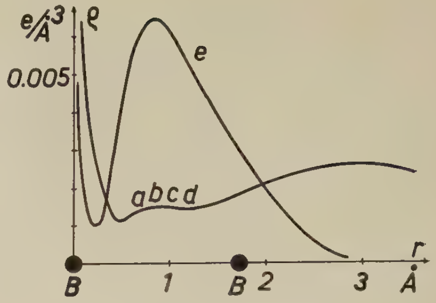

Fig. 5.

Fig. 4. The charge distribution in the surroundings of a B atom, found by maximizing ϱ. — Fig. 5. The charge density, ϱ, found by maximizing ϱ, and given as a function of the atomic distance r in the bond directions.

shows the radial dependence of ϱ in the bond directions, that the d electrons form a new maximum far beyond a bounded B atom. This might also be expected, when we make a comparison with the corresponding diagram in Fig. 3, obtained by the method of maximum probability of orbital composition.

As we see, (17) contains a remarkably large amount of squared $d_{x^2-y^2}$—almost all of the three electrons occupy this state. However, this is incompatible with the PAULI exclusion principle, which disallows more than one electron being in a certain state. (Only one of the two possible spin states is here assumed to be occupied, on account of electron pair bonding with electrons of adjacent atoms.) Since the wave function satisfies the PAULI principle, we must find contradictions in the system of equations (12). In fact, this can easily be shown by investigating five of these equations. Furthermore, the neglect of the C_8 term causes every c_k of the corresponding equation of (12) to disappear. This leads to a contradiction in another of the equations of (12).

The solving of (16) with $C_8 \neq 0$, is much more complicated. However, by applying a certain method which gave a fortuitous value of C_8, the following solution was found:

$$r^I = 0.912 \text{ Å}, \qquad r^{III} = 0.514 \text{ Å};$$

$$\varrho = 0.00314\, s^2 + 0.00233\, (p_x^2 + p_y^2) +$$

$$+ 0.00245\, p_z^2 + 0.00211\, s\, p_z +$$

$$+ 2.40\, (d_{x^2-y^2})^2 - 0.124\, s\, d_{z^2} -$$

$$- 0.0787\, p_z\, d_{z^2} + 0.587\, (d_{z^2})^2.$$

From this, we see that the total number of d electrons is roughly unchanged. The other terms have not undergone very appreciable modifications either. However, it seems impossible to distribute the d electrons in such a way as to satisfy the PAULI principle. Hence, there probably is no solution of (16) which satisfies (12). By assuming that the four equivalent bonds $a\ b\ c\ d$ are curved

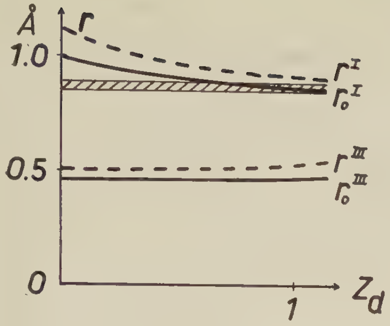

Fig. 6.

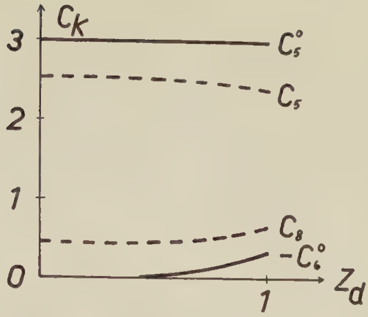

Fig. 7.

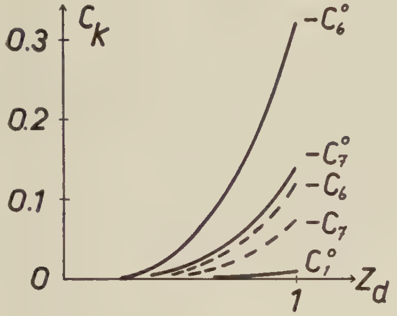

Fig. 8.

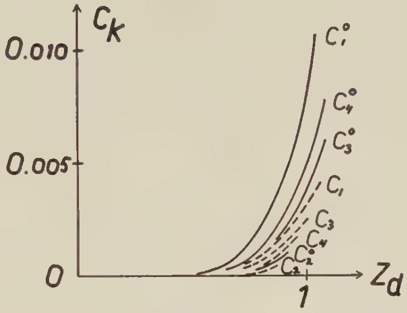

Fig. 9.

Figs. 6–9. Variation of the effective charge, Z_d, of the d orbitals.—r^I, distance of the maximum charge density; r^{III}, distance of the minimum charge density; C_k, coefficients of the ϱ-terms. Index zero indicates $C_8 = 0$. The experimentally found B radii are represented by the marked area in Fig. 6.

between the B atoms, we might find a smaller amount of d orbitals, as in the case with the method used in Section 3. This might give a result more in accordance with the PAULI principle.

7. Variation of the effective charge

If the valence electrons of Me were localized around the B atoms taking part in the covalent B–B bonds, the first equation of (16) should be normalized to a number greater than three. However, this only alters the C_k's with a common factor, and hence is of no special interest. Much more important is the increasing amount of screening of the nuclei, especially for the outer d electrons. Hence, it is advantageous to solve (16) for different values of the effective charge, Z_d. The results from this procedure are seen in Figs. 6–9. The diagrams of these figures show the changes of r^I, r^{III} and the coefficients of the terms in the charge density, when Z_d decreases. The dotted lines, C_k, represent solutions where C_8 has been given arbitrary values apart from zero (see C_8 line). The other lines, C_k^0, represent solutions with $C_8 = 0$. In Fig. 6, the experimental values of the B radii of the various borides of MeB_6 type correspond to the

Table 3

Me	r_B (Å)	Z_d (e)	J (eV)
Ba	0.89	0.69	5.2
Sr	0.87	0.86	5.7
Ca	0.86	0.95	6.1
. . .	. . .	. . .	. . .
Y	0.845	1.09	6.5

marked area (cf. Table 1). It will be seen that the agreement with the calculated values of r^I is extremely good.

If we compare KIESSLING's values, r_B, of the B radii of the investigated borides and the diagram of $r^I(Z_d)$ in Fig. 6 (for simplicity with $C_8 = 0$), we are able to find the effective charge, Z_d, which would give a maximum value of ϱ midway between two bounded B atoms (Table 3). The last column of the table shows the ionization potential, J, of the different metals. We see that J increases at the same time as our hypothetical Z_d value. As is seen, Ba is most easily ionized. If both valence electrons have left the Ba atom, every B atom would have an average value of $3\frac{1}{3}$ valence electrons. Complete screening of the B nucleus (as would be the case for a d electron with all the other electrons inside it [17]), would give $Z_d = 0.67$ in good agreement with the value of Table 3. Thus, BaB_6 probably has the strongest ionic Me–B bonds in accordance with KIESSLING's assumptions.

Also the covalent B–B bonds are strongest here. As a matter of fact, a small value of Z_d corresponds to a large contribution of d functions (cf. Fig. 7) and a large B radius (Fig. 6) which gives considerable overlapping and therefore strong covalent bonds. BaB_6 then seems to be the most stable boride. With an increasing ionization potential of Me, the stability of the borides appears to decrease. It is significant that metals with a higher ionization potential than Y cannot form MeB_6. At a cursory glance, it might be thought that if the energy of the valence bond were large enough to ionize Me, complete ionization would take place. Hence, different screening parameters might not be found, the limit of the ionization potential which permits the formation of the boride being the only thing that matters. However, the more Me electrons that are transferred to the B atoms, the more difficult will it be to ionize still further electrons. This is a possible reason why ionization increases with a decreasing ionization potential of Me. Thus, the high stability of the investigated borides very likely depends on the ionization of Me.

8. Discussion of the results

As we have seen, the numerical results contain many uncertain factors. Qualitatively, however, we have shown that it is possible to write up wave functions which give maximum probability of the orbital composition as well as functions giving maximum charge density in the directions prescribed by the structure of the crystal. The most reliable method seems to be the earlier one which does not require so many excited orbitals, though the neglect of the radial corrrelation in this case is probably the largest source of error, as the bonding electrons belong to different shells. On the other hand, the ionization cannot be described by this method, and hence the second method becomes justified. Undoubtedly, the results show that ionization really is an important factor, though the numerical values cannot be taken too literally. The agreement with the numerical experimental data in Fig. 6 and Table 3, for example, may of course be accidental. In fact, Z_d would be greater on account of the large number of d electrons. (A d electron does not screen another d electron as much as an s or p electron). Nor need the charge maximum of the valence electrons of one B atom necessarily be situated midway between two adjacent B atoms. The indefinite C_8 value is another uncertain factor. Moreover, the bonds probably are curved which decreases the amount of d electrons somewhat. The method in itself is very approximate.

Probably both methods used in the present investigation give far too many $3d$ electrons. In the absence of any experimental energy data, it is difficult to say to what extent excited orbitals participate. However, if we compare the energy differences between the following excited orbitals and the ground state [18],

$$(2s)(2p)^2 \quad 3.57 \text{ eV},$$

$$(2s)^2(3d) \quad 6.79 \text{ eV},$$

we find it reasonable to suppose that d orbitals are included in the wave function, as the energy difference, 3.22 eV, between the two states might not be too great to be compensated by the bonding energy. It is the present author's opinion that the ionized Me electrons, at least, occupy $3d$ states of the B atoms.

Longuet-Higgins and de V. Roberts [4] have succeeded in explaining the stability of MeB_6 without using any $3d$ orbitals at all. There is also room for two ionized valence electrons of Me in the closed shell of each B_6 octahedron which contains 20 MO's, composed of only $2s$ and $2p$ orbitals. The borides with bivalent metals would then be completely ionized and the closed-shell structure would prohibit transition of the electrons to the other states; this yields no metallic conductivity. The low actual conductivity of these borides is explained as being dependent upon impurities or lattice defects of the crystals. The three-valent metals would have delivered two electrons to every B_6 octahedron, and, hence, the remaining valence electron which is likely to move in the Me lattice would be responsible for the large metallic conductivity of these borides. In the present paper, the successively changed degree of ionization of the different metals can explain the low conductivity of the borides of bivalent metals in the same manner.

An agreement between the present method of Section 3 and the results of the MO treatment in [4] is found in the fact that the bonds between adjacent B_6 octahedra are formed by one electron of each octahedron, all the other twelve bonds being described by the remaining twelve (or with ionization, fourteen) electrons. This corresponds with the fact that the inner bonds are not of ordinary covalent type, being greater in number than the electron pairs.

The investigation [4] differs most obviously from the present proposition in the total neglect of the $3d$ orbitals. The question whether these orbitals play an important role or not is open to discussion, but both methods used in the present paper indicate their presence. The potential field of the adjacent B atoms requires a symmetry of the electronic structure which can be obtained with $3d$ orbitals. As a matter of fact, the first attempt made by the present author to describe the bonds with only $2s$ and $2p$ orbitals did not give any peaks of the charge density in the bond directions. It would be interesting later on to make an attempt to use d orbitals in the MO treatment of the B_6 octahedra.

I should like to express my acknowledgments to my teacher, Professor O. KLEIN, for his interest and for all his help and good advice. Similarly, I wish to offer my thanks to Docent I. HJALMARS, who suggested this investigation. Without her guidance and inspiring optimism the work might not have reached the present stage. Financially, the work has been made possible by a grant from *Statens Naturvetenskapliga Forskningsråd.*

Appendix I: The correspondence between the ZIMMERMAN & VAN RYSSELBERGHE (Z & R) *determinantal wave function [8] and* PAULING's *directed HAO's [5] of tetrahedral carbon*

The normalized Z & R determinant with tetrahedral structure is:

$$\Psi = \frac{1}{\sqrt{4!}} \begin{vmatrix} s(1) & s(2) & s(3) & s(4) \\ p_x(1) & p_x(2) & p_x(3) & p_x(4) \\ p_y(1) & p_y(2) & p_y(3) & p_y(4) \\ p_z(1) & p_z(2) & p_z(3) & p_z(4) \end{vmatrix} \text{ or shortly } \begin{vmatrix} s \\ x \\ y \\ z \end{vmatrix}.$$

We now change the form of the determinant by the addition of rows with suitable coefficients:

$$\begin{vmatrix} s \\ x \\ y \\ z \end{vmatrix} = -\tfrac{1}{2} \begin{vmatrix} s \\ s+x-y-z \\ -2y \\ z \end{vmatrix} = -\tfrac{1}{2} \begin{vmatrix} s \\ s+x-y-z \\ -2y-s-x+y+z \\ z \end{vmatrix} =$$

$$= -\tfrac{1}{4} \begin{vmatrix} s \\ s+x-y-z \\ s-x-y-z \\ 2z \end{vmatrix} = -\tfrac{1}{8} \begin{vmatrix} 2s \\ s+x-y-z \\ s-x-y-z \\ s-x-y+z \end{vmatrix} = -\tfrac{1}{8} \begin{vmatrix} s+x+y+z \\ s+x-y-z \\ s-x-y-z \\ s-x-y+z \end{vmatrix}.$$

This is exactly proportional to the determinant formed by PAULING's directed orbitals of tetrahedral carbon. The one-electron AO's, s, x, y and z, used in the

Z & R determinant are all orthogonal which is not the case with all of PAULING's directed orbitals. According to (7), the corresponding density function is

$$\varrho = s^2 + x^2 + y^2 + z^2$$

which is a spherically symmetrical function.

Appendix II: Calculation of the D_{kl} functions

Let us write

$$D_k = \frac{1}{\sqrt{3!}} \text{Det } K,$$

where K is the matrix consisting of the elements $K_p(q)$ of the kth SLATER determinant. Then we get:

$$D_{kl} = \tfrac{1}{6} \iint \text{Det } K \text{ Det } L \, d\tau_2 \, d\tau_3. \tag{18}$$

Shortly, we can write the product of two determinants as follows:

$$\text{Det } K \text{ Det } L = \{\sum_P (-1)^P P(123)\}^2 = \{(123)+(231)+(312)-(321)-(132)-(213)\}^2.$$

Here P is the permutation operator, and the other abbreviated notations will be readily understood. The sequence must be observed closely. After computing the square, we can insert the result in (18), remembering that the integrals embrace the spaces of e.g. the 2nd and 3rd electrons. Every term appears twice, and after rearrangement of the terms we obtain the following formula:

$$\begin{aligned} 3D_{kl} = {} & (11) \left[\int (22) \int (33) - \int (23) \int (32)\right] + \\ & + (12) \left[\int (23) \int (31) - \int (21) \int (33)\right] + \\ & + (13) \left[\int (21) \int (32) - \int (22) \int (31)\right] + \\ & + (21) \left[\int (32) \int (13) - \int (33) \int (12)\right] + \\ & + (22) \left[\int (33) \int (11) - \int (31) \int (13)\right] + \\ & + (23) \left[\int (31) \int (12) - \int (32) \int (11)\right] + \\ & + (31) \left[\int (12) \int (23) - \int (13) \int (22)\right] + \\ & + (32) \left[\int (13) \int (21) - \int (11) \int (23)\right] + \\ & + (33) \left[\int (11) \int (22) - \int (12) \int (21)\right]. \end{aligned} \tag{19}$$

Here, we have used the abbreviations $(ij)=K_i L_j$ and $\int (ij)=\int K_i L_j \, d\tau$. The formula (19) may be written in determinantal form as in (10). This is valid also for determinants of higher order. Hence, we can write in a symbolic form:

$$D_{kl}=\frac{1}{n}\frac{d}{d\tau}\,\mathrm{Det}\int (ij),$$

the participating determinants being of order n. Of course, the space derivation is here only a symbolic sign for the reversal of integration over the whole space.

Institute of Theoretical Physics, University of Stockholm, October 1954.

REFERENCES

1. R. Kiessling, Acta Chem. Scand. 4 (1950) 209.
2. L. Pauling, J. Am. Chem. Soc. 69 (1947) 542.
3. L. Pauling, Proc. Roy. Soc. A 196 (1949) 343.
4. H. C. Longuet-Higgins and M. de V. Roberts, Proc. Roy. Soc. A 224 (1954) 336.
5. L. Pauling, The Nature of Chemical Bond, 2nd ed., Ithaca (1948), p. 76.
6. A. Maccoll, Trans. Faraday Soc. 46 (1950) 369.
7. K. Artmann, Z. Naturforschg. 1 (1946) 426.
8. H. K. Zimmerman jr and P. van Rysselberghe, J. Chem. Phys. 17 (1949) 598.
9. J. W. Linnett and J. Poë, Trans. Faraday Soc. 47 (1951) 1033.
10. Ta-You Wu, J. Chem. Phys. 22 (1954) 1125.
11. I. Fischer, Ark. Fys. 5 (1952) 349.
12. R. McWeeny, Proc. Roy. Soc. A 223 (1954) 63, 306.
13. P. A. M. Dirac, Phil. Soc. Cambr. Proc. 27 (1930/31) 240.
14. R. Hultgren, Phys. Rev. 40 (1932) 891.
15. P. O. Löwdin, J. Chem. Phys. 12 (1951) 1579.
16. W. E. Duncanson and C. A. Coulson, Proc. Roy. Soc. Edinb. A 62 (1943) 37.
17. H. Eyring, J. Walter, and G. E. Kimball, Quantum Chemistry, New York (1944), p. 163.
18. Atomic Energy Levels, Circular of the National Bureau of Standards, Vol. I (1949).

Tryckt den 2 mars 1955

Uppsala 1955. Almqvist & Wiksells Boktryckeri AB

ARKIV FÖR FYSIK Band 9 nr 25

Communicated 24 November 1954 by ERIK HULTHÉN

Emission spectra in the near infra-red

By BENGT KLEMAN and BENGT LILJEQVIST

With 6 figures in the text

A small spectrometer with interchangeable grating and prism has been used for the study of emission spectra in the near infra-red from various conventional light sources. The detector consists of a PbS cell and the amplifying system is based upon the phase-sensitive detector principle. The efficiency of the spectrometer in recording line and band spectra from discharge tubes, King's furnace and an acetylene-air flame is discussed. In the furnace spectrum a new band with its head at 0.86 μ due to CrH is found. The flame spectra of barium, chromium and vanadium are shown to have their main emission concentrated to bands in the near infra-red region.

Introduction

In recent years the PbS cell has been used extensively as detector in near infra-red spectrometry, especially for spectrochemical analyses of absorption spectra. Our own investigations with the PbS cell have been undertaken with the aim of studying the efficiency of the method of recording emission spectra with this cell. We wanted thus to extend the wave-length range, beyond that of the photographic plate and of photocells, for the type of spectroscopy which is usually done at this laboratory, as for instance the analysis of band spectra and intensity measurements of spectral lines for the determination of transition probabilities and dissociation energies.

The useful sensitivity range of the PbS cell is from the visible up to 3.5 μ. According to our experience, the sensitivity of the cell may correspond more or less to that of the photographic plate in the region of 1.0–1.2 μ. Between 1.2 and 3.5 μ its sensitivity exceeds that of all other detectors existing at present. The sensitivity maximum of the PbS cell lies between 2.0 and 2.5 μ. A troublesome thing when working in the near infra-red region is the absorption within large ranges caused by water-vapour and carbon dioxide in the air. For a full utilization of the spectroscopic possibilities in the lead sulfide range a vacuum spectrometer should be used. We have not had the opportunity of carrying out our investigations with a vacuum spectrometer but have had to work with an ordinary spectrometer in air.

The spectrometer

The spectrometer arrangement is shown in Fig. 1. As spectrometer we have used a single monochromator from the firm of Carl Leiss. The monochromator may be obtained from the firm with various prisms which are easily interchangeable. For the present purpose we have used a quartz prism. We have also supplied the spectro-

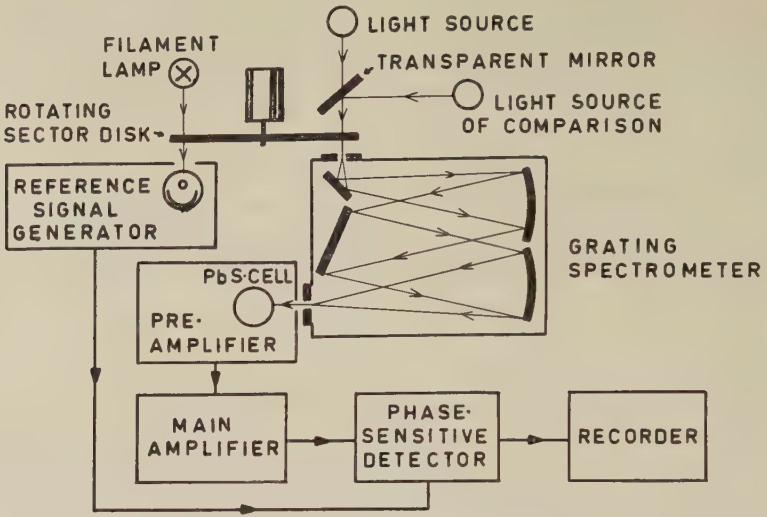

Fig. 1. The spectrometer arrangement.

meter with a plane grating which has 288 rules per mm. The spectrometer is of the Pfund type and the two concave mirrors have a focal length of 30 mm. The dispersion with the grating is about 90 A/mm.

On the spectrometer drum, which is driven by a synchronous motor, is mounted a tooth-wheel which gives signals to the eletromagnetic time-marking system of the recorder. This arrangement is fitted to enable a quick location of the position of an object with the help of calibration curves, but the precision of the driving screw does not permit of an exact determination of the wave-lengths with the time marks. For this purpose we have used references spectra. We shall revert to this later in this paper in connection with the treatment of discharge tubes.

We made a systematic study of the intensity distribution from the grating. Both discharge tubes and a filament lamp served as light sources. It was found that for different orders of the light the intensity distribution as a function of the grating angle differed very much. For example, while there was a particular blaze for the 4th and 5th orders of the visible light to one side of the grating, the first order of infra-red light for these angles showed no counterpart to this.

There are, to the best of our knowledge, no ideal filters for the near infra-red region. For wave-lengths up to 1.6 μ we used a Corning 2540 glass filter for eliminating higher orders of the light. A combination of this filter and a heat-protection filter of interference type (Calflex) served us well up to 2.4 μ. We also used a Kodak remote infra-red filter (200). The drawback with these filters, which may be obtained to cut the light in the region 1–5 μ, is, however, that this cut is rather slow and covers a region of about 2 μ.

The recording and amplifying system

As infra-red detectors we have used PbS cells of the evaporated type [1].

There are many ways of amplifying the signal from the PbS-cell. One of the most widely used amplification systems seems to be that described by WILSON [2]. The

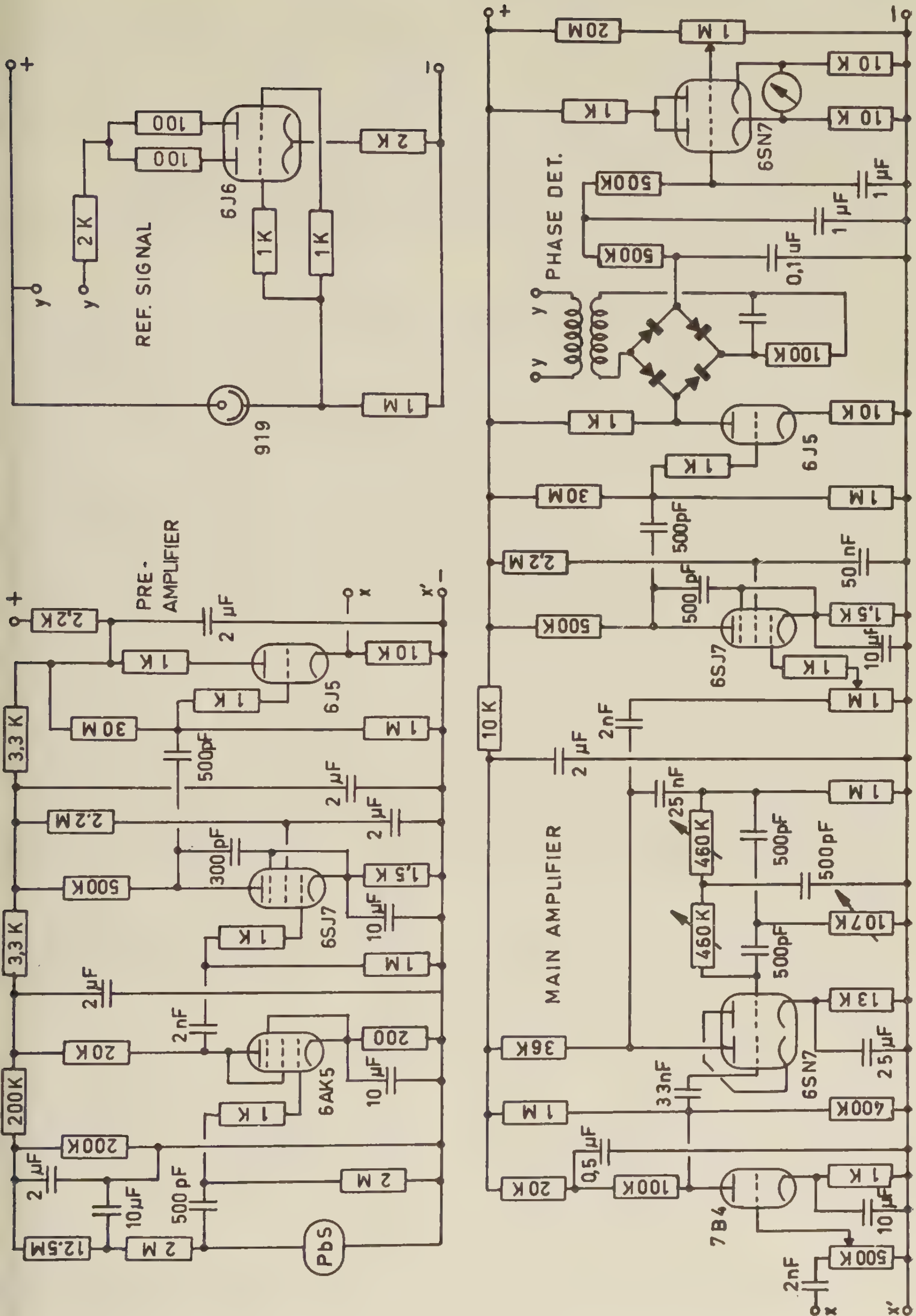

Fig. 2. Wiring diagram of the amplifier system.

light is modulated to a frequency of about 1000 cps and the selectivity of the amplifier is provided by an LC-circuit, with a feedback arrangement which makes it possible to vary the band-width down to 0.5 cps. We first tried an amplifier of this type. With this sharp tuning we had, however, difficulties arising, *inter alia*, from the instability of the line frequency. We therefore decided instead to base the amplifying system upon the phase-sensitive detector principle.

The amplifying system in our arrangement consists of four units, the preamplifier, the main amplifier, the phase-sensitive detector and the reference signal unit. A block-scheme of the system is shown in Fig. 1 and the wiring diagrams are shown in Fig. 2. A rotating sector disk driven by a synchronous motor is used to modulate the signal to a frequency of 975 cps.

The stages in the preamplifier and the main amplifier are resistance-coupled, and in order to eliminate low frequencies the coupling capacitors have been chosen suitably small. The high frequencies are filtered off by capacitors between anode and cathode in the stages. Moreover, a rather broad tuning is obtained with a resistance-capacitance T-filter stage in the main amplifier.

The PbS cell and the preamplifier are mounted on the spectrometer.

The reference signal is obtained in the following way. The light from a filament lamp is modulated by the same sector disk as modulates the signal to be recorded, and falls on a vacuum phototube. The reference signal is then amplified and fed through a coupling transformer into the bridge of four matched germanium diodes in the phase-sensitive detector unit. The correct phase of the reference signal is easily obtained by adjusting the filament lamp-phototube arrangement.

As recorder we used a Hartmann und Braun Lichtpunkt-Linienschreiber.

King's furnace

A King's furnace is a very powerful light source for the production of some spectra of atoms and diatomic molecules requiring low excitation energies.

We have tried the furnace with some suitable metals in an atmosphere of hydrogen or argon. The heating element of the furnace is a carbon tube with thin walls through which a current of 600–900 amp. is sent. Temperatures of up to 2300°C have been used.

When focussing the centre of the heating tube on the entrance slit it cannot be avoided that rather much stray radiation from the walls and the boat, and sometimes from clouds of solid particles, falls on the slit. It is therefore preferable to use a large dispersion with this light source in order to diminish the disturbing influence of the continuum in the study of emission spectra. For this investigation we have thus made use only of the grating in the spectrometer.

The only strong spectral lines in the region 1–3 μ that we observed when running the furnace without loading the liner with any metal are the potassium doublets at 1.17 and 1.25 μ, which seem to be very persistent. Most elements have few transitions between low energy states falling in the region 1–3 μ; and with the metals we tried, as a rule only a few lines appeared, sometimes with considerable strength. Fig. 3 shows a group of calcium lines between 1.9 and 2.0 μ.

We concentrated our investigation with the King's furnace upon the search for hydride spectra. The furnace is known to produce intense spectra of a great number of diatomic metal hydrides.

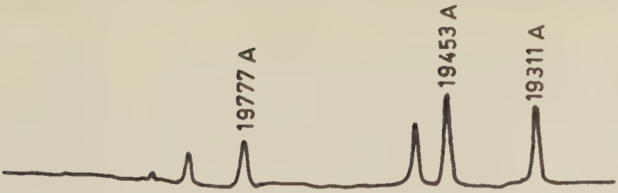

Fig. 3. Ca lines between 1.9 and 2.0 μ obtained with a King's furnace. (Grating; slit-widths 0.05 mm.)

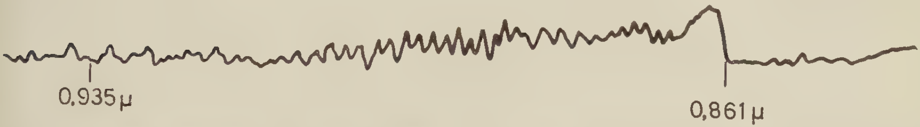

Fig. 4. CrH band obtained in the second order of the grating spectrometer with a King's furnace as light source. (Slit-widths 0.10 mm.)

A review of the lower states of those hydrides whose spectra are known shows that for most groups of elements no electronic transition between low energy states can be expected to fall in the near infra-red region. An exception must, however, be made for some molecules, such as SnH, PbH, BiH, CoH and NiH. These molecules show strong deviations from the normal coupling conditions in their lower states, and the components of the multiplet states behave more or less as separate electronic states. Transitions between such component states may be expected to fall in the near infra-red. The spectra of the above-mentioned molecules do not, however, readily appear in the furnace for various reasons. We therefore tried some metals at random for which the hydride spectra are little known or unknown.

While scanning the region around 1.7 μ a band was observed for chromium, which turned out to be in the second order. It has its head at 0.861 μ and is degraded to the red (Fig. 4). Subsequently, the region between 0.6 and 1.2 μ was photographed and the band identified as the 0,0 band of a system emitted by the CrH molecule. This band system is treated in a separate paper [3].

At 0.9 μ the PbS cell is far from its sensitivity maximum, and the recording of the CrH band shows that the method might be useful for the study of other hydride spectra in the near infra-red, especially in the more favourable region at somewhat longer wave-lengths.

Flame spectra

We have recorded some flame spectra obtained with a Lundegårdh acetylene-air flame.

This flame is astonishingly stable and reproducible in its emission, and it has for this reason often been used for intensity measurements with photoelectric cells [4, 5]. The emission is not, however, very intense, and we have hitherto only used our spectrometer with the quartz prism for the study of flame spectra in the near infra-red.

The flame itself gives an extended emission of water and carbon dioxide bands, commencing with the strong water-band at 1.4 μ and covering much of the region up to 3.5 μ.

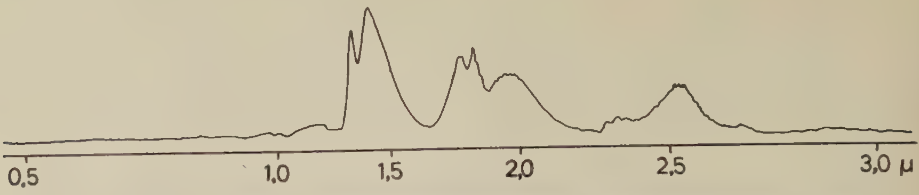

Fig. 5. Emission spectrum of the acetylene-air flame. (Prism; slit-widths 0.03 mm.)

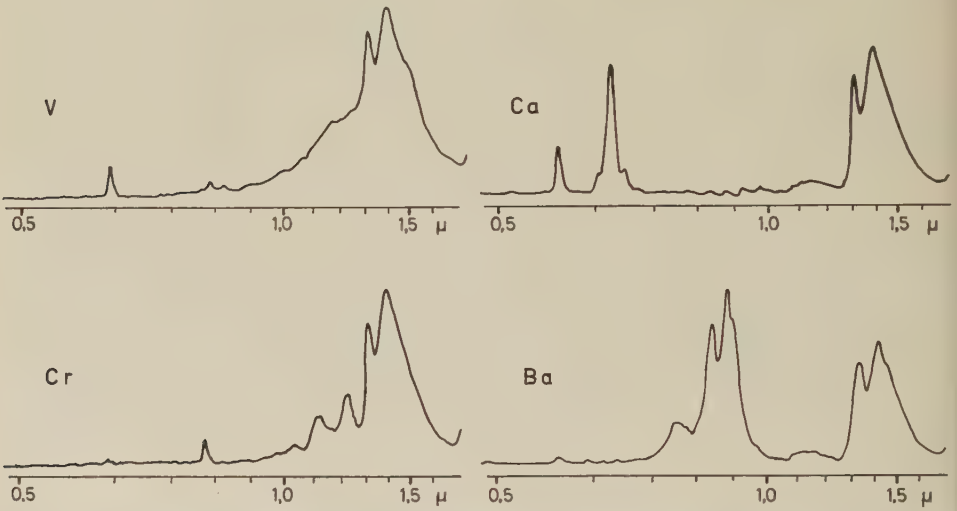

Fig. 6. Flame spectra from the metals; Ca (calcium nitrate), Ba (barium nitrate), Cr (chromium chloride) and V (vanadium chloride). (Prism; slit-widths 0.03 mm.)

To study the flame spectra of some metals water-soluble salts were inserted in the flame. The spectra obtained in this way usually consist of lines of the metal and of bands from the metal oxide or, in some cases, from the diatomic molecule of the metal itself. Fig. 6 shows the spectrum in the region from 0.5 to 1.7 μ from the following metals: Ca (Calcium nitrate), Ba (Barium nitrate), Cr (Chromium chloride), and V (Vanadium chloride). With Ca the green and orange band systems of CaO are obtained, whereas the infra-red system of CaO at 0.9–1.0 μ is less outstanding. With Ba the green and yellow systems of BaO are hardly noticeable, whereas there is a very strong emission in the region 0.8–1.0 μ. The fact that barium has its main emission in the flame spectrum concentrated to bands in this region does not seem to have been pointed out in the literature. Chromium gives a system of bands between 1.0–1.3 μ. The intense emission with vanadium starts at 1.0 μ and, to judge from the deformation of the profile of the 1.4 μ water-band ordinarily obtained, it probably extends to about 1.5 μ.

For a discussion of the origin of the near infra-red emission of barium, chromium and vanadium further experimental study will be necessary. The matter is therefore left open in the present paper.

Discharge tubes

The line spectra from some discharge lamps and tubes have been recorded in order to study their suitability as reference spectra. With a grating, the higher order of the visible and infra-red lines up to 1.5 μ may serve as reference lines in the region 1–3 μ.

Of the commercial spectral lamps tried, the following were found to be of interest. A Na-lamp for the region up to 1.4 μ; the Rb-lamp, which has some very intense lines in the region 1.3–1.5 μ; and, what is probably the most common reference source used for the near infra-red, the mercury lamp, which renders useful reference lines up to 2 μ. The best reference source for the whole near infra-red region was found to be a hollow-cathode discharge with Ne as carrier gas; but this is of course a less handy light source for general purposes than a discharge lamp.

With the flame and furnace it was possible to place the reference light source directly behind the other light source. In cases where this was not possible an aluminium-coated mirror was used to throw the reference light into the same path as that of the light source. The thickness of the coating varied continuously along the mirror, so that by moving the mirror the best ratio of intensity between the light from the two sources could be ensured.

Acknowledgements

Our thanks are due to Dr. R. J. CASHMAN, who kindly supplied us with three PbS cells, to Fil. lic. G. ERLANDSSON for valuable help and suggestions in connection with the designing of the amplifier system, and to Docent L. HULDT for lending us his equipment for the acetylene-air flame. We also want to thank Ing. O. BJÖRKLUND, who superintended the building of the stabilized power supply at the *Fysiska Övningslaboratoriet.*

The work has been financially sponsored by *Statens Naturvetenskapliga Forskningsråd.*

Physics Department, University of Stockholm, November 1954.

REFERENCES

1. CASHMAN, R. J., J.O.S.A. *36*, 356 (1946).
2. KUIPER, G. P., WILSON, W., and CASHMAN, R. J., Astrophys. J. *106*, 243 (1947).
3. KLEMAN, B. and LILJEQVIST, B., Arkiv för Fysik *9*, 345, (1954).
4. HULDT, L. and LAGERQVIST, A., Arkiv för Fysik *2*, 333 (1950).
5. LAGERQVIST, A. and HULDT, L., Zeitschrift f. Naturforsch. *8a*, 493 (1953).

Tryckt den 8 mars 1955

Uppsala 1955. Almqvist & Wiksells Boktryckeri AB

ARKIV FÖR FYSIK Band 9 nr 26

Communicated 24 November 1954 by Erik Hulthén

The band spectrum of the Ag_2 molecule

By Bengt Kleman and Stig Lindkvist

With 2 figures in the text

A vibrational analysis has been carried out for a blue band system of Ag_2. A King's furnace has been used as light source and the spectrum has been photographed both in emission and absorption. The appearance of the system is complicated both by the near equality of the ΔG values for the higher vibrational levels and by the enhancement of the last observed bands due to predissociation. The Ag_2 molecule is found to be somewhat less stable than the Cu_2 and Au_2 molecules.

Introduction

The existence of band spectra due to the molecules Cu_2, Ag_2 and Au_2 were reported by us in a recent paper [1]. The vibrational analyses of the spectra of Cu_2 and Au_2 were treated in papers [1] and [2] respectively. The spectra of Cu_2, Ag_2 and Au_2 have also been observed by Ruamps, who has recently published a preliminary report [3].

The same experimental technique as was used to photograph the spectra of Cu_2 and Au_2 has been used in the case of Ag_2. A King's furnace, with argon as filling gas, served as light source. The spectrograms were taken in the first order of a plane grating in Littrow mounting with a dispersion of about 5 Å/mm. The region 4000–5400 Å was photographed on Ilford Thin Film Half Tone plates. The spectrum was photographed in emission with exposure times varying from a couple of minutes to a quarter of an hour at temperatures of 1700–1800°C. Since self-reversal occurred within the band system, it was found desirable also to photograph the spectrum in absorption at somewhat lower temperatures with a tungsten-band lamp as light source.

Appearance of the bands

The band spectrum of Ag_2 in the region 4000–5200 Å shows many complicated features. In emission at a temperature of about 1700–1800°C there are strong bands which are self-reversed in the region 4200–4600 Å. Towards the violet end of these bands there are weak bands which give a diffuse impression and fade out at about 4000 Å. Around 4700 Å the bands again appear diffuse up to about 4800 Å, where they become sharp and show up in emission. The region 4900–5000 is very crowded with bands and appears almost like a continuum which suddenly ends with two

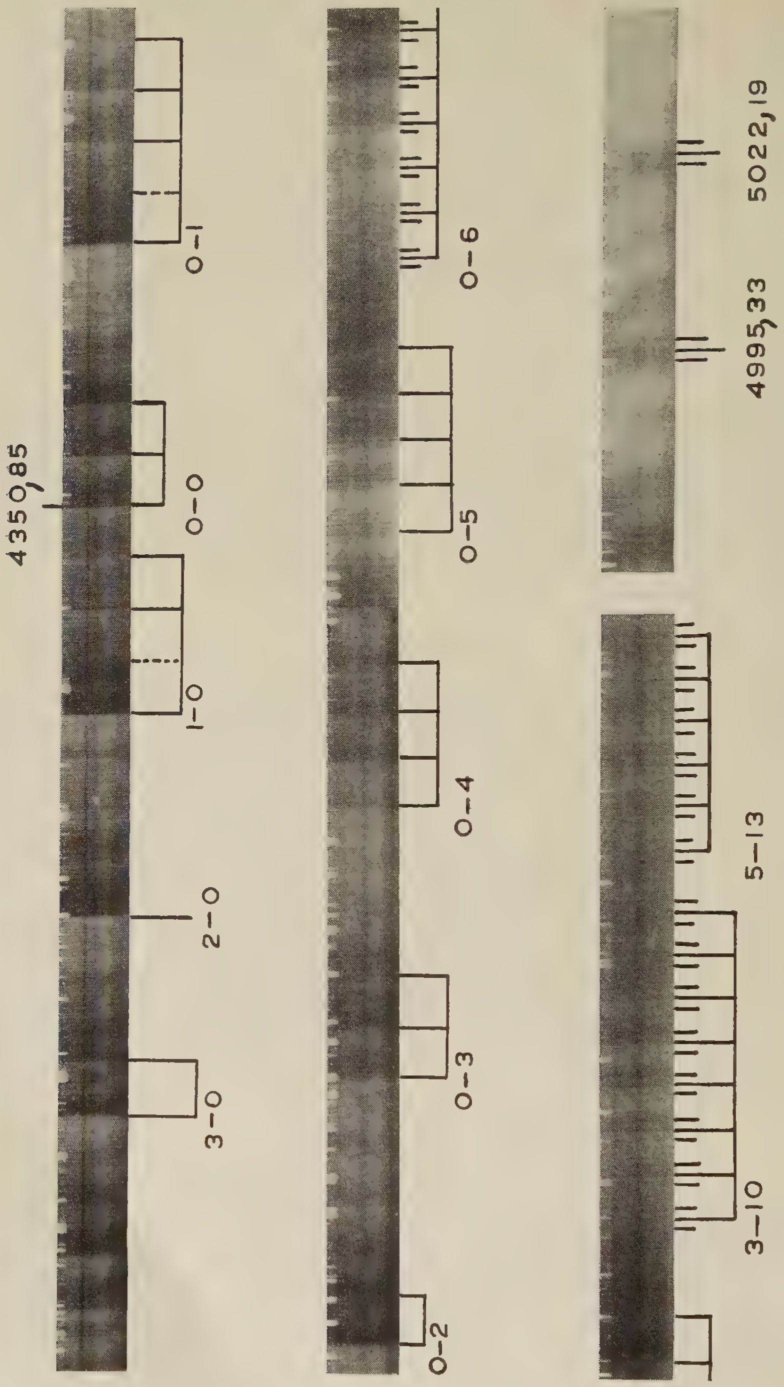

Fig. 1. The blue A–X band system of Ag_2 in absorption.

Table 1. Wave numbers of the band heads *A–X*

Δv	$v' v''$	Ag^{109} Ag^{109}	Ag^{107} Ag^{109}	Ag^{107} Ag^{107}
+5	6.1		23689.5	
+4	4.0		23584.6	
	5.1		23541.2	
+3	3.0		23435.2	
	4.1		23393.1	
+2	2.0		23282.9	
+1	1.0		23130.5	
	– –		– – – –	
	3.2		23052.9	
	4.3		23014.3	
0	0.0		22977.5	
	1.1		22940.0	
	2.2		22901.5	
−1	0.1	22787.4	22786.5	
	– –		– – – –	
	2.3		22714.6	
	3.4		22677.1	
−2	0.2	22598.4	22596.8	
	1.3		22561.8	
−3	0.3	22411.8	22408.4	22405.6
	1.4		22374.2	22371.6
	2.5		22341.2	
−4	0.4	22225.3	22220.7	22217.8
	1.5	22191.4	22188.1	22184.9
	2.6	22159.5	22155.8	22151.9
	3.7		22123.3	22119.4
	4.8		22090.7	22085.5
−5	0.5		22035.0	22031.7
	1.6		22003.3	22199.1
	2.7	21977.1	21972.8	
	3.8	21945.6	21941.4	21936.6
	4.9	21915.2	21910.3	21906.2
	5.10		21879.1	
−6	0.6		21849.8	21845.1
	1.7		21821.0	21815.4
	2.8	21795.9	21790.3	21784.8
	3.9	21766.1	21760.7	21755.7
	4.10	21736.5	21730.8	21725.8
	5.11	21707.1	21701.1	21696.1
	6.12	21678.2	21672.4	21666.6
	7.13	21648.4	21642.7	
−7	3.10		21580.5	21575.2
	4.11		21551.8	21545.8
−7	5.12	21530.3	21523.9	
	6.13		21496.0	21498.3
	7.14	21475.1	21469.1	21463.1
	8.15	21447.3	21440.9	21434.9
	9.16	21420.3	21414.3	
	10.17		21386.6	
−8	5.13		21347.7	21340.8
	6.14	21328.6	21321.9	
	7.15	21302.6	21294.9	21287.9
	8.16	21275.8	21268.0	21261.2
	9.17	21249.5	21241.7	
	10.18		21216.1	21208.2
	11.19	21197.2	21190.2	
	12.20		21165.2	21157.4
	13.21	21147.1	21139.5	
−9	7.16		21123.3	
	8.17		21097.5	
	9.18	21081.1	21072.3	21064.7
	10.19	21055.8	21048.2	21040.2
	11.20	21031.8	21023.4	21014.7
	12.21	21007.6	20999.1	20990.9
	13.22		20975.5	20967.4
	14.23	20959.7	20951.4	20942.9
	15.24	20937.0	20928.2	20920.1
	16.25	20913.8	20904.8	20895.4
	17.26	20888.8	20881.8	20874.0
−10	10.20		20881.8	
	11.21		20857.7	20848.6
	12.22		20835.2	20825.3
	13.23		20811.7	20803.4
	14.24	20798.5	20789.5	20779.9
	15.25		20766.9	20757.9
	16.26	20754.0	20745.8	20735.4
	17.27		20723.8	20714.5
	18.28	20711.4	20701.8	20693.1
	19.29	20690.1	20681.0	20671.8
	20.30	20670.3	20660.5	20650.7
	21.31	20649.7	20639.4	20630.6
	22.32	20628.9	20619.8	
−11	17.28	20576.6	20565.9	20555.9
	18.29	20555.9	20546.7	20535.8
	19.30	20535.8	20526.6	20516.0
	20.31	20516.0	20506.0	20496.9
	21.32	20498.1	20487.5	20478.3
	22.33	20478.3	20468.8	20459.1
	23.34	20459.1	20450.1	
	24.35	20441.8	20432.5	
	25.36	20424.2	20414.6	
	26.37	20407.4	20397.0	20387.5
	27.38		20380.5	

Table 1 (cont.)

Δv	$v' v''$	$Ag^{109}\,Ag^{109}$	$Ag^{107}\,Ag^{109}$	$Ag^{107}\,Ag^{107}$	Δv	$v' v''$	$Ag^{109}\,Ag^{109}$	$Ag^{107}\,Ag^{109}$	$Ag^{107}\,Ag^{107}$
– 12	18.30		20391.9	20380.8		26.38	20262.5	20252.2	
	19.31	20383.0	20372.5			27.39		20236.8	20227.2
	20.32	20364.6	20354.0	20344.7		28.40	20232.3	20222.0	20211.5
	21.33	20346.3	20336.1	20326.6		29.41	20216.3	20206.9	20297.4
	22.34	20329.5	20318.7	20308.8		30.42		20192.8	20282.6
	23.35		20302.2	20391.9		31.43		20178.8	
	24.36		20284.8	20274.7		32.44		20164.8	
	25.37	20278.9	20268.3	20258.0		33.45		20151.5	

strong triple heads at 4995.3 and 5022.2 Å. The subsidiary heads in the triplets have about half the intensity of the central head and are placed at distances of about 1.5 Å from this. At strong exposures very weak bands continue up to a final weak head at 5049 Å. According to our interpretation of the general appearance, all bands belong to the same band system, and the absorption of the bands in the centre of the band system is caused by an abundant occurrence of the Ag_2 molecule in its lower vibrational states within the colder parts of the light source. The related parts of the band system with diffuse appearance may be interpreted as parts in which there is a balance between absorption and emission. The parts which occur in emission belong to transitions which end at higher vibrational levels of the lower state. The simplest explanation for the cut-off of the band system at the heads at 4995.3 and 5022.2 Å is that there occurs a predissociation in the upper electronic state. A certain caution must, however, be observed in connection with this explanation, since the vibrational analysis shows that the sequences should show heads of heads in this region. In absorption there is a further complication due to the appearance of regularly spaced weak headless and diffuse bands which cover the whole observed region from 4000 Å up to 5400 Å. These diffuse bands need not necessarily be caused by the Ag_2 molecule, since they only appear at the lower temperatures used for the absorption exposures and may very well originate from another molecule less stable than Ag_2.

The vibrational analysis

The measurements of the heads up to the 33–45 band (Table 1) have been used in the determination of the equation for the band heads. The constants were determined graphically. The equation for the band heads of $Ag^{107}\,Ag^{109}$ is

$$\sigma_{v',v''} = 22977.5_0 + (154.0_5\, v' - 0.584_0\, v'^2 + 0.0022_8\, v'^3) -$$

$$- (191.7_6\, v'' - 0.642_5\, v''^2 + 0.0003_0\, v''^3).$$

The heads of the isotope molecules $Ag^{107}\,Ag^{107}$ and $Ag^{109}\,Ag^{109}$, which are about half as intense as those of $Ag^{107}\,Ag^{109}$, have been measured for most of the bands in the sequences $\Delta v = -4$ to $\Delta v = -12$. The measured isotope splitting is in agreement with that obtained by applying the theoretical ϱ value to the equation for the band heads of $Ag^{107}\,Ag^{109}$. We are thus confirmed in our assumption that the observed band system is emitted by Ag_2 molecules.

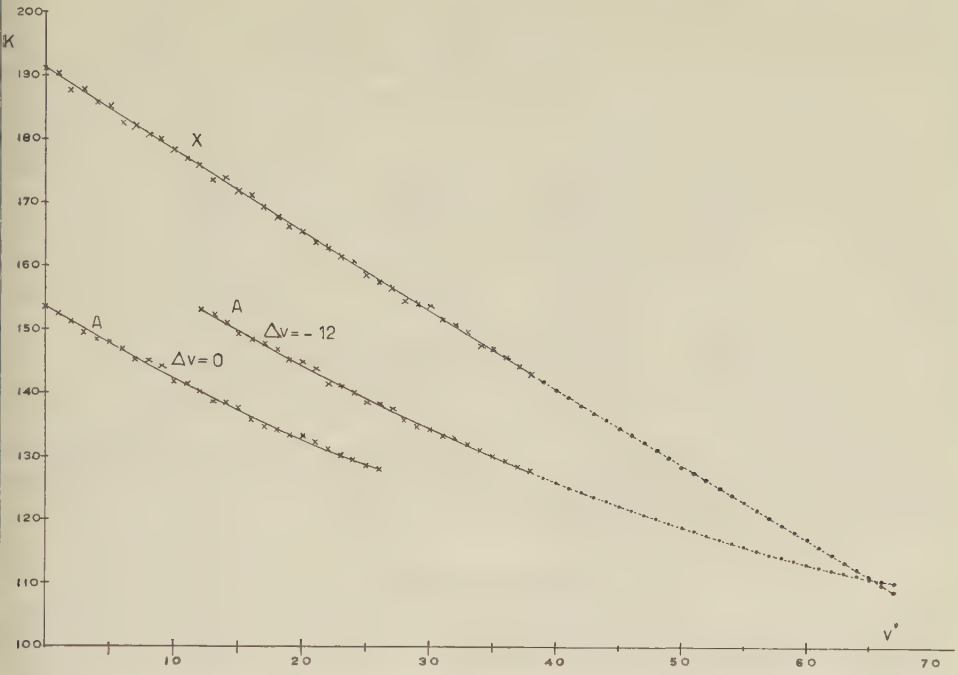

Fig. 2. Graphical determination of the turning point within a seqence of bands by plotting the ΔG values for the lower (X) and the upper (A) states against v (see text).

Above the band (33.45) the clustering of heads becomes very great, and in emission the region looks almost like a continuum ended by the triple heads at 4995.3 and 5022.2 Å; and we have not been able to assign the heads in this area. The complicated appearance is probably due to two phenomena. The ΔG values for the bands in this area rapidly become more and more equal, and the band heads within a sequence converge, consequently, towards a point, where a head of heads is formed. This has been illustrated in Fig. 2, where $\Delta G''(_{v''+\frac{1}{2}})$ is plotted against v'' and $\Delta G'(_{v'+\frac{1}{2}})$ against $v' + |\Delta v|$. The point of intersection between the two curves determines $v'v''$ at the turning point of the sequence $\Delta v = -12$ (see HERZBERG, 4). The extrapolation of the ΔG values by means of the calculated constants to the point of intersection of the curves in Fig. 2 is naturally rather uncertain. It does, however, show that the turning points for the sequences $\Delta v = -12$ and $\Delta v = -13$ are in the vicinity of the triple heads at 4995.3 and 5022.2 Å, though we do not believe that these triple heads represent turning points of the sequences $\Delta v = -12$ and $\Delta v = -13$. This or the following reasons. The turning points occur at a place in the sequences where the intensities of the bands may be assumed to be rather low, and even if two or three heads for each isotope fall together this would not be sufficient to make them as outstanding as they are observed. Secondly, it is difficult to see why there should be such an abrupt change in intensity after the heads at 5022.2 Å. Rather must it be assumed that the enhancement of the triple heads is due to a predissociation in one of the participating states. The isotope splitting in the triple heads is about 7 K,

Table 2

	T_e	ω_e	$\omega_e x_e$	$\omega_e y_e$	D_0^0 e.V.
Cu_2: B . .	21757.8	245.8	2.0	−0.02	
A . .	20433.0	191.9	0.348	−0.018	
X . .	0	266.1	1.025	0.0008	2.1
Ag_2: A . .	22996.4	154.6	0.587	0.0022	
X . .	0	192.4	0.643	0.0003	1.8
Au_2: B . .	25690	177 (ω_0)	—	—	
A . .	19668.1	142.3	0.445	−0.0015	
X . .	0	190.9	0.420	−0.0001	2.7

which indicates that the predissociation occurs not far from the turning points of the sequences. It is estimated that the sequences $\Delta v = -12$ and $\Delta v = -13$ form their heads from bands which have v'' values around 65.

Energy of dissociation

The energy of dissociation for the lower state, which must be presumed to be the ground state, has been analytically extrapolated by means of the formula

$$D_0 = \frac{\omega_0^2}{4\,\omega_0 x_0}\,.$$

The value $D_0^0 = 1.8$ ev was obtained. The Ag_2 molecule thus seems to be somewhat less stable than the Cu_2 and Au_2 molecules.

Summary of constants for Cu_2, Ag_2 and Au_2

In Table 2 the constants obtained from the vibrational analyses of the observed systems in Cu_2, Ag_2 and Au_2 have been summarized. The band system B–X for Au_2 has not been analyzed by us and the constants for the B-state have been taken from the preliminary values calculated by Ruamps [3].

Physics Department, University of Stockholm, November 1954.

REFERENCES

1. Kleman, B. and Lindkvist, S., Arkiv för Fysik *8*, 333 (1954).
2. Kleman, B., Lindkvist, S., and Selin, L.-E., Arkiv för Fysik *8*, 505 (1954).
3. Ruamps, J., Comptes Rendus *238*, 1489 (1954).
4. Herzberg, G., Molecular Spectra and Molecular Structure I. Spectra of Diatomic Molecules, p. 160, Van Nostrand 1950.

Tryckt den 8 mars 1955

Uppsala 1955. Almqvist & Wiksells Boktryckeri AB

ARKIV FÖR FYSIK Band 9 nr 27

Communicated 12 January 1955 by Nils Zeilon

Two flow problems in a viscous fluid

By Adolf Anzelius

With 6 figures in the text

In order to find exact solutions to the equations of hydrodynamics, Hamel (Jahresbericht der Math. Ver. 1916) posed the following question: Do there exist solutions for which the streamlines are as in potential flow but with a differing velocity distribution? In connection with this investigation Hamel demonstrated the existence of spiral movements in fluid media of infinite extent. He further gave an exact solution for the radial source and sink flows in a sector, and thereby demonstrated the essential difference between the flow in the direction of pressure fall from that in the opposite direction. The flow turned out, moreover, to be only incompletely determined, in that the solution involved an arbitrary constant.

The purely radial flow is, however, not practically realizable. It should therefore be of a certain interest to investigate more general solutions of source and sink flows.

The differential equations of motion in two dimensions for a viscous fluid are

$$\left.\begin{aligned}\varrho\left(u\frac{\partial u}{\partial x}+v\frac{\partial u}{\partial y}\right)&=-\frac{\partial p}{\partial x}+\mu\,\Delta u\\ \varrho\left(u\frac{\partial v}{\partial x}+v\frac{\partial v}{\partial y}\right)&=-\frac{\partial p}{\partial y}+\mu\,\Delta v\end{aligned}\right\},$$

where ϱ is the density of the fluid and μ the coefficient of viscosity. Elimination of the pressure p and insertion of the stream function ψ, which determines the velocity components

$$u=\frac{\partial\psi}{\partial y},\quad v=-\frac{\partial\psi}{\partial x}\qquad(\operatorname{div}\,\boldsymbol{v}=0)$$

will characterize the function ψ by means of the equation

$$\mu\,\Delta\,\Delta\,\psi=\varrho\left(\frac{\partial\psi}{\partial y}\frac{\partial\Delta\psi}{\partial x}-\frac{\partial\psi}{\partial x}\frac{\partial\Delta\psi}{\partial y}\right).\tag{1}$$

We now seek a solution of this non-linear differential equation in terms of the series

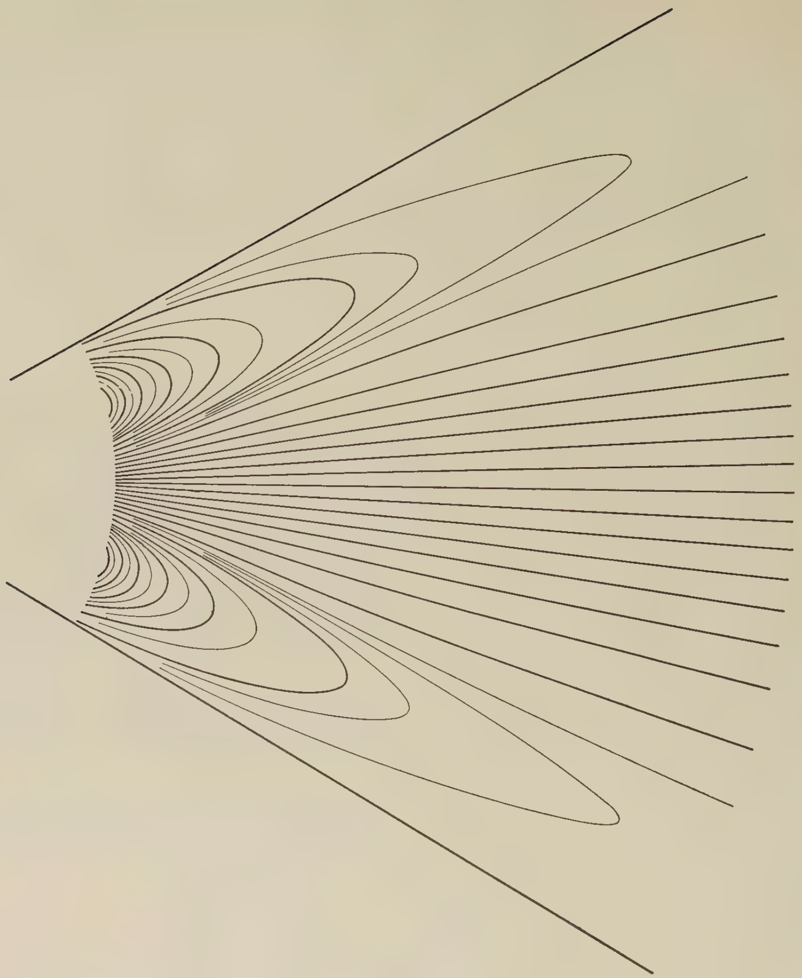

Fig. 1.

$$\psi(x, y) = \sum_{0} \sigma^{\nu} \psi^{(\nu)}(x, y)$$

with

$$\sigma = \varrho/\mu,$$

in which the successive $\psi^{(\nu)}(x, y)$, are determined by the linear differential equations

$$\Delta \Delta \psi^{(0)} = 0, \quad \Delta \Delta \psi^{(\nu+1)} = \sum_{p+q=\nu} \left(\frac{\partial \psi^{(p)}}{\partial y} \frac{\partial \Delta \psi^{(q)}}{\partial x} - \frac{\partial \psi^{(p)}}{\partial x} \frac{\partial \Delta \psi^{(q)}}{\partial y} \right) \quad (\nu = 0, 1, \ldots). \tag{2}$$

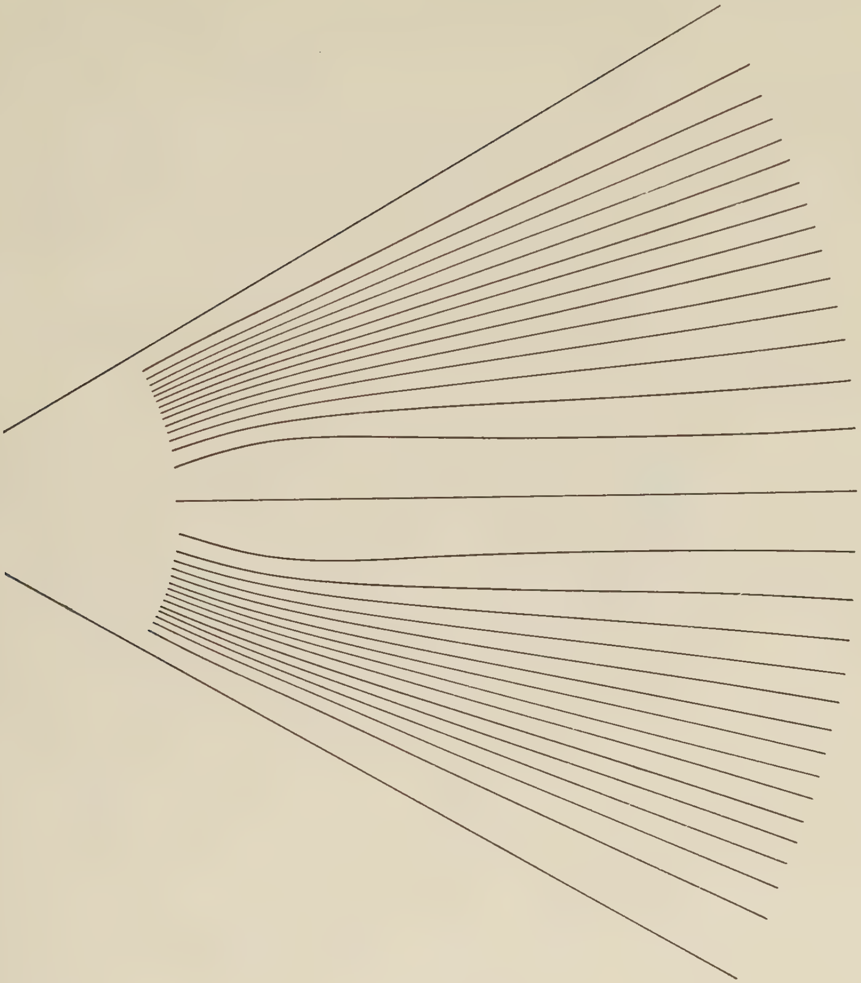

Fig. 2.

1. Flow in the sector $\varphi = \pm\alpha$

In polar coordinates (r, φ), eq. (1) becomes

$$\Delta\,\Delta\,\psi = \sigma \frac{1}{r}\left(\frac{\partial\psi}{\partial\varphi}\frac{\partial\Delta\psi}{\partial r} - \frac{\partial\psi}{\partial r}\frac{\partial\Delta\psi}{\partial\varphi}\right), \quad \Delta = \frac{1}{r}\frac{\partial}{\partial r} r \frac{\partial}{\partial r} + \frac{1}{r^2}\frac{\partial^2}{\partial\varphi^2} \qquad (3)$$

and the velocity components are

$$v_r = \frac{1}{r}\frac{\partial\psi}{\partial\varphi}, \quad v_\varphi = -\frac{\partial\psi}{\partial r}.$$

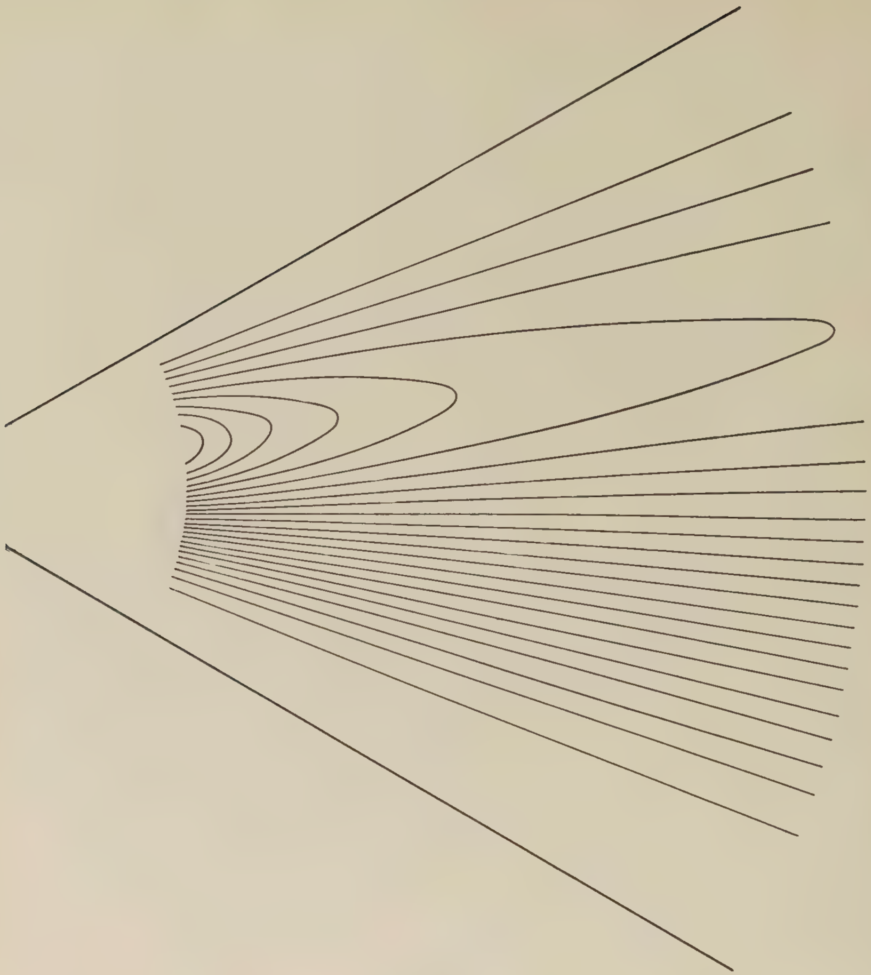

Fig. 3.

For the case of *radial* flow we have that $\psi = \psi(\varphi)$, and eq. (3) becomes

$$\frac{d^4 \psi}{d \varphi^4} + 4 \frac{d^2 \psi}{d \varphi^2} + 2 \sigma \frac{d^2 \psi}{d \varphi^2} \frac{d \psi}{d \varphi} = 0,$$

or, writing

$$\frac{d \psi}{d \varphi} = r v_r = \Phi,$$

$$\frac{d^2 \Phi}{d \varphi^2} + 4 \Phi + \sigma \Phi^2 = \text{const.},$$

which is HAMEL's equation.

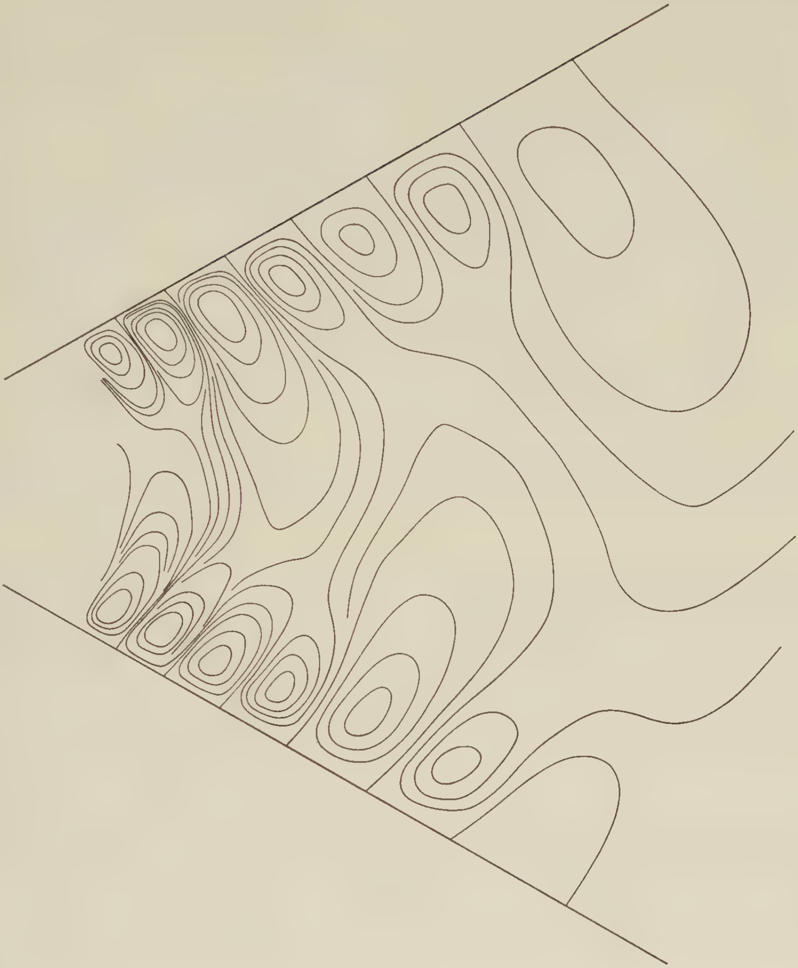

Fig. 4.

For the case of *general* flow, the flow function ψ is a function $\psi(r, \varphi)$ of both r and φ, and it is necessary to determine the successive $\psi^{(\nu)}(r, \varphi)$ from the equations

$$\Delta\,\Delta\,\psi^{(0)} = 0,\quad \Delta\,\Delta\,\psi^{(\nu+1)} = \frac{1}{r}\sum_{p+q=\nu}\left(\frac{\partial\,\psi^{(p)}}{d\,\varphi}\,\frac{\partial\,\Delta\,\psi^{(q)}}{\partial\,r} - \frac{\partial\,\psi^{(p)}}{\partial\,r}\,\frac{\partial\,\Delta\,\psi^{(q)}}{\partial\,\varphi}\right)\quad (\nu = 0, 1, \ldots). \quad (4)$$

The boundary conditions are that the velocity be zero at the boundaries $\varphi = \pm\alpha$ and at ∞. The total quantity of fluid which flows past is

$$\int_{-\alpha}^{+\alpha} v_r\, r\, d\varphi = \psi(+\alpha) - \psi(-\alpha).$$

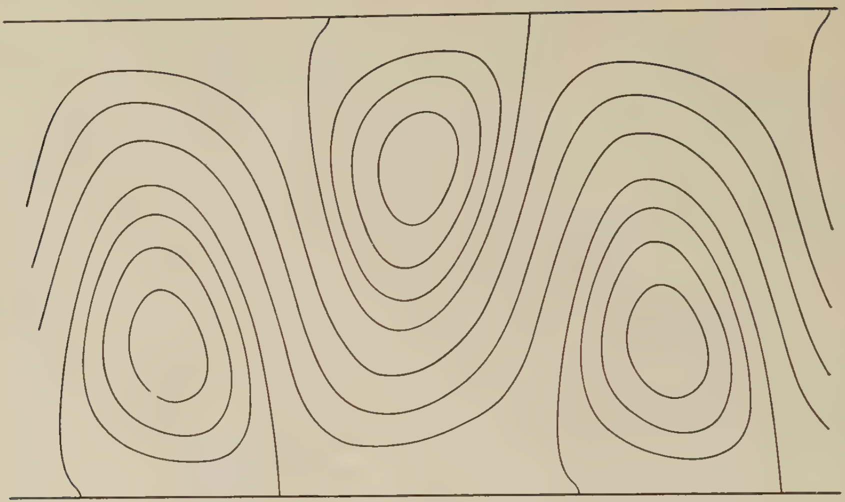

Fig. 5.

We choose as first approximation

$$\psi^{(0)} = Q\,(\sin\,2\,\varphi - 2\,\varphi\,\cos\,2\,\alpha) + \overline{\psi}^{(0)}\,(r, \varphi),$$

where $\overline{\psi}^{(0)}\,(r, \varphi)$ has the form

$$r^{-n}\,[A_n \sin n\,\varphi + B_n \sin\,(n+2)\,\varphi + C_n \cos n\,\varphi + D_n \cos\,(n+2)\,\varphi]. \tag{5}$$

The first term is a radial flow satisfying the boundary conditions, and corresponds to a total flow of fluid which is proportional to Q. The second term corresponds to a superposed curvilinear flow.

The following $\psi^{(\nu)}\,(r, \varphi)$-functions $(\nu > 0)$ are obtained from the linear non-homogeneous equations (4), and have the form

$$\psi^{(\nu)} = \psi_p^{(\nu)} + \overline{\psi}^{(\nu)}$$

in which $\psi_p^{(\nu)}$ is a particular integral containing the arbitrary constants $A_n, \ldots, D_n$. The terms will have the form $r^{-k}\,\varphi^l \begin{smallmatrix}\sin\\ \cos\end{smallmatrix} m\,\varphi$. The term $\overline{\psi}^{(\nu)}$ is the general biharmonic solution of type (5) and its coefficients are determined so that each $\psi^{(\nu)}$ satisfies the boundary conditions. In consequence of the way in which the solution is built up as a product of a function in r and a function in φ, these boundary conditions will also lead to $\psi^{(\nu)} = 0$ on the boundaries $\varphi = \pm\,\alpha$, that is, they represent zero fluid flow. The condition for determining the coefficients in $\overline{\psi}^{(\nu)}$ in this way is that n not satisfy the equation

$$\sin\,2\,(n+1)\,\alpha = \pm\,(n+1)\,\sin\,2\,\alpha, \tag{6}$$

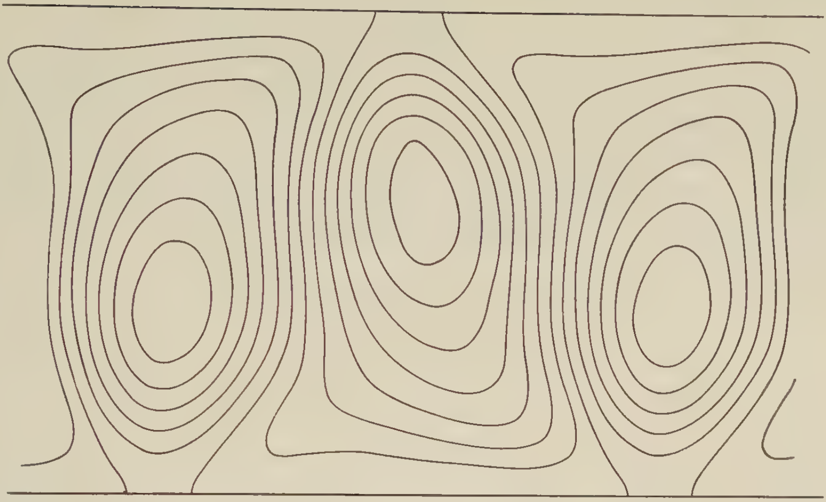

Fig. 6.

the plus and minus signs corresponding to odd and even terms of $\psi^{(\nu)}$. These equations have, for $\alpha < 79.7^\circ$ and $\alpha < 73^\circ$ respectively, no usable real roots.

We have finally only the function $\overline{\psi}^{(0)}(r, \varphi)$ which does not satisfy the boundary conditions, but inasmuch as it is biharmonic it can be eliminated by adjoining a suitable expression to the last approximation $\psi^{(\nu)}$.

An approximate solution has thus been obtained which holds for all $A_n, \ldots, D_n$, and for all n which do not satisfy eq. (6).

The functions $\psi^{(\nu)}$ quickly become complicated, and computations have therefore been carried out for only one or two disturbance-terms in $\overline{\psi}^{(0)}(r, \varphi)$.

Fig. 1 shows the streamlines $\psi =$ const. for $\overline{\psi}^{(0)} = B_2 r^{-2} \sin 4\varphi$, $\alpha = 30^\circ$ and $Q > 0$, corresponding to symmetric outward flow.

Fig. 2 refers to the same solution, but with $Q < 0$, that is, inward flow.

Fig. 3 displays the unsymmetric flow corresponding to the first approximation $\overline{\psi}^{(0)} = D_0 \cos 2\varphi + B_2 r^{-2} \sin 4\varphi$.

Fig. 4 shows the streamlines for the unsymmetric outward flow $\overline{\psi}^{(0)} = D_n r^{-n} \cdot \cos(n+2)\varphi$ with complex-valued $n = 1.5 + 10i$.

2. Flow in the strip $y = \pm a$

In analogy with the preceding cases, we adopt for eq. (2)

$$\varphi^{(0)}(x, y) = Q(3a^2 y - y^3) + S \sin nx \cdot y \cdot \operatorname{sh} ny.$$

Figs. 5 and 6 show the streamlines corresponding to two and three approximations, respectively, to the stream function $\psi(x, y)$, and provide an impression of the practical convergence of the method.

Summary

An approximate solution to the stream function ψ for a viscous fluid is obtained by expanding in powers of ϱ/μ. The streamlines $\psi =$ const. are given for a sector and a strip.

The author wishes to express his thanks to Mr. ERLAND YHLAND, who carried out the laborious numerical computations underlying the ψ-curves.

Tryckt den 20 april 1955

Uppsala 1955. Almqvist & Wiksells Boktryckeri AB

ARKIV FÖR FYSIK Band 9 nr 28

Communicated 26 January 1955 by ERIK HULTHÉN and OSKAR KLEIN

A microwave spectrometer and its applications to some organic molecules

By GUNNAR ERLANDSSON

With 17 figures in the text

Contents

Page
Preface 399
Part I: Description of apparatus 400
  I.1 Introduction 400
  I.2 Arrangement of apparatus 402
  I.3 Microwave components 403
  I.4 Absorption cell 405
  I.5 Electronic equipment 406
    I.5*a* Klystron power supplies 406
    I.5*b* Saw-tooth generator 407
    I.5*c* Stark modulator 407
    I.5*d* Spectrum amplifier 409
    I.5*e* Phase-sensitive detector 410
    I.5*f* Phase-shifter 411
    I.5*g* LF circuits 412
    I.5*h* Frequency standard 412
  I.6 Vacuum system 414
  I.7 Performance 414
    I.7*a* Sensitivity and resolving power 414
    I.7*b* Accuracy of frequency measurements 415
Part II: Investigated spectra 416
  II.1 Energy levels of the asymmetric rotor 416
  II.2 Intensities and selection rules 420
  II.3 Substituted benzene spectra 420
    II.3*a* Fluorobenzene 421
    II.3*b* Chlorobenzene 427
    II.3*c* Benzonitrile 428
  II.4 Cyclopentane compounds 430
    II.4*a* Cyclopentanone 430
    II.4*b* Cyclopentene oxide 431
Summary 433

Preface

When I was finishing my first course in physics in 1948 with some microwave experiments, Professor ERIK HULTHÉN, the head of this institution, drew my attention to the fact that microwaves were becoming important in molecular spectroscopy. He also arranged for me to start working in this field at the institution.

Since the research work here was at the time mainly confined to optical spectroscopy, the available resources in the microwave field were, of course, rather slender. The difficulties in this respect were in the beginning overcome thanks to a generous loan of microwave components from *Försvarets Forskningsanstalt* and later by economic support from *Atomkommittén* and *Statens Naturvetenskapliga Forskningsråd.*

The first simple model of a microwave spectrometer was assembled at the beginning of 1950. After some refinements and the introduction of double source-modulation it was capable of displaying the stronger $N^{15}H_3$ lines in ordinary ammonia. Its application to search for unknown absorption lines, however, encountered difficulties due to sharp resonances in the wave-guide system.

On the occasion of a visit to Dr. BÖRGE BAK's laboratory in Copenhagen Dr. Bak pointed out to me the advantages of Stark-effect modulation. He also gave me much valuable information about the practical arrangement of the apparatus. Following his advice, I rearranged the spectrometer and obtained a much improved performance. My subsequent collaboration with Dr. Bak and his assistant JOHN ANDERSEN has also been of great value to me.

By the time, the instrument was fit for the investigations of unknown spectra most of the linear and symmetric top molecules which were readily available had already been investigated in other laboratories. I therefore turned my attention to the asymmetric tops, and among these I selected some of which the rotational spectra are not too much complicated by internal rotation and centrifugal distortion. The analysis of the spectra has, however, entailed a lot of numerical work. To facilitate this a very promising collaboration has recently been started with the staff of the Computation Machines Board for the making of calculations in the electronic computing machine BESK. I am in this respect much obliged to Dr. STIG KOMET, Fil. lic. G. EHRLING and Fil. lic. G. DAHLQUIST for valuable help and advice.

I have also had the much-appreciated collaboration of colleagues at this institution. Among these I will especially mention Fil. lic. BENGT LILJEQVIST, who has arranged the major part of the vacuum system and advised me in many practical details. I will also mention Mr. BENGT EKSTRÖM, who has built most of the electronic equipment. Mr. OLLE BJÖRKLUND has given me much help and advice on stabilized power supplies.

To the above-mentioned persons and institutions I wish to express my very best thanks. Especially do I wish to express my gratitude to Professor ERIK HULTHÉN for much helpful advice and for his never-failing readiness to place the resources of the institution at my disposal.

Part I: Description of apparatus

I.1. Introduction

The apparatus is intended for the investigation of gas absorption spectra in a wavelength region between one and two centimetres. Its main components are obviously a source of radiation, an absorption cell, a radiation indicator, and means for frequency measurements.

Centimetre waves may be produced by special radio tubes. The type most suitable for spectroscopic purposes is at present the reflex klystron, which is capable of producing continuous and monochromatic radiation at a power level of a few milliwatts. Its frequency may be varied by mechanical tuning within a region of a few thousand megahertz (e.g. the 2K33 between 22000 and 25000 MHz). It may also be tuned electrically by altering the reflector voltage. This type of tuning is limited to a smaller range, which may amount to some 50 MHz.

The waves may be guided in parallel beams through metal pipes whose cross-section dimensions are of the order of the wave length. Such metal pipes, or wave-guides, may thus replace the optical system of an ordinary spectrometer. A length of wave-guide closed at the ends by transparent windows may be used as an absorption cell.

Detectors for microwave radiation are mainly of two kinds, bolometers and crystal rectifiers. The former are sometimes used in microwave spectrometers because of their relative freedom from noise. Crystal rectifiers are, however, more sensitive and more convenient to use. They are therefore more widely used than bolometers. In the present instrument only crystal rectifiers are employed.

Frequency measurements may be performed either by comparison with known standard frequencies or with tunable, calibrated resonators. The latter method is simpler but less accurate. It is based on the occurrence of standing waves usually in a cylindrical cavity of variable length. The accuracy obtainable in this way may amount to a few parts in 10^5. Direct frequency comparisons may give about 100 times better results. Both methods are employed here.

A complete microwave spectrometer may thus consist of a klystron, a wave-guide system with an absorption cell, a crystal detector and a frequency meter. To this equipment must be added a power supply for the klystron and an indicating instrument coupled to the detector. If the klystron frequency is modulated, e.g. by a saw-tooth voltage, the indicating instrument may be a cathode-ray oscilloscope synchronized with the modulating voltage. The absorption lines are then displayed on the oscilloscope screen.

To obtain sharp absorption lines the pressure in the cell must be kept low, generally around 10^{-2} mm Hg. A vacuum system and suitable means for the introduction of the gas sample are therefore required.

Simple as it may seem, the practical realization of the above scheme generally calls for a fairly complicated apparatus. The main reason is that most absorption lines in the microwave region are quite weak. It is therefore necessary to detect very small variations in the output power. These small variations must also be distinguished from much larger variations due to the properties of the klystron and the wave-guide system.

Several methods for the detection of weak absorption lines have been described in literature (See e.g. ref. [1]). One of the most successful and probably the one most widely used nowadays is the Stark-modulation method introduced by HUGHES and WILSON [2]. This method has also been employed here. As the name indicates, it is based upon the Stark-effect splitting of an absorption line in an electric field.

The absorption cell of a Stark-modulation spectrometer contains an electrode whereby the gas may be subjected to various electric fields. If the klystron is tuned to the exact frequency of an absorption line, the output power from the cell will depend on the voltage applied to the electrode. It will show a minimum due to gas absorption when the voltage is zero, and a maximum when the voltage is sufficient to split the line completely. If the electrode voltage alternates between zero and a suitable non-zero value the output power will be modulated with the frequency of this voltage. The spectrum line may then be detected by an amplifier tuned to the modulating frequency. Such an amplifier will of course not react to the steady component of output power, and in general not to variations in power due to other causes than absorption lines. On the other hand, the amplifier will react not only to signals arising from the undisturbed absorption line, but also to signals due to the Stark-effect components. With a sufficiently homogeneous field in the cell it is therefore possible to study the splitting patterns of the lines. The best results are obtained if the modulating voltage alternates between two distinct values, i.e. with a square-wave voltage. Since the signals due to Stark-effect components are 180° out of phase with the main line signals, the two types of signal may be distinguished with a phase-sensitive detector following the tuned amplifier.

The choice of frequency for the Stark-effect voltage depends on several factors. From considerations of sensitivity a high frequency is desired, since the noise generated by the klystron and the crystal detector is smaller at higher frequencies. Considerations of resolving power, on the other hand, call for a low modulating frequency, because additional broadening of the line occurs if the frequency is of the order of the line width. For good resolution it is also essential that the modulating voltage should have a good square-wave shape. Such a wave shape is more easily obtained at a low frequency. A compromise usually arrived at is a frequency of about 100 kHz, which is also chosen here.

I.2. Arrangement of apparatus

A block diagram of the apparatus is shown in Fig. 1. The arrangement is similar to those described by other authors, e.g. McAfee, Hughes and Wilson [3] and Scharbaugh [4]. The microwave power from the klystron is fed through a waveguide system and the absorption cell to a crystal detector. Samples of the power are taken out to a cavity wavemeter and to a mixer crystal for frequency comparison. Two variable attenuators are provided for adjustment of the power level.

The klystron is driven with a stabilized power supply to which a saw-tooth voltage may be applied for frequency modulation.

The Stark-effect electrode in the absorption cell is connected to a 100 kHz square wave generator driven by a quartz crystal oscillator.

The output crystal detector is connected to two amplifiers. One is a low frequency amplifier used for supervision of the microwave power. The other is tuned to 100 kHz and used for the amplification of spectrum line signals. It terminates in a phase-sensitive detector, where the frequency and the phase of the signal are compared to those of a gating signal from the Stark-effect modulator. The output from this detector is fed to a cathode-ray oscilloscope through a mixer, where wavemeter or frequency-marker signals may be superimposed. The oscilloscope sweep is synchronized by the saw-tooth generator.

The cavity wavemeter gives an output signal when the klystron is swept through its resonance frequency. The signal is fed to the mixer through a low frequency amplifier.

In the frequency-marker crystal the klystron frequency is mixed with harmonics from a 10 MHz crystal oscillator. Beat notes are detected by a calibrated communications receiver, which thus measures differences between the klystron frequency and the 10 MHz harmonics. The output from the receiver may be fed to the mixer through the wavemeter amplifier.

A recording instrument may be used instead of the cathode ray oscilloscope. In this case the saw-tooth generator is switched off, and a slow motor drive is applied to the klystron tuning shaft.

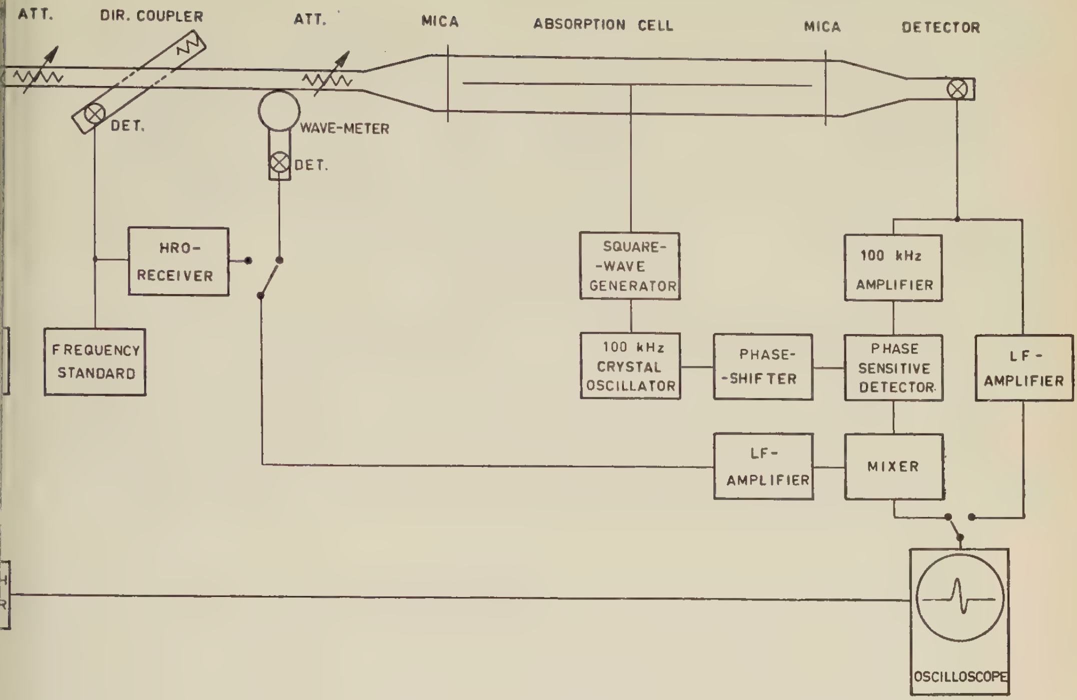

Fig. 1. Block diagram of the spectrometer.

I.3. Microwave components

Three types of klystrons are at present used to cover the frequency region 12000–25000 MHz. These are

X 12	for	12.4–17.5	kMHz	(Varian Bros)
QK 306	,,	18 –22	,,	(Raytheon)
2K33	,,	22 –25	,,	(Raytheon)

The frequency regions given are those specified by the manufacturers. The actual regions covered are generally greater and vary from one tube to another. This seems especially to be the case with early examples of the 2K33. One such tube tried here has been operated down to 16.3 kMHz. Operation at such extreme frequencies, however, requires very careful adjustments and is usually rather unstable. The gap between 17.5 and 18.0 kMHz may, however, be bridged.

The klystron types QK306 and 2K33 have output guides of standard dimension $0.420 \times 0.170''$ i.d., whereas type X12 has $0.622 \times 0.311''$ i.d. Accordingly, two interchangeable sets of wave-guide components preceding and following the absorption cell are used.

The attenuators are of the ordinary flap type. The resistive material is metalized glass with a resistance of about 200 ohms per square. It is made by the evaporation of nichrome as described in [6] section 12.15.

The wavemeters are of the type described by Bleany *et al.* [5]. A cross-section is

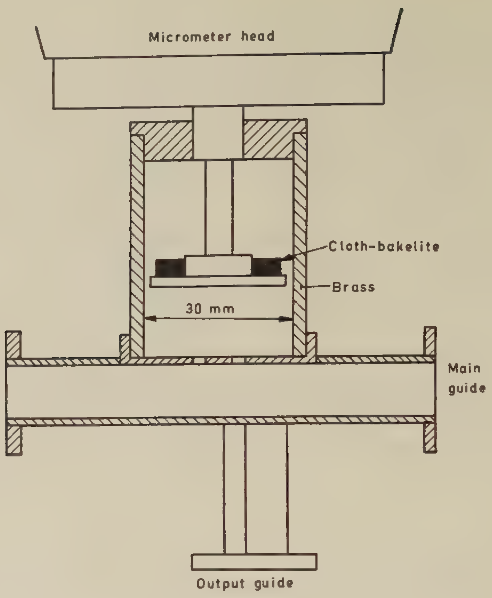

Fig. 2. Wavemeter.

shown in Fig. 2. Power is fed into the cavity through two holes placed symmetrically in the bottom plate. The output power is taken through a third hole placed at a 45° angle to the output holes. The resonant mode employed is the TE_{01n}, i.e. the electric field is circular around the axis. Other modes which may be excited are more strongly coupled to the space beyond the movable plunger, where they are to some extent absorbed by a piece of cloth bakelite.

Three wavemeters of this type are used, two for the smaller wave-guide and one for the larger. One of the former is provided with a $2\frac{3}{4}''$ micrometer head, which may be read to 0.001 mm or better. It has been used within the whole range of 16–26 kMHz with satisfactory results, except at some isolated frequencies where its function is disturbed, probably by the occurrence of unwanted resonant modes. The plunger movement allows of tuning to three different resonances at frequencies above 20 kMHz and to two resonances at lower frequencies. It has been calibrated against a large number of known absorption lines, especially in ammonia and methyl alcohol. It has then been found possible to calculate the frequency values from the wave length in the cavity (λ_g), using the formula

$$\nu = \sqrt{\left(\frac{c}{\lambda_g}\right)^2 + \nu_c^2},$$

where c is the velocity of light. ν_c represents the cut-off frequency and is determined from the calibration measurements. Only one calibration constant is thus necessary. At frequencies above 20 kMHz the errors seldom exceed 5 MHz. The other two wavemeters have smaller micrometer heads but otherwise similar properties. The errors are generally within ± 10 MHz.

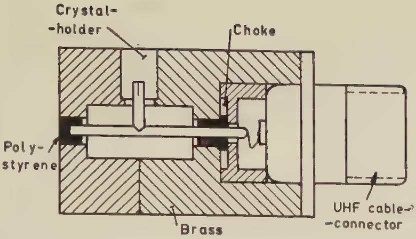

Fig. 3. Crystal mount.

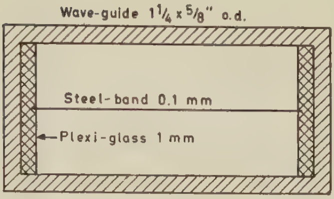

Fig. 4. Cross-section of the absorption cell.

The power to the frequency-comparison crystal is taken through a Bethe hole directional coupler designed for 20 dB attenuation as described in [6] section 14.3.

The crystal detectors used are silicon crystals in coaxial cartridges of type 1N26 (Sylvania). To obtain the best results a good crystal should be selected for each purpose and for each frequency region.

The crystal mounts are of the crossbar type. A cross section is shown in Fig. 3. A short-circuiting plunger is provided for adjustment to different frequency regions. Additional tuning may be obtained by pulling the cartridge slightly out from the mount.

Cable connections to the detector mounts are made with UHF-type coaxial connectors. The crystal mounts and the klystron are insulated from the wave-guide system to avoid the formation of closed circuits through the different cable shields.

I.4. Absorption cell

The absorption cell consists of a standard wave-guide $1\frac{1}{4} \times \frac{5}{8}''$ o.d., and is 3 m long. It is provided with a steel band electrode, 0.1 mm thick and mounted in strips of plexi-glass as shown in Fig. 4.

The cross-section of the absorption cell is considerably larger than that of the other wave-guides. This serves to increase the number of gas molecules involved in the absorption processes and thus makes it possible to increase the microwave power level without encountering saturation effects. The larger cross-section also makes it easier to get the electrode well centered in the guide, which is important for the resolution of Stark-effect components. It is also possible to extend the workable wave length region to 3 and 4 cm without changing the cell.

A disadvantage of the larger cross-section is that it permits several modes of transmission for the microwave power. The original mode from the feeding wave guide may be retained if the cross-section changes gradually, and if no discontinuities occur on the way. Discontinuities cannot, however, be entirely avoided. There are several places where these are likely to occur, e.g. the end-windows, the pumping hole, the ends of the electrode and its supports, and the connection to the electrode. The microwave power converted to unwanted transmission modes is for the most part lost in the cell and may also cause disturbing resonances. No serious trouble of this kind has, however, been encountered in these experiments.

The end-windows are made from thin mica sheets (about 0.05 mm) clamped between flat wave-guide flanges and vacuum-sealed with Apiezon grease.

The pumping hole is a slot 1 mm wide and 6 mm long in the middle of the broad wave-guide side and parallel with the direction of the guide. The current distribution

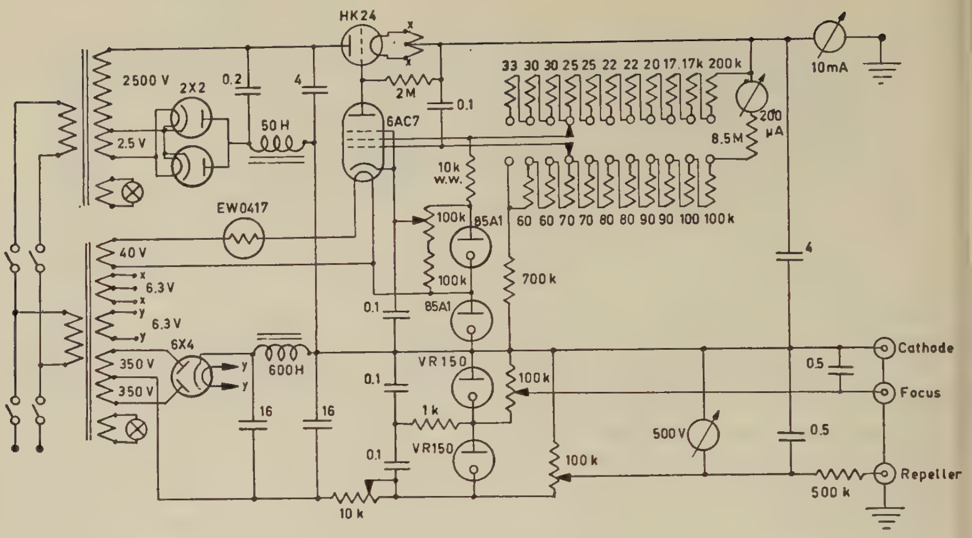

Fig. 5. 2K33 power supply.

in the guide wall is then essentially parallel with the slot and fairly undisturbed by the same.

The electrode is rather thin (0.1 mm) and placed at right angles to the microwave electric field and its disturbing effect on the field is therefore slight. The connecting wire to the electrode is also kept at right angles to the field and brought out through a small hole in the small side of the guide. It is insulated from the guide by a piece of polystyrene and vacuum-sealed with Glyptal enamel.

The choice of plexi-glass for the electrode supports has turned out to be a little unfortunate, since it slowly gives off vapours of methyl alcohol.

The transitions from the larger cross-section of the cell to the smaller wave guide take place through tapered guide sections 12 cm in length. These are milled out of brass blocks in halves, which are soldered together with the join in the middle of the broad side. They are not connected directly to the ends of the cell, but to short pieces of the large size wave guide. The taper sections may thus be exchanged together with the outer guide without disturbing the cell windows.

The absorption cell is placed in a closed wood casing for cooling with dry ice when required.

I.5. Electronic equipment

I.5 *a*. Klystron power supplies

Two different power supplies are used for the klystrons, one for types QK306 and 2K33 and one for type X12. The former types require a beam voltage of 1800 volts and a cathode current of about 10 mA. The latter type requires 600 volts for the beam and a 50 mA cathode current.

Fig. 5 shows the circuit of the high voltage supply. It comprises two rectifiers and two stabilization circuits of standard design. The cathode voltage may be varied between -1000 and -2500 volts, with a ripple amounting to about 20 millivolts rms.

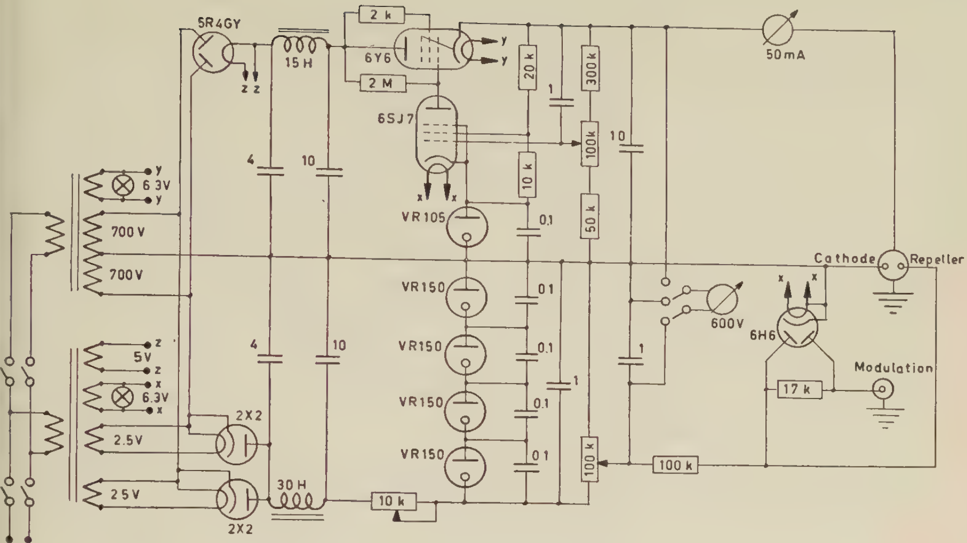

Fig. 6 X12 power supply.

A control grid voltage is variable between 0 and 150 volts negative to cathode. The repeller voltage is variable between 0 and 300 volts negative to cathode. The ripples in these are about 5 millivolts rms referred to cathode. All components carrying high voltages to ground are mounted in plexi-glass with ample clearings to avoid sparking and corona discharges. The shafts of potentiometers and switches are provided with insulated extensions through the panel.

The X12 klystron power supply is shown in Fig. 6. It is similar to the high voltage supply except for voltage and current ratings. The cathode voltage is variable between −300 and −600 volts. The repeller voltage is variable between 0 and 600 volts negative to cathode. Ripples amount to a few millivolts.

The klystron heaters are supplied with 6.3 volts DC from a rectifier to avoid hum and frequency modulation that may occur with AC-heating. The rectifier is a full wave selenium bridge filtered with a 6300 μF condenser (Fig. 7).

I.5 *b.* Saw-tooth generator

The saw-tooth generator (Fig. 8) consists of a conventional thyratron oscillator followed by a pentode amplifier. The sweep frequency is variable between 3 Hz and 1000 Hz. Only the lower frequencies are in general used. The power supply is voltage regulated in order to minimize ripple voltage.

I.5 *c.* Stark modulator

The Stark-effect modulator is designed to give a square-wave voltage with a frequency of 100 kHz and a maximum amplitude of about 600 volts. This voltage is generally biased, with one edge to zero and the other edge positive. An extra DC bias variable from zero to 3000 volts may, however, be superimposed in either direction. The square-wave generator is governed by a quartz-crystal oscillator to keep the frequency constant.

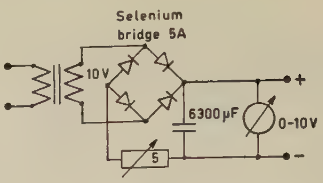

Fig. 7. Klystron heater supply.

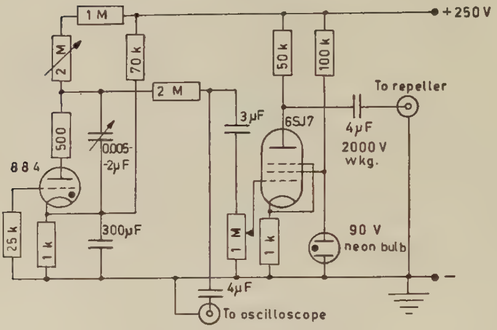

Fig. 8. Saw-tooth generator.

The crystal oscillator (Fig. 9) is a Pierce circuit using one section of a 6SN7. The other section serves as a cathode-follower output stage. A gating signal for the phase-sensitive detector is taken directly from this stage. The master signal for the square-wave generator is taken from a 6L6 amplifier. Another 6L6 drives the DC-bias supply, which consists of an air-core transformer, a high voltage rectifier, and a filter circuit. The heater of the rectifier is driven by a 6.3/2.5 V high voltage insulated transformer.

The square-wave generator is similar to the one described by SCHARBAUGH [3]. The principle is illustrated in Fig. 10. The capacity of the absorption cell is alternatingly charged and discharged from a variable power supply by means of two periodically operated switches. In the actual apparatus these switches are replaced by electron tubes which are normally biased to cut-off, but which are made conducting at the proper times by short pulses applied to their control grids.

The absorption cell capacity amounts to 700 pF. To obtain a satisfactory square-wave shape at a rate of 100 kHz this capacity must be charged and discharged within less than one microsecond. With a maximum of 600 volts the charge is 0.42×10^{-6} coulomb. The average current during the pulse must therefore amount to about 0.5 amps. Since the current flow is not constant during the pulse, the tubes used as switching devices should be able to deliver a peak current of two or three times this value.

The circuit of the square-wave generator is shown in Fig. 11. The switching tubes are type 6CD6. The charging tube is triode-connected, because a pentode connection would require a separate screen-grid supply connected to the cathode. The ground capacity of such a supply would add to the capacity of the cell and increase the requirements on charging current. The same considerations apply to the heater supply, which is therefore a low-capacity transformer 6.3/6.3 volts.

Three 6CD6's in parallel are provided for the discharge circuit, because the dis-

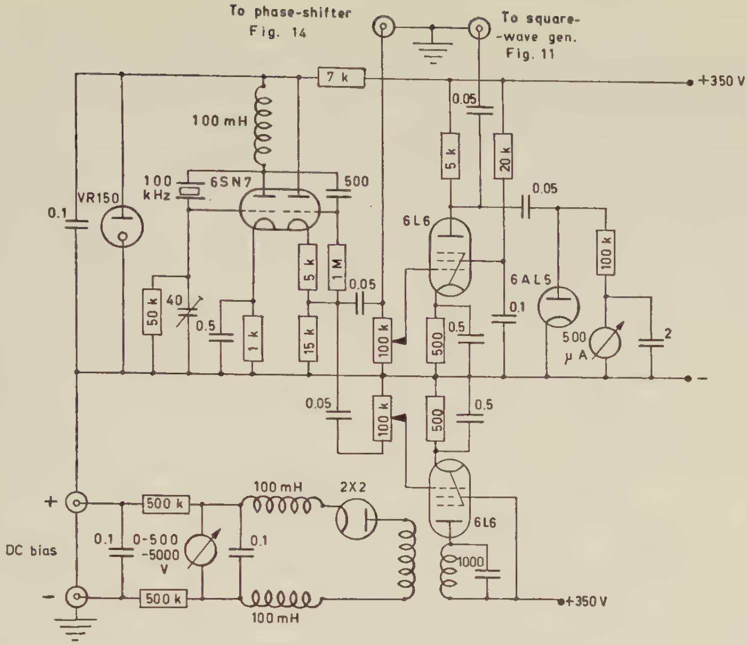

Fig. 9. 100 kHz crystal oscillator and DC bias generator for Stark-effect modulator.

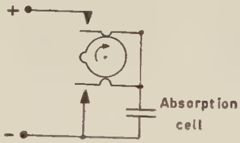

Fig. 10. Principle of square-wave generator.

charge must be very complete. The residual charge would otherwise cause splitting of lines, which are sensitive to Stark-effect voltages.

The control circuit for the switching tubes comprises a 6J5 phase splitting triode dividing the master signal into two signals 180° out of phase. These serve to synchronize two 6SN7 blocking oscillators, which in their turn drive two 6L6 blocking oscillators delivering the pulses for the switching tubes. Each blocking oscillator is preceded by a cathode-follower stage to obtain a low impedance in the synchronizing circuit. The negative grid bias for the switching tubes is obtained through grid leak resistors.

A 450 volt supply is provided for the pulse generators. The charging voltage is taken from a separate rectifier and may be varied by a Variac transformer.

I.5 *d.* Spectrum amplifier

The spectrum amplifier is divided into two parts, a preamplifier mounted directly on the crystal holder, and a main amplifier. This serves to make the input cable to the main amplifier less sensitive to stray pick up especially from the Stark-effect modulator.

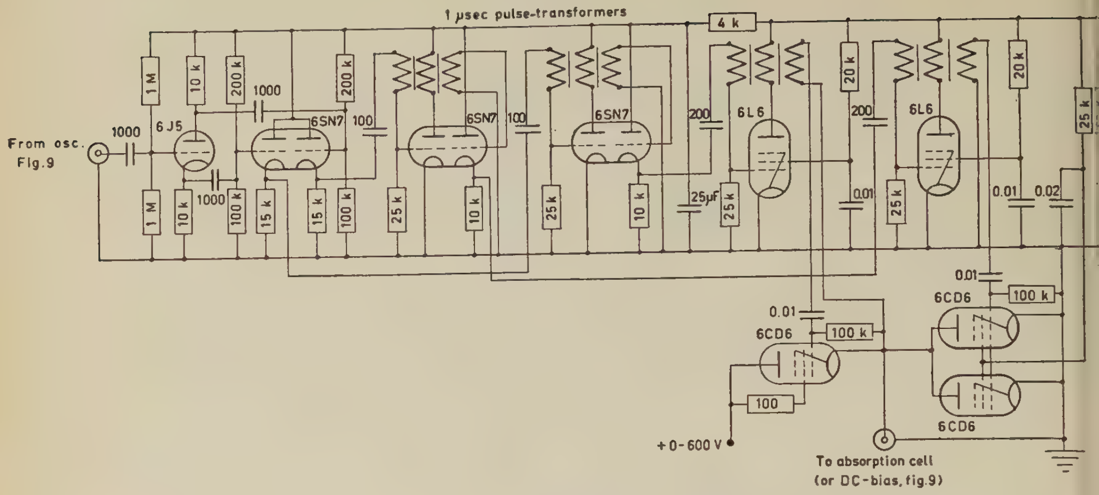

Fig. 11. Square-wave generator.

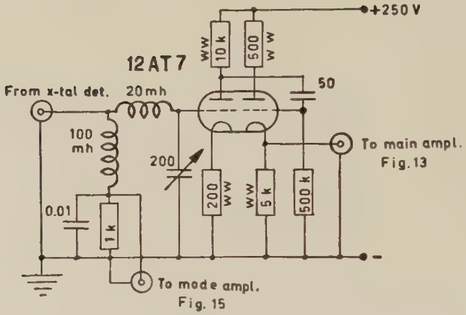

Fig. 12. Preamplifier.

The preamplifier is shown in Fig. 12. It has a series-tuned input circuit like that described by Good [7]. The special low-noise amplifier described in [7] has not been employed here, since klystron and crystal noise are much greater than amplifier noise.

The main amplifier is shown in Fig. 13. It contains three pentode stages. The first and third stages are tuned to 100 kHz with i.f. transformers. The second stage is resistance-coupled in order to reduce interaction between the stages. A cathode-follower output stage is provided as a low impedance source for the detector.

I.5 *e*. Phase-sensitive detector

The detector is essentially an electronic switch closed and opened periodically by a gating signal. If a signal with the same frequency as the gating signal is present at the input of the detector, the output will turn positive or negative according to the relative phases of the two signals. Signals differing in frequency from the gating signal will give rise to beat-frequency output signals. The effective bandwidth may be varied simply by a resistance-capacity filter in the detector output. The actual circuit as

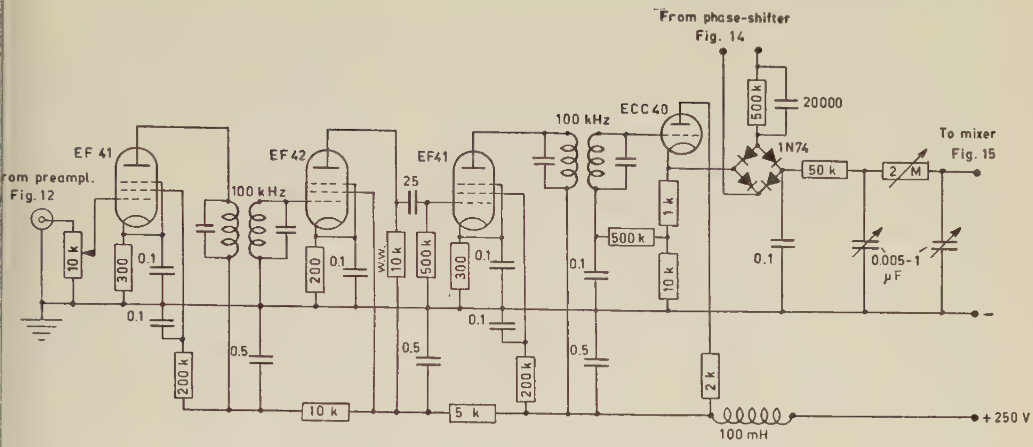

Fig. 13. Main amplifier and phase-sensitive detector.

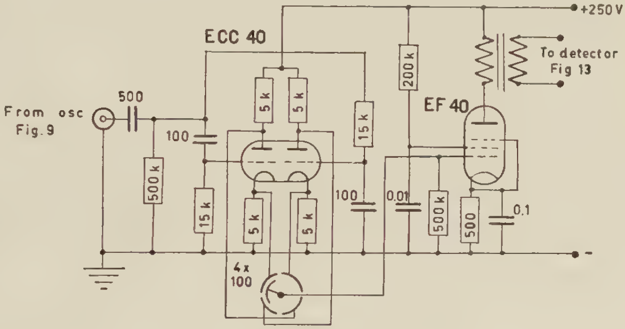

Fig. 14. Phase-shifter.

shown in Fig. 13 consists of four germanium diodes in a balanced bridge. These diodes are biased alternatingly positive and negative by the gating signal.

I.5*f*. Phase-shifter

The phase of the gating signal must be made to coincide with the phase of the spectrum signal. A network allowing a small phase-adjustment might be sufficient for this. It has been found convenient, however, to have a means for adjusting the phase through 360°. This is done by means of a 4–gang condenser having the stators fed with signals in the relative phases 0, 90, 180 and 270° and with the rotors shifted successively 90° to each other. The circuit arrangement is shown in Fig. 14. The reference signal from the Stark modulator is split by an RC bridge into two signals with a 90° phase difference. These drive the grids of a double triode. The cathodes and anodes of this tube furnish signals in the four desired phases.

The output from the phase shifting condenser is amplified by a pentode driving a transformer resonant at 100 kHz.

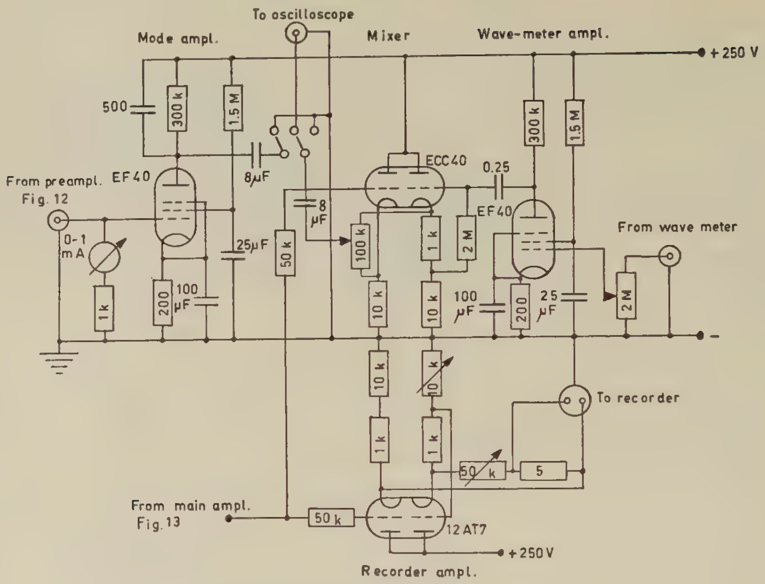

Fig. 15. LF-amplifier circuits.

I.5 *g.* LF circuits

The wavemeter and klystron mode amplifiers are single LF pentode stages as shown in Fig. 15. The mixer consists of two cathode-followers with the signals applied to the grids and with a potentiometer between the cathodes to regulate the relative amplitudes of the two signals.

The recorder is driven by a double triode cathode-follower with the signal applied to one of the grids. The recorder is a 10mV full-scale Brown instrument. It is shunted by a 5-ohm resistor to provide the necessary low input impedance. The amplitude is regulated by a series resistor. The balance is adjusted by the grid voltage of the other triode.

I.5 *h.* Frequency standard

The standard frequencies are derived from a 10 MHz quartz-crystal oscillator. The crystal is mounted in a thermostatic oven keeping the temperature constant within about ± 0.2°C. The oscillator is followed by a buffer amplifier, a quintupler and two tripler stages giving an output frequency from the last stage of 450 MHz. This frequency and samples of the lower frequencies are fed into an 1N26 crystal multiplier. This crystal produces harmonics in the region of the klystron frequency. At the same time it serves as a mixer giving beat-notes between the harmonics and the klystron frequency. Such beat notes falling in the ordinary rf region are detected by a communications receiver, National HRO 7. The arrangement is similar to those described by Good [7] and by Scharbaugh [3].

The circuit diagram of the frequency standard is shown in Fig. 16.

The crystal oscillator is a 7H7 pentode operating essentially in class *A* to ensure good frequency stability. The anode voltage is as low as 75 volts to reduce power dissipation in the crystal. This voltage is electronically regulated.

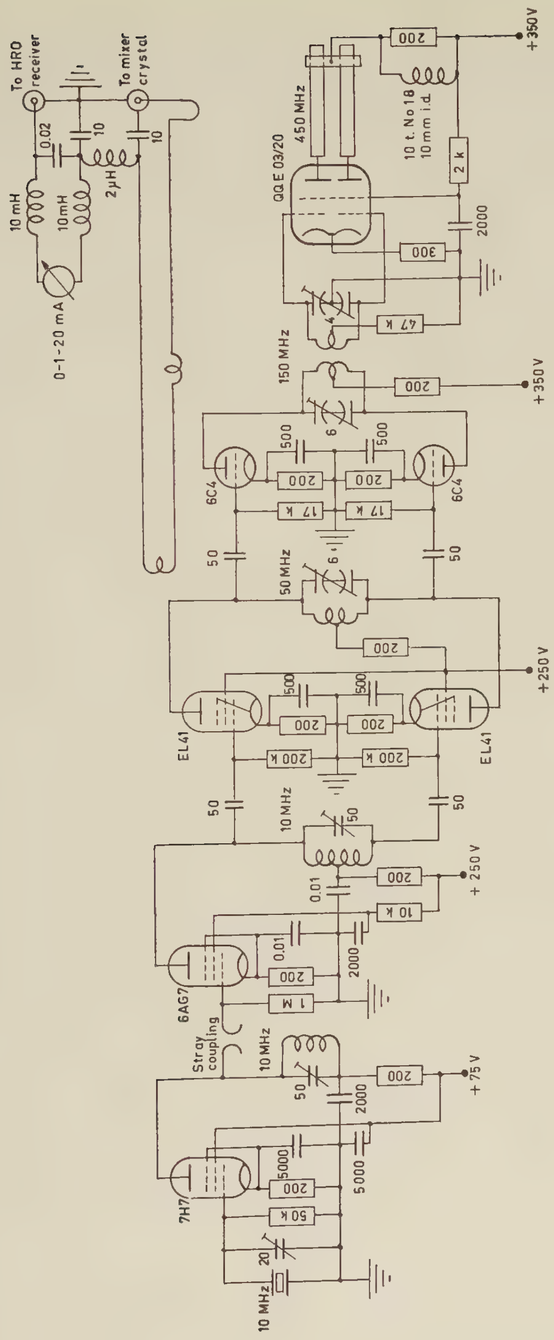

Fig. 16. Frequency standard.

The oscillator is very loosely coupled to the buffer amplifier, which is a 6AG7 pentode working into a phase-splitting tuned circuit. The following multipliers are of the push-pull type. Since the efficiency of a quintupler is rather poor, a pair of 4 W output pentodes (EL41) is used to drive the following 6C4 tripler stage. The final tripler is a QQE 03/20 double tetrode. This tube is capable of delivering 20 W output power at 600 MHz. In the present case the available input power is too slight to drive the tube at its full efficiency. A few watts of output power are, however, obtained at 450 MHz, which is sufficient to give about 20 mA rectified current in the 1N26 silicon-crystal multiplier. This is about the maximum current that may be used with this type of crystal.

The pick-up loop for the standard frequencies and the input coil of the beat-frequency receiver are connected in a series arrangement to the crystal multiplier and mixer. The loop is thereby prevented from loading the receiver input. A filter circuit is provided to by-pass the standard frequencies over the receiver.

I.6. Vacuum system

A three-stage oil diffusion pump preceded by a mechanical fore pump serves to evacuate the absorption cell. The sample to be investigated is placed in a small test tube, which may be evacuated after freezing out the sample with dry ice or liquid air. A small portion of the vapour may be taken out through a lock system consisting of two stopcocks. This vapour is then allowed to expand in a larger chamber, where the pressure may be controlled by a mercury vacustat before letting it out to the absorption cell. The final pressure may then be read on the same vacustat. This is calibrated down to 0.001 mm Hg.

I.7. Performance

I.7 *a*. Sensitivity and resolving power

The sensitivity of the spectrometer is limited mainly by the noise produced by the klystron and the crystal detector. Both of these factors are variable with frequency. A complete specification of instrument sensitivity would therefore require a curve showing minimum detectable absorption versus frequency under optimum conditions, i.e. with the best selection and adjustment of klystron and detector. The compilation of data for such a curve would require the availability of a large number of spectral lines of various and known intensities, and it seems at present to be practically impossible. It may suffice here to mention that absorption lines having absorption coefficients $\alpha \approx 10^{-7}$ cm^{-1} are readily observed on the oscilloscope screen. Examples of such lines are the CH_2O lines at 14362 MHz $\alpha = 1.0 \times 10^{-7}$ cm^{-1} and 19595 MHz $\alpha = 1.5 \times 10^{-7}$ cm^{-1}. With the recorder such lines give fairly strong indications, and the sensitivity may in this case be estimated to be about 10 times better. The HDO-line at 22308 MHz, $\alpha = 1.0 \times 10^{-8}$ cm^{-1} has for example been observed in ordinary water-vapour at a pressure of 0.01 mm Hg.

The possibility of resolving closely spaced lines depends not only on the properties of the instrument, but also on the nature of the molecules investigated. The width of an observed line is in general determined by pressure-broadening. A lower limit for the gas pressure is set by the line strength as compared with the sensitivity of the instrument. Thus in most cases these factors, together with the collision diameter f the molecules, determine the practical resolving power. The comparatively heavy nolecules discussed in the applications (Part II) have rather large collision diameters. he line-widths at 0.01 mm Hg are in the order of a megahertz or more. It has thereore not been possible to resolve lines with theoretical frequencies spaced less than few megahertz apart.

With small molecules and strong absorption lines much better resolution may be btained. For instance hyperfine structure components in the ammonia lines spaced .4 MHz apart are easily resolved completely.

The smallest observed line-widths are about 0.2 MHz, and this figure seems to epresent a limit for the resolving power of the instrument. Factors contributing to his limit are the frequency of the Stark-effect voltage (0.1 MHz), Doppler broadening, nd wall-collision broadening. These factors are discussed in detail in [9]. A further onsideration is frequency instability and hum-modulation in the klystron frequency.

Lines which are especially sensitive to Stark-effect voltages are broadened also y imperfections in the wave-shape of the Stark-effect voltage. This influence has een observed on the internal rotation lines of CH_3OH. The oscilloscope pattern of he lines at 24933.47 and 24934.38 MHz shows a doublet structure at pressures well below 0.01 mm Hg, but the separating minimum and the peak of the high frequency omponent are not clearly visible.

I.7 *b*. Accuracy of frequency measurements

Most of the measurements quoted in the applications discussed in Part II were made before the construction of the frequency standard. They were therefore made vith the cavity wavemeters described in Section I.3., and the accuracy is about ± 5 MHz.

The accuracy obtainable with the frequency standard method depends upon the ccuracy with which the reference frequencies are known. Since the reference frequency and the unknown frequency cannot be checked simultaneously in the instrument used here, the accuracy also depends on the frequency constancy of the rystal oscillator. Other factors of importance are the calibration of the interpolation receiver and the ability of the spectrum receiver to display the correct line-shape. The width and intensity of the absorption line will of course also influence the possibility of setting the frequency-marker exactly on top of the line. A further source of rror may be inability of the Stark modulator to split the line completely, so that the line-shape is distorted by Stark-effect components.

The instrument has no equipment for a comparison of frequencies with standardfrequency broadcasts or other primary standards. The reference frequencies employed are absorption lines measured in other laboratories. The lines most accurately known are the ammonia lines. Ammonia is, however, inconvenient to use, as it is very difficult to get it out of the absorption cell when it has once been introduced. On the other hand, the methyl alcohol lines always appear in the cell owing to the plexiglass insulators (Section I.4). These lines have been measured by Hughes *et al.* [10] to ± 0.1 MHz. Some of these lines have also been remeasured here, using ammonia ines as reference frequencies. The measurements on the ammonia lines are consistent with each other to ± 0.05 MHz (maximum deviation from the results of Good and oles [11]). The results obtained for the methyl alcohol lines may be expected to be of about the same accuracy. These lines are used as references for other lines measured.

The frequency constancy of the crystal oscillator has been tried by measuring an ammonia line every ten minutes during $3\frac{1}{2}$ hours. The deviations observed between these measurements were less than ± 0.015 MHz. The same variations occurred between a series of measurements performed in rapid succession. Since the line-width was about 0.3 MHz, the variations may be ascribed to uncertainty in the receiver settings. Variations in crystal frequency during the time required for the measurements may thus be considered slight as compared with other sources of error.

The interpolation receiver is calibrated against a crystal calibrator giving reference signals every 0.1 MHz, and the scale allows readings to between 1/50 and 1/100 of this value. The calibration is checked from time to time, and the observed variations are slight.

The combined effects of the uncertainties in the frequency measuring system may thus rather safely be considered to give an accuracy of ± 0.1 MHz. Sharp absorption lines with well-resolved Stark effects may be measured to this degree of accuracy if the bandwidth of the spectrum receiver is sufficient for a correct reproduction of the line shape. This condition may be tried by altering the bandwidth or sweep speed and observing that no changes in the relative positions of the line and the frequency-marker occur. For broad lines and lines with more or less unresolved Stark-effect components the errors may be greater.

Part II: Investigated spectra

The spectrometer has been used for the investigation of some organic molecules. It has been found possible to interpret some of the observed spectra as pure rotational spectra of rigid asymmetric rotors. The molecules in question are three mono-substituted benzenes and two cyclopentane compounds. Good agreement between theory and experimental results has been obtained. A short introduction to the theory will be given before the discussion of individual spectra.

II.1. Energy levels of the asymmetric rotor

The quantum mechanical problem of the rigid asymmetric rotor has been treated by several authors, e.g. Witmer [12], Wang [13], Kramers and Ittman [14], Klein [15], and Ray [16]. A treatment of great value for the practical analysis of spectra has been given by King, Hainer and Cross [17]. This paper is in the following referred to as KHC. Reviews of the theory may also be found in [1], [19], and [24]. The details of the theory will not be given here, but only a brief review of the results and the starting points for numerical calculations.

The energy levels of a rigid asymmetric rotor are determined by its three principal moments of inertia, which are generally denoted

$$I_a < I_b < I_c,$$

or the corresponding rotational constants

$$A = h/8\pi^2 I_a,\ B = h/8\pi^2 I_b,\ C = h/8\pi^2 I_c.$$

The rotational angular momentum may be represented by a quantum number J taking on positive integral values. For each value of J there are $2J+1$ distinct energy levels. These cannot be expressed explicitly, but are obtained as the roots of a secular equation of degree $2J+1$ determined by the rotational constants. This equation may be split into four factors of roughly equal order.

The problem may be simplified by a transformation referring the energy levels of an arbitrary asymmetric rotor to those of another rotor, which has fixed values for two of the rotational constants. This may be done in several ways. A transformation introduced by Ray [16] and further developed by KHC uses a reference rotor with rotational constants 1, $\varkappa$, and -1. The intermediate rotational constant $\varkappa$ is determined by

$$\varkappa = \frac{2B-A-C}{A-C},$$

and may be considered as a parameter of asymmetry for the original rotor. It is variable between the limits -1 and $+1$. The former value corresponds to the prolate symmetric rotor $B=C$ and the latter value to the oblate symmetric rotor $A=B$.

With this transformation the desired levels may be expressed as

$$E_\tau(A,B,C) = \tfrac{1}{2}(A+C)J(J+1) + \tfrac{1}{2}(A-C)E_\tau(\varkappa), \tag{1}$$

where $E_\tau(\varkappa)$ are the levels of the reference rotor. τ is a numbering index, which is usually given the integral values $-J \leq \tau \leq J$, from the lowest to the highest level. For a given J the $E_\tau(\varkappa)$ are the roots of four determinantal equations of orders about $J/2$.

In the limiting symmetric cases the levels may be expressed explicitly by the formulas

$$\begin{aligned} E &= BJ(J+1) + (A-B)K^2; \quad (\varkappa=-1) \\ E &= BJ(J+1) + (C-B)K^2; \quad (\varkappa=1). \end{aligned} \tag{2}$$

K is here a quantum number representing the component of rotational angular momentum along the symmetry axis. It may take the $2J+1$ integral values $-J \leq K \leq J$. Since the energy is independent of the sign of K, the levels are doubly degenerate except for $K=0$.

The levels form in the prolate case a series increasing with K and in the oblate case a series decreasing with K. If $\varkappa$ is allowed to vary continuously from -1 to $+1$, the energy levels will also vary continuously from those of the prolate rotor to those of the oblate rotor. No crossings occur between the levels, and therefore the upper level for $\varkappa=-1$ ($K=J$) corresponds to the upper level for $\varkappa=+1$ ($K=0$) and so on. The degenerate pairs in the prolate limit are split up in the intermediate cases, and new pairs are formed in the oblate limit. The situation is illustrated in Fig. 17.

It is easily found that any level for the asymmetric cases may be unambiguously specified by giving J and the K values for the corresponding symmetric rotor levels. This leads to the notation $J_{K_{-1}K_1}$ for the asymmetric rotor levels suggested by KHC. The single index τ defined above is thus replaced by two indices, K_{-1} and K_1. The advantage is that the selection rules for rotational transitions may be expressed in terms of the K's. This type of notation is therefore used in the following.

The fact that the roots $E(\varkappa)$ for a given J depend only on $\varkappa$ makes possible a tabulation of roots which may then be used for the simple calculation of energy levels for arbitrary asymmetric rotors. Such tables have been published by King, Hainer and

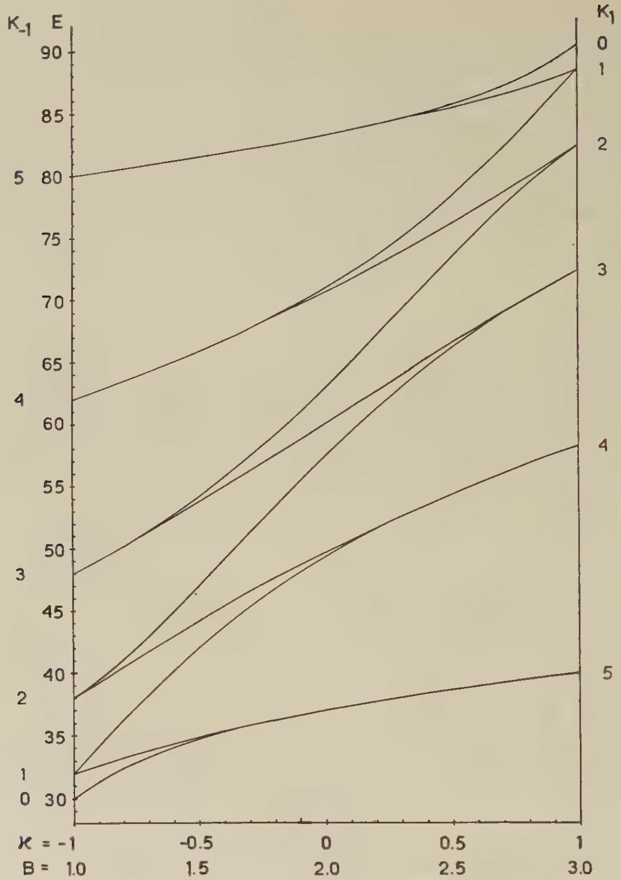

Fig. 17. Energy levels of the asymmetric rotor $J = 5$, $A = 3$, $C = 1$, $1 \le B \le 3$.

Cross [17, 18] for $J \le 12$ and $\varkappa = -1,(0,1),0$. They may also be used for positive values of $\varkappa$ using the relation

$$E_{K_{-1}K_1}(\varkappa) = -E_{K_1K_{-1}}(-\varkappa).$$

These tables are also reprinted in [19]. Unfortunately, interpolation in the tables for intermediate values of $\varkappa$ does not give sufficient accuracy for microwave spectroscopic work. Recently, Turner, Hicks and Reitwiesner [20] have used the computing machine Edvac for tabulating the roots for $J \le 12$ with 0.01 intervals for $\varkappa$. In these tables linear interpolation gives fairly good results. Tables for $13 \le J \le 40$ with 0.1 intervals in $\varkappa$ have also very recently been computed in the electronic machine BESK. The machine program for this purpose was worked out by fil. lic. G. Ehrling. These tables will be published in the *Arkiv för Fysik.*

The BESK program now allows of a rapid computation of roots for any value of $\varkappa$ and any value of $J \le 100$. It is in fact a matter of a few minutes to arrange the machine for the desired computation, and a matter of seconds to get a few roots calculated and typewritten (or punched on a strip for other computations). This means that a very satisfactory method for computing the energy levels of asymmetric rotors has been arrived at.

Most of the spectra discussed in the following were analysed before the tables of Turner and the aid of BESK were available. The roots $E(\varkappa)$ therefore had to be calculated by manual methods. Such calculations involve the solution of algebraic equations of orders about $J/2$. For $J \leq 7$ the equations are at most quartic, and algebraic or trigonometric methods may be used. For $J \geq 8$, equations of fifth and higher orders occur, and other methods must be applied.

The equations for $E(\varkappa)$ may be written in the form

$$\begin{vmatrix} k_0-\lambda & b_1 & 0 & \dots \\ 1 & k_1-\lambda & b_2 & \dots \\ 0 & 1 & k_2-\lambda & \dots \\ \vdots & \vdots & \vdots & \dots k_n-\lambda \end{vmatrix} = 0,$$

where k_m are linear and b_m quadratic expressions in $\varkappa$. Polynomial expansions of the determinant have been given for $J \leq 15$ in [21], [22] and [23]. It is, however, in general more convenient to expand the equations in the form of continued fractions as suggested by KHC.

It is easily found that the determinantal equation may be expanded in the form

$$\lambda = k_m - \cfrac{b_m}{k_{m-1}-\lambda-\cfrac{b_{m-1}}{k_{m-2}-\lambda-\dots}} - \cfrac{b_{m+1}}{k_{m+1}-\lambda-\cfrac{b_{m+2}}{k_{m+2}-\lambda-\dots}},$$

where k_m may be any one of the k's in the determinant. The constants k and b are easily evaluated for any value of J from the expressions and tables given by KHC. If an approximate value of λ is known, this may be inserted on the right hand side of the equation, and a new value is obtained by evaluating the fractions. The process is sometimes convergent, so that the new value is better than the original one. This is not always the case, but if the original value is sufficiently good, the correct value is to be found between this and the new one. The convergence entailed in the method will depend upon what expansion is chosen for the desired root.

The determinantal equation may be set up in three different forms according to the choice of the coordinate system with respect to the molecule. In one of these forms the $b_m = 0$ for $\varkappa = -1$. For this case one obtains $\lambda_m = k_m$, and the energy expressions take the form of equation (2). With another choice of determinantal equation the same occurs for $\varkappa = 1$. For each of these cases there is thus a correspondence between the roots λ_m and k_m. This correspondence may be considered to obtain also for other values of $\varkappa$. For the evaluation of a certain root λ_m it is advisable to choose the determinantal equation that is diagonal in the nearest limit for $\varkappa$ and to start the expansion with k_m corresponding to λ_m. If $\varkappa$ is near zero, a third form of equation, having $k_m = 0$ for $\varkappa = 0$, may be convenient.

The continued fraction method thus offers a straightforward method for the calculation of asymmetric rotor energy levels. It has been used in the present work for all equations of higher degree than the second. It is also used for the computations in BESK.

II.2. Intensities and selection rules

Selection rules for transitions between energy levels of the asymmetric rotor have been derived from symmetry considerations by Dennison [25]. A fairly complete treatment based on intensity calculations has been given by Cross, Hainer and King [26]. Their paper also contains tables for the calculation of relative intensities of spectrum lines.

The transitions to be considered here are those associated with the electric dipole moment of the molecule. For such transitions the general selection rule

$$\Delta J = 0 \text{ or } \pm 1$$

applies. All three cases are possible with asymmetric rotors. Following the practice in band-spectroscopy, the lines are classified as P, Q and R-branch lines depending on whether $\Delta J = -1$, 0 or $+1$. Further selection rules depend on the orientation of the dipole moment in the molecule and may be expressed in terms of K_{-1} and K_1 as follows:

$$\begin{aligned} \mu_a \neq 0&: \Delta K_{-1} = \text{even}, \; \Delta K_1 = \text{odd} \\ \mu_b \neq 0&: \Delta K_{-1} = \text{odd}, \; \Delta K_1 = \text{odd} \\ \mu_c \neq 0&: \Delta K_{-1} = \text{odd}, \; \Delta K_1 = \text{even} \end{aligned}$$

where μ_a, μ_b and μ_c represent the dipole components.

The intensity calculations of Cross, Hainer and King [26] show that transitions having the ΔK's equal to zero and one are strongest and may be regarded as first order permitted lines. Transitions involving one $\Delta K = 2$ or 3 are in general weaker but may still have appreciable intensities. They may be regarded as second order permitted lines. Other transitions may be regarded as forbidden, even though they satisfy the parity rules. They are, however, not strictly forbidden but may in some cases be observed.

II.3. Substituted benzene spectra

The investigations of substituted benzene spectra were started here in January 1953. No spectroscopic data were then available for the dimensions of the benzene ring, and the aim was to see whether some information on this point could be obtained from microwave spectroscopy. Such data, obtained from the Raman spectrum of benzene, were, however, published later in 1953 by Stoicheff [27, 28].

The benzene molecule itself has no electric dipole moment and accordingly no observable rotation spectrum. On the other hand, mono-substituted molecules, C_6H_5X, generally have dipole moments; but the substitution may be suspected to disturb the structure of the benzene skeleton. If this is not the case, different molecules with single atom substitutions such as C_6H_5F and C_6H_5Cl should have equal moments of inertia around the C–X axis (apart from the influence of different zero-point vibrations). The same should be true for molecules with linear substituents such as C_6H_5CN.

The three substances mentioned have been investigated in the microwave spectrometer and the observed spectra interpreted as pure rotation spectra of rigid asymmetric rotors. The values found for the least moments of inertia (I_a) are nearly equal, and the observed differences cannot be considered significant. It has been concluded that the benzene skeleton is fairly undisturbed by the substitutions, and that the value for I_a is a good approximation to the corresponding moment of the benzene molecule itself. Since the structure of this molecule is certainly plane and regularly hexagonal, the only unknowns are the C–H and C–C distances. One equation relating these quantities is furnished by the value for I_a. This is much less influenced by d_{CH} than by d_{CC}. An approximate value for d_{CH} may therefore be inserted to give a fairly good approximation to d_{CC}. The resulting value is about 0.003 Å greater than Stoicheff's value.

II.3 *a*. Fluorobenzene

In the first investigation of this molecule reported in [29] and [30] some 50 absorption lines between 17.7 and 26.7 kMHz were measured to ± 5 MHz with cavity wavemeters. An independent investigation has been made by McCulloh and Pollnow [31], who have reported 15 lines in the region 22.1–27.3 kMHz measured to ± 0.1 MHz. A remeasurement of 30 lines between 15.5 and 25.5 kMHz has also recently been made here to about ± 0.2 MHz.

The procedure employed in the first analysis of the spectrum was to calculate the expected rotation spectrum for a supposed molecular model and to compare this with the observed spectrum. Stark-effect observations could to some extent be used as an aid in the identification of the lines.

The approximate model was based on the electron-diffraction work by Finbak and Hassel [32]. These investigators found the benzene structure to be undisturbed by the fluorine substitution. Their results indicated a plane structure, regularly hexagonal except for the C–F bond, with the following values for bond distances:

$$d_{CC} = 1.40 \pm 0.01 \quad d_{CH} = 1.04 \pm 0.05 \quad d_{CF} = 1.31 \pm 0.03 \text{ Å}$$

These values give the rotational constants

$$A = 5.72 \quad B = 2.57 \quad C = 1.77 \text{ kMHz}$$

and the excentricity parameter $\varkappa = -0.60$.

The axis of least moment of inertia (a-axis) is the symmetry axis through the fluorine atom. The electric dipole moment must coincide with this axis. Hence the first order permitted lines should have $\Delta K_{-1} = 0$ and $\Delta K_1 = \pm 1$. Using the energy level tables of KHC it was found that such lines with $\Delta J = 1$ should be expected in the investigated region for $J = 3$–4, 4–5, 5–6 and 6–7 and with $\Delta J = 0$ for various values of $J \geq 7$. From the tables of relative intensities [26] it was found that the latter should have $J > 10$ in order to be of intensity comparable to the R-branch lines.

Now two of the stronger lines observed were found to have only a few Stark-effect components. They should then be associated with low J values and were therefore supposed to be R-branch lines. This assumption was further justified by observations on the spacings and the relative intensities of resolved Stark-effect components. These were compatible with the formulas given by Golden and Wilson [33] for $\Delta J = 1$, but not with those for $\Delta J = 0$. Comparing the observed frequency values (21 388 and 23 388 MHz) with the expected values for the assumed model, the nearest assignments were found to be

$$\nu\,(4_{2.3} - 5_{2.4}) = 21\,388 \text{ MHz and } \nu\,(4_{2.2} - 5_{2.3}) = 23\,388 \text{ MHz}.$$

The frequency of an R-branch line may be written

$$\nu = \tfrac{1}{2}(A + C)2J'' + \tfrac{1}{2}(A - C)\Delta E$$

where $\Delta E = E''(\varkappa) - E'(\varkappa)$. J'' and E'' refer to the higher level and E' to the lower. The values for $\frac{1}{2}(A + C)$ and $\frac{1}{2}(A - C)$ corresponding to the two assignments mentioned above were calculated from this expression for some $\varkappa$ values around -0.60. Corresponding frequencies for other R-branch lines were then evaluated and compared with the experimental spectrum. It was found that for $\varkappa = -0.590$, $\frac{1}{2}(A - C) = 1.9592$ and $\frac{1}{2}(A + C) = 3.7267$ kMHz, all these lines coincided with experimental lines in so far as they might be expected to appear in the investigated region. The differences between calculated and observed frequencies were in all cases within the expected limits of error (± 5 MHz). These results were published in [29].

Attempts to interpret other lines in the observed spectrum as Q-branch lines were not very successful with the constants thus obtained. The reason was found to be that the Q-branch lines are very sensitive functions of $\varkappa$. A series of more closely spaced $\varkappa$ values around -0.590 was therefore tried and tentative assignments made.

The frequency of a Q-branch line is given by

$$\nu = \tfrac{1}{2}(A - C)\Delta E(\varkappa).$$

The constant $\frac{1}{2}(A - C)$ could therefore be calculated for each $\varkappa$ from one assignment, and corresponding frequencies for other Q-branch lines were thereby determined.

In this way it was found that $\varkappa = -0.5880$ and $\frac{1}{2}(A - C) = 1.94839$ made nine lines to coincide with experimental frequencies. These lines formed two sequences, where J increased in steps of 3 and K_{-1} increased with one unit. The frequencies in one sequence ($J = 17$, 20, 23, 26 and 29) first increased with J and then decreased again. Higher members of the other sequence ($J = 12$, 15, 18 and 21) were therefore calculated. For $J = 39$, 42, 45 and 48 the lines were found to fall in the observable region. Complete agreement between observed and calculated frequencies could not be obtained, but assignments could be made to observed lines showing systematic deviations toward lower frequencies. The experimental sequence could also be extrapolated to $J = 51$, 54 and 57. Attempts were made to adjust $\varkappa$ to fit also the higher J values, but this was found impossible without upsetting the agreement for lower J. It was concluded that centrifugal distortion caused the deviations.

The new values obtained for $\varkappa$ and $\frac{1}{2}(A - C)$ were tried also on the R-branch lines, and a new value for $\frac{1}{2}(A + C)$ was calculated to fit these [$\frac{1}{2}(A + C) = 3.71593$]. The resulting theoretical frequencies for these lines were found to agree still better with the experimental ones than before. These results were published in [30].

The independent investigation of the fluorobenzene spectrum by McCulloh and Pollnow [31] included measurements to ± 0.1 MHz of 15 lines belonging to $J = 4$–5, 5–6 and 6–7. Twelve of these are among those reported in [30]. The assignments made therein are confirmed, and the rotational constants show a fairly satisfactory agreement:

	From [30]	From McCulloh and Pollnow
A	5.6643 ± 0.0003	5.66376 kMHz
B	2.5703 ± 0.0002	2.57076 kMHz
C	1.7675 ± 0.0002	1.76794 kMHz
$\varkappa$	-0.5880	-0.58790 ± 0.00002

The deviations are, however, outside the expected limits of error.

In a later investigation here 19 R-branch lines and 11 Q-branch lines have been measured with the frequency standard technique. The apparatus allows of measurements to ± 0.1 MHz but the width of the fluorobenzene lines (0.5–1.0 MHz) causes an extra uncertainty in the marker settings. The actual accuracy has therefore been estimated as about ± 0.2 MHz. The errors may be greater for some lines owing to the occurrence of nearly coinciding unresolved lines. In fact it has been observed that the R-branch lines are accompanied by a number of weaker satellites, which are probably due to excited vibrational states. It may be suspected that satellites exist which are not resolvable from the ground-state line but may influence the observed line-shape and thereby the measured frequency value.

A fine adjustment of the rotational constants based on the R-branch lines has been carried out in such a way that all the lines considered influence the result equally. The method employed is to assume a value for $\varkappa$ and to calculate the corresponding values for $\Delta E(\varkappa)$. These are inserted in the system of equations

$$\tfrac{1}{2}(A+C)2J_i'' + \tfrac{1}{2}(A-C)\Delta E_i(\varkappa) = \nu_i,$$

which is then solved for $\frac{1}{2}(A+C)$ and $\frac{1}{2}(A-C)$ by the method of least squares. The procedure is repeated for a series of $\varkappa$ values covering the region of interest, and the different results are compared.

Since a lot of numerical work is required, a program following the above scheme has been coded for the electronic computing machine BESK. The machine is given the values for J_i, ν_i and $\Delta E_i(\varkappa)$ for two limiting values of $\varkappa$. A tolerance limit for the errors in the individual equations is also provided. The program then proceeds automatically as follows:

1) The set of equations is solved for one $\varkappa$-limit, and the resulting values for $\frac{1}{2}(A+C)$ and $\frac{1}{2}(A-C)$ are printed. These values are inserted in the individual equations and the resulting errors (δ_i) calculated. The sum $\Sigma|\delta_i|$ is printed.

2) The procedure is repeated for interpolated values of ΔE in ten steps to the other limit for $\varkappa$.

3) The interpolation step giving the least value for $\Sigma|\delta_i|$ is selected, and the number of this step is printed. The corresponding individual errors are compared with the tolerance limit. Equations in which the absolute errors exceed the limit are discarded. The corresponding frequency values are printed.

4) The individual errors for the best step are printed with their proper signs.

5) The whole procedure is repeated from the beginning without the rejected equations.

The use of linear interpolation implies that the limits for $\varkappa$ should be sufficiently narrow. If this is not the case, the results may be used to choose a smaller region, and the procedure may be repeated with the correct values for ΔE within the new limits.

The method described has been applied to the fluorobenzene lines in the interval $-0.5885 \le \varkappa \le -0.5875$ and with the frequency values given in the second column of Table 1. For comparison it was also applied to the frequency values obtained by McCulloh and Pollnow, which are reprinted in the third column of Table 1. The tolerance limit for the errors was set to 0.5 MHz. In the first group of frequencies the machine rejected those at 21997.3 and 22006.1 MHz. In the second group the unresolved pair at 26378.8 MHz was rejected. These rejections caused no appreciable differences in the results.

In both cases $\varkappa = -0.5879$ was found to be the best value in agreement with the results of McCulloh and Pollnow. For the first group, however, $\varkappa = -0.5880$ was found to be almost equivalent. The results given by the machine for these values are

		$\frac{1}{2}(A+C)$	$\frac{1}{2}(A-C)$	$\Sigma\|\delta\|_i$*
$\varkappa = -0.5879$	1)	3715.85	1947.94	2.42 MHz
	2)	3715.85	1947.91	2.23
$\varkappa = -0.5880$	1)	3716.43	1948.54	2.52
	2)	3716.41	1948.50	3.28

1 From lines measured here.
2 From lines measured by McCulloh and Pollnow.
* After the rejections specified above.

The agreement between the rotational constants for the two cases is thus very good. Calculated frequency values corresponding to the two values for $\varkappa$ are given in columns 4 and 5 of Table 1. The rotational constants used are averages of the results in cases 1 and 2 above.

A comparison of the results for the two $\varkappa$ values shows them to be nearly equal. The differences exceed 0.2 MHz in only three cases ($4_{1.3} - 5_{1.4}$, $5_{1.4} - 6_{1.5}$ and $5_{3.2} - 6_{3.3}$), where they are 0.3, 0.6 and 0.3 MHz respectively. It seems scarcely justified from these results to give $\varkappa$ closer than to four decimal places.

A radically different situation is encountered with the Q-branch lines. In Table 2 the observed frequency values for these lines are given together with the calculated values for $\varkappa = -0.5879$ and -0.5880 obtained with the corresponding R-branch values for $\frac{1}{2}(A - C)$. Differences of about 10 MHz occur here between the two calculated values for each line. If the differences between observed and calculated frequencies are plotted against $\varkappa$ it is found that for $J \leq 23$ they all go through zero around $\varkappa = -0.58795$. For higher J's the zeros are displaced towards smaller values for $\varkappa$.

In order to fit both the R-branch and the lower state Q-branch lines the constants of the molecule must be specified as follows:

$$\begin{aligned}
\varkappa &= -0.58795 \pm 0.00001\\
\tfrac{1}{2}(A - C) &= 1948.22 \pm 0.10 \text{ MHz}\\
\tfrac{1}{2}(A + C) &= 3716.13 \pm 0.10 \text{ MHz}\\
A &= 5664.35 \pm 0.15 \text{ MHz}\\
B &= 2570.40 \pm 0.03 \text{ MHz}\\
C &= 1767.91 \pm 0.03 \text{ MHz}.
\end{aligned}$$

With the constants $h = 6.62377 \pm 0.00018 \times 10^{-27}$ ergsec and 1 amu $= 1.65963 \pm 0.00003 \times 10^{-24}$ g the moments of inertia are then:

$$\begin{aligned}
I_a &= 89.239 \pm 0.007 \text{ amu Å}^2\\
I_b &= 196.654 \pm 0.013 \text{ amu Å}^2\\
I_c &= 285.920 \pm 0.020 \text{ amu Å}^2.
\end{aligned}$$

For a plane rigid structure one would have $I_a + I_b = I_c$. If zero-point vibrations are considered, this relation will be valid only for the equilibrium values. The moments

Table 1. R-branch lines C_6H_5F.

Transition	ν_{obs}		ν_{calc}	
	Present results	McCulloh and Pollnow	$\varkappa = -0.5879$	$\varkappa = -0.5880$
$3_{0.3}-4_{0.4}$	16 172.3	—	16 172.6	16 172.7
$3_{1.3}-4_{1.4}$	15 514.1	—	15 513.8	15 513.8
$3_{1.2}-4_{1.3}$	18 637.4	—	18 637.4	18 637.6
$3_{2.2}-4_{2.3}$	17 247.0	—	17 247.0	17 247.1
$3_{2.1}-4_{2.2}$	18 427.2	—	18 427.5	18 427.4
$3_{3.1}-4_{3.2}$	17 588.9	—	17 589.3	17 589.3
$3_{3.0}-4_{3.1}$	17 676.6		17 676.7	17 676.7
$4_{0.4}-5_{0.5}$	19 678.2	—	19 678.2	19 678.4
$4_{1.4}-5_{1.5}$	19 219.8	—	19 220.0	19 219.9
$4_{1.3}-5_{1.4}$	22 941.1	22 940.9	22 940.7	22 941.0
$4_{2.3}-5_{2.4}$	21 389.2	—	21 389.3	21 389.4
$4_{2.2}-5_{2.3}$	23 393.7	23 393.8	23 393.5	23 393.4
$4_{3.2}-5_{3.3}$	22 028.8	—	22 029.0	22 029.0
$4_{3.1}-5_{3.2}$	22 321.9	22 322.2	22 321.8	22.321.7
$4_{4.1}-5_{4.2}$	21 997.3	—	21 996.5	21 996.3
$4_{4.0}-5_{4.1}$	22 006.1	—	22 007.0	22 007.0
$5_{0.5}-6_{0.6}$	23 134.5	23 134.7	23 134.5	23 134.7
$5_{1.5}-6_{1.6}$	22 863.0	22 863.5	22 863.0	22 863.0
$5_{1.4}-6_{1.5}$	—	26 960.2	26 960.2	26 960.8
$5_{2.4}-6_{2.5}$	25 427.1	25 427.4	25 427.4	25 427.6
$5_{2.3}-6_{2.4}$	—	—	28 278.0	28 278.1
$5_{3.3}-6_{3.4}$	—	26 445.2	26 445.1	26 445.1
$5_{3.2}-6_{3.3}$	—	27 163.3	27 163.3	27 163.0
$5_{4.2}-6_{4.3}$	—	26 483.2	26 482.9	26 482.9
$5_{4.1}-6_{4.2}$	—	26 528.9[1]	26 529.3	26 529.2
$5_{5.1}-6_{5.2}$	—	26 378.8[1]	26 378.1	26 378.1
$5_{5.0}-6_{5.1}$	—	26 378.8[1]	26 379.2	26 379.2
$6_{0.6}-7_{0.7}$	—	26 605.3	26 605.2	26 605.3
$6_{1.6}-7_{1.7}$	—	26 460.7	26 460.7	26 460.6

[1] Values uncertain.

of inertia obtained are, however, not equilibrium values but effective values for the lowest vibrational state. They show an "inertia defect"

$$\Delta = I_a + I_b - I_c = -0.027 \text{ amu Å}^2.$$

This value is smaller than the uncertainties involved and is thus not significant except as confirmation of the assumed planarity of the molecule.

As discussed at the beginning of Section II.3, the value for I_a may be supposed to be characteristic not only for fluorobenzene, but also for the benzene molecule

Table 2. Q-branch lines C_6H_5F.

Transition	ν_{calc}			ν_{obs}
	$\varkappa = -0.5879$	$\varkappa = -0.5880$	$\varkappa = -0.58795$	
$12_{3.10}-12_{3.9}$	21 847.6	21 846.2	21 846.9	21 846.3
$15_{4.12}-15_{4.11}$	23 979.1	23 975.4	23 977.3	23 976.8
$17_{5.13}-17_{5.12}$	19 538.0	19 531.1	19 534.6	19 535.1
$18_{5.14}-18_{5.13}$	25 600.5	25 593.9	25 597.2	25 596.4
$20_{6.15}-20_{6.14}$	20 285.6	20 275.7	20 280.7	20 280.9
$23_{7.17}-23_{7.16}$	20 669.8	20 656.7	20 663.2	20 662.1
$26_{8.19}-26_{8.18}$	20 736.9	20 720.5	20 728.7	20 725.5
$29_{9.21}-29_{9.20}$	20 530.4	20 510.7	20 520.6	20 514.5
$42_{13.30}-42_{13.29}$	25 371.6	25 333.8	25 352.7	25 315.0
$45_{14.32}-45_{14.31}$	24 258.1	24 216.9	24 237.5	24 189.7
$48_{15.34}-48_{15.33}$	23 025.0	22 981.0	23 003.0	22 943.9

itself. Assuming a plane, regularly hexagonal structure for this molecule, a relatio between the bond distances d_{CC} and d_{CH} may be derived from I_a. Using $I_a = 89.24 +$ ΔI_a and $d_{CH} = 1.08 + \Delta d_{CH}$, one obtains

$$d_{CC} = 1.40026 + 0.008\ \Delta I_a - 0.13\ \Delta d_{CH};$$

or, with $\Delta d_{CH} = \pm 0.03$ and $\Delta I_a = \pm 0.5$ amu Å^2,

$$d_{CC} = 1.400 \pm 0.008 \text{ Å}.$$

From the Raman spectrum of benzene STOICHEFF [28] has found $I_a = 88.92 \pm 0.0$ amu Å^2. The fluorine substitution thus seems to produce a difference of 0.3 amu Å in the moment of inertia. The bond distances determined by Stoicheff from a com parison of the results for C_6H_6 and C_6D_6 are $d_{CH} = 1.084$ and $d_{CC} = 1.3973$ Å showing that the value found here is about 0.003 Å too great.

The value obtained for I_c may be used to calculate the bond distance d_{CF}, stil assuming an undisturbed benzene skeleton. This calculation may conveniently b started with the benzene molecule, where $I_a = I_b$. Removing one hydrogen atom adding the fluorine atom and transforming to the new center of gravity gives th equation

$$I_b = I_a - m_H r_H^2 + m_F r_F^2 - (m_F r_F - m_H r_H)^2/M,$$

where $r_H = d_{CC} + d_{CH}$, $r_F = d_{CC} + d_{CF}$ and M = total molecular weight. It seems mos reasonable here to use Stoicheff's values for I_a, d_{CH} and d_{CC}. One then obtains

$$d_{CF} = 1.305 + 0.06\ \Delta r_H + 0.02\ (\Delta I_b - \Delta I_a) \text{ Å}.$$

The uncertainties Δr_H and ΔI_b are small as compared with ΔI_a, as the latter mus include the unknown distortion of the benzene skeleton. Putting $\Delta I_a = \pm 0.5$ am Å^2, one obtains

$$d_{CF} = 1.305 \pm 0.010 \text{ Å}.$$

Table 3. $C_6^{12}H_5Cl^{35}$.

Transition	ν_{calc}	ν_{obs}	Transition	ν_{calc}	ν_{obs}
$7_{0.7}$–$8_{0.8}$	21 149	21 151	$8_{0.8}$–$9_{0.9}$	23 584	23 584
$7_{1.7}$–$8_{1.8}$	20 781	—	$8_{1.8}$–$9_{1.9}$	23 303	23 308
$7_{1.6}$–$8_{1.7}$	23 342	23 339	$8_{1.7}$–$9_{1.8}$	26 064	26 063
$7_{2.6}$–$8_{2.7}$	22 231	22 233	$8_{2.7}$–$9_{2.8}$	24 926	24 923
$7_{2.5}$–$8_{2.6}$	23 556	23 554	$8_{2.6}$–$9_{2.7}$	26 615	26 616
$7_{3.5}$–$8_{3.6}$	22 642	22 642	$8_{3.6}$–$9_{3.7}$	25 481	25 483
$7_{3.4}$–$8_{3.5}$	22 829	22 830	$8_{3.5}$–$9_{3.6}$	25 811	25 807
$7_{4.4}$–$8_{4.5}$	22 624	22 628	$8_{4.5}$–$9_{4.6}$	25 483	25 483
$7_{4.3}$–$8_{4.4}$	22 632		$8_{4.4}$–$9_{4.5}$	25 502	25 502
$7_{5.3}$–$8_{5.4}$	22 583	22 578	$8_{5.4}$–$9_{5.5}$	25 428	25 427
$7_{5.2}$–$8_{5.3}$	22 583		$8_{5.3}$–$9_{5.4}$	25 428	
$7_{6.2}$–$8_{6.3}$	22 560	22 560	$8_{6.3}$–$9_{6.4}$	25 395	23 595
$7_{6.1}$–$8_{6.2}$	22 560		$8_{6.2}$–$9_{6.3}$	25 395	
$7_{7.1}$–$8_{7.2}$	22 546	—	$8_{7.2}$–$9_{7.3}$	25 376	25 375
$7_{7.0}$–$8_{7.1}$	22 546	—	$8_{7.1}$–$9_{7.2}$	25 376	
			$8_{8.1}$–$9_{8.2}$	25 363	25 359
			$8_{8.0}$–$9_{8.1}$	25 363	

Electron diffraction measurements by FINBAK and HASSEL [32] have given $d_{CF} = 1.31 \pm 0.03$. The agreement is thus satisfactory.

II.3 *b*. Chlorobenzene

The chlorobenzene spectrum is appreciably more complicated than the fluorobenzene spectrum for several reasons:

(*a*) The molecule is heavier. As a consequence the J values of the observed R-branch lines are higher. The number of lines is correspondingly increased.

(*b*) Owing to the increased mass, lower excited vibrational states occur, and more lines belonging to such states are mixed with the ground-state lines.

(*c*) The molecule is more nearly symmetrical ($\varkappa$ nearer to -1). This causes the R-branch lines to form rather cluttered band-heads for the higher values of K_{-1}.

(*d*) The quadrupole moment of the chlorine nucleus causes a hyperfine structure splitting of the lines. This structure has not been resolved but causes a broadening of the lines that makes the resolution of line-groups more difficult.

(*e*) The occurrence of two isotopes, Cl^{35} and Cl^{37}, increases the number of observable lines.

The observed spectrum showed some regions of closely spaced absorption lines and a number of more isolated ones. Most lines were rather broad and weak. The analysis followed the same lines as the preliminary work on fluorobenzene. The expected spectrum for $C_6H_5Cl^{35}$ should contain two line groups, one for $J = 7$–8 and one for $J = 8$–9, each converging for increasing K_{-1} to something like a band-head. Some of the isolated lines could from their Stark effects be identified as R-branch lines. Several

Table 4. $C_6^{12}H_5Cl^{37}$.

Transition	ν_{calc}	ν_{obs}
$8_{0.8}-9_{0.9}$	23 083	—
$8_{1.8}-9_{1.9}$	22 781	—
$8_{1.7}-9_{1.8}$	25 435	—
$8_{2.7}-9_{2.8}$	24 323	24 318
$8_{2.6}-9_{2.7}$	25 883	—
$8_{3.6}-9_{3.7}$	24 828	24 827
$8_{3.5}-9_{3.6}$	25 110	25 114
$8_{4.5}-9_{4.6}$	24 824	24 827
$8_{4.4}-9_{4.5}$	24 839	24 834
$8_{5.4}-9_{5.5}$	24 774	24 776
$8_{5.3}-9_{5.4}$	24 774	
$8_{6.3}-9_{6.4}$	24 744	24 746
$8_{6.2}-9_{6.3}$	24 744	
$8_{7.2}-9_{7.3}$	24 727	—
$8_{7.1}-9_{7.2}$	24 727	—
$8_{8.1}-9_{8.2}$	24 715	—
$8_{8.0}-9_{8.1}$	24 715	—

different possibilities for the assignment of these were tried until a satisfactory interpretation was obtained. This involved all components of $J = 8–9$ and most components of $J = 7–8$. Calculated and observed frequencies are given in Table 3. The rotational constants are

$$A = 5.667 \pm 0.010 \quad B = 1.5770 \pm 0.0005 \quad C = 1.2333 \pm 0.0005 \text{ kMHz},$$

the asymmetry parameter $\varkappa = -0.845 \pm 0.001$, and the moments of inertia

$$I_a = 89.2 \pm 0.2 \quad I_b = 320.5 \pm 0.2 \quad I_c = 409.9 \pm 0.2 \text{ amu Å}^2.$$

The value for I_a agrees fairly well with the value 89.24 found for fluorobenzene.

From the above results the C–Cl distance was found to be 1.706 Å. This value was used to calculate new values for B and C for $C_6H_5Cl^{37}$.

$$B = 1.5320 \quad C = 1.2063 \text{ kMHz}.$$

It was found possible to fit a number of expected lines for this molecule to observed lines with satisfactory agreement (Table 4). The observed lines are, however, rather weak, and the assignments should be considered as tentative.

The results have been published in [34].

II.3 *c*. Benzonitrile

From assumed dimensions of the benzonitrile molecule its microwave spectrum was expected to be very similar to the chlorobenzene spectrum. This assumption was confirmed by experimental results. The analysis therefore offered no additional

Table 5. C_6H_5CN.

Transition	ν_{calc}	ν_{obs}	Transition	ν_{calc}	ν_{obs}
$7_{0.7}-8_{0.8}$	20 828	20 826	$8_{0.8}-9_{0.9}$	23 228	23 226
$7_{1.7}-8_{1.8}$	20 453	20 449	$8_{1.8}-9_{1.9}$	22 938	22 936
$7_{1.6}-8_{1.7}$	21 854	21 857	$8_{1.7}-9_{1.8}$	25 626	25 628
$7_{2.5}-8_{2.6}$	23 105	23 110	$8_{2.7}-9_{2.8}$	24 506	24 507
$7_{3.5}-8_{3.6}$	22 239	22 238	$8_{2.6}-9_{2.7}$	26 110	—
$7_{3.4}-8_{3.5}$	22 407	22 406	$8_{3.6}-9_{3.7}$	25 028	25 030
$7_{4.4}-8_{4.5}$	22 220	22 220	$8_{3.5}-9_{3.6}$	25 327	25 328
$7_{4.3}-8_{4.4}$	22 226	22 231	$8_{4.5}-9_{4.6}$	25 026	25 030
$7_{5.3}-8_{5.4}$	22 181	22 177	$8_{4.4}-9_{4.5}$	25 043	25 044
$7_{5.2}-8_{5.3}$	22 182		$8_{5.4}-9_{5.5}$	24 974	24 972
$7_{6.2}-8_{6.3}$	22 160	22 157	$8_{5.3}-9_{5.4}$	24 975	
$7_{6.1}-8_{6.2}$	22 160		$8_{6.3}-9_{6.4}$	24 944	24 938
$7_{7.1}-8_{7.2}$	22 147	22 144	$8_{6.2}-9_{6.3}$	24 944	
$7_{7.0}-8_{7.1}$	22 147		$8_{7.2}-9_{7.3}$	24 925	24 924
			$8_{7.1}-9_{7.2}$	24 925	
			$8_{8.1}-9_{8.2}$	24 914	24 912
			$8_{8.0}-9_{8.1}$	24 914	
			$9_{0.9}-10_{0.10}$	25 623	25 625

difficulties. Calculated and observed frequency values are given in Table 5. The following values for the constants were obtained

$$A = 5.654 \quad B = 1.546 \quad C = 1.2145 \text{ kMHz} \quad \varkappa = -0.8505$$

$$I_a = 89.40 \quad I_b = 327.0 \quad I_c = 416.2 \text{ amu Å}^2.$$

The results were published in [35].

An independent investigation of the benzonitrile spectrum was carried out simultaneously by Lide [36], with greater accuracy in the frequency measurements. Lide's results indicate an average error of ± 5.7 MHz in the observed values given in Table 5. This is a little more than usual with the wavemeter in question. The reason for this may be difficulties in the measurements due to weakness of the lines and to the rather considerable line widths, which were a few MHz. The assignments made by Lide agree, however, with those given above. The constants according to Lide are:

$$A = 5.6554 \quad B = 1.54688 \quad C = 1.21443 \text{ kMHz} \quad \varkappa = -0.85027$$

$$I_a = 89.370 \quad I_b = 326.740 \quad I_c = 416.183 \text{ amu Å}^2$$

in good agreement with the results obtained here.

The value for I_a is slightly larger than the value found for fluorobenzene. The deviation may be caused by displacement of hydrogen atoms or by zero-point vibrations of the CN group.

Table 6. Cyclopentanone.

Transition	ν_{calc}	ν_{obs}
$2_{1.1}-3_{1.2}$	18 572	18 573
$3_{0.3}-4_{0.4}$	21 564	21 565
$3_{1.3}-4_{1.4}$	20 864	20 863
$3_{1.2}-4_{1.3}$	24 505	24 503
$3_{2.2}-4_{2.3}$	22 905	22 911
$3_{2.1}-4_{2.2}$	24 382	24 381
$3_{3,1}-4_{3.2}$	23 340	23 335
$3_{3,0}-4_{3.1}$	23 462	23 462
$14_{4.11}-14_{4.10}$	23 548	23 551
$19_{6.14}-19_{6.13}$	20 891	20 893
$22_{7.16}-22_{7.15}$	22 194	22 206
$25_{8.18}-25_{8.17}$	23 251	23 256
$28_{9.20}-28_{9.19}$	24 086	24 089
$31_{10.22}-31_{10.21}$	24 720	24 723
$34_{11.24}-34_{11.23}$	25 169	25 172
$37_{12.26}-37_{12.25}$	25 452	25 460
$40_{13.28}-40_{13.27}$	25 584	25 594
$43_{14.30}-43_{14.29}$	25 580	25 589
$46_{15.32}-46_{15.31}$	25 455	25 464
$49_{16.34}-49_{16.33}$	25 217	25 234
$52_{17.36}-52_{17.35}$	24 883	24 899
$55_{18.38}-55_{18.37}$	24 466	24 484

II.4. Cyclopentane compounds

The five-membered carbon ring in cyclopentane (C_5H_{10}) is, according to the thermodynamic results of Aston, Fink and Schumann [37], not exactly plane but slightly skew. As a check on this point a microwave spectroscopic investigation of cyclopentanone (C_5H_8O) was undertaken [38]. (Cyclopentane itself has no dipole moment and could not be investigated.) The results clearly indicated a non-planarity in the ring. If this is due to repulsion between the hydrogen atoms, it seems reasonable that a similar effect should occur in cyclopentane, although it may be of a different type and magnitude. In connection with this work Dr. Stig Sunner in Lund suggested an investigation of the isomeric molecule cyclopentene oxide, which was also carried out [39].

II.4 *a*. Cyclopentanone

The cyclopentanone molecule has the structure formula

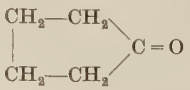

Assuming ordinary bond distances it was found that the rotation spectrum should be similar to the one found for fluorobenzene. The J values of the observable R-branch lines should, however, be about one unit lower. This was readily confirmed by experiments. The analysis was based primarily on the lines $J = 3$–4. Fine adjustment of the constants was made to fit some Q-branch lines with $J \geq 14$. A satisfactory agreement was obtained to about $J = 34$ and a rougher agreement to $J = 55$. Calculated and observed frequency values are given in Table 6. The rotational parameters were found to be

$$A = 6.6189 \quad B = 3.3508 \quad C = 2.4099 \text{ kMHz} \quad \varkappa = -0.5529$$
$$I_a = 76.369 \quad I_b = 150.85 \quad I_c = 209.75 \text{ amu Å}^2.$$

The difference $I_a + I_b - I_c = 17.47$ amu Å^2 is certainly too great to be caused by the hydrogen atoms alone, which may be expected to contribute about 12 amu Å^2. The results therefore indicate a non-planarity of the carbon ring.

The type and magnitude of the non-planarity cannot be derived from these results alone. It seems reasonable, however, to assume that the CO group and the two adjacent C atoms lie in one plane, and that the two opposite C atoms are displaced to different sides of this plane. The order of magnitude of these displacements may be estimated to 0.2 Å.

An estimate of the C–C distances in the ring may be obtained by making some simplifying assumptions. The non-planarity is for this purpose neglected, and the structure is assumed to be regularly pentagonal except for the oxygen atom. The latter is supposed to be on the symmetry axis. The H–C–H angle is set to 110° and the C–H distance to 1.08 Å. One then obtains $d_{\text{CC}} = 1.51$ Å. Under the same conditions the C–O distance is found to be $d_{\text{CO}} = 1.23$ Å.

II.4 *b*. Cyclopentene oxide

Cyclopentene oxide has the same over-all formula (C_5H_8O) as cyclopentanone but a different structure[1]

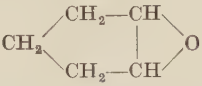

The oxygen atom is certainly not in the (approximate) plane of the carbons. The molecule may therefore have two active components of electric dipole moment. The rotation spectrum may thus be expected to be quite complicated, which was also confirmed by experiment. Sufficient data on the molecular structure were not available for direct application of the methods described in the preceding sections for the analysis. Instead, a systematic search for lines with resolvable Stark effects was carried out. Extensive regions of the spectrum were recorded several times with different DC and AC voltages applied to the Stark-effect electrode. In this way three lines were found, which could be ascribed to transitions $J = 2$–3. Different possibilities of assignments for these lines were tried, and corresponding positions for the two remaining components calculated. (It was clear from structure considerations that the lines should be due to the a-component of the dipole, and the number of components should thus be five.) The lines in question were found near the expected positions for

---

[1] A sample of this substance was obtained as a gift from Dr. STIG ANDERSSON in Lund.

Table 7. Cyclopentene oxide.

Transition	ν_{calc}	ν_{obs}
$2_{0.2}-3_{0.3}$	21 450	21 446
$2_{1.2}-3_{1.3}$	21 095	21 094
$2_{1.1}-3_{1.2}$	24 746	24 751
$2_{2.1}-3_{2.2}$	23 367	23 365
$2_{2.0}-3_{2.1}$	25 286	25 284
$10_{3.7}-10_{5.6}$	22 135	22 140
$11_{4.8}-11_{4.7}$	24 470	24 470
$11_{3.8}-11_{5.7}$	25 301	25 304
$11_{4.7}-11_{6.6}$	22 773	22 775
$12_{5.8}-12_{5.7}$	22 569	22 568
$12_{4.8}-12_{6.7}$	25 128	25 133
$12_{5.7}-12_{7.6}$	24 963	24 968
$10_{7.3}-10_{8.3}$	23 721	23 717
$10_{7.4}-10_{8.2}$	24 221	24 221
$11_{6.6}-11_{7.4}$	23 025	23 028
$11_{7.4}-11_{8.4}$	22 070	22 070
$11_{7.5}-11_{8.3}$	23 902	23 900
$12_{7.6}-12_{8.4}$	24 264	24 262

one of the alternatives tried. Their Stark effects were resolved, and the assignments confirmed.

The data thus available made it possible to identify some Q-branch lines, and the constants were adjusted to a best fit for these. Some of these lines are associated with the a-component and others with the c-component of the dipole moment. The former have $\Delta K_{-1} = 0$ or 2 and $\Delta K_1 = -1$. The latter have $\Delta K_{-1} = \pm 1$ and $\Delta K_1 = 0$ or ± 2. The intensity relations indicate that the two components of the dipole moment are of about equal magnitude. The frequency values are listed in Table 7. The following values were obtained for the constants:

$$A = 5.7086 \quad B = 4.5404 \quad C = 3.2486 \text{ kMHz} \quad \varkappa = 0.0502$$
$$I_a = 88.55 \quad I_b = 111.33 \quad I_c = 155.60 \text{ amu Å}^2.$$

The results allow some rough estimates of molecular structure constants. For this purpose the molecule is assumed to consist of a plane, regularly pentagonal carbon ring with the hydrogen atoms in radial planes and with the oxygen atom in a symmetry plane. The C–H bonds are supposed to be 1.08 Å and to form angles of 55° with the ring plane. One then obtains $d_{\text{CC}} = 1.52$ Å and $d_{\text{CO}} = 1.47$ Å. The angle between the COC triangle and the carbon ring is found to be 98°. Both the bond distances appear rather large as compared with the results for ethylene oxide ($d_{\text{CC}} =$ 1.472, $d_{\text{CO}} = 1.436$) obtained by CUNNINGHAM *et al.* [40]. A considerably smaller value for d_{CO} is, however, obtained if some correction is made for non-planarity in the ring. Probably the ring is also not regularly pentagonal, but has a shorter distance between the carbon atoms connected to oxygen.

Summary

A Stark-modulated microwave spectrometer is described in some detail. Circuit diagrams of the electronic equipment are given.

The instrument has been used to investigate a number of asymmetric top molecules. The observed spectra of three mono-substituted benzenes and two cyclopentane derivatives have been analyzed. The former are C_6H_5F, C_6H_5Cl and C_6H_5CN. From their moments of inertia it has been found that the distortions of the benzene skeleton by the substituents are slight. A value for the C–C distance in the benzene ring has been obtained together with values for the C–F and C–Cl distances. The results agree with those obtained by other methods.

The cyclopentane derivatives investigated are cyclopentanone and cyclopentene oxide, both with the formula C_5H_8O. The results on cyclopentanone confirm the assumption that a non-planarity occurs in the five-membered carbon ring. The assumed structures of the two molecules have also been confirmed.

The values obtained for the principal moments of inertia of the investigated molecules are collected in the following table (in amu Å²)

	I_a	I_b	I_c
Fluorobenzene	89.239	196.65	285.92
Chlorobenzene (Cl^{35})	89.2	320.5	409.9
,, (Cl^{37})	89.2	329.9	419.0
Benzonitrile	89.4	327.0	416.2
Cyclopentanone	76.37	150.9	209.8
Cyclopentene oxide	88.55	111.3	155.6

REFERENCES

1. W. Gordy, W. V. Smith, and R. F. Trambarulo, Microwave Spectroscopy. J. Wiley and Sons, New York, 1953.
2. R. H. Hughes and E. B. Wilson Jr., Phys. Rev. *71*, 562, 1947.
3. K. B. McAfee Jr., R. H. Hughes, and E. B. Wilson Jr., Rev. Sci. Instr. *20*, 821, 1949.
4. A. H. Scharbaugh, Rev. Sci. Instr. *21*, 120, 1950.
5. B. Bleany, J. H. N. Loubser, and R. P. Penrose, Proc. Phys. Soc. *59*, 185, 1947.
6. C. G. Montgomery, Technique of Microwave Measurements. McGraw Hill, New York, 1948.
7. W. E. Good, Proc. Natl. Electronics Conference *6*, 29, 1950.
8. T. Soller, M. A. Star, and G. E. Valley, Cathode Ray Tube Displays. McGraw Hill, New York, 1948.
9. S. Geschwind, Ann. New York Acad. Sci. *55*, 751, 1952.
10. R. H. Hughes, W. E. Good, and D. K. Coles, Phys. Rev. *84*, 418, 1951.
11. W. E. Good and D. K. Coles, Phys. Rev. *71*, 383, 1947.
12. E. Witmer, Proc. Natl. Acad. Sci. U.S. *13*, 60, 1927.
13. S. C. Wang, Phys. Rev. *34*, 243, 1929.
14. H. A. Kramers and G. P. Ittmann, Z. Physik *53*, 553, 1929.
15. O. Klein, Z. Physik *58*, 730, 1929.
16. B. S. Ray, Z. Physik *78*, 74, 1932.
17. G. King, R. M. Hainer, and P. C. Cross, Journ. Chem. Phys. *11*, 27, 1943.
18. R. M. Hainer, P. C. Cross, and G. W. King, Journ. Chem. Phys. *17*, 826, 1949.
19. M. W. P. Strandberg, Microwave Spectroscopy. Methuen, London, 1954.
20. T. E. Turner, B. L. Hicks, and G. Reitwiesner, Ballistic Research Laboratories, Report Nr. 878. Aberdeen Proving Ground, Maryland, U.S.A.
21. H. H. Nielsen, Phys. Rev. *38*, 1432, 1931.

22. H. M. Randall, D. M. Dennison, N. Ginsburg, and L. R. Weber, Phys. Rev. *52*, 160, 1937
23. N. Ginsburg, Phys. Rev. *74*, 1052, 1948.
24. H. H. Nielsen, Rev. Mod. Phys. *23*, 90, 1951.
25. D. M. Dennison, Rev. Mod. Phys. *3*, 280, 1931.
26. P. C. Cross, R. M. Hainer, and G. W. King, J. Chem. Phys. *12*, 210, 1944.
27. B. P. Stoicheff, J. Chem. Phys. *21*, 1410, 1953.
28. B. P. Stoicheff, Can. J. Phys. *32*, 330, 1954.
29. G. Erlandsson, Arkiv för Fysik *6*, 477, 1953.
30. G. Erlandsson, Arkiv för Fysik *7*, 189, 1953.
31. K. E. McCulloh and G. F. Pollnow, J. Chem. Phys. *22*, 1144, 1954.
32. C. Finbak and O. Hassel, Arch. Math. Naturvidenskab *45*, 45, 1941.
33. S. Golden and E. B. Wilson Jr., J. Chem. Phys. *16*, 669, 1948.
34. G. Erlandsson, Arkiv för Fysik *8*, 341, 1954.
35. G. Erlandsson, J. Chem. Phys. *22*, 1152, 1954.
36. D. R. Lide Jr., J. Chem. Phys. *22*, 1577, 1954.
37. J. G. Aston, H. L. Fink, and S. C. Schumann, J. Am. Chem. Soc. *65*, 341, 1943.
38. G. Erlandsson, J. Chem. Phys. *22*, 563, 1954.
39. G. Erlandsson, Arkiv för Fysik *9*, 341, 1955.
40. G. L. Cunningham Jr., A. W. Boyd, R. W. Myers, W. D. Gwinn, and W. J. Le Van, J. Chem. Phys. *19*, 676, 1951.

Tryckt den 15 april 1955

Uppsala 1955. Almqvist & Wiksells Boktryckeri AB

ARKIV FÖR FYSIK Band 9 nr 29

Communicated 1 December 1954 by Oskar Klein and Ivar Waller

On the limiting vibrational frequencies of a cubic ionic lattice

By Stig O. Lundqvist

Summary

The vibrations of a cubic ionic lattice are investigated on the basis of a potential energy, which is a first approximation of the expression for the cohesive energy in the Heitler-London treatment of ionic crystals. Besides ordinary two-particle interactions this potential contains a term which represents a three-body interaction. This term accounts (to a first approximation) for the deviations from the Cauchy relations. The main effect of this term is the introduction of an effective ionic charge. Formulae are derived for the transverse and longitudinal frequencies of long polar vibrations under the assumption that the optical polarisation can be neglected. By expressing the total polarisation in terms of the dielectric constants for static and high-frequency ields more accurate formulae for the frequencies are derived, which are generalisations of those given by Szigeti for the case of central forces. Numerical applications are given for NaCl and KCl.

I. Introduction

The vibrations of an ionic lattice have up to now been investigated essentially only on the basis of the original Born model, according to which the ions in the lattice are regarded as held in their positions by the attractive electrostatic forces between the ions and by repulsive forces of short range. Both the electrostatic and repulsive nteractions are assumed to be central. Under these assumptions the Cauchy relation $c_{12} = c_{44}$ would be fulfilled in those crystals where each ion is a centre of symmetry, whereas it is now well known that the Cauchy relations are in general not valid in onic crystals.

The use of the Born model implies the assumption that in the oscillations the charge cloud of each ion is bodily displaced. In reality, however, the ions in the lattice are not rigid structures and the oscillations result in complicated deformations of the ons. The importance of taking the deformability of the ions into account in many problems has been pointed out especially by Born [5].

According to a well-known theorem by Born and Oppenheimer [8] the potential energy of the lattice is equal to the lowest eigenvalue of the total electronic energy, f the nuclei are held in fixed positions. A first approximation of this eigenvalue has been obtained from the Heitler-London approximation for several ionic crystals by Hylleraas [16], Landshoff [18], Löwdin [23] and others. Their results are in general in rather good agreement with the experimental values. Löwdin pointed out that the overlap of the atomic wave functions introduces interaction terms corresponding to a rather complicated many-body potential. He also computed the elasti constants for several alkali halides taking such terms into account and found that th calculated values agree rather well with the empirical results; the deviations from th Cauchy relations have the correct sign but are too large. In the Heitler-Londo approximation the atomic wave functions are rigidly connected with the nuclei an are supposed not to change in a deformation of the lattice, but this will not impl that the charge density can be written as the sum of the charge densities for a syste of free ions. The reason is that the anti-symmetry of the wave function introduce terms which cause the charge distribution to differ from the sum of densities for fre ions, the differences being most pronounced in the regions where the overlap betwee the atomic wave functions is large. Accordingly the potential energy will contai terms which depend on the distortion of the charge distribution, which is due t the overlap of the wave functions and which appears even if the atomic wave functions are fixed. If the wave functions are assumed to be fixed, such a description o the deformation of the ions in the lattice is certainly not very realistic, especiall when the nuclei are displaced from their equilibrium positions. However, the expression for the total energy in the Heitler-London approximation is valid even i the atomic wave functions are allowed to vary. The change in the wave function can be estimated by minimizing the total energy.

In this paper we shall treat only the long polar vibrations of the lattice and w shall consider only a first order modification of the Born model. This modificatio is obtained by using the approximate expression for the potential energy, obtaine from the so-called S^2 approximation of the Heitler-London approximation, whic has been used by Löwdin in his calculations. This expression contains terms whic represent a three-particle interaction. The magnitude of these terms is less than te percent of the binding energy of the crystal for the alkali halides. By approximatin these terms in a simple way it is possible to relate the frequencies to well-known constants of the crystal, the lattice constant and the three elastic constants c_{11}, c_{12} an c_{44}. The expression for the potential energy can therefore be considered as a semi-empirical form for the interaction between the ions in the lattice and can be usefu in calculations of the vibrations if the empirical constants are known with sufficien accuracy. The optical polarisation of the ions will be neglected in the first part o this paper, but will later be taken into account in a semi-empirical way using certai relations first derived by Lyddane, Sachs and Teller [22] involving the dielectri constants for static and high-frequency fields.

II. The potential energy

Formulae for the energy of an ionic crystal with ions having complete electro shells have been derived in the Heitler-London approximation by Hylleraas [16], Landshoff [18], and Löwdin [23]. Hylleraas formulated the physics of the problem and derived the energy expression for the LiH crystal. Landshoff introduced the convenient calculating device of using approximately ortho-normalized one-electron wave functions, obtained as linear combinations of the one-electron wave functions of the free ions. Later Löwdin derived a mathematically exact energy expression in the Heitler-London approximation by using a mathematically exact method of ortho-normalization. In his calculations, however, he used a series expansion in the overlap integrals defined below and considered and approximation milar to Landshoff's, taking some more terms into account.[1] Löwdin's exact nergy expression is rather complicated and has, except for LiH [20], not yet been sed in any calculation. Therefore we shall here use Löwdin's S^2 approximation.

The complete expression for the potential energy in terms of integrals over the tomic wave functions will not be given here[2] but we shall give a brief account of he different terms in it. Apart from the constant term, which represents the energy f the free ions, the energy can be divided into three distinct parts:

A. The classical electrostatic energy of the lattice, which is obtained by considering he ions as point charges

$$\Phi_A = \frac{e^2}{2} \sum_G \sum_{G'}^{(G)} \frac{\varepsilon_G \, \varepsilon_{G'}}{|\boldsymbol{r}_G - \boldsymbol{r}_{G'}|}. \tag{1}$$

Here ε_G denotes the valency of the ion at the lattice point G, and e is the Electron charge. $\sum_{G'}^{(G)}$ denotes a summation, where the term $G' = G$ shall be mitted.

B. Terms which depend only on the distance between two neighbouring nuclei. These terms give the main contribution to the repulsive potential between the ions. Without specifying the exact form of these terms we can collect them into a potential

$$\Phi_B = e^2 \sum_G \sum_{G'} V'(|\boldsymbol{r}_G - \boldsymbol{r}_{G'}|). \tag{2}$$

C. Terms, which correspond to a three-body potential[3]

$$\Phi_c = e^2 \sum_\mu \sum_\nu \sum_G{}^{(G_\mu G_\nu)} \varepsilon_G \, P_{\mu\nu} (\nu \, G \, \mu). \tag{3}$$

$\sum_G^{(G_\mu G_\nu)}$ denotes a summation, where G is always different from both G_μ and G_ν. $P_{\mu\nu}$ are the elements of a matrix $\boldsymbol{P}$ given by

$$\boldsymbol{P} = \frac{\boldsymbol{S}}{\boldsymbol{1} + \boldsymbol{S}},$$

where $\boldsymbol{S}$ is the Hermitian matrix in which the elements are the overlap integrals

$$S_{\mu\nu} = \int \psi_\mu^* (x) \, \psi_\nu (x) \, d\tau - \delta_{\mu\nu}.$$

ψ_μ are the normalized one-electron wave functions including spin and x means the spin and space coordinates of an electron $x = (\boldsymbol{r}, \zeta)$. The index μ refers to an electron with the quantum numbers n, l, m, s associated with an ion at a certain lattice point

---

[1] In contrast to Landshoff's energy expression, Löwdin's approximate energy expression can be characterized as a consequent S^2 approximation. In this approximation terms which are small of third and higher orders are neglected and only the overlap between nearest neighbours is considered. Cf. ref. [23], p. 38.

[2] P. O. Löwdin, Thesis, Uppsala 1948.

[3] We wish to define Φ_c as a pure many-body potential. This is the case according to (3) for the exact $P_{\mu\nu}$ but for the approximate $P_{\mu\nu}$, which we shall use here, certain terms for $\mu = \nu$ correspond to a two-body potential. These terms are assumed to be excluded in (3) and included in Φ_B.

G_μ. The sign $\int d\tau$ implies integration over the space coordinates and summation ove the spin coordinate. The symbol $(\nu G \mu)$ means the integral

$$(\nu G \mu) = \int \psi_\nu^* (x) \frac{1}{|\boldsymbol{r} - \boldsymbol{r}_G|} \psi_\mu (x) \, d\tau.$$

In the S^2-approximation we put[1]

$$P_{\mu\nu} = S_{\mu\nu} - (S^2)_{\mu\nu} \delta_{\mu\nu}.$$

From the expression for the charge density, which in units of e is given b

$$\varrho(\boldsymbol{r}) = \sum_\zeta \sum_{\mu\nu} T_{\mu\nu} \psi_\nu (x) \psi_\mu^* (x),$$

where $T_{\mu\nu}$ are elements of the matrix

$$\boldsymbol{T} = (\boldsymbol{1} + \boldsymbol{S})^{-1} = \boldsymbol{1} - \boldsymbol{P},$$

we can see that Φ_c represents a correction to the classical electrostatic energ of the lattice due to the overlap of the atomic wave functions. If the overla is zero, then

$$\varrho(\boldsymbol{r}) = \sum_G \varrho_G (\boldsymbol{r}),$$

where $\varrho_G(\boldsymbol{r})$ is the charge density in a free ion at the lattice point G. Th change in the charge density due to the overlap is

$$\Delta \varrho(\boldsymbol{r}) = \varrho(\boldsymbol{r}) - \sum_G \varrho_G(\boldsymbol{r}) = - \sum_\zeta \sum_{\mu\nu} P_{\mu\nu} \psi_\nu (x) \psi_\mu^* (x).$$

The integral of $\Delta\varrho(\boldsymbol{r})$ over the unit cell is zero. Comparing with (3) we fin that Φ_c represents the interaction between this charge distribution of zero ne charge with the ions in the lattice regarded as point charges, except for th ions at G_μ and G_ν.[2]

The expression (3) has earlier been calculated by LÖWDIN and the present write using different methods. LÖWDIN expands the integral in spherical harmonics wit the origin at the lattice point of the positive ion.[3] The expansion converges rapidl if the positive ion is small, but for large positive ions the overlap products $\psi_\nu^* (\boldsymbol{r}) \psi_\mu (\boldsymbol{r}$ will no longer be preferently localized around the nucleus of the positive ion and fo crystals with large positive ions the convergency of the expansion will be rathe slow. An alternative method has been proposed by the present writer [19] accordin to which the integral is expanded in spherical harmonics with the origin at the cente of gravity of the overlap density $\psi_\nu^* (\boldsymbol{r}) \psi_\mu (\boldsymbol{r})$. For NaCl this expansion seems t converge rapidly and it is a good approximation to neglect all but the first term However already the first term will be a rather complicated function of the relativ coordinates of three nuclei because each pair of overlapping orbitals has its ow center of gravity, the coordinates of which will appear in the formulae. As both methods would lead to rather complicated expressions for the coefficients appearing in Section IV, none of them seems to be well suited for the purpose of this investigation.

---

[1] Note that $(\mu G \mu)$ is of zero order in $S_{\mu\nu}$. Cf. ref. [23], p. 38.

[2] Note that the selfpotential of $\Delta\varrho(\boldsymbol{r})$ is of the fourth order in $S_{\mu\nu}$ and will therefore not appea in the S^2 approximation.

[3] This method was first introduced in this problem by LANDSHOFF for NaCl.

In this investigation we can avoid the drawbacks of the methods used earlier in a very simple way. Consider an infinite plane orthogonal to the line $\overline{G_\mu G_\nu}$ through a suitably chosen point between G_μ and G_ν. It is then immediately clear that we can write

$$(\nu\, G\, \mu) = (\nu\, G\, \mu)_{G_\mu} + (\nu\, G\, \mu)_{G_\nu},$$

where $(\nu G \mu)_{G_\mu}$ means that the integration has to be restricted to the half-space containing G_μ and correspondingly for $(\nu G \mu)_{G_\nu}$. We then get[1]

$$\begin{aligned}\Phi_c &= e^2 \sum_\mu \sum_\nu \sum_G^{(G_\mu G_\nu)} \varepsilon_G\, S_{\mu\nu} \{(\nu\, G\, \mu)_{G_\mu} + (\nu\, G\, \mu)_{G_\nu}\} - \\ &\quad - e^2 \sum_\mu \sum_\nu \sum_G^{(G_\mu G_\nu)} \varepsilon_G\, S_{\mu\nu}\, S_{\nu\mu}\, (\mu\, G\, \mu) \\ &= 2\, e^2 \sum_\mu \sum_\nu \sum_G^{(G_\mu G_\nu)} \varepsilon_G\, S_{\mu\nu}\, (\nu\, G\, \mu)_{G_\mu} - \\ &\quad - e^2 \sum_\mu \sum_\nu \sum_G^{(G_\mu G_\nu)} \varepsilon_G\, S_{\mu\nu}\, S_{\nu\mu}\, (\mu\, G\, \mu).\end{aligned} \tag{4}$$

We shall here consider only the overlap between nearest neighbours in which case the integrand vanishes outside a rather small region surrounding G_μ. We can therefore expect to get a rather good first approximation if we replace $\dfrac{1}{|\boldsymbol{r} - \boldsymbol{r}_G|}$ by $\dfrac{1}{|\boldsymbol{r}_{G_\mu} - \boldsymbol{r}_G|}$ both in $(\nu\, G\, \mu)_{G_\mu}$ and in $(\mu\, G\, \mu)$. If this is done and if we sum over the orbitals associated with G_μ and G_ν we can write

$$\Phi_c = e^2 \sum_G \sum_{G'} \sum_{G''}{}^{(G G')} f_G(|\boldsymbol{r}_G - \boldsymbol{r}_{G'}|)\, \frac{\varepsilon_{G''}}{|\boldsymbol{r}_G - \boldsymbol{r}_{G''}|}, \tag{5}$$

where

$$f_G(|\boldsymbol{r}_G - \boldsymbol{r}_{G'}|) = \sum_\mu^G \sum_\nu^{G'} (2\, \lambda_{\nu\mu}^G - 1)\, S_{\mu\nu}\, S_{\nu\mu}, \tag{6}$$

$\lambda_{\nu\mu}^{G_\mu}$ and $\lambda_{\mu\nu}^{G_\nu}$ being defined by $(\mu \neq \nu)$

$$S_{\nu\mu}\, \lambda_{\nu\mu}^{G_\mu} = \int_{G_\mu} \psi_\nu^*(x)\, \psi_\mu(x)\, d\tau$$

$$S_{\nu\mu}\, \lambda_{\mu\nu}^{G_\nu} = \int_{G_\nu} \psi_\nu^*(x)\, \psi_\mu(x)\, d\tau$$

where the integrations are to be extended over the half-spaces containing G_μ

---

[1] The formula is simplified by making use of the fact that all integrals, for which the corresponding $S_{\mu\nu}$ do not vanish, are real, if the axes of quantization are chosen according to LANDSHOFF.

and G_ν respectively. Obviously $\lambda^{G_\mu}_{\nu\mu}+\lambda^{G_\nu}_{\mu\nu}=1$ and therefore it immediately follow that

$$f_G(|\boldsymbol{r}_G-\boldsymbol{r}_{G'}|)=-f_{G'}(|\boldsymbol{r}_G-\boldsymbol{r}_{G'}|),$$

if G and G' denote two neighbouring ions.

For fixed overlap integrals and fixed interionic distance it is easy to see tha $|f_G(|\boldsymbol{r}_G-\boldsymbol{r}_{G'}|)|$ takes its largest value when the positive ion is very small and tha $|f_G(|\boldsymbol{r}_G-\boldsymbol{r}_{G'}|)|$ and therefore also Φ_c tends gradually to zero, when the positive io increases in size. This result is in complete accordance with that given in a previou paper [19].

For the total potential energy of the lattice (apart from a constant term) we no get

$$\Phi=\frac{e^2}{2}\sum_G\sum_{G'}{}^{(G)}\frac{\varepsilon_G\,\varepsilon_{G'}}{|\boldsymbol{r}_G-\boldsymbol{r}_{G'}|}+e^2\sum_G\sum_{G'}V'(|\boldsymbol{r}_G-\boldsymbol{r}_{G'}|)+$$

$$+e^2\sum_G\sum_{G'}\sum_{G''}{}^{(GG')}f_G(|\boldsymbol{r}_G-\boldsymbol{r}_{G'}|)\frac{\varepsilon_{G''}}{|\boldsymbol{r}_G-\boldsymbol{r}_{G''}|}$$

from (1), (2) and (5).

A more accurate expression than (7) would have been obtained by introducing int (4) the whole expansion of $\dfrac{1}{|\boldsymbol{r}-\boldsymbol{r}_G|}$ in spherical harmonics around G_μ. Then we would ge an expansion of Φ_c in which the first term represents a charge correction to the class cal electrostatic energy and the higher terms are contributions from the highe moments of the charge distribution. The first term will be (5) provided that the ove lap products decrease sufficiently rapidly with increasing distance from G_μ. Suppos that the nuclei are slightly displaced from their equilibrium positions. Then the charg density will be slightly deformed in a complicated way. In the Heitler-London ap proximation the one-electron wave functions are supposed to be fixed and rigidl connected with the nuclei, and the distortion of the charge distribution is then du entirely to the overlap of the wave functions. This description of the distortion not completely realistic. Unless we modify the treatment such that the atomic wav functions are allowed to vary, it seems therefore to be appropriate to neglect the highe terms and keep only the leading term, which is least sensitive to the finer detai of the charge distribution. We have computed Φ_c according to (5) and also the elast constants c_{12} and c_{44} for NaCl and found that the results agree well with those ob tained with the methods used earlier. The comparison can be found in an appendi We shall therefore in the following consider a potential energy of the simple form (7

In order to make full use of the symmetry of the lattice it is convenien to include a two-particle term $e^2 f_G(|\boldsymbol{r}_G-\boldsymbol{r}_{G'}|)\dfrac{\varepsilon_{G'}}{|\boldsymbol{r}_G-\boldsymbol{r}_{G'}|}$ in the last sum in (7 Therefore we write

$$\Phi=\frac{e^2}{2}\sum_G\sum_{G'}{}^{(G)}\frac{\varepsilon_G\,\varepsilon_{G'}}{|\boldsymbol{r}_G-\boldsymbol{r}_{G'}|}+e^2\sum_G\sum_{G'}V(|\boldsymbol{r}_G-\boldsymbol{r}_{G'}|)+$$

$$+e^2\sum_G\sum_{G'}\sum_{G''}{}^{(G)}f_G(|\boldsymbol{r}_G-\boldsymbol{r}_{G'}|)\frac{\varepsilon_{G''}}{|\boldsymbol{r}_G-\boldsymbol{r}_{G''}|},$$

here

$$V(|\boldsymbol{r}_G-\boldsymbol{r}_{G'}|)=V'(|\boldsymbol{r}_G-\boldsymbol{r}_{G'}|)-f_G(|\boldsymbol{r}_G-\boldsymbol{r}_{G'}|)\frac{\varepsilon_{G'}}{|\boldsymbol{r}_G-\boldsymbol{r}_{G'}|}.$$

The expression (8) holds for an arbitrary configuration of the nuclei, but in the llowing sections we shall consider only small displacements of the nuclei from their quilibrium positions.

III. The potential energy for small displacements

Let $\boldsymbol{a}_1$, $\boldsymbol{a}_2$, $\boldsymbol{a}_3$ be the vectors determining the elementary cell and $\boldsymbol{r}_k$ the osition vectors of the nuclei in the cell. We write an arbitrary lattice vector as

$$\boldsymbol{r}^l=l_1\boldsymbol{a}_1+l_2\boldsymbol{a}_2+l_3\boldsymbol{a}_3,$$

, l_2, l_3 being integers. The equilibrium position of the particle k in the cell l determined by the vector

$$\boldsymbol{r}_k^l=\boldsymbol{r}^l+\boldsymbol{r}_k.$$

he distance vector between two particles (l, k) and (l', k') is given by

$$\boldsymbol{r}_{kk'}^{ll'}=\boldsymbol{r}_k^l-\boldsymbol{r}_{k'}^{l'}=\boldsymbol{r}^{ll'}+\boldsymbol{r}_k-\boldsymbol{r}_{k'}.$$

onsidering small displacements $\boldsymbol{u}_k^l$ of each particle from its equilibrium position, he vector between the displaced particles is

$$\boldsymbol{R}_{kk'}^{ll'}=\boldsymbol{r}_{kk'}^{ll'}+\boldsymbol{u}_{kk'}^{ll'}.$$

he Cartesian coordinates of $\boldsymbol{r}_{kk'}^{ll'}$ and $\boldsymbol{u}_{kk'}^{ll'}$ are denoted by $\underset{\alpha}{x}{}_{kk'}^{ll'}$ and $\underset{\alpha}{u}{}_{kk'}^{ll'}$, $=1, 2, 3$.

The lattice dynamics in the case of a general potential was first developed by EGBIE and BORN [3], who considered the expansion of the potential energy in pow- rs of the absolute displacements of the particles. The potential (8) which we shall onsider here is given as a function of the relative positions of the nuclei and it seems herefore more natural to expand it according to powers of the relative displacements f the nuclei. The treatment of the normal vibrations of a lattice, when a general otential is expanded in powers of the relative displacements of the nuclei, has been iven by WALLER [29], who gave the general form for the linear and quadratic erms in the displacements, derived a formula for the elastic constants and showed ow normal coordinates can be introduced.[1]

In the expansion of Φ after powers of the relative displacements

$$\Phi=\Phi_0+\Phi_1+\Phi_2+\cdots,$$

Φ_0 is the potential energy of the undisturbed lattice. According to WALLER, Φ_2 a sum, where each term depends only on the relative displacements of three nuclei, and therefore is of the form

---

[1] For shortness he gave the results only for a simple lattice, but the extension to a general lattice obvious.

$$\Phi_2=\tfrac{1}{2}\sum_{l\,l'\,l''}\ \sum_{k\,k'\,k''}\ \sum_{\alpha\beta}\Phi_{\alpha\beta}\begin{pmatrix} l-l' & l-l'' \\ k\,k' & k\,k'' \end{pmatrix}\underset{\alpha}{u^{l\,l'}_{kk'}}\,\underset{\beta}{u^{l\,l''}_{kk''}}. \qquad \text{(9}$$

The coefficients $\Phi_{\alpha\beta}\begin{pmatrix} l-l' & l-l'' \\ k\,k' & k\,k'' \end{pmatrix}$ have the property of being unchanged if th index triples (l', k', α) and (l'', k'', β) are interchanged. For crystals, where eacl ion is a centre of symmetry, WALLER has found the following expression fo the elastic constants

$$C_{\alpha\gamma\beta\delta}=\frac{1}{\Delta}\sum_{l'\,l''}\ \sum_{k\,k'\,k''}\Phi_{\alpha\beta}\begin{pmatrix} l' & l'' \\ k\,k' & k\,k'' \end{pmatrix}\underset{\gamma}{x^{l'}_{kk'}}\,\underset{\delta}{x^{l''}_{kk''}}, \qquad \text{(10}$$

Δ denoting the volume of the elementary cell. The formulae (9) and (10) will be the starting point for the following treatment.

We shall in this paper restrict ourselves to the polar vibrations of long wavelength in which case WALLER's formula (9) can be simplified. From the fact that the relativ displacements of three nuclei (l, k), (l', k') and (l'', k'') are not independent th following identity follows:

$$\underset{\alpha}{u^{l\,l'}_{kk'}}\,\underset{\beta}{u^{l\,l''}_{kk''}}=\tfrac{1}{2}\big[\underset{\alpha}{u^{l\,l'}_{kk'}}\,\underset{\beta}{u^{l\,l'}_{kk'}}+\underset{\alpha}{u^{l\,l''}_{kk''}}\,\underset{\beta}{u^{l\,l''}_{kk''}}-\underset{\alpha}{u^{l'\,l''}_{k'k''}}\,\underset{\beta}{u^{l'\,l''}_{k'k''}}\big]+\tfrac{1}{2}\big[\underset{\alpha}{u^{l\,l'}_{kk'}}\,\underset{\beta}{u^{l\,l''}_{kk''}}-\underset{\beta}{u^{l\,l'}_{kk'}}\,\underset{\alpha}{u^{l\,l''}_{kk''}}\big]. \qquad \text{(11}$$

In the first bracket each term depends only on the relative displacements of two particles, but in the second bracket both terms depend of the relative displacements of three particles. According to (11) we can write (9) as follows:

$$\Phi_2=\Phi_2'+\Phi_2'', \qquad \text{(12}$$

where

$$\Phi_2'=\tfrac{1}{2}\sum_{l\,l'}\sum_{k\,k'}\sum_{\alpha\beta}\underset{\alpha\beta}{C^{l\,l'}_{kk'}}\,\underset{\alpha}{u^{l\,l'}_{kk'}}\,\underset{\beta}{u^{l\,l'}_{kk'}} \qquad \text{(12'}$$

and[1]

$$\begin{aligned}\Phi_2''&=\tfrac{1}{4}\sum_{l\,l'\,l''}\ \sum_{k\,k'\,k''}\ \sum_{\alpha\beta}\Phi_{\alpha\beta}\begin{pmatrix} l-l' & l-l'' \\ k\,k' & k\,k'' \end{pmatrix}\big[\underset{\alpha}{u^{l\,l'}_{kk'}}\,\underset{\beta}{u^{l\,l''}_{kk''}}-\underset{\beta}{u^{l\,l'}_{kk'}}\,\underset{\alpha}{u^{l\,l''}_{kk''}}\big]\\ &=\tfrac{1}{4}\sum_{l\,l'\,l''}\ \sum_{k\,k'\,k''}\ \sum_{\alpha\beta}\left[\Phi_{\alpha\beta}\begin{pmatrix} l-l' & l-l'' \\ k\,k' & k\,k'' \end{pmatrix}-\Phi_{\beta\alpha}\begin{pmatrix} l-l' & l-l'' \\ k\,k' & k\,k'' \end{pmatrix}\right]\underset{\alpha}{u^{l\,l'}_{kk'}}\,\underset{\beta}{u^{l\,l''}_{kk''}},\end{aligned} \qquad \text{(12''}$$

$\underset{\alpha\beta}{C^{l\,l'}_{kk'}}$ being defined by

$$\underset{\alpha\beta}{C^{l\,l'}_{kk'}}=\tfrac{1}{2}\sum_{l''}\sum_{k''}\left[\Phi_{\alpha\beta}\begin{pmatrix} l-l' & l-l'' \\ k\,k' & k\,k'' \end{pmatrix}+\Phi_{\alpha\beta}\begin{pmatrix} l-l'' & l-l' \\ k\,k'' & k\,k' \end{pmatrix}-\Phi_{\alpha\beta}\begin{pmatrix} l''-l & l''-l' \\ k''\,k & k''\,k' \end{pmatrix}\right]. \qquad \text{(13}$$

For the long polar vibrations of a lattice the relative displacements of all particles of the same kind are zero, and the relative displacements of particles of different kinds are the same. From (12″) it therefore immediately follows that Φ_2'' vanishes. The potential energy of the lattice will thus take the simple form[1]

---

[1] Φ_2'' vanishes identically if the coefficients $\Phi_{\alpha\beta}\begin{pmatrix} l-l', & l-l'' \\ k\,k', & k\,k'' \end{pmatrix}$ are symmetric in α and β, a condition which is however fulfilled only for special potentials.

$$\Phi_2 = \tfrac{1}{2} \sum_{ll'} \sum_{kk'} \sum_{\alpha\beta} C^{ll'}_{\substack{kk'\\ \alpha\beta}} \, u^{ll'}_{\substack{kk'\\ \alpha}} \, u^{ll'}_{\substack{kk'\\ \beta}} \qquad \text{(Long polar vibrations.)} \tag{14}$$

According to our original definition (13) of $C^{ll'}_{\substack{kk'\\ \alpha\beta}}$, these coefficients are in general not symmetric in α and β. In (14) we can, however, redefine the $C^{ll'}_{\substack{kk'\\ \alpha\beta}}$ such that they become symmetric in α and β.

IV. Investigation of the coefficients $\Phi_{\alpha\beta}\begin{pmatrix} l-l' & l-l'' \\ kk' & kk'' \end{pmatrix}$ and $C^{ll'}_{\substack{kk'\\ \alpha\beta}}$ for the potential (8)

For the potential (8) the coefficients $\Phi_{\alpha\beta}\begin{pmatrix} l-l' & l-l'' \\ kk' & kk'' \end{pmatrix}$ in (9) are for a lattice of NaCl type[2, 3]

$$\begin{aligned} \Phi_{\alpha\beta}\begin{pmatrix} l-l' & l-l'' \\ kk' & kk'' \end{pmatrix} = e^2 \Bigg[& \tfrac{1}{2}\, \varepsilon_k \left\{\varepsilon_{k'} + 12\, f_{k'}(a_0)\right\} \left\{ \frac{\partial^2}{\partial x_\alpha \, \partial x_\beta} \left(\frac{1}{r}\right) \right\}_{r = r^{ll'}_{kk'}} + \\ & + \left\{ \frac{\partial^2}{\partial x_\alpha \, \partial x_\beta} \left[V(r) + \frac{\varepsilon\, \alpha_M}{a_0} f(r) \right] \right\}_{r = r^{ll'}_{kk'}} \Bigg] \delta_{l''l'}\, \delta_{k''k'} + \\ & + e^2 \left\{ \frac{\partial f_k (R^{ll'}_{kk'})}{\partial X^{ll'}_{\substack{kk'\\ \alpha}}} \right\}_0 \left\{ \frac{\partial}{\partial X^{ll''}_{\substack{kk''\\ \beta}}} \left(\frac{\varepsilon_{k''}}{R^{ll''}_{kk''}} \right) \right\}_0 + \\ & + e^2 \left\{ \frac{\partial f_k (R^{ll''}_{kk''})}{\partial X^{ll''}_{\substack{kk''\\ \beta}}} \right\}_0 \left\{ \frac{\partial}{\partial X^{ll'}_{\substack{kk'\\ \alpha}}} \left(\frac{\varepsilon_{k'}}{R^{ll'}_{kk'}} \right) \right\}_0 , \end{aligned} \tag{15}$$

where $\varepsilon = |\varepsilon_k|$, $f(r) = \frac{\varepsilon_k}{\varepsilon} f_k(r)$, a_0 denotes the interionic distance in equilibrium and α_M is the Madelung constant. For a lattice of the NaCl type $\alpha_M = -1.74756$.

The term in the square brackets, $[\;]$, in (15) has the same form and symmetry as for an ordinary central potential and can be written in the BORN notation [4] as

$$Q^{l-l'}_{kk'}\, x^{ll'}_{\substack{kk'\\ \alpha}}\, x^{ll'}_{\substack{kk'\\ \beta}} + P^{l-l'}_{kk'}\, \delta_{\alpha\beta}.$$

---

[1] Except for the long polar vibrations this simple form is valid only for special deformations of the lattice, e.g. the deformations corresponding to plane waves along certain directions of high symmetry, and is not valid e.g. for the displacements corresponding to an arbitrary homogeneous deformation unless the coefficients $\Phi_{\alpha\beta}\begin{pmatrix} l-l' & l-l'' \\ kk' & kk'' \end{pmatrix}$ are symmetric in α and β.

[2] They are found by expanding (8) in a Taylor series in the relative displacements and by simplifying the results by making use of the simple property of the three-body part that (5) summed over one of the indices is symmetric in the two remaining indices.

[3] From now on the discussion will be restricted to lattices of the NaCl type. The treatment of other types of diatomic ionic lattices where each ion is a centre of symmetry will be completely analogous and the corresponding formulae will differ only with respect to certain numerical factors.

The coefficients $Q_{kk'}^{l-l'}$ and $P_{kk'}^{l-l'}$ can easily be found from (15). The coefficients $P_{kk'}^{l-l'}$ are related to the equilibrium condition in the same way for an ordinary central force interaction[1]

$$\sum_{l}\sum_{kk'} P_{kk'}^{l}\,(r_{kk'}^{l})^{2} = 0.$$

From this relation and WALLER's formula (10) for the elastic constants it follows that the contributions from the square bracket, $\Big[\;\Big]$, in (15) to the elastic constants c_{12} and c_{44} (which contributions we denote by c'_{12} and c'_{44}) satisfy the Cauchy relation. Carrying out the summations we find that

$$c'_{12} = c'_{44} = \frac{e^2}{a_0^4}\,\varepsilon\,[\varepsilon + 12\,f(a_0)]\cdot 0.3477 \tag{16}$$

for a lattice of the NaCl type.

The last two terms in (15) couple the relative displacements of three nuclei. These terms vanish if the overlap of the atomic wave functions is neglected, i.e. if we write the charge density as the sum of the charge densities for free ions. As they depend on the derivatives of $f(r)$, they are associated with the distortion, which the charge density undergoes when the lattice is deformed, and which results even if the atomic wave functions are kept fixed. From (10) we can easily work out the contributions to c_{12} and c_{44} (which contributions we denote by c''_{12} and c''_{44}). We find

$$\begin{aligned} c''_{12} &= -\frac{4\,e^2\,\varepsilon\,\alpha_M}{3\,a_0^3}\left(\frac{df}{da}\right)_0 = \frac{e^2\,\varepsilon}{a_0^3}\left(\frac{df}{da}\right)_0\cdot 2.3301.\\ c''_{44} &= 0. \end{aligned} \tag{17}$$

Adding the contributions from (16) and (17) we get for a lattice of the NaCl type[2]

$$\begin{aligned} c_{12} &= \frac{e^2}{a_0^4}\,\varepsilon\,[\varepsilon + 12\,f(a_0)]\cdot 0.3477 + \frac{e^2\,\varepsilon}{a_0^3}\left(\frac{df}{da}\right)_0\cdot 2.3301\\ c_{44} &= \frac{e^2}{a_0^4}\,\varepsilon\,[\varepsilon + 12\,f(a_0)]\cdot 0.3477. \end{aligned} \tag{18}$$

From (13) and (15) we get

$$\begin{aligned} C_{\substack{kk'\\ \alpha\beta}}^{ll'} &= \frac{e^2}{2}\,\varepsilon_k\,[\varepsilon_{k'} + 12\,f_{k'}(a_0)]\left\{\frac{\partial^2}{\partial x_\alpha\,\partial x_\beta}\left(\frac{1}{r}\right)\right\}_{r=r_{kk'}^{ll'}} + \\ &+ e^2\left\{\frac{\partial^2}{\partial x_\alpha\,\partial x_\beta}\left[V(r) + \frac{\varepsilon\,\alpha_M}{a_0}\,f(r)\right]\right\}_{r=r_{kk'}^{ll'}} + \\ &+ e^2\sum_{l''}\sum_{k''}\left\{\frac{\partial f_{k''}(R_{kk''}^{ll''})}{\partial X_{\substack{kk''\\ \alpha}}^{ll''}}\right\}_0\left\{\frac{\partial}{\partial X_{\substack{k''k'\\ \beta}}^{l''l'}}\left(\frac{\varepsilon_{k'}}{R_{k''k'}^{l''l'}}\right)\right\}_0, \end{aligned} \tag{19}$$

---

[1] Cf. ref. [4].

[2] The formulae (16), (17) and (18) are valid only when we restrict ourselves to the case of overlapping between nearest neighbours.

f we use the fact that certain sums vanish, because each ion is a centre of ymmetry. The last sum in (19) contains only pure three-body terms. It represents a long-range interaction between (l, k) and (l', k') which at large values of $r^{l\,l'}_{k\,k'}$ goes as $\frac{1}{(r^{l\,l'}_{k\,k'})^3}$, i.e. as the contribution from a Coulomb potential. Separating off the leading term, the last sum in (19) can be written

$$2\,e^2\,\varepsilon_k\,a_0\left(\frac{d\,f_{k'}}{d\,a}\right)_0\left\{\frac{\partial^2}{\partial\,x_\alpha\,\partial\,x_\beta}\left(\frac{1}{r}\right)\right\}_{r=r^{l\,l'}_{k\,k'}}+e^2\,\underset{\alpha\beta}{\mathcal{R}^{l\,l'}_{k\,k'}},$$

where the correction term $\underset{\alpha\beta}{\mathcal{R}^{l\,l'}_{k\,k'}}$ can always be chosen symmetrized in α and β. It can be shown that the leading term in $\underset{\alpha\beta}{\mathcal{R}^{l\,l'}_{k\,k'}}$ goes as $\frac{1}{(r^{l\,l'}_{k\,k'})^5}$ for large values of $r^{l\,l'}_{k\,k'}$. The formula (19) can therefore be written

$$\underset{\alpha\beta}{C^{l\,l'}_{k\,k'}}={}^1\underset{\alpha\beta}{C^{l\,l'}_{k\,k'}}+{}^2\underset{\alpha\beta}{C^{l\,l'}_{k\,k'}}+{}^3\underset{\alpha\beta}{C^{l\,l'}_{k\,k'}},\tag{20}$$

where

$${}^1\underset{\alpha\beta}{C^{l\,l'}_{k\,k'}}=e^2\left\{\frac{\partial^2}{\partial\,x_\alpha\,\partial\,x_\beta}\left[V(r)+\frac{\varepsilon\,\alpha_M}{a_0}\,f(r)\right]\right\}_{r=r^{l\,l'}_{k\,k'}}\tag{21}$$

and

$${}^2\underset{\alpha\beta}{C^{l\,l'}_{k\,k'}}=\frac{e^2}{2}\,\varepsilon^*_k\,\varepsilon^*_{k'}\left\{\frac{\partial^2}{\partial\,x_\alpha\,\partial\,x_\beta}\left(\frac{1}{r}\right)\right\}_{r=r^{l\,l'}_{k\,k'}}\tag{22}$$

with

$$\varepsilon^*_k=\pm\sqrt{\varepsilon\left[\varepsilon+12\,f(a_0)+4\,a_0\left(\frac{d\,f}{d\,a}\right)_0\right]}\quad\begin{pmatrix}+\ \text{for the positive ion}\\ -\ \text{for the negative ion}\end{pmatrix}\tag{22'}$$

and ${}^3\underset{\alpha\beta}{C^{l\,l'}_{k\,k'}}$ is a correction term.

${}^1\underset{\alpha\beta}{C^{l\,l'}_{k\,k'}}$ contains the short range terms, i.e. the overlap forces between nearest neighbours. ${}^2\underset{\alpha\beta}{C^{l\,l'}_{k\,k'}}$ represents a long range interaction in which the terms behave as $\frac{1}{r^3}$ for large values of r. ${}^2\underset{\alpha\beta}{C^{l\,l'}_{k\,k'}}$ has the same form as for ordinary Coulomb forces. The three-body forces are however contained in the effective charge ε^*_k. As regards ${}^3\underset{\alpha\beta}{C^{l\,l'}_{k\,k'}}$ it is a correction in which the terms behave as $\frac{1}{r^5}$ for large values of r and will not be considered in the following.

The concept of an effective ionic charge was first introduced by LYDDANE, SACHS and TELLER [22]. Recently SZIGETI [27] has derived a relation from which the effective charge can be estimated semi-empirically. For the alkali halides he found that $\varepsilon^*/\varepsilon$ is smaller than unity (~ 0.8) For a crystal made up by non-polarizable infinitely small ions ε^* equals the valency of the ions. The deviations of $\varepsilon^*/\varepsilon$ from unity is due to the finite extension and deformability of the ions.

V. The natural frequencies for the long polar oscillations

We shall here derive the frequencies of the transverse and longitudinal vibrations of the lattice in the usual approximation, i.e. assuming unretarded forces. The effect of retardation has recently been investigated by HUANG [15]. He found that the longitudinal vibrations are not influenced but that approximately pure transverse lattice vibrations exist only for wavelengths shorter than c/ν_0 ($\sim 10^5$ Å), ν_0 being the infra-red dispersion frequency. This wavelength is, however, very long compared with the lattice distance (~ 1 Å). We shall restrict ourselves to waves, which are very long compared with the lattice spacing but short compared with the dimensions of the crystal. For waves, which are long compared with the dimensions of the crystal, the effective field in the lattice depends[1] on the shape of the specimen, whereas for waves short compared with the crystal dimensions but still very long compared with the lattice spacing the field is independent of the external shape of the material and depends only on the nature of the wave. Since the wave length is assumed to be very long compared with the lattice distance, both the polarisation and the macroscopic electric field can be regarded as uniform within any microscopic domain containing a large number of atoms. The natural frequencies for transverse and longitudinal vibrations are different, but they do not vary with the wavelength down to much shorter waves than those considered here. We can therefore formally consider waves of infinite wavelength when deriving the equations of motion, but we have then to be careful as regards the long-range contributions so as to take that limiting value, which corresponds to the case of waves in an infinite lattice with wavelengths shorter than the crystal dimensions.

Consider a cubic ionic lattice with two particles per unit cell, $k = 1, 2$, and let 1 denote the positive ion and 2 the negative one. According to (14) the force acting on a positive ion is

$$K_{1\alpha} = -\sum_{\beta} D_{\alpha\beta}\, u_{\beta}, \tag{23}$$

where

$$D_{\alpha\beta} = 2 \sum_{l} C^{l}_{\substack{12\\ \alpha\beta}} \tag{24}$$

and

$$u_{\beta} = u_{1\beta} - u_{2\beta}.$$

When performing the summation indicated in (24) for the Coulomb and three-particle terms in (19), the result turns out to be indetermined for an infinite lattice. According to BORN [6] this result corresponds to the limiting case of waves long compared with the dimensions of the crystal. For waves short compared with the dimensions of the crystal the limiting value would, according to Born, be $-\dfrac{4\pi e^2 \varepsilon^{*2}}{3\Delta}\,\delta_{\alpha\beta}$. This corresponds to the contribution from the characteristic term $\dfrac{4\pi}{3}\boldsymbol{P}$ in the Lorentz-Lorenz field, where $\boldsymbol{P}$ denotes the polarisation associated with the displacements of the nuclei (cf. eq. (28)). This result was recently supplemented by HUANG [14][2] who showed, by using EWALD's theta-function transformation, that the Coulomb field also contained the contribution from the macroscopic electric field. The limiting value for the longnge terms ${}^2C^{ll'}_{\substack{kk'\\ \alpha\beta}}$ equals therefore the contribution from the Lorentz-Lorenz field.

---

[1] R. H. LYDDANE and K. F. HERZFELD [21].

[2] See also the discussion in ref. [7].

rom the analysis by Born and Huang it follows that, according to (22), we have to sert the effective instead of the actual ionic charge. It is convenient to redefine $_{\alpha\beta}$ as

$$D_{\alpha\beta} = 2 \sum_{l} {}^1C^{l}_{\substack{12\\ \alpha\beta}} \tag{25}$$

nd then add the contribution from the electric forces.

The Lorentz-Lorenz field is

$$\boldsymbol{F} = \boldsymbol{E} + \frac{4\pi}{3}\boldsymbol{P}, \tag{26}$$

here $\boldsymbol{E}$ is the macroscopic electric field. The use of this expression does not rest olely on the electrostatic treatment of Lorentz and Huang, but follows also from wald's investigation of the propagation of electromagnetic waves in an idealized rystal consisting of bound oscillators.

It has been shown by Lyddane and Herzfeld [21] and by Fröhlich and Mott 11] that[1]

$$\boldsymbol{E} = \begin{cases} 0 & \text{for transverse waves} \\ -4\pi\boldsymbol{P} & \text{for longitudinal waves.} \end{cases}$$

ombining this with (26), we get

$$\boldsymbol{F} = \begin{cases} \dfrac{4\pi}{3}\boldsymbol{P} & \text{for transverse waves} \\[2ex] -\dfrac{8\pi}{3}\boldsymbol{P} & \text{for longitudinal waves.} \end{cases} \tag{27}$$

In the expression (8) for the potential energy we have not included any terms lepending on the polarizability of the ions. The polarisation is therefore entirely lue to the displacements of the ions. From the analysis by Born and Huang it ollows that the ionic charge has to be replaced by the effective charge given by (22′), o we have to take

$$\boldsymbol{P} = \frac{\varepsilon^* |e|}{\Delta}\boldsymbol{u}, \tag{28}$$

vhere

$$\boldsymbol{u} = \boldsymbol{u}_1 - \boldsymbol{u}_2.$$

imilarly the Lorentz force has to be modified, so we have to take

$$\boldsymbol{K}_1^{\text{Lorentz}} = \varepsilon^* |e| \boldsymbol{F}. \tag{29}$$

Performing the summation indicated in (25) and using (21) we can write

$$D_{\alpha\beta} = \frac{e^2}{\Delta} D\,\delta_{\alpha\beta}, \tag{30}$$

---

[1] Compare also ref. [7] and [10].

where

$$D = 8 a_0^3 \left\{ \left(\frac{d^2 V}{d a^2}\right)_0 + \frac{\varepsilon \alpha_M}{a_0} \left(\frac{d^2 f}{d a^2}\right)_0 + \frac{2}{a_0} \left[\left(\frac{d V}{d a}\right)_0 + \frac{\varepsilon \alpha_M}{a_0} \left(\frac{d f}{d a}\right)_0 \right] \right\}. \qquad (30')$$

From (23), (25), (27), (28), (29) and (30) we now get for the total force acting on a positive ion

$$\boldsymbol{K}_1 = \begin{cases} -M \omega_t^2 \boldsymbol{u} & \text{for transverse vibrations} \qquad (31) \\ -M \omega_l^2 \boldsymbol{u} & \text{for longitudinal vibrations,} \qquad (32) \end{cases}$$

where

$$\omega_t^2 = \frac{e^2}{M \Delta} \left(D - \frac{4 \pi \varepsilon^{*2}}{3} \right) \qquad (31')$$

and

$$\omega_l^2 = \frac{e^2}{M \Delta} \left(D + \frac{8 \pi \varepsilon^{*2}}{3} \right), \qquad (32')$$

M being the reduced mass of the two ions in the unit cell.

The equations of motion for the ions are

$$\ddot{\boldsymbol{u}} + \omega_t^2 \boldsymbol{u} = 0 \quad \text{for transverse vibrations}$$

$$\ddot{\boldsymbol{u}} + \omega_l^2 \boldsymbol{u} = 0 \quad \text{for longitudinal vibrations.}$$

We shall now express the frequencies ω_t and ω_l in terms of the compressibility β and the elastic constants c_{12} and c_{44}.[1]

For an ideal undisturbed lattice the binding energy ϕ per cell, considered as a function of the interionic distance a will be

$$\phi = e^2 \left\{ \frac{\varepsilon^2 \alpha_M}{a} + 12 \left[V(a) + \frac{\varepsilon \alpha_M}{a} f(a) \right] \right\},$$

if we take into account only the overlap between nearest neighbours.

From the equilibrium condition $\left(\frac{d \phi}{d a}\right)_0 = 0$ we get

$$\left(\frac{d V}{d a}\right)_0 + \frac{\varepsilon \alpha_M}{a_0} \left(\frac{d f}{d a}\right)_0 = \frac{\varepsilon \alpha_M}{12 a_0^2} [\varepsilon + 12 f(a_0)].$$

From the expression for the compressibility

$$\frac{1}{\beta} = \frac{1}{18 a_0} \left(\frac{d^2 \phi}{d a^2}\right)_0$$

we get

$$\left(\frac{d^2 V}{d a^2}\right)_0 + \frac{\varepsilon \alpha_M}{a_0} \left(\frac{d^2 f}{d a^2}\right)_0 = \frac{3 a_0}{2 \beta e^2} - \frac{\varepsilon \alpha_M}{6 a_0^3} \left[\varepsilon + 12 f(a_0) - 12 a_0 \left(\frac{d f}{d a}\right)_0 \right]$$

---

[1] Since the corresponding relations for the case of a central repulsive interaction between nearest neighbours are in general given in terms of the compressibility, we prefer this alternative to that of expressing ω_t and ω_l in terms of c_{11}, c_{12} and c_{44}.

nd from (16) and (17) we get

$$\left(\frac{df}{da}\right)_0 = -\frac{3a_0^3}{4e^2\varepsilon\alpha_M}(c_{12}-c_{44}).$$

sing these formulae and (18) we get

$$D = \frac{12a_0^4}{e^2}\left(\frac{1}{\beta}+c_{44}-c_{12}\right) \tag{33}$$

nd

$$\varepsilon^{*2} = \frac{a_0^4}{e^2}(1.159\,c_{44}+1.717\,c_{12}). \tag{34}$$

f the overlap is neglected and a central repulsive interaction between nearest eighbours is assumed, it can be shown by inserting the electrostatic expressions r c_{12} and c_{44} that (34) reduces to ε^2.

By inserting (33) and (34) into (31′) and (32′) we finally get

$$\omega_t^2 = \frac{a_0}{M}\left(\frac{6}{\beta}+3.573\,c_{44}-9.595\,c_{12}\right) \tag{35}$$

nd

$$\omega_l^2 = \frac{a_0}{M}\left(\frac{6}{\beta}+10.855\,c_{44}+1.191\,c_{12}\right). \tag{36}$$

The corresponding formulae for the case of a central repulsive interaction etween nearest neighbours are obtained by putting $\varepsilon^*=\varepsilon$ in (31′) and (32′) nd $c_{12}=c_{44}$ in (33).

VI. Semi-empirical treatment of the complete polarisation

The effect of the polarizability of the ions has been completely neglected in (28). he Lorentz field will no doubt cause a displacement of the electrons relative to the uclei, which has not been taken into account in our previous treatment. Moreover, ie effect of the deformation associated with the displacements of the ions in the bsence of a field has not been fully considered, because the formula (22′) for the fective charge is only a first approximation. The considerations of these effects have een essentially based on rather phenomenological theories. The dielectric constants f LiF and MgO for static and high-frequency fields have recently been calculated y YAMASHITA [30], who used LANDSHOFF's expression for the energy as starting oint. His calculated values agree with the empirical results within 10–20 % for iF and within about 50 % for MgO. In his calculations, however, some terms in the nergy expression were not taken into account and therefore, unfortunately, it may em doubtful whether his results are completely significant.[1] We shall now derive the expressions for the frequencies by making use of certain relations involving the dielectric constants for static and high-frequency fields, which were first obtained by LYDDANE, SACHS and TELLER [22]. Because of the lack of a satisfactory quantitative theory of the dielectric properties we will have to use the empirical values.

---

[1] See e.g. the discussion in ref. [20].

Consider the oscillations of homogeneous polarisation (i.e. waves of infinite wavelength) of a sphere in the absence of an external field. In this case the Lorentz field vanishes and we get a unique infra-red frequency ω_s. According to LYDDANE, SACHS and TELLER this frequency is connected to the frequencies of long transverse and longitudinal vibrations by the relations

$$\omega_t^2 = \frac{\varepsilon_\infty + 2}{\varepsilon_0 + 2}\,\omega_s^2 \qquad (37)$$

$$\omega_l^2 = \frac{\varepsilon_0}{\varepsilon_\infty}\,\omega_t^2. \qquad (38)$$

Here ε_0 denotes the static dielectric constant, and ε_∞ is the dielectric constants for frequencies larger than the infra-red dispersion frequency but small compared with the optical resonance frequency.

The frequency ω_s is easily found from the results of the preceding section. We perform the summation in (24) over a large sphere, for infinite wavelength. Only the short range term ${}^1C^{l\,l'}_{\substack{kk'\\ \alpha\beta}}$ will contribute, so we get from (31′), (32′) and (33) by formally putting $\varepsilon^* = 0$

$$\omega_s^2 = \frac{6\,a_0}{M}\left(\frac{1}{\beta} + c_{44} - c_{12}\right). \qquad (39)$$

Inserting (39) in (37) we get for the transverse frequency

$$\omega_t^2 = \frac{\varepsilon_\infty + 2}{\varepsilon_0 + 2}\,\frac{6\,a_0}{M}\left(\frac{1}{\beta} + c_{44} - c_{12}\right). \qquad (40)$$

The corresponding relation in the case of a central repulsive interaction between nearest neighbours, which is obtained by putting $c_{12} = c_{44}$ in (40), has recently been derived by SZIGETI [28] and independently by ODELEVSKI [26], who also introduced a correction for the interaction between nearest neighbouring negative ions.

VII. Comparison with experiments and discussion

The transverse eigen-frequency is connected with the absorption of infra-red radiation. The absorption frequency has been measured directly by BARNES and CZERNY [1, 2], using thin films of the halide crystals. The frequency can also be found from the maximum in the reflecting power, which has been measured by the residual ray method. By estimating the damping from the experimental values of the refractive index, the extinction coefficient and the dielectric constants ε_0 and ε_∞

as been found by ODELEVSKI [26] that the absorption frequency agrees with the en-frequency within 1.5 % in the case of NaCl. The eigen-frequency and the maxim of the reflecting power are connected by relations derived from dispersion theory, ich have been given by FÖRSTERLING [12] and HAVELOCK [13]. ODELEVSKI has own that the frequencies calculated from the residual ray measurements are in od accordance with those found from absorption measurements.

The comparison between theory and experiment will be restricted to NaCl and Cl. Of the crystals investigated theoretically by LÖWDIN, these crystals are the ones which the approximations in the calculations seem to be best justified. For Cl we have made a comparison between the results for Φ_c, c_{12} and c_{44} obtained by WDIN and those obtained according to our approximate formulae. The comrison is found in the appendix. The agreement is good and we can therefore without preciable error use his theoretical values of a_0, β, c_{12} and c_{44} in our formulae. en for KCl we shall use the values found by LÖWDIN, although it may not be ite legitimate. A calculation of Φ_c and its derivatives for KCl according to our rmulae will probably not affect the values of a_0, β and c_{44} so much, but we might pect to get a smaller value for the difference c_{44}–c_{12} than that found by LÖWDIN.

A general feature of LÖWDIN's calculation is that the compressibility comes out o high for all crystals, higher even than the value at room temperature. From (35), 6) and (40) we find that the frequencies depend most sensitively on the compressility, so the frequencies can be expected to agree better with the observed frequens at room temperature than at absolute zero. Due to the uncertainty in the theotical determination of β (and also of c_{12} and c_{44}) it seems in general preferable in vestigations of the frequency spectrum to consider the expression (8) for the pontial energy as a semi-empirical form for the interaction between the ions. The antities $f(a_0)$ and $\left(\frac{df}{da}\right)_0$ can be determined from the empirical values of c_{12} and c_{44} cording to (18) and the values of the other derivatives are determined from a_0 d β (or c_{11}).

Unfortunately a comparison between the theory and the experimental results, ich are available now, will not be very illuminating. The reason is that the formulae ven in this paper are valid only at the absolute zero of temperature,[1] while most pirical data refer to rather high temperatures (~ room temperature). Thus, the served resonance frequencies are measured at room temperature, and, except r NaCl and KCl, most data concerning the constants a_0, c_{11}, c_{12} and c_{44} refer to om temperature. For these reasons the conclusions drawn from the comparison nnot be very decisive.

In the following comparison of theory and experiments the eigen-frequencies ve been calculated from (35), (36), (38) and (40) both for the theoretical and empiril values of a_0, β, c_{12} and c_{44}. As no direct measurements of the compressibility have en made at low temperatures we have instead calculated β from the values of c_{11} d c_{12}. We shall also make a comparison with the result obtained according to the rn model, which is obtained by assuming a central interaction between nearest ighbours. The corresponding expressions are special cases of (35), (36), (38) and (40), tained if putting $c_{12} = c_{44}$ and $\varepsilon^* = \varepsilon$.

---

[1] The zero-point motion of the nuclei is neglected.

Discussion of NaCl:

Table 1. The frequencies ω_t and ω_l for NaCl at $T = 0°$ K.

10^{13} sec^{-}

	Ionic polarisation [1]		Complete polarisation [2]	
	ω_t	ω_l	ω_t	ω_l
From theoretical constants [3] . .	3.28	6.04	3.29	5.19
From empirical constants [4] . . .	3.53	6.20	3.43	5.42
,, ,, ,, [5] . . .	3.59	6.11	3.43	5.42
Assuming central forces [4] . . .	3.04	6.30	3.29	5.20
,, ,, ,, [5] . . .	2.90	6.24	3.22	5.09

Concerning the transverse frequency we note that of the results in the first thre rows the values found from the theoretical constants are the ones which agree bes with the value $\omega_t = 3.09 \times 10^{13}$ sec^{-1} found by BARNES [1] at room temperature This is probably due to the fact that the theoretical compressibility is too high an agrees better with the compressibility at room temperature than with that at $T = 0$ In fact we ought to expect ω_t to be considerably higher at the absolute zero than a room temperature. Therefore the results in the second and third rows ought to b more representative. In the last two columns we have used the values of ε_0 and ε_∞ a room temperature. From the temperature coefficient of ε_0 we can estimate that th values in the third column should be about 2–3 % higher; this estimate is of cours very uncertain. The agreement between the results in the first and third column, overlap is included, is good and is probably improved if we correct for the temperatur variation of ε_0. For the case of central forces the deviations between the results i the first and third column is not unsignificant, and if applying a correction for th variation of ε_0 with temperature the discrepancy will increase. For transvers frequencies it seems as if the results according to (35) and (40) would show a bette consistency in the case where the effect of the overlap is included than if overla is neglected. For the longitudinal frequency, on the other hand, the results obtaine from (36) and (38) do not agree well with each other. As the relation (38) is an exac one it is obvious that the treatment of the polarisation according to (28) is a rathe poor approximation for the longitudinal waves. It seems as if the different contri butions to the polarisation, which are neglected in (28), would cancel to a large exten in the transverse vibrations, but would reinforce each other in the case of longitudina vibrations. FRÖHLICH [10] has divided the total polarisation into two parts

$$\boldsymbol{P} = \boldsymbol{P}_0 + \boldsymbol{P}_{\mathrm{ir}},$$

where $\boldsymbol{P}_0$ is the polarisation caused by the effective field, $\boldsymbol{P}_{\mathrm{ir}}$ the polarisation assoc ated with the displacements of the nuclei in the absence of a field, and has show t the optical polarisation $\boldsymbol{P}_0$ differs in sign and magnitude for transverse and longi- inal vibrations. This seems to explain why the approximate treatment of the po- sation can give good agreement for the transverse waves but fails in the case of gitudinal vibrations. From the approximate agreement between (35) and (40) we not conclude that the optical polarisation would be almost negligible in the trans- se vibrations, but only that the sum of all contributions due to the electronic placements, which are neglected in (28), seems to be small. The electronic polari- ion in the infra-red vibrations has recently been discussed by KRISHNAN and ROY], who concluded that the field tending to displace an ion is just the Lorentz field, that the field tending to polarize it is almost zero. Their argument is based on the t that the total electronic polarisation in the transverse waves seems to be small, since they have not distinguished between the two types of electronic displace- nts, their conclusion seems not quite established.

---

[1] The optical polarisation is neglected. ω_t and ω_l are calculated according to eq. (35) and (36

[2] ω_t and ω_l are calculated according to eq. (38) and (40), using the empirical values of ε_0 an ε_∞, which are $\varepsilon_0 = 5.62$ and $\varepsilon_\infty = 2.25$ (at room temperature).

[3] P. O. LÖWDIN, Thesis, l.c.

[4] The values of the elastic constants are taken from DURAND [9].

[5] The values of the elastic constants are taken from OVERTON and SWIM [25].

Ve have further computed the effective valency ε^* according to (22′) using both theoretical and empirical[1] values of c_{12} and c_{44} and we found in both cases $\varepsilon^* =$ 2. The value determined semi-empirically by SZIGETI [27] is considerably smaller, found $\varepsilon^* = 0.74$. We wish to point out that SZIGETI's value is determined from a of empirical constants at room temperature, whereas our formula is only a first proximation and refers to the absolute zero of temperature; therefore the fig- es may not be strictly comparable.

scussion of KCl:

Table 2. The frequencies ω_t and ω_l for KCl at $T = 0°$ K.

10^{13} sec^{-1}

	Ionic polarisation[2]		Complete polarisation[3]	
	ω_t	ω_l	ω_t	ω_l
rom theoretical constants[4] . .	2.76	4.58	2.73	4.05
rom empirical constants[5] . . .	3.00	4.52	2.82	4.17
ssuming central forces	2.69	4.77	2.77	4.10

The differences between the various results are not so pronounced as in the case NaCl. The transverse frequencies in the first and third rows are all very close to the served value at room temperature, $\omega_t = 2.67 \times 10^{13}$ sec^{-1}. At low temperature we ght, however, expect a somewhat larger value. The longitudinal frequencies in second column are also here all too large, although not to the same extent as NaCl.

For KCl we found the value $\varepsilon^* = 0.91$ from the theoretical values of c_{12} and c_{44}, ile the empirical values gave $\varepsilon^* = 0.86$; the latter value agrees well with SZIGETI's

---

OVERTON and SWIM [25].

The optical polarisation is neglected. ω_t and ω_l are calculated according to eq. (35) and (36).

ω_t and ω_l are calculated according to eq. (38) and (40), using the empirical values of ε_0 and which are $\varepsilon_0 = 4.68$ and $\varepsilon_\infty = 2.13$ (at room temperature).

P. O. LÖWDIN, Thesis, l.c.

The values of the elastic constants are taken from DURAND [9].

value $\varepsilon^* = 0.8$. The first two values are not in good agreement with each other. A
though the theoretical values of the binding energies and lattice constants for Na
and KCl agree equally well with each other, this is not the case with the elast
constants c_{12} and c_{44}.[1] The calculated difference $c_{44} - c_{12}$ is larger than the observed
a factor ~ 5. Part of this discrepancy may possibly be due to the slow conve
gency of the series expansion used by Löwdin, but this cannot explain why the o
served value of c_{44} is so much smaller than the classical electrostatic value.[2] It is possib
that higher order effects in the interaction have to be taken into consideration, bu
the discrepancy may also be due to the fact that the charge distribution differs appr
ciably from that in the Heitler-London approximation. In either case, however,
seems hard to explain why such effects should be more important in KCl than
NaCl.

I wish to express my sincere gratitude to my teacher Professor I. Waller for suggesting th
investigation to me and for much valuable advice and many stimulating discussions during t
course of the work. I am also much indebted to Drs. P. O. Fröman, P. O. Löwdin an
A. Sjölander for their valuable suggestions and criticism concerning my manuscript.

Institute of Mechanics and Mathematical Physics, University of Uppsala.

APPENDIX

The three-body potential Φ_c and the elastic constants c_{12} and c_{44} for Na

In Section II of this paper we have derived a simple approximate form for the ter
Φ_c and we shall now make a comparison with the results found earlier by Löwd
[23] and the present writer in the case of NaCl. For NaCl the overlap is rather sma
and each overlap product is non-vanishing in a rather small region around the nucle
Instead of integrating over the half-space it is sufficient to integrate over the interi
of a cube with the side equal to the interionic distance and with the lattice point
the centre. To simplify the numerical calculation we have, as is usually done, r
placed the cube by a sphere of the same volume.[3] The values of the overlap integra
were taken from Löwdin's investigation. We have calculated Φ_c according to (
and also the elastic constants c_{12} and c_{44}. The formulas for c_{12} and c_{44} are given
Section IV (eq. (18)). The results concerning NaCl are found in Tables I and I
where they are compared with the earlier results.[4] The experimental values have bee
taken from a paper by Overton and Swim [25].

---

[1] P. O. Löwdin: Thesis, p. 113.

[2] Also in the case of NaCl the observed value of c_{44} is smaller than the electrostatic value b
not to the same extent as for KCl.

[3] We wish to point out that this approximation is in fact completely immaterial. The on
thing which matters in the derivation of (4) and (5) is that we have divided the domain of int
gration into two parts, and the way in which this is done is purely a matter of convenience. It
sufficient to verify that it exists at least one such division for which the simple form (5) is a goo
approximation.

[4] I am indebted to Dr. P. O. Löwdin, who kindly placed unpublished tables from his ov
investigation at my disposal, which implied a considerable reduction in the numerical work.

Table I. The term Φ_c for NaCl in kcal/mol.

	Present calc.	LUNDQVIST[1]	LÖWDIN[2]
Φ_c	-7.4	-6.7	-10.9

Table II. The elastic constants c_{12} and c_{44} for NaCl.[3]

10^{11} dyne/cm^2

	Present calc.	LUNDQVIST[1]	LÖWDIN[2]	Emp.
. . . .	1.058	1.032	0.982	0.986
. . . .	1.514	1.515	1.525	1.327

In the earlier calculations of c_{12} and c_{44} the first two non-vanishing terms in the ies expansions of Φ_c mentioned in Section II were taken into account. In LÖWDINS atment the contribution from the second term was a considerable fraction of the al, whereas, when expanding around the center of gravity of the overlap product, second term contributed only a few per cent. Here, however, we have approxi- ted the integral in (3) by only one term. The agreement between the theoretical ults is good; the small differences between the results seem rather unsignificant iew of the limited computational accuracy. As the simple form (5) seems to be able reproduce the results of the earlier calculations with such a good accuracy, the lect of further terms in the expansion of Φ_c seems to be justified for the purpose this investigation.[4]

REFERENCES

BARNES, R. B., Zeit. f. Phys. *75*, 723 (1932).
BARNES, R. B. and CZERNY, M., Zeit. f. Phys. *72*, 447 (1931).
BEGBIE, G. H. and BORN, M., Proc. Roy. Soc. A, *188*, 179 (1947).
BORN, M., Atomtheorie des festen Zustandes. Leipzig 1923.
—— Rev. Mod. Phys. *17*, 245 (1945).
BORN, M. and GÖPPERT-MAYER, M., Handbuch der Physik *24* (2), 623 (1933).
BORN, M. and HUANG, K., Dynamical Theory of Crystal Lattices. Oxford 1954.
BORN, M. and OPPENHEIMER, R., Ann. Phys., Lpz., *84*, 551 (1927).
DURAND, M. A., Phys. Rev. *50*, 449 (1936).
FRÖHLICH, H., Theory of Dielectrics. Oxford 1949.
FRÖHLICH, H. and MOTT, N. F., Proc. Roy. Soc. A, *171*, 496 (1939).
FÖRSTERLING, K., Ann. Phys., Lpz., *61*, 577 (1920).
HAVELOCK, T. H., Proc. Roy. Soc. A, *105*, 488 (1924).
HUANG, K., Phil. Mag. *40*, 733 (1949).
—— Proc. Roy. Soc. A, *208*, 352 (1951).
HYLLERAAS, E. A., Zeit. f. Phys. *63*, 771 (1930).
KRISHNAN, K. S. and ROY, S. K., Proc. Roy. Soc. A, *207*, 447 (1951).
LANDSHOFF, R., Zeit. f. Phys. *102*, 201 (1936).

Ref. [19].

Ref. [23].

In order to find the contribution from Φ_c we have to subtract that from Φ_A, which is $\times 10^{11}$ dyne/cm^2.

Note that Φ_c is in general small compared with Φ_A and Φ_B. For NaCl Φ_c is only $\sim 4\,\%$ of the ing energy of the crystal.

19. LUNDQVIST, S. O., Ark. Fys. *6*, 25 (1953).
20. —— Ark. Fys. *8*, 177 (1954).
21. LYDDANE, R. H. and HERZFELD, K. F., Phys. Rev. *54*, 846 (1938).
22. LYDDANE, R. H., SACHS, R. G., and TELLER, E., Phys. Rev. *59*, 673 (1941).
23. LÖWDIN, P. O., Thesis, Uppsala 1948. Cf. also Ark. f. mat. fys. astr. *35* A, N:o 30; J. Chen Phys. *18*, 365 (1950).
24. MOTT, N. F. and GURNEY, R. W., Electronic Processes in Ionic Crystals. Oxford 1940.
25. OVERTON, W.C. and SWIM, R. T., Phys. Rev. *84*, 758 (1951).
26. ODELEVSKI, V. I., Izv. Akad. Nauk USSR, Ser. Fiz. *14*, 232 (1950).
27. SZIGETI, B., Trans. Faraday Soc. *45*, 155 (1949).
28. —— Proc. Roy. Soc. A, *204*, 51 (1950).
29. WALLER, I., Ark. Fys. (in press).
30. YAMASHITA, J., Progr. Theor. Phys. *8*, 280 (1952).

Tryckt den 21 april 1955

Uppsala 1955. Almqvist & Wiksells Boktryckeri AB

ARKIV FÖR FYSIK Band 9 nr 30

Communicated 12 January 1955 by MANNE SIEGBAHN and BENGT EDLÉN

A study of C III by means of a sliding vacuum spark

By KJELL BOCKASTEN

With 2 plates and 4 figures in the text

Summary

A light source has been devised, using a sliding spark in vacuum, which gives an intense spark spectrum of carbon with small Stark effect perturbations. It has been applied to a study of C III in the region 9950–1900 A. A total of 192 lines has been measured, 121 of which had not been observed before, and the analysis has given 21 new levels. The singlets and triplets have been connected, and the ionization limit has been accurately determined from the *ng* ^3G-series. Some C III lines and the resonance lines of C IV in the vacuum region have been measured on old plates taken by EDLÉN. The whole term system has been recalculated on the basis of the new data.

The original purpose of the investigation was to get the wavelength data needed for the interpretation of stellar spectra. As recently shown by EDLÉN (1954), the new C III data have essentially explained the infrared emission bands in the Wolf-Rayet stars of the carbon sequence.

Introduction

The present investigation was started in 1951 as part of a program that had the primary purpose of providing the laboratory data in the red and infrared parts of the spark spectra of light elements, especially C, N and O, which had become urgently needed through the increased application of infrared plates to the study of stellar spectra.

The first problem was to get a light source suitable for wavelength determinations in the red and infrared region. For his fundamental investigations in the spark spectra of carbon EDLÉN (1934) used a vacuum spark, which gives intense spectra of C III and C IV. In consequence of the high voltage and current densities of this light source, however, broadening and displacements due to Stark effect are troublesome, especially in the region now investigated, where transitions between terms with high quantum numbers are expected to occur.

Since GLAD (1953) had successfully excited the spectrum of C II with a condensed hollow-cathode discharge it was natural to see if this discharge could be made still more violent and give also the spectra of C III and C IV. By putting an aluminium cylinder inside the graphite tube in Glad's light source and making a slit in this hollow cathode from its open end to half its length, it was possible to get quite good C III spectrum but hardly anything of C IV.

A note by Vodar and Astoin (1950) directed the attention to some sort of slidin spark in vacuum, which could be operated at a lower voltage than the ordinar vacuum spark. The resulting light source, which is described in detail below, gave C III spectrum with greater intensity and better line quality than the condense hollow-cathode discharge and a good C IV spectrum as well. It has, in consequenc been used for the present work.

The light source

Vodar and Astoin (1950) used a sliding spark in vacuum between two metalli rings mounted on a commercial carbon resistor. The spark was supplied by th discharge of a condenser charged to 30 kV. With copper rings they obtained, according to their report, in the region 100–2000 A a spectrum similar to that of an ordinar vacuum spark and in addition some carbon lines.

For the work on carbon I have used a vacuum chamber made from a brass cub with three bores crossing in the centre (Fig. 1). To the six openings were applie connection to the pump system, gas inlet, holder for the high voltage electrod holder for the grounded electrode, tube with quartz window towards the spectrograph, and tube with glass window for visual observations. The cylindrical graphit electrodes were pressed against a porcelain disk with a bore along the axis and a sl towards the spectrograph, as can be seen on Fig. 2 *a*. By this arrangement all th sparks appear in the hole, which means a great gain of intensity, compared to th case with the sparks on the outside of a cylinder. It proved to be important that th electrodes were fitting well to the surfaces of the disk, otherwise part of the discharg took place along the outside of the disk. For that reason the lower electrode holde was pressed upwards by a brass bellows and the upper electrode holder was supplie with a double ball-and-socket joint, permitting the upper electrode to move.

The pump system consisted of a Speedivac rotary pump, model 1 S 50, a Speediva oil diffusion pump, model 203, and a moisture trap, all from W. Edwards & Company The light source was connected to the high vacuum side of the pump system throug a cylinder of porcelain and a tombac tubing. After the light source had worked fo some time the inside of this cylinder had a thin coating of particles from the electrode and this resulted in flash-over from the light source over the heating element in th diffusion pump to the supply network. By putting a stop consisting of a disk and rin in the bore leading to the pump system (see Fig. 1), and inserting an insulating tub between the tombac tube and the diffusion pump, this trouble was removed.

The pressure was measured with a vacuum thermocouple gauge, type E, from th Nat. Res. Corp., Boston (Mass.). The light source worked well at 10^{-3} mm Hg or les

Power was supplied by an aggregate giving up to 100 kV. It has been describe by O. Lundquist (1931). A circuit diagram is given in Fig. 3. If no outer spark ga is present, the first sparks will pass when the condenser has been charged to som 30 kV. After a short time, however, the channel in the porcelain disk is covered wit a thin conducting layer of the electrode material, and an auxiliary spark gap in ai has to be inserted in series. At first two brass spheres were used to form this spar gap, and the desired voltage was obtained by varying the distance between th spheres. If this distance was small, their surfaces very soon became rough and the spar

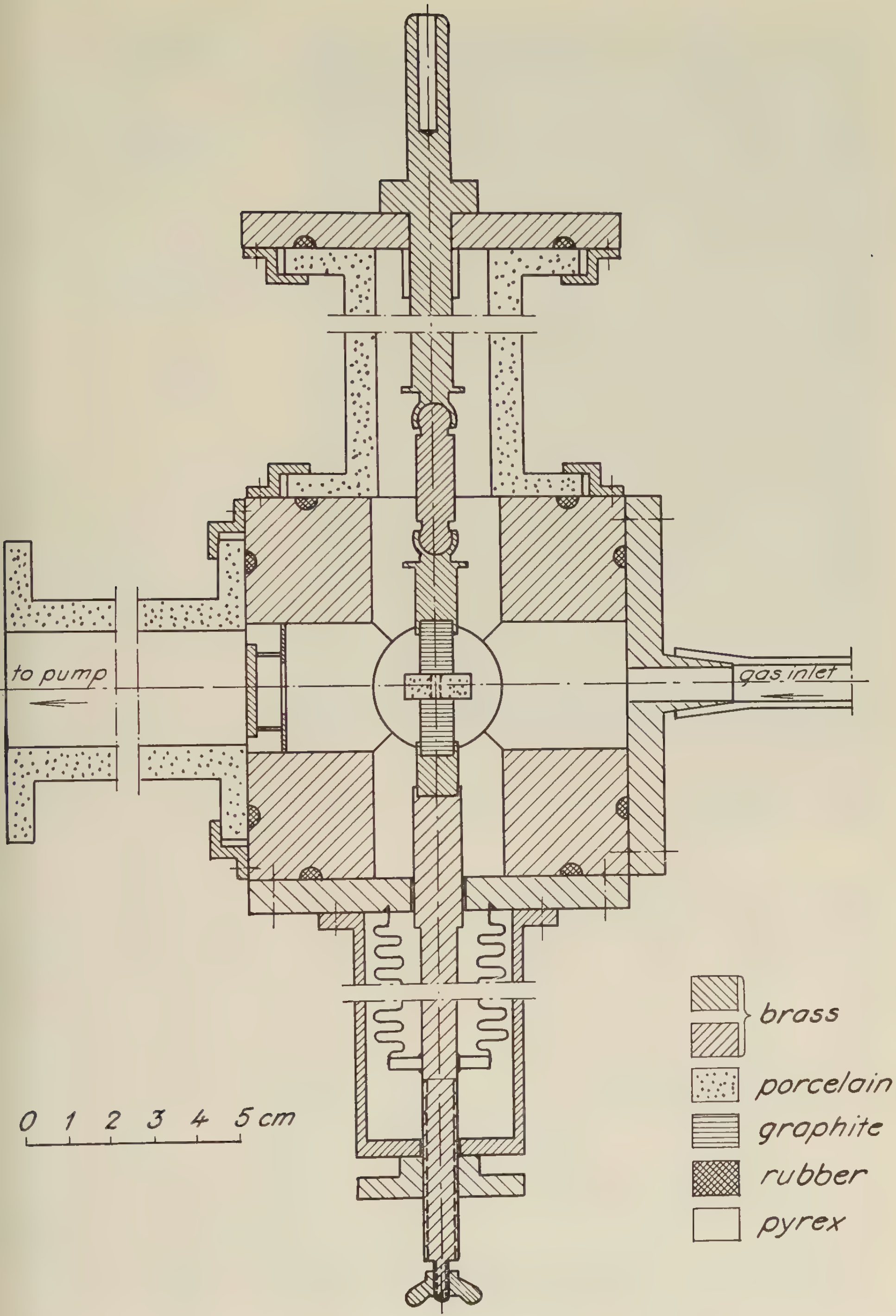

Fig. 1. The spark chamber used for the sliding vacuum spark.

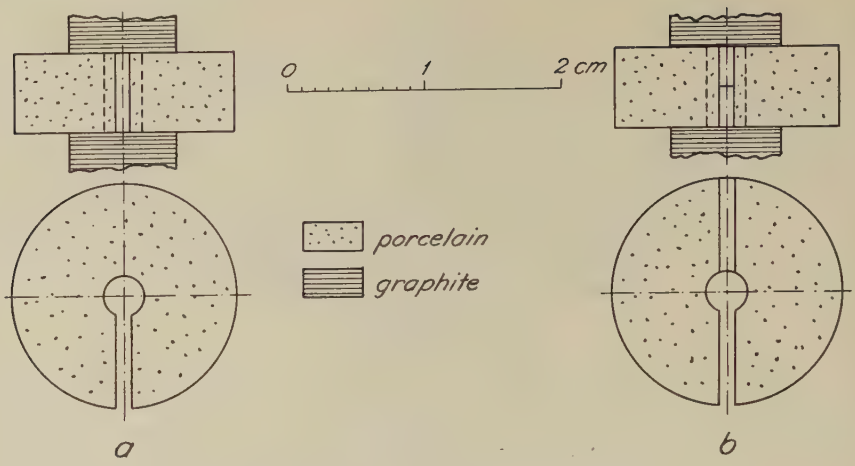

Fig. 2. The insulating disk used for the sliding vacuum spark.

voltage varied. By replacing the spheres by contact screws from the distributing box of a car motor it was possible, however, to get a stable spark potential even if the gap was as small as 0.8 mm, corresponding to a spark voltage of about 4 kV. For spark gaps wider than 5 mm, the spheres worked better than the screws. It is possible to get also the first sparks at low voltage by making a pencil line along the bore of the porcelain disk.

Spectra of different stages of ionization could be separated by means of a self-induction coil. The inductance used was an air coil with 40 cm diameter and 29 turns of 4 mm copper wire. The distance between two turns was 15 mm. By a movable contact the desired number of turns could be joined in the circuit. The sliding spark works perfectly well even with large inductance, which is not the case with the ordinary vacuum spark.

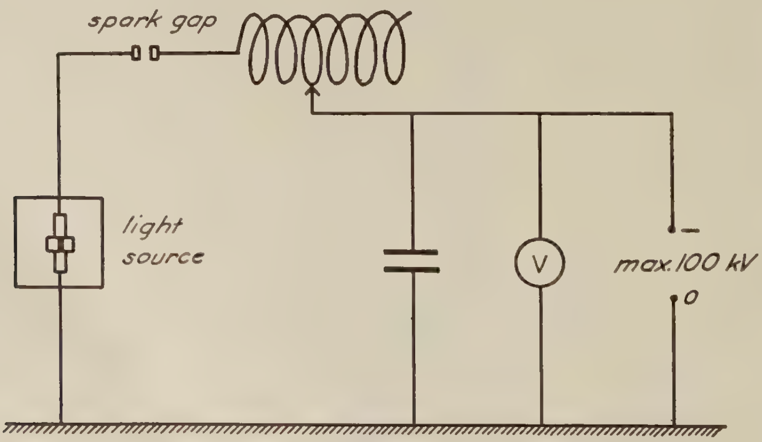

Fig. 3. The electric circuit.

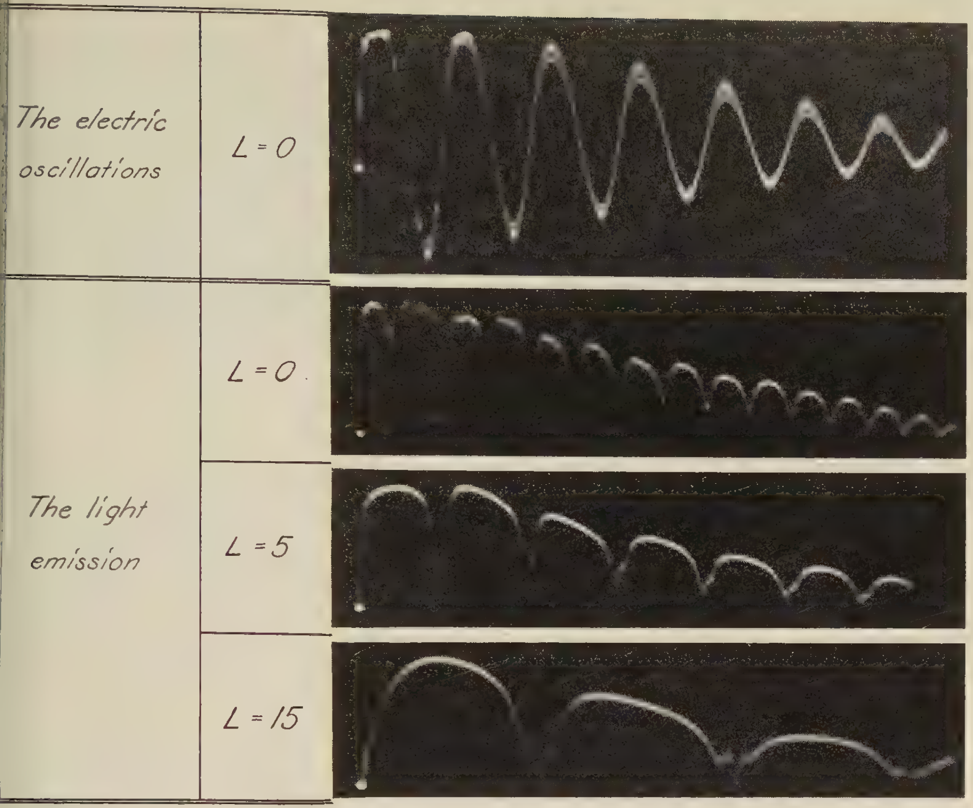

Fig. 4. Oscillograms showing the electric oscillations and the light emission of the sliding vacuum spark. The total length of each oscillogram corresponds to 45 microseconds.

For the work on C III and C IV a spark gap between 1.5 and 4.5 mm was used, orresponding to a spark voltage between 6 and 15 kV. The high voltage set was, as rule, fed with about 2 kVA giving 6–8 sparks per second at 15 kV with a condenser f 0.30 μF. After 1–1 ½ hours run the graphite electrodes had been excavated and the lit of the porcelain disk partly filled with graphite, and it was necessary to clean he disk and to put in new electrodes.

When exposing plates sensitive to the red and infrared, the continuous spectrum rom the hot porcelain disk gave a strong background on the plate. To get good pectrograms in this region it was necessary to use the type of disk shown in Fig. 2 *b*. late I shows spectrograms taken with this type of disk.

The spectrum from a sliding spark contains lines from the electrodes and from he insulator between them. When working with graphite electrodes, the spark chanel was very soon coated with carbon, and the lines due to the porcelain disk became ery weak compared to the carbon lines.

The light source described above has been tried with different metallic electrodes, uch as Be, Al, Fe, Cu, and W, and with insulating disks of different materials, e.g.

quartz and various types of porcelain. With metallic electrodes the light source can work for a long time without any change of electrodes or disk. Strong spectra of Si II–Si IV and O II–O VI can be obtained with a quartz disk if suitable metals are chosen for electrodes. Spark voltages up to 35 kV have been used.

The light emission from the sliding spark has been analysed with a photomultiplier tube and an oscilloscope. Fig. 4 gives the oscillograms. The four curves show the electric oscillations without the self-induction coil and the light emission with 0, 5, and 15 turns of the coil in the circuit. The length of each oscillogram corresponds to 45 microseconds. Although 100 sparks have been exposed on each oscillogram, the contour is rather sharp, which means that the spark cycle is repeated with great regularity. The oscillograms were obtained with the electronic equipment of Dr S. A. E. Johansson, who has kindly helped me with this part of the investigation.

The spectrograms

Spectrograms have been taken in the region 9950 − 1900 A with a stigmatic concave grating spectrograph (Ja 70-15 m, Jarrell-Ash Company). The grating has 15,000 lines per inch and a radius of curvature of 21 feet. The dispersion in the first order ranges from 5.1 A/mm to 4.7 A/mm. For wavelengths shorter than 4700 A the measurements have been made on plates taken in the second order, except for the very weakest lines. In the region 1900–2700 A several lines have been measured in the third order. For the region 3100–3700 A the grating gives greater intensity in the second order than in the first, evidently corresponding to a blaze in the first order red. To separate the spectra of different orders, colour filters from the Jenaer Glaswerk, Schott & Gen., have been used. The slit of the porcelain disk was imaged in the plane of the spectrograph slit by a quartz-fluorite lens with 254 mm focal length and 42 mm diameter.

Eastman spectroscopic plates have been used throughout. In the ultraviolet, Ilford Q 3 plates have been used also. The longest exposure time was as a rule 60–90 minutes. In certain cases, where some line of interest was too weak to be measured, plates were exposed for 3 hours. Then three sets of electrodes had to be used. After the electrodes had been changed, the position of the light source was adjusted, if necessary, so that the image of the slit of the porcelain disk came exactly at the same place on the slit plane of the spectrograph as before. To be able to separate with certainty the different stages of ionization, at least three long exposures with various amounts of self-induction had to be taken for each region.

Lines coming from elements in the porcelain were of very different intensity even on plates where the carbon spectra were equally strong, and could therefore easily be picked out. Furthermore, their shapes were usually different from those of the carbon lines. The impurities of the graphite gave only the strongest lines of the respective elements, and these could easily be found in wavelength tables. As for the carbon spectra, the lines of different ionization stages could be separated by exposures taken with different amounts of inductance. Plate II shows a typical plate with three exposures corresponding to 0, 5, and 15 turns of the induction coil. The C II lines could also be picked out by comparison with Glad's list (1953). C_2-bands appear but are rather weak.

Reference spectra

Reference spectra of solid elements can be obtained easily by dipping the electrodes powder. In the region 1900–2300 A the Fe III wavelength values of Edlén and vings (1942) have been used as standards together with some Cu II wavelengths Burns and Walters (1931 a). Between 2300 and 4400 A the tables of Burns ıd Walters (1929, 1931 b) have given an excellent set of Fe I and Fe II standards. the long-wave region lines of Ne I and A I have been used. Directly after the ding spark spectrum had been exposed, a hollow-cathode discharge was run, ing the hole in the porcelain disk as hollow cathode and an extra electrode, inoduced through the gas inlet, as anode. Using the wavelength list of Burns, Adams ıd Longwell (1950) for Ne I, and the list of Meggers and Humphreys (1934) r A I, a sufficient number of reference lines were available in the region 5850–50 A. In the region 4400–5850 A A II lines measured by Minnhagen (1947), II lines from Beals (1931) and Cu I lines from Burns and Walters (1931 a) ve been used. Iron lines from an arc in air, introduced on the spectrograms by eans of a right angle prism, have been used in some regions to bridge the gaps tween standard lines. Sometimes a small systematic shift between the iron lines ıd the lines from the light source was observed and corrected for. Over the whole avelength region the strongest lines of several elements, such as Na, Mg, Al, Si, , and Ca, have appeared. They are due to impurities in the graphite and to the conituents of the porcelain. Most of them are known with great accuracy and have een used as additional standards.

C III wavelengths in the region 9950–1900 A

The plates have been measured in an Abbe comparator from Carl Zeiss, Jena, hich can be read to 0.0001 mm. The wavelengths have been calculated by linear terpolation except in some regions with few standard lines, where cubic interpolaon has been used.

In Table 1 all the C III lines that have now been measured are listed. The tabulated avelengths are the weighted means of measurements on several spectrograms. nly very faint lines have been measured on less than three spectrograms. Wavength values with three decimals were used when calculating the wave numbers. he vacuum corrections were taken from Edlén's tables (1953). The estimated certainty is equal to or smaller than ten units in the last figure given in the wavength list. σ is used in this paper as symbol for wave number, and the unit cm^{-1} is breviated K (=kayser).

The estimated intensities are given on a logarithmic scale. They refer to the most tense spectrogram that has been obtained, using the kind of plate which is most nsitive in each specific region.

For every line that has been experimentally classified as belonging to C III it has een possible to find the corresponding term combination. This is given in Table 1 Edlén's notation.

Some lines are unsymmetrical and shaded towards one side, especially at the ends the lines, presumably because one or both of the corresponding levels are affected Stark effect. The Stark effect perturbations will act as a mutual repulsion of two vels the quantum numbers of which fulfil the selection rules for electric dipole

Table 1. Complete list of C III lines in the region 9950–1920 A.

Abbreviations in column 1:

bl = blended by
h = hazy
hul = hazy, unsymmetrical, shaded to longer waves
hus = hazy, unsymmetrical, shaded to shorter waves
l = slightly shaded to longer waves
m = masked by
s = slightly shaded to shorter waves
ul = unsymmetrical, shaded to longer waves
us = unsymmetrical, shaded to shorter waves
w = wide
wh = wide, hazy

References to previous measurements:

B = I. S. Bowen (1931).
E = B. Edlén (1934).
F = A. Fowler and E. W. H. Selwyn (1928).
G = A. Gatterer and J. Junkes (1938).
M = T. R. Merton (1915).

Intensity	λ_{air}, A	Previous measurements	σ_{obs}, K	σ_{calc}	Combination
2	9717.73		10 287.65	7.63	$3p\ ^3P_2 - 3d\ ^3D_2$
5	9715.11		10 290.42	0.44	$^3P_2 - \quad ^3D_3$
2	9706.44		10 299.61	9.61	$^3P_1 - \quad ^3D_1$
3	9705.39		10 300.73	0.71	$^3P_1 - \quad ^3D_2$
2	9701.12		10 305.27	5.28	$^3P_0 - \quad ^3D_1$
1	9358.37		10 682.69	2.69	$4s\ ^1S_0 - 4p\ ^1P_1$
3 very wh	8665.22		11 537.22	7.0	$5f\ ^3F_4 - 6g\ ^3G_5$
2 very wh	8663.65		11 539.31	8.9	$^3F_3 - \quad ^3G_4$
1 very wh	8652.6		11 554.1	4.08	$5d\ ^3D_3 - 6p\ ^3P_2$
10	8500.32		11 761.03	1.03	$3s\ ^1S_0 - 3p\ ^1P_1$
2	8358.72		11 960.27	0.27	$4d\ ^3D_2 - 3d'\ ^3F_2$
2	8357.86		11 961.50	1.50	$^3D_3 - \quad ^3F_3$
5	8347.94		11 975.72	5.70	$^3D_1 - \quad ^3F_2$
6	8341.59		11 984.83	4.81	$^3D_2 - \quad ^3F_3$
7	8332.99		11 997.19	7.19	$^3D_3 - \quad ^3F_4$
1+ h	8296.51		12 049.95	9.91	$3d'\ ^3F_4 - 5d\ ^3D_3$
1 h	8272.26		12 085.27	5.17	$^3F_3 - \quad ^3D_2$
1− h	8255.62		12 109.63	9.56	$^3F_2 - \quad ^3D_1$
10 hus	8196.48		12 197.01	7.0	$5g\ ^{3,1}G - 6h\ ^{3,1}H$
1 very hus	8021.14		12 463.63	3.61	$5d\ ^1D_2 - 6f\ ^1F_3$
4	7796.00		12 823.56	3.57	$3p'\ ^3S_1 - 3d'\ ^3P_2$
3	7780.42		12 849.24	9.26	$^3S_1 - \quad ^3P_1$
m O I	—		12 863	3.56	$^3S_1 - \quad ^3P_0$
6	7707.43		12 970.93	0.93	$3p'\ ^1P_1 - 3d'\ ^1D_2$
2	7625.94		13 109.53	9.45	$3s'\ ^3P_2 - 4d\ ^3D_2$
7	7612.65		13 132.41	2.25 2.76	$3d'\ ^3F_4 - 5g\ ^3G_5$ $3s'\ ^3P_2 - 4d\ ^3D_3$
2	7595.29		13 162.43	2.40	$^3P_1 - \quad ^3D_1$
5 l	7592.28		13 167.65	7.66	$3d'\ ^3F_3 - 5g\ ^3G_4$
4	7586.40		13 177.85	7.83	$3s'\ ^3P_1 - 4d\ ^3D_2$
4 l	7578.16		13 192.18	2.20	$3d'\ ^3F_2 - 5g\ ^3G_3$
2	7576.68		13 194.76	4.73	$3s'\ ^3P_0 - 4d\ ^3D_1$

ble 1 (cont.)

Intensity	λ_{air}, A	Previous measurements	σ_{obs}, K	σ_{calc}	Combination
3 hus	7486.52		13 353.67	3.45	$5d\ {}^3D_1 - 6f\ {}^3F_2$
				3.59	$^3D_3 - {}^3F_4$
				3.60	$^3D_2 - {}^3F_3$
0	7353.96		13 594.37	4.52	$3p'\ {}^1D_2 - 3d'\ {}^1P_1$
1 very wh	7212.29		13 861.41		$5p\ {}^3P_1 - 6d\ {}^3D_2$
2 very wh	7210.52		13 864.81	4.80	$^3P_2 - {}^3D_3$
7 h	7037.25		14 206.17	6.17	$3s'\ {}^1P_1 - 4d\ {}^1D_2$
1	6899.64		14 489.51	9.41	$3p'\ {}^3P_2 - 5p\ {}^3P_2$
1	6881.09		14 528.57	8.56	$3p'\ {}^3D_3 - 3d'\ {}^3D_2$
4	6872.05		14 547.67	7.71	$^3D_3 - {}^3D_3$
1	6868.80		14 554.57	4.62	$^3D_2 - {}^3D_1$
3	6862.71		14 567.48	7.53	$^3D_2 - {}^3D_2$
2	6857.27		14 579.04	9.10	$^3D_1 - {}^3D_1$
1	6853.70		14 586.64	6.68	$^3D_2 - {}^3D_3$
1	6851.20		14 591.97	2.01	$^3D_1 - {}^3D_2$
0	6774.93		14 756.23	6.19	$3d'\ {}^3P_2 - 6s\ {}^3S_1$
1	6773.37		14 759.63	9.59	$3s'\ {}^3P_2 - 3p'\ {}^3D_1$
4	6762.17		14 784.06	4.07	$^3P_2 - {}^3D_2$
7	6744.38		14 823.07	3.04	$^3P_2 - {}^3D_3$
5 bl C II	6742.24		14 827.78	7.97	$^3P_1 - {}^3D_1$
6	6731.04		14 852.45	2.45	$^3P_1 - {}^3D_2$
6 bl C II	6727.39		14 860.50	0.30	$^3P_0 - {}^3D_1$
0 w	6460.33		15 474.80	4.90	$5p\ {}^1P_1 - 6d\ {}^1D_2$
2 h	6350.76		15 741.80	1.78	$3p'\ {}^1D_2 - 5f\ {}^1F_3$
5	6205.56		16 110.13	0.13	$4p\ {}^1P_1 - 5s\ {}^1S_0$
0	6163.96		16 218.84	8.84	$4d\ {}^3D_3 - 3d'\ {}^3D_2$
0	6159.97		16 229.36	9.24	$^3D_2 - {}^3D_1$
3	6156.68		16 238.02	7.99	$^3D_3 - {}^3D_3$
2	6155.09		16 242.22	2.15	$^3D_2 - {}^3D_2$
1	6154.13		16 244.76	4.67	$^3D_1 - {}^3D_1$
0	6149.23		16 257.70	7.58	$^3D_1 - {}^3D_2$
0	6147.81		16 261.46	1.30	$^3D_2 - {}^3D_3$
3	5894.07		16 961.50	1.51	$3p'\ {}^3D_3 - 3d'\ {}^3P_2$
1	5880.54		17 000.53	0.48	$^3D_2 - {}^3P_2$
2	5871.69		17 026.15	6.17	$^3D_2 - {}^3P_1$
1	5863.24		17 050.71	0.65	$^3D_1 - {}^3P_1$
1	5858.35		17 064.92	4.95	$^3D_1 - {}^3P_0$
7	5826.42	7.1 E; 6.7 M	17 158.44	8.45	$4d\ {}^1D_2 - 3d'\ {}^1F_3$
2 hul	5771.66		17 321.22	1.24	$3d'\ {}^1F_3 - 6g\ {}^1G_4$
2	5695.92	6.0 E; 6.0 M	17 551.57	1.57	$3p\ {}^1P_1 - 3d\ {}^1D_2$
2	5359.95		18 651.71	1.79	$4d\ {}^3D_3 - 3d'\ {}^3P_2$
0 bl band	5353.12		18 675.50	5.10	$^3D_2 - {}^3P_2$
1 bl band	5345.84		18 700.94	0.79	$^3D_2 - {}^3P_1$
0	5341.46		18 716.27	6.22	$^3D_1 - {}^3P_1$
0	5337.42		18 730.43	0.52	$^3D_1 - {}^3P_0$

Table 1 (cont.)

Intensity	λ_{air}, A	Previous measurements	σ_{obs}, K	σ_{calc}	Combination
2 very hul	5305.10		18 844.54	4.5	$5f\ {}^3F - 7g\ {}^3G$
6	5272.53	2.56 F	18 960.95	0.98	$3s'\ {}^3P_2 - 3p'\ {}^3S_1$
5	5253.58	3.55 E	19 029.35	9.36	${}^3P_1 - {}^3S_1$
4 l	5249.11	9.6 E	19 045.54	5.54	$4d\ {}^1D_2 - 5p\ {}^1P_1$
3	5244.67	4.5 E	19 061.67	1.69	$3s'\ {}^3P_0 - 3p'\ {}^3S_1$
0 w	4859.6		20 571.9	1.9	$5d\ {}^3D_3 - 7f\ {}^3F_4$?
2	4739.66		21 092.66	2.65	$3p'\ {}^3D_3 - 5p\ {}^3P_2$
1	4730.16		21 135.03	4.93	${}^3D_2 - {}^3P_1$
1 bl band	4724.33		21 161.11	1.80	${}^3D_1 - {}^3P_0$
6	4673.95	3.91 E	21 389.18	9.18	$3s'\ {}^3P_2 - 3p'\ {}^3P_1$
8	4665.86	5.90 E	21 426.27	6.28	${}^3P_2 - {}^3P_2$
6	4663.64	3.53 E	21 436.47	6.47	${}^3P_1 - {}^3P_0$
5	4659.06		21 457.56	7.56	${}^3P_1 - {}^3P_1$
5	4652.06		21 489.84	9.89	${}^3P_0 - {}^3P_1$
11	4651.47	1.35 E; 1.35* B	21 492.55	2.55	$3s\ {}^3S_1 - 3p\ {}^3P_0$
5	4651.01		21 494.70	4.66	$3s'\ {}^3P_1 - 3p'\ {}^3P_2$
13	4650.25	0.16 E; 0.16* B	21 498.22	8.22	$3s\ {}^3S_1 - 3p\ {}^3P_1$
14	4647.42	7.40 E; 7.40* B	21 511.29	1.30	${}^3S_1 - {}^3P_2$
1 very wh	4593.3	3.47 E	21 764.8	4.8	$4f'\ {}^3D_3 - 5g'\ F_{(4)}$
0 very wh	4587.6		21 791.7		${}^3D - F$
6 l	4516.77	6.93 E	22 133.51	3.42	$4p\ {}^3P_2 - 5s\ {}^3S_1$
5 l	4515.78	6.02 E	22 138.37	8.21	${}^3P_1 - {}^3S_1$
3 l	4515.33		22 140.59	0.46	${}^3P_0 - {}^3S_1$
2 bl O II	4443.08		22 500.60	0.24	$4d\ {}^1D_2 - 3d'\ {}^1P_1$
4	4388.016	8.24 E	22 782.94	2.93	$4d\ {}^3D_3 - 5p\ {}^3P_2$
2	4383.544	3.24 E	22 806.18	6.24	${}^3D_2 - {}^3P_2$
3	4382.898		22 809.55	9.55	${}^3D_2 - {}^3P_1$
2	4379.952	9.97 E	22 824.89	4.98	${}^3D_1 - {}^3P_1$
2	4379.481		22 827.34	7.37	${}^3D_1 - {}^3P_0$
3 h	4367.50	8.14 bl C II E	22 890.0	0.0	$4f'\ {}^3F_4 - 5g'\ G_{(5)}$
4 wh	4361.87	1.85 E	22 919.5		$F - G$
2 very wh	4358.90		22 935.1	5.	$4f'\ {}^3G_5 - 5g'\ H_{(6)}$
8	4325.560	5.70 E	23 111.90	1.89	$3s'\ {}^1P_1 - 3p'\ {}^1D_2$
3 wh	4315.44		23 166.1	6.	$4d'\ {}^3D_3 - 5f'\ {}^3F_4$
2	4257.894		23 479.18	9.18	$4f\ {}^3F_4 - 5d\ {}^3D_3$
1	4256.455		23 487.12	7.14	${}^3F_3 - {}^3D_2$
1	4255.42		23 492.84	2.89	${}^3F_2 - {}^3D_1$
4	4247.308	7.56 E	23 537.70	7.68	$3p'\ {}^1P_1 - 5p\ {}^1P_1$
9 h	4186.900	7.05 E	23 877.29	7.29	$4f\ {}^1F_3 - 5g\ {}^1G_4$
2	4173.089		23 956.31	6.32	$4f\ {}^1F_3 - 5d\ {}^1D_2$
1	4166.95		23 991.60	1.47	$3p'\ {}^1D_2 - 6p\ {}^1P_1$
2	4163.26		24 012.85	2.93	$3p'\ {}^3D_3 - 5f\ {}^3F_3$
7	4162.86	2.80 E	24 015.16	5.08	${}^3D_3 - {}^3F_4$

* BOWEN's λ_{vac} have here been converted to λ_{air}.

le 1 (cont.)

ntensity	λ_{air}, A	Previous measure-ments	σ_{obs}, K	σ_{calc}	Combination
	4156.76		24 050.44	0.53	$3p'\,{}^3D_2 - 5f\ {}^3F_2$
	4156.49	6.50 E	24 051.97	1.90	${}^3D_2 -\ {}^3F_3$
	4152.512	2.43 E	24 075.02	5.01	${}^3D_1 -\ {}^3F_2$
l	4121.843	2.05 E	24 254.15	4.14	$4p\,{}^1P_1 - 5d\ {}^1D_2$
	4070.261	0.30 F	24 561.52	1.52	$4f\ {}^3F_4 - 5g\ {}^3G_5$
	4068.912	8.97 F	24 569.66	9.63	${}^3F_3 -\ {}^3G_4$
	4067.940	7.87 E	24 575.53	5.53	${}^3F_2 -\ {}^3G_3$
	4056.062	6.06 E	24 647.49	7.50	$4d\ {}^1D_2 - 5f\ {}^1F_3$
very wh	4001.56*	= E	24 983.2		$4d'\,{}^3F - 5f'\,{}^3G$
very wh	3999.92*	= E	24 993.4	3.	${}^3F_4 -\ {}^3G_5$
	3889.475		25 703.13	3.21	$4d\ {}^3D_3 - 5f\ {}^3F_3$
	3889.144	9.18 F	25 705.32	5.36	${}^3D_3 -\ {}^3F_4$
	3885.941	5.99 F	25 726.50	6.52	${}^3D_2 -\ {}^3F_3$
	3883.816	3.80 E	25 740.58	0.58	${}^3D_1 -\ {}^3F_2$
hus	3703.71	3.52 E	26 992.28	2.38	$3p'\,{}^1P_1 - 3d'\,{}^1P_1$
	3609.625	9.61 E	27 695.81	5.42	$4p\ {}^3P_2 - 5d\ {}^3D_2$
				5.85	${}^3P_2 -\ {}^3D_3$
	3609.063	8.96 E	27 700.13	0.06	${}^3P_1 -\ {}^3D_1$
				0.21	${}^3P_1 -\ {}^3D_2$
	3608.81		27 702.05	2.31	${}^3P_0 -\ {}^3D_1$
	3262.272	2.23 E	30 644.64	4.67	$4s\ {}^3S_1 - 3d'\,{}^3P_2$
	3259.541	9.44 E	30 670.32	0.36	${}^3S_1 -\ {}^3P_1$
	3258.00	7.90 E	30 684.81	4.66	${}^3S_1 -\ {}^3P_0$
h	3170.016	0.16 E	31 536.46	6.52	$4s\ {}^1S_0 - 5p\ {}^1P_1$
	3161.92		31 617.25	7.43	$3s'\,{}^3P_2 - 5s\ {}^3S_1$
	3155.09		31 685.67	5.81	${}^3P_1 -\ {}^3S_1$
	3151.85		31 718.24	8.14	${}^3P_0 -\ {}^3S_1$
	3038.91		32 897.00	7.19	$4d\ {}^1D_2 - 6p\ {}^1P_1$
	2982.106	2.20 E	33 523.57	3.46	$3d\ {}^1D_2 - 3s'\,{}^1P_1$
	2874.722	4.69 E	34 775.76	5.81	$4s\ {}^3S_1 - 5p\ {}^3P_2$
	2874.43		34 779.33	9.12	${}^3S_1 -\ {}^3P_1$
	2874.24		34 781.65	1.51	${}^3S_1 -\ {}^3P_0$
us	2863.712	3.65 E	34 909.46	9.46	$4d\ {}^1D_2 - 6f\ {}^1F_3$
	2857.013		34 991.32	1.22	$4s\ {}^1S_0 - 3d'\,{}^1P_1$
wh	2854.13		35 026.6		$4f'\,{}^3F - 6g'\ G$
wh	2853.13		35 038.9	8.9	${}^3F_4 -\ G_{(5)}$
	2849.050	9.08 E	35 089.11	9.11	$3s'\,{}^1P_1 - 3p'\,{}^1S_0$
	2844.117		35 149.97	9.97	$2p\ {}^1P_1 - 2p'\,{}^3P_2$
	2808.07		35 601.18	1.18	$4d\ {}^3D_3 - 6p\ {}^3P_2$
	2806.31		35 623.43	3.43	${}^3D_2 -\ {}^3P_1$
	2805.13		35 638.41	8.07	${}^3D_1 -\ {}^3P_0$
				8.86	${}^3D_1 -\ {}^3P_1$

* These wavelengths are from EDLÉN's list (1934), Table 41.

Table 1 (cont.)

Intensity	λ_{air}, A	Previous measurements	σ_{obs}, K	σ_{calc}	Combination
4 wh	2799.47	9.38 E	35 710.54	0.41	$3p'\,{}^3D_3 - 6f\ {}^3F_4$
3 wh	2796.46	6.40 E	35 748.97	8.96	${}^3D_2 -\ {}^3F_3$
2 wh	2794.56	4.40 E	35 773.21	3.14	${}^3D_1 -\ {}^3F_2$
5 hul	2777.714	7.90 E	35 990.20	0.16	$4f\ {}^1F_3 - 6g\ {}^1G_4$
3 hul	2751.828		36 328.73	8.73	$4p\ {}^1P_1 - 6d\ {}^1D_2$
7 ul	2725.90	5.90 F	36 674.3	4.4	$4f\ {}^3F_4 - 6g\ {}^3G_5$
7 l	2725.30	5.29 F	36 682.4	2.6	${}^3F_3 -\ {}^3G_4$
6 l	2724.85	4.87 F	36 688.4	8.5	${}^3F_2 -\ {}^3G_3$
7 bl C IV	2697.75		37 057.0	6.73	$4p\ {}^3P_2 - 6s\ {}^3S_1$
3	2697.42		37 061.44	1.52	${}^3P_1 -\ {}^3S_1$
5 hus	2672.959	2.77 E	37 400.61	0.69	$4d\ {}^3D_3 - 6f\ {}^3F_4$
4 hus	2671.318	1.28 E	37 423.58	3.58	${}^3D_2 -\ {}^3F_3$
3 hus	2670.240	0.12 E	37 438.68	8.71	${}^3D_1 -\ {}^3F_2$
4	2616.627	6.66 E	38 205.74	5.75	$3d\ {}^3D_1 - 3s'\ {}^3P_0$
5	2614.478	4.49 E	38 237.13	6.98 8.08	${}^3D_2 -\ {}^3P_1$ ${}^3D_1 -\ {}^3P_1$
6	2610.020	0.02 E	38 302.45	2.55	${}^3D_3 -\ {}^3P_2$
1	2609.83		38 305.19	5.36	${}^3D_2 -\ {}^3P_2$
4 h	2480.861	0.76 E	40 296.42	6.48	$4p\ {}^3P_2 - 6d\ {}^3D_3$
4 h	2480.502		40 302.25		${}^3P_{1,0} -\ {}^3D_{2,1}$
16	2296.870	6.89 E; 6.86 G	43 524.09	4.09	$2p\ {}^1P_1 - 2p'\,{}^1D_2$
1	2202.54		45 387.9	8.17	$4s\ {}^1S_0 - 6p\ {}^1P_1$
4	2176.963	6.99 E; 6.97* F	45 921.17	1.34	$3d\ {}^1D_2 - 4p\ {}^1P_1$
9	2162.944	2.96 E; 2.91* F	46 218.77	9.16	$3d\ {}^1D_2 - 4f\ {}^1F_3$
0 w	2145.58		46 592.7		$3p'\,{}^3P_{2,1} - 4s'\,{}^3P_{1,0}$
1	2142.49		46 660.0	0.0	${}^3P_2 -\ {}^3P_2$
1 w	2140.92		46 694.2		$3d'\,{}^3D_{1,2} - 4p'\,{}^3P_{0,1}$
1	2139.86		46 717.4	7.4	${}^3D_3 -\ {}^3P_2$
0	2100.46		47 593.6	4.06	$4s\ {}^3S_1 - 6p\ {}^3P_2$
6	2091.999	2.03 E; 2.40 F	47 785.98	3.43 4.58 5.68 6.56 9.37	$3d\ {}^3D_1 - 4p\ {}^3P_0$ ${}^3D_2 -\ {}^3P_1$ ${}^3D_1 -\ {}^3P_1$ ${}^3D_3 -\ {}^3P_2$ ${}^3D_2 -\ {}^3P_2$
1 very wh	2016.84	6.92 F	49 566.5	6.5	$3d'\,{}^3P_2 - 4f'\,{}^3D_3$
0 very wh	2015.7		49 594		${}^3P -\ {}^3D$
5	2010.094	0.11 E; 0.18 F	49 732.84	2.87	$3p\ {}^3P_2 - 4s\ {}^3S_1$
4	2009.570	9.60 E; 9.67 F	49 745.80	5.95	${}^3P_1 -\ {}^3S_1$
2	2009.327		49 751.81	1.62	${}^3P_0 -\ {}^3S_1$

* FOWLER and SELWYN give as λ_{air} 2177.66 and 2163.60. The above values have bee obtained assuming that FOWLER and SELWYN have actually given wavelengths in vacuu

Table 1 (cont.)

Intensity	λ_{vac}, A	Previous measurements	σ_{obs}, K	σ_{calc}	Combination
1	1979.62	9.79 F	50 514.7		$3d'\,{}^3D - 4f'\,{}^3F$
2	1979.16	9.35 F	50 526.4	6.4	${}^3D_3 - {}^3F_4$
				1.75	$3d\,{}^3D_2 - 4f\,{}^3F_2$
2	1923.31	3.40 E	51 993.7	2.85	${}^3D_1 - {}^3F_2$
		3.33 B		4.84	${}^3D_3 - {}^3F_3$
4	1923.14	3.22 E	51 998.2	7.65	${}^3D_2 - {}^3F_3$
5	1922.93	3.01 E; 2.98 B	52 003.9	3.23	${}^3D_3 - {}^3F_4$

transitions. Transitions involving such levels will give hazy and unsymmetrical lines because the electric field strength varies in the light source. Table 1 gives many examples of such lines with appearance notations of the type "hul". A comparison of the new wavelength values with those of EDLÉN (1934) shows that the divergences (e.g. in λ 3703 and λ 4121) can be explained by the large Stark effect displacements in the vacuum spark used by Edlén. This can also be found from the term values. In Table 2 have been collected pairs of terms, T_1 and T_2, whose sensitivity to Stark effect can be traced from the character of lines in Table 1. The differences $T_1 - T_2$ are also given, using for separated triplets the centres of gravity. For comparison, the values $T_1 - T_2$ have been calculated from Edlén's term table. As can be expected, his vacuum spark gives larger distances between the terms, implying that the Stark effect repulsion is larger in the vacuum spark than in the sliding spark. In cases where only two terms affect each other, half the difference between the two values of $T_1 - T_2$ can be taken as a minimum value for the displacement in the vacuum spark.

To get a consistent set of term values one therefore ought to measure all lines on plates taken with the same electric conditions. To investigate the influence of the electric data upon the wavelength values, one of the most unsymmetrical of the observed lines, λ 3703, has been measured on plates taken with various values of

Table 2. Pairs of terms subjected to a mutual Stark effect repulsion.

Repelling terms		$T_1 - T_2$	
T_1	T_2	BOCKASTEN	EDLÉN (1934)
$5d\,{}^1D_2$	$3d'\,{}^1P_1$	54.39	57.1
$6d\,{}^1D_2$	$6f\,{}^1F_3$	389.02	396.7
$6g\,{}^1G_4$	$6f\,{}^1F_3$	429.77	433.3
$6g\,{}^1G_4$	$6h\,{}^1H_5$	84.1	
$5s\,{}^3S$	$3d'\,{}^3P$	180.13	182
$5g\,{}^3G$	$5f\,{}^3F$	574.54	576.3
$6g\,{}^3G$	$6f\,{}^3F$	158.1	161
$6g\,{}^3G$	$6h\,{}^3H$	84.0	
$7g\,{}^3G$	$7f\,{}^3F$	70.6	
$7g\,{}^3G$	$7h\,{}^3H$		

Table 3. Displacements of the C II doublet λ 3831.

Combination	EDLÉN (1934) Vacuum spark	GLAD (1953) Condensed hollow-cathode discharge		BOCKASTEN Sliding spark	
	λ	$\lambda_{\max}$	$\lambda_{\min}$	$\lambda_{L=0}$	$\lambda_{L=15}$
$4p\ ^2P_1 - 3p'\ ^2D_2$	3836.10	5.80	5.730	5.680	5.661
$^2P_2 - \quad ^2D_3$	3832.12	1.81	1.743	1.648	1.639

spark gap and self-induction. The wavelength values varied from 3703.693 t 3703.727 in rather good correlation with the electric circuit data. The variation is however, not much larger than the variation between different measured values fo other hazy but not unsymmetrical lines in the same wavelength region. As this line i one of the most critical ones, it has been considered as safe to combine measurement from spectrograms obtained at different electric conditions. Thus, strong lines coul be measured on spectrograms taken with much self-inductance where they are shar and narrow, and weak lines on plates taken with little self-inductance, the onl spectrograms on which they appear.

In his work on C II GLAD (1953) studied the Stark effect perturbation of th term $3p'\ ^2D$ at various voltages across the hollow cathode by observing the displacements of lines arising from combinations with that term. He also made a compariso with the values obtained in the vacuum spark. To get an idea about the Stark effec in the sliding vacuum spark, some of the C II lines in question were measured o spectrograms with 12 kV spark voltage and with 0 or 15 turns of the induction coil The results for the doublet at 3831 A are given in Table 3 where the values of Gla and Edlén are also included. The Stark effect will displace these lines towards longe wavelengths. It is obvious that the sliding vacuum spark used in the present investigation gives a smaller Stark effect than any of the other two light sources.

Wavelengths in the vacuum region

In order to connect the deep levels (principal quantum number = 2) with the syste of higher terms it is necessary to use lines falling in the vacuum region. Some line in this region have now been measured on some plates taken by Edlén in 1937 usin the two-meter normal incidence vacuum spectrograph at the Massachusetts Institut of Technology, described by COMPTON and BOYCE (1934). The light source was condensed spark in nitrogen at a pressure of 0.5 atm. Table 4 gives the resultin wavelengths, including the resonance lines of C IV. The C III lines were measure in the second order against Cu II and Fe II standards of BURNS and WALTER (1931 a, 1931 b) and the C IV doublet in the first order against Fe II lines from a lis of working standards prepared by EDLÉN and referred to in his work on Fe II (1942). The carbon lines were very sharp and the values should be reliable to a fe units in the third decimal place. Included for comparison are the values of BOYC and RIEKE (1935), EDLÉN (1934) and BOWEN and INGRAM (1926).

Table 4. Wavelengths of some C III and C IV lines in the region 1600–1100 A.

Intensity	λ_{vac}, A	Previous measurements			σ_{obs}, K	σ_{calc}	Combination
		BOYCE & RIEKE (1935)	EDLÉN (1934)	BOWEN & INGRAM (1926)			
							C IV:
4	1550.771	.790	.768	.774	64 484.05		$2s\ {}^2S_1 - 2p\ {}^2P_1$
5	1548.185	.214	.195	.189	64 591.76		${}^2S_1 - \quad {}^2P_2$
							C III:
3	1247.383	.387	.368	.391	80 167.84	7.84	$2p\ {}^1P_1 - 2p'\ {}^1S_0$
3	1176.370	.370	.351	.359	85 007.27	7.29	$2p\ {}^3P_2 - 2p'\ {}^3P_1$
3	1175.987	.986	.973	.988	85 034.95	4.95	${}^3P_1 - \quad {}^3P_0$
5	1175.711	.716	.700	.711	85 054.92	4.90	${}^3P_2 - \quad {}^3P_2$
2	1175.590	.582	.566	.577	85 063.67	3.65	${}^3P_1 - \quad {}^3P_1$
3	1175.263	.259	.248	.261	85 087.34	7.34	${}^3P_0 - \quad {}^3P_1$
3	1174.933	.934	.916	.922	85 111.24	1.26	${}^3P_1 - \quad {}^3P_2$

The term system

EDLÉN (1934) has given a quite complete term table for C III. The new data have not caused any change in his classifications and most of the new lines are due to transitions between his terms. In the system with the limit (${}^2S$) the new terms $5s\ {}^1S$, $6p\ {}^3P$, $7f\ {}^3F$, $7g\ {}^3G$ and $6h\ {}^{3,1}H$ have now been found. In some cases, previously unresolved terms have now been split into separate levels. Tables 5 and 6 give the term system of C III with the values recalculated as described further on.

High terms of the (${}^2P$)-system. The terms with higher quantum numbers ($n \geqq 4$) belonging to the (${}^2P$)-system present a special problem. They are situated near or above the first series limit, and there are very few lines that can be ascribed to transitions involving these terms. It has not been possible to get more than one connection for each of the new terms derived from these lines. The classification has been made so as to give reasonable values of n^*, and has been confirmed by the character of the lines. Levels of the type $np'\ P$, $nd'\ D$, $nf'\ F$ and $ng'\ G$ (i.e. $l = L$) should not be affected by autoionization, and the lines now identified as combinations between them are actually the sharpest ones of this type of transitions. The lines of the groups at 4593 A and 3999 A, on the other hand, are extremely wide and hazy and are the only lines that appear fainter in the sliding vacuum spark than in Edlén's vacuum spark, the last group being so faint that it has been impossible to measure them at the large dispersion used in the present work. They have been classified as transitions between levels one or both of which are subject to autoionization.

Most of these lines appear as close pairs. It has not been considered possible, however, to calculate the fine structure splitting of the terms on the basis of these diffuse lines. For high L- values the singlet and triplet levels will merge and the LS-coupling can be expected to pass over to Jl-coupling. For terms arising from the ng' configuration the sign of multiplicity has therefore been dropped. As a rule, the level with the

Table 5. The term system of C III: Singlet terms.

Term symbol	Term value	n^*	Term symbol	Term value	n^*
$2s\ ^1S_0$	386 213.9		$2p'\ ^1S_0$	203 694.02	
$2p\ ^1P_1$	283 861.86		$^1D_2$	240 337.77	
		Limit: $2s\ ^2S_1$ $(=0)$			
$3s\ ^1S_0$	139 043.64	2.66510	$3d\ ^1D_2$	109 731.04	3.00002
$4s\ ^1S_0$	74 492.39	3.64110	$4d\ ^1D_2$	62 001.41	3.99106
$5s\ ^1S_0$	47 699.57	4.55021	$5d\ ^1D_2$	39 555.56	4.99672
$3p\ ^1P_1$	127 282.61	2.78550	$6d\ ^1D_2$	27 480.97	5.99477
$4p\ ^1P_1$	63 809.70	3.93410	$7d\ ^1D_2$	20 186*	6.9946
$5p\ ^1P_1$	42 955.87	4.79487	$4f\ ^1F_3$	63 511.88	3.94331
$6p\ ^1P_1$	29 104.22	5.82520	$5f\ ^1F_3$	37 353.91	5.14186
$7p\ ^1P_1$	21 318*	6.8064	$6f\ ^1F_3$	27 091.95	6.03766
$8p\ ^1P_1$	16 288*	7.7867	$5g\ ^1G_4$	39 634.59	4.99173
			$6g\ ^1G_4$	27 521.72	5.99033
			$6h\ ^1H_5$	27 437.6	5.99951
		Limits: $2p\ ^2P_2$ $(-64\ 591.8)$; $2p\ ^2P_1$ $(-64\ 484.1)$			
$3s'\ ^1P_1$	76 207.58	2.64843 $(^2P_2)$	$3d'\ ^1P_1$	39 501.17	3.08019 $(^2P_2)$
$3p'\ ^1S_0$	41 118.47	3.05654 $(^2P_2)$	$^1D_2$	53 522.62	2.89291 $(^2P_1)$
$^1P_1$	66 493.55	2.74593 $(^2P_1)$	$^1F_3$	44 842.96	3.00408 $(^2P_2)$
$^1D_2$	53 095.69	2.89683 $(^2P_2)$	$4d'\ ^1D_2$	396.7*	3.9015 $(^2P_1)$
$4p'\ ^1P_1$	5 108.5*	3.7671 $(^2P_1)$	$^1F_3$	− 2 559*	3.9900 $(^2P_2)$
$^1D_2$	575.8*	3.8929 $(^2P_2)$	$5d'\ ^1D_2$	− 23 469*	4.9070 $(^2P_1)$
$5p'\ ^1P_1$	− 21 217*	4.7776 $(^2P_1)$			
$^1D_2$	− 23 292*	4.8901 $(^2P_2)$			

highest J value has been considered to join in the strongest line, but this line ma contain combinations with other J values too, and the classification has therefor been written, e.g., $5g'\ F_{(4)}$, to indicate that the line has been used when calculatin the level $5g'\ ^3F_4$.

Two of the classifications are transitions between terms that cannot be connecte to the rest of the system. In these cases the term values have been estimated an given in Table 6 with additive constants, x and y, the absolute values of which ar probably less than 50 K.

As long as the nf' and ng' terms have not been confirmed by more combination or by extended analyses of homologous spectra, they must be regarded as tentative

Calculation of term values. For the major part of levels below the first series limit the wavelengths observed in the region 9950–1900 A give a well-connected network of transitions for each of the singlet and triplet systems. Levels included in these networks have been calculated by the method of least squares. Details of the procedure are given in the Appendix. The calculation has been carried on with four decimals until the successive corrections have converged enough to give the term values correctly when shortened to the second decimal. Those levels that were not included in this calculation were afterwards connected individually to the main systems.

From the term values the σ_{calc} in Table 1 have been computed. The weighted mean of $|\sigma_{\text{obs}}-\sigma_{\text{calc}}|$ for lines included in the networks are for the singlets 0.01 K and for the triplets 0.03 K.

The triplet transition at 1922 A showed some departure from its predicted position and was therefore not used in the calculation of term values. The observed wavelength values are 0.022–0.032 A larger than the values computed from the term table. This could indicate a systematic error in the wavelength determination. The lines have been measured in the first, second and third order, however, and with different sets of reference lines, and the uncertainty has been estimated to only 0.010–0.015 A. The observed intensities 5, 4, and 2 do not answer very well to the theoretical relative intensities, which are on a logarithmic scale with the base 2 : 5.0, 4.4, and 3.9. The lines are in a region where atmospheric absorption is very strong and are indeed the most short-wave lines observed. It may therefore be possible that the lines have been mis-shaped by atmospheric absorption bands. This could explain the deviations in wavelength as well as in intensity.

Singlet-triplet connection. In the region, where the intense transitions $5g\ G$–$6h\ H$ should be looked for, only one C III line has been found, namely λ 8196.48 (see Plate I). This line must therefore be assumed to include all transitions $5g\ G$–$6h\ H$. The term $6h\ H$ being near hydrogen-like, $6h\ ^1H$ and $6h\ ^3H$ must be very nearly coincident, which means that $5g\ ^1G$ and $5g\ ^3G$ coincide within an estimated range of ± 0.4 K. In this way the singlet and triplet systems have been connected. Afterwards the assumption has been confirmed in several ways. The values of $6g\ ^1G$ and $6g\ ^3G$, independently obtained from combinations with F terms, will then also coincide. In the Al II spectrum, which is analogous to C III and where intersystem combinations connecting the singlet and triplet systems have been found, the observations by PASCHEN and RITSCHL (1933) indicate that the two multiplicities of the $ng\ G$ and $nh\ H$ terms are coincident. VAN VLECK and WHITELAW (1933) have given a theoretical explanation of this for the G terms. Finally, after this connection of the singlets and triplets in C III, the C III line λ 2844.117 (see Plate II d), which is otherwise unidentified, can be explained as the intersystem combination $2p\ ^1P_1$–$2p'\ ^3P_2$. This combination is analogous to the transition $2p\ ^1P_1$–$2p'\ ^1D_2$ which gives the most intense line (λ 2296) in the whole region investigated. The intercombination may be considered as an indication of some interchange of combination properties between the levels $2p'\ ^1D_2$ and $2p'\ ^3P_2$. This would also explain why combinations with the remaining two levels, $^3P_1$ and $^3P_0$, do not appear on the plates.

The connection of the singlets and triplets has caused an increase of the singlet term values of 51.7 K relative to the triplets. This invalidates a tentative identification (EDLÉN, 1934) of the line λ 339.773. No alternative identification of this line has been found.

Table 6 a. The term system of C III: Triplet terms, normal system.

Term symbol	Term value		n^*	Term symbol	Term value		n^*
$2p\,^3P_2$	333 766.79	56.36		$2p'\,^3P_2$	248 711.89	47.61	
$^3P_1$	333 823.15	23.69		$^3P_1$	248 759.50	28.70	
$^3P_0$	333 846.84			$^3P_0$	248 788.20		
			Limit: $2s\,^2S_1$ $(=0)$				
$3s\,^3S_1$	148 000.90		2.58319	$5d\,^3D_3$	40 716.75	0.43	4.92495
$4s\,^3S_1$	76 756.73		3.58699	$^3D_2$	40 717.18	0.15	4.92493
$5s\,^3S_1$	46 279.18		4.61951	$^3D_1$	40 717.33		4.92492
$6s\,^3S_1$	31 355.87		5.61215	$6d\,^3D_3$	28 116.12		5.92667
$7s\,^3S_1$	22 601*		6.6104	$7d\,^3D$	20 576*		6.9280
$3p\,^3P_2$	126 489.60	13.08	2.79422	$8d\,^3D$	15 715*		7.9274
$^3P_1$	126 502.68	5.67	2.79408	$9d\,^3D$	12 386*		8.9294
$^3P_0$	126 508.35		2.79402	$4f\,^3F_4$	64 195.93	8.39	3.92225
$4p\,^3P_2$	68 412.60	4.79	3.79945	$^3F_3$	64 204.32	5.90	3.92199
$^3P_1$	68 417.39	2.25	3.79931	$^3F_2$	64 210.22		3.92181
$^3P_0$	68 419.64		3.79925	$5f\,^3F_4$	39 058.49	2.15	5.02841
$5p\,^3P_2$	41 980.92	−3.31	4.85023	$^3F_3$	39 060.64	1.37	5.02827
$^3P_1$	41 977.61	−2.39	4.85042	$^3F_2$	39 062.01		5.02818
$^3P_0$	41 975.22		4.85056	$6f\,^3F_4$	27 363.16	0.42	6.00766
$6p\,^3P_2$	29 162.67	1.06	5.81935	$^3F_3$	27 363.58	0.30	6.00761
$^3P_1$	29 163.73	0.79	5.81925	$^3F_2$	27 363.88		6.00758
$^3P_0$	29 164.52		5.81917	$7f\,^3F_4$	20 144.9?		7.00174
$3d\,^3D_3$	116 199.16	2.81	2.91533	$5g\ ^3G_5$	39 634.41	0.28	4.99174
$^3D_2$	116 201.97	1.10	2.91529	$^3G_{4,3}$	39 634.69		4.99173
$^3D_1$	116 203.07		2.91528	$6g\ ^3G_5$	27 521.5	0.2	5.99035
$4d\,^3D_3$	64 763.85	23.31	3.90501	$^3G_{4,3}$	27 521.7		5.99033
$^3D_2$	64 787.16	15.43	3.90431	$7g\ ^3G$	20 215.5		6.98950
$^3D_1$	64 802.59		3.90384	$6h\,^3H$	27 437.6		5.99951

The deep levels. The terms $2s\,^1S$, $2p\,^1P$, $2p'\,^1S$, $2p'\,^1D$, $2p\,^3P$ and $2p'\,^3P$ have bee connected to each other using the lines of Table 4, the lines λ 2296 and λ 2844 fro Table 1 and the value λ 977.020 for $2s\,^1S$–$2p\,^1P$ given by BOYCE and RIEKE (1935) After this it would be sufficient to use one accurately measured line to connect th system of deep levels with the rest of the term system. At present no such line o outstanding accuracy can be singled out, but EDLÉN's wavelength tables (1934 give a large number of lines connecting the two groups of levels. Using the best 2 of these lines with wavelengths from 1310 to 310 A and weighted according to thei estimated accuracy, the connection has been made with an estimated uncertainty o ± 0.5 K, allowing for the possibility of a small systematic error in the wavelength used. It may be of interest to mention that if the assumed intercombination lin λ 2844 were disregarded, and the deep levels of singlets and triplets were attache

Table 6 b. The term system of C III: Triplet terms, displaced system.

Limits: $2p\ ^2P_2$ (−64 591.8); $2p\ ^2P_1$ (−64 484.1)

Term symbol	Term value		n^*
$3s'\ ^3P_2$ $^3P_1$ $^3P_0$	77 896.61 77 964.99 77 997.32	68.38 32.33	2.63268 ($^2P_2$)
$4s'\ ^3P_2$	9 810.3		3.6433 ($^2P_2$)
$3p'\ ^3S_1$	58 935.63		2.82753 ($^2P_2$)
$^3P_2$ $^3P_1$ $^3P_0$	56 470.33 56 507.43 56 528.52	37.10 21.09	2.85617 ($^2P_2$)
$^3D_3$ $^3D_2$ $^3D_1$	63 073.57 63 112.54 63 137.02	38.97 24.48	2.78133 ($^2P_2$)
$4p'\ ^3P_2$ $^3P_1$	1 808.5 1 849*	40	3.8566 ($^2P_2$)
$^3D_3$ $^3D_2$	4 204* 4 243*	39	3.7889 ($^2P_2$)
$5p'\ ^3P_2$	−22 711*		4.8560 ($^2P_2$)
$^3D_3$	−21 612*		4.7935 ($^2P_2$)
$6p'\ ^3P_2$	−35 805*		5.8572 ($^2P_2$)
$^3D_3$	−35 218*		5.7984 ($^2P_2$)
$7p'\ ^3P_2$	−43 550*		6.8509 ($^2P_2$)
$^3D_3$	−43 183*		6.7919 ($^2P_2$)
$3d'\ ^3P_2$ $^3P_1$ $^3P_0$	46 112.06 46 086.37 46 072.07	−25.69 −14.30	2.98681 ($^2P_2$)

Term symbol	Term value		n^*
$3d'\ ^3D_3$ $^3D_2$ $^3D_1$	48 525.86 48 545.01 48 557.92	19.15 12.91	2.95477 ($^2P_2$)
$^3F_4$ $^3F_3$ $^3F_2$	52 766.66 52 802.35 52 826.89	35.69 24.54	2.90089 ($^2P_2$)
$4d'\ ^3P_2$	− 2 279*		3.9811 ($^2P_2$)
$^3D_3$	− 1 483*		3.9559 ($^2P_2$)
$^3F_4$	388 + x		3.8985 ($^2P_2$)
$5d'\ ^3P_2$	−24 678*		4.9742 ($^2P_2$)
$^3D_3$	−24 371*		4.9552 ($^2P_2$)
$6d'\ ^3P_2$	−36 895*		5.9714 ($^2P_2$)
$^3D_3$	−36 718*		5.9524 ($^2P_2$)
$4f'\ ^3D_3$	− 3 454.4		4.0192 ($^2P_2$)
$^3F_4$	− 2 000.5		3.9722 ($^2P_2$)
$^3G_5$	− 1 911 + y		3.9694 ($^2P_2$)
$5f'\ ^3F_4$	−24 649		4.9724 ($^2P_2$)
$^3G_5$	−24 605 + x		4.9697 ($^2P_2$)
$5g'\ ^3F_4$	−25 219.2		5.0083 ($^2P_2$)
$^3G_5$	−24 890.5		4.9875 ($^2P_2$)
$^3H_6$	−24 846 + y		4.9847 ($^2P_2$)
$6g'\ ^3G_5$	−37 039.4		5.9870 ($^2P_2$)

separately by the help of Edlén's wavelength values, the values of the deep singlets would become only 0.1 K smaller and the deep triplets 0.1 K greater. This confirms the identification of λ 2844.

The connection of some high levels. Those higher terms of EDLÉN's term table (1934) that are not involved in any combination in the region now investigated have been corrected for the shift in term values caused by the present recalculation of the term system. They have been marked with an asterisk in the term table and are of lower accuracy than the rest.

WHITELAW and MACK (1935) have suggested that the terms 7, 8, and $9d\ ^3D$ in Edlén's term table, which have been computed from three unresolved lines due to transitions to $2p\ ^3P$ with intensities *3dd*, *1dd*, and *0dd* respectively, ought to be calculated with respect to the centre of gravity of the term $2p\ ^3P$. When calculating $7d\ ^3D$, using a line with observed intensity *3dd*, this would seem all right, because five components can be expected to have given contributions on the plate. As for

Table 7. Calculated C III wavelengths suitable as standards in the region 575–290 A

Combination	σ_{calc}, *K*	λ_{calc}, *A*	λ_{obs} (Int) [EDLÉN (1934)]
$2p\ ^1P_1-3d\ ^1D_2$	174 130.82	574.2809	.279 (12)
$2p'\ ^1D_2-4f\ ^1F_3$	176 825.89	565.5280	.530 (7)
$2p\ ^3P_2-3s\ ^3S_1$	185 765.89	538.3120	.312 (13)
$^3P_1-\ ^3S_1$	185 822.25	538.1487	.150 (12)
$^3P_0-\ ^3S_1$	185 845.94	538.0801	.075 (11–)
$2p'\ ^1D_2-3d'\ ^1D_2$	186 815.15	535.2885	.288 (10)
$2p'\ ^1D_2-3d'\ ^1F_3$	195 494.81	511.5225	.527 (10)
$2p'\ ^1D_2-5f\ ^1F_3$	202 983.86	492.6500	.649 (7)
$2p\ ^1P_1-4s\ ^1S_0$	209 369.47	477.6246	.625 (3)
$2p\ ^1P_1-3p'\ ^1P_1$	217 368.31	460.0487	.050 (8)
$2p\ ^1P_1-4d\ ^1D_2$	221 860.45	450.7338	.732 (9)
$2p\ ^1P_1-3p'\ ^1D_2$	230 766.17	433.3391	.337 (8)
$2p\ ^1P_1-3p'\ ^1S_0$	242 743.39	411.9577	.958 (3)
$2p\ ^3P_2-4s\ ^3S_1$	257 010.06	389.0898	.090 (7)
$^3P_1-\ ^3S_1$	257 066.42	389.0045	.005 (6)
$^3P_0-\ ^3S_1$	257 090.11	388.9687	.965 (5–)
$2s\ ^1S_0-3p\ ^1P_1$	258 931.3	386.2028	.203 (14)
$2p\ ^3P_2-3p'\ ^3S_1$	274 831.16	363.8598	.864 (6)
$^3P_1-\ ^3S_1$	274 887.52	363.7852	.790 (5)
$^3P_0-\ ^3S_1$	274 911.21	363.7538	.761 (4)
$2s\ ^1S_0-3s'\ ^1P_1$	310 006.3	322.5741	.575 (8)
$2s\ ^1S_0-4p\ ^1P_1$	322 404.2	310.1697	.171 (7)
$2s\ ^1S_0-5p\ ^1P_1$	343 258.0	291.3261	.330 (5)

the line $2p\ ^3P$–$9d\ ^3D$, however, with the observed intensity 0*dd*, only the stronges component of the multiplet ought to be able to give developable traces on the plate and the term value $9d\ ^3D$ has therefore been calculated with respect to the leve $2p\ ^3P_2$. In the case of $2p\ ^3D$–$8d\ ^3D$, finally, with the observed intensity 1*dd*, it ha been assumed that the observed line is due to the two strongest components of th multiplet, each contributing according to its theoretical intensity.

Calculated wavelength standards. In the region 575–291 A some strong lines c good quality have been selected from EDLÉN's list (1934). The wavelengths of thes lines, calculated from the term system, are given in Table 7. The estimated uncer tainty of ±0.5 K of the deep levels will correspond to ±0.0017 A for the longes and ±0.0004 A for the shortest wavelengths. The observed values are included i the table.

Determination of the series limits. The effective quantum numbers

$$n^* = \sqrt{9R/T_n}$$

have been calculated with the Rydberg constant for carbon, $R = 109\ 732.3$ K. As first approximation the (^2S)-limit was obtained by assuming for 6*h H* the hydroge like value $9R/6^2$. This will certainly place the limit too low. Different series hav then been tried to improve the limit, but unfortunately all the series with the lim (^2S) are more or less perturbed by terms of the (^2P)-system. The *ng* ^3G series ha inally been chosen, because the lowest perturbing term, $4f'\,{}^3G$, is situated well above he observed part of the series, and the perturbations can be expected to be small. Using the terms with $n = 5$, 6, and 7 of this series, the limit has to be raised 4.50 K f they are to fit the simple Ritz formula $n^* = n - \alpha - \beta T_n$. The experimental uncertainty of these terms has been estimated to ± 0.2, ± 0.2, and ± 0.4 K respectively, and the limit determination has, therefore, an uncertainty of at least ± 1 K. The limit may still be slightly too low, because the possible perturbation of the ${}^3G$ series would have the effect of lowering the calculated limit, but it has been considered the best value attainable at present. The connection of the two systems and the new limit determination have given as result an average increase in absolute term values of 1.8 K for the triplets and 53.5 K for the singlets.

The position of the two limits ${}^2P_1$ and ${}^2P_2$ of the $({}^2P)$-system is directly obtained from the C IV doublet $2s\,{}^2S$–$2p\,{}^2P$ in Table 4. When deciding what levels shall be assigned to each of the two components of the $({}^2P)$-limit the rule has been used that levels with equal J values approach their limits without crossing each other.

Series perturbations. The term $5p\,{}^3P$ is inverted, evidently due to perturbation from the wide inverted triplet $3d'\,{}^3P$. The interaction between these terms can also be traced from the intensities of lines in the vacuum region (EDLÉN, 1934). Thus the lines of $2p'\,{}^3P$–$5p\,{}^3P$ are considerably stronger than those of $2p'\,{}^3P$–$4p\,{}^3P$, and $2p'\,{}^3P$–$3p\,{}^3P$ has not even been observed. It must be assumed that $3d'\,{}^3P$ has given some of its combination properties to $5p\,{}^3P$ and, to a smaller extent, to $4p\,{}^3P$. In return, the combinations with $3d'\,{}^3P$ are weaker than expected. For instance, $2p'\,{}^3P$–$3d'\,{}^3P$ is only little stronger than $2p'\,{}^3P$–$4d'\,{}^3P$.

Most of the term series of the $({}^2S)$-system are strongly perturbed by terms belonging to the $({}^2P)$-system. An attempt has been made to represent these series by formulae of the type suggested by SHENSTONE and RUSSELL (1932). The results of these calculations will be published later on.

APPENDIX

The calculation of term values from a network of observed transitions using the method of least squares

Formulae. The wave number of an observed line corresponding to the transition A_i–B_k is labelled $\pm\sigma_{ik}$ where σ_{ik} is given the same sign as $A_i - B_k$. All A_i are levels with one parity and all B_k levels with the opposite parity. The observed wave number σ_{ik} is given a weight p_{ik} inversely proportional to the square of its probable error. Then, according to the method of least squares, the best term values are those which make the function z a minimum:

$$z = \sum_{ik} p_{ik}\,(A_i - B_k - \sigma_{ik})^2. \tag{1}$$

Making in turn the partial derivatives with respect to the individual A_i and B_k equal to zero, one obtains

$$\sum_i p_{ik}(A_i - B_k - \sigma_{ik}) = 0, \qquad (k = 1,\ 2,\ \dots\ n), \qquad (2$$

$$\sum_k p_{ik}(A_i - B_k - \sigma_{ik}) = 0, \qquad (i = 1,\ 2,\ \dots\ m). \qquad (3$$

Between these $m + n$ equations there is one linear connection: the sum of the lef hand sides of the equations (2) is identical with the same sum of the equations (3 This means, as is physically self-evident, that the term values can be determined bu for an additive constant.

The system can be solved by successive approximations. The successive correc tions to a set of preliminary term values a_i and b_k are labelled $\alpha_i^{(r)}$ $(r = 0,\ 1,\ 2,\ \dots$ and $\beta_k^{(s)}$ $(s = 0,\ 1,\ 2,\ \dots)$. Thus

$$A_i = a_i + \sum_{r=0}^{\infty} \alpha_i^{(r)}, \qquad (4$$

$$B_k = b_k + \sum_{s=0}^{\infty} \beta_k^{(s)}. \qquad (5$$

Introducing these expressions in equations (2) and (3) and putting

$$a_i - b_k - \sigma_{ik} = \Delta_{ik} \qquad (6$$

one obtains

$$\sum_i p_{ik}\left(\Delta_{ik} + \sum_{r=0}^{\infty} \alpha_i^{(r)} - \sum_{s=0}^{\infty} \beta_k^{(s)}\right) = 0, \qquad (7$$

$$\sum_k p_{ik}\left(\Delta_{ik} + \sum_{r=0}^{\infty} \alpha_i^{(r)} - \sum_{s=0}^{\infty} \beta_k^{(s)}\right) = 0. \qquad (8$$

From equation (7) one may take as a first approximation

$$\beta_k^{(0)} = \frac{\sum_i p_{ik}\Delta_{ik}}{\sum_i p_{ik}}, \qquad (9$$

and then, similarly, from equation (8), using this value of $\beta_k^{(0)}$,

$$\alpha_i^{(0)} = \frac{\sum_k p_{ik}(\beta_k^{(0)} - \Delta_{ik})}{\sum_k p_{ik}}. \qquad (10$$

The equations (7) and (8) will now be reduced to

$$\sum_i p_{ik}\left(\sum_{r=0}^{\infty} \alpha_i^{(r)} - \sum_{s=1}^{\infty} \beta_k^{(s)}\right) = 0, \qquad (11$$

$$\sum_k p_{ik}\left(\sum_{r=1}^{\infty} \alpha_i^{(r)} - \sum_{s=1}^{\infty} \beta_k^{(s)}\right) = 0. \qquad (12$$

hese equations will be satisfied if the successive $\beta_k^{(s)}$ and $\alpha_i^{(r)}$ are calculated lternately according to the following formulae:

$$\beta_k^{(r)} = \frac{\sum_i p_{ik}\,\alpha_i^{(r-1)}}{\sum_i p_{ik}}, \qquad (r>0), \tag{13}$$

$$\alpha_i^{(r)} = \frac{\sum_k p_{ik}\,\beta_k^{(r)}}{\sum_k p_{ik}}, \qquad (r>0). \tag{14}$$

rom (9), (10), (13) and (14) the following relations, useful for checking the numerical alculations, can be derived:

$$\sum_i \alpha_i^{(r)} \sum_k p_{ik} = 0, \qquad (r \geqq 0), \tag{15}$$

$$\sum_k \beta_k^{(r)} \sum_i p_{ik} = 0, \qquad (r>0). \tag{16}$$

The question of the convergence of the series of corrections has not been theoetically investigated. The rapidity of convergence seems to be favoured, however, if he levels are well connected by observed lines and if the weights are not too different. n the hypothetical case when all squares in the rectangular array are assumed to e filled and all weights equal, all higher $\alpha_i^{(r)}$ and $\beta_k^{(s)}$ beyond $r=0$ and $s=0$ will anish.

Calculation schedule

1. From good lines a set of preliminary term values a_i and b_k is calculated. The irst level can be chosen arbitrarily. Only levels involved in the network of closed neshes of the term diagram should be included. The remaining levels can easily be onnected afterwards. If they were included they would considerably retard the rocedure. If the network can be resolved in two or more separate networks, having nly one level in common, then each one of these networks should be calculated eparately and connected afterwards by means of the common level.

2. The preliminary term values are tabulated with odd levels along one axis of rectangular array and even levels along the other. Each observed wave number, orresponding to the transition A_i–B_k, then has its own square in this array, in which $_{ik}$ and p_{ik} can be written down, σ_{ik} with the sign of a_i–b_k.

3. Compute the Δ_{ik} of (6) and write down the results in the squares of the array. Then calculate from (9) the $\beta_k^{(0)}$ and write them in the margin.

4. Compute and tabulate in the same way the $(\beta_k^{(0)}-\Delta_{ik})$ and the $\alpha_i^{(0)}$ according to 10).

5. Calculate in turn $\beta_k^{(1)}$, $\alpha_i^{(1)}$, $\beta_k^{(2)}$, $\alpha_i^{(2)}$, ... from (13) and (14). The successive esults can be written at the margins of a rectangular array, in which only the values f p_{ik} are needed. The calculation must be carried on with 1 or 2 decimals more than re wanted in the final term values in order that the series shall converge normally. t has to be judged from the series of corrections when the sums of the remaining orrections are small enough to be neglected.

6. The final term values are calculated from (4) and (5).

7. If desired, the successive sets of α_i and β_k can be checked using (15) and (16).

ACKNOWLEDGEMENTS

This investigation was suggested by Professor Bengt Edlén, to whom I am deeply indebte for his sustained interest and invaluable advice, both of which have been a source of encouragement and inspiration.

I consider myself fortunate to have been introduced to the principles of spectroscopic techniqu under the skilful guidance of Fil. lic. Sven Glad, who has ever since readily allowed me to profi from his great experience.

I also wish to thank Dr. Sven Bertil Nilsson for valuable suggestions as to the formulae i the Appendix.

Finally I wish to acknowledge, with thanks, the financial support received from the Swedis Natural Science Research Council.

The Physical Laboratory, University of Lund, December 1954.

REFERENCES

Beals, C. S., Monthly Not. Roy. Astron. Soc. *91*, 531 (1931).
Bowen, I. S., Phys. Rev. *38*, 128 (1931).
Bowen, I. S., and Ingram, S. B., Phys. Rev. *28*, 444 (1926).
Boyce, J. C., and Rieke, C. A., Phys. Rev. *47*, 653 (1935).
Burns, K., Adams, K. B., and Longwell, J., J. Opt. Soc. Amer. *40*, 339 (1950).
Burns, K., and Walters, Jr., F. M., Publ. Allegheny Obs. *6*, 159 (1929).
—— Publ. Allegheny Obs. *8*, 27 (1931 a).
—— Publ. Allegheny Obs. *8*, 39 (1931 b).
Compton, K. T., and Boyce, J. C., Rev. Sci. Instrum. *5*, 218 (1934).
Edlén, B., Nova Acta Reg. Soc. Sci. Ups. *9*, No. 6, 51 (1934).
—— J. Opt. Soc. Amer. *43*, 339 (1953).
—— Vistas in Astronomy. Pergamon Press Ltd, London (in press 1954).
Edlén, B., and Swings, P., Astrophys. J. *95*, 532 (1942).
Fowler, A., and Selwyn, E. W. H., Proc. Roy. Soc. London *A 120*, 312 (1928).
Gatterer, A., and Junkes, J., Ricerche Spettroscopiche, Specola Vaticana, *1*, No. 1 (1938).
Glad, S., Ark. Fys. *7*, 7 (1953).
Lundquist, O., Diss., Gleerupska Universitetsbokhandeln, Lund (1931).
Meggers, W. F., and Humphreys, C. J., J. Res. Nat. Bur. Stand. *13*, 293 (1934).
Merton, T. R., Proc. Roy. Soc. London *A 91*, 498 (1915).
Minnhagen, L., Ark. Mat. Astr. Fys. *34 A*, No 22 (1947).
Paschen, F., and Ritschl, R., Ann. der Phys. [5], *18*, 872 (1933).
Shenstone, A. G., and Russell, H. N., Phys. Rev. *39*, 415 (1932).
Van Vleck, J. H., and Whitelaw, N. G., Phys. Rev. *44*, 551 (1933).
Vodar, B., and Astoin, N., Nature *166*, 1029 (1950).
Whitelaw, N. G., and Mack, J. E., Phys. Rev. *47*, 677 (1935).

Description of Plates I–II

The spectrograms are from a sliding vacuum spark with graphite electrodes and an in-lating disk of porcelain. A stigmatic 21-foot concave grating spectrograph has been used the first order (5 A/mm) for spectrograms I a, b, c, d and II a, b, c, and in the second der (2.5 A/mm) for spectrogram II d. The short lines are from an iron arc in air. The ectrograms have been magnified 2.9 times. Spark data and time of exposure for each ectrogram were as follows:

Spectrogram	Condenser, μF	Spark gap, mm	Induction coil, number of turns	Exposure time
I a	0.30	2.5	4	3 hours
I b	0.30	2.5	12	2 hours
I c	0.30	2.5	2	3 hours
I d	0.30	2.5	2	3 hours
II a	0.30	2.5	2	65 min.
II b	0.30	2.5	8	35 min.
II c	0.30	2.5	15	35 min.
II d	0.30	4.0	4	90 min.

Tryckt den 25 april 1955

Uppsala 1955. Almqvist & Wiksells Boktryckeri AB

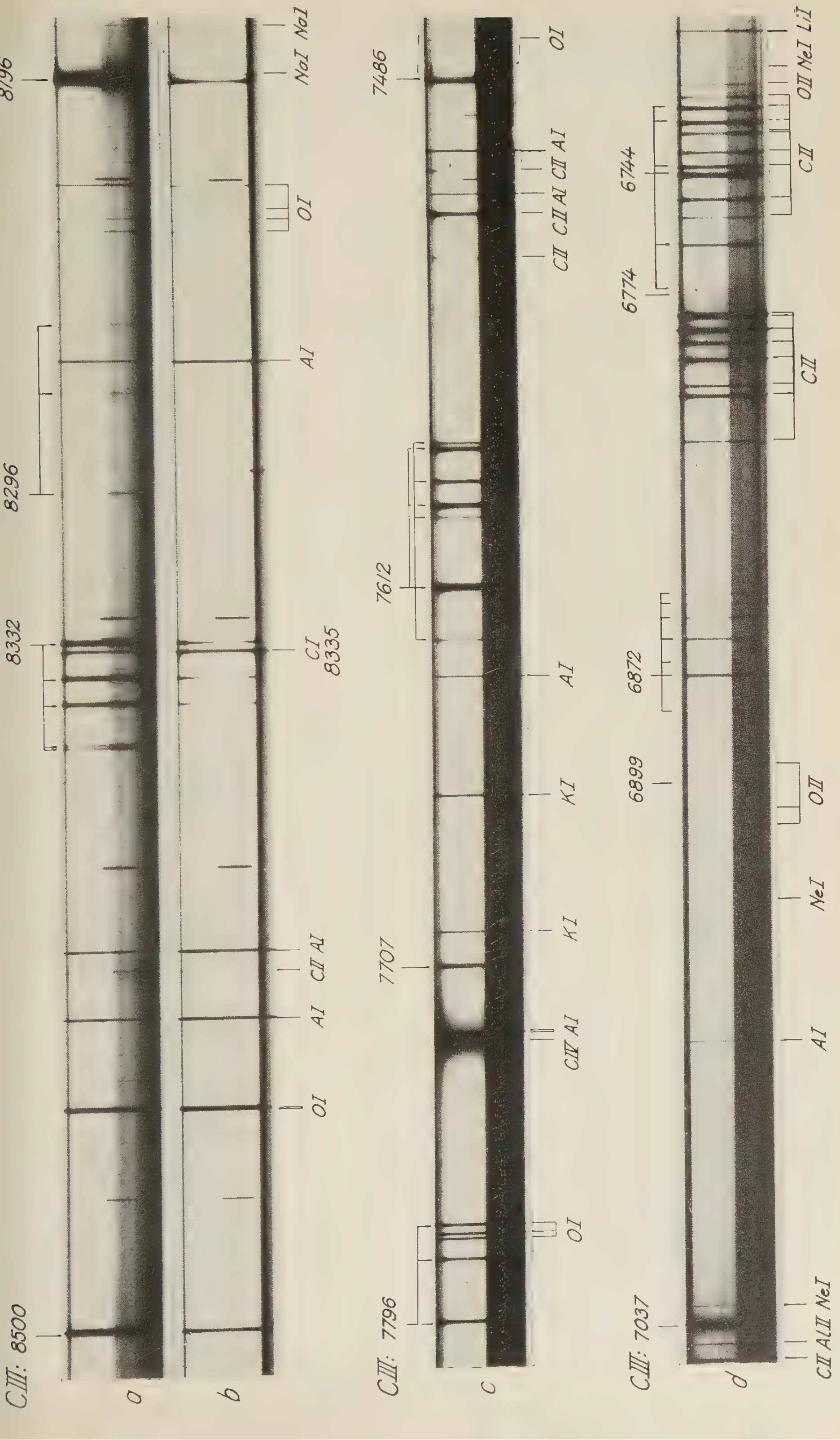
CIII: 8500
8332
8296
8196
a
b
NaI NaI
OI
AI
CI
8335
CII AI
AI
OI
CIII: 7796
7707
7612
7486
c
OI
CII CII AI CII AI
AI
KI
KI
CIV AI
OI
CIII: 7037
6899
6872
6774
6744
d
OII NeI LiI
CII
CII
OII
NeI
AI
CII AlII NeI

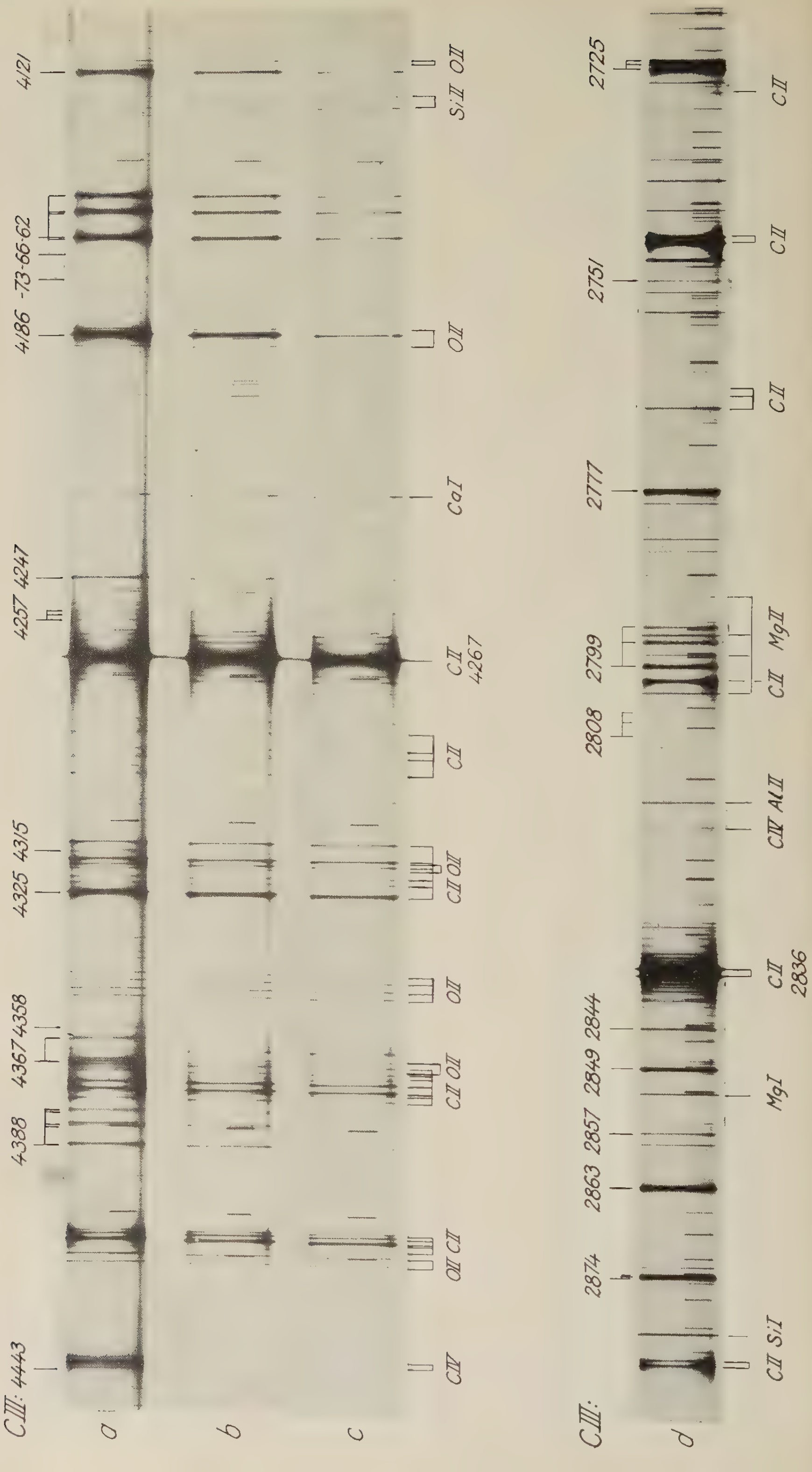
CIII: 4443
4388
4367 4358
4325 4315
4257 4247
4186 -73-66-62
4121
a
b
c
CIV
OII CII
CII OII
OII
CII OII
CII
CII 4267
CaI
OII
SiII OII
CIII:
2874
2863
2857
2849
2844
2808
2799
2777
2751
2725
d
CII SiI
MgI
CII 2836
CIV AlII
CII MgII
CII
CII
CII
CII

ARKIV FÖR FYSIK Band 9 nr 31

Communicated 12 January 1955 by MANNE SIEGBAHN and BENGT EDLÉN

The spectrum of singly-ionized magnesium, Mg II

By PERCY RISBERG

With 2 plates and 3 figures in the text

Summary

he spectrum of singly-ionized magnesium has been observed between 11 620 A 2790 A with a hollow-cathode discharge. Wavelengths have been determined 93 lines, 26 of which fall above 7896 A, the upper limit of previous observations. term system has been revised and extended, and series formulae have been com-ed. Wavelengths in the vacuum-ultraviolet have been calculated for use as stan-d wavelengths.

Introduction

g II has been ranked as one of the best known spectra ever since the early in-tigation by FOWLER (1914, 1922) who observed the spectrum using an arc in uum. His observations in the red and the infrared were very incomplete, however, it seemed desirable to extend the observations using the improved photographic ulsions now available, especially in view of the astrophysical interest of Mg II. urther reason for a complete reinvestigation of this spectrum derives from the that the term system of Mg II, if accurately determined, is very well suited for alculation of wavelengths in the vacuum-ultraviolet for use as standards. Such evision should be performed with a light source giving undisturbed levels, e.g. ollow cathode.

Experimental details

he investigation has been carried out with a hollow cathode which has the desir- property of giving sharp lines even for very high principal and azimuthal ntum numbers. The anode and cathode parts of the light source are separated by ort porcelain tube (Fig. 1), the joints being sealed by O-rings. These three parts he light source are held together by small clamps not shown in the figure. Between iron cylinder that formed the hollow cathode, and the cathode block there was all heat-insulating space in order to get the temperature inside the hollow cathode able for the evaporation of the magnesium metal. The inner dimensions (not ical) of the hollow cathode were: length 40 mm, diameter 8 mm, the opening being

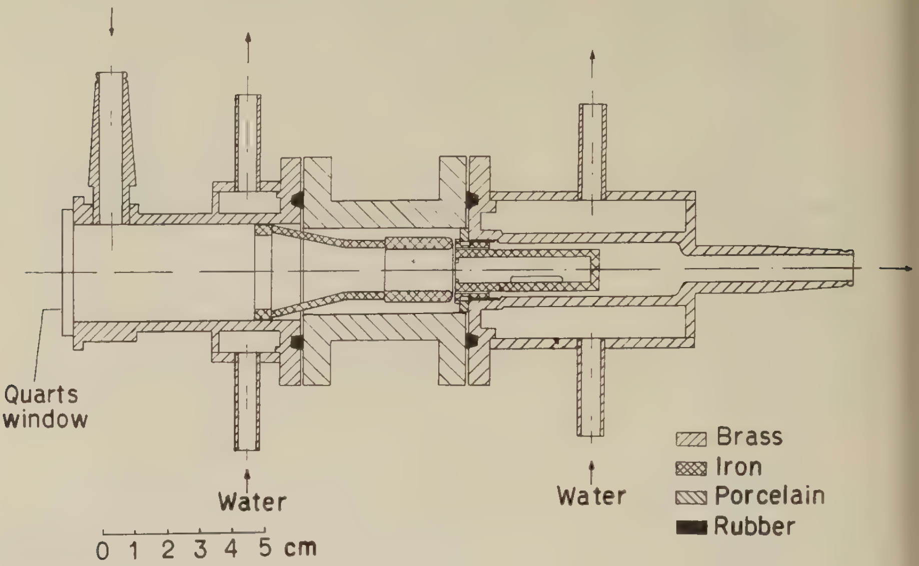

Fig. 1. A section through the hollow-cathode light source used for Mg II.

constricted to 5 mm. The hollow cathode was charged with a piece of metallic magne
sium of 10–20 mm length and 2–3 mm thickness.

The magnesium line 10092 A was very strong in comparison with the availabl
standard wavelengths. In order to overcome this difficulty the heat-insulate
hollow cathode was replaced by a water-cooled hollow cathode of aluminium. I
this way it was possible to get a suitable intensity relation between the line 10092 A
and the standard lines. Without any risk of continuous temperature radiation th
current could be raised to give a conveniently short exposure time.

In front of the cathode at a distance of 1 mm there is a hollow iron cylinder, con
nected with the anode by means of two iron pins. Thanks to this iron cylinder, whic
is easy to replace through the front of the light source, the discharge stays entirel
inside the hollow cathode, and the evaporated metal will deposit almost exclusivel
on the inside of the cylinder. To exchange this cylinder for a cleaned one and to re
charge the hollow cathode it is only necessary to remove the quartz window whic
is attached to the front of the anode by means of apiezon grease.

Neon was used as the carrier gas at a pressure of some tenths of a millimeter c
mercury. The current and the voltage generally varied from about 120 mA an
450 V to about 200 mA and 325 V. The gas circulating system was of the conventiona
type, including purifying traps and glass bulbs containing a supply of He, Ne, A
and Xe. When using Ar or Xe the charcoal trap must be turned off. For Xe it
necessary to turn off the empty liquid air trap too.

The spectrograms were obtained with a grating spectrograph in Wadsworth
mounting described by Lidén (1949). The dispersion is about 7.5 A/mm in the fir
order. Eastman spectroscopic plates were used over the whole range. The improve
type I–Z(2) for the region above 10000 A has been of special value. Plates of the typ
I–N, I–M and I–Z(2) were hypersensitized in a solution of 12 cc ammonia (24 %)

Table 1. Wavelengths of Mg II lines in the region 11 620–2790 A.

ntensity	λ_{air}, *A*	Previous measurements	σ_{obs}, cm^{-1}	σ_{calc}	Combination
3	11 620.14		8 603.39	*H**	$5g\,^2G - 7h\,^2H$
3	11 600.56		8 617.92	.90	$5f\,^2F - 7g\,^2G$
4	11 256.35		8 881.44	.45	$5d\,^2D_2 - 7f\,^2F_3$
5	11 255.93		8 881.78	.78	$^2D_3 - {}^2F_4$
10	10 951.78		9 128.43	.44	$3d\,^2D_2 - 4p\,^2P_1$
7	10 915.27		9 158.97	.96	$^2D_2 - {}^2P_2$
11	10 914.23		9 159.84	.83	$^2D_3 - {}^2P_2$
6	10 392.23		9 619.94	.95	$4f\,^2F_4 - 5d\,^2D_3$
5	10 391.76		9 620.37	.38	$^2F_3 - {}^2D_2$
14	10 092.16		9 905.97	*G*	$4f\,^2F - 5g\,^2G$
11	9 632.435		10 378.74	.74	$4d\,^2D_2 - 5f\,^2F_3$
12	9 631.888		10 379.33	.33	$^2D_3 - {}^2F_4$
10	9 340.544		10 703.08	*H*	$5g\,^2G - 8h\,^2H$
10	9 327.545		10 717.99	8.00	$5f\,^2F - 8g\,^2G$
13	9 244.266		10 814.55	.55	$4s\,^2S_1 - 4p\,^2P_1$
14	9 218.248		10 845.07	.07	$^2S_1 - {}^2P_2$
11	8 835.082		11 315.41	.41	$5p\,^2P_2 - 7s\,^2S_1$
10	8 824.323		11 329.20	.20	$^2P_1 - {}^2S_1$
11	8 745.657		11 431.11	.11	$5p\,^2P_2 - 6d\,^2D_3$
10	8 734.990		11 445.07	.07	$^2P_1 - {}^2D_2$
11	8 234.639		12 140.49	.49	$4p\,^2P_2 - 5s\,^2S_1$
10	8 213.989		12 171.01	.01	$^2P_1 - {}^2S_1$
7−	8 233.194		12 142.62	*H*	$5g\,^2G - 9h\,^2H$
7	8 222.924		12 157.78	.79	$5f\,^2F - 9g\,^2G$
8	8 120.434		12 311.23	.23	$4d\,^2D_2 - 6p\,^2P_1$
9	8 115.220		12 319.14	.13	$^2D_3 - {}^2P_2$
13	7 896.368	.37	12 660.57	.56	$4p\,^2P_2 - 4d\,^2D_3$
12	7 877.051	.13	12 691.62	.61	$^2P_1 - {}^2D_2$
4	7 790.978		12 831.83	.83	$5s\,^2S_1 - 6p\,^2P_1$
5	7 786.500		12 839.21	.21	$^2S_1 - {}^2P_2$
3	7 589.558		13 172.37	*H*	$5g\,^2G - 10h\,^2H$
4	7 580.764		13 187.65	*G*	$5f\,^2F - 10g\,^2G$
2	7 166.676		13 949.63	*G*	$5f\,^2F - 11g\,^2G$
8	6 819.270		14 660.28	.28	$5p\,^2P_2 - 8s\,^2S_1$
7	6 812.860		14 674.07	.08	$^2P_1 - {}^2S_1$
8	6 787.851		14 728.14	.14	$5p\,^2P_2 - 7d\,^2D_3$
7	6 781.451		14 742.04	*D*	$^2P_1 - {}^2D_2$
6	6 620.569		15 100.27	.27	$4f\,^2F_4 - 6d\,^2D_3$
5	6 620.440		15 100.57	.57	$^2F_3 - {}^2D_2$

* A letter in this column indicates that the high term was determined from this line
ne.

Table 1 (cont.)

Intensity	λ_{air}, A	Previous measurements	σ_{obs}, cm^{-1}	σ_{calc}	Combination
11	6 545.973	.80	15 272.35	G	$4f\,^2F - 6g\,^2G$
9	6 346.962	.67	15 751.21	F	$4d\,^2D_2 - 6f\,^2F_3$
10	6 346.737		15 751.77	F	$^2D_3 - {}^2F_4$
4	5 943.499		16 820.45	.45	$5p\,^2P_2 - 9s\,^2S_1$
3	5 938.629		16 834.24	.24	$^2P_1 - {}^2S_1$
4	5 928.233		16 863.76	D	$5p\,^2P_2 - 8d\,^2D_3$
3	5 923.366		16 877.62	D	$^2P_1 - {}^2D_2$
6	5 918.158		16 892.47	P	$4d\,^2D_2 - 7p\,^2P_1$
7	5 916.429		16 897.41	P	$^2D_3 - {}^2P_2$
2	5 464.136		18 296.07	.07	$5p\,^2P_2 - 10s\,^2S_1$
1	5 460.019		18 309.87	.87	$^2P_1 - {}^2S_1$
masked	(5 455.4)		(18 325.4)		$5p\,^2P_2 - 9d\,^2D_3$
1	5 451.259		18 339.29	D	$^2P_1 - {}^2D_2$
4	5 434.039		18 397.41	.40	$4f\,^2F - 7d\,^2D$
9	5 401.543	.05	18 508.08	.09	$4f\,^2F - 7g\,^2G$
7	5 264.368	.14	18 990.35	.34	$4d\,^2D_2 - 7f\,^2F_3$
8	5 264.215		18 990.90	.90	$^2D_3 - {}^2F_4$
3	5 069.802		19 719.14	P	$4d\,^2D_2 - 8p\,^2P_1$
4	5 068.937		19 722.50	P	$^2D_3 - {}^2P_2$
2	4 868.845		20 533.02	.01	$4f\,^2F - 8d\,^2D$
7	4 851.082	.10	20 608.20	.19	$4f\,^2F - 8g\,^2G$
5	4 739.712	.59	21 092.43	F	$4d\,^2D_2 - 8f\,^2F_3$
6	4 739.588		21 092.98	F	$^2D_3 - {}^2F_4$
1	4 631.405		21 585.68	P	$4d\,^2D_2 - 9p\,^2P_1$
2	4 630.878		21 588.13	P	$^2D_3 - {}^2P_2$
6	4 534.291	.26	22 047.98	.97	$4f\,^2F - 9g\,^2G$
13	4 481.327	.327	22 308.56	.56	$3d\,^2D_2 - 4f\,^2F_3$
14	4 481.130	.129	22 309.54	.56	$^2D_3 - {}^2F_4$
4	4 436.598	.48	22 533.47	F	$4d\,^2D_2 - 9f\,^2F_3$
5	4 436.486		22 534.04	F	$^2D_3 - {}^2F_4$
9	4 433.990	.991	22 546.72	.72	$4p\,^2P_2 - 6s\,^2S_1$
8	4 427.994	.995	22 577.25	.25	$^2P_1 - {}^2S_1$
10	4 390.564	.585	22 769.72	.68	$4p\,^2P_2 - 5d\,^2D_3$
9	4 384.637	.643	22 800.50	.50	$^2P_1 - {}^2D_2$
2	4 242.543	.47	23 564.13	F	$4d\,^2D_2 - 10f\,^2F_3$
3	4 242.445		23 564.68	F	$^2D_3 - {}^2F_4$
7	3 850.385	.40	25 964.07	.06	$3d\,^2D_2 - 5p\,^2P_1$
8	3 848.209	.24	25 978.74	.73	$^2D_3 - {}^2P_2$
3	3 615.583	.64	27 650.17	.17	$4s\,^2S_1 - 5p\,^2P_1$
4	3 613.781	.80	27 663.96	.97	$^2S_1 - {}^2P_2$
8	3 553.366	.51	28 134.29	.30	$4p\,^2P_2 - 7s\,^2S_1$
7	3 549.516	.61	28 164.81	.83	$^2P_1 - {}^2S_1$

Table 1 (cont.)

Intensity	λ_{air}, A	Previous measurements	σ_{obs}, cm^{-1}	σ_{calc}	Combination
8	3 538.813	.86	28 249.99	50.00	$4p\ {}^2P_2 - 6d\ {}^2D_3$
7	3 534.972	5.04	28 280.68	.69	${}^2P_1 - {}^2D_2$
7	3 175.783	.84	31 479.19	.18	$4p\ {}^2P_2 - 8s\ {}^2S_1$
6	3 172.706	.79	31 509.72	.70	${}^2P_1 - {}^2S_1$
6	3 168.951	.98	31 547.06	.04	$4p\ {}^2P_2 - 7d\ {}^2D_3$
8	3 104.809	.805	32 198.75	.79	$3d\ {}^2D_2 - 5f\ {}^2F_3$
9	3 104.722	.713	32 199.66	.72	${}^2D_3 - {}^2F_4$
10	2 936.509	.496	34 044.08	.07	$3p\ {}^2P_2 - 4s\ {}^2S_1$
9	2 928.634	.625	34 135.63	.64	${}^2P_1 - {}^2S_1$
12	2 802.704	.698	35 669.32	.32	$3s\ {}^2S_1 - 3p\ {}^2P_1$
13	2 795.528	.523	35 760.87	.88	${}^2S_1 - {}^2P_2$
10	2 797.998	.989	35 729.30	.31	$3p\ {}^2P_2 - 3d\ {}^2D_3$
9	2 790.776	.768	35 821.76	.75	${}^2P_1 - {}^2D_2$

100 cc methyl alcohol and 100 cc water. The plates were kept in the bath for 5 minutes at a temperature not above 10°C and then bathed in methyl alcohol for 1 minute, the temperature still being below 10°C, and finally dried with a fan. Hypersensitized plates were developed in Kodak D19 for 4–4.5 minutes.

Wavelength measurements

The two lines 11 620 A and 11 600 A were measured on three spectrograms. All the other lines have been measured on at least four plates. Lines above 7000 A and the three lines 5464 A, 5460 A, and 5451 A have been measured in the first diffraction order only. All other lines were measured in the second order. On every spectrogram standard wavelengths in the same order were used. On some plates above 10 000 A, however, the sparsely occurring standards were supplemented with second order lines. The main part of the standard wavelengths have been the Ne I wavelengths given by BURNS, ADAMS and LONGWELL (1950) and by MEGGERS and HUMPHREYS (1934), supplemented with some lines in the infrared the wavelengths of which have been calculated from accurately determined term values. In some cases use has been made of interferometrically measured lines in He, Ar and Xe. Wavelengths of iron lines (vacuum-arc values) were of great value in the visible and the

Table 2. Interferometric measurements of $3s$–$3p$ in Mg II.

Reference	λ_{air} A, number of obs.	
BURNS, SULLIVAN (1948)	2 802.701 (2)	2 795.531 (5)
BURNS (1948)	2 802.704	2 795.527
WAGMAN (1937)		2 795.520 (1)

Table 3. Comparison of some Mg II lines with solar data.

Combination	Present investigation		Solar data		
	Intens.	λ_{air}, *A*	λ	Intens.	Ident.
$3d\,^2D_2 - 4p\,^2P_1$	10	10 951.78	1.82	0	Mg II *p*
$^2D_3 - \quad ^2P_2$	11	10 914.23	4.25	2	Mg II *p*
$4f\,^2F_4 - 5d\,^2D_3$	6	10 392.23	2.18	− 3	
$4f\,^2F - 5g\,^2G$	14	10 092.16	2.15	− 2	
$4d\,^2D_3 - 5f\,^2F_4$	12	9 631.888	1.87	− 2	⊙
$4s\,^2S_1 - 4p\,^2P_1$	13	9 244.266	4.25	0NN	Mg II *p*
$^2S_1 - \quad ^2P_2$	14	9 218.248	8.251	3	Mg II *p*
$4p\,^2P_2 - 4d\,^2D_3$	13	7 896.368	6.378	− 1	Mg II
$^2P_1 - \quad ^2D_2$	12	7 877.051	7.059	0	Mg II
$3d\,^2D_2 - 4f\,^2F_3$	13	4 481.327	1.340	0	Mg II
$^2D_3 - \quad ^2F_4$	14	4 481.130	1.142	0	Mg II
$4p\,^2P_2 - 5d\,^2D_3$	10	4 390.564	0.542	0	
$3d\,^2D_2 - 5f\,^2F_3$	8	3 104.809	4.780	− 3	
$^2D_3 - \quad ^2F_4$	9	3 104.722	4.715	− 1	

ultraviolet. The hollow cathode served as the source of the iron spectrum after the magnesium metal had been quite evaporated from it by raising the current for a while. The iron wavelengths were taken from WILLIAMS and MIDDLETON (1939) and from BURNS and WALTERS Jr. (1929, 1931). Finally, it was also possible to use interferometrically measured Mg I lines (MEISSNER, 1938).

The limits of error in the wavelength measurements are estimated to range from 0.02 A at 11 600 A to 0.003 A at 3000 A. Vacuum corrections ($\lambda_{\mathrm{vac}} - \lambda_{\mathrm{air}}$) were taken from the tables calculated by EDLÉN from his dispersion formula for standard ai (1953).

The measured wavelengths are given in Table 1. A few more lines were observed but not measured as being of little value for fixing the term system. The previous observations listed in the third column of Table 1 are all from FOWLER (1922) For the resonance doublet 3*s*–3*p* some interferometric observations exist, which are collected in Table 2. A comparison with the present grating observations show that these lie within the range of variation of the different interferometer values The grating observations have been used in computing the term values.

The intensities given in Table 1 are only roughly estimated values and are consistent only over a short range of wavelengths.

A comparison with the solar spectrum in the photographic region is given in Tabl 3. The solar data are from BABCOCK and MOORE (1947) in the region 10951–7877 A and from ST. JOHN, MOORE, WARE, ADAMS, and BABCOCK (1928) for shorter wavelengths. Computed lines falling above the photographic region do not seem to appea in the solar spectrum as recorded by MOHLER, PIERCE, MCMATH and GOLDBERG (1953). This may be explained by the relatively high excitation potentials for th levels involved.

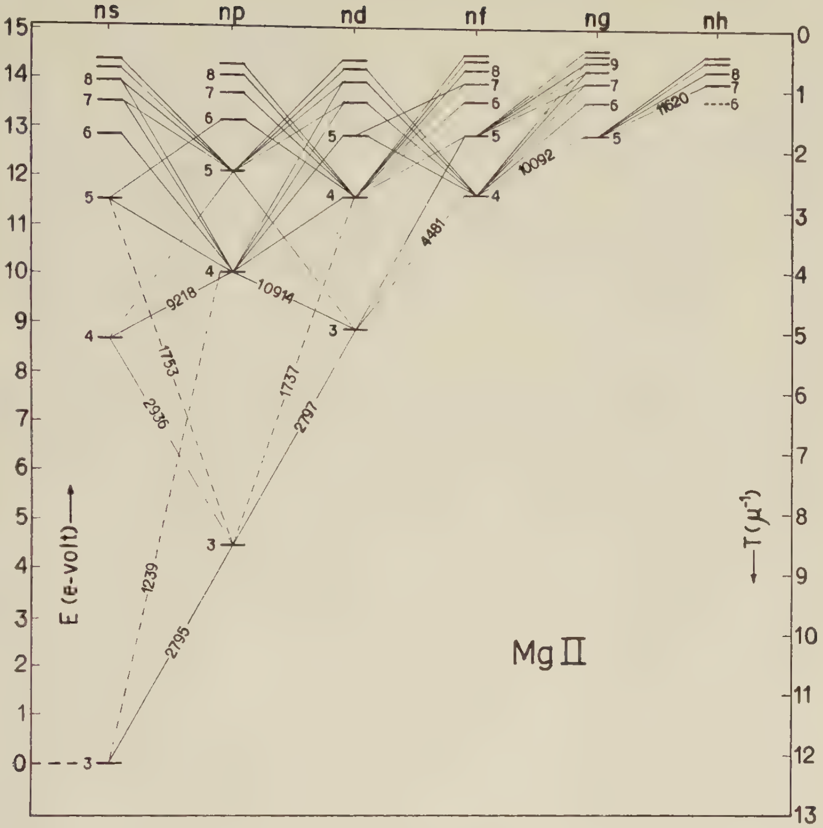

Fig. 2. Term system of Mg II. Measured transitions are indicated by solid lines.

The term system

The simple one-electron system of Mg II is illustrated by the term diagram shown in Fig. 2. The term values are given in Table 4. In order to facilitate a comparison with existing term tables both *E* values, counted from the ground state, and *T* values, counted from the series limit, are given.

The term values have been calculated from weighted wave numbers with 3 decimal places using the method of least squares. A convenient procedure for this calculation has been described by Bockasten (1955). It seemed to be most suitable to do this calculation in two steps due to the fact that the ^2F terms combine with ^2D terms giving separated doublets and with ^2G terms giving unseparated lines. First, the splittings of the ^2F terms were computed from all the weighted lines except those due to ^2F–^2G transitions. Weighted transitions ^2F–^2G were then theoretically resolved with regard to these splittings and used with all the other weighted lines for a final determination of the term values.

Table 4. Term values of Mg II.

Term symbol	E, cm^{-1}	ΔE	T, cm^{-1}	n^*	Δn^*
$3s\,{}^2S_1$	0.00		121 267.61	1.902 523	
$4s\,{}^2S_1$	69 804.95		51 462.66	2.920 493	
$5s\,{}^2S_1$	92 790.51		28 477.10	3.926 037	
$6s\,{}^2S_1$	103 196.75		18 070.86	4.928 478	
$7s\,{}^2S_1$	108 784.33		12 483.28	5.929 770	
$8s\,{}^2S_1$	112 129.20		9 138.41	6.930 538	
$9s\,{}^2S_1$	114 289.36		6 978.25	7.931 02	
$10s\,{}^2S_1$	115 764.99		5 502.62	8.931 36	
$3p\,{}^2P_1$	35 669.31	91.56	85 598.30	2.264 486	0.001 212
${}^2P_2$	35 760.88		85 506.73	2.265 698	
$4p\,{}^2P_1$	80 619.50	30.53	40 648.11	3.286 110	0.001 234
${}^2P_2$	80 650.02		40 617.59	3.287 344	
$5p\,{}^2P_1$	97 455.12	13.80	23 812.49	4.293 386	0.001 244
${}^2P_2$	97 468.92		23 798.69	4.294 630	
$6p\,{}^2P_1$	105 622.34	7.38	15 645.27	5.296 765	0.001 250
${}^2P_2$	105 629.72		15 637.89	5.298 015	
$7p\,{}^2P_1$	110 203.58	4.41	11 064.03	6.298 622	0.001 257
${}^2P_2$	110 207.99		11 059.62	6.299 879	
$8p\,{}^2P_1$	113 030.25	2.84	8 237.36	7.299 754	0.001 259
${}^2P_2$	113 033.09		8 234.52	7.301 013	
$9p\,{}^2P_1$	114 896.79	1.93	6 370.82	8.300 50	0.001 26
${}^2P_2$	114 898.72		6 368.89	8.301 76	
$3d\,{}^2D_2$	71 491.06	−0.87	49 776.55	2.969 545	−0.000 026
${}^2D_3$	71 490.19		49 777.42	2.969 519	
$4d\,{}^2D_2$	93 311.11	−0.52	27 956.50	3.962 423	−0.000 037
${}^2D_3$	93 310.59		27 957.02	3.962 386	
$5d\,{}^2D_2$	103 420.00	−0.30	17 847.61	4.959 207	−0.000 041
${}^2D_3$	103 419.70		17 847.91	4.959 166	
$6d\,{}^2D_2$	108 900.19	−0.17	12 367.42	5.957 482	−0.000 040
${}^2D_3$	108 900.03		12 367.58	5.957 442	
$7d\,{}^2D_2$	112 197.16	−0.10	9 070.45	6.956 453	−0.000 038
${}^2D_3$	112 197.06		9 070.55	6.956 415	
$8d\,{}^2D_2$	114 332.74	−0.06	6 934.87	7.955 79	−0.000 04
${}^2D_3$	114 332.68		6 934.93	7.955 75	
$9d\,{}^2D_2$	115 794.41		5 473.20	8.955 33	
$4f\,{}^2F$	93 799.70	0.13	27 467.91	3.997 509	
$5f\,{}^2F$	103 689.89	0.06	17 577.72	4.997 134	
$6f\,{}^2F$	109 062.34	0.03	12 205.27	5.996 925	
$7f\,{}^2F$	112 301.47		8 966.14	6.996 801	
$8f\,{}^2F$	114 403.55		6 864.06	7.996 72	
$9f\,{}^2F$	115 844.60		5 423.01	8.996 68	
$10f\,{}^2F$	116 875.25		4 392.36	9.996 63	
$5g\,{}^2G$	103 705.66		17 561.95	4.999 378	
$6g\,{}^2G$	109 072.05		12 195.56	5.999 311	
$7g\,{}^2G$	112 307.79		8 959.82	6.999 267	
$8g\,{}^2G$	114 407.88		6 859.73	7.999 24	
$9g\,{}^2G$	115 847.67		5 419.94	8.999 23	
$10g\,{}^2G$	116 877.54		4 390.07	9.999 23	
$11g\,{}^2G$	117 639.51		3 628.10	10.999 24	

ble 4 (cont.)

Term symbol	E, cm^{-1}	ΔE	T, cm^{-1}	n^*	Δn^*
$6h\ ^2H$	109 074.0†		12 193.6†	5.999 79†	
$7h\ ^2H$	112 309.06		8 958.55	6.999 763	
$8h\ ^2H$	114 408.74		6 858.87	7.999 74	
$9h\ ^2H$	115 848.28		5 419.33	8.999 73	
$10h\ ^2H$	116 878.04		4 389.57	9.999 79	

† Extrapolated values.

Some indication of the accuracy of the observations is given by the average of the solute values of the differences between observed and calculated wave numbers:

$$\frac{\sum|\sigma_{\mathrm{obs}}-\sigma_{\mathrm{calc}}|}{\text{number of lines}}=\frac{0.556}{71}=0.008\ \mathrm{cm}^{-1}.$$

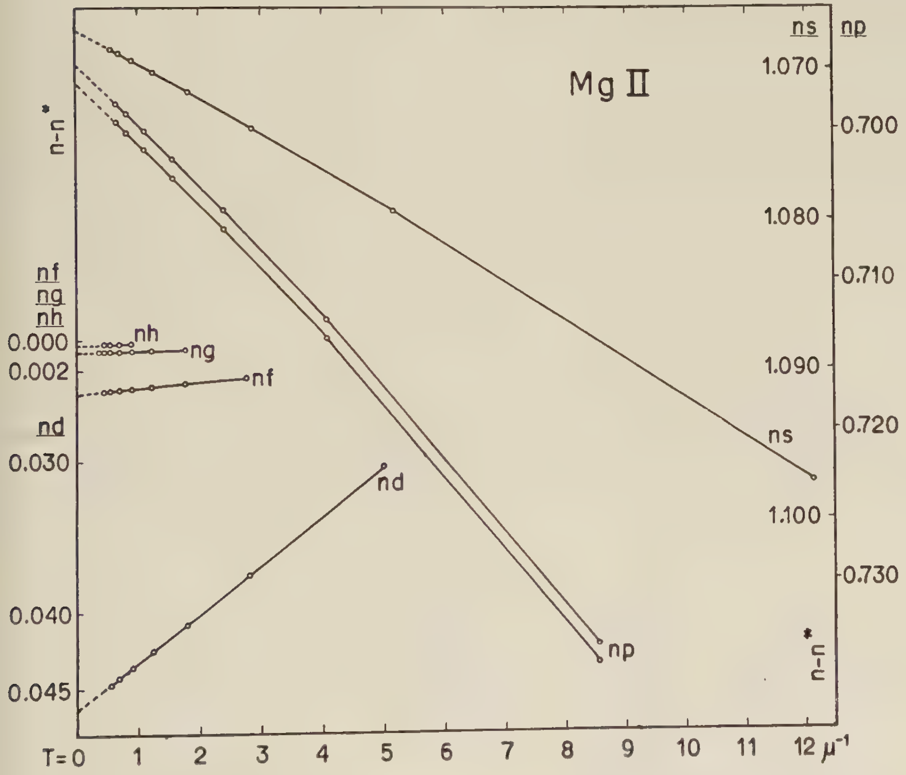

Fig. 3. The quantum defect $n-n^*$ for the series of Mg II as a function of the term values.

Table 5. Differences between observed term values and term values computed fro
the series formulae given below. The figures are $T_{\text{obs}}-T_{\text{calc}}$ in cm^{-1}.

n	$^2S_1$	$^2P_2$	$^2P_1$	$^2D_3$	$^2D_2$	^2F	^2G	^2H
3	—	—	—	—	—			
4	—	—	—	—	—	+0.002		
5	—	—	—	—	—	−0.012	+0.001	
6	—	—	—	+0.002	+0.015	+0.008	−0.003	
7	+0.001	−0.021	−0.013	−0.004	+0.010	+0.006	+0.005	—
8	−0.001	−0.019	−0.015	−0.002	+0.013	+0.008	−0.001	—
9	+0.015	−0.025	−0.026		+0.011	−0.011	−0.001	−0.002
10	+0.008					+0.001	−0.015	−0.066
11							−0.027	

As the estimated limit of error in the term values is of the order of 0.02 cm^{-1} i
has seemed appropriate to give the term values in Table 4 abbreviated to two decima
places. Unabbreviated values have been used in the calculation of ΔE and n^* i
Table 4, σ_{calc} in Table 1, σ and λ_{vac} in Table 6, and ΔT in Table 5.

No ^2H-levels were previously known, nor was the lowest ^2G-level. Of the ^2D term
only $3d\ ^2D$ had been given as double. The line 4481 A ($3d$–$4f$) was resolved by KIN
(1913) who found that the violet component was the strongest, indicating tha
$3d\ ^2D$ were inverted. The same doublet was observed by MUNDIE and MEISSNE
(1944) and resolved in two components with the separation 1.000 ± 0.002 cm^{-}
This checks well with the present observation of 0.98 cm^{-1}. Now it is shown (Table 4
that also the higher ^2D terms are inverted. On the other hand, the ^2F terms are foun
to be separated in the normal way. It may be remarked that the term values o
^2F given in Table 4 correspond to the centres of gravity of the two component
$^2F_3$ and $^2F_4$.

A comparison between the term values in Table 4 and those in *Atomic Energ*
Levels (1949) shows several differences greater than 1 cm^{-1}, also among the lowe
levels, indicating that the average errors in the term values have now been reduce
by a large factor.

The series limit has been determined from the five lowest ^2G terms by fitting the
to a Ritz formula with the method of least squares. The effective quantum number
$n^* = \sqrt{4R/T_n}$, were calculated with $4R = 438\,939.33$. Fig. 3 shows $\delta = n - n^*$ plotte
against the term values for the various spectral series. These series can be represente
by the following extended Ritz formulae, suggested by EDLÉN (1954), wher
$t = (n^*)^{-2}$:

$^2S_1,\ \delta = 1.067\,391\,3 + 0.098\,620\,0\,t + 0.042\,497\,t^2 - 0.019\,155\,t^3$

$^2P_2,\ \delta = 0.695\,758\,8 + 0.170\,099\,5\,t + 0.128\,363\,t^2 + 0.072\,47\,t^3$

$^2P_1,\ \delta = 0.697\,025\,9 + 0.169\,484\,6\,t + 0.130\,371\,t^2 + 0.064\,51\,t^3$

$^2D_3,\ \delta = 0.046\,389\,2 - 0.134\,570\,9\,t - 0.050\,313\,t^2$

$^2D_2,\ \delta = 0.046\,342\,5 - 0.134\,462\,9\,t - 0.049\,679\,t^2$

$^2F\ ,\ \delta = 0.003\,538\,6 - 0.016\,741\,t$

$^2G\ ,\ \delta = 0.000\,844 \quad - 0.005\,54\,t$

$^2H\ ,\ \delta = 0.000\,323 \quad - 0.004\,22\,t$

Table 6. Mg II. Calculated wavelengths.

Combination	σ, cm^{-1}	λ_{vac} A
$3p\ ^2P_2 - 5s\ ^2S_1$	57 029.63	1753.4744
$^2P_1 - \quad ^2S_1$	57 121.19	1750.6637
$3p\ ^2P_2 - 4d\ ^2D_3$	57 549.71	1737.6283
$^2P_2 - \quad ^2D_2$	57 550.23	1737.6124
$^2P_1 - \quad ^2D_2$	57 641.80	1734.8523
$3p\ ^2P_2 - 6s\ ^2S_1$	67 435.87	1482.8903
$^2P_1 - \quad ^2S_1$	67 527.43	1480.8797
$3p\ ^2P_2 - 5d\ ^2D_3$	67 658.83	1478.0037
$^2P_2 - \quad ^2D_2$	67 659.13	1477.9972
$^2P_1 - \quad ^2D_2$	67 750.69	1475.9998
$3p\ ^2P_2 - 7s\ ^2S_1$	73 023.45	1369.4231
$^2P_1 - \quad ^2S_1$	73 115.01	1367.7082
$3p\ ^2P_2 - 6d\ ^2D_3$	73 139.15	1367.2568
$^2P_2 - \quad ^2D_2$	73 139.31	1367.2537
$^2P_1 - \quad ^2D_2$	73 230.88	1365.5442
$3p\ ^2P_2 - 8s\ ^2S_1$	76 368.32	1309.4434
$^2P_1 - \quad ^2S_1$	76 459.89	1307.8754
$3p\ ^2P_2 - 7d\ ^2D_3$	76 436.18	1308.2809
$^2P_2 - \quad ^2D_2$	76 436.28	1308.2792
$^2P_1 - \quad ^2D_2$	76 527.85	1306.7139
$3p\ ^2P_2 - 9s\ ^2S_1$	78 528.49	1273.4232
$^2P_1 - \quad ^2S_1$	78 620.05	1271.9402
$3p\ ^2P_2 - 8d\ ^2D_3$	78 571.80	1272.7212
$^2P_2 - \quad ^2D_2$	78 571.86	1272.7202
$^2P_1 - \quad ^2D_2$	78 663.43	1271.2388
$3s\ ^2S_1 - 4p\ ^2P_1$	80 619.50	1240.3947
$^2S_1 - \quad ^2P_2$	80 650.02	1239.9252
$3s\ ^2S_1 - 5p\ ^2P_1$	97 455.13	1026.1133
$^2S_1 - \quad ^2P_2$	97 468.92	1025.9681
$3s\ ^2S_1 - 6p\ ^2P_1$	105 622.34	946.7694
$^2S_1 - \quad ^2P_2$	105 629.72	946.7032
$3s\ ^2S_1 - 7p\ ^2P_1$	110 203.58	907.4115
$^2S_1 - \quad ^2P_2$	110 207.99	907.3752
$3s\ ^2S_1 - 8p\ ^2P_1$	113 030.25	884.7189
$^2S_1 - \quad ^2P_2$	113 033.09	884.6967

From Table 5, which contains the differences $T_{\text{obs}} - T_{\text{calc}}$ it is clear that these rmulae describe the series within the observational errors. A dash in Table 5 means at the term has been used for the determination of the series constants. For $n\ ^2F$ e terms $n = 4, 5, 6, 7$ and for $n\ ^2G$ the terms $n = 5, 6, 7, 8, 9$ have been used for these terminations by applying the method of least squares.

Calculation of vacuum-ultraviolet standards of wavelength

Owing to the favourable positions of the deep levels the term system is very well ited for the calculation of accurate wavelengths in the vacuum-ultraviolet. The fferences $3s$–$3p$, $3p$–$4s$ and $3p$–$3d$ (Fig. 2) have nearly the same size, the wavengths falling between 2790 A and 2936 A, and are well determined. The calculated es in the vacuum-ultraviolet belong to the principal, sharp and diffuse series and e collected in Table 6. An estimated error limit in σ of 0.05 cm^{-1} would correspond a wavelength error ranging from 0.0015 A at 1750 A to 0.0004 A at 880 A.

ACKNOWLEDGEMENTS

The author wishes to thank Professor Bengt Edlén for his invaluable advice and constant terest in this investigation. Also to Fil. Dr. Lennart Minnhagen the author is greatly indebted r many valuable discussions.

The work has been financially supported by the Swedish Natural Science Research Council, hich is gratefully acknowledged.

The Physical Laboratory, University of Lund, December 1954.

REFERENCES

Babcock, H. D., and Moore, Ch. E., Carnegie Inst. Wash. Publ. *579* (1947).
Bockasten, K., Arkiv för Fysik (1955) (in press).
Burns, K. (1948), see Burns and Sullivan (1948).
Burns, K., Adams, K. B., and Longwell, J., J. Opt. Soc. Am. *40*, 339 (1950).
Burns, K., and Sullivan, F. F., Science Studies, St. Bonaventure College *14*, No. 3 (1948).
Burns, K., and Walters Jr., F. M., Publ. Allegheny Obs. *6*, 159 (1929); *8*, 39 (1931).
Edlén, B., J. Opt. Soc. Am. *43*, 339 (1953).
—— Proceedings of the Rydberg Centennial Conference, Lund (1954) (in press).
Fowler, A., Phil. Trans. *A 214*, 225 (1914).
—— Report on Series in Line Spectra, p. 118. Fleetway Press, London, 1922.
King, A. S., Astrophys. J. *38*, 327 (1913).
Lidén, K., Arkiv för Fysik *1*, 229 (1949).
Meggers, W. F., and Humphreys, C. J., J. Res. Nat. Bur. Stand. *13*, 293 (1934).
Meissner, K. W., Ann. der Phys. (5) *31*, 505 (1938).
Mohler, O. C., Pierce, A. K., McMath, R. R., and Goldberg, L., Astrophys. J. *117*, 41 (1953)
Moore, Ch. E., Atomic Energy Levels, Circular 467, Nat. Bur. Stand. (1949).
Mundie, L. G., and Meissner, K. W., Phys. Rev. *65*, 265 (1944).
St. John, Ch. E., Moore, Ch. E., Ware, L. M., Adams, E. F., and Babcock, H. D., Carnegie Inst. Wash. Publ. *396* (1928).
Wagman, N. E., Univ. Pittsburgh Bull. *34*, 1 (1937).
Williams, W. E., and Middleton, A., Proc. Roy. Soc. *A 172*, 159 (1939).

Description of Plates I–II

The plates show enlarged spectrograms obtained with a hollow cathode and a grating spectrograph in Wadsworth mounting. The original dispersion is about 7.5 A/mm in the first order. The Mg II lines were observed in the first order with Ne as filling gas. In some cases second order lines have been superimposed on the first order spectrum during a part of the exposure time, as is remarked in parenthesis in the data list given below. When standard wavelengths of Ar or Xe were used, these lines were obtained by means of a separate discharge either before or after the main Mg exposure. All plates were hyper-sensitized. The magnification is 4 times except for I d which is magnified 13 times.

	Plate type	Discharge in Ne		Supplementary discharge		
I a	I–Z (2)	5 hours (second order:	120 mA 30 min)			
I b	I–Z (2)	90 min (second order:	120 mA 10 min)			
I c	I–Z (2)	33 min (second order:	700 mA 2 min)	Xe	1 min	450 mA
I d	I–M	35 min	100 mA	Ar + Xe	15 min	100 mA
II a	I–M	20 min	125 mA	Ne + Ar	1 min	200 mA
II b	I–N	90 min	100 mA	Ar	2 sec	150 mA
II c	I–N	3.5 hours	110 mA	Ar	6 sec	150 mA

Tryckt den 29 april 1955

Uppsala 1955. Almqvist & Wiksells Boktryckeri AB

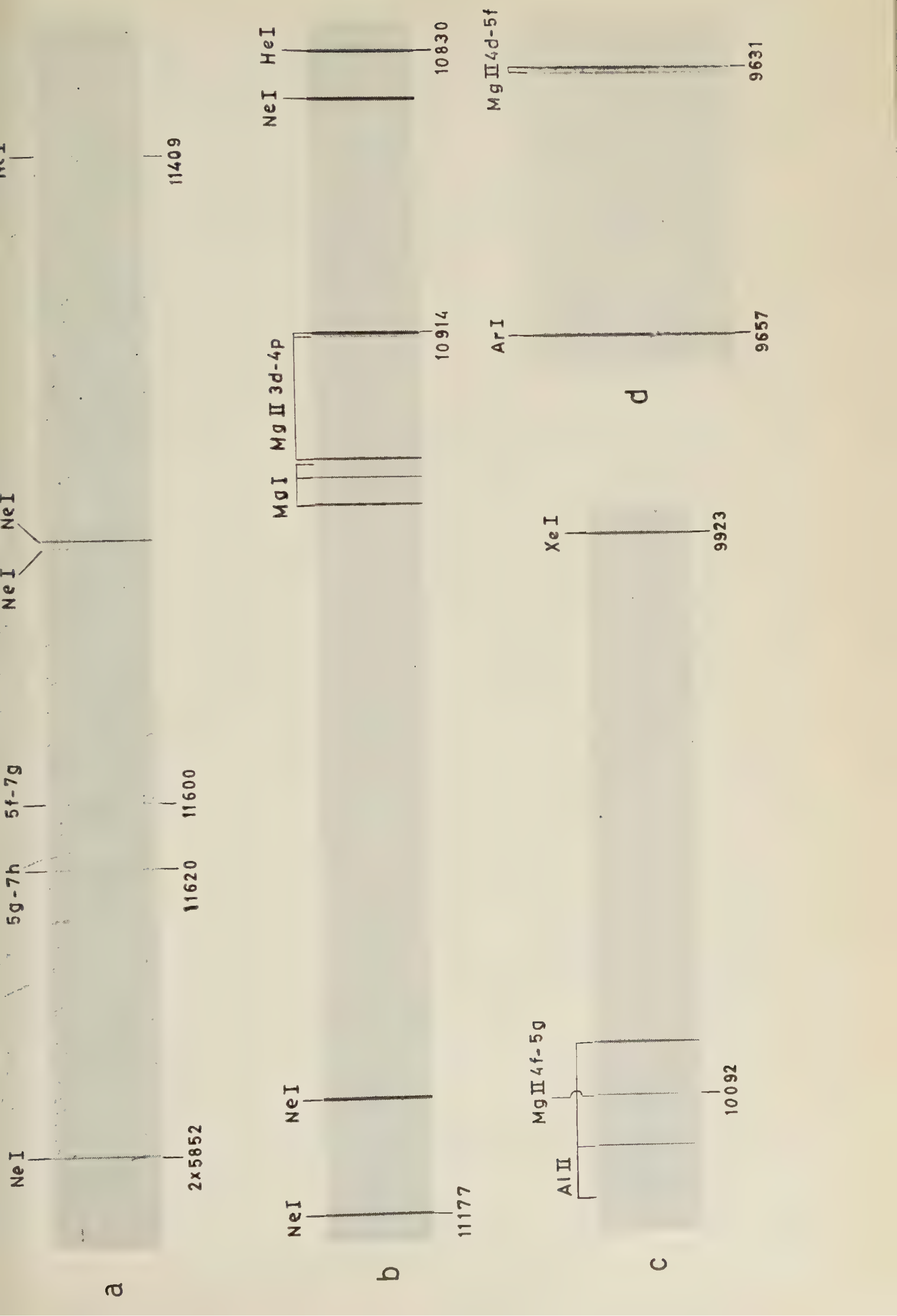
a
11409
Ne I
Ne I
5f-7g
11600
5g-7h
11620
Ne I
2x5852
b
Ne I
He I
10830
Mg II 3d-4p
10914
Mg I
Ne I
Ne I
11177
c
d
Mg II 4d-5f
9631
Ar I
9657
Xe I
9923
Mg II 4f-5g
10092
Al II

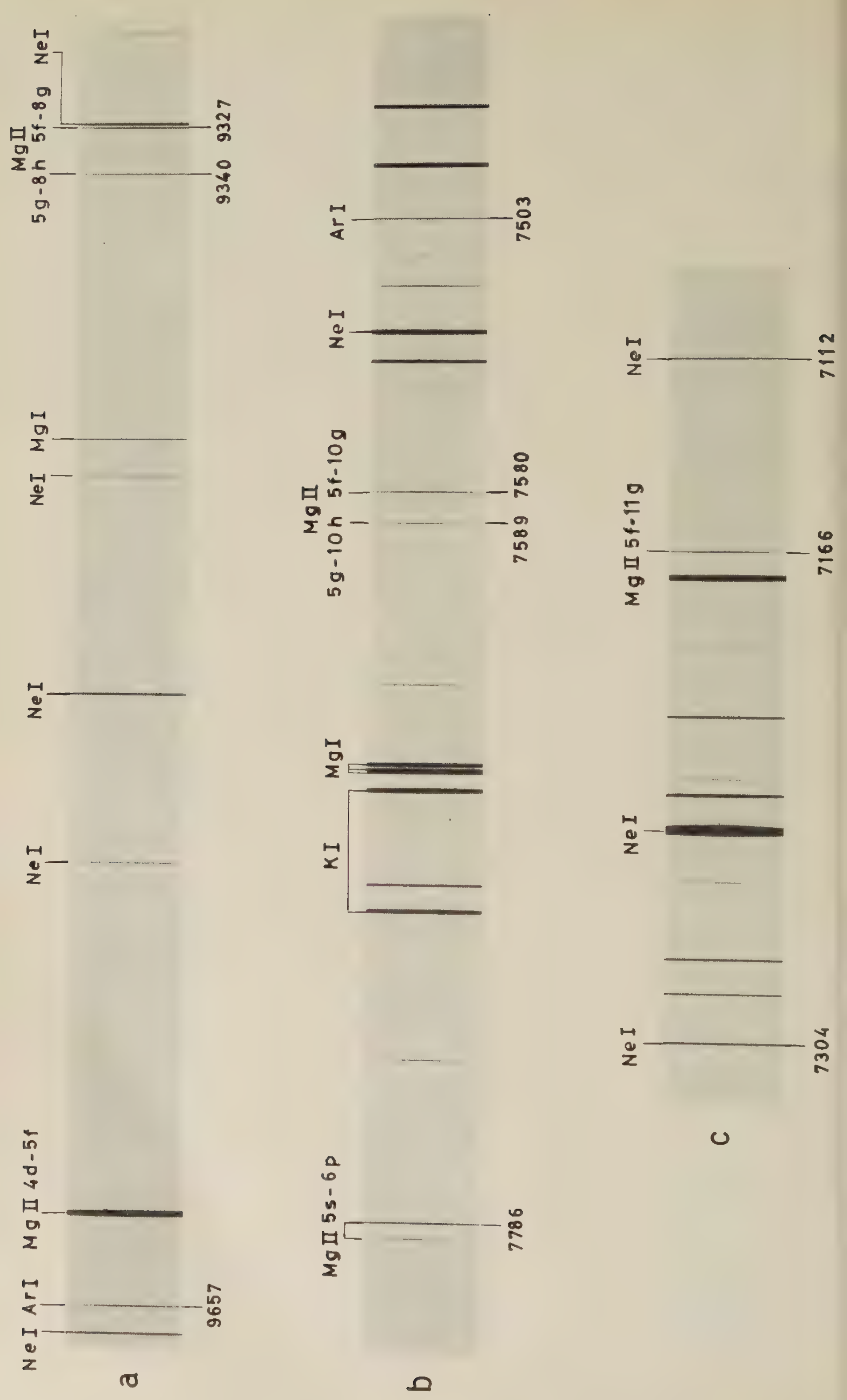
NeI
MgII
5g-8h 5f-8g
9327
9340
MgI
NeI
NeI
NeI
MgII 4d-5f
ArI
NeI
9657
a
ArI
7503
NeI
MgII
5g-10h 5f-10g
7580
7589
MgI
KI
MgII 5s-6p
7786
b
NeI
7112
MgII 5f-11g
7166
NeI
NeI
7304
c

ARKIV FÖR FYSIK Band 9 nr 32

Communicated 23 February 1955 by Manne Siegbahn and Gunnar Hägg

Relative intensities of the X-ray K lines of heavier elements

By Olof Beckman

With 19 figures in the text

Contents

Acknowledgements 495
Chapter I. Introduction 496
Chapter II. Experimental arrangements 497
  1. The van de Graaff generator 497
  2. The voltmeter 499
  3. Target arrangements 499
  4. The current integrator 501
  5. The spectrometer 502
  6. The scintillation counter 505
  7. Shielding 505
Chapter III. Recordings with the spectrometer 506
  1. Adjustment 506
  2. Procedure 507
Chapter IV. Computation of the X-ray intensities 507
  1. The efficiency of the scintillation counter 513
  2. Absorption of the X-ray beam 514
  3. X-ray absorption in the target 514
  4. Reflection properties of the quartz crystal 516
Chapter V. Discussion of the results 519
  1. General remarks on K-spectra 519
  2. Earlier investigations 520
  3. The present measurements 521
Chapter VI. The KL_1-transition 526

Acknowledgements

The investigation reported in this paper was carried out at the Physical Laboratory of Uppsala University. I am greatly indebted to Professor Axel E. Lindh, formerly head of the Physical Laboratory, for the kind interest and constant encouragement he has provided throughout my work.

I wish to express my sincere gratitude to Professor Per Ohlin, who made the first designs of the van de Graaff machine essential to this work, for the valuable help he has offered me during this investigation.

My sincere thanks are also due to Professor Kai Siegbahn, Laborator Arne Sandström and Docent Gösta Brogren, who have given freely of their time in discussions of problems that have arisen.

The experimental measurements in the concluding part of the study were assiste to a large extent and in a very skilful manner by Fil. kand. PÄR BERGWALL.

Finally my thanks are due to Professor HARRISON SHULL for correcting my Englis

Uppsala, March, 1955.

CHAPTER I

Introduction

In spite of the great number of investigations on X-ray spectra only a few measurements have been made of the intensities of the lines. Intensity measurements ar most easily carried out in the case of K-spectra, where all lines are excited at the sam voltage and consequently the intensity ratios are independent of the mode of excitation. Investigations of the K line intensities of elements in the middle of the periodi system have been made by MEYER [1929] ($Z = 23$–49) and by WILLIAMS [193 ($Z = 24$–52). KLIEVER [1939] has measured the intensities of the K lines of tungste and platinum by means of an X-ray spectrometer and an ionization chamber. method with different absorption filters has been applied by VOTH [1942] in an investigation of several heavy elements.

Theoretical calculations in this field have been made by PINCHERLE [1933] and b MASSEY and BURHOP [1936], but their results are not satisfactorily checked by th rather few results that have been obtained experimentally. Thus it was of grea interest to measure the K line intensities of as many of the heavier elements as migh be available and to study the change in the line intensities with the atomic number, Z

Such an investigation could conveniently be carried out with the van de Graaf generator of the Physical Laboratory. A high luminosity spectrometer with a counte of high efficiency would probably give enough intensity for registering even th weaker lines of the K-spectrum.

X-ray intensity measurements employing pulse-counting devices require constan conditions for long periods of time. One possible way of meeting these conditions i to stabilize both voltage and current in the X-ray tube and to count the X-ra quanta entering the counting tube for a known time. It is very difficult, howeve to stabilize satisfactorily the tube current of van de Graaff generators, and thus i would be better to use some type of monitor method. In the present experiments i seemed most suitable to use the electron beam as a monitor. The target is insulate from the earth and connected to a current integrator. The counter that registers th X-rays is switched on for the same period of time in which the current integrato records the charge reaching the target. Since the X-ray yield in the target varie very rapidly with the energy of the electrons, the high voltage must be well stabilized Furthermore it is necessary to keep the focal spot in a fixed position on the target

It is essential to have an X-ray spectrometer of high luminosity and high dispersion These demands are met by the curved crystal spectrograph and, for the short wavelengths in question (100–220 XU), the transmission type is the only one available

In this spectrometer the radiation from an extended focal spot (Fig. 1) is reflecte at the inner atomic planes in the crystal and focussed to a point on the Rowlan circle. Radiation from different points of the focal spot is reflected by different part of the crystal; thus the focal spot corresponds to a "reflecting area" of the crystal If the crystal aperture is large enough, radiation from the whole focal spot is utilized On the other hand, if the crystal opening is too small, the whole crystal aperture i filled with radiation, but only a part of the focal spot is used. In the latter case, fluc

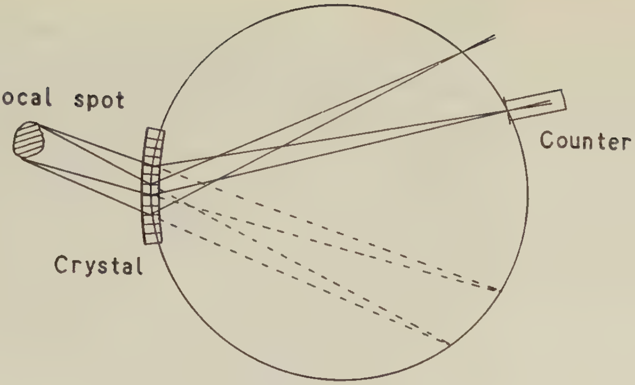

Fig. 1. Principle of the curved crystal spectrometer.

tuations in the intensity distribution from the focal spot may cause changes in the intensity of the X-rays reflected by the crystal, even though the electron beam current is constant. This may introduce severe errors when the electron beam itself is used as a monitor. Thus there must not be any limiting aperture or slit between the X-ray tube and the counter-slit.

As shown in Fig. 1, the crystal is mounted in a fixed position, limiting the spectrograph to only a rather narrow wavelength region. Different wavelengths are reflected from different parts of the crystal, and it is difficult to ascertain the wavelength at which the crystal holder starts to screen the X-ray beam.

The spectrometer should be constructed preferably in such a manner that the crystal is moved simultaneously with, and at half the angular speed of the counter-slit. Moreover, the crystal opening must be broader than the width of the focal spot. By this arrangement always the same (central) part of the crystal is used for X-ray reflection. In order to minimize the broadening of the lines the vertical height of the X-ray beam must be low. This is accomplished by making the angle between the target and the plane of the Rowland circle rather small.

Because of their good elastic qualities, quartz crystals are very useful in curved crystal spectrographs. The short wavelengths make it necessary to use a crystal plane with a low grating constant, but at the same time the plane must, of course, have good reflecting properties. Suitable planes are, for instance, quartz $13\bar{4}0$, $22\bar{4}3$ and $50\bar{5}2$. For the present spectrograph, $22\bar{4}3$ was chosen. This plane has a grating constant of 1012.75 XU and a crystal structure factor of 15.6. The wavelength region 100–220 XU then corresponds to the Bragg angles 2°.9–6°.2. In the case of tungsten some measurements were also made employing the plane $13\bar{4}0$ with the grating constant 1177.63 XU and structure factor 20.9.

CHAPTER II

Experimental arrangements

1. The van de Graaff generator

The van de Graaff generator (Fig. 2) is an open-air machine with two charging belts driven by three-phase asynchronous motors. The velocity of the belts is 20 m/sec,

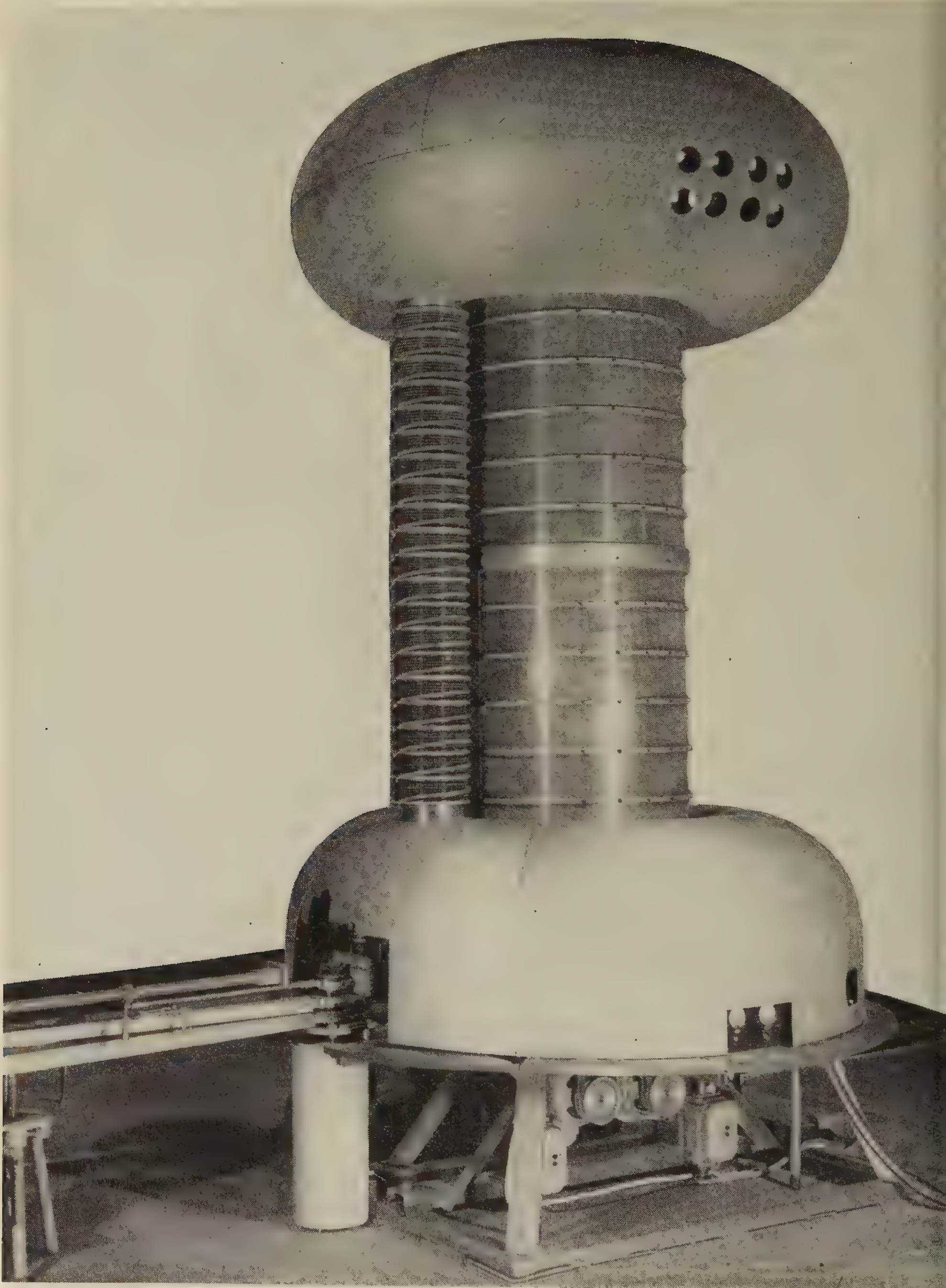

Fig. 2. The van de Graaff generator. To the left of the insulating column is the accelerating tube with the potential divider. Part of the spectrometer is seen to the left.

ielding a short circuit current of 600–700 μA. The highest obtainable voltage is bout 800 kV at 300 μA electron beam.

The accelerating tube consists of 20 porcelain insulators separated by aluminium lates, which support funnel-shaped electrodes. Along the whole accelerating tube here is mounted a resistor chain in order to obtain a stabile voltage distribution. This chain contains 400 ordinary radioresistors of 20 MΩ each. The current through hese resistors is measured by a μA meter on the control panel in order to get a rough alue of the high voltage.

The electron gun has been previously described, OHLIN, BECKMAN [1949]; only he electric feeding has been changed. The filament is made of 0.25 mm diam. tungten wire. The first anode immediately in front of the filament has a constant voltage f 300 V relative to the filament. The next anode is an electrode of the same kind as hose in the accelerating tube. This anode is connected to a variable high tension et of max. 10 kV. In addition, the high voltage conductor of the machine contains n AC generator for 220 V, 2 A, 50 c, driven by one of the upper rollers. Filament urrent and focussing voltage can be controlled from the earth side by means of ylon cords that operate variable transformers in the high voltage terminal.

2. The voltmeter

The problem of measuring the voltage of van de Graaff generators is a difficult one. t is necessary to use an instrument whose load on the machine is a minimum. The nost widely used instrument is the generating voltmeter, in which a sectory rotor lternately screens and unscreens stator plates. An AC signal proportional to the lectric field is thus induced on the plates. The generating voltmeter used here is f a different type, in which the moving system is vibrating instead of rotating, ECKMAN [1949]. The vibrating type has the advantage that one can use higher requencies for the AC signal and that it is easier to give this signal a sine form. The nstrument employs an ordinary loudspeaker, from which the cone has been removed. Attached to the coil is a small circular plate exposed to the field from the high oltage terminal.

A small AC voltage is induced on the vibrating plate. Immediately in front of the late is a grid, which can be given a suitable DC potential, thus compensating the ield from the van de Graaff and making the AC signal zero. The grid potential at ompensation is directly proportional to the field strength and consequently to the an de Graaff voltage. The grid voltage is stabilized within 0.2 per cent. The AC ignal from the moving plate is amplified and rectified in a phase-sensitive rectifier. The signal can be read on a meter, which indicates the degree of compensation. The ensitivity of the meter is such that full scale deflection to each side indicates a deviaion of the high voltage by about 1 per cent.

The rectified signal is used also for stabilization of the van de Graaff voltage. The ignal is put on the grids of two 2A3 tubes which control the primary current to the pray voltage set. This type of stabilization is not very rapid, but it has worked well, nd the high voltage could be kept constant within 1 per cent for a long period of ime.

3. Target arrangements

The target-plate *1* (Fig. 3) is tightly screwed to a water-cooled copper block *2* t the bottom of a tube. The electron beam passes through a 5 mm wide aperture *3*

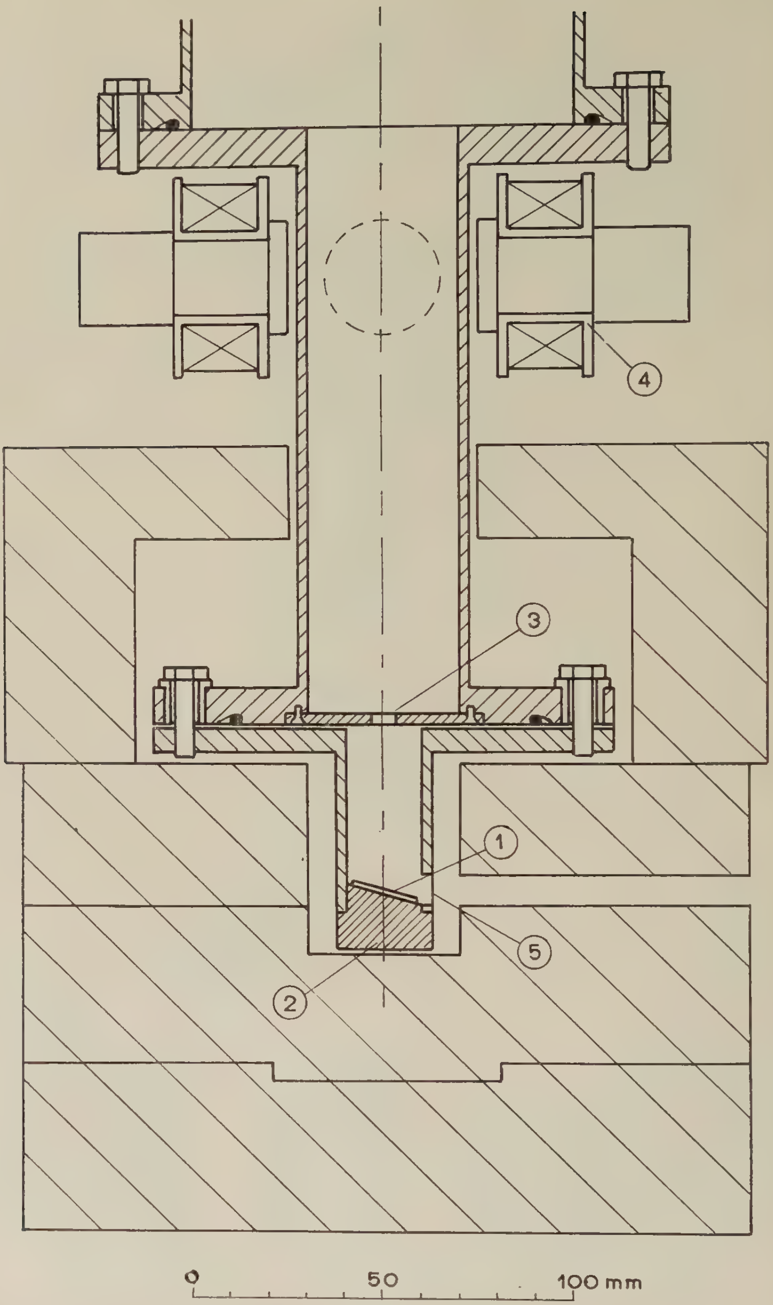

Fig. 3. The lower part of the accelerating tube showing the target arrangement and lead shields.

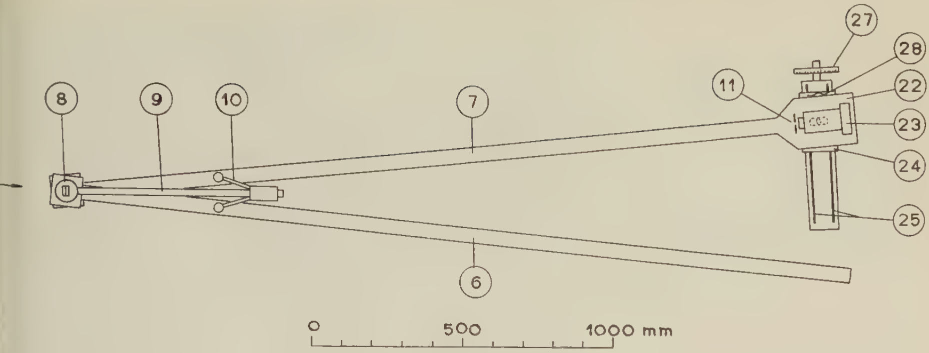

4. Schematic drawing of the spectrometer. The arrow to the left indicates the incoming X-ray beam. The curved crystal is seen at *8*; *11* is the spectrometer slit and *23* the scintillation counter.

well-cooled copper plate. Two pairs of coils *4* produce two crossed magnetic fields a plane perpendicular to the beam. By varying the currents in these coils it is sible to direct the beam through the hole *3* down to the target. The voltages on two pairs of coils are further connected to the horizontal and vertical deflection tes in a small oscilloscope on the control panel. Thus it is easy to control the posi- of the focal spot continually during the measurements. The X-ray beam passes ough a window *5* of 0.1 mm brass. Because of the intense X-radiation, the target the lower part of the accelerating tube must be well shielded with lead blocks. these blocks there is a channel of 8 × 20 mm cross-section for the X-ray beam. or target materials, Ta, W and U were available as 1 mm thick plates. The Ir, and Th samples consisted of 0.2–0.3 mm thick foils. In the latter cases it was essary to use a copper plate as a distance piece in order to get the focal spot at right height. Au, Tl, Pb and Bi were fastened to copper plates. The Hg target sisted of silver amalgam packed in a depression in a copper plate. Some mer- y evaporated when the electron beam hit the target and the line intensities dually decreased to about 80 per cent of the initial value during the meas- ments. This makes of course the intensity values for Hg more uncertain than the other elements, but the evaporation occurred at a constant rate, so that was possible to correct for it. Re and Os could be obtained only as metal wder, which was pressed into scores in copper plates. All the targets used were ck enough to stop the 500 keV electrons.—The vacuum system was evacuated to out 10^{-5} mm Hg by a mechanical pump and two oil diffusion pumps.

4. The current integrator

The X-ray intensity is measured relative to a constant electric charge falling on the get. Since the electron beam fluctuates a little, it is necessary to integrate the target rent. The current charges a capacitor, which is discharged by an electronic circuit enever the total charge on the capacitor reaches a predetermined fixed amount. us at each discharge one obtains a pulse corresponding to this fixed amount of arge. The latter must not change over a considerable period of time and must be ependent of target current (within the limits of the normal fluctuations).

The integrator used is in principle the same as the one described by Elmor and

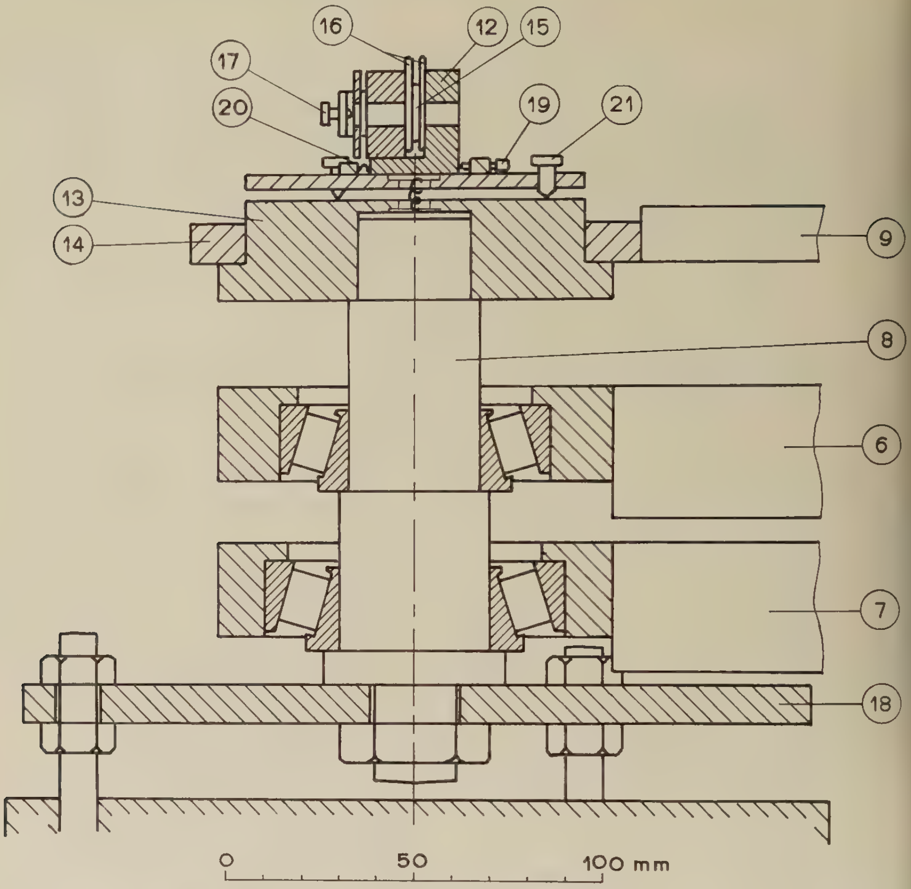

Fig. 5. The spectrometer axis with the mounting of the aluminium beams and the crystal table.

Sands [1949] p. 405. The circuit was changed a little to register negative currents. The integrator shows very good stability and is reliable within some tenths of a per cent. Each pulse means about 2 μ coulomb.

The pulses from the integrator are counted by a Philips predetermined count scaler PW 4035. This scaler also gives pulses to switch on and off the electronics registering the X-ray intensity.

5. The spectrometer

The principal construction of the spectrograph is shown in Fig. 4. One end of each of two aluminium beams *6* and *7* are pivoted on a common vertical axis *8*. The steel rod *9* also pivoted on the axis *8*, coincides with the bisector of the angle between the aluminium beams. This is accomplished by the link system *10*. The beam *6* is fixed in the direction of the primary X-ray beam and the rod *9* is clamped to the crystal table, so that the crystal normal falls along the rod. Radiation of the wavelength

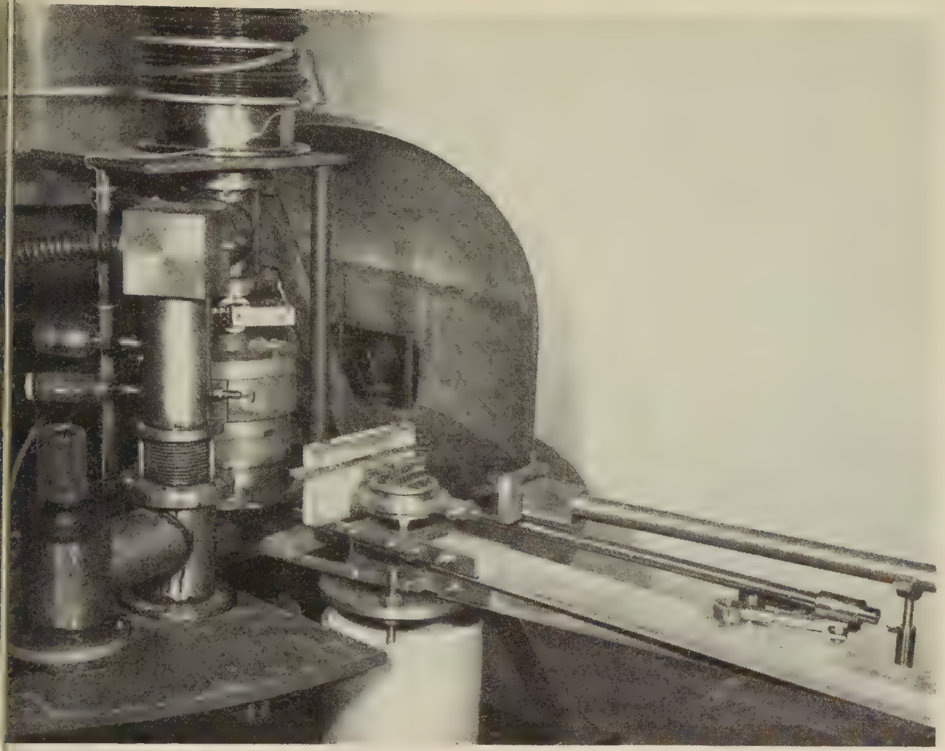

. 6. Part of the spectrometer. In the middle, the crystal holder and the steel rod with the pling links to the right. Above this coupling is the brass tube for the shielding of the racted X-ray beam. To the left, the accelerating tube and beneath this the lead shield at the target with the exit hole for the X-radiation.

t satisfies the Bragg equation will thus be directed along the beam *7* and focussed the slit *11*. In every position of the spectrometer the same central part of the crys- is used for reflection. The vertical axial support *8* (Fig. 5) is mounted on an iron te *18*, which can be leveled by means of the nuts on three bolts, cast into a concrete lar. The two beams *6* and *7* are connected to the axis *8* by means of conical roller arings. The crystal-holder *12* is placed on a brass block *13*, which also can rotate ound the axis *8*. The steel bar *9* can be clamped to this brass block by means of the g *14*.

The crystal holder is of the type described by Brogren [1951]. The quartz crystal is curved between two pairs of steel pins *16*, fitted in grooves in two brass blocks. e pressure at the crystal and consequently also the curvature of the crystal can be ntrolled by the screws *17*. The four pins are strictly parallel to each other. With s crystal holder it is possible to bend the crystal to an arbitrary radius and yet tain good focussing conditions.

The crystal holder is clamped to the crystal table by means of two screws *19* and pring *20*. The crystal table is then fixed to the brass block *13* by a spring and three ews *21*, so that the table can be tilted a small angle in any direction.

The link system (Figs. 4, 6) must be constructed with the utmost precision. The

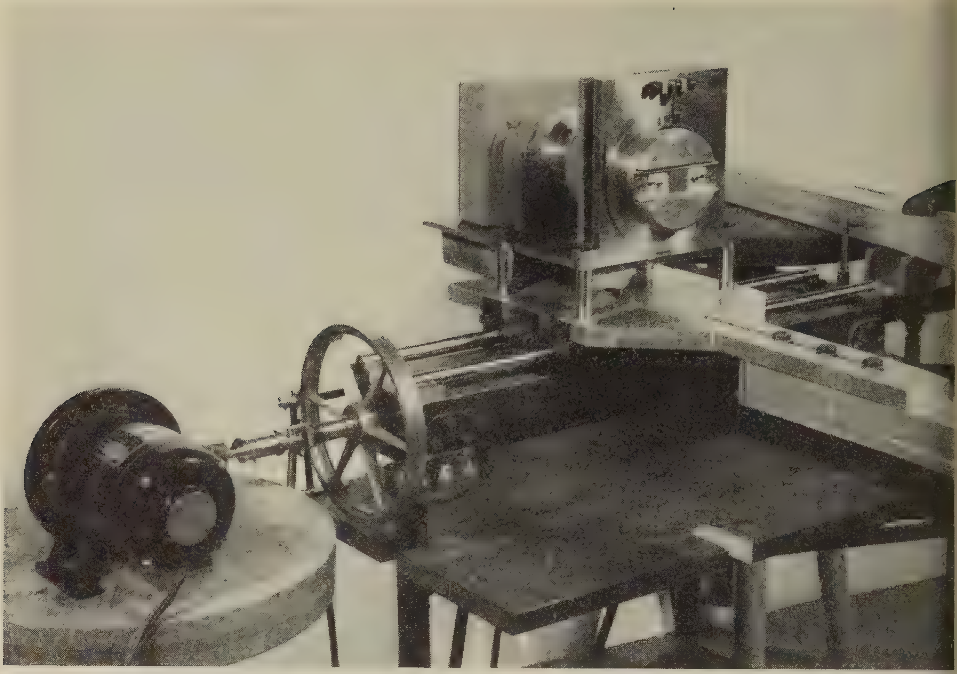

Fig. 7. Part of the spectrometer with the scintillation counter. All lead shields are removed in order to show the mounting of the spectrometer slit with the scintillation counter behind. To the right, the fixed aluminium beam *6* and the movable beam *7*. (The figures *6* and *7* refer to Fig. 4.) The beam *7* can be moved by the motor (left).

two links *10* are mounted on the beams *6* and *7* by means of ball bearings. The other ends of the links are connected to a common pivot on a coupling, which is free to move along the well-ground steel bar *9*. The lengths of the links and the distance from the ball-bearing pivots to the center *8* can be adjusted so that the steel rod always bisects the angle between the aluminium beams.

The reflected X-ray beam is directed along the beam *7* (Fig. 4) and focussed on the slit *11*, mounted in a holder which is screwed to the aluminium plate *22*. As the beam is moved, radiation of successive wavelengths passes through the slit into the scintillation counter *23*. The plate *22* rests on a brass plate *24* sliding on two steel rods *25*. The brass plate can be moved by means of a precision screw with a pitch of 1 mm. The position of the slit is read on a mm scale and on the wheel *27*, marked with a scale of 500 divisions. The screw is driven slowly by a motor (Fig. 7). The plate *24* is supplied with a short pin that fits into a slot in the upper plate *22*. A slot is necessary, because the upper plate moves along an arc of a circle, while the lower plate moves along a straight line. By means of the spring *28* the upper plate is pressed against the pin.

The scintillation counter is surrounded on all sides by 5 mm lead in order to minimize stray radiation. This lead shield has a considerable weight, and in order to decrease the load on the steel rods and on the precision screw, the lead shield is balanced by a counter weight connected to the shield by a wire laid over two pulleys.

Because of the short wavelengths the spectrometer slit must be made of a heavy ent. The jaws of the slit consist of two gold plates, 1 mm thick, soldered to pieces ver, also 1 mm thick. The silver absorbs the K-radiation from the gold. The jaws e slit are further shielded by two lead blocks. The slit is mounted within a ring hich is attached a short lever, as shown in Fig. 7. By means of two screws the hus can be rotated until it is parallel to the spectral lines.

6. The scintillation counter

scintillation counter is a very suitable detector for the X-radiation. If the counter mbined with a single channel discriminator, the radiation of energies other than of the X-ray lines is discarded, and in this way it is possible to maintain a very background.

ne scintillation counter used in these experiments contains a cylindrical NaI tal, 25 mm in diameter and 25 mm high. Such a crystal registers radiation of gies up to about 300 keV with almost 100 per cent efficiency. The NaI crystal is osed in a thin-walled aluminium box, supplied with a glass window, which is rect contact with the photomultiplier. MgO is used as a reflector.

ne photomultiplier used is an EMI 6260, operated at 90 V per stage. The pre- lifier, with one 6AK5 tube as cathode follower, is placed in the same cage as multiplier tube. The pulses are led through a 4 m long coaxial cable to a linear lifier, Model 100 (Elmor and Sands [1949]), at the control panel. The single nel discriminator (Åström, [1954]) selects the amplified pulses which have a corresponding to the energy of the K-radiation. The pulses are recorded by a e-of-64 (Atomic Instrument Company Model 101-A). Since, on the one hand, es from a scintillation counter are very short (about 1 μ sec) and, on the other, counting rates never exceeded 300 pulses per second, there was no problem of d-time corrections.

7. Shielding

he scintillation counter must be very carefully shielded against stray radiation rder to decrease the background. The high energy of the electron beam (500 keV) the small angle between the direct and reflected X-ray beam (minimum angle make the difficulties of shielding rather great. Fortunately, because of the use he channel discriminator, which discards all pulses of energy different from that he registered K lines, the demands on shielding are not so high as would be the e if, for instance, a GM tube was used. On the other hand, extra pulses of wrong rgy in the scintillation counter are, of course, not desirable.

he target itself is placed at the center of a lead block, 20 cm in diameter and 20 in height, with a small channel for the X-ray beam. The parts of the vacuum tem above the target are shielded by 5–10 mm lead.

rather strong radiation, however, comes from the lower parts of the accelerating e because of stray electrons. Furthermore, secondary X-rays may be emitted from st parts of the machine. In order to avoid this rather weak radiation, the reflected m is guided through a brass tube extending almost the entire distance from the stal to the counter slit, as shown in Figs. 2 and 6. The scintillation counter is ced in a lead housing made of 5 mm lead with an extra lead shield on the front side. n this way it has been possible to eliminate almost all stray radiation. Only about per cent of the background in the registered curves is attributable to stray radia- n, probably largely arising from scattering in the crystal holder.

CHAPTER III

Recordings with the spectrometer

1. Adjustment

1. The crystal holder was placed at the same height as the target. By pinhole camera photographs of the focal spot it was checked that the line from the center of the focal spot through the center of the crystal holder was horizontal.

2. The aluminium beam *6* in Fig. 4 was adjusted horizontally and fixed in the direction of the primary X-ray beam.

3. The crystal was placed in the holder and bent to approximately the desired radius (about 2.5 meters). A slit lamp was placed on the beam *6* and the image of the slit reflected by the crystal used as a concave mirror, was examined.

4. When the crystal was bent satisfactorily, the exact focus was determined by examining the sharpness of X-ray lines recorded on films placed at every 10th centimeter on both sides of the assumed focus.

5. The axis *8* was made vertical and by means of a centering microscope the crystal was adjusted so as to have its center on the axis *8*.

6. By means of adjusting screws at the table carrying the scintillation counter the beam *7* was leveled horizontally. At the same time the rods *25* were adjusted horizontally.

7. The surface of the crystal was made parallel to the rotation axis by the adjusting screws *21*.

8. The link system was now adjusted so that the image of the slit lamp placed on the beam *6* coincided with the counter slit for all positions of the spectrometer. The rod *9* was then the bisector of the angle between the aluminium beams.

9. The spectrometer slit was set parallel to the X-ray lines. An X-ray film was placed in front of the slit and illuminated from behind for a moment. On the same film X-ray lines were also exposed. By examination of the film in a microscope it was possible to determine the angle between the two images.

10. On a film placed in front of the slit two X-ray spectra were exposed with the crystal in two different positions. At the same time several exposures were made of the counter slit. It was thus ascertained that the spectrum lines and the slit were moving parallel to each other.

The radius of curvature of the quartz crystal ($22\bar{4}3$) was 2660 mm. This curvature resulted in a linear dispersion of 0.382 XU/mm. Because of the small reflecting angles ($< 6°$) the dispersion can be assumed constant through the whole wavelength region, and the spectrometer readings in mm could be set proportional to the wavelength in XU. The length of the spectrometer screw was 200 mm and thus a wavelength region of 76 XU could be covered at one time. The spectrometer was first adjusted for the wavelength region 150-225 XU and then for the region 100-175 XU. In both regions the steel rods *25* (Fig. 4) were adjusted perpendicular to the aluminium beam *7*, when the spectrometer was set at the middle of the wavelength region.

The slit width was 0.1 mm and the height of the slit 15 mm. The approximately circular focal spot had a diameter of 5 mm. Since the angle between the target surface and the horizontal plane was 15°, the vertical dimension of the focal spot was only 2 mm. This involves only a negligible broadening of the spectral lines under the geo-

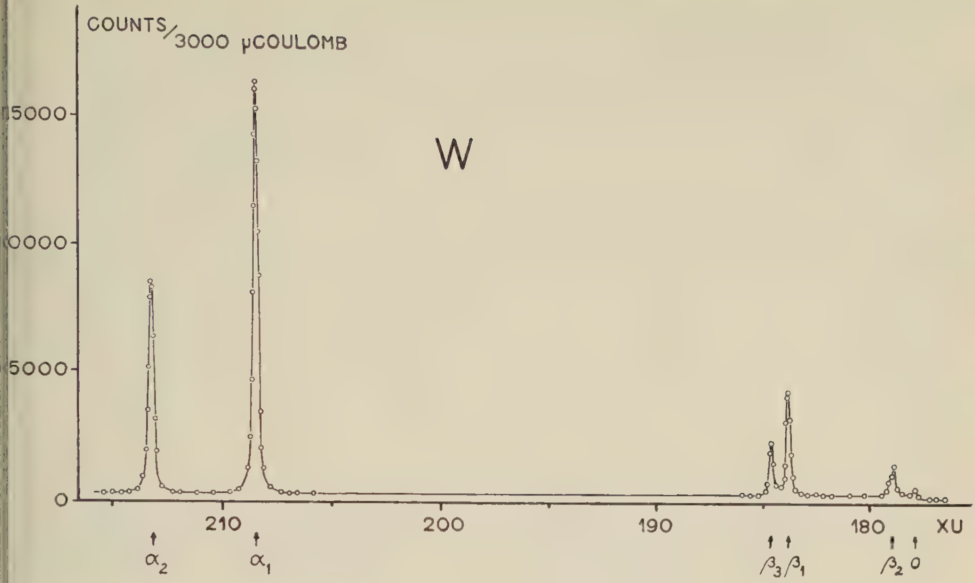

Fig. 8. General view of tungsten *K*-spectrum.

metrical conditions prevailing. Furthermore it is evident that only a small central part (2 × 5 mm) of the crystal was used for reflection. The quartz crystal had the dimensions 1 × 15 × 25 mm and the aperture of the crystal holder was 6 × 13 mm. It was thus easy to avoid screening of the X-ray beam by the crystal holder.

2. Procedure

During the measurements the channel discriminator must be set at a pulse-height that corresponds to the energy of the X-ray line being measured. Prior to each run the spectrometer was set at the peak of either the α_1 or β_1 lines and the pulse spectrum was recorded by varying the channel discriminator. In this way a curve with a flat top was obtained and from this curve the discriminator setting was determined. Such pulse spectra were always taken for the α_1 and β_1 lines. The electronic circuits were found to be very stabile, and the discriminator setting was almost the same from one day to another for the same line.

When recording an X-ray line the scintillation counter was switched on for the time during which the charge was registered by the integrator. The integrator counted from about 300 to 3000 pulses for each point, depending on the intensity of the X-radiation. The van de Graaff voltage was maintained at 500 kV for all spectrograms, and the electron beam current was about 80 μA. Only the most intense lines α_1 and α_2 sometimes required a decrease in the electron beam current in order to avoid too high counting rates.

CHAPTER IV

Computation of the X-ray intensities

Fig. 8 shows the general appearance of a complete spectrum. Since the spectra of all elements are very similar, the spectrum of only one element, tungsten, is published.

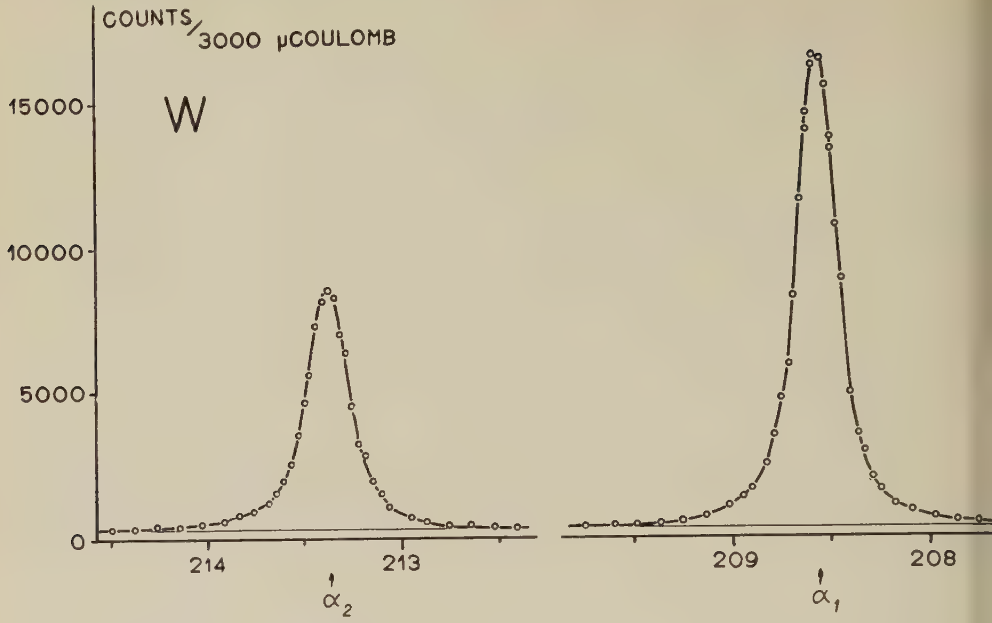

Fig. 9. Tungsten *K*-spectrum. The α lines.

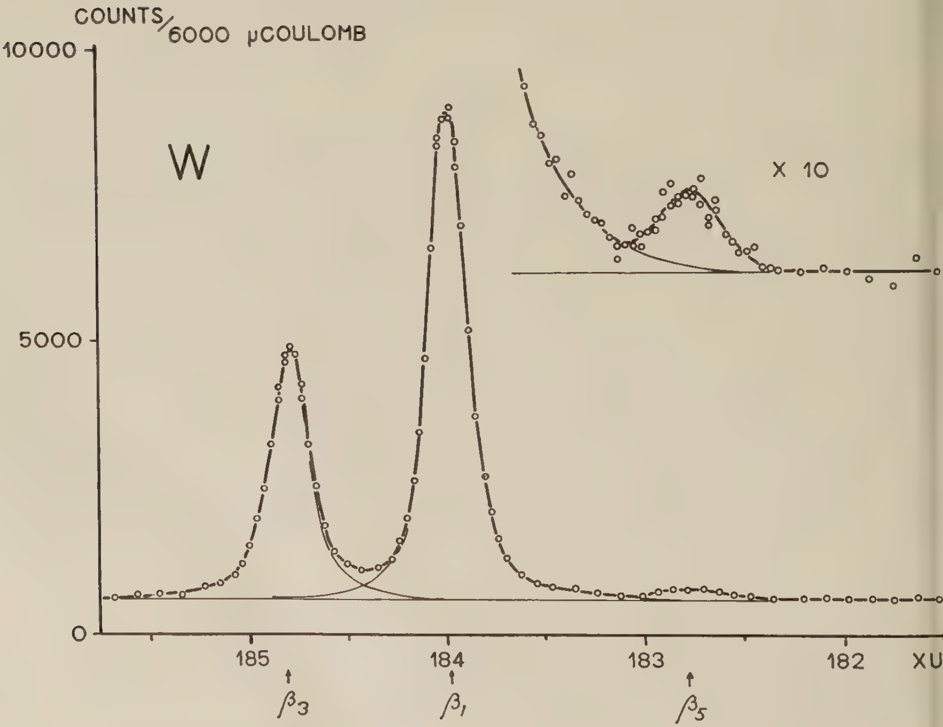

Fig. 10. Tungsten *K*-spectrum. The dipole lines β_1 and β_3 and the quadrupole line β_5

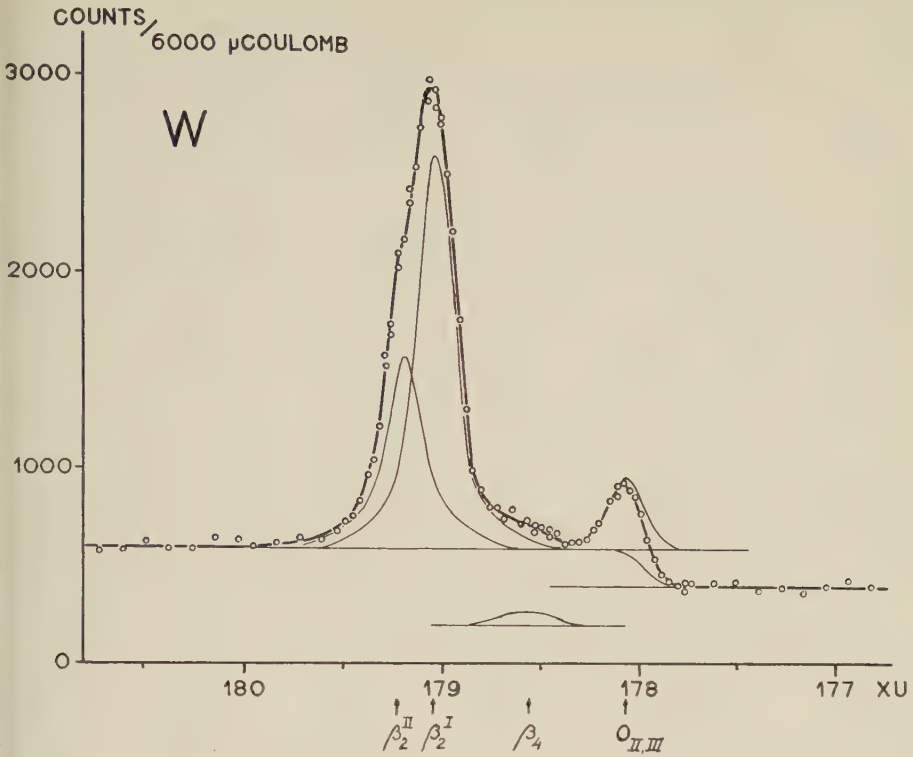

ig. 11. Tungsten K-spectrum. The β_2 line resolved in its components, the $KO_{II,\,III}$ line and the K-edge. Between the β_2 and $KO_{II,\,III}$ lines is seen the weak quadrupole line β_4.

he details of the tungsten spectrum are seen in Figs. 9, 10, 11. The registered spectra ere plotted on a large scale and the areas under the curves measured by means of a lanimeter (G. Coradi, Zürich). Before the planimeter measurements were made, the ackground was drawn in as a straight line parallel to the abscissa axis. Neighbouring nes were also separated from each other. This was not difficult in the case of $_1$, β_3 and β_5. The β_2 line consists of two components belonging to the transitions N_{II} and KN_{III}. The line can be separated (see Fig. 11), but this cannot be done ithout some knowledge of the intensity distribution between the components and herefore only intensity values referring to the unseparated line are given. The rea under the weak line β_4 was measured, but the neighbouring lines β_2 and $O_{II,\,III}$, f course, make the result very uncertain. Because the continuous radiation forming he background is partly absorbed in the target itself, there is a considerable change the background from one side of the K-edge to the other (see Fig. 11). This change ffects the profile of the $O_{II,\,III}$ line considerably. It was necessary to adopt a trial nd error method for the separation of this line from the edge. In the case of tungsten he result thus obtained was confirmed by recording an ordinary absorption spectrum. W foil of 0.1 mm thickness was put in the X-ray beam using a Pt target. The W -edge thus obtained showed the same profile as the one separated from the $O_{II,\,III}$ line.

The lines in each of the three groups represented by Figs. 9, 10 and 11 were always easured in the same recording. The ratios of the areas of the lines in these groups are

Table 1. Measured values of the areas under the recorded curves, quartz 22$\bar{4}$3.

Element	α_2/α_1	β_3/β_1	β_5/β_1	β_4/β_2	$O_{\text{II III}}/\beta_2$
73 Ta	0.543	0.505	0.021	0.007	0.090
	525	539	25	13	102
	537	515	24	6	74
	545	521	23	12	82
Mean	**0.538**	**0.520**	**0.023**	**0.010**	**0.087**
74 W	0.577	0.561	0.025	0.024	0.091
	529	593	21	14	113
	524	522	20	13	95
	559	558	21	14	109
	579	520	24	13	108
	542	514	22	18	98
	569	507			
Mean	**0.554**	**0.539**	**0.022**	**0.016**	**0.102**
75 Re	0.580	0.504	0.022	0.023	0.113
	502	507	30	27	102
	583	547	17	21	130
	593	538	24	18	93
Mean	**0.565**	**0.524**	**0.023**	**0.022**	**0.110**
76 Os	0.561	0.573	0.027	0.019	0.132
	536	490	22	18	102
	608	519	28	22	70
	567	508	30	33	138
Mean	**0.568**	**0.523**	**0.027**	**0.023**	**0.111**
77 Ir	0.564	0.552	0.019	0.021	0.136
	573	484	28	22	95
	543	534	27	21	136
	544	554	32		
	556				
	554				
Mean	**0.554**	**0.531**	**0.026**	**0.021**	**0.122**
78 Pt	0.577	0.513	0.025	0.024	0.104
	564	563	32	25	138
	572	534	31	18	125
	542	527	25	25	121
	531	516			
	572				
	578				
Mean	**0.562**	**0.531**	**0.028**	**0.023**	**0.122**
79 Au	0.557	0.507	0.026	0.020	0.126
	538	524	35	13	108
	543	529	28	28	139
	548	517		16	90
	525	521		16	138
	563	512			
Mean	**0.546**	**0.518**	**0.030**	**0.018**	**0.120**

ble 1 (cont.)

Element	α_2/α_1	β_3/β_1	β_5/β_1	β_4/β_2	$O_{\mathrm{II\,III}}/\beta_2$
80 Hg	0.575 555 494 526	0.55 45	0.027 25		0.14 23
Mean	**0.538**	**0.50**	**0.026**		**0.18**
81 Tl	0.608 583 583	0.535 506 608	0.025 25 25	0.020 19 22	0.164 174 175
Mean	**0.591**	**0.550**	**0.025**	**0.020**	**0.171**
82 Pb	0.608 590 520 539	0.585 515 539	0.027 31 27	0.024 23 26	0.146 154 159
Mean	**0.564**	**0.545**	**0.028**	**0.024**	**0.153**
83 Bi	0.569 585 600 541 643	0.497 492 528	0.028 26 33	0.026 23 23	0.133 141 139
Mean	**0.588**	**0.506**	**0.029**	**0.024**	**0.138**
90 Th	0.568 610 547	0.535 493 480	0.032 33 39	0.026 57	0.276 284 221
Mean	**0.575**	**0.503**	**0.035**	**0.041**	**0.260**
92 U	0.616 595 606 597	0.532 521 482	0.032 38 36	0.044 41 33	0.213 254 275
Mean	**0.604**	**0.512**	**0.035**	**0.039**	**0.247**

ted in Table 1, as they were obtained from the separate runs. Table 2 contains the tios β_1/α_1 and β_2/β_1. These ratios could not be determined with the same accuracy the other ratios because the lines were not registered in sequence. The difference accuracy is small, however, since the intensity of a given line showed only small riations from one day to another (about 5 per cent).

Tables 1 and 2 contain the results obtained with the plane $22\bar{4}3$. The tungsten specum was also measured employing the plane $13\bar{1}0$ (Table 3). As shown there, the two ystal planes give the same values of the relative intensities, indicating that the flecting properties of the two crystal planes are the same.

The peak intensities of the registered lines can be used for computation of intensity tios if the lines are of the same width which is approximately the case for the K nes. The peak intensity of the strongest lines α_1, α_2, β_1 and β_3 was measured (Table

Table 2. Measured values of the areas under the recorded curves, quartz $22\bar{4}3$.

Element	β_1/α_1	β_2/β_1
73 Ta	0.227	0.311
74 W	0.228	0.334
75 Re	0.223	0.337
76 Os	0.225	0.340
77 Ir	0.216	0.309
78 Pt	0.217	0.356
79 Au	0.225	0.328
80 Hg	0.23	0.36
81 Tl	0.220	0.399
82 Pb	0.222	0.369
83 Bi	0.226	0.360
90 Th	0.227	0.397
92 U	0.220	0.412

Table 3. Measured values of the areas under the recorded curves, quartz $13\bar{4}0$.

Element	α_2/α_1	β_3/β_1	β_5/β_1	β_4/β_2	$O_{\text{II III}}/\beta_2$	β_1/α_1	β_2/β_1
74 W	0.527 510 539 558	0.545 553 505	0.022 23	0.019 16	0.092 83		
Mean	**0.534**	**0.534**	**0.022**	**0.018**	**0.088**	**0.226**	**0.334**

Table 4. Measured peak values of the recorded lines, quartz $22\bar{4}3$.

Element	α_2/α_1	β_3/β_1	β_1/α_1
73 Ta	0.529	0.502	0.235
74 W	0.537	0.520	0.252
75 Re	0.547	0.513	0.230
76 Os	0.560	0.519	0.235
77 Ir	0.553	0.500	0.232
78 Pt	0.543	0.514	0.237
79 Au	0.525	0.502	0.246
80 Hg	0.538	0.53	0.24
81 Tl	0.572	0.515	0.229
82 Pb	0.544	0.531	0.226
83 Bi	0.573	0.526	0.234
90 Th	0.563	0.536	0.235
92 U	0.608	0.517	0.232

4). The other lines of the spectrum are double, and a separation into the components in order to determine the peak intensities cannot possibly be carried out with any accuracy. A comparison between the peak and the area values shows that there is a marked difference only for the β_1/α_1 ratio. The difference (about 5 per cent) may be attributed to the different width of the α and β lines.

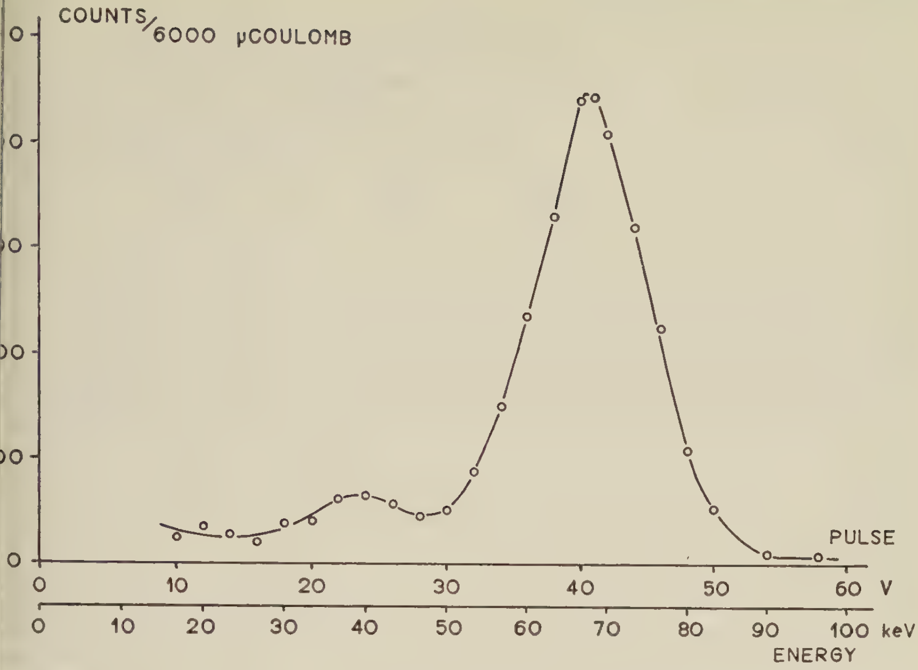

12. Pulse spectrum of the scintillation counter; the spectrometer set at the Au $K\alpha_1$ Channel width 3 volts. The photopeak is at 69 keV, and the iodine K-escape peak at 40 keV.

n calculating the relative transition probabilities and intensities of the X-ray lines n the experimentally determined quantities, it is necessary to take several factors consideration. The ratio of the intensities of two lines may be influenced by the owing factors:

. Varying efficiency of the scintillation counter at different wavelengths.
. Absorption of the X-ray beam from the target to the counter.
. X-ray absorption in the target itself.
. Reflection properties of the quartz crystal.

he absolute intensity of an X-ray line is greatly influenced by these factors, but relative intensity values are influenced only if these factors depend on the wavegth. It was found necessary to correct the experimentally determined intensity io only when the lines differed greatly in wavelength. The corrections were in eral appreciable only for the ratio between the β_1 and α_1 line intensities and were ally negligible in other cases.

1. The efficiency of the scintillation counter

ig. 12 shows a typical pulse spectrum from the scintillation counter, when the ctrometer was placed at the Au $K\alpha_1$ line. The channel width was 3 volts. The diam shows that about 90 % of the radiation is detected at the right pulse height e photopeak). The small peak of lower energy is the iodine K-escape peak. The oming quantum has excited the K-shell in an I atom and the emitted K-radiation

Table 5. Correction factors for the ratio β_1/α_1.

Element	Escape prob.	Absorption, X-ray beam	Absorption, target	Crystal refl.
73 Ta	0.98	0.96	0.79	1.29
79 Au	0.98	0.97	0.83	1.29
82 Pb	0.98	0.98	0.84	1.28
92 U	0.99	0.99	0.89	1.28

has escaped from the NaI crystal. The difference between the two peaks is 29 keV which is in agreement with the energy of the K lines of iodine.

When the scintillation counter was used in the spectrometer, the channel width was set at 20 volts. Thus the whole photopeak was utilized and about 90 per cent of the X-radiation was recorded by the counting devices. The wide channel has the advantage that the pulse spectrum shows a flat top, almost a plateau, which makes the discriminator setting less critical. A change of 1 volt corresponds to a change of less than 1 per cent in the registered X-ray intensity. Since only the part of the radiation that corresponds to the photopeak is registered in the spectrometer, it is necessary to know the iodine escape probability and how it changes with the energy of the X-ray quanta.

Complete pulse spectra with a narrow channel were registered for the α_1 lines of tungsten, gold and thorium (photon energies 59.2, 68.7 and 93.2 keV). The escape probability thus obtained (10.9, 9.7 and 3.6 per cent respectively) is in agreement with the results of other investigators, Lidén and Starfelt [1954], Axel [1954] and Meyerhof and West [1954]. The variation of escape probability with photon energy introduces only small corrections to the intensity ratios. (Table 5.)

2. Absorption of the X-ray beam

The X-rays are subject to absorption at the following points: (1) the window of the vacuum system, (2) the quartz crystal, and (3) the aluminium container for the NaI crystal of the counter.

The correction necessary as a result of these effects is greatest for Ta and decreases to very small values for U. The total correction, calculated for β_1/α_1, for several elements is shown in Table 5. The main part of the correction arises from absorption in the X-ray tube window (0.11 mm brass). The absorption in the air is negligible.

3. X-ray absorption in the target

The absorption in the target is due to the penetration of the electrons into the target with the result that the X-rays are emitted from different depths. The emitted X-rays are partly absorbed by the target to an extent that is rather wavelength dependent. The correction that must be applied is very difficult to calculate. The method used here is similar to the one used by Williams [1933]. The problem is discussed also by Compton and Allison [1935] in detail.

The electrons are assumed to go in a straight path into the target, at the same time being successively retarded. The X-rays under consideration are emitted at an angle of 90° to the electron beam. Atoms excited by electron impact at the depth x (measl in the direction of the electron beam) emit X-ray quanta that pass through get material for a distance $\frac{x}{\operatorname{tg}\alpha}$ where α is the angle between the X-ray beam and target surface. The number of quanta dN_λ at the target surface emitted from the t dx of the electron beam is

$$d N_\lambda = k \cdot T_\lambda \cdot F(U) \cdot e^{-\frac{\mu_\lambda \cdot x}{\operatorname{tg}\alpha}} dx, \tag{1}$$

ere k is a constant, T_λ the radiation transition probability for quanta of wavelength μ_λ the absorption coefficient of the target material and $F(U)$ the ionization ction for K-excitation. U is the energy of the electrons measured in units of K-itation energy. Integrating from the target surface to the depth x_0, at which the tron energy is just equal to the K-excitation energy of the target material, gives total number of emitted X-ray quanta in the appropriate direction,

$$N_\lambda = k \cdot T_\lambda \int_0^{x_0} F(U) \cdot e^{-\frac{\mu_\lambda \cdot x}{\operatorname{tg}\alpha}} dx. \tag{2}$$

$F(U)$ has been measured by WEBSTER, HANSEN and DUVENECK [1933] who give following equation as a good fit for the experimentally determined values:

$$F(U) = \text{const.} \frac{6}{U\left[\left(\dfrac{\pi}{2 \arccos\sqrt{\dfrac{1}{U}}}\right)^2 - 1\right]}. \tag{3}$$

n addition it is necessary to know U as a function of x, that is, the electron rgy at various depths in the target. Experimental data on the stopping of electrons matter are obtained from GOODMAN [1947] and SIEGBAHN [1955]. The values of X-ray absorption coefficient are given by VICTOREEN [1949]. It is necessary to aluate the integral (2) graphically. The corrections thus obtained are listed in Table or the ratio β_1/α_1.

The above calculation of the target absorption involves two simplifying assump-ns. No account has been taken of the scattering of the electrons in the target ce the electron path is assumed to be a straight line, and the target atoms are as-med to be excited only by electron impact. The latter is a rather severe assumption, ce photoexcitation is certainly important too. These effects are, however, very ficult to calculate.

Because of the uncertainties in the calculated target corrections it seemed wise to rify them experimentally. For that purpose, the α_1 and β_1 lines were recorded with ferent target arrangements. Besides the thick target with $\alpha = 15°$ used throughout investigation, in these cases a thick target with $\alpha = 45°$ and a thin target with $= 15°$ were tried. The thick target with $\alpha = 45°$ requires a smaller correction than target with $\alpha = 15°$. The thin target consisted of a 5 μ layer of gold evaporated copper. In such a thin target the X-ray absorption in the gold layer is negligible. ble 6 contains the experimental values of the β_1/α_1 ratio for the three cases, and

Table 6. Experimental values of the ratio β_1/α_1 for various gold targets.

	Thin target	Thick target $\alpha = 45°$	Thick target $\alpha = 15°$
	0.181	0.207	0.221
	0.205	0.217	0.232
	0.192	0.221	0.227
Mean	**0.193**	**0.215**	**0.227**

Table 7. Correction factors for target absorption; gold β_1/α_1.

	Thick target $\alpha = 45°$	Thick target $\alpha = 15°$
Exp.	0.90	0.85
Theor.	0.93	0.83

from these figures the correction for thick gold targets are calculated. The corrections thus obtained agree within the limits of error with the theoretically estimated values as shown in Table 7.

4. Reflection properties of the quartz crystal

An X-ray line profile, as it is obtained from the spectrometer recording, is composed of the X-ray line itself and the diffraction pattern of the curved crystal. Suppose the true X-ray line can be described by the function $f(x)$ and the crystal pattern by $g(x)$ where x is a variable proportional to the spectrometer scale readings. At the small reflecting angles used here, the wavelength values, the spectrometer readings, and the Bragg angles all can be assumed to vary linearly with each other. The recorded line is then described by the function $F(x)$,

$$F(x) = \int_{-\infty}^{+\infty} f(\xi)\, g(x-\xi)\, d\xi . \tag{4}$$

The total number of quanta falling into the counter when recording a line is expressed by

$$\int_{-\infty}^{+\infty} F(x)\, dx = \int_{-\infty}^{+\infty}\int_{-\infty}^{+\infty} f(\xi)\, g(x-\xi)\, d\xi\, dx . \tag{5}$$

This expression can be rearranged to

$$\int_{-\infty}^{+\infty} F(x)\, dx = \int_{-\infty}^{+\infty} f(\xi)\, d\xi \left[\int_{-\infty}^{+\infty} g(x-\xi)\, dx\right] \tag{6}$$

which is equal to

$$\int_{-\infty}^{+\infty} F(x)\,dx = \int_{-\infty}^{+\infty} f(\xi)\,d\xi \cdot \int_{-\infty}^{+\infty} g(x)\,dx. \tag{7}$$

e different integrals can be expressed by M, T and R

$$M = T \cdot R, \tag{8}$$

ere M is the total number of quanta reflected by the crystal. Since the slit geometry he same for all positions of the spectrometer, M is proportional to the area under curves obtained from the records. T is the number of quanta falling into the crys- under certain geometrical conditions. T is proportional to the probability of the ission of quanta belonging to a certain transition in the atom. R, which is known the integrating reflection coefficient of the crystal, is the area under the diffraction ttern of the crystal, when a monochromatic and parallel beam of X-rays is falling o it. The ratio of the emission transition probabilities of two lines can therefore expressed by

$$\frac{T_1}{T_2} = \frac{M_1}{M_2} \cdot \frac{R_2}{R_1} \tag{9}$$

ovided that the geometrical conditions are constant, which is true in the actual ectrometer arrangement used here. It is obvious that the variation of the reflection efficient with wavelength must be known. A thorough investigation of the reflec- n properties of quartz crystals has been made by Lind, West and DuMond 950] in connection with their work on the two-meter curved crystal gamma-ray ectrometer. In the theoretical part of their paper they treat the cases of a thick rfect crystal and a mosaic crystal with low primary and secondary extinction. The flection coefficient for a perfect crystal is:

$$R = \frac{r_0 \cdot d \cdot K}{2 \cos \theta_0} \cdot \frac{|F_H|}{V} \cdot \lambda, \tag{10}$$

d for a mosaic crystal

$$R = \frac{r_0^2 \cdot d \cdot K^2 \cdot a}{\cos^2 \theta_0} \cdot \left(\frac{|F_H|}{V}\right)^2 \cdot \lambda^2. \tag{11}$$

Here r_0 equals e^2/mc^2, d is the lattice constant for the crystal plane in question, is the polarization factor for the X-rays, F_H the crystal structure factor and V e volume of the unit cell. The crystal has the thickness a and the Bragg angle for diation of wavelength λ is θ_0. The conditions of low primary and secondary extinc- on are certainly fulfilled at the short wavelength in question.

Lind, West and DuMond studied the reflection properties of the $13\bar{4}0$ plane of artz in the wavelength region 500 to 9 XU. Their measurements show a variation R with λ^2 which is an indication that quartz behaves as a mosaic crystal when it elastically bent. Their measurements on an unstressed crystal plate show that is behaves more nearly as a perfect crystal.

Since their results obviously indicate that an elastically bent quartz crystal reflects a mosaic crystal, the value of R from eq. (11) was adopted. Because of the small lues of θ, the factor cos θ can be assumed to be equal to 1, and the variation of the

Table 8. Radiation transition probabilities for the K lines of heavy elements relative to $K\alpha_1 = 100$.

Element	α_2	α_1	β_3	β_1	β_5	β_2	β_4	$O_{\text{II III}}$
73 Ta	53.6	100	11.1	21.5	0.49	6.7	0.07	0.6
74 W	54.4	100	11.8	21.9	0.48	7.3	0.13	0.7
75 Re	56.0	100	11.3	21.7	0.50	7.3	0.16	0.8
76 Os	56.3	100	11.4	22.1	0.60	7.6	0.17	0.9
77 Ir	54.3	100	11.2	21.4	0.58	6.7	0.14	0.8
78 Pt	55.0	100	11.4	21.7	0.61	7.7	0.18	0.9
79 Au	53.3	100	11.7	22.8	0.68	7.6	0.14	0.9
80 Hg	52.4	100	12	24	0.61	8.6		1.5
81 Tl	57.6	100	12.3	22.7	0.57	8.7	0.17	1.5
82 Pb	54.8	100	12.4	23.1	0.65	8.6	0.21	1.3
83 Bi	57.0	100	11.9	23.6	0.68	8.6	0.21	1.2
90 Th	55.0	100	12.4	25.1	0.88	10.1	0.41	2.6
92 U	57.5	100	12.4	24.6	0.86	10.3	0.40	2.5

Table 9. Intensities of the K lines of heavy elements relative to $K\alpha_1 = 100$.

Element	L_{I}[1] KL_{I}	α_2 KL_{II}	α_1 KL_{III}	β_3 KM_{II}	β_1 KM_{III}	β_5 $KM_{\text{IV V}}$	β_2 $KN_{\text{II III}}$	β_4 $KN_{\text{IV V}}$	$O_{\text{II III}}$ $KO_{\text{II III}}$
73 Ta		52.4	100	12.5	24.3	0.57	7.8	0.08	0.7
74 W	0.16	53.2	100	13.3	24.8	0.56	8.5	0.14	0.9
75 Re		54.7	100	12.8	24.6	0.57	8.5	0.19	1.0
76 Os		54.9	100	12.9	25.0	0.69	8.9	0.20	1.0
77 Ir		53.0	100	12.7	24.3	0.64	7.8	0.16	1.0
78 Pt		53.6	100	12.9	24.6	0.69	9.0	0.21	1.1
79 Au	0.22	51.9	100	13.2	25.8	0.77	8.8	0.16	1.1
80 Hg		51.0	100	13.1	26.6	0.72	10.0		1.8
81 Tl		56.0	100	13.9	25.7	0.65	10.1	0.20	1.7
82 Pb		53.2	100	14.0	26.2	0.74	10.0	0.24	1.5
83 Bi		55.3	100	13.4	26.8	0.80	10.0	0.24	1.4
90 Th		53.0	100	14.0	28.4	0.98	11.8	0.48	3.1
92 U		55.3	100	14.0	27.8	0.98	12.0	0.47	3.0

[1] Regarding the KL_{I}-transition, see Chapter VI, p. 526.

polarisation factor K with wavelength considered negligible. Equation (9) can thus be written:

$$\frac{T_1}{T_2} = \frac{M_1}{M_2} \cdot \frac{\lambda_2^2}{\lambda_1^2}. \tag{12}$$

The transition probabilities for emission of X-ray quanta were calculated from eq. (12) after correction for the X-ray absorption discussed in the preceding sections. In the main part of this investigation the plane $22\bar{4}3$ has been used. In the case of tungsten some measurements have been made using the plane $13\bar{4}0$ (Table 3). The intensity ratios for tungsten obtained from the two crystal planes are equal, showing that the reflecting properties are equal for the two planes.

The quantity T is proportional to the radiation transition probability, whereas he intensity I of an X-ray line is proportional to the emitted energy. Since the energy f each quantum is $h\nu$, one has

$$I = T \cdot h\nu. \tag{13}$$

The final values of the transition probability for quantum emission are listed in Table 8, while in Table 9 are tabulated the intensity values. In each case the α_1 line s put arbitrarily equal to 100.

CHAPTER V

Discussion of the results

1. General remarks on *K*-spectra

The elements investigated have an electron configuration, where the four first hells (K, L, M, N) are completely filled. The N-shell is completed at 71 Lu, the last f the rare earth elements. For 73 Ta the electron arrangement is:

K-shell: $1s^2$
L-shell: $2s^2 2p^6$
M-shell: $3s^2 3p^6 3d^{10}$
N-shell: $4s^2 4p^6 4d^{10} 4f^{14}$
O-shell: $5s^2 5p^6 5d^3$
P-shell: $6s^2$

The following elements until 78 Pt are characterized by the filling of the $5d$-level. At 81 Tl the first $6p$ electrons appear, and this subshell is filled at the rare gas 86 Rn. At 90 Th the electrons enter the $5f$ subshell at the beginning of the actinide group. The outer shells at 92 U have the following configurations:

O-shell: $5s^2 5p^6 5d^{10} 5f^3$
P-shell: $6s^2 6p^6 6d$
Q-shell: $7s^2$

K-spectra are obtained if an $1s$-electron is removed and the vacancy in the K-level s filled by an electron jump from an outer level. Since the K-shell contains only one evel, the K-spectra are very simple in their structure. The initial state is always an s^{-1} state with the total angular momentum 1/2 and even parity ($1/2^+$). The final states of the transitions occurring in the K-spectra have the following J-values and parities:

s $1/2^+$
p $1/2^-$ $3/2^-$
d $3/2^+$ $5/2^+$
f $5/2^-$ $7/2^-$

The radiation emitted in a transition is characterized by its multipole order L, where L combines vectorially with the quantum numbers J_i and J_f of the initial and final states of the atom. The radiation occurs with or without parity change according to the following rules:

$$\begin{array}{ll}\text{electric radiation} & (-1)^{L} = \pm 1 \\ \text{magnetic radiation} & (-1)^{L-1} = \pm 1\end{array}$$

where the result -1 means parity change and $+1$ means no parity change.

The strongest lines arise always from electric dipole transitions ($E1$), where $L = 1$. According to the selection rules this transition occurs between states of different parity. In the K-spectra this means transitions from the $1s$-state to a p-state, that is to the levels L_{II}, L_{III}, M_{II}, M_{III}, N_{II} N_{III}, O_{II} O_{III} and P_{II} P_{III}. The electric quadrupole ($E2$) and magnetic dipole ($M1$) transitions are considerably less probable, and the corresponding X-ray lines are very weak. $E2$-transitions give rise to the $1s$–nd lines, namely $KM_{\mathrm{IV},\,\mathrm{V}}$ (β_5) and $KN_{\mathrm{IV},\,\mathrm{V}}$ (β_4). Two s-states can only combine with $L = 1$. A transition between two s-levels, which must occur without parity change, is thus only permitted as magnetic dipole radiation ($M1$). The very faint KL_{I} line on the long wavelength side of the α_2 line is of this type. Electric octupole ($E3$) transitions can occur between the $1s$-level and the $4f$-level, but the line resulting from this transition is surely not detectable owing to the very small intensity.

2. Earlier investigations

A systematic study of the intensity relations in K-spectra has been made by Meyer [1929] and by Williams [1933]. Meyer has investigated elements from 23 V to 49 In, using a crystal spectrometer and the photographic-photometric method for obtaining the intensity of the lines. This includes, however, some very uncertain corrections regarding the sensitivity of the photographic plate. The intensity values given by Williams [1933] for several elements from 24 Cr to 52 Te are probably more reliable, since he used an ionization chamber as detector. Furthermore the efficiency of the detector was studied carefully and the results were corrected for X-ray absorption, for reflection properties of the crystal and for the target absorption.

With respect to the heavy elements only a few papers have appeared in the later years.[1] Kliever [1939] studied 74 W and 78 Pt with a double crystal spectrometer and ionization chamber. His results were corrected for the detector efficiency and the absorption of the X-ray beam, but the target correction was not estimated. The intensity relations for spectra of some heavy elements have been studied by Voth [1942] using an absorption method. He measured the intensity of the secondary X-rays emitted from a radiator with and without different filters. The absorption filters were made of elements having their K-edges between the α and β lines as well as on the long and short wavelength side of the lines of the element used as radiator. In this way he was able to measure the intensity ratio between the α-group and the β-group for the elements 75 Re to 82 Pb. For some elements it was possible to use filters with the K-edge between the α_1 and α_2 lines or between the two β-groups of the K-spectrum of the radiator, and thus the α_2/α_1 ratio and some other intensity ratios could be determined for a few elements. This absorption method offers some advantage because of the simple experimental arrangement (no spectrograph is needed), but it is doubtful if it can give the same accuracy as the spectrometer method. Though one avoids the corrections for crystal reflection, other errors are introduced, for instance those arising from the Compton scattering in the radiator. Furthermore it is necessary to know the absorption coefficients very accurately. Voth's results, together with those of the above-mentioned investigators, are plotted in the Figs. 13–18.

---

[1] Regarding earlier measurements see Duane and Stenström [1920], Siegbahn [1931] and Compton and Allison [1935].

Theoretical calculations of the intensities of X-ray lines are very difficult to make cause of the very complicated wave functions for the heavy elements. A calculation sed on screened hydrogen eigenfunctions modified by relativistic effects has been ade by Pincherle [1933] for 74 W and by Massey and Burhop [1936] for 51 Sb, Au and 92 U. Ramberg and Richtmyer [1937] have calculated the radiation and ger transition probabilities for 79 Au. Their values are here converted to in- nsity values.

3. The present measurements

The intensities of the dipole-lines as compared with the α_1 line are plotted against in Figs. 13, 14, 15 and 16. The ratios β_5/β_1 and β_4/β_2 of the quadrupole line inten- ies to those of the neighbouring dipole-lines are shown in Figs. 17 and 18. The rtical lines marked at some points in the diagrams indicate the estimated errors cluding both statistical and systematic errors. The statistical errors, which depend the uncertainty in the voltage and current integrator measurements and in fluc- ations in the focal spot, amount to about 5 per cent for the stronger lines and to –20 per cent for the weaker ones. Systematic errors arise mainly from target cor- ction and crystal reflection factors. In the case of the $KO_{\mathrm{II,III}}$ line errors are troduced because of the K-edge, which strongly affects the profile of the line. s earlier pointed out, the separation of the line from the edge is very difficult make since the shape and wavelength value of the edge is not accurately own. Further the target correction for the line is difficult to calculate because the abrupt change in the absorption coefficient for the target material at the -edge. The correction applied here is the same as for the β_2 line, which might use the $KO_{\mathrm{II,III}}$ line intensities to be some per cent too low.

The dipole lines

As mentioned above the dipole lines arise from electron jumps from levels $L_{\mathrm{II,\,III}}$, $_{\mathrm{II,\,III}}$, $N_{\mathrm{II,\,III}}$, $O_{\mathrm{II,\,III}}$ and $P_{\mathrm{II,\,III}}$ to the K-level. Transitions to the L- and M-levels re- ult in the well separated doublets $\alpha_1\,\alpha_2$ and $\beta_1\,\beta_3$. The β_2 line ($KN_{\mathrm{II,\,III}}$) shows marked symmetry and can be resolved into its components (Fig. 11), but the $KO_{\mathrm{II,\,III}}$ ne is recorded as a single line. The first electrons in the $P_{\mathrm{II,\,III}}$-level appear for element 1 Tl, but no line resulting from the $KP_{\mathrm{II,\,III}}$-transition has been detected even in 90 h and 92 U. Obviously the line is suppressed by the neighbouring much stronger $O_{\mathrm{II,\,III}}$ line.

The intensity of the lines in the dipole doublets is proportional to the statistical eight $2J+1$, of the doublet levels, which gives the well-known value 0.50 for the ntensity ratios α_2/α_1 and β_3/β_1. It is assumed, however, that these intensity ratios ould be changed for heavy elements as a result of relativistic effects, since the bind- g energy of the inner electrons is rather great (~ 70 keV for Au). Theoretical cal- ulations by Massey and Burhop with regard to relativistic effects show that the $_2/\alpha_1$ ratio should decrease with increasing Z. All calculations of transition probabili- es in heavy atoms must necessarily include rather severe approximations, however, nd Massey and Burhop state that their calculations do not give a value that efinitely differs from the non-relativistic value 0.50.

It is noticeable that all values for the ratio α_2/α_1 obtained in this investigation are reater than 0.50; the mean value being 0.537. Voth reports the α_2/α_1 ratio as 0.593 nd Kliever's Pt value is 0.52, which he states to be more reliable than the W value .47. It seems therefore to have been established that the α_2/α_1 ratio, that is 0.50

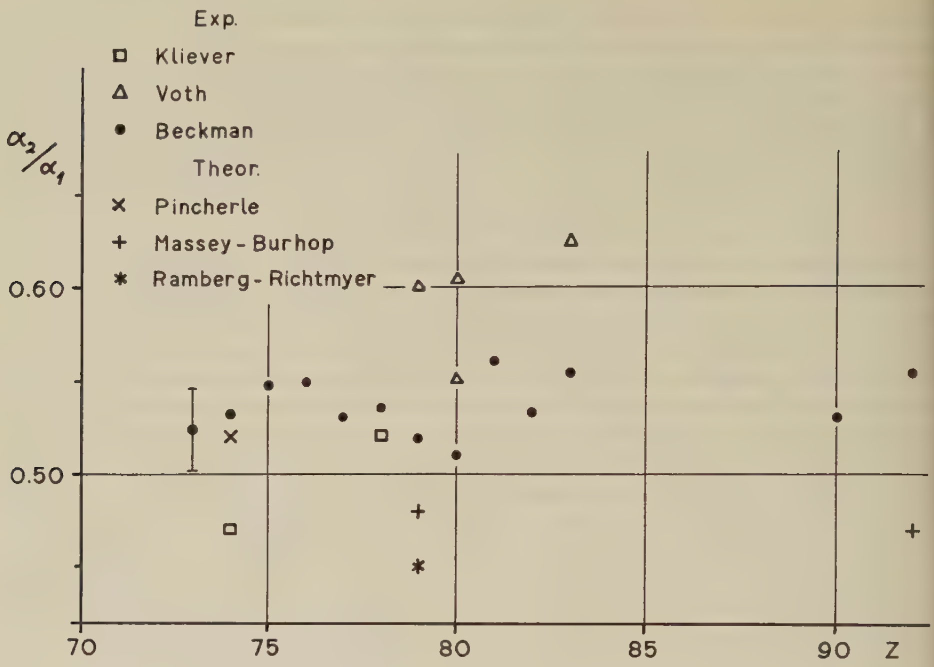

Fig. 13. The intensity ratio α_2/α_1 as a function of the atomic number Z.

for atoms in the middle of the periodic system, increases somewhat for heavy elements. The β_3/β_1 ratio obtained here (0.516) is likewise higher than 0.50, though the difference is not definitely established.

The ratios $(\beta_1 + \beta_3)/\alpha_1$ and β_2/α_1 are plotted in Figs. 14 and 15, for Z varying from 20 to 90. For elements with low Z it is impossible to resolve the β_1 and β_3 lines, and therefore MEYER's and WILLIAMS' values are compared with the $\beta_1 + \beta_3$ values obtained here for the heavy elements. WILLIAMS makes no clear distinction between transition probabilities and intensities, but since he used an ionization chamber as detector, his results are assumed to be intensity values. The values obtained by WILLIAMS and by the author are in excellent agreement in the case of $(\beta_1 + \beta_3)/\alpha_1$, but some discrepancy is shown for β_2/α_1.

The $KO_{\text{II, III}}$ line shows a rather steep increase in intensity in the Z range 73–92. An extrapolation to zero intensity for this line results in a Z value of about 65, and this would indicate that $O_{\text{II, III}}$-electrons do not appear for elements with $Z < 65$. The electrons start to enter the $O_{\text{II, III}}$-level at the element 49 In, however, and the shell is completed at 54 Xe. Further INGELSTAM [1937] reported the $KO_{\text{II, III}}$ line at 49 In and for several higher elements, so the line does exist for these elements. Obviously the $KO_{\text{II, III}}$ line intensity does not show the same steady increase with Z as do the β_1 and β_3 lines, for instance. After an initial increase for the elements just following 49 In, the line intensity then must be constant or vary only slowly until $Z \sim 72$, where the steep rise shown in Fig. 16 appears. The intensity of the line thus would show a variation with Z, similar to that of the term value ν/R of the 5p-level (SIEGBAHN [1931] p. 389). The anomalous behaviour of the $KO_{\text{II, III}}$ line is obviously

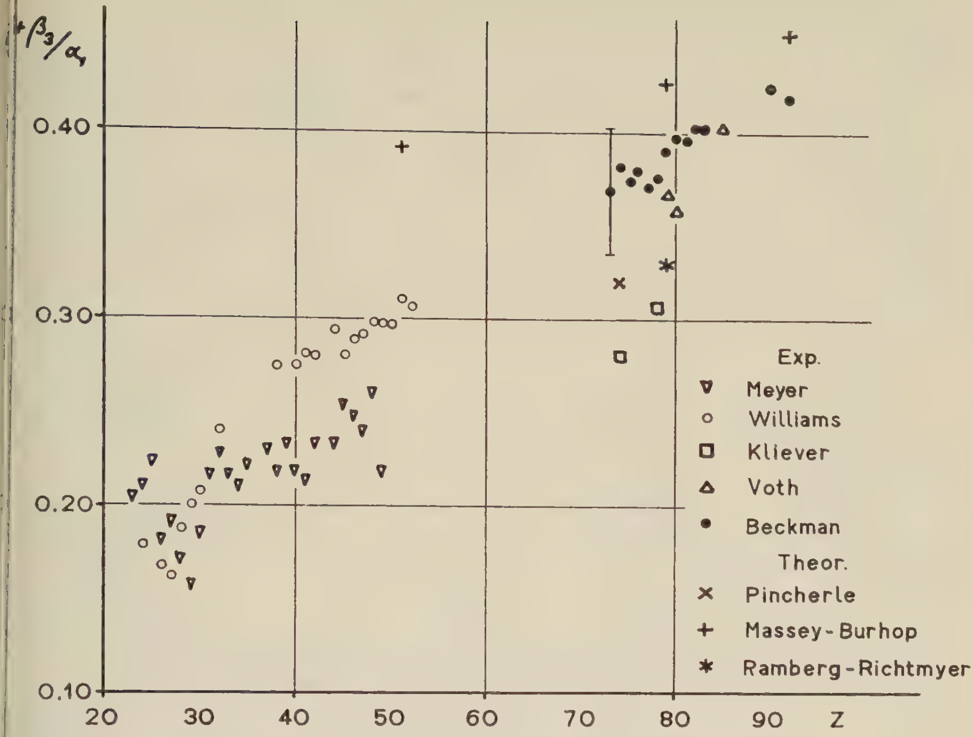

Fig. 14. The intensity ratio $(\beta_1+\beta_3)/\alpha_1$ as a function of the atomic number Z.

used by the filling up of the $4f$-level at the rare earth elements (Z, 58–71). The me effect, but not so pronounced, is also shown by the term value of the $N_{\mathrm{II},\,\mathrm{III}}$-level d an indication of a plateau in the intensity curve for the β_2 line might explain e small discrepancy between WILLIAMS' and the author's values (Fig. 15). The me effect is reported by BRIL [1947] for the β_2 line in L-spectra (transition $_{\mathrm{II}}N_{\mathrm{V}}$). The intensity of this line as measured relative to the $L\beta_1$ line ($L_{\mathrm{II}}M_{\mathrm{IV}}$) creases rapidly as Z varies from 44 to 55. In the region of the rare earths e line intensity is constant and then starts to increase slowly for $Z>72$.

The quadrupole lines

The two quadrupole lines, which arise from the transitions $KM_{\mathrm{IV},\,\mathrm{V}}$ and $KN_{\mathrm{IV},\,\mathrm{V}}$, e both doublets. The J values for the final levels are 3/2 and 5/2 respectively, hich gives the theoretical intensity ratio 2:3 between the components. The β_5 ie is reported separated by INGELSTAM [1937] and a slight asymmetry of the line as seen in most recordings in the present investigation too, but no attempt was made resolve the line into its components.

The β_5/β_1 values are in general agreement with the values obtained by KLIEVER r 78 Pt and with the theoretical calculations by MASSEY and BURHOP. WILHELMY 934] measured the β_5 and β_4 lines of 44 Ru, and reported the ratio $\beta_5/\alpha_1=0.0025$, hich fits fairly well the present values for the heavy elements. MASSEY and BURHOP ve calculated the β_5/α_1 ratio at 51 Sb to be 0.0012, which shows a great discrepancy

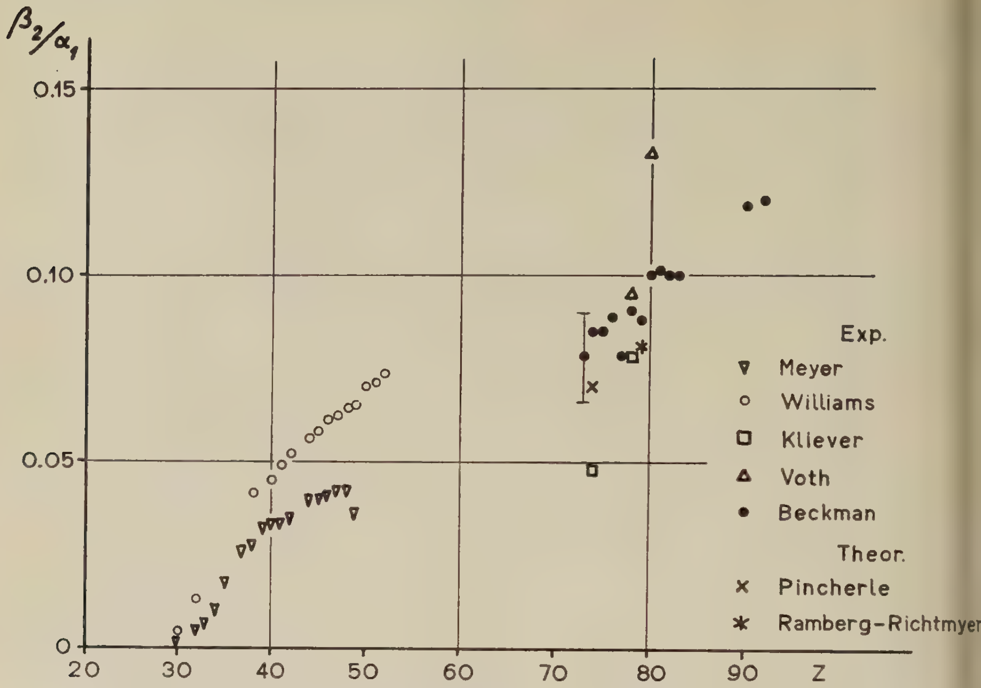

Fig. 15. The intensity ratio β_2/α_1 as a function of the atomic number Z. The values by VOTH include the $KO_{\text{II III}}$ line.

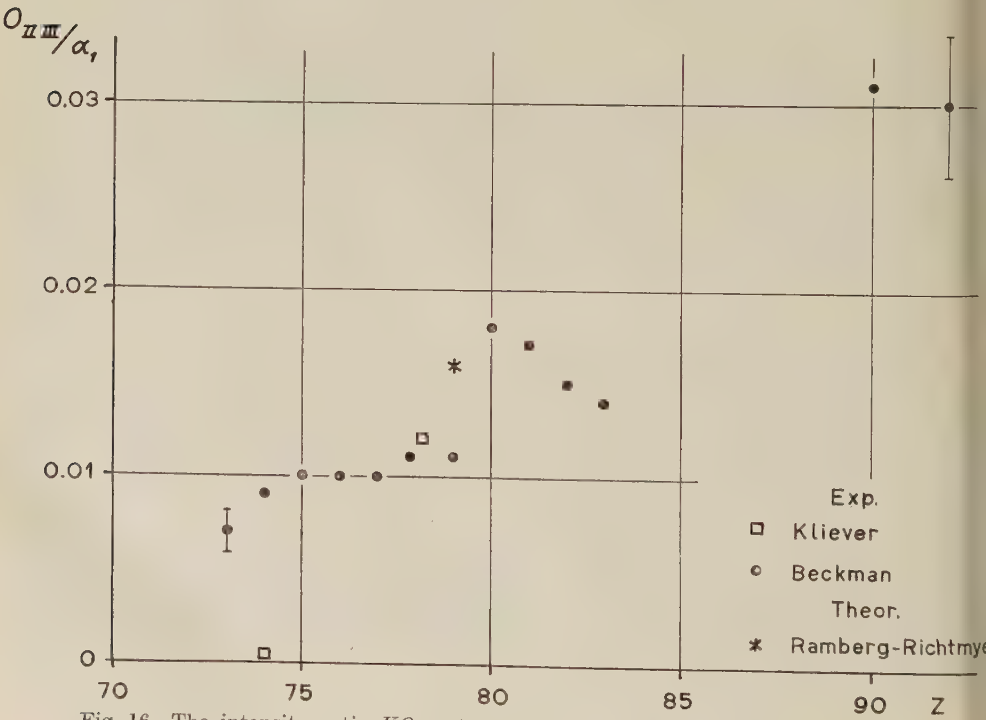

Fig. 16. The intensity ratio $KO_{\text{II, III}}/\alpha_1$ as a function of the atomic number Z.

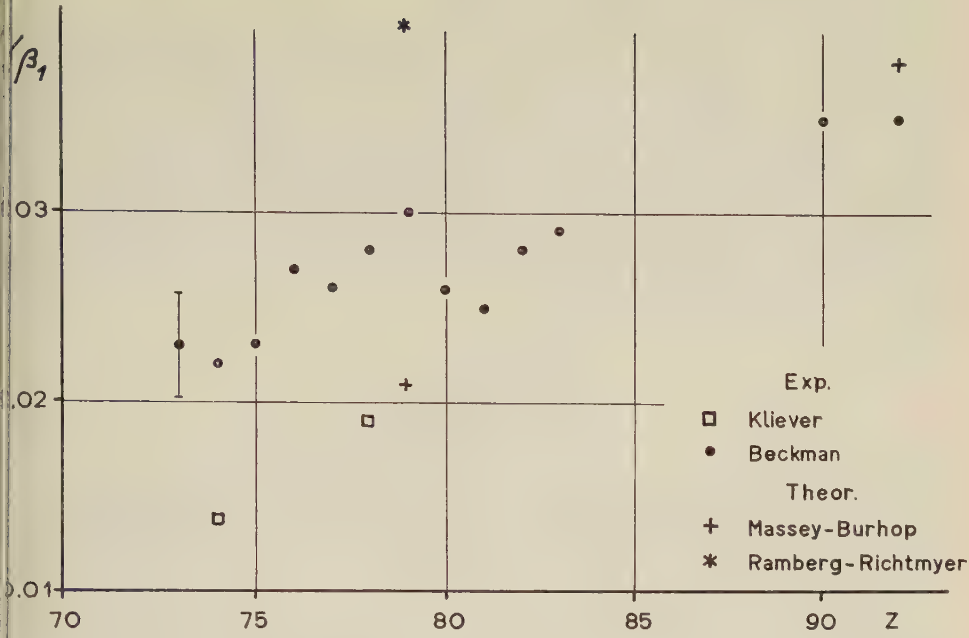

17. The intensity of the quadrupole line β_5 compared with the intensity of the neighbouring dipole line β_1 as a function of Z.

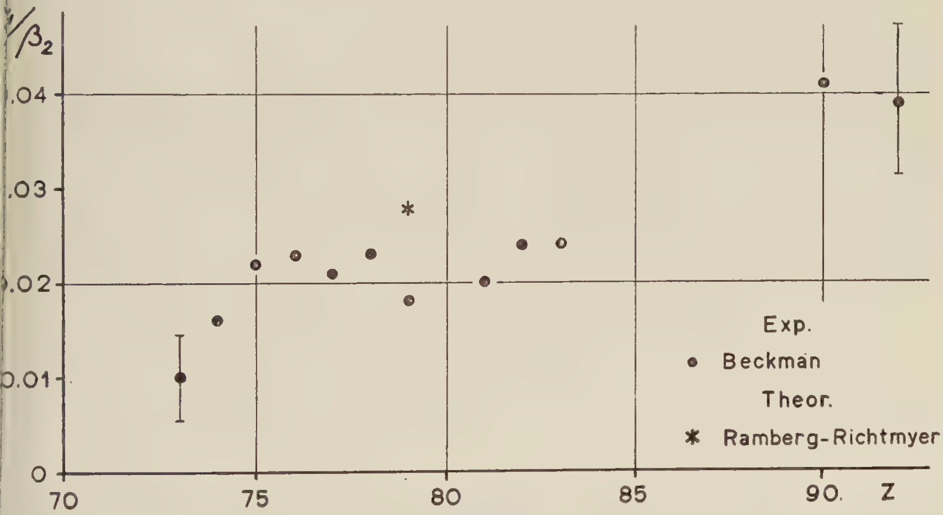

. 18. The intensity of the quadrupole line β_4 compared with the intensity of the dipole line β_2 as a function of Z.

ative to WILHELMY's value. A rough calculation shows that the intensity of a adrupole line relative to a dipole line of the same series increases as Z^2 UBINOWICS and BLATON [1932]). Such a Z-dependence is shown by the β_5 line; ratio β_5/β_1 varies approximately as Z^2.

The other quadrupole line β_4 shows a much stronger Z-dependence: β_4/β_2 increases as Z^4. The β_4 line is very weak, however, and the two adjacent lines β_2 and $KO_{\mathrm{II,III}}$ make the intensity determination very uncertain. WILHELMY reported $\beta_4/\alpha_1 = 0.006$ at 44 Ru, which seems to be in complete disagreement with the present results ($\beta_4/\alpha_1 = 0.001$ for 73 Ta). HULUBEI [1935] pointed out, however, that the β_4 line of the elements 42 Mo and 45 Rh is double and only one of the components can be referred to the $KN_{\mathrm{IV,V}}$-transition. The other component is a non-diagram line β_{4x} (INGELSTAM [1937]). INGELSTAM followed the β_{4x} line up to the element 58 Ce; in the heavy elements this line is not detectable and only the quadrupole line β_4 is visible.

CHAPTER VI

The KL_{I}-transition

The K and L_{I}-levels are both s-levels with the total angular momentum $J = 1/2$. The KL_{I} line is thus forbidden both as electric dipole and quadrupole radiation. The transition can, however, occur as a magnetic dipole radiation (see p. 520). The line would thus be hard to detect but should have an intensity comparable with that of the electric quadrupole lines.

A weak line on the long wavelength side of α_2 was reported in W by DUANE and STENSTRÖM [1920] and by MAZUMDER [1927], but the identification of this line with the KL_{I}-transition is doubtful. More recently HULUBEI [1947] observed satellite X-ray lines on the long wavelength side of the α_2 line of several elements in the region Z, 32–42. Such satellites were also studied by GROVEN and MORLET [1951] for the elements 30 Zn and 33 As–36 Kr. The lines do not coincide in wavelength with the calculated value of the KL_{I} line but were assumed to be satellites of this line.

The ordinary K-satellites are caused by double-ionization of the atom. The intensity of these lines decreases roughly as Z^3 (RICHTMYER [1936]) and thus they should be extremely weak in the spectra of the higher elements. In fact they have never been observed for these elements. Instead a higher order line such as the KL_{I} line would probably increase in intensity with increasing Z, and since the satellites of the line

Table 10. Wavelength and intensity values of the KL_{I} line of 74 W and 79 Au.

Element	Wavelength XU	Intensity ($\alpha_1 = 100$)	
		Exp.	Theor. M-B.
74 W	215.33	0.14	
	53	0.22	
	54	0.12	
Mean	**215.47**	**0.16**	
79 Au	186.37	0.20	
	29	0.24	
Mean	**186.33**	**0.22**	**0.42**

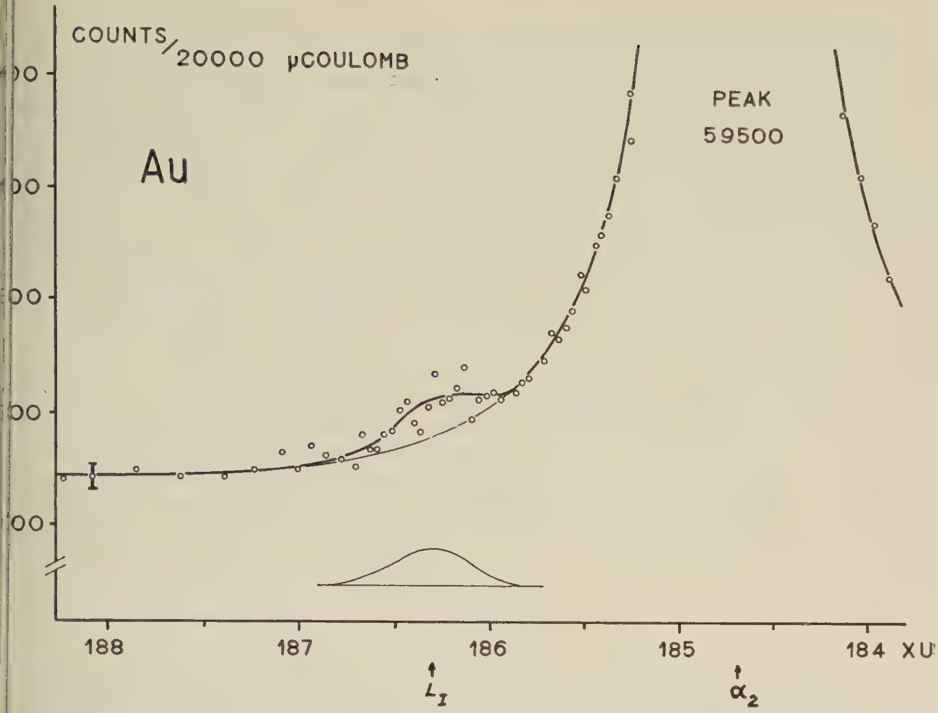

Fig. 19. The magnetic dipole line arising from the transition KL_{I} in gold.

observed in the spectra of elements with low Z, the line itself might be observable the spectra of the heaviest elements.

pecial attention was thus paid to possible faint lines in the α-group of the K-ctra in the present investigation, and a very faint line was then found near the ine for each of tungsten and gold, the two elements which were investigated in s respect. The wavelength values obtained for these faint lines are in agreement h the values computed from ν/R data for some K and L lines of these elements. e observed line undoubtedly arises from the magnetic dipole KL_{I}-transition. This iclusion is supported by the work of MASSEY and BURHOP [1936] who calculated intensity ratio of the Au KL_{I} line to the α_1 line to be 4.2×10^{-3}, which agrees derately well with the experimental values obtained here (2×10^{-3} for Au KL_{I}). ble 10 contains the wavelengths and intensities obtained in the various recordings this line in W and Au, and Fig. 19 shows one of the recordings for the Au KL_{I} e. The wavelength values of the lines were determined relative to the α_1 and α_2 es, the latter wavelengths being obtained from INGELSTAM [1937]. It is further ticeable that the line is rather broad; the width of the line as obtained directly m the records is nearly double the width of the other K lines.

A transition between two levels in an atom does not necessarily give rise to emitted X-ray quantum. The excitation energy can be transferred to an outer ctron instead, with the result that this electron is ejected (Auger effect). The ger transition probability is best known for the K-shell. For elements of low the Auger transition is more probable than the radiation of a quantum, but in the heavy elements only a few per cent of the atoms excited in the K-shell emit Auger electrons (SIEGBAHN [1955]). The relative intensities of the Auger electrons have been calculated by several investigators using various electron wave functions, but the agreement with the values experimentally obtained is not good (SIEGBAHN [1955]). HILL [1953] has used another method in a calculation of the Auger intensities in the case of mercury. HILL treated the Auger effect as an internal conversion process, and assumed that the conversion coefficients for nuclear gamma-rays might be applicable to the conversion of the X-ray K-radiation in the L-subshells. This approximation would not be serious for the heavy elements where the K-shell is close to the nucleus. On account of the high conversion probability of $M1$ radiation in the L_I-subshell HILL was able to explain the great intensity of the Auger KL_IL_I line assuming a probability of the KL_I-transition of only about 1.5 per cent of the total $E1$ X-ray radiation, which agrees with the estimation of the intensity of the satellite lines reported by GROVEN and MORLET [1951]. In the present investigation it has been found, however, that the KL_I line is still weaker. The intensity is only 0.2 per cent of the α_1 line, which gives too small a value of the intensity of the Auger KL_IL_I line. The discrepancy that obviously exists may possibly be caused by the application of the gamma conversion coefficient on the X-ray K-radiation.

SUMMARY

1. A 2.5 meter focussing curved crystal X-ray spectrometer of the transmitting type is described. The spectrometer is designed for the wavelength region 100–220 XU, using the $22\bar{4}3$ plane of quartz.

2. The X-radiation has been registered by a scintillation counter with a NaI (Tl) crystal and a single channel discriminator.

3. A stabilized 800 kV van de Graaff generator was used as the high voltage source.

4. The X-ray K-spectra have been obtained for the elements 73 Ta–83 Bi, 90 Th and 92 U at 500 kV and 60–90 μA. The high luminosity of the spectrometer and the low background have made it possible to detect even the weak β_5 and β_4 lines.

5. The intensity ratios between the K lines and the $K\alpha_1$ line have been calculated. Corrections have been made for varying efficiency of the scintillation counter and for X-ray absorption within the target and in the X-ray beam between the target and the counter. The variation of reflecting properties of the crystal with the wavelength has been taken into account.

6. The theoretical calculation of the target absorption has been experimentally verified in the case of gold.

7. The calculated intensities are in general agreement with the theoretically determined values. A slight deviation from the 2 : 1 rule for the intensity ratio of some doublets is observed, however; the mean α_2/α_1 ratio is found to be 0.537 and that for β_3/β_1 is 0.516 for the elements investigated. See Table 9 and Figs. 13–18.

8. A weak line resulting from the transition K to L_I has been detected in the spectrum of tungsten and gold. The wavelength is: W KL_I 215.47 ± 0.08 XU and Au KL_I 186.33 ± 0.08 XU. The intensity in each case is 0.2 : 100 relative to that of the α_1 line.

REFERENCES

RÖM, B., Arkiv f. Fysik *7*, 241 (1954).
EL, P., Rev. Sci. Inst. *25*, 391 (1954).
KMAN, O., Arkiv f. Fysik *1*, 329 (1949).
L, A., Physica *13*, 481 (1947).
GREN, G., Arkiv f. Fysik *3*, 515 (1951).
PTON, A. H. and ALLISON, S. K., X-rays in Theory and Experiment, London 1935.
ANE, W. and STENSTRÖM, W., Proc. National Acad. *6*, 477 (1920).
MOR, W. and SANDS, M., Electronics Experimental Techniques. New York 1949.
DMAN, C., The Science and Engineering of Nuclear Power. Cambridge U.S.A. 1947.
VEN, L. and MORLET, J., Bull. Acad. Roy. Belge CI. Sci. *37*, 630 (1951).
L, R. D., Phys. Rev. *91*, 770 (1953).
LUBEI, H., C. R. Acad. Sci. Paris *201*, 1356 (1935).
– C. R. Acad. Sci. Paris *224*, 770 (1947).
ELSTAM, E., Die *K*-Spektren der Schweren Elemente, Diss. Uppsala 1937.
EVER, W. H., Phys. Rev. *56*, 387 (1939).
ÉN, K. and STARFELT, N., Arkiv f. Fysik *7*, 427 (1954).
D, D. A., WEST, W. J., and DUMOND, J. W. M., Phys. Rev. *77*, 475 (1950).
SSEY, H. S. W. and BURHOP, E. H. S., Proc. Cambr. Phil. Soc. *32*, 461 (1936).
ZUMDER, K. C., Zs. f. Phys. *46*, 449 (1927).
YER, H.-T., Wissenschaftliche Veröffentlichungen aus dem Siemens-Konzern *7*, 108 (1929) (ref. SIEGBAHN 1931).
YERHOF, W. E. and WEST, H. I., Rev. Sci. Inst. *25*, 1025 (1954).
LIN, P. and BECKMAN, O., Arkiv f. Fysik *1*, 323 (1949).
CHERLE, L., Accad. Lincei. Atti *17*, 560 (1933).
MBERG, E. G. and RICHTMYER, F. K., Phys. Rev. *51*, 913 (1937).
HTMYER, R. D., Phys. Rev. *49*, 1 (1936).
BINOWICZ, A. and BLATON, J., Ergebn. d. exakt. Naturwiss. *11*, 176 (1932).
GBAHN, K., Beta- and Gamma-Ray Spectroscopy, Amsterdam 1955.
GBAHN, M., Spektroskopie der Röntgenstrahlen, Berlin 1931.
TOREEN, J. A., Journ. of Appl. Phys. *20*, 1141 (1949).
TH, G., Ann. der Physik, *41*, 375 (1942).
BSTER, D. L., HANSEN, W. W., and DUVENECK, F. B., Phys. Rev. *42*, 141 (1932).
LHELMY, E., Phys. Rev., *46*, 130 (1934).
LLIAMS, J. H., Phys. Rev. *44*, 146 (1933).

Tryckt den 28 april 1955

Uppsala 1955. Almqvist & Wiksells Boktryckeri AB

ARKIV FÖR FYSIK Band 9 nr 33

Communicated 13 April 1955 by Harald Norinder and Ivar Waller

Energy loss of fast electrons

investigation into the absolute total cross-section for Bremsstrahlung in nuclear research emulsions

By A. G. Ekspong

With 11 figures in the text

Introduction

Since the appearance of the electron-sensitive nuclear research emulsions in 1948–49, ich make possible the study of tracks of singly charged particles of any energy, ny papers have appeared which deal with research on electrons[1], derived both m accelerators and from the soft component of the cosmic radiation. In the course the investigation of the gamma-radiation from neutral π-mesons and its subsequent oducts, the electron pairs, by Hooper, King and the author [1], the problem of energy loss by radiation presented itself. It was felt that this loss of energy, ich in certain cases was strikingly demonstrated, might well be the subject of a ecial investigation by means of the photographic emulsion technique.

Both from the theoretical and from the experimental point of view the radiation s problem has been one of long standing. In the following we will limit the discus- n to the case of high energy electrons, where the energy loss by radiation equals outweighs in magnitude that by ionization and excitation. In 1933–34 Bethe and eitler [2, 3] lay the theoretical foundation and presented a solution in the Born proximation, which, as recent theoretical investigations show [4, 5], requires less rrection than might be expected. At extremely high energies there should be no rrection at all contrary to the situation for pair production where the cross-section lowered by about 10 % in the case of lead. For some years this theory was believed break down at high energies (above about 200 MeV), because energetic cosmic ray rticles observed traversing lead or copper plates in cloud chambers [6, 7, 8] did t radiate to the extent predicted by the theory. As is well known, the solution to is puzzling situation led to the discovery of the μ-meson on the one hand, and to new confidence in the theory of Bremsstrahlung on the other.

Experimental investigations of radiation loss may be based on a study either of e radiation emitted or of the energy loss of the electron, as was pointed out in the review article by Corson and Hanson [9]. Recent experiments have dealt with various aspects of the process. One striking feature of the theory is that it predicts a broad intensity distribution of the emitted gamma-radiation, roughly constant over nearly the entire range from zero energy up to the full energy of the electron. All the recent experiments in the high energy region, with but one exception [10], have dealt with the investigation of the shape of the intensity distribution (for γ's) or of the shape and the absolute magnitude (for electrons). Measurements on the γ-radiation have been performed at various electron energies [11–16], and there is found general agreement between the experimental results and the theoretical predictions with respect to the shape of the intensity distribution.

---

[1] Throughout this paper the term electron is used to cover both negative and positive electrons less otherwise stated.

Two recent experiments based on measurements of the energy of electrons before and after traversing a foil in a cloud chamber have been limited to cases involving large losses only, and these two also demonstrated general agreement with the theory as to the shape in the region corresponding to high energy photons. Curtis [17] studied 60 MeV electrons traversing a lead foil and found the absolute magnitude of the partial cross-section to be a few per cent lower than the theoretical value. Fisher [18] studied 250 MeV negative and positive electrons traversing Au-foils and found the partial cross-section of the Bethe-Heitler theory to be $8.7 \pm 2.3\,\%$ too high.

Other aspects of the process have been studied at 17 MeV by Lanzl and Hanson [10], who found the nuclear cross-section to follow the Z^2-law within 1 % and also found agreement with respect to the angular distribution, which in their case is due to the combined effect of the intrinsic distribution of the radiation process and of the overlapping distribution from the multiple scattering in the target. These authors point out the difficulties associated with absolute measurements of the total cross-section based on the γ-radiation from betatron electrons. They have devised an experiment along these lines based on catching all the radiation in an ionization chamber. The difficulties in this approach involve the response of the chamber to the radiation and also the measurement of the electron beam current. Their result for Au is 10 % below the theory with an estimated error of about 10 %.

Reviewing the two main lines of experimental attack on the problem, we may say that investigations based on the γ-rays are more direct than those based on the energy left to the electron. Corson and Hanson point out in their review article [9] that the second method suffers from an incomplete knowledge of what happens to the electron in the foil. It is clear from the review of recent experiments, however, that the second method is at present more suited for absolute cross-section measurements.

The nuclear emulsion technique gives an insight into the processes responsible for the energy loss, and if the decrease of the average energy due to invisible processes as a function of the distance traversed is followed, this technique will also in principle be suitable for an absolute determination of the total cross-section.

The aim of the present investigation is to study in some detail the energy loss of fast electrons in the nuclear emulsion, to discard from the material that portion of the data in which electrons lose energy by visible processes, and to treat the rest in a statistical way in order to obtain a value of the total cross-section for Bremsstrahlung or—which is equivalent—a value of the radiation length in the nuclear research emulsion.

ection I. Survey of the theory and principle of the experimental method

§ 1. Theory

e differential cross-section for one-quantum radiation was derived by Bethe Heitler [2] for the case in which the interactions of the electron with the atomic and the radiation field can be treated as perturbations. It has already been ioned that the criteria for the validity of this solution seem to be too stringently d as has been shown by recent investigations by Bethe, Maximon, and Low by Bethe and Maximon [4], and by Davies, Bethe, and Maximon [5]. The rated cross-section, ϕ_k, is shown to be proportional to the square of the nuclear ge, Z, and to be essentially inversely proportional to the energy, k, of the quantum ted. Consequently the number of low energy quanta emitted is greater than number of high energy quanta, and hence the intensity $k\,\phi_k$ is only slightly ndent on k. The form of the intensity distribution, which seems to be verified ecent experiments [11–18], implies that in investigations on electrons a conable straggling in the energy loss will occur.

dealing with the average energy lost per cm, $\frac{dE}{dx}$, a cross-section, ϕ_{rad}, for the gy lost by radiation is defined by

$$-\frac{d\,E_0}{d\,x} = N\,E_0\,\phi_{\text{rad}}, \tag{1}$$

re E_0 is the energy of the electron and N the number of atoms per cm^3. From theory, ϕ_{rad} is given by

$$\phi_{\text{rad}} = \frac{1}{E_0}\int_0^1 k\,\phi_k\,d\left(\frac{k}{E_0-\mu}\right), \tag{2}$$

re μ is the restmass of the electron. When applying (2) to neutral atoms, one st take into consideration the screening of the nuclear Coulomb field by the mic electrons and further add the cross-section which is due to the radiation cesses in the Coulomb field of the electrons. Generally the integration in (2) must performed numerically for a given model of the charge distribution (Thomasmi). At extremely high energies or for complete screening, the analytical result iven by the energy-independent expression

$$\phi_{\text{rad}} = \bar{\phi}\,\{4\log\,(183\,Z^{-1/3}) + \tfrac{2}{9}\}, \tag{3}$$

ere

$$\bar{\phi} = \frac{Z\,(Z+A)\,r_0^2}{137}.$$

s the classical electronic radius. The quantity A which accounts for the contribu by the atomic electrons, is close to one [3], and in this paper is taken equal 1.0. important point in connection with the present investigation is that ϕ_{rad} is ected to vary only very slowly with the energy of the electron when this is high 100 MeV).

§ 2. Principle of the method

Starting from the definition of $\phi_{\rm rad}$ in eq. (1) and assuming this quantity to b a constant in the energy region considered, we obtain an exponential decrease of th average energy. Eq. (1) is then equivalent to

$$E_x = E_0 \exp\left(-\frac{x}{R}\right) \qquad (4$$

where $R = \dfrac{1}{N\,\phi_{\rm rad}}$ has the dimension of a length and is in this paper called the radiation length. The method proposed is based on eq. (4) and consists of measuring th average value of E_x / E_0 in a sample of electrons as a function of the distance traversed x. The energy of the electrons is measured in a microscope by the multiple scatterin method due to FOWLER [20], and the distance x is simply measured along the pat by an accurate micrometer screw attached to the microscope. The energy stragglin may cause large statistical errors in the average energy ratio. There exists, of course no way of eliminating this effect entirely, but one can eventually diminish th error caused by the straggling. This statistical problem is formulated and treated i Appendix 1.

The method proposed above has some advantages. First, the formation of the mea of the observed energy ratios at a given distance x will smooth out not only th intrinsic straggling but also the errors due to the limited energy resolution of th multiple scattering method. Second, it is based directly on the definition equatio of the total cross-section (to the approximation that this is a constant). Finally, th efficiency is rather good even with regard to the straggling, as is shown in Appendix 1

Section II. Source of electrons. Measurements

§ 1. The selection of electron tracks

The present investigation is based on electrons in the cosmic radiation obtaine in high altitude balloon flights. The first sample of tracks was measured in plate from the Bristol HA21-flight; further samples were obtained from a flight for N.R.L in the U.S.A. in 1950 (12 USC-plates) and from one flight in Sardinia (flight No. 21 1953) (12 Pd-plates).[1]

The thickness of the emulsions in the first two batches was 400 μ, the thicknes of the Pd-plates was 600 μ. The size of the plates was 7.5 × 7.5 cm and 10 × 15 cm respectively. The type of emulsion was in all cases Ilford G5.

The plates have been examined for electron pairs and tridents besides the ordinar search for nuclear interactions and meson events. From a total of about 2300 electro pairs and 75 tridents, representing about 4800 electron tracks, those have bee selected whose lengths in the emulsion exceed 10,000 μ, which requires that the proceed nearly parallel to the plane of the emulsion. The reason for this selectio criterion is that the multiple scattering measurements are performed on a 5000 μ segment of the track. The present method will give an average value of $\phi_{\rm rad}$ over th

---

[1] I would like to express my gratitude to all those engaged in arranging these flights.

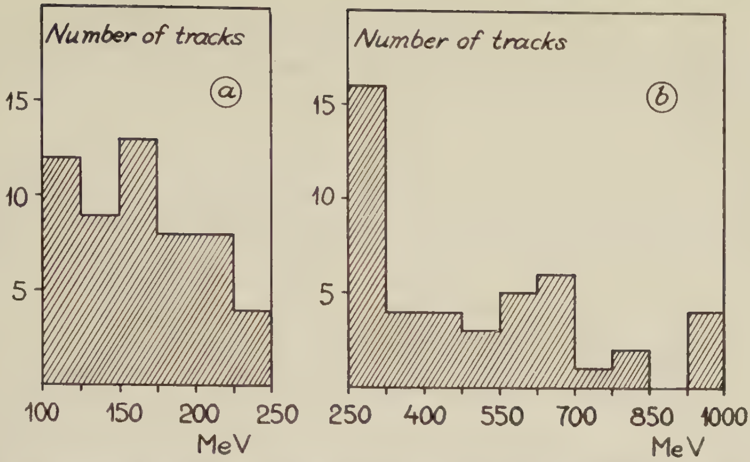

Fig. 1. The distribution of primary electron energies in the regions 100–250 MeV and 250–1000 MeV.

energy region studied. The emphasis has therefore been laid on energies higher than 100 MeV where the cross-section is expected to vary but slowly. An attempt has been made, however, to obtain a group of electrons centered around 75 MeV, but the number of such tracks turned out to be insufficient for a reliable determination of the cross-section to be made.

The majority of the tracks selected are due to pair created particles. A few tracks belonging to soft showers have also been included, if grain counting and scattering measurements showed that the particle had a mass less than that of known mesons.

In this way a total of 137 tracks have been selected, representing a total track length of 2400 mm. This length corresponds to about 80 radiation lengths. The distributions of the primary energies in the two energy regions of main interest, viz. 100–250 MeV and 250–1000 MeV, are shown in Fig. 1.

Whether there may be any admixture of particles other than electrons in this sample is a question that may be raised. That the majority of the tracks are due to electrons is not doubted. In the case of pairs the initial angle ω between the electron momenta was in two cases found to be rather large as compared to the average for the corresponding energy. In one case with $p\beta c$ equal to 170 ± 20 and 45 ± 5 MeV the angle was measured to be 4°.1. This angle may be compared with the angle $\omega_0 = \frac{k \cdot m c^2}{E_1 E_2}$ [21], where E_1 and E_2 are the energies of the electrons, k the energy of the quantum, and $mc^2 = 0.51$ MeV. The ratio was then found to be $\omega/\omega_0 = 4.7$, a rather large value but not improbably so. Furthermore, grain counting showed that the mass of the 45 MeV-particle was definitely less than that of known mesons. This pair was therefore accepted as being due to electrons. The second case had $p\beta c = 5.4 \pm 1.8$ GeV and $p\beta c = 1.0 \pm 0.2$ GeV respectively. The measured angle was found to be 0°.14, whereas $\omega_0 = 0°.03$; thus again a high ratio $\omega/\omega_0 = 4.7$ is obtained. If this pair is supposed for the moment to be due to mesons, the one of lower energy is expected to have a grain density slightly less than the plateau-value (about 0.96). The higher energy track provides the plateau-value for comparison in the same region of the emulsion. The result of the grain counting was that both tracks were at platea ionization, the 1.0 GeV-particle even slightly above but not significantly differen from the other. The pair is then probably due to electrons. There has been no reaso to doubt any other case.

§ 2. The measurements

The multiple scattering measurements were performed according to the metho described in detail in another paper [22]; thus the signal-to-noise ratio was kept i the vicinity of 3. In order to compute the energy, a knowledge of the scatterin factor K_0 is required. But it must be pointed out that the energy ratio E_x/E_0 is t a great extent independent of K_0. The dependence comes in only to the extent t which K_0 varies with the cell size. The present investigation is based on a total o about 16,000 individual scattering angles. The estimation of E_0, E_1 etc. along th track requires that the measurements be performed on a finite track length, calle here the segment, in order to keep the error within reasonable limits. Too long segment will, however, complicate the situation because the electron then tends t lose too much energy by radiation within the segment. In the present investigatio the segment was, as a general rule, taken to be 5000 μ, corresponding to a standar deviation in the energy ranging from 10 % to 20 % for electrons between 50 and 40 MeV respectively. At 1000 MeV this error is about 28 % and increases rapidly fo even higher energies. The systematic study made on samples of electrons has therefor been limited to energies below 1000 MeV.

To a first approximation the energy is considered constant within the segmen and the x-value assigned is the midpoint of the segment. If the electron loses muc energy within the ordinary 5 mm segment, which appears as increased scatterin signals, the segment is shortened (or alternatively the preceding one is lengthened so as to correspond to an approximately constant energy. Any slow energy decrease will then influence all segments in approximately the same way. Therefore th distance (Δx) between points where the energy is E_1 and E_2 is taken as the distanc between the midpoints of the corresponding segments. Thus Δx between adjacen segments may be calculated from the number of cells (m_1 and m_2 resp.) and thei size (c_1 and c_2 resp.) by the following formula

$$\Delta x = \frac{m_1 c_1 + m_2 c_2}{2} - \frac{c_1 - c_2}{2}.$$

As the tracks are always nearly parallel to the microscope stage movement, th Δx-measurements are very accurate (generally $\lesssim 2‰$ error).

When we deal with a sample of electrons and form the mean value of E_x/E_0, new problem arises because the x-values vary somewhat around the points $x = 5.0$ $x = 10.0$, $x = 15.0$ mm etc. This variation of x among the individual electrons i caused by (1) varying cell sizes, (2) varying nominal segment lengths in case thes have been shortened or lengthened. Now it is easy to show that the mean valu ($\bar{x}$) of the x's in the vicinity of a given point may be taken to represent the poin where $\overline{\left(\frac{E}{E_0}\right)} = \exp\left(-\frac{\bar{x}}{R}\right)$ holds. The argument is as follows: at each point x the measured ratio E_x/E_0 belongs to a distribution in energy with a mean $\exp\left(-\frac{x}{R}\right)$. If th x's are distributed as $f(x)dx$ then the mean energy of the sample is given by

$$\overline{\left(\frac{E}{E_0}\right)} = \frac{\int \exp\left(-\frac{x}{R}\right) f(x)\,dx}{\int f(x)\,dx} = \exp\left(-\frac{\bar{x}}{R}\right)\left\{1+\frac{\mathrm{var}\,x}{2R^2}+0\left(\frac{1}{R^3}\right)\right\},$$

ich is found by a series expansion of exp $-\left(\frac{x-\bar{x}}{R}\right)$. In the experiments var x found to be between $0.1-0.3$ mm^2 (var x = mean value of $(x-\bar{x})^2$). The st order correction within the parenthesis (with $R \simeq 30$ mm) amounts then less than 0.2 ‰.

Section III. Corrections

There are three corrections to be applied due to (1) distortion, (2) ionization and citation, and (3) outscattering. No correction for cascade processes is needed.

Because of the small dip of the tracks selected for measurements, distortion will general have a negligible effect on the energy measurements. The USC-plates are t free from distortion, however, as judged by some measurements carried out th the distortion vector method [23], and special care has been exercised in case e tracks have dips occasionally greater than the usual (< 2°-3°), and/or have ch high energy that large cells are required. In the Pd-plates distortion cor-ction was found unnecessary, and these plates show also in general low distortion r tracks with a large dip. Two tracks in the USC-plates caused by very high energy ctrons (estimated to 3 and 1.5 GeV respectively) with dip angles about 2° had to entirely rejected. In three other cases the end portions (5, 3, and 2 mm respectively) the tracks were left out, the tracks approaching one edge of the plate. In three rther cases the end portions of tracks had to be corrected slightly with a result of ss than 5 % increase of the estimated energy. One case of local distortion caused a 10 μ wide extraneous obstacle led to the rejection of 300 μ of the track, but easurements before and after were judged to be reliable.

The loss of energy per unit path length due to ionization and excitation may in is experiment be considered a constant, because almost all the electrons have ergies above 10 MeV and high energy transfers are detected separately. According Fowler [20] the loss may be taken as 0.59 MeV per mm. Most electrons studied re have such high energies ($\gtrsim 100$ MeV) that this correction is relatively unim-rtant. At lower energies (20–30 MeV) this loss of energy is in magnitude about ual to that by Bremsstrahlung. In this experiment the correction has been applied all tracks irrespective of their energy. If the primary energy of the electron is E_0, s energy E_x after a distance x mm is reduced to

$$E_x = E_0 - 0.59\,x_1 - q_1 - 0.59\,(x_2 - x_1) - q_2 \ldots = E_0 - 0.59\,x - \Sigma\,q_i$$

which it is supposed that a number of photons of energies q_i are emitted at the ints x_i. The application of the correction $+\,0.59\,x$ MeV to the measured E_x removes e effect of ionization and excitation energy loss. Both the emitted radiation and her sources of energy loss cause a change of energy of the electron from point to int along its path. It is, however, a consequence of the definition of the cross-ction in eq. (1), that its energy dependence is very slow. The variation is logarithmic in E for an unscreened Coulomb potential, and, in the case of a partially screened field, much slower.

The most important correction is that due to outscattering. The corrections discussed above apply to the electrons as individuals, whereas the third correction i applied to the energy sampling distribution of many electrons. The scattering of the electrons is such that they tend to leave the emulsion through the surface or the bottom. The thickness of the emulsions used in this experiment is 400 or 600 μ. As the outscattering is energy-sensitive the sample of electrons with a certain track length will be biased against tracks of electrons that have lost considerable energy. It is thus only the energy-sensitive part of the outscattering that needs to be corrected for. The aim will be to assign a weight to each electron which is found at the point of measurement such that electrons which apparently have suffered no loss of energy are given the weight 1.0. As mentioned in Appendix 2, the probability of finding the electron at the distance x with the lateral deflection z (perpendicular to the plane of the emulsion) is given by the normal frequency curve. The proof requires in fact an infinitely thick emulsion, but to solve the problem with proper boundary conditions imposed by the limited thickness of the emulsion is not a very attractive task. Because of the strong positive correlation between the perpendicular deflection and the angle to the original direction, which lies approximately in the plane of the emulsion, a fast electron will rarely scatter back into a layer which it has already left. It is therefore considered to be a fair approximation to apply the result of the calculations in Appendix 2 to this problem. The probability distribution for deflections z for electrons with initial energy E_0 MeV, which after a distance x_1 mm is reduced to energy E_1, is described by the standard deviation σ_z.

$$\sigma_z^2 = \frac{x^3}{e_0^2} + (x - x_1)^3 \left(\frac{1}{e_1^2} - \frac{1}{e_0^2}\right); \quad e = \frac{E}{1.5} \cdot$$

The next step is to average this increased variance over the x_1-values. The nature of the quantum process studied suggests that a sufficient approximation is to give all elements of the x-axis the same probability. This leads to the average value:

$$\sigma_z^2 = \frac{x^3}{4\,e_0^2}\left\{3 + \left(\frac{E_0}{E_1}\right)^2\right\}.$$

The case of no energy loss (normal outscattering) is dependent on a smaller variance, viz.

$$\sigma_z^2 = \frac{x^3}{e_0^2}.$$

The fraction of non-outscattered tracks (q) is then given by $q = 2\,F\left(\frac{d/2}{\sigma_z}\right) - 1$, where F is the normal distribution function, and d the thickness of the emulsion. This fraction is a function of σ_z, and in particular a function of the energy ratio E_1/E_0. With x and E_0 constant we have a constant fraction q_0 defined for the normal outscattering case, and a varying q_1 for the case of energy loss. The weight factor f is defined as the ratio q_0/q_1. Thus f may be written

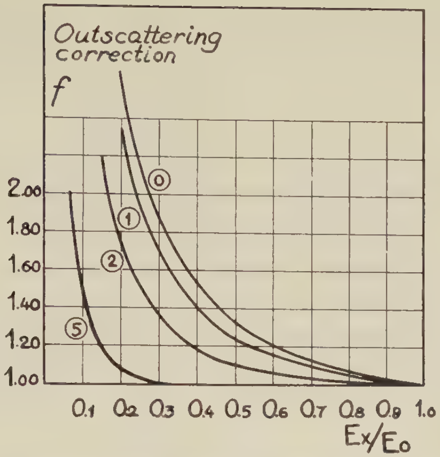

ig. 2. The correction for outscattering is made by assigning a weight $f \geq 1$ to each electron. he weight factor f is a function of the energy ratio E_x/E_0 and the parameter p (see text). The curves shown have been calculated for $p = 5$, 2, 1, and the limiting case $p = 0$.

$$f = \frac{2\,F(p) - 1}{2\,F(p/y) - 1}, \quad \text{where} \quad p = \frac{E_0\,d}{3\,x^{3/2}}, \quad y = \tfrac{1}{2}\sqrt{3 + \left(\frac{E_0}{E_1}\right)^2}, \quad \text{and}$$

$$F(p) = (2\,\pi)^{-\frac{1}{2}} \int_{-\infty}^{p} \exp\left(-\tfrac{1}{2}\,u^2\right) d\,u, \quad (E_0 \text{ in MeV, } d \text{ in mm and } x \text{ in mm}).$$

To each measured energy belongs a p-value and a y-value. An electron which has ot lost any energy has $y = 1$ and therefore $f = 1$, irrespective of its p. Very long racks of rather low energy electrons have small p-values, provided the thickness d s small. For $p \ll 1$ the limiting form $f = y$ holds, as is shown by a series expansion of F.

The weight factor is shown as a function of the energy ratio with p as a parameter n Fig. 2. It is seen that small energy losses require very little correction, and that arge p-values, i.e. high primary energy or thick emulsion or small distances, require ractically no correction. The largest weight given to any track in the present inestigation is $f = 3$. In all, 30 % of the total number of about 400 measured energies ave led to the assignment of a weight factor larger than 1.05. The procedure for alculating the mean value of $\varepsilon_i = \frac{E_x}{E_0}$ at a given distance x is simply to evaluate

$$\bar{\varepsilon} = \frac{\Sigma\, f_i\, \varepsilon_i}{\Sigma\, f_i}.$$

t is noted that it is the combined effect of a spread in ε and f that makes this correcion effective. Experimentally it is found that this correction corresponds to the emoval of a systematic error of 16 and 14 % in the total cross-section in the cases f 100-250 MeV electrons and 250–1000 MeV electrons respectively. It is difficult to stimate the uncertainty in the final results due to this correction. As it is worked ut in this section the weight factor depends only on the p-parameter and the nergy ratio. A 50 per cent increase of the p-parameter for all tracks was found to ield an increase of the radiation length by only 1.3 per cent. Therefore, the exact alue of the p-parameter has but a slight influence in the present case. The other factor, the energy ratio, is of greater importance. As the energy loss is a stochastic variable, the uncertainty due to this factor is to its greatest part included in the statistical error, which is worked out in Section V, § 1.

Section IV. Selected events

In this section a few selected events will be described in some detail. In Fig. 3 a and b are shown two examples where large losses have been observed, one at about 275 MeV, the other at about 300 MeV. Fig. 3 b also contains examples in certain regions showing apparent increase of energy due to the limited resolution of the multiple scattering method. In some cases the first stages of the development of a soft cascade shower have been observed, in which a new pair starts near the track under investigation and proceeds nearly parallel to it. Measurements of the energy of the electron and of the parallel pair shows in general that the γ-ray producing the pair has an energy that is equal to that lost by the electron within the limits of error. Examples are shown in Fig. 4 and Fig. 5.

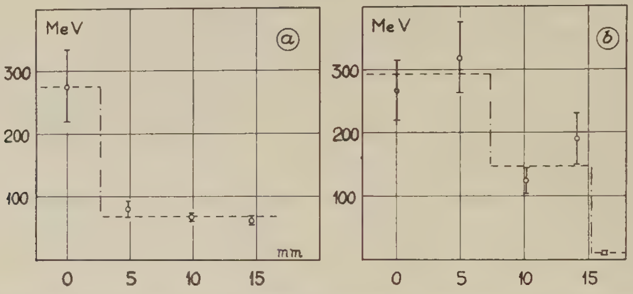

Fig. 3. Two typical cases with large energy losses observed. The energy of the electron as a function of the distance traversed. The errors are standard deviations.

A sudden large energy loss appears as increased scattering signals. Suppose this effect occurs at the end of the track segment under investigation, then most of the larger signals are eliminated by the cut-off procedure employed, in which all scattering angles larger than four times the mean are left out. Therefore the measured energy tends to remain at the higher level. If the midpoint of the segment is shifted forward along the track, more of the larger signals enter into the measurements resulting in a rapid decrease of the energy down to the lower level. One expects, therefore, that an analysis of the track made in such a way that the midpoint of the segment is gradually shifted forward will result in a high energy region and a low energy region with a transition region in between. Fig. 6 shows an actual case where the energy ratio is about 1:4.

The development of a small shower, which has been studied in considerable detail, is shown in the schematic drawing, Fig. 7, outlining the positions of the events involved. The energy of the 33.4 mm long electron track is, when measured in succeeding 10 mm intervals, $E_0 = 310 \pm 45$, $E_1 = 320 \pm 45$, $E_2 = 280 \pm 40$, and $E_3 = 10.0 \pm 1.5$ MeV. The large loss of energy is apparently connected with the relatively large angular deflection of 4°.8. There is no visible recoil at the point of deflection. One would expect, on the basis of these measurements, that one high energy photon (285 ± 25 MeV) has been emitted. The available path length for such a photon in

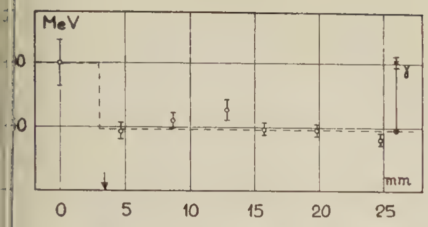

4. A case of a large energy loss accompa- d by the appearance of an electron pair at point marked by an arrow. The energy with standard error of the new pair is shown to the right.

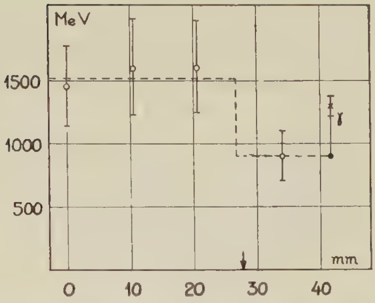

Fig. 5. A case of a large energy loss accompanied by the appearance of an electron pair at the point marked by an arrow. The energy with its standard error of the new pair is shown to the right.

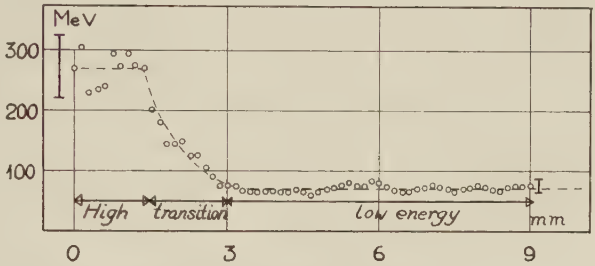

. 6. A detailed energy analysis made by gradually shifting forward the midpoint of the track ment. Each point is the result of 33 angular deflections. Every second point shown in the re. Two regions having approximately a constant energy are obtained. The standard errors refer to the first and the last point.

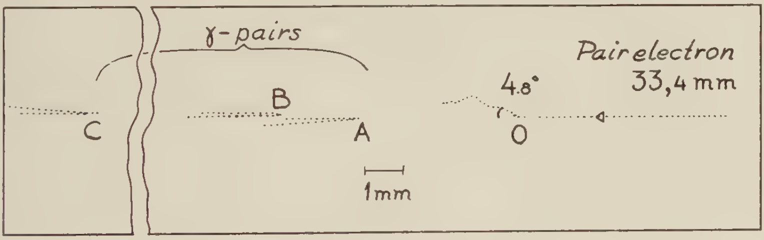

. 7. A small shower containing the three pairs A, B, and C, probably related to the primary ctron. The schematic drawing outlines the position of the events involved. The scale refers to the horizontal axis only.

e emulsion is estimated to be about one mean free path, the probability of finding materializing in the emulsion therefore being about 0.65. A very careful scan of e corresponding volume yielded no such photon, but instead the three pairs A, and C which all pointed very close to the point O in Fig. 7. These pairs are probably lated in some way to the original event, because the probability of finding one ay pair pointing close to O in this volume is less than 1:100; the probability of all ree being independent is about $1:10^6$. This figure is based on the known density

Table 1. Data on the events in Fig. 7.

	Event		
	A	B	C
Total energy in MeV	19±2	63±7	87±13
Distance to O (mm)	4.3	6.3	48.0
Nuclear recoil (*mc*) (see text) . .	0.5	2.0	–
Recoil angle	76°	83°	–

and angular distribution of pairs. Some data about these events are collected in Table 1, showing that the three pairs represent altogether about 170 MeV. The current view of shower development would then require a rapid emission of several photons (at least B, C, and one at O) in the last few millimeters' path length of the original electron, where a loss of energy would escape detection by the present method. A rough estimation of this probability yields a value of about 1:200. It is thus an odd case when so interpreted. It should be mentioned that there is no feature of the present observation that would absolutely exclude an interpretation of the event as due to a true multiple process, i.e. simultaneous emission of several photons. In particular the nuclear momentum in the pair creations at A and B can be estimated from the measured positions of the pair tracks relative to the point O and from the energy of each pair electron. The results are given in Table 1, showing the magnitude to be of the order of *mc* and the direction sideways, as expected [3, 26, 27]. Multiple processes, which are typical quantum effects, have been observed in other high energy fields, such as double pair formation [28] and three quanta annihilation of positrons [29].

The analysis of two cases of electron-electron collisions will be described in detail, because these provide an independent check of the reliability of the multiple scattering measurements and because of their intrinsic interest as examples showing strong relativistic effects. Both cases have an appearance in the microscope as shown schematically in Fig. 8, with rather small angles α and β. The only possible interpretation is that the struck particle is also an electron. As is well known, the sum of the angles α and β is 90° for elastic scattering between like particles in the non-relativistic case. Therefore the deviation from 90° is attributed to relativistic effects and further, one can utilize a measurement of these angles for an independent estimate of the three energies involved. The exact expressions are given in Appendix 3. In Table 2 the results of the measurements are collected. An unfortunate circumstance in the

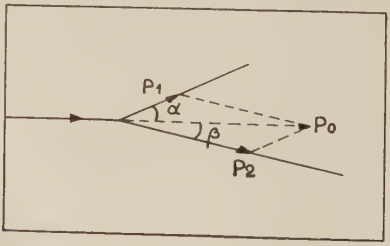

Fig. 8. Schematic drawing of an electron-electron collision. The full-drawn lines correspond to the electron tracks.

le 2. Electron-electron collisions at about 215 MeV and 13 MeV. The kinetic gies of the three electron tracks (p_0, p_1, p_2) by two independent methods. The rs have been calculated from the estimated standard errors in the measurements.

nary rgy eV	Method	Energy in MeV of tracks			Angles	
		p_0	p_1	p_2	α	β
15	Collision angles	290 ± 180	250 ± 180	37 ± 5	$1^\circ\!.3 \pm 0^\circ\!.8$	$8^\circ\!.7 \pm 1^\circ\!.3$
	Multiple scattering. . . .	286 ± 100	180 ± 20	33 ± 3		
13	Collision angles	14 ± 3	5.7 ± 1	8 ± 2	$17^\circ\!.5 \pm 1^\circ\!.5$	$12^\circ\!.3 \pm 1^\circ\!.5$
	Multiple scattering	13 ± 1	5.4 ± 0.7	8 ± 1		

event is that track p_0 is short (1.85 mm) and consequently does not lend itself more accurate multiple scattering measurements. Otherwise the energy balance ld have been tested more accurately in order to see if any energetic γ-ray was en off during the collision. The agreement between the energy estimations for k p_2, which is subject to least relative error, is very good. The rather low energy he second event and the sufficient length of the tracks allow the energy determinations by multiple scattering to be made with about 10% error. The energy ance indicates that no appreciable fraction of the energy is carried off as γ-radia. The energies based on the collision angles agree very well with those based on tiple scattering. Finally it should be mentioned that the coplanarity of the nts has been tested, and no deviation from coplanarity was found greater than errors of measurement ($0^\circ\!.5$ and 2° respectively).

Section V. The radiation length

§ 1. Experimental results

The sample of electron tracks studied in this section is free from events where ble energy losses occur. A further feature of the present method is that there is danger of confusing the track under investigation with other tracks in the development of showers. After the correction for ionization and excitation energy loss has n made it is supposed that the remaining loss observed is due to Brehmsstrahlung. The high energy group (≥ 100 MeV) has been divided into one sample containing electrons with primary energies in the region 100–250 MeV, and one with energies)–1000 MeV. The end portions of very long tracks have been added to the sample responding to its energy. The energy of the second group of electrons (mean rgy $\simeq 500$ MeV) seems to be the highest for which cross-section measurements re been published. Relevant data on the two samples are collected in Tables 3 l 4. Table 5 contains the total sample. The steady decrease of the average energy io is obvious. The error, σ, of the ratio is rather large. This error depends on the rinsic straggling of the radiation process, on the errors in the energy measurements l finally on the number of tracks (n) in the sample. One may write

$$\sigma = \frac{\sigma_t}{\sqrt{n}}$$

Table 3. Experimental results for 100–250 MeV electrons. Average energy-ratio, E_x/E_0, as a function of the distance traversed, x. The number of tracks in the sample $= n$, when corrected for outscattering $= n'$; σ is the standard error of E_x/E_0.

x mm	n	n'	$\left(\overline{\frac{E_x}{E_0}}\right)$	σ
0.00	62	62	1.000	0.020
4.82	62	68.01	0.821	0.037
9.83	42	47.93	0.763	0.045
15.07	19	23.54	0.596	0.067

Table 4. Experimental results for 250–1000 MeV electrons. Average energy-ratio, E_x/E_0, as a function of the distance traversed, x. The number of tracks in the sample $= n$, when corrected for outscattering $= n'$; σ is the standard error of E_x/E_0.

x mm	n	n'	$\left(\overline{\frac{E_x}{E_0}}\right)$	σ
0.00	50	50	1.000	0.031
4.94	50	52.39	0.854	0.041
9.77	39	45.41	0.664	0.046
14.93	23	30.48	0.589	0.060
20.25	13	16.38	0.570	0.080

Table 5. Experimental results for 100–1000 MeV electrons. This table summarizes the results of Tables 3 and 4.

x mm	n	n'	$\left(\overline{\frac{E_x}{E_0}}\right)$	σ
0.00	112	112	1.000	0.018
4.87	112	120.40	0.835	0.027
9.80	81	93.34	0.715	0.032
14.99	42	54.02	0.592	0.045

where σ_t is the total "straggling". This quantity has been estimated from the E_x/E_0 distributions of all these electrons. The values found are 0.27 ± 0.02, 0.28 ± 0.02, 0.29 ± 0.03, and 0.26 ± 0.04 at $x = 5, 10, 15$, and 20 mm respectively. For the evaluation of errors σ a common value $\sigma_t = 0.29$ has been adopted. The logarithmic diagrams with straight lines fitted to the experimental points are shown in Fig. 9 and Fig. 10. Each point has been given a weight inversely proportional to the corresponding variance of the logarithm. The slope, k, has been calculated by the method of least squares. The first point corresponds to $\frac{E_0'}{E_0}$, where E_0' is the true value of the energy,

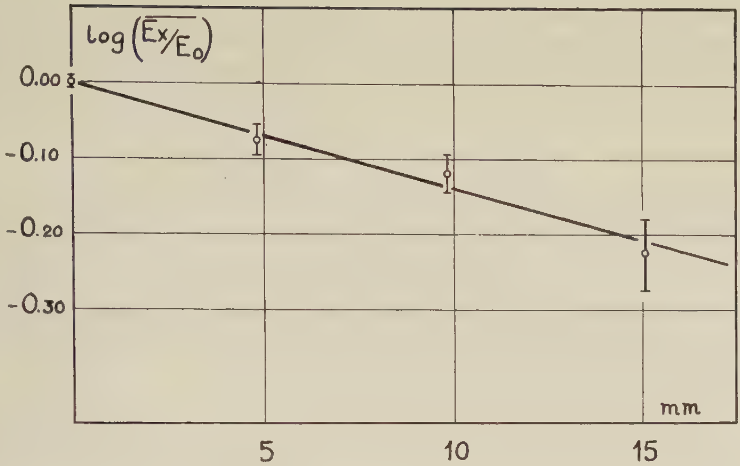

9. The logarithmic decrease of the average energy ratio as a function of the distance traversed. The figure refers to the 100–250 MeV electrons of Table 3.

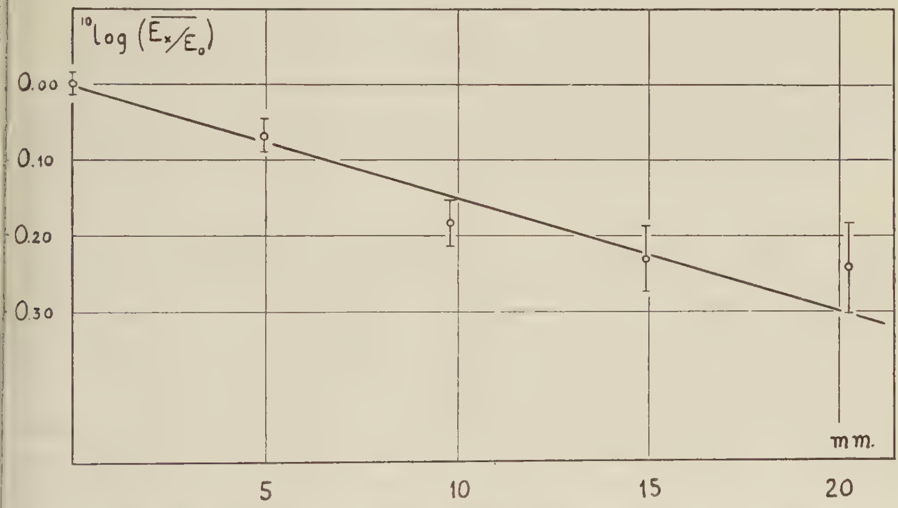

10. The logarithmic decrease of the average energy ratio as a function of the distance traversed. The figure refers to the 250–1000 MeV electrons of Table 4.

l E_0 the one estimated by the measurements. The ratio is close to 1.0, the error gned is due to the errors in the energy measurements. With the notation y = g $(\overline{E_x/E_0})$ one finds k from the relation

$$k = \frac{\overline{xy} - \bar{x} \cdot \bar{y}}{\overline{x^2} - (\bar{x})^2},$$

where the bar denotes the weighted mean of the quantity beneath. The error in is mainly due to the error in the y's. It is thus not evaluated from the residuals a this would overestimate the accuracy. From a consideration of the errors in y_i on finds

$$\frac{1}{\text{var } k} = [\overline{x^2} - (\bar{x})^2] \cdot \sum \frac{1}{\text{var } y_i}.$$

The radiation length is given by $R = \frac{{}^{10}\log e}{|k|}$, and its standard error, σ, by $\frac{\sigma}{R} = \frac{\sqrt{\text{var } k}}{|k|}$

The final results are collected in Table 6. The variation of R with energy is statisticall not significant. Therefore the total sample, 100–1000 MeV, has been formed, se Tables 5 and 6. These results are admittedly of rather low statistical weight, mainl due to the limited number of tracks available.

Table 6. The radiation length, R. Experimental results according to Tables 3, 4 and 5. Theoretical values averaged over the energy distribution; $R_{\max}$ and R_{mi} refer to the extremes of the energy region. The errors are standard deviations

Energy region MeV	R mm		Variation (theory)	
	Exp.	Theory	$R_{\max}$	$R_{\min}$
100 – 250	31 ± 5	30.3	30.6	29.6
250 – 1000	29 ± 4	29.4	29.6	28.8
100 – 1000	29 ± 3	29.8	30.6	28.8

In conclusion, some remarks on the present method may be made. Clearly it i limited to those atoms which can build up the emulsion. In the present case th cross-section is dominated by the silver and bromine atoms. More accurate result could be obtained by a further development in which a stack of stripped emulsion is exposed to mono-energetic electrons from an accelerator. The gain thereby obtaine would be (1) a larger number of measurable tracks, (2) outscattering greatly reduced and (3) primary energy known, if a magnetically analysed beam is used.

The determination of the radiation length in nuclear emulsions may have som importance for other investigations. Thus the Bremsstrahlung process has bee utilized for the detection of the β-decay of K-mesons [31]. The present investigatio shows that most electrons (about 85 %) have an E_x/E_0 less than 0.75 after a traversa of 20 mm in the emulsion; a 10 mm track length will only occasionally be suitabl for a determination of the electronic nature of the particle, whereas at length greater than 25 mm the probability of at least one significant energy loss seems to b high.

§ 2. Comparison with the theory. Discussion on results

In computing ϕ_{rad} for the emulsion the following formula is used:

$$\phi_{\text{rad}} = \frac{N_1 \phi_1 + N_2 \phi_2 + \cdots}{N_1 + N_2 + \cdots},$$

ϕ_1, ϕ_2 etc. being the cross-sections of the various constituents of the emulsion, and N_1, N_2 etc. the number of atoms per cm^3. The calculation is based on the manufacturers data of the composition of the Ilford G5 emulsion. It is observed that the Ag ($Z=47$) and Br ($Z=35$) atoms account for 94.5 % of the total cross-section. In the case of complete screening, the result was $R_\infty = 28.0$ mm (by neglecting the contribution from the atomic electrons $R_\infty = 28.8$ mm). In the high energy region the variation of ϕ_{rad} with the energy is slow, and the relative variation is rather insensitive to Z. If we start from the computed value in the case of complete screening and adopt the same relative variation as for Pb [3], the radiation length at high energies may be found. As a justification of this procedure a numerical integration was performed at $E_0 = 200\ \mathrm{mc}^2$ for Ag [30]. The relative decrease of ϕ_{rad} was found to be 9.1 %, whereas for Pb it is about 9.2 % [3]. The theoretical values are given in Table 6 together with the experimental results. In the last two columns the variation of R with energy is given according to theory. The theoretical values may be regarded accurate to about 2 per cent. Part of the uncertainty lies in the contribution from the atomic electrons, part in screening effects. There is also some uncertainty as to the exact composition of the emulsion. According to recent calculations [4, 5] a slight correction to the Born approximation is expected which would increase R. The exact magnitude of the correction has not yet been published, but it seems to be less than 3 per cent in the present case [3, 4, 5]. The experimental results do not differ significantly from the theoretical values. The agreement is in fact somewhat better than might be expected with regard to the experimental errors. It was pointed out in Section III that it is difficult to estimate the uncertainty in the systematic error correction, but that it is essentially included in the statistical error. In the case of the statistically best group of electrons, viz. 100—1000 MeV, the experimental result corresponds to a total cross-section for Bremsstrahlung which is 4 ± 10 per cent larger than that derived from theory.

Appendix 1: Energy straggling and estimation problem

The physical process studied in this paper is in fact what is called a stochastic process with the energy of the electron entering as a stochastic variable. The probability distribution of this variable depends on the distance travelled. The mean free path enters as a parameter. It is thus not out of place to consider the statistical problem of the estimation of the parameter. A fairly good approximate formula describing the probability distribution has been given by BETHE and HEITLER [2, 3]. They introduce the new variable y, by the relation $E = E_0 \exp(-y)$. The probability distribution of y is then in this approximation given by

$$\omega(y)\,dy = \frac{e^{-y}\,y^{bl-1}}{\Gamma(bl)}\,dy; \tag{1}$$

l is the distance traversed by the electron; b is related to the mean free path (R) or to ϕ_{rad} by the relation

$$b \ln 2 = N\,\phi_{\mathrm{rad}} = \frac{1}{R}. \tag{2}$$

In the emulsion $b^{-1} \simeq 20$ mm.

The problem of finding the best value of R, i.e. one with least standard error, from the energy decreases observed for a number of electrons is thus equivalent to finding the most efficient estimator of b from a sample drawn from the population (1). What function of the observed energies should then be formed in order to determine b? In the following discussion the approach to this problem and the conceptions used may be found in M. G. KENDALL, *The Advanced Theory of Statistics* [24].

The mean value of some function of the observations may be expected to be useful, although other ways might also be found. We will in the following encounter the mean of y, of e^{-y} and of $\ln y$. Any of these will provide a solution, which is called an estimator. From (1) it is seen that a sufficient estimator exists [24]. The property of sufficiency is such that no other estimator can add anything to our information about b; it is further not a limiting property, but holds also in the case of small samples. The value of b must then be found from the equation

$$\frac{d \ln \Gamma(b\,l)}{d\,(b\,l)} = \frac{1}{n} \Sigma \ln y_i \tag{3}$$

where n is the number of electrons in the sample. It is remarkable that the best method for estimating the mean free path involves the mean logarithm of the logarithm of the energy ratio. Next the intrinsic accuracy, I, may be found. This quantity provides a standard with which all other estimators may be compared. In this case it is given by

$$I = \int_0^\infty \left[\frac{\partial \ln \omega}{\partial b}\right]^2 \omega\, d y = -\int_0^\infty \frac{\partial^2 \ln \omega}{\partial b^2}\, \omega\, d y.$$

Finally
$$I = l^2 \frac{d^2 \ln \Gamma(b\,l)}{d\,(b\,l)^2}. \tag{4}$$

This function may be found from tables [25]. $(n\,I)^{-1}$ is the variance of the sufficient estimator (3). Now that the intrinsic accuracy is known for this distribution we may calculate the efficiency of any other more convenient estimator than that given by (3). Two other estimators will be considered here.

1) The mean value of the logarithm E_0/E. This estimator has been considered earlier, see HEITLER [3], and used in the experiments by BLACKETT and WILSON. The b-value is then found from

$$l\,b_1 = \frac{1}{n} \sum \ln \frac{E_0}{E}. \tag{5}$$

The variance is given by

$$\operatorname{var} b_1 = \frac{1}{n}\frac{b}{l}. \tag{6}$$

2) The mean of the energy-ratio, E/E_0, i.e. the mean of e^{-y} in (1). The b-value is then found from

$$\frac{1}{n} \sum \frac{E}{E_0} = 2^{-b_2 l} = e^{-l/R}, \tag{7}$$

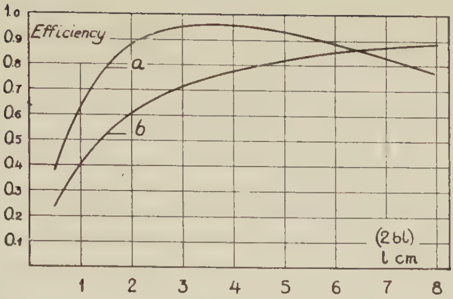

Fig. 11. The statistical efficiency of two estimators: a, the logarithm of the mean energy ratio (used in this paper), b, the mean logarithm of the energy ratio.

a relation which displays the exponential decrease of the average energy. The variance of b_2 is then given by

$$\operatorname{var} b_2 = \frac{1}{n} \frac{1}{(\ln 2)^2 l^2} \{(\tfrac{4}{3})^{bl} - 1\}. \tag{8}$$

The efficiency of a given estimator is for large samples defined by the ratio of the variance of (3) to that of (5) or (7) respectively. The efficiency is always ≤ 1; at best the equality holds. The efficiency of each estimator has been calculated for various values of l. The value of b is in these calculations assumed to be 0.50 cm^{-1} for the emulsion. The result is given in graphical form in Fig. 11. The curves may also be applied to materials other than the nuclear emulsion if the abscissa is taken as $2\,b\,l$, a dimensionless quantity.

In the first few millimeters of path length, the efficiencies of the two estimators considered are rather low. In the first few centimeters the method involving the mean energy is superiour to that based on the mean of y, and it is practically as good as the best method in the region from 3–5 cm, i.e. in the bl-region 1.5–2.5. Practically, these curves may be interpreted to express the following: we may need say, 100 electron tracks to obtain a desired statistical accuracy if we solve b from eq. (3); if we use a less efficient estimator, we can compensate the loss by increasing the number of tracks. The mean-energy estimator then needs about 160 tracks, and the estimator based on the mean logarithm of the energy about 250 tracks at $l = 10$ mm. The corresponding figures at $l = 20$ mm are 112 and 165, respectively. The conclusion to be drawn from energy-straggling considerations is that the mean-energy estimator is the better one of the two estimators investigated when applied to this investigation.

Appendix 2: Deduction of the formula for σ_z^2 when energy loss occurs

A beam of electrons initially moving in a material medium parallel to the x-axis with energy E_0 will be spread out in angle θ to the x-axis and lateral displacement y from the same axis such that at the point x the joint distribution of y and θ in the small angle approximation is given by (see Rossi-Greisen [32])

$$F(x, y, \theta) = \frac{e_0^2}{\sqrt{3}\,\pi}\,\frac{1}{x^2}\,\exp\left[-\tfrac{2}{3}e_0^2\left(\frac{\theta^2}{x} - \frac{3\,y\,\theta}{x^2} + \frac{3\,y^2}{x^3}\right)\right]. \qquad (1$$

(The formula has been rewritten to apply to the emulsion with x and y in mm θ in radians, and $e = \frac{E}{1.5}$, where E is the energy in MeV, when a scatterin factor $K = 30$ degrees × MeV × $(100\,\mu)^{-1/2}$ is adopted.) The variances of y and and the covariance of y and θ may be computed. These are

$$\overline{(y-\bar{y})^2} = \text{var}\; y = \frac{x^3}{e_0^2} \qquad (2$$

$$\text{var}\;\theta = \frac{3\,x}{e_0^2} \qquad (3$$

$$\text{cov}\;(y, \theta) = \frac{3\,x^2}{2\,e_0^2}. \qquad (4)$$

It is seen that y and θ are correlated with correlation coefficient:

$$\varrho = \frac{\text{cov}\;(y, \theta)}{\sqrt{\text{var}\; y\; \text{var}\;\theta}} = \sqrt{\frac{3}{2}} \simeq 0.87,$$

independent of the distance x and the energy E_0. If the electrons arrive at x with energy practically unaltered (E_0), then the joint distribution of y and θ is given by the above bivariate normal distribution $F_0\,(x, y, \theta)$ where the index denotes that the energy is E_0. When the electrons proceed further to L with the energy E_1 the problem is to find the joint distribution of the variables z and φ at the point L. The lateral displacement is z and the angle to the original axis is φ. This new distribution is denoted by $F\,(L, z, \varphi)$ and a little reflection shows that it is given by

$$F\,(L, z, \varphi) = \int\limits_y \int\limits_\theta F_0\,(x, y, \theta)\, F_1\,[(L-x), (z - y - \{L-x\}\,\theta), (\varphi - \theta)]\, d\,y\, d\,\theta \qquad (5)$$

where F_1 is the same function as (1) but with the variables stated and the energy E_1. It may be shown that $F\,(L, z, \varphi)$ is a bivariate normal distribution in z and φ with zero means. The quantity of interest is the standard deviation of z, denoted by σ_z. It will be a function of L, x and the two energies E_0 and E_1. By definition this quantity is given by the expression

$$\sigma_z^2 = \int\limits_z z^2\, d\,z \int\limits_\varphi d\,\varphi \int\limits_y \int\limits_\theta F_0\,(x, y, \theta)\, F_1\,[(L-x), (z - y - \{L-x\}\,\theta), (\varphi - \theta)]\, d\,y\, d\,\theta. \quad (6)$$

If the order of integration is changed, one obtains

$$\sigma_z^2 = \int\limits_y \int\limits_\theta d\,y\, d\,\theta\, F_0 \int\limits_z \int\limits_\varphi z^2\, F_1\, d\,z\, d\,\varphi.$$

change of the variables φ and z is made to new variables u and ψ such that $= u + y + (L-x)\,\theta$, and $\varphi = \psi + \theta$, yielding,

$$\sigma_z^2 = \int_y \int_\theta d\,y\,d\,\theta\,F_0 \int_u \int_\psi [u^2 + y^2 + (L-x)^2\,\theta^2 + 2\,u\,(y + \{L-x\}\,\theta) + $$

$$+ 2\,(L-x)\,y\,\theta] \cdot F_1\,[(L-x), u, \psi]\,d\,u\,d\,\psi \qquad (7)$$

$$\sigma_z^2 = \int_y \int_\theta d\,y\,d\,\theta\,F_0 \cdot \left[\frac{(L-x)^3}{e_1^2} + y^2 + (L-x)^2\,\theta^2 + 2\,(L-x)\,y\,\theta\right],$$

here the mean $\bar{u} = 0$ and the mean of u^2, i.e. var $u = \dfrac{(L-x)^3}{e_1^2}$, according to q. (2).

The next integration yields directly

$$\sigma_z^2 = \frac{(L-x)^3}{e_1^2} + \text{var}\,y + (L-x)^2\,\text{var}\,\theta + 2\,(L-x)\,\text{cov}\,(y, \theta)\,.$$

Vith the help of equations (2), (3), and (4), the end result is

$$\sigma_z^2 = \frac{L^3}{e_0^2} + (L-x)^3\left(\frac{1}{e_1^2} - \frac{1}{e_0^2}\right). \qquad (8)$$

he following checks on this formula are made. First, if the energy is constant through- ut the distance up to L, then σ_z should be independent of x and equal L^3/e_0^2. Second, f the loss of energy does not occur until $x = L$, the same result is expected, and third, f the loss of energy has already occurred at the start, one would expect $\sigma_z^2 = L^3/e_1^2$. ll these expected results are obtained from formula (8).

Appendix 3: Elastic collision between like particles

Relativistic formulae expressing the relation between the angles and the energy f the particles.

Symbols used: γ = total energy in units of the restmass of the particles
p = linear momentum
α and β = angles of collision
$\theta = \alpha + \beta$ = angle between outgoing particles.

ompare Fig. 8.

The conservation laws of momentum and energy in the frame of reference where ne particle is originally at rest, may be written:

$$p_1 = p_0\,\frac{\sin\beta}{\sin\theta}, \qquad (1)$$

$$p_2 = p_0 \frac{\sin \alpha}{\sin \theta}, \tag{2}$$

$$\gamma_1 + \gamma_2 = \gamma_0 + 1. \tag{3}$$

The relation between momentum and energy of particles with restmass ε, $p^2 c^2 = \varepsilon^2 (\gamma^2 - 1)$, is inserted in the squared relations (1) and (2) and their difference may be written

$$\gamma_1^2 - \gamma_2^2 = (\gamma_1 - \gamma_2)(\gamma_1 + \gamma_2) = (\gamma_1 - \gamma_2)(\gamma_0 + 1) = (\gamma_0^2 - 1)\frac{\sin^2 \beta - \sin^2 \alpha}{\sin^2 \theta}.$$

This relation, together with eq. (3), forms a simple system of equations:

$$\gamma_1 - \gamma_2 = (\gamma_0 - 1)\frac{\sin^2 \beta - \sin^2 \alpha}{\sin^2 \theta}$$

$$\gamma_1 + \gamma_2 = \gamma_0 + 1.$$

The solution is given by:

$$\gamma_1 = \frac{\sin \alpha \cos \beta + \gamma_0 \cos \alpha \sin \beta}{\sin \theta}$$

$$\gamma_2 = \frac{\gamma_0 \sin \alpha \cos \beta + \cos \alpha \sin \beta}{\sin \theta}.$$

Any of these relations together with the corresponding squared relations (1) or (2) produces the desired formulae:

$$\gamma_0 + 1 = 2 \cot \alpha \cot \beta, \tag{4}$$

$$\gamma_1 + 1 = \frac{2 \cos \beta}{\sin \alpha \sin \theta}, \tag{5}$$

$$\gamma_2 + 1 = \frac{2 \cos \alpha}{\sin \beta \sin \theta}. \tag{6}$$

All the energies (γ_0, γ_1, γ_2) are given by the collision angles α and β, according to the exact relations (4)–(6).

In the case of electrons the small angle approximation is given by the very simple system:

$$E_0 = \frac{1}{\alpha \beta} \text{ MeV},$$

$$E_1 = \frac{1}{\alpha\,\theta}\,\mathrm{MeV}\,,$$

$$E_2 = \frac{1}{\beta\,\theta}\,\mathrm{MeV}\,.$$

angles are measured in radians; 2 mc^2 has been approximated by 1 MeV.

nstitute of Physics, University of Uppsala, Sweden, April 1955.

REFERENCES

Carlson, A. G., J. E. Hooper, and D. T. King, Phil. Mag. *41*, 701 (1950).
Bethe, H., and W. Heitler, Proc. Roy. Soc. A *146*, 83 (1934).
Heitler, W., The Quantum Theory of Radiation, 3rd ed. Oxford (1954).
Bethe, H. A., and L. C. Maximon, Phys. Rev. *93*, 768 (1954).
Davies, H., H. A. Bethe, and L. C. Maximon, Phys. Rev. *93*, 788 (1954).
Anderson, C. D., and S. H. Neddermeyer, Phys. Rev. *50*, 263 (1936).
Blackett, P. M. S., Proc. Roy. Soc. A *165*, 11 (1938).
Wilson, J. G., Proc. Roy. Soc. A *166*, 482 (1938).
Corson, D. R., and A. O. Hanson, Ann. Rev. of Nucl. Sci. *3*, 67 (1953).
Lanzl, L. H., and A. O. Hanson, Phys. Rev. *83*, 959 (1951).
Koch, H. W., and R. E. Carter, Phys. Rev. *77*, 165 (1950).
De Wire, J. W., and L. A. Beach, Phys. Rev. *83*, 476 (1951).
Powell W. M., W. Hartsough, and M. Hill, Phys. Rev. *81*, 213 (1951).
Stokes, R. H., Phys. Rev. *84*, 991 (1951).
McDiarmid, I. B., Phil. Mag. *43*, 1003 (1952).
Motz, J. W., W. Miller, and H. O. Wyckoff, Phys. Rev. *89*, 968 (1953).
Curtis, C. D., Phys. Rev. *89*, 123 (1953).
Fisher, P. C., Phys. Rev. *92*, 420 (1953).
Bethe, H. A., L. C. Maximon, and F. Low, Phys. Rev. *91*, 417 (1953).
Fowler, P. H., Phil. Mag. *41*, 169 (1950).
Baroni, G., A. Borsellino, L. Scarsi, and G. Vanderhaeghe, Nuovo Cim. *10*, 1653 (1953).
Ekspong, G., Ark. Fys. *9*, 49 (1954).
Cosyns, M., and G. Vanderhaeghe, Bull. Cent. Phys. Nucléaire Bruxelles, No 15, (1950).
Kendall, M. G., The Advanced Theory of Statistics, Vol. I & II. Ch. Griffin & Co., Ltd., London (1948).
Jahnke-Emde, Tables of Functions. Dover Publications, New York.
Modesitt, G. E., and H. W. Koch, Phys. Rev. *77*, 175 (1950).
Jost, R., J. M. Luttinger, and M. Slotnick, Phys. Rev. *80*, 189 (1950).
Hooper, J. E., and D. T. King, Phil. Mag. *41*, 1194 (1950).
Wu, C. S., and I. Shaknow, Phys. Rev. *77*, 136 (1950).
See e.g. E. Segré, Experimental Nuclear Physics, Vol. I, p. 260. John Wiley & Sons, Inc., New York (1953).
Friedlander, M. W., D. Keefe, M. G. K. Menon, and L. van Rossum, Phil. Mag. *45*, 1043 (1954).
Rossi, B., and K. Greisen, Rev. Mod. Phys. *13*, 240 (1941).

Tryckt den 30 april 1955

Uppsala 1955. Almqvist & Wiksells Boktryckeri AB

ARKIV FÖR FYSIK Band 9 nr 34

Communicated 26 January 1955 by AXEL E. LINDH and HARALD NORINDER

Photographs of the light phenomena of positive corona

By REINHARDS SIKSNA

With 3 figures in the text

References may be found in the literature that light phenomena around a orona electrode were changed in dependence on the magnitude of the potential pplied in the case of positive corona [2, 3, 5, 6]. The principal subject of the vestigations quoted was, however, not the light phenomena of corona and herefore they were described as by-phenomena observed. It seemed to us that he investigation of the corona light phenomena has been disregarded until now nd our first intention was, therefore, to find the conditions for a better documentation of the phenomena in question. Results of an attempt of photographing the light phenomena due to positive corona are described in this paper.

The photographic camera used was equipped with a 4.5 cm diameter quartz bjective of F:4.6 which in some cases was stopped down to F:11. The corona evices used were: (1) one with a cylindric arrangement of the electrodes, and 2) the ends of razor blades of two different shapes towards a plane.

Results

1. *With the cylindric arrangement.*—An aluminium cylinder with the inner dia-meter of 30 mm was connected with the negative terminal of a high tension ource. Along the axis of this cylinder, a kanthal wire of 0.5 mm diameter and 0 mm long was placed and connected with the positive terminal of the high ension source. A brass sphere of 5 mm diameter was fixed on the free end of he corona wire to prevent discharge on the sharp end.

At a potential of approx. 10 kV applied to the wire a noise and a light phenomenon starting from the wire and reaching the negative cylinder were observed. ntense pulses were observed simultaneously on a cathode-ray oscillograph conected with the corona device. By increasing the potential these phenomena ncreased in intensity reaching a maximum at approx. 11 kV and decreased in ntensity at higher potentials. This phenomenon is that called by us "noisy brush" n accordance with a name introduced by FITZSIMMONS [1]. The photographs of his stage of the positive corona are shown in Fig. 1 as pictures *2*, *3* and *5* btained by photographing the phenomenon on plates being exposed initially for btaining the shape of the electrodes, and in pictures *6* and *7* obtained when hotographing solely the corona light phenomenon. As may be seen, the diffuse ght starting from the wire is not evenly distributed on the surface of the wire, ut is coming from single points. This fact might be explained by an assumption

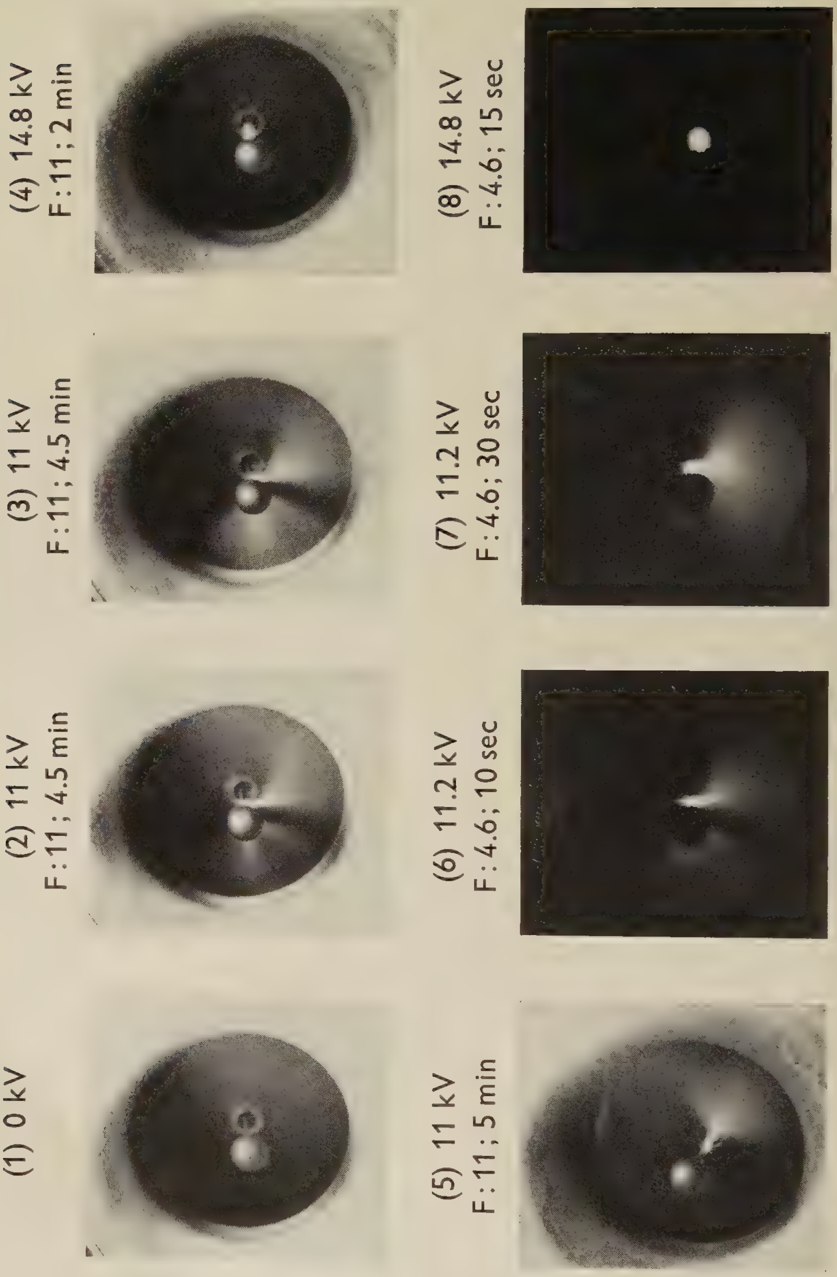

(1) 0 kV

(2) 11 kV
F : 11 ; 4.5 min

(3) 11 kV
F : 11 ; 4.5 min

(4) 14.8 kV
F : 11 ; 2 min

(5) 11 kV
F : 11 ; 5 min

(6) 11.2 kV
F : 4.6 ; 10 sec

(7) 11.2 kV
F : 4.6 ; 30 sec

(8) 14.8 kV
F : 4.6 ; 15 sec

Fig. 1. Light phenomena of positive corona around a wire in a cylinder.

t the surface was no more completely even after some time of working but corroded at certain points or small areas. Thus, local points might be formed the initially even surface, the electrical field might be higher at these points the discharge might be centred on these points. As mentioned above, by easing the potential the entire "noisy brush" phenomenon decreased in intenand ceased at a certain potential. A bluish light layer appeared now near corona wire (Fig. 1, pictures *4* and *8*). This was the light phenomenon of steady positive corona.

. *From a rounded end of a razor blade.*—As may be seen on the photographs in . 1, a part of the light phenomena obtained in the cylindric arrangement of electrodes was shadowed at the end of the corona wire and photographs ld be obtained only obliquely to the wire. Therefore, another arrangement s tried. A sphere towards a plane would be the ideal, but the potential essary for the sphere of a reasonable diameter would be comparatively high. was observed in other experiments with corona a reasonable arrangement can, wever, be built by using a positive electrode with two different radii of curture: one of which is great and the other small [4]. Such an electrode can simply built of a comparatively thin wire bent in form of a loop with a ater radius of curvature. A mechanically more stable arrangement was obtained using a razor blade (0.1 mm thick) one end of which was rounded and used the positive electrode (Fig. 2, above). All stages considered above of the charge were observed with this arrangement of the electrodes and the corrending light phenomena were obtained very clearly as shown in Fig. 2 (below) comparatively low potentials applied. The lucid cylinder near the positive ctrode and the diffuse light beam reaching the negative electrode and relating the noisy brush stage of the corona discharge are shown in the first two tures (Fig. 2, below) at potentials of 13.2 and 13.4 kV. Besides the main beam, me by-discharges can be noted. When increasing the potential the main disarge increased in intensity at the beginning and decreased at a higher potential, ile the by-discharges increased farther in order to decrease and cease at a ll higher potential. A new stage with the blue light layer was observed at prox. 14 kV in the nearest surroundings of the positive electrode. This light yer increased in intensity by increasing of the potential but did not extend the space to the cathode. By a farther increasing of the potential, a spark oke down the gap. When after reaching the stage with the blue layer (at prox. 14 kV) the potential decreased (by discharging of the rectifier condenser the corona current) an opposite succession of the stages was observed: the ue layer near the positive electrode diminished in intensity and ceased, the ht beams appeared, increased in intensity, diminished and ceased at the end. ie points were the same on the positive electrode at which the beams with e lucid cylinders were initiated independently whether decreasing or increasing e potential. Thus it seemed that the origin of the noisy brush was centred certain points of the positive electrode. It can be assumed that local small ievennesses were the points at which an intense field was present, and this is the cause for the formation of the "noisy brush". A fact can be added to nfirm this assumption: after a sparking through the gap, the points on the zor blade from which the noisy brush was initiated, were not the same as fore, new unevennesses may be built on the electrode by the sparking.

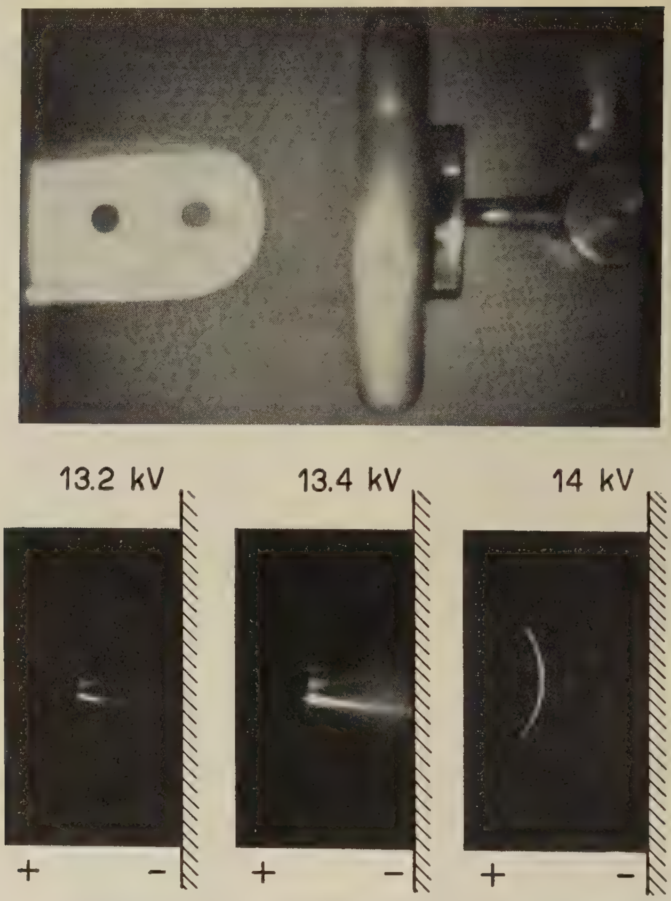

Fig. 2. Light phenomena of positive corona around the rounded end of a razor blade.

3. *From the more complicated end of a razor blade.*—The centring of the origin of the noisy brush discharge on certain points of the positive electrode was more marked by using a more complicated end of a razor blade, as shown in Fig. 3 where, above, the arrangement of the electrodes is shown, and below the pictures of the discharge at different potentials applied.

As may be seen on the photographs, the bright shining cylinders or points are shown very markedly near the sharp points on the positive electrode. The diffuse beams follow along the lines of forces. It can be assumed that the highest field is where the light phenomena appeared at the beginning. When increasing the potential the field increases too and it can reach values sufficient for initiating of the noisy brush discharge also at other points on the positive electrode. More points were built gradually at which noisy brush could be initiated. Moreover, the intensity of the light phenomena diminished now on the points where they were built at the beginning when the potentials was lower. It is difficult to assume that the field was diminished at these points by increasing the potential.

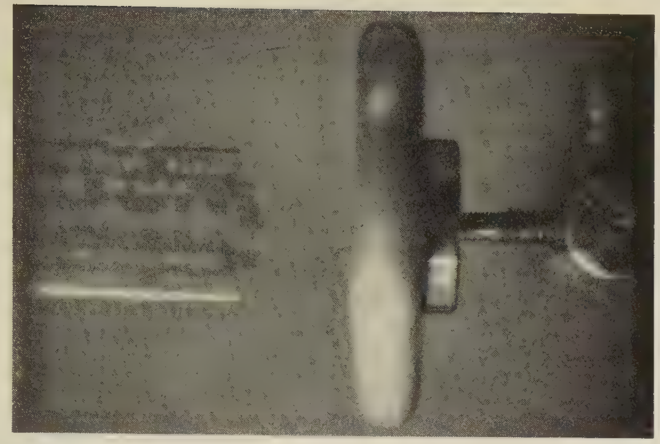

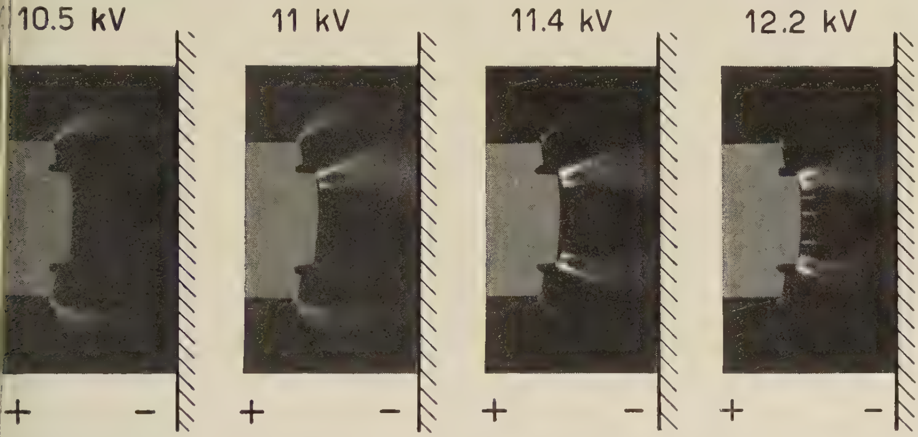

;. 3. Light phenomena of positive corona from a razor blade with complicated shape of the end.

could, therefore, be assumed that an interval of the field strength exists vouring initiation of the noisy brush. If the field increases farther the noisy ush ceases. When decreasing the potential the observed phenomena appeared the opposite succession. At repeated increasing and decreasing of the potential plied the points were the same on the positive electrode where the noisy brush s initiated. For the shape of the positive electrode considered here it was not ssible to increase the potential so hight that the noisy brush stage of the scharge would be passed over because the discharge current through the gap s so high that the power of the high tension source used did not suffice the necessary supply.

Acknowledgements

The author is grateful to the Director of the Institute of High Tension Research of the iversity of Uppsala, Professor H. Norinder, for providing him with facilities to carry out this work and for his interest in its progress. The Swedish Natural Science Research Council deserves to receive thanks for placing means at the disposal of the Institute to perform this investigation. The author gratefully acknowledges the assistance of Mr. A. METNIEKS.

Institutet för högspänningsforskning vid Uppsala Universitet, November 1954.

REFERENCES

1. FITZSIMMONS, K. E., Threshold field studies of various positive corona phenomena. Phys. Rev. *61*, 175–182 (1942).
2. GÄNGER, B., Die elektrische Festigkeit verdichteter Gase. Arch. f. Elektrotechnik *34*, 633–652 (1940).
3. LOEB, L. B., Recent developments in analysis of the mechanisms of positive and negative coronas in air. J. Appl. Phys. *19*, 882–897 (1948).
4. SIKSNA, R., Two different breakdowns between a positive electrode with small curvature and a plane. Ark. fysik *9*, Nr 6, 77–82 (1954).
5. UHLMANN, E., Der elektrische Durchschlag von Luft. Dissertation 1929, T. H. Braunschweig.
6. WAGNER, L., Korona-Entladungen an der Spitze-Platte-Funkenstrecke. Arch. für Elektrotechnik *40*, 331–342 (1952).

Tryckt den 18 augusti 1955

Uppsala 1955. Almqvist & Wiksells Boktryckeri AB

ARKIV FÖR FYSIK Band 9 nr 35

Communicated 23 February 1955 by MANNE SIEGBAHN and BENGT EDLÉN

The RaC–RaC′ decay

By SVEN A. E. JOHANSSON

With 3 figures in the text

Summary

The RaC–RaC′ decay has been investigated by means of a coincidence scintillation spectrometer. The gamma-gamma and beta-gamma coincidence ralations have been studied in detail. 20 gamma-rays have been arranged in a consistent level scheme, which is in good agreement with the energy spectrum of the long-range alpha particles from RaC′.

Introduction

The hard gamma-radiation from a radium source is emitted in the decay RaC–RaC′. This radiation has been studied for a long time, almost since the discovery of radioactivity. v. BAYER, HAHN, and MEITNER [1] discovered and measured a number of conversion lines. This work was repeated and extended by RUTHERFORD and ROBINSON [2]. Later, ELLIS and co-workers [3, 4] made a series of careful measurements of the internal conversion lines. They also studied the gamma-radiation by means of the photo-electric effect. ITOH and WATASE (5) used the Compton recoil electrons to stydy the gamma-radiation. LATYSHEV and co-workers [6] studied the radiation from RaC carefully, using various methods. In addition to the internal conversion spectrum, they also studied the gamma-radiation by recording Compton electron spectra and positron spectra from the pair-production due to the high-energy gamma-rays. More recently MANN, OZEROFF, and PEARCE [7, 8] investigated the photo-electron spectrum. MIWA and KAGEYAMA [9], as well as CORK and co-workers [10], measured the internal conversion spectrum. KAGEYAMA [11] studied the gamma-radiation by determining the Compton recoil spectrum. Quite recently, the internal conversion spectrum was remeasured by MLADJENOVIC and SLÄTIS [12] and the Compton spectrum of the gamma-radiation by MLADJENOVIC and HEDGRAN [13].

The continuous beta-spectrum has been analyzed by LATYSHEV [6] and by KAGEYAMA [14].

The agreement between the various measurements is not entirely satisfactory. Some of the older works are, of course, rather unreliable. But the modern works, too, disagree on many points. A number of strong gamma-rays are well established. Several weak rays have, however, been reported in some measurements but not been found in others. The intensity values show considerable variations.

Table 1. Relative gamma-ray intensities.

Energy keV	Ellis	Latyshev	Kageyama	Mladjenovic-Hedgran
609	100		100	100
769	10		14	22
935	10		12	11
1120	31	30	29	76
1238	10	7	11	28
1281		5		
1378	10	15	10	32
1509		9	8	11
1620		7		
1690		5		
1764	39	30	36	61
1849		5	2.5	6
2117		5		
2204	11	12	11	20
2432		6	6	7

Apparently only one attempt has been made to set up a decay scheme for the transition RaC–RaC′, viz. by Ellis in 1934 [15]. The decay scheme comprises no less than 55 gamma-rays. The energy values were taken from the measurements of the internal conversion spectrum. The intensity was known for only 9 of these gamma-rays. The procedure used for setting up the scheme is open to serious objections. Twelve levels were taken from the energy values of the long-range alpha-particles from RaC′. Twelve more levels were added in order to accomodate all the gamma-rays. A rather large tolerance was allowed in the energy fit; as a result a variety of different level systems could be proposed. All except one were ruled out by intensity considerations. For most of the gamma-rays, however, the intensity was not known. Therefore spin values were assigned to the different levels and the intensity values were calculated from the known intensity values of the internal conversion lines. This procedure must be regarded as somewhat arbitrary.

The safest way to establish a decay scheme, especially a complicated one, is to perform coincidence measurements. The aim of the present work was to do this in the case of the decay RaC–RaC′. The coincidence measurements made it possible to set up a consistent decay scheme. This scheme was in good agreement with the energy values reported. After the present work had been completed, the paper of Mladjenovic and Slätis [12] on the internal conversion spectrum appeared. Their very accurate energy values show especially satisfactory agreement. Their values have therefore been used in the present paper.

The radiation of RaC

The relative intensity values of four of the more extensive measurements are listed in Table 1. The values of Ellis [3] and Kageyama [11] are in good agreement. The values of Latyshev *et al.* have been normalized so as to get the same value for the 1120 keV gamma-ray as the mean of the two first-mentioned measurements, after which a good agreement is obtained. This fact is especially gratifying since the measurements were performed according to several different methods; photo-electron, Compton electron and positron spectra were measured. The intensity values of Mla-

Table 2.

nergy keV	Intensity of gamma-rays, % of disintegrations	Intensity of conversion lines, % of disintegrations × 10^2	K conversion coefficients × 10^3	Multipole assignments	Multipole assignments according to Latyshev
609	39.4	37	9.4	$E2$	
769	6.0	4.2	7.0	$E2$	
935	4.3	4.3	9.9	$E2$, $M1$	
1120	16.3	12.6	7.7	$E2$, $M1$	
1155	—	1.8	—	—	
1238	5.5	5.6	10.2	$M1$, $E2$	
1281	2.0	1.2	6.0	$E2$, $M1$	
1378	6.6	2.9	4.3	$E2$	$E2$
1416	—	28	—	—	
1509	3.7	1.5	4.1	$E2$, $M1$	$E2$
1620	2.8	—	—	—	
1690	2.0	—	—	—	
1728	—	0.8	—	—	
1764	16.3	4.5	2.7	$E2$	$E2$
1849	1.8	0.6	3.3	$E2$, $M1$	$E2$
2017	—	0.4	—	—	
2117	2.0	0.4	2.0	$E2$	
2204	5.3	1.2	2.2	$E2$	$E2$
2432	2.5	—	—	—	$E2$

jenovic and Hedgran are also shown in the table. The agreement with the other hree measurements is not entirely satisfactory. The ratio between the intensity alues for low-energy and high-energy gamma-rays is different. In the following iscussion we have used the mean values of the four series in Table 1.

All the gamma-rays reported are listed in Table 2. The energy values are taken om the internal conversion spectrum of Mladjenovic and Slätis. The values for vo additional gamma-rays are from the paper of Latyshev. Table 2 also gives the bsolute intensity values in per cent of the total number of disintegrations, calculated sing the mean of the relative values of Table 1. To do this calculation it is necessary know the decay scheme and the branching ratios of the beta-radiation. We have sed the scheme resulting from the coincidence measurements reported in this paper. he branching ratios are taken from Latyshev *et al.* The resulting intensity values e listed in Column 2 of Table 2. Column 3 shows the intensity values of the internal onversion K lines in per cent of the total disintegrations. The values listed are the ean of the values reported by Ellis [3], Latyshev [6] and Mladjenovic and lätis [12]. It is then possible to calculate the internal conversion coefficients of the shell which are listed in Column 4. A comparison with the theoretical K conversion oefficients of Rose *et al.* [16] makes it possible to find the multipole character of e gamma-rays. Column 5 shows the result of this comparison. If the experimental alue is close to the theoretical value for electric quadrupole or magnetic dipole, is denoted with a single symbol. If it lies between the theoretical values, both symols are used, the first symbol giving the nearest theoretical value. Finally, Column shows the multipole assignments made by Latyshev using the internal conversion ositron spectrum. They check well with the other assignments.

For the beta-radiation, LATYSHEV [6] reports two components with end points at 3170 and 1650 keV and intensities of 23 and 77 per cent, respectively. KAGEYAMA [14] found three components at 3200, 1650 and 1000 keV. The intensity values reported are 23, 57 and 20 per cent, respectively.

The apparatus

The apparatus used in this work has been described in detail elsewhere [17]. It consists of two scintillation spectrometers connected in coincidence. Each one can be used either as a beta- or gamma-spectrometer, depending on the crystal material. The source is mounted between the crystals of the two spectrometers. One of the spectrometers is provided with a single channel analyzer which is used to select a certain part of the radiation registered by the spectrometer. One can, for example, put the channel on a peak in the pulse-distribution of a gamma-spectrum, thereby selecting a certain gamma-ray. It is also possible to select beta-particles of a certain energy in a beta-spectrum. The apparatus records those pulses from the second spectrometer which are in coincidence with the selected pulses from the first spectrometer. The pulses are displayed on an oscilloscope and the pulse distributions are obtained by photographing the screen of the oscilloscope. The pictures are analyzed by means of a microphotometer. The pulse distributions are finally calculated from the photometer traces by means of calibration curves.

Experimental results

Fig. 1 shows a microphotometer trace of the gamma-ray spectrum of RaC. Most of the gamma-rays are easily discernible. The 1378 keV peak is unusually broad and might correspond to two gamma-rays of about the same energy. This fact has also been noted by MLADJENOVIC and HEDGRAN [13].

A number of coincidence measurements have been performed. The coincidence spectra are similar to the spectrum in Fig. 1, although some gamma-rays are missing. In this way a fairly complete information about the coincidence relations can be obtained.

First the channel of the analyzer was set to select the 609 keV gamma-ray and the corresponding coincidence gamma-spectrum was recorded. The photometer trace is shown in Fig. 2. It shows definitely that the following gamma-rays are in coincidence with the 609 keV ray: 769, 935, 1120, 1238, 1509 and 1620 keV.

Next, the channel was set to select beta-rays of different energies and the corresponding coincidence gamma-spectra were recorded. The channel was set at 650, 870, 1090, 1300, 1520, 1740, 1960, 2180, 2400, and 2620 keV. The channel width was 200 keV. When the channel was moved towards higher energies, the shape of the coincidence spectra were changed. The gamma-ray peaks disappeared one after the other. At the lowest settings the coincidence spectra are similar to the total spectrum in Fig. 1, except that the highest peak around 2200 keV, attributed to the 2204 keV gamma-ray, has disappeared. The very weak peak around 1620 keV is also absent. The next gamma-rays to become weaker are the rays at 1764, 1238, and 1120 keV. They are almost gone at a beta-ray energy of 1500 keV. The next gamma-rays to disappear are the ones at 1509 and 935 keV. The only ones remaining are the 609, 769 and 1378 keV rays. The last two disappear for beta-ray energies between 1700 and 1900 keV. The 609 keV gamma-ray remains up to about 2500 keV. It is, however,

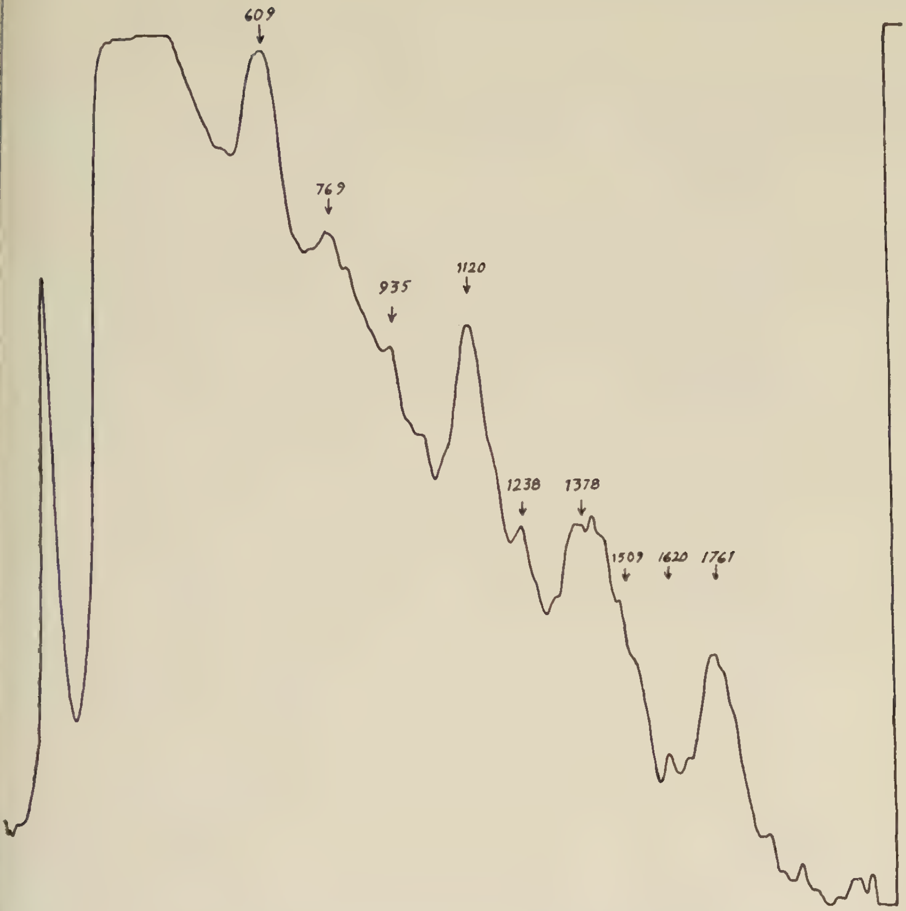

Fig. 1. Microphotometer trace of the gamma-ray spectrum of RaC.

eaker than expected if it is assumed that the high energy beta-groups goes to the)9 keV level. We must therefore assume that only a weak beta-ray group with an ıd point at about 2500 keV goes to the 609 keV level. Its intensity can be estimated › about 10 per cent of that of the highest beta-group, i.e. 2 per cent.

The decay scheme

The coincidence measurements make it possible to set up a consistent decay heme, shown in Fig. 3. The gamma-gamma coincidence measurements give sufficient formation to arrange most of the gamma-rays. The gamma-rays in coincidence ith the 609 keV gamma-ray establish a number of levels. Most of the other gamma-ıys fit in this level system as cross-over transitions. The fit is surprisingly good; ıe mean error for five of the gamma-rays is 0.05 per cent which indicates a very ›od accuracy in the energy measurements of MLADJENOVIC and SLÄTIS [12]. In the

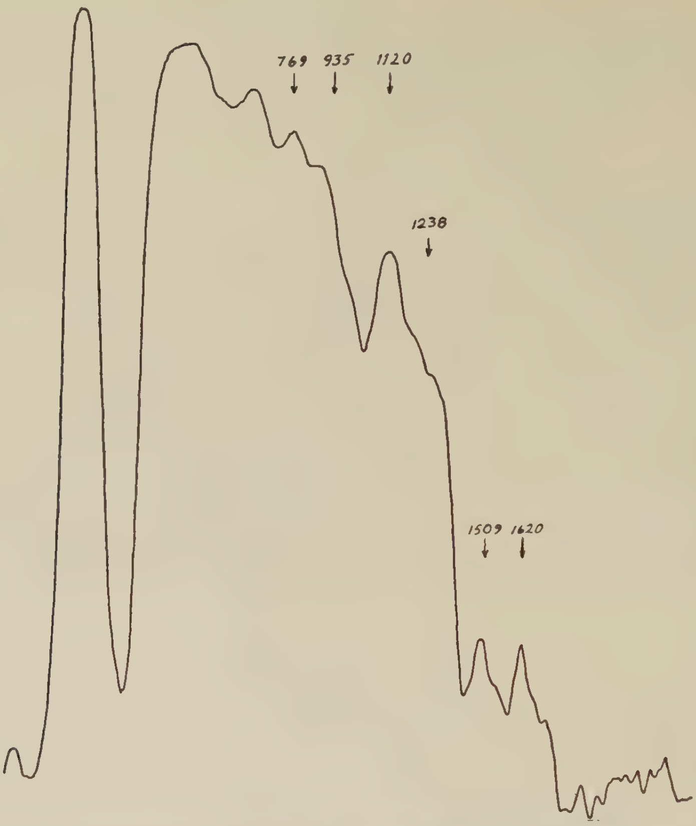

Fig. 2. Microphotometer trace of the gamma-ray spectrum in coincidence with the 609 keV gamma-ray.

case of the 2204 keV gamma-ray the fit is considerably less good, due to uncertainty in the energy value of the 1620 keV gamma-ray, known only from the measurements of LATYSHEV *et al.* [6]. The 1764 and 2432 keV gamma-rays are assumed to go to the ground state since they show no coincidence effect with the 609 keV gamma-ray. The 1416 keV gamma-transition is only known from the strong lines in the internal conversion spectrum. No corresponding gamma-ray has been found. It seems to be completely converted and is therefore assumed to be a zero-zero transition going from a 0 + state to the ground state.

All but three of the gamma-rays listed in Table 2 have now been incorporated in the decay scheme. The remaining three rays at 1281, 1690 and 2017 keV are all so weak that no information can be obtained from coincidence measurements. However, the energy spectrum of the long range alpha-particles from RaC′ [18] makes it possible to find the position of these gamma-rays in the scheme. Among the long-range alpha-group there are three with energy values corresponding to levels at 1283, 1663 and 2015 keV. The agreement in energy is so good that the three gamma-rays are likely to be transitions from these levels to the ground state.

The beta-gamma coincidence measurements are in good agreement with the decay

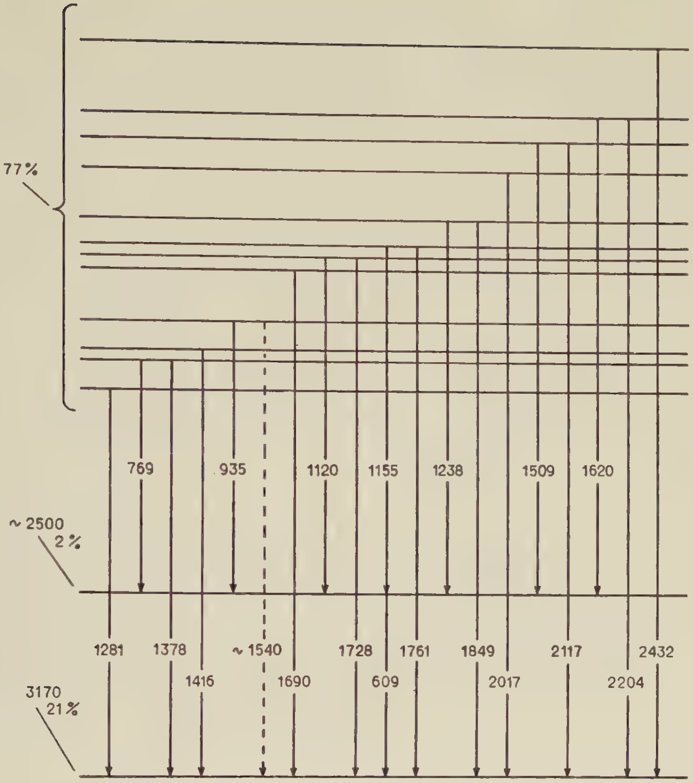

Fig. 3. The proposed decay scheme. The dotted transition is only tentative.

scheme proposed. There is, however, one inconsistency. The peak at 1509 keV does not disappear until the channel is set on beta-ray energies between 1500 and 1700 keV. A possible explanation may be that the 1509 keV peak is due to two gamma-rays, one at 1509 keV and the other one at a slightly different energy. The second one might be a transition from the 1545 keV level. This would be in good agreement with the coincidence measurements.

According to the proposed decay scheme, one should expect several beta groups to go to the various levels. According to the published beta-ray spectra there are only two or three groups. There is, however, a certain agreement in energy values. The levels of RaC′ are approximately arranged in groups. One group has a mean energy of about 1450 keV. This corresponds to a beta-ray energy of 1700 keV, which is close to the reported value for one of the beta-ray groups. There is another group of levels with a mean energy of about 2200 keV, corresponding to a beta-ray energy of about 1000 keV, i.e. exactly the value reported by Kageyama for the third beta-group of RaC. Hence the general trend of the beta-spectrum is in agreement with the decay scheme. If, however, there is a beta-group going to each level, one should expect the Fermi plot to be composed of several small straight portions. They would not be resolved but give a general bending of the plot. However, this is true only on the assumption that the beta-components have an allowed shape. If the spin assignments, which will be discussed later, can be trusted, then all the beta-groups in question have a forbidden shape. It is easy to show that, by adding two forbidden components of the same intensity but with somewhat different end-points, one can obtain a distribution which is reasonably straight in the upper end. There is a possibility, therefore, that the experimental beta-spectrum is consistent with the assumption of many beta-groups.

Another possibility is that some levels are fed not by a beta-ray group but by a gamma-transition from higher levels. However, no gamma-rays belonging to RaC and with the right energy values, have been reported. It seems likely that there are gamma-transitions between the higher levels. The question is whether their intensity is sufficiently high to affect appreciably the branching ratios of the beta-ray groups.

The intensity values listed in Table 2 provide a check of the proposed decay scheme. The sum of the intensity values of the gamma-rays going to the 609 keV level, is 38.6 per cent. The intensity of the 609 keV gamma-ray, minus the intensity of the weak beta-ray group going to the 609 keV level, is 37.4 per cent, a very satisfactory agreement.

The experimental results provide some information about the spin and parity of the levels in RaC′. The ground state has, of course, the spin 0 +. The 609 keV gamma-ray is an $E2$ transition according to the multipole assignment of Table 2. Hence the 609 keV level has the spin 2 +. This agrees with the general rule of the spin of the first excited state in even-even nuclei. The log *ft*-value of the 3170 keV beta-group is 7.8 and that of the beta-group going to the 609 keV level approximately 8.7. The spin of RaC is then presumably 0 −. It is interesting to compare this value with the predictions of the shell model. RaC has one proton in the $h_{9/2}$ shell and the odd neutron in the $g_{9/2}$ shell. According to the NORDHEIM rules [19] the spins subtract, giving the total spin 0 −.

The multipole assignments of Table 2 give information about the spin values of some levels in RaC′. The ground state transitions from the levels at 1378, 1764, 1849, 2117, 2204, and 2432 keV seem to be rather pure $E2$ transitions, which indicates that these levels have the spin 2 +. The multipole character of the ground state transitions from the 1544 and 1728 keV levels is not known. The transitions to the 609 keV level are mixed $M1 + E2$ transitions. It seems rather likely that these levels also have the spin 2 +. The 1416 keV level has the spin 0 + as discussed above.

It is interesting to compare the proposed decay scheme with the level system obtained from the energy spectrum of the long-range alpha particles from RaC′ [18]. The following levels were found: 608, 1283, 1412, 1663, 1844, 2015, 2138, 2268, 2439, 2513, 2697, and 2880 keV. The first seven levels are found in the decay scheme, if levels corresponding to the weak gamma-rays 1281, 1690 and 2017 keV are included. Four of the highest levels are not found in the decay scheme. The excitation of these levels is probably so weak that the corresponding gamma-rays are too weak to be detected.

On the other hand, there are several levels in the decay scheme with no corresponding long-range alpha-group. This means, of course, that these levels have a shorter lifetime than the others. It is possible to get quantitative information about the lifetime of a level from the intensity of the corresponding alpha-group and the half-life of RaC′. For the 609 keV level, the lifetime is calculated to 10^{-10} sec. The same value is obtained when using Weisskopf's lifetime formula (20) for an $E2$ transition. This agreement supports the spin assignment for the 609 keV level.

ACKNOWLEDGEMENTS

he present work was performed at the Institute for Atomic Research and Department of sics, Iowa State College, Ames, Iowa, U.S.A. The author wants to express his sincere appre- ion of the hospitality extended to him during his stay in Ames.

REFERENCES

O. v. Bayer, O. Hahn, and L. Meitner, Phys. ZS *12*, 1099 (1911).
E. Rutherford and H. Robinson, Phil. Mag. Ser. 6, *26*, 717 (1913).
C. D. Ellis and G. H. Aston, Proc. Roy. Soc. *129 A*, 180 (1930).
C. D. Ellis, Proc. Roy. Soc. *143 A*, 350 (1934).
J. Itoh and Y. Watase, Proc. Phys.-Math. Soc. Jap. Ser. 3, *23*, 142 (1941).
G. D. Latyshev, Rev. Mod. Phys. *19*, 132 (1947).
K. C. Mann and M. J. Ozeroff, Can. J. Res. *27 A*, 164 (1949).
R. M. Pearce and K. C. Mann, Can. J. Phys. *31*, 592 (1953).
M. Miwa and S. Kageyama, J. Phys. Soc. Jap. *5*, 416 (1950).
J. M. Cork *et al.*, Phys. Rev. *83*, 681 (1951).
S. Kageyama, J. Phys. Soc. Jap. *7*, 93 (1952).
M. Mladjenovic and H. Slätis, Arkiv för Fysik *8*, 65 (1954).
M. Mladjenovic and A. Hedgran, Arkiv för Fysik *8*, 49 (1954).
S. Kageyama, J. Phys. Soc. Jap. *8*, 689 (1953).
C. D. Ellis, International Conference on Physics, London 1934, 43.
M. E. Rose, G. Goertzel, B. I. Spinrad, J. Harr, and P. Strong, Phys. Rev. *83*, 79 (1951).
Sven A. E. Johansson and S. Almquist, Arkiv för Fysik *5*, 427 (1952).
W. B. Lewis and B. V. Bowden, Proc. Roy. Soc. *145 A*, 235 (1934).
L. W. Nordheim, Rev. Mod. Phys. *23*, 322 (1951).
V. F. Weisskopf, Phys. Rev. *83*, 1073 (1951).

Tryckt den 18 augusti 1955

Uppsala 1955. Almqvist & Wiksells Boktryckeri AB

ARKIV FÖR FYSIK Band 9 nr 36

Communicated 10 March 1954 by MANNE SIEGBAHN and ERIK HULTHÉN

Low energy levels in N^{16}

By R. T. PAULI

With 15 figures in the text

Table of contents

1. Introduction 572
2. Principle of the present investigation 572
3. Experimental arrangements 573
4. Targets 573
5. Beam energy 573
6. Angle measurement 573
7. Calibration of the spectrometer 574
8. Evaluation of the spectral lines 574
9. External layers on target 575
10. Results 577
11. Errors 578
12. Search for other α-groups 578
13. Conclusion 581
14. Discussion 582
15. Analogous states in N^{16} and O^{16} 582

Appendix

I. Production of thin targets of O^{18} 586
  1. Types of targets used 586
  2. Energy spread due to finite thickness of target 586
  3. The ratio $n_t\,\Delta E_2$ for oxygen targets on different backings 587
  4. Production of surface-oxidized targets 587
  5. Thin targets produced by magnetic separation 588
  6. Method for analysis of O^{18}-distribution. 588
  7. Collecting efficiency and O^{18}-distribution 588
  8. External layers on target 590
  9. Foil target backings 593
  10. Preparation of foil target backings 594
II. Measurement of angle 595
  1. Measurement of angle 595
  2. Angular sensitivity of spectrometer 597
III. Spectrometer characteristics 598
  1. Measurement of the dispersion 598
  2. Line width on different parts of the plate 599
  3. Beam spot height 599
  4. Solid angle of the spectrometer 600

1. Introduction

N^{16} is β-active with a half-life of 7.35 sec. (Ref. 1). It is the residual nucleus of several nuclear reactions, and therefore many determinations of its energy levels are reported, but only one level has been measured with great accuracy (Ref. 5).

Bleuler *et al.* (Ref. 1) measured the β-spectrum and found it complex with 18% going to the ground state of O^{16} and having $E_\beta = 10 \pm 1$ MeV (Wilson chamber) and most of the rest to the 7.1 and 6.1 MeV levels in O^{16}. E_β of these components $+ E_\gamma$ was measured to be 10.5 ± 0.5 MeV. (These figures give the difference between the atomic masses of the ground states of N^{16} and O^{16}.) The authors showed that the β-decay to the ground state of O^{16} was a first forbidden transition, while the decay to the γ-ray emitting levels were allowed. From these results it may be deduced that the ground state of N^{16} has a spin of 2 and odd parity ($J = 2^-$) (see also Ref. 7).

The α-spectrum from $F^{19}(n, \alpha)N^{16}$ was investigated by Bleuler and Rossel (Ref. 2) with ionization chamber and pulse analysis. The most energetic α-group they found had a Q-value of -0.73 ± 0.25 MeV (corresponding to $N^{16} - O^{16} = 9.7$ MeV). A second α-group was assigned to a transition to an excited level in N^{16} at 1.6 MeV. The pulse distribution also indicated excited levels at lower energies, but the resolution did not permit their identification. Jelly and Paul (Ref. 3) found for the same reaction a Q of -1.2 ± 0.9 MeV corresponding to $N^{16} - O^{16} = 10.2$ MeV.

The reaction $N^{15}(d, p)N^{16}$ has been studied by Wyly (Ref. 4) at $E_d = 3.4$ MeV. The energy of the protons was determined from their range in air. Two proton groups are reported, one with $Q = 0.23 \pm 0.15$ MeV corresponding to the (presumed) ground level, and a second corresponding to an excited level at 0.3 MeV in N^{16}. From the reported Q-value the difference $N^{16} - O^{16}$ is calculated to be 10.43 MeV.

Malm and Buechner (Ref. 5) used 1.43 MeV deuterons for the same reaction and determined the proton-energies with a magnetic spectrometer. They report only one proton group and its Q-value -0.034 ± 0.005 MeV corresponds to $N^{16} - O^{16} = 10.70$ MeV. The authors assigned the group to a transition to the excited level in N^{16} at 0.3 MeV reported by Wyly.

Lillie (Ref. 6) studied the disintegration of O^{16} when it was bombarded with 14.1 MeV neutrons in a Wilson chamber. He found three proton groups from the reaction $O^{16}(np)N^{16}$ which he assigned to four levels in N^{16}: one of the groups was namely rather broad. He gives the following values: A ground level corresponding to $N^{16} - O^{16} = 10.7$ MeV, and excited levels at 0.3, 1.7, and 2.6 MeV.

N^{16} is of a certain interest in connection with the theory for isotopic spin multiplets. According to theory (Ref. 8) the ground level of $N^{16}(T = 1)$ should correspond to an excited level in O^{16} at about 12.5 MeV. Five levels in O^{16} in this range (12.41 – 13.24 MeV) are fairly well known (Ref. 9, 10, 11, 25, see Fig. 5). It is therefore of interest to determine the ground level and possible levels at low excitation energy in N^{16} and see to what extent correspondence can be established.

2. Principle of the present investigation

In the present investigation the nuclear reaction $O^{18}(d, \alpha)N^{16}$ was used for determination of levels of low excitation energy in N^{16}. Thin targets of O^{18} were bombarded with deuterons of 850 keV energy. The energies of the α-particles produced were measured with a double focusing magnetic spectrometer. The Q-values for the found α-groups were calculated from the measured energies according to the eq. in ref.

and the energies (= masses) of the corresponding states of the residual N^{16} could en be determined with the eq.:

$$M(\mathrm{N}^{16}) = M(\mathrm{O}^{18}) + M(\mathrm{D}^{2}) - M(\mathrm{He}^{4}) - \frac{Q}{c^{2}}$$

ecause the masses of O^{18} (Ref. 13) and of He^4 and deuterium (Ref. 9) are known. he masses $M(N^{16})$, $M(\mathrm{O}^{18})$ etc. in the equation are atomic masses.)

3. Experimental arrangements

The apparatus used has earlier been described (Ref. 12) and also the experimental rrangements used in investigations of the same kind as the present (Ref. 13, 14, 15). e shall therefore discuss some details only. A treatment at some length can be ound in the accompaning appendix.

4. Targets

Details of the target preparation are described in appendix I. For the Q-value easurements we used a copper disk coated with a thin oxide layer by oxidation n an atmosphere enriched in O^{18} to ca. 50 %. The layer had some keV stopping ower to 875 keV protons (see Appendix I, 4). An α-spectrum from the $O^{18}(p, \alpha)N^{15}$ eaction on this target is shown in Fig. 3 A c.

Later during the investigations thin targets prepared on steel and stainless steel n the magnetic isotope separator and free of external layers became available Appendix I, 5–I, 7) and they were partly used for taking the survey spectra shown n Fig. 4.

For measurement at an angle of 45° to the beam a target on aluminium foil backing was used in order to get better resolution as described in Appendix I, 9.

5. Beam energy

The energy of the incident deuterons was measured by a comparison of the $H\varrho$ for 873 keV protons elastic scattered against aluminium at 135° with the $H\varrho$ of the deuterons scattered against beryllium as described in Ref. 16. The accuracy of the measurement was about ± 4 keV (0.5 %). The energy of the incident deuterons was determined by the condition that the beam should pass one slit before and a second slit after a magnet which deflects the beam 90°. Variation in energy during one run was about ± 1.5 keV (0.2 %) and is due to variations of the field strength of the deflecting magnet and also to changes in current distribution over the entrance slit.

Because the magnetic spectrometer was calibrated with nuclear reactions of known Q-value which had nearly the same energy dependence $\delta E_2/\delta E_1$ (E_1 refers to the incident deuteron, E_2 to the emitted particle) as the investigated reaction, the absolute value of the beam energy E_1 need not be known very accurately, but, of course, it was necessary that the beam energy should vary as little as possible during each run.

6. Angle measurement

The measurement of the angle θ between the incident beam and the center of gravity of the ray pencil accepted by the spectrometer is described in Appendix II.

The values of θ for the angular positions of the spectrometer used in the present investigation are given in Table 3 A.

In most cases the energy of a particle group was determined form the high energy edge of its spectral line and then the minimum angle $\theta - \Delta\theta_1$ (Fig. 7 A) was used in the calculations of the Q-value. In order to be able to compute this angle from eq. 10 A the east-west position (d and b Fig. 7 A) of the beam spot on the target was determined for every run by turning the target out from the beam path so that the position of the beam could be observed on the fluorescent screen at the window in the target chamber (see Fig. 7 A).

All measurements were done with full opening of the spectrometer ($\omega_0 = 0.0031$ sterad and $\Delta\theta_1 = 1.9°$, $\Delta\theta_2 = 1.75°$, compare Appendix II and III).

7. Calibration of the spectrometer

The nuclear reactions $N^{14}(d, p)N^{15}$ with $Q_1 = 3.339 \pm 0.005$ MeV and $Q_2 = 3.310 \pm 0.005$ MeV (a double line) and $C^{12}(d, p)C^{12}$ with $Q = 2.223 \pm 0.006$ MeV (Ref. 9) were used for calibration of the spectrometer.

The N^{14}-target was a tantalum foil which had been bombarded with N^{14}-ions in the isotope separator, the C^{12}-target was the carbon deposit formed on the ordinary O^{18}-target during one experiment.

By a measurement of the α-energy of an unknown α-group from $O^{18}(d,\alpha)N^{16}$ this was first photographed on the nuclear-track plate in the spectrometer and directly afterwards the proton-group form the calibration reaction was photographed at the same spectrometer field strength. The difference in position of the spectral line from the unknown α-group and that from the protons gives the difference in $H\varrho$ if the dispersion of the spectrometer is known (see Appendix III, 1 and Table 2 A).

The stray fields of the spectrometer deflects the incident beam somewhat, and therefore the exact position of the beam spot on the target varies both with spectrometer field strength and angular position of the spectrometer. At the same time as the east-west position of the beam was observed on the above-mentioned window in connection with the angle measurement, the height of the spot was determined and so that correction for changes in it could be applied (see Appendix III, 3). Such correction was only necessary when the calibrating and the unknown reactions were taken at different angles.

For computation of the α-energy from the $H\varrho$ value we used the eq. given in Ref. 17, according to which the energy of an α-particle ($E_{\alpha\,\mathrm{ekv}}$) and a proton (E_p) with the same $H\varrho$ are related by

$$\frac{E_{\alpha\ \mathrm{ekv.}}}{E_p} = \frac{4\left(M_{p0} + \frac{1}{2}\frac{E_p}{c^2}\right)}{\left(M_{\alpha 0} + \frac{1}{2}\frac{E_p}{c^2}\right)}$$

M_{p0} and $M_{\alpha 0}$ are the rest masses of the proton and α-particle.

8. Evaluation of the spectral lines

The position of a spectral line was determined by the position of its high energy edge, which is the simpliest method when calibration is performed by means of a particle group of known energy. In order to avoid difficulties when the front of the es were concave we have chosen to read the front edge at a $^1/_{10}$ of the maximum e height. Of course, this will cause some errors if the distributions of target atoms the target backing surface is not the same for O^{18} as for the calibrating element ^{14} or C^{12}), but the errors are thought to be smaller than the uncertainty in the ergy of the calibrating proton group and no further analysis of line shape was made.

Because the photographic plates are not placed in the exact image plane of the ectrometer the width of a spectral line will depend upon its position along the plate. t will be broadest where the plate position has its largest deviations from the age plane.) This line broadening, of course, affect the position of the high energy ge. The measured distance between the edges of two lines (the calibrating and the known line) must therefore be corrected according to eq. 11 A in Appendix III. his correction is not very exact, however, and we have therefore tried to chose the bserving angles so that the distance between calibrating and unknown line along e plate is as small as possible (compare Figs. 1 and 2).

9. External layers on target

The investigation of the targets, described in appendix I, showed that before ombardment with the deuteron beam the external layer on target was negligible $\leq$ 0.2 keV to 875 keV protons). In one case, this is due to the mode of target produc- on, oxidation of a clean copper surface in an enriched atmosphere, and in the case f isotope separated targets the use of a liquid air trap adjacent to the target in the eparator obviously effectively prevented the formation of an external layer during he bombardment in the separator.

When the O^{18}-targets were used for Q-value measurement, a new not earlier ombarded part of the target was used for every run and therefore the external yer was due only to deposition on target under the deuteron bombardment during he experiment itself. The thickness of the external layer was measured after every xperiment by elastic scattering of deuterons against 1) the used target spot and) a clean surface of the backing metal.

If the high energy edge of a spectral line is used for energy determination one hould only correct for the slowing down in the external layer which is present at he beginning of the run, that is: there should be no correction at all if the surface is nitially clean. (On the other side, if the center of gravity of a spectral line had been sed for the energy determination, the slowing down in a layer equal to the mean hickness during the experiment would have been corrected for.)

The external layer was not measured at the beginning of every run, it was relied n the measurements done on two different unused parts of the targets which showed hat thickness of external layer on an unbombarded part of the target was less than .2 keV to 875 keV protons. In order to account for a possible external layer at the eginning of the measurements we have chosen to correct for an energy absorption n an external layer which thickness was 25 % of the thickness measured after the -value measurement, and put an uncertainty to the correction of equal magnitude ± 25 % of measured layer). The layer formed on the target under the deuteron ombardment was of the order of 1 keV stopping power to 850 keV deuterons and he corrections calculated on the basis of an external layer of 25 % of this thickness mounted to ca. 1.3 keV in the calculated Q-value.

The external layers on the calibrating targets were only measured for the N^{14}- arget by scattering deuterons against the N^{14}-target (on tantalum) and on a clean old surface. (The C^{12} target has no external layers, in fact the C^{12} itself is a part of

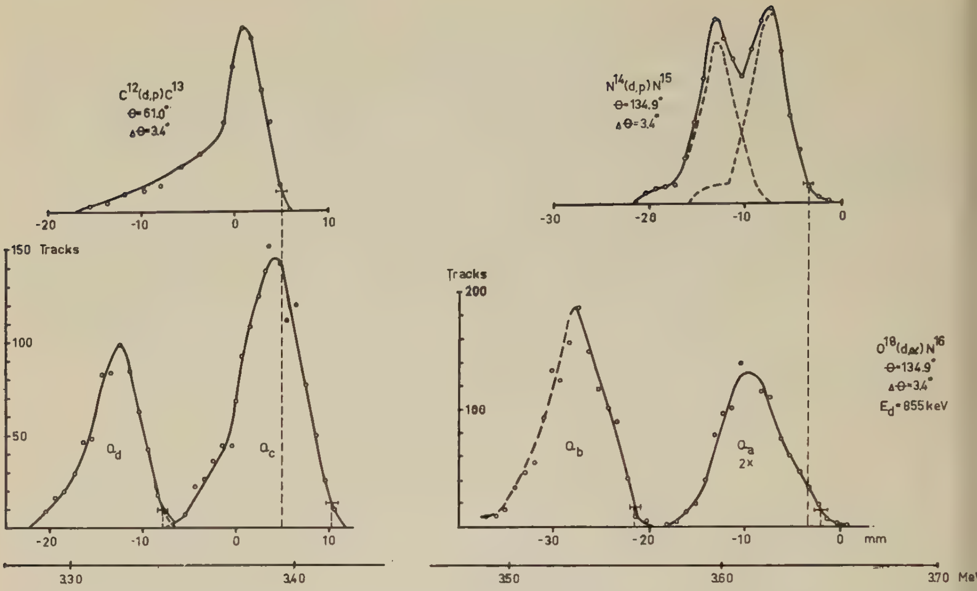

Fig. 1. The four α-grops Q_a–Q_d from $O^{18}(d, \alpha)N^{16}$ at 134.9°. Target Cu_2O^{18} on Cu. Yield for Q_a and Q_b: 1 track = 0.05 α/μC. sterad. keV, for Q_c and Q_d : 1 track = 0.04 α/μC. sterad. keV.

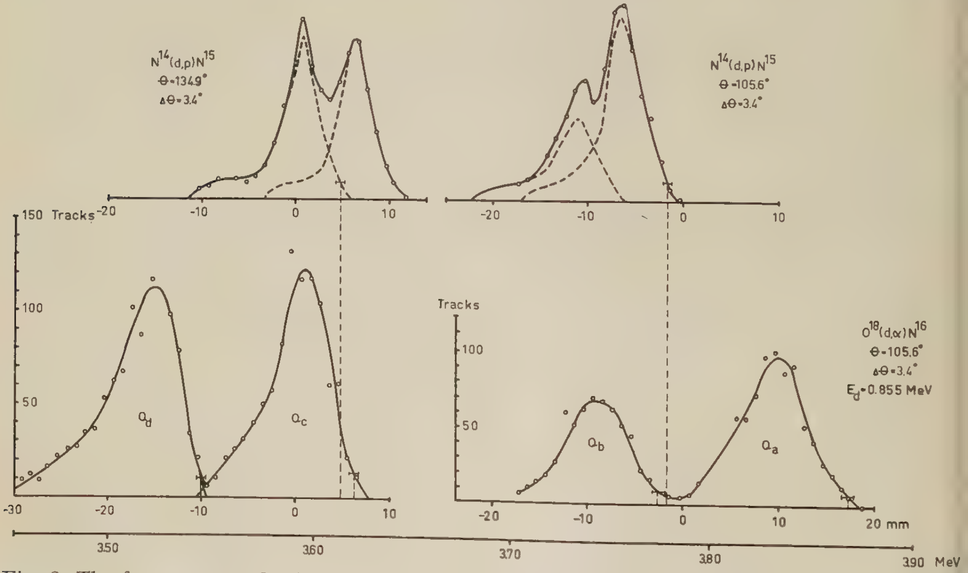

Fig. 2. The four α-group Q_a–Q_d from $O^{18}(d, \alpha)N^{16}$ at 105.6°. Target Cu_2O^{18} on Cu. Yield for Q_a and Q_b: 1 track = 0.03 α/μC. sterad. keV, for Q_c and Q_d: track = 0.04 α/μC. sterad. keV.

the external layer).) The layer on N^{14} was very small and no corrections were made. As an extra control we took a (d, p) spectrum of the used in N^{14} target and also of a N^{14} target prepared by evaporating a drop of NH_3Cl-solution to dryness on *able I.* Q-values for $O^{18}(d,\alpha)N^{16}$ calculated from the spectra of Fig. 1 and 2. $Q(O^{17})$ d $Q(F^{19})$ are calculated from the same energy values under the assumption that the target nuclei are O^{17} and F^{19} instead of O^{18}.

Group	Angle	Q-value	$Q(O^{17})$	$Q(F^{19})$
Q_a	134°9	4238 ± 8	4334	4153
	105°6	4236 ± 10	4320	4165
Q_b	134°9	4124 ± 10	4218	4040
	105°6	4120 ± 8	4200	4049
Q_c	134°9	3939 ± 10	4031	3857
	105°6	3936 ± 9	4014	3867
Q_d	134°9	3845 ± 12	3935	3765
	105°6	3847 ± 10	3924	3780

Table II. Weighed mean Q-values.

Q_a	4237 ± 9 keV
Q_b	4121 ± 9 keV
Q_c	3937 ± 10 keV
Q_d	3846 ± 11 keV

clean Ag surface. The external layer on this target cannot be expected to be of y importance. The high energy edges of the p-spectra from this target and the rget used for calibrating coincided within less than 1 keV.

10. Results

Four α-groups form $O^{18}(d,\alpha)N^{16}$ were found. Fig. 1 and Fig. 2 show the spectra tained. (Because their small energy difference two groups could be photographed each photographic plate.) The target used in the exposures is the same as in Fig. Ac of Appendix I.

The points on the lines used for energy determination are indicated, and also the certainty due to scattering of the measuring points.

In order to acertain that none of the groups was due to some contamination on e target backing, their energies were measured both at 134.9° and 105.6° to the cident beam.

The Q-values calculated from the measured energies are shown in Table I. In lumn 4 and 5 are shown which Q-values are obtained if one assumes that the rget nuclei were O^{17} or F^{19}. Under these assumptions the Q-values in 135° and 5° differ by 9–18 keV which shows that all four groups can be ascribed to $O^{18}(d,\alpha)N^{16}$ th a high degree of probability. In order to make the identification still more re, the spectra were also taken at 45° to the beam. In order to get a good resolution O^{18}-target on an aluminum foil backing was used in a position where the α-particles d to escape through the foil, as described in Appendix I, 9. The spectra obtained e shown in Fig. 3. The position which the spectral lines would have had if any of

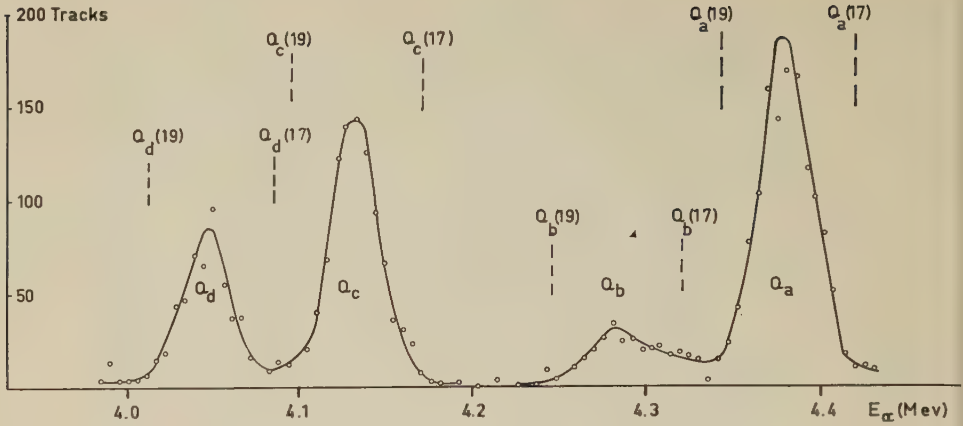

Fig. 3. The four α-groups Q_a–Q_d from $O^{18}(d, \alpha)$ at 45°. Target H_2O^{18} on Al-foil.

the lines of Fig. 1 were due to $O^{17}(d,\alpha)$ or $F^{19}(d,\alpha)$ are indicated. It is quite obvious that all four α-groups are associated with the $O^{18}(d,\alpha)N^{16}$ reaction.

From the spectra Figs. 1, 2, and 3, it can be seen that some of the groups are strongly anisotropically distributed. Differences in target intensities are approximately corrected for and the vertical scales are chosen so that the line heights in the figs. give an approximately correct picture of the relative intensity of the four groups.

11. Errors

Different sources of errors are discussed in Ref. 13. A summary of their actual magnitude is given in Table III.

Table III. Partial errors and total probable error in keV.

	Q_a		Q_b		Q_c		Q_d	
Angle of observation	134.9°	105.6°	134.9°	105.6°	134.9°	105.6°	134.9°	105.6°
Source of error:								
Q of calibrating reaction	6.0	5.9	6.0	5.9	7.6	5.8	7.6	5.6
Deuteron energy .	1.9	2.0	1.9	2.0	3.6	1.8	4.6	1.8
Angle measurement	0.7	1.2	0.7	1.2	3.0	3.5	3.0	3.5
Reading of spectral lines	4.3	6.0	6.0	4.3	5.1	5.7	6.0	6.0
Dispersion	0.5	3.0	3.7	0.2	0.8	0.5	2.2	3.0
External layers . .	1.4	1.4	1.4	1.4	1.7	1.6	1.7	1.6
Total prob. error .	7.8	9.5	9.6	7.8	10.4	9.2	12	9.7

12. Search for other α-groups

The four α-groups from $O^{18}(d, \alpha)N^{16}$ represent transitions to four levels in N^{16}. Before the ground state of N^{16} is known it might be appropriate to refer to the energy of these levels to the ground state of O^{16}, and this can be done by means of the following four reactions with known Q-values:

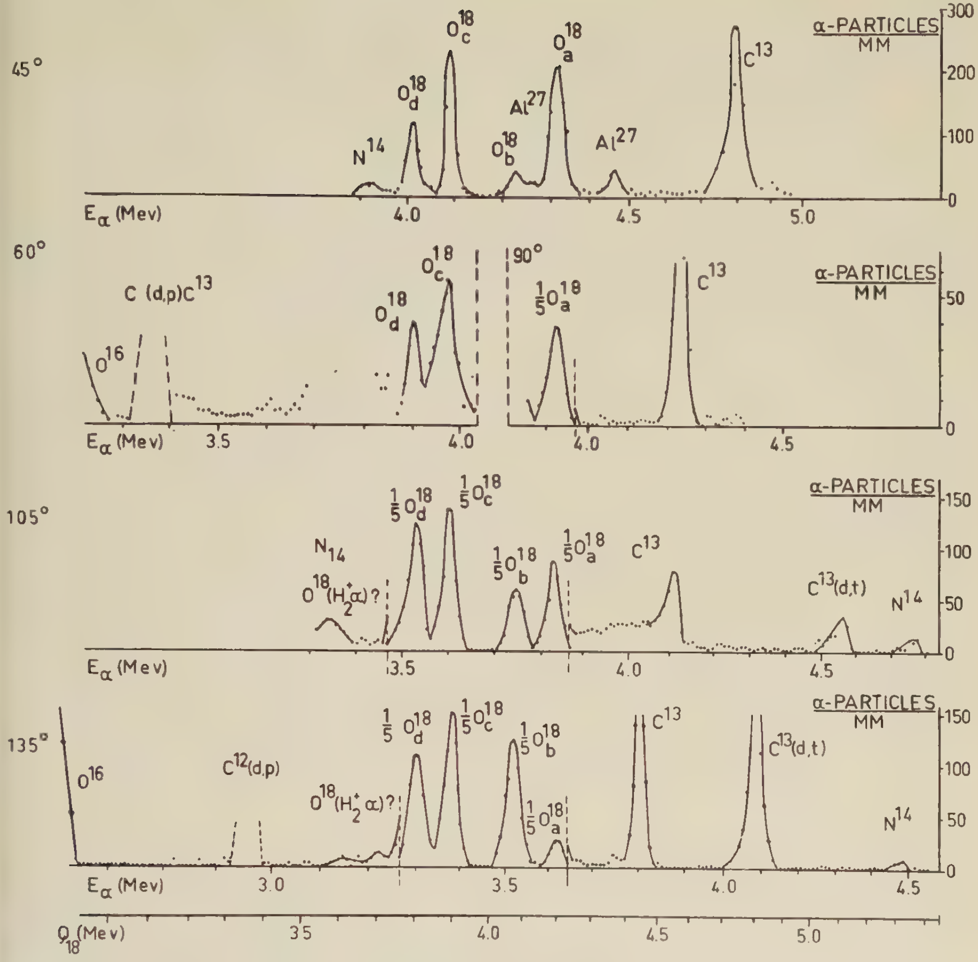

Fig. 4. Survey spectra of $O^{18}(d,\alpha)N^{16}$. The Q^{18} scale refer to the Q-value of this reaction. The vertical scales refer to number of α-particles per mm along the nuclear-track plate at ca. 2000 μC bombardment. Targets H_2O^{18} or $N^{14}O^{18}$ on Cu, Fe and Al backings. The letters refer to target nuclei for (d,α) reactions. When other particles are involved, the complete reaction is given. The strong background around 4 MeV at 105° depends on the carbon in the target backing of polished steel.

$O^{16}(d,\alpha)N^{14}$	$Q = 3.116 \pm 0.004$ MeV	(Ref. 9)
$N^{14}(d,p)N^{15}$	$Q = 8.614 \pm 0.009$ MeV	(Ref. 9)
$O^{18}(p,\alpha)N^{15}$	$Q = 3.961 \pm 0.009$ MeV	(Ref. 13)
$O^{18}(d,\alpha)N^{16}$	$Q = Q_a, Q_b, Q_c$ or Q_d	(see Table II)

If we form a chain of these four reactions, and insert the known values of the atomic masses of the hydrogen, deuterium and He^4 taken from Ref. 9, we get the following values of the $N^{16} - O^{16}$ atomic mass differences (the N^{16}-levels are labeled after the corresponding α-groups):

Table IV. Energy levels of N^{16} referred to the ground state of O^{16}. (The differences refer to differences in atomic masses.)

$N^{16} - O^{16}$ MeV	N^{16}-level
10.385 ± 0.030	Q_a
10.501 ± 0.030	Q_b
10.685 ± 0.030	Q_c
10.776 ± 0.030	Q_d

The lowest of these levels, Q_a, might be the ground state of N^{16}. Its energy, 10.39 MeV over the ground state of O^{16}, is in accordance with the value 10.5 ± 0.5 MeV for the difference between the ground states of N^{16} and O^{16} given by BLEULER *et al.* (Ref. 1) who measured the β- and γ-energies of the radioactive decay of N^{16} to O^{16}. The uncertainties of earlier measurements are however, so large that one can expect the ground level of N^{16} to be less than 10 MeV over the ground state of O^{16}. In order to investigate the possible existence of levels in N^{16} below the Q_a-level, a thorough search for α-groups was undertaken in the energy range corresponding to Q-values of 4.24–5.4 MeV (that is $N^{16} - O^{16} = 10.39$ to 9.23 MeV). The spectra obtained can be seen in Fig. 4. Spectra were taken at several angles, and in Fig. 4 the energy scales of the different spectra are displaced just enough to compensate for the angular energy-dependence of the $O^{18}(d,\alpha)N^{16}$ reaction. α-groups from this reaction therefore will appear at the same Q_{18}-value in all spectra in Fig. 4, independently of the angle at which the spectrum was taken, but α-groups from target nuclei other than O^{18} will be displaced in the horizontal direction when one goes from the spectrum at one angle to the spectrum at another.

An inspection of the spectra of Fig. 4 showed that there was no α-group from $O^{18}(d,\alpha)N^{16}$ of higher energy than the Q_a-group which was strong enough to appear in Fig. 4. If there was any, it must have been weaker than 0.05 of the weakest of the four identified α-groups. Of course one must consider the possibility that α-groups from unavoidable contaminants i.e. $C^{13}(d,\alpha)B^{11}$ have hidden some weak α-group from $O^{18}(d,\alpha)N^{16}$. But because spectra were taken at several angles and the energy dependence of the disturbing groups were different from $O^{18}(d,\alpha)N^{16}$-groups, all parts of the studied energy interval were free from disturbing groups at least at one angle. All α-groups found in the investigated energy interval could be ascribed to earlier known reactions. Even the weak $N^{14}(d,\alpha)C^{12}$ to the 7.68 MeV level in C^{12} appears on our plates. It originates from surface contamination with N^{14}. A separate calibration of this line with a $Be^9(d,p)Be^{10}$ line gave a Q-value for $N^{14}(d,\alpha)C^{12}$ of 5.910 ± 0.015 MeV which corresponds to a 7.66 ± 0.02 MeV excited state of the residual C^{12} nuclei. This value is 20 keV lower than reported elsewhere (Ref. 24).

The search for α-groups from $O^{18}(d,\alpha)N^{16}$ was also extended to energies below the Q_d-group, corresponding to levels in N^{16} of higher excitation than the Q_d-level. According to Ref. 2 and 6 there should be levels in N^{16} at 1.6 and 2.6 MeV over the ground state of N^{16} (not O^{16}). If we tentatively assume that the Q_a-level is the ground state of N^{16}, there would consequently be α-groups with $Q = 2.64$ MeV and $Q = 1.64$ MeV. In the energy range where the first of these two groups can be expected, there is a strong interference from $C^{13}(d,\alpha)B^{11}$ and $O^{16}(d,\alpha)N^{14}$ and the second group will partly interfere with scattered deuterons at the beam energy available. We therefore limited our search for α-groups to energies greater than the disturbing $O^{16}(d,\alpha)N^{14}$ group. In the range between Q_d and the α-group from $O^{16}(d,\alpha)N^{14}$ ($Q = 3.8 - 3.0$ MeV) the most complete spectrum was taken at 135° (Fig. 4). At this angle one weak α-group was observed just below Q_d, with an intensity of 15 % of the Q_a α-group. (The latter is the least intense α-group from $O^{18}(d,\alpha)N^{16}$ at 135°.) If the α-group belonged to the $O^{18}(d,\alpha)N^{16}$-reaction it should also appear in the spectra taken at other angles. Unfortunately these spectra showed a rather high background in the range of interest so the identification of the α-group is not possible until better spectra at other angles than 135° are obtained.

The α-group might also be due to α-particles form the reaction $O^{18}(p,\alpha)N^{15}$ produced with molecular hydrogen ions present in the deuteron beam. (The α-energy would be 3.26 MeV.) Each H_2^+-ion gave two protons of 430 keV (deutron energy 860 keV), and a comparation of the cross sections of the $O^{18}(d,\alpha)N^{16}$-reaction for the production of the Q_a α-group at $E_d = 860$ keV and the cross section of the $O^{18}(p,\alpha)N^{15}$-reaction at $E_p = 430$ keV (ratio 1 : 7, Ref. 35, 36) showed that the observed intensities of the α-groups corresponded to a molecular beam current of 1 % of the deuteron current, which in turn could be explained if the deuterium gas to the ion source was contaminated with 10 % hydrogen. This high value was not impossible considering the arrangements for the deuterium gas production although it was not very probable.

In the other parts of the energy range $Q = 3.8 - 3.0$ MeV no α-group was observed at 135° with an intensity larger than 5 % of the Q_a-group. At $Q = 3.4$ MeV however the strong proton group from $C^{12}(d,p)C^{13}$ prevent any observation of α-groups and the spectra at other angles showed here a high background, hiding possible α-groups of low intensity.

Thus we can say that in the range $Q = 3.8 - 3.0$ MeV no α-groups from $O^{18}(d,\alpha)N^{16}$ with an intensity comparable to the weakest of the four groups identified were observed, but the existence of α-groups from this reaction with 15 % or less of this intensity at $Q = 3.8$ and 3.4 MeV, and less than 5 % of the same intensity in the rest of the energy range, $Q = 3.8 - 3.0$ MeV can not be excluded.

13. Conclusion

From the investigation we can conclude that the reaction $O^{18}(d,\alpha)N^{16}$ gives transitions to four levels in N^{16} in the energy interval $(N^{16} - O^{16}) = 9.3 - 11.6$ MeV. If there are further levels in N^{16} in this energy interval, the transitions to them at $E_d = 850$ keV are weaker than $0.05 - 0.15$ (see above) of the weakest of the four transitions observed. A consideration of the spin and parities of the ground states of $O^{18}(=0^+)$ and $N^{16}(J = 2^-$, Ref. 1) shows that the transition to the ground state of N^{16} should not be particularly discouraged by spin-parity selection rules. Therefore the lowest of the levels observed, 10.39 ± 0.03 MeV above the O^{16}-ground state, is probably the ground state of N^{16}. Under this assumption we get the following result:

1.[1] *Atomic mass of* $N^{16} = 16.01116 \pm 0.000032$ *a.m.u. (atomic mass defect* 10.385 ± 0.030 *MeV).*

2.[1] N^{16} *has excited states at* 116 ± 6 *keV,* 300 ± 12 *keV and* 391 ± 12 *keV.*

---

[1] *Note added in proof.*
Since this work had been completed, W. Whaling reports (private communication) that he has investigated the reaction $N^{15}(d,p)N^{16}$ and found the same four levels as we in N^{16}. His preliminary values are ground level Q-value 286 keV which gives $N^{16} - O^{16} = 10.375$ MeV and excited states at 0.128, 0.308 and 0.404 MeV over the ground state. The discrepancy between his values and ours is mainly that the energy of his ground level is 10 keV lower than ours.

3. No levels found at excitation energy 391–1240 keV. (intensity limits 15–5 % of Q_a, see Paragraph 11).

14. Discussion

Earlier determinations of the ground state of N^{16} and our value are compared in Table V (the energies are referred to the ground state of O^{16}).

It is possible to check one of our Q-values with a closed cycle. The $N^{15}(d,p)N^{16}$ transition reported by MALM and BUECHNER (Ref. 5) goes namely to the level in N^{16} we have labeled Q_c. The third reaction in the cycle is $O^{18}(p,\alpha)N^{15}$, the Q-value of which was measured by MILEIKOWSKY (Ref. 13). Table VI shows the three reactions in the cycle and their Q-values. The sum of the Q-values deviates only 10 keV from zero, which must be considered quite satisfactory.

Table V.

$N^{16} - O^{16}$		
10.5 ± 0.5 MeV	$E_\beta + E_\gamma$ for $N^{16}(\beta, \lambda)O^{16}$	ref. 1
10 ± 0.5 »	from $N^{18}(d, p)N^{16}$	ref. 4
10.39 ± 0.03 »	from $O^{18}(d, \alpha)N^{16}$	our value

Table VI.

$+N^{15}(d,p)N^{16}$	$Q = -0.034 \pm 0.005$ MeV
$+O^{18}(p,\alpha)N^{15}$	$Q = 3.961 \pm 0.009$ MeV
$-O^{18}(d,\alpha)N^{16}$	$Q = -3.937 \pm 0.010$ MeV
	-0.010 ± 0.014 MeV

15. Analogous states in N^{16} and O^{16}*

If the specific nuclear forces are charge independent there will be states of O^{16} with isotopic spin $T = 1$ which are analogous to the states of N^{16} (Ref. 8, 18). The difference in binding energy between a state of N^{16} and its analogous O^{16}-state is due to the neutron-proton mass difference and difference in Coulomb energy. The latter can only be calculated approximately within some tenths of a MeV because the configuration of the nucleons is not exactly known. There is also a small magnetic contribution to the binding energy that will change when a proton is changed into a neutron and the change in energy will depend on the l and j of the individual nucleons. Therefore the difference in energy between two states which are analogous to each other is not necessarily the same for all analogue pairs, shifts of 0.1 to 0.3 MeV being not uncommon.

Estimates of the Coulomb energy difference can be made in different ways. INGLIS (Ref. 8) computed it to be 3.49 MeV by comparison with the adjacent mirror pair N^{15}, O^{15}. BROWN *et al.* (Ref. 17) give a formula based on the assumption of a constant nuclear density out to a radius of $R_0 A^{1/3}$ and this gives in our case, with $R_0 = 1.4 \times \times 10^{-13}$ cm, the Coulomb difference = 3.43 MeV. If neutron-proton mass difference

---

* Section 15 was written after a discussion with Prof. T. LAURITSEN and added in proof.

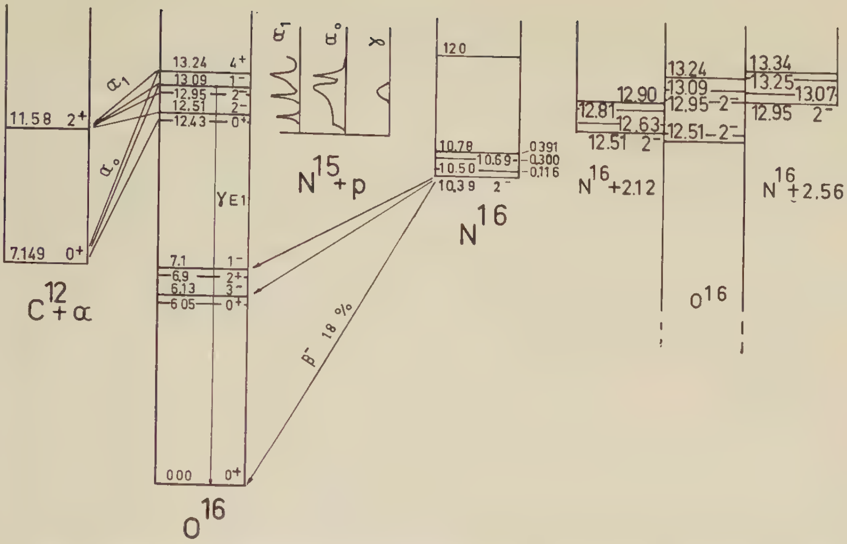

Fig. 5. Level scheme for O^{16} and N^{16} and two different possibilities for matching N^{16} and O^{16} levels. Except the four lowest levels of N^{16}, which are taken from the present investigation, the data are taken from Ref. 9 and 19.

is subtracted we get that the difference between analogous states of O^{16} and N^{16} should amount to ca. 2.68 MeV. The analogue to the (presumed) ground state of N^{16} should thus be a O^{16} state of $10.39 + 2.68 = 13.07$ MeV excitation energy. (Compare Fig. 5.) Five levels are known in O^{16} in this range, at 12.43, 12.51, 12.95, 13.09 and 13.24 MeV excitation energy (Ref. 9, 10, 11, 25). Their spins and parities are rather well established (Ref. 10, 25), but their isotopic spins are less certain. We will give a survey of what is known about the isotopic spin of the actual O^{16} levels.

First it must be stressed that isotopic spin is not necessarily a good quantum number at this high excitation energy: the states can be mixed $T = 0$ and $T = 1$. The 13.09 level in O^{16} can decay by $E1$ radiation to the ground state of O^{16}, which demands that its T-value should be $= 1$ (Ref. 19), but it also decays with a broad resonance into $C^{12} + \alpha$, which suggests that it is $T = 0$ because ΔT shall be $= 0$ in a particle reaction (Ref. 20), and both of the end products C^{12} and α have $T = 0$. The possibility that there are two very closely adjacent levels at 13.09 MeV in O^{16}, one with $T = 1$ and a second with $T = 0$, cannot be ruled out, but does not seem very probable.

According to the last mentioned rule ($\Delta T = 0$), O^{16}-levels with $T = 1$ would not decay into $C^{12} + \alpha$ because both these particles are assumed to have $T = 0$ in the states acutal in this case. It is not expected, however, that the $\Delta T = 0$ selection rule will be very strong and therefore the decay into C^{12} (ground state or 4.43 MeV state) $+ \alpha$, which in fact is observed at all five levels, does not exclude the possibility that some of them have $T = 1$.

The N^{16} ground state has almost certainly spin $J = 2^-$ (odd parity) (Ref. 1). Its analogue in O^{16} might therefore be the 12.51 or the 12.95 MeV level, which both are $J = 2^-$. (Analogous states shall have the same spin and parity.) Both these levels are formed as compound states in the $N^{15}(p, \alpha, \gamma)C^{12}$-reaction where they show very sharp resonances (Ref. 11). They cannot decay into the ground state of C^{12}

Table VII.

O^{16}-level	Γ_p	Γ_α	γ_p	γ_α	$R \cdot \gamma_p$	$R \cdot \gamma_\alpha$	Alternative
Excitation energy and N^{15} (p, α, γ) C^{12} reasonance parameters	keV		keV		10^{-13} cm keV		
12.51 MeV $E_{\text{res}} = 0.429$ MeV $\sigma_0 = 0.3$ barn $\Gamma = 0.9$ keV	0.03	0.87	290	580	1 420	3 150	I
	0.87	0.03	7 980	21	39 000	115	II
12.95 MeV $E_{\text{res}} = 0.898$ MeV $\sigma_0 = 0.8$ barn $\Gamma = 2.2$ keV	1.62	0.58	310	15	1 510	82	I′
	0.58	1.62	110	40	540	217	II′

by emission of long-range α-particles because of spin and parity selection rules. On the assumption that the resonance widths of these levels in the $N^{15}(p, \alpha, \gamma)C^{12}$-reaction are entirely due to the possible emission of a proton or an α-particle, that is $\Gamma_p + \Gamma_\alpha = \Gamma$, we have calculated the reduced widths γ_p and γ_α from the values of σ_0 and Γ given in Ref. 11 (see Table VII). The single level formula of Breit-Wigner was used for the determination of the Γ_p and Γ_α. The reduced widths were computed according to eq. VIII, 7.15 of Ref. 22, and the penetration factor v_l in this equation was calculated from the $F(R)$ and $G(R)$-values of Ref. 21. The reactions take place with d-protons and the emitted α-particles have angular momentum $l = 1$. For the channel radius R we used $R = 1.4 \times 10^{-13}(A_x^{1/3} + A_s^{1/3})$. At each level there are two alternatives, due to the ambiguity of the computation of the partial widths with the Breit-Wigner formula.

For the level 12.51 alternative II does not seem probable because of the very high proton width, and we therefore adopt alternative I for the reduced widths of level 12.51.

At the 12.95 level it is not possible to judge which of the two alternatives I′ or II′ is the most probable. The reduced widths should be of the order of magnitude $\gamma_p \approx D/(\pi \cdot R \cdot K)$ (Ref. 22, Chapter VIII), where D is the energy spacing between levels of the same J and parity, and K the wave number of the emitted particle inside the nucleus. In our case $D \approx 500$ keV and $K \approx 10^{13}$ cm^{-1} (Ref. 22) and thus

$$\gamma_p \approx 30 \text{ keV and } R \cdot \gamma_p \approx 170 \times 10^{-13} \text{ cm keV}.$$

The values for γ_p in the alternatives I, I′ and II′ are all much larger than predicted by the expression above, but they are of the same order of magnitude as the γ_p for $B^{11} + p$, $C^{12} + p$ and $C^{13} + p$ tabulated in Ref. 23 ($\gamma \lambda_s^2$ in the paper referred to is identical with our $R\gamma_p$, tabulated in the next last column of Table VII). In Ref. 23 $R\gamma_p/D$ for the three reaction mentioned varies between 1.4 and 3.2×10^{-13} cm, our values give $R\gamma_p/D = 3.0$ à 1.0×10^{-13} cm.

The essential point to us is however that the reduced α-width, γ_α, of level 12.95 is much smaller than the γ_α of the 12.51 level (which is true, independently of which of the alternatives I′ and II′ we chose) and this fact might indicate that the 12.95

eV level has $T = 1$, so that its decay to $C^{12} + \alpha$ is discouraged by the $\Delta T = 0$ rule. he evidence is, however, not very strong, γ_α of the 12.95 level is small compared γ_α for the 12.51 level but not relative to the value predicted in the text above redicted value $\gamma_\alpha \approx 30$ keV, measured $\gamma_\alpha = 40$ or 15 keV).

Finally, we will compare the spacings of the four N^{16} levels with the spacings of fferent O^{16} levels, even if such a comparison may be of doubtful value for the entification of analogous states because the level spacings in one isobar may differ om the spacings of the analogous states of another isobar by some tenths of a MeV. Fig. 5 we have shown two alternative ways of comparing of the N^{16} and O^{16} level acings. According to the first of them the presumed ground state of N^{16} is matched the 12.51 MeV level of O^{16} and the N^{16}-levels are all displaced 2.12 MeV, which is 56 MeV less than the estimate made at the beginning of this paragraph. The 4th vel of N^{16} agrees reasonably well with the 12.95 level, but the 3rd and 2nd levels N^{16} have no known counterparts in O^{16}.

In the second case, the ground state of N^{16} is matched to the 12.95 MeV level of ^{16}, which according to this alternative should be the lowest $T = 1$ level of O^{16}, suggestion that is supported by the small value of γ_α of this level (see above). he energy displacement in this case is 2.56 MeV, that is 0.12 MeV less than the lculated value 2.68 MeV. There is a good agreement between the 13.09 MeV vel and the 2nd level of N^{16} and also between the 13.24 MeV level and the 3rd vel of N^{16}. But the 4th level of N^{16} has no known counterpart in O^{16}. If this level, e hypothetical analogue in O^{16} to the 4th level in N^{16} were $J = 0^-$*, its decay into $^{2} + \alpha$ by either short or long range α-particles is forbidden by spin and parity selec- on rules (the C^{12} level is $J = 2^+$ and $J = 0^+$ respectively), and these circumstances ight account for the fact that the level does not appear (as a resonance) in the $^{15}, p)$ reactions. Its radiative decay by $E1$ would only be possible to a $J = 1^+$, $= 0$ level.

From the survey given we can conclude that there is no clear evidence for cor- spondence between the four low levels in N^{16} and the levels in O^{16} around 13 MeV citation energy. In order to clarify the case it would be necessary to measure the in and parities of the N^{16} levels for instance by angular distribution measurements protons from $N^{15}(d,p)N^{16}$ and also from $O^{18}(d,\alpha)N^{16}$. Knowledge of spin and pari- es cannot decide but indicate whether two levels are analogous to each other nembers of the same isotopic multiplet) or not. One should also investigate O^{16} r more levels in the actual range, for instance by elastic scattering of protons gainst N^{15}. This reaction has the advantage that it does not discriminate against $= 1$ levels in O^{16}. Inelastic scattering of high energy (~ 20 MeV) α-particles and otons against O^{16} would indicate which levels are $T = 0$ and which are $T = 1$, ecause the levels with $T = 1$ would appear weakly or not at all in the $O^{16}(\alpha,\alpha')O^{16}$ actions because of the $\Delta T = 0$ rule.

Acknowledgments

The author is indebted to Professor MANNE SIEGBAHN for his interest in this ork and to Professor K. CLUSIUS for the gift of the enriched O^{18}-gas sample. Thanks e also due to Professor T. LAURITSEN and Professor L. HULTÉN and to Docent . MILEIKOWSKY, who proposed the investigation, for valuable discussions. Tekn. . S. THULIN gave generously help by the preparation of targets and Tekn. lic. . AHNLUND has given much valuable help by the runs.

---

* According to Ref. 8 a level of this kind, $J = 0^-$, $T = 1$, is possible among the lower states N^{16}.

Appendix I. Production of thin targets of O^{18}

I, 1. Types of targets used

Small metal disks 2 × ⌀ 14 mm of stainless steel (71 % Fe, 17 % Cr, 10 % Ni) or copper were used as target backings. In order to get a highly polished surface we also used polished carbon steel (Johansson gauges).

The disks were cleaned before use by machining, and the gauge pieces by washing in carbon-tetrachloride and absolute alcohol.

Thin targets of O^{18} were deposited on the backings in two ways: 1) By surface oxidation in an atmosphere enriched in O^{18} to 50 %. 2) By bombardment in a magnetic isotope separator (Ref. 30) with a beam containing O^{18}.

The enriched gas was kindly supplied to us by professor K. CLUSIUS, Zürich. As well as O^{18} it also contained O^{16}, N^{14}, N^{15} and ca. 2 % O^{17}.

Both types of targets contained the O^{18} atoms in a minute surface layer, consisting of a mixture of a) O^{18}-atoms, b) atoms of the backing material and of c) possible contaminations.

I, 2. Energy spread due to finite thickness of target

When the target is bombarded with a beam of particles which produce nuclear reactions with the target nuclei the yield is proportional to the surface density n_t of target nuclei, the cross section σ of the reaction, the beam current I_1, and $1/\cos\theta_1$ if θ_1 is the angle of incidence (Fig. 1 A).

$$Y = n_t \cdot \sigma \cdot I_1 \cdot \frac{1}{\cos\theta_1} \tag{1 A}$$

Secondary particles produced in the reactions at different depths in the surface layer suffer different energy losses on their way out, and this causes an energy spread among them, which is given[1] by (for simplicity we neglect possible contaminations)

$$\Delta E_2 = n_t \cdot \varepsilon_{\text{eff}, t} + n_b \cdot \varepsilon_{\text{eff}, b} \tag{2 A}$$

$\varepsilon_{\text{eff}, t}$ and $\varepsilon_{\text{eff}, b}$ are the effective stopping powers of the target and backing atoms respectively, and n_t and n_b are the surface densities of the target and backing atoms within the surface layer. ε_{eff} accounts for the energy loss of the produced particle

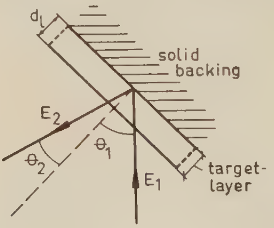

Fig. 1 A. Definition of angles when a solid target backing is used.

---

[1] In the following we use the notations:
suffix 1 refers to the incident particle (ex. E_1, M_1),
suffix 2 refers to the produced particle,
suffix 3 refers to the residual nuclei.

ue both to slowing down of the incident particle before reaction and also to the loss f energy of the produced particle after the reaction has occurred (Ref. 17):

$$\varepsilon_{\text{eff}} = \frac{\varepsilon_1}{\cos\,\theta_1} \cdot \frac{\delta E_2}{\delta E_1} + \frac{\varepsilon_2}{\cos\,\theta_2} \qquad (3\ \text{A})$$

$\frac{E_2}{E_1}$ is calculated from the parameters of the nuclear reaction involved and ε_1 and $_2$ are the stopping powers to the incident and produced particle respectively and $_1$ and θ_2 the angles of the travelling directions to the target surface normal (see ig. 1 A).

I, 3. The ratio $n_t/\Delta E_2$ for oxygen target on different backings

We will compare different backing materials on the basis of the ratio of $n_t/\Delta E_2$ or thin layers of their oxides, because the higher value of this ratio the smaller is he energy spread at a giving yield. From the equations above we get:

$$\frac{n_t}{\Delta E_2} = \frac{1}{\varepsilon_{\text{eff},\,t} + \varepsilon_{\text{eff},\,b} \cdot (n_b/n_t)} \qquad (4\ \text{A})$$

The denominator is the stopping power of the target layer (an oxide) per oxygen tom. Its value for some metal oxides relative to the stopping power of oxygen is abulated in Tab. 1 A. The values are taken from Ref. 32 and are valid for 1 MeV protons, 4 MeV α-particles or 2 MeV deuterons.[1]

Table 1 A. Stopping power of different oxides *per oxygen atom* relative to stopping power of pure oxygen.

O	H_2O	BeO	Al_2O_3	NiO	Fe_2O_3	Cu_2O	MoO_2	Ag_2O	Au_2O
1	1.4	1.7	1.9	3	2.4	5.4	2.4	6.6	8

In computing Table 1 A it is assumed that the stopping number of a chemical compound is the sum of the stopping numbers of its components. (Ref. 27, 28, 29.)

From this table it is evident that Be, Al and Fe are suitable for use as backing metals for targets produced by surface oxidation, provided that the oxide can be made to the desired thickness. Less suitable are Cu and Ag. Backings of Be must be used in the form of thin films evaporated on for instance Ag, because thick Be-backings give a continuous background of protons and alpha-particles due to the $Be^9(d,p)Be^{10}$ and $Be^9(d,\alpha)Li^7$ reactions.

I, 4. Production of surface-oxidized targets

Iron and copper were used as backings. After cleaning by washing in warm trichlorethylene and absolute alcohol the backing plates were put into a small vacuum vessel, which after a thorough evacuation was filled with the enriched gas to a pressure of about 1 mm Hg. By gentle high-frequency heating the iron plate was oxidized, the amount of oxygen used up being controlled by the magnitude of pressure decrease. Iron oxidizes very easily down to pressures below 0.1 mm Hg. The copper disks were heated to a faint red glow in vacuum and the oxygen let into the vessel when they were still glowing. One of the copper backings which happened to show the thinnest layer was used as a target for the $O^{18}(d,\alpha)N^{16}$ investigations in spite of the high stopping power of copper-oxide. An α-line taken with the reaction $O^{18}(p,\alpha)N^{15}$ with this target is shown in Fig. 3 A c. The advantage of the oxidized targets in comparison with those produced by isotope separation is mainly that in the former case one is sure that the oxygen is bound to backing atoms only and not partly absorbed in a possible external layer. This simplifies the energy correction due to external layers (see below).

---

[1] At other energies figures in table 1 will change but not very much.

I, 5. Thin target produced by magnetic separation

The second way to produce thin targets is to bombard the backings in an isotope separator (Ref. 30), with a beam containing the desired isotope, which then will be absorbed in the lattice of the backing. We used two different ways of producing an O^{18}-beam in the separator: either the ion-source was charged with water vapour enriched to 5 % in O^{18}, and H_2O^{18}-ions were collected on mass-number 20, or the source was loaded with the afore-mentioned gas enriched to ca. 50 % in O^{18}, and O^{18} collected as $N^{14}O^{18}$ ion. Because of the nitrogen content of the gas sample this ion had the largest intensity. For details of the separation see Ref. 31.

I, 6. Method for analysis of O^{18}-distribution

Collecting efficiency and the depth of the O^{18}-layer for different backing materials and types of ions were investigated by means of the reaction $O^{18}(p,\alpha)N^{15}$. The targets were bombarded with 873 keV protons and the spectral line of the α-group (ca. 4 MeV) detected photographically in a double focusing spectrometer of 40 cm radius (Ref. 14, 15). The distribution of the O^{18}-atoms in the surface of a target backing could then be determined by analysis of the shape of the α-line.

In this analysis (Ref. 33) one needs the window curve of the spectrometer, that is the shape of a spectral line formed by a particle group with an angular energy dependence equal to that ot the α-particles from the $O^{18}(p,\alpha)N^{15}$ but produced with an infinitely thin target.

The window curve was experimentally determined from the spectral line of protons from the reaction $C^{12}(d,p)C^{13}$. The angular energy dependence of the protons was $(dE_2/d\theta)\cdot(1/E_2) = 0.160$ % per degree, and for the $O^{18}(p,\alpha)N^{15}$ reaction 0.155 % per degree, and this small difference is easily corrected for. Due to the very high cross section of the $C^{12}(d,p)C^{13}$ reaction, practically infinitely thin targets could be used (the carbon layer formed on an initially clean metal surface after some beam bombardment).

The analysis of the O^{18}-distribution was done rather simply with rectilinear distribution functions, which do not give finer details. The accuracy of the curves (Fig. 2 A) can be estimated to be 20 %.

I, 7. Collecting efficiency and O^{18}-distribution

First the collecting efficiency and distribution of the O^{18}-atoms in target backings of stainless steel (71 % Fe, 17 % Cr, 10 % Ni), copper and silver were investigated when O^{18} was collected as H_2O^{18}-ions. In order to eliminate the influence of fluctua-

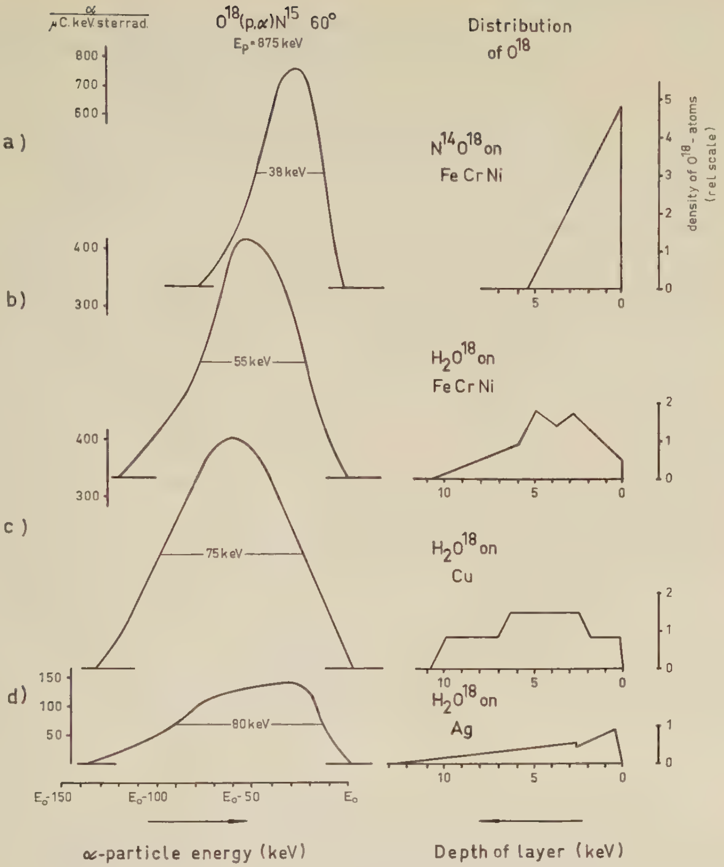

ig. 2 A. α-lines from the reaction $O^{18}(p, \alpha)N^{15}$ produced with different targets and the distri-ution of O^{18} in them. Density of O^{18}-atoms per keV stopping power is given in a unit, which the same for all four curves. Depths of layers are given in stopping power to 875 keV protons. $\vartheta_0 = 60°$, see Fig. 7 A.)

ions in the separator beam, the target backings were bombarded in pairs of two ith half the beam spot on each disk. (Ag + stainless steel disk no. 1 in the first run nd copper and stainless steel disk no. 2 in the second.) Fig. 2 A b–d shows the α-lines rom these targets produced with the reaction $O^{18}(p, \alpha)N^{15}$. The height of the spectral ines are corrected for the (small) difference between the targets on stainless steel isk nos. 1 and 2. All four target backings were exposed to ca. 15,000 μC/cm² $\left(0.9 \cdot 10^{17} \frac{\text{ons}}{\text{m}^2}\right)$ in the separator on mass-number 20, which mainly contains H_2O^{18}. The O^{18} ontent for the three different backing materials show the ratio 2 : 2.3 : 1 for stainless teel, copper and silver respectively. The depth to which the O^{18} distribution extends s given in stopping power to 875 keV protons and is about the same in all three aterials: the depth of the centre of gravity of the distribution is 3.5, 5 and 3.5 eV below the surface.

The density, which is the number of O^{18}-atoms in a volume of 1 cm^2 base area and of a height corresponding to 1 keV, is given in an arbitrary scale, common to all four curves.

If all ions ($0.9 \cdot 10^{17}$ cm^{-2}), which hit the surface were collected, the stopping power to 873 keV protons of the oxides formed would have been 0.6 keV as pure oxygen, 1.3 keV as Fe_2O_3, 2.9 keV as Cu_2O and 4 keV as Ag_2O. If these figures are compared with the extension of the distribution curves it is apparent that the layers are by no means complete oxides of the backings.

The difference between $N^{14}O^{18}$-ions and H_2O^{18}-ions may be seen from a comparison of Fig. 2 A a and b. In both cases stainless steel was used as backing. The most obvious difference is that the $N^{14}O^{18}$-ions penetrate into the backing only half as much as the H_2O^{18}-ions. In both separations the energy of the ions was 40 keV but due to the larger mass of the $N^{14}O^{18}$-ions the kinetic energy of the O^{18} atoms is 22 keV in the $N^{14}O^{18}$-case, but 36 keV in the H_2O^{18}-case, which may explain the difference observed.

The higher density of the O^{18}-atoms in the target in Fig. 2 A a is not due to better collecting efficiency: the bombardment during the production of the target in Fig. a was about 3 times greater than in case Fig. 2 A b–d.

Separation of $N^{14}O^{18}$ on steel (highly polished gauge pieces) and stainless steel with half the beam spot on each backing showed that the collecting efficiency of steel was 2 times better than that of stainless steel. Aluminium and beryllium have been used in separations with single targets only, so that no accurate comparison is possible, but measurements indicate that these two materiels are at least as good as steel.

The absolute magnitude of the collecting efficiency was not determined, but a comparison with the yield of targets produced by oxidation of iron and copper in the gas enriched in O^{18} to 50 % shows that most of the O^{18} atoms, which hit the backing are collected.

For our purpose we can draw the *following conclusions*:

1. In the production of thin O^{18} targets through isotopic separation on backings of steel, stainless steel, copper and silver, the collections efficiencies are as 4 : 2 : 2.3 : 1. That of beryllium and aluminium are equal to or better than steel.

The absolute magnitude of the best collecting efficiency is better than 10 %.

2. The depths of the O^{18} layers measured in stopping power to protons is about equal for the four materiels, but the layers produced with $N^{14}O^{18}$-ions are only half as deep as those produced with H_2O^{18}-ions.

I, 8. External layers on target

All surfaces inside the vacuum volume are covered by a thin film of condensed pump oil vapour. During the beam bombardment this film will carbonise on the spot where the beam hits the target, and a carbon layer approximately proportional to the total charge of the bombardment will grow up. Both incident and emitted particles are slowed down in this layer and it is therefore necessary to correct for it. The thickness of the layer is measured by means of scattering protons or deuterons first against a clean and then against the exposed target. From the diplacement of the scattering edge, counted in energy units, the thickness of the external layer is calculated from the equation:

$$\Delta E_2 = \Delta E_L \left(\frac{1}{\cos \theta_1} \frac{\delta E_2}{\delta E_1} + \frac{1}{\cos \theta_2} \cdot \frac{\varepsilon(E_2)}{\varepsilon(E_1)} \right) \tag{5 A}$$

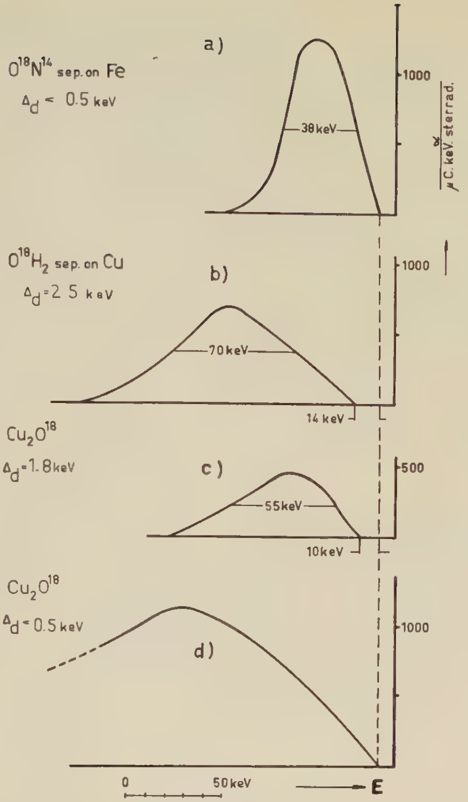

g. 3 A. α-lines from the reaction $O^{18}(p, \alpha)N^{15}$ produced with different targets for comparison external layers. Δ_d are thicknesses of external layers given in stopping power to 850 keV deuterons. ($\theta_0 = 60°$, see Fig. 7 A.)

E_2 = displacement of scattering edge.
E_1 = energy of incident particle.
E_2 = energy of scattered particle.
E_1) = atomic stopping power of carbon to incident particle.
E_2) = atomic stopping power of carbon to scattered particle.
E_L = stopping power of the layer to the incident beam.

When targets are made by surface oxidation of target backings, the surface is itially clean and layers are only due to exposure to a deuteron or proton beam. o target atoms are present in the layer, so the whole measured thickness of the yer can be used as a correction.

When targets are produced in the isotope separator, external layers can be formed ıring the bombardment in the separator, and it is then possible that an unknown ırt of the separated isotope will be absorbed in the carbon layer formed, so that ıcertainty arises as to how to correct for energy absorption in the external layer.

In order to investigate these questions, we took α-spectra of the reaction $^{18}(p, \alpha)N^{15}$ with different types of targets. Due to the high yield of this reaction only μC proton bombardment was required on each target, so the external layers

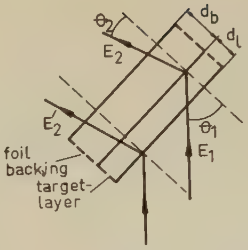

Fig. 4 A. Definition of angles when a foil target backing is used.

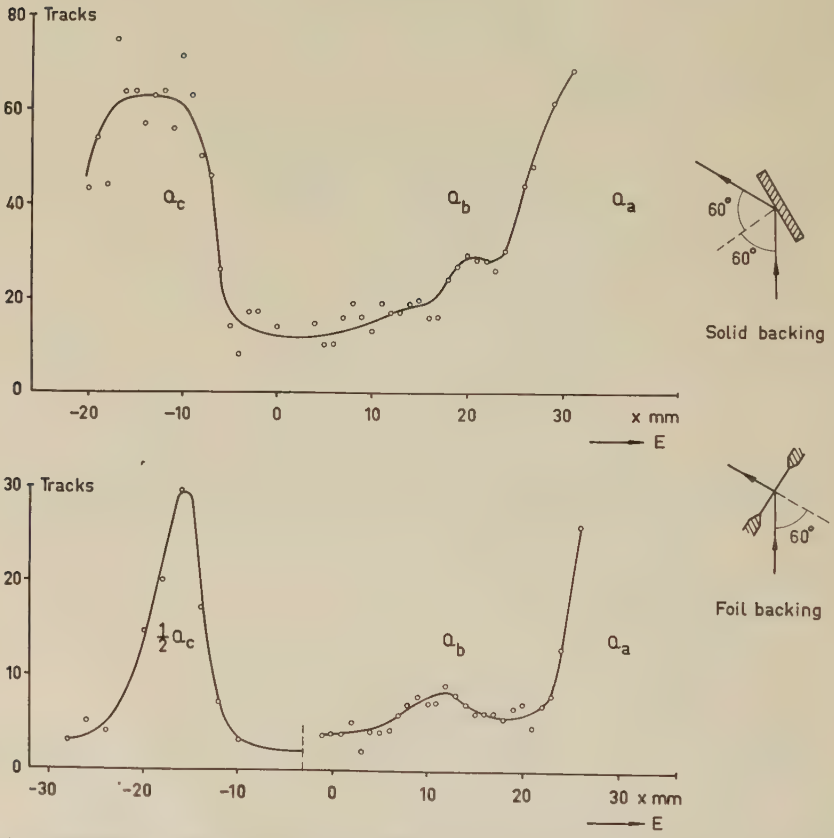

Fig. 5 A. α-spectra of three α-groups form $O^{18}(d, \alpha)N^{16}$, Q_a, Q_b and Q_c , at 60° taken with a) a solid target backing, b) a foil target backing, showing difference in energy spread from different types of targets. The lower spectrum is displaced towards higher energy ca. 100 keV in order to correct for slowing down in the foil.

formed during these exposures need not be accounted for. (External layers grow with a velocity of ca. 1 keV per 1000 μC bombardment for protons.) The lines obtained are shown in Fig. 3 A.

Curve 3 A d is made with a surface-oxidized copper disk, and contains the O^{18} as a copper oxide. Scattering on this target showed an external layer of less than 0.1 keV to 875 keV protons and therefore the high energy edge of this line needs no correction for external layers.

Curve 3 A b is displaced 14 keV, corresponding to an external layer of 1.5 keV to 875 protons. The target was produced in the isotope separator by collecting H_2O^{18} on a copper backing. The separation was performed without cold trap. In contrast to this, Fig. 3 A a shows the α-line of a target also produced in the isotope separator, but with a liquid air cold trap. No displacement relative to the line 3 A d is detectable, which means that the external layer is smaller than 0.1 keV in spite of an exposure in the separator to ca. 10^5 μC/cm². Scattering gave a layer of less than 0.3 keV.

Finally, Fig. 3 A c shows the line from a target consisting of a thin oxide layer on a copper backing. In this case there is a displacement of 10 keV, corresponding to an external layer of 1.1 keV stopping power to protons. Scattering of deutrons gave a thickness of only 0.9 keV to 875 keV protons. The difference must be due to errors in the two measurements. The external layer has been formed by bombardment with $5 \cdot 10^4$ μC/cm² of deuterons. Liquid air trap was used.

From this investigation we can conclude that production of separated targets in the isotope separator give targets nearly free from external layers if a liquid air cold trap is used. (10^5 μC/cm² give layer < 0.2 keV to 875 keV protons.) In the high tension set a liquid air trap adjacent to the target (Ref. 26) does not eliminate target layers completely, but they grew much slower than without the trap, and at a velocity of about 1 keV to 875 keV protons after $5 \cdot 10^4$ μC/cm². A comparison with the separator shows that the layer growth in the high tension set ought to be much less than it actually is. Better baffles in the diffusion pump would probably help somewhat.

I, 9. Foil target backings

The target nucleus in a nuclear reaction may be identified by the dependence of the energy of the emitted particle upon angle of emission. It is therefore necessary to take spectra of particle groups both at backward and forward directions to the incident beam.

When spectra are taken in a forward direction with a solid target backing, the angles θ_1 and θ_2 in Fig. 1 A approach 90° and therefore the apparent thickness of the target layer $d/\cos\theta$ will become large. This gives a large energy spread, and the resolution of particle groups adjacent in energy will become poor, especially when they are of different intensities. To avoid this difficulty, foil target backings can be used, which are so thin that they permit the produced particle to escape through the foil (Fig. 4 A). It is possible to choose an angle of incidence which nullifies the energy spread due to target layer thickness. The condition is ($E_2' = E_2$ in Fig. 4 A):

$$\frac{\varepsilon_1}{\cos\theta_1}\frac{\delta E_2}{\delta E_1} = \frac{\varepsilon_2}{\cos\theta_2} \qquad (6\text{ A})$$

where ε_1 and ε_2 are the stopping power of target layer to incident and emitted particle respectively. The latter particle is however slowed down by the passage through the foil backing, and targets of this type are therefore not suitable for absolute energy measurement unless some calibrating reaction of known energy can be produced with the same target. The energy spread among members of a certain particle group

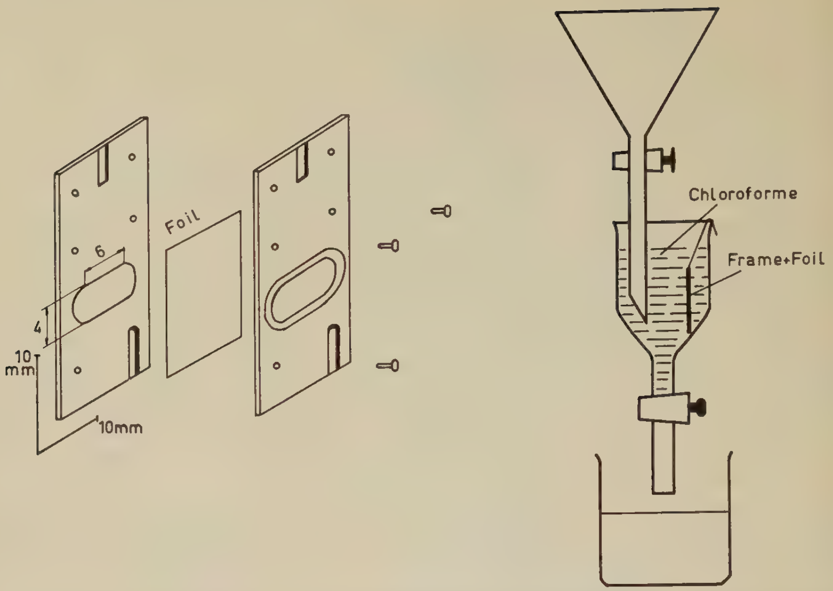

Fig. 6 A. Frame for mounting foil target backings, and arrangement for soaking the mounted foil in chloroform.

from such a target is due to angular-dependence of the energy and to straggling in the foil backing.

The improvement, which can be achieved by the use of a foil target in the way described is shown in Fig. 5 A, which shows the spectrum of two adjacent groups Q_a, Q_b and Q_c from $O^{18}(d,\alpha)N^{16}$ at 60° to the beam taken with a solid target and $\theta_1 = \theta_2 = 60°$, and also with a foil target and $\theta_1 = 60°$ but $\theta_2 = 0°$. The weak line Q_b is hardly visible in the former case, Fig. 5 A. The energy loss of the produced 4 MeV α-particles by the passage through the foil backing was about 100 keV.

I, 10. Preparation of foil target backings

Glass-plates, washed with soap, rinsed in distilled water, and thoroughly dried, were coated with a Formvar film by dipping them *twice* in a chloroform solution of Formvar. The plates were dried thoroughly between the first and second dippings, and the resulting film thickness on the glass surface was about 200 $\mu g/cm^2$. After 24 hours drying the plates were put into a vacuum chamber and coated with aluminium (70 $\mu g/cm^2$) by means of evaporation. The distance between glass plate and evaporation spiral (tungsten loaded with aluminium) should be at least 10 cm to avoid damage the film by heat radiation.

The aluminium film was loosened from its backing by soaking the plates in chloroform. It was found that this procedure was more successful if the glass plates had been dipped twice in the chloroform solution as described above.

The aliminium could be picked up from the soaking bath in the form of small flakes of some cm^2 area. These flakes were mounted between two frames serving as holder and afterwards washed by rinsing in chloroform in order to clean them from possible traces of Formvar. (See Fig. 6 A.)

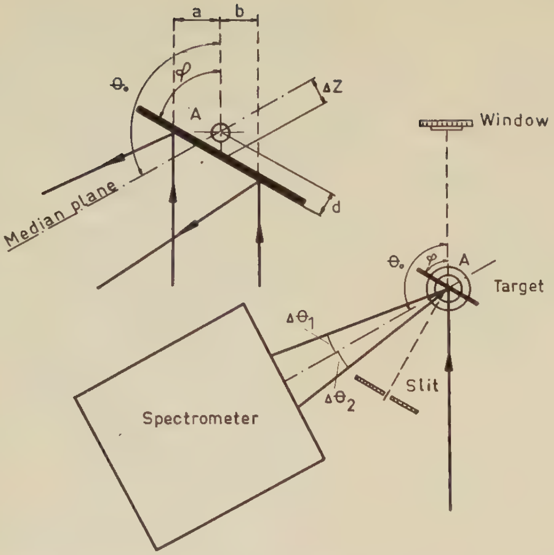

Fig. 7 A. Arrangement for measuring the angle θ_0 between beam and particles accepted by the spectrometer.

The mounted aluminium foils had a free surface of 0.4 × 0.8 cm, and were quite resistent to beam bombardment. Isotopes could be separated on them with a beam intensity of ca. 0.1 W/cm^2.

The energy loss of 850 keV deuterons in the foils was about 20 keV, and a deuteron beam of 0.5 μA made a foil glow dark red during bombardment, but in spite of this foils loaded with O^{18} did not loose oxygen and could be used as oxide targets during long experiments.

Rolled aluminium foils of 150 μg/cm^2 are commercially available, and therefore more convenient to use than evaporated ones, but the latter can be made thinner and more homogeneous in structure.

Appendix II, 1. Measurement of angle

The angle between the travelling directions of the incident beam and of the emitted particles accepted by the spectrometer must be measured with an accuracy of a few tenths of a degree, because errors in this angle give rise to errors in the calulated Q-value of the order of 5–10 keV/degree (Ref. 13).

Fig. 7 A shows a schematic view of the arrangements. For details see Ref. 26. By means of a double conical ground joint, a slit mounted on an arm could be moved around the target in a circle of 110 mm radius. Protons were scattered at the target and detected in the spectrometer by a scintillation counter. The number of proton counts per μC of incident beam versus angular position of the slit was determined a) when the slit intercepted the beam (curve A), b) when it intercepted the scattered protons (curve B) see Fig. 9 A. If the angular distance between the centre of gravity of the curves A and B is θ', and θ_0 is the horizontal projection of the angle between the beam direction and the center of gravity of the ray pencil admitted by the spectrometer, we have (on the condition that $\varphi = \frac{1}{2}\,\theta_0$):

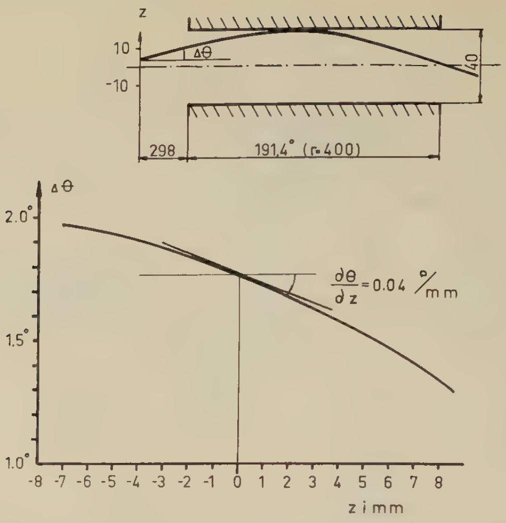

Fig. 8 A. Angle $\Delta\theta$ of marginal beam in the spectrometer at different positions z of the source.

$$\theta_0 = 180 - \theta' - \frac{\Delta z}{110} 57.3 + \frac{\delta\,\theta_0}{\delta z}\Delta z \tag{7 A}$$

where Δz is the source displacement from the median plane of the spectrometer in mm (compare Fig. 7 A). The first correction term in the expression above accounts for a possible displacement (d in Fig. 7 A) of the target-plane with respect to the axis around, which the slit moves:

$$\Delta z = 2d \cdot \cos\frac{\theta_0}{2} \tag{8 A}$$

The second correction term is due to the fact that the mean angle between the spectrometer median plane and the ray pencil accepted by the spectrometeter is not zero but varies when the source is displaced out from the median plane. The derivative $\delta\,\theta_0/\delta\,z$ depends upon the nature of the aperture limiting the ray pencil in the spectrometer. Under the assumption that the walls of the spectrometer chamber (width 4.0 cm) form the aperture, we have used first order ray equations (Ref. 34) to calculate the paths of the margin rays (see Fig. 8 A). The geometrical extension of the spectrometer field is 180° ($r_0 = 40$ cm) but fringing fields make the effective length equal 191.4° because 4.0 cm is added to each edge (Ref. 15). Distance between target and geometrical field edge is 33.8 cm, that is 29.8 cm from the edge of the effective field. The angle of the margin beam to the median plane is plotted as a function of source displacement z in Fig. 8 A. In the neighbourhood of $z = 0$ the derivative $\delta\,\theta_0/\delta\,z = -0.04°/\text{mm}$. (Obs. that the mean angle of the ray pencil has the same derivative as the margin beams.)

θ_0 is the horizontal projection of the angle between incident beam and emitted particles. To get the true angle θ we must correct for the inclination to the horizontal plane of the ray pencil accepted by the spectrometer. This correction is (Ref. 13)

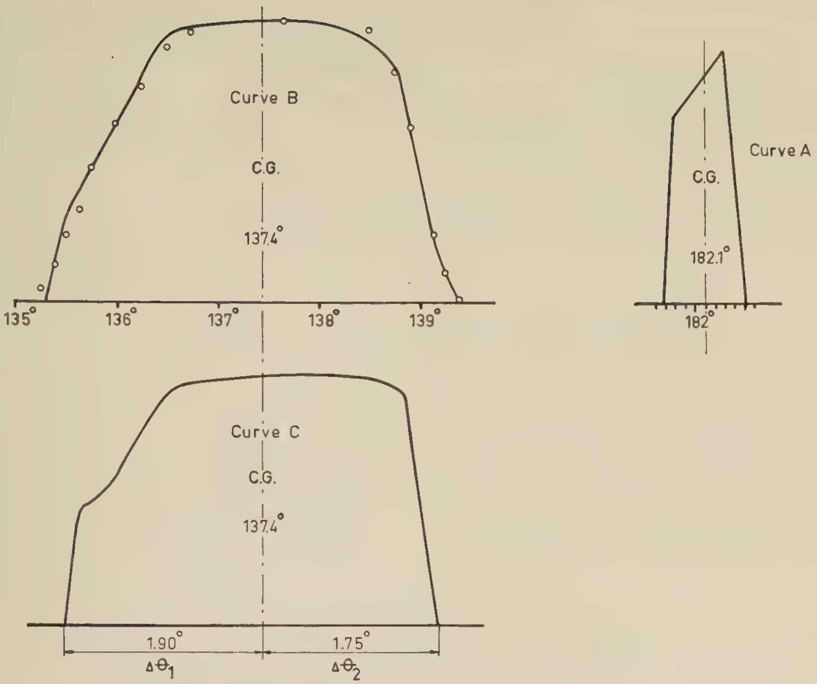

ig. 9 A. Scattered protons versus angular position of the slit at angle measurement. Curve A: lit intersepting the beam, curve B: slit intercepting the scattered protons. Curve C is the resulting ngular sensitivity of the spectrometer. Curve C folded on to the reflected A-curve gives the small ircles in curve B. Centers of gravity (C. G.) of the curves are shown with dash-dotted lines.

$$\theta = \theta_0 + \frac{1}{2}\frac{\nu^2}{\operatorname{tg}\theta_0} \tag{9 A}$$

where ν is the mean angle between the horizontal plane and the ray pencil accepted by the spectrometer. ν is $= 5°$ (Ref. 13).

II, 2. Angular sensitivity of spectrometer

θ_0 is the angle between the incident beam and the centre of gravity of the angular interval $\Delta\theta_1 + \Delta\theta_2$, Fig. 7 A admitted by the spectrometer. Often the high energy edge of a spectral line is used for energy determination. This part of a line is formed by particles, which are emitted in the most forward direction $\theta - \Delta\theta_1$, Fig. 7 A. One therefore needs the value of $\Delta\theta_1$.

$\Delta\theta_1 + \Delta\theta_2$ is the width of the angular sensitivity curve C (Fig. 9 A) of the spectrometer. This curve can be computed from the curves *A* and *B* (see II, 1 above), then because of the finite width of the beam and the slit, curve *B* is a superposition of *A* and the true angular sensitivity curve (*C*) we are seeking for. The determination of a *B* and an *A* curve to be used in the computation of *C* should be done with as small beam- and slit-widths as possible because this simplifies the computation. From Fig. 9 A can be seen that

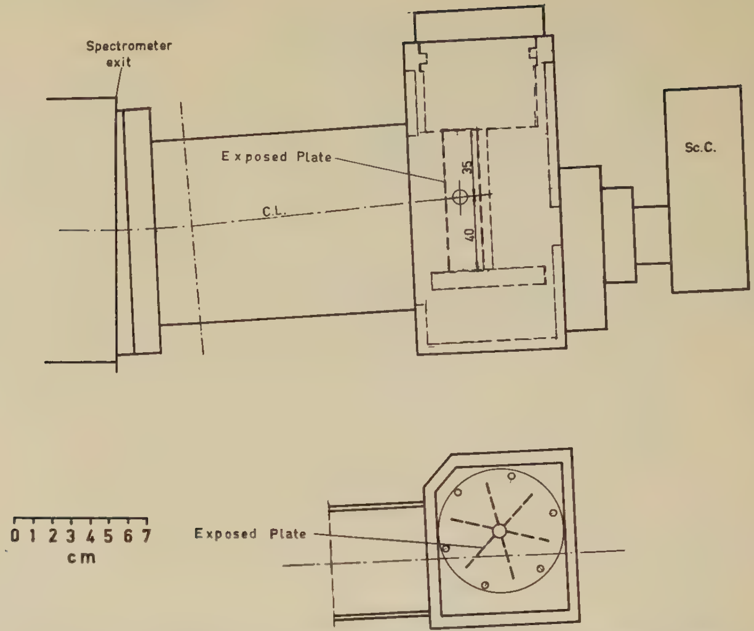

Fig. 10 A. Camera for maximum six nuclear-track plates used at the spectrometer. The position of a plate in exposured position is shown and also the intersection point between the plate and the central line (C. L.) of the spectrometer. The extension of the field when corrected for fringing fields is also shown with dash-dotted line. Sc. C. = scintillation counter to use alternatively to nuclear-track plate.

$$\Delta\theta_1 = 1.9^\circ \qquad \Delta\theta_2 = 1.75^\circ.$$

When the beam has a finite width the dimensions *a* and *b* Fig. 7 A have finite values. The minimum angle to the beam among the particles admitted by the spectrometer is then:

$$\theta_{\min} = \theta - 1.9 - 0.04\left(b + 2d\cos\frac{\theta}{2}\right) \qquad (10\text{ A})$$

The magnitude of *b* and *d* Fig. 7 A was measured with the help of a window inserted in the wall of the target chamber behind the target in the direction of the beam. A millimeter scale was engraved on the window and a small object glass on the inside of the window was used as a fluorescent screen. By turning the target so that $\varphi = 0^\circ$ and 180°, the magnitude of d and b can be determined from the positions of the shadows on the screen.

The measured values of θ, the angle between the incident beam and the center of gravity of the ray pencil admitted by the spectrometer are given in Table 3 A.

Appendix III. Spectrometer characteristics

III, 1. Measurement of the dispersion

Dispersion of the spectrometer was measured by scattering protons first on a copper and then on a silver target with unchanged spectrometer field. The distance between the scattering edges on the photographic plate corresponds to ca. 2%

fference in energy. Scattering figures were taken at five somewhat different fields that the dispersion $E_0(dx/dE)$ could be determined over the whole plate. he total range of one plate at unchanged field is 7.5 % in energy.) The result of the easurements can be seen from the second column of table 2 A, where it is given change of energy per mm displacement along the plate in parts of the energy $x=0$ ($x=0$ is where the central axis of the spectrometer crosses the plate, see g. 10 A). The figures are of course valid only for the plate position used. How is located can be seen from the drawing of the camera, Fig. 10 A. Errors are ainly due to uncertainty in reading the positions of the scattering edges on the ates.

III, 2. Line width on different parts of the plate

Nuclear track plates were used as detectors in the spectrometer (Ref. 13). They ere placed in a camera, which could be loaded with 6 plates at the same time. Due lack of space this camera had to be placed in a position where the exposed plate did ot coincide with the image plane, and the spectral lines therefore had different idths on different parts of the plate. The distance along the plate is counted positive the direction of increasing energy with zero at the point where the central axis of e spectrometer crosses the plate plane. The central axis is a tangent to the central rcle $r=40$ cm), and is inclined 5.7° to the horizontal plane (Ref. 13).

In order to determine the variation of the line width along the plate, lines of the .73 MeV α-group from ThC were photographed at four somewhat different field tensities in the spectrometer. The half width and extrapolated base width of the nes at different positions along the plate is given in Table 2 A.

The measured base widths were used for the correction of the positions of the high nergy edges of spectral lines of particle groups from nuclear reactions. If the energy ifference between two lines taken at the same spectrometer field is to be determined, he corrected distance between their high energy edges is:

$$x_k = x_1 - x_2 - \tfrac{1}{2}(\Gamma_1 - \Gamma_2), \tag{11 A}$$

where x_k is the corrected distance, x_1 and x_2 the measured positions of the high nergy edges and Γ_1 and Γ_2 the base widths of lines at x_1 and x_2 according to the ourth column of Table 2 A.

III, 3. Beam spot height

The stray field of the spectrometer deflects the incident beam a little, and therefore he exact position of the beam spot on the target relative to the central axis of the pectrometer varies both with field strength and angular position of the spectrometer. The magnification of the spectrometer is 0.95 (Ref. 15), thus the displacement of a pectral line from a given particle group on the detecting photographic plate is .95 of the shift in spot height. The latter was determined by observation of the eam spot on the fluorescent screen at the window W (Fig. 7 A) in the target chamber vhen target was partially turned out of the beam path. As the beam always has to ass a fixed slit 300 mm before the target, and the distance slit-fluorescent screen s ~ 420 mm, the shift in target spot height is ca. 0.7 and the shift in spectral line osition of the photographic plate is $0.95 \times 0.7 \approx 0.65$ of the spot displacement bserved at the fluorescent screen.

With no magnetic shield the shift in target spot position was ca. 1 mm when the spectrometer field was increased from zero to a field strength corresponding to 9 MeV α-particles (ca. 11,000 gauss). (At spectrometer angles $< 90^\circ$ upwards, at angles $> 90^\circ$ downwards.) Later a magnetic shield consisting of a soft iron tube, diameter $= 30$ mm, thickness 2 mm, was used, which enclosed the beam path form the exit of the deflecting magnet onto the target chamber. The maximum shift in beam spot height decreased below 0.3 mm, and it was not necessary to correct for it.

Deflection of the beam between the exit of the deflecting magnet and the slit before the target, which might have influenced the value to which the stabilizer adjusted the beam energy, was very small even with no magnetic shield. This was controlled by taking the $F(p,\alpha,\gamma)O^{16}$ resonance at 873.5 keV at various spectrometer field strengths. The resonance peak always occurred at the same deflector field strength independently of the spectrometer field strength.

Table 2 A. Dispersion, relative solid angle and line widths at plate position according to Fig. 10 A.

x mm	$\frac{1}{E_0}\frac{dE}{dx}\cdot 10^3\cdot \mathrm{mm}^{-1}$	$\frac{\omega_x}{\omega_0}$	Γ_b mm	$\Gamma_{1/2}$ mm
-30	1.34 ± 0.04	0.83 ± 0.05	5.5 ± 0.3	2.2 ± 0.3
-20	1.33 ± 0.04	0.94 ± 0.05	6.3 ± 0.3	2.7 ± 0.3
-10	1.32 ± 0.04	1.00 ± 0.05	7.1 ± 0.3	3.9 ± 0.3
0	1.31 ± 0.04	1.00 ± 0.05	8.3 ± 0.3	4.9 ± 0.3
10	1.30 ± 0.04	0.93 ± 0.05	9.0 ± 0.3	5.4 ± 0.3
20	1.31 ± 0.04	0.79 ± 0.05	8.8 ± 0.3	5.5 ± 0.3
30	1.32 ± 0.04	0.63 ± 0.05	7.8 ± 0.3	5.3 ± 0.3

x = position along plate (x is $= 0$ where central axis crosses plate and is positive towards increasing particle energy).

E_0 = particle energy at $x = 0$.

ω_x = solid angle at x.

ω_0 = solid angle at $x = 0$, $\omega_0 = 0.0031 \pm 0.0003$ sterad.

Γ_b = base-widths of lines.

$\Gamma_{\frac{1}{2}}$ = do. for widths at ½ max height.

Table 3 A. Values of θ, used in the investigation. θ is the angle between the incident beam and the center of gravity of the ray pencil admitted by spectrometer. The values given are corrected for the inclination of the ray pencil to the horizontal plane ($\nu = 5^\circ$) and refer to the case $\Delta z = 0$ (that is when the target spot coincides with center around which the target can be turned). The values of $\theta_{\min} = \theta - \Delta\theta_1$, are also given:

$\theta =$	61°0 ± 0°3	105°6 ± 0°3	121°0 ± 0°3	134°9 ± 0.3
$\theta_{\min} =$	59°1 ± 0°3	103°7 ± 0°3	119°1 ± 0°3	133°0 ± 0.3

III, 4. Solid angle of the spectrometer

n connection with the determination of the line width on different parts of the
te, the solid angle of the spectrometer could also be determined by a comparison
he number of α-tracks in the α-lines at different positions along the plate and the
face density of α-tracks in a plate exposed at the entrance of the spectrometer
cm from the ThC-source. The solid angle was found to vary over the plate: the
tive magnitude at different x is given in the third column of Table 2 A. The ab-
ute value of ω_0 was determined to 0.0031 ± 0.0003 sterad.

REFERENCES

Bleuler, E., Scherrer, P., Walter, M., Zünti, W., Helv. Phys. Acta *20*, 96 (1947).
Bleuler, E., Rossel, J., Helv. Phys. Acta *20*, 445 (1947).
Jelly and Paul, Proc. Cambridge Phil. Soc. *44*, 133 (1948).
Wyly, L. D., Phys. Rev. *76*, 316 (1949).
Malm, R., Buechner, W. W., Phys. Rev. *80*, 771 (1950).
Lillie, A. B., Phys. Rev. *87*, 716 (1952).
Millar, C. H., Bartholomew, G. A., Kinsey, B. B., Phys. Rev. *81*, 150 (1951).
Inglis, D. R., Rev. Mod. Phys. *25*, 390 (1953).
Ajzenberg, F., Lauritsen, T., Rev. Mod. Phys. *24*, 321 (1952).
Cohen, A. V., French, A. P., Phil. Mag. *44*, 1259 (1953).
Schardt, A., Fowler, W. A., Lauritsen, C. C., Phys. Rev. *86*, 527 (1952).
Mileikowsky, C., Pauli, R. T., Ark. f. fys., *4*, nr 12, 287 (1952).
Mileikowsky, C., Ark. f. fys., *7*, nr 8, 89 (1953).
Mileikowsky, C., Ark. f. fys., *4*, nr 16, 337 (1952).
Mileikowsky, C. Ark. f. fys., *7*, nr 3, 33 (1953).
Mileikowsky, C., Ark. f. fys., *7*, nr 10, 117 (1953).
Brown, A. B., Snyder, C. W., Fowler, W. A., Lauritsen, C. C., Phys. Rev. *82*, 159 (1951).
Lauritsen, T., Annual Rev. Nucl. Science *1*, 67 (1952).
Wilkinson, D. H., Phys. Rev. *90*, 721 (1953).
Adair, R. K., Phys. Rev. *87*, 1041 (1952).
Bloch, I. *et al.*, Rev. Mod. Phys., *23*, 147 (1951).
Blatt, J. M., Weisskopf, V. F., Theoretical Nucl. Phys. N.Y. and London 1952.
Teichmann, T., Wigner, E. P., Phys. Rev. *87*, 123 (1952).
Dunbar, D.N.F., Pixley, R. E., Wenzel, W. A., Whaling, W., Phys. Rev. *92*, 649 (1953).
Krauss Jr., A. A., French, A. P., Fowler, W. A., Lauritsen, C. C., Phys. Rev. *89*, 299 (1953).
Ahnlund, K., Ark. f. fys., *7*, no. 14, 155 (1953).
Hirschfelder, J. O., Magee, J. L., Phys. Rev. *73*, 207 (1948).
Wenzel, W. A., Whaling, W., Phys. Rev. *87*, 499 (1952).
Sternheimer, R. M., Phys. Rev. *88*, 851 (1952).
Bergström, I., Thulin, S., Svartholm, S., Siegbahn, K., Ark. f. fys., *1*, nr 11, 281 (1949).
Ahnlund, K., Thulin, S., Pauli, R. T., Ark. f. fys. (1954) (to be publ.).
Livingstone, M. S., Bethe, H. A., Rev. Mod. Phys. *9*, 245 (1937).
Snyder, C. W., Rubin, S., Fowler, W. A., Lauritsen, C. C., Rev. Scient. Instr. *21*, 852 (1950).
Judd, D. L., Rev. Scient. Instr. *21*, 213 (1950).
Mileikowsky, C., Pauli, R. T., Ark. f. fys., *4*, nr 13, 299 (1952).
Cohen, A. V., Phil. Mag. *44*, 583 (1953).

Tryckt den 10 september 1955

Uppsala 1955. Almqvist & Wiksells Boktryckeri AB

ERRATUM

Line 3 from the bottom of page 581 should read:

1. Atomic mass of N^{16} = 16.01116 ± 0.00003 a.m.u. (atomic mass defect 10.39 ± 0.03 MeV).

Erratum:

e use of the $^{3}T\,(d, n)\,He^{4}$ reaction for a comparison of some methods for the absolute measurement of a fast neutron flux

The yield of a Ra-α-Be source

Arkiv f. Fysik, Bd 9 Nr 18, p. 293 (1955)

By Karl-Erik Larsson

Appendix II

Calculation of the mean energies $\bar{E}_H$ and $\bar{E}_C$ of the recoil nuclei

Formula (4) page 331 should be read:

$$\bar{T} = \frac{2\,m_r\,m_n}{(m_r + m_n)^2}\,E_n\left\{1 + \frac{1}{4}\left(\frac{m_r - m_n}{m_r + m_n}\right)^2\beta^2\right\}$$

here $E_n = m_n\,c^2\,(\gamma - 1)$.

Formula (5) page 331 should be read

$$\bar{E}_H = \frac{E_n}{2}$$

ormula (6) page 331 should be read

$$\bar{E}_C = 0.142\,E_n\,(1 + 0.18\,\beta^2)$$

The table on page 332 is changed to the following:

Neutron energy (MeV)	β^2	Mean energies of recoil nuclei in MeV	
		$\bar{E}_H$	$\bar{E}_C$
13.00	0.028	6.50	1.86
13.50	0.029	7.75	1.93
14.00	0.030	7.00	2.00
14.50	0.031	7.25	2.07
15.00	0.032	7.50	2.14

As a results of this change of the mean energies, the factor $2\,\sigma_H \bar{E}_H + \sigma_C \bar{E}_C$ given in figure 16 p. 312 is decreased by about 2.5 %, and consequently the values of $\left(\frac{I_n}{I_\alpha}\right)_{\text{exp}}$ and $\left(\frac{I_n}{I_\alpha}\right)_{\text{c.m.}}$ given in table 2 on page 313 and table 3 on page 314 should be increased by the same amount. The final value given on page 317 as the ratio between the fluxes measured by the homogenous ionization chamber and the associated particle method is increased by 2.5 %, so that the final ratio becomes 1.06 ± 0.04.

Finally the value of the yield of the RaBe source as given in column two, line four of table 9 on page 327 is changed from 2.73 ± 0.12 to 2.81 ± 0.12, and the ratio given in column three, line four, is changed from 1.03 to 1.06.

AB Atomenergi, Department of Physics, Stockholm.

THE UNIVERSITY OF ILLINOIS AT CHICAGO
3 8198 314 370 089